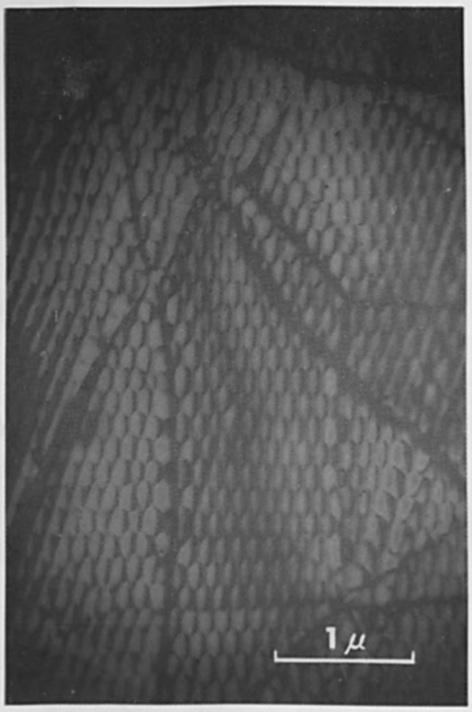

Photo 1

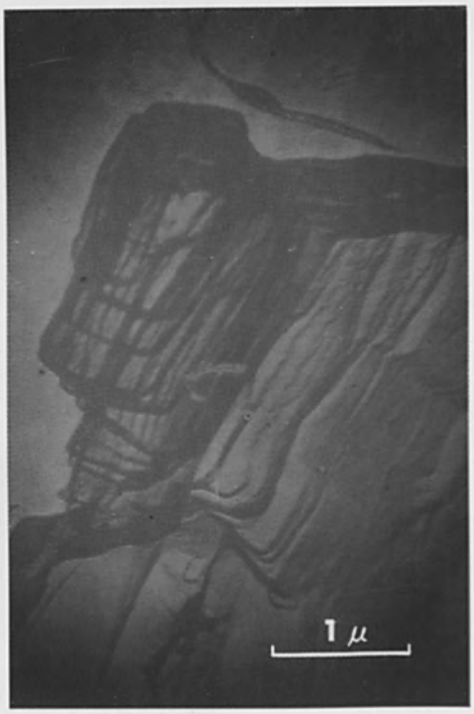

Photo 2

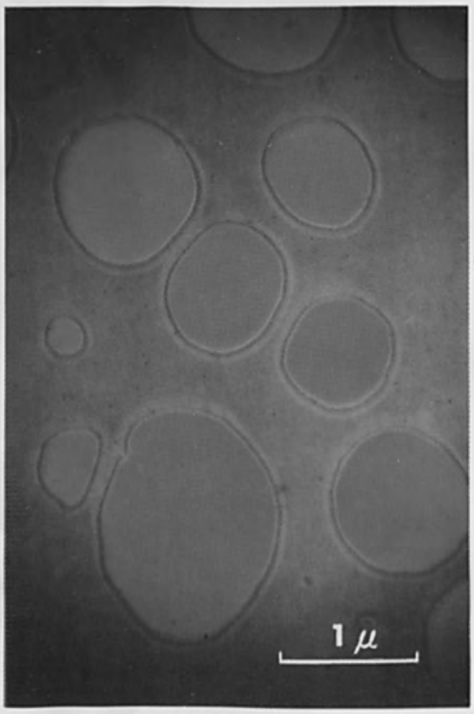

Photo 3

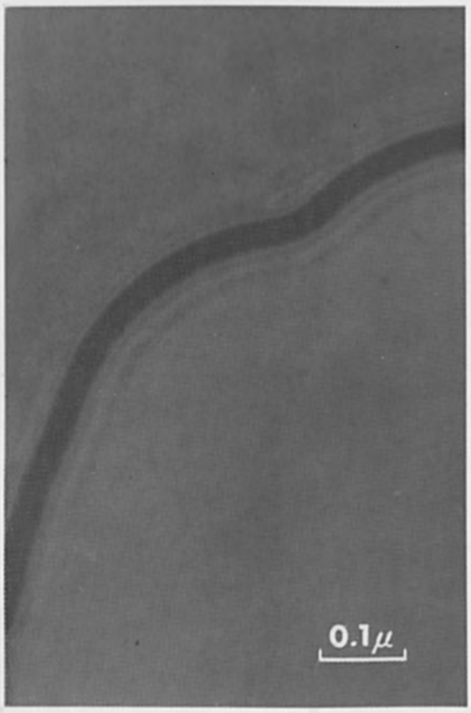

Photo 4

K. KANAYA, H. KAWAKATSU, A. ATODA, et al.

RECORD

of the

10th Symposium on Electron, Ion, and Laser Beam Technology

Gaithersburg, Maryland, 21-23 May 1969

L. MARTON
Editor

IEEE Catalog No. 69 C 22-ED

Sponsored by
Group on Electron Devices of the
Institute of Electrical and Electronics Engineers, Inc.
American Vacuum Society
University of Maryland
National Bureau of Standards

and with the support of

National Science Foundation
Office of Naval Research

San Francisco Press, Inc.

255 12th Street, San Francisco, California

Copyright © 1969 by Institute of Electrical and Electronics Engineers, Inc.

All rights reserved

Library of Congress catalog card 62-51780

Printed in the United States of America

PREFACE

The 10th Symposium on Electron, Ion and Laser Beam Technology was held at the National Bureau of Standards, Gaithersburg, Maryland, May 21 to 23, 1969. It was a pleasant occasion both for the visitors and the hosts. The visitors could see a brand new campus with many improved features; the hosts enjoyed to see many of their friends and hear their contributions to the growing field of energy beam technology.

There were a few innovations. Breaking with the established pattern, instead of annual symposia, the Steering Committee established, at least for the time being, a bi-annual pattern. Two years have elapsed since our Berkeley meeting (the 9th) and we agreed to hold the 11th Symposium in 1971 in Boulder, Colorado.

Another break with tradition was our attempt to broaden the base of our activities. This was accomplished by gaining the sponsorship of the American Vacuum Society, in addition to the IEEE. We are very grateful for the renewed support of the Group on Electron Devices, IEEE; as well as to the Vacuum Metallurgy Division, AVS, for joining us. Added sponsorship should be gratefully acknowledged to the Office of Naval Research and to the National Science Foundation, for their grants, permitting the invitation of distinguished foreign scientists. The list of sponsors is not complete without thanking the University of Maryland and the National Bureau of Standards for all the help given to the Symposium.

Of the 60 technical papers, about 65% were related to electron beam technology, about 30% to lasers and about 5% to ion beam technology. There were 7 invited papers, with the rest contributed.

Those attending the banquet enjoyed an excellent speech by Dr. E. R. Piore, Vice-President, IBM Corporation. He touched on the current situation of R&D funds, the inter-relation between military and civilian organizations and the responsibilities of the University faculties and of the faculty members created by growing unrest on the campuses.

The Steering Committee (composed of F. Barnes, T. E. Everhart, B. W. Schumacher, K. H. Steigerwald, C. Süsskind, and myself), was fortunate in finding a great number of devoted individuals to help its task of preparing the symposium. The Local Committee members (C. O. Alley, F. Byrne, W. H. Culver, E. S. Dayhoff, K. F. Heinrich, K. Mielenz, S. Penner, S. K. Poultney, R. Reed, A. Shostak, J. A. Simpson) as well as members of the Program Committee (F. Byrne, J. E. Davey, T. E. Everhart, F. J. Grundhauser, R. D. Haun, Jr., D. B. Medved, K. Mielenz, J. R. Morley, S. V. Nablo, S. Newberry, B. W. Schumacher, H. J. Schwarz, J. A. Simpson, J. F. Smith, G. K. Wehner, N. Winogradoff) deserve the thanks of all the participants for their untiring labors.

We had a distinguished International Committee, providing us with advice. Last, but not least, I wish to mention the Publication Committee. Composed of five members, taken from the Steering Committee and the local Committee, it was fortunate enough to secure the services of Prof. Süsskind as the coordinator of this "Record," which contains, with a few exceptions, the complete output of the Symposium.

No conference, or symposium can be successful without the cooperation of all participants. This we had and my thanks go to all those whose help and enthusiasm made the 10th Symposium a going concern.

L. MARTON

Gaithersburg, Maryland, 1969

TABLE OF CONTENTS (Cont'd)

Page

"An application of the laser in contour measurement," 249; Tencza, Angelo, "Selective removal of Teflon insulation from wire using CO_2 and argon lasers," 259; Schumacher, Taylor, "Rock breakage by means of electron beam piercing (laboratory tests)," 271; White, "Phenomena associated with electron-beam evaporating," 285; Zimmermann, "Energy broadening in accelerated electron beams by Coulomb interaction," 297.

LASER EXCITATION & INSTRUMENTATION; NEW MICROANALYTICAL TOOLS 305

Nasini, Redaelli, "Ceramic plasma container for ion lasers," 307; Rocherolles, "Focusing of intense laser beams," 311; Beck, "Laser requirements for magneto-optical recording," 317; Schwarz, Hora, "Observation of electron diffraction pattern on nonluminescent target caused by laser interaction," 323; Fóti, "Feedback control of high intensity triode guns," 329; Helmer, Weichert, "Induced electron emission spectroscopy," 337; Simpson, "Electron impact spectroscopy," 345; Heinrich, "Electron and ion microprobe analysis," 353.

ELECTRON MICROSCOPES; ELECTRON OPTICS; ELECTRON SCATTERING 361

Plows, Nixon, "Further developments in stroboscopic scanning electron microscopy," 363; Banbury, Nixon, "Improved contrast in scanning electron microscopy," 364; Weiner, "Transmission scanning electron microscope using field emitters and liquid helium," 365; Tighe, Hockey, "Ion thinning of electron microscope specimens," 375; Kanaya, Kawakatsu, Atoda, "Color observation of electron microscope images," 381; Steigerwald, Meyer, Scheffels, "A new type of electron gun," 389; El-Kareh, "Design and analysis of symmetrical and asymmetrical electrostatic immersion lenses using a digital computer," 393; El-Kareh, Parks, "Computer analysis of symmetrical magnetic lenses with unsaturated pole pieces," 407; McWhirter, "Paraxial electron trajectories with space charge," 429; Wolter, "High-speed high-resolution deflection system," 435; Hughes, "Long-life, high-brightness sources for demountable guns," 441; Yamazaki, Everhart, "Point-cathode electron gun analysis," 453; Hoff, Everhart, "Direct measurement of electron energy loss in solids," 454; Schubert, "Computation of small-angle scattering and its importance for electron beam welding," 459; Hart, "Angular distribution of backscattered electrons," 473.

BIOLOGICAL AND CHEMICAL APPLICATIONS OF LASERS 483

Süsskind, "Biological research with lasers (invited paper)," 484; Riggle, "Q-switched neodymium laser effects on tissue," 487; Namba, Kim, Taki, "Laser-induced chemical reaction," 493; Wilhelmi, Szews, "Laser detection of visible air pollution," 501.

APPENDIX 507

Wells, "Bibliography on the scanning electron microscope," 509.

AUTHOR INDEX 543

PART I

WELDING AND MICROMACHINING

[illegible] CONTENTS (Cont'd)

Page

"An application of [illegible] lasers in contour measurement," 269; Toerke, Angelo, "Selective removal of Teflon insulation from wire using CO_2 and argon lasers," 279; Schumacher, Taylor, "Rock breakage by means of electron beam piercing laboratory tests," 271; White, "Phenomena associated with electron-beam evaporation," 285; [illegible], "Energy broadening in accelerated electron beams by Coulomb interaction," 297.

LASER EXCITATION & INSTRUMENTATION: NEW MICROANALYTICAL TOOLS 305

[illegible], Manzelli, "Ceramic plasma container for ion lasers," 307; Rocherolles, "Focusing of intense laser beams," 311; Beck, "Laser requirements for [illegible]," 317; Schwarz, Hora, "Observation of electron diffraction pattern on nonluminescent target caused by laser interaction," 323; [illegible], "Feedback control of high intensity triode guns," 329; Helmer, Weichert, "Induced electron emission spectroscopy," 337; [illegible], "Electron impact spectroscopy," 343; Heinrich, "Electron and ion microprobe analysis," 353.

ELECTRON MICROSCOPES; ELECTRON OPTICS; ELECTRON SCATTERING 361

[illegible], Nixon, "Further developments in stereoscopic scanning electron microscopy," 363; Banbury, Nixon, "Improved contrast in scanning electron microscopy," 364; [illegible], "Transmission scanning electron microscope using field emitters and liquid helium," 365; Tighe, Hockey, "Ion thinning of electron microscope specimens," 375; Kanaya, Kawakatsu, [illegible], "Color observation of electron microscope images," 381; Steigerwald, Mayer, Scheifels, "A new type of electron gun," 389; El-Kareh, "Design and analysis of symmetrical and asymmetrical electrostatic immersion lenses using a digital computer," 395; El-Kareh, Parks, "Computer analysis of symmetrical magnetic lenses with unsaturated pole pieces," 407; McWhirter, "Paraxial electron trajectories with space charge," 415; [illegible], "High-speed high-resolution deflection system," 435; Hughes, "Long-life, high-brightness sources for demountable guns," 441; [illegible], Everhart, "Point-cathode electron gun analysis," 459; Hoff, Everhart, "Direct measurement of electron energy loss in solids," 465; Schubert, "Computation of small-angle scattering and its importance for electron-beam welding," 473; Hart, "Angular distribution of backscattered electrons," 479.

BIOLOGICAL AND CHEMICAL APPLICATIONS OF LASERS 483

Susskind, "Biological research with lasers (invited paper)," 484; [illegible], "Q-switched mechanism laser effects on tissue," 487; [illegible], Kim, Taki, "Laser-induced chemical reaction," 493; [illegible], [illegible], "Laser detection of visible air pollution," 501.

APPENDIX 557

Wells, "Bibliography on the scanning electron microscope," 559

AUTHOR INDEX 643

SOME LESS-KNOWN FACTS ABOUT ELECTRON BEAM WELDING

ROBERT BAKISH*

Bakish Materials Corp., Englewood, N. J.

It is my pleasure to speak at this forum some 10 years after my initial involvement in it. Electron beam (EB) welding, which was then only an intellectual curiosity, is today a well-established powerful technique with its uses and users increasing daily.

Before I begin with the substance of my talk let me briefly outline for the uninitiated EB welding as it is practiced in 1969. In essence it is a joining technique which has three operational modes using the electron beam as a heat source. The first mode is the hard vacuum, the second is referred to by any of the three names (soft, partial, or "commercial" vacuum), and the third, the so-called inert-atmosphere EB welding or EB welding in air, is pressure dependent with the ambient pressures of 10^{-4} Torr or less, 100 to 300 μ and 1 atm being the respective operating pressures. Figure 1 gives the schematics of the machines for the conduction of these three modes. (These illustrations show the Hamilton Standard point of view, but the systems of the other manufacturers are similar.)

There are a number of problem areas which have been of concern to me over the years that have been intimately connected with this powerful joining technology virtually since its invention. Nevertheless, they remain at best known only to those actually and intimately involved with the process and its applications because they occur usually under special circumstances. It is these which I will plan to discuss in my presentation.

In addition I wish to refer to a rather interesting recent finding which even though not strictly welding deals very much with fusion-zone properties. I should also like to comment on the interrelation of focal spot location and fusion-zone configuration. Last but not least I should like to comment briefly on the business of the high depth-to-width capability of the electron beam and its importance to the user in terms of actual tasks to be performed. It is my hope that wider realization of the existence of these problems and peculiar facts should bring, where needed, research and development effort to bear so that positive procedures to avoid these problems are developed. Better understanding here and the solutions derived should provide even greater impetus to the growth of EB welding in the future. On the other hand realization of the other items might prove highly advantageous to some.

Let me begin with the area of EB defects as I believe it is of greatest importance to apprise a potential user of EB welding equipment that they do exist. He should know that he will encounter these defects in the course of welding with electron beams and he will have to find ways to avoid them. Let me hasten to say that knowledge of the existence of

---

*Adj. Prof., Fairleigh Dickinson University, Teaneck, N. J.

Record of 10th Symposium on Electron, Ion, and Laser Beam Technology (L. Marton, ed.); San Francisco Press, Inc.

Copyright © by The Institute of Electrical and Electronics Engineers, Inc.—Printed in the U.S.A.

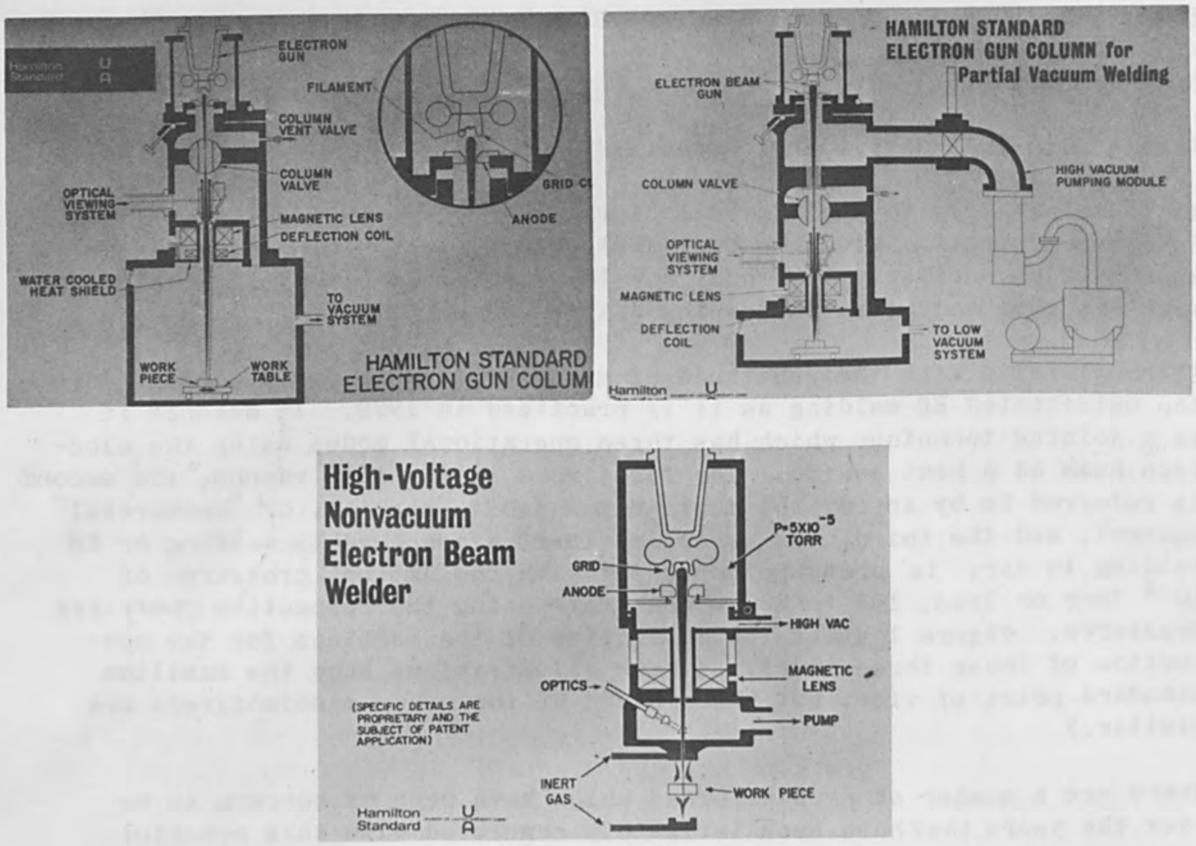
Hamilton Standard
ELECTRON GUN
FILAMENT
COLUMN VENT VALVE
COLUMN VALVE
OPTICAL VIEWING SYSTEM
MAGNETIC LENS
DEFLECTION COIL
WATER COOLED HEAT SHIELD
TO VACUUM SYSTEM
WORK PIECE
WORK TABLE
GRID C
ANODE
HAMILTON STANDARD ELECTRON GUN COLUM
HAMILTON STANDARD ELECTRON GUN COLUMN for Partial Vacuum Welding
ELECTRON BEAM GUN
COLUMN VALVE
OPTICAL VIEWING SYSTEM
MAGNETIC LENS
DEFLECTION COIL
HIGH VACUUM PUMPING MODULE
TO LOW VACUUM SYSTEM
Hamilton
High-Voltage Nonvacuum Electron Beam Welder
P=5X10^{-5} TORR
GRID
ANODE
HIGH VAC
MAGNETIC LENS
OPTICS
PUMP
(SPECIFIC DETAILS ARE PROPRIETARY AND THE SUBJECT OF PATENT APPLICATION)
INERT GAS
WORK PIECE
Hamilton Standard

FIG. 1.—Schematics of EB welding machines. (Courtesy: Hamilton Standard.)

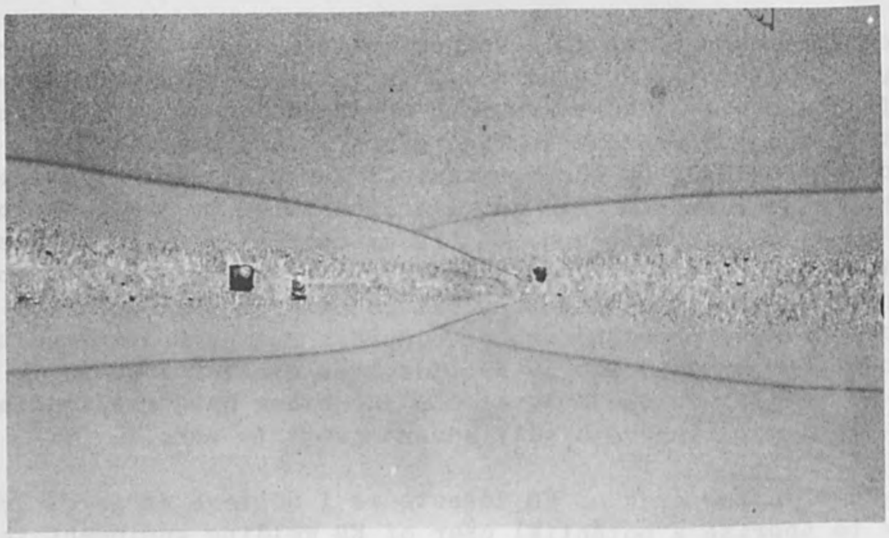

FIG. 2.—Gross porosity: two-pass bead on plate in HP 9-4-25, 1.5 in. thick, 5X. (Courtesy: J. Gerken, TRW.)

potential problem areas should under no circumstances deter from the tremendous capabilities of the technique. It is my intention to focus on these areas and develop awareness which should contribute to effort by those using or about to use EB welding leading to eventual elimination of defects through better understanding of conditions leading to them. This to be certain will permit better utilization of this technology and even broader acceptance.

Several types of defects have been observed in the course of EB welding. Many of them are common to fusion welding processes in general though some are typically EB related and many occur with greater frequency here. The degree of these defects is alloy- and very likely mode-dependent though at this stage virtually no information on the mode dependence is available. Their severity and incidence as a rule increases with the thickness of the material welded and this is so regardless of mode. Porosity, spatter, cracking, shrinkage voids, undercutting, cold shuts, and missed joints are perhaps the seven most commonly observed defects in the course of EB welding.

Porosity can result from a number of causes. Vaporization of one or more of the alloy constituents with particularly serious problems potentially existing in alloys containing widely divergent vapor pressure constituents is one of the important causes for porosity (Fig. 2).[1] High gaseous content can contribute to porosity in numerous instances. Decomposition of nonmetallic inclusions often common in many metallic materials and particularly important in the carbon steels is also a serious cause of porosity. Existence of carbides, nitrides, and similar case-hardening constituents also can lead to porosity and welding problems.

Though without the benefit of much experimental data from studies concentrated in these areas, it can be said that the vacuum processed materials (and those processed by EB melting in particular) have a reduced propensity for porosity in relation to nonvacuum-melted comparable materials, though vacuum processing of the material by no means assures absence of porosity. In terms of acquisition of data related to porosity it can be said that it is at best scarce and whatever information can be found here has been generated using the hard vacuum mode. The higher operating pressure of the alternate two modes could alleviate the porosity problem slightly in some cases but lacking concrete information on the extent of this improvement continued awareness of the potential danger of porosity should be maintained. With the greater usage of electron beams for welding of steels the danger of nonmetallic inclusion-induced porosity here should be kept in proper perspective. In joining of surface-treated parts one should be particularly careful as real problem areas exist here (Fig. 3).[2]

Another potential danger area is that of work with rimmed and semikilled steels, where deoxidants (for example, aluminum) should be added in the vicinity of what will be the fusion zone to permit deoxidation in the process of welding. The irons, i.e., cast irons which contain large amount of carbon, are virtually unweldable because of the high degree of gas evolution caused by the oxidation of the carbon in the process. This is also the case with the steels containing phosphorus or sulfur in

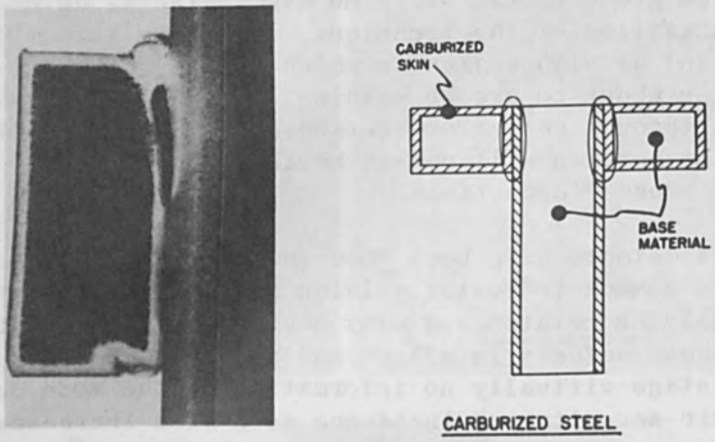
CARBURIZED SKIN
BASE MATERIAL
CARBURIZED STEEL

FIG. 3.—Welding of carburized material at the weld interphase. (Courtesy: J. R. King, Sciaky.)

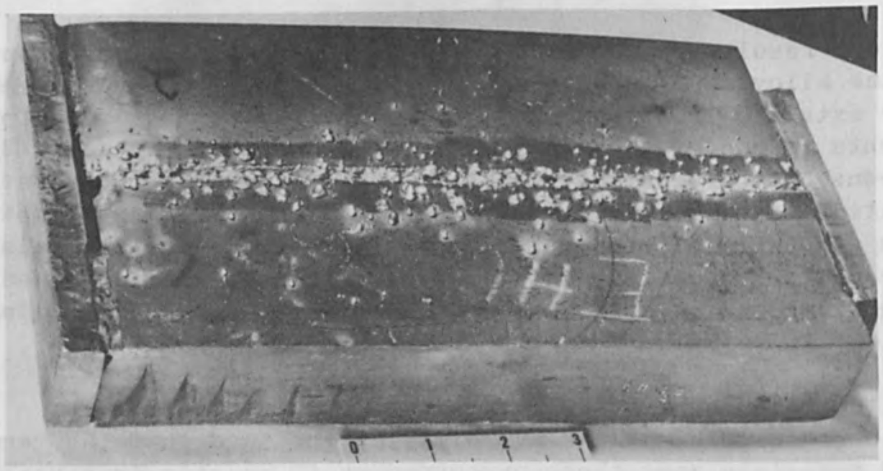

FIG. 4.—Spatter on surface of weld in 1.5-in. HP 9-4-25. (Courtesy: J. Gerken, TRW.)

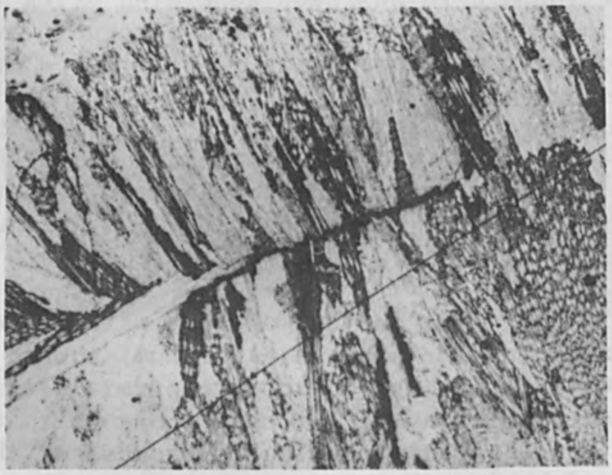

FIG. 5.—Shrinking in FZ solidification center line in A-286. (Courtesy: J. Pasoja, Fusion Division of EBTEC.)

excess of 0.03%.

The expansive release of highly heated gases from the fusion zone in the many cases referred to above leads also to spatter (Fig. 4).[1] Although this effect is readily observed and can be rectified by refinishing of the surface of the fusion zone and its vicinity it nevertheless is a matter of concern as it leads to the added cost of the refinishing. The problem of spatter can be of extreme importance in life-support systems. Here the danger of entrapment (of small solid metal droplets in the astronauts' breathing systems, for example) can have most serious consequences. Because of lack of 100% reliable means to locate all possible spatter-related particles in life-support systems recommendations to avoid EB welding for these systems have been made.[3]

Shrinkage voids are another type of important defect which is encountered in EB welding. Unlike porosity, where we usually are dealing with spherical configurations or curvilinear outlines of the defect, here we often run into rather complex void configurations. These are more often encountered in material known for volumetric shrinkage. As the fusion-zone solidification proceeds normal to its walls, shrinkage cavities can be developed almost along the solidification center line (Fig. 5). As in other defects only limited information specifically related to this problem in EB welding has reached the literature. It is believed its occurrence should be more pronounced in EB welding relative to the alternate fusion welding process by virtue of the higher welding speeds and consequential higher solidification rates. It should improve at least to some extent in partial and IAEB welding modes, both of which have lower solidification rates. As a way of dealing with the problem in all the three modes, reduction of weld speeds and beam oscillation both aimed at reduction of the rates of cooling,are suggested as possible remedies.

Cracking has been one of the more severe problems in welding technology and it continues to prevail. EB welding in its three operational modes has unfortunately not eliminated the problem. Many of the materials which are susceptible to cracking when joined with the miscellaneous arc welding processes are also susceptible to cracking either during or subsequent to EB welding. Some nickel base alloys,[1] for example Inco 718, Rene 41, and hardenable steels of the 4340 and D6A1 types are all subject to cracking problems.

In these alloys, as is the case with other similar situations, good understanding of metallurgical parameters including structural and dimensional changes brought about by heat treating and its relation to the joining process is a must if one is to overcome the problem. Preheating or postheating of specific nature for each and every alloy which suffers from such cracking problems based on the production of suitable metallurgical structure and reduction of internal stresses brought about by the welding are absolutely necessary. In addition there is no substitute for most careful design both of the components and fixtures aiming at reduction of constraints. One should always design for low constraint if one wishes to minimize cracking occurrence.

An interesting case pertaining to cracking is for example the behavior of A-286, a Ni-base alloy. Here it was established[4] that the weldability of the material was grain-size dependent. This in itself is not strange but it is the only incidence of the problem known by the writer related to EB welding. The specific case which revealed this fact was the preparation of a part containing a butt weld between two pieces of this material, one in forged condition and the other a bar stock. The user kept obtaining most inconsistent results when a stated part was subjected to fatigue testing. The first item which was established in the study was that the grain size of the material in the forged condition varied over a considerable range because of poor forging temperature control. In addition it was also established that fatigue cracks abounded on the large-grain-size specimen (Fig. 6). The establishment of maximum allowable grain size eliminated the problem.

Certain grades of tool steels in general and the M grades in particular have the tendency to carbide liquation in the vicinity of the fusion zone. Such steels have low ductility as in the welded condition because of the formation of eubectic carbides. Extensive pre- and post-treatments have been devised and are successfully used to rectify the problem also in these cases.

There is no information whatsoever permitting any statements pertaining to the changes of cracking susceptibility as one switches from the one to the other EB welding modes, though no major changes are expected. As already mentioned best results in overcoming cracking problems have been obtained either through application of carefully selected heat treatments or through suitable design aimed in minimizing constraints in the system. No sufficient information has accrued on which to base more specific guidelines for the users here.

As cracking itself is brought about by a variety of thermally induced stress configurations brought about by phase transformations and related metallurgical factors, nondestructive X-ray studies should be very valuable in establishing the stress patterns associated with EB weld joints. In aiming to better our understanding of happenings here much study will be needed. Although activities in this area have begun[5] by virtue of a great many variables involved in joint preparation, joint design, materials, and EB mode, it will take some time before even the initially generated data will be of practical use to those in the shop. I hope the difficulty and the tedious nature of the generation of such information will not discourage a potential investigator. The rewards of a clear understanding and sound knowledge of stresses produced in EB welding will be notable.

Undercutting is another problem area in EB welding, with all factors which tend to remove metal from the fusion zone contributing to it. As a consequence of jigs, fixtures, work-piece configuration, and occasionally metal build up in the center of the bead also contribute to undercutting. Sometimes bottom drop-through leads to undercutting. Though several approaches can be used to overcome this problem, the exact details very much depend on the specific case. Beam parameter adjustments, a thin shim of material placed on the surface, filler metal, a smoothing pass with a defocused beam, and for that matter even a TIG manicuring pass can be used to good advantage to overcome undercutting when it has been observed. The problem can occur in all the three modes and yet there has been virtually no mention of it in reference to the higher pressure modes.

Missed joints or beam bending within the joint leading to only partial weld is a problem that those using EB welding must face occasionally. Here two manifestations, which can be referred to as missed joints, take place. Though these two types of defects are not truly related, the ultimate results have much in common. The first occurs when fine joints are made and when a small deviation of the beam in its path of travel bypass the seam, leaving nonwelded segments along the joint with the fusion seam wandering to the left or right of it. This fault is most often due to fields formed in the vicinity of the work leading to beam deflection from the seam zone with the beam entering one or the other of the parts to be joined. The second is brought about by deflection of the beam by fields within the material. This type of problem occurs most often when dissimilar materials or different cross sections are joined. Magnetic and nonmagnetic material combinations are particularly susceptible to this type of problem, which leads to bending of the beam within the material and missing of part of the joint. Programmed oscillation of the beam at rates to be experimentally determined for different cases and which tends to neutralize the fields within the material has been shown as most helpful for elimination of problems of this variety.

The cold shut is last weld defect in this group. Detailed explanation of this defect is not well agreed upon by all concerned. It is further the defect which is rather difficult to detect by nondestructive testing means. An example of such defect is seen in Fig. 7, though perhaps one of the most interesting types of cold shut was observed for the first time by Gerken and Groves[1] (Figs. 8 and 9). These indicate the three-dimensional configuration of this cold shut. It is suspected that the very fast cooling rates typical of EB welding are responsible. But the details of this type of configuration are by no means clearly understood. They are possibly related to the suggestion that the beam moves in step fashion even though it is continuously displaced. It is suggested that this stepwise beam motion is associated with plasma focusing at the surface of the workpiece being irradiated by the beam. The actual configuration of the cold shut itself might be due to the very high thermal gradients which are created by the electron beam. Actually the root of the weld is characterized by three-dimensional heat flow in contrast with two-dimensional flow on the walls of the weld and as a consequence there is a greater frequency of cold shuts in the root of welds.

Another interesting defect which has not been fully resolved was recently reported by Hicken[6] (Fig. 10). Here all attempts to derive a correlation among any known beam parameters and the frequency of the variation of the root of the fusion zone have failed to date. Bradburn et al.[7] also encountered this problem on UR 3.5 Ti alloy in attempting to produce controlled penetration welds. Like Hicken they were able to remedy but not eliminate the situation by beam oscillation.

To summarize the first subject of my discussion, defects: EB welding is not different in essence from other fusion-welding processes and welding

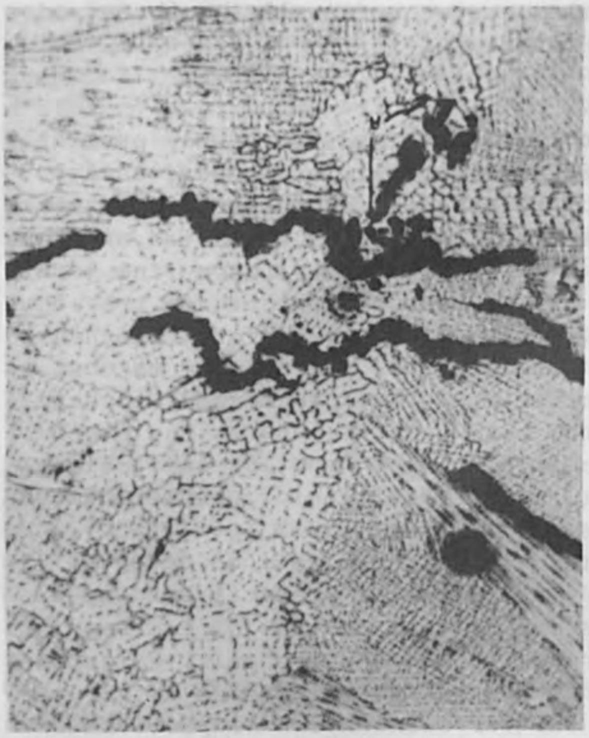

FIG. 6.—A-286 cracking in coarse grained structure. (Courtesy: J. Pasoja, Fusion Division of EBTEC.)

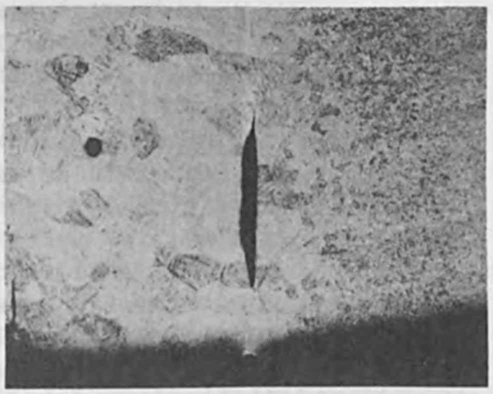

FIG. 7.—Cold shut and porosity in Ti 6 Al 4V. (Courtesy: J. Gerken, TRW.)

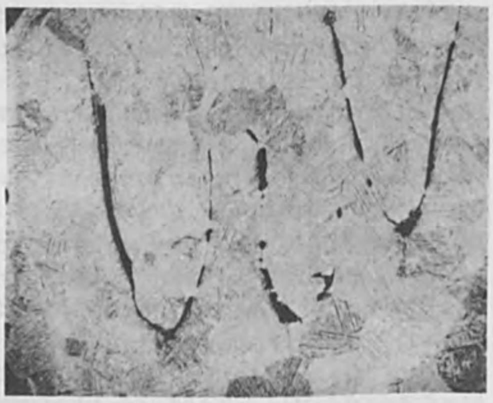

FIG. 8.—Cold shut, Ti 6 Al 4V. (Courtesy: J. Gerken, TRW.)

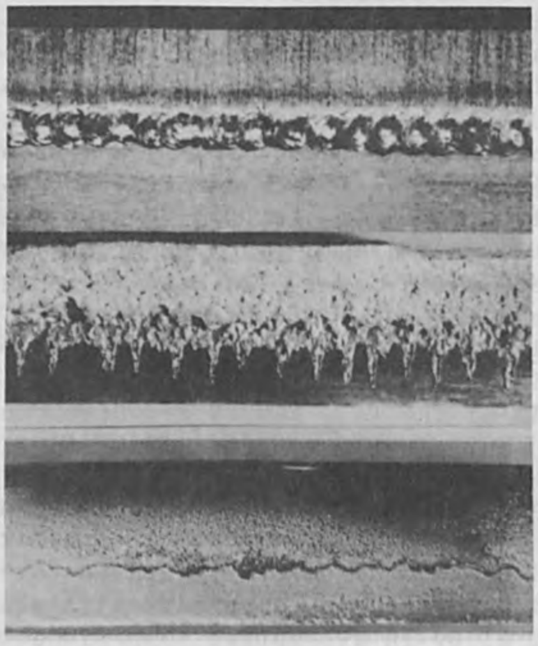

FIG. 10.—Root profile fluctuation in aluminum (top) and uranium alloys (bottom). (Courtesy: K. Hicken, Dow Chemical.)

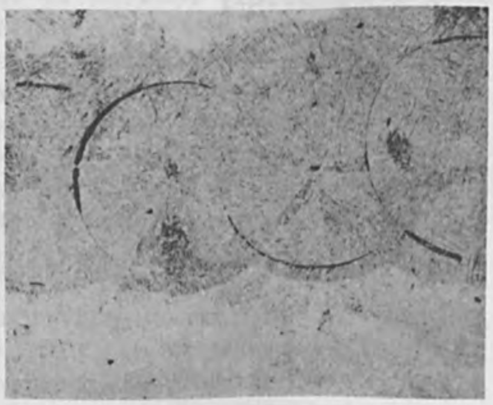

FIG. 9.—Flat section in Ti 6 Al 4V through above cold-shut zone. (Courtesy: J. Gerken, TRW.)

defects exist also here. Considerable betterment in the awareness of their existence is needed before effort to improve the understanding of causes leading to these defects is initiated. Only through understanding and establishing of proven and general remedial procedures will the importance of EB weld defects as a problem area be reduced.

The second topic to be discussed is that related to the interrelation of the beam, its focus spot, and fusion-zone configuration. Although it is implied that long-focal-distance systems (i.e., long-working-distance EB welding systems) permit considerable freedom in welding, the specific location of the focal spot in relation to the surface of the work piece is of considerable importance in relation to the shape and reproducibility of the fusion zone. Attention to this matter was drawn for the first time by Olshansky[8] (Fig. 11); since then the problem has been investigated with considerable additional details by Boncoeur and Rapin.[9] These two studies were conducted with low-voltage Pierce-type guns. It was hoped that utilization of the telefocus type of gun might tend to reduce the spread of fusion-zone configuration in relation to these low-voltage systems. The writer also conducted recently limited experiments on 3.5-in.-thick AISI 304 and on 6-in.-thick aluminum AA 5083 alloy. These bead-on-plate experiments conducted with the assistance of Hamilton Standard indicate that the telefocus system might possibly reduce the problem somewhat, but the variation of fusion-zone configuration still exists and must be taken in consideration (Fig. 12).

Based on these three investigations it can be stated that for all thin-gage joining operations and all planar joining tasks on heavier-gage materials the above does not present a problem. However, if one is concerned with joining over some important range of depth, unless one can compensate for it either with gun displacements or through changes in beam parameters, one will have considerable variation in the fusion-zone geometry of the joints and consequent property variation.

By virtue of its configuration the electron beam as a heat source leads to the creation of very rapid cooling rates in the fusion zone. This behavior has been usually associated only with welding, but some rather interesting facts are revealed by consideration of the fusion-zone metal as specially processed material.[19] The results are shown in Table I.

TABLE I

Alloy	Vickers* hardness	Tensile strength	Percent elongation
Al 11 Si			
Base metal	60	20.6	7.5
		14.9	-
EB fusion zone	115	35.0	4.4
		36.0	4.5
Al 6 Mn			
Base metal	50	12.5	4.8
		12.7	5.1
EB fusion zone	75	21.4	8.6
		19.6	6.6

*Averages of several measurements.

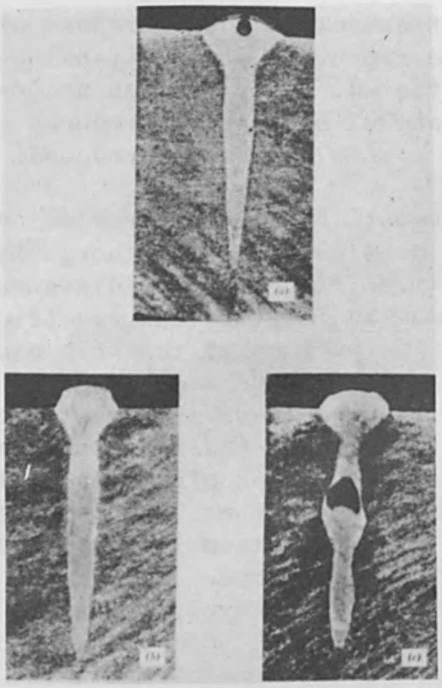

FIG. 11.—Dependence of fusion-zone geometry on site of beam focusing. (Courtesy: N. A. Olshansky, Moscow Power Institute.)

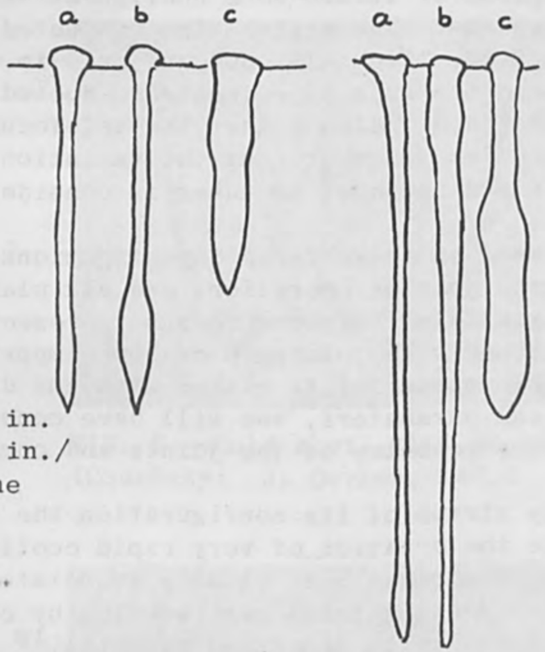

FIG. 12.—Dependence of fusion-zone geometry on site of beam focusing; fusion-zone traces produced in AISI 3.5 in. thick (left), and AA 5083 6 in. thick (right), 150 kV and 167 mA, 8 in./min. Focusing (a) 2 in. above, at the surface, and (c) 2 in. below.

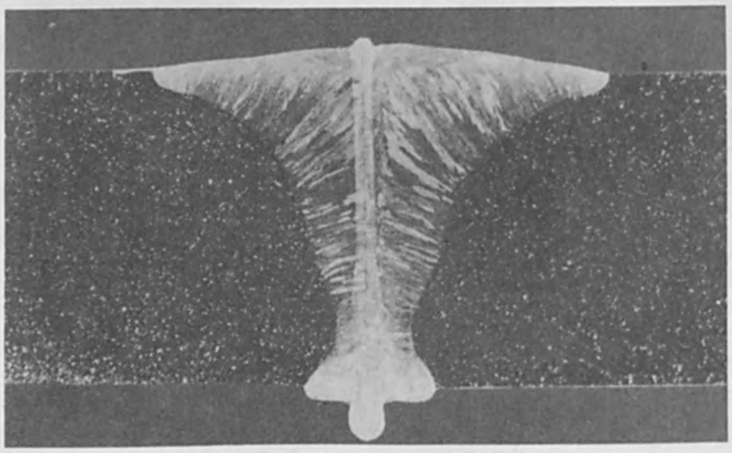

FIG. 13.—"Trademark" of EB weld: 304 stainless steel, 0.5 in. thick.

Note the important increase of hardness for both the Al 11 Si and the Al 6 Mn. These properties are due to extreme structure refinement brought about by the extreme chill rates. It is not impossible that some of the EB weld properties obtained are related to this particular aspect of the process and perhaps reevaluation along these terms might reveal interesting information.

Here is also a potential area of application of the electron beam, i.e., for the production of unusual and perhaps high-strength structures; one might refer to this as "restructuring." Needless to say, this is not by any means a commercial process at this juncture but it does have some most intriguing possibilities for preparation of ultrafine cast structures and in turn perhaps most unusual properties in a variety of suitably selected alloys.

Let me next refer to the "trademark" of the EB weld (Fig. 13). Much has been said about the high depth-to-width capabilities of the EB process and indeed it is the process which permits the preparation of the highest depth-to-width ratios possible in welding technology. Though electron beams are capable of these high depth-to-width ratios, there is a large area of application where these are not necessary at all. This being the case a considerable waste in capital investment occurs by any user who needs EB welding but does not need high depth-to-width ratios. One could facetiously say that these people acquire high performance Masserati or Ferrari racing vehicles to use them for daily commuting in traffic-jammed highways. One should also not forget that in some limited instances it was even shown that the very high depth-to-width ratio fusion zones actually have an adverse effect and wide fusion zones superior properties, though this is not truly pertinent to the point that I wish to make.

What I am really attempting to say in this brief reference to the high depth-to-width ratios is that with greater discretion exercised by a potential purchaser of an EB welding machine he could effect substantial savings. Needless to say when you buy a piece of experimental equipment one should get the best and most versatile system he can afford and acquire it from the most reliable supplier one can find. In the past two manufacturers have won laurels for making the best available equipment in the U.S. I am afraid, however, that in most cases customers have bought what these suppliers have wanted to sell rather than the most efficient and economic machine to do the job. This status is certain to change with the growth in the field and when the two main suppliers encounter serious challenge from potential newcomers in the field.

Last but not least I wish to mention an item which has been somewhat perturbing to me for some time. EB welding, and in particular the high depth-to-width of penetration nugget configuration, leads to formation of some rather sizable internal stresses. I already stated that they are only now being investigated. The exact interrelation of these stress patterns and the behavior of these structures in fatigue is at best not known. As best as I can gather only limited data on the subject are available and though I cannot say this with certainty I do not know a single paper specifically directing attention to the subject to have reached the welding journals. The base of application of EB welding continues to broaden. We know of early applications and we hear more and more talk about the use of EB welding in very-high-performance aircraft. We even know that virtually all important airlines have EB welders at their service and maintenance facilities. Further, helicopter rotators are often EB welded. Yet no data appear to exist which would permit a user, actual or potential, to do away with existing concern as to the soundness of these joints. The writer wonders if a major program of study of interrelations of EB welding in structural applications and fatigue is not overdue.

In conclusion let me say that I have attempted here to dwell on four items related to EB welding that seldom get the attention that they deserve to my mind. It is my hope that as awareness of these real and potential problem areas is developed corrective steps will be taken. It is only in this manner that the steady and uninterrupted growth of EB welding can continue without unexpected unpleasant surprises which might affect its future.

ACKNOWLEDGMENT

The writer wishes to express thanks to all those who provided illustrations used in this paper.

REFERENCES

1. M. T. Groves and J. M. Gerken, AFM 2-TR-66-22.
2. J. R. King, SAE Preprint 680048, Jan. 1968.
3. K. Miller, private communication.
4. D. Pasoja, private communication.
5. R. Prummer, Proc. 3rd Beam Techniques Colloquium, SLV Manheim, to be published.
6. K. Hicken, in Proc. 3rd Int. Conf. Electron & Ion Beams in Sci. and Techn. (R. Bakish, ed.), New York: ECS, 1968.
7. E. M. Bradburn, P. W. Turner, and R. A. Huber, AWS Spring Meeting, Philadelphia, 1969.
8. N. A. Olshansky, in Proc. 1st Int. Conf. Electron and Ion Beams in Sci. and Techn. (R. Bakish, ed.), New York: Wiley, 1965.
9. M. Boncoeur, J. Y. Marhic, and M. Rapin, Proc. 3rd Conf. Electron & Ion Beams in Sci. and Techn. (R. Bakish, ed.), New York: ECS, 1968.
10. W. Hiller, La Métallurgie, 100: No. 1, Jan. 1968.

USE OF SECONDARY, THERMAL, AND BACKSCATTERED ELECTRONS IN THE ELECTRON-BEAM WELDING PROCESS

M. BONCOEUR

Commissariat d'Énergie Atomique, Paris

I. DIFFERENT ELECTRON CURRENTS PRESENT DURING WELDING

An electron beam, all the characteristics of which are assumed to be invariable, strikes a metallic target of known composition. Under the impact of the electrons this target may heat up and melt if the energy provided is high enough; if not, it remains at room temperature. The electron currents differ in the two cases.

1. THE TARGET IS NOT HEATED. The various types of electrons in movement in this case are illustrated in Fig. 1(a). The incident electrons strike the sample and penetrate the metal, where some remain fixed while others escape again. The latter are elastically or inelastically backscattered primary electrons, and secondary electrons due to the collision of primary particles with the electrons of the metallic lattice. Secondary electrons are distinguished from backscattered particles by their low energy, which is assumed to be less than 50 eV.[1,2]
The current I_p passing in the sample is equal to the difference between the incident current I_b and the currents I_s and I_r due to secondary and backscattered electrons:

$$I_p = I_b - (I_s + I_r) \tag{1}$$

If we assume that the incident electrons are monoenergetic and follow parallel paths, the secondary current I_s is given by the expression

$$I_s = \Delta I_b \tag{2}$$

where Δ is the number of secondary electrons emitted by incident electron. As we can see in Table I taken from the work of Weinryb,[1] the value of Δ increases with the atomic number of the target and decreases with the energy of the incident electrons. The backscattered current I_r is obtained from the expression

$$I_r = \eta I_b \tag{3}$$

η being the number of elastically or inelastically backscattered electrons per incident primary electron. The η values obtained by Weinryb for targets of increasing atomic number and for various primary electron energies are given in Table II. The coefficient η increases with the atomic number and as the incidence of the primary electrons diverges from the perpendicular. The direction in which η varies with the energy of the primaries is uncertain since the results obtained

Record of 10th Symposium on Electron, Ion, and Laser Beam Technology (L. Marton, ed.); San Francisco Press, Inc.
Copyright © by The Institute of Electrical and Electronics Engineers, Inc.—Printed in the U.S.A.

TABLE I.—Secondary-emission coefficient Δ according to Weinryb.[2]

Z	Element	Δ	
		28 keV	4.5 keV
4	Be	0.05	0.19
6	C	0.09	0.29
13	Al	0.09	0.21
22	Ti	0.08	0.31
26	Fe	0.06	0.28
27	Co	0.06	0.28
28	Ni	0.07	0.27
33	As	0.08	0.26
41	Nb	0.11	0.34
47	Ag	0.10	0.33
50	Sn	0.10	0.34
74	W	0.08	0.33
83	Bi	0.12	0.34
92	U	0.14	0.36

TABLE II.—Backscattering coefficient η according to Weinryb.[1]

Z	Element	$\eta \, 10^2$		
		4.5 keV	11 keV	28 keV
4	Be	6.4	4.05	2.3
6	C	8.3	5.86	5.5
13	Al	18.6	14.3	13.5
22	Ti	26.2	23.6	22
26	Fe	30.7	26.6	25.3
27	Co	31.6	28	26.5
28	Ni	34.7	30	28.5
33	As	38	31.7	30.8
41	Nb	39.3	34.7	33.3
47	Ag	42	36.5	36.1
50	Sn	42.5	37	38
74	W	47.3	43.3	43.4
83	Bi	48	44.7	44.8
92	U	48.2	45.5	46.2

by the authors are contradictory.[1] The currents I_s and I_r vary also with the shape and surface state of the target.

2. THE TARGET IS HEATED AND MELTS UNDER THE IMPACT OF THE ELECTRONS. This case is illustrated in Fig. 1(b). In addition to the electrons described above a new type is present: thermoelectrons. The metal melted under the impact of the particles is a thermoelectron emitter which gives off low-energy thermal electrons outside the metal. If I_t is the current corresponding to the latter the current passing through the sample becomes

$$I_p = I_b - (I_s + I_r + I_t) \tag{4}$$

Thermoelectron emission is governed by the Richardson-Dushman law

$$J_t = AT^2 e^{-Q/kT} \tag{5}$$

where J_t , expressed in amperes per square centimeter of emitting surface, is the maximum current density obtainable from the metal; T the absolute temperature of the emitter; A a constant of the material; Q the electron work function expressed in electron volts; and k the Boltzmann constant. This relationship shows that for a given metal the current I_t increases with the temperature and surface area of the emitter.

The various currents involved in (1) change as we vary the focusing of the electron beam during welding. In fact we know that changes occur under these conditions in the temperature of the liquid metal and in the width and depth of the zone it occupies, i.e., the thermoelectron emission surface; according to (5) the same applies to the current I_t . Varying the focusing also modifies the form of the molten zone and the incidence of primary electrons on it, and therefore the values of the currents I_s and I_r . According to (4) the current I_p passing through the target varies with the focusing of the beam to which we shall refer in terms of the value of the current I_f passing through the electromagnetic focusing coils.

Blisters or cracks pre-existing in the bulk of metal melted by beam are microscopic Faraday cages. The result is that as soon as the beam passes through these defects the currents I_r and I_s decrease, and consequently I_p increases. A solid inclusion or a gas-filled blister which explodes in vacuum alters the permanent electron flow conditions and changes the values of I_r , I_s , I_t , and I_p . By recording these currents during welding it is thus possible to detect immediately any anomaly which can point to the presence of a defect in the line of the weld. We shall give results relative to variations in the currents passing through or leaving the target, as a function of the focusing current I_f on the one hand, and during passage of the beam over a defect pre-existing in the metal on the other hand.

II. VARIATION IN THE CURRENT LEAVING OR PASSING THROUGH THE TARGET, AS A FUNCTION OF THE FOCUSING CURRENT

1. EXPERIMENTAL METHOD. Figure 2 shows the device used to record curves giving the current I_p passing through the sample as a function of the focusing current I_f . A motor mounted on the axis of the I_f adjustment potentiometer causes this current to vary constantly during the welding operation. The voltages collected at the terminals of two calibrated resistances R_1 and R_2 connected in the focusing coil supply circuit and between the target and the earth respectively, are fed into an x-y recorder. The curves showing the current I_p as a function of I_f are thus obtained directly. The variations in the current $(I_s + I_r + I_t)$ leaving the target are measured by means of the device shown in Fig. 3: a small Faraday cage placed under the gun collects part of the current and is connected to a recording device similar to that described above. We studied the variations of the currents leaving and passing through the sample for targets of widely differing atomic numbers: aluminum, steel, uranium, tantalum.

We used electron guns of the high-voltage triode type or the medium-voltage Pierce type. We shall describe the results obtained with a diode gun of the latter type built by the Sciaky Co.

2. FORM OF THE CURVES. The gun-sample distance and the welding rate being constant we observe in Fig. 4, for a steel target, that the power of the incident beam considerably influences the form of the $I_p = f(I_f)$ curves. This relationship changes continuously as a function of the power, but four characteristic situations are found to arise. At very low power the curve is essentially horizontal: changes in the focusing current I_f have little effect on the current I_p . The curve becomes V-shaped when the power rises slightly. At higher power the curve takes the form of a W with asymmetrical arms. At high powers the inner peak of the W expands and the curve takes the form of a peak. It should be noted that the V minima and the crest of the central peak of the W are characteristic points. They are always obtained for fixed values of I_f when the $I_p = f(I_f)$ curves are recorded several times, the welding parameters and the composition of the target remaining constant.

The shape of the curves and the position of the characteristic points are modified by a change in one of the following parameters: acceleration voltage, bombardment current, rate of variation of the focusing current, welding rate, or composition of the target. The influence of these various parameters is shown in the diagrams of Fig. 5. It is worth noting in Fig. 5(b) that the current leaving the sample may be higher than the incident bombardment current when the target metal is a very good thermoelectron emitter, this being the case for molybdenum, tantalum, and uranium.

The curves giving the variation of the current $I_b - I_p$ escaping from the target as a function of the focusing current obviously develop in a way opposite to that of the $I_p = f(I_f)$ curves; for the same abscissa in fact the slopes of the two curves are equal in absolute value but opposite in sign. The results obtained from a study of the current leaving the sample are thus identical with those given previously.

If the shape of the $I_p = f(I_f)$ curves are compared with the

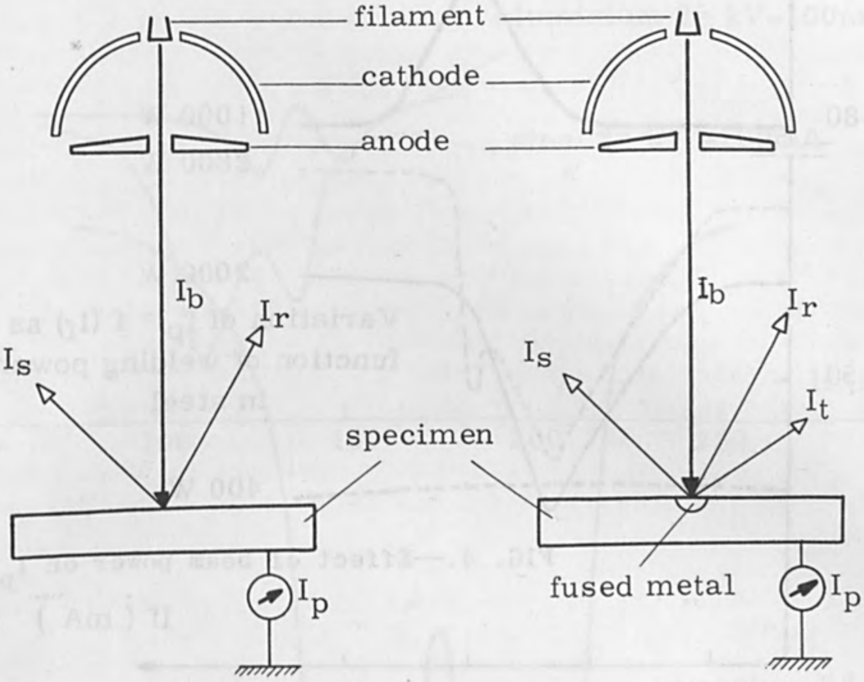
filament
cathode
anode
I_b
I_r
I_s
I_t
specimen
fused metal
I_p

FIG. 1.—Types of electrons without fused metal (left) and with fused metal (right).

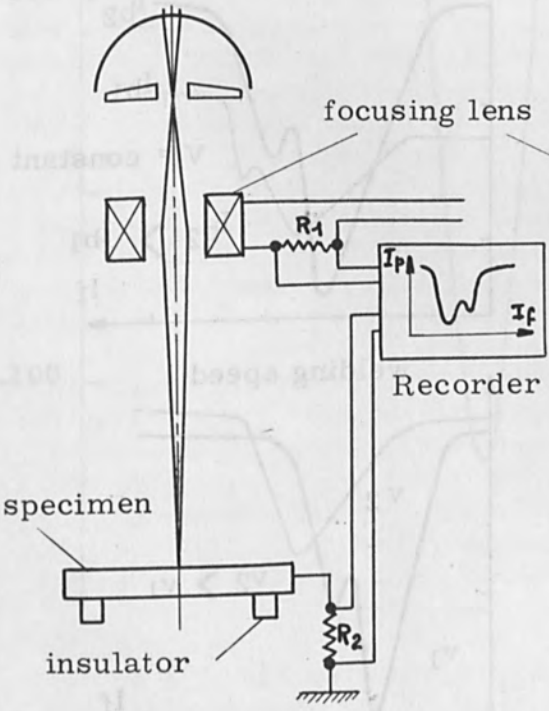
focusing lens
R_1
I_p
I_f
Recorder
specimen
insulator
R_2

FIG. 2.—Device used in making current measurements.

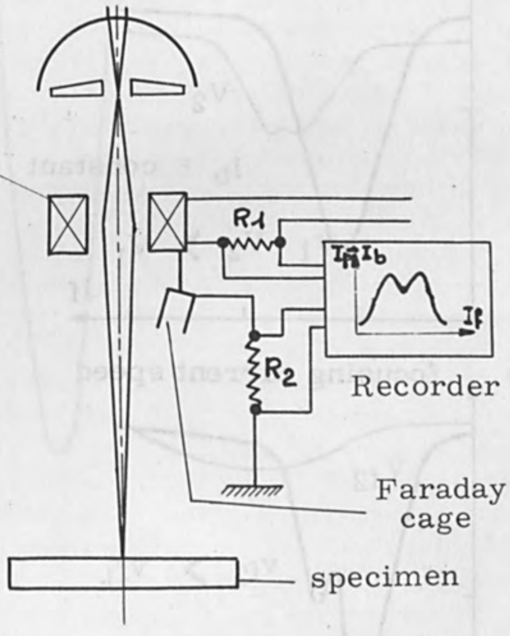
R_1
$I_f \cong I_b$
I_f
Recorder
R_2
Faraday cage
specimen

FIG. 3.—Experimental arrangement for measuring variations in current from target.

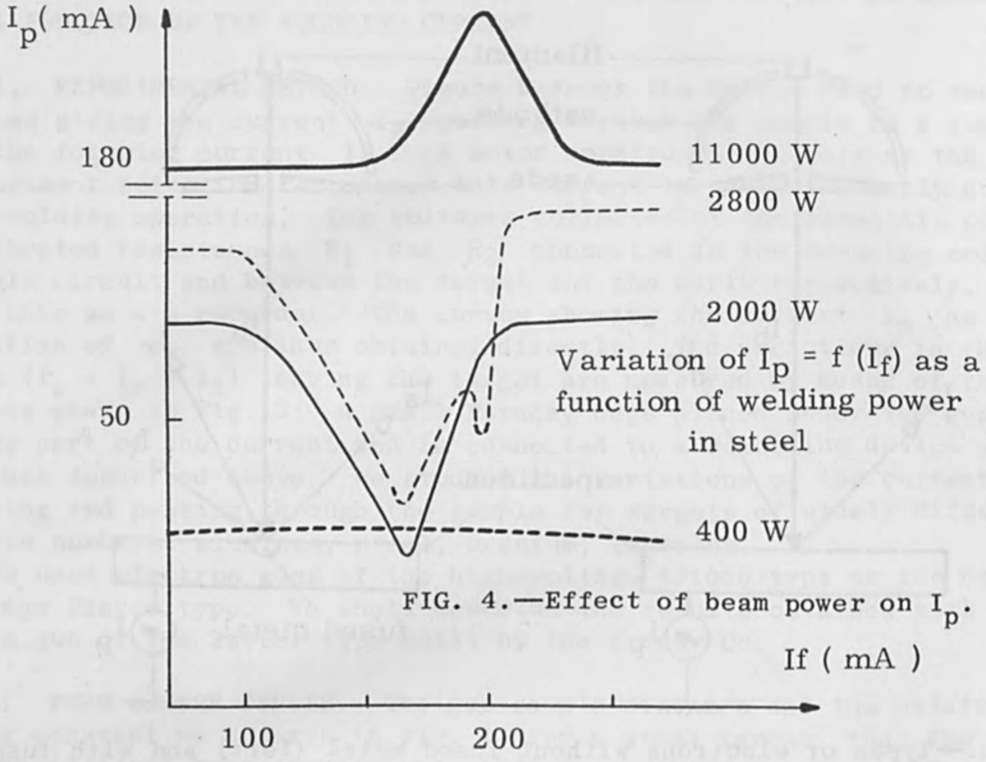

FIG. 4.—Effect of beam power on I_p.

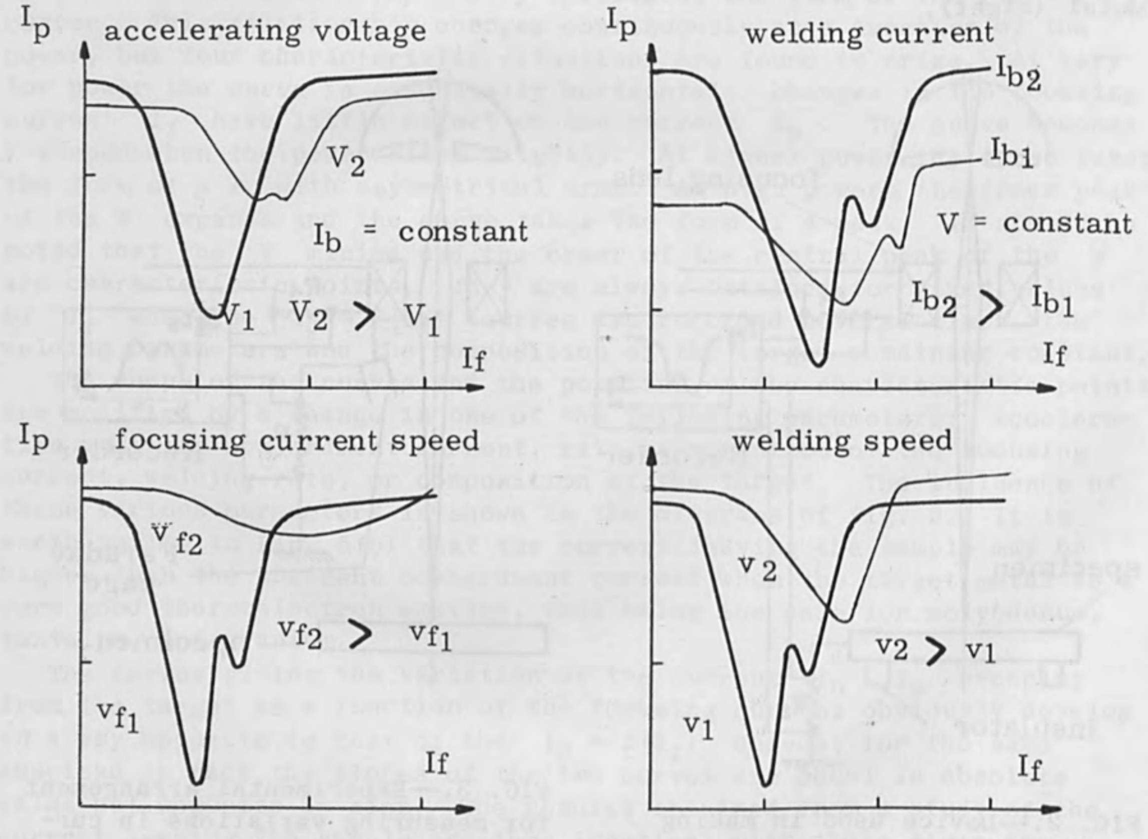

FIG. 5(a).—Effect of welding parameters (steel target).

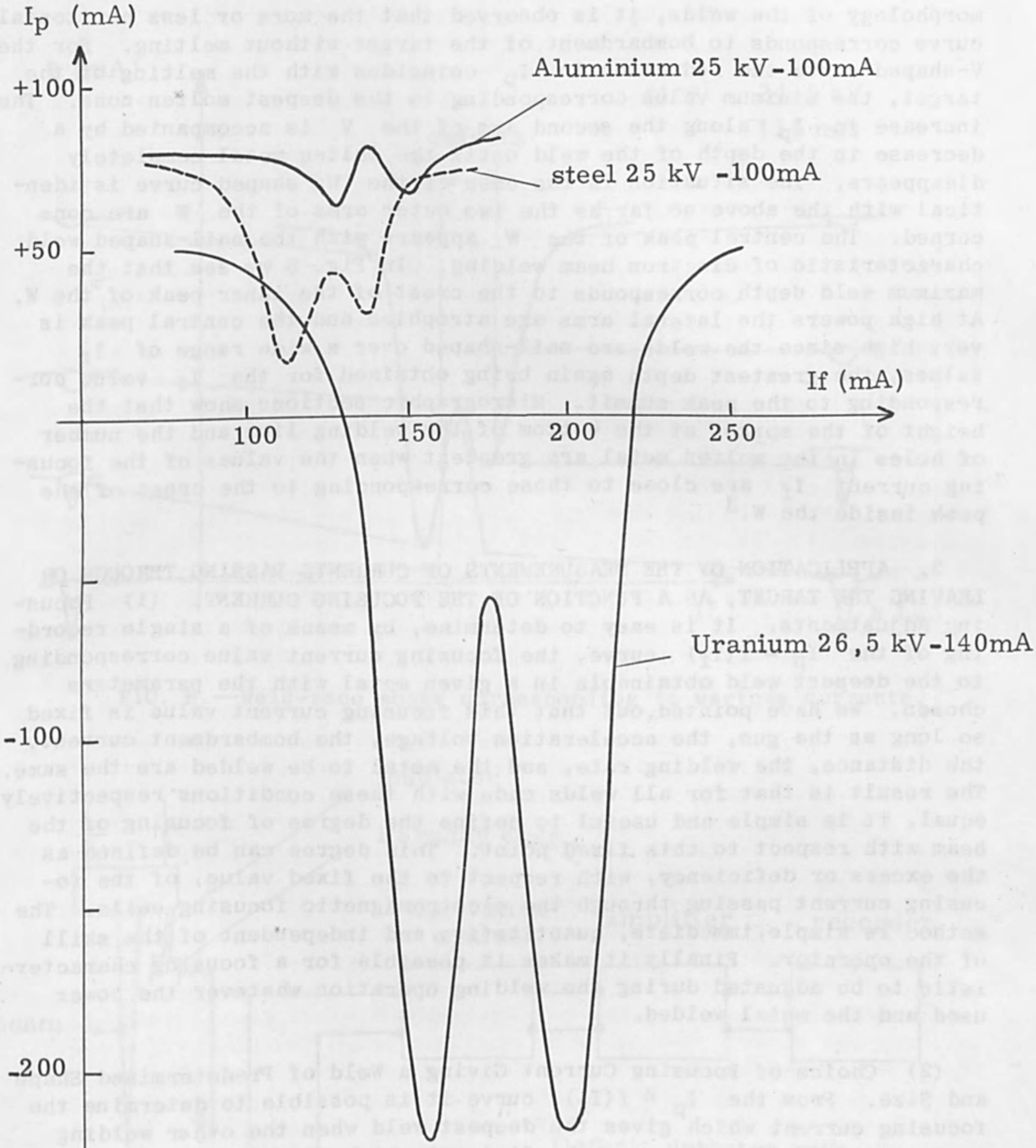

FIG. 5(b).—Effect of target composition. (Current leaving uranium part can be higher than the incident impact current.)

morphology of the welds, it is observed that the more or less horizontal curve corresponds to bombardment of the target without melting. For the V-shaped curve the reduction in I_p coincides with the melting of the target, the minimum value corresponding to the deepest molten zone. The increase in I_p along the second arm of the V is accompanied by a decrease in the depth of the weld until the molten metal completely disappears. The situation in the case of the W shaped curve is identical with the above so far as the two outer arms of the W are concerned. The central peak of the W appears with the nail-shaped weld characteristic of electron beam welding. In Fig. 6 we see that the maximum weld depth corresponds to the crest of the inner peak of the W. At high powers the lateral arms are atrophied and the central peak is very high since the welds are nail-shaped over a wide range of I_f values, the greatest depth again being obtained for the I_f value corresponding to the peak summit. Micrographic sections show that the height of the spikes at the bottom of the welding line and the number of holes in the molten metal are greatest when the values of the focusing current I_f are close to those corresponding to the crest of the peak inside the W.[3]

3. APPLICATION OF THE MEASUREMENTS OF CURRENTS PASSING THROUGH OR LEAVING THE TARGET, AS A FUNCTION OF THE FOCUSING CURRENT. (1) Focusing Adjustments. It is easy to determine, by means of a single recording of the $I_p = f(I_f)$ curve, the focusing current value corresponding to the deepest weld obtainable in a given metal with the parameters chosen. We have pointed out that this focusing current value is fixed so long as the gun, the acceleration voltage, the bombardment current, the distance, the welding rate, and the metal to be welded are the same. The result is that for all welds made with these conditions respectively equal, it is simple and useful to define the degree of focusing of the beam with respect to this fixed point. This degree can be defined as the excess or deficiency, with respect to the fixed value, of the focusing current passing through the electromagnetic focusing coils. The method is simple, immediate, quantitative, and independent of the skill of the operator. Finally it makes it possible for a focusing characteristic to be adjusted during the welding operation whatever the power used and the metal welded.

(2) Choice of Focusing Current Giving a Weld of Predetermined Shape and Size. From the $I_p = f(I_f)$ curve it is possible to determine the focusing current which gives the deepest weld when the other welding parameters are already known, to find out which I_f ranges give welds with or without the "nail" characteristic of electron bombardment, and finally to avoid I_f values likely to correspond to welding lines containing numerous defects such as shrinkage holes and periodic depth variations.

(3) Immediate Detection of a Large Accidental Change in a Welding Parameter. We have shown that the position of the characteristic points on the $I_p = f(I_f)$ curves is fixed if all the welding parameters are constant and conversely that a change in one parameter leads to a displacement of these points. By plotting a single curve it is therefore possible to check that none of these parameters has changed appreciably.

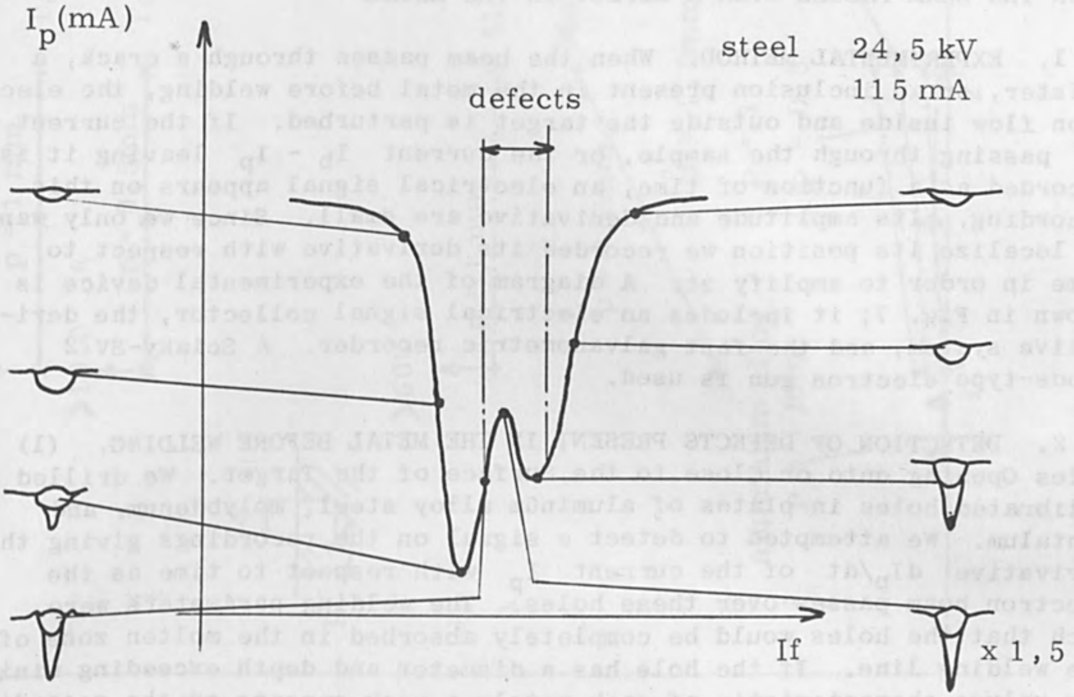

FIG. 6.—Weld-zone shape corresponding to various currents.

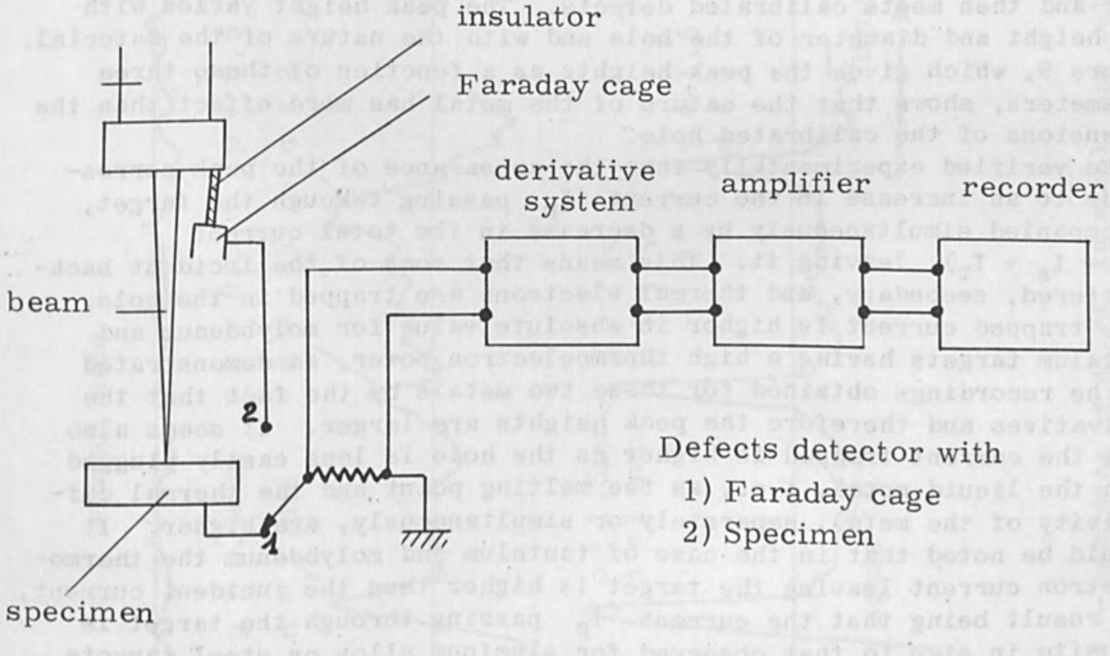
insulator
Faraday cage
derivative system
amplifier
recorder
beam
2
1
specimen
Defects detector with
1) Faraday cage
2) Specimen

FIG. 7.—Defects detector with Faraday cage (1) or specimen (2).

III. VARIATION IN THE CURRENT PASSING THROUGH OR LEAVING THE TARGET WHEN THE BEAM PASSES OVER A DEFECT IN THE METAL

1. EXPERIMENTAL METHOD. When the beam passes through a crack, a blister, or an inclusion present in the metal before welding, the electron flow inside and outside the target is perturbed. If the current I_p passing through the sample, or the current $I_b - I_p$ leaving it is recorded as a function of time, an electrical signal appears on this recording. Its amplitude and derivative are small. Since we only want to localize its position we recorded its derivative with respect to time in order to amplify it. A diagram of the experimental device is shown in Fig. 7; it includes an electrical signal collector, the derivative system, and the fast galvanometric recorder. A Sciaky-SV 2 diode-type electron gun is used.

2. DETECTION OF DEFECTS PRESENT IN THE METAL BEFORE WELDING. (1) Holes Opening onto or Close to the Surface of the Target. We drilled calibrated holes in plates of aluminum alloy steel, molybdenum, and tantalum. We attempted to detect a signal on the recordings giving the derivative dI_p/dt of the current I_p with respect to time as the electron beam passes over these holes. The welding parameters were such that the holes would be completely absorbed in the molten zone of the welding line. If the hole has a diameter and depth exceeding minimum values characteristic of each metal, a peak appears on the recording as the beam passes through it. This can be verified on Fig. 8, which shows, in the case of a semihard steel, recordings of the derivative of the current I_p with respect to time obtained when the beam does not meet and then meets calibrated defects. The peak height varies with the height and diameter of the hole and with the nature of the material. Figure 9, which gives the peak heights as a function of these three parameters, shows that the nature of the metal has more effect than the dimensions of the calibrated hole.

We verified experimentally that the appearance of the peak corresponds to an increase in the current I_p passing through the target, accompanied simultaneously by a decrease in the total current $(I_r + I_s + I_t)$ leaving it. This means that some of the incident backscattered, secondary, and thermal electrons are trapped in the hole. This trapped current is higher in absolute value for molybdenum and tantalum targets having a high thermoelectron power, as demonstrated on the recordings obtained for these two metals by the fact that the derivatives and therefore the peak heights are larger. It seems also that the current trapped is higher as the hole is less easily plugged with the liquid metal, i.e., as the melting point and the thermal diffusivity of the metal, separately or simultaneously, are higher. It should be noted that in the case of tantalum and molybdenum the thermoelectron current leaving the target is higher than the incident current, the result being that the current I_p passing through the target is opposite in sign to that observed for aluminum alloy or steel targets.

(2) Cracks Opening onto or Close to the Surface of the Target. Cracks were simulated by arranging a calibrated gap between the two faces of a flat joint perpendicular to the direction of welding as shown in the drawing of Fig. 10. With semihard steel and aluminum alloy we observed peaks on the dI_p/dt recording as the beam passed above

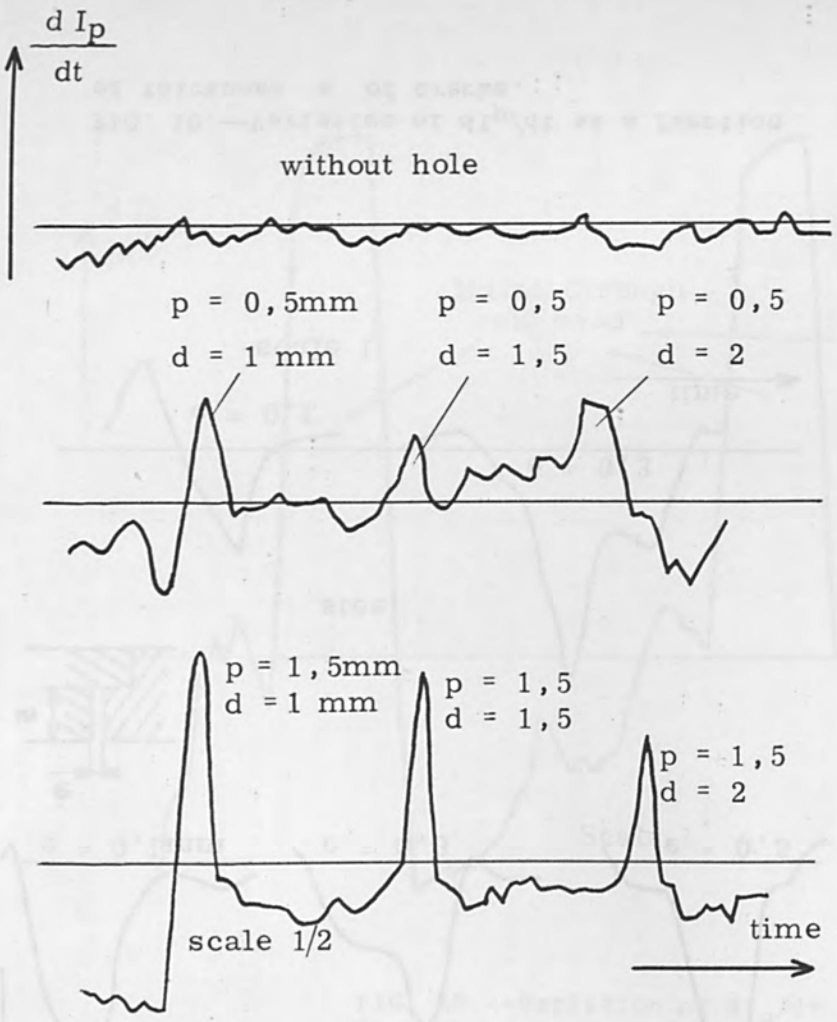

FIG. 8.—Recording of dI_p/dt in steel, one weld without hole and two welds with holes.

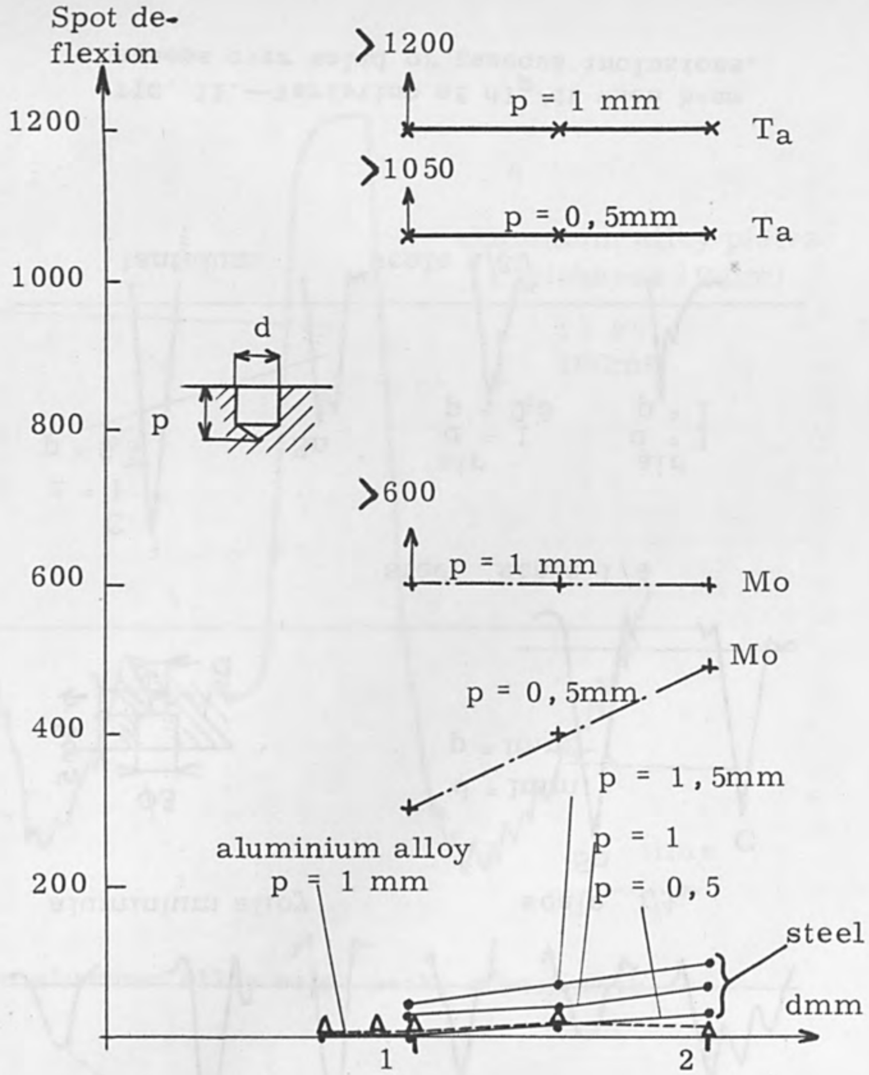

FIG. 9.—Recorder spot deflection as a function of hole depth and diameter.

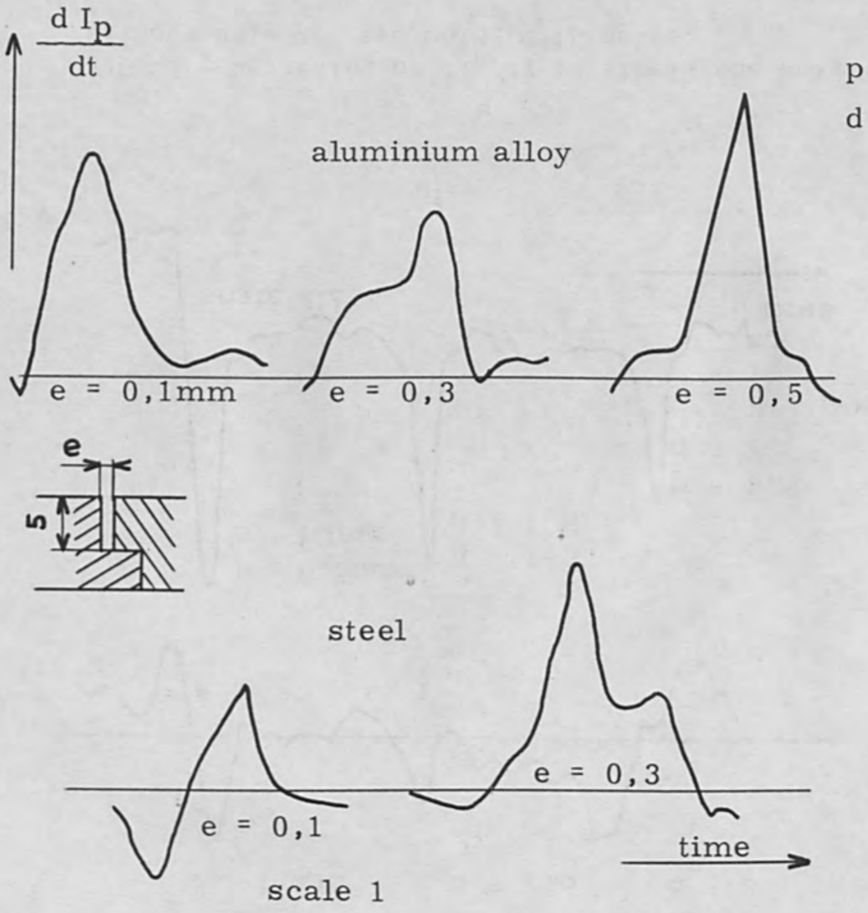

FIG. 10.—Variation of dI_p/dt as a function of thickness e of cracks.

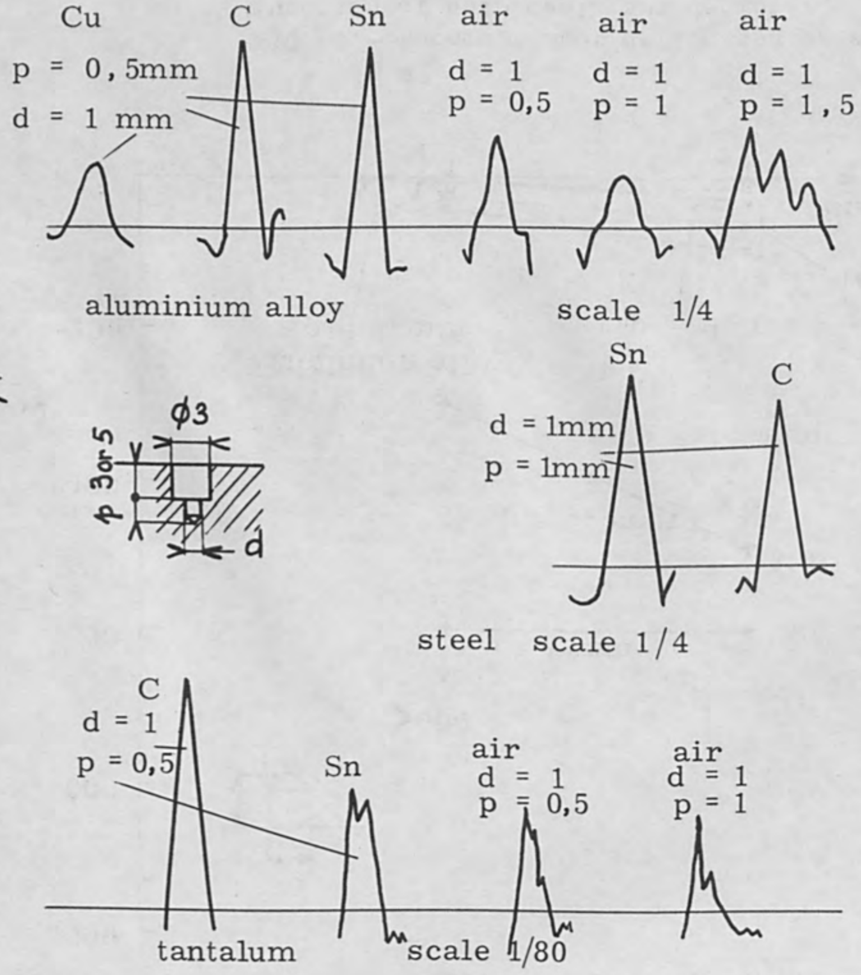

FIG. 11.—Variation of dI_p/dt when beam sweeps over solid or gaseous inclusions.

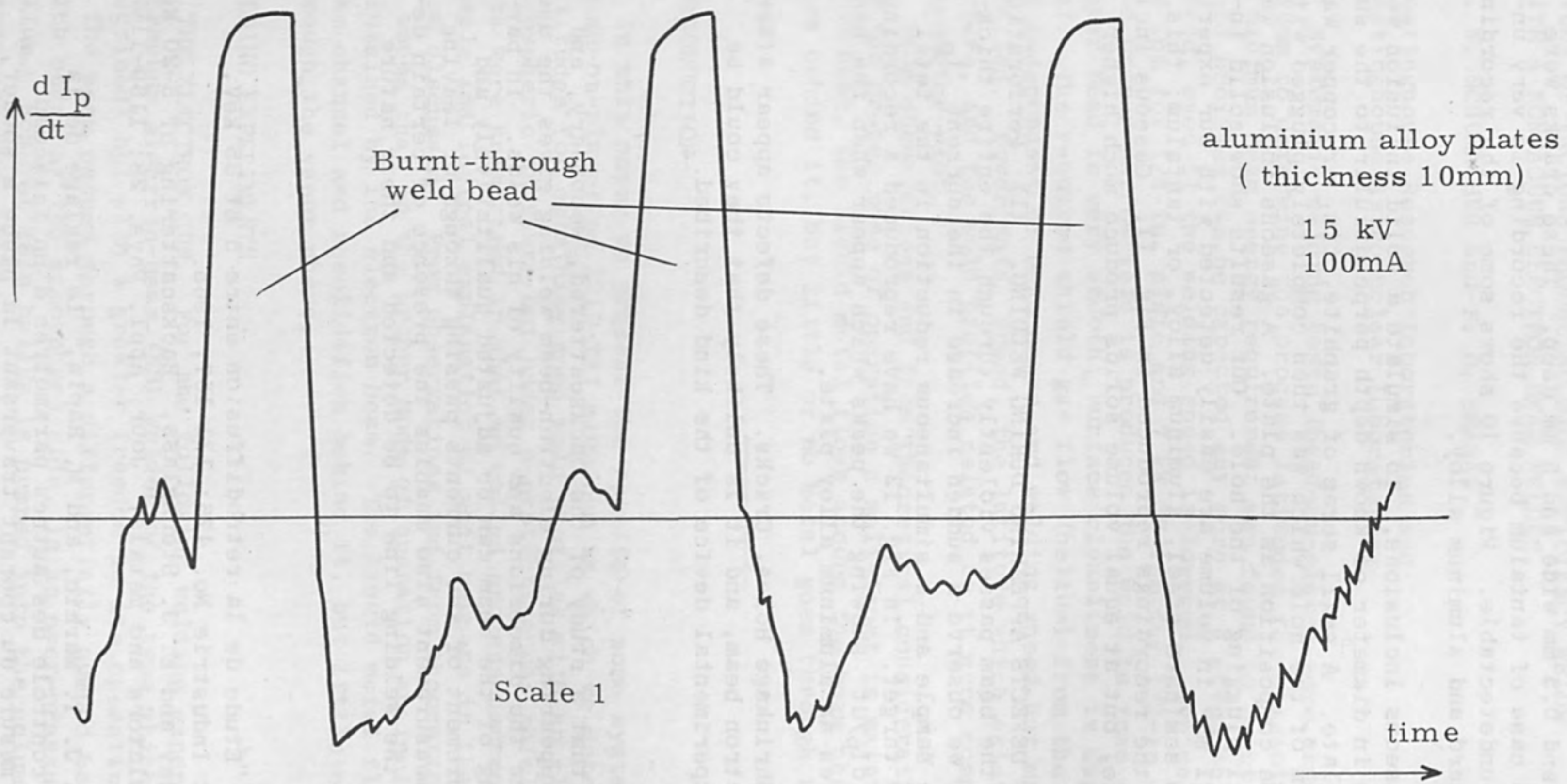

FIG. 12.—Variation of dI_p/dt in aluminum alloy weld: peaks appear with burn-through weld bead.

cracks between 0.1 and 0.5 mm wide and 5 mm deep. These cracks were not revealed in the case of tantalum because the recording is very uneven and the peaks undetectable. Figure 10 shows some of the recordings obtained with semihard and aluminum alloy.

(3) Solid or Gaseous Inclusions. To simulate a solid inclusion we drilled a hole 1 mm in diameter of known depth perpendicular to the surface of the metal plate. A small scrap of graphite, tin, or copper was placed at the bottom of the hole which was then completely plugged with material of the same composition as the plate. A gaseous inclusion was simulated by partial plugging of the hole. Our results show solid inclusions less than 1 mm^3 in volume are easily detected with our experimental apparatus in semihard steel, aluminum alloy, or tantalum; this can be verified on the recordings reproduced in Fig. 11. Gaseous inclusions are detectable, but at equal volume solids produce much higher peaks.

3. DETECTION OF DEFECTS APPEARING DURING WELDING. (1) Perforation of the Target. If the beam passes violently through the entire thickness of the target, we observe a sudden increase in the current I_p passing through the sample and a simultaneous reduction in the total current leaving the target. In Fig. 12 we have reproduced a recording of the derivative dI_p/dt showing the peaks which appear when the beam completely perforates an aluminum alloy plate.

(2) Blisters, Shrinkage Holes, Cracks. These defects appear after passage of the electron beam, and it is unlikely that they could be detected with an experimental device of the kind described.

IV. CONCLUSION

We have shown that a study of the backscattered, secondary, and thermal electrons appearing during electron-beam welding gives the user greater control over the dimensions and quality of his welds. In particular the focusing of the beam can be adjusted qualitatively and accurately by measurement of the currents passing through or leaving the sample. This measurement also enables the presence of certain defects appearing in the welding line to be detected and their nature analyzed.

REFERENCES

1. E. Weinryb, "Étude de la retrodiffusion entre 5 et 35 keV," Métaux-Corrosion et Industrie No. 476: 131-157, 1965.

2. J. E. Holliday and E. J. Sternglass, "Backscattering of 5-20 keV electrons from insulators and metals," Jour. Appl. Phys. 28: 1189-1193, 1957.

3. M. Boncoeur, J. Y. Marhic, and M. Rapin, "Le réglage de la focalisation et le contrôle des autres paramètres d'un faisceau d'électrons par la mesure du courant traversant la pièce à souder," Soud. Tec. Com. 5-6, 1969.

STUDY OF FACTORS PRODUCING HIGH EFFICIENCY WELDS WITH A NONVACUUM ELECTRON BEAM WELDER

B. W. SCHUMACHER and F. D. SEAMAN

Westinghouse Research Laboratories and
Westinghouse Astronuclear Laboratories

Systematic welding tests (bead-on-plate) were made on 2219-T87 aluminum to determine the process latitudes for obtaining good weld profiles. A minimum beam energy requirement was found to exist below which no good weld profiles can be expected any more at a given thickness of the work piece, even if the welding speed is lowered. Typical values are 4 kW 57 ipm for 1/4-in. plate and 7 kW 38 ipm for 1/2-in. plate. Whenever the proper narrow weld is produced the weld is free of porosity and the upper bead is very smooth; surface cleanliness is apparently not critical. The required shield gas flow (helium) from the electron gun nozzle is independent of beam power and welding speed but must be closely controlled. Power data, speed, the latitude which exists in these parameters, and the weld profiles related to it were compiled in a process parameter plot.

From observations and from theoretical considerations it seems that in the proper mode of operation a melt-front is maintained by the electron beam, the liquid metal flows around the beam channel and resolidifies behind it, but little or no metal goes through the vapor phase.

INTRODUCTION

In this paper we present the results of some systematic welding tests (bead-on-plate) on 2219-T87 aluminum in which we determined the process latitudes for obtaining good weld profiles with an electron beam at atmospheric pressure but under a protective gas shield of helium. The data were summarized in what we called process parameter plots. A simple and logical explanation of what happens in the welding process is also discussed. From observations and from theoretical considerations it seems that in the proper mode of operation an inclined melt front is maintained by the electron beam. The liquid metal flows around the beam channel and resolidifies behind it, but little or no metal goes through the vapor phase.

WELDING EXPERIMENTS

THE ELECTRON GUN. For the following welding experiments we used a nonvacuum electron-beam (EB) welder of the type which has been previously described[1] but with a greater freedom in its operating parameters.

The beam passes through a differentially pumped beam transfer column which ends, at the atmosphere side, in an over-pressure chamber with helium. Some of this helium is pumped into the column, some enters the atmosphere through the same hole as the electron beam. The effluent helium acts as a shield gas in the welding. If the effluent gas jet gets too violent it blows the liquid metal out of the weld. If the amount of effluent helium is not high enough it does not replace all the air in

Record of 10th Symposium on Electron, Ion, and Laser Beam Technology (L. Marton, ed.); San Francisco Press, Inc.
Copyright © by The Institute of Electrical and Electronics Engineers, Inc.—Printed in the U.S.A.

the gap between gun (beam exit nozzle) and workpiece. In a 1/8-in. air gap the electron beam would nearly double its width owing to scattering, as calculations show. If the helium pressure is so low that even some air is sucked into the transfer column, the beam power density is affected because of increased scattering inside the gun.

In all our tests the total helium flow was measured. In some cases the effluent part flushing the workpiece was determined separately. In some tests additional helium shield gas (not co-axial with the electron beam) was also applied, but had no effect on the welds.

MEASUREMENT OF BEAM CURRENT DENSITY. The EB current density was measured, prior to or after the welding, with a spinning disk which had a pinhole. It was moved quickly through the beam and the fraction of the current which passed through the pin hole was displayed on an oscilloscope. This yielded, after suitable calibration, the beam width and peak power density at any desired plane through the beam. The following data refer always to measurements at a level identical with the top surface of the work piece. Further details about gas flow and power density calibrations will be reported elsewhere.

WELDING PROCEDURES. Several series of welding tests were made. Three series comprised 60 to 100 welds each. This was followed by a number of shorter test series to check on the influence of just one or the other of the parameters. All together 420 welds have been produced; of these over 300 have been radiographed.

For each series of tests the beam power was set at definite values, for instance 7, 5, 4, and 3 kW, with the beam voltage maintained at 150 kV. The total beam power to the workpiece was measured prior to welding with a Faraday cup. Therefore different scatter losses in the beam transfer column would not affect the beam power used for welding. However the beam power distribution and the beam profile could well be different. The power density and beam width was measured, with the beam analyzer described above, at the end of each welding pass.

All welding tests were made as bead-through-plate in 2219-T87 aluminum, mostly with 1/4-in. plate and a gap of 1/8 in. between the beam exit nozzle and the workpiece. A few data were taken at 1/4-in. working distance and/or 3/8-and 1/2-in. plate. The distance was set for each weld to an accuracy of ± 0.01 in. by means of shims.

The upper surface of the workpiece was scraped to remove a heavy gray mill oxide film, in order to prevent it from interfering with the normal flow of metal and obscuring bead formation. In order to provide a source of H_2, which is a major source of porosity in aluminum, the underside was not scraped to remove the mill oxide. (The hydrogen comes from the moisture and hydrocarbons trapped in the mill oxide.) All the helium used was "welding grade." Gas lines were copper to minimize contamination of the gas during transmission to the gun.

With the above parameters at a fixed setting, a series of welds was produced by varying systematically the welding speed as well as the flow rate of helium into the overpressure chamber. Three to four-inch long bead-through-plate welds were made side by side, about 1/2 in. apart, on aluminum plates 4 X 12 in. in size.

RELATIONSHIP BETWEEN MEASURED BEAM CURRENT DENSITY AND WELD WIDTH. The appearance and quality of these welds was evaluated by visual inspection and classification. Where indicated, radiographs with a 2% sensitivity level for porosity were taken. Process parameter plots were developed, showing the latitudes in the process parameters graphically.

Typical operating parameters are listed in Table I. A transition from wide to narrow welding conditions occurred for Beam A very near 125 CFH total gas flow. Yet it does not seem that at that gas flow a significant change in the beam parameters occurred. The fact that for Beam A a slight peak in the power density occurs at 125 CFH can be interpreted that at this value the gun-to-work gap is just completely filled with helium. At higher helium flow (and pressures) the beam begins to deteriorate in the transfer column. For Beam B a slight peak occurs at 115 CFH total flow which is lower than for A because the beam nozzle was narrower. It was also observed that with a longer exit nozzle (e.g., 0.06 in. dia. x 0.25 in. long) the optimum flow was always less than with a shorter one, probably because it assured better laminar-flow conditions. The minimum helium flow rate at which a narrow weld could be produced (dependent upon beam nozzle diameter) was called "transition flow rate."

TABLE I.—Comparative characteristics of two electron beams (7 KW 150 KV, 0.125 in. nozzle-work spacing).

	BEAM A			BEAM B		
Pressure in transfer column	P_2 = 1.5 to 2.5 Torr			P_2 = 0.6 Torr		
Appearance of Welds	Maximum intensity (A/cm^2)	Beam width (in.)	Gas flow (CFH)	Maximum intensity (A/cm^2)	Beam width (in.)	Gas flow (CFH)
Wide weld (see Fig. 2 Weld 3-6)	6.6	0.0235	110	5.17	0.025	110
Narrow weld (see Fig. 2 Weld 3-7)	7.05	0.0200	125	6.35	0.024	115
Slightly excessive gas flow (see Fig. 2 Weld 3-10)	5.07	0.024	135	6.09	0.024	135
Excessive gas flow (more gouging than 135 CFH)	---	---	---	4.82	0.026	145
Greatly excessive gas flow (severe gouging)	---	---	---	5.05	0.025	155

Representative welds are shown in Fig. 2.

GENERAL OBSERVATIONS REGARDING THE NARROW WELD PROCESS. Since the objective of these welding series was to establish the influence of the machine settings and the process variables like power, welding speed, and workpiece distance on the appearance and quality of the welds, the welds were subdivided into the type-classification of Table II according to the appearance of the upper surface and the degree of penetration.

TABLE II.—Classification of welds.

Name	Description	Symbol Clear weld	 Porous weld
Type A	Wide Welds: penetration through the full workpiece thickness.	□	⊞
Type B	Wide Welds: incomplete penetration of the workpiece.	■	⯐
Type C	Narrow Welds: penetration through the full workpiece thickness.	◍	⌖
Type D	Narrow Welds: incomplete penetration of the workpiece.	●	⨁
Type E	Narrow Welds: undercut (gouged) upper bead surface; penetration through the full plate thickness.	△	⟁
Type F	Narrow Welds: undercut alternating with regularly spaced sectors of normal or excessive crown on the upper surface of the bead; incomplete or marginal penetration of the workpiece.	▲	⏶

Plots were made with gas flow on the vertical axis and welding speed on the horizontal axis. Each weld was entered in the plot with a symbol showing to what type it belongs. Porosity was also determined radiographically for these welds. Where porosity was found the symbol in the process-parameter-plot was given a superimposed cross mark.

This sorting process revealed some interesting relationships. First, it became evident that the change from the wide to the narrow weld configuration, as far as it is influenced by the helium gas flow, always occurred at the same flow regardless of welding speed and beam power. In other words, gas flow is not a process variable but rather a machine setting which is to be kept at a certain level within certain limits. The margins for this setting under various operating conditions will be discussed below. It became further evident that the tolerance for variations in welding speed are larger at higher power levels than at lower ones, which can also be understood.

EFFECTS OF SPEED AND GAS FLOW ON WELD APPEARANCE AT 7 kW OF POWER, 1/4-in. PLATE THICKNESS. Figure 1 shows a classification of the welds in a plot as just described. The symbols indicate the appearance of the weld, the location of the symbol indicates the process parameters under which it was obtained. The gas flow on the vertical scale is given as CFH above or below the transition gas flow, the point where the appearance of the weld changes from wide to narrow. The absolute value for this transition flow changes with the size of the beam exit nozzle as previously mentioned.

We see that symbols for similar welds are grouped in certain areas of this two-dimensional representation of process variables. These areas are indicated by dashed lines. However, these lines are not meant to suggest an abrupt transition but rather a transition zone. Typically for any welding process such transition manifests itself in an increasing probability for obtaining a particular type of weld as the variables are adjusted to move away from the boundaries and into the center of the various regions.

Of considerable importance is the observation that the transition gas flow falls on a straight line, in other words is constant and unaffected by speed or power. It is not a variable in the process but a machine parameter. Nevertheless, separating the results into these various areas suggests some important features of the narrow weld process as it is effected by the gas flow and speed.

As is the case with any fusion process, welds exhibiting lack of penetration become more prevalent as speed is increased, without regard to gas flow. However, changes in gas flow complicate this phenomenon. For example, as gas flow is increased above the transition line a narrow weld not fully penetrating the plate can be expected to increase in penetration. Especially the narrow gouging process (triangular symbol) goes from partial penetration to full penetration as the flow is increased, as shown by the line BD. In simple language, the high-speed gas jet blows the liquid metal out of the slot. In the range of the wide welds (square symbol) the gas flow apparently chills the workpiece so that gas flow must be reduced if the speed is increased in order to maintain full penetration. Shielding gas has a similar effect in the arc welding processes. As a result the boundary line from C to E has a negative slope.

Between these exposures lie the narrow, high-efficiency welds, as described above in Table II. Figure 2 shows typical cross sections for the various types of welds.

In Fig. 1 an extension of the line BD down to A on the transition-gas-flow line encloses the area of acceptable welds. The low-speed end of the process, at about 110 ipm, has been established by the appearance of the undercut. There were no wide welds to provide a better definition of this transition at the 7-kW power level. However it seemed remarkable that a direct transition from gouging to cutting might occur, if the process is slowed to a point that from the vastly overwelded joint the liquid metal falls out of the slot. In fact, later tests at 5 kW showed such an effect. Besides, the beam can begin to vaporize metal, leaving a hole.

From a practical point of view, Fig. 1 suggests that the process is more tolerant of a variation in speed than it is of a variation in gas flow. But this may have something to do with the way in which the gas flow was measured. The optimum gas flow appears to be 2 to 5 CFH above the transition.

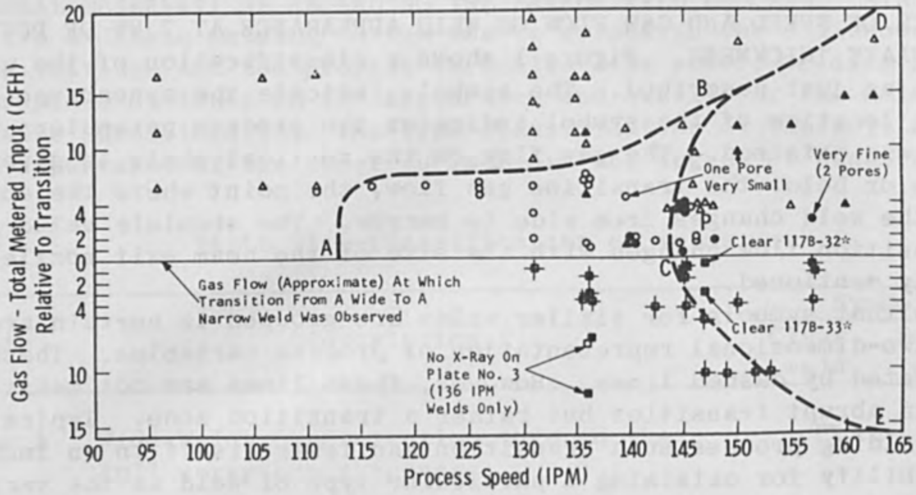

FIG. 1.—Classification of welds.

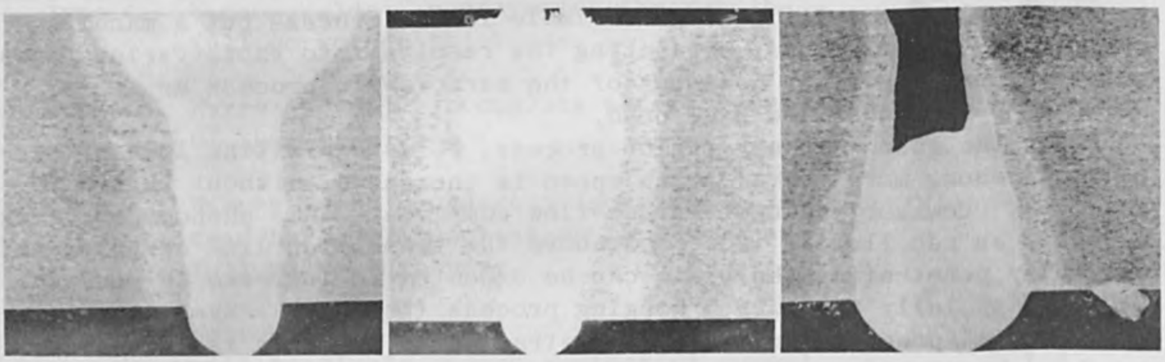

(a) (b) (c)

FIG. 2.—Typical cross sections through welds produced with Beam A of Table I at 136 IPM: (a) wide weld No. 3-6 (110 CFH total effluent gas flow); (b) narrow weld No. 3-7 (125 total effluent gas flow); (c) "gouge" weld No. 3-10 (135 total effluent gas flow).

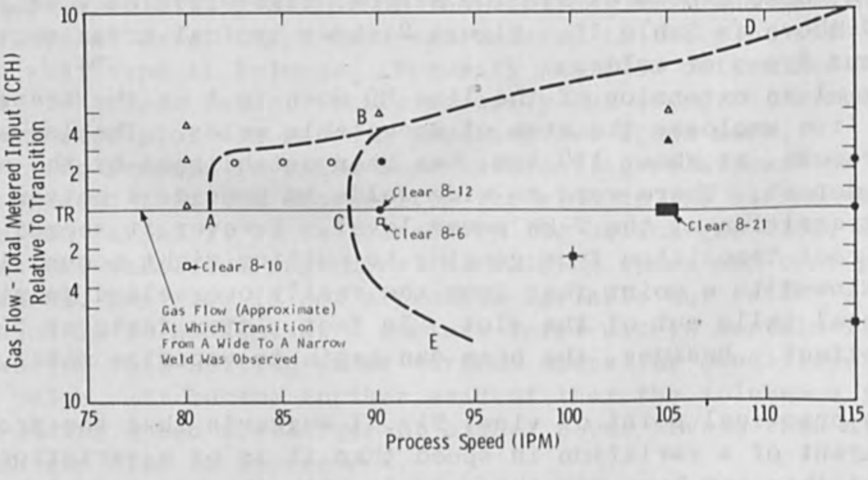

FIG. 3.—Process-parameter plot of weld configurations with welding speed and helium gas flow as independent variables; 150 kv, beam power 5 kW, 1/4-in. plate of 2219-T87 aluminum, 1/8 in. working distance. (For symbols see Table II.)

EFFECTS OF SPEED AND GAS FLOW AT 5, 4, AND 3 kW OF POWER, 1/4-in. PLATE THICKNESS. Welds made at a power level of 5 kW are classified in Fig. 3 in the previously adopted manner. There is a region A-B-C where acceptable welds can be produced. Point A, the slowest speed at which acceptable welds result, is 30 ipm slower at 5 kW than it was at 7 kW. But the high speed limit for the process has changed more. Point C moved from 145 ipm to 88 ipm, a reduction by some 55 to 60 ipm. Thus the speed range of the 5-kW process is only about 10 ipm, whereas the range of the 7-kW process was 35 ipm. This suggests that the process cannot be applied below some minimum power. Assuming a continued, proportional reduction in latitude the lowest level would appear to be 3 kW. Further tests with 4 kW of power showed that there is only a 9% latitude in speed left where the process gives acceptable welds. In 36 tests with 3 kW of power no acceptable welds could be obtained.

EFFECT OF SPEED AND GAS FLOW AT 7 kW OF POWER, 3/8- AND 1/2-in. PLATE THICKNESS. Some welds were produced in 3/8-in. thick plate of 2219-T87 aluminum following all the procedures described before. To get full penetration in this thicker plate at the 7 kW power level requires, of course, a slower welding speed. The classification of the welds made on 3/8-in. plate is shown in Fig. 4. The over-all effect of increasing plate thickness is much like reducing power; with the 1/2-in. plate the welding process at 7 kW performs much as the 4 kW does on 1/4-in. plate. The power level of 7 kW is marginal for welding 1/2-in.-thick materials, but narrow welds were produced successfully in 1/2-in.-thick plate at this relatively low power level and could be easily produced at slightly higher power levels. A cross section through some of several narrow welds is shown in Fig. 5.

EFFECT OF CHANGE OF WORKING DISTANCE FROM 1/8 TO 1/4 in. For all the work discussed so far the working distance, i.e., the gap which the beam must cross from the beam exit nozzle to the workpiece, was 1/8 in. If it is increased to 1/4 in. the welding speed must be reduced to get the same penetration. At 4 kW for 1/4-in. plate little, if any, process latitude remains. Further studies were not made at this time.

PROCESS LATITUDES. The latitude which the narrow-weld process permits in the setting of gas flow rate and process speed varies with power, and the relevant data are summarized in Fig. 6. That there is a minimum power below which the process no longer works at all, is understandable on the basis of energy-balance considerations to be discussed below. Tolerances for variations in the process variables as a function of plate thickness are shown in Fig. 7 for the 7-kW process.

As is evident even from these limited data, it is always advantageous to have excess power available and run at higher speeds.

EFFECT OF SPEED AND GAS FLOW ON POROSITY. The welds are subjected to radiography at the sensitivity level of 2-2T (that is, using an appropriate penetrameter with a thickness equal to 2% of the specimen being radiographed and adjusting the radiographic procedure so as to define a hole in the penetrameter with a diameter equal to twice the penetrameter thickness). In reading the radiographs data were taken from a 1.5-in. section of weld. The first 1/2 in. of weld was disregarded, as was the last 1/2 in. of the weld, to avoid end effects caused by the entry of

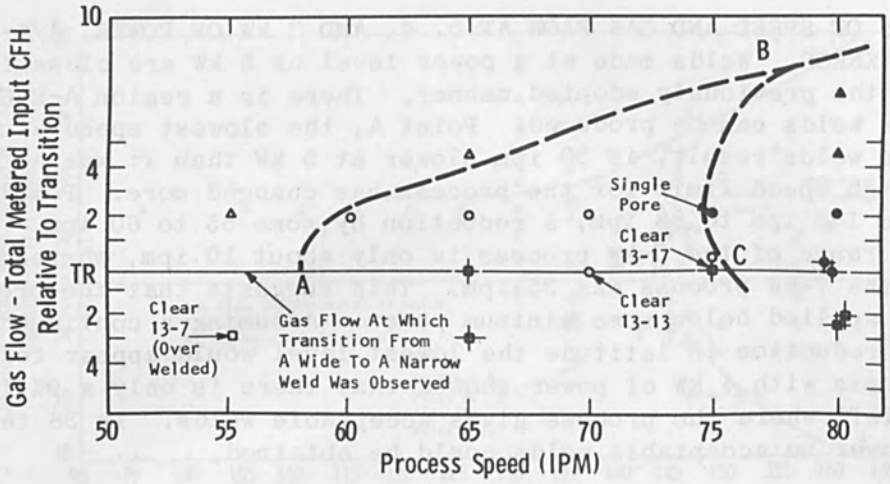

FIG. 4.—Classification of welds, 3/8-in. plate.

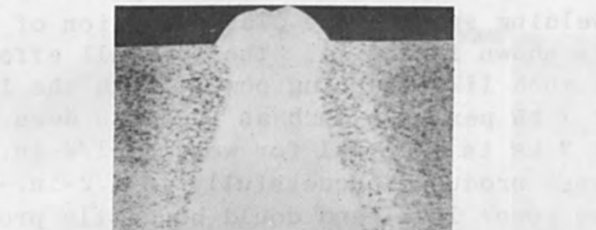

(a)

(b)

FIG. 5.—Cross sections of narrow welds in 2219-T87 aluminum: (a) 7 kW, 150 kv, 39 IPM, 1/8 in. working distance, 1/2-in. plate; (b) two welds, both at 7 kW, 150 kv, 140 IPM, 1/8 in. working distance, 1/4-in. plate.

the process onto the plate (and by its termination in the plate) influencing the results. Gouged welds were not subjected to individual interpretation if it appeared from the film that the joint thickness was beyond the limits of radiographic sensitivity. All visible porosity was noted. The detectable minimum was about 0.030 in. The number, distribution, and size of the pores were noted. However, it was felt that the sample size (length of the weld) was too small to permit conclusions to be drawn regarding trends in these effects. Therefore only the presence or absence of porosity in the sample is reported. Only in some exceptional cases, which seemed anomalous, the severity of the porosity (which was always very low) was noted.

In order to display any relationship that might exist between porosity and the major process variables, the existence of porosity in a particular weld was marked in our process parameter plots by a vertical cross over the symbol of those welds which showed porosity. The symbols of clear welds were left unchanged.

The most remarkable result is that no porosity appears as soon as the process yields a narrow weld. Even where the narrow-welding process becomes marginal, as with lower power or thicker material, porosity is low; most of the narrow welds in 1/2-in.-thick material produced with 7 kW of power would meet conventional aerospace porosity standards and would easily meet the ASME Code for Unfired Pressure Vessels.

It is quite plausible that when the process latitudes become marginal the probability that instabilities can trap vapor or gas during the freezing process is greater, and thereby produces pores. The welds made at 7 kW of power in 1/2-in. materials were indeed made where the tolerance limits of the process are very narrow. In addition, in thicker material the height of the column of liquified metal is longer and therefore more likely to be unstable; at the same time the cooling rate increases as a result of the larger mass of metal. The first condition would encourage the formation of cavities and the second would tend to trap them in the weld. Unfortunately we could not extend the present studies at this point to include welds made with higher-power beams.

THE WELD PROCESS

GENERAL CONSIDERATIONS. It has been indicated in earlier papers that electrons with an energy of the order of 100 keV which arrive at a metal surface at a relatively low rate, say with a current density of 1 mA/cm^2, will only penetrate into the metal to the depths of their so-called range, this being in the order of 100-200 microns, or a few milligrams per square centimeter. For these very low beam currents the penetration range depends upon the kinetic energy of the individual electron (given by the beam voltage). When the beam-current density becomes high the range depends also on the current as has been mentioned and observed many years ago;[2] if the high-power beam hits a stationary metal target it melts and finally vaporizes the metal and drills a hole. This continues as long as the beam stays confined enough and has enough power to vaporize the metal in its path.

Vaporization of the target by a high-power electron beam was used for drilling holes of small diameter (e.g., through 1-in.-thick quartz glass) long before it was ever used for welding. It is impossible for 100-kV electrons to penetrate through either liquid or solid metal to any appreciable depths. Any statement to the contrary is misrepresenting the

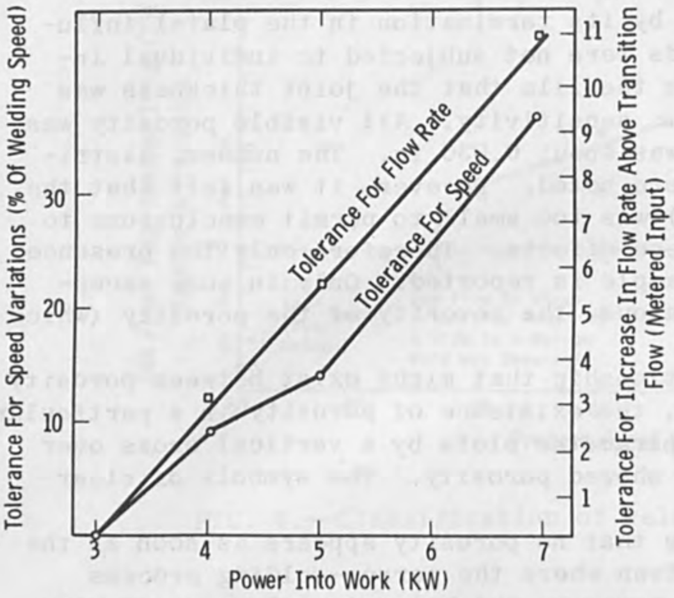

FIG. 6.—Process latitudes of narrow welds.

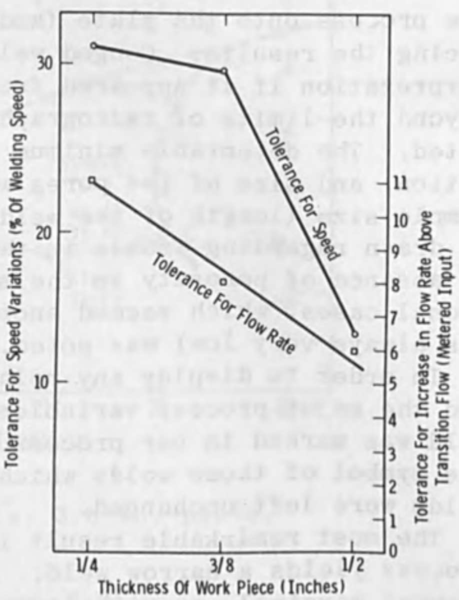

FIG. 7.—Tolerances for narrow-weld process.

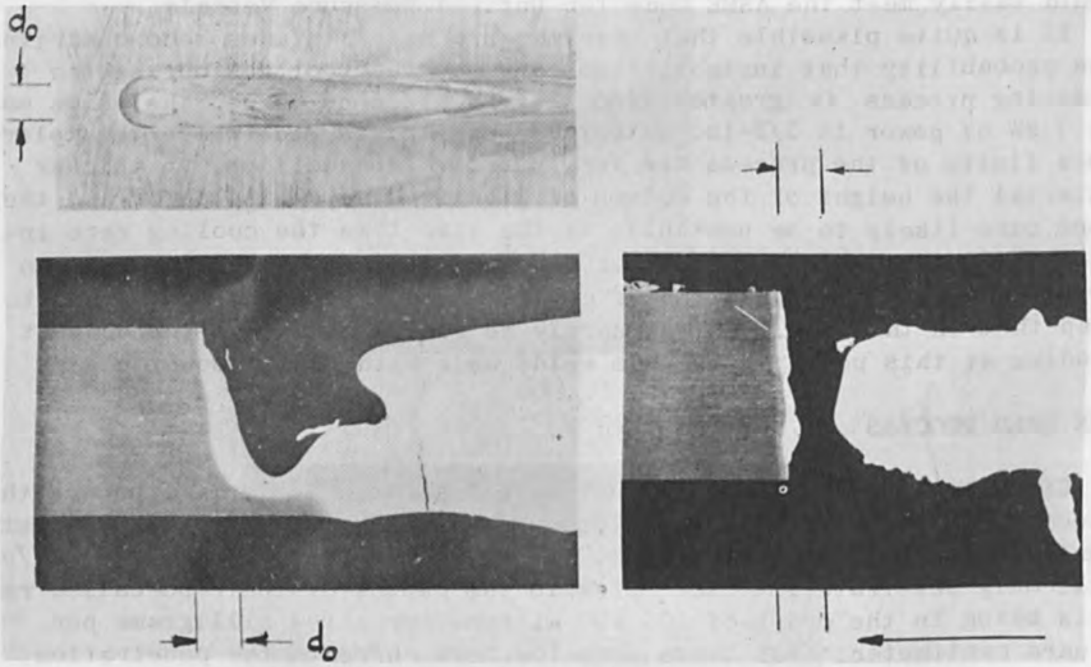

FIG. 8.—Upper left: weld termination (beam turned off) from the top; beam moves from right to left; inclined melt front on the left. Bottom left: cross section through similar weld termination in 1/4-in. plate; since beam diameter b_0 is only 0.06 in., it is evident that without scattering all of the beam inpinges on slanted front face; scattering in the gas may broaden impingement area somewhat, but not much, as calculations show; scattering from solid or liquid impingement area may amount to 10-30 per cent in all directions. Bottom right: cross section through termination of gouge weld; inclined melt front is too steep to intersect all of the beam (feed rate of cold metal not high enough), leading to over-melting and burn-through on the bottom; shape of re-solidification front is essentially determined by surface tension forces.

physical facts.

In a recent paper we have discussed at which power density level the laws for the penetration of the individual electrons become invalid and power phenomena begin to appear.[3] The power density in EB welding is always so high that power phenomena dominate.

Since a beam channel or hole has to be formed first the EB welding process has been called a "keyhole" process. It is usually assumed that the beam channel is filled with metal vapor. But even then, as shown by Schwarz,[4] most of the energy of the electron beam is deposited at the bottom of this hole and little energy is absorbed in the metal vapor itself. This can hardly be otherwise, because energy absorption from the electron beam is associated with scattering which would limit the power density and the range of the beam. We have recently confirmed this fact by a theoretical study on the electron scattering in the weld zone[5] and by some observations on electron beams under water.[6] That the EB energy is mainly deposited at the bottom of the welding cavity implies also that we cannot rely on electron scattering to distribute this energy equally over the depths, or over the wall area, of the weld cavity. Hence we face the very interesting question, how this energy is, in fact, distributed. Schwarz[4] has argued that the vapor produced at the bottom of the cavity and hitting the walls in the upper region of the cavity can account for the energy transport. This may be compared to a violent boiling process, and indeed Schwarz has shown motion pictures of in-vacuum welding where the cavity is closed by a liquid metal film which is periodically rupturing owing to the vapor pressure. Although this mechanism seems to explain the energy redistribution properly, it presupposes that the weld cavity is closed at the bottom, even in a full-penetration-weld with a noticeable underbead, and that capillary forces are holding the liquid in the welding gap. It is understandable that this mode of operation requires a rather delicate equilibrium between power input and melting rate, i.e., welding speed.

WELDING WITH A MELT-FRONT. In welding aluminum in air (under helium) with a 0.08-in.-wide beam and a weld depth of 1/4 to 1/2 in. the top of the keyhole cavity is certainly not closed by a liquid metal film, as one can readily observe by eye (and a small telescope). The open top forms such a large escape hole that a process of energy redistribution by means of vapor can hardly be effective.

We believe there is another mechanism for the energy distribution, as follows. The electron beam, which has a finite width and is moving forward at a finite speed, produces an inclined "melt front" in the forward direction of the beam movement. If this front is properly sloped in relationship to beam width and speed, then the beam energy is distributed over the full height of the front. A combination of vapor pressure, gas pressure, beam pressure, and surface tension causes the liquid metal to flow around the center of the beam to the rear, where it resolidifies. Next to no metal needs to be vaporized, except perhaps in the beginning when the beam cavity is initially formed. Even this seems unnecessary if the beam cuts into the metal piece from the edge.

Many observations suggest that there is indeed an inclined melting front in the forward direction of the beam movement. Such a front can be seen whenever the beam power is suddenly shut off; then the weld terminates in a crater with a sloping front. Very often a hole right through the metal is seen (which means no liquid metal at the bottom of the weld cavity), and a rearward face which looks as if it were mainly formed by surface tension. Figure 8 shows cross section and top view of a weld termination showing this sloping front face. The above description of the melting process is also consistent with the observation that when "good welds" are made little "smoke" is seen and no black deposits afterwards. The hydrodynamic process which accomplishes the metal transport will need some further study and will not be further discussed here, but it may be noted in passing that the triangular groove which can be observed on the surface near an abrupt termination of a weld (e.g., Fig. 8) resembles the funnel which can be seen on the inlet of continuous casting machines; there it is a prerequisite for a sound, pore-free casting.

We may ask now what conditions must be fulfilled to achieve and to optimize this mode of operation. Another question would be whether this mode of operation promises advantages over a mode with violent boiling. Obviously, power input, traveling speed, and workpiece thickness are again most critically interrelated. Because there is a postulated geometrical relationship between the beam diameter and the slope of the melt front one would also expect that this process might be more stable if the diameter of the electron beam were not too small compared with the depth of the weld. The process may therefore be most suitable for producing welds with depth-to-width ratio in the order of 2:1 to 4:1 as was the case in the above described experiments.

ENERGY RELATIONSHIPS REGARDING MELTING, VAPORIZATION, PENETRATION-DEPTH AND WELDING SPEED

MINIMUM THEORETICAL ENERGY EXPENDITURE. A narrow weld or cut in 2219-T87 aluminum, made in atmosphere under helium shield gas, is typically 0.08 in. wide. A simple calculation shows how much energy is needed to melt a 1-in. long slot of this width in a 1-in.-thick plate, assuming all the energy goes for melting and nothing is lost by heat conduction, namely 3.54 kW-sec/in./in. For the 0.25-in.-thick specimens used in our tests this means a minimum of 0.885 kW-sec/in. to melt a 0.08-in. slot. As seen from the tests it takes a minimum energy expenditure of 18 kJ/in./in. (or 4.5 kJ/in. in 1/4-in.-thick material) to produce a weld at the lowest possible power level which the process will permit, namely 3 kW, at a speed of 0.66 in./sec. Hence under those conditions the process is less than 20% efficient, 80% of the energy is carried away by heat conduction. At higher power and speed (7 kW, 2.3 in./sec) the energy expenditure is only 3 kJ/in., which means the energy efficiency has risen to 30%. We know from other experiments that the efficiency improves at higher powers and welding speeds.

The conditions under which 100% energy utilization can be achieved have been analyzed recently.[3] In short, the energy must be supplied to the surface at a rate sufficiently high or within a time interval sufficiently short so that during the melting process no significant amount of heat is lost by conduction. For example, with a 9-kW beam going into a 1-mm^2 spot on a molybdenum surface it would require a time of $\Delta T = 3 \times 10^{-5}$ sec to bring the molybdenum to the melting point. This time is not short enough to make the energy transfer quasi-adiabatic, i.e., insensitive to heat conduction. The power density would have to be increased by an order to magnitude to achieve quasi-adiabatic melting. We see that in this respect theory and experimental observations are compatible.

Let us finally look at the postulated sloping-front theory of narrow, out-of-vacuum welding in the view of the energy transfer calculations of Klemens.[7] In the narrow welding mode that part of the energy which is not used for melting never goes into vaporization (at least not a significant amount) as Klemens has shown. He also showed why a minimum power density in the beam is a prerequisite for deep penetration, in case vaporization temperatures are reached or exceeded, and in case we have a vapor-filled keyhole. But apart from the power density argument Klemen's calculations, including the relations for the change in depth with welding speed, remain valid also in the case of a sloping-melt-front process. The absolute values of the welding speed and the width of the weld depend, of course, upon power density as well as upon power.

CONCLUSIONS

The latest EB welding tests at atmospheric pressure have shown that narrow welds with high depth-to-width ratio can be produced within a fair range of the process parameters.

A controlled flow of helium from the exit gas nozzle of the welder was necessary to produce the narrow welds over a variety of power levels and weld speeds. The controlled helium flow rate must replace the air between the electron gun and workpiece; calculations of electron scattering showed that the beam would roughly double its width across a 1/8-in. air gap. In addition, the controlled exit gas flow may be replacing the metal vapor in the beam path, thus again reducing beam scattering.

The possibility of hydrodynamic effects caused by the gas flow could not be directly observed within the scope of this program. It is obvious, however, that the narrow gouge-type welds or cuts which occur at higher helium flow rates are related to the exertion of excessive force on the liquid metal. The proper exit gas flow required to transform the welding process from a wide to a narrow weld was found to be the same for all beam-power levels and welding speeds; it may be considered a machine parameter.

For a given workpiece thickness, the process requires a minimum beam power below which narrow welds can no longer be obtained at any combination of speed, gas flow, or power. For every beam-power level above the minimum, there is a range of welding speeds within which narrow welds are obtained, the latitude in the operational parameters being larger at higher powers and faster welding speed. The practical minimum power for getting narrow welds in 1/4-in. plate of 2219-T87 aluminum is 4 kW (speed 57 ipm); for 1/2-in. plate it is near 7 kW (speed 38 ipm). At 7 kW, 1/4-in. plate can be welded conveniently (speed 120 to 145 ipm).

These data refer to 1/8-in. gun-to-work distance and 150-kV electron beams; yet even at 1/4-in. gun-to-work distance, narrow welds could still be obtained.

At the termination of the welds, a formation can be seen that looks like a resolidified melting front, inclined in the forward direction. It seems that the projection of this melt-front onto a plane perpendicular to the beam is as wide as the electron beam, and that the beam melts the metal over the full depth of the weld more or less uniformly. This finding would be compatible with various considerations about the energy transfer from the electron beam to the metal.

The molten metal appears to flow around the beam region and resolidifies in the rear. It seems significant that if this model of the welding process is correct, vaporization of metal is not a condition for narrow deep welding, at least out-of-vacuum. It would avoid local overheating and boiling, therefore give smoother weld beads, and reduce the likelihood of entrapped vapor causing porosity, in agreement with the observations.

Radiography showed that all narrow welds which were produced, and even some of the wide ones, were free of porosity. In this connection, it is also important that no particular care was taken to clean the plates prior to welding.

The process latitudes at each power level and specimen thickness, as a function of welding speed, work distance, and gas flow setting can be clearly displayed in graphs so that the process can be applied with confidence.

ACKNOWLEDGMENTS

The authors express their most sincere appreciation to Mr. C. R. Taylor for the conscientious and careful performance of all the welding experiments reported herein. The study has been financed in part by NASA/MSFC under Contract NAS8-11929, Task F.

REFERENCES

1. J. Lempert, IEEE Transactions IGA-3: 438, 1967.
2. B. W. Schumacher, Ann. Phys. 13: 404, 1953.
3. B. W. Schumacher, "Power density limits for the particle penetration laws and the onset of energy phenomena in electron beam targets," in Electron and Ion Beam Science and Technology, Third International Conference, R. A. Bakish, Ed., New York: Electrochemical Society, 1968.
4. H. J. Schwarz, "Mechanism of high-power-density electron-beam penetration in metal," in Electron and Ion Beam Science and Technology, R. Bakish, Ed., New York: Wiley and Sons, 1965.
5. D. C. Schubert and B. W. Schumacher, "Effect of electron scattering in the metal vapor on the energy dissipation in the cavity present during electron beam welding," in Electron and Ion Beam Science and Technology, Third International Conference, R. W. Bakish, Ed., New York: Electrochemical Society, 1968.
6. B. W. Schumacher, "Some observations on high-power electron beams under water," ibid.
7. P. G. Klemens, "Energy considerations in electron beam welding," ibid.

CORRELATION BETWEEN DIMENSIONS OF AN ELECTRON BEAM AND THOSE OF WELDS OBTAINED WITH IT

M. BONCOEUR and M. RAPIN

Commissariat d'Énergie Atomique, Paris

I. INTRODUCTION

Among all the other welding parameters, the dimensions and the current-density distribution of the electron beam in planes normal to its axis must have a considerable influence on the dimensions and quality of the weld. Several authors have described devices by which these two characteristics can be measured.[1-5] So far however the systematic study of the envelope of the beam and its current-density distribution variation in different cross sections normal to its axis, and also the establishment of correlations between these two characteristics and the dimensions or quality of the welds, seem to have been neglected, and very few publications have appeared on the subject. We propose to describe some of the results we obtained in the course of such a study carried out for beams from a Pierce-type gun.

II. EXTERNAL FORM OF THE BEAM

We studied two beams produced in vacuum by a Sciaky-SV 3 gun built according to the principles laid down by Pierce. The electrical power involved in their production was 1.5 and 2.3 kW, respectively, and they were obtained with the parameters shown in Table I. If we assume that the beams are axially symmetrical, the beam envelope is known when we know the dimensions of an axial cross section. We plotted the latter after measuring the diameter of the beam at increasing distances from the electron gun, using the device shown in the diagram of Fig. 1.

TABLE I.—Parameters used to produce the two beams with a Sciaky-SV 3 gun.

	BEAM 1	BEAM 2
Electrical power in kW	1.5	2.3
Acceleration voltage in kV	16.2	19.3
Bombardment current in mA	90	120
Focusing current in A	2.90	3.35

A rapidly rotating 350-mm-diameter copper disk cuts into the beam perpendicularly to its axis. The maximum diameter of the beam in one of its cross sections equals the length along which the disk must be displaced in order for the current collected in the Faraday cage to decrease from its maximum value to zero. The curve giving the variation of the current collected in the Faraday cage as a function of the length of penetration of the disk into the beam is recorded on a galvanometric apparatus. In order to eliminate errors owing to inaccurate localization of the points where the current collected is at a maximum or zero, we plotted the first derivative of the above curve and assumed arbitrarily

Record of 10th Symposium on Electron, Ion, and Laser Beam Technology (L. Marton, ed.); San Francisco Press, Inc.

Copyright © by The Institute of Electrical and Electronics Engineers, Inc.—Printed in the U.S.A.

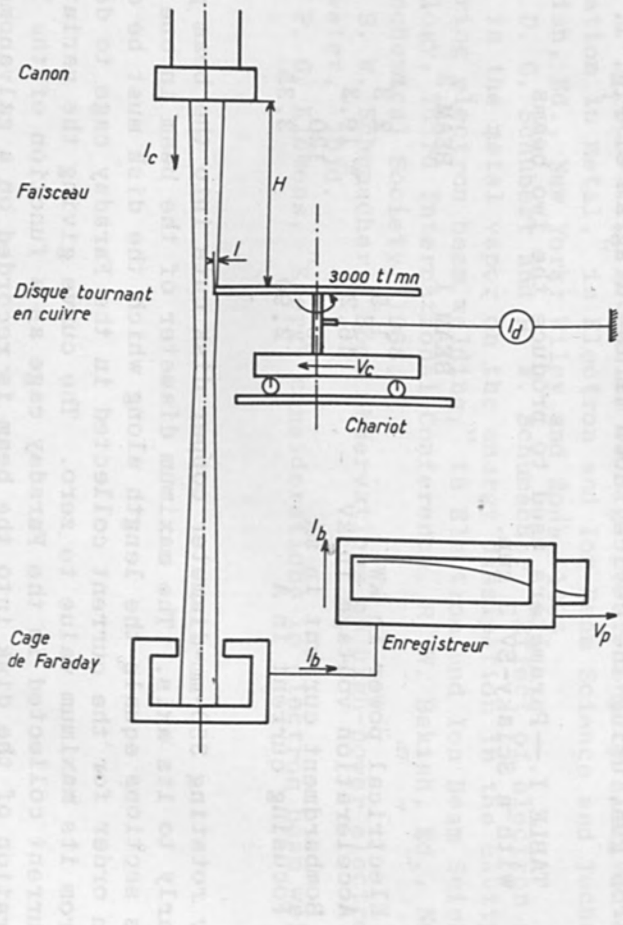
Canon
I_c
Faisceau
H
l
Disque tournant en cuivre
3000 t/mn
I_d
V_c
Chariot
I_b
Enregistreur
V_p
Cage de Faraday
I_b

FIG. 1.—Experimental device.

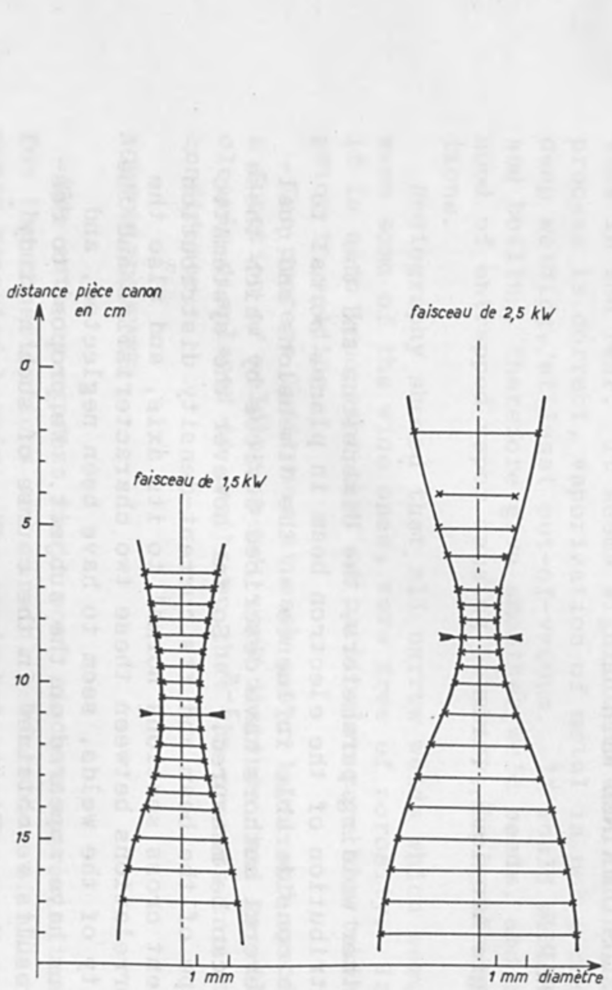

FIG. 2.—Axial cross sections of the two beams.

that the beam diameter was the width of this derived peak measured at a distance from its summit equal to 95% of its height.

The axial cross sections of the two beams are plotted in Fig. 2. In both cases we observe a narrow region about 1.1 mm in diameter and 20 mm long. Above and below this region the beams widen rapidly.

III. CURRENT-DENSITY DISTRIBUTION IN THE BEAM

We attempted to calculate the current-density distribution in the electron beams at various distances from the gun. We used the method described by Harker,[6] which allows this distribution to be obtained from the derivatives of the current mentioned above. The current densities calculated by this method are subject to numerous errors of a magnitude difficult to estimate, which means that the value of the current density distributions is only semiquantitative. However, for a given beam they can be compared, and it is possible to follow their variation for beam cross sections situated at increasing distances from the electron gun.

Figure 3 shows the curves giving the current density distribution in cross sections of the 1.5 and 2.3 kW beams situated at various distances from the gun. The current density is low but relatively uniform over the whole cross section for the region near the gun. It reaches its maximum value in the narrowest section of the beams. Beyond this it decreases at the center of the beam but does not tend to become uniform again throughout the cross section.

IV. DEPTH AND WIDTH OF WELDS AS A FUNCTION OF THE BEAM DIAMETER IN THE WELDING PLANE

Figure 4 shows the curves giving the depth of welds made in stainless steel and in uranium with a 2.3-kW beam, as a function of the beam diameter, measured in the plane of the welded sample. The number beside each point refers to the distance in centimeters between this plane and the lower face of the gun. We observe that the weld depth does not increase regularly with the inverse of the beam cross-section diameter in the welding plane, as we might have expected, and in particular the deepest weld is not that obtained when the surface of the sample lies in the smallest cross section. The curve presents three parts. In the first the weld depth increases inversely as the diameter, up to a maximum value reached when the weld is made in the plane containing the smallest cross section of the beam. This first part corresponds to welds made when the welding plane lies between the gun and the narrow section of the beam. The second part of the curve lies above the first: the depth increases as the beam diameter decreases, and reaches a maximum for a beam cross section greater than the narrowing zone. This is the highest value on the entire curve and is obtained when the welding plane is situated at a distance between 10 and 15 mm from the narrow section. This second part of the curve corresponds to welds made in planes lying beyond the minimum cross section. The third part is more or less rectilinear and joins the two points corresponding to the two maximum depths observed on the first and second parts of the curve. It must be noted that in this part the weld depth increases with the diameter of the beam cross section. It is important to observe that the penetration depths are different for welds carried out in two planes of equal beam cross-section diameter, one lying above and the other below the narrow section.

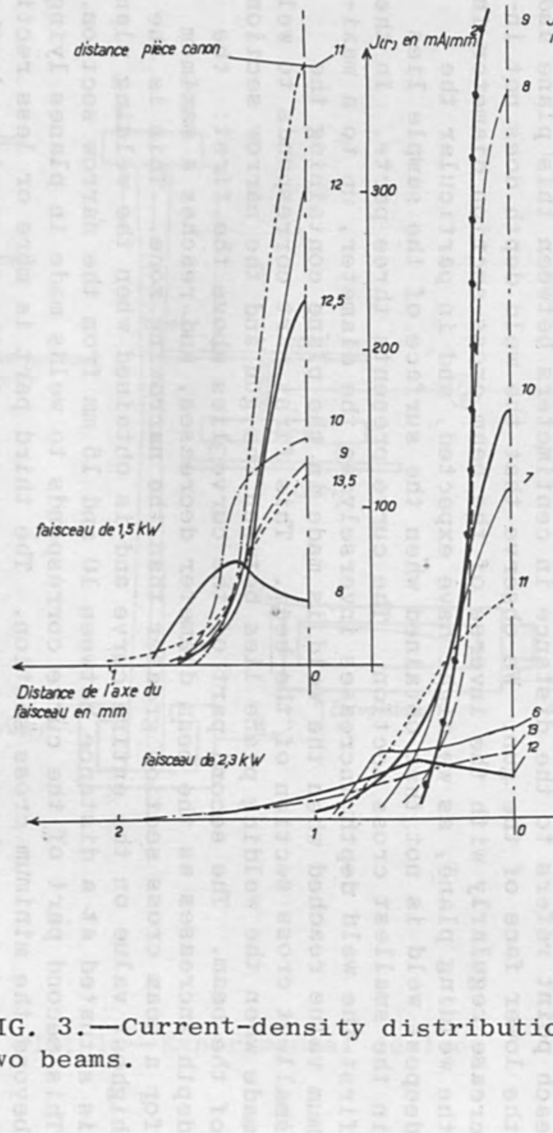

FIG. 3.—Current-density distribution in the two beams.

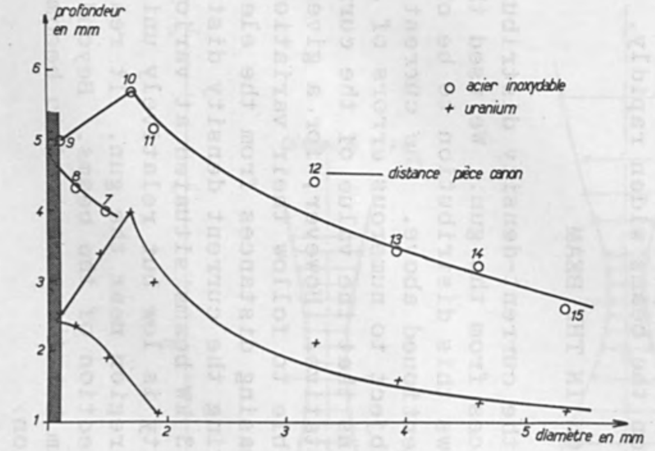

FIG. 4.—Weld depth as a function of the beam diameter in the welding plane (2.3-kW beam).

The diameter of the beam in the welding plane does not therefore account for the variations in the weld dimensions. The curves of Fig. 5, which we plotted for welds made in stainless steel, uranium, and aluminum alloy with the 1.5-kW beam, are similar to those of Fig. 4, which confirms this result.

On Fig. 6 are plotted the curves showing the width of the welds, measured on the surface of the sample, as a function of the 2.3-kW beam diameter. We notice that the curves present three distinct parts having as abscissas the same limiting diameters as those seen on Fig. 4 for the curves giving the weld depths. We also plotted the straight line corresponding to an equal width of the weld and the beam. We observe that welds made in uranium and stainless steel can be narrower than the beam diameter when this becomes large. It is probable that the electron density is low on the periphery of the beam, and that electrons located on the outside of a cross section approximately as wide as the weld are absorbed or reflected by the target without causing the metal to melt.

V. INFLUENCE OF THE CURRENT DENSITY DISTRIBUTION ON THE DIMENSIONS OF THE WELDS

In Fig. 7 we again plotted the curves giving the depths of the welds as a function of the beam diameter in the welding plane, for welds made in uranium with the 2.3-kW beam and for those made in aluminum alloy with the 1.5-kW beam, respectively; near each experimental point we have sketched the curve giving the current density distribution at this point and shown the calculated value of the maximum current density on the beam axis. We prove that the mean current density and the current density on the axis are the highest in the narrow section of the beam, but the greatest weld depths are obtained when the welding plane passes through beam cross sections with lower current densities. On the curve obtained with the 1.5-kW beam we observe that, for a given beam cross-section diameter, the welds are deeper when the current density is very high near the beam axis than when it is low and uniform throughout the cross section. The same result can be seen on the curve plotted for the 2.3-kW beam.

The diameter of a beam of constant power, measured under the conditions described in Sec. II, gives no indication on the concentration of power in the beam. Our results show that the penetration is greater as the current density, i.e., the energy, is concentrated in the beam. When the total power is constant this concentration rises as the beam cross section decreases and as, within this cross section, the current density is concentrated near the beam axis. To account for these two power concentration parameters it would be better to define the beam diameter, in a given welding plane, as the diameter of the cross section inside which passes a defined proportion of the power of the beam. To achieve this, using the curves showing the current density distribution in various cross sections of a beam, we would have to plot the curves giving the power distribution in the same cross sections. It would then suffice to measure the diameter of the cross section containing the proportion of power defined. For the two beams studied the relative positions of the diameters measured remain the same whatever the definition chosen for the diameter, and our conclusions are identical.

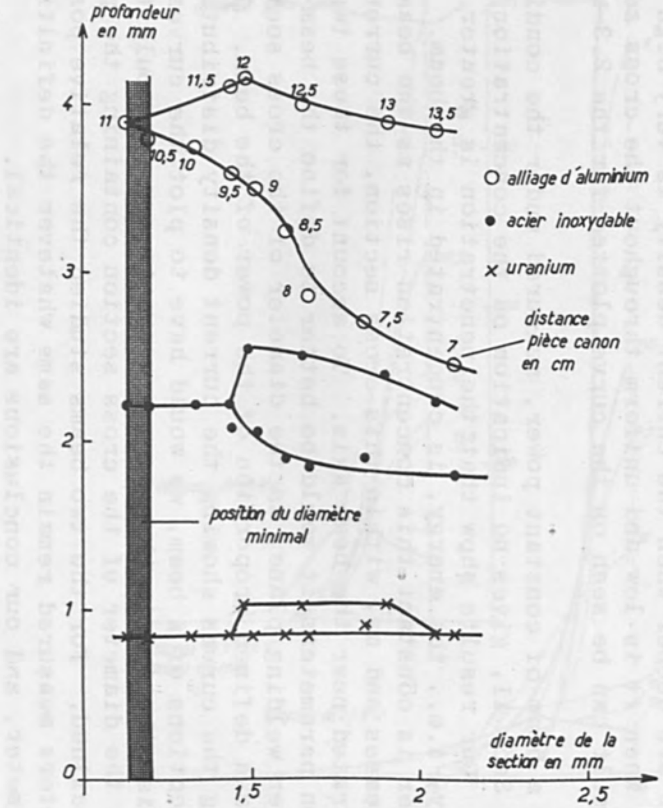

FIG. 5.—Weld depth as a function of the beam diameter in the welding plane (1.5-kW beam).

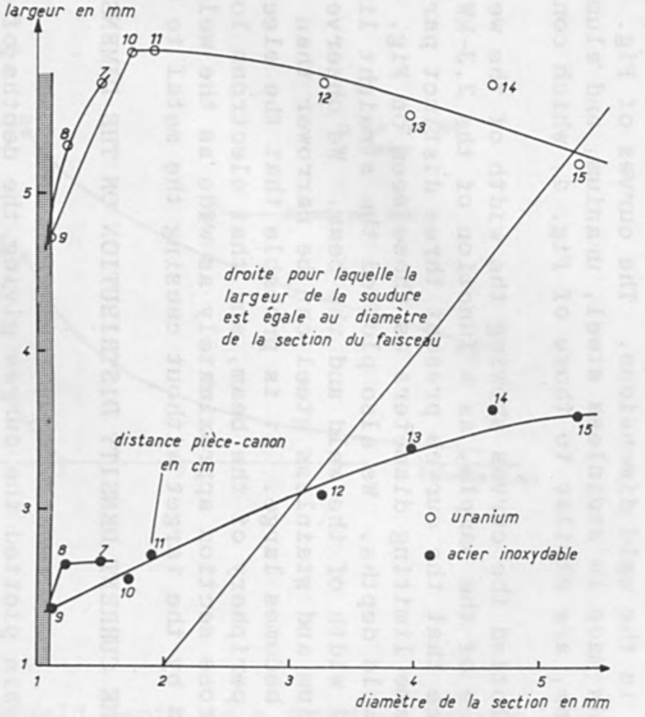

FIG. 6.—Weld width as a function of the beam diameter for 2.3-kW beam.

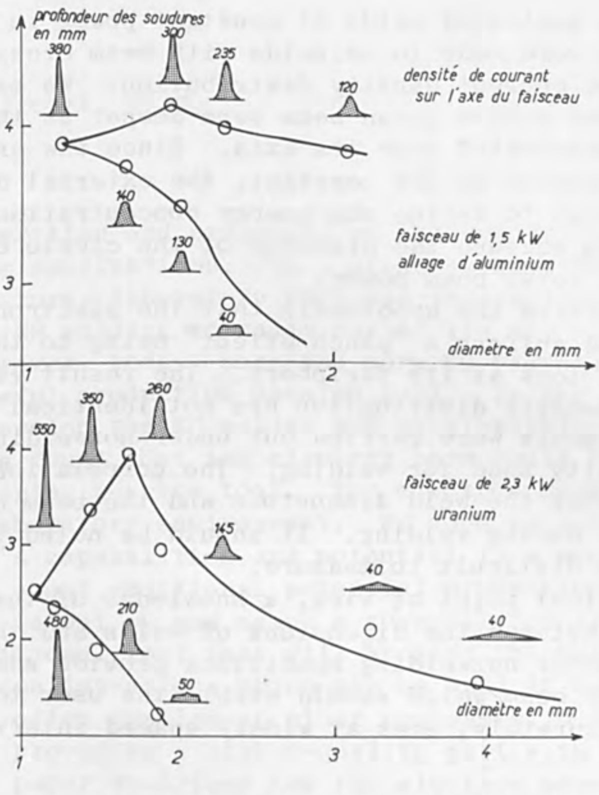

FIG. 7.—Effect of current-density distribution on weld depth.

VI. DEFORMATION OF THE BEAM DURING WELDING

We have shown experimentally that the position of the narrowing point of the 2.3-kW beam, estimated visually by the operator during welding, was 20 mm lower than its earlier position measured when no target was being matted. This confirms the results of authors who have pointed out that the presence of a cloud of metallic ions around the beam could reduce the spreading effect due to its space charge and produce a "pinch effect," reducing its cross section and changing its current density distribution.[1,7] This "pinch effect" exists if the beam energy concentration is great enough in the welding plane for the target to melt and vaporize; its amplitude varies with the quantity of metal melted and vaporized. The weld dimensions are thus bound up directly with the characteristics assumed by the deformed beam during welding, and not with those it possesses under nonwelding conditions. This explains why in Figs. 4 and 5 the welds are not the deepest at the level of the beam cross section which, under nonwelding conditions, has the smallest diameter and the most concentrated energy.

CONCLUSION

We performed a series of welds at constant power in metal plates, the surfaces of which were made to coincide with beam cross sections of known diameter and current density distribution. We established the fact that welds obtained with a given beam were deeper as the energy of the beam was more concentrated near its axis. Since the energy distribution in a beam cross section is not constant, the external diameter of the latter is not enough to define the energy concentration at this level. It is necessary to measure the diameter of the circle containing a fixed proportion of the total beam power.

We have put forward the hypothesis that the electron beam is deformed during welding and suffers a "pinch effect" owing to the presence of a cloud of metallic ions at its periphery. The result is that the envelope and the current density distribution are not identical in the beam on which our measurements were carried out under nonwelding conditions and in the beam actually used for welding. The correlations should therefore be made between the weld dimensions and the beam characteristics as they actually are during welding. It should be noted that these characteristics will be difficult to measure.

From the practical point of view, a knowledge of the correlations we have established between the dimensions of welds and the beam characteristics measured under nonwelding conditions provide additional parameters connected with the beam which should enable the user to reproduce the same weld more accurately, even at widely spaced intervals of time.

REFERENCES

1. E. B. Bas and G. Cremosnik, "Experimental investigation of the structure of high-power density electron beam," First Intern. Conf. on Electron and Ion Beam Sci. and Techn. 108-132, Toronto, 1964.
2. L. H. Stauffer, "Current density distribution in beams from cold hollow cathodes," Third Intern. Conf. on Electron and Ion Beam Sci. and Techn. 206-220, Boston, 1968.
3. A. Matting and G. Sepold, "Basic research on welding with electron beams of high intensity," ibid. 318-334.
4. P. Dumonte and M. Gabbay, Dispositif Sciaky (France).
5. A. Sanderson, "Electron beam delineation and penetration," Bull. Weld. Jour. 509-523, October 1968.
6. K. J. Harker, "Use of scanning slits for obtaining the current distribution in electron beams," J. Appl. Phys. 28:11, 1354-1357, 1957.
7. N. A. Olshanskyi and O. K. Nazarenko, "The current state of electron beam welding in the USSR," First Intern. Conf. on Electron and Ion Beam Sci. and Techn., 587-605, Toronto, 1964.

UTILIZATION OF THE ELECTRON BEAM IN PRODUCTION

R. R. COLLEGE

IBM Corp., SMD Endicott, N. Y.

INTRODUCTION

Much has been written and presented on the subject of electron beam (EB) metal working applications. To a great extent the material was of an experimental nature, laboratory work was theoretical; but little has been published on EB welding actually paying its way within a manufacturing plant. However, today, more and more EB technology is proving itself to be a useful production machine tool. In the early stages of this project to develop the EB welder and metal-working techniques for production, it was found that the electron beam could be advantageously used as an engineering service tool. The electron beam is no longer restricted to a laboratory environment. We hope to inform others of the electron beam's capabilities and potential in a manufacturing plant and help to bring about additional potential production applications. The electron beam is not by any means a cure-all for assembly problems, but rather an additional tool that will broaden the material combinations and design configurations which may be used in modern manufacturing. It may also often supplement other processes to speed up fabrication and assembly providing a higher-quality part with fewer subsequent operations. This paper describes how the electron beam has been used by IBM's Advanced Manufacturing Engineering to service a production organization and shows the breadth of possible service applications for EB metal working.

HISTORY

Approximately three years ago, the Systems Manufacturing Division at IBM Endicott entered the field of EB technology. The entry was accomplished by acquiring a hard-vacuum, high-voltage EB welder (Fig. 1). Primarily, this welder was to be utilized to join the hammer assembly for the 2203 Printer used in System/360 (Fig. 2).

INITIAL APPLICATION

The 2203 Hammer Assembly consists of a chrome-plated 2.5% silicon steel hammer and a chrome-plated mild-steel socket plus two copper-plated special stainless-steel springs. The capabilities of the EB welder to join dissimilar materials plus the ability to accomplish this joining under rigid requirements and specifications provided a perfect solution to an otherwise difficult manufacturing problem. Some of the rigid requirements and specifications that had to be met in this assembly included:

1. The precise location and repeatability of the weld spots.
2. Minimum weld spot diameter.
3. Weld penetration.
4. Very close and precise tolerances.
5. Minimum heat.
6. Minimal distortion.

Record of 10th Symposium on Electron, Ion, and Laser Beam Technology (L. Marton, ed.); San Francisco Press, Inc.

Copyright © by The Institute of Electrical and Electronics Engineers, Inc.—Printed in the U.S.A.

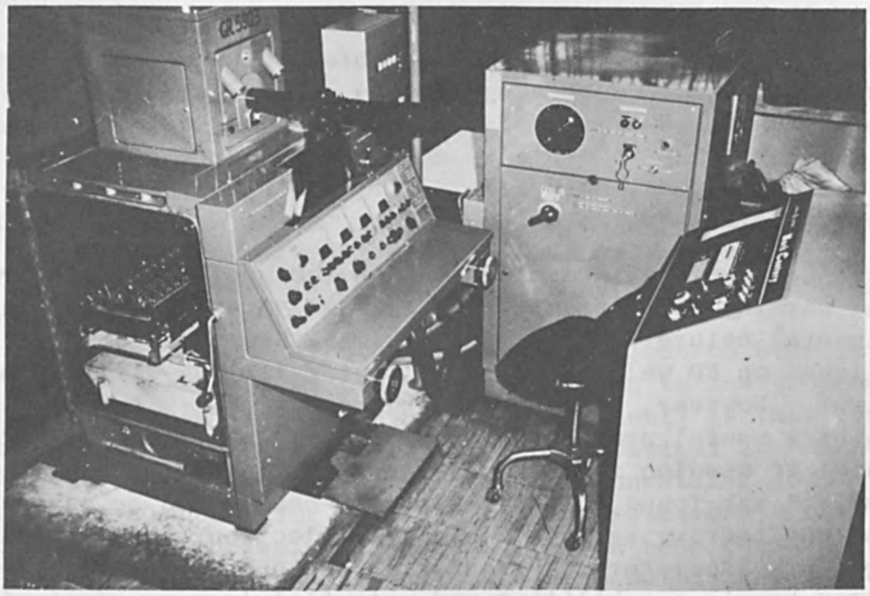

FIG. 1.—EB welder with N/C controller on the production floor.

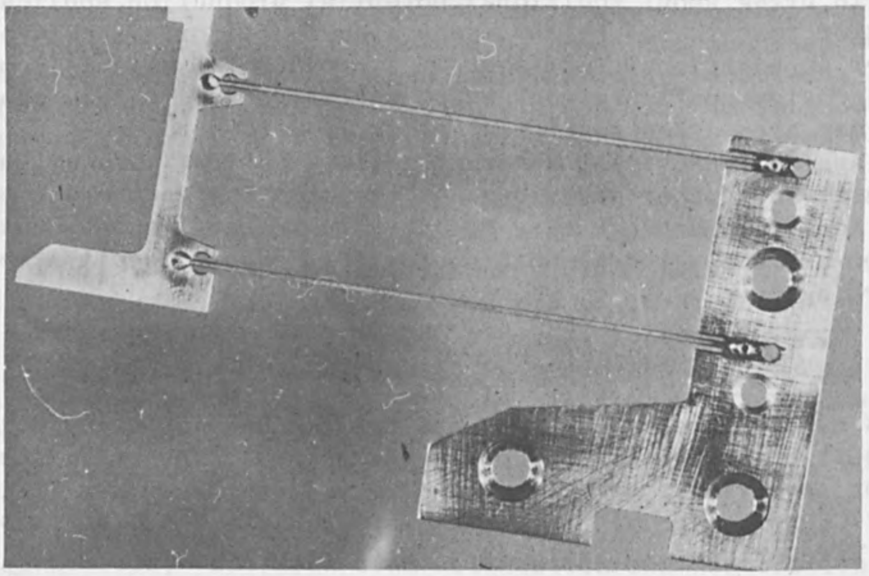

FIG. 2.—A 2203 Hammer assembly after EB welding.

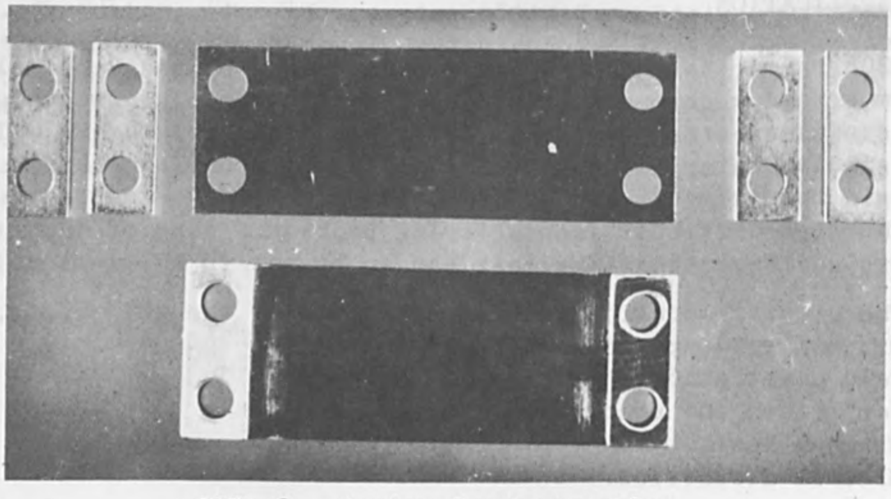

FIG. 3.—Spring-leaf assembly.

These specifications had to be met repeatedly to render the process economically feasible for the production requirements that had been dictated.

Initially, the welding of this assembly was accomplished by positioning the point of impingement or the desired location of the weld spot on the hammer assembly under the electron gun and triggering the beam manually. This process required the positioning of the hammer assembly and the triggering of the beam four times for each assembly.

PROCESS AUTOMATION

As the production requirements increased, IBM developed and built an automatic deflection system. This system was coupled to the EB welder and resulted in increased production capacity. With the automated deflection system incorporated, we now had to position only once for each hammer assembly. This was accomplished by positioning the center of the weld pattern for each hammer assembly under the electron gun and manually triggering the deflection circuitry. The beam would then automatically deflect from a central location to the number one weld spot for a predetermined length of time and then automatically switch the deflection load to the number two weld spot, and the beam would again be fired for a predetermined time. This process was repeated until all four weld spots per assembly were welded.

Because of the potential and capabilities of this new technology and its impact on the production industry in the field of assembly, an additional electron beam welding unit was purchased. Also, at this time, a project was established to attempt to automate the positioning of the hammer assembly to increase the productivity and capabilities of the equipment.

The first attempt at automating the positioning was to evaluate several mechanical systems. These attempts were unsuccessful as the speed, accuracy, and repeatability that were required could not be successfully or economically achieved. The next endeavor was to attempt numerical control positioning. From our initial investigations, we learned that it was feasibly impossible to acquire a dc motor that would operate in a high vacuum. This requirement was necessary if we were to accomplish the task with minimum disturbance to the vacuum work chamber. Some of the problems that were encountered in this task were:

1. A positioning table had to be found or built physically to fit the vacuum work chamber.
2. The height of this table could not exceed 22" from the floor of the work chamber owing to the necessary distance below the heat shield that was required to provide a proper field of range for the deflection pattern.
3. The positioning table had to support a minimum of a 50-lb static load.
4. A point-to-point N/C positioning system with an accuracy of ± 0.001 and a repeatability of 0.0005 had to be acquired.
5. A table move of 1 IPS was required.
6. Dc motors had to be acquired that would operate in a 1×10^{-4} mm of Hg vacuum environment at temperatures of 78° to 150°F.
7. All of these requirements including design, construction, installation, and debugging of the entire system had to be accomplished within

four months at a comparable estimated cost.

No commercial tables were available that would physically fit the vacuum work chamber. Consequently, a special table had to be developed and built. Two special dc motors were also developed and built that would operate in the vacuum environment as specified. The Numerical Control System that was adopted for this project was a G.E. Mark Century 120 with an accupin feedback system.

The complete system was developed, built, installed, and debugged in 5 months. The N/C control system was married to the automated program deflection system.

The final results that were realized with this new automated positioning and deflection system were as follows:

1. A positioning table was designed and built that was compatible to the vacuum work chamber.
2. A point-to-point Numerical Control System was achieved that could position a 50-lb static load to an accuracy of ± 0.001 with 0.0005 repeatability and variable speeds of 0 to 120 IPM.
3. Two special dc motors were developed, designed, and built that would operate in the temperature range of 78° to 150°F and 1×10^{-4} mm of Hg vacuum environment.
4. The system was developed, designed, built, installed, and debugged in the projected time span and at a comparable cost. The reliability of the system has far exceeded our expectations.

The system has been utilized almost continuously for the past 2 years with complete trouble-free operation.

With the installation of this automated positioning system the operation now consists of obtaining a proper vacuum and setting the predetermined parameters on the EB welder, then depressing the cycle start button. The positioning table automatically positions a hammer assembly under the center of the electron gun then sends a signal to the deflection system. The deflection system automatically fires the four deflected weld spots, then signals the N/C Controller to position the next hammer assembly. The deflection system can be altered for various weld patterns simply by inserting new logic cards in the deflection controller.

PRODUCTION APPLICATIONS

After the major concerns for joining the 2203 hammer assembly were under control, new production welding applications were sought. One such application that was adopted to EB welding was the previously bonded spring leaf assembly (Figs. 3 and 4).

Figures 5-9 show the many potentials and versatilities of the EB welder which can be utilized to accomplish the majority of assembly applications found on the production floor today.

DEVELOPMENT UTILIZATION

EB welding can also be used in developing and evaluating new ideas and design configurations. This eliminates the building of prototype parts many times from raw material (Figs. 10 and 11). EB welding can also be utilized in the producing of pilot or prototype production orders (Figs. 12-14).

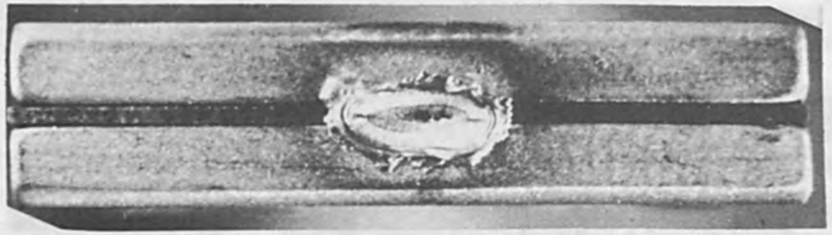

FIG. 4.—End view of the spring-leaf assembly showing the elliptical weld spot.

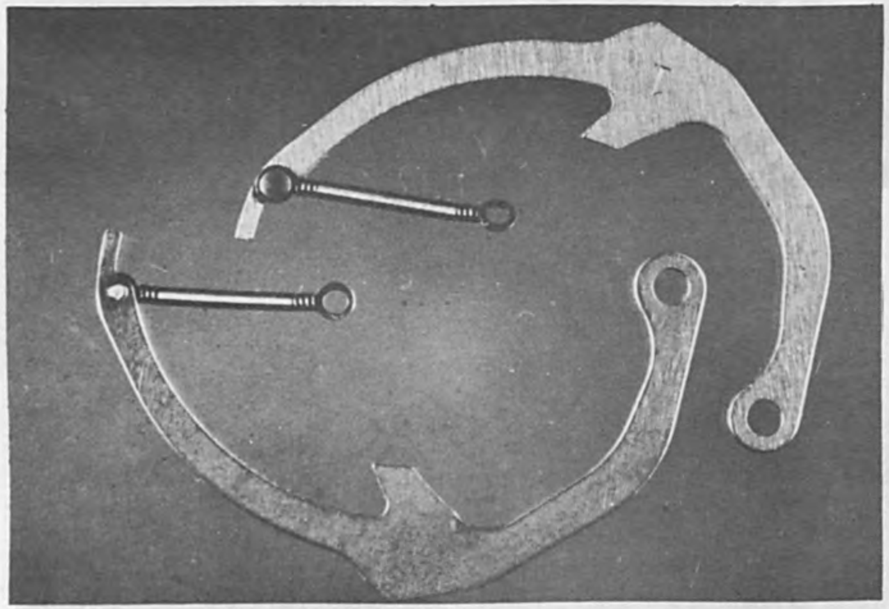

FIG. 5.—Latch assembly in which EB welder is used to attach rivet, allowing the spring to rotate freely.

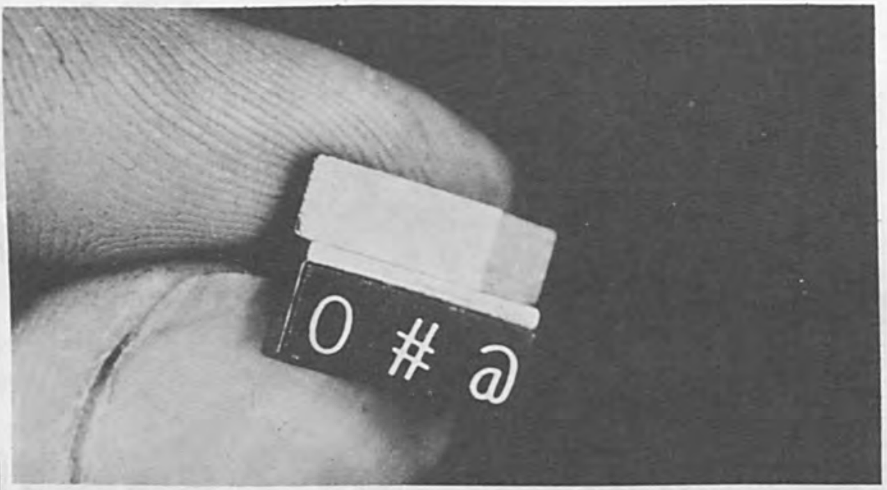

FIG. 6.—Carbide type face EB-welded to heat-treated sintered metal type carrier.

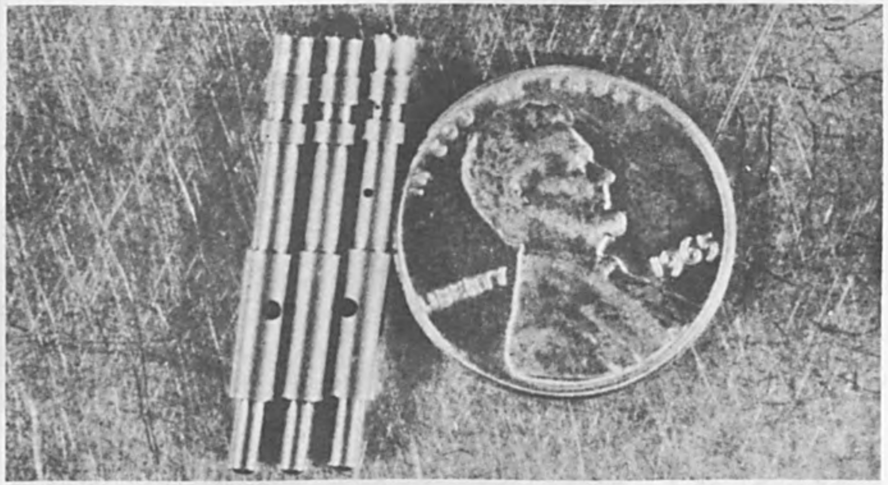

FIG. 7.—Piston type plunger with EB-welded ball-bearing plugging end access hole.

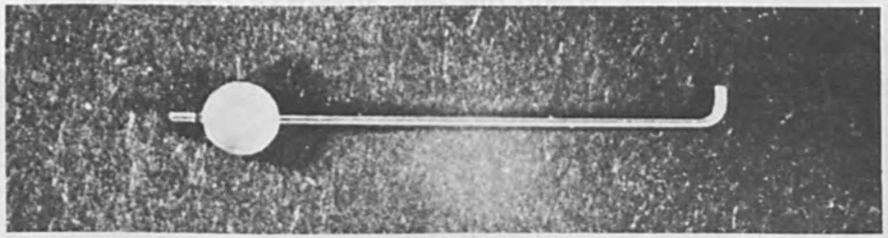

FIG. 8.—Mild-steel nugget beam-welded to a 0.022-in. diam. stainless-steel wire.

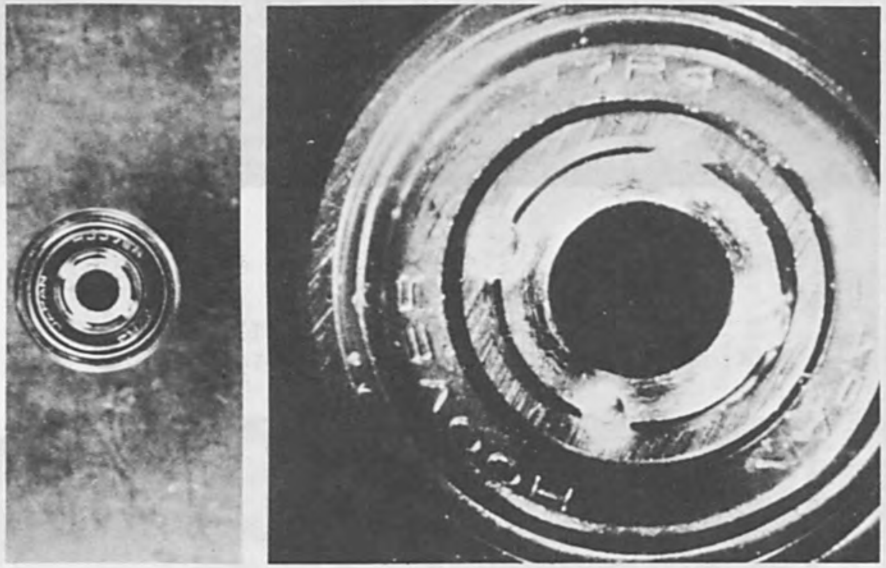

FIG. 9.—Attachment of ballbearings and bushings to heat-treated gear shafts.

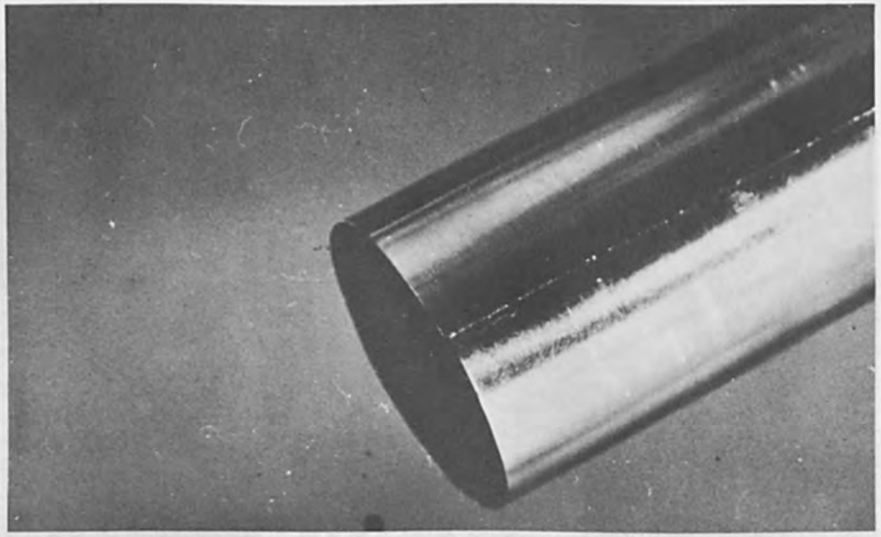

FIG. 10.—Stainless-steel sleeve of 0.008-in. wall thickness EB-welded with 0.004-in. weld penetration.

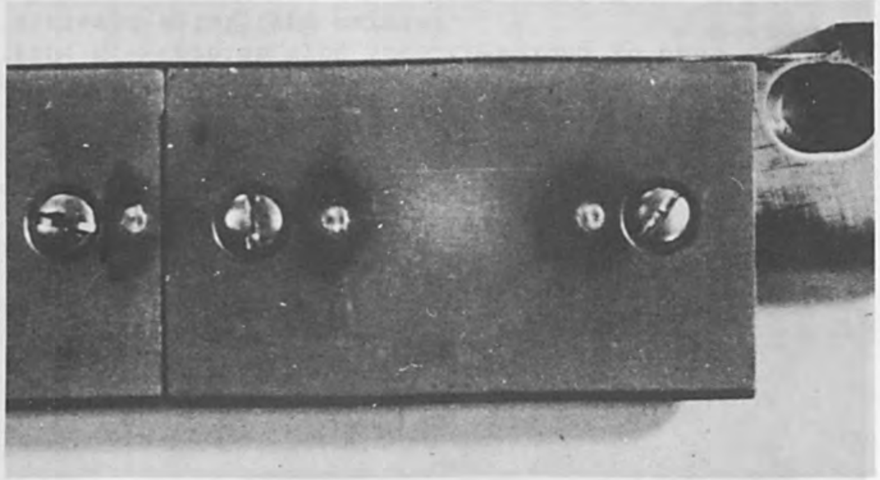

FIG. 11.—Replacement of screw and dowels for assembling component parts by utilizing EB welding.

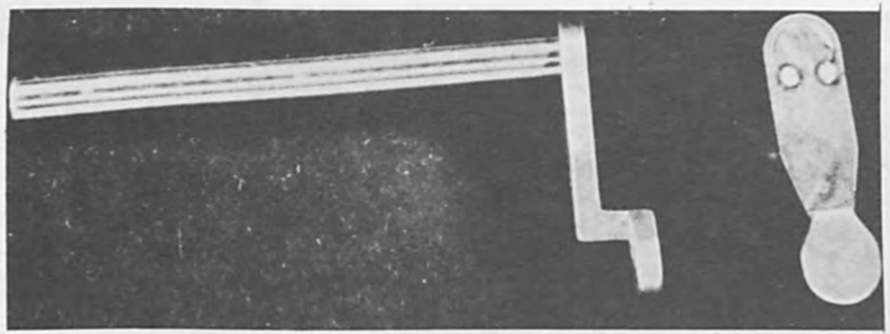

FIG. 12.—Wiper blade is attached to a shaft utilizing spot welding in place of staking.

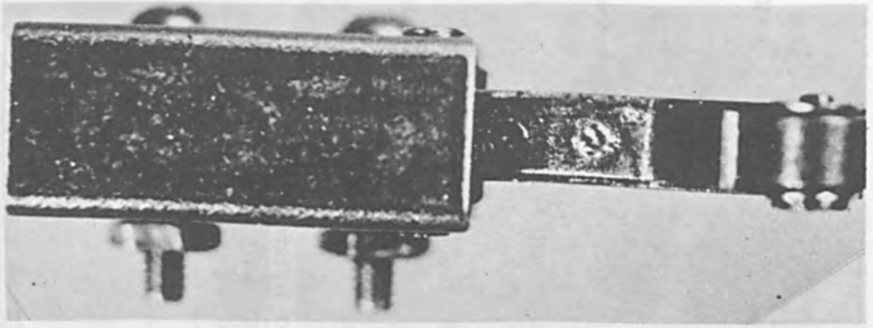

FIG. 14.—EB welder utilized to attach angle bracket to actuating arm of microswitch.

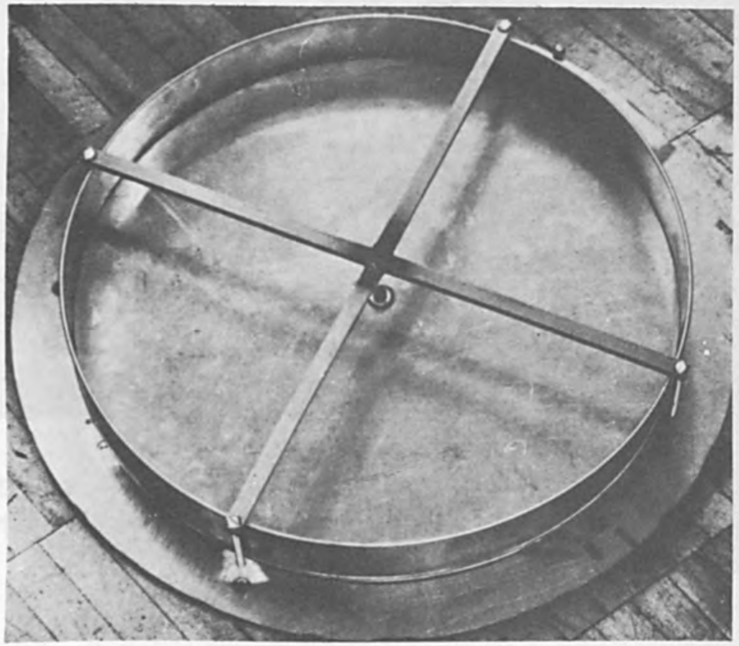

FIG. 13.—Stainless-steel drum assembled with EB welder and rotary table eliminates the much-needed straightening operations of conventional welding practice.

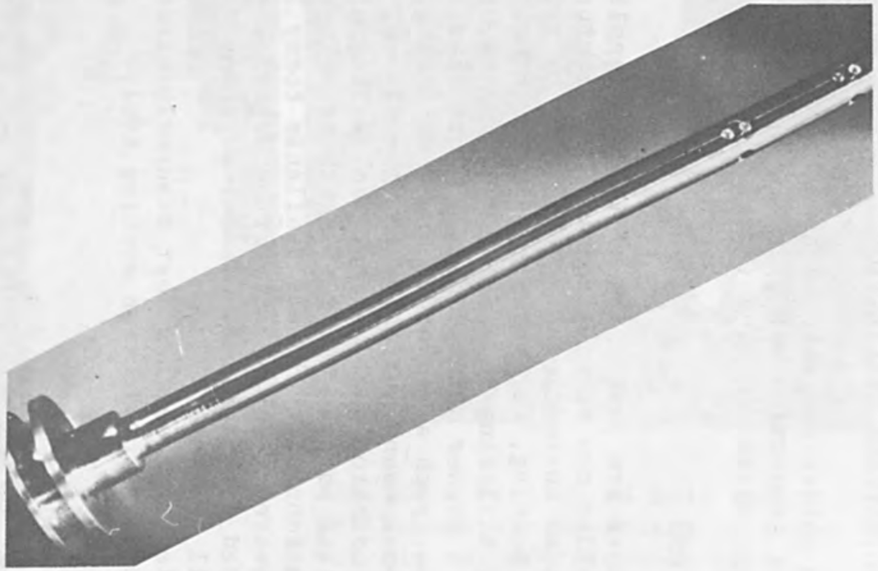

FIG. 15.—Pulley and shaft assembly in which out-of-tolerance holes are plugged by EB welder.

REPAIR AND SALVAGE UTILIZATION

The EB welder can also be used most advantageously in the repair and salvage of production parts and in the area of build, repair, and salvage of tooling, molds and dies (Figs. 15-22).

CONCLUSIONS

The above are just a few of the many applications and their use where the EB welder can be utilized in a manufacturing facility. Many of the applications currently being assembled by riveting conventional welding, staking, bonding, screw and dowels, brazing, etc., can be economically joined by utilizing EB welding. In the majority of cases, EB welding produces a higher quality part in less time and with fewer subsequent operations, such as straightening, deburring, etc., than any of the other conventional means currently being employed.

For production application, the quality of the tooling involved plays an essential part in the results to be achieved. The various models and configurations of equipment available today leave no product or application uncovered. The variety of accessories and equipment that also can be obtained with the EB equipment enhances the potentials of this technology all the more.

The electron beam has most assuredly earned a place as a competent and competitive production machine tool.

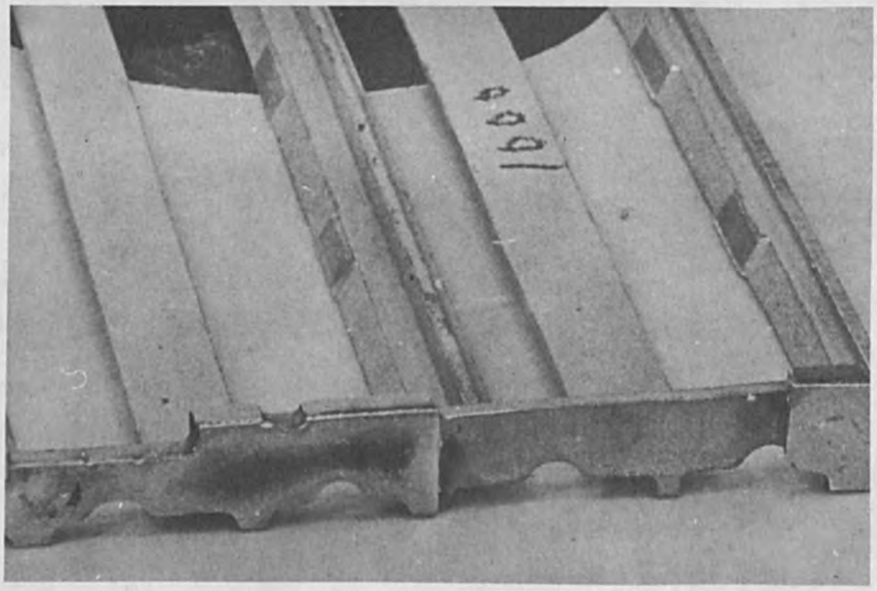

FIG. 16.—EB welder used to build up undercut area of aluminum cast frame.

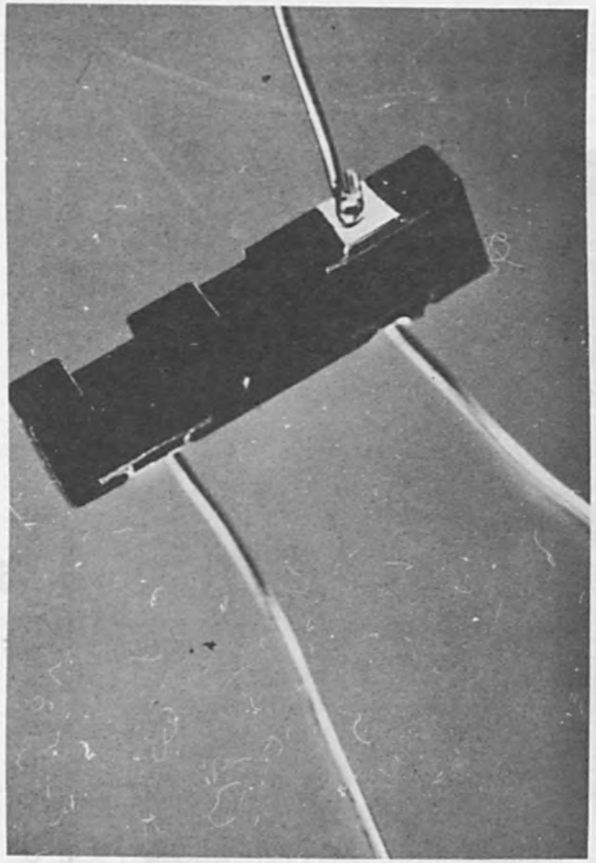

FIG. 17.—EB welder used to attach small wires to electrical components.

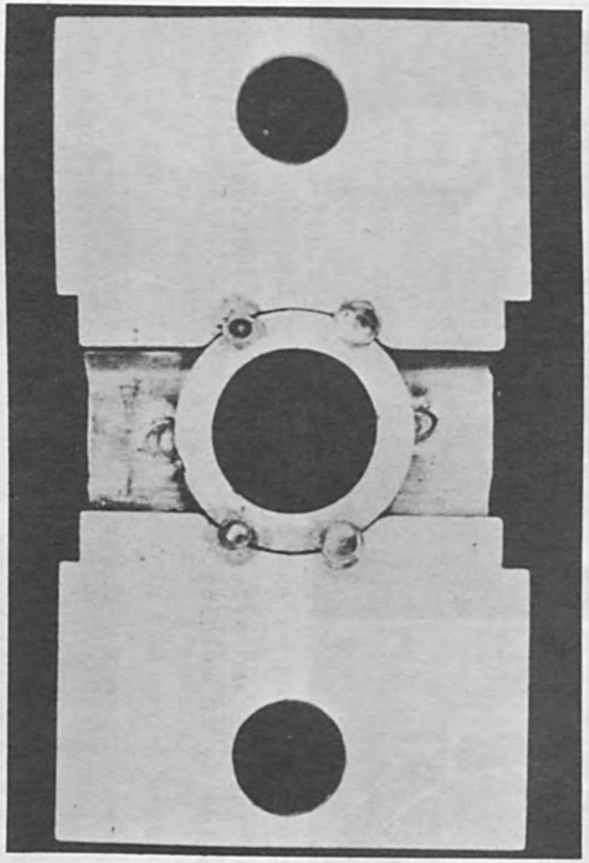

FIG. 18.—Guide block for polymer mold has bushing permanently located by EB welder.

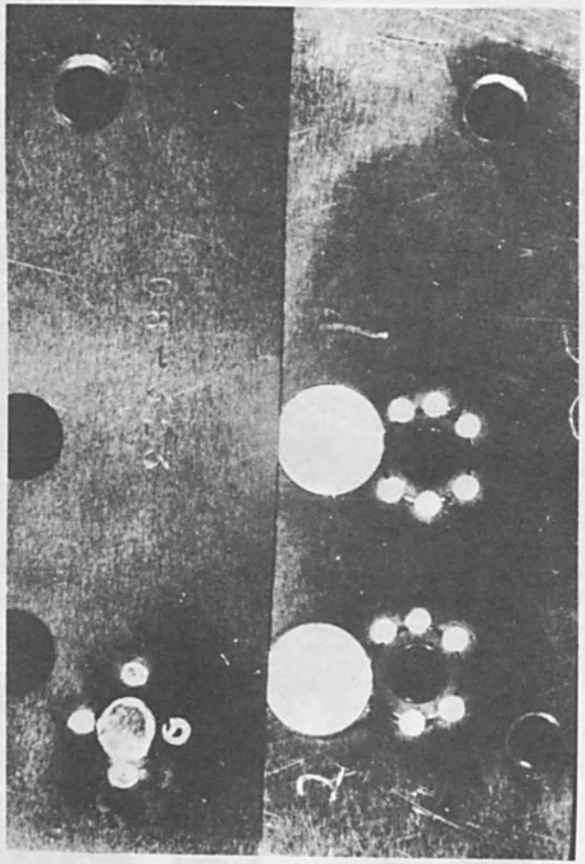

FIG. 19.—Portion of mold cavity has drill bushings EB-staked in place to correct out-of-tolerance holes.

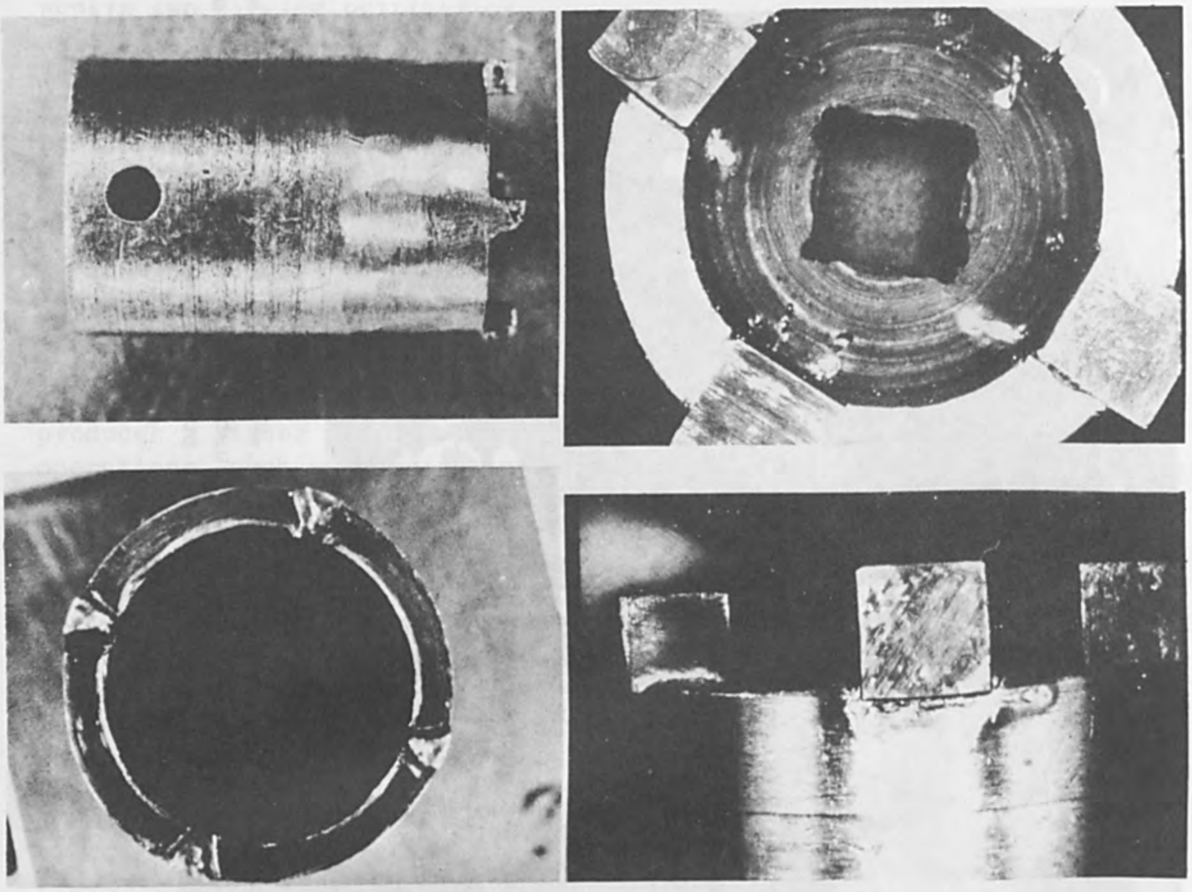

FIG. 20.—Air wrench (before and after) utilized on production equipment has new plugs installed by EB welding.

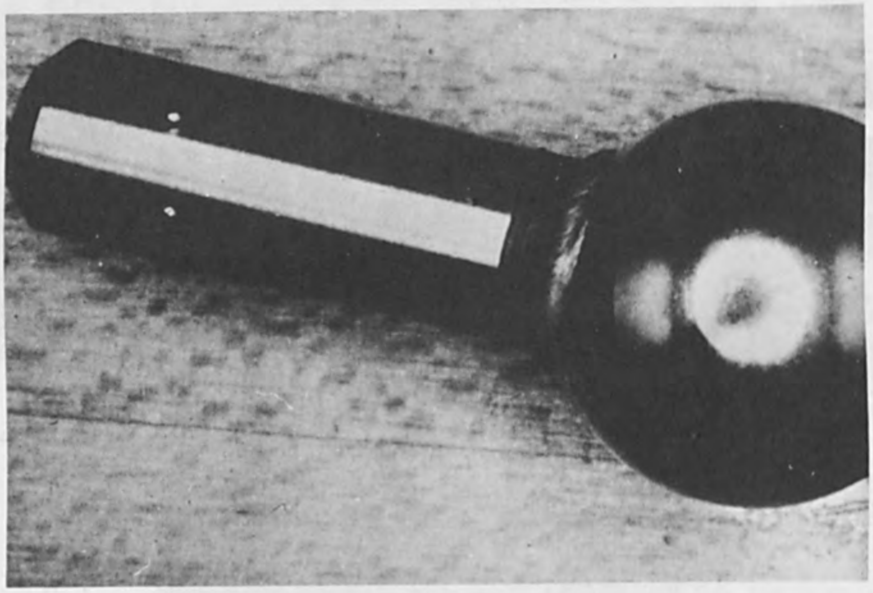

FIG. 21.—Ball bearing, 0.5-in. in diameter, welded to a 3/16-in.-diam. dowel pin to produce an accurate locator.

ELECTRON BEAM WELDING OF STRUCTURAL STEELS

A. MATTING and G. SEPOLD

Technical University of Hannover (Institute for Materials Research), Germany

1. INTRODUCTION

Unalloyed and low-alloy structural steels are among the most important structural materials of our time. They can be joined, e.g., by welding, without difficulty to form complex structural components and fabrications and, because of their high degree of economy, are being used in all areas of technology. That does not mean, however, that the welding of these materials is entirely without problems; on the contrary, problems do arise, for example from the wide welding zones and the metallurgical notches associated therewith and, in the case of heavier sections, from long and hence uneconomic welding times. In contrast to the disadvantages attendant upon the welding of structural steels by conventional methods, electron beam (EB) welding produces extremely narrow and deep welds, the welded component exhibiting but a minimal amount of cross and angular contractions, very small heat-affected zones, and correspondingly favorable strength values under static and/or dynamic loading. Over and above that, EB welding has proven economical when applied to parts of 10- to 50-mm thickness as these can be butt-welded within a very short time and often require neither subsequent heat treatment nor machining even if close tolerances are involved.

The wide application of EB welding has hitherto been prevented by a number of unsolved problems which are in part due to ignorance of the capabilities inherent in, and hence of the design and engineering possibilities afforded by, this process, but mainly to the inadequate and defective joints produced in ordinary steels (Fig. 1). The left-hand part of the future depicts a crack in the cross section of the weld caused by structural transformation and high cooling rates. The next two illustrations depict piping which can be regarded as typical of welds whose penetration depth is less than the cross section of the work piece. The two pores in the right-hand illustration are so-called frozen bubbles of vaporized metal which were unable to rise to the surface of the welding zone because of excessively rapid solidification of the overheated weld pool. Defects of this kind render the strength of the welded joint doubtful. In consequence, extensive investigations and experiments designed to discover ways and means by which to prevent the formation of pores and cracks were required. In addition, it was necessary to obtain data on the mechanical-technological properties of the welded joint so as to facilitate a comparison between the welded and unwelded materials.

2. MATERIALS

The investigations included two unalloyed structural steels, Grades C 22 and TT St 35 and, for purposes of comparison, the low-alloy Grade 13 CrMo 44. Each grade had been heat-treated. Table I gives their composition.

Record of 10th Symposium on Electron, Ion, and Laser Beam Technology (L. Marton, ed.); San Francisco Press, Inc.
Copyright © by The Institute of Electrical and Electronics Engineers, Inc.—Printed in the U.S.A.

TABLE I.—Welded steels.

Steel Grade	C	Si	Mn	P	S	Cr	Mo
C 22 = approx. AISI C 1020	0.19	0.22	0.42	0.014	0.022	-	-
TT St 35	0.14	0.30	0.47	0.008	0.024	-	-
13 Cr Mo 44	0.14	0.24		0.015	0.017	0.93	0.45

With the exception of a higher carbon content of 0.19%, the normalized C 22 Steel Grade had a composition very similar to that of TT St 35, which is a grade tailored for applications requiring high toughness at lower temperatures. The wall thickness in each case was 10 mm. Prior to welding the butt-joint the flanks of the parts were ground so as to obtain a good match.

3. WELDING EQUIPMENT

The experiments were conducted with the aid of a Carl Zeiss Model ES 1013 EB welding machine which is designed as a medium power unit delivering 3 kW at a maximum acceleration voltage of 150 kV.

The power densities attained in the focal spot can be as high as, and in excess of, 10^7 W/cm^2 so that, locally, the melting of narrow areas and even vaporization of metal in the center of the impinging beam may occur. If the high voltage transformer is connected in series to a voltage stabilizer, this will produce adequate stabilization of the acceleration voltage and the emitted beam, which means constant average intensities in the focal spot. A self-developed focusing device permitted reproducible adjustment of the beam current, which is not always assured, particularly at high beam currents of more than 10 mA, by focusing the beam on a block of tungsten and examining the point of impingement of the electrons through an enlarging eyepiece.[1] The focusing device consists of a motor rotating at high speed and having a long piece of metal fixed to its shaft end. Placed underneath the piece of metal and electrically insulated from it is a piece of copper which acts as a cage for the electrons. The piece of metal rotates above the copper cage so as to interrupt the flow of electrons at intervals. The more precise the focusing of the beam, the shorter the period of interruption of electron flow by the rotating piece of metal. This appears on an oscilloscope as a signal with a steep flange. Focusing can be regarded as optimum if the flange of the signal attains maximum steepness.

4. CONDUCT OF EXPERIMENTS

The metal specimens, which had been carefully cleaned with carbon tetrachloride, were clamped in a fixture in abutting relation to each other. The beam was focused on the work piece surface prior to the actual welding operation.

Before welding the front faces of the two specimens it was considered advisable to make a few welds side by side in the solid so as to develop approximate operating parameters for welding down to a depth corresponding to the thickness of the specimens. It was not until the top and bottom weld beads had been tested macroscopically that useful data for butt-weld joints could be established.

5. RESULTS OF EXPERIMENTS

WELDING PARAMETERS. X-ray pictures of the joints indicated porosity in the weld. Unetched micrographs of the center of the weld taken parallel to the welding direction indicated these defects to be located predominantly in the vicinity of the root (Fig. 2). The left-hand micrograph of Fig. 2 illustrates a weld whose depth of penetration falls short of the wall thickness of the specimen resulting in large oblong pores along the root. The weld depicted in the middle of Fig. 2 has a poorly formed root which will act as a notch when the weld is subjected to loading. Again, there is some porosity in the weld indicating a high cooling rate.

These unsatisfactory results were obtained in the initial experiments making it clear that more elaborate and sophisticated investigations were necessary. These tests involved variation of welding parameters, i.e., beam current, voltage, and feed rate. Moreover, the intensity distribution in the focal spot was varied, the beam was wobbled at 50 Hz in the x and y directions, and the specimens were finally preheated to 200°C by applying a defocused electron beam. The results of these experiments can be summarized as follows.

When welding with rising energy per centimeter of weld, that is to say with greater energy than was required to melt the cross section of the material, porosity was reduced to a minimum. Thus, when applying 3100 J/cm of weld length, nonporous joints were obtained; whereas at lower energy rates down to 1400 J/cm of weld length the melting of the material over its entire cross section was still accomplished but was accompanied by a considerable increase in defect size and frequency. The application of energy in excess of 3100 J/cm up to a maximum of 8000 J/cm of weld length, which was associated with a reduction of beam intensity by reason of higher beam current and lower voltage values, produced deep penetration notches on the surface of the weld. Hence an upper limit was imposed on the amount of energy to be applied to exceed which yielded no advantage. However, it was found that even optimum combinations of welding data did not altogether prevent the odd occurrence in the weld of spherical cavities up to 0.01 in. in diameter. Furthermore, the weld roots were apt to "sag," i.e., protrude by as much as 1 mm, whereas a protruding top bead, such as is often observed on EB-welded joints, did not occur. Smoothing of the wavy top face of the joint was accomplished by subsequently remelting the material with a beam of lower intensity. Preheating of the work pieces was dispensed with for economic reasons although the welding results of a few tentative experiments showed a considerable improvement even with work pieces which had not been melted over their entire cross section.

The following welding data were found to be usable:

Acceleration voltage	$U = 130$ kV
Beam current	$I = 16$ mA
Feed rate	$v = 0.7$ cm/sec
Focal distance	$a = 10$ cm

(measured from center of lens to work piece surface)

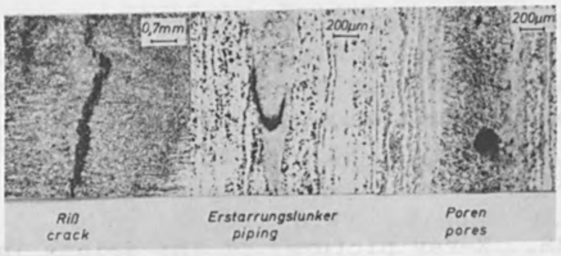
0,7mm
200µm
200µm
Riß
crack
Erstarrungslunker
piping
Poren
pores

FIG. 1.—Defects in the weld.

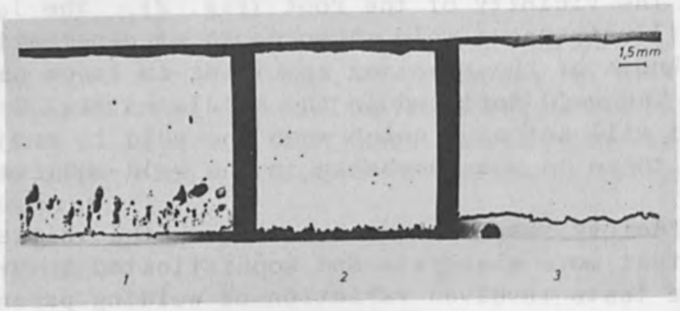

FIG. 2.—Longitudinal seam (cross section) in TT St 35 steel.

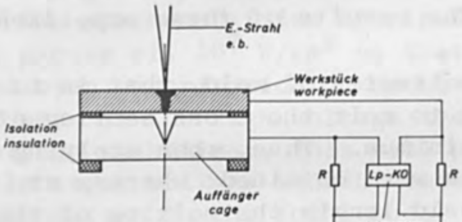
E.-Strahl
e.b.
Werkstück
workpiece
Isolation
insulation
Auffänger
cage
R
Lp-KO
R
visicorder

FIG. 3.—Test setup.

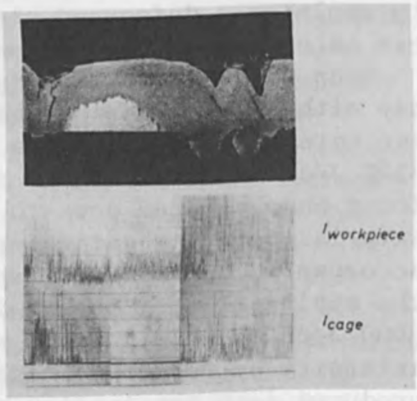
$I_{workpiece}$
I_{cage}

FIG. 4.—Bead formation in a longitudinal seam and resulting currents.

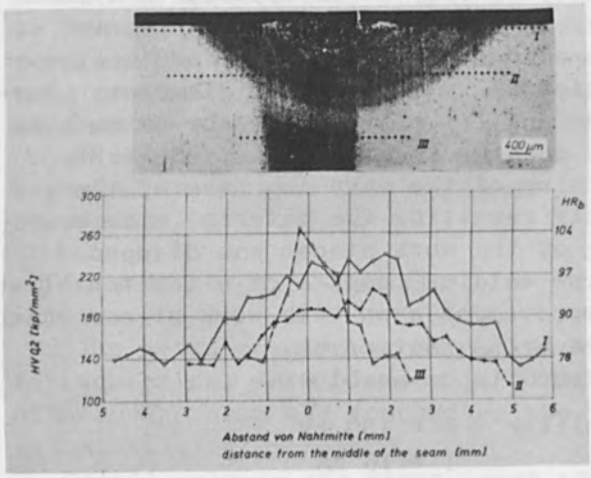

FIG. 5.—Hardness curves for C 22 steel EB welded and postheat-treated.

material	yield strength $\sigma_{0,2}$ [kp/mm^2] required	actual	ultimate strength σ_B [kp/mm^2] required	actual
TT St 35 V	24/26	28	35/50	43
C 22 N	24	27	42/50	42
13 Cr Mo 44	29	28	44/56	45

FIG. 6.—Tensile strength of structural steels.

In order to record reproducible welds, a simple measuring device was used permitting collection of the electrons emerging from the root of the weld (Fig. 3). The electrical signal could be compared subsequently to the macroscopic and metallographic findings of the weld (Fig. 4).

If the work piece, shown in Fig. 3 in cross section and appropriately insulated, is penetrated by the electrons of the beam, the latter are collected in an insulated copper cage positioned below the work piece. The current is displayed on a Visicorder. The electrons impinging upon the work piece can be measured in the same way. Figure 4 illustrates the currents impinging upon cage and work piece, and the metallographic finding of a longitudinal weld in Grade C 22 structural steel. During the welding operation the beam power was reduced and then increased, resulting first in a full-cross-section weld and then in a partial-cross-section weld followed again by a more pronounced formation of the weld root. This is reflected in the associated current curve which drops to zero at partial depth of penetration, only to rise again towards its peak as root formation improves. Thus, if used in conjunction with more sophisticated measuring techniques,[2] a control quantity would be available, making it possible for welding speed as well as beam or lens current to be controlled in such a way as to assure the formation of a uniform weld root.

MECHANICAL-TECHNOLOGICAL PROPERTIES. The preliminary experiments had proved that electron-beam welding will produce virtually flawless welds in structural steels; this did not, however, mean that the welds would also have optimum mechanical-technological properties. The very thin but intensive beam (its diameter was approximately 0.5 mm) produced very narrow welding zones which, by reason of the very steep temperature gradient, led to the assumption that a structure of very high hardness and hence drastically reduced elongation and impact strength would result.

Hardness curves across the welding zone confirmed that assumption. In the center of the weld, Rockwell hardness values up to 42 HR_c were found in respect of 13 CrMo 44 and C 22 Steel Grades compared with 34 HR_c for Grade TT St 35. It was therefore logical to attempt to reduce these hardness peaks by the subsequent application of a defocused electron beam, thereby avoiding more elaborate and hence costly post-treatment such as normalizing the parts in a furnace. The result of these investigations is shown in Fig. 5. The hardness across the weld in C 22 follows the path represented by the curves I to III in dependence on the distance from the work piece surface. A total energy of 12 000 J was applied during this post-treatment with the result that at no point of the weld down to a depth of 2.5 mm did hardness values exceed 23 HR_c. Subsequent heating of EB-welded joints additionally effected some kind of stress-free annealing whereby residual stresses caused by welding were reduced.

Figure 6 shows the result of tensile tests on specimens which had not undergone subsequent heat treatment. The specimen size corresponded to German Standard Specification DIN 50120. The nominal values of round specimens were compared with the actual values of welded joints. Representation of the elongation at fracture of welded specimens was dispensed with because a fracture occurred in the heat-affected zone of grade C 22 for example, and the value for elongation was found to be appropriately low. The results are average values for each of the three specimens tested. As a rule, strength values of the welded joints equalled

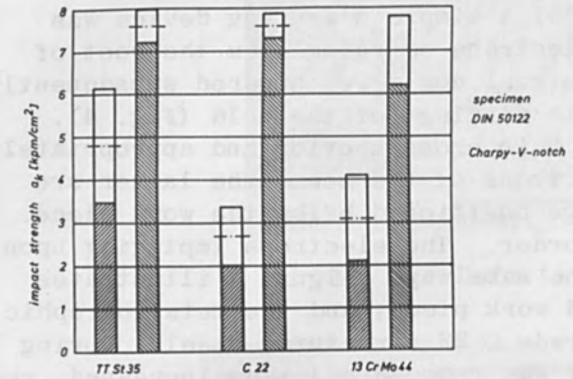

FIG. 7.—Impact strength of welded and unwelded steels at room temperature.

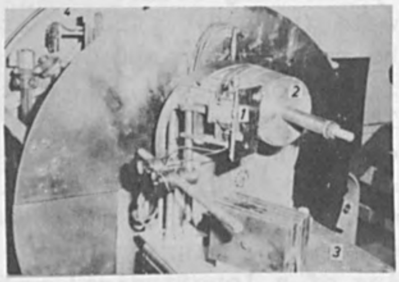

FIG. 8.—Setup for tube welding.

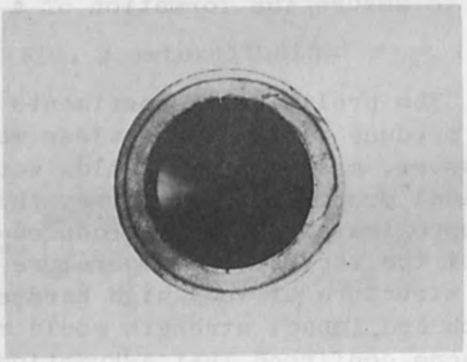

FIG. 9.—Cross section of EB-welded tube.

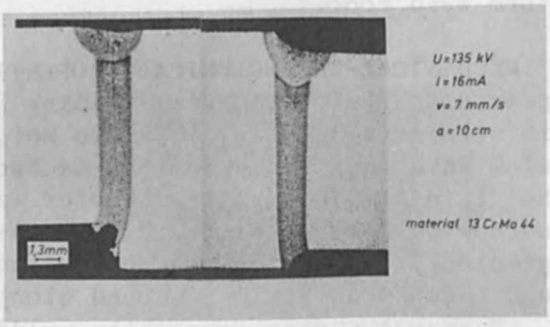
U=135 kV
I=16mA
v=7 mm/s
a=10 cm
material 13 Cr Mo 44
1,3mm

FIG. 10.—EB welding of dissimilar cross sections.

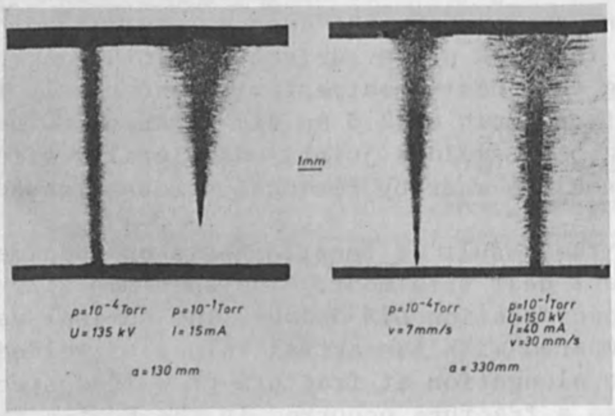
1mm
p=10⁻⁴ Torr
U=135 kV
p=10⁻¹ Torr
I=15mA
a=130 mm
p=10⁻⁴ Torr
v=7mm/s
p=10⁻¹ Torr
U=150 kV
I=40 mA
v=30 mm/s
a=330mm

FIG. 11.—Deep-penetration welding of C 22 steel.

those of unwelded specimens. A slight deviation of the yield strength from the nominal figure for 13 CrMo 44 steel grade should not be overrated. The fractures of the TT St 35 and 13 CrMo 44 specimens which were tested for tensile strength occurred mainly in the parent metal or could be interpreted as a mixed fracture starting in the parent metal and reentering it after crossing the welded joint. Bending tests according to German Standard Specification DIN 50121 consistently resulted in bending angles of 180°. It, therefore, appeared meaningful to conduct the bending tests at right angle to the welding direction as the weld would still be subjected to genuine bending stresses even if bending mandrels of somewhat larger diameter were used.

The EB-welded joints were also tested for brittleness by subjecting them to V-notch impact bending tests. In view of the very narrow welds, the specimen according to German Standard Specification DIN 50122 with Charpy-V-notch proved particularly favorable as it covered the entire weld from the root to the top bead and was positioned parallel to the direction of rolling. Blows were applied to the specimens at room temperature, the results being subsequently evaluated statistically and compared with those of unwelded specimens (Fig. 7). A striking point to note here is that the welded specimens have a wider value scatter band than do the unwelded specimens which, among other things, is an indication that the transition temperature from high to low position had been reached. In no one instance, however, did V-notch impact strength fall below 2 kpm/cm^2.

Annealing the welded specimens for a period of 0.5 hr at 890°C resulted in V-notch impact strength values identical to those of the parent metal. We therefore intend to conduct further experiments designed to improve the impact strength of structural steels by post-treatment for example, involving the application to the weld of a defocused electron beam.

WELDING OF TUBES. The results of the mechanical-technological tests provided the incentive to attempt to butt-weld structural steel tubes of the aforementioned grades using the electron beam welding technique. To accomplish this, the experimental set-up shown in Fig. 8 was devised. The welding system is composed of four main components:

1. Focusing device
2. Work holding fixture
3. Welding table
4. Feed units

The focusing device 1 enabled optimum current density distribution to be obtained in the focal spot. The block of copper placed below the focusing device served as a cage and had been generously dimensioned to avoid melting which a block of smaller size would undergo upon application of the high beam powers involved.

The surface speed of the tubes was capable of being varied infinitely from outside the welding chamber. After evacuation of the welding chamber down to approximately 10^{-4} Torr, the intensity pattern in the focal spot on the work piece surface was first displayed and checked on an oscilloscope, compared with previously determined patterns, and, if necessary, corrected by adjusting the lens current.

In welding the tubes, the same machine settings were used as those which had been found and used previously in the production of longitudinal welds. Subsequent smoothing of the scaly top face of the weld was accomplished by reducing the acceleration voltage from 135 to 110 kV, which entailed a drop in beam current to 7 mA and a diminishing of intensity in the focal spot, with the electric field of the electromagnetic lens remaining constant. This technique of smoothing by means of a defocused electron beam was advisable whenever the top face of the weld had sunk somewhat as a result of the slight "sagging," i.e., protruding, of the weld root. The macroscopic finding of the tube welds was supplemented by micrographs taken parallel to the welding direction (Fig. 9). In this figure, the dark zone near the top of the weld denotes the depth of the fusion zone produced by post-treatment of the top bead with a defocused electron beam whereby the metal was remelted near its surface. The wavy transition from the root to the top bead results from a reduction of beam power which was effected by manual adjustment of the machine. By means of a slope device which permits, for example, control of voltage across the Wehnelt cup, the operation of weld-smoothing, that is to say the transition from focused to defocused beam, can be initiated automatically.

In manufacturing, the application of EB welding to the joining of components of nonuniform wall thickness constitutes a further problem as it is questionable whether such components can be joined satisfactorily. Components falling into this category are especially those of heavier cross section which undergo changes in wall thickness by reason of the particular manufacturing techniques employed such as casting or forging. In welding such components, it may happen that the mutually abutting weld flanges are offset by more than 1 mm. To obtain some more specific information on this problem it was necessary to simulate experiments with geometrically simple shapes for which purpose tubes of different inside and outside diameters were joined by welding. The maximum and minimum wall thicknesses were 12 and 10 mm, respectively. The beam was focused in all cases on the surface of the tube having the largest cross section, which means that it was applied at the shortest focal distance applicable in the circumstances. The results of welds produced in tubes with mutually offset edges are shown in Fig. 10, which depicts micrographs taken at right angle to the welding direction. The steel grade used for the experiment was 13 CrMo 44. The left-hand micrograph shows the surfaces to be offset by 2 mm; the right-hand micrograph indicates the outside and inside diameters to be offset by 1 mm each. These micrographs illustrate very clearly that EB welding is possible without the need for repeated adjustment of current and voltage even if amounts of edge offset greater than those stated above are involved. Moreover, it appeared that, in view of the relatively high beam power, it was of no consequence whether the beam was focused on the work piece surface or on a point 2 mm lower since complete penetration of the entire cross section consistently occurred. This meant that, with a small image aperture, i.e., an almost parallel beam, the pattern of beam intensity distribution in the focal spot was similar to that obtaining at a distance of 2 mm. With beams of small image aperture it would also be possible to weld components of uniform wall thickness but complex shape along the joint, that is to say at different focal distances without the need for complicated adjustments of beam or work piece.

6. WELDING AT HIGHER PRESSURES

Welding at higher pressures of 10^{-1} to 10^{-2} Torr requires shorter pumping times, yielding shorter cycle times and hence improved economy of electron beam welding as such. Except for reactive metals on which conclusive experimental data are not yet available, many materials are capable of being welded also at higher chamber pressures. It must be expected, however, that materials welded at a pressure of 10^{-1} Torr will require a higher beam power than those welded at 10^{-4} Torr since a certain amount of energy will be lost in the chamber owing to the electrons of the beam colliding with residual gas molecules. Therefore, a few tentative experiments were made for the purpose of determining the depth of penetration of the electrons in structural steels in various vacua. The equipment used was a k-kW unit, Model ESW 500, made by Leyboldt-Heraeus. The results of these experiments are shown in Fig. 11.

Using the same welding parameters, i.e.,

Acceleration voltage	$U = 135$ kV
Beam current	$I = 15$ mA
Focal distance	$a = 130$ mm
Feed rate	$v = 7$ mm/sec

with the electron beam focused on the work-piece surface, different fusion-zone depths resulted as a function of pressure. Although pressure of 10^{-4} Torr yielded satisfactory fusion welds, complete fusion of the material over its entire cross section was no longer obtained at a pressure of 10^{-1} Torr. Increasing the focal distance to 330 mm but otherwise retaining the same operating conditions resulted in a shallower depth of penetration than was produced in the weld made at a lower pressure. This result is attributable to divergence of the beam at increasing focal distances due to greater lens aberrations and electrostatic repulsive forces. With increased beam power it was possible to produce a butt-welded joint between 10-mm-thick specimens of C 22 structural steel plate even at a higher pressure. A striking point to note in this connection was that, in terms of applied energy per centimeter of weld length, the joint produced at a higher pressure required less energy, i.e., 2000 J/cm, than the one produced at a lower pressure; here, the energy requirement was found to run to 2900 J/cm. It should be noted, however, that the deep-penetration joints produced at 10^{-4} Torr were narrower than those produced at the higher pressure of 10^{-1} Torr.

7. SUMMARY

EB welding of unalloyed structural steels is possible. Under specific operating conditions, reproducible and virtually nonporous welded joints can be produced. Increases in hardness up to 42 HR_c in the region of the weld are unavoidable; these are, however, confined to a very narrow zone of less than 1 mm and need not be regarded as critical. Besides, a reduction in hardness can be effected by post-heat-treatment of the weld with a defocused beam. Under static loading, the mechanical-technological properties of the joints were found to meet the specifications laid down in the relevant German Industrial Standards (DIN-Standards).

The virtually flawless welding of tubes of different cross section is possible, the welding parameters determined for longitudinal welds being fully transferable to the production of circular welds. The top beads of the welds can be smoothed by repeated remelting of the weld to a shallow depth which, however, may entail some increase in residual stresses within the area of the weld. In welding structural components, shorter cycle times, resulting from shorter pumping times for example, should be aimed at with a view to improving economy. Here, automatic welding at a pressure of 10^{-2} Torr constitutes a modern development which however necessitates higher beam power at increased welding speed if complete penetration of the work piece is to be achieved. Tentative experiments in this respect yielded data on resultant increases in the width of the welds and the heat-affected zones as well as on the virtually complete absence of porosity in these welds.

8. ACKNOWLEDGMENTS

Thanks are due to the sponsors of the 10th Symposium on Electron, Ion, and Laser Beam Technology for their invitation to Drs. Matting and Sepold, who are also taking this opportunity of gratefully acknowledging the outstanding cooperation and assistance of the Siepmann-Werke in the Federal Republic of Germany throughout the conduct of their investigations.

REFERENCES

1. A. Matting and G. Sepold, Basic research on welding with electron beams of high intensity, Third Intern. Conf. on Electron and Ion Beam Science and Technology, Electrochemical Society, 1968.
2. F. Eichhorn and D. Neef, Strahltechnisches Kolloquium III, Mannheim 1969; will be published at the end of 1969 in the "DVS-Berichte."

ELECTRON BEAM WELDING OF COPPER PLATES

RAJ K. RAHEJA

IBM Corp. (Components Division), East Fishkill, N. Y.

The physical structural properties of electron beam welds in copper plates have been investigated. The actual weld region consists of a dendrite grain morphology. On the basis of dendrite axial orientations determined by Laue X-ray techniques, the actual kinetics of dendrite growth seem to conform to those theoretically calculated. Nonisotropic growth kinetics can explain the striations observed in the dendritic weld regions. Other microstructural features are explained by using temperature distribution profiles. A slight decrease in the tensile strength of the cold rolled top copper plate is caused by the recrystallization of grains adjoining the actual weld region.

INTRODUCTION

The purpose of the investigation was to evaluate both the physical (structural) and mechanical properties of electron beam (EB) welds of two copper plates. In the semiconductor industry such welds are useful since they prevent damage to the surrounding regions by preventing exposure to high temperatures.

EXPERIMENTAL RESULTS AND DISCUSSION

The welds were made using a Hamilton Standard EB welding machine. The electron gun operating conditions were: 100 kV high voltage, 3 mA beam current, and 1.75 A filament current. Figure 1 is a schematic of a beam weld cross section. Figures 2 and 3 show representative photomicrographs of weld regions at the surface and cross section, respectively. In the actual weld region, where the copper of both the ground plane and the bit plate was molten and subsequently rapidly solidified, the copper grains are seen to be columnar or dendritic. Adjoining this the grains of the copper ground plane have been recrystallized to some distance from the weld.

Dendritic growth occurs when the difference in Gibbs free energy ΔG between the liquid and solid phase, is positive and increases with distance ahead of the interface. In the case of the pure copper to copper bit plate weld, the dendritic morphology develops in those regions where the temperature gradient in the liquid copper is negative at the liquid/solid interface. In the case of palladium plated bit plates where we have copper-palladium alloy liquid, the dendritic structure may have developed even with a positive temperature gradient in the liquid, provided the solute distribution was such that $d(\Delta G)/dZ > 0$ at the interface. It can be shown that the stablest condition is one where the growth velocity is maximum.

Since most metals are nonisotropic in character, two types of crystal faces have to be considered in dendritic growth: (1) the face growing in the axial direction, the fastest (0-direction) and (2) the slowest growing crystal faces, usually the closest packed faces--(111) for copper

Record of 10th Symposium on Electron, Ion, and Laser Beam Technology (L. Marton, ed.); San Francisco Press, Inc.

Copyright © by The Institute of Electrical and Electronics Engineers, Inc.—Printed in the U.S.A.

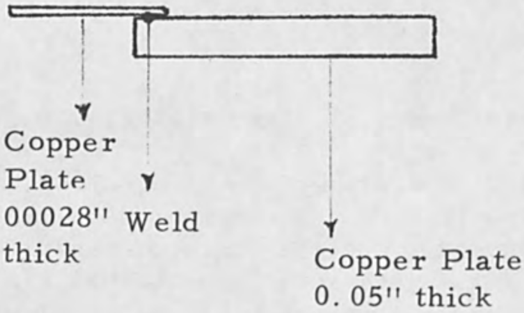
Copper
Plate
00028'' thick
Weld
Copper Plate
0. 05'' thick

FIG. 1.—Schematic illustration of a cross section of EB weld.

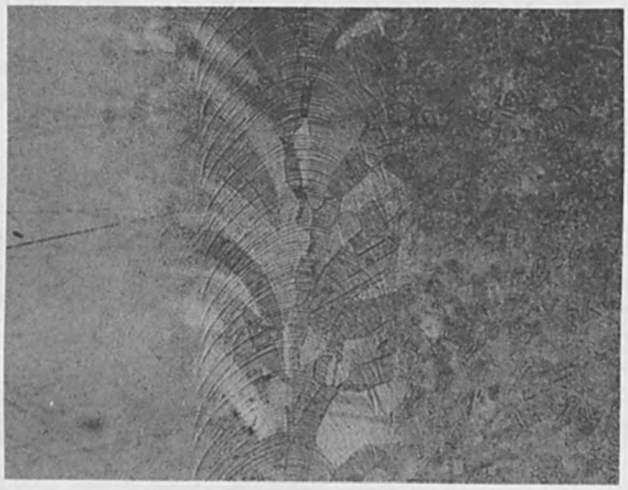

FIG. 2.—Photomicrograph showing scalloped edge of columnar grained EB weld region (mag. 100X).

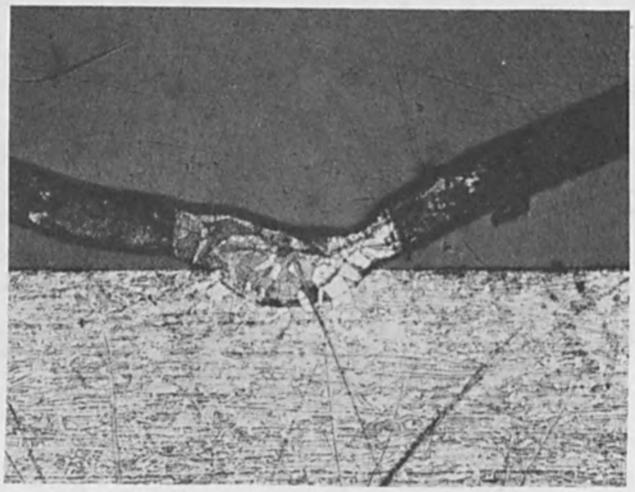

FIG. 3.—Photomicrograph of cross section of EB weld (mag. 100X).

and Cu-Pd alloy--(Ø-direction) make an angle Ø with the dendritic axis.

These faces make angles Ø with the specimen axis (symmetrical faces). If ρ is the radius of curvature of the tip of the dendrite, it can be shown that the dendrite growth velocity V is inversely proportional to this radius of curvature ρ for a constant $\delta T(0)$. For a diffuse interface:

$$\rho = \frac{2G(0)}{S\,\delta T(0)} \cdot \frac{1 - \frac{G(\O)}{2G(0)} \cos \O \, (1 + \cos^2 \O)}{\frac{\mu(0)}{\mu(\O)} \cos \O - 1}$$

Here μ is the atomic kinetic coefficient, Ø is a primary crystallographic direction (slowest growing faces), and G is the free energy. For a constant $\delta T(0)$ as we have in our case, the growth direction that minimizes ρ in the equation above is the preferred dendrite growth direction. The dendritic growth direction is one in which $\mu(0)/\mu(\O)$ is maximum.

One would expect that the atomic kinetic coefficient would decrease as the atomic packing of the crystallographic faces increases, so that for closest packed planes the atomic kinetic coefficient would be minimum, i.e., $\mu(\O)$ is minimum for Ø in the direction of the closest packing. This would maximize $\mu(0)/\mu(\O)$. The closest packed planes in Cu and CuPd are $\{111\}$ planes. The preferred growth directions for face centered cubic materials would then be the axis of a pyramid of the four sets of $\langle 111 \rangle$ planes. This was shown by Weinberg and Chalmers a few years ago. The axial growth direction is thus $\langle 100 \rangle$. The axial directions of the dendrites have been verified by Laue X-ray techniques to be close to $\langle 100 \rangle$ directions. Figures 4 and 5 represent Laue back reflection micrographs of small regions of the dendritic weld and copper plate respectively.

The four significant microstructural features observed are (1) dendritic structure of the actual weld region with the dendrites following $\langle 100 \rangle$ axis, (2) scalloping of the edges of some weld regions (Fig. 2), (3) striations in the weld regions themselves probably due to anisotropy of atomic freezing kinetics (Fig. 6), and (4) recrystallization of regions adjoining the actual weld.

Items (1) and (2) can be explained readily by the use of temperature distribution profiles (Fig. 7). It is assumed here that (a) the shape of the electron beam on the work is circular and (b) the shape of the temperature profile across any diameter of the beam spot is Gaussian with a half-width of approximately 10 μ . It is seen from these profiles that higher-energy peaks T_2 , T_n give rise to deep notches. An increase in the relative rates of translation between the work piece and the electron beam would give rise to increased scalloping of the weld edges. In addition, the copper grains on either side of the actual weld region (temperature $T > T_R$) will be recrystallized as observed.

A microscopically layered temperature interface between liquid and solid may be caused by an inconstancy in $\delta T(0)$ across the liquid/solid interface owing to (1) electron beam and/or specimen table vibration and/or a slight periodic electron density or flux variation associated with the beam, and (2) anisotropy of atomic kinetics. This second reason appears quite likely (Fig. 8a). For a microscopically smooth

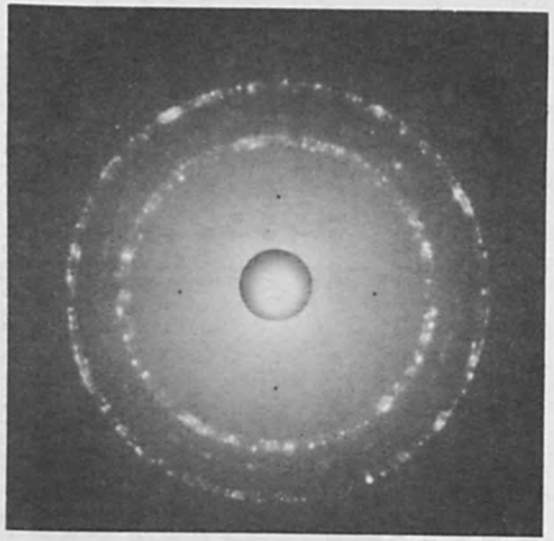

FIG. 4.—Laue back-reflection micrograph of columnar grained weld region.

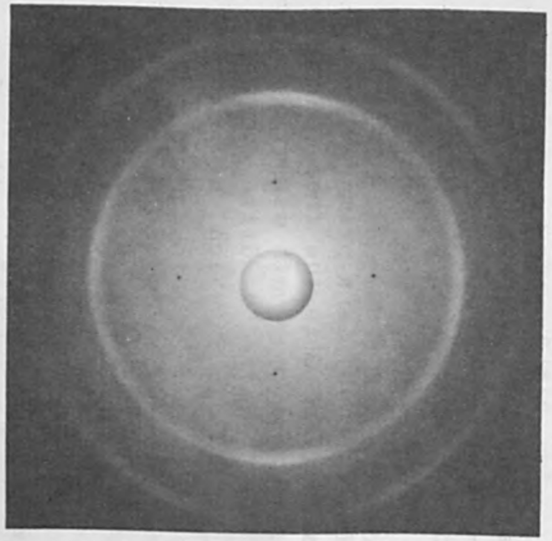

FIG. 5.—Laue back-reflection micrograph of copper sheet.

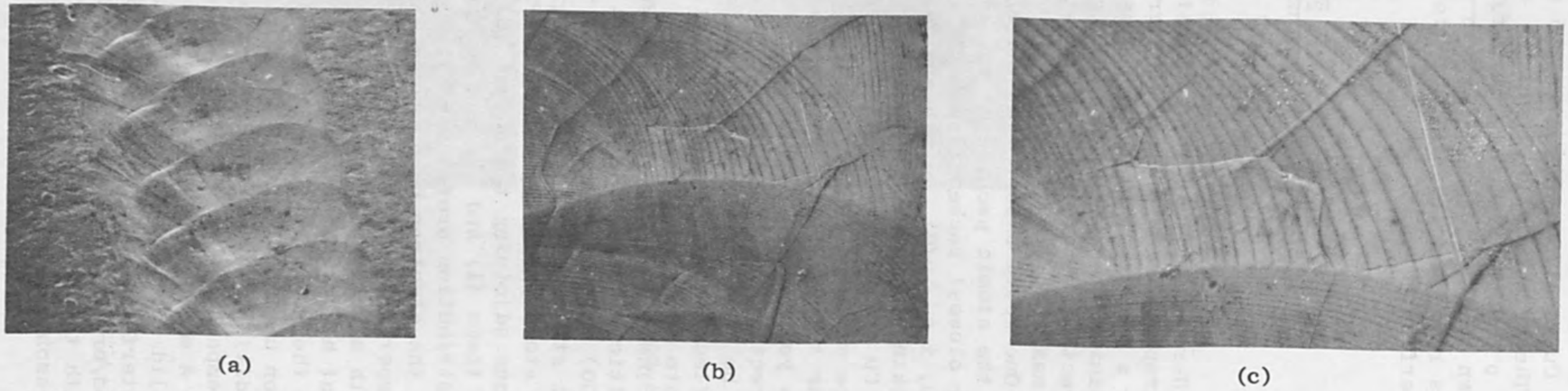

(a) (b) (c)

FIG. 6.—Scanning electron micrographs showing striations in dendritic grains: (a) mag. 93.5X, (b) mag. 468X; (c) mag. 935X.

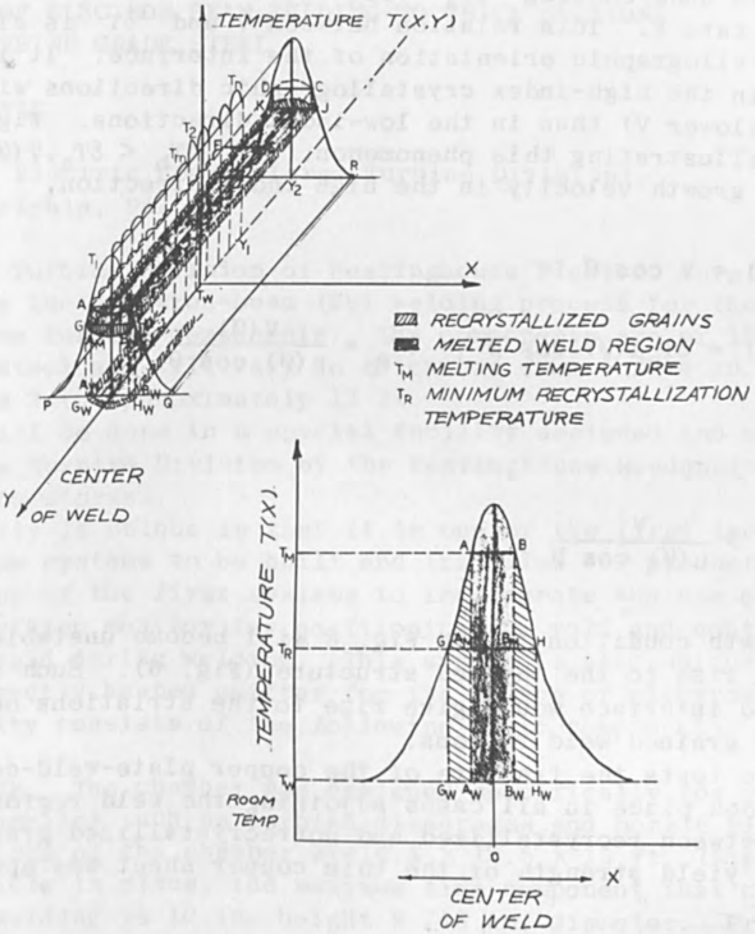
TEMPERATURE T(X,Y)
T3
C
K
J
T2
Tm
S
Y2
R
T1
Y1
A
G
B
X
TW
GW
AW
HW
BW
P
Q
▨ RECRYSTALLIZED GRAINS
■ MELTED WELD REGION
TM MELTING TEMPERATURE
TR MINIMUM RECRYSTALLIZATION TEMPERATURE
CENTER
Y OF WELD
TEMPERATURE T(X)
TM
TR
TW
A
B
G
H
GW AW BW HW
ROOM TEMP
0
X
CENTER OF WELD

FIG. 7.—Temperature distribution profiles.

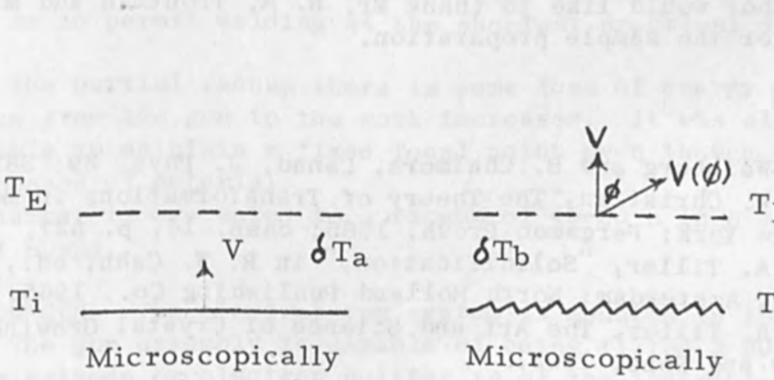
TE
V
δTa
Ti
V
ø
V(ø)
TE
δTb
Ti

Microscopically smooth interface

(a)

Microscopically layered interface

(b)

FIG. 8.—Schematic illustration of undercooling δT necessary to cause dendritic solidification at a rate V. T_E is the equilibrium freezing temperature and T_i is the interface temperature: (a) microscopically smooth interface, (b) microscopically layered interface.

interface some undercooling δT_a will cause the transformation to occur at a certain rate V. This relation between V and δT is also a function of crystallographic orientation of the interface. It is expected that growth in the high-index crystallographic directions will occur at a lower δT (lower V) than in the low-index directions. Figure 8(b) is a schematic illustrating this phenomenon. If $\delta T_b < \delta T_a, V(\phi) > V$ and $V(\phi)$ is the growth velocity in the high index direction,

$$V(\phi) = V \cos \phi$$

$$V(\phi) = \delta T_a \mu(\phi) \cos \phi \ ; \quad \delta T_a = \frac{V(\phi)}{\mu(\phi) \cos \phi}$$

therefore,

$$\delta T_a > \frac{V}{\mu(\phi) \cos \phi}$$

Thus the growth condition (1) in Fig. 8 will become unstable and (2) will occur giving rise to the layered structure (Fig. 6). Such a microscopically layered interface would give rise to the striations observed in the columnar grained weld regions.

In tensile tests the fracture of the copper plate-weld-copper plate composites took place in all cases adjoining the weld region at the transition between recrystallized and nonrecrystallized grains. The reduction in yield strength of the thin copper sheet was approximately 20%.

ACKNOWLEDGMENTS

The author would like to thank Mr. H. A. Troutman and Miss Doris E. Braddock for the sample preparation.

REFERENCES

1. F. Weinberg and B. Chalmers, Canad. J. Phys. 29: 382, 1951.
2. J. W. Christian, The Theory of Transformations in Metals and Alloys, New York: Pergamon Press, 1965; chap. 14, p. 527.
3. W. A. Tiller, "Solidification," in R. W. Cahn, ed., Physical Metallurgy, Amsterdam: North Holland Publishing Co., 1965.
4. W. A. Tiller, The Art and Science of Crystal Growing, New York: John Wiley and Sons, 1963.

APPLICATION OF ELECTRON BEAM WELDING TO THICK SECTIONS OF 12% Cr TURBINE GRADE STEEL

L. J. PRIVOZNIK

Westinghouse Electric Corp. (Large Turbine Division),
South Philadelphia, Pa.

The Large Turbine Division of Westinghouse Electric Corp. is preparing to use the electron-beam (EB) welding process for the welding of selected steam turbine components. The components are of 12% Cr turbine-grade alloy steel and will vary in thickness from 1 to 4 in. and in diameter from 2 to approximately 12 ft.

Welding will be done in a special facility designed and manufactured for the Large Turbine Division by the Westinghouse Headquarters Manufacturing Laboratories.

The facility is unique in that it is one of the first large-chamber partial vacuum systems to be built and installed for production welding. It is also one of the first systems to incorporate the use of a closed-circuit television monitor for positioning the weld and continuously viewing the weld during welding. This system is also unique in that it uses an indirectly heated emitter for its source of electrons.

The facility consists of the following basic components:

1. CHAMBER. The chamber was designed specifically for welding flat circular assemblies such as turbine diaphragms and nozzle blocks. The inner dimensions of the chamber are 4.5 X 12.5 X 15 ft. (Fig. 1). With the rotary table in place, the maximum size component that can be accommodated for welding is 10 in. height X 148 in. diameter. Provision for welding components of greater height can be made by replacing the existing table with one of more compact design. The table has three axes of motion: vertical, horizontal, and rotary. The vertical motion was incorporated so as to permit welding at the shortest practical distance from the gun.

Because of the partial vacuum there is some loss of energy of the beam as the distance from the gun to the work increases. It was also considered desirable to maintain a fixed focal point even though welding various thicknesses of material.

The work chamber is evacuated to a vacuum of 45-50 μ in 8 min using two mechanical pumps.

2. ELECTRON GUN. The electron gun system is mounted in the roof of the chamber. The gun assembly is capable of being tilted $\pm 30^\circ$ from the vertical. The cathode or electron emitter is of the indirect-heat type. The cathode consists of a polished tungsten rod heated by a noninductive, helically wound tungsten filament. The emitting rod, heater filament, and heat shield are mounted in a standard multiple-pin type tube plug. This arrangement permits simple and fast replacement of the cathode into the mating female socket. The electron gun system of our production facility is presently rated at 12.0 kW.

The anode plate, focus coil, and deflection coils are mounted below the cathode. Mounted below the deflection coil is the intermediate orifice system. This stage is pumped down to a vacuum level intermediate between the chamber and the gun and prevents entry of metallic vapors or

Record of 10th Symposium on Electron, Ion, and Laser Beam Technology (L. Marton, ed.); San Francisco Press, Inc.

Copyright © by The Institute of Electrical and Electronics Engineers, Inc.—Printed in the U.S.A.

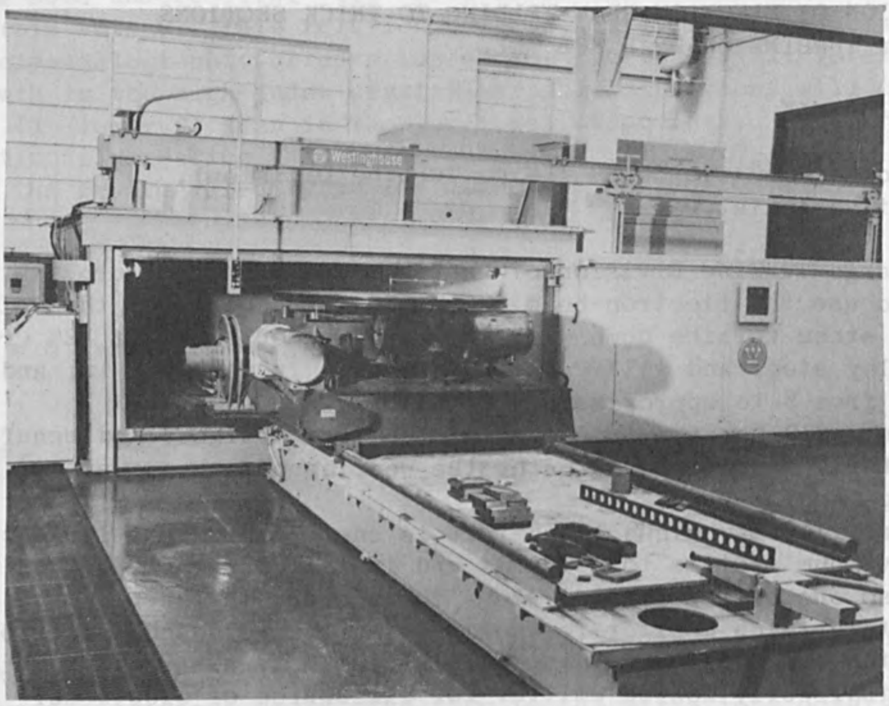

FIG. 1.—Partial-vacuum EB welding facility.

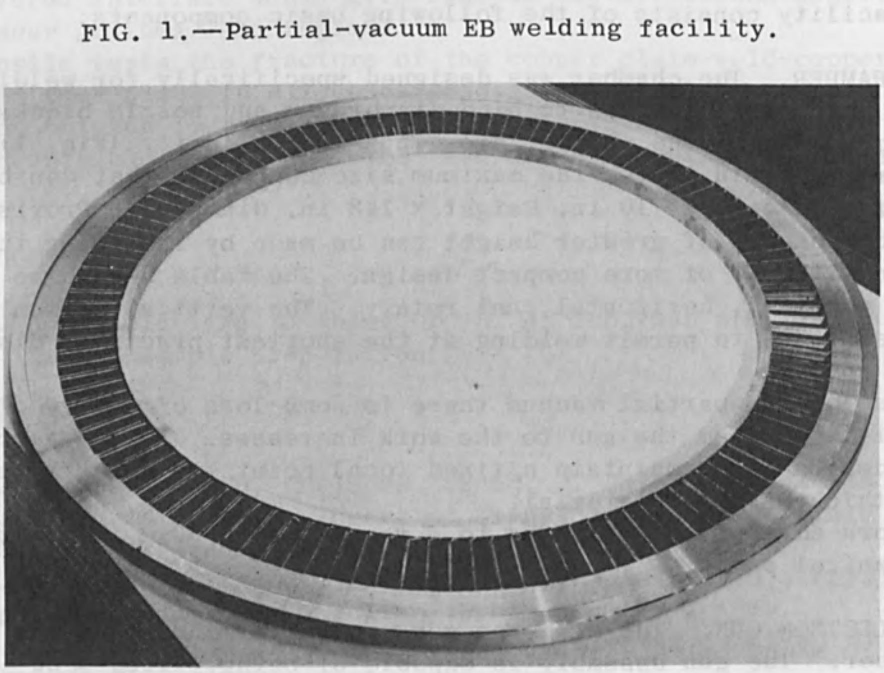

FIG. 2.—Completed diaphragm assembly after welding and machining but prior to cutting apart.

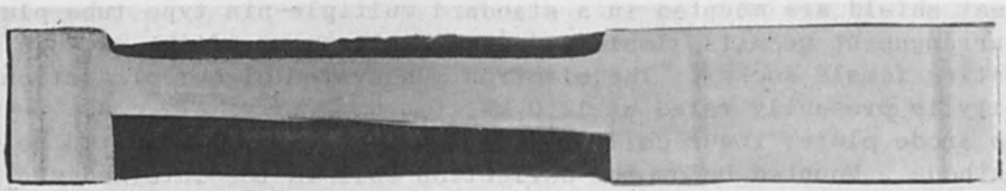

FIG. 3.—Cross section of typical diaphragm showing location of full-penetration EB welds.

other particles into the gun system.

3. POWER SUPPLY. For ease of maintenance, the electrical components of the power supply are mounted in an ASME code pressure vessel and insulated with SF_6 gas maintained at approximately 42 psi of pressure, rather than the more conventional type of oil insulation. All of the electrical components are mounted on a monorail system inside the tank. This construction also contributes to easy maintenance. Power input to the power supply is provided by a motor generator set operating at 960 Hz. The power supply is rated at 25 kW.

MAJOR APPLICATION

Although several applications are being qualified for this facility, the major application is the welding of reaction diaphragms, i.e., stationary vane assemblies that redirect the flow of steam from one row to another row of rotating blades.

Reaction diaphragms are installed in high-pressure, intermediate-pressure, and low-pressure cylinder sections. Each diaphragm has up to 120 vane segments. Each vane segment is in the shape of a "dog bone" with the welds joining the heavy ends. The individual vane segments are assembled into a full circle and welded as a ring. In the past, weld metal was deposited by the MIG process in grooves machined at the inner and outer circumference in a plane perpendicular to the central axis of the diaphragm. Present plans call for welding these assemblies with the electron beam process instead of the MIG process. Instead of filling in grooves with weld metal at the inner and outer circumferences, the welds will be made from the surface parallel to the central axis of the diaphragm. Penetration will be through the full thickness. Figure 2 shows a completed diaphragm assembly after welding and machining but prior to cutting apart. The cross section of a typical diaphragm, indicating location of the welds, is seen in Fig. 3.

Changing from the MIG process to the EB process required a change in weld joint design. The MIG welds are large in cross-sectional area and in width. The electron beam welds are considerably smaller in cross-sectional area and are narrow. Based on engineering design requirements and the results of destructive tests of prototype diaphragms, the number, location, and cross-sectional area requirements for EB welds for the diaphragms were established.

Two welds are required at both the inner and outer circumference. The location and cross-sectional area requirements of the welds at the inner circumference are more critical than those at the outer circumference, particularly for those diaphragms that will be installed in the high-pressure cylinder.

Normally EB weld applications call for very narrow welds with a large depth-to-width ratio. In developing weld parameters emphasis is normally placed on penetration and weld shape with no particular emphasis on weld width.

For the diaphragm application, primary emphasis is placed on weld width and weld shape with penetration being dictated by the thickness of the material being welded. Literature contains much data and information relating to the effect of parameter changes on depth of penetration for EB welds. However, very little information is available concerning the effects of parameter changes on the width of EB welds, particularly those made in heavy sections in partial or soft vacuum. In addition to the rigid requirements for location and area of the welds, there is a rigid requirement as to the quality of the welds. There is a general feeling that since the welds are relatively narrow, the presence of even small-size defects occurring in multiple number would have a detrimental effect, particularly since they inherently occur as linear-type defects.

Preliminary welds made in 12% Cr turbine-grade steel indicated that welds made at too high a travel speed or made under conditions that produced an excessively wide weld were susceptible to centerline cracking. Electron microprobe analysis indicated that cracking occurred in alloy-enriched ferrite areas segregated along the centerline of the weld. Therefore, it was considered mandatory to establish parameters with controlled limits that would not produce conditions which would lead to cracking.

In order to satisfy the rigid requirements for the diaphragm welds and to prove out the repetitiveness of settings and the reliability of the equipment, an extensive testing and evaluation program was conducted. The program consisted of a designed experiment to assist in establishing optimum parameters and to determine which parameters had a significant influence on the critical weld characteristics. Another goal was the development of data that could be used to predict effects of small changes in parameters on weld depth, width, and quality. Since this program is not completed at this date, the results of this program will not be included in this paper. The results of an earlier experiment (designed primarily to evaluate the characteristics of the welder) are presented instead.

EVALUATION OF EB WELD CONFIGURATION

A preliminary designed experiment was conducted on a duplicate welder to evaluate the effects of the major parameters on the configuration of the EB weld. This experiment involved the definition of the parameters, the limits of these parameters, the variations and combinations of these parameters, and finally the preparation of 81 sample welds.

The following parameters were chosen as major independent variables:

VARIABLES	LIMITS
S = Speed	8-12 IPM
V = Accelerating voltage	120-140 kV
I = Beam current	60-80 mA
F_0 = Focus current	0.38-0.44 A
F_r = Frequency of circle generator	150-250 Hz
D = Cathode-to-work distance	27.75-29.25 in.

Other variables such as chamber pressure (vacuum), beam deflection, and work temperature were maintained constant at fixed values. We were interested in the effects of variations in values of the independent variables on the following dependent variables:

L = weld depth
W = average weld width
L/W = depth-to-width ratio

After completion of the weld samples, the dependent variables were measured and tabulated for computer processing. The experiment was evaluated using regression analysis. The equations generated by the computer are as follows:

A. Depth of the weld, L:

$$\begin{aligned} L = {} & 7.974 - 0.427S - 0.192V - 0.0286C + 51.843F_O \\ & + 0.0033F_r - 0.0992D + 0.019S^2 + 0.001VC \\ & + 0.324VF_O - 0.204CF_O - 101.09F_O^2 \end{aligned}$$

B. Width of the weld at half length, W:

$$\begin{aligned} W = {} & - 1.129 + 0.0855S + 0.0118V - 0.000076C - 2.532F_O \\ & - 0.0019F_r + 0.0426D - 0.0032SD - 0.00004VC \\ & - 0.0231VF_O + 0.0135CF_O + 6.09F_O^2 + 0.000037F_r^2 \end{aligned}$$

C. Length-to-width ratio, L/W:

$$\begin{aligned} L/W = {} & 107.195 - 22.632S - 2.997V - 0.0858C + 952.768F_O \\ & + 1.235F_r - 5.107D + 0.800SD + 0.0166VC + 4.999VF_O \\ & - 4.602CF_O - 1469.341F_O^2 - 0.863F_OF_r - 0.0276F_rD \end{aligned}$$

From the equations generated by the computer the depth, width, and depth-to-width ratio of an EB weld can be calculated for a given set of variables within the stated limits. These equations are obviously long and tedious to use. Our interest at this time was to determine the general effect of the independent variables; therefore, a different approach was taken to present the equations in a simplified form. The equations were transformed to vectors, all of the cross terms broken down to components and summarized, and from the minimum values of the independent variables a new constant was generated for each equation. A nomogram was then set up for each equation, with the length of the line representing the amount of contribution of the independent variable to the dependent variable, and the direction of the line representing positive (+) or negative (-) contribution. By this method, it is possible to indicate the contribution of the six linear terms to each dependent parameter (L, W, L/W) on a single nomogram. The nomograms are presented in Fig. 4.

Since the equations represent an exponential expression (parabola), their use for quantitatively predicting weld depth and width must be confined to specified limits of the independent variables. Although the usefulness of the equations or nomograms for predicting welding parameters is limited, it is felt that the direction of contribution and the relative magnitude of the contributor can be predicted on a wider range.

As part of the evaluation of the production welder an investigation to determine the reproducibility of results with different cathode assemblies was conducted. Three welds were made with each of six different cathode assemblies with identical welding parameters. The welds were sectioned and etched and measurements were made of depth and width. To summarize the results of the cathode evaluation, the greatest variation among the measurements was found to be less than 5% based on a single cross section per weld. The average weld depth of each test weld was 1.30 in. with a variation of ± 0.03 in. Therefore, reproducibility from cathode to cathode was considered excellent.

After operating with a single cathode assembly at power levels between 8 and 10 kW for a total accumulated time in excess of 30 hr there was no

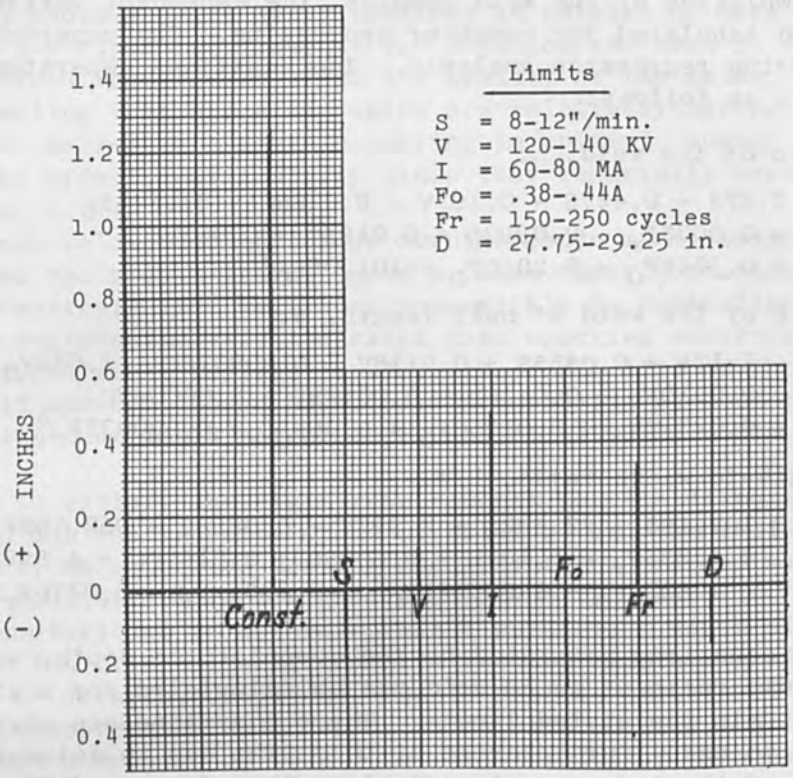
Limits
S = 8-12"/min.
V = 120-140 KV
I = 60-80 MA
Fo = .38-.44A
Fr = 150-250 cycles
D = 27.75-29.25 in.
INCHES
1.4
1.2
1.0
0.8
0.6
0.4
0.2
(+)
0
(-)
0.2
0.4
Const.
S
V
I
Fo
Fr
D

(a)

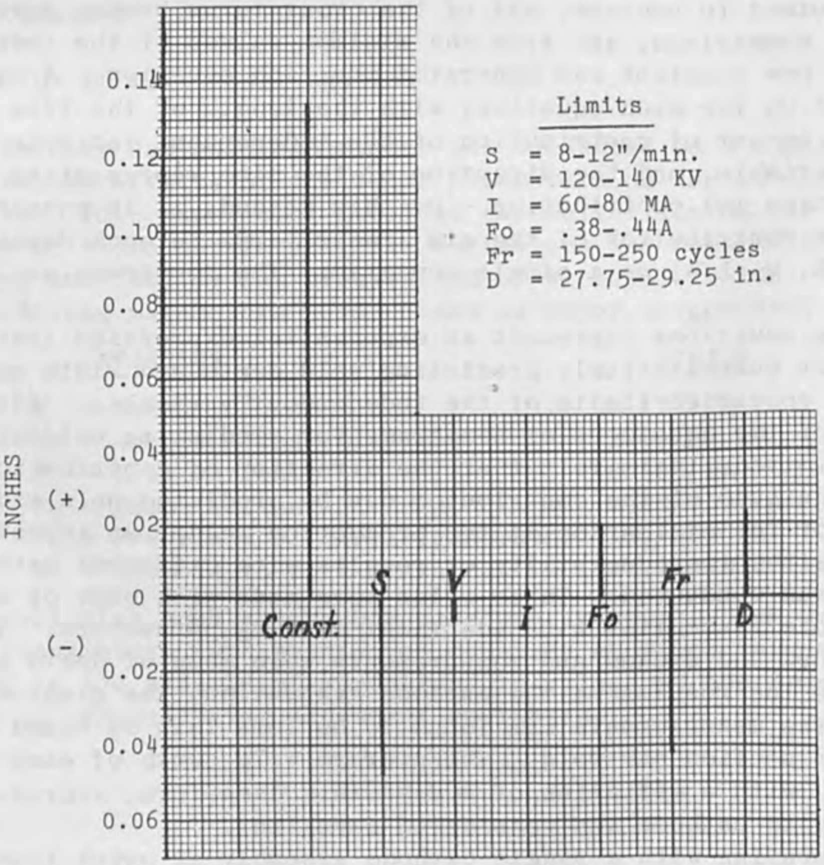
Limits
S = 8-12"/min.
V = 120-140 KV
I = 60-80 MA
Fo = .38-.44A
Fr = 150-250 cycles
D = 27.75-29.25 in.
INCHES
0.14
0.12
0.10
0.08
0.06
0.04
(+)
0.02
0
(-)
0.02
0.04
0.06
Const.
S
V
I
Fo
Fr
D

(b)

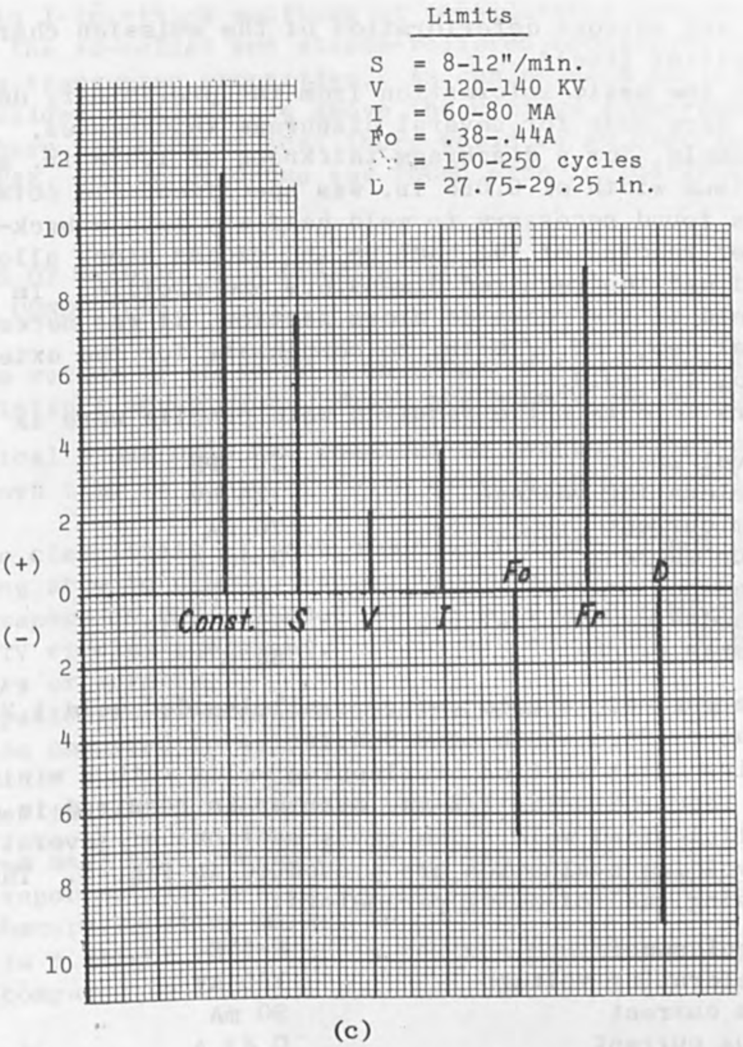

FIG. 4.—Nomograms for predicting dimensions of EB weld in T-304 stainless steel: (a) depth, (b) width, (c) depth-to-width ratio.

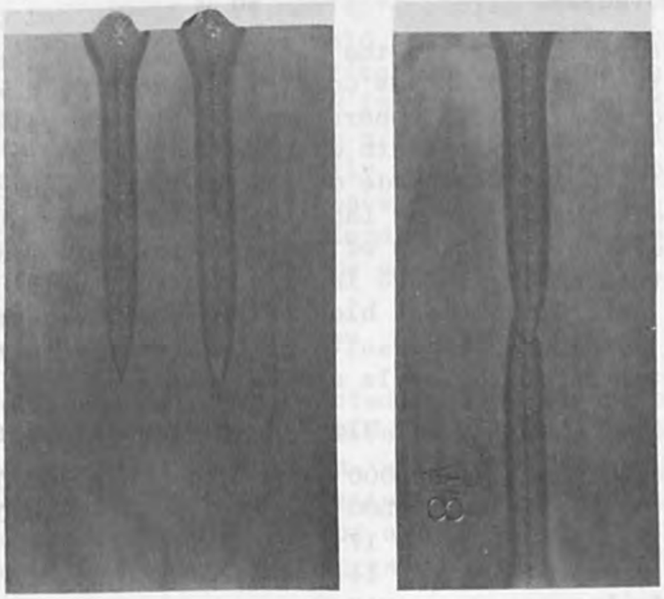

FIG. 5.—Partial-vacuum EB welds in 12% Cr steel 4 in. thick.

ACKNOWLEDGMENTS

A number of personnel were responsible for advancing the state of the art of EB welding to the status presented in this paper. In particular, credit should be given to the following: R. Wien, R. Kugler, L. Mano, and T. Csakvary from the Westinghouse Headquarters Manufacturing Laboratories, who were instrumental in the design and manufacture of the equipment, and J. Heverly, S. Barton, and L. Wagner of the Large Turbine Division, who were instrumental in conducting the development programs and evaluating and qualifying the equipment prior to production.

NEW DEVELOPMENTS IN EB-DRILLING AND PERFORATING PROCESSES

K. H. STEIGERWALD, W. E. MEYER, and D. KÖNIG

Steigerwald Strahltechnik, Munich

During the last few years processes for removal of material using an electron beam (EB) have developed so far that today we have production application in various fields of industry. It will be seen that especially EB drilling will soon reach an extent equal to EB welding or even greater. These methods open new possibilities in aircraft industries, turbine production, filter techniques, application of plastic materials, and a great deal more. This paper describes some important characteristics of these material-removing processes and gives numerous examples of present-day applications.

Contrary to EB welding, where for most purposes a steady beam is used, for material removing a pulsed electron beam is normally chosen. A lot of experiments have shown that the pulse effect alone is by far not sufficient to remove material precisely, reproducibly, and with optimal efficiency.

For this reason we have developed a number of processes using the specific properties of electron beams under optimized conditions. They make it possible

- to remove any material in portions exactly defined by beam parameters;
- to make the process highly reproducible; and
- to work under maximal efficiency of beam power in order to realize very high working speeds.

With these properties the important preconditions for production application had been achieved.

Of course, parallel to this process research, a lot of improvements on the machine (especially on the gun) had to be made. Today we can say that without having made some fundamental changes all of the possibilities now to be reported would not exist.

First, I want to comment on terms EB drilling and EB perforation. Both techniques are used to make holes. Depending on the material thickness it is necessary to work with a series of EB pulses to get a hole or it is sufficient to use a single but more powerful pulse. A few years ago we thought there was a limit to the single-pulse process in thicknesses of about 0.5 mm (about 20 mil), and that it was possible to make holes 5 mm deep or more only with multipulse techniques. But this picture has changed rapidly as new guns with improved electron optics and power supplies have become available. With multipulse drilling, where the hole diameter normally is determined by the amplitude of some kind of circular deflection, holes can be realized in thicknesses of up to nearly 1 in. Tests have been made in which we obtained first holes 2 in. deep and more, but I think it is still too early to talk more about this.

The range of diameter begins with about 0.1 mm and has in principle no upper limit; normal application requires values between 0.1 and 2 mm.

Record of 10th Symposium on Electron, Ion, and Laser Beam Technology (L. Marton, ed.); San Francisco Press, Inc.

Copyright © by The Institute of Electrical and Electronics Engineers, Inc.—Printed in the U.S.A.

Drilling time goes from a few tenths of a second (for example to get holes 0.3 mm in diameter in a 1-mm steel plate) up to 1-2 min to drill a 1-mm-diameter hole 20 mm deep. The shape of holes and *surface quality* are determined by the beam parameters and, of course, by certain special process characteristics. Normal surface roughness inside of the holes is of the order of about 10 µm; in some cases we realized figures smaller than 5 µm.

Diameter setting and *reproducibility* normally lie within 5%, but values of 1% have been realized.

The figures above relate to the drilling of metals, since most applications today concentrate on these materials. Of course drilling of metals which cannot be tooled with other methods or the tooling of which is very expensive and time-consuming is of great interest. Therefore, machines are operating to produce holes, for example, in *turbine blades* and other turbine parts, where very exotic materials had to be used.

In those fields where *high precision* holes are necessary, for instance injection holes, the EB-drilling method has become increasingly important.

Moreover, the drilling of ceramics, graphite, semiconductors, and glasses should be mentioned. These applications play a secondary role today, but become increasingly important, since many attractive results have been achieved.

Single-pulse drilling we call "perforation." This process naturally was first applied to make holes in thin metals and plastic sheets, but today we are able to shoot holes through steel plates *10 mm thick*.

Pulse times range from a few microseconds to several milliseconds, so that we can reach *very high drilling speeds*; this single-pulse process is thus increasingly replacing the multipulse method used so far.

Properties of the holes, such as diameter, conicity, quality of entrance, and exit are determined by the EB parameters, especially the distribution of the power density in the working spot.

As a result of the extremely short drilling time this process has been applied to perforate metals and plastics in the same intense way.

Hole diameters go from a minimum of 1-2 µm to values of about 1 mm. Commonly it is interesting to know the smallest diameter possible in a certain thickness. The relation is shown in Fig. 1.

The accuracy of holes and the reproducibility attain values of a few per cent, as we shall see.

Figure 2 shows the relation between the attainable perforation frequency (holes per second) and material thickness, since with increasing thickness, pulse time has also to be increased. The dotted line shows the frequency of about 20 kHz reached in our machines to date.

Very high hole densities can be obtained. We have found that the

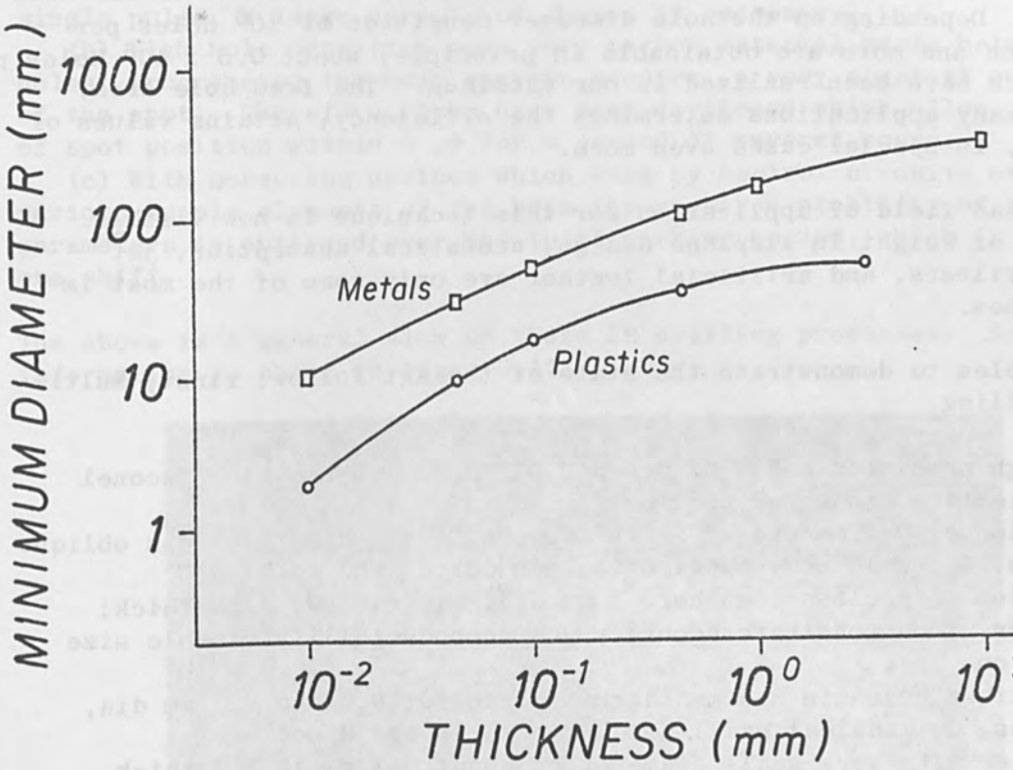

FIG. 1.—Minimum diameter of EB perforation as a function of material thickness for metals and plastics.

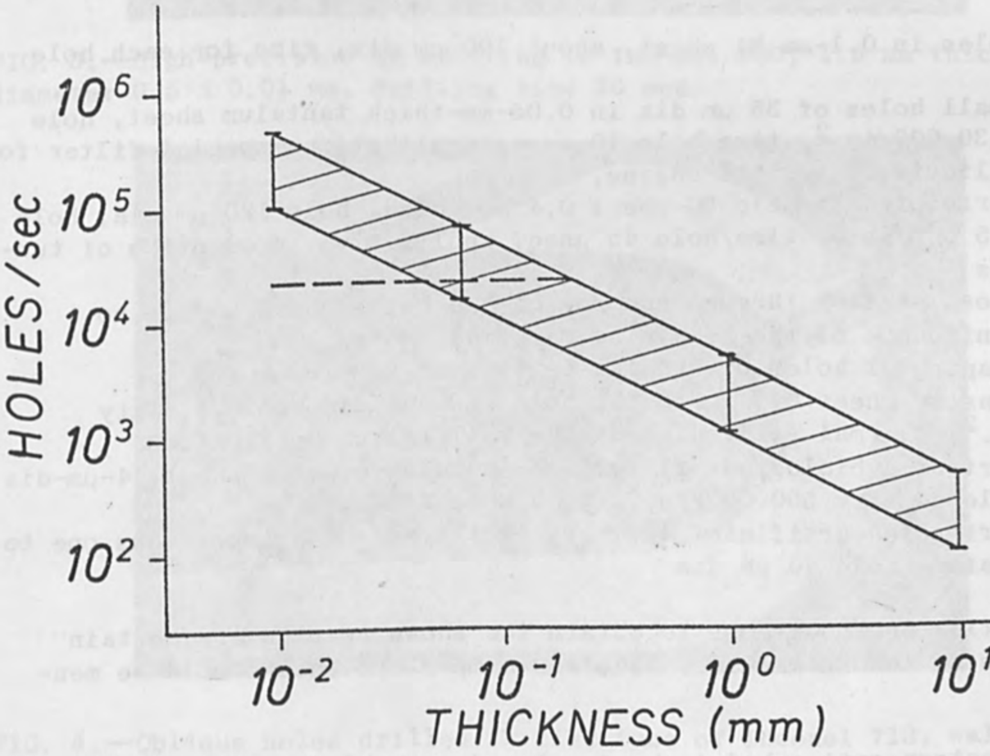

FIG. 2.—Perforation rate as a function of material thickness.

material between two holes in normal cases should be 0.1-0.5 of the hole diameter. Depending on the hole diameter densities of 10^6 holes per square inch and more are obtainable in principle; about 0.5 X 10^6 holes per square inch have been realized in our machines. The free hole area, which in many applications determines the efficiency, attains values of up to 50%, in special cases even more.

A widespread field of application for this technique is now visible. Reduction of weight in airplane design, acoustical absorption, jet engines, filters, and artificial leather are only some of the most important ones.

Some examples to demonstrate the state of the art follow; first, multipulse drilling.

(a) high-precision holes of 0.5 ± 0.01 mm in 1.5-mm-thick Inconel 600; application, injector nozzles

(b) holes of 0.5 mm dia in a flat tube of 1 mm wall thickness oblique to surface, 5 and 10 sec, application, injection and cooling

(c) holes very close together, 1 mm dia, Nimonic 90, 1 mm thick; application, to demonstrate accuracy and reproducibility of hole size and position

(d) oblique holes in 3.3 mm thick Nimonic 90, 0.2 and 0.7 mm dia, clean edges, cylindrical small hole, time: 15 and 3 sec

(e) holes with very small diameter of about 0.1 mm in 3.3 thick Nimonic 90

Here some samples for perforation:

(a) holes in 0.1-mm Ni sheet, about 100 μm dia, time for each hole 20 μsec

(b) small holes of 35 μm dia in 0.05-mm-thick tantalum sheet, hole density 130 000/in.^{2}, time/hole 10 μsec, application, special filter for hot fuel liquid in turbine engine,

(c) perforated Nimonic 90-sheet 0.4 mm thick, hole 120 μm dia, hole density 15 000/in.^{2}, time/hole 45 μsec, application, production of turbine parts

(d) cross section through one row of the holes shown before,no thermal influence of the remaining material

(e) shaping of holes by special setting of EB parameters

(f) plastic sheet 0.1 mm thick, hole 90 μm dia, hole density 20 000/in.^{2}, thermal stiffening of the wall,filter application

(g) part of a biological filter, 12-μm thick plastic sheet, 4-μm-dia holes, hole density 500 000/in.^{2}, time/hole 2 μsec

(h) perforated artificial leather, two layers, the impervious one to be perforated, hole 40 μm dia

The essential preconditions to obtain the shown results are certain properties of the EB machine. The most important ones should be mentioned:

(a) Electron optics had to be developed, capable not only of producing power densities of up to 10^9 W/cm^2 and more, but also of allowing variations of power density distribution within wide limits. Especially for perforation, where all properties of the holes have to be made by a single pulse, a large variety of shapes is necessary.

(b) High hole densities mean very narrow material parts between the holes; programming the hole pattern require a very constant position of the spot. Therefore, guns have been developed which allow constancy of spot position within 5 μm for a period of several hours.

(c) With measuring devices which work by control circuits on the various supply elements of the beam the required stability of the beam parameters is obtained over the total working period, which is at least one shift.

The above is a general view on these EB drilling processes. Additional information is shown in Figs. 3-17.

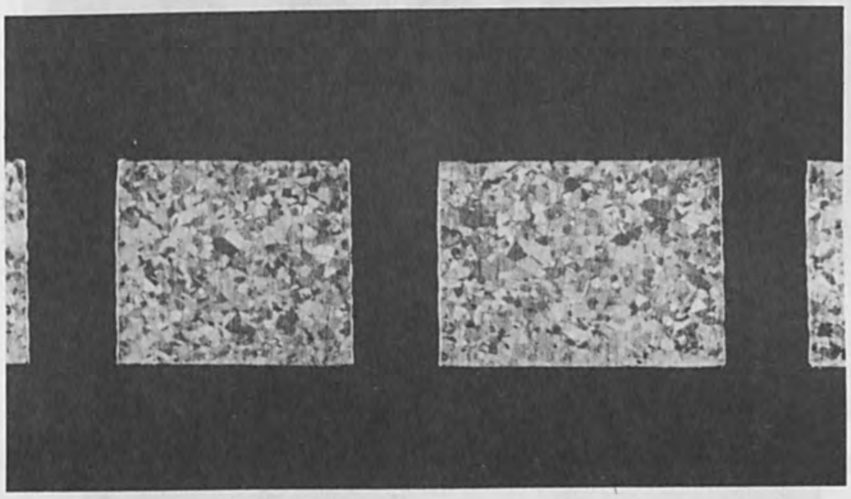

FIG. 3.—High-precision EB drilling in Inconel 600, 1.5 mm thick; diameter 0.5 ± 0.01 mm, drilling time 20 sec.

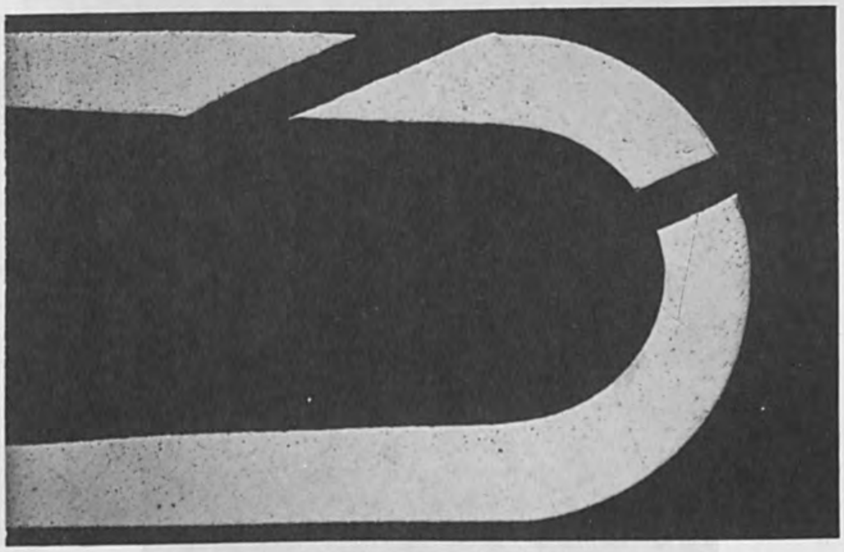

FIG. 4.—Oblique holes drilled in flat tube of Inconel 713, wall thickness 1.5 mm; diameter 0.75 mm, drilling time 5 and 10 sec.

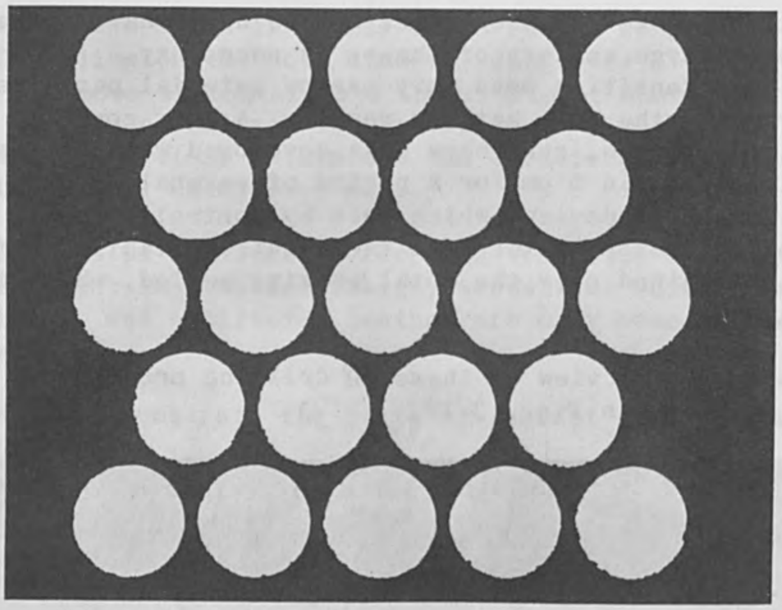

FIG. 5.—High-density EB drilling in stainless steel, 1.5 mm thick; diameter 1.0 mm, drilling time 15 sec.

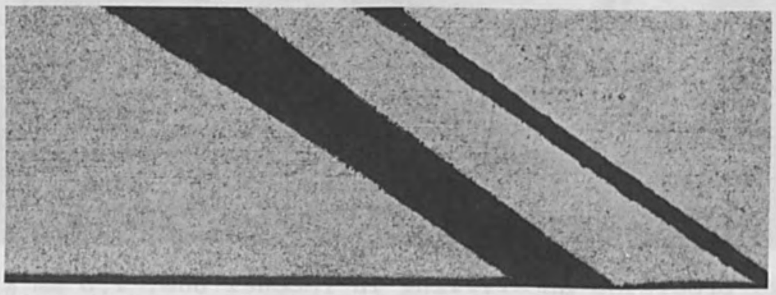

FIG. 6.—Oblique holes drilled in Ni alloy, 3.3 mm thick; hole length 5.2 mm, angle to surface 35°, diameters 0.7 and 0.2 mm, drilling time 15 and 3 sec.

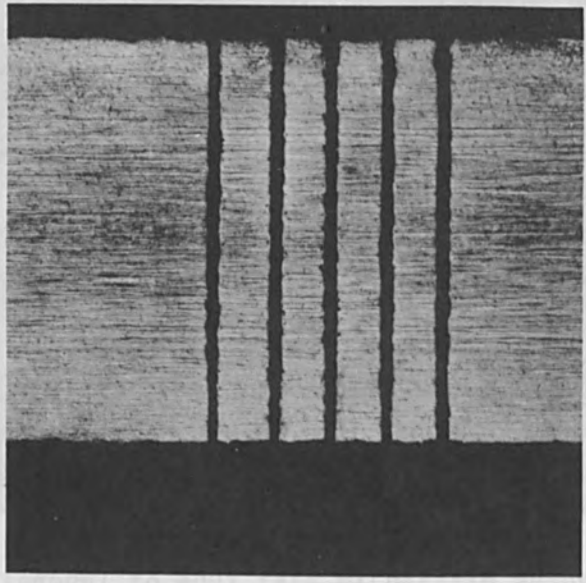

FIG. 7.—Small-diameter holes in Ni alloy, 3.3 mm thick; diameter 0.1 mm, drilling time 1 sec.

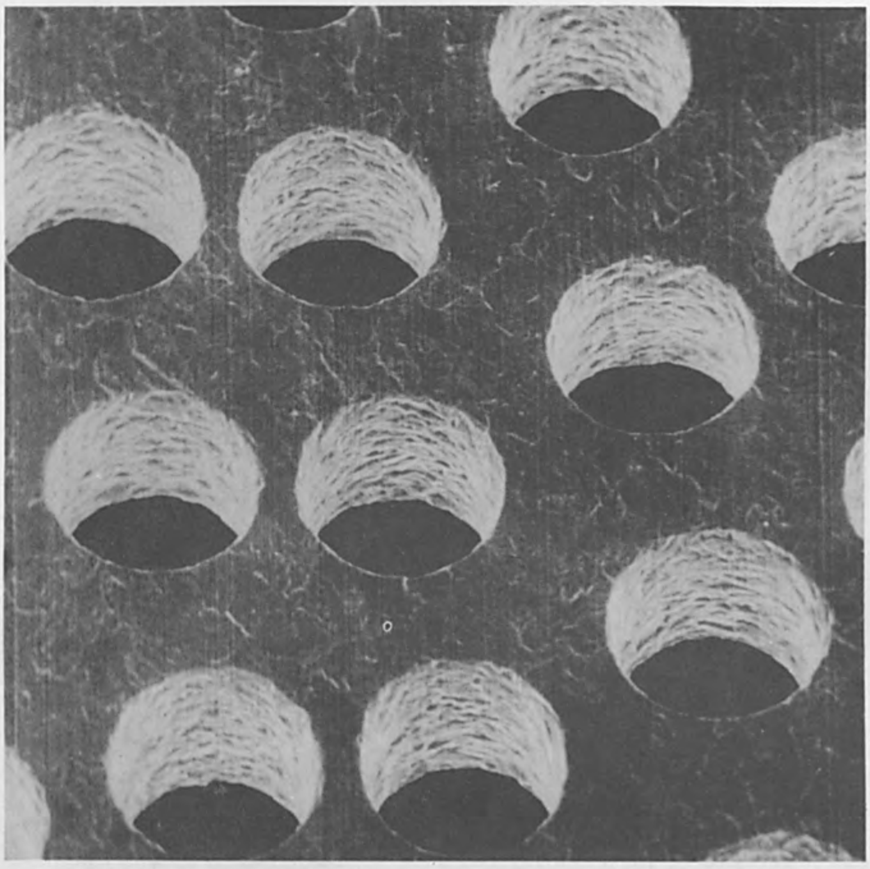

FIG. 8.—EB perforation of nickel, 0.1 mm thick; diameter 0.1 mm, hole density 2000/cm^2, time per hole 15 μs.

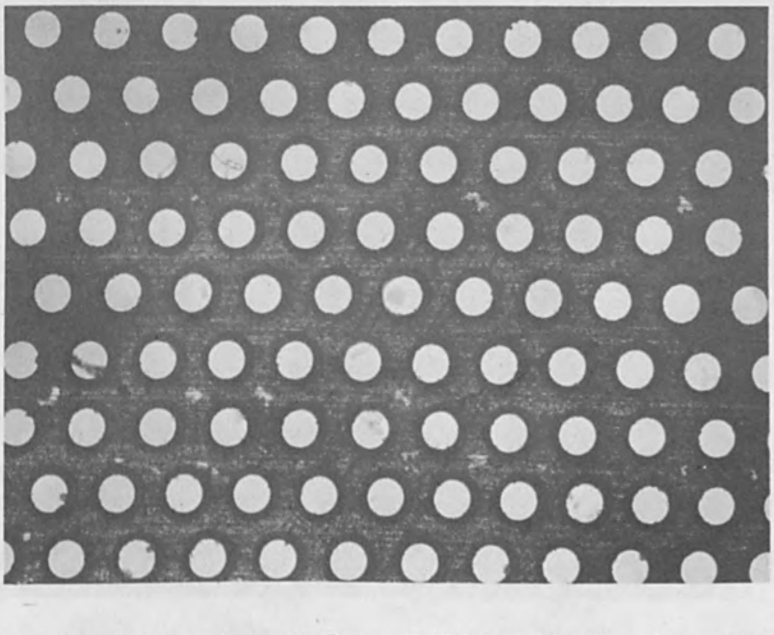

FIG. 9.—EB perforation of tantalum, 0.05 mm thick; diameter 35 μm, hole density 16 000/cm^2, time per hole 10 μs.

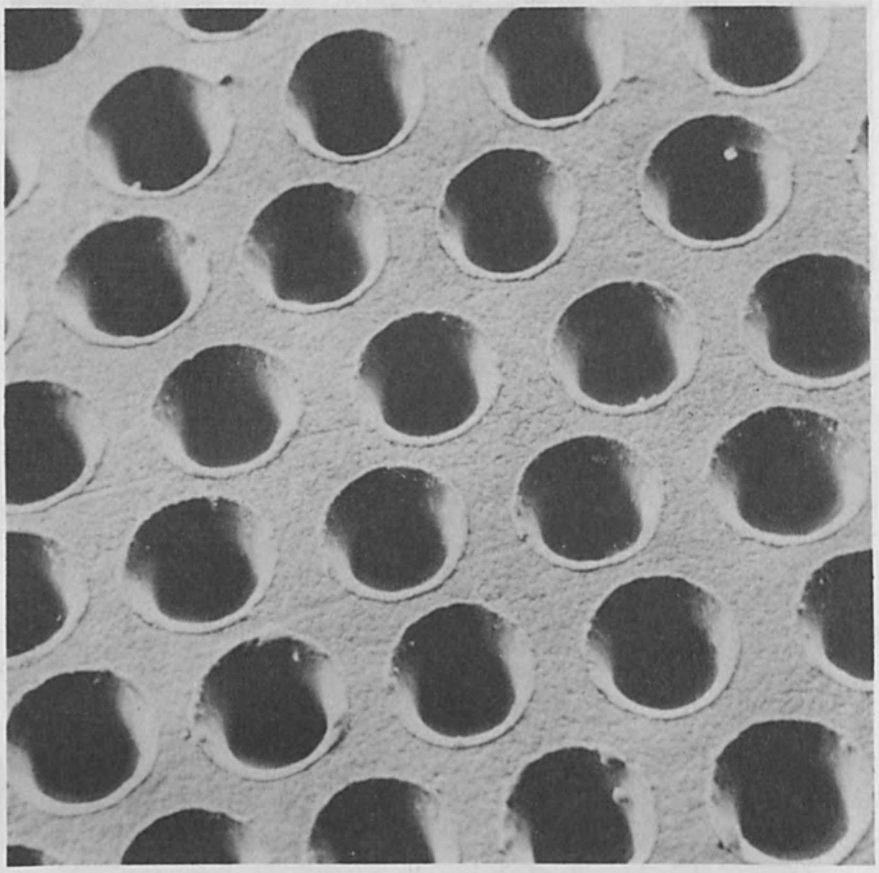

FIG. 10.—EB perforation of Nimonic 90, 0.4 mm thick; diameter 120 μm, hole density 2000/cm^2, time per hole 45 μs.

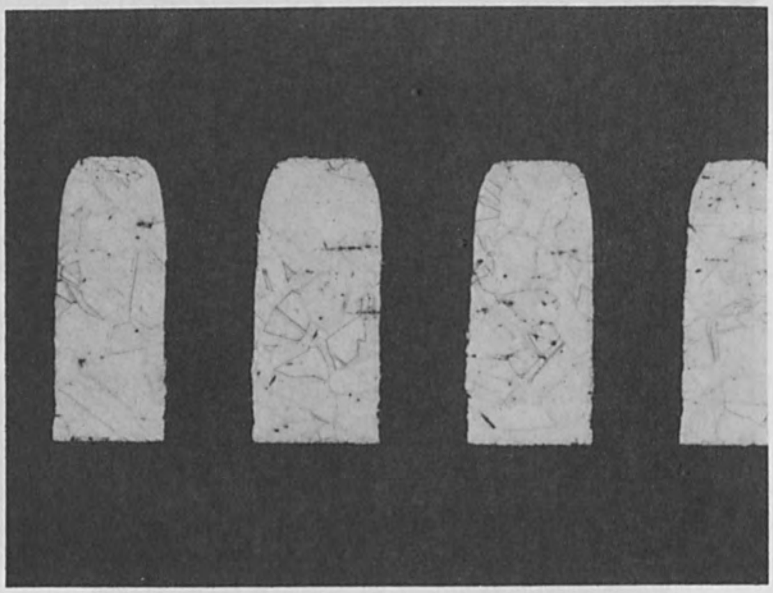

FIG. 11.—Cross section of EB perforation of Fig. 10.

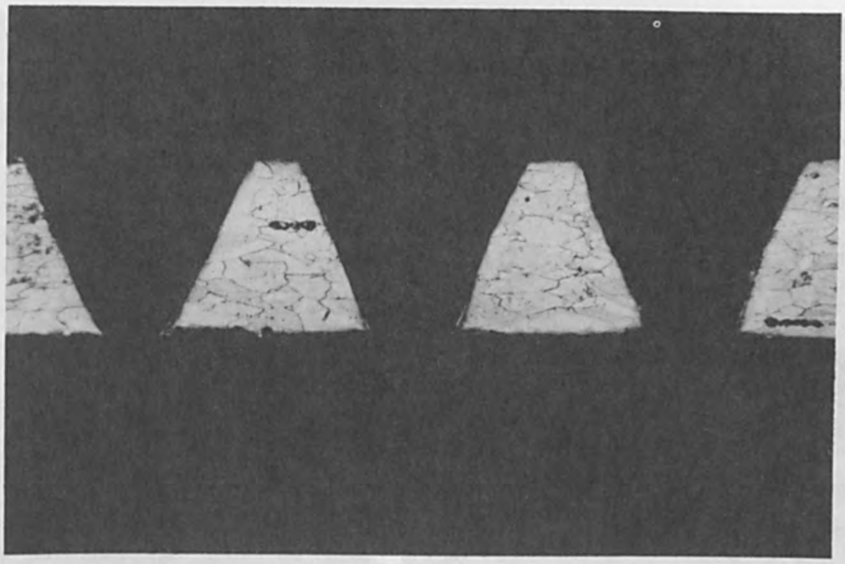

FIG. 12.—Cross section of EB perforation of Nimonic 90, 0.2 mm thick; diameters 280 μm (entrance) and 110 μm (exit), time per hole 20 μs.

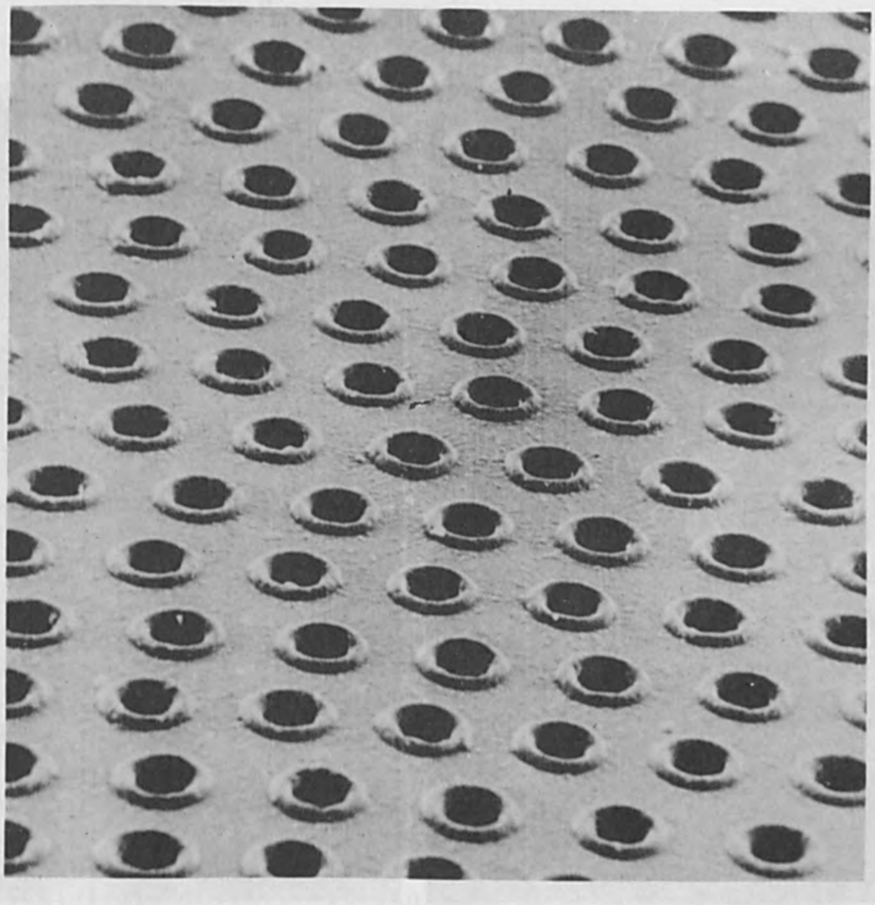

FIG. 13.—EB perforation of Hostaphan, 0.1 mm thick; diameter 90 μm, hole density 3500/cm^2, time per hole 2 μs.

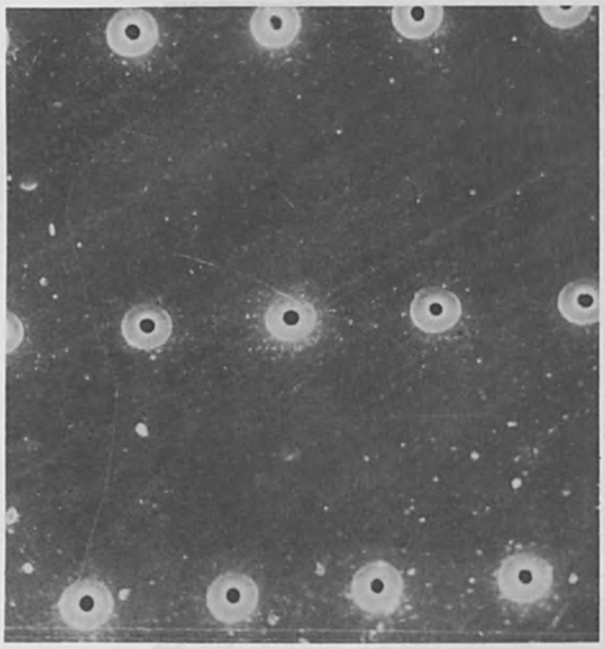

FIG. 14.—EB perforation of Hostaphan, 12 μm thick; diameter 4 μm, hole density 70 000/cm^2, time per hole 2 μs.

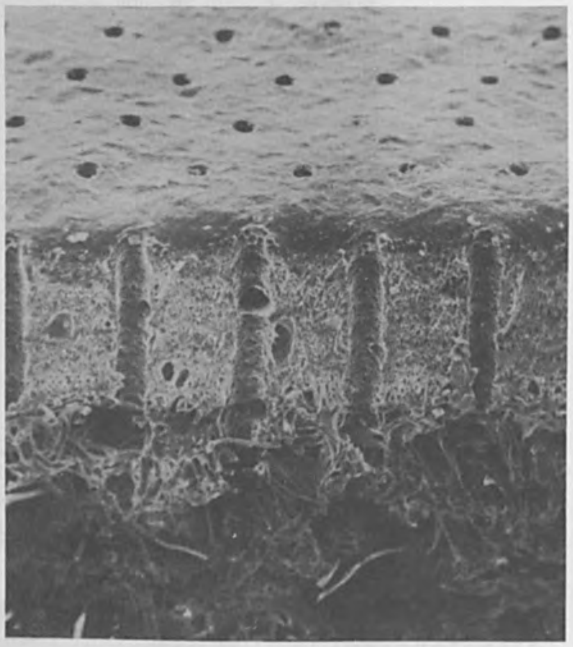

FIG. 15.—EB perforation of artificial leather, perforated thickness 0.3 mm; diameter 40 μm, hole density 2500/cm^2, time per hole 10 μs.

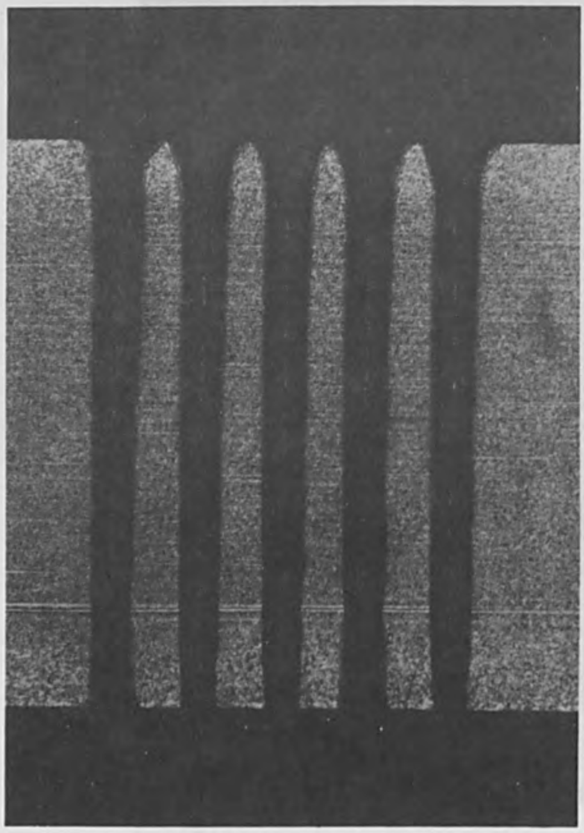

FIG. 16.—EB perforation of stainless steel, 10 mm thick; diameter 0.8 mm, time per hole 3 ms.

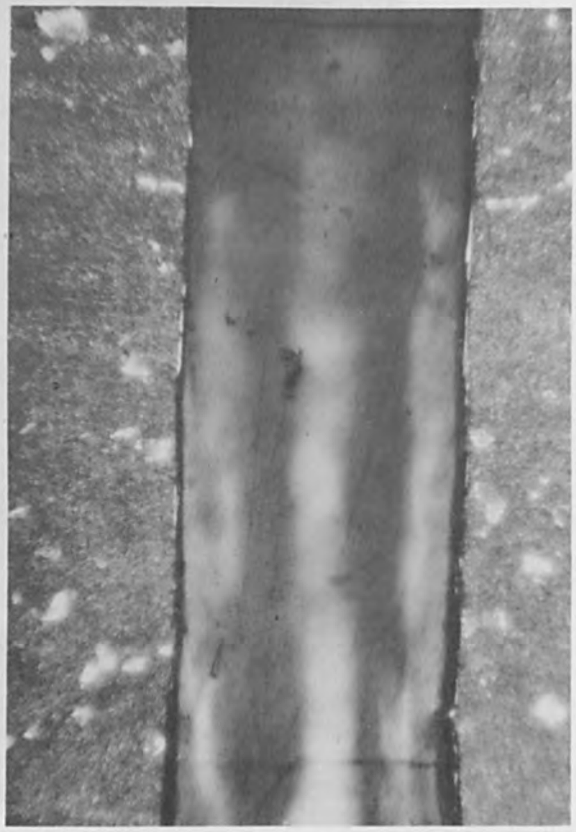

FIG. 17.—Part of a hole obtained by EB perforation of EPK-24, 2 mm thick; diameter 0.3 mm, time per hole 1 ms.

A HIGH RESOLUTION ELECTRON-BEAM SYSTEM FOR MICROCIRCUIT FABRICATION

T.H.P. CHANG and A.D.G. STEWART

Cambridge Scientific Instrument Co., Cambridge, U.K.

INTRODUCTION

Electron-beam (EB) methods offer the possibility of improving on the performance of light-optical methods for the fabrication of microcircuits. The main advantages are (1) significant improvement in resolution; (2) ease of control, which makes the technique more amenable to automation; and (3) ability to initiate certain chemical reactions not possible with the light beam.

It is generally believed that microcircuits and microstorage elements with dimensions smaller than those possible with light optics will become necessary in the near future. It is therefore logical to study EB techniques for this application.

This paper describes a high-resolution EB system which has been developed and some experimental results obtained with it.

GENERAL DESCRIPTION OF THE SYSTEM

It is clear that for any studies of high-resolution EB fabrication technique to be meaningful, an inspection method with a resolution at least comparable to that of the fabrication must be adopted. The present system is constructed around a high-resolution scanning electron microscope. This microscope is used both for fabrication and inspection. A general view of the system is shown in Fig. 1.

The scanning electron microscope used is the Stereoscan IIa.[1] The standard version of this microscope has an electron optical-column with a conventional electron gun and three magnetic lenses. Beam accelerating voltage can be varied from 1 to 30 kV and beam current in the final probe can be varied from 10^{-12} amp to tens of microamperes. For inspection purposes this microscope has a resolving power of about 100 Å.

Some of the attachments which have been added to the standard microscope are:

(a) A beam blanking unit which cuts off the electron beam by deflecting it away from its axis. The unit can be triggered by an external signal and has a switching time of approximately 400 ns.

(b) A specimen current amplifier capable of measuring 10^{-12} to 10^{-4} amp. This unit has sufficient bandwidth to enable a visual picture to be displayed.

(c) A second video display which allows both a secondary electron picture and a specimen current picture to be displayed simultaneously.

(d) A scan rotation unit which enables the scan direction to be altered electronically through 360°.

(e) An ion source and an evaporation unit built into the specimen chamber. The specimen carriage can be moved 1 and 2 in. in the X and Y directions, respectively. It can also be driven by stepping motors to give programmable movements.

In addition the deflection unit of the microscope has been modified

Record of 10th Symposium on Electron, Ion, and Laser Beam Technology (L. Marton, ed.); San Francisco Press, Inc.

Copyright © by The Institute of Electrical and Electronics Engineers, Inc.—Printed in the U.S.A.

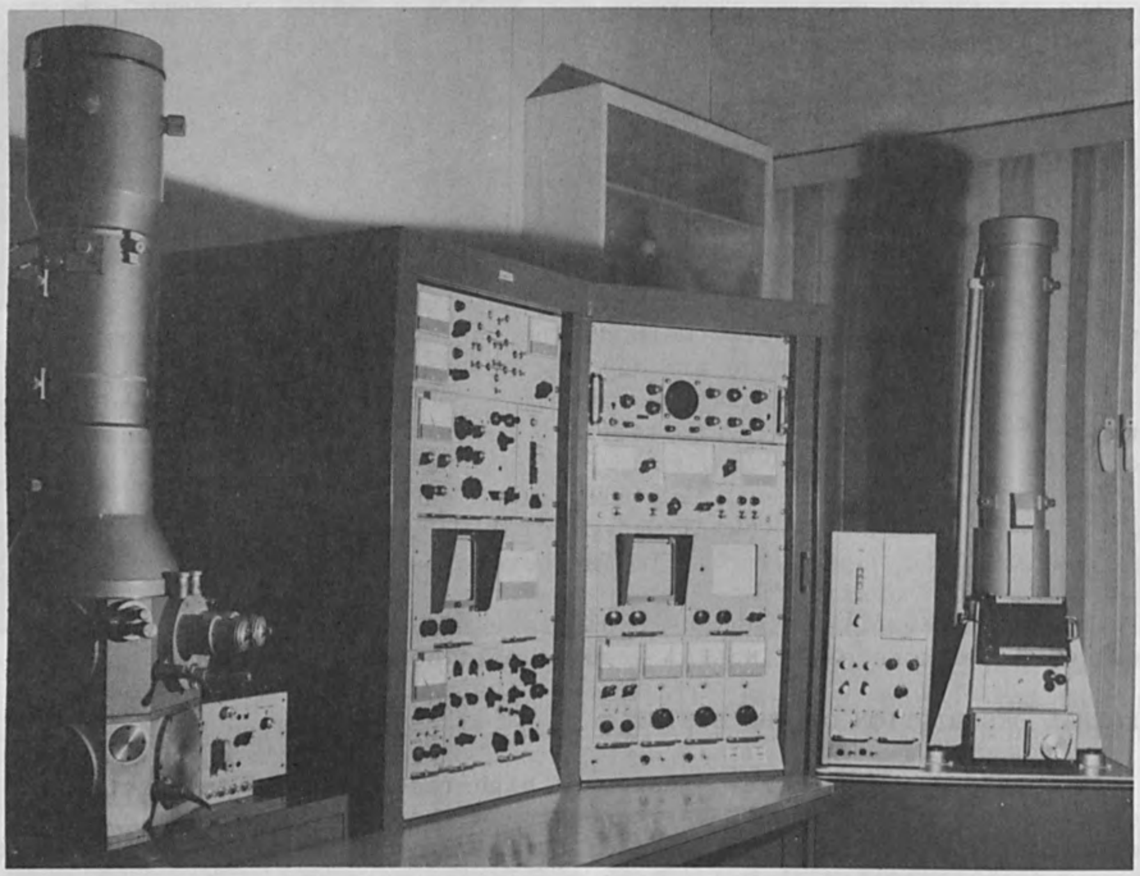

FIG. 1.—General view of the EB system.

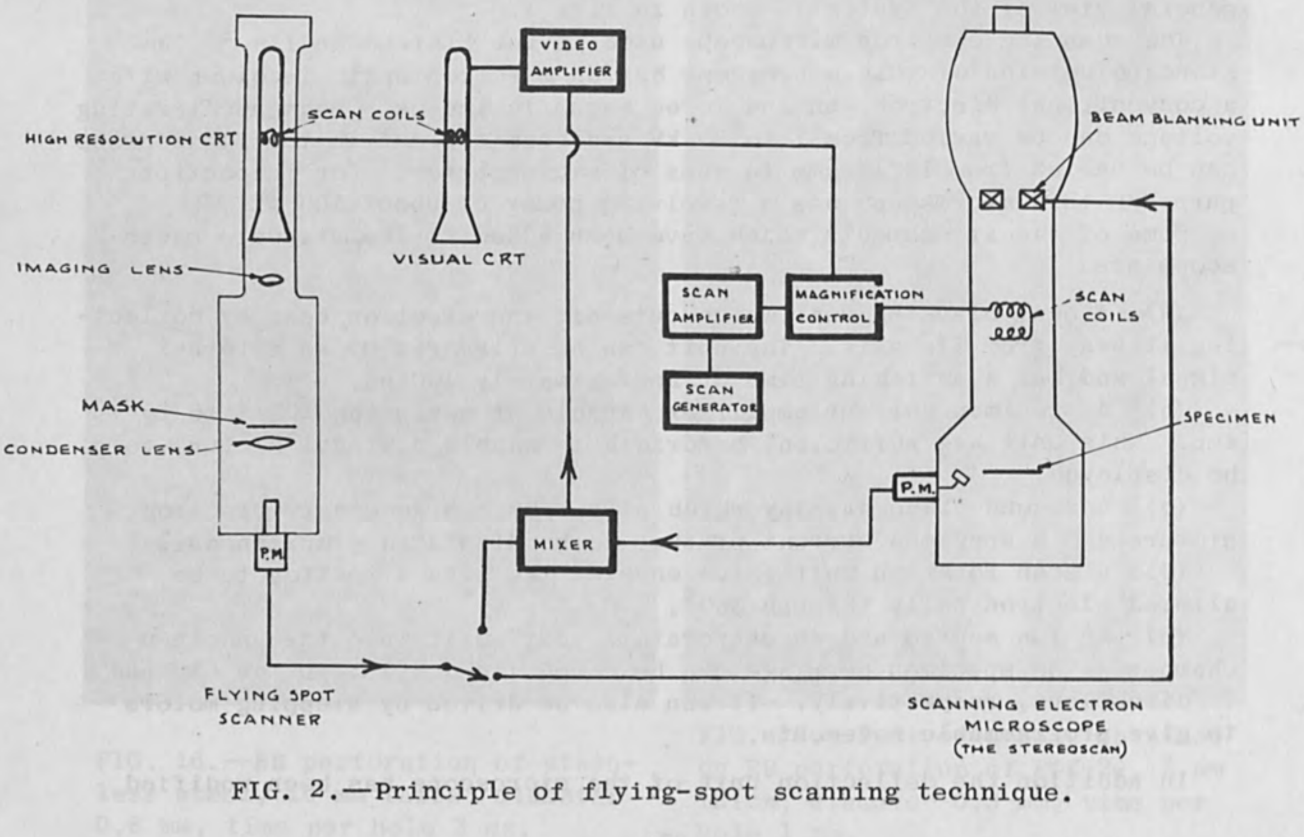
VIDEO AMPLIFIER
SCAN COILS
HIGH RESOLUTION CRT
BEAM BLANKING UNIT
IMAGING LENS
VISUAL CRT
SCAN AMPLIFIER
MAGNIFICATION CONTROL
SCAN COILS
SCAN GENERATOR
MASK
CONDENSER LENS
SPECIMEN
P.M.
P.M.
MIXER
FLYING SPOT SCANNER
SCANNING ELECTRON MICROSCOPE (THE STEREOSCAN)

FIG. 2.—Principle of flying-spot scanning technique.

because, for fabrication, it is necessary to have several sets of deflection coils for (a) alignment, (b) dc deflection, and (c) conventional scanning. The new unit consists of three sets of coils and one set of deflection plates. The ranges that can be covered by each set of coils and plates are approximately as follows at a working distance of 1 cm:

	Fabrication mode	Microscopy mode
Alignment	± 50 μm or more	± 10 μm
Dc deflection	± 2.5 mm	
Scanning (coil)	± 200 μm	± 2.5 mm
(plate)	± 100 μm	± 100 μm

For fabrication, it is necessary to control the electron beam to generate complicated circuit patterns. Several techniques were considered; a high-resolution flying-spot scanner was selected for the initial evaluation.

The operating principle of a flying-spot scanner is illustrated in Fig. 2. The four main components of the unit are: (a) the cathode-ray-tube (crt) assembly, (b) the imaging lens, (c) the mask assembly, and (d) the photomultiplier. The performance of the unit depends on crt resolution, imaging lens resolution, mask quality, and signal-to-noise ratio of the light detector.

One additional feature of using a scanner unit is that it can also be used to produce high-quality microscope pictures. A mirror assembly is introduced halfway down the column to enable pictures to be taken at a side port.

The scanner uses a 3-in. flat-face high-resolution crt with a very fine-grain, short-persistence phosphor (50 ns to 50% amplitude). The masks for the scanner, which are 4 × 4 in., can be produced from 4 × 5-in. standard photographic plates and are held in a carrier which can be controlled externally to give ± 10° rotation for alignment. An 8-in.-diam. condenser lens is placed immediately after the mask, and it focuses the imaging lens on to the screen of the photomultiplier for efficient collection of light. The output signal from the unit can be mixed with that from the microscope and displayed on a visual crt for alignment purposes. When a pattern is to be generated, the output of the scanner is connected directly to the beam blanking unit which switches the microscope beam on and off. Measurement of resolution shows that the crt can produce a spot of approximately 20 μm at the center; with the application of dynamic correction the scanner is capable of resolving more than 2000 lines over the mask.

FIELD OF COVERAGE

For fabrication purposes, it is essential to know the maximum area that can be covered by the electron beam for the resolution to be kept within a certain tolerance. It is also highly desirable to devise means of increasing this field of coverage. Experiments have been carried out to evaluate the various relevant factors.

One important factor which limits the field of coverage is deflection aberrations. It is well known that an electron beam becomes defocused and distorted when deflected away from its axial position. The magnitude of this deterioration depends on several factors such as angle of deflection, working distance, solid angle of the beam, deflection-coil configuration, etc. To restore the beam diameter to its original value, it is necessary to apply both focus and astigmatism corrections.

To measure the effect of deflection aberrations and also the corrections required to counteract them, a series of experiments have been performed in which the electron beam in the microscope was given a static deflection, the amplitude of which could be varied, and a series of scanning electron micrographs were taken with the beam at this deflected position by feeding the normal deflection waveforms to an independent set of scan coils.

Figure 3 shows the estimated deterioration of resolution with deflection. Two curves are shown for working distances of 1 cm. Curve A represents the case where no correction is applied and Curve B represents the case when both focus and astigmatism corrections are used. The semi-angular aperture of the beam is 5×10^{-3}. The comparison of the two curves shows that an increase in the field of coverage can be achieved by applying the corrections. It is estimated that with no correction, the maximum field of coverage for a resolution of 0.1 μm is approximately 1 mm^2; with correction this area can be increased by a factor of roughly 2 at a working distance of 1 cm.

The results also confirmed that for best performance it is necessary to apply corrections to both focus and astigmatism. A detailed measurement of the magnitude of the corrections required as a function of deflection amplitude in the X direction and the Y direction has been performed. It was found that in the case of focus correction an $(X^2 + Y^2)$-law was followed. In the case of astigmatism correction for an eight-pole stigmator, the correction for quadrupoles A and quadrupoles B follows roughly laws of $(Y^2 - X^2)$ and 2XY, respectively. These results agree with previous published work,[2] but measurements were necessary because the effects of nonparaxial-electron paths and the small pinholes in the final electron lens were not fully known.

The field of coverage can also be limited by the need to position the electron beam accurately. For example, if an electron beam is to be positioned to an accuracy of 0.1 μm by use of a deflection drive with a stability of 1 part in 1000, the maximum distance that it can be deflected is limited to 100 μm. Deflection drives with stability approaching 1 part in 10^4 are possible if the environment of the driving unit can be properly controlled, but this stability cannot be fully utilized unless all other parameters which affect magnification and spot position are controlled to the same degree of accuracy. It seems unlikely that with this type of system, it will be economical to provide over-all stability to allow more than a 3000 lines raster to be used at one time.

Positioning accuracy can also be affected by hysteresis in the deflection coils. Although the deflection coils of the microscope are wound on air-core formers, the unit is inside the final magnetic lens, and flux linkage with the soft-iron polepiece could give rise to hysteresis. Measurements were performed by applying a dc deflection of known value to the electron beam and measuring the position shift after this deflection current was switched on and off and varied over a wide range. The shift was measured from high magnification scanning electron micrographs

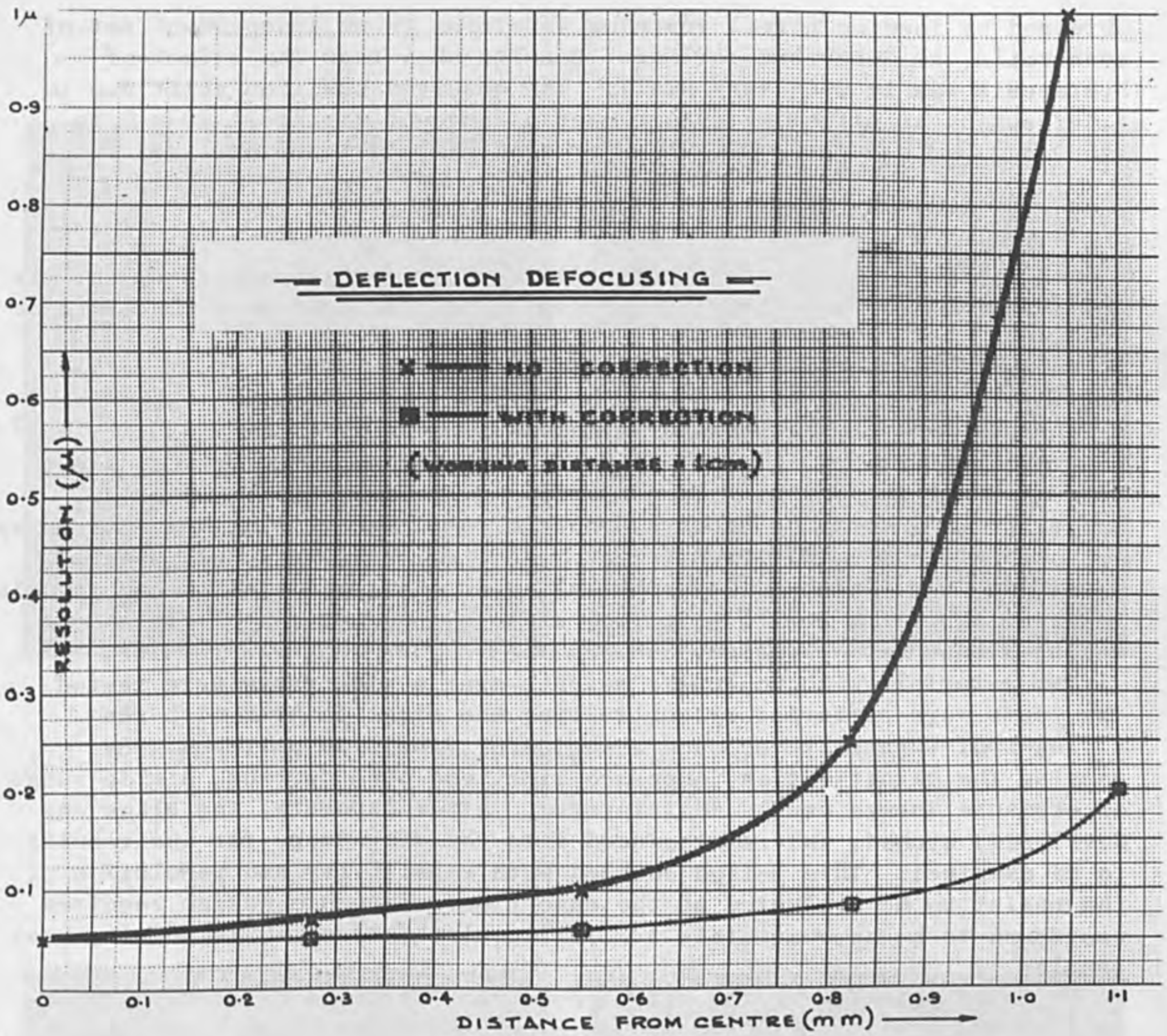

FIG. 3.—Resolution vs deflection with and without corrections.

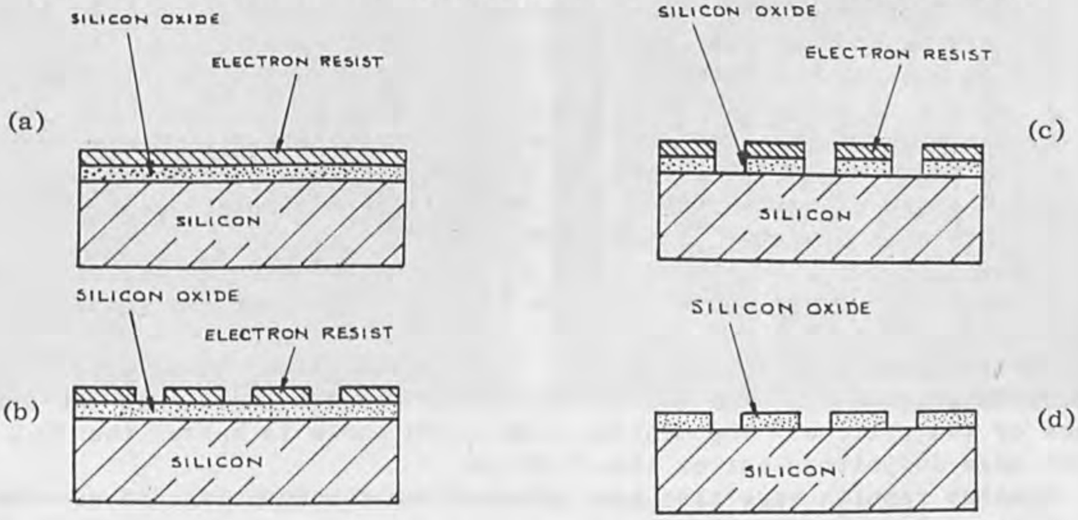
(a)
SILICON OXIDE
ELECTRON RESIST
SILICON
(b)
SILICON OXIDE
ELECTRON RESIST
SILICON
(c)
SILICON OXIDE
ELECTRON RESIST
SILICON
(d)
SILICON OXIDE
SILICON

FIG. 4.—Formation of patterns with the electron resist: (a) before exposure; (b) resist exposed and developed (areas exposed by electron beam are removed during development); (c) silicon oxide etched (chemically); (d) resist stripped.

obtained by feeding normal scanning waveforms to an independent set of scan coils, as described earlier. Results show that the effect of hysteresis was in fact very small. The observed position shift due to a deflection in either direction over a range of distances from 0 to ± 500 μm was less than ± 0.1 μm over a working distance of 1 cm.

FABRICATION OF HIGH-RESOLUTION PATTERNS

The photoresist materials generally used in light-optical methods are not suitable for EB methods. A special kind of resist must therefore be developed.

Several electron resist materials can be used. Thin organic films polymerized by an electron beam from various oil vapors have been used as a resist to form patterns of fine lines 0.05 μm wide in metal films.[3,4] However, this type of resist has relatively low sensitivity and cannot stand some of the strong etchants used for microcircuit fabrication. Recently IBM's Yorktown Heights Group[5] reported the use of PMM (polymethyl methacrylate) as an electron resist. That material was used for this work. The electron beam degrades the polymer and renders it more soluble to a particular solvent. Hence the areas exposed by the electron beam can be subsequently removed, whereas the surrounding area remains.

PMM materials with molecular weights over a wide range were tested. The tests were performed by controlling the electron beam with the flying-spot scanner to produce a series of fine line patterns. By varying the magnification, exposure time, and beam current, a wide range of exposure dosage can be administered. After exposure, the slice was developed, etched, and reintroduced into the microscope for the results to be examined. This method enabled both sensitivity and resolution of the resist to be evaluated at the same time. Exposure dosage required was found to be approximately 5×10^{-5} coulomb/cm^2 at 10 kV for the best samples.

By using this PMM resist, high-resolution patterns have been etched on passivated silicon slices by the procedure shown in Fig. 4. Some results are shown in Fig. 5 to Fig. 8. In all these examples, the oxide of the silicon slices used is approximately 0.15 μm thick.

Figure 5 shows a MOST circuit pattern etched in the oxide with the line width of the central channel 0.5 μm wide. The lettering at the corner is less than 1 μm high, with line width of approximately 0.25 μm. Edge definition of the lines is better than 0.05 μm.

Figure 6 shows the same MOST circuit pattern as in Fig. 5 with the negative image exposed, so that the pattern consists of a series of isolated areas of oxide raised from the surface of the silicon. The line width at the center is less than 0.5 μm.

Figure 7 shows a series of lines etched in the oxide at two different spacings, 0.75 μm and 1.5 μm for the top and bottom series, respectively. The line width is 0.5 μm.

Figure 8 shows writing etched in the silicon slice. The letters are approximately 0.5 μm high and are formed by lines of oxides on the surface of the silicon. The minimum line width shown is better than 0.2 μm, with edge definition better than 0.05 μm.

Similar results have also been obtained on chrome films and on other metallic films.

Several problems have been encountered when working at dimensions of less than 1 μm. For example, it has been found that line width depends

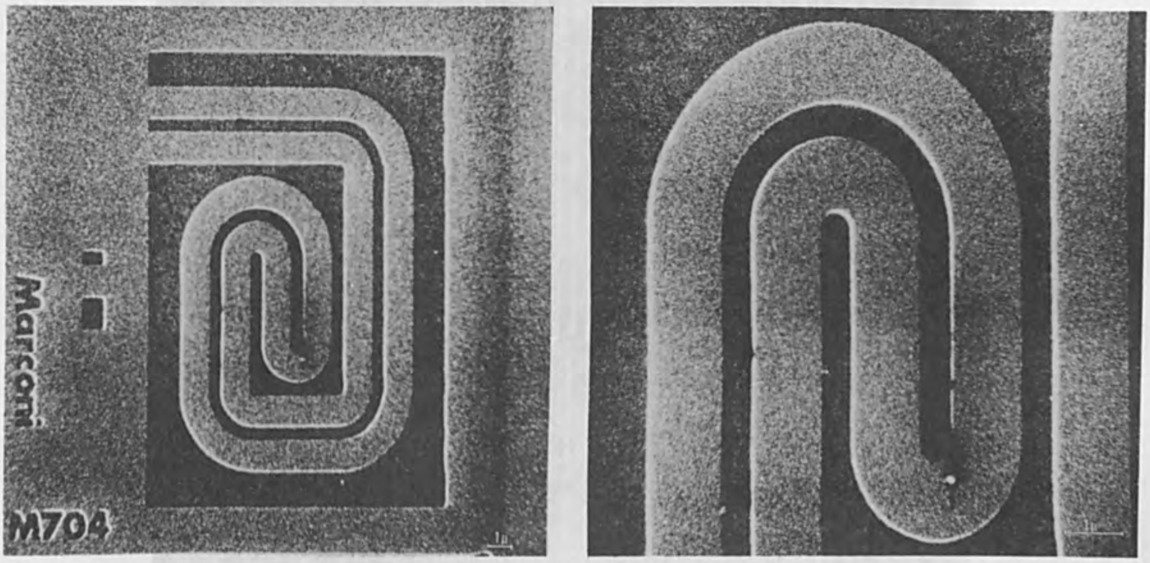
Marconi
M704

(a) (b)

FIG. 5.—MOST circuit pattern etched in silicon: (a) 6000X, (b) 15 000X.

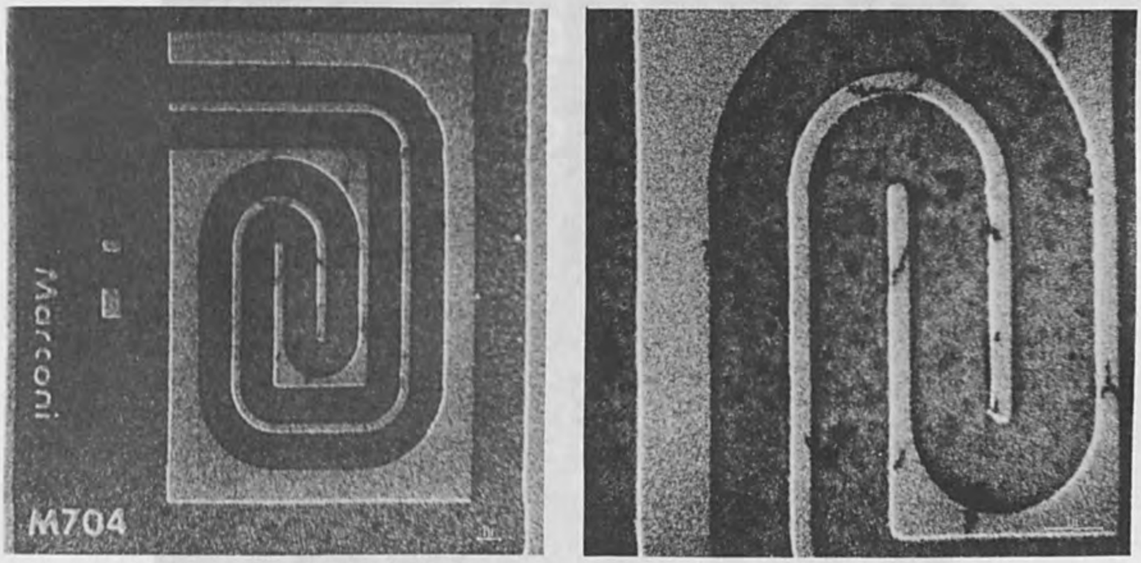
Marconi
M704

(a) (b)

FIG. 6.—Another MOST circuit pattern etched in silicon: (a) 6000X, (b) 15 000X.

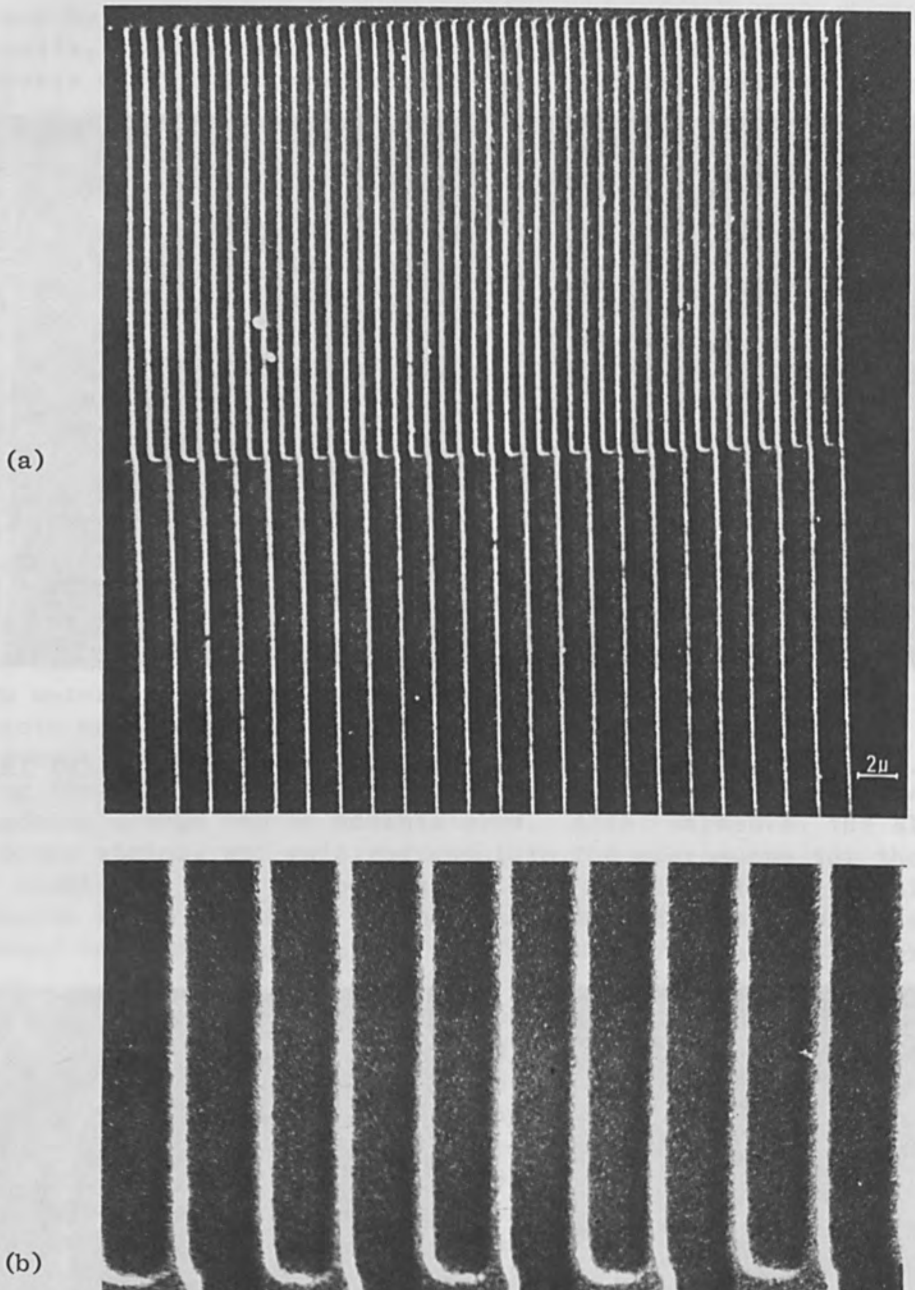

FIG. 7.—0.5 μm line etched in silicon oxide: (a) 8000X, (b) 20 000X.

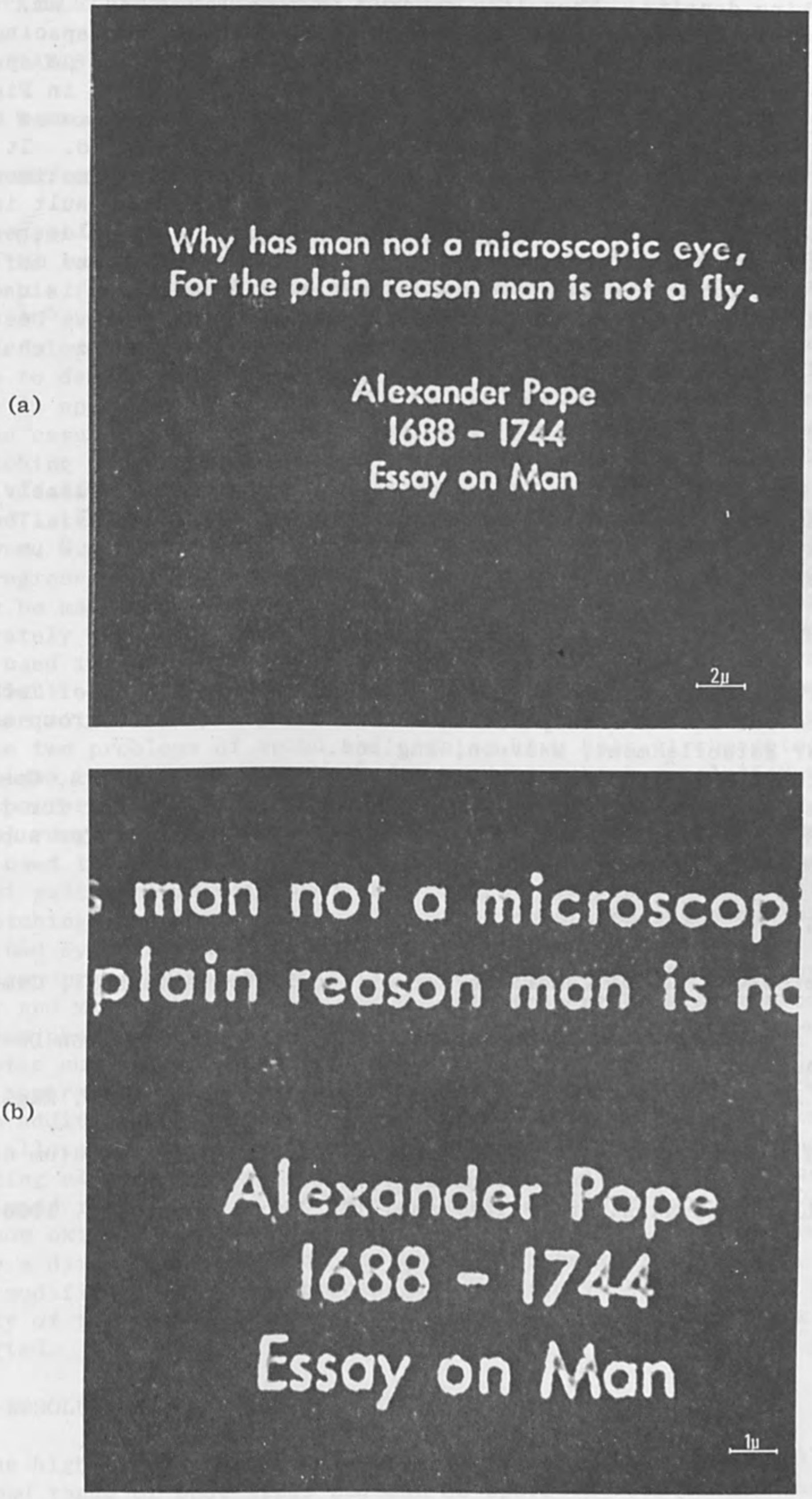
(a)
Why has man not a microscopic eye,
For the plain reason man is not a fly.
Alexander Pope
1688 - 1744
Essay on Man
2μ
(b)
s man not a microscop
plain reason man is no
Alexander Pope
1688 - 1744
Essay on Man
1μ

FIG. 8.—Writing standing proud of silicon with line width less than 0.2 μm: (a) 5000X, (b) 10 000X.

on the packing density. When line spacing is made less than 1 μm, there is a noticeable increase in the line width obtained when the spacing is large. Typically, it was found that for 0.5-μm lines at 0.75 μm spacing, the line width can in some cases increase by 10-15%, as shown in Fig. 7. The exposure dosage required to reproduce the pattern also becomes more and more critical as the dimension of the patterns are reduced. It has also been noticed that lines adjacent to sharp corners can sometimes show a slight displacement, as shown in Figs. 5, 6, and 7. This fault is believed to be a result of slight localized charging by the electron beam itself; the charge produces a high field at the corner and deflects the beam. The effect is much reduced when higher beam energy is used, which tends to reinforce the above theory. No experiments have been made with thin conducting coatings or other methods to minimize charging problems.

CONCLUSION

It has been shown that an EB system can be used to form reliably complex patterns on passivated silicon and thin metallic films. The initial experiments have achieved a line width of less than 0.2 μm with an edge definition of 0.05 μm.

ACKNOWLEDGMENT

The work has been done under a contract from the Ministry of Technology and carried out in close cooperation with the electron-beam group at the Royal Radar Establishment, Malvern, England.

The authors also wish to thank A. C. Prior of R.R.E., Dr. A. Goss of Marconi Ltd., and M. F. Cousins and D. J. Hills of C.S.I. Co. for their advice and assistance. Thanks are also due to Marconi Ltd. for supplying the MOST masks.

REFERENCES

1. Stereoscan IIa of Cambridge Scientific Instruments Ltd., Cambridge, England.
2. K. Schlesinger and R. A. Wagner, IEEE Trans. on Electron Devices 478-484, August 1965.
3. A. N. Broers, Ph.D. dissertation, Cambridge University, England, 1965.
4. T.H.P. Chang and W. C. Nixon, Record of IEEE 9th Symposium on Electron, Ion, and Laser Beam Technology, 1967; pp. 123-134.
5. Haller, Hatzakis, and Srinivasan, IBM Journal, 251-256, 1968.

HIGH-RESOLUTION ELECTRON-BEAM FABRICATION

M. HATZAKIS and A. N. BROERS

T. J. Watson Research Center, Yorktown Heights, N. Y.

INTRODUCTION

Several electron-beam (EB) fabrication techniques have been reported over the last ten years, all of which offer resolution beyond that available from optical processes, i.e., line widths of 0.5 micron and below.[1-5] These processes have been difficult to apply to the building of useful devices and have only been used to fabricate elementary structures to demonstrate their resolution capability. The difficulties that arise in applying EB processes to making real devices are the slow speed in the case of the vapor-resist methods, and the difficulty in finding an etching process which produces edge definition consistent with the small dimensions.

The latter problem can be overcome with the added complexity of ion etching, but ion etching still has the limitation that the resist layer is progressively removed as well as the material from which the device is to be made, and the structure to be fabricated cannot therefore be accurately defined in the initial resist pattern. Chemical etching has been used in conjunction with a vapor resist in one case to produce excellent edge definition, but in general it necessitates a compromise between satisfactory edge definition and sufficient film thickness.

The two problems of speed and etching have been circumvented in the technique reported by Hatzakis[5] for producing high-resolution metalization patterns. In this process the resist, with a sensitivity in the normal range of 10^{-4}-10^{-5} coulomb/cm^2, is coated on to the sample rather than used in the vapor phase, and after exposure and development the resist pattern itself is used as a contact evaporation mask eliminating the etching step altogether. This paper describes high-resolution results obtained by this method in conjunction with a new high-resolution electron-probe system built by A. Broers[6] for scanning electron microscopy and microfabrication. The new electron-probe system produces a minimum probe size of 30 Å at a working distance of 7 mm. Working acoustic surface-wave devices with 3000-Å dimensions have been built with this apparatus, as well as metallic patterns with 1000-Å line widths.

In addition to the microfabrication processes a technique is described that allows precise measurements to be made in the high-resolution scanning electron microscope of the cross section of the exposed and developed resist lines, the fabricated metal lines, and slots etched in silicon oxide. The observation of the exposed volume in the resist layer gives a direct indication of the electron penetration profile.

A modified development process which effectively increases the sensitivity of the methyl-methacrylate resist used in all this work is also reported.

HIGH-RESOLUTION ELECTRON-PROBE SYSTEM

The high-resolution probe system (Fig. 1) has been designed to produce a broad range of spot sizes and can be operated with two or three condenser lenses to demagnify the crossover formed by the electron gun.

Record of 10th Symposium on Electron, Ion, and Laser Beam Technology (L. Marton, ed.); San Francisco Press, Inc.

Copyright © by The Institute of Electrical and Electronics Engineers, Inc.—Printed in the U.S.A.

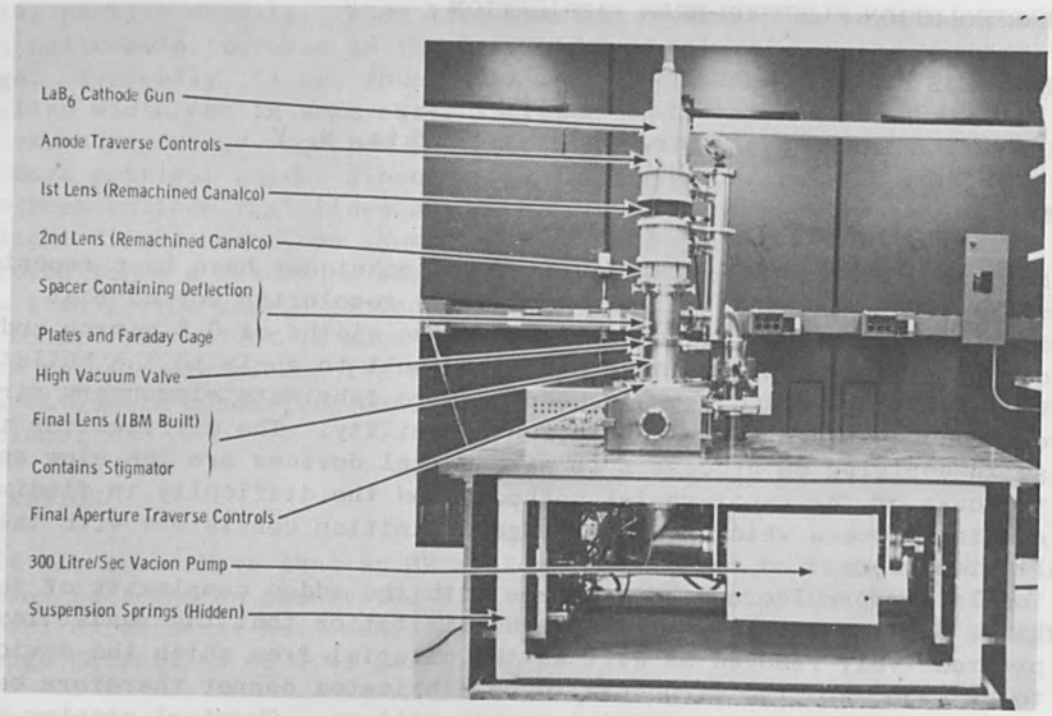
LaB$_6$ Cathode Gun
Anode Traverse Controls
Ist Lens (Remachined Canalco)
2nd Lens (Remachined Canalco)
Spacer Containing Deflection
Plates and Faraday Cage
High Vacuum Valve
Final Lens (IBM Built)
Contains Stigmator
Final Aperture Traverse Controls
300 Litre/Sec Vacion Pump
Suspension Springs (Hidden)

FIG. 1.—High-resolution probe system.

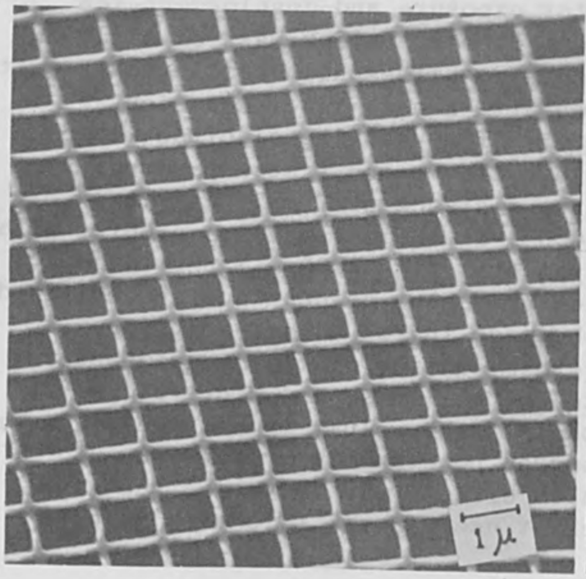

FIG. 2.—Palladium-gold microgrid fabricated with high-resolution probe.

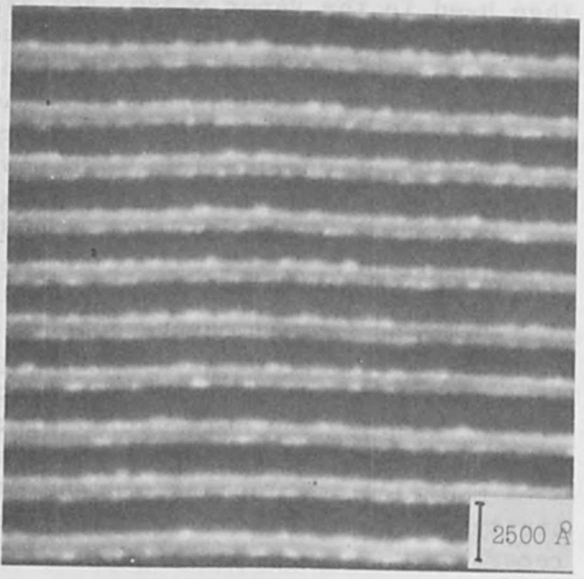

FIG. 3.—1000 Å wide gold-palladium wires fabricated with high-resolution probe.

The column is prealigned (except for the gun anode and the final aperture) to allow for simple operation and assembly. An electron gun with a lanthanum hexaboride cathode capable of producing approximately 5 times the brightness available from a conventional tungsten hairpin electron gun is used as the electron source. The increase in brightness over guns using tungsten hairpin cathodes is believed to result from the lower operating temperature of the LaB_6 cathode (resulting in smaller velocity spread) and the finer point on the rod cathode increasing the accelerating field at the cathode surface and minimizing the effects of space charge. The electron gun and column can be operated up to accelerating potentials of 40 kV.

The system is pumped with an ion pump and a combination of mechanical and absorption roughing pumps and employs techniques which reduce the deteriorating effects of vibration and stray-field interference below significant levels. The instrument produces a minimum probe diameter of 30 ± 7 Å with a current of 10^{-12} amp at a working distance of 7 mm and an accelerating voltage of 23 kV. This result closely approximates the theoretical minimum useful diameter of 27 Å as calculated from the formulas of Smith.[7] In the reflection scanning-electron-microscopy mode, point-to-point resolution of 50 Å has been measured. In general for high resolution microfabrication, probe diameters between 100 and 200 Å are used with currents between 10^{-10} and 10^{-9} amp. A probe of 3000 Å containing 10^{-6} amp can be formed for higher speed and lower resolution applications, as for example in the formation of contact pads.

An electronic pattern generation system is used in conjunction with beam blanking plates to write the desired patterns in the resist layer. An ac signal can be superimposed perpendicular to the scanning signal to control accurately the width of the exposed lines.

MICROFABRICATION OF METAL PATTERNS

In the fabrication process, the electron resist is first coated on the sample surface by conventional spinning methods. After baking at about 170°C for 20 min the resist is then exposed with the electron beam and developed, which removes the resist from the areas where the metal is required. Following development the metal is evaporated over the entire surface and the unwanted metal is removed by stripping the remaining unexposed resist. This stripping is possible because the undercut in the resist, caused by electron scattering, results in a discontinuity between the metal in the slot and that over the resist layer (as long as the metal thickness is kept below that of the resist) and this discontinuity allows solvent to penetrate to the unexposed resist and remove the resist and the unwanted metal as well.

The edge definition is determined by the edge definition in the resist and is generally better than 200 Å. The width of the line is equal to the narrow top of the resist slot and is not degraded by the undercut in the resist. However, the undercut can place a limit on the proximity of one line to another.

Figures 2-5 are structures made in the matter described above with the high-resolution electron probe. The palladium-gold microgrid in Fig. 2 has a grid spacing of 1 micron and a line width of 1400 Å. The gold-palladium wires in Fig. 3 are 1000 Å wide and separated by 0.25 micron. Figure 4 is an optical micrograph of an acoustic wave transducer on a $LiNbO_3$ crystal which operates at 1.8 GHz. Figure 5 is a scanning

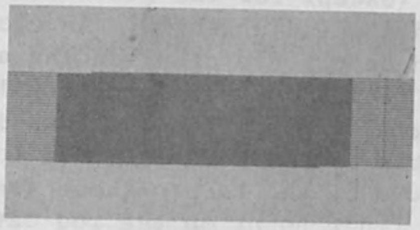

FIG. 4.—Optical micrograph of an acoustic-wave transducer fabricated with high-resolution probe on $LiNbO_3$ crystal.

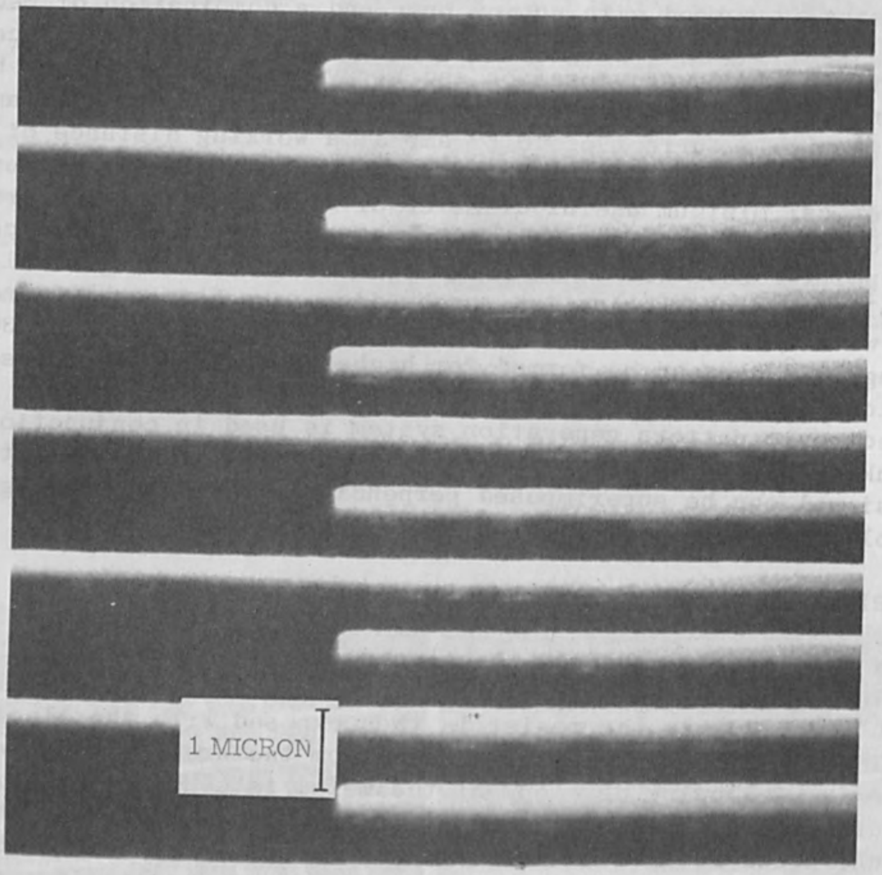

FIG. 5.—Scanning electron micrograph of the acoustic-wave transducer fabricated on a silicon wafer.

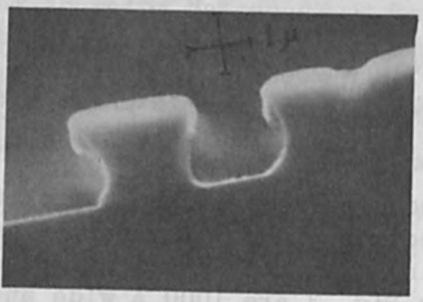

FIG. 6.—Scanning electron micrograph of cross section of lines exposed by beam on thick methacrylate resist layer.

electron micrograph of the same transducer structure but built on a silicon substrate so that it can be examined in the scanning electron microscope without specimen charging. The line width is 3000 Å and the center-to-center spacing of the fingers 0.9 micron.

MEASUREMENT OF RESIST AND METAL PROFILES

In order to examine the cross section of the exposed and developed resist lines, and the cross section of the final fabricated metal lines, monitor experiments are made on silicon wafers which are then cleaved at right angles to the lines and the edges examined in the SEM. This method allows the cross section to be measured to an accuracy determined by the resolution of the scanning electron microscope.

Figure 6 is such a micrograph showing the profile of a line exposed and developed in a thick resist film. The undercut due to electron scattering is clearly visible in the bottom of the developed line. If this pattern were to be used for metalization by evaporating through the resist one could achieve a height-to-width ratio in the metalized pattern in excess of one-to-one. Figure 7a shows schematically the metalization steps and Fig. 7b shows an actual resist profile after aluminum evaporation through the resist. The cross section of the metal line at the bottom of the resist slot and the discontinuity between the metal over the resist and the metal line can be seen in this micrograph. The line width is approximately 3000 Å and the metal thickness is 1500 Å.

The cross section of an acoustic wave transducer made on a silicon substrate is shown in Fig. 8. Finger spacing is approximately 0.9 micron for this device and finger width is 3000 Å. The metal thickness is 2000 Å.

RESIST SENSITIVITY IMPROVEMENT

As already reported[5] methacrylate resist can be used as a mask for HF etching of silicon oxides in semiconductor fabrication with much higher resolution than conventional light-exposed photoresists. However, the exposure sensitivity of the resist is relatively low (5×10^{-5} coul/cm^2), making it difficult to use with a high throughput microfabrication system. In order to increase sensitivity a new development procedure which effectively increases the resist sensitivity to 5×10^{-6} coul/cm^2 has been developed.

When making a liquid solution for sample coating, the methacrylate resist is initially dissolved in methyl-isobutyl-ketone and is usually spin-coated on the sample. After EB exposure the resist is developed in a mixture of liquids consisting of methyl-isobutyl-ketone, which is a resist solvent, and isopropyl alcohol, a nonsolvent.[6] The proportion of liquids in the developer is adjusted so that very little of the unexposed portion of the resist is removed during development. If the developer consists of the resist solvent only it is obvious that the entire resist layer will be removed during development. However, it was found that if the resist is baked after coating and before exposure to a temperature of 160-170°C for a period of 30 min or longer, it becomes partially insoluble in methyl-isobutyl-ketone. In fact it was found that the original baked resist thickness was reduced by only 50% after a 4-min development in methyl-isobutyl-ketone. This change in solubility cannot be easily explained since no chemical change of the polymer is expected

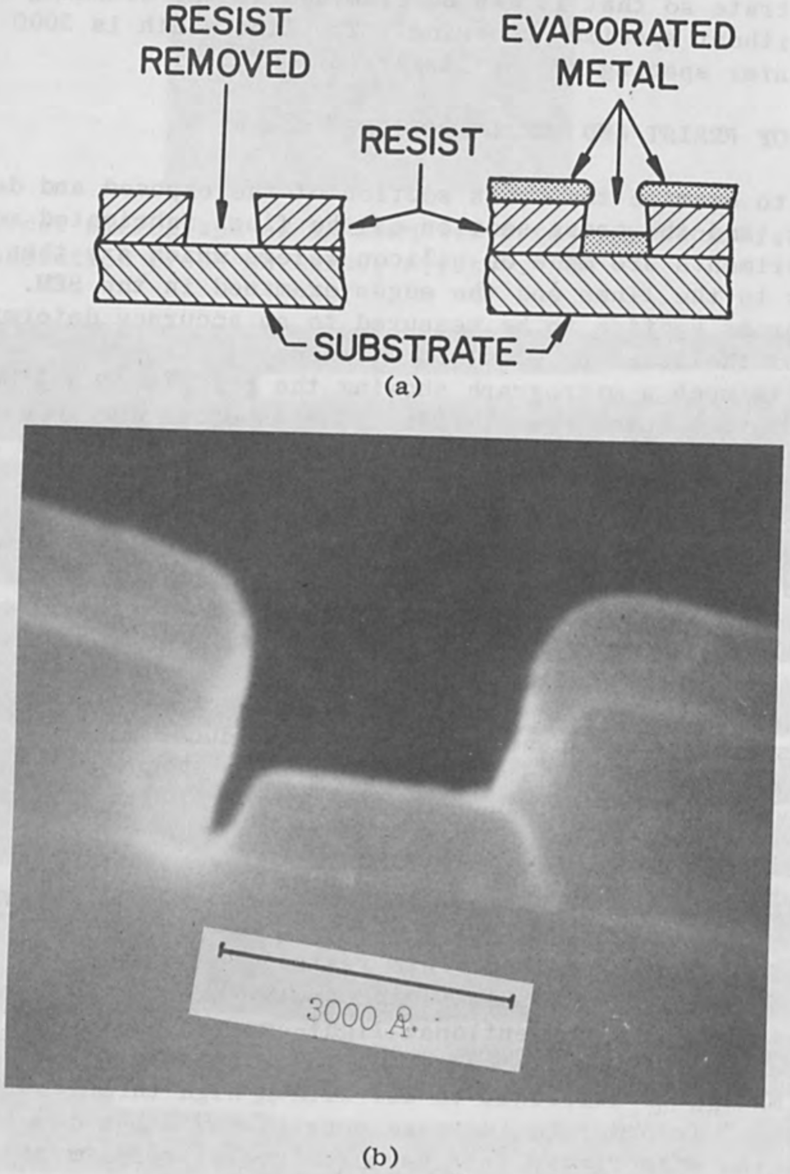
RESIST REMOVED
EVAPORATED METAL
RESIST
SUBSTRATE
(a)
3000 Å
(b)

FIG. 7.—(a) Schematic of the metalization steps; (b) scanning electron micrograph of cross section of aluminum line evaporated through methacrylate resist.

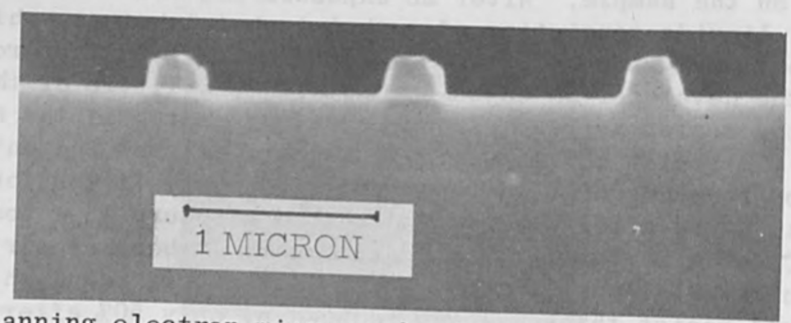

FIG. 8.—Scanning electron micrograph of cross section of an acoustic wave transducer fabricated with the high-resolution probe system.

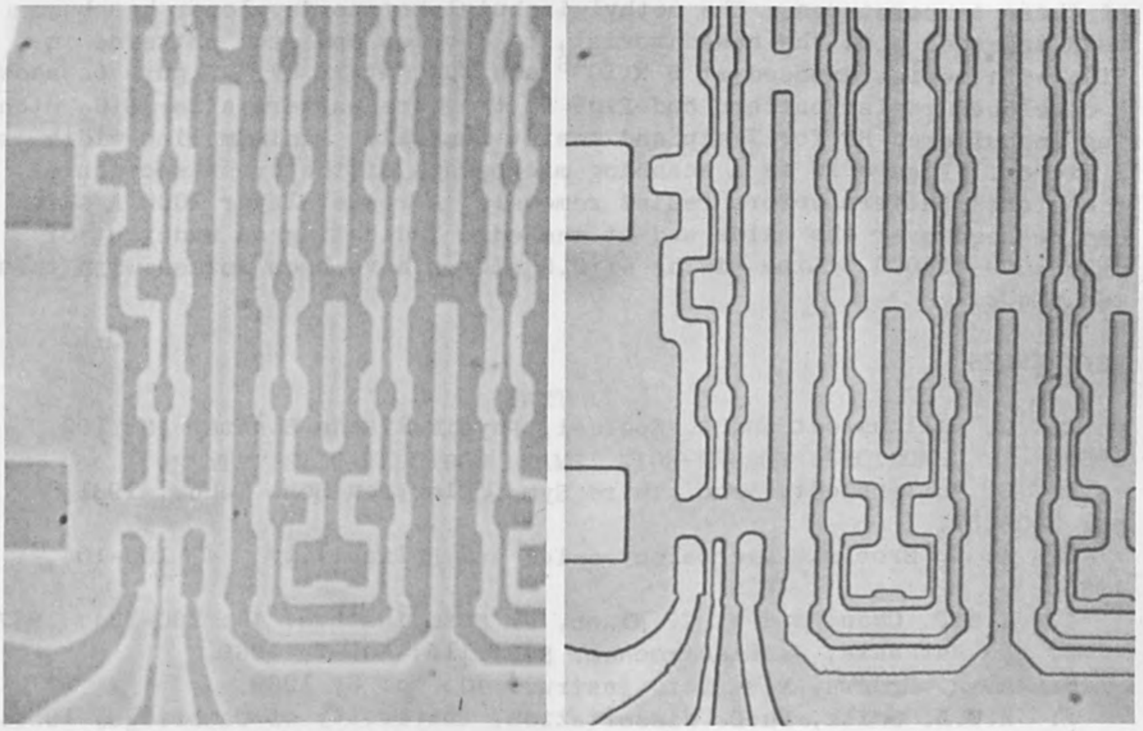

(a) (b)

FIG. 9.—(a) Developed resist pattern exposed by 12-kv beam at 5 X 10^{-6} coul/cm^2; (b) same pattern after SiO_2 etching in buffered HF for 7 min; resist removed.

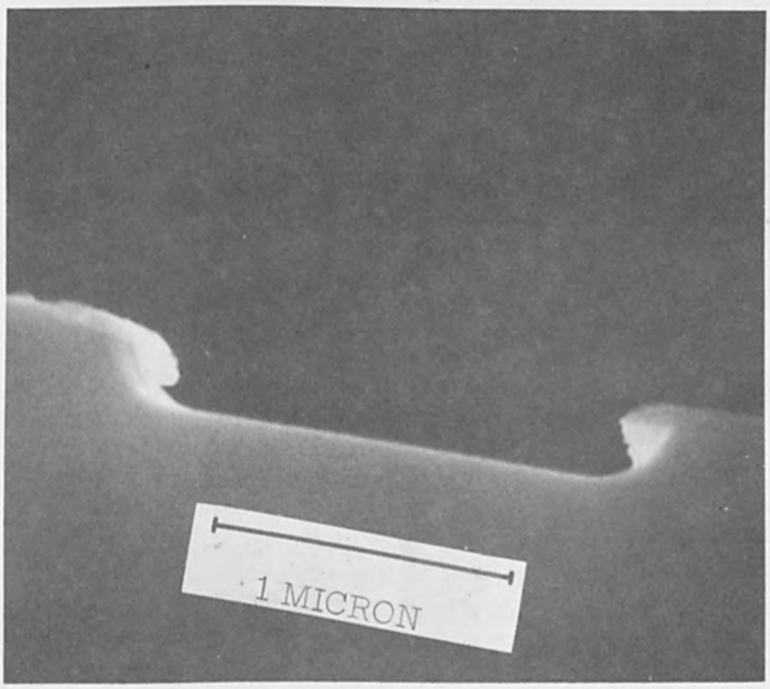

FIG. 10.—Scanning electron micrograph of cross section of part of pattern shown in Fig. 9 after SiO_2 etching but before resist removal, indicating undercut in SiO_2 of only 1500 Å.

at these temperatures. The methyl-isobutyl-ketone developer has been used together with the baked resist, to develop and etch patterns in SiO_2 with resist exposed at 5×10^{-6} coul/cm^2 at 12 kV. Figure 9a shows a developed resist pattern and Fig. 9b the same pattern after SiO_2 etching in buffered HF for 7 min and resist removal. Minimum line width is 1 micron. Figure 10 is a scanning micrograph of the cross section of the etched pattern before resist removal. A resist layer 1000 Å thick can be seen over the oxide and at the edge indicating an undercut of only 1000-1500 Å. Line widths of 0.5 micron have been formed with this technique.

REFERENCES

1. G. Möllenstedt and R. Speidel, Physikalische Blätter 16: 192, 1960.
2. G. Möllenstedt, Proc. Third Symp. Electron Beam Tech., 1961; pp. 340-357.
3. A. N. Broers, Microelectronics and Reliability 4: 103-104, 1965.
4. T.H.P. Chang and W. C. Nixon, J. Sci. Instrum. 44: 230-234, 1967.
5. M. Hatzakis, J. Electrochem. Soc. 116: No. 7, 1969.
6. A. N. Broers, Rev. Sci. Instrum. 40: No. 8, 1969.
7. K.C.A. Smith, Ph.D. dissertation, University of Cambridge, 1956.

PART II

RELATIVISTIC ELECTRON BEAMS; HIGH-ENERGY ELECTRONS

at these temperatures. The methyl-isobutyl-ketone developer has been used together with the baked resist, to develop and etch patterns in SiO_2 with resist exposed at 5×10^{-5} coul/cm^2 at 15 kV. Figure 9a shows a developed resist pattern and Fig. 9b the same pattern after SiO_2 etching in buffered HF for 7 min and resist removal. Minimum line width is 1 micron. Figure 10 is a scanning micrograph of the cross section of the etched pattern before resist removal. A resist layer 1000 Å thick can be seen over the oxide and at the edge indicating an undercut of only 1000-1500 Å. Line widths of 0.5 micron have been formed with this technique.

REFERENCES

1. G. Möllenstedt and R. Speidel, Physikalische Blätter 16: 192, 1960.
2. G. Möllenstedt, Proc. Third Symp. Electron Beam Tech., 1961, pp. 340-357.
3. A. N. Broers, Microelectronics and Reliability 4: 103-104, 1965.
4. T.H.P. Chang and W. C. Nixon, J. Sci. Instrum. 44: 230-234, 1967.
5. M. Hatzakis, J. Electrochem. Soc. 116: No. 7, 1969.
6. A. N. Broers, Rev. Sci. Instrum. 40: No. 8, 1969.
7. K.C.A. Smith, Ph.D. dissertation, University of Cambridge, 1956.

HIGH-CURRENT RELATIVISTIC ELECTRON BEAM ACCELERATORS AT CORNELL UNIVERSITY*

J. J. CLARK, M. URY, M. L. ANDREWS, D. A. HAMMER, and S. LINKE

Cornell University (Laboratory of Plasma Studies), Ithaca, N. Y.

The Laboratory of Plasma Studies at Cornell University entered into experimental high-current relativistic beam research in July of 1967 when, under the guidance of Mr. J. C. Martin's group of the AWRE, England, construction of an 800-kV pulsed electron beam accelerator was started at the Pulse Power Laboratory. The first beam was extracted into a drift space five months later. Since then, experiments have been performed on aspects of beam production, propagation, self-pinching effects, and magnetic-field interactions, with almost 2000 events to date. Peak diode currents in excess of 100 kA and voltages greater than 600 kV have been obtained. Operation at approximately two-thirds of these values is routine.

Within economic limits, the optimum system developed as a slow energy-store (conventional Marx generator) discharging into a submicrosecond store (planar transmission line), which is fast-switched to produce a 50-ns pulse. An end-fed planar diode, using a "plasma" cathode, injects the electron beam through a thin anode foil into a drift space. This system is relatively economical to maintain and is normally operated by one person at a rate of 3 to 4 firings per hour.

I. MARX GENERATOR

The Marx generator employs 16 0.5-μf ICSE capacitors conservatively rated at 100 kV, 25% reversal for 100 000 firings (Fig. 1). When charged in parallel to a maximum of ± 60 kV, up to 960 kV is obtained when eight pressurized spark gaps fire in a cascade mode to place the capacitors in series. A trigger pulse is applied to the number 2 gap to fire the machine on command. Envelopment in Freon-12 at atmospheric pressure is necessary above 450 kV to prevent occurrence of corona discharge. The generator feeds either one of two accelerator systems (3.5 ohms, 600 kV and 4 ohms, 800 kV) through quick-disconnect flexible steel tubes. The lower-impedance transmission line presents a 29-nf load to the 31-nf Marx generator. When losses in both systems are considered, 56% peak energy transfer can occur between the two storage systems.

II. TRANSMISSION LINE

The planar pulse-forming transmission line is arranged in a folded Blumlein configuration to produce an output voltage on a diode load equal to the charging voltage V_0 under matched impedance conditions, or as much as $2V_0$ when feeding an open circuit (Fig. 2). With this scheme,

---

[*] This research is funded by Office of Naval Research (ONR) Contract Number N00014-67-A-0077-0003.

Record of 10th Symposium on Electron, Ion, and Laser Beam Technology (L. Marton, ed.); San Francisco Press, Inc.

Copyright © by The Institute of Electrical and Electronics Engineers, Inc.—Printed in the U.S.A.

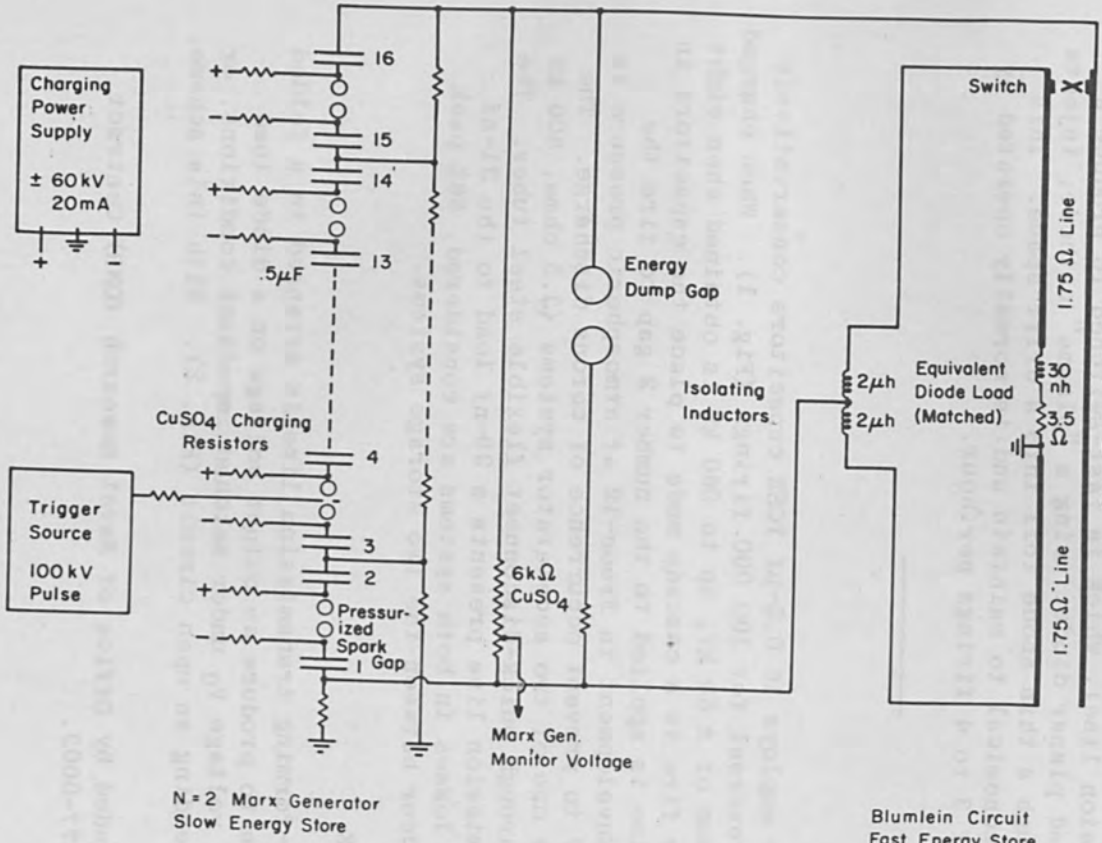
Charging Power Supply
± 60 kV 20 mA
Trigger Source
100 kV Pulse
16
15
14
13
.5μF
4
3
2
Pressurized Spark Gap
1
CuSO4 Charging Resistors
N = 2 Marx Generator Slow Energy Store
Energy Dump Gap
Isolating Inductors
6 kΩ CuSO4
Marx Gen. Monitor Voltage
2μh
2μh
Equivalent Diode Load (Matched)
30 nh
3.5 Ω
Switch
1.75 Ω Line
1.75 Ω Line
Strip Transmission Line
Blumlein Circuit Fast Energy Store

FIG. 1.—Simplified system schematic.

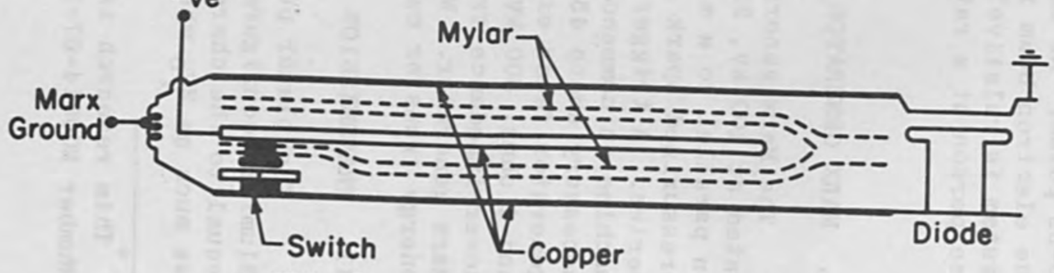
-Ve
Marx Ground
Mylar
Switch
Copper
Diode

FIG. 2.—Folded Blumlein assembly.

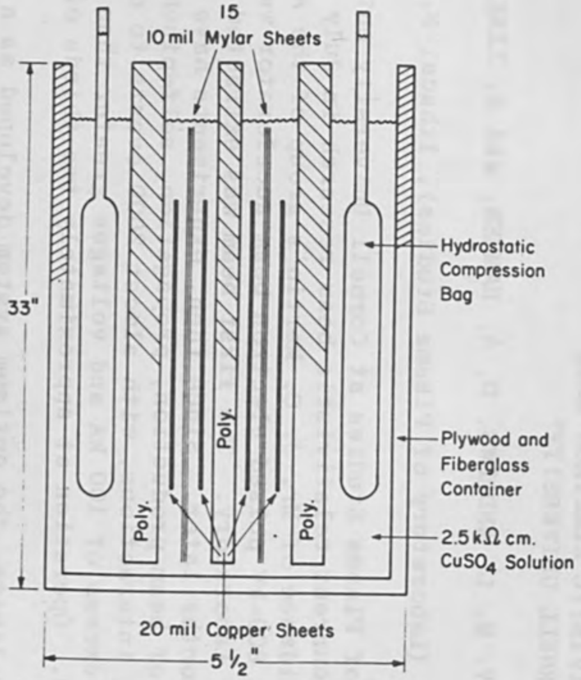
15
10 mil Mylar Sheets
33"
Hydrostatic Compression Bag
Poly.
Poly.
Poly.
Plywood and Fiberglass Container
2.5 kΩ cm. CuSO4 Solution
20 mil Copper Sheets
5 1/2"

FIG. 3.—Transmission-line assembly.

the system need not be stressed above the voltage desired at the load under matched conditions.

The pulse-forming section utilizes copper and mylar strip lines compressed between polyethelene by hydraulic pressure (Fig. 3). In the form of thin sheets, mylar provides the greatest breakdown strength of any insulating material available for this application, as well as excellent energy-transmission and storage characteristics. The 3.5-ohm machine utilizes 1.4 X 10^4 cc of mylar in the fully stressed region. AWRE studies indicate an inverse dependence of pulse-breakdown strength on the total volume stressed, but above 10^3 cc (for 10-mil mylar sheets) the breakdown strength remains constant at approximately 3 MV/cm. These data are used[1] to suggest an approximate statistical expression for expected failure prediction:

$$\left(\frac{\text{Mean breakdown voltage}}{\text{Operating voltage}}\right)^n = \begin{array}{l}\text{The average number of expected}\\ \text{operations without failure}\end{array}$$

The exponent n is normally taken to be 8 and gives an average of 170 firings between failures at 600-kV operation on 15 sheets of 10-mil mylar. With operation between 300 and 400 kV, the maximum number of firings between failures has been 368. This result is an order of magnitude below that predicted at this voltage. All failures, with only one exception, have occurred at field-enhanced areas and were not what could be considered statistical insulation failures.

The entire transmission line is immersed in a grading solution of copper sulfate and water. Field enhancement at the edges of the 20-mil copper strips is thus reduced by allowing the voltage gradient to diffuse out along the channel created between the mylar and polyethelene. If the channel is treated as an R-C transmission line,

$$V(x,t) = V_0[1 - \operatorname{erf}(x/2\sqrt{t/rc})]$$

for a step input of voltage, V_0 with x being the distance along the channel. The requirement that the breakdown strength of water never be exceeded leads to the approximation:

$$\rho = \frac{t\tau}{y^2 c}$$

where

ρ = resistivity of the grading solution
t = time to 1/2 peak voltage
c = capacitance/unit area of channel
$y = \dfrac{\text{peak charging voltage}}{\text{dielectric breakdown strength of water}}$
τ = channel thickness

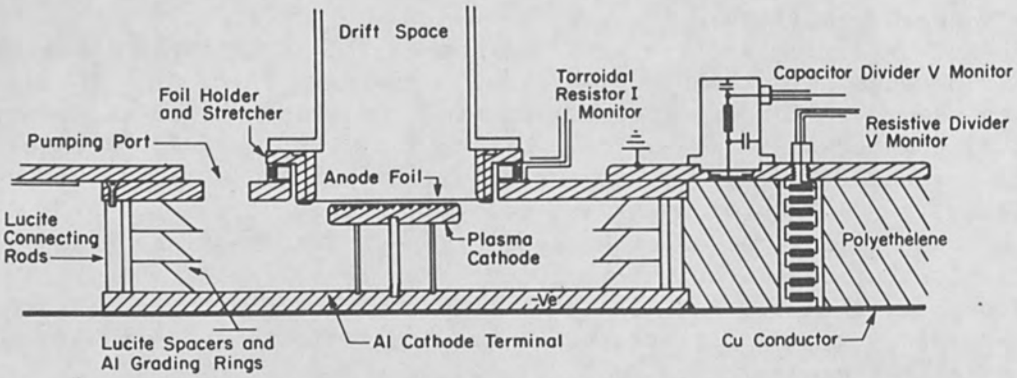
Drift Space
Foil Holder and Stretcher
Pumping Port
Torroidal Resistor I Monitor
Capacitor Divider V Monitor
Resistive Divider V Monitor
Anode Foil
Lucite Connecting Rods
Plasma Cathode
Polyethelene
-Ve
Lucite Spacers and Al Grading Rings
Al Cathode Terminal
Cu Conductor

FIG. 4.—Diode assembly (approx. 1/10 full size).

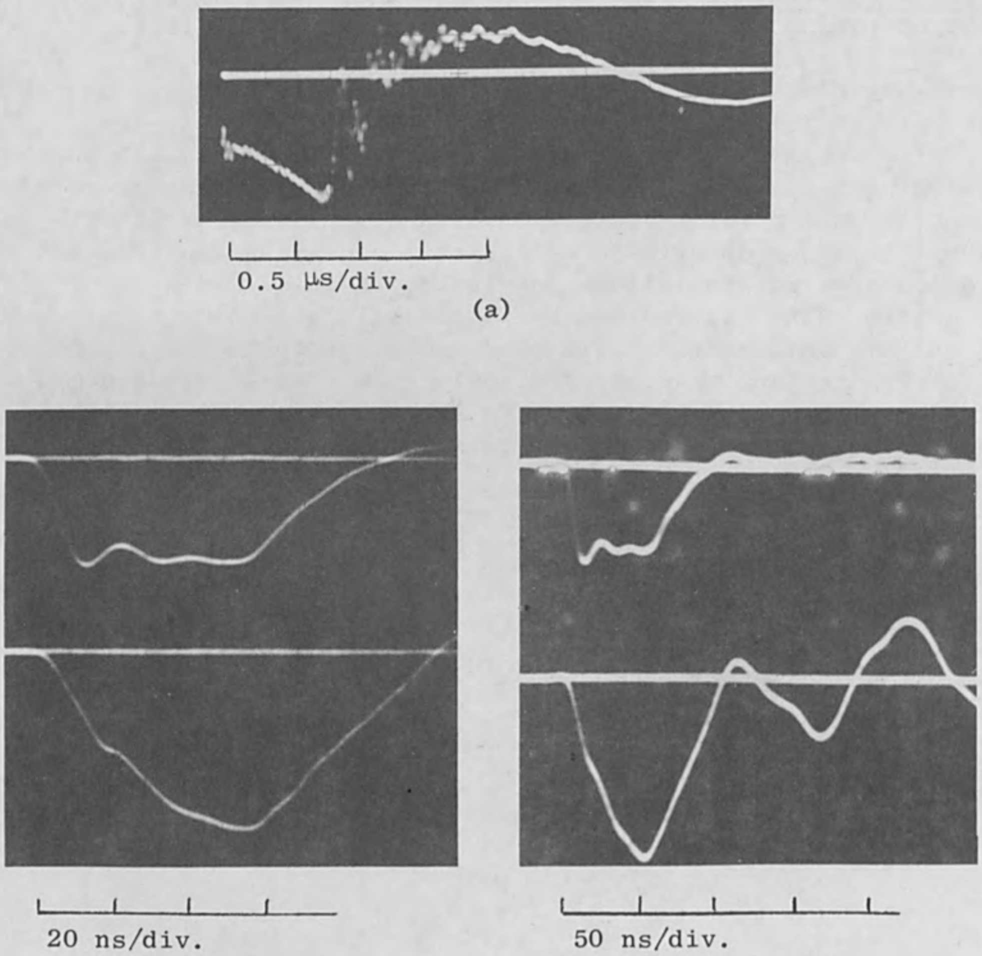

(a)

(b)

(c)

FIG. 5.—Oscillographs: (a) Marx generator voltage; (b) diode voltage (top) and current (bottom), V = 380 kv, I_{peak} = 82 kA; (c) V = 315 kv, I_{peak} = 80 kA.

III. SWITCHING

Switches are slabs of 1/4-in. low-density polyethelene into which a 1/16-in. chrome-steel ball bearing has been automatically heated and pressed to a preset depth. The slab is inserted into one section of the transmission line and the polyethelene remaining between the ball and an electrode (20-80 mils) breaks down when the transmission line is charged past a critical voltage. When operating in the 300- to 400-kV range a standard deviation of ± 4% for breakdown voltage may be obtained with a pulse-voltage rise time of 7 ns.

If a switch fails to fire, the Marx generator continues to charge the system and a ringing condition exists which eventually reverses the polarity of charge on the transmission line. Water breakdown is lower for positive polarities and the increased stress time on various surfaces in the machine will cause breakdown that results in mechanical damage. This undesirable behavior is eliminated by use of an energy dump gap. Charging voltages are set 25% above the desired switch breakdown point while an adjustable spark gap is set to close at approximately 10% over this breakdown point. If the switch fails to fire, unwanted energy is discharged through a critically damped circuit.

IV. DIODE AND INSTRUMENTATION

Insulation in the field-emission diode consists of three 1-in. Lucite spacers (four in the 800-kV diode) tapered at 45° and capacitively graded (Fig. 4). When the spacers are lightly coated with diffusion-pump oil, the diode will withstand over 600 kV. The "plasma" cathode is mounted on an adjustable stalk to vary the impedance of the diode. It is a solid brass disk, 4.0 in. in effective diameter and 5/8 in. thick, with rounded edges to decrease field enhancement. The emitting surface contains about 200 conical indentations approximately 1/8 in. in diameter at the cone base. These holes may be filled with Lucite or epoxy to form plastic "studs." The anode, consisting of 1/2- to 2-mil aluminum or titanium foil, is stretched over the opening to the drift space which has an effective diameter of 5-3/4 in.

Beam current is monitored by a resistive torroidal shunt located in a path between the anode foil and the anode terminal (Fig. 5). Consisting of two hundred 10-ohm 1/2-W resistors in parallel, this monitor produces a 5-kV signal at its maximum operating current of 100 kA. The short pulse duration precludes breakdown while the large output is useful in overcoming the RFI environment. Low-resistance, quality carbon resistors appear to display negligible frequency effects up to 100 kHz.

Diode voltage is monitored with one or two voltage dividers. Two hundred 10-ohm 2-W carbon resistors are assembled in a noninductive series chain with the last five connected to give a 50-ohm output. The chain is potted in an epoxy rectangle to withstand 600-kV pulses. The attenuation ratio is calibrated with relative ease but the output-pulse shape tends to be distorted owing to inductive and stray-capacitance effects. A capacitive divider developed at the Naval Research Laboratory gives almost perfect frequency response allowing 2-ns resolution.[3] Care must be taken to provide adequate shielding for the low-level output (1 V/300 kV).

TABLE I.—Comparison of measured field-emission diode impedances and Child-Langmuir predictions.

CHILD-LANGMUIR	$Z_{C-L} \cong \frac{136}{V^{1/2}}\left(\frac{d}{r}\right)^2$ ohms	$I_{C-L} = 2.34 \times 10^{-6}\, \frac{V^{3/2}}{d^2}$ A (in amp/m^2) (Space-Charge limited flow)
FACILITY	Z_D (MEASURED)	REMARKS
PHYSICS INTERNATIONAL San Leandro, Calif.	$Z_D \approx \frac{115}{V^{1/2}}\left(\frac{d}{r}\right)^2$	V_D = 200KV-5MV, r = 3.5 cm d = 2-10 mm $\langle I_D \rangle \approx 100$ KA
E.G.&G. Brookline, Mass.	$Z_D \approx Z_{C-L}$	V_D = 80-300 KV, I_D = 10-80 KA r_c = 0.8 cm, τ_D = 30 nsec
A.W.R.E. Aldermaston, U.K.	$Z_D \approx Z_{C-L}$	V_D = 200-500 KV, I_D = 50-100 KA
CORNELL	$Z_D \approx \frac{80}{V^{1/2}}\left(\frac{d}{r}\right)^2$	V_D = 200-500 KV, I_D = 50-125 KA r_c = 5cm, d = 2-10 mm, τ = 50 nsec $p = 5 \times 10^{-2}$ to 10^{-5} torr
NAVAL RESEARCH LAB. Washington, D.C.	$Z_D \approx \frac{136}{V^{1/2}}\left(\frac{\lambda_D}{r}\right)^2$	I_D = 200-500 KA, V_D = 750 KV r_c = 2.5 cm, d ≅ 7 mm λ_D = Debye length = $740\sqrt{\frac{W}{n_e}}$

V. DIODE OPERATIONAL CHARACTERISTICS

Since the diode impedance Z_D does not collapse or droop appreciably, some form of space-charge-limited current flow is expected and a comparison with the classical predictions of the Child-Langmuir equation is made in Table I for the Cornell and other accelerator facilities. It is seen that most of the measured diode impedances agree within a factor of 2 with Z_{C-L}. The factor can be accounted for by considering the space-charge neutralization effects of beam-generated ions (collisions) in the anode-cathode gap.[4]

If an imbalance of more than a few percent in the charging impedance of the Blumlein occurs, a "pre-pulse" voltage may exist across the diode during the Marx-to-Blumlein energy-transfer cycle, prior to the firing of the solid dielectric switch. Since the charging cycle lasts about a microsecond, the diode gap has sufficient time to become plasma filled and upon arrival of the main pulse V_D the diode impedance collapses. The Cornell Blumlein has been measured to be balanced within 1.5% but the results of gross line imbalance have been observed to cause main-pulse collapse very similar to that of short-circuit test shots. It is believed that a line imbalance of approximately 10% explains in part, at least, the difference between the measured impedance of the NRL facility (Table I) and the other listed results.

VI. BEAM ENTRANCE CONDITION STUDIES

Since the propagation characteristics of the electron beam in the drift tube are largely determined by the spatial current distribution and angular spread of the electron trajectories at the anode plane, measurements of these "beam-entrance" conditions have been made.

A. TIME-INTEGRATED CURRENT DISTRIBUTION STUDIES.

X-ray pinhole camera measurements (magnification 1/2) were made of the "plasma" cathode for a variety of input voltages, pressures and anode-cathode gaps. Most radiographs of the plasma cathode showed a honeycomb type emission pattern, the resolution of which indicated reasonably laminar flow, as predicted by J. C. Martin,[1] who originally suggested the plasma-cathode design. In addition the pattern was quite uniform in intensity and regularity across the cathode surface (Fig. 6a). However, a number of radiographs gave evidence of a distinct skewing of the beam to the downstream side of the diode (Fig. 6b) and in certain cases (Fig. 6c), both a skewing and a radial compression or "pinching" of the beam were evident.

A simple model for the prediction of this pinch condition in the diode-gap region may be obtained by assuming that the self-generated magnetic field at the stream edge makes the Larmor radius of the edge electrons just equal to the anode-cathode gap d. The force equations are then solved for the current, I_{critical}, that satisfies this condition. Such a solution yields[5]

$$I_{\text{critical}} = 8500 \frac{r}{d} \beta\gamma$$

where

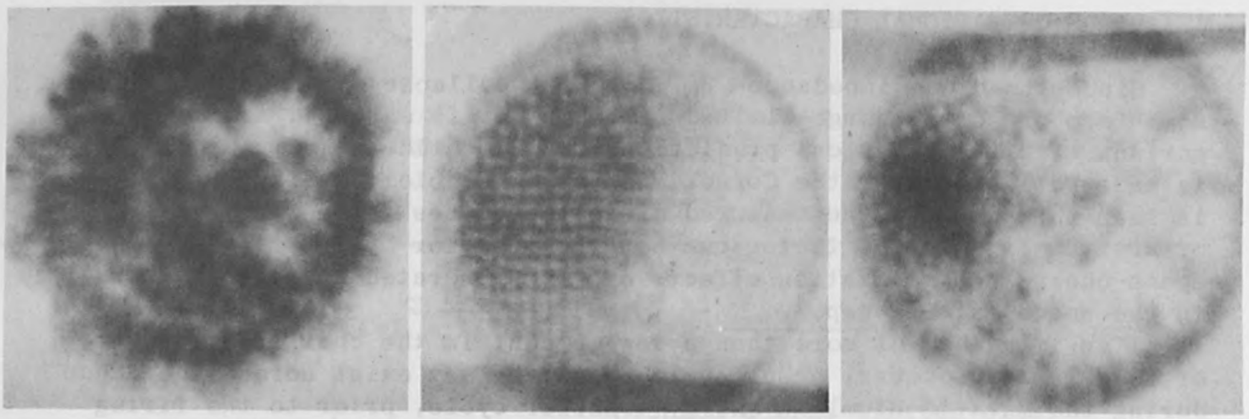

(a) (b) (c)

FIG. 6.—Radiographs of 4-in.-diam. planar plasma cathode.

Figure	(a)	(b)	(c)
	Uniform emission	Skewed emission	Skewed and pinched emission
V_D (kv)	457	366	372
I_D (kA)	56	78	71.5
Z_D (ohms)	7.85	4.7	5.2
Gap (in.)	0.351	0.290	0.290
ν/γ critical	2.83	3.45	3.45
ν/γ measured	1.86	3.31	2.93

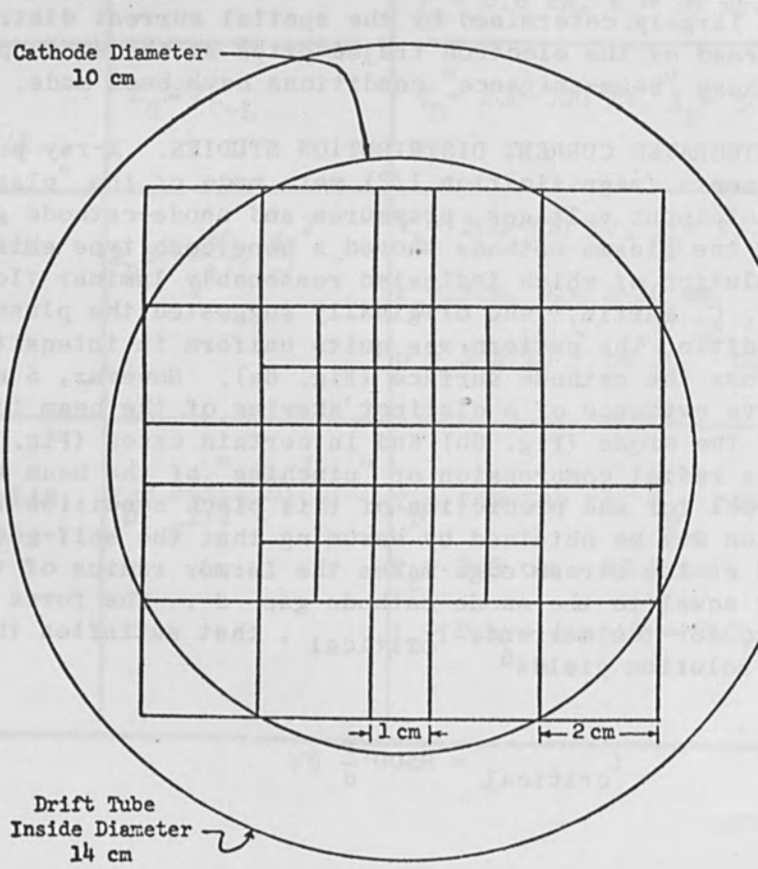
Cathode Diameter
10 cm
1 cm
2 cm
Drift Tube
Inside Diameter
14 cm

FIG. 7.—Forty-one-point segmented calorimeter array.

r = beam or cathode radius
d = anode-cathode gap

or, in terms of the Lawson model,[5] where

$$I_{\text{Lawson}} = 17\,000 \quad \beta\gamma \quad \text{and} \quad \nu = \gamma$$

$$\left(\frac{\nu}{\gamma}\right)_{\text{critical}} \geq \frac{r}{2d}$$

A comparison of the measured values of ν/γ for the radiographs of Figures 6(a-c), with $\nu/\gamma_{\text{critical}}$ and measured Z_D shows the general departure from laminar flow as $\nu/\gamma_{\text{measured}}$ approaches $\nu/\gamma_{\text{critical}}$. It is notable that the beam pattern which is both skewed and pinched occurs for a lower relative value of ν/γ but a higher value of Z_D than for the skewed beam only. This phenomenon has occurred consistently but cannot be explained at present.

This diode-pinch mode has been further studied for ν/γ both less than and greater than $\nu/\gamma_{\text{critical}}$ by means of a segmented graphite calorimeter[7] mounted 1 mm behind the anode foil (Figs. 7 and 8). The data of Fig. 8 represent about 30% of the initial beam energy since a fine stainless-steel mesh, which is only 30% transparent to the beam electrons, was used as the anode. The net transmitted energy measured by the calorimeter agrees within approximately 15% of that obtained from the beam-current-and-voltage monitor data. Again it can be seen that the higher the relative ratio of ν/γ, the more pronounced is the pinching tendency.

Other Cornell data[7] reveal that there is a strong tendency for the pinch to be perpetuated as the beam propagates down the drift tube. The pinch position at the diode is always on the downstream (left) side, as is the general beam skewing, and this condition is believed at present to be caused by the asymmetrical feed of the Cornell system.

B. TIME-DIFFERENTIATED CURRENT DISTRIBUTION STUDIES. A time-history of the beam "instabilities" in the diode was accomplished by a masking technique (Fig. 9) used to decrease the primary beam current to a level that can be tolerated by a fast-rising (3-ns) scintillator material. Since the electrons which reach the scintillon are more effective (by a factor of at least 10^3) in producing optical photons in the scintillon than those anode-generated X rays which reach the scintillon, a scintillon sheet thin enough to pass the X rays with little optical excitation allows one to discriminate against the X rays and, in effect, photograph the electron spatial distribution.

Figure 10(a) shows a time-integrated photograph and Fig. 10(b) a 5 ns/frame photograph of the plasma cathode for the following conditions:

$$V_D = 360 \text{ kV} \ , \quad I_D = 61 \text{ kA} \ , \quad Z_D = 5.9$$

$$\left.\frac{\nu}{\gamma}\right|_{\text{measured}} = 2.60 \ , \quad \left.\frac{\nu}{\gamma}\right|_{\text{critical}} = 2.95$$

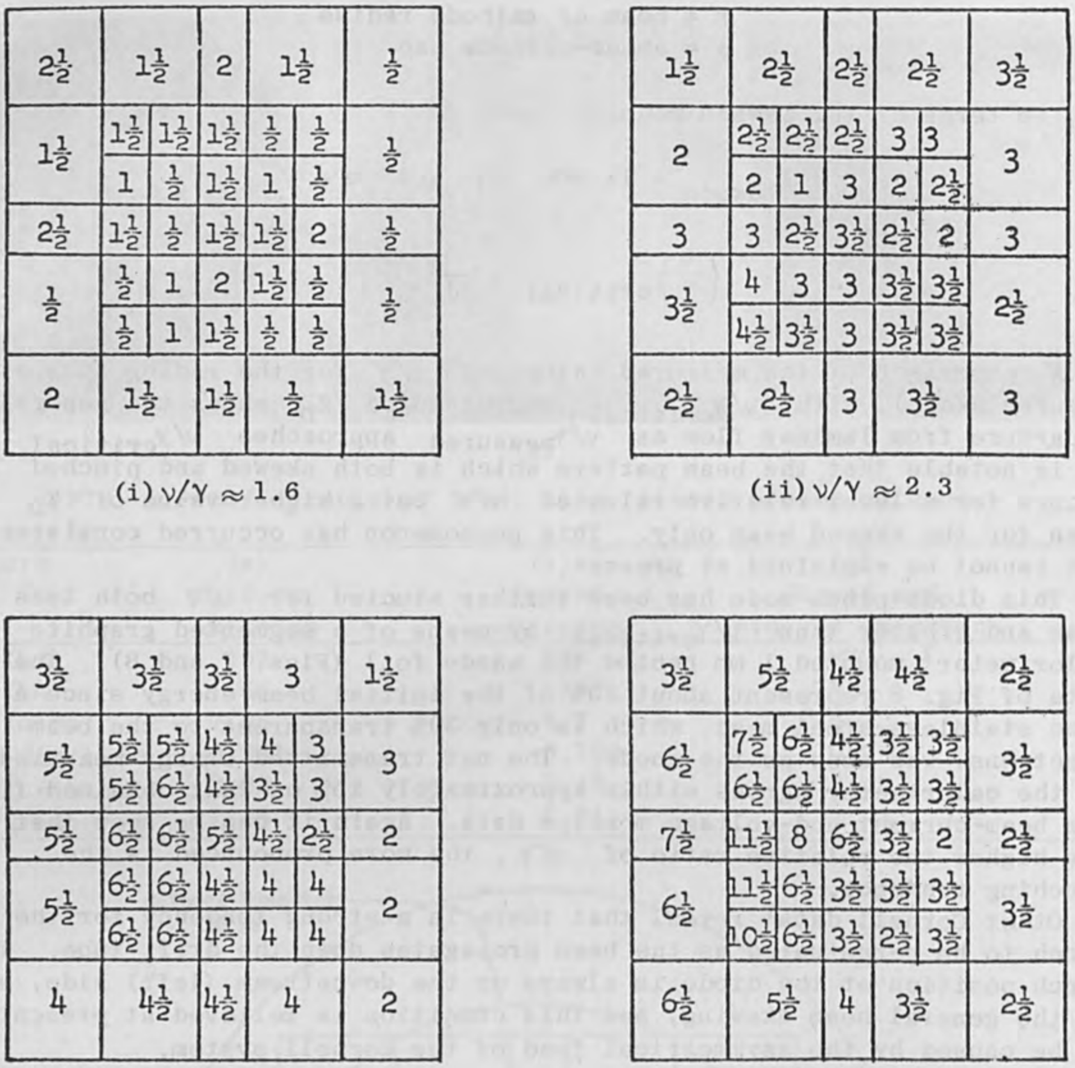
2½ 1½ 2 1½ ½
1½ | 1½ 1½ 1½ ½ ½ | ½
1 ½ 1½ 1 ½
2½ | 1½ ½ 1½ 1½ 2 | ½
½ | ½ 1 2 1½ ½ | ½
½ 1 1½ ½ ½
2 1½ 1½ ½ 1½
1½ 2½ 2½ 2½ 3½
2 | 2½ 2½ 2½ 3 3 | 3
2 1 3 2 2½
3 | 3 2½ 3½ 2½ 2 | 3
3½ | 4 3 3 3½ 3½ | 2½
4½ 3½ 3 3½ 3½
2½ 2½ 3 3½ 3
3½ 3½ 3½ 3 1½
5½ | 5½ 5½ 4½ 4 3 | 3
5½ 6½ 4½ 3½ 3
5½ | 6½ 6½ 5½ 4½ 2½ | 2
5½ | 6½ 6½ 4½ 4 4 | 2
6½ 6½ 4½ 4 4
4 4½ 4½ 4 2
3½ 5½ 4½ 4½ 2½
6½ | 7½ 6½ 4½ 3½ 3½ | 3½
6½ 6½ 4½ 3½ 3½
7½ | 11½ 8 6½ 3½ 2 | 2½
6½ | 11½ 6½ 3½ 3½ 3½ | 3½
10½ 6½ 3½ 2½ 3½
6½ 5½ 4 3½ 2½

(i) $\nu/\gamma \approx 1.6$ (ii) $\nu/\gamma \approx 2.3$

(iii) $\nu/\gamma \approx 2.8$ (iv) $\nu/\gamma \approx 3.4$

FIG. 8.—Segmented calorimeter data at 1 mm. (Numbers represent temperature rise in deg C.)

Test Data	(i)	(ii)	(iii)	(iv)
Test number and date	5 - 3/15/69	2 - 3/19/69	3 - 3/15/69	11 - 3/19/69
Drift tube pressure	Same as diode pressure	-	less than 0.0005 torr	
Diode voltage (Ave.), kv	400	320	430	350
Diode current (Peak), kA	44	49	75	77

(Listed ν/γ was calculated from peak current. Average values are about 70% of those listed; $\nu/\gamma|_{\text{critical}} = 2.81$.)

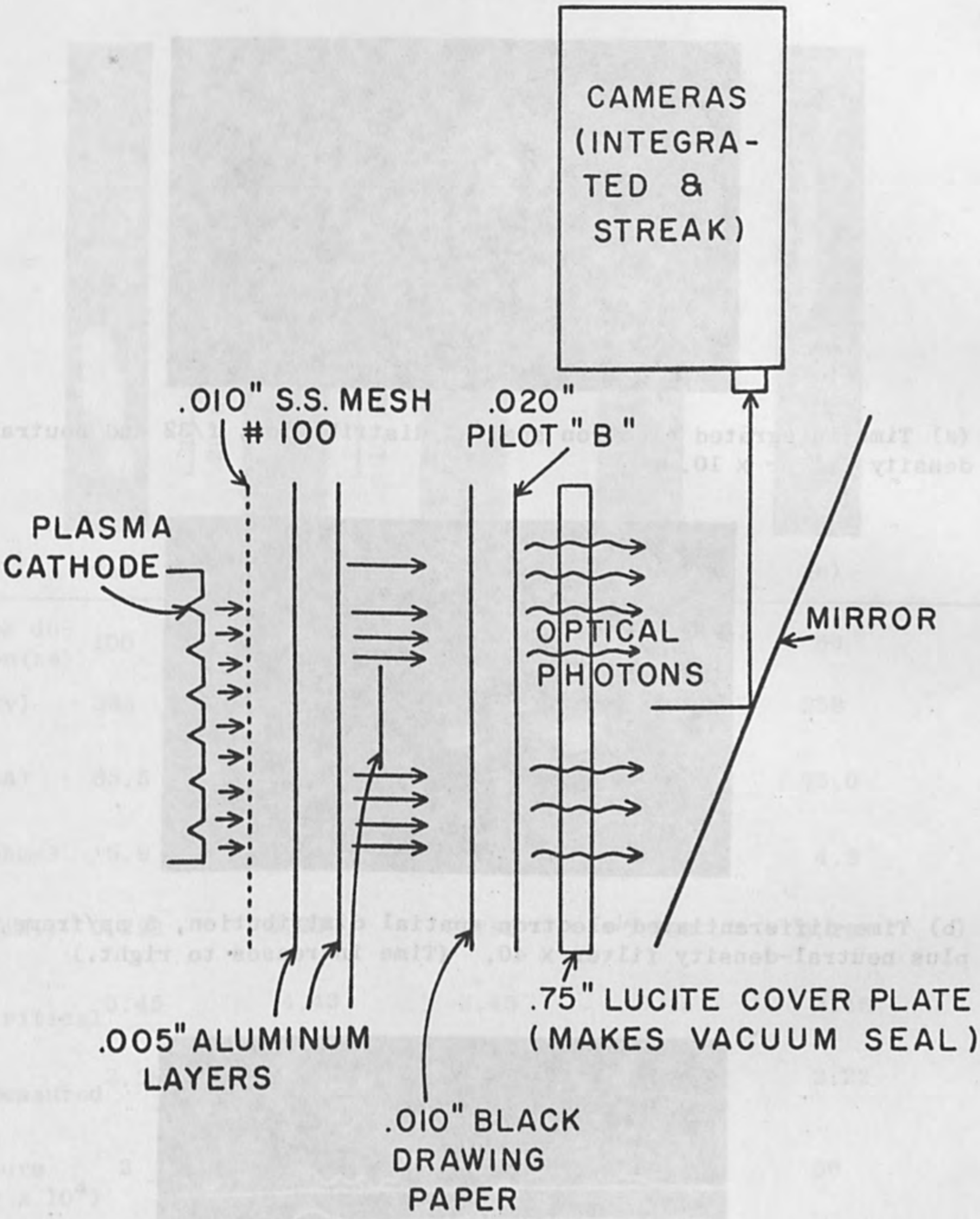
CAMERAS (INTEGRATED & STREAK)
.010" S.S. MESH # 100
.020" PILOT "B"
PLASMA CATHODE
OPTICAL PHOTONS
MIRROR
.75" LUCITE COVER PLATE (MAKES VACUUM SEAL)
.005" ALUMINUM LAYERS
.010" BLACK DRAWING PAPER

FIG. 9.—Masking technique for time-differentiated EB studies.

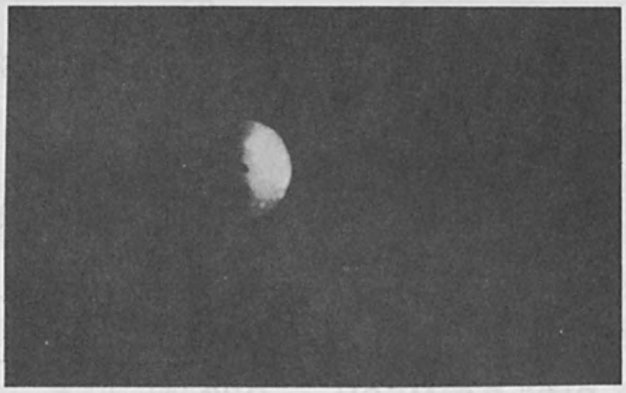

(a) Time-integrated electron spatial distribution, f/32 and neutral-density filter X 10.

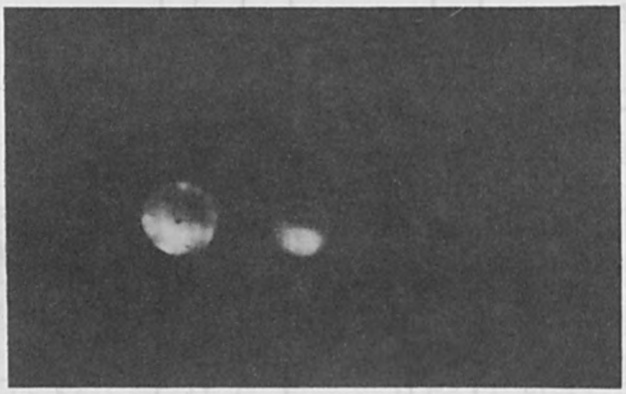

(b) Time-differentiated electron spatial distribution, 5 ns/frame, f/2 plus neutral-density filter X 40. (Time increases to right.)

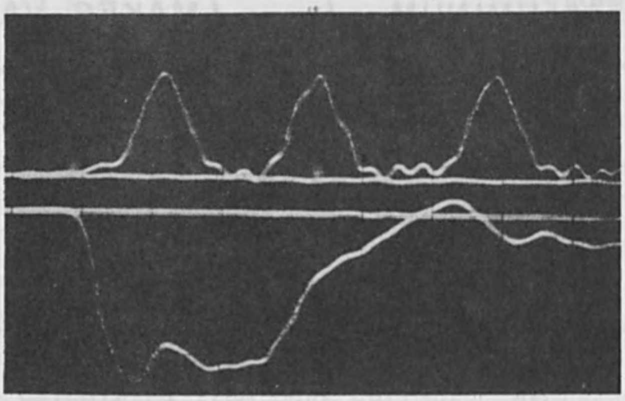

(c) Time-synchronized diode voltage V_D (lower trace) and TRW framing camera marking pulses (20 ns/cm).

FIG. 10.—Framing camera study: Test 22-4-69, 360 kv, 61 kA, 5.9 ohms, $\nu/\gamma|_{\text{critical}} = 2.95$, $\nu/\gamma_{\text{measured}} = 2.59$.

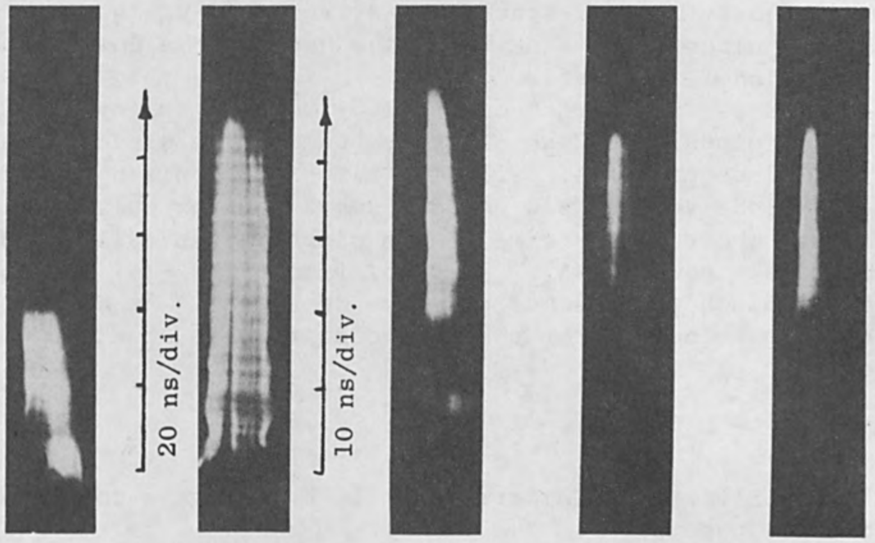

	(a)	(b)	(c)	(d)	(e)
Streak duration (ns)	100	50	50	50	50
V_D (kv)	386	254	350	329	358
I_D (kA)	65.5	73.2	76.2	70.0	75.0
Z_D (ohms)	5.9	3.5	4.6	4.7	4.8
Gap (in.)	0.290	0.226	0.290	0.290	0.290
$\nu/\gamma\|_{critical}$	3.45	4.43	3.45	3.45	3.45
$\nu/\gamma\|_{measured}$	2.58	3.87	3.28	3.16	3.22
Diode pressure (torr $\times 10^4$)	2	2	1	10	50
Test number and date (1969)	11 5/8	8 5/14	7 5/7	12 5/7	19 5/7

FIG. 11.—Streak camera study.

Figure 10(c) shows the time-synchronized trace of V_D vs the framing-camera marker pulses. The skewing of the beam to the downstream side of the line (diode) is notable.

Figure 11 shows fast streak-camera (50-100 ns/5 cm) evidence of the skewing and/or pinching of the electron beam in the diode, as a function of ν/γ and diode pressure. From the time-synchronized oscilloscope trace of the diode voltage and streak-camera monitor pulse, it is estimated that the build-up time of the pinch is typically about 25 ns. The approximately equal $\nu/\gamma_{\text{measured}}$ of Figs. 11(c)-(e) indicate that the degree of pinch is somewhat pressure dependent. An estimate of the radial collapse velocities of the beam electrons is about 10^8 cm/sec (Fig. 11e).

REFERENCES

1. J. C. Martin, AWRE, Aldermaston, U. K., private communications and unpublished papers.

2. J. Clark, Operational Characteristics and Entrance Conditions of a High-Current Relativistic Electron Beam Accelerator, Ph.D. Thesis, Cornell University, Ithaca, N. Y.; 1969.

3. G. E. Leavitt, J. D. Shipman, and I. M. Vitkovitsky, "Ultrafast high voltage probe," Rev. Sci. Instr. 35: 1371-1372, 1965.

4. I. Vitkovitsky, Plasma Physics Division, Naval Research Laboratory, Washington, D. C., private communication.

5. F. Friedlander, R. Hechtel, H. Jory, and C. Mosher, Megavolt-Megampere Electron Gun Study, Final Report, DASA 2173, Defense Atomic Support Agency, Washington, D. C.; September 1968.

6. J. D. Lawson, "Perveance and the Bennett pinch relation in partially neutralized electron beams," J. Elect. and Control 5: 146, 1958.

7. D. Hammer, Studies of High-Current Relativistic Electron Beam Propagation, Ph.D. Thesis, Cornell University, Ithaca, N. Y.; 1969.

PRODUCTION AND DIAGNOSTICS OF HIGH-CURRENT PULSED RELATIVISTIC ELECTRON BEAMS

JOHN J. CONDON

Naval Research Laboratory, Washington, D. C.

This paper reviews the work on high-current diodes used for the generation of electron beams at the Naval Research Laboratory. The work is directed at seeking answers to questions of high-current beam focusing and associated instabilities.

The methods for measuring voltage and current of the pulse supplied to the diode and procedures used to calibrate the voltmeters and the current meter are outlined. Types of cathodes which have been examined and the diagnostic methods which were used to measure their characteristics are described. Comparison is made between available theoretical predictions and the experimental values.

Blumlein generators[1] were used to provide a 50-ns pulse of up to 500 kV to the diode. One was a low-current generator with a maximum of 12 kA into a matched 41-ohm load which used oil as the dielectric. The other generator used de-areated water as the dielectric and had a maximum current of 72 kA into a matched 7-ohm load.[2] The principal features of this 7-ohm generator are shown in Fig. 1, together with an ideal pulse shape into a matched load. The generator is unbalanced due to the equal spacing of the two concentric pipes, giving a transmission line impedance of 5.1 ohms for the center conductor and 1.9 ohms for the intermediate pipe. The effect of this unbalancing is shown in the "staircasing" pulse shape which has about 82% of the available stored energy (maximum of 2200 joules at 500 kV) delivered in the first 50 ns and 42% of the remaining energy in each subsequent reflection.

Generator voltages were measured with capacitive or resistive dividers shown in Figs. 2 and 3. The first used capacitive coupling through the dielectric to the stressed high-voltage electrode, which in the case of water had a resistivity of 10-15 megohm-cm. In the circuit diagram shown in Fig. 2, the 1-nf capacitance was obtained by wrapping the small cylinder[1] with three layers of 1-mil Mylar before insertion into the hollow cylinder.[2] In practice the attenuation with these voltmeters is about 114 to 125 db, which yields a signal voltage of less than 1 volt in most cases. The attenuation is found by calibration but can be calculated from the product of the ratio of the capacities and resistances. In Fig. 2 the capacitive ratio of 1 nf/1 pf is 10^3 and the resistive ratio of 50 K/50 is 10^3, giving a total attenuation of 10^6. The size of the capacitive coupling tip, which can be seen to vary in the photograph of the assembled voltmeters,[3] is determined by the dielectric constant. Further details regarding this type of voltmeter, which we have used for several years, can be found in Ref. 3.

Photographs and a circuit diagram of the resistive divider are shown in Fig. 3. The liquid resistor is aluminum chloride. The ratio of the

Record of 10th Symposium on Electron, Ion, and Laser Beam Technology (L. Marton, ed.); San Francisco Press, Inc.
Copyright © by The Institute of Electrical and Electronics Engineers, Inc.—Printed in the U.S.A.

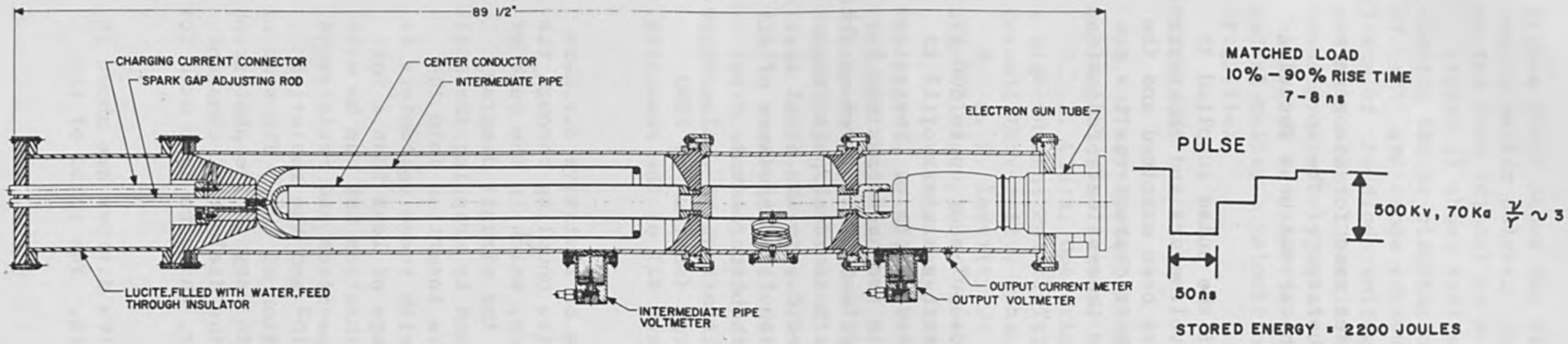
89 1/2"
CHARGING CURRENT CONNECTOR
SPARK GAP ADJUSTING ROD
CENTER CONDUCTOR
INTERMEDIATE PIPE
ELECTRON GUN TUBE
LUCITE,FILLED WITH WATER,FEED THROUGH INSULATOR
INTERMEDIATE PIPE VOLTMETER
OUTPUT CURRENT METER
OUTPUT VOLTMETER
MATCHED LOAD
10% - 90% RISE TIME
7-8 ns
PULSE
500 Kv, 70 Ka ν/γ ∼ 3
50 ns
STORED ENERGY = 2200 JOULES

FIG. 1.—Seven-ohm unbalanced Blumlein generator used to provide a high-current 5-ns pulse to the diode.

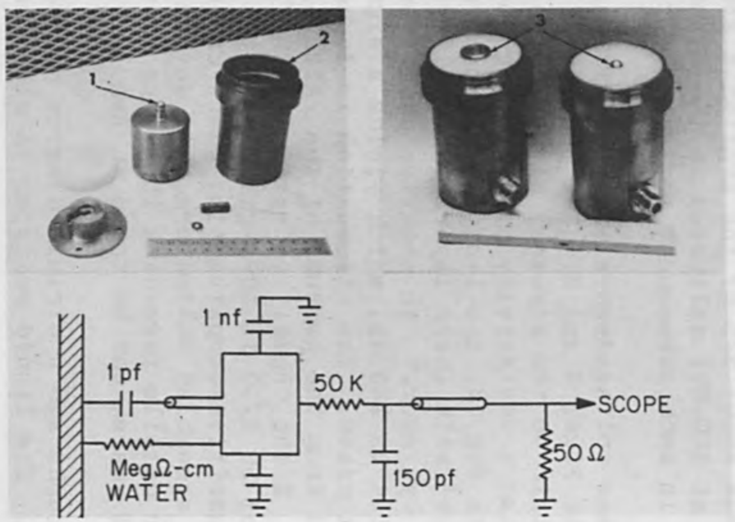
1
2
3
1 nf
1 pf
50 K
SCOPE
MegΩ-cm
WATER
150 pf
50 Ω

FIG. 2.—Capacitive voltage-divider circuit and components before and after assembly.

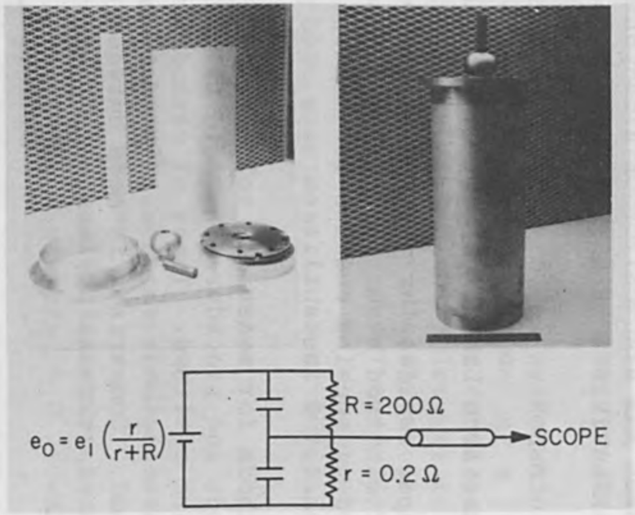
R = 200 Ω
$e_0 = e_I \left(\frac{r}{r+R}\right)$
SCOPE
r = 0.2 Ω

FIG. 3.—Resistive voltage-divider circuit and components before and after assembly.

resistance of the liquid in the tube to that between the plates, which are 200 ohms and 0.2 ohms, respectively, gives an attenuation of about 1000:1, which yields signal voltages of the order of 100 volts. The capacitance of the liquid (dielectric constant about 80) in the long tube is compensated for by adjusting the spacing and capacity of the plates so that the time constants for both resistive-capacitive circuits are equal. The length of the long tube determines the maximum voltage that can be measured with this type of voltmeter.

Calibration is usually done by pulse charging a much larger capacitance than the generator capacitance and measuring its charged voltage with an electrostatic voltmeter. The capacitor is then switched into the generator and the signal from the voltmeter to be calibrated is measured with an oscilloscope.[4] Another procedure uses an rf signal to null out the inductance and capacitive components at the resonant frequency, leaving only the resistive, which can be compared to a known resistance.[5] With these generators the measured diode voltage is very nearly the same as the electron accelerating voltage, since the inductive voltage drop between the diode and the voltmeter is small.

Current measurement is done by integrating a rate of change of current signal from a single-turn loop mounted flush with the inner wall of the generator. Calibration is done by short-circuiting the generator and measuring the voltage as described in the previous paragraph. The current is calculated from $i = V/R$, where R is the known generator resistance, and compared with the integrated signal on an oscilloscope. The accuracy of the calibration is estimated to be 5%.

To determine some of the effect of the cathode and anode configuration on the EB characteristics both plane and conical cathodes were used. An example of a plane cathode consisting of about 55 needle emitters is shown in Fig. 4. The Ta anode was parallel with the cathode face and separated from it by about 16 mm. A corona ring (shown in the upper photograph) was placed around the needle array to help give a uniform field distribution over the needle tips. Pressure in the cathode-anode region was in the range of 10^{-7} torr. The cathode emission pattern is shown in the lower photograph, as recorded by a remote closed-circuit TV screen. The TV camera was focused on a phosphor disk that was in good contact with the anode surface. A solenoid coil was placed around the end of the electron gun and a high-current pulse passed through the coils, generating a magnetic field whose flux lines were parallel with the electron paths and provided a guide path for the electron streams from each emitter.

Emission from the steel corona ring was considerable and probably accounts for most of the electron flow. Recently some thought has been given to using the ring as a source of hollow electron beams which could be accelerated and subsequently compressed to a smaller radius--the so-called electron ring accelerator. The scope traces in the center show that the beam was nearly a constant impedance of 60 ohms.

Results using another type of nearly flat cathode that was in the shape of a dome or hemisphere with a maximum height of 3 mm are shown in Fig. 5. The TV picture shows the appearance of a ring of bright emission

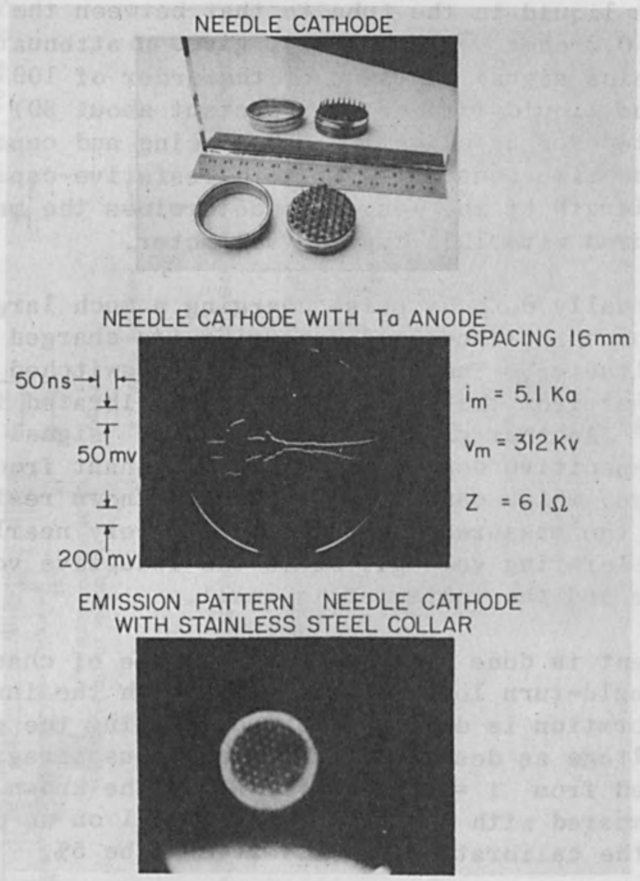
NEEDLE CATHODE
NEEDLE CATHODE WITH Ta ANODE
SPACING 16 mm
50 ns
50 mv
200 mv
i_m = 5.1 Ka
v_m = 312 Kv
Z = 61 Ω
EMISSION PATTERN NEEDLE CATHODE WITH STAINLESS STEEL COLLAR

FIG. 4.—Needle cathode before assembly into diode and during emission, and scope traces of current and voltage.

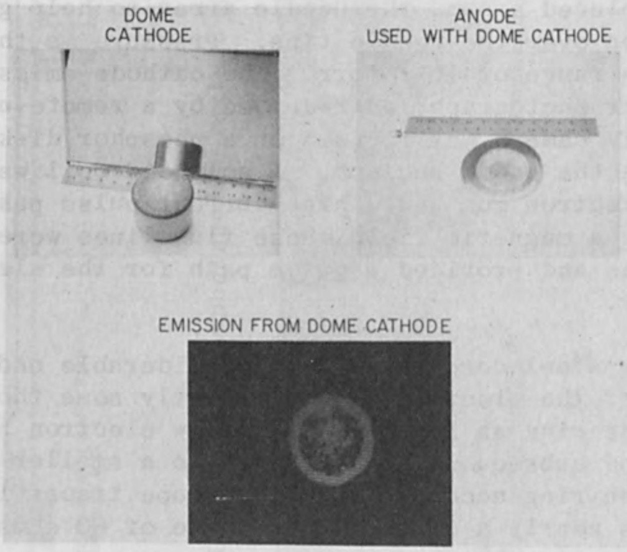
DOME CATHODE
ANODE USED WITH DOME CATHODE
EMISSION FROM DOME CATHODE

FIG. 5.—Dome cathode before assembly and during emission.

around the outside edge that is similar to the emission from the corona ring in the previous figure. The diameter of the circle of pit marks on the anode matches a diameter on the cathode face which is slightly smaller than the maximum diameter. Some of individual emission points on the face of the smooth cathode are also visible.

The current obtained with these planar-type cathodes can be compared to that determined by one-dimensional Child's law for relativistic electrons. In Fig. 6 the calculated current for various anode-cathode voltages given by the solid lines was reproduced from Ref. 6. The complete expression is given by the series expression shown and is asymptotic at the low-voltage end by the classical type Child's law of $V^{3/2}$ and in the ultrarelativistic range by the expression given for V . In nearly all cases, the experimental data fall below these curves, indicating that at a given voltage, more current is obtained than would be expected on the basis of this simple model. Results for the needle cathode, the dome cathode, and one of the cone cathodes are shown in Fig. 6. The cone cathodes were attempts to give a more convergent flow. It is shown here that, indeed, greater current density can be obtained by such design.

Any realistic model of the high-current diodes must of course account for the effects of the self-magnetic field which tends to compress the beam by overcoming some of the electrostatic repulsion of the electrons. An attempt to do so is described in Ref. 7, where it is conjectured that the electron flow could be divided into a core current and sheath current. As shown in Fig. 7 (reproduced from Ref. 7) the core current is similar to low-current, nonrelativistic flow across equipotential lines (equipotential flow) in contrast to the parapotential sheath where the flow is along equipotential lines (parapotential flow), and may account for most of the flow in relativistic diodes. Based on these considerations, an approximate expression for the conductance is derived and shown in the figure.

For the case of the needle cathode, at 16 mm separation (see Fig. 4) the impedance was about 61 ohms. Using the derived expression, a value of about 30 ohms is calculated for this condition.

Any of these time-independent models can only be approximations, since our results generally show a time-dependent current and voltage. Recently, work has begun to obtain a time-dependent code for computer analysis of these flows. It is now giving correct results for low-voltage diodes in a time-dependent calculation. The effort now will be to keep the code time dependent and solve numerically the equations for various geometries for these high-current flows.[8]

Our attempt to achieve convergent flows has been to use conical cathodes. The first of two cones that we have used is designated P1 , and the photographs in Fig. 8 show the cathode and corresponding current and voltage traces. The results shown here were obtained with the 40-ohm generator. (Results for the same cathode obtained with the higher-current generator--7-ohm, water-dielectric Blumlein--are given below.) As can be seen in the photograph, the tip of the cone is the region of most deterioration.

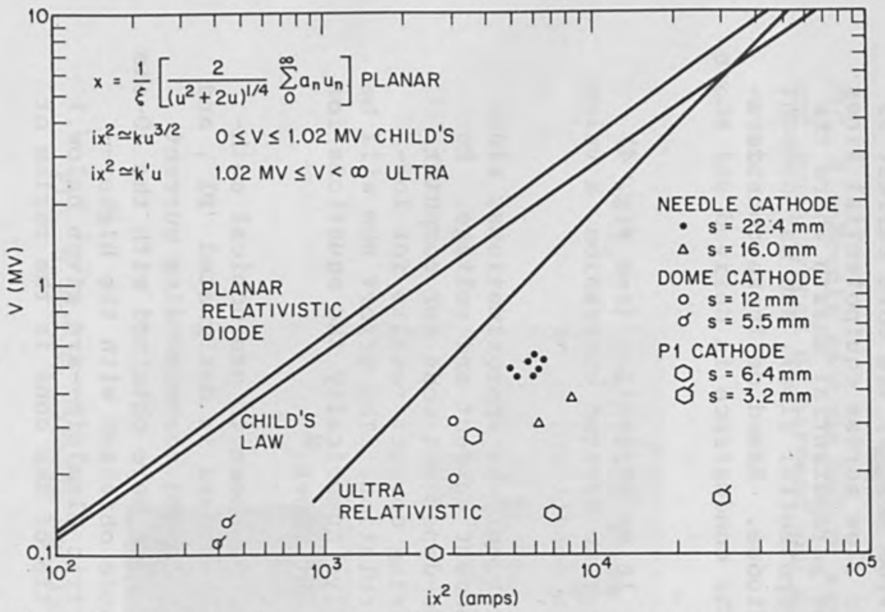

FIG. 6.—Comparison of calculated and measured current for parallel-plane diode.

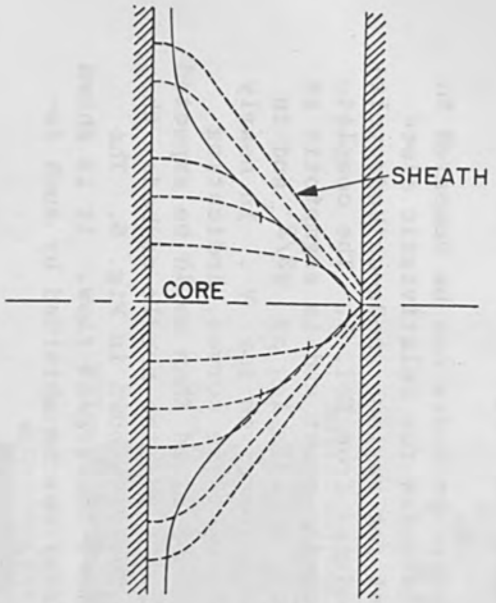
SHEATH
CORE

$1/R = 0.017(1+1/V_{MV})^{1/2}(r_o/d) \cdot$ mhos

FIG. 7.—Core and sheath currents based on the parapotential model and the expression for conductance.

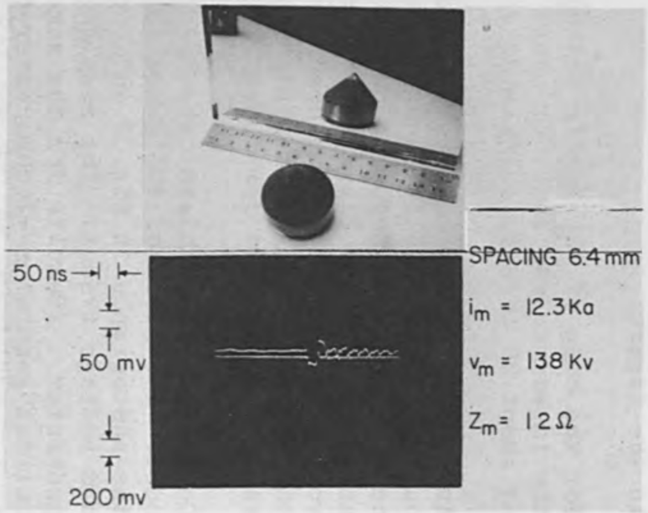
50 ns
50 mv
200 mv
SPACING 6.4 mm
i_m = 12.3 Ka
v_m = 138 Kv
Z_m = 12 Ω

FIG. 8.—P1 cathode and associated current and voltage traces.

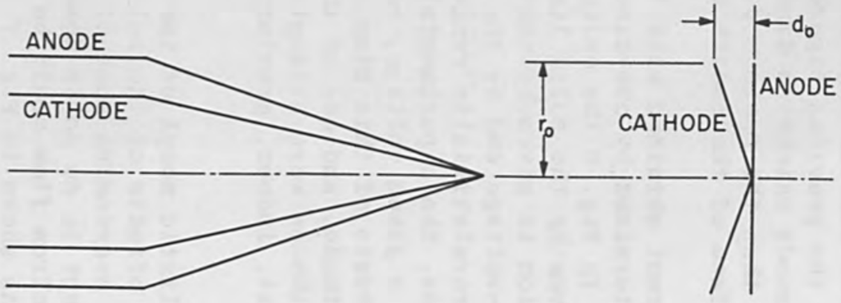
ANODE
CATHODE
d_o
r_o
ANODE
CATHODE

$5.74\ d_o/r_o$ ohms

FIG. 9.—Cone-cathode configuration defining quantities that are measured for impedance calculation using parapotential concepts.

In the example shown here, the impedance is nearly a constant value of 12 ohms. This can be compared to a value calculated on the basis of the assumptions previously outlined for parapotential flow. The cone configuration and the derived expression for impedance are shown in Fig. 9. For these conditions, the calculated impedance was about 11 ohms. The agreement is encouraging, but it must still be demonstrated that flow of this type does in fact exist in these diodes.

Two problems in particular arise in high-current-density beams such as these. The first has to do with diode breakdown and the second with beam focusing. We used two cone-cathode configurations in these initial experiments, one of them the P1 cathode previously described and a more convergent cone designated as P2 (Fig. 10). The configuration was fixed by the 90° and 20° cones and the cathode-anode spacing (held at about 3 mm). The anode material was Ta , except in one case where it was Ti . The high-current, 7-ohm generator was used, where the prepulse was kept at 2%.* The residual gas pressure in the cathode-anode region was either 10^{-7} or 10^{-4} torr. Essentially we are examining the effects of these two pressures on the two cone configurations. Figures 11 and 12 show examples of results obtained for the P1 and P2 cathodes, respectively. With P1 the pulse was shortened for either pressure but was twice as long at 10^{-7} as at 10^{-4} torr. The time was determined by the duration of the photon emission from the anode as observed with a photodiode-scintillator detector. The total photon energy, determined with thermoluminescent dosimeters (TLD), was considerably different in both cases. The impedance values shown in Fig. 11 indicate that it was changing during the entire pulse with the maximum value achieved at the beginning of the pulse. The calculated impedance as previously described in Fig. 9 was about 7 ohms or approximately the same as the peak value at 10^{-7} torr. The results with this P1 cathode on the higher current generator are in marked contrast to those obtained with the low-current generator previously described in Fig. 8. There, the pulse was a "nonbreakdown" type, whereas it now has the characteristics of a breakdown pulse, i.e., the current continues to change rapidly during the entire pulse and never levels off, and the duration of the pulse is much less than the 50 ns that the generator can provide. Vacuum baking of the diode to remove adsorbed gases from the surfaces had no substantial effect on these P1 results. It is noted that the photon yields at the two pressures are comparable on the basis of the voltage ratio squared multiplied by the ratio of pulse duration times.

In contrast to these results, the P2 diode behaved as a nearly constant-impedance device at 10^{-7} torr over most of the pulse duration, but at 10^{-4} torr it was remarkably similar to the P1 results, with about the same range of impedance in both cases. The calculated impedance of about 35 ohms is much higher than observed values. The photon energy is not available at 10^{-4} torr with the P2 cathode but the value at 10^{-7} torr

---

* The prepulse is due to the charge that builds up on the inner conductor while the intermediate pipe is charging and can ionize the gas in the cathode-anode gap prior to arrival of the main pulse. This condition can be controlled by holding the inner pipe near ground potential while the intermediate pipe is charging (note coil in Fig. 1 between the center conductor and ground).

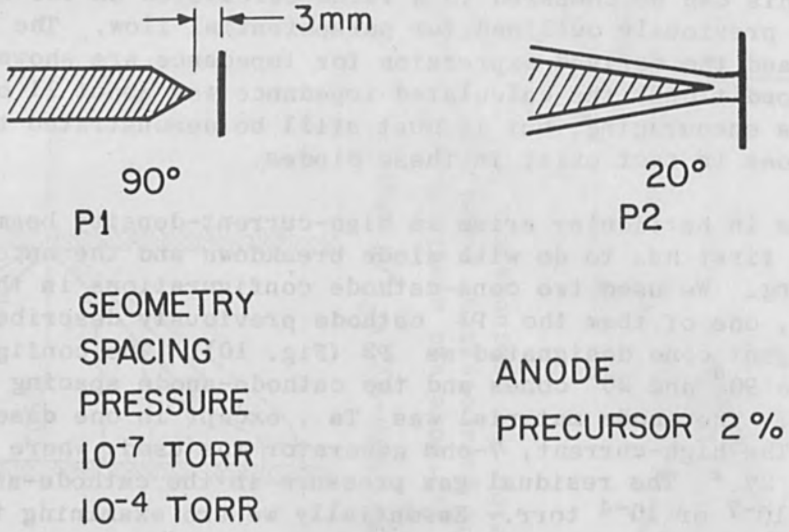
3mm
90°
P1
20°
P2
GEOMETRY
SPACING
PRESSURE
10-7 TORR
10-4 TORR
ANODE
PRECURSOR 2 %

FIG. 10.—Outline of experimental plan for determining pressure effect on parapotential-diode performance.

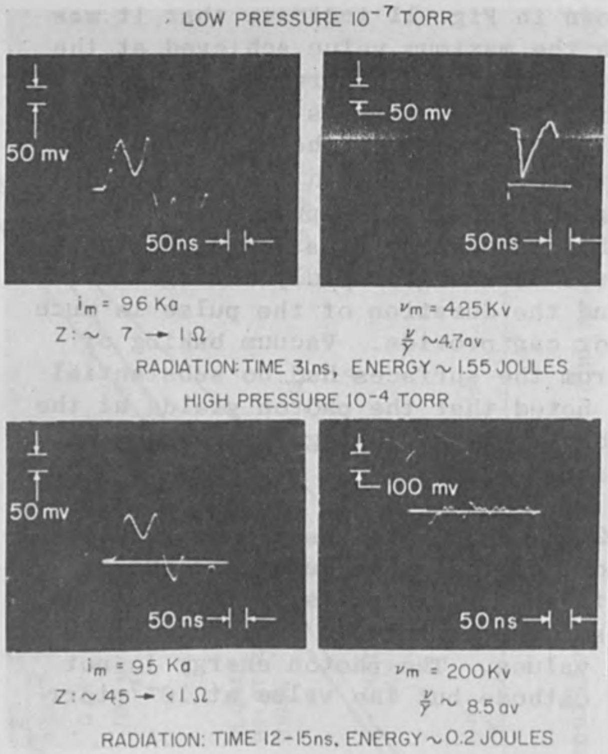

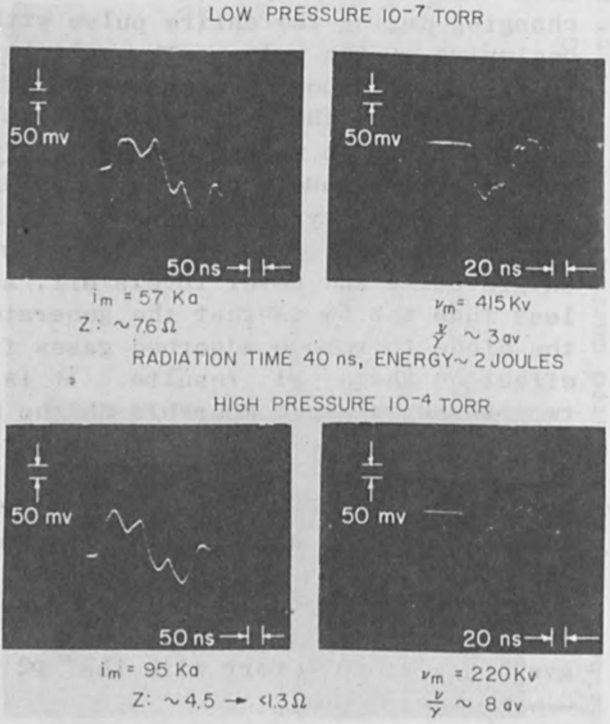

FIG. 11.—Current and voltage traces of P1 cathode at 10^{-4} and 10^{-7} torr.

FIG. 12.—Current and voltage traces of P2 cathode at 10^{-4} and 10^{-7} torr.

can be compared with the P1 result by multiplying the P2 energy by the ratio of the radiation time for each diode.

These results are too limited to form any general conclusion, but it does appear that the pulse-time duration is longer at low pressure with the impedance higher and that the higher pressure masks the differences arising from the cone geometry.

The second problem, that of beam focusing, has only recently received attention, so that any results are very preliminary. One of the means used to investigate has been to measure the energy distribution in the beam by carbon calorimetry. Nonuniformity in beam-energy distribution would partially explain lack of focusing in some cases. An example of this calorimetry measurement is given in Fig. 13, where a map of the beam energy density is shown. The beam was produced with a parallel-plane multipoint cathode and extracted through a transmission anode into a drift chamber, as indicated in the drawing in the center of Fig. 13. A carbon calorimeter shown in the lower left was positioned 0.5 cm from the anode. The calorimeter consisted of 25 bars of carbon with thermocouples in the back whose output was recorded on the oscillograph shown in the lower right. The map at the top was made by arranging the results into energy intervals. The lowest energy density is all shaded. The next highest has one diagonal line and the next two and three. Finally, the highest is in the upper left corner, showing that this beam was not very symmetrical in the energy distribution. The decrease in energy density of the beam, as the calorimeter is moved away from the anode, is shown in Fig. 14, where the energy density decreases from about 22 to 2 cal/cm^2.

Focusing of the beam depends on a symmetric emission of electrons from the cathode, since the forces acting on the beam become unbalanced and lead to unreproducible discharges. One of the ways to enhance symmetric emission is to coat the cathode surface with a clean, fresh layer of metal. The importance of cathode preparation is still being examined.

Another diagnostic method for examining diode behavior is to determine the electron and photon spectra from the anode. Knowledge of electron spectra is needed for input information for computer codes to calculate photon spectra and also for data reduction. At this time, we are calculating the spectra from the current and voltage traces. This procedure is facilitated by reducing the current and voltage profiles to values on punched cards by a digitizing device.[9] An example is given in Fig. 15 with the original scope trace on the right and the digitized version on the left reproduced from punched cards.

An example of an electron spectrum calculated from measured current and voltage is shown in the upper part of Fig. 16, where the data were processed from the punched cards in the manner just described. In this example, most of the electrons had an energy of about 375 keV. Shown in the lower portion of the figure is a calculated photon spectrum for this electron spectrum. The photon spectra were determined with a transport code called ELECTREX. In this code the electron distribution in the converter is assumed to be governed by the Bethe-Rose-Smith equation, which is derived from the Boltzmann equation. The code computes the

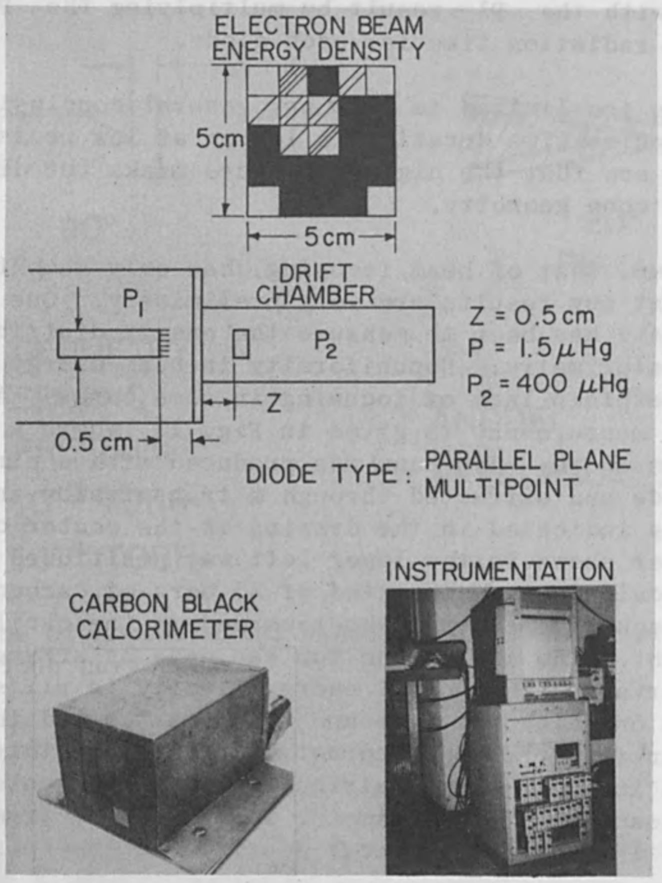
ELECTRON BEAM ENERGY DENSITY
5cm
5cm
DRIFT CHAMBER
P1
P2
Z = 0.5 cm
P = 1.5 μHg
P2 = 400 μHg
Z
0.5 cm
DIODE TYPE: PARALLEL PLANE MULTIPOINT
INSTRUMENTATION
CARBON BLACK CALORIMETER

FIG. 13.—Measurement of electron-beam energy density using carbon block calorimeter.

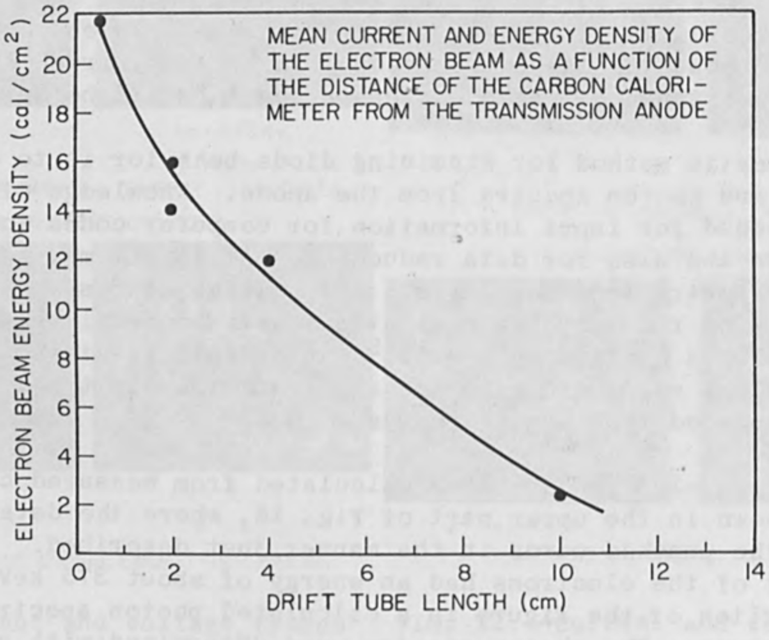

FIG. 14.—Electron-beam energy density measured at various distances from transmission anode.

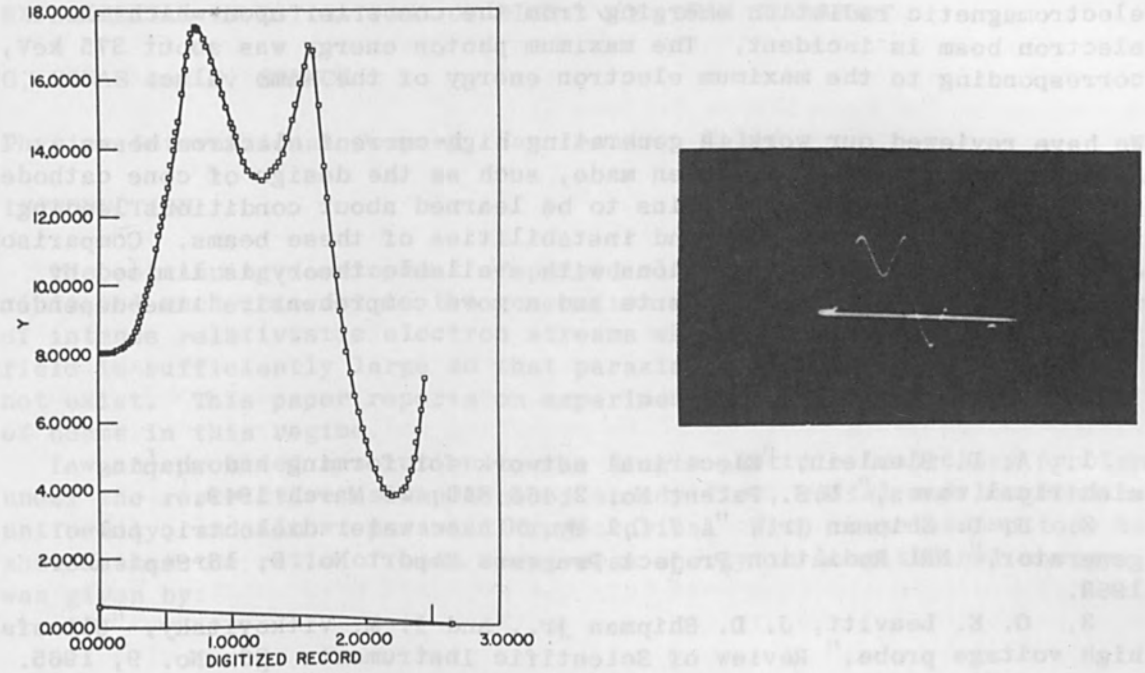

FIG. 15.—Comparison of original scope trace with reproduction from digitized record on punched cards.

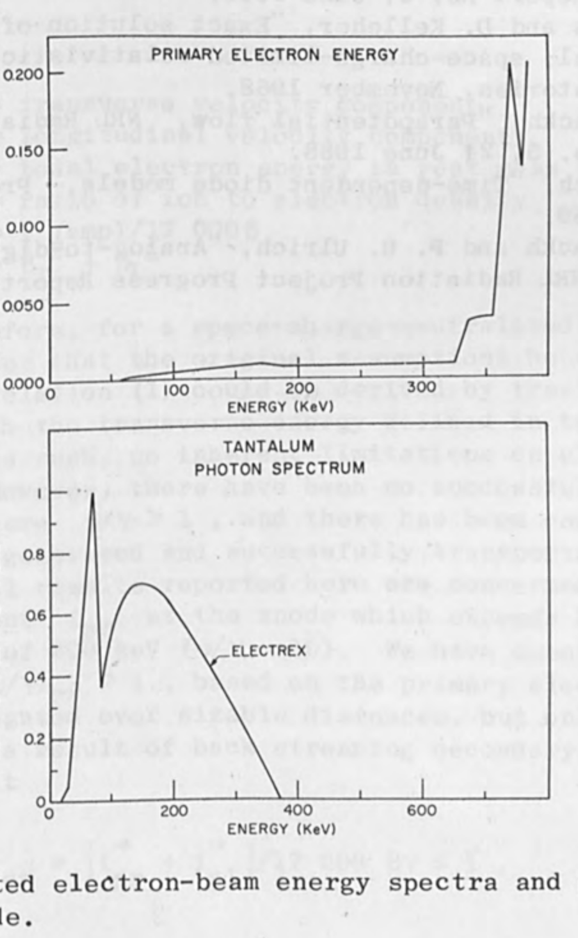

FIG. 16.—Calculated electron-beam energy spectra and photon spectra using ELECTREX code.

electromagnetic radiation emerging from the converter upon which the electron beam is incident. The maximum photon energy was about 375 keV, corresponding to the maximum electron energy of the same value.

We have reviewed our work in generating high-current electron beams. Although advancements have been made, such as the design of cone cathodes, it is apparent that much remains to be learned about conditions leading to interelectrode breakdown and instabilities of these beams. Comparison of various cathode configurations with available theory is limited by lack of more refined measurements and a more comprehensive time-dependent theory.

REFERENCES

1. A. D. Blumlein, "Electrical network for forming and shaping electrical waves," U.S. Patent No. 2 465 840, 29 March 1949.
2. J. D. Shipman jr., "A 7 Ω,1 Mv, 50 nsec water dielectric pulse generator," NRL Radiation Project Progress Report No. 8, 16 September 1968.
3. G. E. Leavitt, J. D. Shipman jr., and I. M. Vitkovitsky, "Ultrafast high voltage probe," Review of Scientific Instruments 36: No. 9, 1965.
4. J. K. Burton, "High-voltage probe calibration" (to be published).
5. J. J. Condon, "Measurement of Bremsstrahlung radiation produced with high-current diodes and coaxial Blumlein generators," NRL Radiation Project Progress Report No. 6, June 1969.
6. J. E. Boers and D. Kelleher, "Exact solution of Poisson's equation for one-dimensional, space-charge-limited relativistic flow," SC-RR-68-536, Sandia Laboratories, November 1968.
7. D. C. de Packh, "Parapotential flow," NRL Radiation Project Progress Report No. 5, 24 June 1968.
8. P. B. Ulrich, "Time-dependent diode models," Proceedings DASA Meeting, April 1969.
9. D. C. de Packh and P. B. Ulrich, "Analog-to-digital system for film recording," NRL Radiation Project Progress Report No. 9, 11 March, 1969.

EXPERIMENTAL INVESTIGATIONS OF HIGH ν/γ BEAM TRANSPORT

G. YONAS and P. SPENCE

Physics International Company, San Leandro, Calif.

INTRODUCTION

The continuing development of pulsed electron accelerators has precipitated much interest in the generation and propagation characteristics of intense relativistic electron streams where the beam self-magnetic field is sufficiently large so that paraxial electron trajectories can not exist. This paper reports on experimental and analytical studies of beams in this regime.

Lawson[1] provided a solution to the single particle trajectory problem under the restrictive assumptions of steady flow, radial and longitudinal uniformity, and almost paraxial trajectories. With these assumptions he showed that the ratio of beam transverse energy to longitudinal energy was given by:

$$\frac{\langle\beta_T{}^2\rangle}{\langle\beta_L\rangle^2} \approx \frac{\nu}{\beta_L{}^2\gamma}\left(\beta_L{}^2 + f - 1\right) \qquad (1)$$

where

$c\beta_T$ = transverse velocity component
$c\beta_L$ = longitudinal velocity component
γ = total electron energy in rest mass units
f = ratio of ion to electron density
ν = I (amp)/17 000β
$\beta^2 = \beta_T{}^2 + \beta_L{}^2$

He required, therefore, for a space-charge-neutralized beam, that $(\nu/\gamma) \ll 1$ in order that the original assumptions be valid. Lawson also showed that relation (1) could be derived by treating the beam as a linear pinch with the transverse energy defined in terms of a kinetic temperature, and as such, no inherent limitations on electron trajectories existed. However, there have been no successful orbit calculations for cases where $\nu/\gamma > 1$, and there has been concern as to whether such beams can be generated and successfully transported.

The experimental results reported here are concerned with beams of primary beam current I_{pr} at the anode which exceeds 200 000 A at mean electron energies of 200 keV ($\nu/\gamma \sim 10$). We have concluded that beams with values of $(\nu/\gamma)_{pr} > 1$, based on the primary electron beam current, can be propagated over sizable distances, but only if current neutralization as a result of back streaming secondary electrons, I_{pl}, can occur such that

$$(\nu/\gamma)_{net} = \left|\vec{I}_{pr} + \vec{I}_{pl}\right| / 17\,000\ \beta\gamma \le 1 \,. \qquad (2)$$

Record of 10th Symposium on Electron, Ion, and Laser Beam Technology (L. Marton, ed.); San Francisco Press, Inc.

Copyright © by The Institute of Electrical and Electronics Engineers, Inc.—Printed in the U.S.A.

The major emphasis of this work was, then, to relate beam transport properties to current neutralization and neutralization to the time dependence of the beam currents in terms of the electromagnetic fields generated by the beam-plasma system.

APPARATUS

Throughout this work considerable emphasis has been placed on developing low-inductance-diode and drift-chamber diagnostics. Diode accelerating voltage and current probes, as well as net and primary current probes have been used to instrument the Physics International Model 730 Pulserad, shown in Fig. 1. The pulser consists of a Marx generator used to pulse charge an 8.5-ohm oil-filled coax whose load impedance can be varied in the 1- to 9-ohm range by adjusting the cathode-anode gap. Typical operation at pulse charge voltages of 3.5 MV yields beams with mean electron energies from 180 keV to 1 MeV, at mean current levels of 200 kA to 100 kA respectively, and with a 50-ns pulse duration (FWHM). The anode consists of a 0.00025-in. aluminized Mylar window that allows injection of the electron beam into the separate drift chamber region.

A resistive voltage divider, consisting of a capacitively and resistively graded column of copper sulfate solution, was used to directly monitor the cathode voltage.[2] The diode current was monitored by a self-integrating magnetic fluxmeter, which consisted of a single-turn loop in series with an integrating resistor ($L/R \approx 600$ ns). Calibration was performed under machine operating conditions by comparing the monitor output to the current measured in a Faraday cup placed at the anode to test the credibility of the diode diagnostics. The total beam energy was measured by a totally absorbing graphite calorimeter and compared with

$$\int_0^\infty V(t)I(t)\,dt$$

This test was performed at both high $[(\nu/\gamma)_{pr} \sim 8]$ and low $[(\nu/\gamma)_{pr} \sim 1.6]$ current levels. At low current levels, the agreement was within 5%. At higher current levels, which necessitated placing the calorimeter further from the anode to avoid its destruction by the intense beam, the measured total energy was low by 10%. This discrepancy is consistent with a loss in beam energy during transport from the anode to the calorimeter. The electron energy deposition-vs-depth profile was calculated from voltage and current data by the use of a Monte Carlo electron transport code. At low current levels the agreement was quite good. However, measurements of low-energy, high-current deposition profiles typically showed a more steep profile near the front surface and a higher front surface dose than that calculated. This effect was most pronounced at 200 keV, was only slightly apparent at 500 keV, and could not be resolved at energies above 700 keV. The excellent agreement for net currents sufficiently low so that the self-magnetic field of the beam does not influence the electron trajectories, confirms the independent calibrations of the diode diagnostics. The high ν/γ data point to the existence of transverse energy components in the electron beams. This deduction is discussed more fully in the next section.

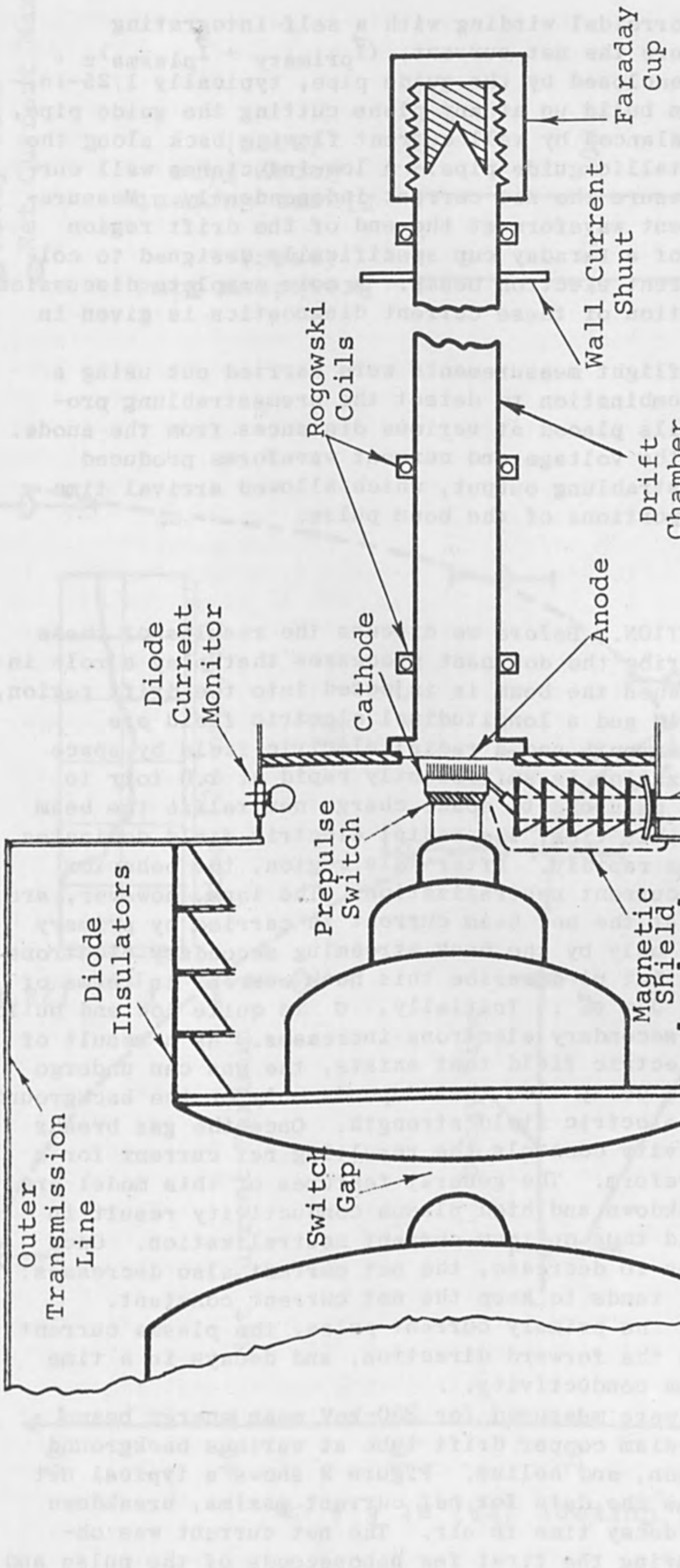
Outer Transmission Line
Switch Gap
Diode Insulators
Prepulse Switch
Magnetic Shield
Diode Current Monitor
Cathode
Diode Voltage Monitor
Anode
Drift Chamber
Rogowski Coils
Wall Current Shunt
Faraday Cup

FIG. 1. — Diode and drift chamber region with diagnostics.

The Rogowski coil, a torroidal winding with a self-integrating resistor, is used to measure the net current, $(\vec{I}_{\text{primary}} + \vec{I}_{\text{plasma}})_z$, flowing through the area enclosed by the guide pipe, typically 1.25-in.-diam. Since no charge can build up at any plane cutting the guide pipe, the net current must be balanced by wall current flowing back along the conducting wall of the metallic guide pipe. A low-inductance wall current shunt was used to measure the net current independently. Measurements of the primary current waveform at the end of the drift region were accomplished by use of a Faraday cup specifically designed to collect low-energy, high-current electron beams. A more complete discussion of the design and calibration of these current diagnostics is given in Ref. 3.

Electron beam time-of-flight measurements were carried out using a scintillator photodiode combination to detect the bremsstrahlung produced in thin tantalum foils placed at various distances from the anode. Oscillations inherent in the voltage and current waveforms produced oscillations in the bremsstrahlung output, which allowed arrival time measurements for various portions of the beam pulse.

RESULTS AND DISCUSSION

A. CURRENT NEUTRALIZATION. Before we discuss the results of these measurements we must describe the dominant processes that play a role in current neutralization. When the beam is injected into the drift region, an azimuthal magnetic field and a longitudinal electric field are generated by the rising current, and a radial electric field by space charge. Collisional ionization is sufficiently rapid at 1.0 torr to provide enough background gas ions to space charge neutralize the beam in about 2 ns. Prior to this time, the radial electric field dominates and the beam front expands rapidly. After this region, the behavior depends on the degree of current neutralization. The ions, however, are relatively immobile so that the net beam current is carried by primary electrons and is canceled only by the back streaming secondary electrons within the beam channel. Let us describe this back current in terms of a scalar conductivity σ; $\vec{J} = \sigma\vec{E}$. Initially, σ is quite low and builds as the number density of secondary electrons increases. As a result of the large longitudinal electric field that exists, the gas can undergo avalanche breakdown with a delay time that depends only on the background gas pressure for a given electric field strength. Once the gas breaks down, the plasma conductivity controls the resulting net current for a given primary current waveform. The general features of this model are that rapid avalanche breakdown and high plasma conductivity result in maximum plasma current and thus optimum current neutralization. Once the primary current begins to decrease, the net current also decreases; but now the induced emf tends to keep the net current constant. Finally, after the end of the primary current pulse, the plasma current continues to flow, now in the forward direction, and decays in a time that depends on the plasma conductivity.

Net current waveforms were measured for 250-keV mean energy beams propagated in a 1.25-in.-diam copper drift tube at various background gas pressures of air, argon, and helium. Figure 2 shows a typical net current waveform and gives the data for net current maxima, breakdown time, and plasma current decay time in air. The net current was observed to rise steeply during the first few nanoseconds of the pulse and

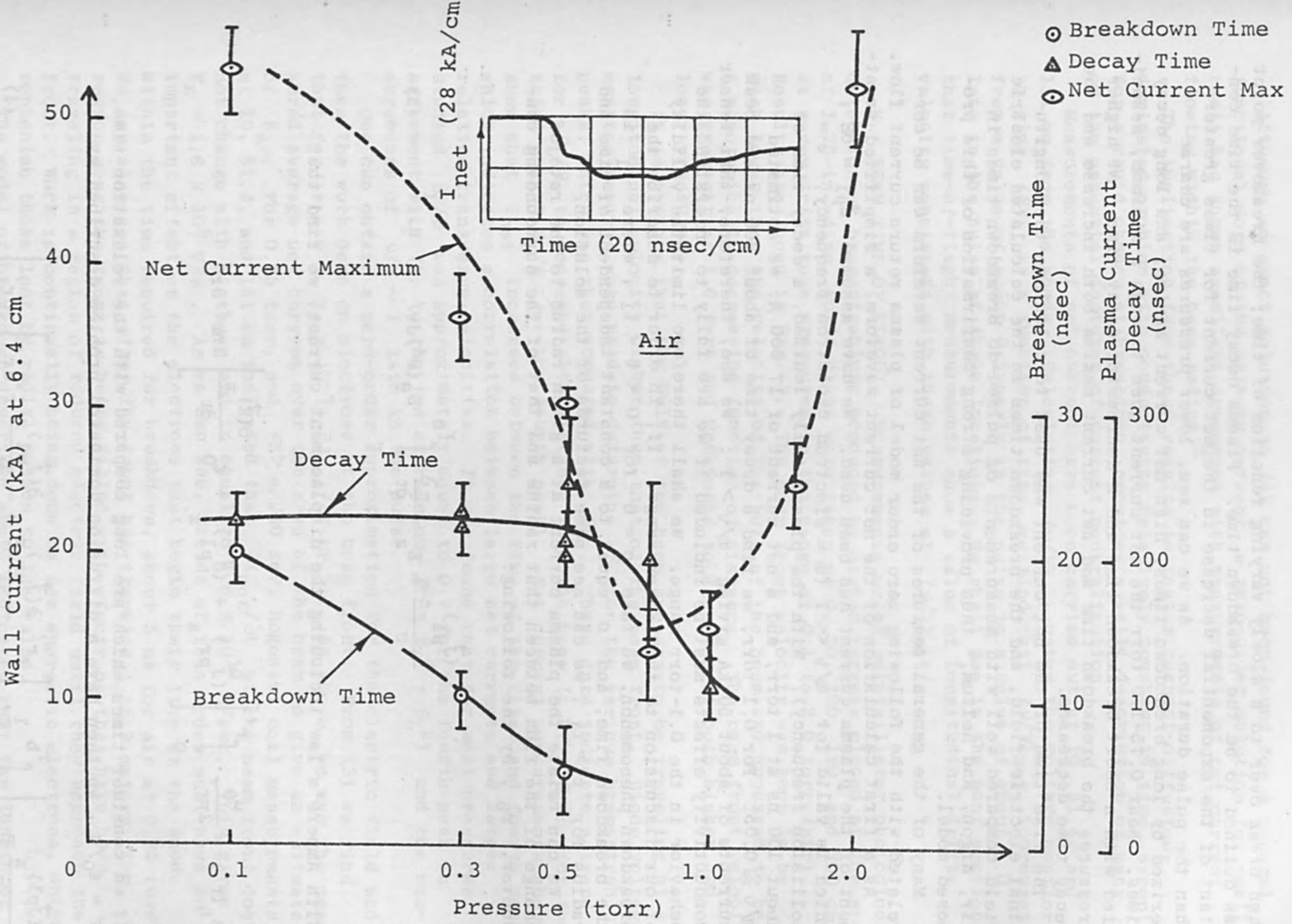

FIG. 2.—Net current, plasma current decay time, and breakdown time vs pressure in air.

then break over to a slowly varying function of time; the breakover point was defined to be the breakdown time. Plasma decay time is the time constant of the exponential decrease in the net current for times greater than the pulse duration. As we can see, lower pressures are characterized by long breakdown times. high net current maxima, and long decay times. Near 0.75-1.0 torr the net current goes through a minimum, associated with a short breakdown time and a decreasing decay time. At higher pressures the breakdown time and net current maxima both increase and the decay time decreases.

The rise time of the net current was used to calculate the longitudinal electric field, and the breakdown times in the calculated electric field compared well with measurements of pulsed-dc breakdown times in air, argon, and helium,[4] thus providing strong confirmation of this proposed model.

Many of the general features of the net current waveform can be correlated with the following zero order model of plasma return current flow.

As a first calculation of the net current waveform, a simplified treatment of the plasma current has been used. We have assumed $\vec{J}_{pl} = \sigma\vec{E}$, which is valid for $\omega/\nu \ll 1$ (ω = electron cyclotron frequency, ν = collision frequency). With the plasma fully ionized, a decay time of about 100 ns at 1 torr, and a net current of 17 000 A, we estimated $\omega/\nu \approx 0.05$. For 0.1 torr, we find a decay time of about 200 ns and peak currents of about 50 kA giving $\omega/\nu > 1$. We see, therefore, that tensor conductivity effects must be included if we are fully to understand the behavior in the 0.1-torr range. We shall therefore limit the validity of our discussion to the 1-torr range. If, in order to describe the breakdown phenomenon, we take $\sigma = 0$ for $0 < t < t_1$, where t_1 is the breakdown fime, and σ equal to a constant independent of time and radius for $t > t_1$, we can see some features of the solution.

We can relate the plasma current at a given radius to the rate of change of the flux between that radius and that of the surrounding conductor, r_b, by the following:

$$\frac{(\vec{J}_{pl})_z}{\sigma} = E_z = \frac{-\partial}{\partial t}\int_r^{r_b} B_\theta(r')\,dr' \qquad (3)$$

With Ampere's law including the displacement current, we find that

$$B_\theta(r') = \frac{\mu_0}{2\pi r'}\int_0^{r'}\left[(\vec{J}_{pr})_z + (\vec{J}_{pl})_z + \epsilon_0\frac{\partial(\vec{E})_z}{\partial t}\right]2\pi r''\,dr''$$

If we consider times which are long compared with the relaxation time, $\tau = \epsilon_0/\sigma$, we then have a diffusion dominated problem described by:

$$\frac{(\vec{J}pl)_z}{\mu_0\sigma} = -\left\{\int_r^{r_b}\frac{1}{r'}\left[\int_0^{r'}\frac{\partial(\vec{J}_{pr})_z}{\partial t} + \frac{\partial(\vec{J}_{pl})_z}{\partial t}\,r''dr''\right]dr'\right\} \qquad (4)$$

Although an exact solution to (4) has not been found for a general functional form of the primary current, a zero-order solution for small radii has shown excellent agreement with measurements of net current flowing within the beam radius.[3]

The implication from these results is that a current-diffusion-dominated problem with conductivity relatively constant in time, except for a rapid change at breakdown, provides a valid description of many of the essential features of current neutralization.

Measurements of net current have been carried out at 10, 51.4, and 154 cm from the anode. Calculating $(\nu/\gamma)_{net}$ using the voltage monitor to give $(\beta\gamma)$ as a function of time, we find that $(\nu/\gamma)_{net}$ increases from a value of about 0.5 early in the pulse to a value of about 1.0 late in the pulse at these locations. We shall see in the next section, that time-of-flight measurements show a value of longitudinal drift velocity consistent with these values of $(\nu/\gamma)_{net}$.

B. BEAM TIME OF FLIGHT. Measurements using scintaillator photodiode detection of bremsstrahlung produced by high-Z targets placed at the ends of 1.25-in.-diam. guide pipes were taken at 0, 50, 120, 190, and 300 cm at seven drift tube pressures in the range of 0.1 to 2.0 torr (air). Results are shown in Fig. 3. The beam front velocity was seen to be much lower than the velocity of the bulk of the beam and appeared to be a monotonically decreasing function of distance. The beam front velocity was greatest at 1.0 torr and was found to decrease at both higher and lower pressures.

It is obvious that the bulk of the beam appears to be traveling at a longitudinal velocity higher than that of the beam front. Diode voltage monitor records were used to determine β for the various bremsstrahlung peaks, which was then compared with β_L . These data indicate a trend for β_L/β to decrease with distance into the beam (i.e., β_L/β for the third peak $>$ β_L/β for the fourth peak). Net current measurements above, show that I_{net} increases between the time of the first and fourth peak, which indicates a correlation between large net currents and larger relative transverse velocities. It was found that for most pressures studied β_L/β was approximately equal to 0.7 for the fourth peak in agreement with (1) (using the expression $\beta^2 = \beta_T^2 + \beta_L^2$) and the measurements of $\nu/\gamma \sim 1$ late in the pulse.

One can obtain a zero-order approximation for the electric field and then the work done on electrons at the beam front. From (3) we find that for $r \approx 0$, $E_z = 10^{-7} \, \partial J_{net}/\partial t \, \pi r_b^2$. As above, we use the measured average net current over the area of the beam to give an estimate of E_z . For 0.75 torr, and $\langle E \rangle \approx 230$ keV, Rogowski coil measurements at 10, 51.4, and 151 cm indicated that $\partial I_{net}/\partial t$ at the beam front does not change with distance and is equal to 1.6×10^{12} A/sec. This gives $E_z = 1.6 \times 10^5$ V/m . As we can see, fields of this order must have an important effect on the electrons that begin their life at the anode within the time required for breakdown, about 5 ns for air at 0.75 torr . We can also see that after the front has traveled 1 to 2 meters, the region near the front is being filled with electrons that have been traveling in a region of reduced electric field until they approach the front. Work is continually being done on new energetic electrons, which replenish those lost by radial motion to the walls.

The model of breakdown described above indicates that the length of this region of large electric field at the beam front should increase as

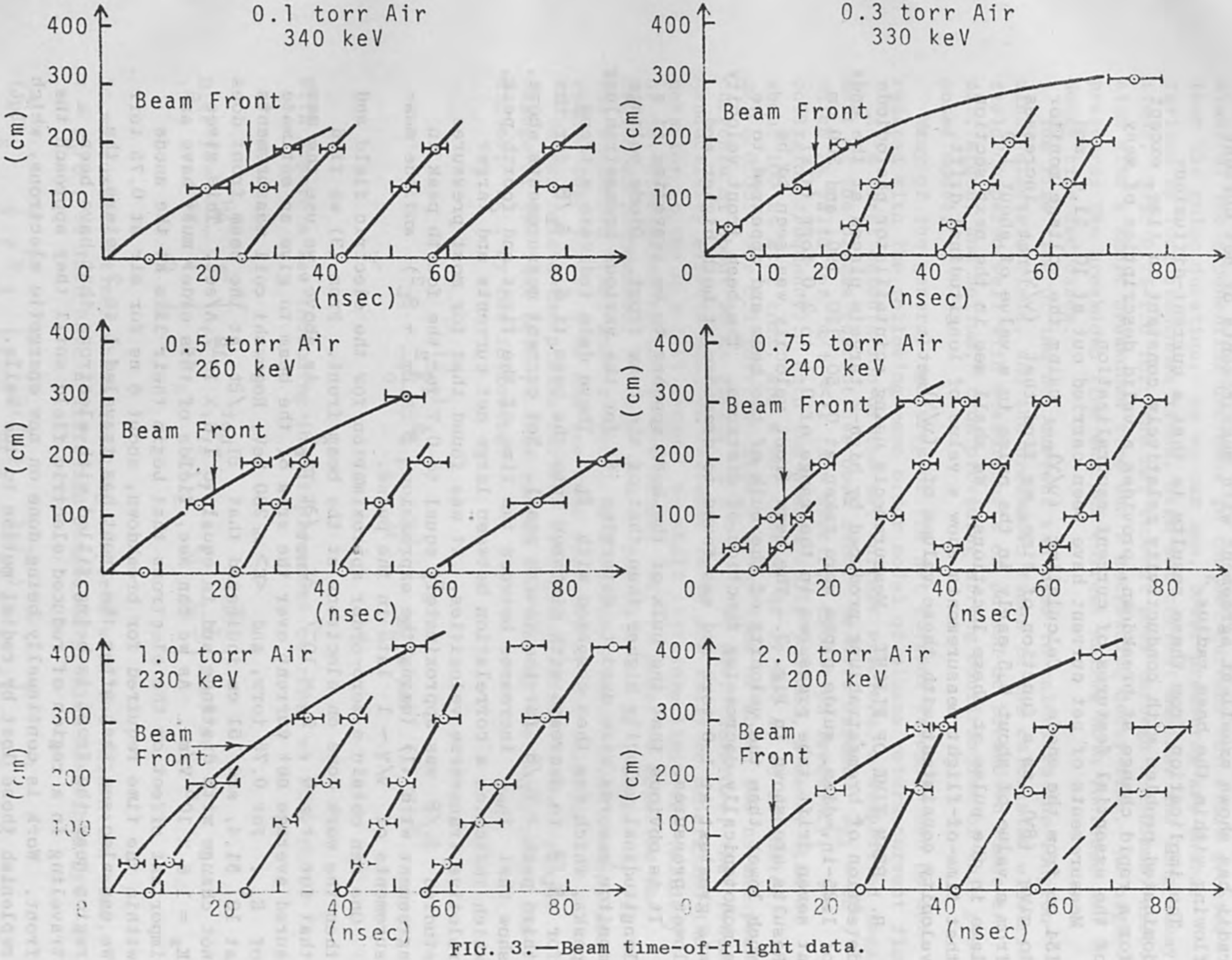

FIG. 3.—Beam time-of-flight data.

the pressure is decreased from 1.0 to 0.1 torr. Since the energetic electrons must pass through this region to reach the front, this would predict a larger beam front velocity for higher pressures, as is observed.

C. ELECTRON DEPOSITION AND ELECTRON TRANSMISSION MEASUREMENTS. Net current and beam time of flight measurements were found to suggest the existence of substantial transverse energy in beams with $(\nu/\gamma)_{net} \approx 1$. Energy deposition versus depth profiles, measured by thin-foil dosimetry, lend further support to this interpretation. As a first approximation to the description of transverse energy in the beam, Monte Carlo electron transport calculations were performed with (1) voltage and current waveforms used to define the electron energy spectrum, and (2) a single mean angle of incidence $<\theta> = \tan^{-1} (<\beta_T{}^2>/\beta_L{}^2)^{\frac{1}{2}}$, which was taken to be constant over the pulse duraton . Results of a series of such calculations are consistent with experimental data with $<\theta>$ between 45 and 60°.

Measurements of electron deposition were also made at the end of a 12-cm guide tube by use of a Faraday cup behind filters of various thicknesses. Figure 4 shows the fractional number of transmitted electrons versus material thickness, and gives results of electron transport calculations. The data suggest $<\theta> \simeq 50\text{-}60^\circ$ at 0.5 torr and $<\theta> \approx 40\text{-}50^\circ$ at 0.75 torr. Simultaneous measurements of net current indicated $(\nu/\gamma)_{net} \approx 2.5$ and 1.0 at 0.5 and 0.75 torr, respectively, giving approximate agreement with the relation $\tan \theta = \sqrt{(\nu/\gamma)_{net}}$.

D. ELECTRON BEAM TRANSPORT IN GUIDE TUBES. Transport efficiency ε was found to be an exponential function of tube length, $\varepsilon = e^{-\lambda/L}$, for transport in a 1.25-in. guide tube for $10 \text{ cm} < L \leq 3 \text{ m}$. The characteristic length λ appeared to be greatest at 0.75 torr where $\lambda \simeq 250$ cm. Absolute energy transport depended upon both distance and pressure. For pressures lower than 0.75 torr the beam energy at $L = 10$ cm was found to increase with decreasing pressure down to 0.1 torr. However, λ for transport to greater distances was found to decrease. This effect was interpreted to arise from better initial containment, at lower pressures, of the high fraction of transverse energy beam components coupled with a stronger energy loss mechanism for high $(\nu/\gamma)_{net}$. At distances $L \sim 50$ cm, $(\nu/\gamma)_{net}$ was found to be nearly 1.0 at all pressures, and for these longer distances energy loss at the beam front appeared dominant. Although it is clear that the substantial longitudinal electric field contributes to energy loss at the beam front, a correlation with the observation of exponential decay is lacking.

E. BEAM MANIPULATION AND SHAPING. Several interesting experiments have been carried out that rely on the image currents generated in nearby conductors by these beams. It was found that by injecting the beam into a shallow angle cone, extremely flat fluence distributions could be produced over areas as large as 3 cm^2. Fluence uniformity over the cone exit area was investigated with (1) calorimetry, (2) front-surface crater formation in materials, and (3) pinhole photography of the bremsstrahlung produced by a tantalum target. All diagnostics indicated essentially no fluence variation except at the very edge of the beam. The use of guide cones to provide uniform fluence distributions has been demonstrated over the full range of Model 730 Pulserad operating conditions, 0.2-1 MeV, with the general observation that changes in drift chamber pressure

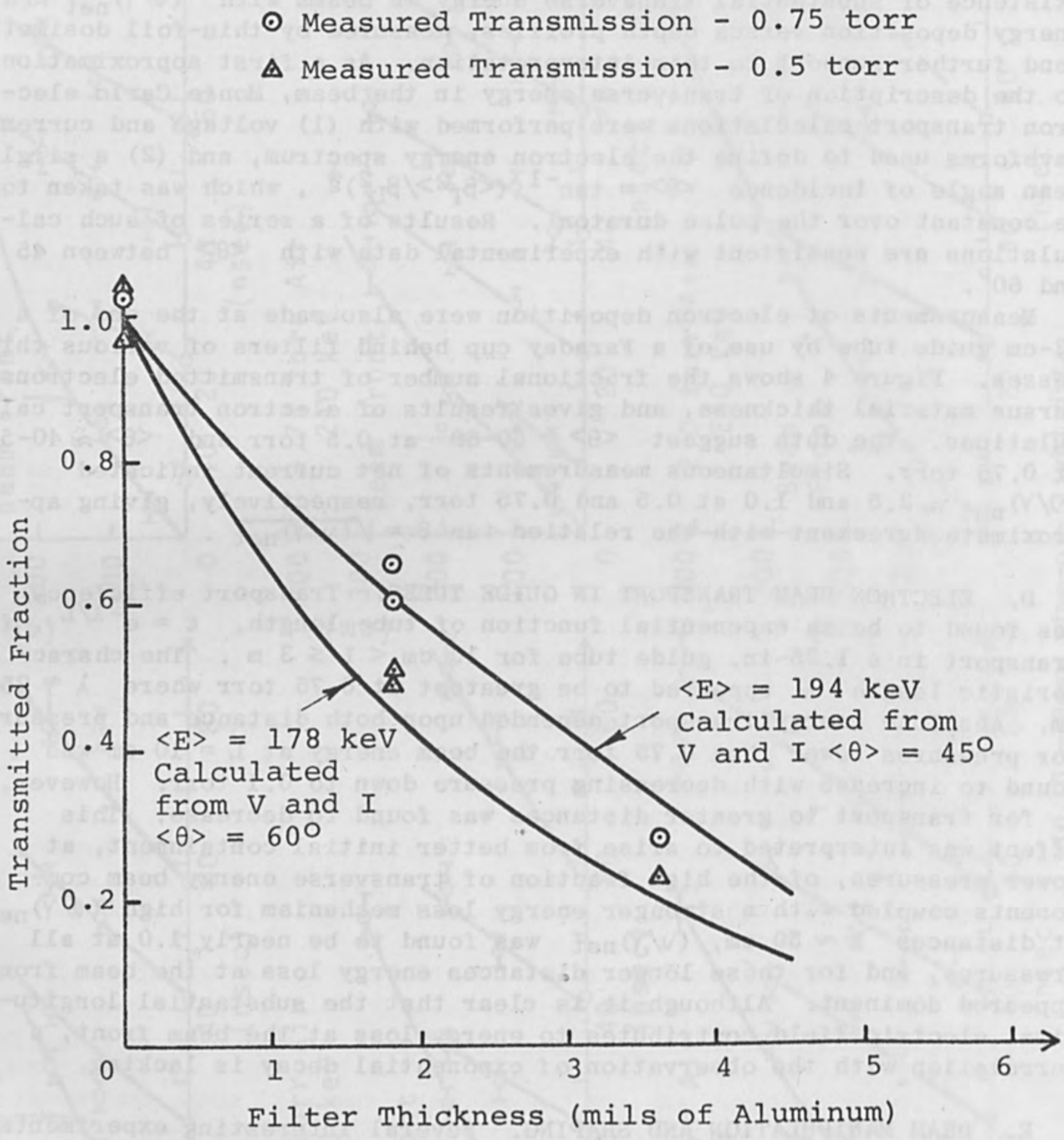

FIG. 4.—EB transmission through aluminum filters.

affect the magnitude of the fluence levels while preserving fluence uniformity in the 0.5- to 0.8-torr pressure range.

Other observations include (1) the splitting of a single beam into two or more separate beams by the use of sharp-edged metallic planes inserted into a guide pipe, and (2) the transport of electron beams through curved guide tubes with no apparent change in transport efficiency over that observed for straight pipes. Other experiments, directed at the re-injection of the beam into its own wake by the use of curved guide configurations, are in process.

CONCLUSION

The major conclusions of this paper relate to the observation of $(\nu/\gamma)_{net} \approx 1$ for beams transported in the 0.5- to 1.0-torr range, and definite evidence of beam electron trajectories with non-negligible components of transverse velocity. Time-of-flight, deposition profile, and transmission measurements indicate that

$$\frac{\langle \beta_T^2 \rangle}{\langle \beta_L \rangle^2} \sim 1$$

giving consistent agreement with an extension of Lawson's model or an interpretation of the beam behaving as a linear pinch. Time-dependent measurements of net and primary current have been correlated with a diffusion-dominated model of current neutralization that depends on the rise time of the primary current and two background gas parameters: (1) avalanche breakdown time, and (2) plasma conductivity. Measurements of energy loss with distance were presented; primary electron energy degradation in the inductively induced electric field, near the beam front, was suggested as a major loss mechanism.

In order to test many of the features of this model of high ν/γ beam transport it is suggested that pre-ionization of background gas can provide effectively a zero value of breakdown time and, if our model is correct, lower values of net current, energy loss rate, and β_T. The other parameter of considerable importance is the primary current; it should be varied through both considerably higher and lower ranges. The 1- to 2-mA, 100-keV Mylar and copper sheet strip line pulser now under development under DASA support should provide an ample test for many of these concepts.

The authors are indebted to several individuals who played invaluable roles in this work: D. Pellinen, who developed the voltage and current diagnostics; B. Ecker and S. Heurlin, who carried out much of the data collection and analysis; and S. Putnam, J. Creedon, and Ian Smith, who participated in many helpful discussions during the course of this program. This work was supported by the Defense Atomic Support Agency under contract number DASA-01-68-C-0096.

REFERENCES

1. J. D. Lawson, "On the classification of electron streams," J. Nucl. Energy, Part C: Plasma Physics 1: 31-35, 1959.

2. G. Yonas and P. Spence, "Experimental investigation of high ν/γ electron beam transport," PIFR-106, DASA 2175, Physics International Co., San Leandro, Calif., October, 1968.

3. G. Yonas, P. Spence, D. Pellinen, B. Ecker, and S. Heurlin, "Dynamic effects of high ν/γ beam plasma interaction," PITR-106-1, Physics International Co., San Leandro, Calif., April, 1969.

4. P. Felsenthal and J. M. Proud, "Nanosecond-pulse breakdown in gases," Phys. Rev. 139: A 1796, September, 1965.

BEAM CHARACTERISTICS OF INTENSE RELATIVISTIC ELECTRON ACCELERATORS

J. R. UGLUM, W. H. McNEILL, and S. E. GRAYBILL

Ion Physics Corp., San Leandro, Calif.

INTRODUCTION

The rapid advance of pulsed-power technology over the past several years has led to the development of pulsed accelerators which produce very intense relativistic electron beams. These beams have now been used to generate high-density plasmas and there is a large effort now being carried out to investigate the behavior of relativistic beam propagation in a plasma environment.

It is clear that the propagation characteristics of the beam must depend strongly on injection parameters and any attempt to correlate experimental data with theoretical models must take this dependence into account. This paper reviews the diagnostic tools, both time resolved and time integrated, which have been developed at Ion Physics Corp. for measuring the injection parameters. The quantities which are measured are:

(1) Injected current (time resolved)
(2) Electron energy
(3) Radial current density profile
(4) Emittance
(5) Divergence

Finally, a brief description is given of computer calculations made to predict some of the beam parameters.

ACCELERATOR

Figures 1 and 2 show a typical dc charged accelerator used at Ion Physics Corp. The coaxial-transmission-line capacitor is dc charged by a Van de Graaff generator and then end switched to a capacitively graded tube which houses a cold-cathode electron gun. The electron beam which is produced passes through the thin anode plane into a drift-tube region, where a plasma is formed via interactions of the beam with the background gas. Precise synchronization between firing of the machine and a command pulse (± 5 ns jitter) has been attained through the use of advanced trigatron switching technology. This synchronization has allowed correlated time measurements to be made of the beam parameters.

CURRENT MEASUREMENTS

Two techniques have been employed for time resolved measurements of the beam current. The first is a Rogowski coil (Fig. 3), which has been used to measure the beam current in the drift tube region. The Rogowski coil can be considered to be a current transformer, with the beam acting as the primary. The coil is self-integrating when the inequality

$$L_{coil}/R_{load} \gg \text{beam pulse width}$$

Record of 10th Symposium on Electron, Ion, and Laser Beam Technology (L. Marton, ed.); San Francisco Press, Inc.

Copyright © by The Institute of Electrical and Electronics Engineers, Inc.—Printed in the U.S.A.

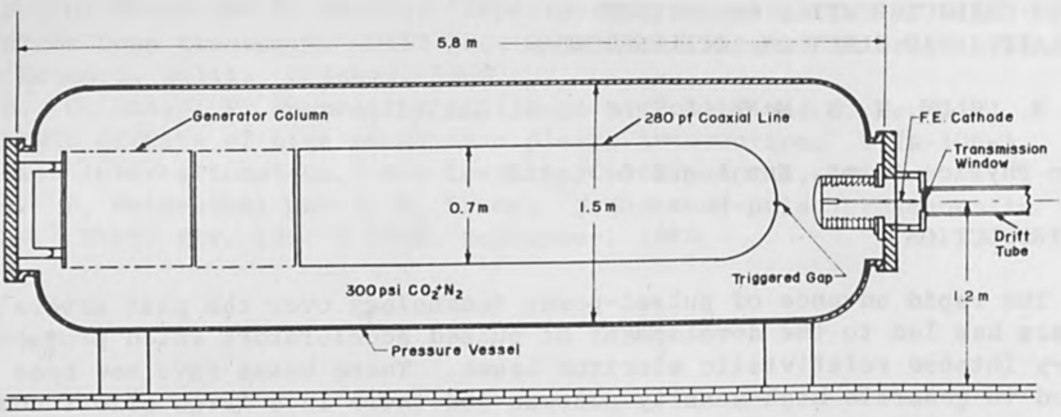
5.8 m
Generator Column
280 pf Coaxial Line
F.E. Cathode
Transmission Window
0.7 m
1.5 m
Drift Tube
Triggered Gap
1.2 m
300 psi CO2-N2
Pressure Vessel

FIG. 1.—Configuration of 4-Mv coaxial generator.

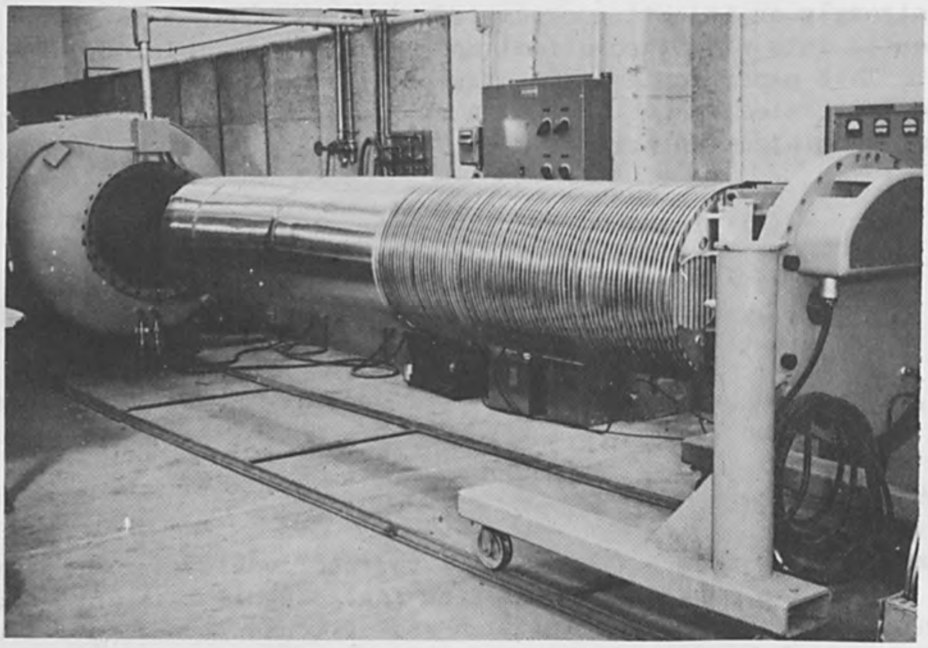

FIG. 2.—FX-1 machine with charging column and line withdrawn.

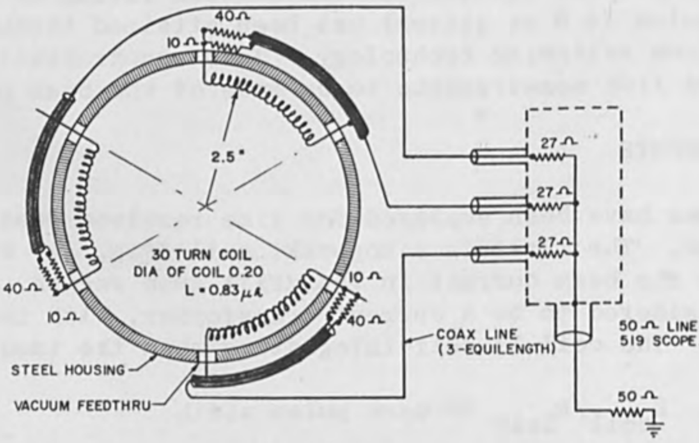
40 Ω
10 Ω
2.5"
27 Ω
27 Ω
27 Ω
30 TURN COIL
DIA OF COIL 0.20
L = 0.83 μH
40 Ω
10 Ω
10 Ω
40 Ω
COAX LINE
(3-EQUILENGTH)
50 Ω LINE TO
519 SCOPE.
STEEL HOUSING
VACUUM FEEDTHRU
50 Ω

FIG. 3.—Parallel-element Rogowski coil.

is satisfied, and this is the mode in which it is normally used. When the coil completely surrounds the beam it can be shown that the response is nearly independent of exact beam location.

Since the Rogowski coil responds to the azimuthal magnetic field due to the net current (beam current minus induced plasma current) carried inside it, it affords an ideal way to measure net current, and hence plasma current, in the drift-tube region. Some results of this type of measurement are shown in Fig. 4, where the currents at 10 and 20 ns after the start of the pulse are plotted against drift tube pressure. It shows that maximum net current, and hence minimum return current, occurs at about 0.1 torr. At higher pressures the return current increases, presumably owing to a higher plasma density and corresponding higher plasma conductivity, up to pressures where the conductivity is reduced by increased collision frequency.

Time-resolved current measurements are made with resistive shunts, which interrupt either the drift-tube or field-emission outer conductor with a large number of parallel resistors, as shown in Fig. 5. The voltage across them is proportional to the current induced in the outer conductor by the primary current. The current shunts are all calibrated with a constant-impedance transmission-line pulser. The risetime has been shown to be less than 1 ns when checked by a square wave pulser and a sampling scope. Some results of time-resolved data taken from a field-emission current shunt mounted on the IPC FX-1 machine are shown in Fig. 6. The two curves correspond to different cathodes, one consisting of a circular array of 20 pins, the other a blunt-tipped single-point cathode.

ELECTRON ENERGY

A capacitive voltage divider has been found useful for measuring the energy of beams produced by high-impedance accelerators. In order to get sufficient sensitivity without degrading response time, a metal strip completely encircling the inside of the outer conductor of the field-emission tube was used (Fig. 7). The metal strip is insulated from the outer conductor by Mylar tape. The metal strip is connected to the center conductor of a coaxial cable leading to a Tektronix 519 oscilloscope through a resistor. The resistance is chosen to give a time constant $RC \simeq 500$ ns. The risetime of the voltage monitor has been shown to be less than 1 ns when checked with a constant-impedance transmission-line square-wave pulser and sampling scope. Calibration is accomplished by using the photodisintegration threshold of beryllium at 1.67 MeV and of deuterium at 2.22 MeV.

Results of voltage measurements are shown in Fig. 8, together with current pulses for the single-point and multipoint cathodes. From the time-resolved measurements of voltage and current, the time-dependent diode impedance $Z(t)$ can be determined. Figure 9 shows $Z(t)$ for the 20-pin cathode. The impedance in this case reaches a steady state after about 10 ns.

A separate measurement of the beam energy spectrum has been made by use of a magnetic spectrometer (Fig. 10). The spectrometer is a 180° fixed-field type, with charge collectors arranged to give a 45 β keV energy resolution. The spectrometer can be used to measure the time-resolved spectrum by replacing the charge collectors with current detectors.

Results of time-integrated magnetic spectrometer measurements for two

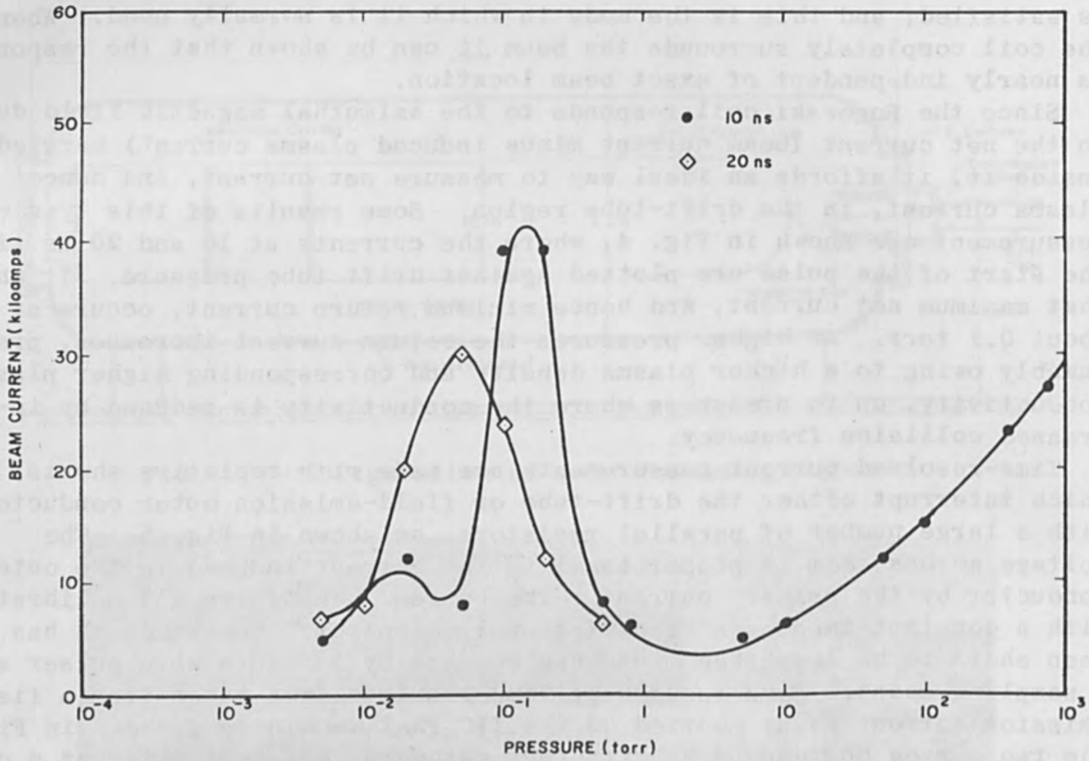

FIG. 4.—Rogowski-coil measurement of net current as a function of drift-tube pressure.

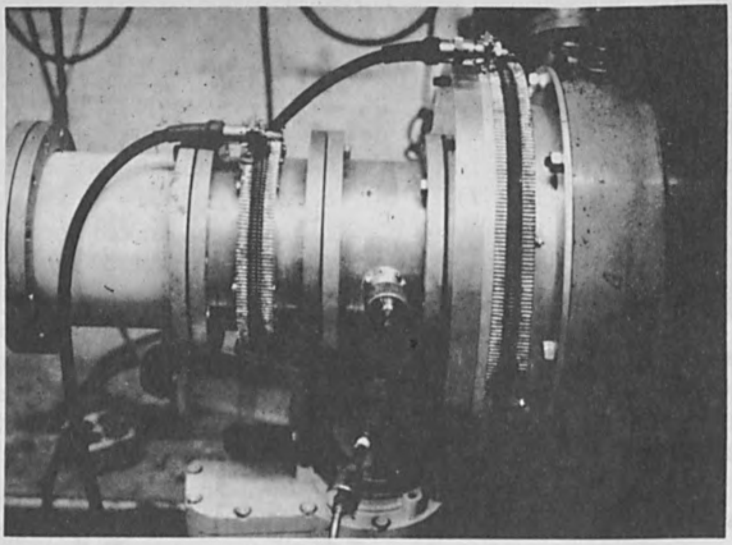

FIG. 5.—Drift-tube and field-emission-tube current shunts.

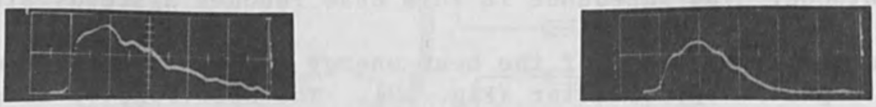

(a) (b)

FIG. 6.—Current profiles of FX-1 field-emission cathode: (a) single-point cathode, hor. scale 20 ns/div, vert. scale 13 kA/div, I_{max} = 22 kA; (b) 20-point cathode, hor. scale 20 ns/div, vert. scale 32 kA/div, I_{max} = 39 kA.

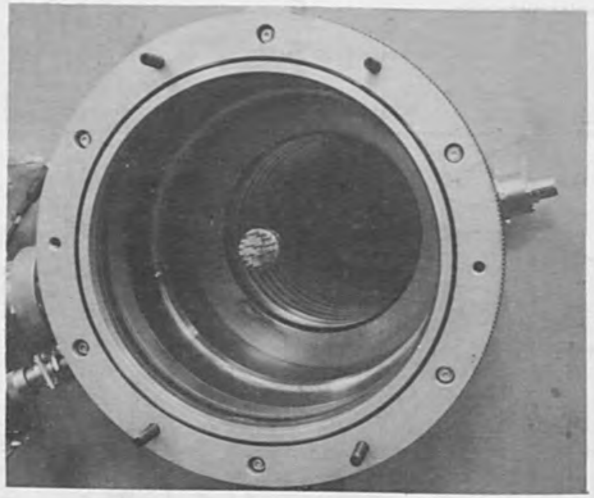

FIG. 7.—Capacitive voltage monitor and return-current shunt.

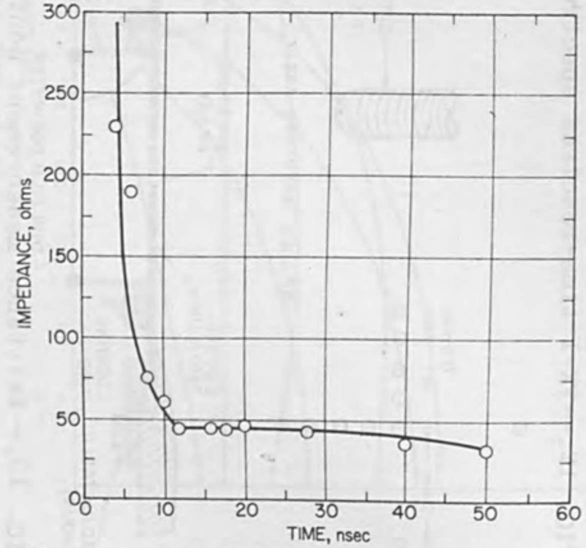

FIG. 9.—Impedance vs time for 20-pin cathode, 20-cm gap.

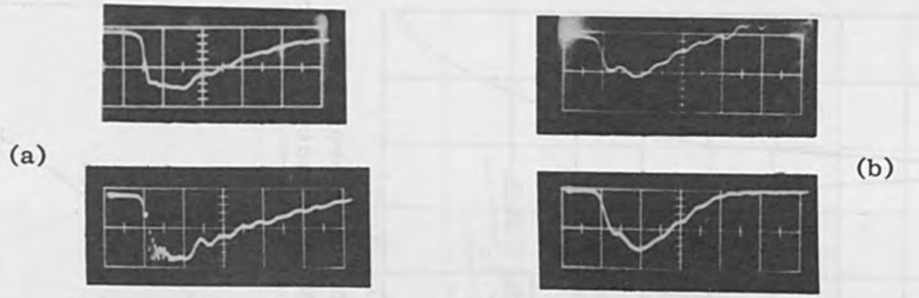

FIG. 8.—Voltage and current pulses (hor. scale 20 ns/div): (a) 1/8-in.-diam. hemispherical cathode, 2.7-cm gap, 1.7 Mv/div (top), 13 kA/div (bottom); (b) 20-point cathode, 2.0-cm gap, 1.7 Mv/div (top), 26 kA/div (bottom).

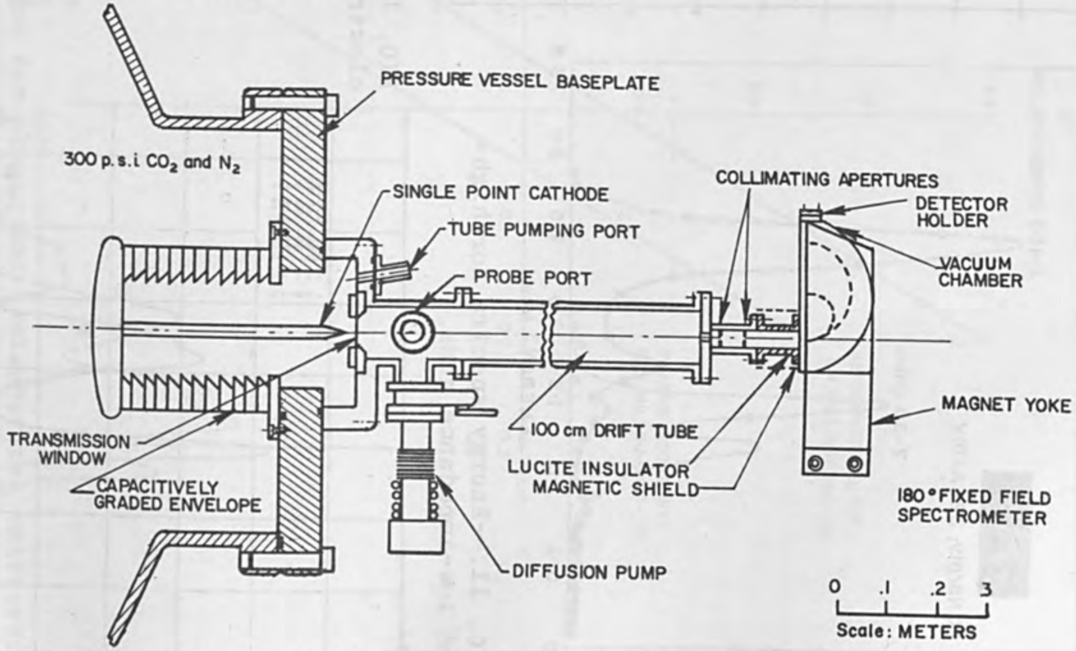
PRESSURE VESSEL BASEPLATE
300 p.s.i CO₂ and N₂
SINGLE POINT CATHODE
TUBE PUMPING PORT
PROBE PORT
COLLIMATING APERTURES
DETECTOR HOLDER
VACUUM CHAMBER
MAGNET YOKE
TRANSMISSION WINDOW
CAPACITIVELY GRADED ENVELOPE
100 cm DRIFT TUBE
LUCITE INSULATOR
MAGNETIC SHIELD
180° FIXED FIELD SPECTROMETER
DIFFUSION PUMP
0
.1
.2
3
Scale: METERS

FIG. 10.—Configuration for electron-beam spectrum-analysis experiment.

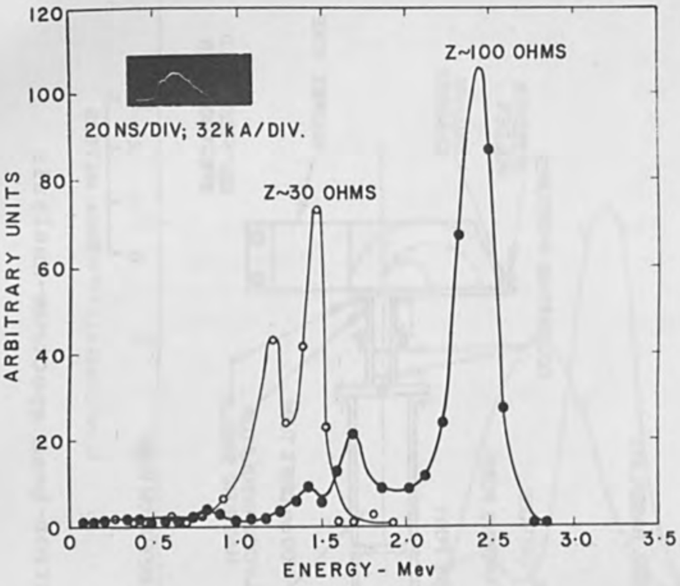

FIG. 11.—Energy spectra for high- and low-impedance guns.

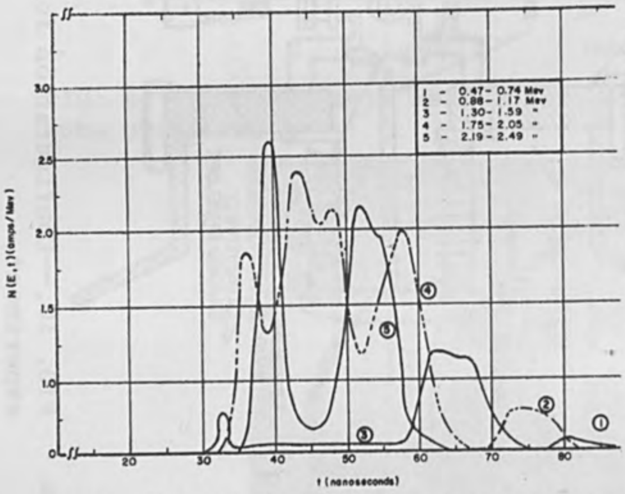

FIG. 12.—FX-1 time-resolved spectrum.

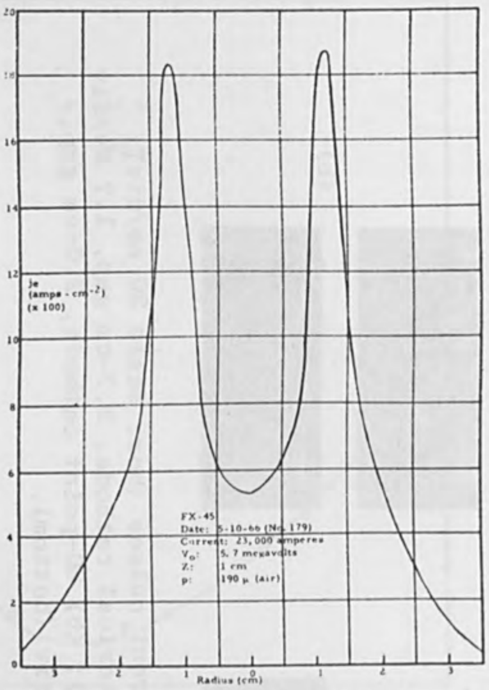

FIG. 13.—Entrance beam profile of electron field-emission accelerator.

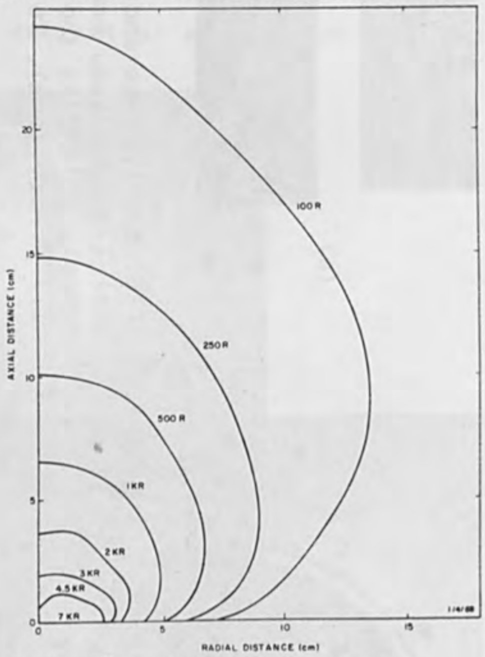

FIG. 14.—FX-1 dose map.
(Charging voltage 4 Mv.)

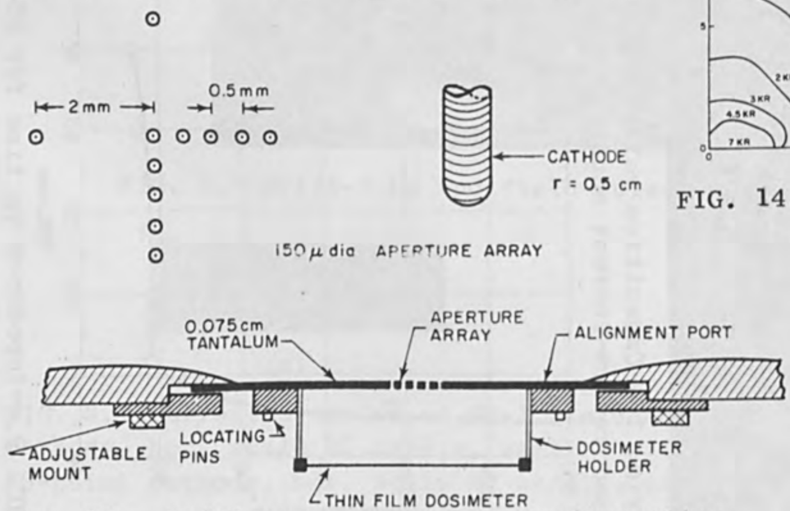
2 mm
0.5 mm
CATHODE
r = 0.5 cm
150 μ dia APERTURE ARRAY
0.075 cm
TANTALUM
APERTURE
ARRAY
ALIGNMENT PORT
ADJUSTABLE
MOUNT
LOCATING
PINS
DOSIMETER
HOLDER
THIN FILM DOSIMETER

FIG. 15.—Emittance measurement configuration.

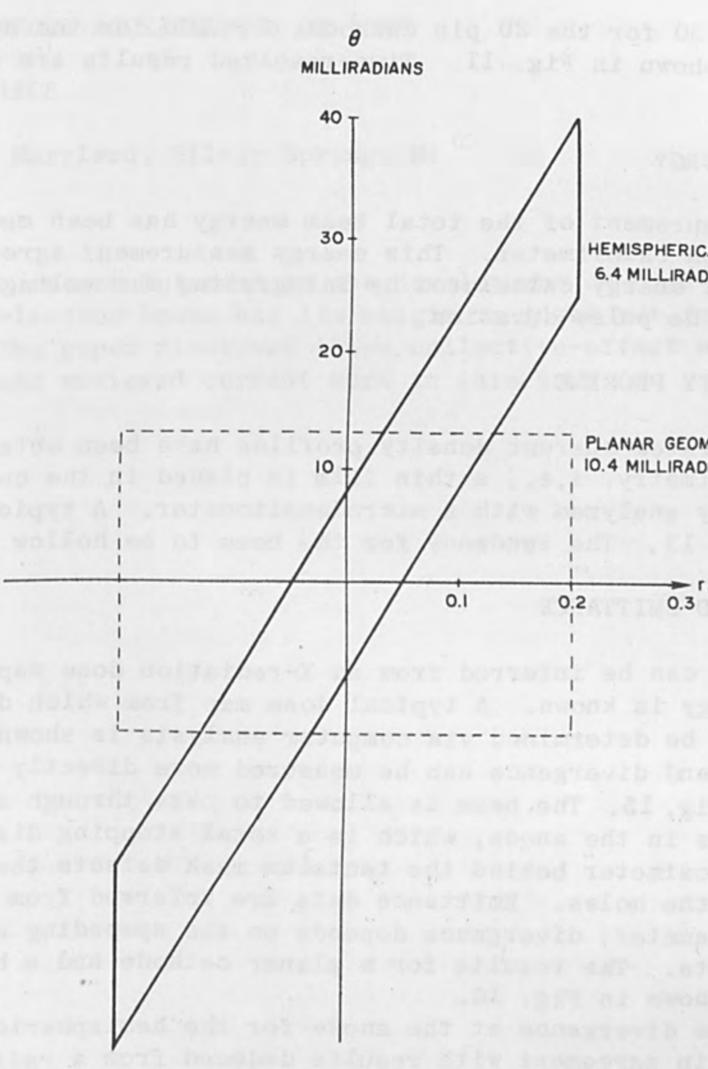

FIG. 16.—Emittance diagrams for planar and hemispherical emitters.

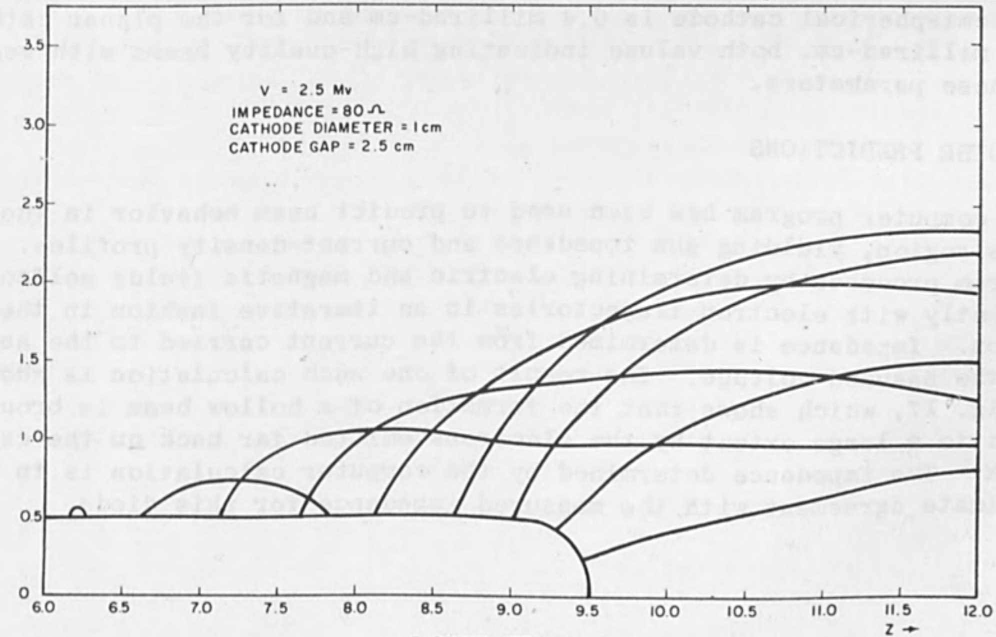

FIG. 17.—Trajectories for electron gun.

cathodes (Z ~ 30 for the 20 pin cathode, Z ~ 100 for the single point cathode) are shown in Fig. 11. Time-resolved results are shown in Fig. 12.

TOTAL BEAM ENERGY

Direct measurement of the total beam energy has been made using a total stopping carbon calorimeter. This energy measurement agrees within 10% with the total energy calculated by integrating the voltage-current product over the pulse duration.

CURRENT-DENSITY PROFILE

Time-integrated current density profiles have been obtained by using thin film dosimetry, i.e., a thin film is placed in the beam path and then optically analyzed with a microdensitometer. A typical result is shown in Fig. 13 . The tendency for the beam to be hollow should be noted.

DIVERGENCE AND EMITTANCE

Divergence can be inferred from an X-radiation dose map if the input electron energy is known. A typical dose map from which divergence at the anode can be determined via computer analysis is shown in Fig. 14.

Emittance and divergence can be measured more directly using a scheme depicted in Fig. 15. The beam is allowed to pass through an L-shaped array of holes in the anode, which is a total stopping distance thick. A thin-film dosimeter behind the tantalum mask detects the beamlets that pass through the holes. Emittance data are inferred from the spreading of beamlet diameter; divergence depends on the spreading of the center of the beamlets. The results for a planar cathode and a hemispherical cathode are shown in Fig. 16.

The average divergence at the anode for the hemispherical cathode is $< \theta > \sim 12^\circ$, in agreement with results deduced from a radiation map. The planar cathode shows no divergence at the anode. The emittance for the hemispherical cathode is 6.4 millirad-cm and for the planar cathode, 10.4 millirad-cm, both values indicating high-quality beams with respect to these parameters.

COMPUTER PREDICTIONS

A computer program has been used to predict beam behavior in the diode region, yielding gun impedance and current-density profiles. The program proceeds by determining electric and magnetic fields selfconsistently with electron trajectories in an iterative fashion in the gap region. Impedance is determined from the current carried to the anode and the assumed voltage. The result of one such calculation is shown in Fig. 17, which shows that the formation of a hollow beam is brought about to a large extent by the electrons emitted far back on the cathode shank. The impedance determined by the computer calculation is in approximate agreement with the measured impedance for this diode.

COLLECTIVE EFFECT--ACCELERATION OF IONS

A. W. TRIVELPIECE

University of Maryland, Silver Spring, Md.

SUMMARY

Some of the recent interest in the development of high-current relativistic electron beams has its origin in ideas put forward by Veksler and others. The paper discussed these collective-effect schemes for ion acceleration and reviewed current work in this area.

PARTICLE BEAMS IN THE SOLAR TERRESTRIAL ENVIRONMENT (Invited Paper)

S. J. BAUER

Laboratory for Space Sciences, NASA Goddard Space
Flight Center, Greenbelt, Md.

SUMMARY

Energies of particle beams in the solar terrestrial environment range from hundreds of MeV for solar protons to a few keV for electrons responsible for auroras. Solar protons associated with strong solar flares cause ionization deep within the terrestrial ionosphere, called polar cap absorption events (PCA), i.e., radio blackout. The intensities of these solar protons exceed the galactic cosmic rays by several orders of magnitude. In addition to these high-energy particles which are associated with disturbances on the sun, there is a steady outflow of charged particles from the sun called the solar wind. The solar wind consists primarily of protons and electrons (with a small fraction of heavier constituents) having a bulk flow velocity of about 300 km/sec, which is supersonic in the interplanetary medium, and a density of about 5-10 particles/cm^3; the characteristics of the solar wind change with solar activity. The interaction of this solar wind with the geomagnetic field leads to the formation of a magnetosphere with a shock front and a magnetopause behind which the terrestrial geomagnetic field is contained. As the results of the interaction of the solar wind with the earth's magnetic field, field lines are swept back into a tail behind the earth extending to very great distances. Within the magnetosphere, into which charged particles from the outside can only enter through limited regions, there are energetic particle populations whose origins are not well understood. In addition to the trapped particle population of the radiation belts, there are particle beams of a few keV, especially in the auroral zone and over the polar cap, which may possibly be the result of "local" acceleration processes in the magnetosphere.

Particle beams traveling in the sun-earth environment can also lead to the generation of radio noise by means of the Čerenkov mechanism. For instance, charged particles emitted from the sun during disturbances lead to radio bursts which are observed in space and on the ground. Similarly, particles precipitated in the terrestrial environment can lead to radio noise which has been observed in the magnetosphere and ionosphere.

Recently a space-borne electron-beam experiment proposed and implemented by W. N. Hess of NASA was performed by means of a rocket launched from Wallops Island. An artificial aurora was generated as the result of an electron beam of a few keV injected along magnetic field lines. A slender, rayed aurora was observed by ground-based image orthicon cameras. Based on this successful test, it appears that electron beams launched from spacecraft can be used to study, under controlled conditions, a number of phenomena in the earth's magnetosphere.

ELECTRON TRANSMISSION, ENERGY LOSS, AND RADIATION DAMAGE AT HIGH BEAM VOLTAGES (Invited Paper)

V. E. COSSLETT

Cavendish Laboratory, University of Cambridge, Cambridge, England

INTRODUCTION

The recent development of electron microscopy to high voltages (1 MV and more) has revealed considerable gaps in our knowledge of the transmission and energy loss of electrons in thin films. By "thin" is meant here a film thickness equal to a few mean free paths for elastic scattering. It is timely to review the situation in order to see how far theory can be relied upon and where further experimental measurements are needed. It will appear that many situations of practical importance for electron microscopy are too complex for any comprehensive theoretical treatment, particularly of energy loss and hence of the limits of observation as set by chromatic aberration. In respect of radiation damage by ejection of atoms from a lattice, however, the predictions of theory accord closely with observation.

ELECTRON TRANSMISSION IN AMORPHOUS AND POLYCRYSTALLINE MATERIALS

The main reason for using high voltages in electron microscopy is to obtain images from thicker specimens than can be observed at 100 kV. So interest centers on the factors that limit transmission through relatively thick specimens and into the small collection angle of the objective aperture α_0 (order of 10^{-2} radian). Much work, both theoretical and experimental, has been done on this problem at normal operating voltages. It has been established that results agree fairly well with the plural scattering theory of Lenz (1954) in respect of the fraction of the beam transmitted through thicknesses up to about ten elastic mean free paths, and its variation with α_0 and beam voltage V_0. The fit can be made even closer by using two independent atomic parameters (Lippert and Friese 1962) instead of the single one (the mean atomic radius R) used by Lenz. Although Lenz's treatment is based on scattering (elastic and inelastic) by isolated atoms, and so is not strictly applicable to anything except a gas, it is found to agree well with results for polycrystalline as well as for amorphous materials (Reimer 1965). The anomalous conditions of transmission through a perfect crystal require a quite different treatment, as outlined later.

The first attempt to predict how transmission would change with increasing beam voltage was made by Burge and Smith (1962). They showed that it should increase more rapidly for carbon than for gold, owing to the greater inelastic and smaller elastic scattering in the former, and also that the increase would become almost linear if a relatively large aperture (5×10^{-3}) were to be used (at all voltages). Since Burge and Smith's treatment is based on a very different model of the atom from Lenz's, it was not prima facie clear how reliable their predictions might be. It was also evident from work done at 50-100 kV that their scattering theory (Smith and Burge 1963) did not agree so well as did Lenz's with experiment. So we set out to measure transmission through carbon and gold as a function of voltage and aperture, and also calculated

Record of 10th Symposium on Electron, Ion, and Laser Beam Technology (L. Marton, ed.); San Francisco Press, Inc.

Copyright © by The Institute of Electrical and Electronics Engineers, Inc.—Printed in the U.S.A.

what would be predicted by the plural theory of Lenz (in relativistic form).

The experiments were carried out in the Cavendish high-voltage electron microscope (Smith, Considine, and Cosslett 1966) at voltages up to 700 kV. Measurements were made on three thicknesses of carbon and two thicknesses of gold at three values of α_0. Full details of the procedure have been given by Curtis (1968) and a preliminary account of the results by Curtis, Cosslett, and Ferrier (1968). Dr. Lippert has since made available an extrapolation of the Lippert and Friese empirical relation into the relativistic region, taking plural scattering into account.

Figures 1 and 2 show the results obtained for a carbon film of mass-thickness 0.26 $mg.cm^{-2}$ with $\alpha_0 = 1.1 \times 10^{-3}$ and 5.5×10^{-3} radian, respectively. Transmission T is plotted against beam voltage V_0, where T is defined by

$$T = (\log_e I_0/I)^{-1}$$

It is evident that the experimental points are close to the curve predicted by the plural theory of Lenz (LP), which lies just below them at 1.1×10^{-3} and just above them at 5.5×10^{-3}. The empirical curve of Lippert and Friese (LFP) rises too steeply with voltage. Burge and Smith do not give a plural scattering curve for these conditions, but it would probably fall between the LP and LF curves in the same way as for the single scattering curves (L, BS, LF).

The results for gold are shown in Fig. 3, where curves A and B are calculated from Lenz's plural theory with $\alpha_0 = 1 \times 10^{-3}$ and 5×10^{-3}, respectively. The experimental points lie higher in each case, by much more than the experimental error. The curves BS are the corresponding predictions of the Smith and Burge (1963) plural theory. They show a much greater change in transmission with aperture than do Lenz's curves, so that for $\alpha_0 = 5.5 \times 10^{-3}$ there is fair agreement with experiment at very high voltages, whereas for 1.1×10^{-3} the BSP curve lies far below both the Lenz curve and the measured points. No curve is shown for the Lippert-Friese plural treatment, as Lippert was not able to get consistent enough results over a range of apertures and voltages sufficient to justify an empirical relation.

The method of presentation adopted in Figs. 1-3 seems to show a rather slow rise in transmission with voltage. This is partly due to the use of a logarithmic scale on the ordinate, but also reflects a fact of real physical significance. With a film of given thickness, as here, single-scattering conditions are approached at very high voltage. As the voltage is decreased, the mean number of scattering acts increases and there is an increasing tendency for electrons to be scattered back into the aperture in a second or subsequent act. So the decrease in T due to the increase in scattering cross section is partly masked in plural conditions, and the curve falls less steeply than expected.

A more direct measure of the increase in effective penetration is provided by plotting the thickness which produces a given attenuation of the beam, I/I_0. A set of such constant intensity-ratio curves is shown in Fig. 4 for carbon and Fig. 5 for gold, in each case for $T = 0.25$ (i.e., $I/I_0 = e^{-4}$), as calculated from the plural theory of Lenz. The slope of the thickness-voltage curve changes dramatically with aperture,

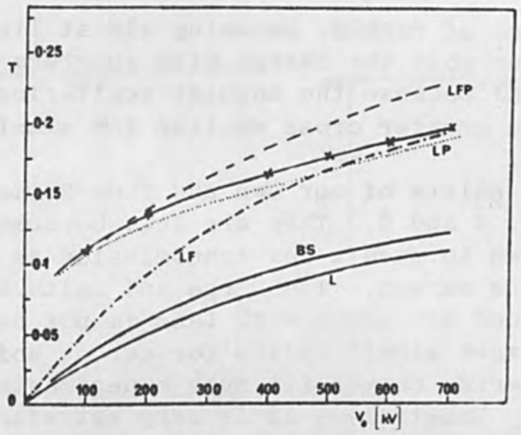

FIG. 1.—Electron transmission T through a carbon film of mass-thickness 260 μg cm^{-2} as function of accelerating voltage V_0, for $\alpha_0 = 1 \times 10^{-3}$, calculated from the single-scattering theories of Lenz (L), Burge and Smith (BS), and Lippert and Friese (LF), and the plural scattering theories of Lenz (LP) and Lippert and Friese (LFP). Crosses = experimental points of Curtis (1968) for $\alpha_0 = 1.1 \times 10^{-3}$.

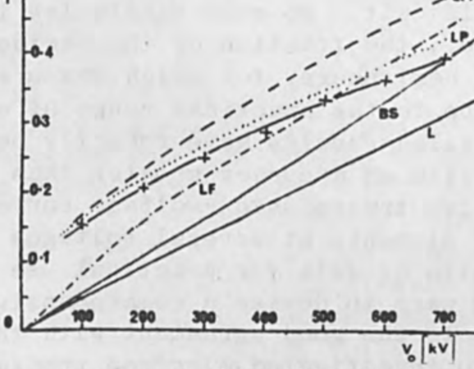

FIG. 2.—Electron transmission T through a carbon film of mass-thickness 260 μg cm^{-2} in function of accelerating voltage V_0, for $\alpha_0 = 5 \times 10^{-3}$, calculated from the theories listed under Fig. 1. Crosses = experimental points of Curtis (1968) for $\alpha_0 = 5.5 \times 10^{-3}$.

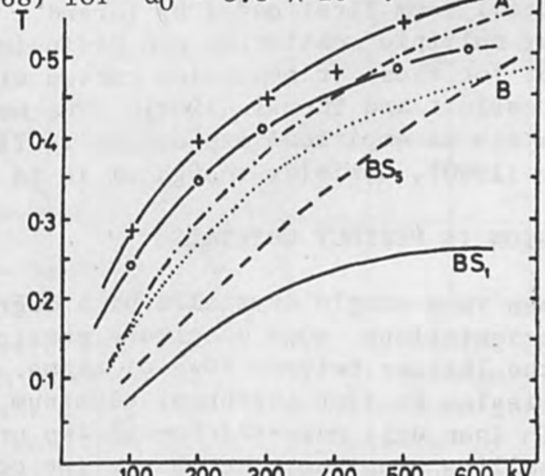

FIG. 3.—Electron transmission T through a gold film of thickness 450 Å in function of accelerating voltage V_0, calculated from the plural scattering theories of Lenz (A, B) and Burge and Smith (BS_5, BS_1) for $\alpha_0 = 5 \times 10^{-3}$ and 1×10^{-3} in each case, compared with the experimental points of Curtis (1968) for $\alpha_0 = 5.5 \times 10^{-3}$ (crosses) and 1.1×10^{-3} (circles).

especially in the case of carbon, becoming almost linear for $\alpha_0 = 5.5 \times 10^{-3}$. For gold the change with aperture is less marked even at 10^{-2} (Curve C) because the angular scattering distribution is wider, reflecting the greater cross section for elastic scattering as compared with carbon.

Some experimental points of our own and from Reimer and Sommer (1968) are included in Figs. 4 and 5. They are few, because measurements are not usually taken down to such a low transmission as e^{-4} , but they agree well with Lenz's curves. The Burge and Smith curves lie appreciably lower. The good agreement with Lenz is not surprising, since he chose values of the mean atomic radius for carbon and gold which made his calculated scattering curves fit such experimental evidence as existed at the time. Nonetheless it is very satisfactory that agreement remains good at relativistic voltages, from the almost linear variation of thickness with voltage at large aperture to the nearly $(v/c)^2$ curve at very small aperture.

So far we have been concerned with transmission in the axial direction into an aperture of the order of 10^{-2} radian, which obeys an approximately exponential law for foil thicknesses up to a few elastic mean free paths. For thicker foils the intensity becomes so small as to make measurement difficult. No such simple law is obeyed by the total transmission, i.e., the fraction of the incident beam emerging into the whole forward hemisphere, for which measurements can be made with film thicknesses up to the practical range of electrons of the incident voltage. Detailed results have recently been obtained by Dupouy et al. (1965b) with an accuracy greater than any earlier work at high voltages. They give transmission-voltage curves for given thicknesses of a variety of elements at several voltages from 100 to 1200 kV, making available a wealth of data for practical use and also for the theoretician who might care to devise a comprehensive theory to fit them. It is interesting to note the good agreement with the very early results of Crowther (1910), who investigated electron transmission at 600 kV. Figures 6 and 7 show his results for aluminum and platinum, plotted as transmission-thickness curves, with the Dupouy et al. results added. The shape of the curves is similar to that for lower voltages, tailing off to the exponential form first noted by Lenard. A discussion of the various theories of multiple scattering and diffusion which have been advanced to account for these transmission curves will be found in Scott (1963) and Cosslett and Thomas (1964). The most successful of the attempts to obtain an empirical expression to fit them is probably that due to Makhov (1960), unwieldy though it is to use.

ELECTRON TRANSMISSION IN PERFECT CRYSTALS

When the specimen is a single crystal a high degree of channeling can occur in certain orientations, some electrons passing almost unhindered down the gaps in the lattice between rows of atoms. The resulting "anomalous" transmission in (for instance) aluminum is great enough to give a value of T (per unit mass-thickness) two or three times higher than for polycrystalline aluminum, the absorption coefficient (μ) being one-half to one-third the normal value. The wave treatment of Hashimoto, Howie, and Whelan (1960, 1962) gives a satisfactory explanation so far as thin specimens are concerned. In its two-beam form it predicts fairly closely the variation in T (or $1/\mu$) with voltage in thin films

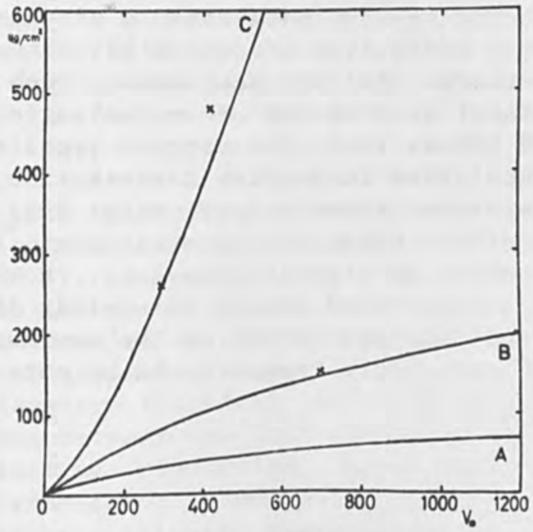

FIG. 4.—Mass-thickness of carbon for a transmission of e^{-4} when the objective aperture is 10^{-5} (A), 10^{-3} (B), and 5×10^{-3} (C), calculated from the plural-scattering theory of Lenz. Crosses = experimental points of Curtis (1968) for $\alpha_0 = 1.1 \times 10^{-3}$ and 5.5×10^{-3}.

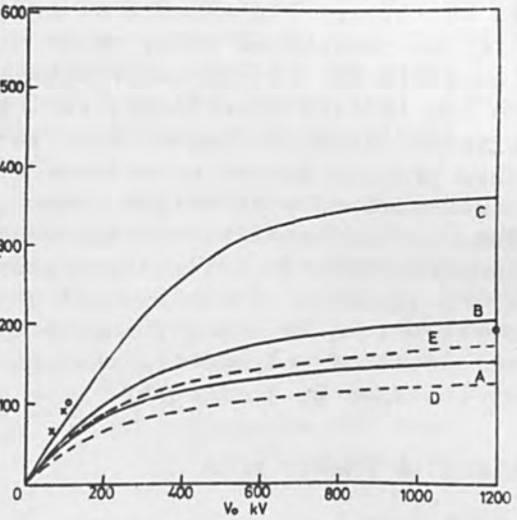

FIG. 5.—Mass-thickness of gold for a transmission of e^{-4} when the objective aperture is 10^{-5} (A), 10^{-3} (B), and 10^{-2} (C), calculated from the plural scattering theory of Lenz. D, E are from the plural scattering theory of Burge and Smith for $\alpha_0 = 10^{-3}$ and 5×10^{-3}, respectively. Crosses = experimental points of Curtis (1968) for $\alpha_0 = 5.5 \times 10^{-3}$, and circles = experimental points of Reimer and Sommer (1968) for $\alpha_0 = 1.5 \times 10^{-3}$.

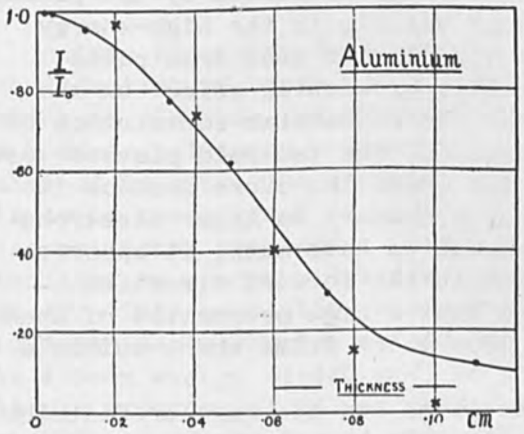

FIG. 6.—Total forward transmission (I/I_0) through aluminum as function of thickness for electrons of 600 kV as measured by Crowther (1910) (continuous curve). Crosses = experimental points of Dupouy et al. (1965b).

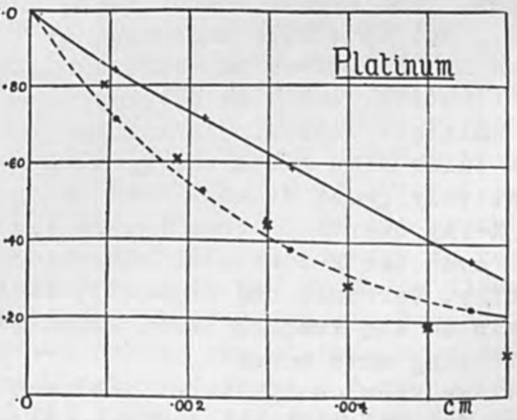

FIG. 7.—Total forward transmission (I/I_0) through platinum as function of thickness for electrons of 600 kV as measured by Crowther (1910) (continuous curve). Crosses = experimental points of Dupouy et al. (1965b).

(Dupouy et al., 1965a, Mazel and Ayroles, 1968) by introducing an imaginary term into the refractive index, the physical basis of which is not clear. In essence we need to bring in some mechanism to attenuate the channelled beam, which otherwise could pass through a lattice indefinitely. It seems probable that thermal diffuse scattering, due to the lattice vibrations, is the dominant process but other inelastic effects cannot be neglected. In thick films, where the various types of loss process become convoluted with each other in angular distribution, discussion of attenuation cannot be separated from that of energy loss. This is difficult within the confines of the anomalous transmission theory, which is initially concerned only with elastic processes. However, Ichimiya (1968) has put forward an empirical theory to explain the observations by himself and by Uyeda and Nonoyama (1968) on the maximum thickness of molybdenite through which acceptable images could be obtained at voltages up to 1200 kV.

ELECTRON ENERGY LOSS

A variety of energy-loss processes have to be taken into account: plasmon and phonon excitations, ionization, and electron-shell excitations of all types, including X-ray levels. Greatest attention has been paid to the characteristic losses due to plasma oscillations, especially by the anomalous transmission theorists (see Hirsch and Humphreys, 1968). The angular spread of the loss electrons is very narrow, so that for single crystals one or two mean free paths thick they make the chief contribution to the energy spread in the imaging beam and hence to the chromatic aberration in an electron micrograph. The mean free paths for some other loss processes, however, are of the same order and some are possibly smaller. Even those for low-level X-ray excitations differ only by one or two orders of magnitude and being individually of large energy may make an appreciable contribution to the total energy loss.

From thin films the loss distribution is thus dominated by the plasmon "lines," the higher losses being only just visible in the high-energy tail. But in a film thickness of (say) ten plasmon mean free paths, these higher losses may have a significantly broadening effect on the distribution, which is already widened by the Poissonian convolution of the multiple losses. In carbon, for instance, the ten-fold plasmon loss peak falls near the K-energy (280 eV), for which the cross section is relatively great (though most of the energy appears as Auger electrons not X-ray quanta). From recent measurements we have made, it appears that even the K-loss electrons are peaked in the forward direction (Wittry, Ferrier, and Cosslett, 1969) so that a high proportion of them remain in the imaging beam, especially from thick films where multiple scattering acts occur.

If we knew enough about the mean free paths and the angular distributions for the separate loss processes, it would be possible to calculate the over-all loss distribution, which is characterized by the position of the peak (E_p) and the half-width of the peak at half-height (ΔE_W). The convolution procedure is not significantly more difficult than that for multiple plasmon losses (see Metherell 1968; Misell 1968; Burge and Misell, 1968). In our present state of ignorance we can only resort to the less detailed treatment of energy loss due to Landau (1944), which requires only the mean effective energy loss, and look for experimental evidence to test it. The measurements of Knop et al. (1961) on Al, Cu, Ag, and Au at 1 MV are the only extensive results available for conditions approaching those of electron microscopy. They show conclusively that Landau's expressions for E_p and ΔE_w are obeyed in thick films, but that as thickness decreases the peak gets more asymmetrical and the half-width becomes narrower than the Landau prediction. But if the high-energy losses of low probability are omitted from the theoretical calculations, dropping the K-, L-, and M-level contributions successively, good agreement with experiment is obtained.

The only detailed measurements of E_p and ΔE_w made actually in an electron microscope are those of Kamiya on magnesium oxide at 200 kV and 500 kV, as reported by Uyeda (1968). Full details have not yet been published, but it was stated that the results agree with Landau's theory. The problem of reconciling the observed energy spread with the electron microscopical resolution obtained in similar conditions is discussed elsewhere (Cosslett 1969). Surprisingly there was only a small difference between the loss distributions in the Bragg reflecting and nonreflecting orientations, which supports the view that simple anomalous transmission is swamped by multiple-loss processes in thick films. Kamiya's thinnest specimen was 1 μm thick, corresponding to 7 or 8 mean free paths for plasmon loss at his lowest voltage (200 kV).

Clearly more experimental evidence is required. Verdier (1968) has attempted to derive the loss distribution from the chromatic aberration in electron micrographs, but this is a doubtful procedure as the scatter of his results shows. Only a direct determination will give the accuracy needed to check the Landau theory, as modified by Knop et al. We are in process of making measurements in the Cavendish high-voltage microscope with a magnetic energy analyzer of the Ichinokawa type (1968). Owing to the difficulty of maintaining the required stability over the 20 to 30 min needed for recording a wide range of energy losses, we have not yet obtained sufficiently consistent results to report here.

RADIATION DAMAGE

A type of energy loss that is peculiar to high-voltage operation is the ejection of atoms from a lattice by the "knock-on" mechanism, in which an electron transfers all or nearly all its energy to an atom in a head-on collision. Since the electron mass is so much smaller than that of an atom, the incident energy must be very high if enough energy is to be transferred to overcome the binding energy. Relativistic collision theory predicts a threshold energy of 495 kV for an electron beam incident on a copper lattice, assuming the displacement energy to be 25 eV. This prediction has now been closely confirmed by Makin (1968) in experiments carried out in the Cavendish high-voltage microscope. At a beam energy of 490 keV, no radiation damage was visible even after 15-min exposure at an incident current density of about 1 $A.cm^{-2}$, but at 500 keV slight damage occurred and the amount increased rapidly at 510 keV, 520 keV, and finally 600 keV. An accurate test of the change with voltage of the theoretical cross section for ejection is difficult, because individual atomic events are below the resolution of the microscope and damage becomes visible only by diffusion and aggregation of interstitial atoms (or vacant sites), but qualitative confirmation has been obtained (Fig. 8).

Detailed studies are now being made of the variation in threshold energy, rate of production of damage and of annealing it out, as

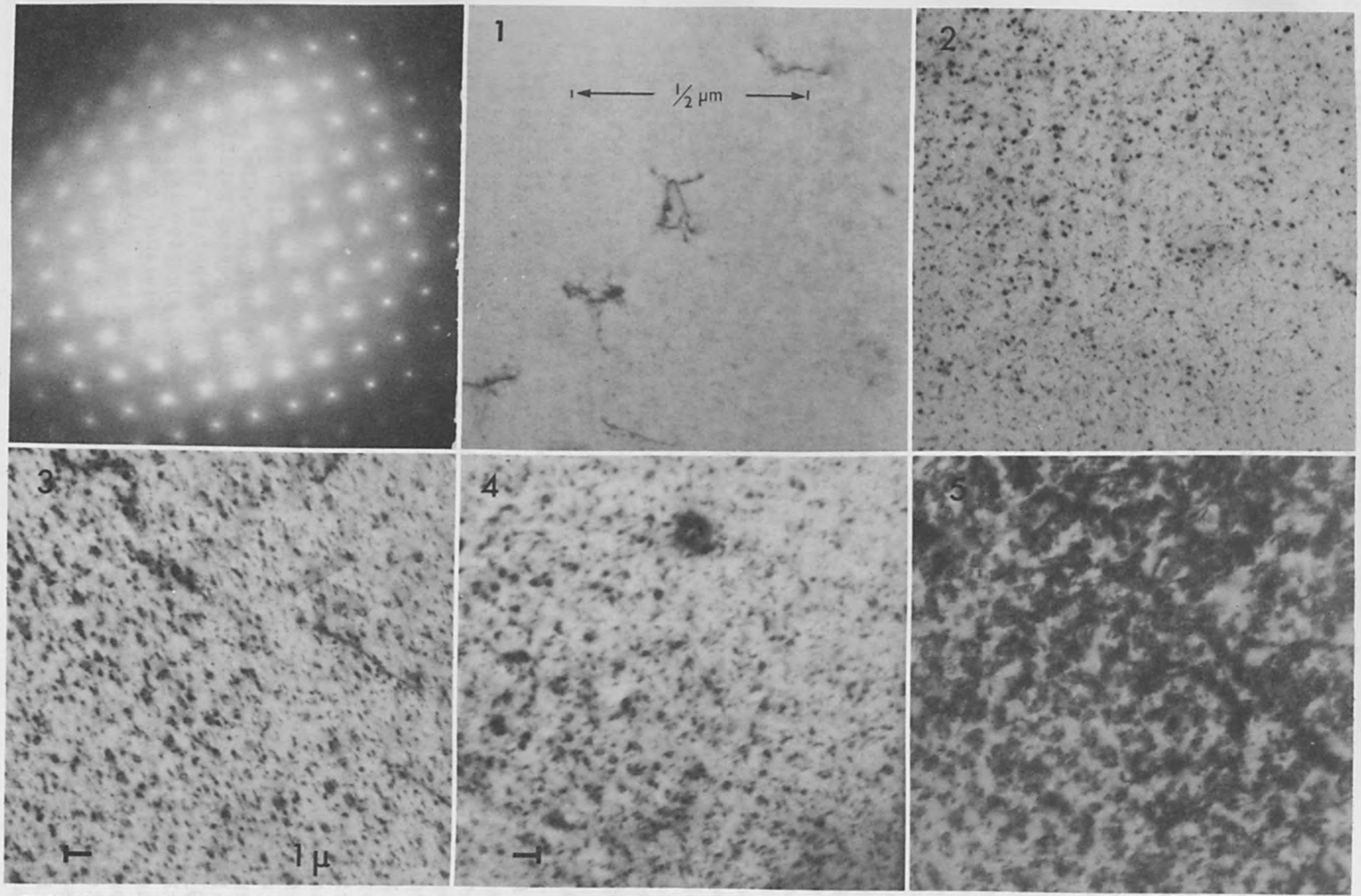

FIG. 8.—Radiation damage in copper after 15-min exposure to an electron beam at (1) 490 kV, (2) 500 kV, (3) 510 kV, (4) 520 kV, and (5) 600 kV, in the Cavendish high-voltage microscope [courtesy of Dr. M. J. Makin (1968)].

influenced by experimental conditions, especially specimen temperature and lattice orientation. It has already been shown by Steeds and Valdrè (1968) that radiation damage in the form of dislocation loops readily occurs in lead at liquid helium temperatures, but that it quickly disappears on warming to room temperature. We are finding that the annealing process is very sensitive to experimental conditions, and also that the threshold energy varies more strongly with orientation than had been predicted. There is a considerable field opening here for the metal physicist, one example of which is the effect of radiation damage in destroying the coherence between a precipitate and its matrix (Woolhouse 1968). If nothing else, these investigations have brought home to us the value of having designed the Cavendish high-voltage microscope to be variable over a very wide voltage range, from 75 kV to 750 kV.

REFERENCES

Burge, R. E., and Misell, D. L. (1968), Phil. Mag. 18: 251 and 261.
Burge, R. E., and Smith, G. H. (1962), Nature 195: 140.
Cosslett, V. E. (1969), Z. angew. Physik (in the press).
Cosslett, V. E. and Thomas, R. N. (1964), Brit. J. Appl. Phys. 15: 883.
Crowther, J. A. (1910), Proc. Roy. Soc. A84: 226.
Curtis, G. H. (1968), Thesis, University of Cambridge.
Curtis, G. H., Cosslett, V. E., and Ferrier, R. P. (1968), Electron Microscopy 1968, Rome: Tipografia Poliglotta Vaticana; vol. 1, p. 61.
Dupouy, G., Perrier, F., Uyeda, R., Ayroles, R., and Mazel, A. (1965a), J. Microscopie 4: 429.
Dupouy, G., Perrier, F., Verdier, P., and Arnal, F. (1965b), C. R. Acad. Sci. Paris 260: 6055.
Hashimoto, H., Howie, A., and Whelan, M. J. (1960), Phil. Mag. 5: 967.
Hashimoto, H., Howie, A., and Whelan, M. J. (1962), Proc. Roy. Soc. A261: 80.
Hirsch, P. B., and Humphreys, C. J. (1968), Electron Microscopy 1968, Rome: Tipografia Poliglotta Vaticana; vol. 1, p. 49.
Ichimiya, A. (1968), Jap. J. Appl. Phys. 7, 1425.
Ichinokawa, T. (1968), Jap. J. Appl. Phys. 7: 799.
Knop, G., Minten, A., and Nellen, B. (1961), Z. Physik 165: 533.
Landau, L. (1944), J. Phys. U.S.S.R. 8: 201.
Lenz, F. (1954), Z. Naturforsch. 9a: 185.
Lippert, W., and Friese, W. (1962), Proc. 5th Internat. Cong. Electron Microscopy, Philadelphia, New York: Academic Press, vol. 1, AA1.
Makhov, A. F. (1960), Soviet Physics, Solid State 2: 1934, 1942, and 1945.
Makin, M. J. (1968), Phil. Mag. 18: 637.
Mazel, A., and Ayroles, R. (1968), J. Microscopie 7: 793.
Metherell, A.J.F. (1968), Jap. J. Appl. Phys. 7: 99.
Misell, D. L. (1968), Thesis, University of London.
Reimer, L. (1965), Quantitative Electron Microscopy (ed. Bahr, G. F., and Zeitler, E. H.), Baltimore: Williams and Wilkins; p. 201.
Reimer, L., and Sommer, K. H. (1968), Z. Naturforsch. 23a: 1569.
Scott, W. T. (1963), Rev. Mod. Phys. 35: 231.
Smith, G. H., and Burge, R. E. (1963), Proc. Phys. Soc. 81: 612.
Smith, K.C.A., Considine, K. T., and Cosslett, V. E. (1966), Electron Microscopy 1966, Tokyo: Maruzen; vol. 1, p. 99.

Steeds, J. W., and Valdrè, U. (1968), Electron Microscopy 1968, Rome: Tipografia Poliglotta Vaticana ; vol. 1, p. 43.
Uyeda, R. (1968), Electron Microscopy 1968, Rome: Tipografia Poliglotta Vaticana; vol. 1, p. 55.
Uyeda, R., and Nonoyama, M. (1968), Jap. J. Appl. Phys. 7: 200.
Verdier, P. (1968), J. Microscopie 7: 775.
Wittry, D. B., Ferrier, R. P., and Cosslett, V. E. (1969), Proc. 5th Internat. Cong. on X-ray Optics, Tübingen. Heidelberg: Springer; in press.
Woolhouse, G. R. (1968), Nature, 220: 573.

PART III

ION IMPLANTATION

Steeds, J. W., and Valdre, U. (1968). Electron Microscopy 1968, Rome: Tipografia Poliglotta Vaticana; vol. 1, p. 43.
Uyeda, R. (1968). Electron Microscopy 1968, Rome: Tipografia Poliglotta Vaticana; vol. 1, p. 55.
Uyeda, R., and Nonoyama, M. (1968). Jap. J. Appl. Phys. 7: 200.
Verdier, P. (1968). J. Microscopie 7: 775.
Wittry, D. B., Ferrier, R. P., and Cosslett, V. E. (1969). Proc. 5th Internat. Cong. on X-ray Optics, Tübingen. Heidelberg: Springer; in press.
Woolhouse, G. R. (1968). Nature, 220: 573.

A VERSATILE ARC SOURCE FOR ION IMPLANTATION SYSTEMS

T. C. SMITH

Ion Physics Corporation, Burlington, Mass.

An arc discharge ion source which has been operational in the Van de Graaff accelerator of a 2-MV implantation system is described. Ions are obtained from either four gases or two gases and one solid in any arbitrary sequence without opening the pressure vessel of the accelerator. An ion source test stand has been used to determine source operating conditions for many materials prior to running on the accelerator. Operating experience and typical target currents are reviewed.

INTRODUCTION

Several recent survey articles discuss the various types of ion sources which might be adapted to provide ions of many elements required for implantation purposes.[1-3] Several considerations led to the development of an arc discharge source of the Nielsen type[4] for use in the Van de Graaff accelerator. The rf ion source is most frequently used in such accelerators; the duoplasmatron ion source is also employed. The ions provided by these sources are usually limited to those derived from gases. Some of these gases cannot be run in sequence without a drastic deterioration in source output and problems of contamination and condensation. With the rf source, the output ion current degrades with time and useful source lifetimes are limited to about 50 hr for some vapors.

Greater flexibility is possible with the arc discharge source since the discharge chamber is thermally isolated and the high wall temperature prevents condensation. This allows source operation with gases run in sequence as well as with materials having vapor pressures of the order of 10^{-3} torr at temperatures up to 1000°C. Several modes of operation are possible with charge material fed from an attached vaporizer or placed directly inside the discharge chamber. The use of a support gas is usually not necessary.

ION SOURCE DESCRIPTION

The principle of operation of this type of source is as follows: Ions are created by electron bombardment of neutral molecules which have been introduced into the cylindrical discharge chamber. Electrons emitted from an incandescent filament at cathode potential are accelerated toward the discharge chamber walls at anode potential. An axial magnetic field generated by an electromagnet increases the electron path length and an arc discharge is initiated. The ion beam is extracted from the boundary of the plasma at the source aperture. A schematic diagram of the source for operation on gases is shown in Fig. 1.

In general, the beam current is proportional to the ion density in the plasma and therefore to the arc current. For any charge material, the total beam current and the distribution of the various ionic species obtained depend upon the particular combination of extracting electric field, discharge chamber pressure, source magnetic field intensity,

Record of 10th Symposium on Electron, Ion, and Laser Beam Technology (L. Marton, ed.); San Francisco Press, Inc.
Copyright © by The Institute of Electrical and Electronics Engineers, Inc.—Printed in the U.S.A.

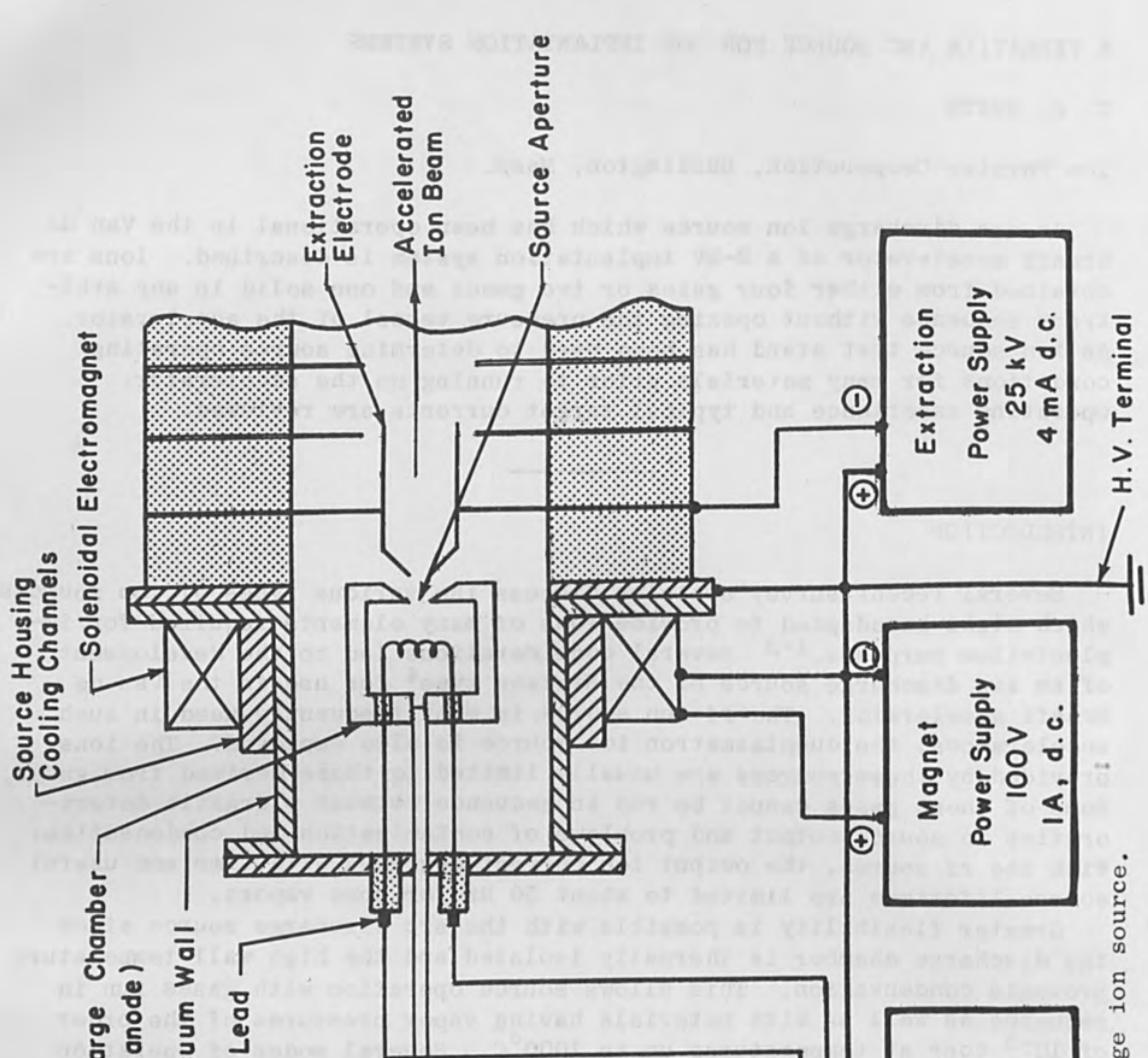
Source Housing
Cooling Channels
Solenoidal Electromagnet
Discharge Chamber
(anode)
Vacuum Wall
Filament Lead
Variable Leak
Gas Feed Line
Gas Supply
Extraction
Electrode
Accelerated
Ion Beam
Source Aperture
Filament
Power Supply
5V
30A, d.c.
Arc
Power Supply
100V
2A, d.c.
Magnet
Power Supply
100V
1A, d.c.
Extraction
Power Supply
25 kV
4 mA d.c.
H.V. Terminal
−
+
−
+
+
−
+
−

FIG. 1.—Schematic diagram of arc discharge ion source.

emitted electron current, arc voltage, and arc current. For most elements the magnitude of the doubly charged ion current is usually several percent of the singly charged component. The relative yield of the multiply charged ion species increases with increasing arc voltage.

The ion source assembly, with the vaporizer attached, is shown in Fig. 2. The temperature of the vaporizer is sensed by the thermocouple and maintained at the desired operating level within ± 1°C by means of a temperature controller. The arc discharge chamber is made of high-purity graphite. The tungsten filament is crimped into tantalum holders and insulated from the graphite anode by alumina sleeves. The remainder of the materials of construction are stainless steel.

When the material to be vaporized is placed inside the discharge chamber, a simple modification of the same basic source provides an auxilliary filament at anode potential to produce additional heat. With radiation shields, internal temperatures in excess of 1100°C have been attained. The total power dissipated within the source assembly proper can be as much as 500 W, so that proper cooling is imperative. The source assembly in the accelerator is cooled by circulating the high-pressure (300 psi) insulating gas through cooling ducts on the source housing and mounting flange.

SOURCE TEST STAND

A testing system shown in Fig. 3 simulates the conditions of the accelerator terminal and was employed for initial evaluation of the arc discharge source. It has also been utilized in a continuing development program with a source assembly identical to that in use on the accelerator. Proper source operating conditions for many materials have been determined prior to running on the accelerator. This test system also incorporates a mass spectrometer with high resolving power to obtain data on the yield of the ion desired for implantation.

A broad range of information is obtained from data taken on the test stand. This includes factors affecting reliability, such as filament lifetimes, materials compatibility, and cooling requirements. When operating with the vaporizer, the proper working temperatures and resulting charge consumption rates are observed. An evaluation of several charge materials yielding a given ion can be carried out to select the one which results in optimum source performance. In the current development program, this source has been operated on 24 different materials including 9 elemental metals.

ION SOURCE IN ACCELERATOR

In addition to the many considerations which must be taken into account for reliable source performance, some special problems are associated with the horizontal Van de Graaff accelerator. The constraints upon the size, weight, power, control and cooling requirements are considerable. The ion source is inaccessible inside the terminal of the accelerator, and is operated by remote control with no readout of the source operating parameters. The pressure vessel is evacuated to a pressure of 10 μ before being backfilled to 300 psi with an insulating gas mixture. All mechanical and electrical components in the terminal must be able to withstand this vacuum/pressure cycle.

To date, the filament lifetime has not been a serious problem.

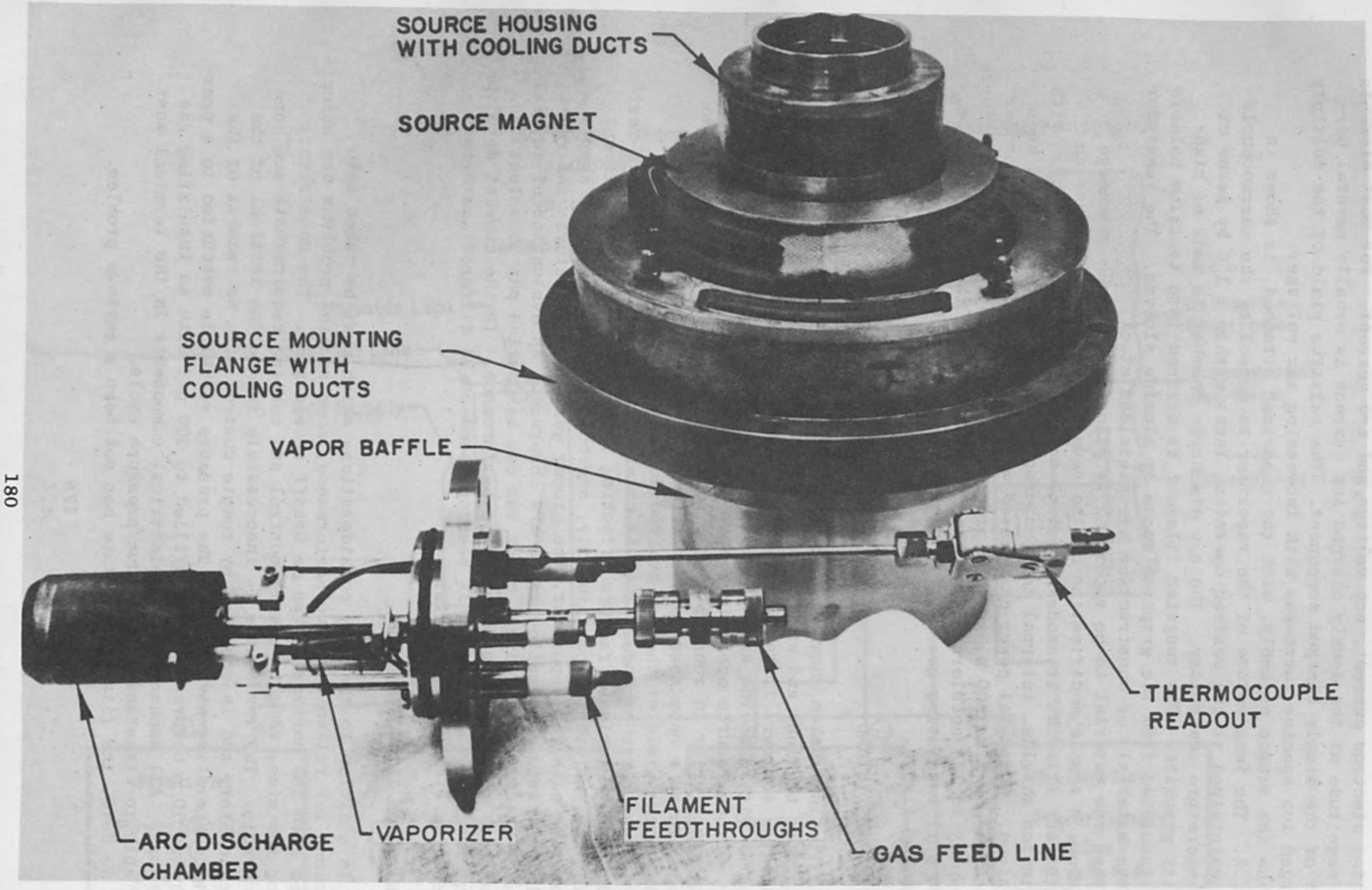
SOURCE HOUSING WITH COOLING DUCTS
SOURCE MAGNET
SOURCE MOUNTING FLANGE WITH COOLING DUCTS
VAPOR BAFFLE
THERMOCOUPLE READOUT
ARC DISCHARGE CHAMBER
VAPORIZER
FILAMENT FEEDTHROUGHS
GAS FEED LINE

FIG. 2.—Arc discharge source for accelerator application.

Implantation operations have only been interrupted once because of filament burnout and this occurred after 124 hrs. Many filaments have been intact after operating for 70 to 100 hr. The capacity of the vaporizer is sufficient to hold enough material for at least 400 hr of operation at the present charge consumption rates.

The total power required to drive the source and its associated power supplies and cooling blower is less than 1 kW. The cooling system described above can remove 1 kW of heat with a 9°F temperature rise in the insulating gas.

In this particular installation, the remote controls allow source operation on any one of four gases or two gases and one solid in arbitrary sequence without opening the pressure vessel of the accelerator.

OPERATING EXPERIENCE IN 2-MV IMPLANTATION SYSTEM

The arc discharge source has been operated in the 2 MV accelerator for more than 1000 hr. Different combinations of five gaseous charge materials and three pure metals have been run at various times. No cross contamination and no degradation in typical source output for a given ion has been observed after switching back and forth. The gases used include: BF_3, PH_3, 15% AsH_3/85% He mixture, N_2, and Ar. Zn and Se have been fed from the attached vaporizer and Ag has been vaporized directly inside the discharge chamber, so that all three modes of source operation have been demonstrated in this implantation system. The performance of the source in the accelerator has been similar to that seen on the test stand.

Considerable effort was involved in determining the proper conditions to provide vapors of Zn or Se when required but to keep the feed rate low when operating on either of the two gases. Because heat is conducted from the discharge chamber, the minimum temperature of the vaporizer is approximately 250°C for any of the interconnecting feed tubes. The vacuum conductance of the feed tube must be such that the feed rate at this minimum temperature is negligibly small. In practice,

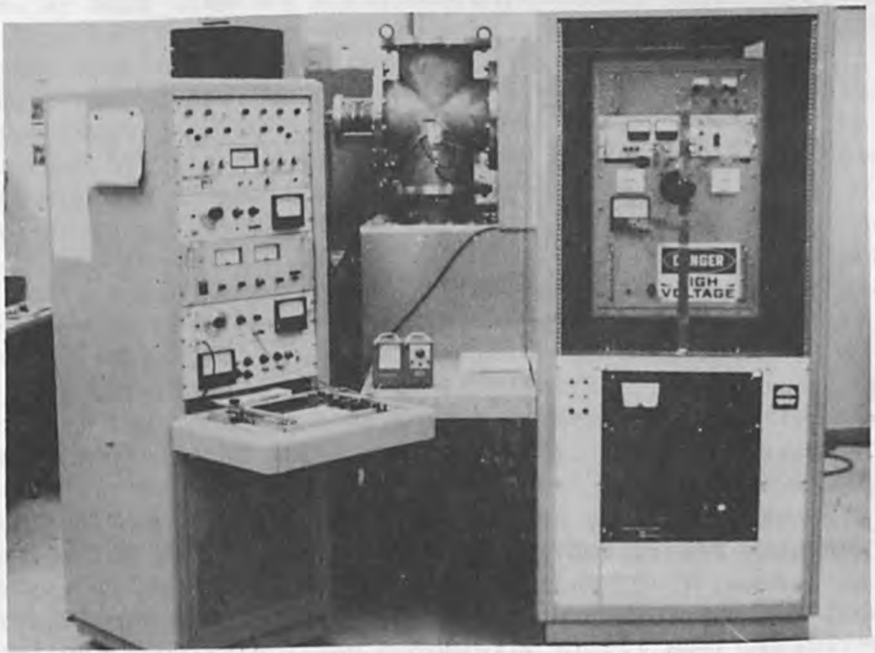

FIG. 3.—Ion source test stand.

when running on phosphine with zinc in the vaporizer, the $^{64}Zn^{+}$ current is less than 1% of the $^{31}P^{+}$ current. The average charge consumption rate for runs with the pure metals have ranged from 1 to 8 mg/hr.

The beam current delivered to the implantation target depends upon the transmission of the complete source, accelerator, analyzer, and scanner system. The total accelerated ion current which corresponds to acceptable focus at the target in our system is in the range of 20 to 40 μA . The focused spot is typically 1 to 4 mm in diameter. The source itself is capable of producing several hundred microamperes, so that the limitation at present is in the ion optical system.

Typical target currents for some of the ions implanted to date with this system are given in Table I. Over the working range of voltage for this accelerator (0.2 to 2.0 MV), these target currents may vary somewhat from the quoted values. The versatility of the arc discharge ion source in providing ions for implantation has been demonstrated in the accelerator as well as on the test stand.

ACKNOWLEDGMENTS

The support of the Corning Glass Works in this program is gratefully acknowledged. The assistance of G. Goosney, W. Butts, and A. Boom in the course of the development effort has been appreciated.

TABLE I.—Typical target currents for arc discharge ion source in 2-MV implantation system.

Ion species	Isotopic abundance (%)	Typical target current (μA)
^{11}B	80.2	1.0
^{14}N	99.6	6.0
^{19}F	100.0	1.0
^{31}P	100.0	7.5
^{40}Ar	99.6	20.0
^{64}Zn	48.9	10.0
^{75}As	100.0	6.0
^{80}Se	49.8	5.0
^{107}Ag	51.8	10.0

REFERENCES

1. G. R. Brewer and R. G. Wilson, Proc. IEEE Eighth Conference on Tube Techniques, 1966.

2. V. W. Hughs and H. L. Shultz, Methods of Experimental Physics, New York: Academic Press, 1967; vol. 4, part A, chap. 1.4.

3. D. E. Davies, T. C. Smith, and R. N. Cheever, Technology of ion implantation, Ion Physics Corp. TR-No. 808-TR-336; also in Solid State Technology 11: 33, 1968.

4. K. O. Nielsen, Nuc. Instr. and Meth. 1: 289, 1957.

DEFECTS IN SILICON DURING ION IMPLANTATION

T. IKEDA, T. TSUCHIMOTO, and T. TOKUYAMA

Central Research Laboratory, Hitachi, Ltd., Tokyo

1. INTRODUCTION

When a crystal is bombarded by high-energy ions, the Frenkel-type defects as well as many vacancy clusters are supposed to be generated by an elastic collision of bombarding ions against the crystal lattice. By an increase of bombarding dose, these defects overlap each other and apparently an amorphous layer is usually observed. These amorphous layers could be recovered into the perfect lattice by thermal annealing at suitable conditions, but in some cases, there are difficulties in recovering the lattice structures even by a long-time thermal annealing.

We have observed that the dose to form such an amorphous layer depends on energies and the species of ions. The distribution depth of these defect layers in the substrate surface is also observed to depend on the mass and the energy of ions. In our experiments, ions are hydrogen, helium, boron, and argon at the accelerating energy of 100 keV, and ion doses are varied from 10^{14} to $10^{17}/\mathrm{cm}^2$. The substrates were silicon single crystal, (111) oriented, n-type, 1 ohm-cm. The channeling phenomena will occur even in (111) alignment directions, but when the lattice disorders are generated and are accumulated, these irradiations can be considered as off channel.

2. EXPERIMENTAL RESULTS AND DISCUSSIONS

We have chosen the electron diffraction pattern as a measure of lattice disorders and measurements are carried out to determine the depth of defective regions through successive layer removal technique by anodic oxidation. Between perfect lattice patterns and amorphous patterns, we have observed a region of substrate indicating weak Kikuchi lines. This latter case seemed to correspond to the state of substrate having many defective structures.

Figure 1 represents the change of electron diffraction pattern from the silicon substrate surface to the depth direction, when the sample was bombarded by nitrogen ions of 100 keV energy, $10^{16}/\mathrm{cm}^2$ dose. The substrate surface showed the perfect crystal pattern, and at 0.1 μ depth, the pattern changed to show weak Kikuchi lines. These patterns then changed to amorphous at 0.2 and 0.3 μ depth. At 0.5 μ, the perfect crystal patterns appeared again. This result showed that there is a buried defective zone which was produced by the bombardment of high-energy ions. When ions are injected into the substrate, in the first process, ions lose their energy by an electronic collision process. In this process, the incident ions do not generate Frenkel-type defects and lose their energy by an inelastic collision. When the incident ions are slowed down by the above process, they begin to lose their energy by a nuclear-collision process successively. In this process, the ions generate many of defects by an elastic collision. Therefore, the buried defects zone is produced below the surface.

Figure 2 shows the etched cross section of hydrogen and helium bombarded silicon substrate. The bombarding energy was 100 keV and the

Record of 10th Symposium on Electron, Ion, and Laser Beam Technology (L. Marton, ed.); San Francisco Press, Inc.

Copyright © by The Institute of Electrical and Electronics Engineers, Inc.—Printed in the U.S.A.

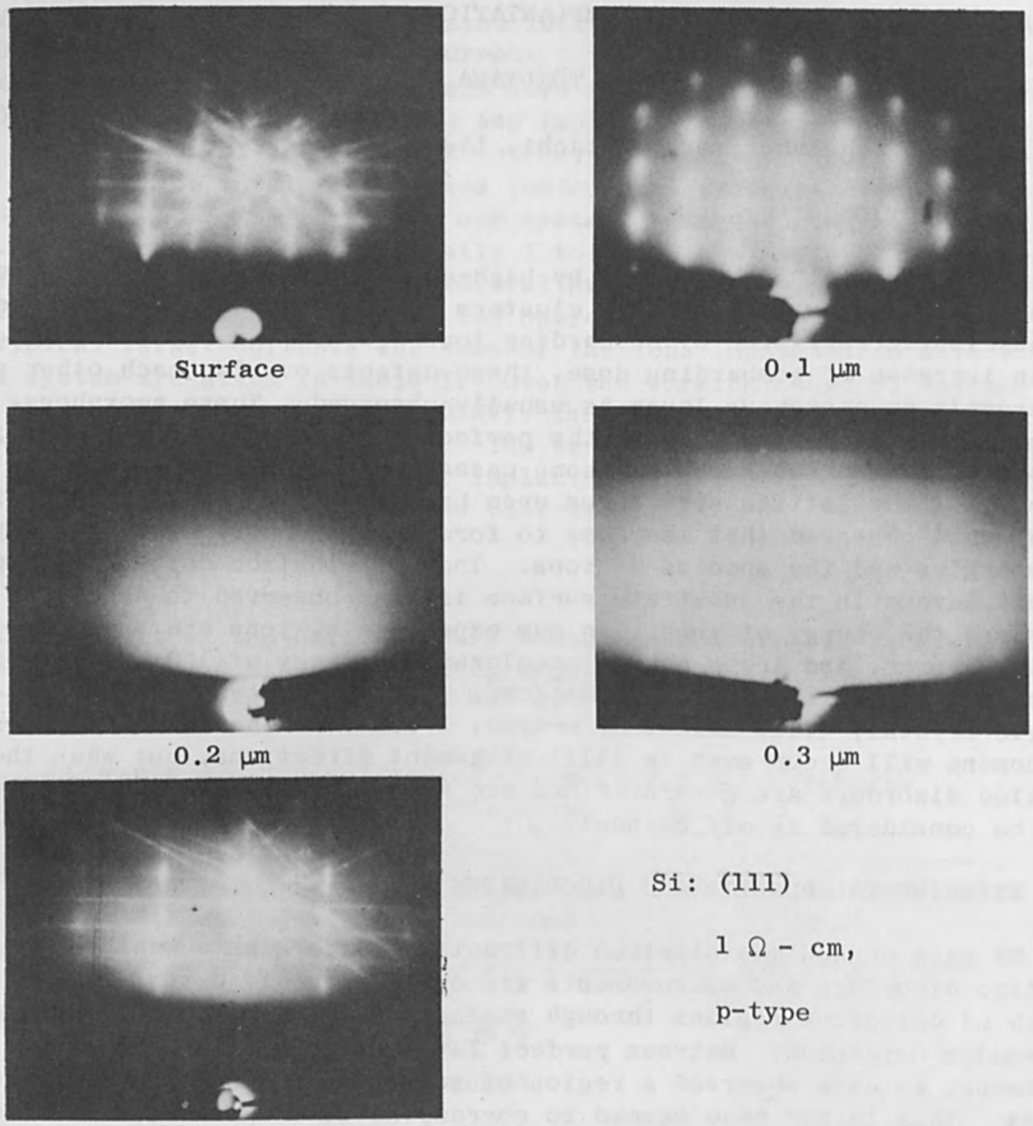

Surface

0.1 μm

0.2 μm

0.3 μm

0.5 μm

Si: (111)

1 Ω - cm,

p-type

FIG. 1.—Change of electron diffraction pattern from surface to depth. (Nitrogen-implanted silicon substrate, 100 keV, 1 × 10^{16}/cm^2.)

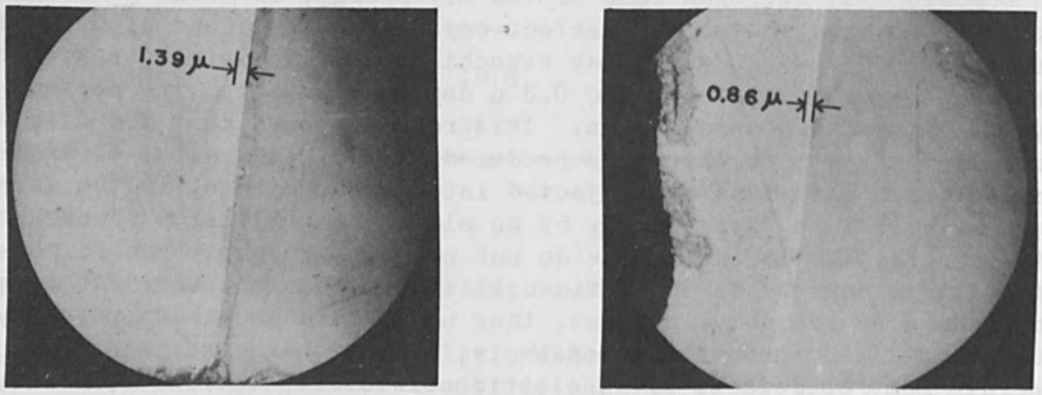

H, 100 keV, 1 × 10^{16}/cm^2

He, 100 keV, 1 × 10^{17}/cm^2

FIG. 2.—Etched region by Sirtl etching after angle lapping. [Substrate: Silicon, (111) 1 Ω - cm, p-type.]

bombarding doses were 10^{16} and $10^{17}/cm^2$, respectively. Etching by Sirtl's solution after angle lapping was carried out. From these figures, we can see the etching zone in the depth of the substrate. In the case of hydrogen bombardment, although we have not found the buried defective zone region by an electron diffraction method, the etching method revealed that there is an etched zone below the surface. The etching by Sirtl's solution seems to be very sensitive in these cases. In the helium bombardment case, the electron diffraction showed weak Kikuchi lines.

These results are summarized in Fig. 3. In the figure, the dashed line represents the etching zone, 1.3 to 1.5 μ from the substrate surface, as in the case of hydrogen bombardment. The dotted line represents the region which showed very weak Kikuchi lines, and the solid line represents an amorphous region. In the case of helium bombardment, there is only a very weak Kikuchi line zone from 0.7 to 0.9 μ from the substrate surface, but in the nitrogen case, $10^{16}/cm^2$ bombardment, there are weak Kikuchi line zones above and below an amorphous zone. Increasing the mass numbers, from boron to nitrogen and argon, this buried defective layer moves towards the surface and the surface becomes amorphous. In the case of argon, amorphous patterns are observed at the substrate surface, and these are followed by a weak-Kikuchi-line region.

Figure 4 represents schematically the results of preceding figure. The abscissa represents mass numbers and the ordinate represents the bombarding doses. The dotted and solid line in the figure represents the critical dose that puts the amorphous region both in or at the surface of substrate. The bombarding condition was 100 keV, room temperature. The amorphous zone is recovered to the single crystal by adequate thermal annealing treatment. The recovery was assured by the electron diffraction method, that is, the change of amorphous pattern to single-crystal pattern. Beside the critical dose, there is another critical dose that yields an amorphous zone in a polycrystal when the bombarded substrate is annealed. This also assured that the amorphous pattern changed to the polycrystal pattern. Therefore, it may be possible to draw another critical-dose line that separates these amorphous samples into two groups. One group leads to the single crystal and the other group to the polycrystal when these samples are annealed. From the figure, it is seen that the irradiations by large mass number have a tendency to make the latter. Therefore the smaller mass number ion is suitable for ion implantation. In the case of the large mass number and high density implantation, these relations must be taken into consideration.

Figure 5 represents one example of the annealing characteristics of boron-implanted silicon substrate. The implantation condition was 100 keV, $10^{14}/cm^2$, and room-temperature implantation. The carrier density changes with annealing temperature, and between 800 and 900°C, the value of the carrier density reaches saturation. The means that the substrate is annealed out completely in this condition. The annealing times were set to 5 and 100 min, but there are no differences in these time intervals in the annealing characteristics. This seems to indicate that the annealing does not depend on the time but the temperature in this implantation condition. The hole mobility was also measured vs temperature and also settles to a constant value between 800 and 900°C. These values are also compared with the value that was obtained from

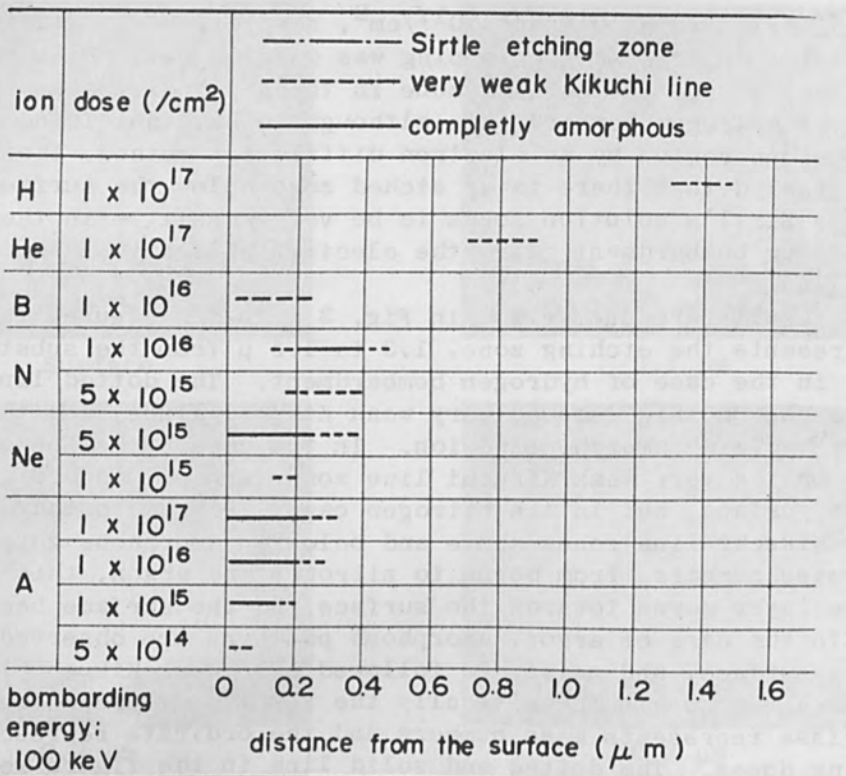

FIG. 3.—Amorphous generation condition and depth.

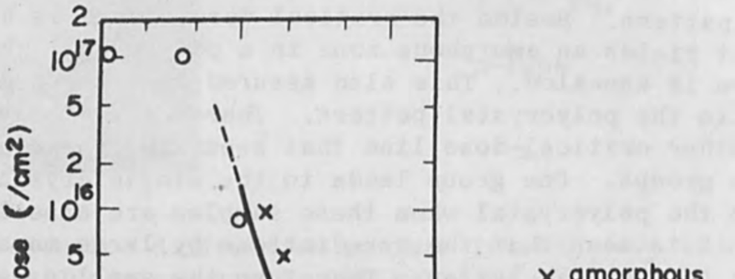

FIG. 4.—Critical bombarding dose vs mass number (x amorphous, o single crystal).

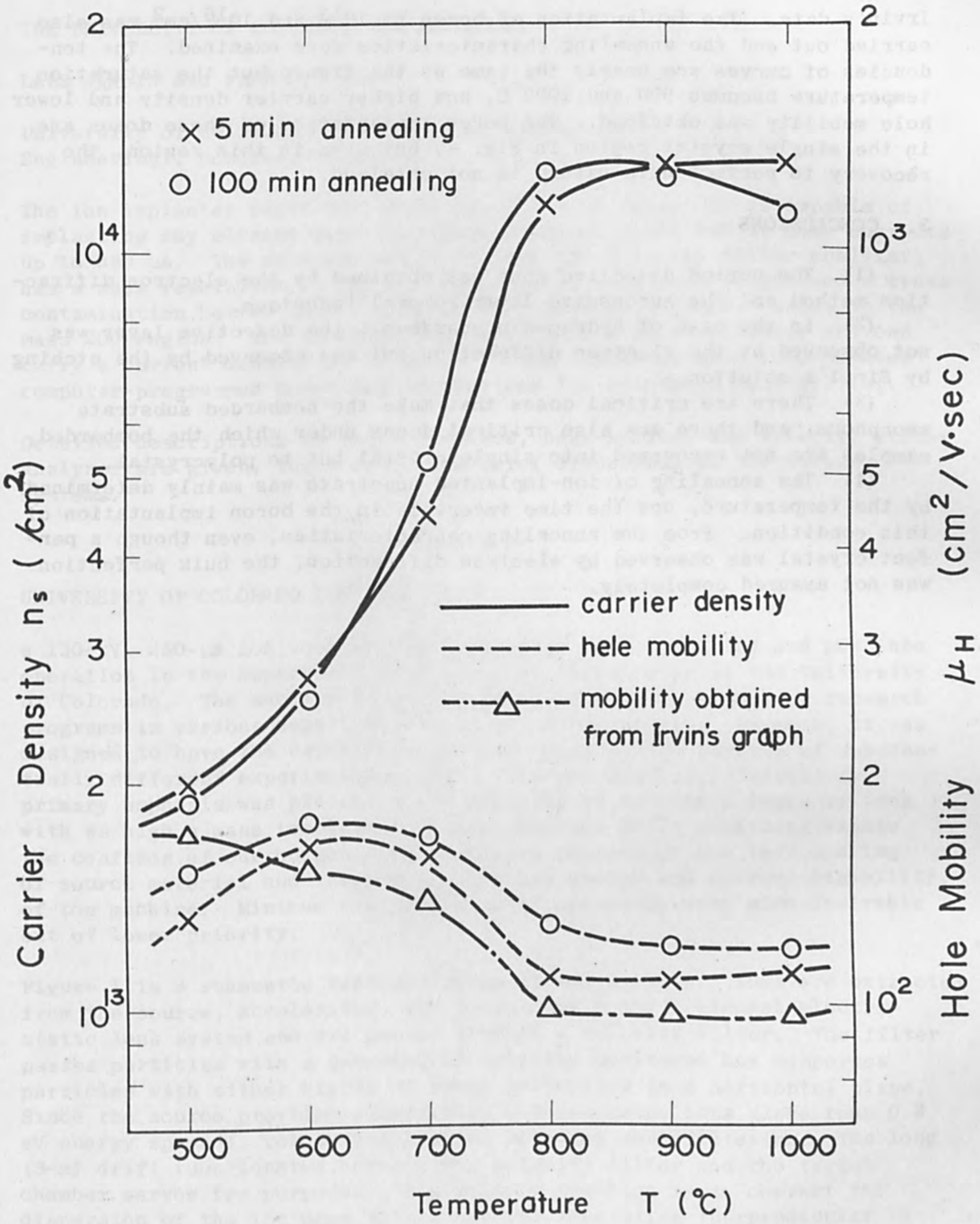

FIG. 5.—Annealing characteristics of boron-implanted silicon substrate (100 keV, 1 × 10^{14}/cm^2).

Irvin's data. The implantation of boron to 10^{15} and $10^{16}/cm^2$ was also carried out and the annealing characteristics were examined. The tendencies of curves are nearly the same as the figure but the saturation temperature becomes 900 and 1000°C, and higher carrier density and lower hole mobility was obtained. The boron implantation of these doses are in the single crystal region in Fig. 4, but even in this region, the recovery to perfect bulk nature is not obtained.

3. CONCLUSIONS

(1) The buried defective zone was obtained by the electron diffraction method and the successive layer removal technique.

(2) In the case of hydrogen bombardment, the defective layer was not observed by the electron diffraction but was observed by the etching by Sirtl's solution.

(3) There are critical doses that make the bombarded substrate amorphous, and there are also critical doses under which the bombarded samples are not recovered into single crystal but to polycrystal.

(4) The annealing of ion-implanted substrate was mainly determined by the temperature, not the time intervals in the boron implantation of this condition. From the annealing characteristics, even though a perfect crystal was observed by electron diffraction, the bulk perfection was not assured completely.

THE UNIVERSITY OF COLORADO ION IMPLANTER

LARS WÅHLIN and FRED CHERNOW

University of Colorado (Department of Electrical
Engineering), Boulder, Colorado

The ion implanter described is of the Colutron type. It is capable of implanting any element over an energy range of 5-260 keV at beam currents up to 250 μA. The machine, which employs the velocity filter analyzer, has a mass resolution of $M/\Delta M$ over 3000 at half peak height and a cross contamination better than 1 part in 10^{-5} between adjacent masses in the mass 200 region. The unmasked beam size is 0.4 mm in diameter and can carry a current density of 10 $\mathrm{mA/cm^2}$. The implanter also incorporates computer-programmed beam-handling devices for automatic beam writing.

Detailed descriptions of the ion source, beam optics, and velocity filter analyzer are given, together with a brief discussion of the vacuum systems.

UNIVERSITY OF COLORADO ION IMPLANTER

a 130-kV, 250-μA ion implanter has recently been completed and put into operation in the Department of Electrical Engineering at the University of Colorado. The machine is providing service for a number of research programs in various departments within the University. As such, it was designed to have the capability of performing a wide variety of substantially different experiments. Aside from the need for flexibility, primary emphasis was placed on the delivery of as wide a range of ions with as high a mass resolution as was possible while remaining within the confines of our budget. Of secondary importance was fast cycling of source material and targets and the ion energy and current capability of the machine. Minimum size and ease of operation were also desirable but of lower priority.

Figure 1 is a schematic representation of the machine. Ions are extracted from the source, accelerated, and focused by a three-element electrostatic lens system and are passed through a velocity filter. The filter passes particles with a preselected velocity unaltered but disperses particles with either higher or lower velocities in a horizontal plane. Since the source provides essentially monoenergetic ions (less than 0.2 eV energy spread), velocity filtering provides mass filtering. The long (3-m) drift tube located between the velocity filter and the target chamber serves two purposes. Its primary function is to convert the dispersion of the ion beam into a spatial separation (perpendicular to the direction of motion of the ions) at the target chamber. Thus a small orifice in the target chamber can be used to select the specific ion desired for implantation. The drift tube also serves to trap any neutral beam that is formed prior to filtering. One set of electrostatic deflection plates, located in the drift tube, direct the ion beam to bypass the neutral trap. A variety of electrical, mechanical, and optical feedthroughs can be mounted on the eight 2.75-in. ports that circumscribe the

Record of 10th Symposium on Electron, Ion, and Laser Beam Technology (L. Marton, ed.); San Francisco Press, Inc.
Copyright © by The Institute of Electrical and Electronics Engineers, Inc.—Printed in the U.S.A.

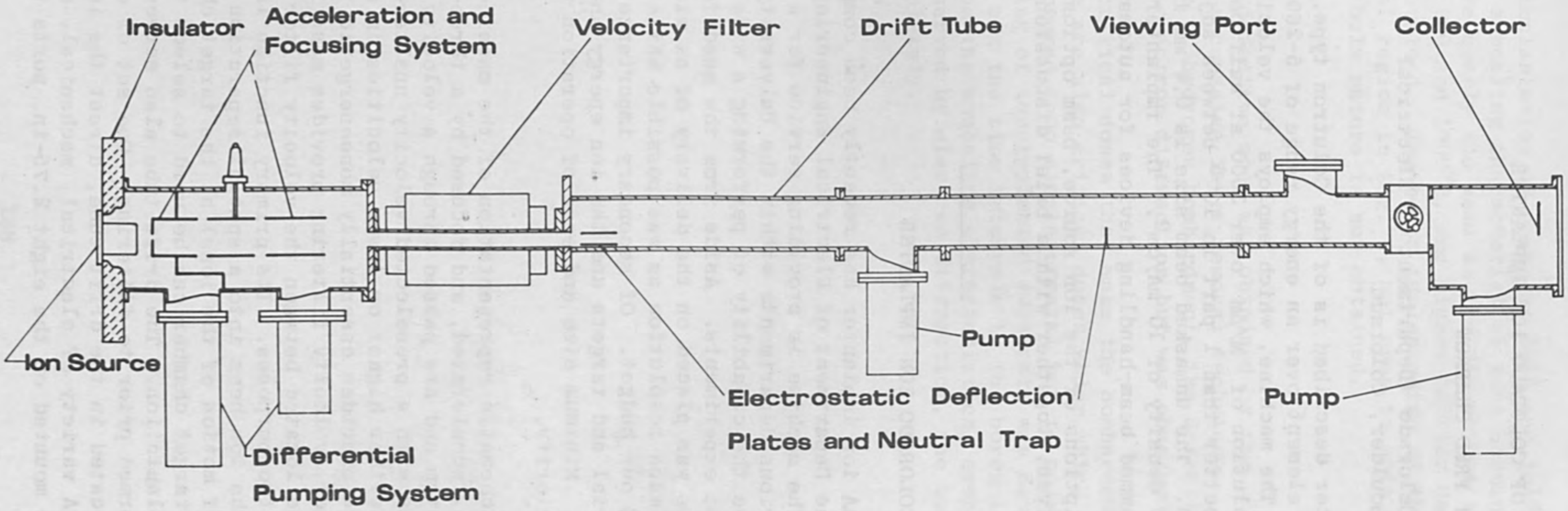
Insulator
Acceleration and Focusing System
Velocity Filter
Drift Tube
Viewing Port
Collector
Ion Source
Pump
Electrostatic Deflection Plates and Neutral Trap
Pump
Differential Pumping System

FIG. 1.—Schematic representation of ion implanter.

target chamber. The end of the target chamber is removable so that entire experimental units may be plugged into the chamber.

The vacuum pumping system was designed to maintain the system oil free,* provide an operating pressure in the mid-10^{-9} Torr range in the drift tube, and reach operating pressures overnight. Rough pumping is performed by three molecular absorption pumps operating at liquid nitrogen temperature. Two of these pumps are located at the acceleration chamber and the third at the target chamber. Low-pressure pumping is accomplished by ion and titanium sublimation pumping. The total peak pumping speed is approximately 5000 liters/sec for nitrogen. The acceleration chamber is differentially pumped to optimize the vacuum in the drift tube while pumping against the constant leak from the ion source (10^{-4} Torr liters/sec). It is necessary to maintain a low pressure in the drift tube to minimize the interaction between the ion beam and the residual gas after filtering the beam. At the present time a vacuum of 2×10^{-8} Torr is achievable in the drift tube. A 250°C automatic bakeout system is being installed to reduce the outgassing load. In principle, this addition should lower the pressure to the mid-10^{-9} Torr range. A 3-in. bakable gate valve separates the target chamber from the drift tube. The target chamber can be independently pumped. In this manner targets may be altered without venting of the entire machine to atmospheric pressure. Replacement of targets and cycling of the target chamber requires approximately 2 hr. Cycling of the machine for purposes of repair or replacement of the source chamber requires overnight pumping. The automatic bakeout system will not alter this time element but rather utilize it to achieve lower operating pressures. The machine utilizes both standard crushed copper and reusable polyimide gaskets. The polyimide gaskets are machined to washer-like configurations and sealed with obtuse (120°) knife edges machined into the mating stainless steel flanges. A large 18-in.-diam., 2-in.-thick disk of polyimide is simultaneously used as the back wall of the acceleration chamber and to insulate the ion source from ground potential.

The ion source shown in Fig. 2 is of the confined plasma variety. It is constructed of carbon and boron nitride to permit high-temperature operation. To prevent heating of the acceleration chamber, it is surrounded by a kerosene-cooled jacket. A tungsten filament is used as a heater and electron source. The pressure in the source is maintained at 10 microns by a variable leak utilizing pure nitrogen with solid source materials or the particular gas when gaseous materials are employed. Solids are mechanically driven into the source through a vacuum lock. A potential developed between the filament and front plate of the source confines the plasma to a small region of the chamber. A pin hole (0.020 in. in diameter) located in the front plate serves as an egress for the positively charged ions which are extracted from the plasma by the grounded extraction lens in the acceleration chamber. The monoenergetic nature of the ion beam results from the extraction of the ions from a plasma. Control of the source is by means of servo motors and

---

* Systems contaminated with pump oil tend to suffer from oil deposits on implanted surfaces. The oil is apparently dragged by the ion beam and deposited on the target.

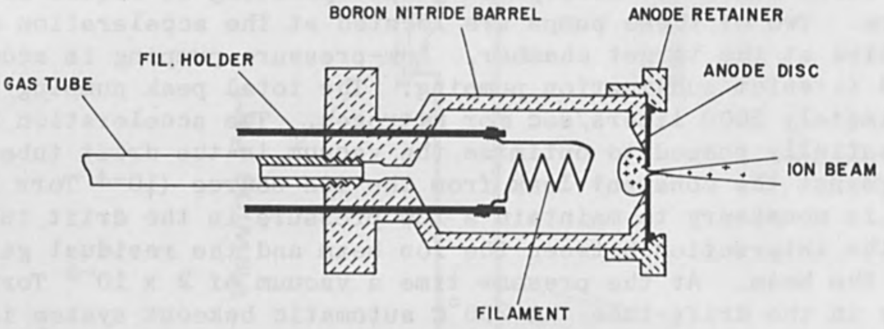
BORON NITRIDE BARREL
ANODE RETAINER
FIL. HOLDER
ANODE DISC
GAS TUBE
ION BEAM
FILAMENT

FIG. 2.—Ion source.

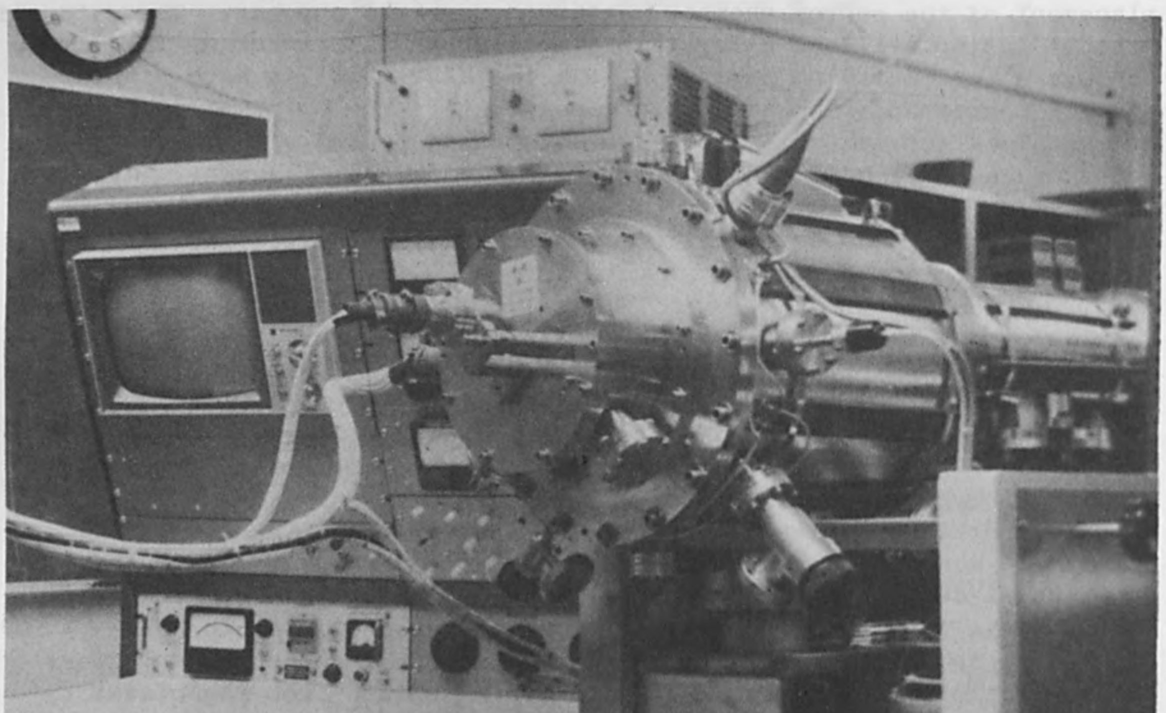

FIG. 3.—Target chamber.

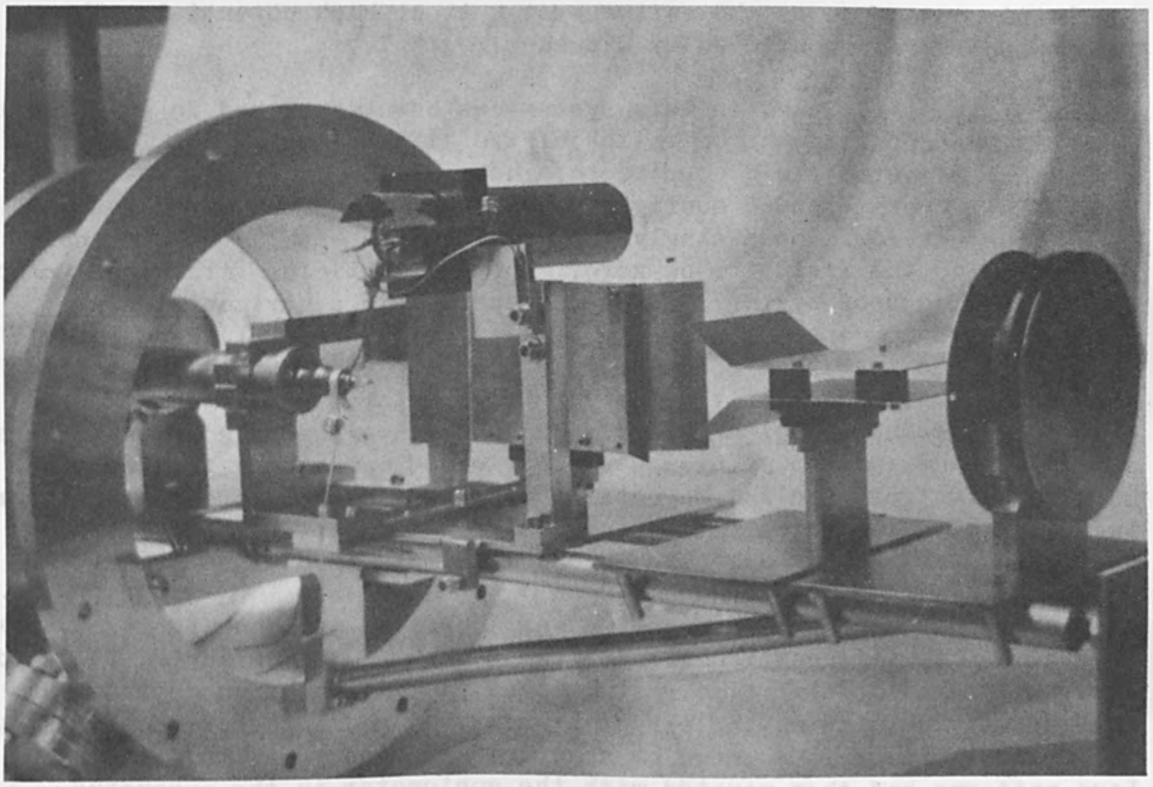

FIG. 4.—Experimental plug-in unit.

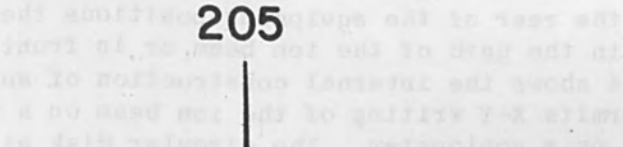

FIG. 5.—Thallium mass spectra.

insulated connectors as the entire system is at high potential. The power supplies are monitored by closed-circuit TV.

The velocity filter used in this system has been described in an earlier paper.[1] Conceptually the operation of the filter is straight forward. A vertical magnetic field coupled to a horizontal electrostatic field result in a cross E and H configuration. The fields can be adjusted to permit the net force on a singly ionized particle with a velocity perpendicular to the fields to be zero. Ionized particles with other velocities are acted upon by the field and dispersed in a horizontal plane. Although this concept for particle separation has been utilized since the 1930s, the intrinsic focusing effect of the velocity filter limited its use. For this reason the ion detector or targets have been mounted at the end of the velocity filter. This practice precludes sizable mass separation and in turn high mass resolution. To surmount this problem both the electrostatic and magnetic fields have been tapered. The tapering virtually eliminates the cylindrical focusing effect of the filter, making the use of long drift tubes and high mass resolution practical.

The target chamber with an experimental apparatus attached to it is shown in Fig. 3. In this particular experiment Bi^{210} was implanted in a CdS crystal for radioactive tracer studies of the implantation depth. The ion current incident on the target is measured and integrated externally. The crystal itself is mounted on a goniometer head, oriented with X-ray Laue patterns and then mounted with the goniometer in the apparatus. A Geiger counter has been mounted in the target chamber permitting in situ radioactive counting. The apparatus is arranged so that the external arm at the rear of the equipment positions the goniometer and crystal either in the path of the ion beam or in front of the Geiger counter. Figure 4 shows the internal construction of an experimental arrangement that permits X-Y writing of the ion beam on a target crystal that is mounted on a goniometer. The circular disk at the right of the apparatus provides an orifice for the incoming beam. Sets of vertical and horizontal wires mounted behind the orifice measure any spatial drift of the ion beam and are utilized in feedback loops to correct its position. The deflection plates are capable of moving the beam 1 cm in the vertical or horizontal directions. With the target rotated out of the path of the beam, a second set of vertical and horizontal wires (not visible in Fig. 4) measures the sensitivity of the electrostatic displacement element. The various elements are mounted on an optical-type bench for ease in alterations and cleaning. This particular experimental apparatus is for a study of ion-implanted devices. The implanter is currently being interfaced with a hybrid computer that will be eventually utilized to measure and control device characteristics as ions are being implanted.

The machine has been used for implantations ranging from hydrogen to bismuth. Beam currents of 250 μA have been readily achieved. The mass resolution (M/ΔM at the half height) has been measured to be more than 4100 at mass 205. Figure 5 shows the mass spectra of thallium from which the resolution was determined.

REFERENCE

1. L. Wåhlin, Proc. of the Int. Conf. on E & M Isotope Separators, North Holland Press, 1965, pp. 133-139.

PART IV

SEMICONDUCTORS AND SEMICONDUCTOR LASERS; MATERIALS PROCESSING WITH LASERS; MISCELLANEOUS LASER AND EB APPLICATIONS

insulated connectors as the entire system is at high potential. The power supplies are monitored by closed-circuit TV.

The velocity filter used in this system has been described in an earlier paper.[1] Conceptually the operation of the filter is straight forward. A vertical magnetic field coupled to a horizontal electrostatic field result in a cross E and H configuration. The fields can be adjusted to permit the net force on a singly ionized particle with a velocity perpendicular to the fields to be zero. Ionized particles with other velocities are acted upon by the field and dispersed in a horizontal plane. Although this concept for particle separation has been utilized since the 1930s, the intrinsic focusing [illegible] of the velocity filter limited its use. For this reason the ion detector or targets have been mounted at [illegible] [illegible] [illegible] with [illegible] [illegible] [illegible] mass separation [illegible] [illegible] [illegible] problem both the electrostatic and magnetic fields have been tapered. The tapering virtually eliminates the cylindrical focusing effect of the filter, making the use of long drift tubes and high mass resolution practical.

The target chamber with an experimental apparatus attached to it is shown in Fig. 3. In this particular experiment Rn^{210} was implanted in a CdS crystal for radioactive tracer studies of the implantation depth. The ion current incident on the target is measured and integrated externally. The crystal itself is mounted on a goniometer head, oriented with X-ray Laue patterns and then mounted with the goniometer in the apparatus. A Geiger counter has been mounted in the target chamber permitting in situ radioactive counting. The apparatus is arranged so that the external arm at the rear of the equipment positions the goniometer and crystal either in the path of the ion beam or in front of the Geiger counter. Figure 4 shows the internal construction of an experimental arrangement that permits X-Y sweeping of the ion beam on a target crystal that is mounted on a goniometer. The circular disk at the front of the apparatus provides an orifice for the incoming beam. Sets of vertical and horizontal wires mounted behind the orifice measure any [illegible] drift of the ion beam and are utilized in feedback loops to correct the position. The deflection plates are capable of moving the beam [illegible] in vertical or horizontal directions. With the target rotated [illegible] the path of the beam, a second set of vertical and horizontal wires [illegible] to Fig. 4) measures the sensitivity of the electrostatic [illegible] element. The various elements are mounted on an optical bench for ease in alterations and cleaning. This particular experimental apparatus is for a study of ion-implanted devices. The implanter is currently being interfaced with a hybrid computer that will be [illegible] utilized to measure and control device characteristics as ions are being implanted.

The machine has been used for implantations ranging from hydrogen to bismuth. Beam currents of 250 µA have been readily achieved. The mass resolution (M/ΔM at the half height) has been measured to be more than 1100 at mass 205. Figure 5 shows the mass spectra of thallium from which the resolution was determined.

REFERENCE

1. E. [illegible] in: Proc. of the Int. Conf. on E & M Isotope Separators, North Holland Press, 1965, pp. 133-139.

ELECTRON-BEAM-PUMPED CdS LASER

S. NAMBA, H. ARITOME, and K. MASUDA

Osaka University (Faculty of Engineering Science), Toyonaka, Osaka

The penetration of electrons into CdS crystal is examined by the microscope method based on the luminous figure adopted by Ehrenberg and King. From the differential energy loss obtained by this method, the threshold conditon of electron-beam-pumped CdS laser is calculated. The agreement between the calculated and experimental results is reasonable.

Laser oscillation was also observed for the crystal grown with bismuth added. Its threshold current density is lower than that of undoped crystals as in the case of Cd-rich crystals. The reason is not understood at the present stage.

I. INTRODUCTION

The threshold condition of the electron beam pumped laser is first presented by Klein[1] and discussed in the case of GaAs. Recently it has been theoretically treated for CdS by Haug[2] from the quantum-mechanical basis. But so far little has been said about the threshold conditions and the impurity effects on it.

In this paper only the preliminary results obtained at the present stage are described and discussed on the basis of the expression given by Klein. First, electron penetration depth into CdS crystal is measured as a function of the electron energy by the microscope method based on the luminous figure adopted by Ehrenberg and King.[3] Then from the differential energy loss obtained by this method, the threshold condition of CdS laser is calculated and compared with the experimental results. The agreement is reasonable in the case of undoped crystals.

The dependence of threshold current density on the beam voltage is also shown. It was tentatively explained by the surface effects. Laser oscillations were also observed for CdS crystals grown with bismuth added and Cd rich CdS crystals. They were briefly presented.

II. EXPERIMENTAL PROCEDURES

1. ELECTRON PENETRATION. Figure 1 shows the principle of the method employed for examining electron penetration. An electron beam through the aluminum hole of about 40 μm in diameter was focused so as to impinge upon a flat cleaved face of the undoped vapor-grown CdS single crystal and the resultant luminous glow was photographed through the microscope using the Kodak Tri-X Pan Film. The magnification of the microscope was 100. An electron gun of a Pierce type was used. Its maximum capacity was 22 mA at the beam voltage of 40 kV. This corresponds to the maximum current density of 7 A/cm^2. Current was supplied in about 500-ns pulses at a repetition rate of 20-200 Hz. The exposed film was developed and then traced by a microphotometer.

2. LASER OSCILLATION. Three kinds of CdS crystals were used for

Record of 10th Symposium on Electron, Ion, and Laser Beam Technology (L. Marton, ed.); San Francisco Press, Inc.
Copyright © by The Institute of Electrical and Electronics Engineers, Inc.—Printed in the U.S.A.

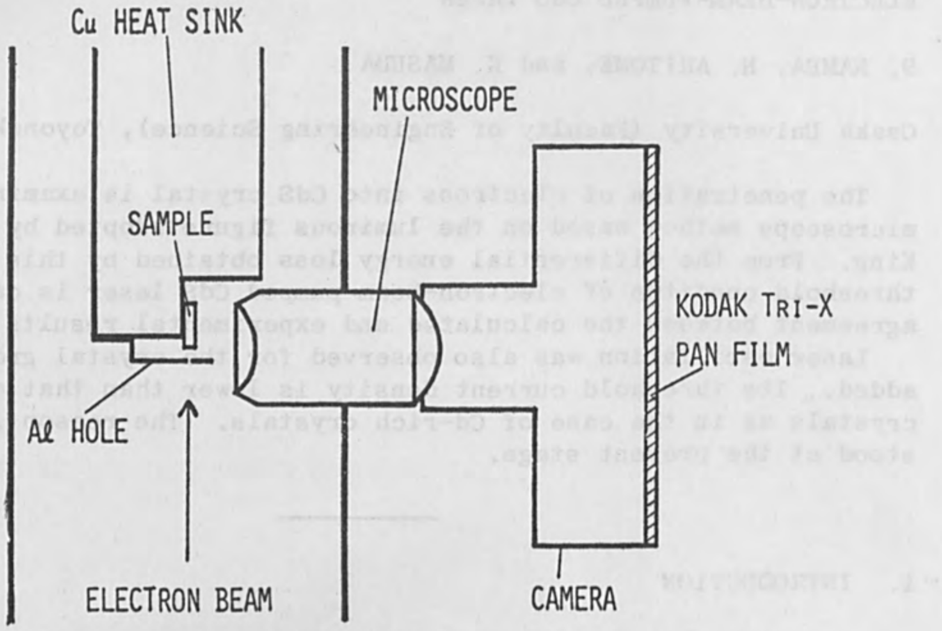
Cu HEAT SINK
MICROSCOPE
SAMPLE
KODAK Tri-X
PAN FILM
Aℓ HOLE
ELECTRON BEAM
CAMERA

FIG. 1.—Schematic diagram of arrangement to study glow in CdS.

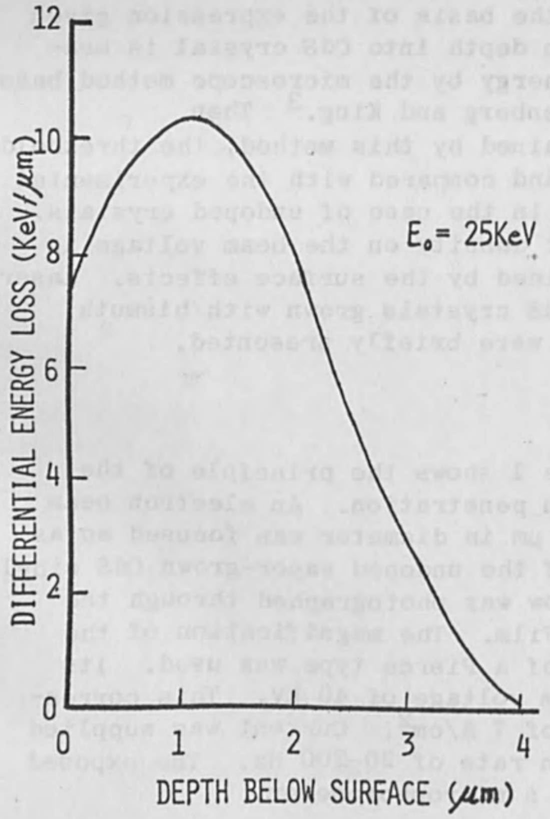

FIG. 2.—Distribution of energy loss of electrons with depth in CdS crystal at 80°K. (Electron energy in 25 keV.)

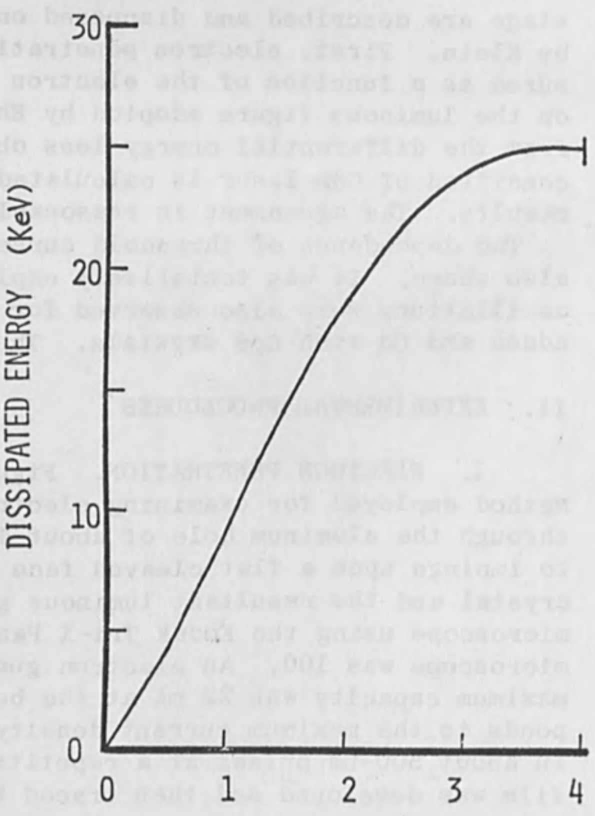

FIG. 3.—Dissipated energy in CdS crystal at 80°K. (Electron energy is 25 keV.)

observing laser oscillation: undoped crystals, those grown with bismuth added, and Cd-rich crystals. They were all vapor-grown platelets. The optical cavity was formed by cleaving along two parallel $(10\bar{1}0)$ faces, which were normal to the surface of the platelet and parallel to the c-axis. The width of the samples (i.e., the dimension of the optical cavity), varied from 50-500 μm; all were about 1 mm long and 1-20 μm thick. The samples were then attached to the copper heat sink with vacuum grease. The pulsed electron beam was incident on the platelet surface and the radiation was emitted normal to the beam from the cavity face. The distribution in the beam in the radial direction was approximately Gaussian, i.e., the current density J(r) was given by $J(r) = (I_0/2\pi\sigma^2)\exp(-r^2/2\sigma^2)$, where I_0 is the total current and σ was measured to be 0.23 mm. The variation of the current density over the sample thus did not exceed ±3% for the 140-μm cavity sample, ±5% for the 200-μm cavity sample, and ±10% for the 280-μm sample, respectively. Laser radiation was detected by an RCA 1P28 photomultiplier through a monochromator and observed by a dual-beam synchroscope.

III. ELECTRON PENETRATION

Figure 2 shows an example of the microphotometer trace of photographed films of luminescence converted to the distribution of energy loss of electrons with depth at 80°K. The electron energy was 25 keV. For the determination of the distribution of energy loss per unit length, it was necessary to assume that the luminous intensity from any elemental volume within the glow was proportional to the energy dissipated within the volume. The integrated area was normalized to give the incident energy E_0. It was graphically integrated and is shown in Fig. 3 to give the dissipated energy. The depth at which the dissipated energy is equal to the incident energy was defined as the ultimate range. A theory for the total electron penetration depth was first presented by Bethe.[4]

For nonrelativistic electrons, Bethe gives as the average energy loss per unit of path length,

$$-\frac{dE}{dX} = \frac{4\pi N q^4}{mv^2} \ln\left[\frac{mv^2}{2\bar{I}}\left(\frac{e}{2}\right)^{\frac{1}{2}}\right] \quad \text{(erg/cm)} \tag{1}$$

$$N = \frac{Z\rho}{AN_a} \tag{2}$$

where N is the number of electrons per cubic centimeter of material, q is the charge of the electron, e = 2.718..., $\bar{I}$ is the average excitation potential of the atoms, Z is the atomic number, A is the atomic weight, ρ is the mass density of the material, and N_a is Avogadro's number.

The total range R_B may then be calculated from

$$R_B = \int_0^{E_0} \left(\frac{dE}{dX}\right)^{-1} dE \tag{3}$$

with (1) substituted in the integrand, where E_0 is the incident energy. For compound materials, the effective values of (Z/A) and $\bar{I}$ were used.[5] For compounds of the formula $(Z_1)_{n_1}(Z_2)_{n_2}$, the effective values of (Z/A) and $\bar{I}$ were obtained from

$$\left(\frac{Z}{A}\right)_{eff} = \frac{n_1 Z_1 + n_2 Z_2}{n_1 A_1 + n_2 A_2} \tag{4}$$

$$\ln \bar{I}_{eff} = \frac{n_1 Z_1 \ln \bar{I}_1 + n_2 Z_2 \ln \bar{I}_2}{n_1 Z_1 + n_2 Z_2} \tag{5}$$

For the CdS crystal, $(Z/A)_{eff} = 0.443$ and $I_{eff} = 360$ eV were used which were calculated from (4) and (5) using the values in stopping power experiments for protons.[6] With these values and $\rho = 4.82$, (3) was graphically integrated. The result is shown in Fig. 4 for comparison of the experimental results. The range R_B increased with energy as $R_B \propto E_0^{1.75}$. Accurate comparison cannot be made because it is understood that Bethe's model of the electron transmission through metals does not give the accurate coincidence with the experimental values.[7] But it is noted from this experiment that the exciton or ambipolar diffusion seems to be unimportant at this temperature when the beam voltage is sufficiently high.

IV. LASER OSCILLATION THRESHOLD

Table I shows the representative experimental results of laser oscillations. Laser oscillation condition for electron pumping is given by Klein.[1]

TABLE I.—Representative experimental results at 80°K.

Crystal	Doping	Dimension (μm X μm X mm)	Threshold Current Density at 25kV (A/CM^2)	Wavelength (Å)
A	undoped	140 X 20 X 1	1.3	4960
B	doped	280 X 10 X 1	0.2	4940
C	Cd-doped	200 X 10 X 1	0.2	4940

Carrier generation rate Z excited by an electron beam is given by

$$Z = \frac{J}{q} \frac{1}{\varepsilon} \frac{dE}{dX} \tag{6}$$

where J is the beam current density, q is the electronic charge, and ε is the average energy for creating one electron hole pair. For the CdS crystal, ε of 7.5 eV is given.[8] Laser action occurs when this generation rate exceeds the threshold value Z_{th} determined by the internal loss. Z_{th} is given at very low temperature,

$$Z_{th} = \frac{8\pi}{h^3 c^2} \frac{n_0^2 (h\nu)^2 \Delta(h\nu)}{\eta_q} \left(\alpha + \frac{1}{L} \ln \frac{1}{R}\right) \tag{7}$$

where h is Plank's constant, c is the light velocity in vacuum, $h\nu$ is the emitted photon energy, $\Delta(h\nu)$ is the half line width of the emission spectrum, η_q is the quantum efficiency, n_0 is the refractive index, α is the absorption coefficient, L is the cavity length, and R is the reflectivity of the material. At the elevated temperature, the additional carrier excitation is necessary to maintain the quasi-

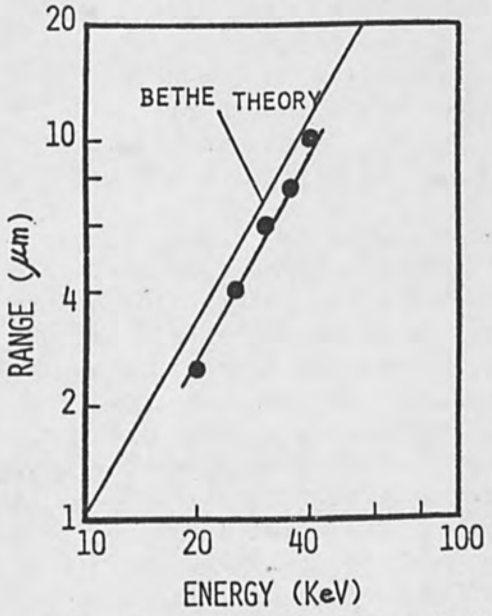

FIG. 4.—Range-energy relation in CdS crystal at 80°K.

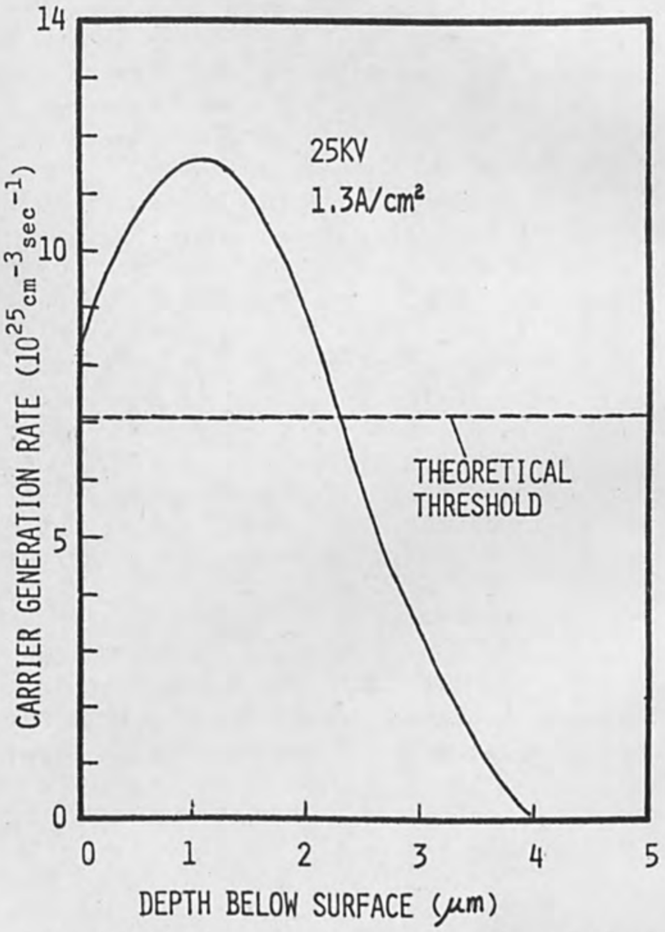

FIG. 5.—Carrier generation pattern in CdS crystal at threshold condition at 80°K.

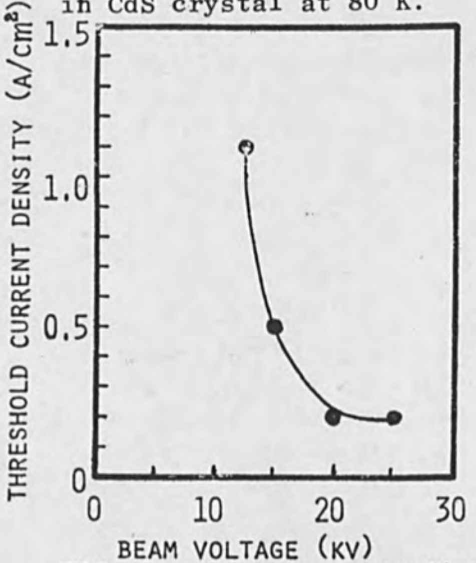

FIG. 6.—Dependence of threshold current density on beam voltage at 80°K.

Fermi level at its 0°K position. So (7) is valid only at very low temperature, but it was also used at 80°K using the parameters at 80°K, as the precise data at very low temperatures is not available. This is not strictly true but may not be absurd because according to Hurwitz's results,[9] the difference of the threshold current density at 77°K and 4.2°K is 20% (1.2 A/cm^2 at 77°K and 1.0 A/cm^2 at 4.2°K at the beam voltage of 50 kV). So, for CdS crystals, $n_0 = 2.8$, $\alpha = 16\text{cm}^{-1}$, $R = 0.22$, and $\Delta(h\nu) = 0.03$ eV were used for the oscillation wavelength of 4960 Å at 80°K; η_q was assumed to be 1.

Figure 5 shows the threshold carrier generation rate calculated from (7) and the carrier generation rate calculated from (6) using the experimental energy loss per unit length shown in Fig. 2. The agreement is reasonable. Their difference may be explained by the additional excitation necessary above 0°K.

For the crystal B and C, the threshold current density is considerably lower than that for the crystal A as shown in Table I. The reason the threshold current density is so low for the crystal B as in the crystal C is not clear, but may be due to the increased crystal homogenity. The reason for the shift of oscillation wavelength toward the shorter side is also not clear, but it is most probably that the sample heating of the crystal B is not so great as in the case of the crystal A because the threshold current is lower.

The dependence of the threshold current density on the beam voltage for the crystal B is shown in Fig. 6. The threshold current density increases as the beam voltage decreases. The electron penetration depth at beam voltages of 12.5 and 25 kV can be estimated about 1 and 4 μm, respectively, from Fig. 4. As the electron penetration depth increases with energy greater than E_0^1, the peak energy loss per unit length increases, so the peak carrier generation rate increases, as the electron energy decreases. Owing to the carrier recombinations, however, the situation becomes different because the recombination effect is significant at at the surface. It is necessary to solve the differential diffusion equation involving the surface recombination for precise analysis. But it was tentatively attributed qualitatively to the surface effect.

ACKNOWLEDGMENT

We wish to thank Dr. D. C. Reynolds of Aerospace Research Laboratory, Dr. S. Ibuki of Mitsubishi Electric Corporation, and Dr. J. Chikawa of NHK Broadcasting Science Research Laboratories for supplying CdS crystals.

REFERENCES

1. C. A. Klein, Appl. Phys. Letters 7: 200, 1965.
2. H. Haug, J. Appl. Phys. 39: 4687, 1968.
3. W. Ehrenberg and D.E.N. King, Proc. Phys. Soc. 81: 751, 1963.
4. H. A. Bethe, Handbuch der Physik, vol. 24, pt. 1): 519, 1933.
5. R. O. Lane and D. J. Zaffarano, Phys. Rev. 94: 960, 1954.
6. C. J. Bakker and E. Segrè, Phys. Rev. 81: 489, 1951.
7. V. E. Cosslett and R. N. Thomas, Brit. J. Appl. Phys. 15: 1283, 1964.
8. N. F. Malyuk et al., Sov. Phys. - Solid State 8: 2513, 1967.
9. C. E. Hurwitz, Appl. Phys. Letters 8: 243, 1966.

GaAs LASER BY ELECTRON BEAM EXCITATION

SUSUMU NAMBA and SOHACHI IWAI

Institute of Physical and Chemical Research, Yamato-machi Saitama, Japan

The laser emission was observed in GaAs by the excitation of 27-keV electron beams. The temperature dependence of threshold current density was measured in n-type and p-type samples from 100 to 300°K. The threshold current increased with $T \sim T^{1.5}$ in samples with impurity concentration of 10^{17} and 10^{18} cm^{-3}.

I. INTRODUCTION

The temperature dependence of laser threshold has been studied in detail for injection lasers. An approximately T^3 dependence was reported elsewhere.[1-3] In the case of injection laser the active region of the semiconductor was heavily doped and compensated. Since an impurity gradient exists, the impurity concentration in an active region cannot be determined exactly. On the contrary in this case, the electron-beam pumping method enables one to excite the homogeneous material with any impurity concentration and to investigate n-type and p-type materials separately. This method is useful for determining the laser parameters of injection lasers. It is also a powerful method to investigate stimulated emission from many semiconductors in which p-n junctions are difficult to make, for example II-VI compounds.

In this paper are described the laser emission from GaAs and the temperature dependence of threshold current density and photon energy in the region from 100 to 300°K. The dependence is discussed by a simple calculation.

II. EXPERIMENTAL PROCEDURE

The optical cavity was formed by the two parallel polished surfaces separated by 0.2 mm. In some cases one of the polished surfaces was coated with evaporated aluminum. The surface to be bombarded by electron beams was cleaved in a (110) plane, perpendicular to the polished surfaces. The sample was soldered with Sn or In in a groove of a copper heat sink, which was attached to a cold finger of a liquid nitrogen cryostat.

The block diagram of the experimental arrangement is shown in Fig. 1. The electron-beam energy was 30 keV maximum, the pulse duration time from 0.1 to 0.5 μsec, and the repetition rate from 10 to 1000 Hz. The beam current was observed on a synchroscope by measuring the terminal voltage drop through a low resistance between the cryostat and the earth. The beam had a diameter of 1 mm on the sample surface and the maximum current density was 4.5 A/cm^2. The threshold current density was measured within an error of about ± 5%. The temperature of the sample as measured by a thermocouple was controlled by heating the heat sink. The emitted light was detected by a photomultiplier after being passed through a spectrometer and then observed by a synchroscope.

Record of 10th Symposium on Electron, Ion, and Laser Beam Technology (L. Marton, ed.); San Francisco Press, Inc.

Copyright © by The Institute of Electrical and Electronics Engineers, Inc.—Printed in the U.S.A.

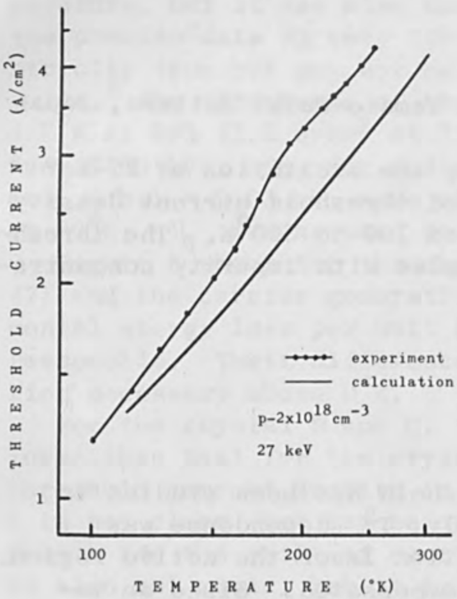

FIG. 1.—Block diagram of experimental arrangement.

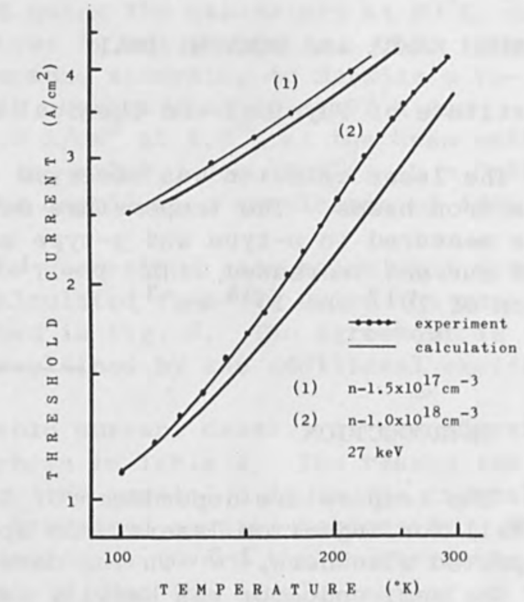

FIG. 2.—Temperature dependence of threshold current density in p-GaAs laser by excitation with 27-keV electron beam.

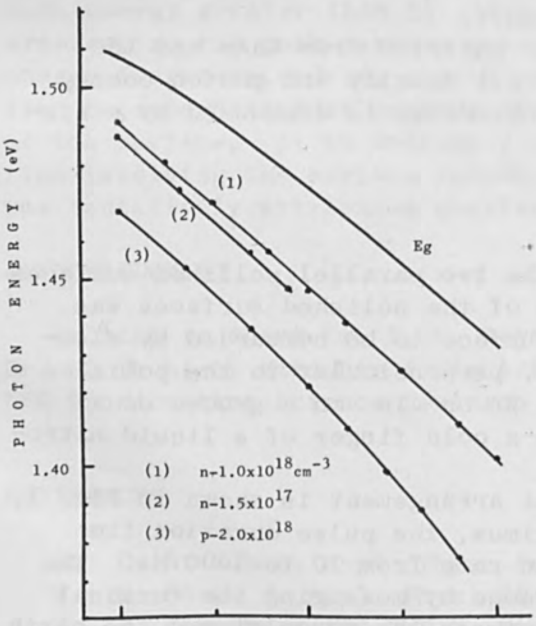

FIG. 3.—Temperature dependence of threshold current density in n-GaAs laser by excitation with 27-keV electron beam.

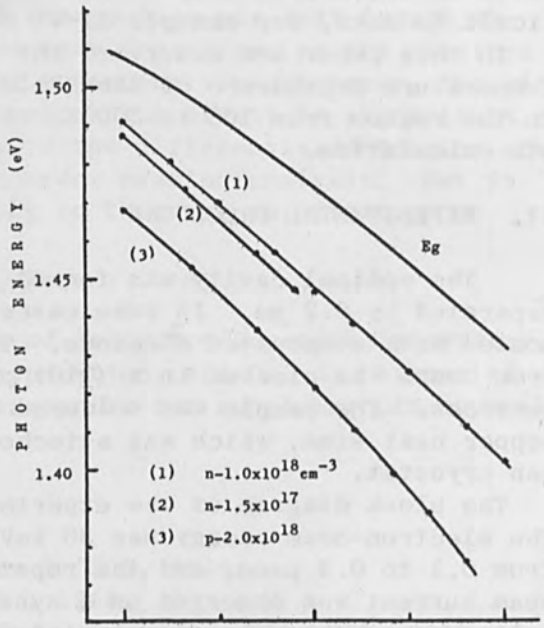

FIG. 4.—Temperature dependence of photon energy of laser emission. Change of band gap (E_g) in pure GaAs is also shown.

III. EXPERIMENTAL RESULTS

As shown in Table I, the laser emission occurred at 8306 Å in Te-doped samples and at 8440 Å in Zn-doped samples with impurity concentrations of 10^{18} cm^{-3} at 100°K. The threshold current density was 1.1 A/cm^2 for Te-doped and 1.2 A/cm^2 for Zn-doped samples at 100°K with an electron-beam energy of 27 keV. The minimum electron energy for lasing was 15 keV at 100°K and 25 keV at 300°K in both samples.

TABLE I. The experimental values in GaAs laser by the excitation with a 27-keV electron beam at 100°K.

Impurity (cm^{-3})	Wavelength (Å)	Photon energy (eV)	Threshold (A/cm^2)
Te - 1.5 X 10^{17}	8330	1.488	2.5
Te - 1.0 X 10^{18}	8306	1.492	1.1
Zn - 2.0 X 10^{17}	8340	1.486	4.0
Zn - 2.0 X 10^{18}	8440	1.468	1.2

In Te-doped samples with 1.5 X 10^{17} cm^{-3} impurities the wavelength of laser emission was 8330 Å, which is longer than that of the samples with 1 X 10^{18} cm^{-3} impurities. On the other hand, in Zn-doped samples with 2 X 10^{17} cm^{-3} impurities the wavelength of laser emission was 8340 Å, which is shorter than that of the samples with 2 X 10^{18} cm^{-3} impurities and which is almost the same wavelength as in the case of the Te-doped samples with 1.5 X 10^{17} cm^{-3} impurities. Before lasing, the peak of spectra of emitted light of Te-doped samples was about 8310 Å, but that of Zn-doped samples with 2 X 10^{17} cm^{-3} impurities was about 8400 Å under a low excitation and shifted gradually to shorter wavelengths with increasing beam current, and the laser emission occurred at 8340 Å.

As the temperature rises, the threshold current density increases as shown in Fig. 2 for p-type and in Fig. 3 for n-type. The threshold current increases with an approximately $T^{1.5}$ dependence both in n-type and p-type samples with 10^{18} cm^{-3} impurities. In the n-type samples with 10^{17} cm^{-3} impurities, the temperature dependence of the threshold current is weaker than that of 10^{18} cm^{-3} doped samples and the absolute values of the threshold current density are larger than that of heavily doped samples. A similar temperature dependence of threshold current was reported recently.[4]

The wavelength of laser emission shifted to longer wavelength with increasing temperature. The temperature dependence of photon energy above threshold is shown in Fig. 4 in which the change of the band gap of pure GaAs is also shown. The temperature dependence of the photon energy was slightly larger than that of the band gap.

Though the power of laser emission was not measured strictly, its temperature dependence was stronger than that of the threshold and the power decreased rapidly when the sample was heated above 200°K.

IV. DISCUSSION

At very low temperature the threshold current density of an electron-beam pumped laser is given by

$$J_{th} = 6.3 \times 10^{-3}\, n^2 E^2\, \Delta E(\alpha + \ln R^{-1}/L)\, \varepsilon_p d/\eta\, sV \quad (\mathrm{A/cm^2}) \tag{1}$$

where n, η, and R are the index of refraction, the internal quantum efficiency, and the reflectivity, respectively, E and ΔE are the photon energy at the peak of the spontaneous emission and the line width at half of maximum in eV respectively, α is the internal and diffraction loss in $\mathrm{cm^{-1}}$, ε_p is the pair creation energy (eV), d is the penetration depth (μ), and s is the energy fraction of penetrating electron and V the electron energy (keV).

At very low temperatures, the electrons completely occupy the states below the electron quasi-Fermi level F_e when the stimulated emission occurs. With increasing temperature the electrons distribute over a broader energy range above F_e, and additional electrons must be generated by increased excitation in order for a population inversion to be established.

In general, the density of electrons in the conduction band is represented by

$$n = 2 \int N(\varepsilon) f(\varepsilon)\, d\varepsilon \tag{2}$$

where $N(\varepsilon)$ is the density of state and $f(\varepsilon)$ is a Fermi-Dirac function. For a parabolic energy surface, n is given

$$n = 4\pi(2m^*/h^2)^{3/2} \cdot \int_0^\infty \frac{\sqrt{\varepsilon}\, d\varepsilon}{\exp[(\varepsilon - \varepsilon_f)/kT] + 1}$$

$$= 4\pi(2m^*kT/h^2)^{3/2}\, F(\varepsilon_f/kT) \tag{3}$$

where m^* is the conduction band effective mass, h the Plank's constant, k the Boltzmann's constant, T the absolute temperature, ε_f the Fermi energy measured from the bottom of the conduction band and the function $F(x)$ is defined by the integral

$$F(x) = \int_0^\infty \frac{\sqrt{t}\, dt}{e^{t-x} + 1}$$

In the p-type samples with 2×10^{18} and $2 \times 10^{17}\ \mathrm{cm^{-3}}$ impurities, the laser emission at 100°K occurred at 1.468 eV and 1.486 eV, respectively, which are smaller than the band-gap energy by 20 to 40 meV. This implies that the transition occurred from conduction band to acceptor level (or band). The density of electrons generated by the electron beam at the threshold is given by

$$N_{th} = 0.625 \times 10^{26} \, J_{th} \, \tau sV/\varepsilon_p d \quad (\mathrm{cm}^{-3}) \tag{4}$$

where τ is a radiative lifetime (about 10^{-9} sec), which is much longer than the thermal relaxation time of the electrons in the conduction band.

From (3), N_{th} is also represented as follows,

$$N_{th} = 4\pi(2m^*kT/h^2)^{3/2} \quad F(F_e/kT) \tag{5}$$

where F_e was the electron quasi-Fermi level for the metastable state under electron-beam excitation and the conduction band is assumed to be parabolic. The value of N_{th} at 100°K was calculated by substitution of the experimental value of J_{th} (at 100°K) for (4) and F_e was determined from (5). The following are parameters used in the calculation:

$$s = 0.8, \; \varepsilon_p = 4.6 \text{ eV}, \; d = 2.5 \; \mu, \; V = 27 \text{ keV}, \; m^* = 0.072 \; m_0$$

where m_0 is the free electron mass.

From (4) and (5), J_{th} is formulated as follows:

$$J_{th} = AT^{3/2} \quad F(F_e/kT) \tag{6}$$

By assuming that F_e is constant, the relation between J_{th} and T is calculated as shown in Fig. 2.

In n-type samples, the laser emission occurred at 1.488 eV for 10^{17} cm^{-3} doped samples, and this photon energy was almost the same energy as in the case of lightly doped p-type samples. This result implies that the transition occurs from a conduction band to a valence band through acceptor levels about 30 meV above the top of the valence band, which are formed by residual acceptor centers. In 10^{18} cm^{-3} doped n-type samples, the photon energy of laser emission was 1.492 eV. In this case, the transition occurs from upper states in the conduction band. The role of residual acceptors has been reported earlier.[6]

The total electron density in the conduction band at threshold is

$$n_{th} = n_0 + N_{th} \tag{7}$$

where n_0 is the electron density in equilibrium and N_{th} is the generated electrons, which are given by (4) and n_{th} is given by

$$n_{th} = 4\pi(2m^*kT/h^2)^{3/2} \; F(F_e'/kT) \qquad (8)$$

where the conduction band is also assumed simply to be parabolic. The value of N_{th} at 100°K is calculated by substituting the experimental value of J_{th} for (4), and n_0 is assumed to be equal to impurity concentration. The electron quasi-Fermi energy at 100°K is obtained from (8), which is measured from the bottom of the conduction band.

From (4), (7), and (8), J_{th} is formulated as follows:

$$J_{th} = AT^{3/2} \; F(F_e'/kT) - Bn_0 \qquad (9)$$

where

$$A = \frac{4\pi(2m^*k/h^2)^{3/2}}{0.625 \times 10^{26}} \frac{\varepsilon_p d}{\tau sV}$$

$$B = \frac{1}{0.625 \times 10^{26}} \frac{\varepsilon_p d}{\tau sV}$$

At higher temperature, n_{th} was calculated under the condition that the electron quasi-Fermi level is constant as in the case of the p-type samples. In this calculation, however, the value of F_e' used was reduced by about 30%, because the actual position of the quasi-Fermi level is depressed by the tail of conduction band states.[7] The difference of temperature dependence between a lightly doped and heavily doped sample is calculated from (9) as shown in Fig. 3.

V. CONCLUSION

The agreement between the calculated and the observed temperature dependencies of the threshold current is fairly satisfactory as shown in Figs. 1 and 2, and the slight differences between them might be attributed to the omission of the weak temperature dependency of F_e. It has been shown that the temperature dependency of the threshold current density of the electron beam excited laser was much weaker than that of the injection laser which is about T^3.

REFERENCES

1. G. C. Dousmain, H. Nelson, and D. L. Staebler, Appl. Phys. Letters 5: 174, 1964.
2. G. Lasher and F. Stern, Phys. Rev. 133: A553, 1964.
3. F. Stern, Phys. Rev. 148: 186, 1966.
4. O. V. Bogdankevich, N. A. Borisov, I. V. Krjukova, and B. M. Lavrushin, Proc. 9th Int. Conf. Phys. Semiconductor, Moscow, 1968; p. 575.
5. M. D. Sturge, Phys. Rev. 127: 768, 1962.
6. D. A. Cusano, Appl. Phys. Letters 15: 151, 1965.
7. J. I. Pankove, Phys. Rev. 140: A2059, 1965.

ELECTRON BEAM PARAMETERS FOR PUMPING SEMICONDUCTORS TO MULTIMEGAWATT STIMULATED LIGHT LEVEL

J. L. BREWSTER

Field Emission Corporation, McMinnville, Ore.

Stimulated light outputs of 10, 2.5, and 2 MW, with corresponding pulse half-widths of 2, 9, and 18 ns, have been obtained by electron pumping large-area semiconductor targets. The effect of beam parameters such as kilovoltage, current density, and pulse duration on semiconductor output and life is discussed. Choice of semiconducting materials and beam energy depends on end applications such as fluorescent decay measurements, flash photography, or flash photolysis.

Successful electron beam-pumped semiconductor lasers were first reported in 1964, for CdS,[1,2] InSb,[3] and InAs.[3,4] Such lasers have the advantages of very high output per unit volume, fairly high efficiency and wavelength choice--by selection of the proper compound or alloy--from UV to IR. As a result, extensive investigations[5-7] have been conducted by several groups. Several types of laser diodes are produced commercially, but with power levels and wavelengths not suitable for some applications such as photography. The cathodes and accelerating configurations in most electron-beam systems have limited peak currents and current densities. As a result, electron-pumped lasers have apparently been confined to laboratory studies. This paper presents data showing stimulated, although not true laser, emission at substantially higher levels, using several commercially available electron accelerators.

The very simple technique, shown in Fig. 1, involves fastening the semiconductor crystals to an electron-transparent support foil. This assembly is then placed directly over the electron tube output window of the accelerator, at room temperature. We recently reported[8] research data as shown in Fig. 2 for CdS platelets,[9] indicating an efficiency of about 1 per cent at room temperature. The current density was varied over the range indicated by simply changing the tube-to-sample spacing. The 3-ns accelerator[10] was pulsed, recording light output with a planar photodiode and traveling-wave oscilloscope. The initial steep slope, at low current densities, is characteristic of the transition from fluorescent to stimulated emission. The subsequent linear region has an efficiency of about 1 per cent, consistent with the room-temperature reported value of Nicoll.[11] The platelet did not have parallel (Fabry-Perot reflector) surfaces, and consequently the output was noncoherent and approximately isotropic.

The peak output of 200 kW thus obtained, with only a small portion of the beam area used, suggested the source design of Fig. 3. Many small semiconductor crystals are attached to a reflective aluminum foil window with clear plastic. Such sources have proven highly uniform in brightness, with typical large-area-source Lambert's-law radiation pattern.

Sources of this type have been used on several systems. Figure 4 shows

Record of 10th Symposium on Electron, Ion, and Laser Beam Technology (L. Marton, ed.); San Francisco Press, Inc.

Copyright © by The Institute of Electrical and Electronics Engineers, Inc.—Printed in the U.S.A.

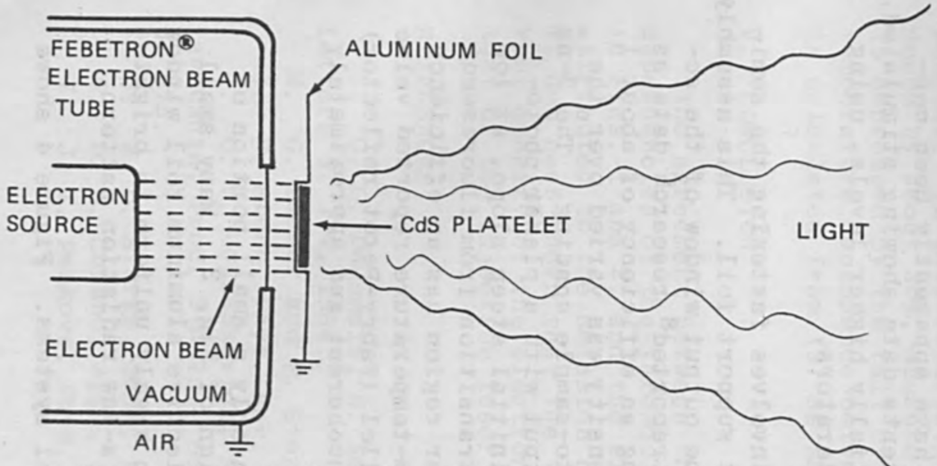
FEBETRON®
ELECTRON BEAM
TUBE
ALUMINUM FOIL
ELECTRON
SOURCE
CdS PLATELET
LIGHT
ELECTRON BEAM
VACUUM
AIR

FIG. 1.—Schematic indicating semiconductor mounting and excitation method.

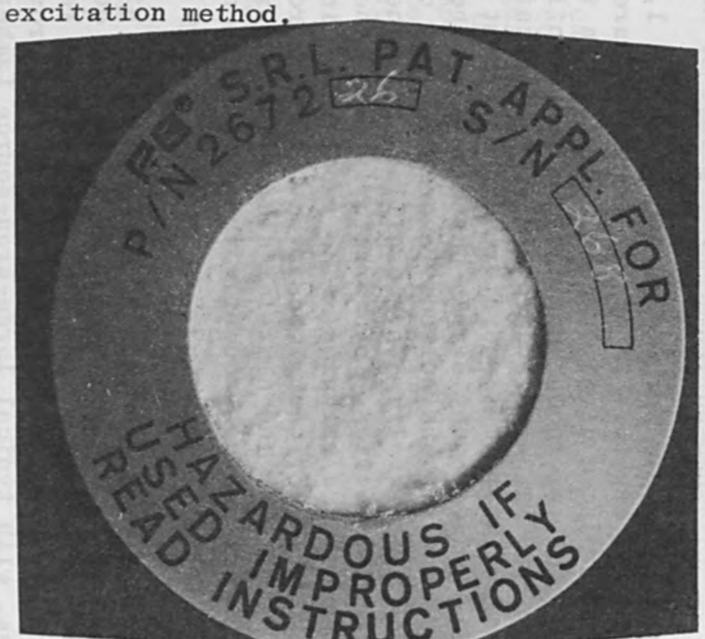
P/N 2672
S.R.L. PAT. APPL. FOR
S/N
HAZARDOUS IF
USED IMPROPERLY
READ INSTRUCTIONS

FIG. 3.—Photograph of multiple-crystal semiconductor source.

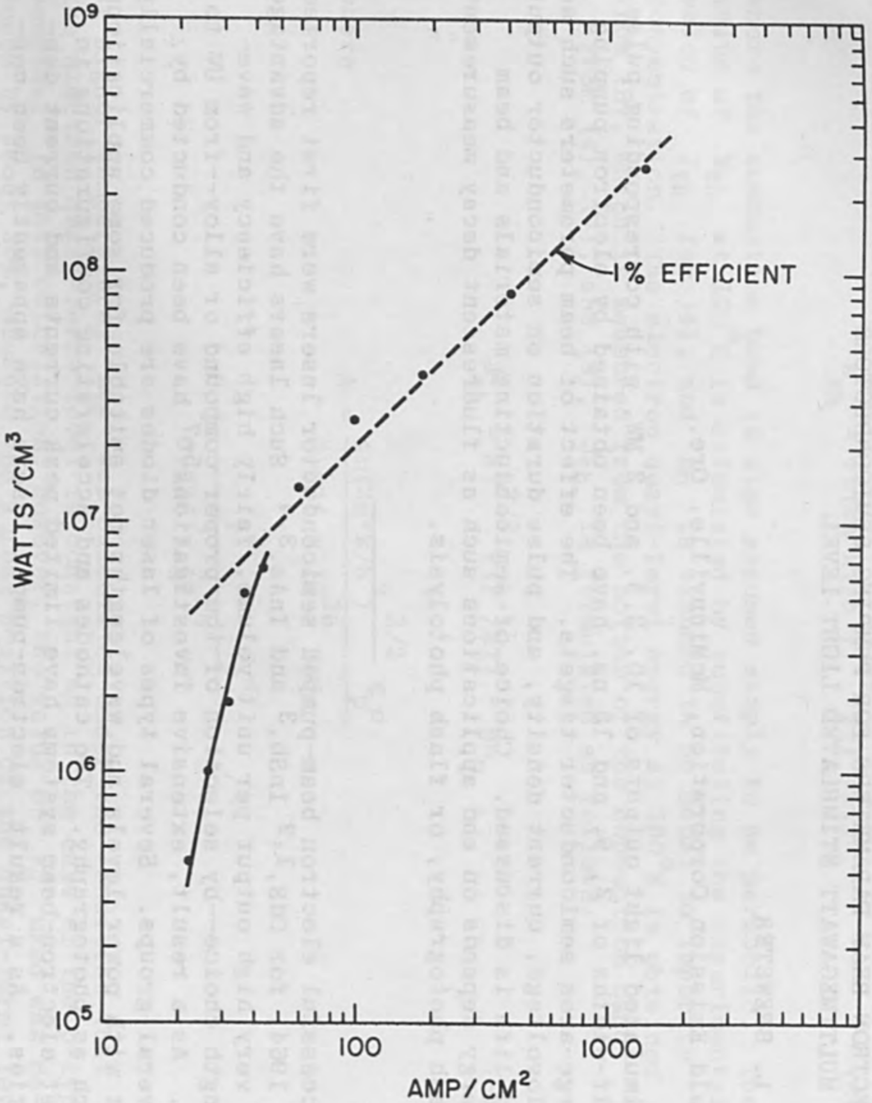

FIG. 2.—Specific light output of CdS crystal vs current density, at room temperature.

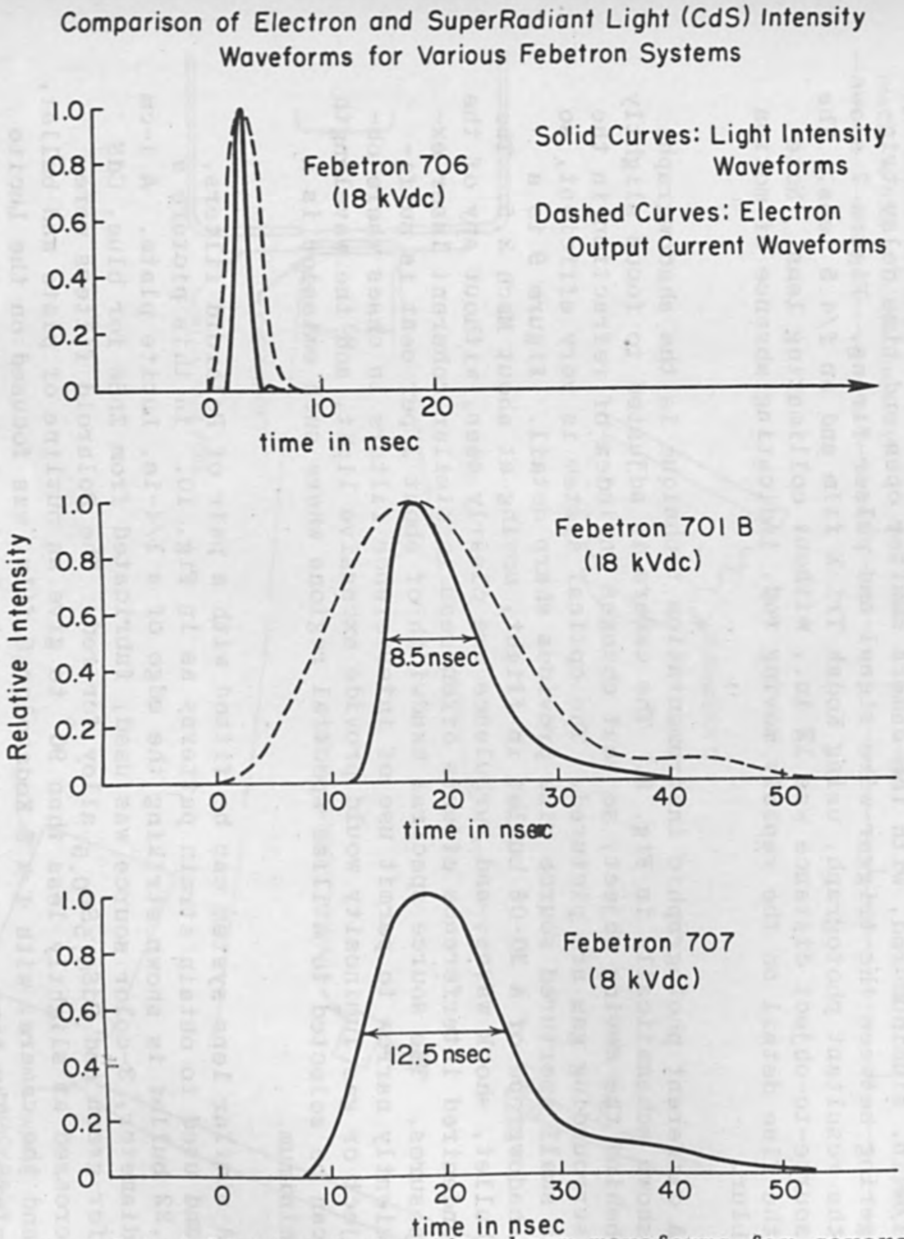

FIG. 4.—Stimulated light and exciting beam waveforms for several systems.

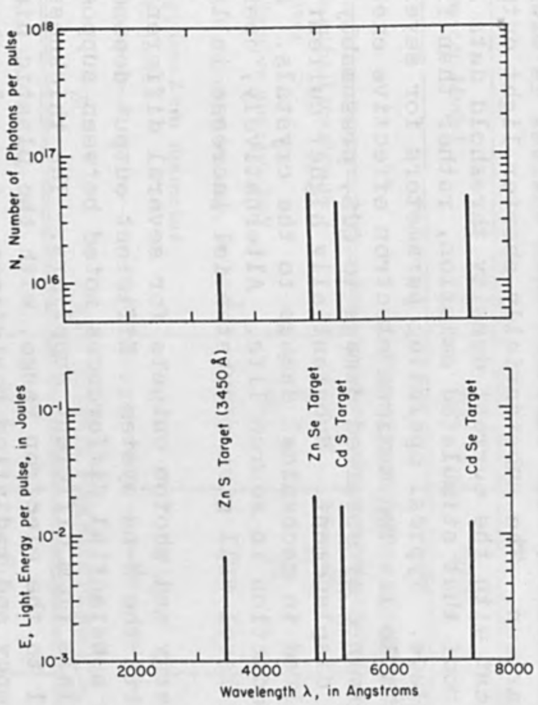

FIG. 5.—Output of several semiconductor compounds for 3-ns system.

typical light output waveforms, with electron-beam current waveforms superimposed for comparison. The substantially shorter light output durations are consistent with the current density threshold data shown previously, further proof that stimulated emission, rather than fluorescence, is taking place. Typical operating parameters for several systems are shown in Table I. The maximum electron effective energy of about 380 keV is determined by observed damage to CdS, presumably a result of cadmium ion displacement. Substantially higher current density loading has also resulted in mechanical damage to the crystals. Either will give a sizable reduction in source life. Alternatively, operation at a slightly reduced level will give a substantial increase in life.

Figure 5 shows the energy and photon outputs for several different materials, obtained with the 3-ns system. Efficient output depends on material purity, with substantial differences noted between supposedly the same purity materials from different suppliers. The thickness should be approximately equal to the electron range, with the plastic binder selected for transparency and radiation resistance. Several other materials have been used, giving different wavelengths, including semiconductor alloys.

The light outputs are sufficient for direct photography. Figure 6 is a schematic for such an application. A .22 caliber bullet is shot at a 1/4-in. aluminum rod, with the camera shutter open and time delay triggering between the trigger-wire signal and pulser firing. Figure 7 shows the resultant photograph, using Kodak Tri-X film and an f/4.5 lens. The source-to-object distance was 12 in., without collimating lens. Note the fine detail on the rapidly moving rod, indicating absence of motion blur.

A different photographic instrumentation technique is the shadowgraph, shown schematically in Fig. 8. The camera is adjusted to focus slightly behind the moving object, so that changes in index of refraction in the surrounding gas are pictured. The optical system is very efficient, so a small apertured source size provides sharp detail. Figure 9 is a shadowgraph of a 30-06 bullet in flight, moving at about Mach 2.5. The bullet, shock waves, and turbulence are clearly seen, without any of the undesired interference effects often seen in similar coherent laser exposures. The source spectral bandwidth of about 1 per cent is sufficiently narrow to permit use of interference filters in cases where object or gas luminosity would provide excessive light, and the wavelength can be selected to utilize spectral regions where such emission is a minimum.

A similar lens system can be fitted with a pair of Polaroid filters, and used to obtain strain patterns as in Fig. 10. In this picture a .22 bullet is shown striking the edge of a 1/4-in. Lucite plate. A 1-cm diameter, 3-color source was used, fabricated from ZnSe for blue, CdS for green and $CdS_{0.5}Se_{0.5}$ alloy for red. The Polaroid filters were crossed at slightly less than 90° to give an outline of plate and bullet, and the camera, with 4 X 5 Kodacolor S film, was focused on the Lucite plate. The three exposures are separate tests, with slightly different delay time settings. Since the velocity of sound in plastic is faster than the speed of the .22 caliber bullet, the shock waves are well in

TABLE I.—Table of several electron-beam and CdS light parameters for four systems.

Febetron Model	706	701B	707	705
ELECTRON BEAM PARAMETERS				
Pulse width at half maximum intensity, nsec	3.5	17.5	Approx. 30	Approx. 45
Electron effective energy, keV	380	370	370	400
Approx. peak current density, A/cm^2	800	230	150	280
Beam energy into 2 cm diameter SRL source, joules	3	5	6	18
SRL OUTPUT PARAMETERS FOR CdS				
Pulse width at half maximum intensity, nsec	1.4	8.5	12.5	18
Peak power, megawatts	8.6	2.6	1.33	2.0
Total output, joules	.015	.024	.020	.046
Peak source brightness, megastilbs	500	160	80	120
Approximate life, in pulses (decay to 65% of initial intensity)	400	400	200	100

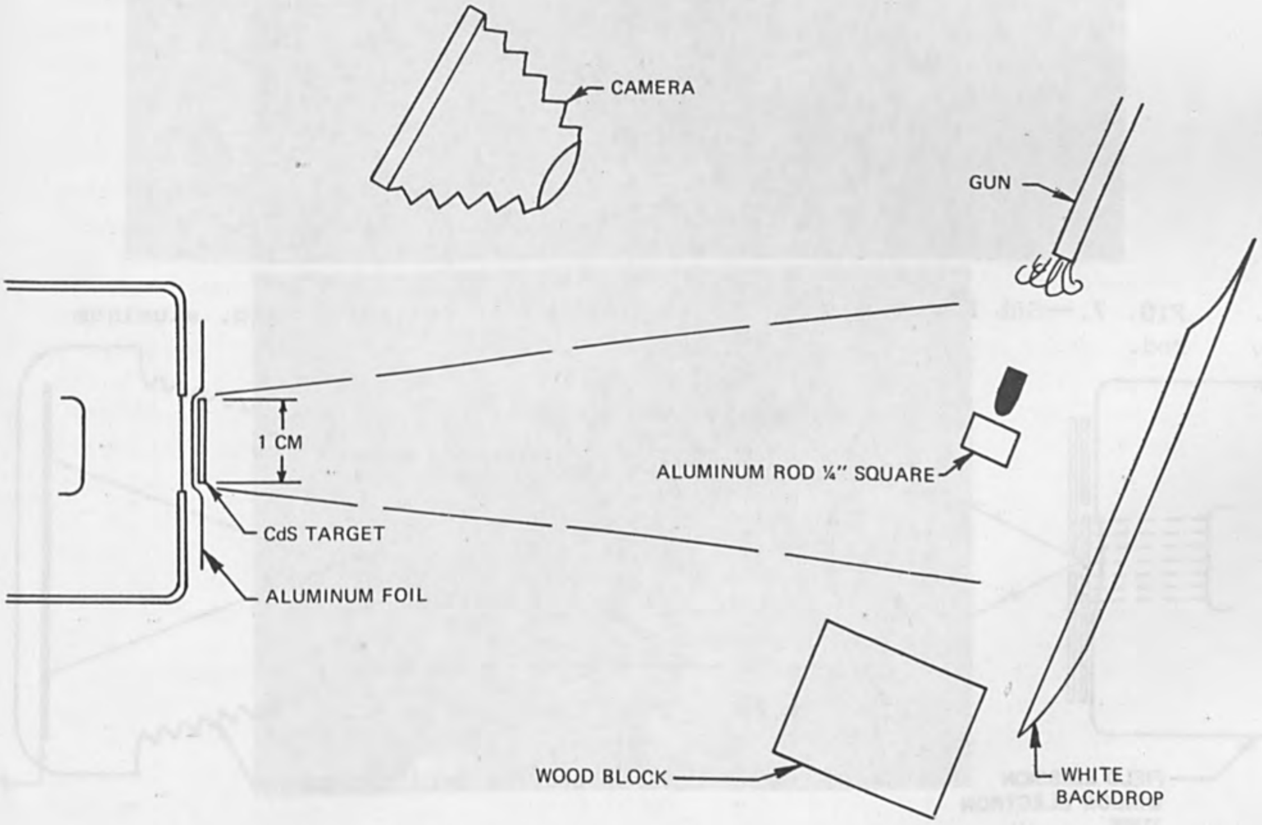
CAMERA
GUN
1 CM
ALUMINUM ROD ¼" SQUARE
CdS TARGET
ALUMINUM FOIL
WOOD BLOCK
WHITE BACKDROP

FIG. 6.—Schematic indicating direct photography technique.

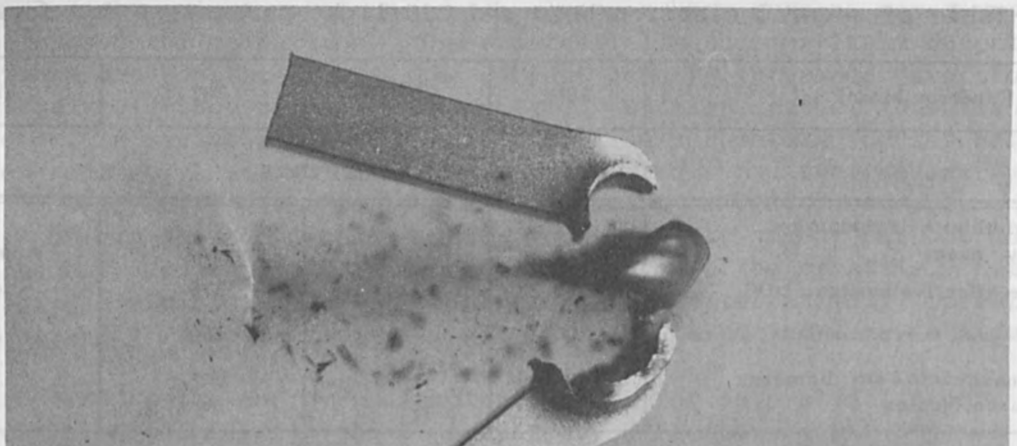

FIG. 7.—SRL Photograph of .22 caliber bullet cutting 1/4-in. aluminum rod.

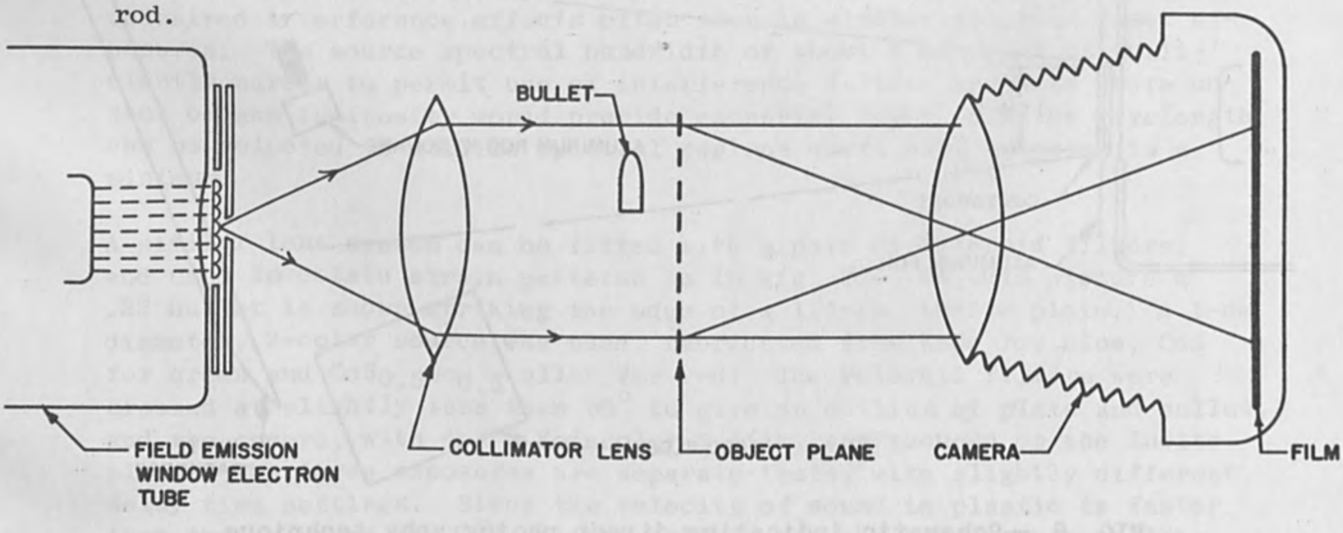
BULLET
FIELD EMISSION WINDOW ELECTRON TUBE
COLLIMATOR LENS
OBJECT PLANE
CAMERA
FILM

FIG. 8.—Schematic indicating shadowgraph technique.

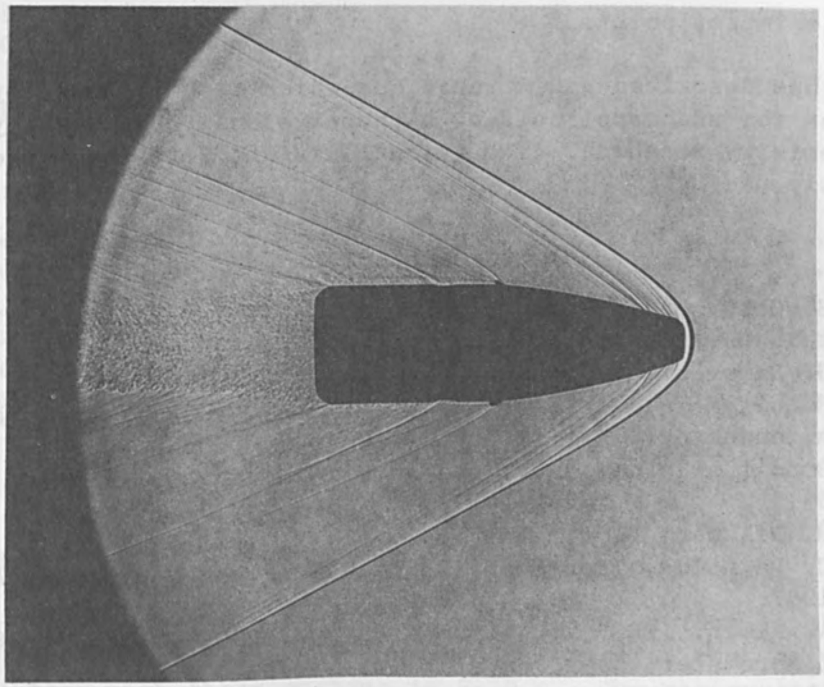

FIG. 9.—Shadowgraph of 30-06 bullet in flight.

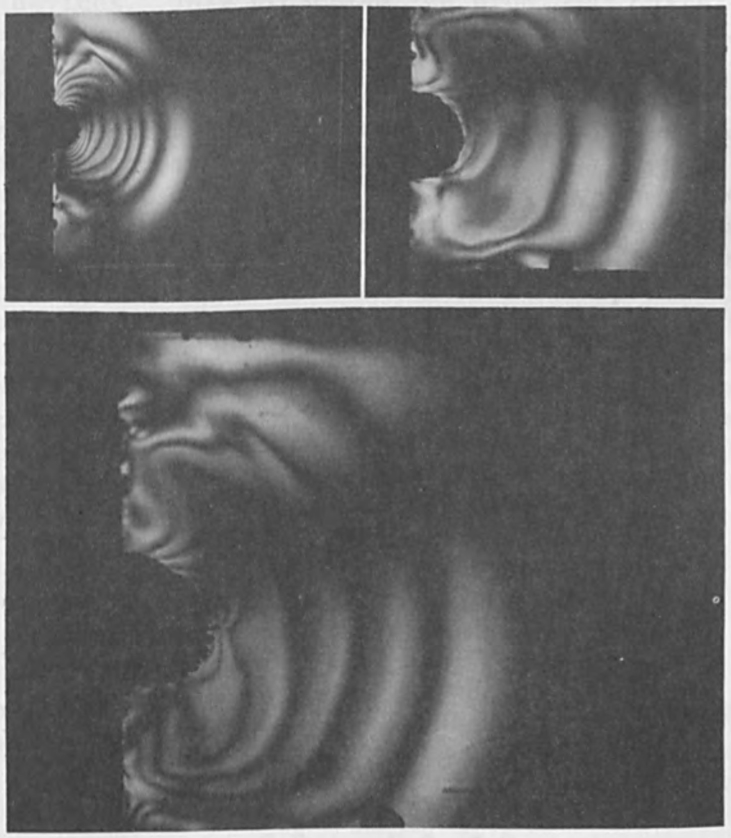

FIG. 10.—Crossed Polaroid color stress wave photograph of .22 caliber bullet entering 1/4 X 2 X 2-in. Lucite plate.

front of the impact point.

This paper has described a new technique which is being used by several laboratories for such applications as hypervelocity photography and radiation chemistry research. The versatility and intensity levels are significantly useful.

REFERENCES

1. N. G. Gasov and O. V. Bogdankevich, Radiative Recombination in Semiconductors, Paris: Dunod, 1964; p. 225.
2. N. G. Basov et al., Sov. Phys.-Doklady 9: 288, 1964.
3. C. Benoit à la Guillaume and J. M. Debever, Radiative Recombination in Semiconductors, Paris: Dunod, 1964; p. 255.
4. C. Benoit à la Guillaume and J. M. Debever, Solid State Comm. 2: 145, 1964.
5. M. H. Pilkuhn, Phys. Stat. Sol. 25: 9, 1968.
6. D. C. Reynolds, Trans. of the Metallurgical Society of AIME, 239: 300, 1967.
7. C. A. Klein, IEEE J. Quantum Electronics QE-4: 186, 1968.
8. J. L. Brewster, Appl. Phys. Lett. 13: 385, 1968.
9. Supplied by D. C. Reynolds of Wright-Patterson AFB, Ohio.
10. J. L. Brewster et al., Proc. Nat. Elect. Conference 23: 737, 1967.
11. F. H. Nicoll, Appl. Phys. Lett. 10: 69, 1967.

LASER PROBE FOR CHARACTERIZATION OF SEMICONDUCTOR SURFACE STATES

L. A. KASPRZAK

IBM Corp. (Components Division), East Fishkill, N. Y.

A system is described for the measurement of the surface photovoltaic response of semiconductor devices as a function of position on the device surface. A laser is used for the excitation of the surface carriers. The system has been used to measure minority carrier lifetimes and the location of surface inversion layers. It can also be used to measure conductivity gradients, work functions of metal-semiconductor contacts and bulk lifetimes.

INTRODUCTION

A number of investigators[1-4] have constructed systems capable of displaying photoresponses of semiconductor devices. The maximum attainable resolution with these systems is 5-10 μ. The photovoltaic effect[5] is the source of information for all of these systems, as it is for the system described below. Our particular application for such a system required a resolution of 1 μ or less, as well as the ability to study "passivated" devices. This presented two problems: first, the optics would be critical; and second, the signal level would be very low and buried in noise. The selection of a laser as a source of illumination simplified the optics. A Pockel's cell was chosen to amplitude modulate the laser beam intensity, thereby producing a photoresponse at the amplitude modulation frequency of the Pockel's cell. A lock-in amplifier, with a reference input at the amplitude modulation frequency, is used to amplify the photoresponse to the desired level and reject all noise.

The photoresponse of a P-N junction is explained in terms of a photovoltage which arises when carriers are generated near the junction, for example, by illumination. The nonequilibrium minority carriers are swept across the high field junction region and cause an external voltage drop across the device. If the area of illumination is restricted to a spot, and a path normal to the junction selected, a photoresponse of the surface is obtained that is similar to that shown in Fig. 1. This photoresponse leads directly to a measure of the diffusion length[6] of the surface minority carriers ($L_{n,p}$).

$$V(x) = V(0)\, e^{-|x|/L_{n,p}} \tag{1}$$

The diffusion length, mean lifetime ($\tau_{n,p}$), and diffusion constant ($D_{n,p}$) are related as follows:

$$L_{n,p} = \sqrt{D_{n,p}\, \tau_{n,p}} \tag{2}$$

Record of 10th Symposium on Electron, Ion, and Laser Beam Technology (L. Marton, ed.); San Francisco Press, Inc.

Copyright © by The Institute of Electrical and Electronics Engineers, Inc.—Printed in the U.S.A.

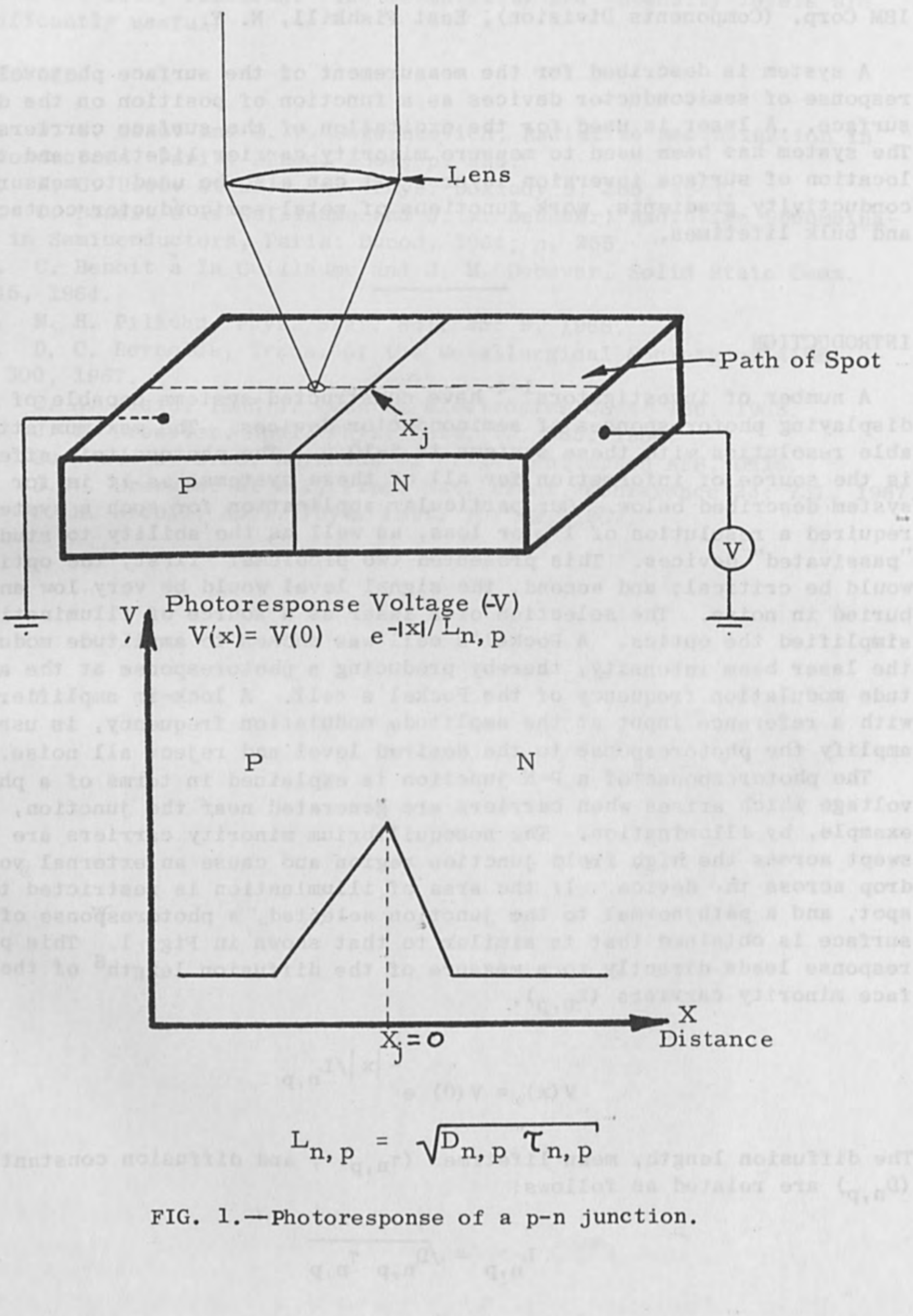
Lens
Path of Spot
X_j
P
N
V
Photoresponse Voltage (-V)
V(x)= V(0) e^{-|x|/L_{n, p}}
V
P
N
X
Distance
X_j = 0

$$L_{n, p} = \sqrt{D_{n, p}\, \tau_{n, p}}$$

FIG. 1.—Photoresponse of a p-n junction.

If one now measures $L_{n,p}$ and knows either $\tau_{n,p}$ or $D_{n,p}$ the other can be readily determined. The photovoltaic effect can also be used to measure conductivity gradients, work functions of metal-semiconductor contacts, and the location and characteristics of surface inversion layers.

PHYSICAL ARRANGEMENT OF LASER PROBE

A schematic diagram of the physical arrangement of the laser probe is shown in Fig. 2. A collimated beam from a 6328-Å cw (He-Ne) laser is initially polarized (P_1). The beam then passes through a Pockel's cell and an analyzer (P_2). The function of the Pockel's cell is to rotate the plane of polarization of the beam as a function of the voltage applied to its terminals. Thus the amplitude of the light emerging from the analyzer can be controlled. The rise time of the Pockel's cell employed is less than 10 ns. Therefore, the Pockel's cell can be used to generate amplitude modulated light at amplitude modulation frequencies into the megahertz range. The Pockel's cell can also be used to generate pulses of light.

The beam next passes through a 48-mm focal length lens positioned 48 mm from a mirror used to reflect the beam through 90° into a microscope ocular. Finally the beam is focused to a 1-μ spot on the device under investigation by a 500X, 0.85 numerical aperture, microscope objective.

The device to be studied is mounted on a scanning stage modified to move in y-increments of 1 μ. The scanning stage moves in a raster beneath the microscope objective to effectively move the spot in a raster over the device surface. The area of the raster thus generated is controlled by microswitches on the scanning stage. The position of the spot is monitored by sliding pot resistors mounted on the sides of the scanning stage as shown in Fig. 2. The voltages from these pots generate a raster on an oscilloscope screen.

The signal from the device is

$$V(x,t) = V(0)e^{-|x|/L_{n,p}} \left|\sin 2\pi ft\right| \qquad (3)$$

where

x = distance from a junction, and
f = amplitude modulation frequency.

This signal is amplified by a lock-in amplifier whose reference frequency is the same as the amplitude modulation frequency of the Pockel's cell. This is accomplished by driving the wave amplifier for the Pockel's cell and the lock-in amplifier reference input by a common small signal wave generator. The end result is that the signal from the device at the amplitude modulation frequency is amplified and all noise is rejected. This complete noise rejection allows very low signals to be measured (nanovolt range). The amplified signal is used to intensity modulate the raster on the oscilloscope thereby generating a TV-like picture of the photovoltage response of a given area of the device. The

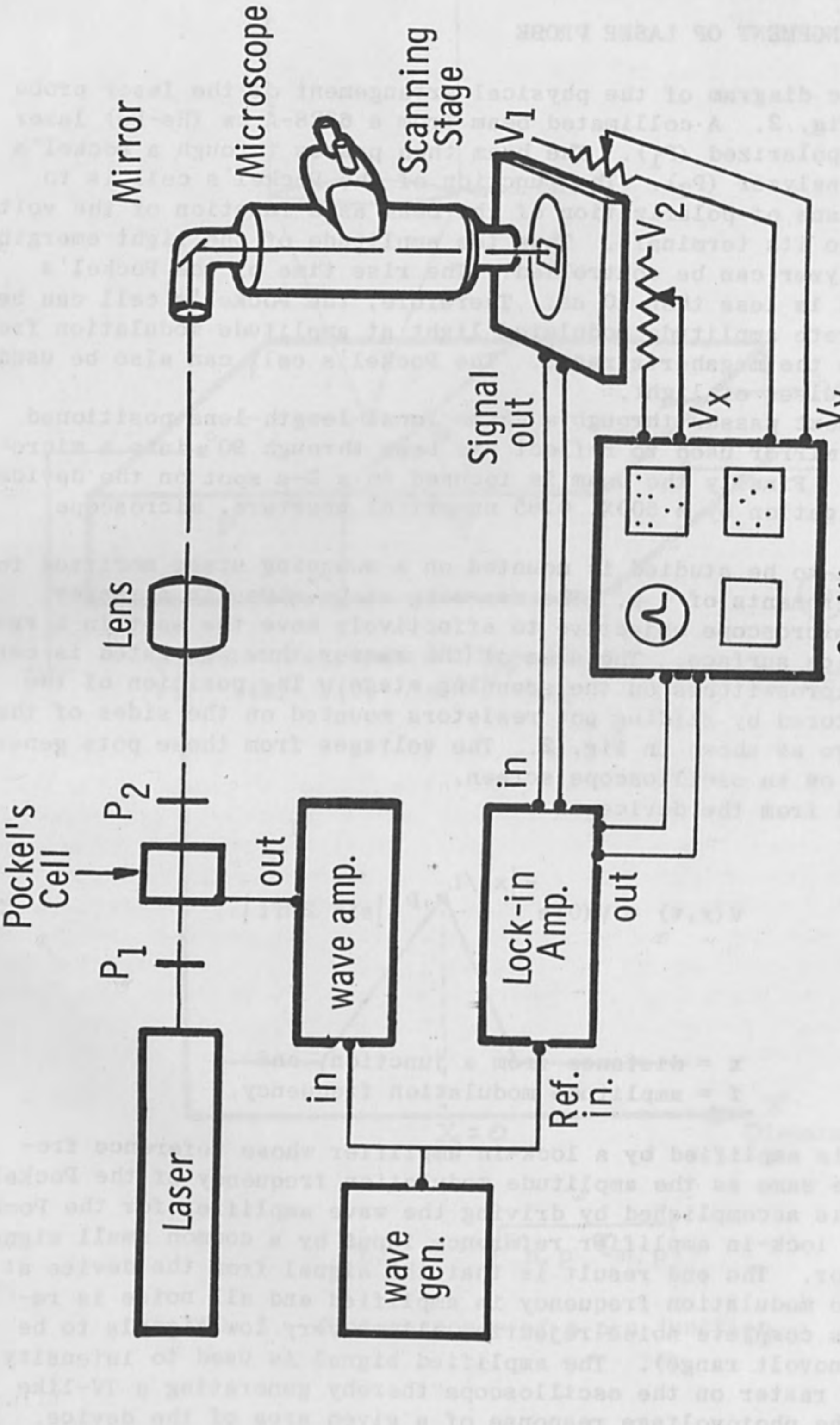
Wave gen.
Laser
in
wave amp.
out
P$_1$
Pockel's Cell
P$_2$
Lens
Mirror
Microscope
Scanning Stage
V$_1$
V$_2$
Signal out
V$_x$
V$_y$
Oscilloscope
Ref. in.
Lock-in Amp.
out
in

FIG. 2. —Schematic diagram of laser probe.

signal can also be used to generate sequential line scans, which results in a quantitative three dimensional topograph of the photoresponse as a function of position on the device surface. When necessary, single line scans can also be generated. Finally, if the spot is kept stationary the waveform of the device output can be measured.

APPLICATIONS

The very first application of the system was in mapping (by use of sequential line scans) the normal surface photovoltaic response of a typical transistor (Fig. 3). The response of the device (Fig. 4) was as expected, i.e., the junctions (collector-base and emitter base) responded as P-N junctions. The same device was also displayed in the intensity modulation mode (Fig. 5).

A similar transistor (Fig. 6) with a slightly inverted curve-tracer characteristic was scanned using intensity modulation (Fig. 7). Area A in Fig. 7 was identified as suspicious and a sequential line scan was generated (Fig. 8). The inverted area was clearly discernible. As can be seen in the single-line scan (Fig. 9), Area A did indeed have an abnormally high photoresponse. The effect of the amplitude modulation frequency and scanning speed can be seen in Fig. 9, where the photoresponse of the collector-base junction is seen to be non-Gaussian. This curvature at points P on Fig. 9 is due to long lifetime surface minority carriers, which could not reach equilibrium with a scanning speed of 16 mil/sec and an amplitude modulation frequency of 10 kHz. The amplitude modulation frequency must be an order of magnitude or so slower than the minority carrier lifetimes. Also the scanning speed must be selected such that the spot does not move appreciably during one cycle of amplitude modulation. Unfortunately the minority carrier lifetimes are not known before the fact.

This sensitivity of the system to carrier lifetime can be used to separate responses with respect to the lifetime of the carriers. For example, if the amplitude modulation frequency is zero and the scanning speed is very slow, minority carriers of all lifetimes present should be able to respond and contribute to the photoresponse. Now as the amplitude modulation frequency and scanning rate are increased, the response of the slower states eventually washes out and only the response due to the fast carriers is observed.

Finally, the lifetime[7,8] of the minority carriers at a given position on the device can be measured directly by applying a square pulse or wave across the Pockel's cell, and measuring the waveform of the device response (Fig. 10).

$$V(t) = V(x)_{\max}[1 - e^{-(t-t_0)/\tau_{n,p}}] \qquad t_0 < t < t_1 \qquad (4)$$

$$V(t) = V(x)_{\max}e^{-(t-t_2)/\tau_{n,p}} \qquad t_1 < t < t_2 \qquad (5)$$

The laser illuminates the area from $t = t_0$ to $t = t_1$ and the illumination is turned off from $t = t_1$ to $t = t_2$. The rise time of the input

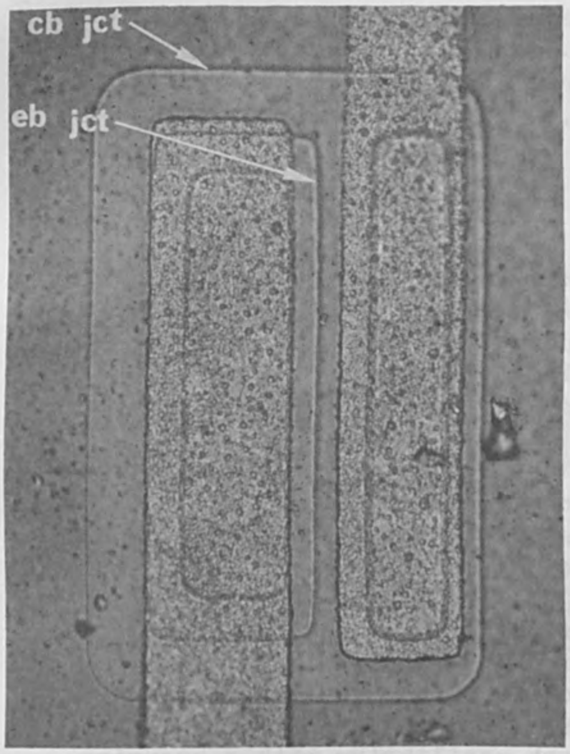

FIG. 3.—Typical transistor (500 X).

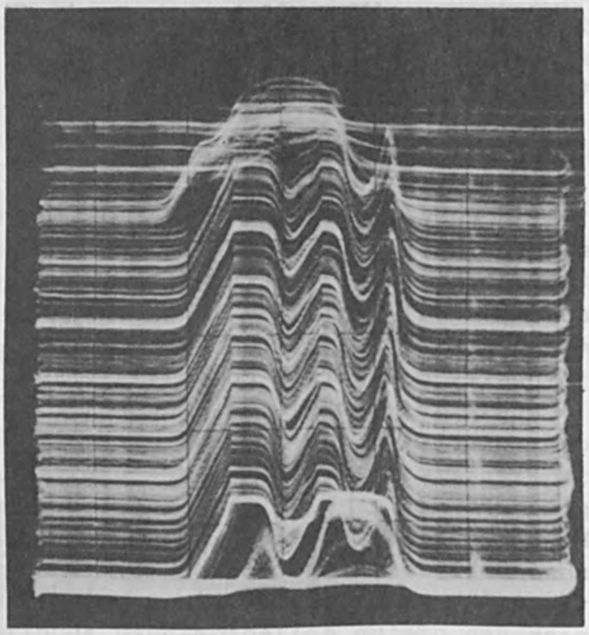

FIG. 4.—Sequential line scans of transistor in Fig. 3 (≈ 300 X).

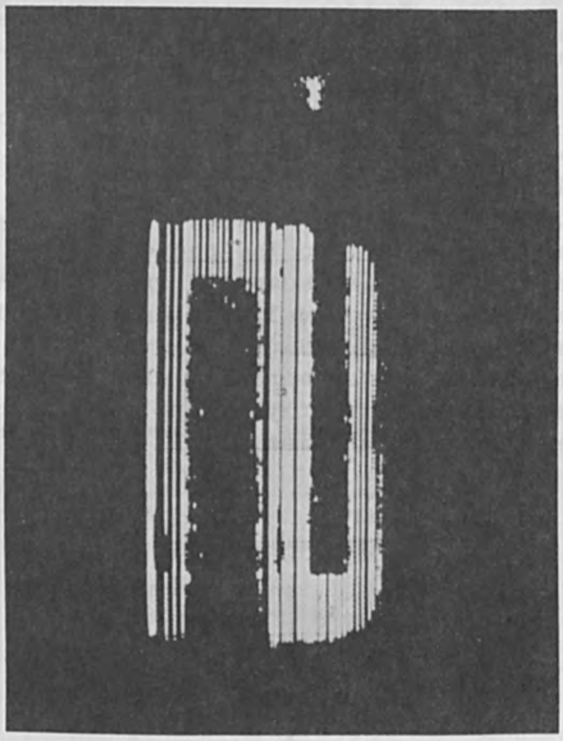

FIG. 5.—Intensity-modulation scan of transistor in Fig. 3 (≈ 300 X).

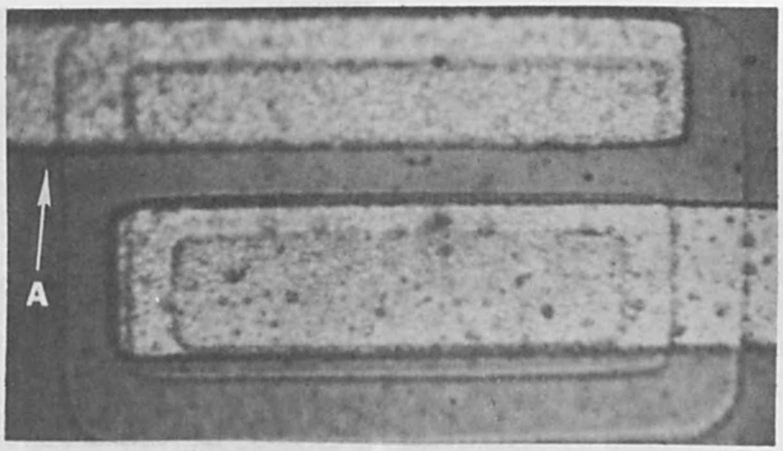

FIG. 6.—Typical transistor (500 X).

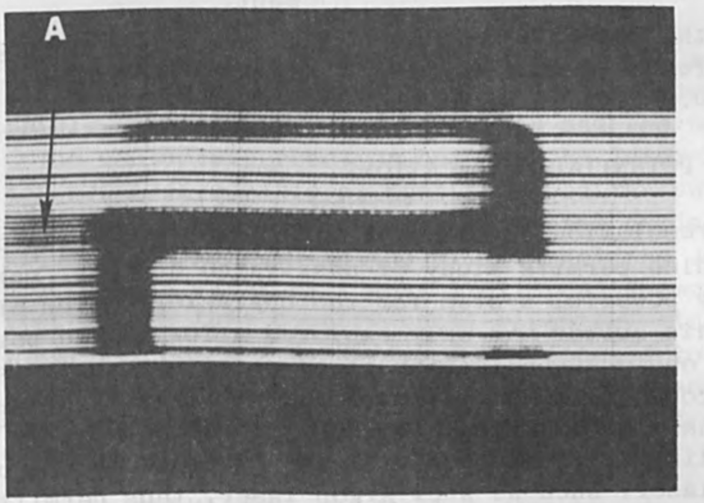

FIG. 7.—Intensity-modulation scan of transistor in Fig. 6 (≈ 300 X).

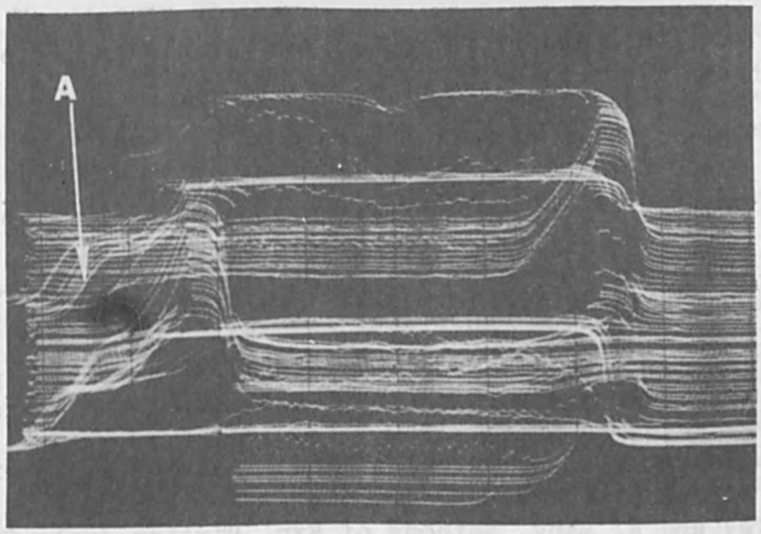

FIG. 8.—Sequential-line scans of transistors in Fig. 6 (≈ 300 X).

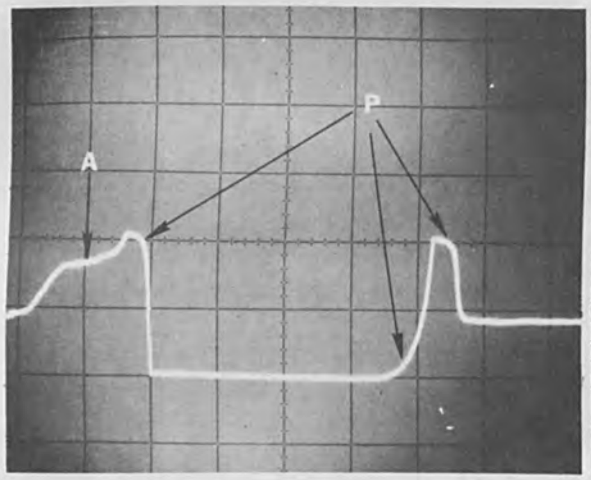

FIG. 9.—Single-line scan of Line A, Fig. 6.

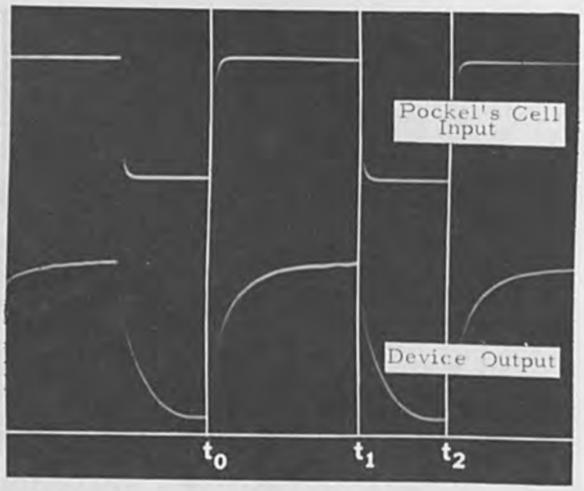

FIG. 10.—Typical lifetime measurement.

voltage to the Pockel's cell must be a few orders of magnitude faster than the lifetime of the carriers. The lifetime of the carriers in Fig. 10 is 0.85 msec.

SUMMARY AND POTENTIAL APPLICATIONS

The 1-μ resolution coupled with the laser as source of excitation of carriers, which permits study of passivated devices, makes the laser probe a very powerful system for the characterization of semiconductor devices. This author has only explored a few of the possible applications. The obvious application is as a failure analysis tool. However, the system could be used to experiment with any light sensitive devices and phenomena; for example, localized photoconductivity measurements. The versatility of the system could be enhanced by the use of a multiple-wavelength laser, such as a cw argon laser, thus permitting measurement of parameters which depend upon wavelength.

ACKNOWLEDGMENTS

I should like to thank Mr. J. Greco for his aid in the physical construction of the laser probe.

REFERENCES

1. C. N. Potter and D. E. Sawyer, Physics of Failure in Electronics Conf. 1966.
2. J. R. Haberer, ibid.
3. J. Tihanyi and G. Pasztor, Solid State Electronics, 20: 235-239, 1967.
4. R. A. Summers, Solid State Technology, March, 1967, p. 12.
5. J. J. Loferski and P. Rappaport, Methods of Exp. Physics (vol. 6B), New York: Academic Press, 1959.
6. C. Munakata, Microelectronics & Reliability, 5: 267-270, 1966.
7. Shyh Wang, Solid State Electronics, New York: McGraw Hill, 1966.
8. R. Bray and A. Many, Methods of Exp. Physics (vol. 6B), New York: Academic Press, 1959.

SOME NOVEL APPROACHES IN THE UTILIZATION OF LASERS IN MATERIALS PROCESSING

R. B. BARBER and D. L. LINN

Laser Systems Corp., Ann Arbor, Mich.

Since their conception, lasers have held great promise, especially to some of us, as machine tools. But as with most new discoveries, the step from laboratory curiosity to production line tool has been a slow one. Recent reports in industry journals[1] and in conferences such as this one[2] make it clear, however, that lasers are now being successfully used as economical materials processing machines.

The purpose of this paper is to discuss some techniques which we have found significantly increase the potential of lasers for cutting and machining.

Considerable attention, including ours, has been directed toward the use of an auxilliary gas jet, in conjunction with continuous-wave lasers used to cut materials. The gas is usually oxygen and the materials are usually metals. The exothermic reaction between the laser-heated metal and the oxygen jet provides additional heat to speed the cutting process, and the jet also acts to eject molten metal and metal oxides from the cut. This technique was described in the British Welding Journal by Sullivan and Houldcroft as early as August 1967,[3] but seems not to have received much attention in this country until recently. In that early article a 300-W, ac, 100-Hz, CO_2-N_2-He laser was focused to a 0.016-in.-diameter spot and oxygen was delivered from a 1/10-in.-diameter co-axial nozzle to produce cuts with 0.020-in. kerf, at the rate of 40 IPM in 0.10-in.-thick steels.

An extremely narrow (0.003-in.) heat-affected zone was produced, and the focused diameter of the laser beam was found to do more to determine the width of the cut than did the oxygen flow.

Recently a pulsed CO_2 laser in our laboratory has achieved cutting rates of 24 in. per minute in steels of various thicknesses and up to 400 IPM in 0.036-in.-thick titanium alloy sheet. This latter figure is all the more interesting when one considers that for a pulse rate of 250 pps, succeeding focused pulses are separated by as much as 2.5 spot diameters, with the oxygen jet carrying the cut along between.

With the oxygen the kerf in titanium was 0.060 in. and the heat-affected zone was 0.010 in. wide (not optimum conditions); whereas without the oxygen, kerf was 0.008 in. (focal-spot diameter) but with 0.015 in. HAZ. Without the oxygen jet, the cutting rate for titanium was 12 IPM.

Of the many things happening at once as a given metal is being cut by the oxy-laser method, the most interesting process is that of oxidation. The list in Table I compares heats of formation of the oxides of several metals. Certainly other quantities are also important: heat of fusion, heat of vaporization, thermal conductivity, etc.; but a rough correlation exists between the exothermic heat of oxide formation and the

Record of 10th Symposium on Electron, Ion, and Laser Beam Technology (L. Marton, ed.); San Francisco Press, Inc.

Copyright © by The Institute of Electrical and Electronics Engineers, Inc.—Printed in the U.S.A.

cutting rate, as seen here for the cases of iron and titanium mentioned.

We have also had considerable success using oxygen-jet assist to drill individual holes in metal parts of irregular thickness. Here, the oxygen serves not only as a producer of heat energy in bringing the hole to the desired size and depth consistently, but also serves to keep the hole clear of debris and speeds cooling. Splattered material tends to be in the form of surface-oxidized beads which do not bond strongly to the surrounding metal, facilitating clean-up of the finished part.

Along with the earlier investigators, we find that there is a definite minimum rate of clean cutting, which is a function of the material, the laser beam power, the focusing optics, and the oxygen delivery system. All our successful oxygen-delivery nozzles have had a small-diameter orfice (around 1/10 in.) located co-axially with the focused laser beam, and operated at moderate pressures (10-30 psi).

The second novel approach to materials processing involves a special optical device which increases the size of holes that may be drilled, or circles that may be heated or welded with a laser. A conventional lens system can focus a laser beam to a very small spot, ranging from microns to perhaps 0.025-in. in diameter, depending on focal length, beam divergence of the laser, and laser wavelength. But most applications involve much larger diameters.

This deficiency in capability has been the source of several ingenious and, usually, expensive techniques, including rotating the work beneath the laser, rotating an offset laser beam above the work, and using an x-y controlled work platform programmed for circles and special toroidal lenses. All these methods have their particular shortcomings, primarily that of expense, and engineers tend not to design parts with these processes in mind.

The device we have developed as a solution to this problem is not entirely new to the optics industry and is known somewhat descriptively as an axicon. It usually consists of an element having a conically ground and polished upper surface, and a flat lower surface, although other configurations are possible.

Taken in cross section (Fig. 2), the axicon is seen to be an afocal device which deviates parallel light through a fixed angle with respect to the system axis, in the manner of a Fresnel biprism, but with circular symmetry.

The system is completed with the addition of a conventional positive lens, whose function is to bring all parallel rays to the same focus. Parallel rays entering a lens at an angle are focused at a point off the axis, so that the resulting focused pattern is that of a ring rather than a disk. When this device was first used in this way in our laboratory, its utility was limited by available laser energy, but this problem has been greatly alleviated with the advent of high-power gas lasers which may have output beams of large diameter and of relatively uniform intensity.

TABLE I.—Heats of formation of various metallic oxides.

	Δ H (kcal/mole)
Copper	38 - 44
Nickel	58 - 59
Iron	60 - 277
Chromium	141 - 142
Titanium	125 - 586
Vanadium	299 - 1076

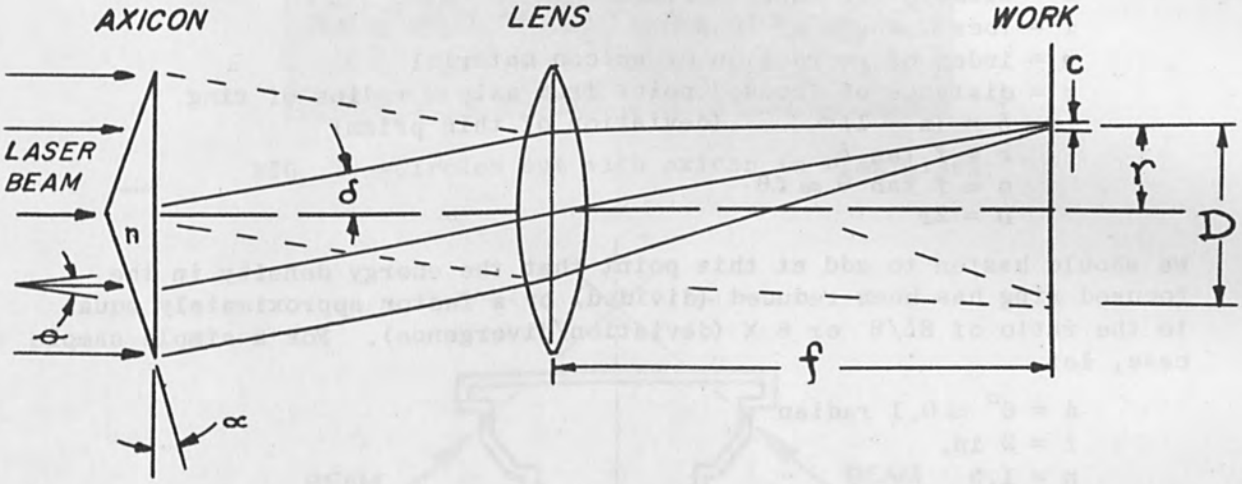
AXICON
LENS
WORK
LASER BEAM
n
δ
θ
∝
c
r
D
f

FIG. 1.—Axicon-lens system cross section, with resulting pattern.

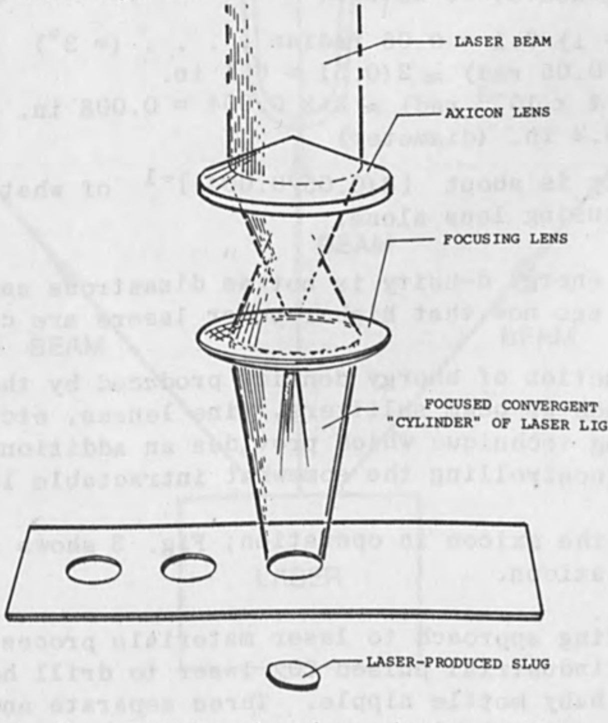
LASER BEAM
AXICON LENS
FOCUSING LENS
FOCUSED CONVERGENT "CYLINDER" OF LASER LIGHT
LASER-PRODUCED SLUG

FIG. 2.—Sketch of axicon in operation.

Functionally, the diameter of the focused ring is determined by both the "wedge angle" (or "edge angle") of the axicon and the focal length of the lens. Thus, the size of the ring can be changed by a change in the associated lens element, requiring fewer different axicons to be manufactured.

With reference to Fig. 1, which shows the effect of the axicon in only one plane, the important formulas are:

∞ = wedge angle of axicon
δ = angle through which light is deviated
c = diameter of focused spot $\equiv$ width of ring
θ = beam divergence of laser
D = diameter of focused ring
f = focal length of lens
n = index of refraction of axicon material
r = distance of focused point from axis = radius of ring
$\delta = (n - 1)\infty$ (deviation of thin prism)
$r = f \tan \delta$
$c \approx f \tan \theta \approx f\theta$
$D = 2r$

We should hasten to add at this point that the energy density in the focused ring has been reduced (divided) by a factor approximately equal to the ratio of $8\delta/\theta$ or 8 × (deviation/divergence). For a simple sample case, let

$a = 6^\circ \approx 0.1$ radian
$f = 2$ in.
$n = 1.5$
$d = 4 \times 10^{-3}$ radian

From the formulas above, we obtain:

$b = (1.5 - 1)\ 0.1 = 0.05$ radian . . . . $(= 3^\circ)$
$r = 2(\tan 0.05 \text{ rad}) \approx 2(0.5) = 0.1$ in.
$c = 2(\tan 4 \times 10^{-3} \text{ rad}) \approx 2 \times 0.004 = 0.008$ in. (width)
$D = 2r = 0.2$ in. (diameter)

The energy density is about $[8(0.05/0.004)]^{-1}$ of what it would have been with the focusing lens alone.

This decrease in energy density is not as disastrous as it would have been a few years ago now that higher-power lasers are commonly available.

In fact, the reduction of energy density produced by the axicon (and by other methods, such as beam splitters, line lenses, etc.) may be thought of as a modulating technique which provides an additional and advantageous means of controlling the somewhat intractable laser beam.

Figure 2 depicts the axicon in operation; Fig. 3 shows some cuts made in plastic using an axicon.

One last interesting approach to laser materials processing is found in our design of an industrial pulsed CO_2 laser to drill holes in a non-metallic part--a baby bottle nipple. Three separate and diversely located holes are drilled simultaneously with a timed pulse burst, as

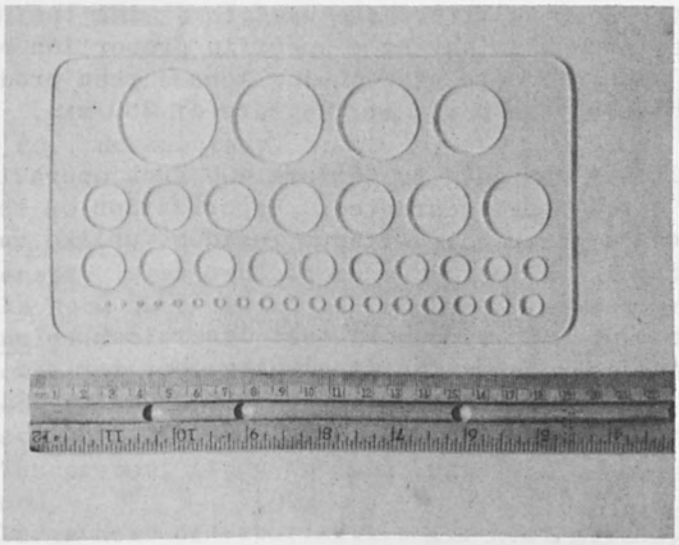

FIG. 3.—Circles cut with axicon in Plexiglass.

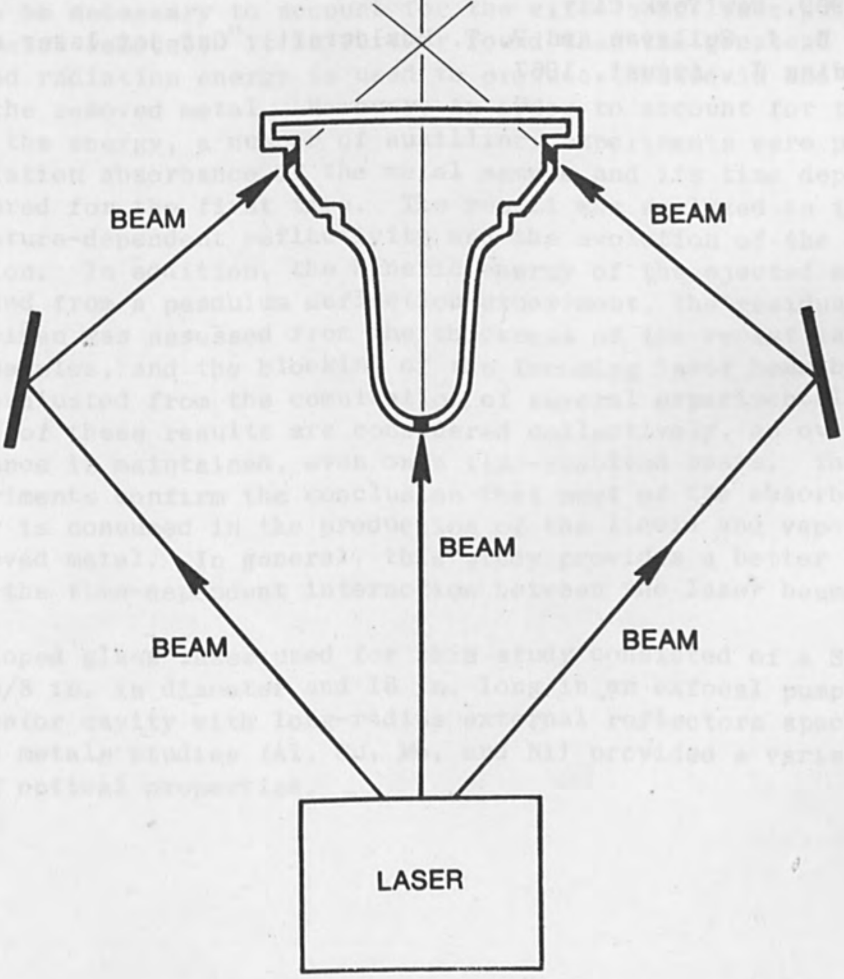
BEAM
BEAM
BEAM
BEAM
BEAM
LASER

FIG. 4.—Diagram of beam trisection in laser drill.

shown in Fig. 4. Beam splitters are used to divide the single laser beam into three, each beam having a specific proportion of the total energy. Three separate sets of focusing lenses then produce the correctly sized holes on the part, at the rate of 250/min.

The laser itself was designed to perform 400 such operations per minute, with a 2000-hr operational guarantee. Vaporization of the rubber material produces a clean hole without residue, unlike various mechanical means of punching the holes.

In defense of our opening statement that lasers can be economical tools, the cost of this laser operation, including operator and amortization of equipment cost over a two-year period of approximately \$1/1000 pieces. A pre-laser method would have cost about \$4/1000 pieces.

REFERENCES

1. J. F. Smith, "Drilling, trimming, welding," Laser Focus, March, 1969.

2. J. Longfellow and D. J. Oberholzer, "The application of the CO_2 laser to cutting ceramic substrates," IEEE International Convention, Spring, 1969, New York City.

3. A. B. J. Sullivan and P. T. Houldcroft, "Gas-jet laser cutting," Brit. Welding J., August, 1967.

INTERACTION OF HIGH-INTENSITY LASER BEAMS WITH METALS

M. K. CHUN

General Electric Co., Schenectady, N. Y.

ABSTRACT

With high-intensity laser radiation, such as that from a focused laser beam, metals have been melted and vaporized in the process of hole drilling. The analysis of this process is very complicated, since the simultaneous interaction of complex physical phenomena is involved. Prior reported work has been incomplete since some of the factors that use up a substantial fraction of the energy of the incident laser beam have not been measured. The present study includes detailed measurements of all significant factors.

Because of a large heat of vaporization for most metals, the amount of energy required to remove a given mass depends strongly on the liquid/vapor ratio. Therefore, the total amount of metal removed was measured, together with the time-dependent ratio of mass ejected as liquid to that expelled as vapor. The measurement of the time dependence of this ratio is shown to be necessary to account for the effects of laser pulse duration upon metal removal. It is further found that the greatest part of the absorbed radiation energy is used to produce the liquid and vapor phases of the removed metal. However, in order to account for the remainder of the energy, a number of auxilliary experiments were performed.

The radiation absorbance of the metal sample and its time dependence was considered for the first time. The result was analyzed in terms of the temperature-dependent reflectivity and the evolution of the crater configuration. In addition, the kinetic energy of the ejected material was estimated from a pendulum deflection experiment, the residual heat in the specimen was assessed from the thickness of the recast layer in sectioned samples, and the blocking of the incoming laser beam by ejected metal was evaluated from the combination of several experimental data.

When all of these results are considered collectively, an over-all energy balance is maintained, even on a time-resolved basis. The auxilliary experiments confirm the conclusion that most of the absorbed laser beam energy is consumed in the production of the liquid and vapor phases of the removed metal. In general, this study provides a better over-all picture of the time-dependent interaction between the laser beam and the metal.

The Nd-doped glass laser used for this study consisted of a Schott glass rod 5/8 in. in diameter and 18 in. long in an exfocal pump cavity and a resonator cavity with long-radius external reflectors spaced 3 m apart. The metals studies (Al, Cu, Mo, and Ni) provided a variety of thermal and optical properties.

Record of 10th Symposium on Electron, Ion, and Laser Beam Technology (L. Marton, ed.); San Francisco Press, Inc.

Copyright © by The Institute of Electrical and Electronics Engineers, Inc.—Printed in the U.S.A.

INTERACTION OF HIGH-INTENSITY LASER BEAMS WITH METALS

M. K. CHUN

General Electric Co., Schenectady, N. Y.

ABSTRACT

With high-intensity laser radiation, such as that from a focused laser beam, metals have been melted and vaporized in the process of hole drilling. The analysis of this process is very complicated, since the simultaneous interaction of complex physical phenomena is involved, so prior reported work has been incomplete since some of the factors that use up a substantial fraction of the energy of the incident laser beam have not been measured. The present study includes detailed measurements of all significant factors.

Because of a large heat of vaporization for most metals, the amount of energy required to remove a given mass depends strongly on the liquid/vapor ratio. Therefore, the total amount of metal removed was measured, together with the time-dependent ratio of mass ejected as liquid to that expelled as vapor. The measurement of the time dependence of this ratio is shown to be necessary to account for the effects of laser pulse duration upon metal removal. It is thus found that the greatest part of the absorbed radiation energy is used to produce the liquid and vapor phases of the removed metal. However, in order to account for the remainder of the energy, a number of auxiliary experiments were performed.

The radiation absorbance of the metal sample and its time dependence was considered for the first time. The result was analyzed in terms of the temperature-dependent reflectivity and the evolution of the crater configuration. In addition, the kinetic energy of the ejected material was estimated from a pendulum deflection experiment, the residual heat in the specimen was assessed from the thickness of the recast layer in sectioned samples, and the blocking of the incoming laser beam by ejected metal was evaluated from the combination of several experimental data.

When all of these results are considered collectively, an over-all energy balance is maintained, even on a time-resolved basis. The auxiliary experiments confirm the conclusion that most of the absorbed laser beam energy is consumed in the production of the liquid and vapor phases of the removed metal. In general, this study provides a better over-all picture of the time-dependent interaction between the laser beam and the metal.

The Nd-doped glass laser used for this study consisted of a Schott glass rod 5/8 in. in diameter and 18 in. long in an exfocal pump cavity and a resonator cavity with long-radius external reflectors spaced 3 m apart. The metals studies (Al, Cu, Mo, and Ni) provided a variety of thermal and optical properties.

Record of 10th Symposium on Electron, Ion, and Laser Beam Technology (L. Marton, ed.), San Francisco Press, Inc.

Copyright © by The Institute of Electrical and Electronics Engineers, Inc. — Printed in the U.S.A.

EXPERIMENTAL USE OF A LASER TO PENETRATE URANIUM[*]

H. Y. SPITZ

Technical Division, National Lead Company of Ohio

I. INTRODUCTION

The work described here was undertaken to study the feasibility of using a laser beam to replace conventional tools for cutting uranium metal. To be an efficient drilling or cutting tool, the laser beam must have (a) an intensity sufficiently great to evaporate the target material; (b) an adequate penetration depth; and (c) the ability to make a hole of sufficient size to preclude its being closed by refrozen material.

II. THEORY

Let a laser beam of radius r_b be focused by a lens of focal length f to a spot of radius r_f ; r_f will always be finite, although it may become very small. From Fig. 1, the double truncated light cone has its vertices a distance ϵ away from the focal plane. It follows that

$$r_f/\epsilon = (r_b - r_f)/f = \tan\theta \tag{1}$$

The gaussian intensity distribution is given by

$$I(\rho) = [P_0/(\pi\alpha^2)]\ (k^2/2)\ \exp[-\ (k^2/2)(\rho^2/\alpha^2)] \tag{2}$$

where P_0 is the total power of the beam, α is the radius of a circle containing a fixed fraction of the total power, ρ is the variable radius in the cross section of the beam, and $k^2/2$ is a constant whose significance is shown below. The power contained within a circle of radius ρ is

$$P(\rho) = 2\pi\int_0^\rho I(\rho)\rho d\rho = P_0\ \{1 - \exp[-\ (k^2/2)(\rho^2/\alpha^2)]\} \tag{3}$$

For the limitimg case, when $\rho = \alpha$, this simplifies to

$$P(\alpha) = P_0[1 - \exp\ (-\ k^2/2)] \tag{4}$$

With

$$r_f \le R \le R_1 \tag{5}$$

---

[*] Work performed under AEC Contract No. AT(30-1)-1156.

Record of 10th Symposium on Electron, Ion, and Laser Beam Technology (L. Marton, ed.); San Francisco Press, Inc.

Copyright © by The Institute of Electrical and Electronics Engineers, Inc.—Printed in the U.S.A.

we wish to define the radius of a circle on which the intensity I is equal to a fixed value. Thus

$$I(r) = [P_0/(\pi R^2)]\ (k^2/2)\ \exp[-\ (k^2/2)\ (r^2/R^2)] \tag{6}$$

However, with increasing distance s from the focal plane, r decreases, until it vanishes at s_1. There

$$I_{r=0} = [P_0/(\pi R_1^2)]\ (k^2/2) \tag{7}$$

Equating the right-hand sides of (6) and (7) gives

$$r = (2/k)R(\ell n\ R_1/R)^{1/2} = (2/k)\ (r_f/\epsilon)s(\ell n\ s_1/s)^{1/2} \tag{8}$$

Differentiation of (8) with respect to s shows that a maximum will occur at $s = s_1e^{-1/2}$ with

$$r_{max} = (2/k)\ (r_f/\epsilon)s_1(2e)^{-1/2} \tag{9}$$

The volume V_0 enclosed by $r(s)$ for $\epsilon \leq s \leq s_1$ is

$$V_0 = \pi \int_{\epsilon}^{s_1} r^2 \cdot ds = (2\pi/9)\ [f/(r_b - r_f)]\ (2/k^2)r_f^3[(s_1/\epsilon)^3 - \ell n(s_1/\epsilon)^3 - 1] \tag{10}$$

If it is desired to express the volume in original rather than in derived quantities, use can be made of (8) and the initial condition $s = \epsilon$ when $r = r_\epsilon$.

Assume now that the laser beam is focused onto the surface of the target and that I is the minimum intensity required to evaporate material. It is evident that s_1 is the maximum depth of penetration and V_0 is the maximum volume of material that can be evaporated; i.e., these are the steady-state expressions. The only quantity to be measured is r_ϵ. This measurement can be achieved with fairly good precision by focusing the laser beam just below the surface and exposing the sample to a large number of shots.

III. EXPERIMENTAL

A Lear-Siegler pulsed CO_2 laser emitting at 10.6 μ was used. The beam had a cross-sectional radius of 0.9525 cm, which was reduced to a spot with a radius of 0.762×10^{-2} cm by means of a 2.54-cm focal length NaCl lens. The laser was operated at 95 W, 245 pps. The pulse width was 1×10^{-6} sec at the half-power point. Thus, the energy flow was

0.194×10^6 w, assuming a nearly triangular pulse. It was necessary to irradiate the uranium sample in an inert atmosphere to prevent its oxidation and also to prevent contamination of the area with evaporated material. Therefore, a special apparatus was designed. After the sample was placed in position, the container was closed and the air was purged with an argon stream which was stopped just before irradiation began.

Four different samples were subjected to irradiation by the laser beam. Each sample was machined to a slab having a square base 2.54 cm on a side. Prior to irradiation, the samples were exposed to air to oxidize the surface and thus reduce reflectivity. The samples are described in Table I. All samples were subjected to five series of shots, consisting of 1, 3, 6, 9, and 12 shots. Each shot, comprising 245 pulses, lasted 1 sec, and the interval between successive shots was 6 sec. Samples 1 and 2 were irradiated parallel to the rolling direction.

TABLE I.—Characteristics of samples.

Sample No.	Thickness (cm)	Hardness (R_G)	Density (g/cm^3)	Condition	Additives (ppm)			
					C	Fe	Si	Al
1	0.6350	61.0-78.5	19.04	As rolled & recrystallized	52	49	14	32
2	0.3175	79.0	19.04	As rolled & recrystallized	52	49	14	32
3	0.3175	75.7	18.95	As cast	219	230	227	222
4	0.3175	87.5	18.61	As cast	1030	945	841	981

IV. RESULTS

A metallographic examination of the holes showed large variations. In samples 1, 2, and 3, a zone of molten and recrystallized material can be recognized (Fig. 2). Sample 4 (Fig. 3) exhibited a different type of behavior. The holes are oddly shaped and there is a mass of what had been molten material on the surface at one side of the crater. This mass appears to have frozen instantaneously.

From the dimensions of the holes, one can calculate the volumes excavated. These volumes can be fitted to a curve of the form

$$V = V_0 \, [1 - \exp(-\alpha S)] \tag{11}$$

where V_0 is the maximum volume that can be removed with the apparatus described, S is the number of shots, and α is a constant. Both V_0 and α are characteristics of the target material. The individual equations are:

$$\left.\begin{array}{ll} \text{Sample No. } 2 & V = 0.000\,1671\,[1 - \exp(-\,0.0472\,S)]\ \text{cm}^3 \\ 3 & V = 0.000\,2381\,[1 - \exp(-\,0.0557\,S)]\ \text{cm}^3 \\ 4 & V = 0.000\,0485\,[1 - \exp(-\,0.0438\,S)]\ \text{cm}^3 \end{array}\right\} \quad (12)$$

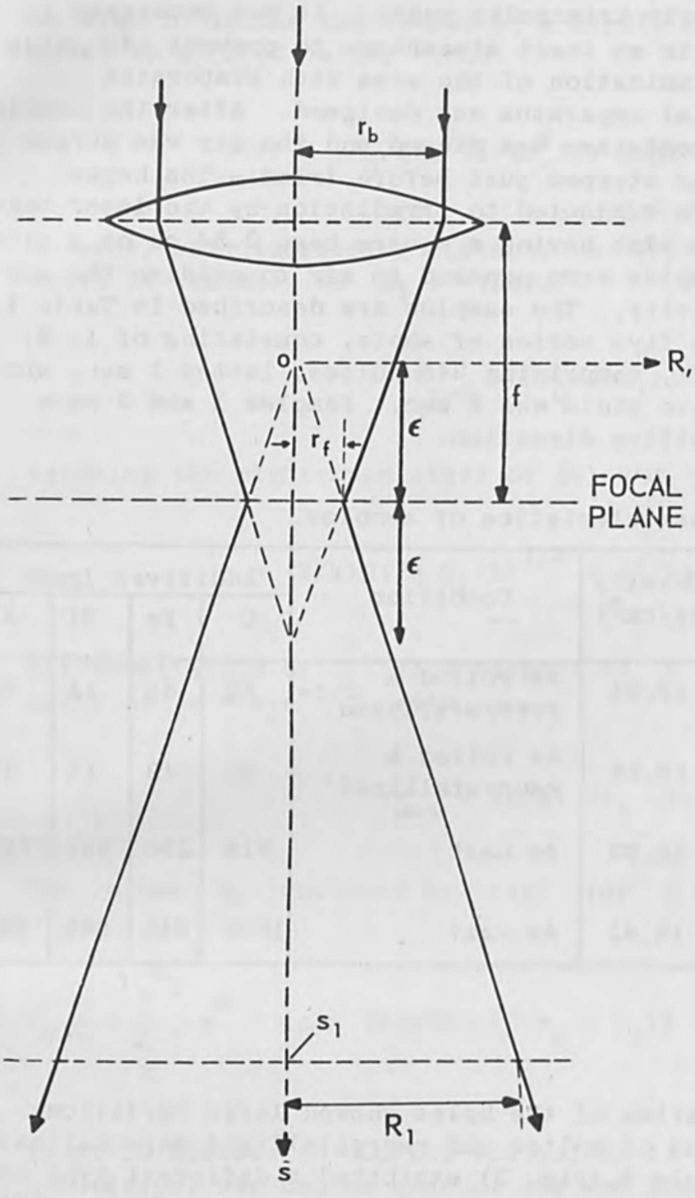

r_b
o
R, r
f
ϵ
r_f
FOCAL PLANE
ϵ
s_1
R_1
s

FIG. 1.—Configuration of focused laser beam.

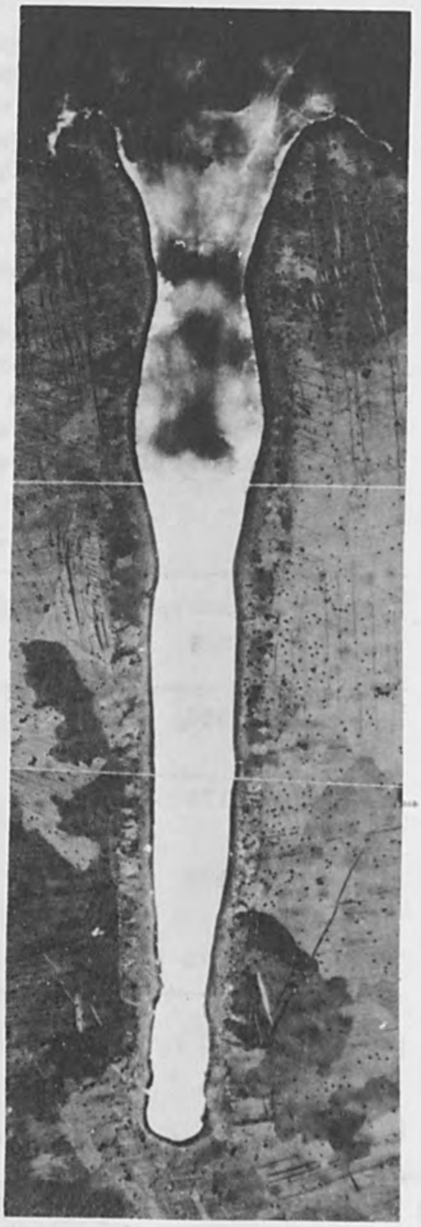

FIG. 2.—Sample No. 3: Uranium with 219 ppm C, 230 ppm Fe, 227 ppm Si, and 222 ppm Al. Hardness 75.7R_G, 12 shots, polarized light (100 X). Focal plane is slightly beneath the surface, its position indicated by topmost constriction of pit.

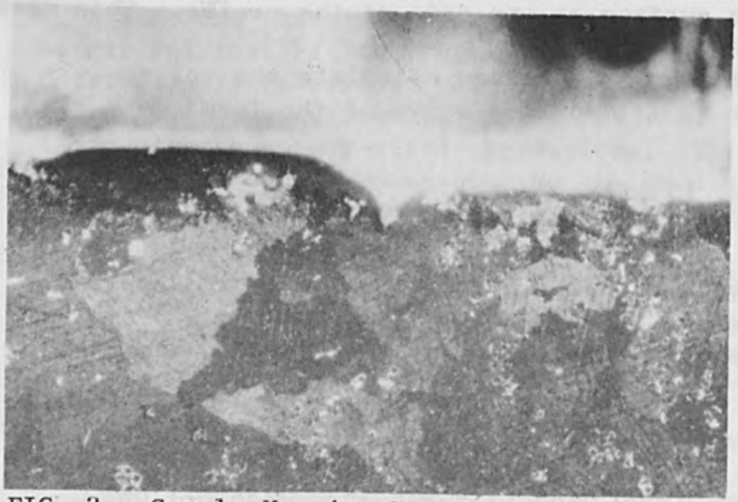

FIG. 3.—Sample No. 4: Uranium with 1030 ppm C, 945 ppm Fe, 841 ppm Si, and 981 ppm Al. Hardness 87.5R_G, 6 shots, polarized light (100 X).

The observed values and the fitted curves are shown in Fig. 4. The coefficients V_0 and α decrease with increasing hardness. (Sample No. 1 is omitted because it was found on inspection after the experiment that considerable inhomogeneity existed in its surface hardness.)

We shall now apply the theory developed in Section II to these experimental results. Let I be the minimum intensity required to evaporate a material, and let the target be placed so that the focal plane of the lens is on the surface of the target; then s_1 is the maximum depth of penetration and V_0 is the volume of material removed, provided the distance between lens and target remains constant, and provided the exposure consists of an infinite number of shots.

In the experiment described here, $f = 2.54$ cm , $r_f = 0.7620 \times 10^{-2}$ cm, $r_b = 0.9525$ cm, and $P_0 = 0.194 \times 10^6$ W , where f = focal length of the lens, r_f = radius of laser beam in the focal plane, r_b = radius of the incident laser beam, and P_0 = total power in the laser beam. We let $k^2/2 = 5$, since $1 - e^{-5} = 0.99326$, which means that 99.326% of the total power in the beam is being considered. Thus,

$$s_1 = 2.05 \times 10^{-2} \exp (4.30 \times 10^4 r_\varepsilon^2) \text{ cm} \tag{13}$$

$$I = 5.31 \times 10^9 \exp(- 8.61 \times 10^4 r_\varepsilon^2) \text{ w/cm}^2 \tag{14}$$

$$V_0 = 0.166 \times 10^{-6} [\exp(12.92 \times 10^4 r_\varepsilon^2)-12.92 \times 10^4 r_\varepsilon^2-1] \tag{15}$$

The method described here for the calculation of the maximum penetration depth s_1 , the critical intensity I , and the maximum removable volume V_0 has definite advantages over the purely empirical approach. There, measurements had to be made of the average radius and depth of each hole, from which the individual volumes were calculated. These calculated volumes had then to be curve-fitted. This process had to be repeated for each sample. But the method outlined in Sec. II necessitates the measurement of only a single quantity for each sample, namely r_ε .

Substitution of the measured values of r_ε into (13), (14), and (15) gives the maximum penetration depth, critical intensity, and maximum removable volume, as summarized in Table II. The good agreement of the values of V_0 in Table II with those shown in (12) is noteworthy.

TABLE II.—Maximum penetration depth, critical intensity, and maximum removable volume.

Sample No.	$r_\varepsilon (10^{-2}$ cm)	s_1 (cm)	$I (10^8 \text{w/cm}^2)$	$V_0 (10^{-4} \text{cm}^3)$
2	0.735	0.210	0.507	1.768
3	0.750	0.231	0.418	2.362
4	0.665	0.137	1.176	0.485

Figure 5 gives plots of r(s) for samples No. 2, 3, and 4. The excellent correlation between the upper region of the cavity in Sample 3 (Fig. 2) and the calculated longitudinal cross section of this sample can be seen clearly in Fig. 6.

Thus far, the hardness of the samples has not been considered. This is readily done by writing (11) in the form

$$V = V_0[1 - \exp(-\beta P_0 t/H)] \tag{16}$$

where β is a constant, P_0 is the total power in the beam, t is the time of exposure, and H is the Knoop hardness of the material. Solving the equations $\alpha_i S = \beta P_0 t/H_i$ gives $\beta = 0.128$. The results are listed in Table III. The removed volume can now be written

$$V = 0.166 \times 10^{-6}\,[\exp(12.92 \times 10^4 r_\epsilon^2) - 12.92 \times 10^4 r_\epsilon^2 - 1]$$

$$\times\,[1 - \exp(-\,0.128\,P_0 t/H)]\ \mathrm{cm}^3 \tag{17}$$

or more specifically,

$$\left.\begin{aligned} \text{Sample No. 2:}\quad & V = 0.000\,1768\,[1 - \exp(-\,0.000\,5311\,P_0 t)]\ \mathrm{cm}^3 \\ 3:\quad & V = 0.000\,2362\,[1 - \exp(-\,0.000\,5565\,P_0 t)]\ \mathrm{cm}^3 \\ 4:\quad & V = 0.000\,0485\,[1 - \exp(-\,0.000\,4555\,P_0 t)]\ \mathrm{cm}^3 \end{aligned}\right\} \tag{18}$$

TABLE III.—Effective hardness on material removed.

Sample No.	Hardness		α	β	V_0 Obs. ($10^{-4}\mathrm{cm}^3$)	V_0 Calc. ($10^{-4}\mathrm{cm}^3$)
	R_G	Knoop				
2	79.0	241	0.0472	0.128	1.671	1.768
3	75.7	230	0.0557	0.128	2.381	2.362
4	87.5	281	0.0438	0.128	0.485	0.485

V. DISCUSSION

The interaction of laser beams with solid targets has been subject to extensive investigations. Attempts have also been made at theoretical treatments of the heating of metals by laser radiation.[1-3] Among the few articles describing or mentioning the craters formed by laser radiation, Ready's[4] is the most complete; but a good comparison of his results with those described here cannot be made because he did not expose his samples to more than a single pulse in any given area. Khan[5] and his co-workers made the same observation that is reported here. Consoli[6] et al. found that crater sizes increase with decreasing pressures. Ehler[7] determined the evaporated mass by weighing before and after irradiation.

It is unfortunate that no mention is made in the literature of any metallography of areas exposed to laser radiation. Elion[8] states that

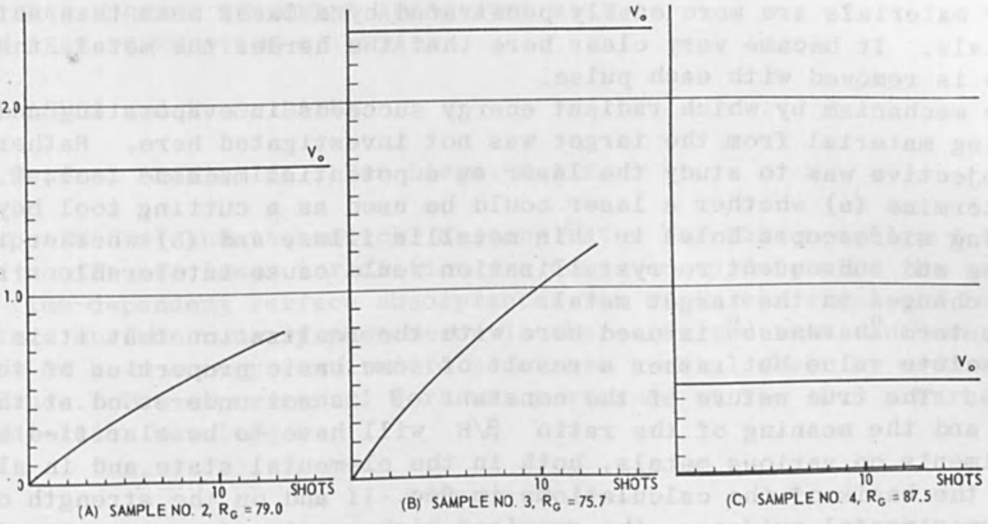

FIG. 4.—Volume of uranium removed vs number of laser shots. (V_0 is maximum removable volume according to Eq. 12.)

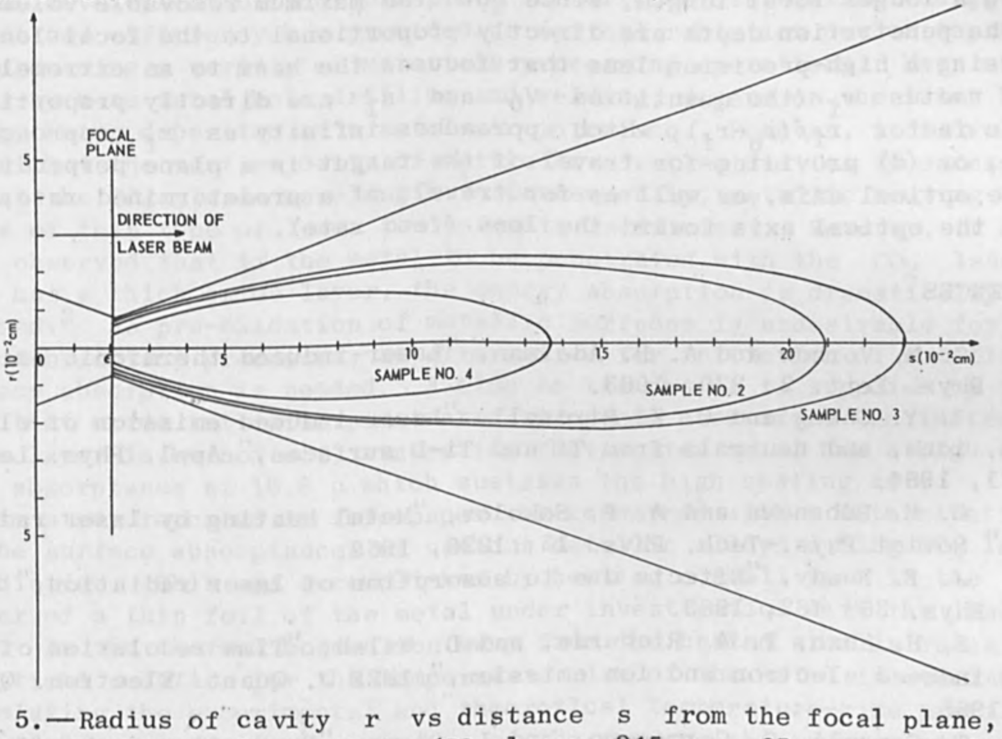

FIG. 5.—Radius of cavity r vs distance s from the focal plane, for infinite number of laser shots (CO_2 laser, 245 pps, 95 w output, 2.54-cm focal-length NaCl lens).

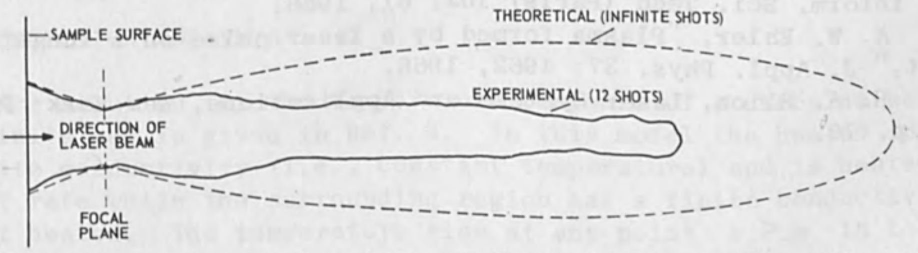

FIG. 6.—Comparison of experimental and theoretical results for sample No. 3. Experimental outline is taken from Fig. 3; theoretical curve is from Fig. 6. Note good agreement near sample surface.

harder materials are more easily penetrated by a laser beam than softer materials. It became very clear here that the harder the metal, the less volume is removed with each pulse.

The mechanism by which radiant energy succeeds in evaporating and ejecting material from the target was not investigated here. Rather, our objective was to study the laser as a potential machine tool; i.e., to determine (a) whether a laser could be used as a cutting tool beyond drilling microscopic holes in thin metallic films, and (b) whether the melting and subsequent recrystallization would cause intolerable structural changes in the target metal.

The term "hardness" is used here with the realization that it is not an absolute value but rather a result of some basic properties of the sample. The true nature of the constant β is not understood at this time, and the meaning of the ratio β/H will have to be clarified by experiments on various metals, both in the elemental state and in alloys.

On the basis of the calculations in Sec. II and on the strength of the experimental evidence, the required higher rate of evaporation for cutting bulk metal with a laser could be achieved by one or more of the following means: (a) increasing the power output; (b) using a lens having a longer focal length, since both the maximum removable volume and the penetration depth are directly proportional to the focal length; (c) using a high-precision lens that focuses the beam to an extremely small radius r_f (the quantities V_0 and s_1 are directly proportional to the factor $r_f/(r_b-r_f)$, which approaches infinity as r_f approaches zero); or (d) providing for travel of the target in a plane perpendicular to the optical axis, as well as for travel, at a predetermined rate, along the optical axis toward the lens (feed rate).

REFERENCES

1. C. M. Verber and A. H. Adelman, "Laser-induced thermionic emission," Appl. Phys. Lett. 2: 220, 1963.

2. T. Y. Chang and C. K. Birdsall, "Laser-induced emission of electrons, ions, and neutrals from Ti and Ti-D surfaces," Appl. Phys. Lett. 5: 171, 1964.

3. G. M. Rubanova and A. P. Sokolov, "Metal heating by laser radiation," Soviet Phys.-Tech. Phys. 12: 1226, 1968.

4. J. F. Ready, "Effects due to absorption of laser radiation," J. Appl. Phys. 36: 462, 1965.

5. S. H. Khan, F. A. Richards, and D. Walsh, "Time resolution of laser induced electron and ion emission," IEEE J. Quant. Electron. QE-1: 359, 1965.

6. T. Consoli, G. Gormezano, and L. Slama, "Production de bouffées de plasma dense par focalisation d'un faisceau laser sur une cible," Bull. Inform. Sci. Tech (Paris) 102: 61, 1966.

7. A. W. Ehler, "Plasma formed by a laser pulse on a tungsten target," J. Appl. Phys. 37: 4962, 1966.

8. H. A. Elion, Laser Systems and Applications, New York: Pergamon, 1967; p. 76.

NONLINEAR SURFACE PHENOMENA ASSOCIATED WITH LASER BEAM PENETRATION OF METALS

J. F. ASMUS and F. S. BAKER

Gulf General Atomic Inc., San Diego, Calif.

Experimental and theoretical heating rates for thin metallic foils under continuous laser irradiation are compared to determine the effective time-dependent surface absorptances for stainless steel and brass. In air a surface runaway phenomenon is characterized that can lower the amount of beam energy required to penetrate a metal sheet by orders of magnitude. The experimental work was performed at the 10.6 μ carbon-dioxide-laser wavelength.

INTRODUCTION

The development of the 10.6-μ CO_2 laser with its available high-power output and efficiency has provided an optical radiation device capable of performing a variety of materials-processing operations. Many of them, such as metal hole drilling and welding, depend on the laser beam energy being deposited at a metal-air interface. However, it is well-known that the vast majority of metals have reflectivities in excess of 90% at the CO_2 laser wavelength.[1] Consequently, metallic heating by means of this type of laser can be quite inefficient. However, it has been observed that if the metal to be penetrated with the CO_2 laser beam has a thick oxide layer, the energy absorption is dramatically increased.[2] As pre-oxidation of metallic surfaces is undesirable for many microfabrication processes, an alternative for initiation of metallic-surface absorption is needed. A clue to the answer is supplied by the fact that oxide initiated penetration proceeds even after the initial oxide layer is burned off, suggesting that molten metal has a high surface absorptance at 10.6 μ which sustains the high heating rate.

The study reported in this paper was concerned with a determination of the surface absorptances of various metallic alloys during CO_2 laser irradiation. This was accomplished by heating a small spot in the center of a thin foil of the metal under investigation with the laser beam. As the thermal conduction away from the heated area is radial an analytical solution for the temperature rise of the metal is available.[3] Correlating the experimental and theoretical temperature-rise profiles then yields a quantitative measure of the surface absorptance at early times and a qualitative measure at late times.

THERMAL-CONDUCTION ANALYSIS

The exact solution for the temperature response of a circular segment of an infinite web is given in Ref. 3. In this model the heated spot has infinite conductivity (i.e., constant temperature) and is heated at a constant rate while the surrounding region has a finite conductivity and is not heated. The temperature rise at any point $r > a$ in the web can be written in the form

Record of 10th Symposium on Electron, Ion, and Laser Beam Technology (L. Marton, ed.); San Francisco Press, Inc.
Copyright © by The Institute of Electrical and Electronics Engineers, Inc.—Printed in the U.S.A.

$$\Delta T = \frac{2P(1-R)}{\pi^2 \rho a^2 t C_p \alpha} \int_0^\infty \left(1 - e^{-\alpha U^2 \tau}\right) f(U,r)\, dU$$

where

a = spot radius
ρ = web density
C_p = web specific heat
t = web thickness
α = web thermal diffusivity
P = power
R = reflectivity
τ = time
U = complex variable of integration having units of $(\text{length})^{-1}$
$f(U,r)$ = expression containing first- and second-kind Bessel functions

For the case $r = a$, which gives the temperature of the heated region, numerical values for the solution of the above equation are given in Ref. 3. Figure 1 has been prepared from this information. The dimensionless parameters are:

$$\theta\ (\text{temperature}) = \frac{kt\,\Delta T}{P(1-R)}$$

$$Y\ (\text{time}) = \frac{\alpha\tau}{a^2}$$

where

k = web thermal conductivity

The experimental temperature-rise curves of the next section were caused to coincide with the theoretical curve of Fig. 1 at low temperatures. This was accomplished by assuming that the thermodynamic parameters for the materials are constant with temperature and then finding that reflectivity R that causes the experimental curve to fall on the curve of Fig. 1.

EXPERIMENTAL MEASUREMENTS

The temperature rises for several metals were measured with the apparatus shown schematically in Fig. 2. The beam from a 1-kW CO_2 flowing gas laser passes through a programmed shutter and power monitoring device to impinge upon a concave mirror. The optical axis of the mirror is oriented 10° off the laser beam axis so that the radiation converges on the center of the sample foil located to one side. The radius of the heated zone, a, is controlled by adjusting the mirror to sample distance. The radiant power density at the sample is a function of the spot radius a and the total laser power which may be varied between

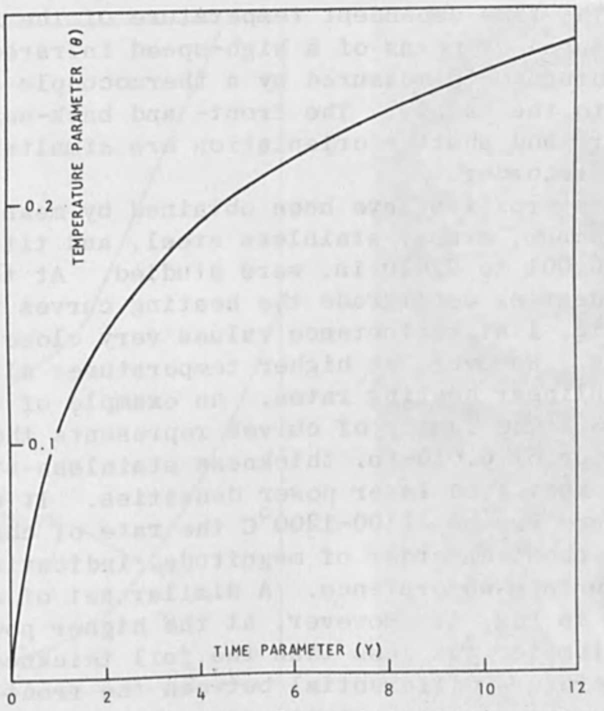

FIG. 1.—Theoretical temperature rise of infinite web when heated in center.

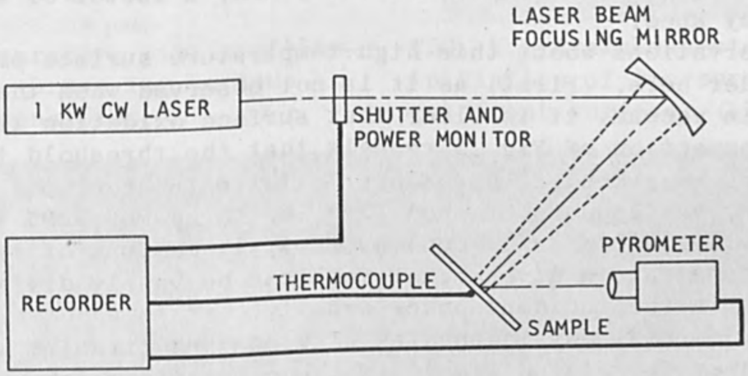
LASER BEAM
FOCUSING MIRROR
1 KW CW LASER
SHUTTER AND
POWER MONITOR
PYROMETER
THERMOCOUPLE
RECORDER
SAMPLE

FIG. 2.—Experimental apparatus for measuring dynamic reflectivity of metal foils.

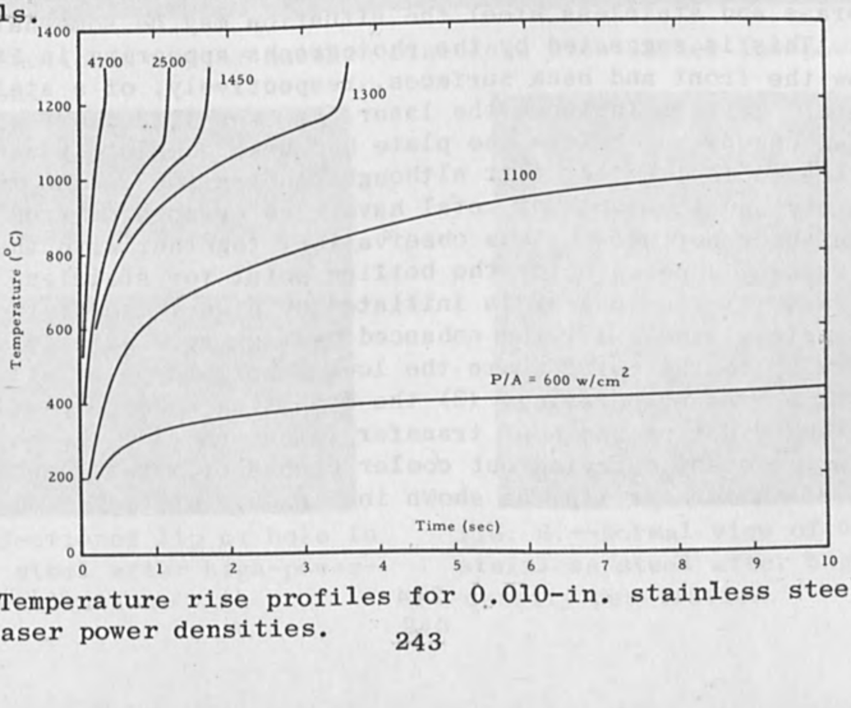

FIG. 3.—Temperature rise profiles for 0.010-in. stainless steel for various laser power densities.

200 and 1000 W. The time-dependent temperature of the front surface of the sample is measured by means of a high-speed infrared pyrometer. The back surface temperature is measured by a thermocouple of 0.0005-in. wire spot welded to the sample. The front- and back-surface temperatures, laser power, and shutter orientation are simultaneously displayed on a multichannel recorder.

Temperature rise profiles have been obtained by means of the Fig. 2 apparatus for aluminum, brass, stainless steel, and titanium. Foil thicknesses from 0.001 to 0.020 in. were studied. At temperatures up to a few hundred degrees centigrade the heating curves for these metals matched that of Fig. 1 at reflectance values very close to the published[1] magnitudes. However, at higher temperatures all of the above metals exhibit nonlinear heating rates. An example of this phenomenon is shown in Fig. 3. The family of curves represents the measured temperatures at the center of 0.010-in. thickness stainless-steel foils when irradiated at the indicated laser power densities. It can be seen that when the temperature reaches 1100-1200°C the rate of change of temperature increases by about an order of magnitude, indicating a corresponding increase in the surface absorptance. A similar set of curves for 0.010-in. brass appears in Fig. 4. However, at the higher power density the irradiated spot diameter was less than the foil thickness, leading to a considerable temperature differential between the front and back surfaces. This example represents a less extreme case than the stainless steel in that the surface absorptance increases by only a factor of about three at the runaway knee.

A few observations about this high-temperature surface phenomenon may be in order here. First, as it is not observed when the heating takes place in vacuum, it is clear that surface oxidation is involved. Second, an inspection of Fig. 3 reveals that the threshold for the onset of the runaway is exceedingly sharp. It fails to occur out to 10 sec at 1100 W/cm^2, yet appears at about 3.5 sec for a mere 20% increase in power density to 1300 W/cm^2. Consequently, the amount of laser energy required to penetrate a given metal foil can be vastly different for a modest change in the incident power density.

For pure elemental metals such as aluminum and titanium it appears that the runaway is related simply to the oxidation which proceeds rapidly when a critical temperature is reached. In the case of alloys such as brass and stainless steel the situation may be somewhat more involved. This is suggested by the photographs appearing in Fig. 5. These show the front and back surfaces, respectively, of a stainless-steel plate. In this instance the laser beam was turned off after the runaway had begun, but before the plate had been completely penetrated. Of significance is the fact that although penetration is incomplete, approximately equal amounts of metal have been evaporated from both the exposed and back surfaces. This observation, together with the fact that the runaway appears below the boiling point for stainless steel suggests that (1) the runaway is initiated by high-temperature oxidation of the stainless steel, (2) the enhanced heating rate quickly brings the temperature up to the point where the lowest-boiling-point alloying constituent begins evaporating, (3) the resulting alloy depletion further enhances the oxidation and heat transfer rates, and (4) the boiling becomes rather violent carrying out cooler chunks of material which are deposited at the crater lip, as shown in Fig. 5.

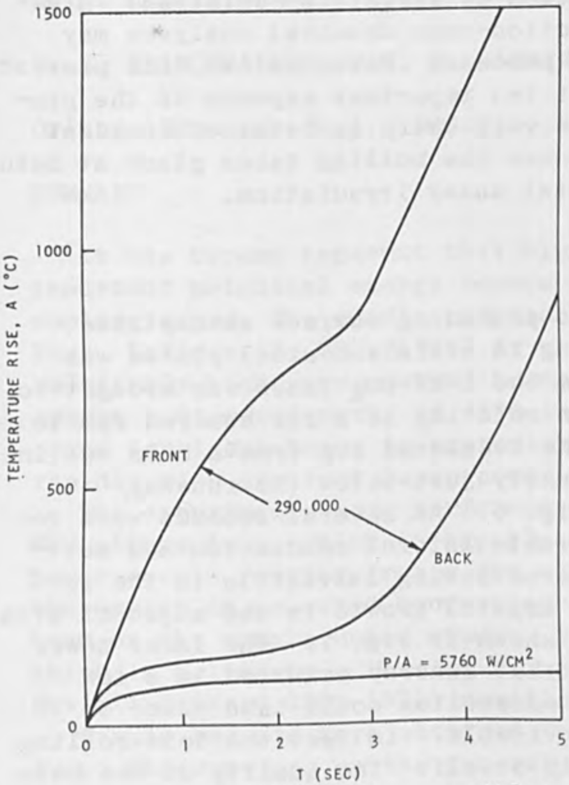

FIG. 4.—Temperature rise profiles for 0.010-in. brass for various laser power densities.

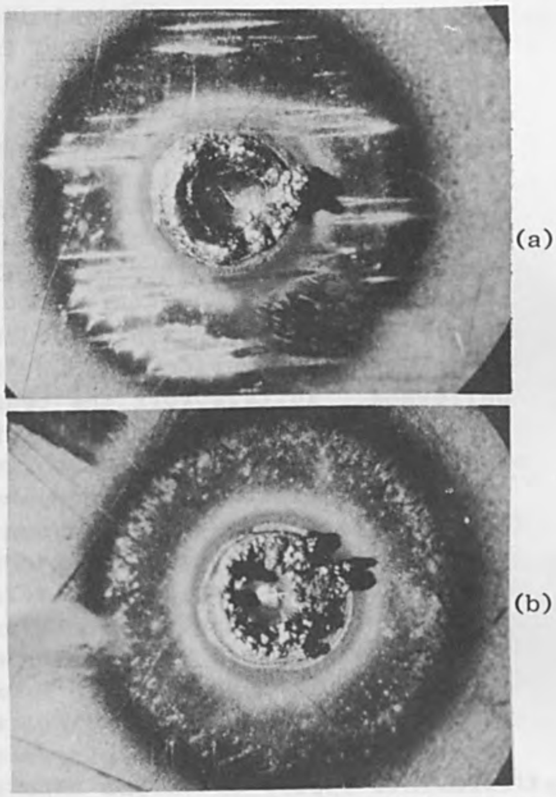

FIG. 5.—Stainless-steel plate after initiation of the surface run-away: (a) front surface; (b) back surface.

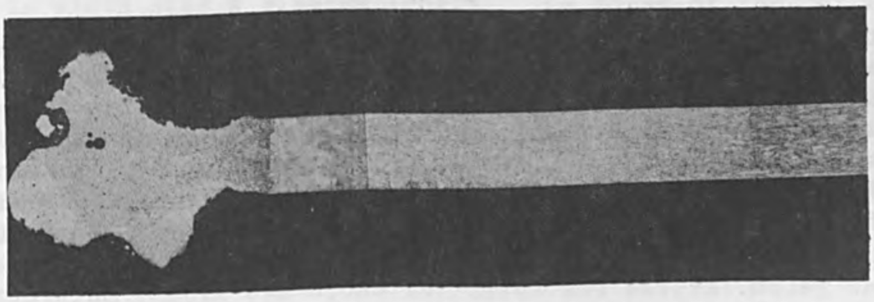

FIG. 6.—Sectioned lip of hole in stainless steel after low-power-density penetration.

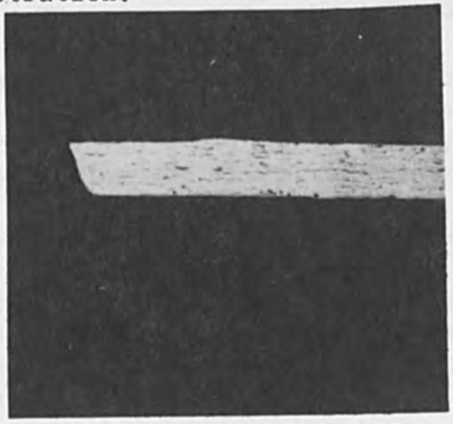

FIG. 7.—Sectioned lip of hole in stainless steel after high-power-density penetration.

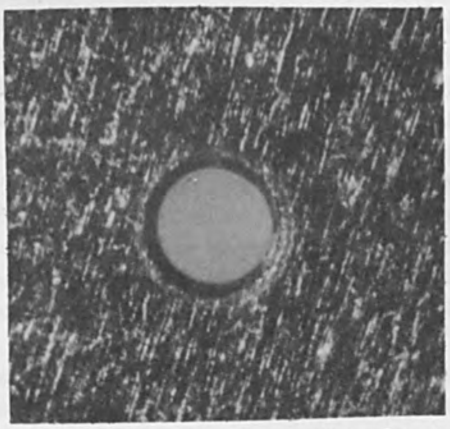

FIG. 8.—Normal view of hole in stainless steel after high-power-density penetration.

The above phenomenological description is largely speculation. High-speed photographic studies and interaction-zone chemical analyses may lead to a fuller understanding of the process. Nevertheless, the present investigation has illuminated at least two important aspects of the process. First, the runaway threshold is very sharp in terms of incident power density. Second, in many instances the boiling takes place at both the front and back surfaces of the metal under irradiation.

EXPERIMENTAL HOLE DRILLING STUDIES

From the background provided by the preceding surface absorptance study an investigation of hole drilling in stainless-steel plates was performed. In this work the beam from the 1-kW CO_2 laser was brought to a focus on the metal surface as it was rotating at a few hundred rpm to insure that the hole was circular. The sectioned lip from a hole cut in this manner with an incident power density just below the runaway threshold at 1000 W/cm^2 is shown in Fig. 6. As several seconds were required to penetrate the metal considerable lateral conduction and melting took place. A high density of microcracking is visible in the resolidified lip along with substantial crystal growth in the adjacent area.

In contrast note the sectioned lip shown in Fig. 7. The laser power density was increased to 10^5 W/cm^2 so that runaway occurred in a few milliseconds. As very little lateral conduction could take place on this time scale, no crystal growth is visible. In fact the cold-rolling filaments appear to extend into the lip itself. The quality of the hole is further revealed in the planar view displayed in Fig. 8.

DISCUSSION

The studies reported in this paper have shown that when designing a laser beam machining operation it is necessary to consider the dynamic aspects of the surface absorptance. For sufficiently high power densities the absorbed energy may be as much as an order of magnitude greater than that inferred from low-temperature measurements. If maximum use is to be made of this phenomenon, high power densities are required which materially improve the quality of the cut by lessening the heating of adjacent material.

REFERENCES

1. C. D. Hodgman et al., Handbook of Chemistry and Physics, 42nd ed., p. 2951.

2. J. Hobart, Coherent Radiation Laboratories, private communication.

3. H. S. Carslaw and J. C. Jaeger, Conduction of Heat in Solids, London: Oxford University Press, 2nd ed., 1965.

METAL MACHINING WITH AN ARGON LASER BEAM

D. E. FLINCHBAUGH and G. M. BARNARD

Orlando Research Corp., Orlando, Fla.

SUMMARY

It has become apparent that high-power blue-green laser light is an important potential energy source for industrial machining and cutting applications. The anodic-bore ion laser tube (see W. H. McMahan, Appl. Phys. Letters 12: 383, 1968) is particularly suitable for generating relatively high power output beams with a compact, efficient, laser system. At wavelengths of 4880 and 5145 Å, the effect of concentrated argon ion laser beams is appreciable and material removal rates increase rapidly with incident laser power once a threshold level is attained.

The experiments were performed with a modified Orlando Research Model 800 plasma tube, which is capable of generating argon laser beams at power levels ranging from a few milliwatts to 10 W (cw). Just outside the cavity an uncoated converging lens (focal length 35 mm) focuses the beam on the sample under study. Samples are bolted flat to a holder which is driven by a Moseley X-Y plotter at speeds controlled by a Hewlett-Packard 180A-1821A oscilloscope and time-base generator.

Sample results were obtained for stainless steel type 301 and tantalum. Observations on the general appearance and measurements of machining parameters were made on a Bausch and Lomb Dynazoom steroscopic microscope with a B & L bright line stage micrometer. A 30-sec scan across the 0.002-in.-thick stainless steel yielded a cleanly cut slit averaging 0.16 mm in width over a 9.14-mm length. The edges of the cut were smooth. Vapor plumes during the cutting and the absence of ridges or sputtered particles on the surface indicate that the irradiated material was cleanly removed. Also, it was observed that the airstream from a small blower assisted in removing the vapor from the laser beam, resulting in much smoother, more even slit edges. The edges were feathered for about 0.09 mm on the side where the laser beam was incident; on the back side the taper to the original surface measured about 0.05 mm in width. The surface immediately surrounding the slit appeared tarnished for about 1 mm.

The tantalum sample was 0.005 in. thick and several holes were cut through this material with a laser power output of 5.2 W measured with a Coherent Radiation power meter. The argon laser tube was operating at a 35-A current level. The time required to drill a very clean, round 6.25-μ-diam. hole was 105 sec. Larger holes could be drilled by moving the sample in the focal plane. This material did not emit a vapor plume as had the stainless steel, but crater ridges were formed and sputtered particles were evident on the surface surrounding the holes. On the side facing the laser, the surface acquired an irregular ridge averaging 25 μ in diameter for the 6.25-μ hole. On the back side, however, the surface was clean and a barely detectable depression appeared at the edges.

Some factors influencing the effectiveness of argon laser metal machining appear to be (1) color and surface finish, (2) thermal conductivity, (3) thickness, (4) hardness and physical structure, and (5) surface tension of the molten material. Paper, wood, and other fibrous dielectric materials burn readily when exposed to the unfocused beam. Some quantitative explanations of the observed differences have been attempted on the basis of physical properties of materials tested.

APPLICATION OF HELIUM-NEON LASERS FOR PROCESS DIMENSIONAL CONTROL

SHELDON MINKOWITZ

Laser Engineering Instrument Division, The Perkin-Elmer Corp.

SUMMARY

The laser generates a new type of light beam, one that is intense, monochromatic, and coherent. By applying these characteristics, measurements once considered impractical or impossible become feasible.

Laser tooling has already made significant contributions in the areas of aircraft jig alignment and machine tool fabrication over distances and to accuracies not previously possible.

The laser tooling system makes use of the brightness and unidirectionality of the laser only. The distance-measuring laser interferometer depends on the monochromaticity and spatial coherence of the laser. The interferometer utilizes a stabilized single-frequency laser source. Thus, the user has a length standard essentially "built in" to his distance-measuring instrument, the great advantage being that the same instrument may be utilized for measuring ranges from 0 to 150 ft.

Results of typical applications of the laser interferometer and laser tooling system were presented.

AN APPLICATION OF THE LASER IN CONTOUR MEASUREMENT

SHIGERU ANDO,* KAZUNARI SATO,** MASAO AOKI*
KAZUO OKADA,* MAKOTO KIKUCHI,** and TSUTOMU SUGANO**

Mitsubishi Electric Corp., Japan

An optical profiling system, in which a light beam serves for a stylus, will be described. A helium-neon 6328-Å laser and a light-emitting diode are used as a light source respectively. The helium-neon laser enables the stylus to have a minute light spot, which results in a sensitivity better than 1 μ. In the case of the light-emitting diode, the signal-to-noise ratio can be greatly improved by modulating light at a medium frequency and narrowing the receiving bandwidth. The scanning speed can be exceedingly increased by rapid scanning with correction for displacement.

1. INTRODUCTION

If the profiling for contour measurement in industry were made without contact instead of a mechanical stylus, there would be remarkable conveniences. When a mechanical stylus weighing 1 g is kept in contact with a surface perpendicularly at a circle 10 μ in diameter, the pressure amounts to 1.3 ton/cm^2. Since the contact pressure is generally high, a serious problem arises as to the deformation of the surface to be measured. Requirement for high accuracy with a sharp stylus contradicts that for high speed and high fidelity in the profiling operation. The problem can be settled by substituting a light spot for the top of a mechanical stylus. Now that the helium-neon 6328-Å laser and the light-emitting diode are available, a light spot whose diameter or width is within a few microns is practical.

In the case of the profiling milling machine, the optical stylus does not help to avoid the error caused by cutter curvature, or simply "cutter error," which is usually avoided by using a mechanical stylus of the same diameter as the cutter. The optical profiling system is essential to the model scanning in a mechanical automation system, which makes an integrated work of contour measurement, smoothing, fairing, programing for cutting, and die cutting. Other important applications are the inspection of machine parts, the position control in the machine tool and measurement of the surface roughness.

2. APPARATUS

The block diagram of the optical profiling system using a helium-neon 6328-Å laser is shown in Fig. 1. A laser beam emitted from an objective lens serves for a stylus, which keeps the distance between the lens and the surface constant in the same way as reported previously.[1] Three kinds of improvement have been made since the previous

---

* Central Research Laboratory, Amagasaki.

** Kakamura Works.

Record of 10th Symposium on Electron, Ion, and Laser Beam Technology (L. Marton, ed.); San Francisco Press, Inc.

Copyright © by The Institute of Electrical and Electronics Engineers, Inc.—Printed in the U.S.A.

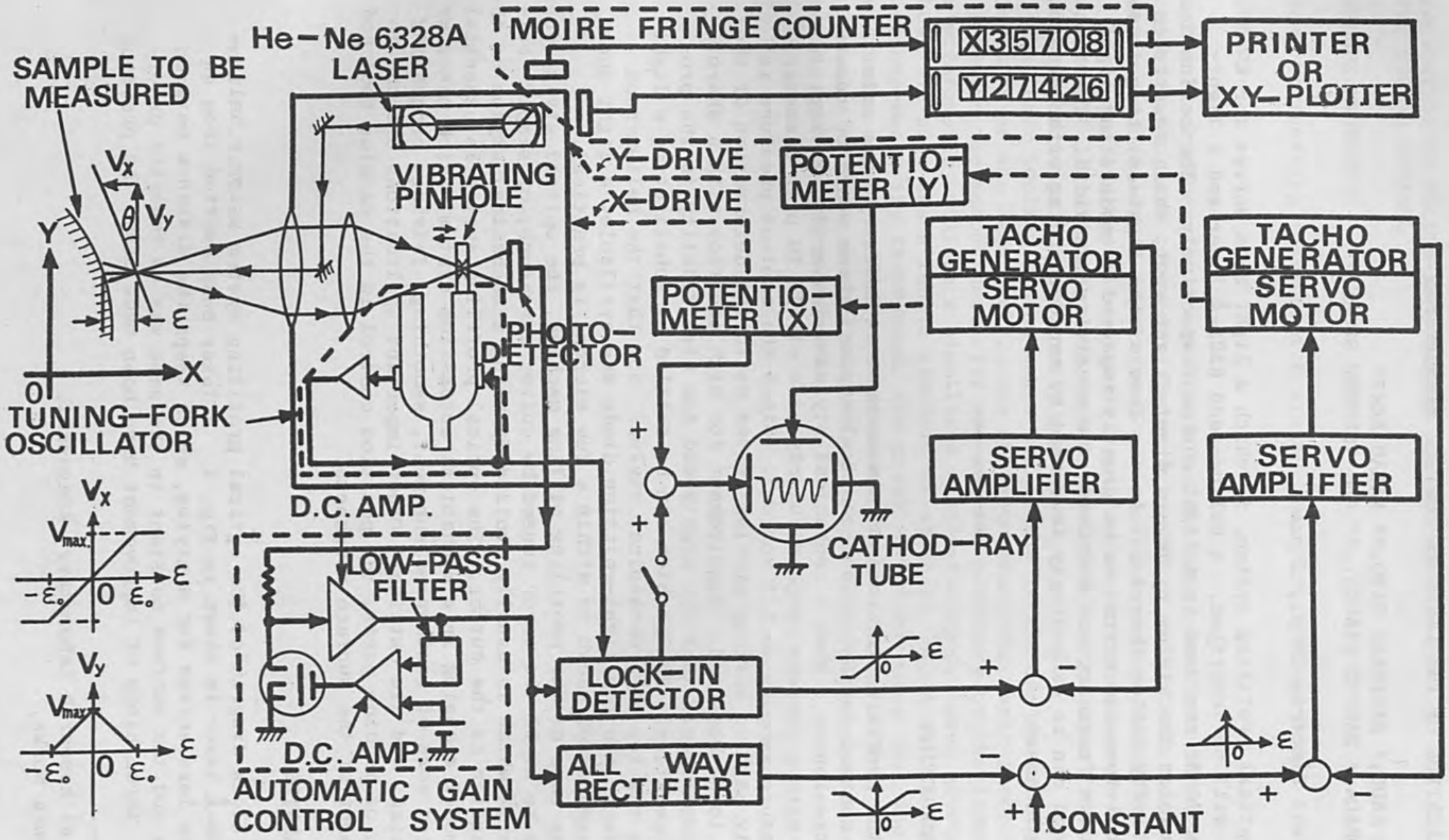
SAMPLE TO BE MEASURED
He – Ne 6328A LASER
MOIRE FRINGE COUNTER
X35708
Y27426
PRINTER OR XY–PLOTTER
Vx
Vy
θ
Y
ε
X
0
VIBRATING PINHOLE
Y–DRIVE
X–DRIVE
POTENTIO–METER (Y)
POTENTIO–METER (X)
PHOTO–DETECTOR
TUNING–FORK OSCILLATOR
TACHO GENERATOR
SERVO MOTOR
SERVO AMPLIFIER
CATHOD–RAY TUBE
D.C. AMP.
LOW–PASS FILTER
D.C. AMP.
AUTOMATIC GAIN CONTROL SYSTEM
LOCK–IN DETECTOR
ALL WAVE RECTIFIER
CONSTANT
Vmax
–ε₀
ε₀
+
–

FIG. 1.—Block diagram of optical profiling system using He-Ne 6328-Å laser.

report, as follows:

(1) An automatic gain control system has been developed to compensate a range of about a thousand times of variation in the intensity of received light.

(2)

$$V_x + V_y = V_{max} = \text{constant} \tag{1}$$

where V_x and V_y denote components of velocity.

(3) The time required for measurement can be reduced by rapid scanning with correction for displacement.

The profiling system using a light-emitting diode is illustrated in Fig. 2. The 7700-Å light emitted from the diode is modulated at 455 kHz and the received signal is amplified by a narrow band amplifier whose center frequency and half width are 455 kHz and 1.5 kHz respectively. Other part not shown in Fig. 2 is the same as Fig. 1.

3. DESIGN CONSIDERATIONS

As far as the author is aware, few papers[2] concerning the optical profiling system have been published. As for the optical system for detecting focus, very few papers[3] have been published. In this chapter, the comparison between those systems and design considerations will be described.

The optical profiling systems are generally simplified as shown in Fig. 3. Using the notations shown in the figure, received power P_r can be written as follows,

$$P_r = (BS\Omega_s) \cdot K_t \cdot (\sigma\Omega_r) \cdot K_r \tag{2}$$

Fidelity of measured contour is improved as the area of the light spot decreases and therefore as the area of light source S does. As can be seen from Fig. 6, the lowest efficiency factor of scattering σ corresponds to the surface of low diffusibility such as polished metal with large angle of incidence. In order to measure low σ surface at a high accuracy, the helium-neon 6328-Å laser is essential because of its extremely high brightness.[1] In the case of the light-emitting diode, signal-to-noise ratio can be greatly improved by modulating light at a medium frequency and narrowing the receiving bandwidth.

The optical systems for detecting focus are classified into longitudinal and transversal method. Comparison between the two methods is made as shown in Table I. In the case of the transversal method and $\alpha = 90^\circ$, the system is suitable for position control but not for profiling. The system corresponding to the condition $0 < \alpha < 90^\circ$ is applicable to the profiling and relatively small α is desirable considering the sharpness of the stylus. It should be noted that accuracy and sensitivity decrease with α and are limited by the spot size. The spot size is limited by the spherical aberration and the diffraction of lenses.

In the case of the longitudinal method and $\alpha = 0$, the accuracy is limited by the spherical aberration of lenses. Since the angle of incidence θ changes unceasingly during the profiling operation and so

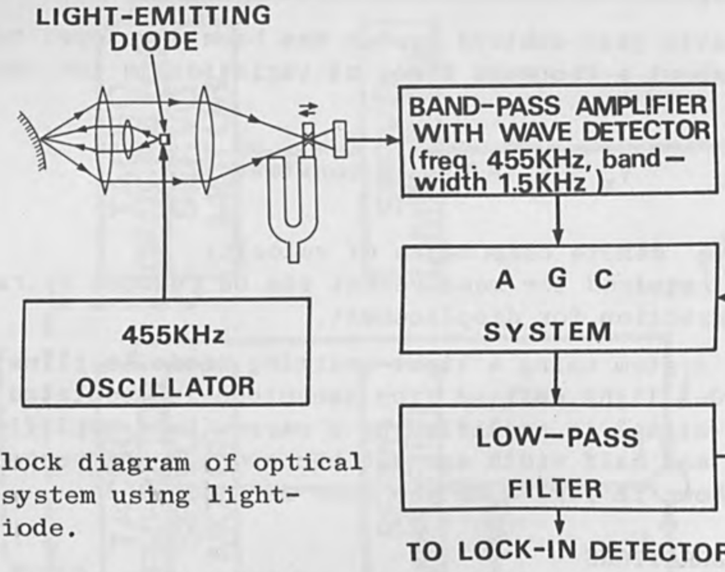
LIGHT-EMITTING DIODE
BAND-PASS AMPLIFIER WITH WAVE DETECTOR (freq. 455KHz, band-width 1.5KHz)
A G C SYSTEM
455KHz OSCILLATOR
LOW-PASS FILTER
TO LOCK-IN DETECTOR

FIG. 2.—Block diagram of optical profiling system using light-emitting diode.

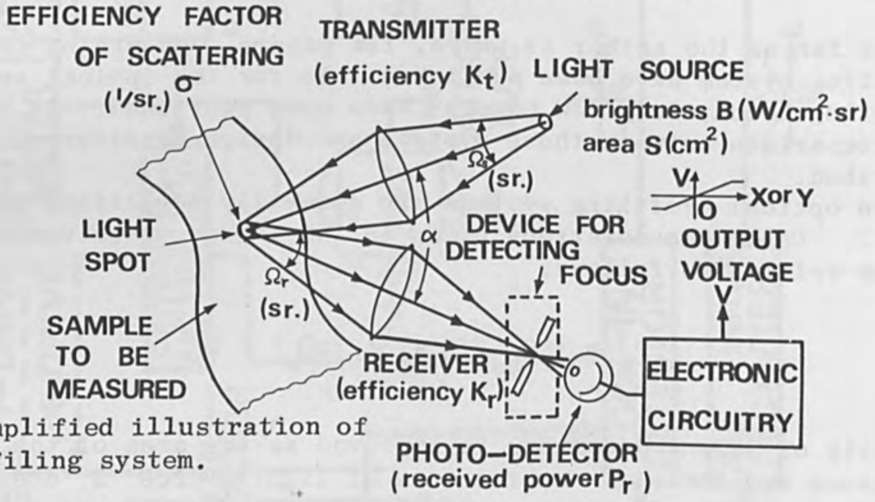
EFFICIENCY FACTOR OF SCATTERING σ (1/sr.)
TRANSMITTER (efficiency K_t)
LIGHT SOURCE
brightness B (W/cm²·sr)
area S (cm²)
Ω_s (sr.)
V
O
X or Y
LIGHT SPOT
α
DEVICE FOR DETECTING FOCUS
OUTPUT VOLTAGE
V
Ω_r (sr.)
SAMPLE TO BE MEASURED
RECEIVER (efficiency K_r)
ELECTRONIC CIRCUITRY
PHOTO-DETECTOR (received power P_r)

FIG. 3.—Simplified illustration of optical profiling system.

TABLE I.—Comparison between two methods of focusing.

	Most effective case	α	What is the accuracy limitted by?	What is the sensitivity limitted by?	Optics
Longi-tudinal method	$\alpha = 0$	0°	Spherical aberration of lenses		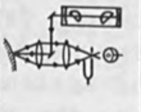
Trans-versal method	$\alpha = 90^\circ$	90°	Diffraction limit, spherical aberration of lenses		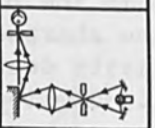
		$0 < \alpha < 90^\circ$	Spot size (spherical aberra-tion of lenses or diffraction limit)		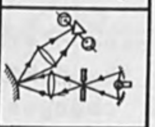

does the intensity distribution of scattered light on the lens surface, the focal point moves about within the limit of spherical aberration along optical axis.[1] On the contrary, the sensitivity is not limited by the spherical aberration, as shown later on.

Several systems for detecting focus and their characteristics are shown in Figs. 4 and 5, respectively. In the figures, ε indicates the direction in which the displacement of the light spot is detected; V_1 and V_2 denote the output voltage of photodetectors. System A is sometimes used for an inspecting lens. Its characteristic is shown in Fig. 5(a). In this case, the intensity distribution of light is required to be uniform on the surface of lens. If the distribution is not uniform, that is, V_1 and V_2 characteristics are not symmetric such as V_1 and V_2' in consequence of the change in θ, an error corresponding to X' enters. The characteristics of system A′, B, and B′ are shown in Fig. 5(b). In the case of A′, the uniformity of light intensity is required for the same reason as in A. In the case of A, A′, B, and B′, a change in the sensitivity of a photodetector such as V_2' results in an error corresponding to X' as shown in Fig. 5. The systems C and C′ are free from the problems illustrated by Fig. 5. Because of the existence of the error signal V for large absolute value of ε, the system A is preferable to the servo-system. According to the design considerations mentioned above, we have adopted system C as shown in Figs. 1 and 2.

Unlike the mechanical stylus, if any automatic compensation is not employed, the voltage-to-displacement ratio K in Fig. 3 changes unceasingly during the profiling operation. In this case, K is proportional to the efficiency factor of scattering σ and consequently to the received power P_r. The received power P_r vs θ measured by the apparatus of Fig. 1 is shown in Fig. 6. In the case of the profiling for brass surfaces, the received power P_r varies more than a hundred times as θ varies from zero to 70°. An automatic gain control system shown in Fig. 1 is adopted to compensate the variation. Since the unmodulated component of received light is proportional to P_r, the amplifier gain is controlled in such a way that the dc component of the output voltage is held to a constant value E. Thus the ratio K is kept to be constant for a thousandfold change in P_r.

Design considerations concerning servo-characteristics of the optical profiling system will be described next. Fidelity of profiling can be much improved by employing a two-dimensional servo-system in the same way as the mechanical profiling cutter. The system has the stationary-state characteristics as shown in Fig. 1, where (1) holds, and

$$V_x = V_{max} \cdot \varepsilon/\varepsilon_0 \tag{3}$$

$$V_y = (1 - |\varepsilon|/\varepsilon_0) \cdot V_{max} \tag{4}$$

$$V_x/V_y = \tan\theta \tag{5}$$

and stationary-state displacement

$$\varepsilon = \varepsilon_0 \tan\theta/(1 + \tan\theta) \tag{6}$$

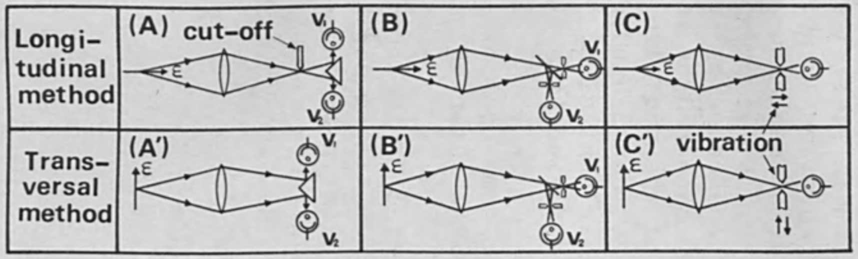
Longi-tudinal method
(A) cut-off
V_1
V_2
(B)
(C)
Trans-versal method
(A')
(B')
(C') vibration
ε

FIG. 4.—Several systems for detecting focus.

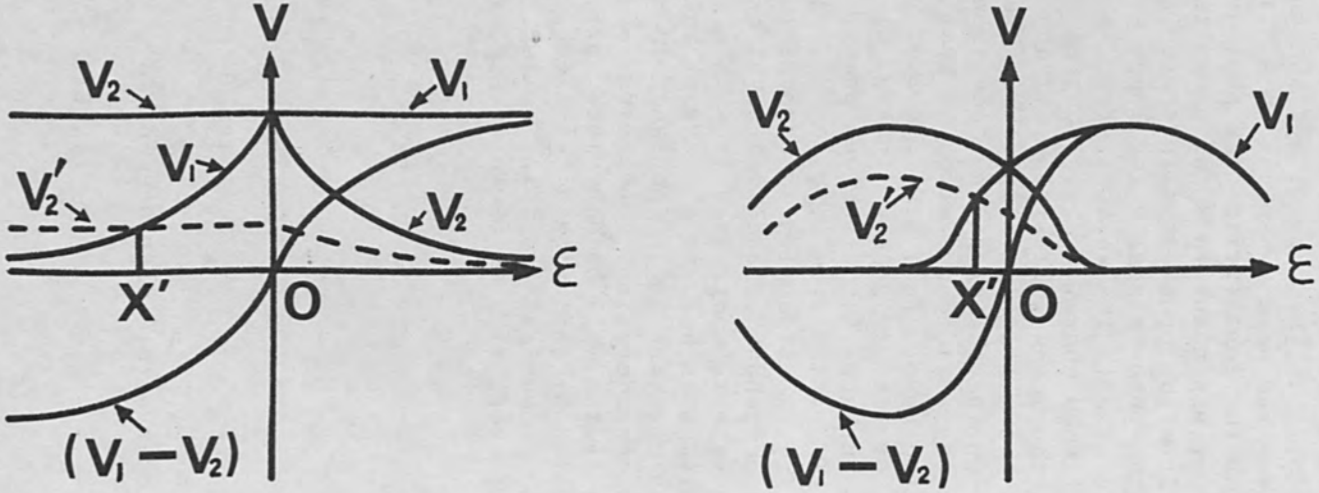

(a)

(b)

FIG. 5.—Characteristics for detecting focus.

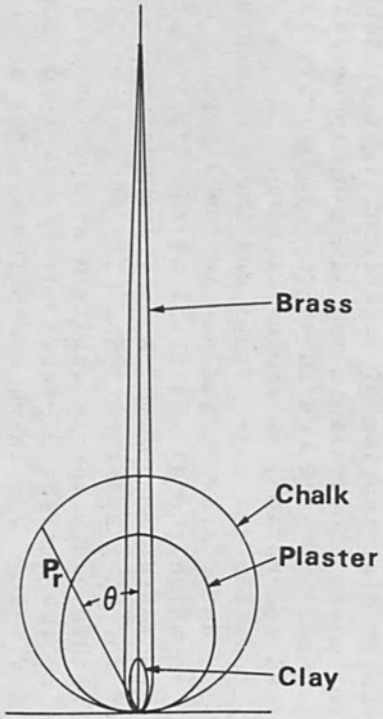

FIG. 6.—Received power P_r vs angle of incidence θ.

For the transient state,

$$d\epsilon/dt = V_y \tan \theta - V_x \tag{7}$$

The system can be represented by transfer functions as shown in Fig. 7, where K_p and K_v denote constant gain, T_m is the time constant of the servo-motor of the mechanism carrying the optical system, and N is the ratio of V_x to the shaft velocity of the servo-motor. The dynamic response to a zero-to-θ step change is observed by an analog computer to determine the condition of critical damping. One of the results is shown in Fig. 8, where stationary-state displacement ϵ vs v_{max} is given for various values of T_m. As can be seen from the figure, ϵ is proportional to the maximum speed V_{max}.

4. RESULTS AND DISCUSSIONS

The lenses used in the experiment are designed to reduce the spherical aberration, especially at the focus. Observable errors caused by spherical aberration are shown in Fig. 9 for these lenses. The sample in Fig. 1 is replaced by a plane mirror and only the V_x loop is actuated while the V_y loop is stopped. Then displacement in X direction is plotted for the angle of incidence θ when the plane mirror is rotated with the light spot as the central point. When the reflected laser beam moves from center to edge of the objective lens as θ increases, maximum error caused by spherical aberration is observed as shown in Fig. 9. The results agree with the design of lenses under test. The test is also necessary for optical alignment of the profiling system. In the experiment, the divergence angle of the laser beam is about 10^{-3} radian and diameters of the light spot are 15, 27, 36, and 120 μ for the lenses of focal length 15, 25, 35, and 100 mm, respectively. In the previous work,[1] no design considerations were given to reduce the spherical aberration of lenses and diameter of the light spot was 0.2 mm for the lens of 60-mm focal length. We find that when the V_y loop is stopped, the sensitivity or the repeatability of X in the system shown in Fig. 1 is better than 1 μ for both cases of low and large aberration lenses. These results confirm what is described in Table I.

The performance of the automatic gain control system is shown in Fig. 10 for brass, which is a most severe case. As can be seen from the figure, the output voltage from lock-in detector V' is perfectly compensated for the change in θ ranging from zero to 80° and the width of linear part L increases by about 40% because of the saturation effect of the system.

Observed contours for various samples are shown in Fig. 11. These contours involve errors shown in Table 2. The lower limit of the spot diameter is 5 μ because of difficulty in servo-control owing to smaller L, which is several times as long as the diameter. Though the stationary-state displacement ϵ predominates in error, particularly for rapid scanning, the value of ϵ is indicated by the lock-in detector as shown in Fig. 12(b). Superposition of two curves in Fig. 12(b) yields curve (c) which is similar to curve (a), settling the problem of error caused by ϵ. Using this method of correction, ϵ smaller than L/2 is allowable. In the case of the He-Ne 6328-Å laser, L/2 ranges from 130 to

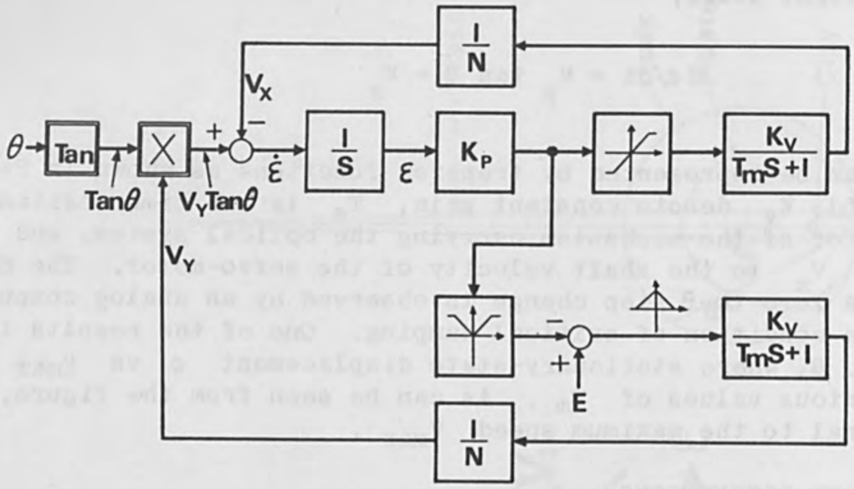
θ
Tan
Tanθ
V_Y Tanθ
V_X
+
−
ε̇
1/S
ε
K_P
K_V / (T_m S+1)
1/N
V_Y
−
+
E
K_V / (T_m S+1)
1/N

FIG. 7.—Block diagram of transfer functions for optical profiling system shown in Fig. 1.

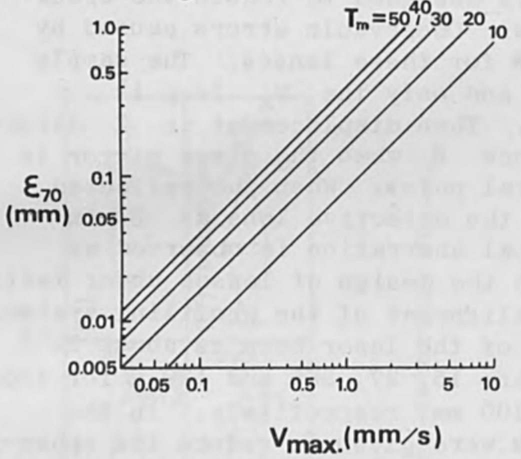

FIG. 8.—Stationary-state displacement ϵ_{70} (ϵ for $\theta = 70^\circ$) vs V_{max} under condition of critical damping.

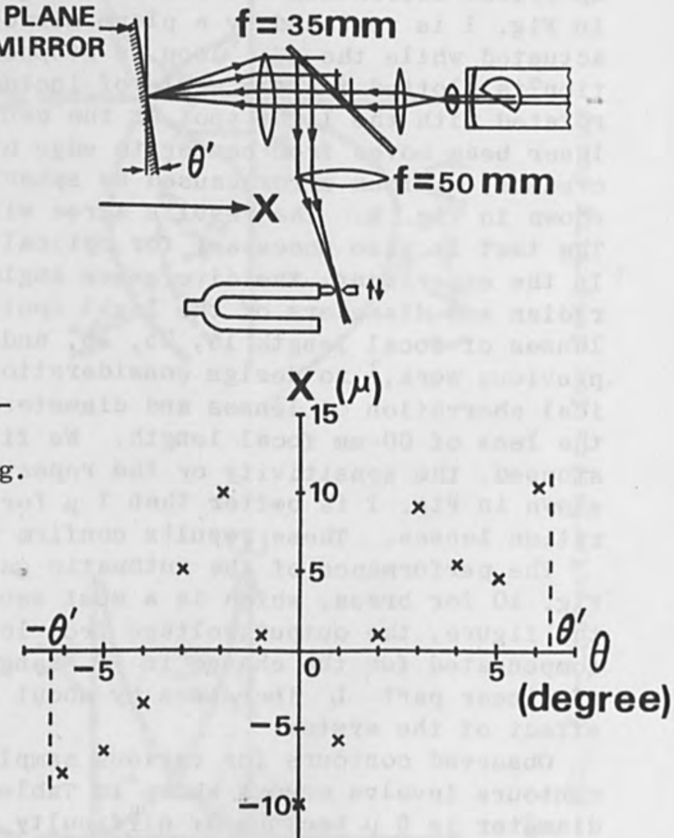

FIG. 9.—Observable error caused by spherical aberration.

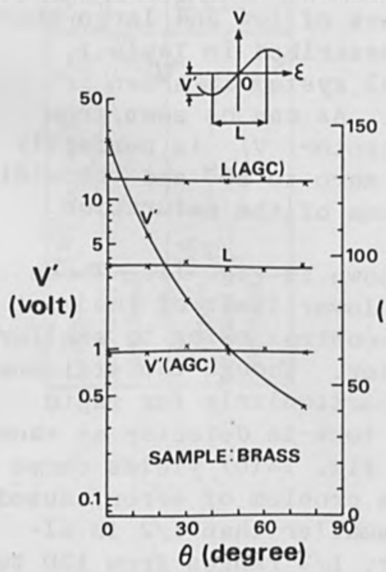

FIG. 10.—Performances of automatic gain control system.

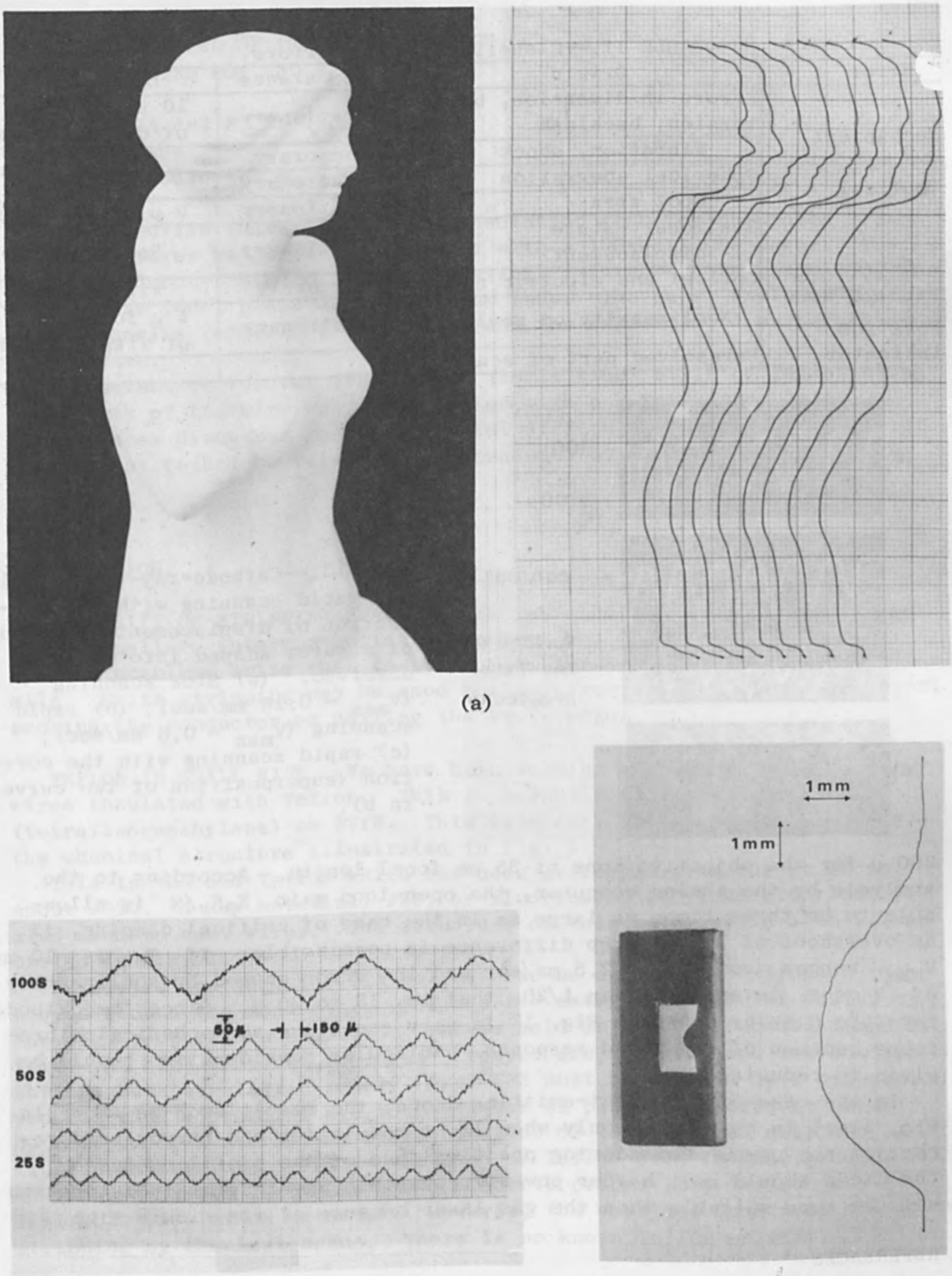

FIG. 11.—Observed contours of various samples: (a) plaster statue, (b) standard sample of surface roughness, (c) hollow clay model. Contours (a) and (b) are observed by using He-Ne laser, contour (c) by using light-emitting diode.

TABLE II.—Classification of errors.

Error	Origin	Appearance	Lower limit
Mechanical	Errors in dimension, bend torsion, backlash	Stationary	10 μ for 25 cm of displacement
	Vibration, shock	Temporary	
Optical	Spherical aberration	Stationary	5 μ
	Spot area	Stationary	5 μ of diameter
Servo-	Stationary-state displacement	Stationary	See Fig. 8
	Optical and electric noise	Temporary	Within 1 μ
Position indicator	Nonlinearity of scale	Stationary	1 μ for 25 cm of displacement
	Unresolved part of scale		1 μ

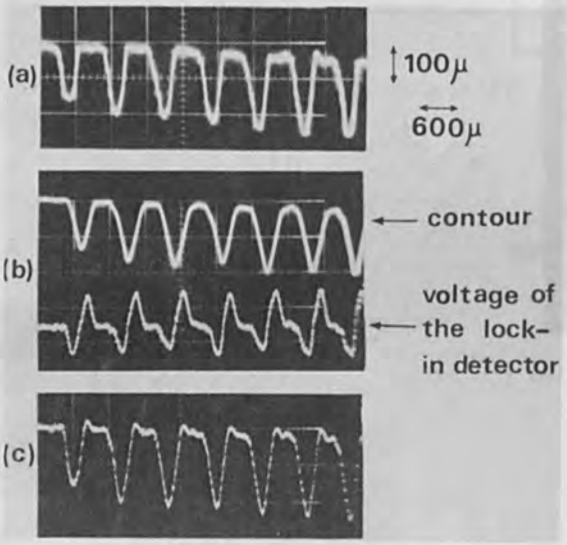

FIG. 12.—Cathode-ray-tube display for rapid scanning with the correction of displacement. Contour of a screw shaped into chalk is observed. (a) Slow scanning (V_{max} = 0.16 mm/sec); (b) rapid scanning (V_{max} = 0.6 mm/sec); (c) rapid scanning with the correction (superposition of two curves in b).

200 μ for the objective lens of 35 mm focal length. According to the analysis by the analog computer, the open-loop gain K_pK_V/N is allowable to be three times as large as in the case of critical damping, if an overshoot of 10% of step difference is permissible. If T_m is 10 ms, V_{max} ranges from 4.8 to 7.5 mm/sec and the error caused by nonlinearity of V vs ε is smaller than L/20, that is, 13 to 20 μ. Since the cathode-ray-tube display shown in Fig. 12 is very sensitive to mechanical vibrations because of its rapid response, particular consideration should be given to reducing it.

In the case of the light-emitting diode, the result such as shown in Fig. 11(c) is obtainable only when light modulation and narrow-band reception are used. Considering practical use of the profiling system, the diode should emit higher power for visible wavelengths in future and will be more suitable than the gas laser because of its minute size.

REFERENCES

1. S. Ando et al., IEEE J. Q. E. QE-3: 576, 1967.

2. A. Kamoi and I. Ogura, "Laser stylus for a layout machine, 1967 Conference on Laser Engineering and Applications, 6-8 June 1967, Washington, D.C.; and E. M. Bailey, U. S. Patent 3 016 464.

3. R. C. Gunter jr. et al., U. S. Patent 2 897 722; C. J. Glasser, U. S. Patent 2 385 503; S. Ando et al., Applied Optics 5: 1961, 1966.

SELECTIVE REMOVAL OF TEFLON INSULATION FROM WIRE USING CO_2 AND ARGON LASERS

A. D. TENCZA and R. W. ANGELO

IBM Corp., Endicott, N. Y.

The selective removal of Teflon insulation from Teflon-coated 3.5-mil-diam. wires has been demonstrated with a 100-watt CO_2 laser. The technique demonstrated employs a rotating fixture to permit rotating the wire in the focal plane of a germanium lens. The paper includes photographs showing removal of the Teflon and the exposed gold on beryllium copper wire.

The selective removal of a narrow (1-mil wide) strip of Teflon along the length of the wire was demonstrated with a 2-watt argon laser.

The paper discusses the experimental difficulties and limitations of the present technique relative to subsequent bonding operations.

INTRODUCTION

NECESSITY OF STRIPPING SMALL WIRES. As electronic packaging has become smaller, interconnecting conductors had to be reduced in size. Special problems arise when the wire diameter is approximately 3.5 mils. Knife stripping may be used but requires care in order to prevent scoring the conductor or dulling the knife edges.

TEFLON IN SMALL WIRE. We have been working with such small-diameter wires insulated with Teflon. This is DuPont's tradename for poly (tetrafluoroethylene) or PTFE. This material, also known as TFE, has the chemical structure illustrated in Fig. 1.

This is the old Teflon which has been available from DuPont since about 1950. A new material, FEP, or fluorinated ethylene-propylene is also used to coat wires. The structure of this material is also illustrated in Fig. 1.

As a wire coating, the FEP polymer can be applied by extrusion techniques around the conductor. FEP has the extended molecular chains of the high-temperature extrusion process held in place by normal temperature. At high temperature these stresses are relieved and the coating shrinks back by elastic memory. But TFE must be applied by a dispersion process that does not leave the stresses of plastic memory; it cannot be removed from microwires by application of temperatures near the extrusion temperature. TFE is the type of Teflon used in this study.

Because of its inertness and dielectric properties, Teflon is a desirable insulation material. However, the chemical inertness eliminates stripping by chemical means. There is no known Teflon solvent.

THERMAL DEGRADATION OF TEFLON. Not only is Teflon chemically inert, but it is thermally one of the more resistant polymers. It is, for example, used as a frying-pan coating. However, the material does degrade almost completely at temperatures on the order of 500°C. Figure 2, taken from Madorski, shows the percentage of sample volatilized as a function of time at 460, 475, and 485 °C.

Record of 10th Symposium on Electron, Ion, and Laser Beam Technology (L. Marton, ed.); San Francisco Press, Inc.

Copyright © by The Institute of Electrical and Electronics Engineers, Inc.—Printed in the U.S.A.

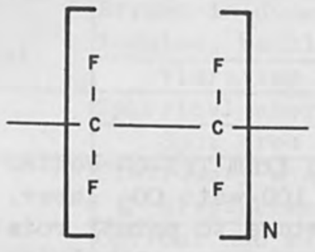

TFE
POLY (TETRAFLUORETHYLENE)

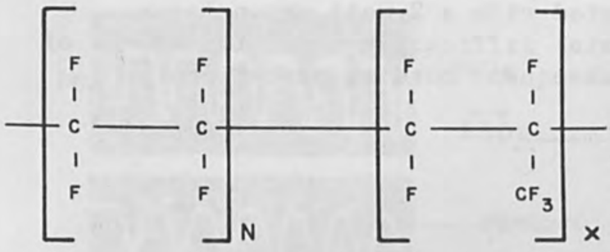

FEP
FLUORINATED ETHYLENE-PROPYLENE

FIG. 1.—TFE and FEP Teflon.

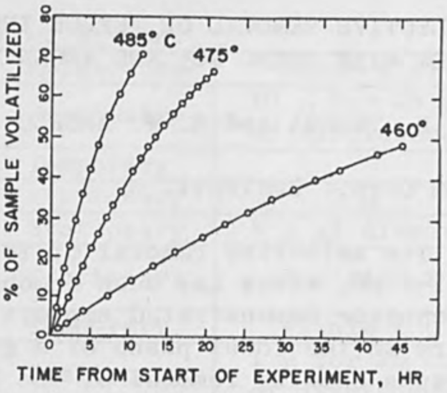

FIG. 2.—Cumulative volatilization of Teflon at low temperature as a function of time.[3]

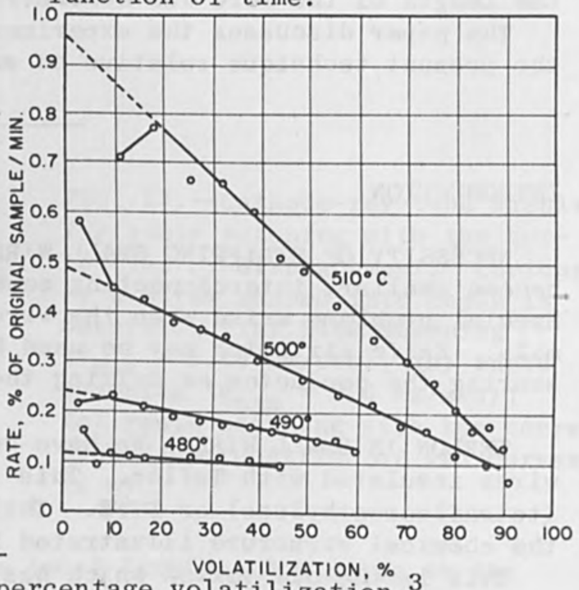

FIG. 3.—Rates of thermal degradation of Teflon in the tungsten-spring balance as a function of percentage volatilization.[3]

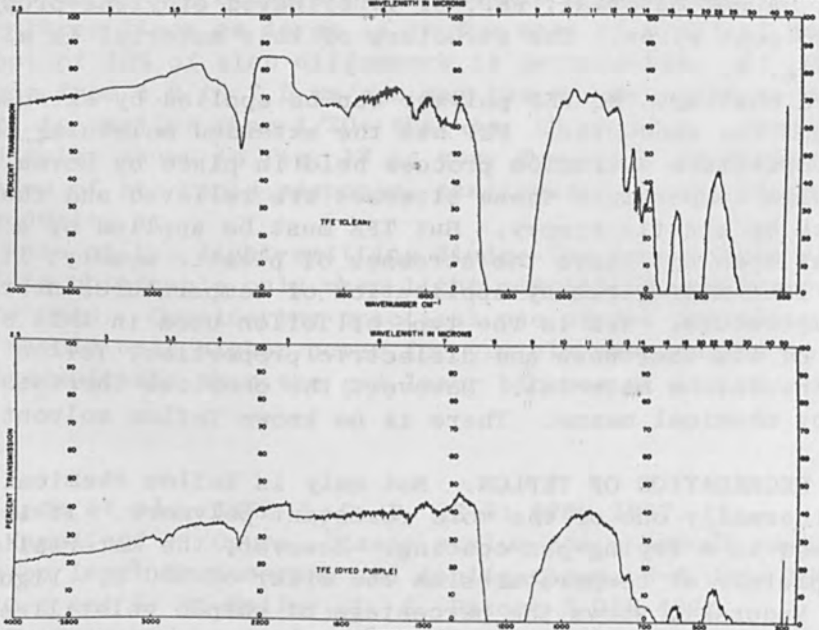

FIG. 4.—IR spectra of TFE (clear) and TFE (dyed).

Similar studies plotted as rate of degradation vs percent volatilization at various temperatures are shown in Fig. 3. The data indicate that the rate of degradation falls to zero only when 100% of the sample has been volatilized.

ABSORPTION OF CO_2 LASER RADIATION BY TEFLON. Figure 4 (top) shows the infrared spectral absorption of a 2-mil-thick clear film of poly (tetrafluoroethylene). The CO_2 laser emits radiation at 10.6 microns. At this wavelength, the 2-mil TFE transmits 68% of the radiant energy.

The relationship determining the absorption of light by a material is a function of thickness, in accord with the Lambert law. If I is the intensity of transmitted light and I_0 is the intensity of the incident light, then each increment of material absorbs a fraction of the light,

$$dI = -kI \ db$$

where b is the thickness of the material and K is a constant. Integration yields

$$\ln (I/I_0) = -kb$$

Substituting the transmittance value at 10.6 microns from Fig. 4 (top) and converting to base 10 logarithms yields the equation:

$$\log (I/I_0) = \log 0.682 = \frac{-K_{clear}}{2.303} (2 \text{ mils})$$

which yields the constant K for the clear Teflon,

$$K_{clear} = 0.193 \text{ mil}^{-1}$$

A sample of TFE stripped from the wire and pressed into a 1.4-mil-thick pellet produced the IR absorption spectrum shown in Fig. 4 (bottom). In the 10.6-micron region the percent transmittance is about 40%, corresponding to a constant K for the purple Teflon coating of

$$K_{dyed} = 0.655 \text{ mil}^{-1}$$

The increased value for the dyed Teflon may not be due to the purple dye, since the effect is approximately the same throughout the spectral region. More probably it is due to the particulate nature of the wire coating, which would cause an increase in light scattering in comparison with the more uniform sheet material.

Assuming that all the radiation is reflected from the gold the total path length for the laser light is then twice the thickness of the Teflon insulation on the wire or approximately 1 mil. Using the value of K for the purple of coating and neglecting curvature results in a percent transmittance of 52% for the insulation.

The absorption of light can also be expressed as absorbance or optical density A . The relationship between absorbance and transmittance is given by

$$\%T = 100\ I/I_0$$

$$A = \log\ (I_0/I) = 2 - \log\ \%T$$

The absorbance of the 1-mil-thick dyed TFE is then 0.28 and that of the clear TFE is 0.08.

Table I summarizes the transmittance and absorbance calculations.

TABLE I.—Absorbance and transmittance calculations.

%T	I/I_0	$\log I/I_0$	K (mil)	b (mil)
68	0.68	-0.167	0.1934	2.0 clear
82	0.82	-0.084	0.1934	1.0 clear
40	0.40	-0.398	0.6547	1.4 dyed
52	0.52	-0.284	0.6547	1.0 dyed

EXPERIMENTAL

APPARATUS. A 100-watt 10.6-micron Korad CO_2 cw (120-Hz) laser served as the source; the focusing element was a 3-in. focal length germanium lens. The small-diameter wire produced a number of unique handling problems. In order to provide uniform exposure to the focused laser energy, precision wire rotation fixtures were designed and built (Figs. 5 and 6). The single-spindle fixture (Fig. 5) was a convenient design for exposing a few samples quickly without having to load and thread the 3.5-mil-diam Teflon wire after each sample. The over-all length of the free end of Teflon wire was limited by the tendency of the wire to twist and kink the Teflon coating. Approximately 2 ft of free wire was found to be optimum and provide several well-spaced samples.

The narrow focused beam width of the CO_2 laser indicated a need for a precision rotation fixture. In the single-spindle fixture, precision rotation was accomplished by passing the wire over two nonrotating brass "pulleys." A 20-g magnet clamp provided tension of the free end.

The dual-drive fixture was designed for greater precision in positioning. In this scheme (Fig. 6), both ends of the wire rotate. Precision-bored and pre-aligned caps and holes served as only a rough guide for the wire. A hole diameter of approximately 12 mils in the caps was used because of the difficulty in threading 3.5-mil wire.

Elimination of the remaining irregular wire motions was achieved by raising the Teflon wire with the Teflon wire support illustrated in Fig. 7. The support was positioned by a precision xyz positioning device.

The wire-support mechanism itself was designed to provide minimum friction and to allow locating the region of focus of the beam. Minimum friction was achieved by routing the wire between two adjacent ball

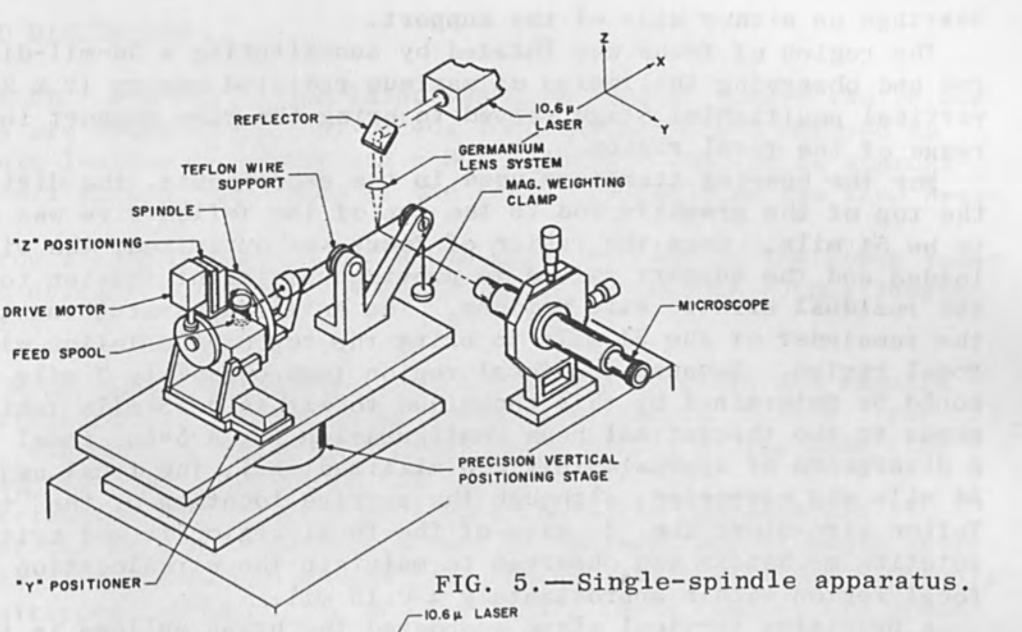
Z
X
Y
REFLECTOR
10.6μ LASER
GERMANIUM LENS SYSTEM
TEFLON WIRE SUPPORT
MAG. WEIGHTING CLAMP
SPINDLE
"Z" POSITIONING
DRIVE MOTOR
MICROSCOPE
FEED SPOOL
PRECISION VERTICAL POSITIONING STAGE
"Y" POSITIONER

FIG. 5.—Single-spindle apparatus.

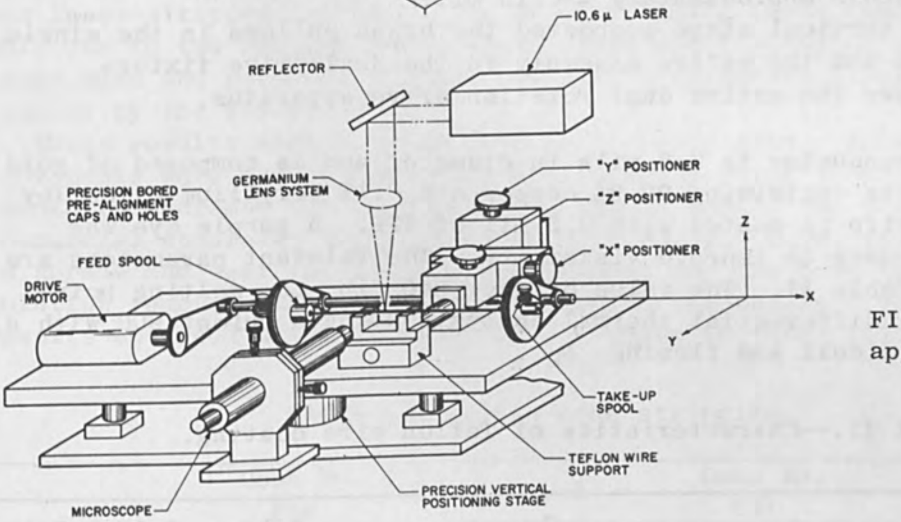
10.6μ LASER
REFLECTOR
"Y" POSITIONER
GERMANIUM LENS SYSTEM
"Z" POSITIONER
PRECISION BORED PRE-ALIGNMENT CAPS AND HOLES
Z
"X" POSITIONER
FEED SPOOL
DRIVE MOTOR
X
Y
TAKE-UP SPOOL
TEFLON WIRE SUPPORT
MICROSCOPE
PRECISION VERTICAL POSITIONING STAGE

FIG. 6.—Dual-drive apparatus.

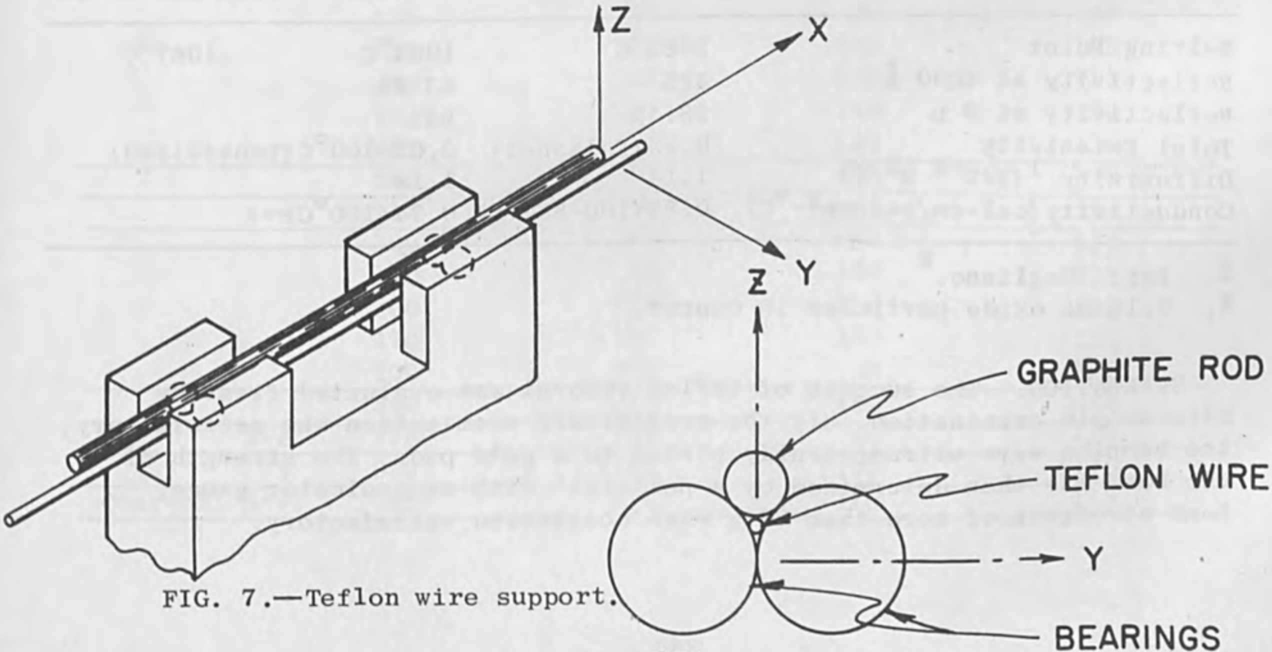
Z
X
Z
Y
GRAPHITE ROD
TEFLON WIRE
Y
BEARINGS

FIG. 7.—Teflon wire support.

bearings on either side of the support.

The region of focus was located by substituting a 36-mil-diam graphite rod and observing the region of maximum radiated energy (Y & Z). The vertical positioning stage served to bring the wire support into the range of the focal region.

For the bearing diameters used in the experiments, the distance from the top of the graphite rod to the top of the Teflon wire was calculated to be 54 mils. Once the region of focus was optimized, the wire was loaded and the support raised to provide sufficient tension to remove the residual erratic wire motions. The entire apparatus was then raised the remainder of the 54 mils to bring the top of the Teflon wire into the focal region. Because the focal region (approximately 7 mils in diameter), could be determined by this technique to within ± 25 mils (which corresponds to the theoretical beam configuration for a 3-in. focal length and a divergence of approximately 2.5 milliradians), the final adjustment of 54 mils was warranted, although the precise location of the "top" of the Teflon wire along the Z axis of the focal region is not critical. The rotating mechanism was observed to maintain the wire location in the focal region within approximately ± 0.15 mil.

A precision vertical stage supported the brass pulleys in the single spindle fixture and the entire assembly in the dual-drive fixture.

Figure 8 shows the entire dual rotation drive apparatus.

WIRE. The conductor is 2.5 mils in diameter and is composed of gold plating on a core containing 99.9% copper and 0.1% beryllium oxide (by weight). The wire is coated with 0.5 mil of TFE. A purple dye was added by the vendor to improve visibility. The relevant parameters are summarized in Table II. The value of the BeO in Cu melting point was obtained by differential thermal analysis using a DuPont 900 with a high-temperature cell and flowing N_2 .

TABLE II.—Characteristics of Teflon wire coating.

	Copper	Gold	0.1% BeO in Cu[2]
Melting Point	1083°C	1063°C	1067°C
Reflectivity at 4880 Å	42%	43.6%	
Reflectivity at 9 μ	98.4%	98%	
Total Emissivity	0.15 (Polished)	0.02@100°C (Unoxidized)	
Diffusivity [1] ($X10^{-4}$ M^2/S)	1.14	1.18	
Conductivity (cal-cm/sec-cm^2-°C)	0.85 (100-837°C)	0.74 (100°C)	

1. Ref: Gagliano.[2]
2. 0.1% Be oxide particles in copper.

EVALUATION. The success of Teflon removal was evaluated first by microscopic examination. If the preliminary examination was satisfactory, the samples were ultrasonically bonded to a gold pad. The strength of the bond was then determined by a pull test with an indicator gauge. Bond strengths of more than 80 g were considered satisfactory.

RESULTS AND DISCUSSION

ARGON LASER. A 2-watt argon laser was also used to remove the Teflon. The results are shown in Fig. 9. A 40x focusing objective removed an approximately 1-mil-wide region and a 20x objective removed an approximately 1.5-mil region. Swelling of the heat affected zone was also present.

The narrow stripped region limits the applicability of the argon laser since it is desired to remove completely an approximately 10-mil length of insulation.

RESULTS WITH SINGLE-SPINDLE APPARATUS. Figure 10 shows the results of laser stripping of 25 wires using the single-spindle fixture. For comparison, the bond strength of control wires bonded at the same time are given in the upper portion of the figure.

The distribution of bond strengths shows both the problems and the potential of the method. Some bonds were of satisfactory strength (over 80 g). This first technique showed poor reproducibility of both controls and laser-stripped samples. The scatter in the laser samples was probably due to two factors: nonreproducible positioning of the wire in the laser beam and possible residues (a thin transparent layer of Teflon not removed by the laser).

These results were obtained early in the program. Subsequently, improvements were made in the wire and in the bonding technique which tended to increase the bond strength and to reduce the scatter. The commercial apparatus illustrated in Fig. 11 uses twin fiberglass cones to abrade and tear the insulation. Except for the long length of insulation removed, this apparatus performed adequately. For comparison, results obtained using this method are shown in Table III.

TABLE III.—Twin-cone stripping.

	Cone No. 640	Control	Cone No. 661	Control
	110	120	90	60
	130	135	125	135
	120	140	130	125
	115	125	145	120
	85	130	130	130
	560	650	620	570
Ave.	112	130	124	114
	120	85	60	125
	0	60	100	125
	60	125	120	120
	110	130	120	135
	100	105	80	100
	390	505	480	605
Ave.	78	101	96	125
T	950	1155	1100	1175
Over-all Ave.	95	116	110	118

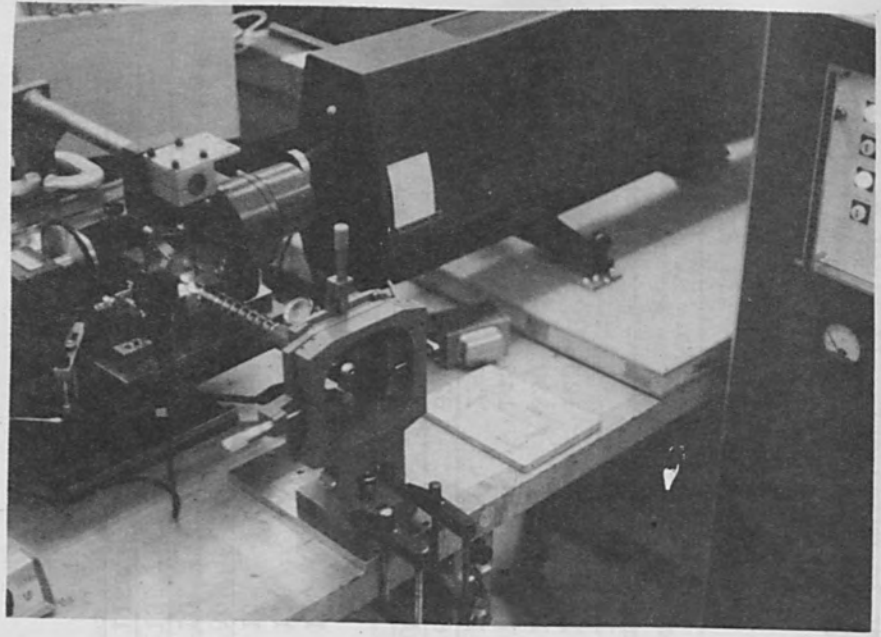

FIG. 8.—Dual-drive apparatus.

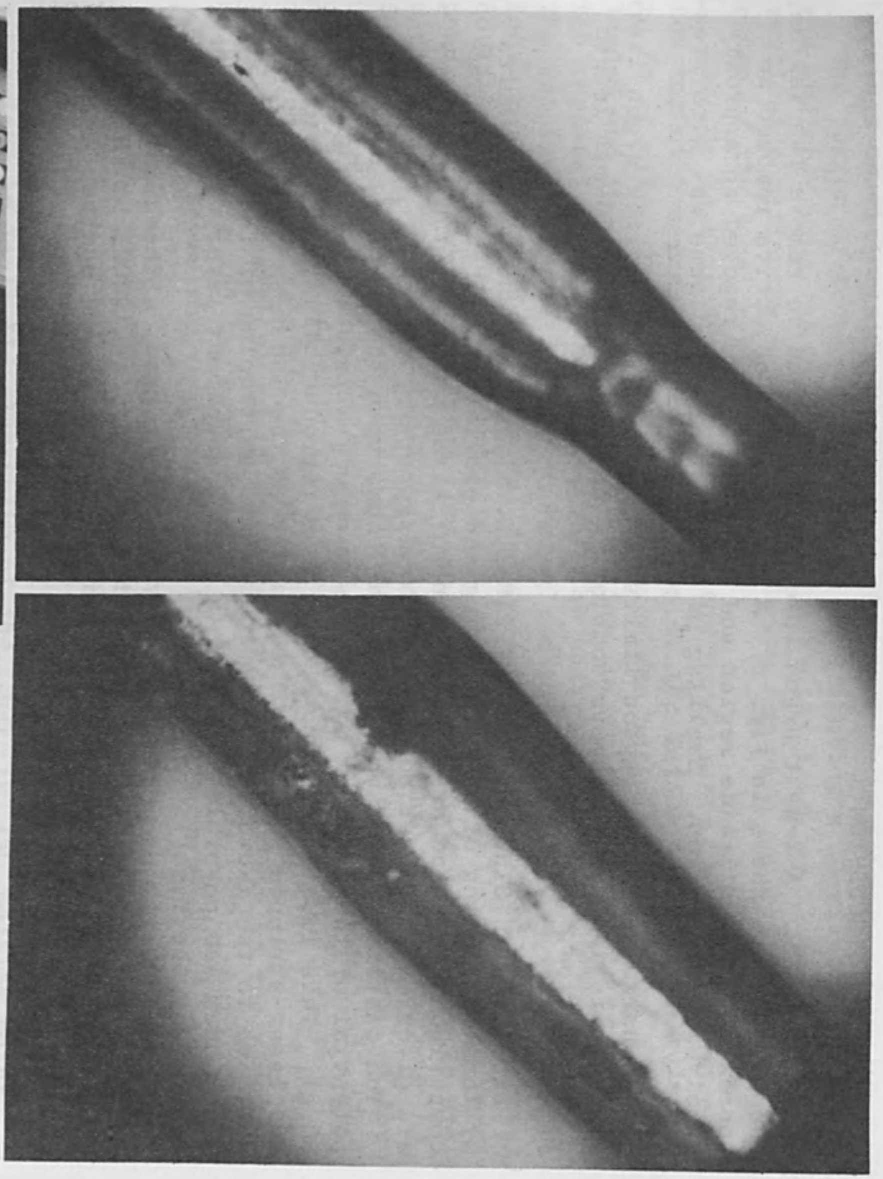

FIG. 9.—Teflon removal: with 40X objective (top) with 20X objective (bottom).

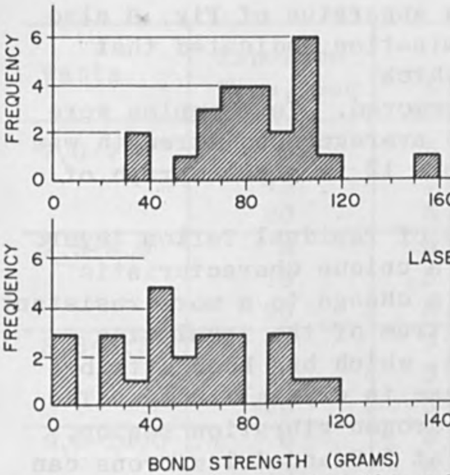

FIG. 10.—Bond strengths of laser-stripped wire and of controls.

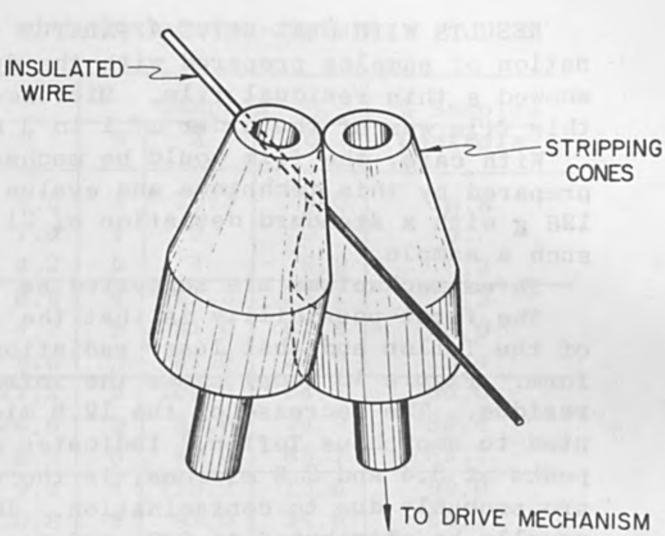
INSULATED WIRE
STRIPPING CONES
TO DRIVE MECHANISM

FIG. 11.—Twin-cone stripping apparatus.

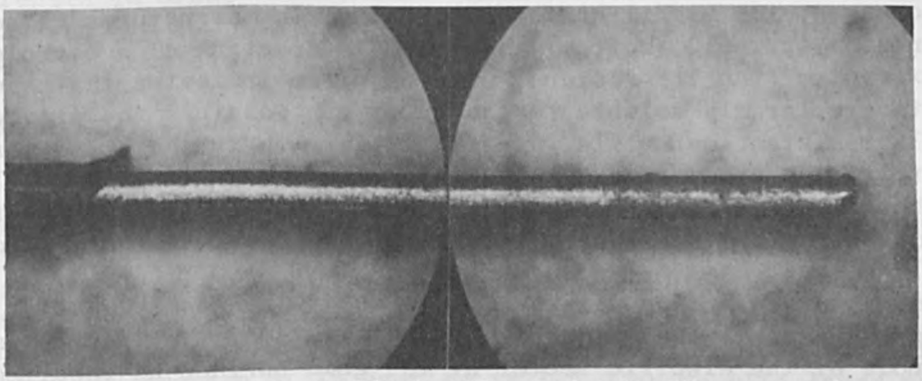

FIG. 12.—Laser residual film mechanically removed.

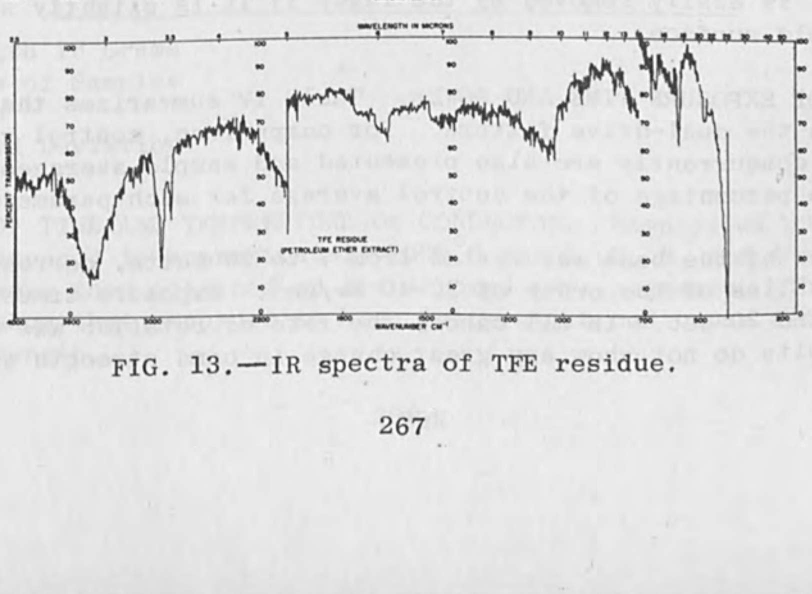

FIG. 13.—IR spectra of TFE residue.

RESULTS WITH DUAL-DRIVE APPARATUS (RESIDUAL FILM). Microscopic examination of samples prepared with the dual-drive apparatus of Fig. 6 also showed a thin residual film. Microscopic examination indicated that this film was of the order of 1 to 3 microns thick.

With care, the film could be mechanically removed. Ten samples were prepared by this technique and evaluated. The average bond strength was 126 g with a standard deviation of 21 g. Figure 12 is a photograph of such a sample.

Three mechanisms are suggested as the cause of residual Teflon layer.

The first possibility is that the layer is a unique characteristic of the Teflon and that laser radiation causes a change to a more resistant form. Figure 13 (top) shows the infrared spectrum of the insulation residue. The decrease of the 12.8 micron peak, which has been attributed to amorphous Teflon,[4] indicates an increase in crystallinity. The peaks at 3.4 and 2.8 microns, in the carbon-hydrogen vibration region, are probably due to contamination. The peaks at 5.8 and 6.1 microns can usually be attributed to C=O and to C=C , respectively. Whether the carbonyl is due to a contamination or the result of laser action in the presence of oxygen is not known. If the spectrum truly represents laser-caused changes, the significance of the resulting structures is not yet determined. Figure 13 (bottom) shows the IR spectrum of a petroleum ether extract of the TFE residue. The spectrum indicates that the contaminants are largely soluble in the extract. Possibly the products are thermally resistant materials which would survive further treatment. Alternately, the products are intermediates which would be volatilized by further laser energy. Separating the residual layer slightly from the gold surface and subsequent laser exposure does, in fact, remove the residue.

A second possible cause is the coherence of the laser energy. A standing wave established by the coherent nature of the laser beam would have a node of the electric vector at the gold surface as required by Maxwell's equations. Between the node and the first quarter wavelength (region of maximum intensity), the energy would range from zero to maximum. The effective wavelength λ/N (where λ is the wavelength of incident light and n is the index of refraction, 1.35) is 7.8 microns. Somewhat less than a quarter wavelength (less than 1.9 microns) would be the maximum thickness of the layer. In addition, the focused laser energy would form a high temperature plasma which would tend to obliterate the layer structure.

A third possible cause is the high thermal conductivity of gold in conjunction with the high reflectivity of gold at 10.6 microns. This is judged to be the most likely cause, since the layer (thickness greater than $\lambda/4$) is easily removed by the laser if it is slightly separated from the gold surface.

EFFECT OF EXPOSURE TIME AND POWER. Table IV summarizes the data obtained with the dual-drive fixture. For comparison, control values determined concurrently are also presented and sample averages are presented as a percentage of the control average for each parameter combination.

The power of the beam was varied from 7 to 10 watts, corresponding to energy densities of the order of 30-40 kw/cm^2. Exposure times were set at 6, 15, and 20 sec. In all cases, the rate of rotation was 34 rpm.

The results do not show any great change in bond strength with time.

TABLE IV.—Data obtained with dual-drive fixture.

Watts	Exposure Time, Sec	Controls			Samples			% Samples/Controls
		N	$\bar{X}$	σ	N	$\bar{X}$	σ	
7.0-7.3	6	5	134.0	6.5	4	22.5	5.0	16.8
	15	5	139.0	7.4	4	0	0	0
	20	5	124.0	4.2	5	4	8.9	3.2
7.5-8.0	6	5	136.0	8.9	4	11.3	13.1	8.3
	15	5	131.0	4.2	5	51.0	61.9	38.9
	20	5	136.0	9.6	5	21.0	21.9	15.4
8.3-9.3	6	5	120.0	27.2	5	102.0	24.1	85.0
	15	5	128.0	26.6	5	81.0	34.9	63.4
	20	5	131.0	8.2	5	82.0	68.7	62.7
9.0-10.0	6	5	135.0	9.4	4	133.7	13.8	99.0
	15	5	134.0	10.8	5	93.0	34.6	69.4
	20	5	135.0	10.0	6	121.7	23.8	90.2

Bond Strength in Grams
All at 34 rpm
N = Number of Samples
$\bar{X}$ = Average
σ = Standard Deviation

This finding may be due to poor control of the laser output. However, as the power increases, the average bond strengths also increase, until the range of 9.0 to 10.0 watts gives averages as high as 99.0% of the controls. The same data are presented in Table V with the exposure times averaged out. The average bond strength increases rapidly with increased power until the average of 15 samples is 115.3 grams with laser power at 9.0 to 10.0 watts.

TABLE V.—Data of Table IV with averaged exposure times.

Watts	N	$\bar{X}$	σ
7.0-7.3	13	8.5	11.4
7.5-8.0	14	28.9	40.9
8.3-9.3	15	88.3	44.3
9.0-10.0	15	115.3	29.6

Bond Strength in Grams
N = Numbers of Samples
$\bar{X}$ = Average
σ = Standard Deviation

EFFECT OF TIME AND TEMPERATURE ON CONDUCTOR. Samples of uninsulated wire were exposed to approximately 1000°C for 1, 2, 3, and 4 sec. Bond strengths were then obtained on the exposed wire segments. The results (Fig. 14) show that exposure to high temperature can cause a decrease in bond strength.

SUMMARY AND CONCLUSIONS

We have demonstrated feasibility for laser stripping of Teflon-insulated small-diameter wires. A comparatively low power range (30-40 kw/cm^2) was investigated at 6, 10 and 20 sec. By averaging the results over this time span, 15 samples gave an average of 115.3 grams at 9.0 to 10.0 watts. Further, the results show an increase in bond strength with increased power over the range explored.

The problems of handling the wire and of bringing the laser energy to the insulation have been overcome. A suitable mechanical device has been built. By using a graphite rod, the micro wire may be easily located in the focal region.

IR studies show that the residue is probably unvolatilized Teflon. The cause of this layer is probably protection by the thermal conductivity of the metal. In spite of this residue problem, proper parameter selection gave samples with bond strengths of 99% of control values.

ACKNOWLEDGMENTS

The authors wish to acknowledge the assistance of H. Houghtalen for evaluation of the samples by ultrasonic bonding. The apparatus was built by R. Taber and A. Wood. G. Ogden helped run the laser experiments. Finally, we should like to express our appreciation to the Materials and Process Group of IBM Owego for permission to use the CO_2 laser and to M. Chaffee for his assistance in obtaining the experimental data.

R. Boyce obtained the IR absorption data and with R. Pizzo prepared the IR samples. D. Berg performed the differential thermal analysis.

REFERENCES

1. Handbook of Chemistry and Physics.

2. F. P. Gagliano, R. M. Lumley, and L. S. Watkins, "Lasers in industry," Proc. IEEE, February, 1969.

3. S. L. Madorski, Thermal Degradation of Organic Polymers, New York: John Wiley and Sons, pp. 133-134.

4. G. M. Kline, ed., Analytical Chemistry of Polymers, Part 1, New York: Interscience, 1959; p. 182.

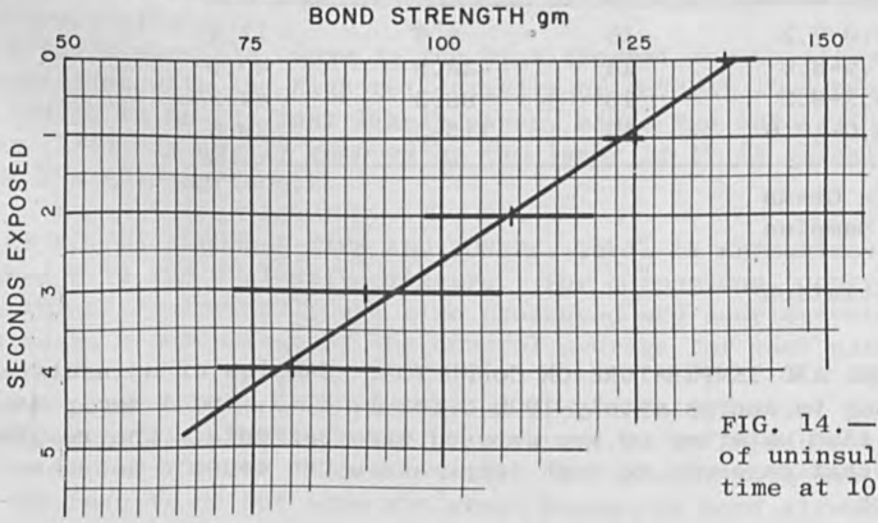

FIG. 14.—Bond strength of uninsulated wire vs time at 1000°C.

ROCK BREAKAGE BY MEANS OF ELECTRON BEAM PIERCING (LABORATORY TESTS)

B. W. SCHUMACHER and C. R. TAYLOR

Westinghouse Research Laboratories, Pittsburgh, Pa.

A stationary electron beam of 9 kW will pierce any rock, forming a narrow melt-cavity 2 to 4 in. deep. Most of the beam energy is deposited at the bottom of this cavity and leads to a temperature distribution with steep gradients. Consequently high thermal stresses develop which can break the rock. Laboratory tests showed that the energy efficiency of this mode of rock breakage is better than for conventional methods and other novel methods of drilling or rock breakage which have been investigated in recent years. So-called specific energy figures have been obtained of 240 J/cm^3 in diorite, 230 J/cm^3 in sandstone, and 112 J/cm^3 in granite. Even limestone breaks with an energy expenditure of less than 250 J/cm^3. The energy transfer from the electron beam to the rock is particularly efficient. The conversion efficiency from electrical energy into electron beam energy is also better than 90%. Therefore, based on energy requirements, the process can be considered competitive with any other rock breaking method.

INTRODUCTION

In a previous paper[1] we have shown how an electron beam can be used to cut rocks by making what has been called a melt-cut. Because of the high power and power density available in the electron beam the rock may be melted or even vaporized in a narrow channel less than 1/8 in. wide at the top and less than 5/8 in. wide at a depth of 2 to 3 in. It was discussed how by means of this slicing method prismatic sections can be cut from a solid rock face. It was also shown that thermal stress cracking may occur in some rocks producing breakage far beyond the region of the actual melt-cut. But this breaking action was not further discussed or analyzed.

Here we want to report on some new experiments where we have investigated the thermal cracking of the rock. The electron beam used was stationary or traveling across the rock face at slow speeds. In the stationary mode the electron beam drills or pierces a cavity into the rock until a certain equilibrium depth is reached. During this piercing process, as well as after the cavity has fully formed, nearly all the input power is deposited at the bottom or the lower quarter of the cavity heating a thin layer of the rock very quickly to the melting point. The temperature gradients which are produced in the adjacent rock are very steep because of the high power and power density. They lead to thermal-stress cracking of the rock regardless of whether or not the rock is of the "spalling" type. With this piercing mode of operation we get higher efficiencies for rock breakage than for instance with surface spalling. The latter can also be produced by an electron beam provided its power density is reduced, or provided it is swept over the surface at a very high speed.[2]

For measuring the efficiency of any rock-breaking method a parameter

Record of 10th Symposium on Electron, Ion, and Laser Beam Technology (L. Marton, ed.); San Francisco Press, Inc.
Copyright © by The Institute of Electrical and Electronics Engineers, Inc.—Printed in the U.S.A.

has come into use which is called specific energy. It is defined[5] as the energy expended divided by the volume of debris produced. It has been claimed that with this figure one may extrapolate from small-scale tests to large-scale tests safely. Applying it to our recent experiments we obtained figures for the efficiency of electron-beam rock breakage which compare very favorably with the figures for older methods.

MAIN FEATURES OF THE ELECTRON BEAM

A beam of 150-keV electrons can be focused to an energy density of 10^6 W/cm^2 and yet a narrow beam angle of a few degrees can be maintained at this power density level. When this beam hits a target all substances melt immediately and if there were no other impediments the melt front in the beam spot could proceed with speeds of 3 m/sec or more. Usually vaporization takes place as well, and the electron beam melts and vaporizes a hole for itself, thereby piercing the target to a considerable depth within a few seconds. It is essential that the melt front of the target material is not propagated via heat conduction; the individual electrons penetrate the surface of the solid or liquid target to some depth, regardless of its heat conduction properties.

The vapor which forms will not unduly impede the electrons either. In this selfgenerated hot-vapor channel, which represents a rarefied gas atmosphere, the electrons can travel a considerable distance before being scattered. Scattering of the electrons does, however, limit the depths to which the electron beam can pierce a target. In the equilibrium stage a cavity is present which is somewhat wider at the bottom than at the top as schematically shown in Fig. 1. It is typical for the electron-beam process that most of the power input is dissipated at the bottom of this cavity.[3] It is also significant that practically all of the power is transmitted to the rock because very little energy escapes as kinetic energy of the vapor jet which blows from the top of the cavity.[4] We may assume the walls of the cavity to be at the melting temperature of the rock $T = T_M$. The cavity grows to a final size where all the incoming power can just be dissipated by heat conduction through the walls under the molten surface layer of the cavity. This final size of the cavity is approached slowly; just before it is reached the power input is so high, and the coupling of the power to the rock so good, that very steep temperature gradients are produced around the bottom of the cavity. In first approximation we may assume the temperature distribution to be nearly spherical. In the center, which lies about 3 in. below the rock surface, it reaches the melting temperature T_M . It obviously induces high thermal stresses with a tendency to lift off the sections of the rock surrounding the cavity. This has indeed been observed. A more detailed analysis of the thermal stresses shall be given elsewhere.

EXPERIMENTS

In Figs. 2 and 3 we show once more what happens if a 9-kW electron beam travels across a rock surface at slow speed, namely 4 in./min. In Fig. 2 a piece of volcanic lava was subjected to the electron beam. It melted away rapidly and the liquid flowed out of the path of the electron beam owing to the fact that the piece was relatively thin and a slot was cut. Some, but not much, stress cracking can be seen. In Fig. 3 a piece

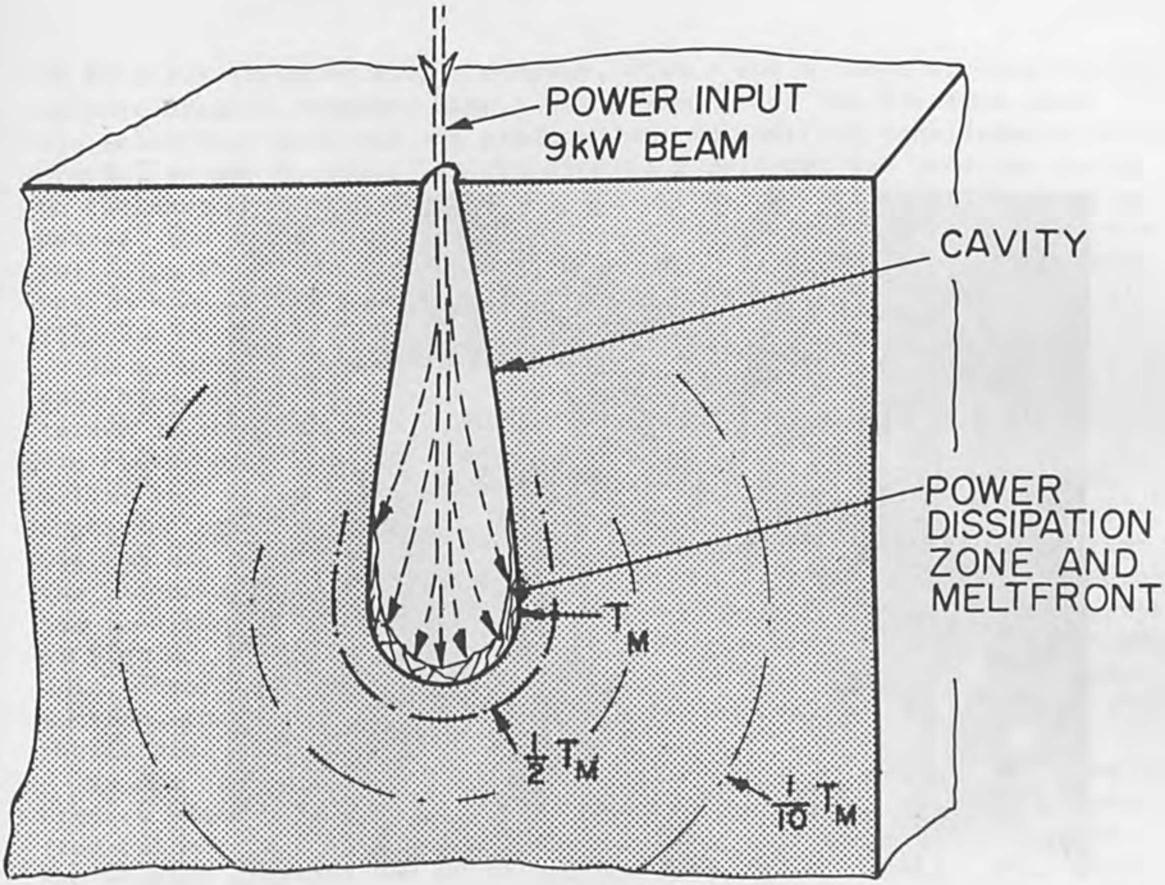
POWER INPUT
9kW BEAM
CAVITY
POWER DISSIPATION ZONE AND MELTFRONT
T_M
$\frac{1}{2}T_M$
$\frac{1}{10}T_M$

FIG. 1.—Cavity drilled into a rock by a stationary electron beam, power dissipation zone at the bottom of this cavity, and temperature distribution; schematic.

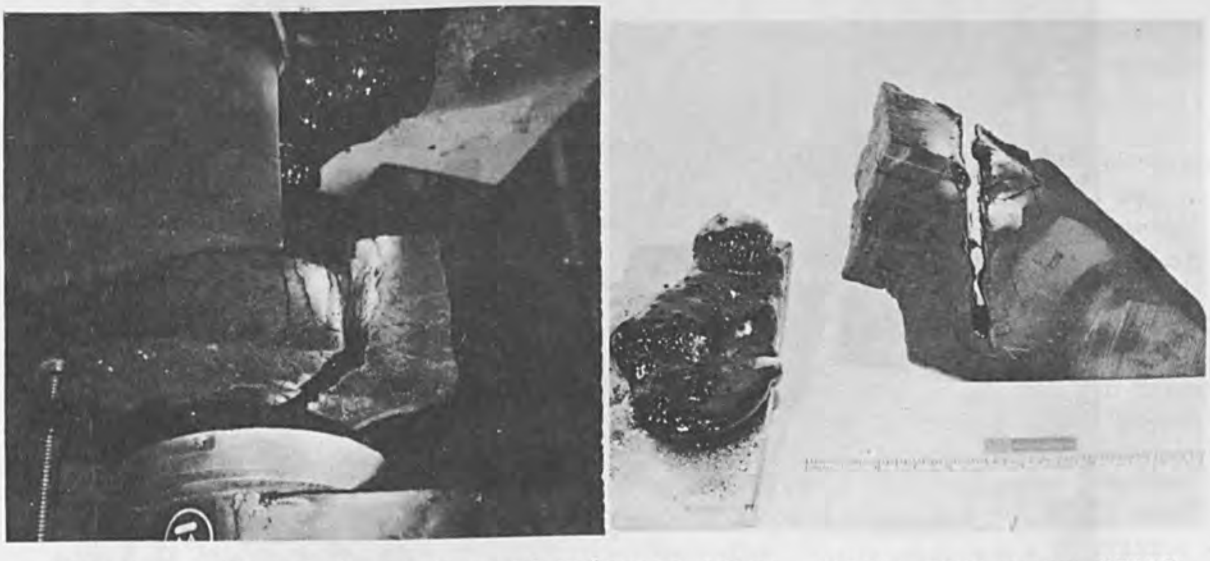

FIG. 2.—Melt-cut in a piece of volcanic lava: (left) rock piece under the electron gun; (right) view of slot and melted material.

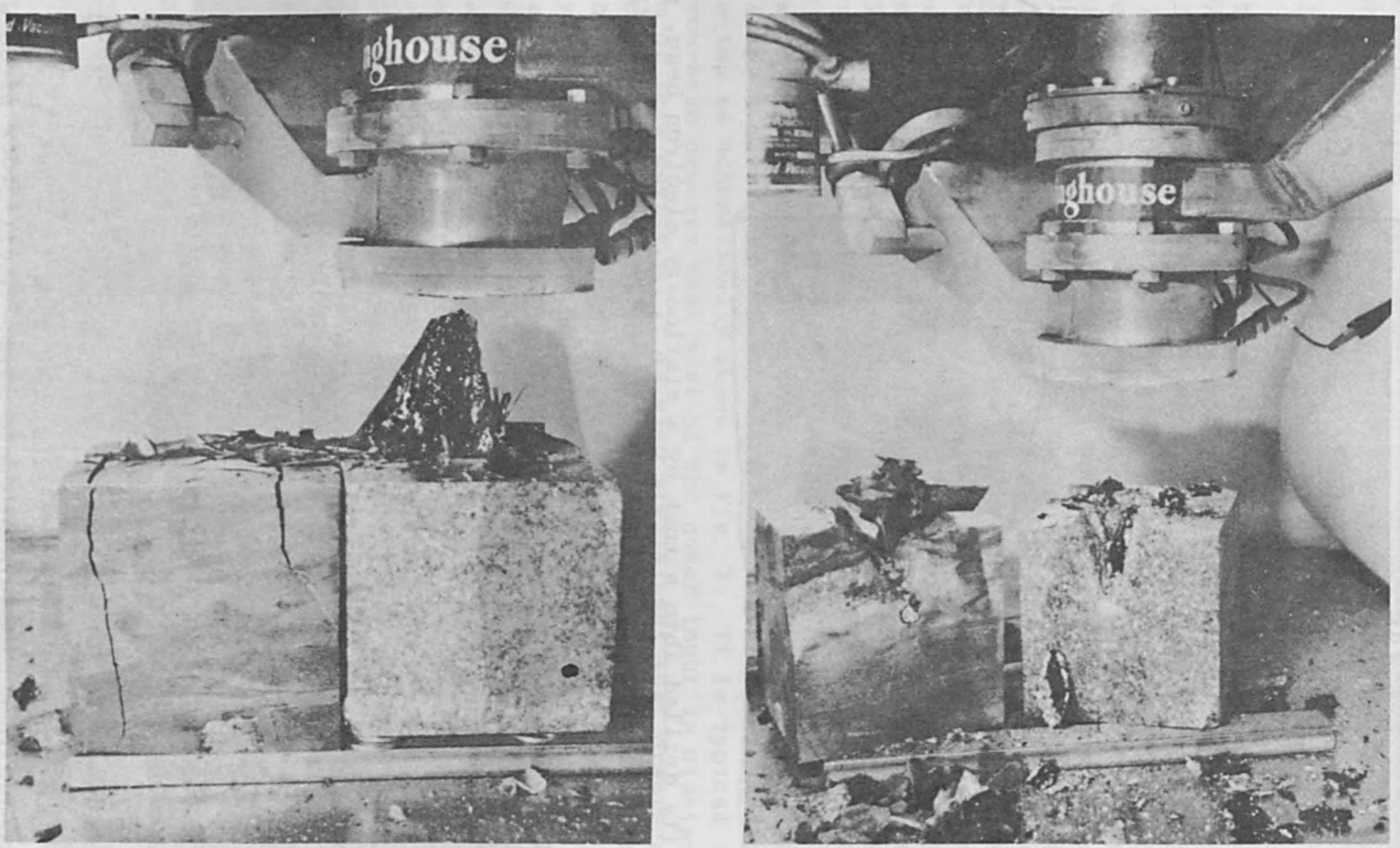

FIG. 3.—Melt cut in a 4 1/8-in. cube of Reserve taconite and a block of charcoal granite or Granodiorite. Pronounced thermal stress cracking occurred on the taconite but none in the diorite. The melt cut is equally deep in both blocks (1 7/8 in.). Beam power 9 kW at 150 kv, travel speed 4 IPM.

of taconite (Reserve Mining Company, Minn.) and a piece of diorite (Cold Springs Granite Company, Minn.) was placed under the electron beam. In the taconite a melt-cut was produced and in addition considerable stress cracks, as can be seen. In the diorite a melt-cut was produced going to the same depths as in the taconite but no thermal stress cracks appeared; the molten diorite, in this instance, stuck to the gun and was pulled up while still red hot when the work-piece table with the rocks was lowered. This produced the peculiar shape in the left picture of Fig. 3.

In a subsequent test other specimens of the same types of rocks were subjected to a stationary electron beam. Figure 4 shows the results obtained on the diorite or charcoal granite. A 9-kW beam was going into the center of the block with dimensions 4 X 4 X 4 in. and a weight of 6 lb 7 oz. It took 27.5 sec until breakage occurred as shown in the upper photograph of Fig. 4. The moment of breakage is very distinct. One can see light flashing through the cracks. To take the photograph the block was very carefully lifted off the work-piece table, photographed, and then broken apart by a slight blow as shown in the lower photograph of Fig. 4. There it can be seen that the electron beam cavity went about 3 in. deep into the rock. The cavity walls broke loose as a separate section, the tube-like structure that can be seen in the middle of the photograph.

It is, of course, hard to say how much longer it would have taken to break a block of twice the volume shown here. Some tests are planned to find out more about this dependence. Using just the present data we see we have expended 250 kJ to produce 1040 cm^3 of debris. This gives a specific energy figure of 240 J/cm^3.

The breakage of a block of taconite is shown in Fig. 5. The energy expenditure was slightly less. Figure 6 shows the breakage of a block of coarse-grained granite. It took the 9 kW beam 37 sec to achieve breakage; with the volume of the block being 5 X 8 X 4-3/8 in. or 2850 cm^3, a specific energy figure of 112 J/cm^3 results.

A fine-grained granite from Vermont was subjected to the stationary electron beam as well as to a beam traveling at 4 in./min. The breakage which resulted is shown in Fig. 7. It took nearly equal times in both modes of operation until breakage occurred. If we count half the volume of the block as debris then a specific energy figure of 315 J/cm^3 results.

A sandstone (of unknown origin) is shown in Fig. 8. It took 59 sec until it broke apart under the 9-kW beam. If we consider the two parts as the debris which was produced then we get a specific energy figure of 230 J/cm^3. The block is 4-1/16 in. thick and the melt cavity produced by the electron beam reaches right to the bottom. In this case the fused material adhered to the wall of the cavity and split in half with the block. Figure 9 shows a block of Sioux or Jasper quartzite (Jasper Stone Company, Jasper, Minn.). When hit by the 9-kW beam it broke apart after 9 sec. If we count two-thirds of the volume of the block as debris, then we get a specific energy figure of 244 J/cm^3. In the lower photograph of Fig. 9 one can see that the resolidified material, forming the walls of the beam cavity, sticks together and breaks away as a tubular piece, as we have observed in all the granites. Figure 9 shows very well how narrow the beam input channel is at its upper end.

A piece of copper ore is shown in Fig. 10. It originated from the dark gray massive zone of the White Pine Copper Company, Mich. The 9-kW beam was run across the surface at a speed of 4 in./min resulting in a

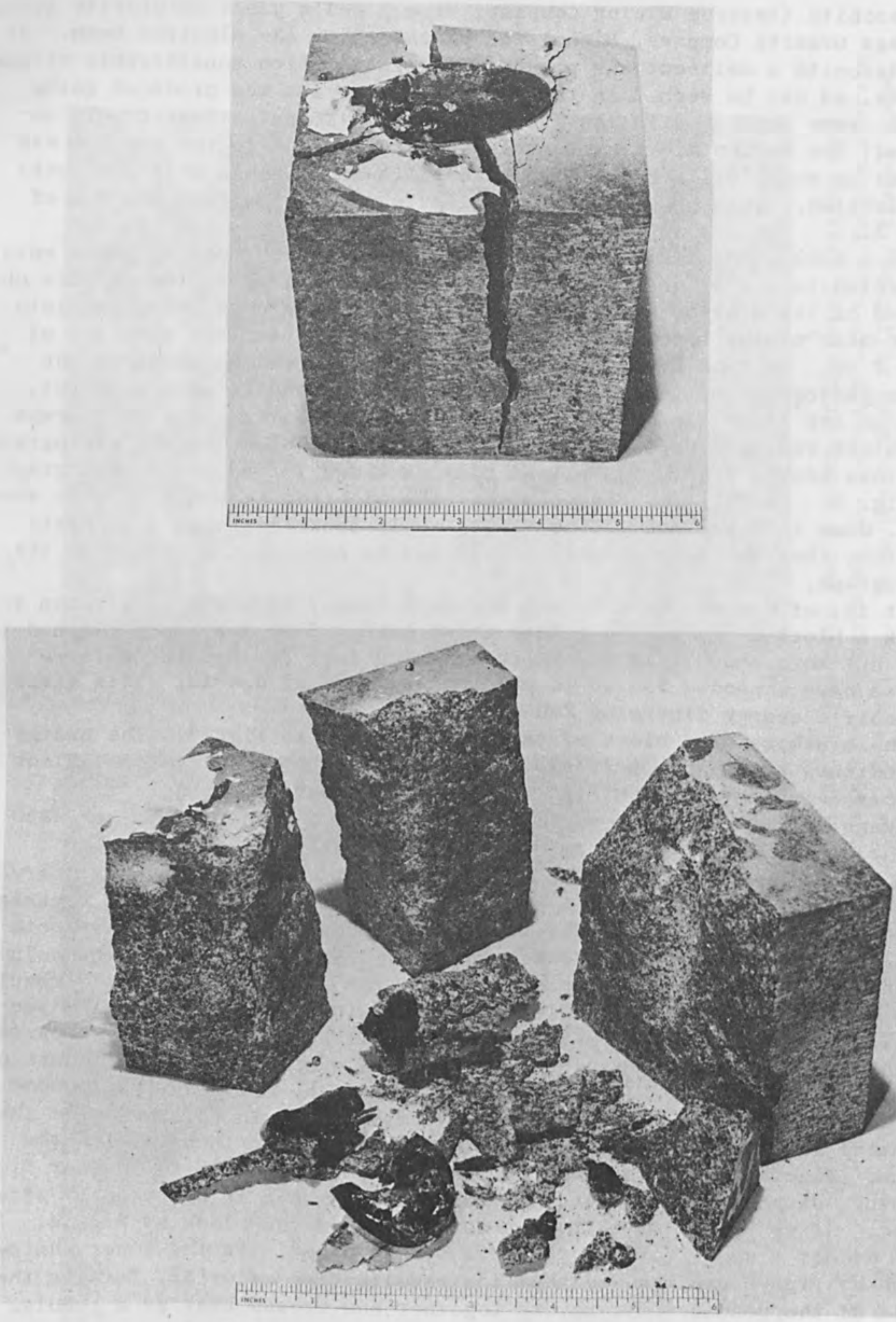
INCHES
1
2
3
4
5
6
INCHES
1
2
3
4
5
6

FIG. 4.—Piercing of a block of Granodiorite with stationary 9-kW electron beam; time to breakage 27.5 sec. Top: block carefully taken from the electron gun; bottom: broken by a slight blow.

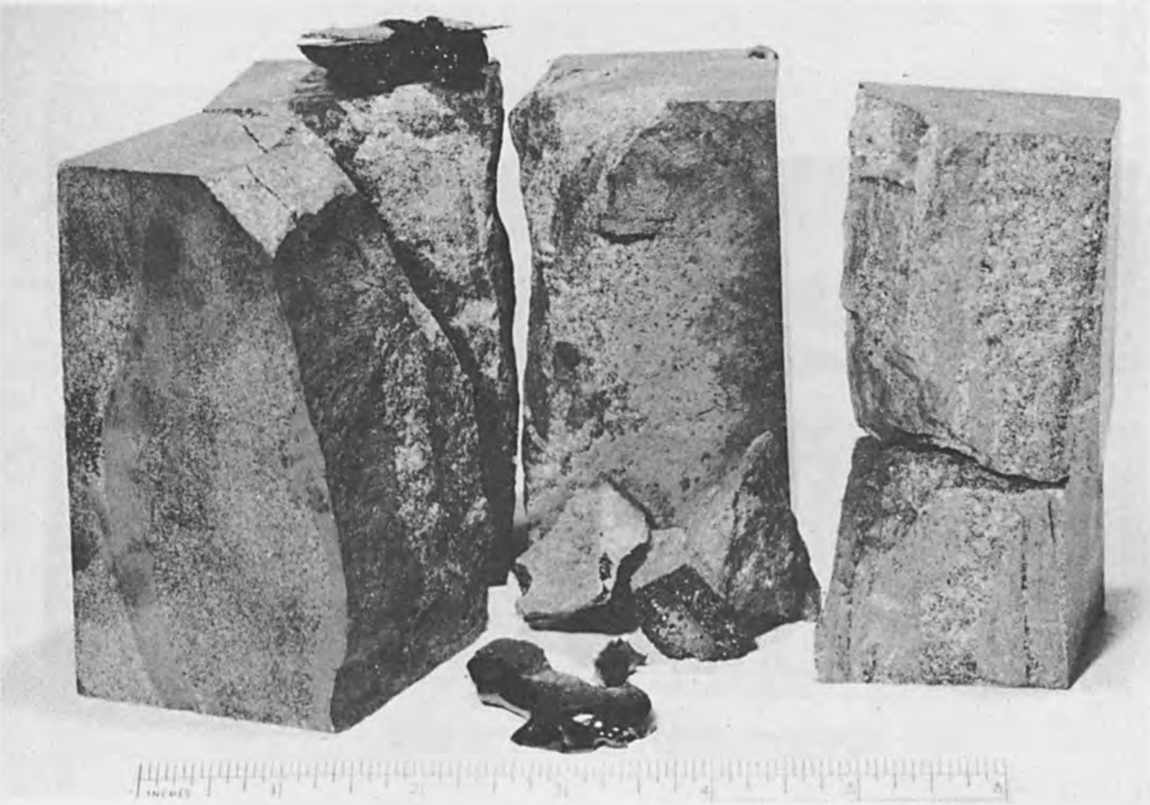
INCHES
1
2
3
4
5
6

FIG. 5.—Reserve taconite, thermal-stress cracking produced by stationary electron beam.

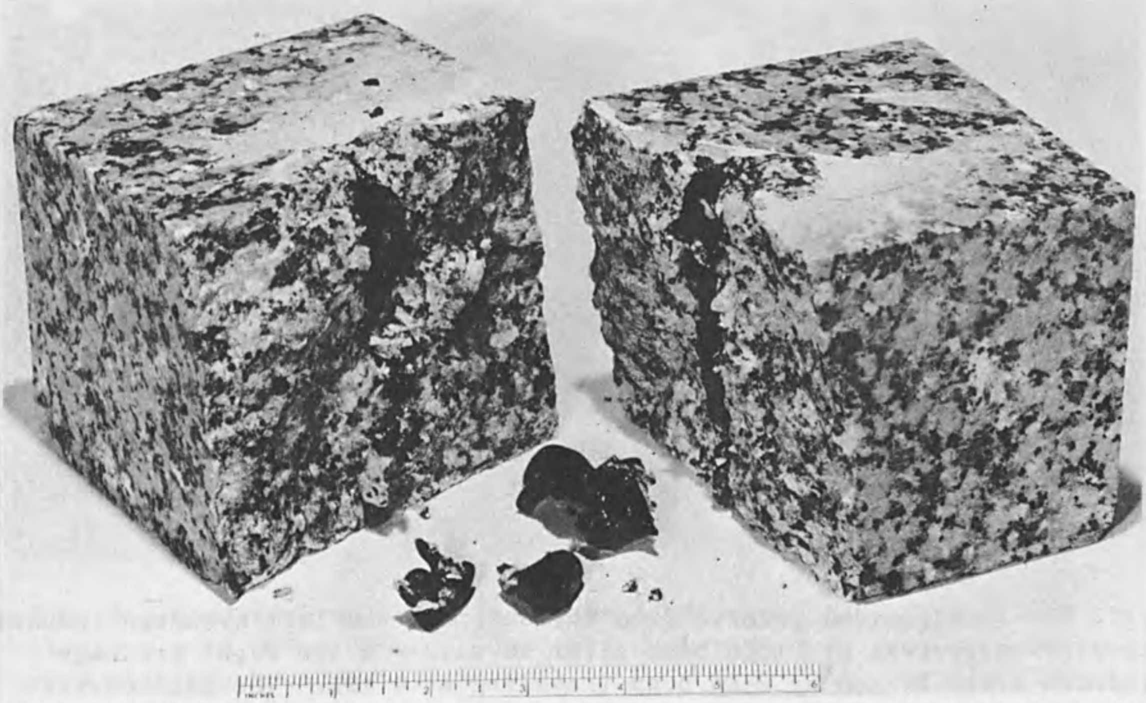
INCHES
1
2
3
4
5
6

FIG. 6.—Coarse grained granite broken by 9-kW, 150-kv electron beam in 37 seconds. Melt cavity is nearly 4 in. deep.

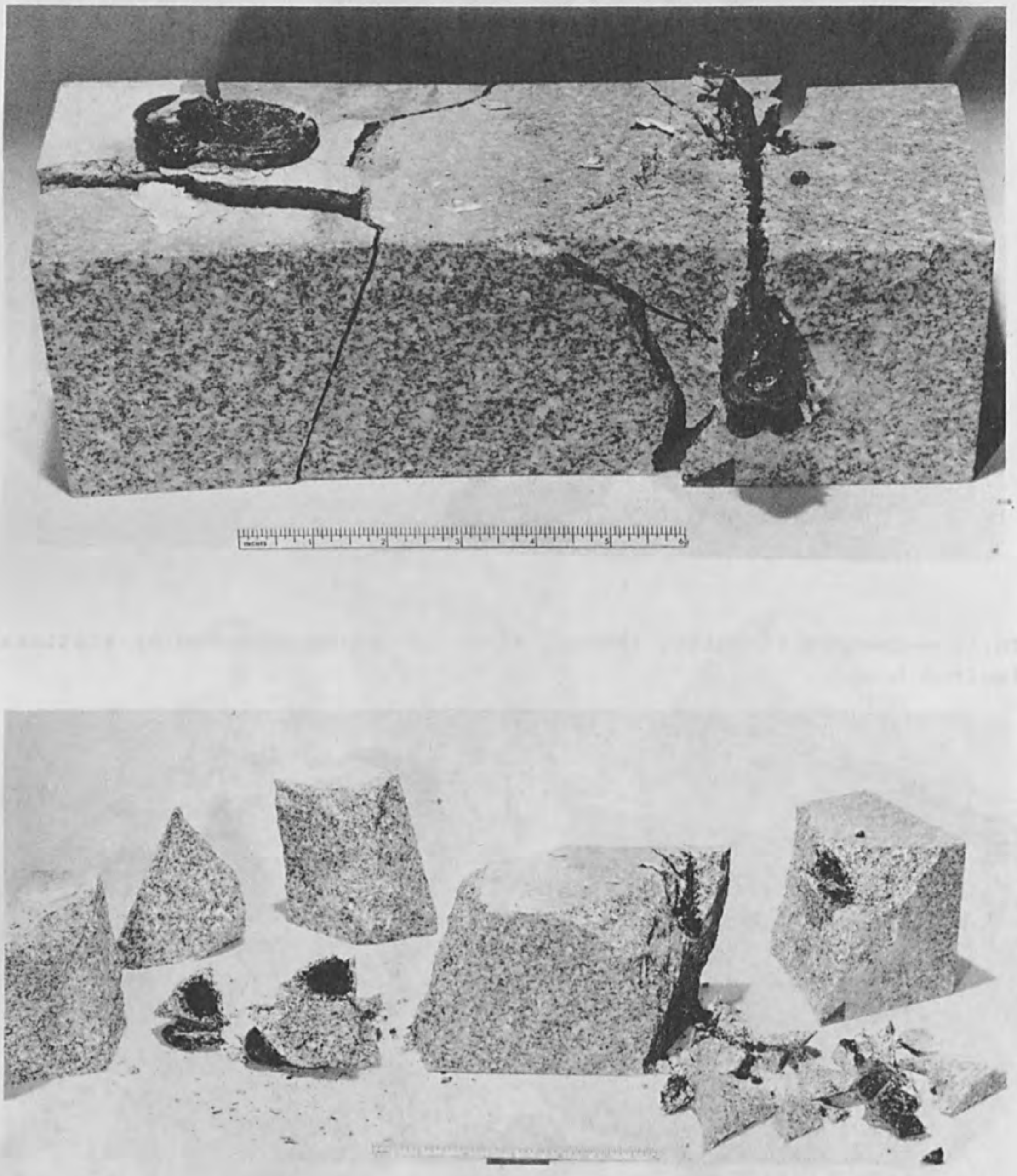

FIG. 7.—Fine grained granite from Vermont. On the left breakage induced by stationary 9-kW electron beam after 56 sec. On the right breakage induced after 57 sec by 9-kW beam traveling at 4 IPM. The melt-cavity broke away from the block as a separate tubular piece.

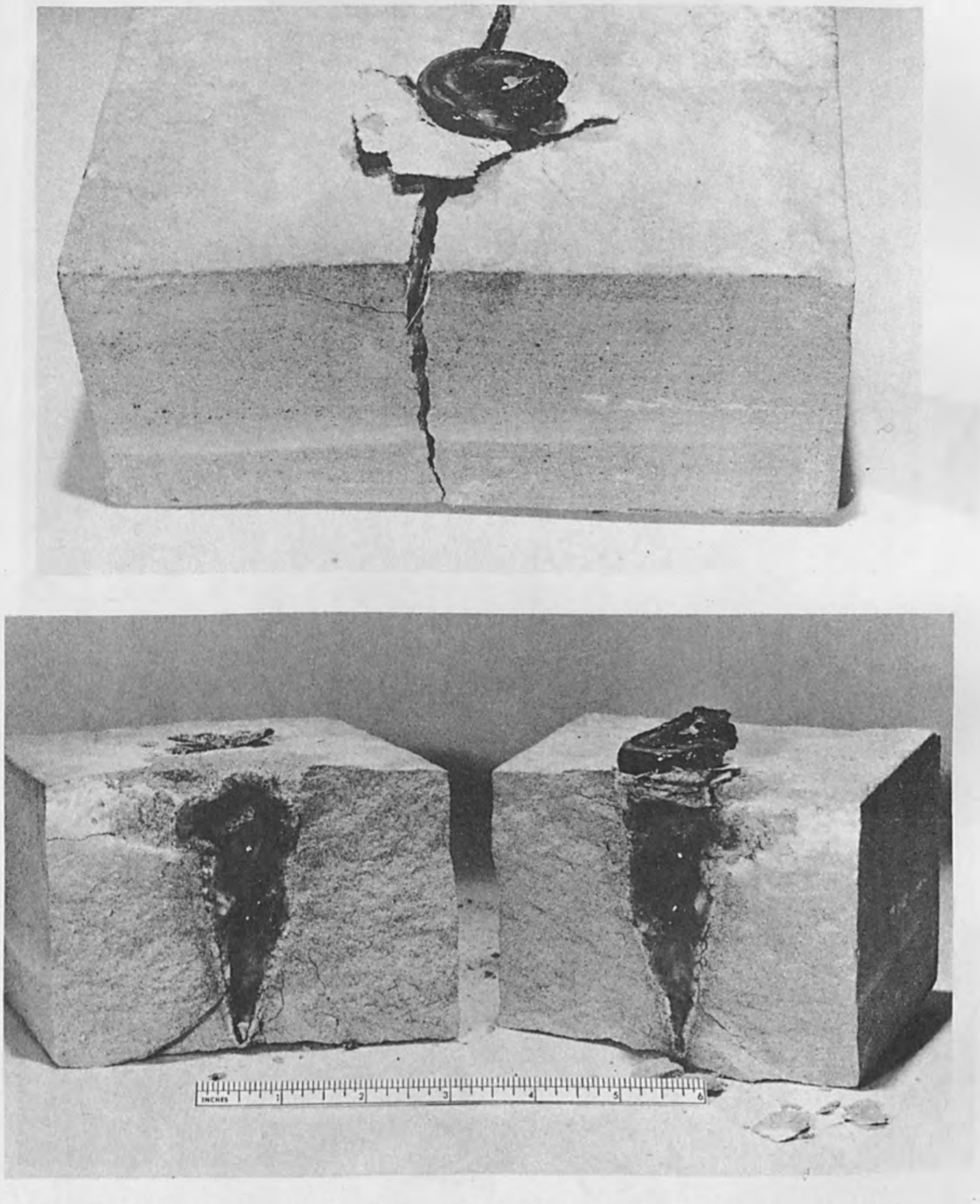

FIG. 8.—Sandstone split by the thermal stresses induced by a 9-kW electron beam after 59 sec. The melt cavity is 4 in. deep and has split open with the breakage of the rock.

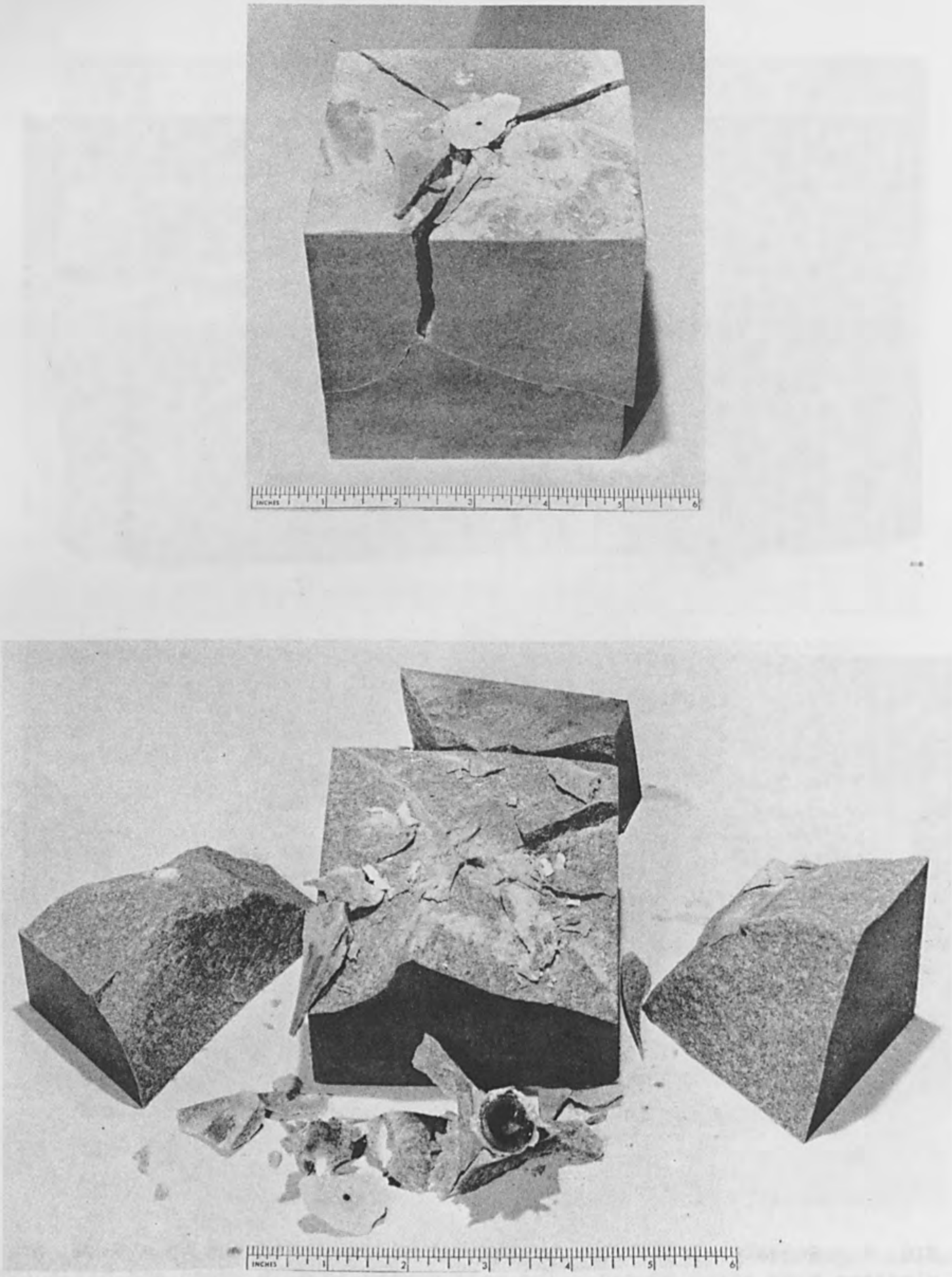

FIG. 9.—Sioux or Jasper Quartzite split after 9 sec under a 9-kW, 150 kV electron beam. The melt cavity, about 2 in. deep, broke away as a separate unit, seen in the center of the lower photograph.

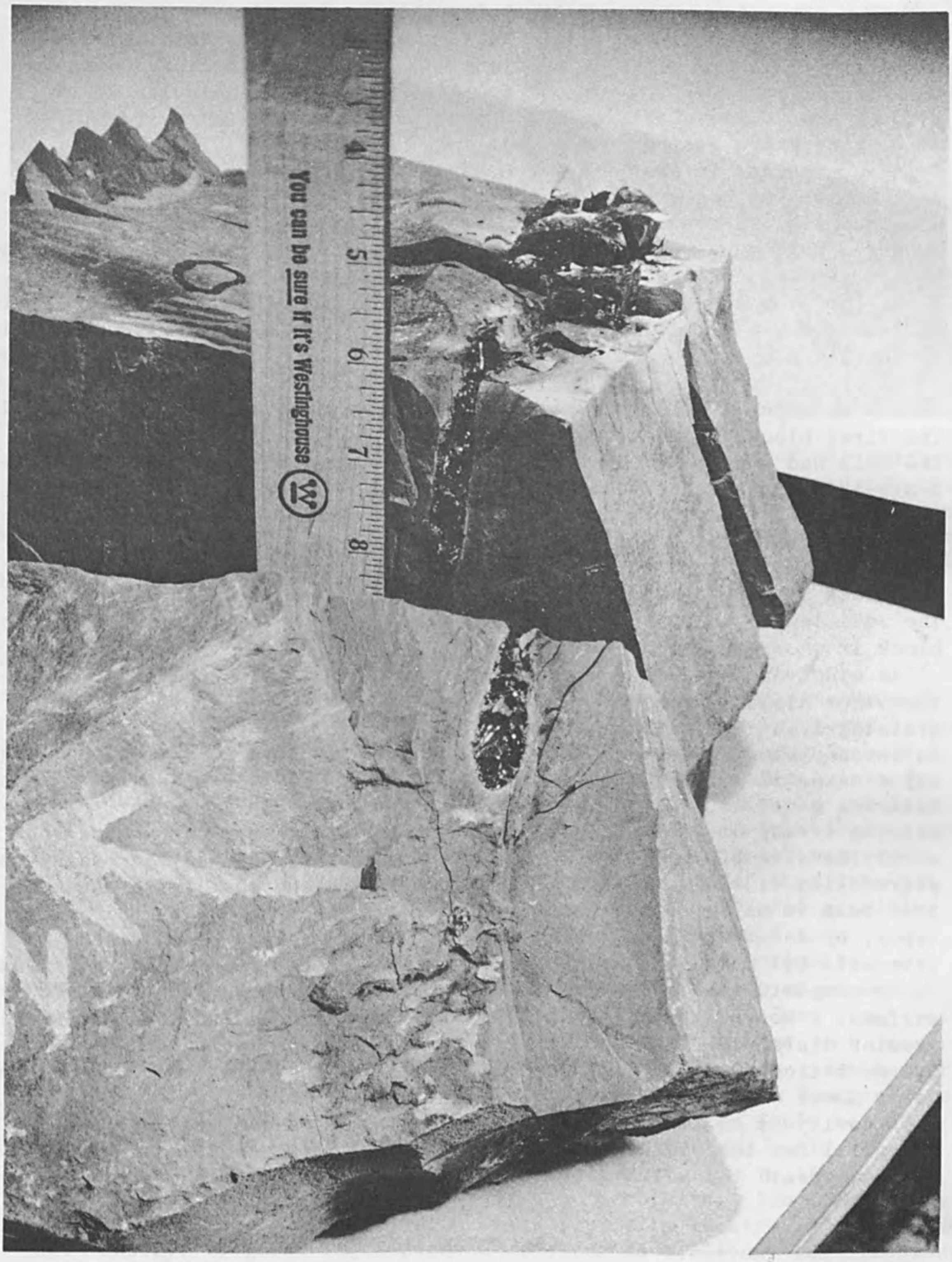
You can be sure if it's Westinghouse
4
5
6
7
8

FIG. 10.—Copper ore with 2-in.-deep melt cut and concurrently induced extensive thermal-stress cracking. Beam: 9 kW, traveling at 4 IPM.

melt-cut 2 in. deep, as is typical for this power and speed. The melt-cut region can be clearly seen. While the block was traversing under the beam it split several times along its natural laminations owing to the thermal stresses. Many such breakage planes perpendicular to the melt-cut can be seen in Fig. 10. Deriving a specific energy for this kind of breakage was not attempted.

Of particular interest is the behavior of limestone when subjected to the electron beam. Limestone cannot be pierced by a flame jet.[5] As noted earlier[1] limestone does not show extensive stress cracking in or around a melt cut. But when pierced by a stationary beam it can nevertheless break into two parts. A block 3-3/8 in. thick, 5 in. wide, and 8 in. long was subjected to the electron beam of 9 kW. A hole was drilled through the 3-3/8-in. thickness of the block in 58 sec. Towards one side of the block a thin crack appeared across the full thickness. In another block of different origin (the exact origin of none of the blocks was known) in which a hole was drilled in 39 sec, a one-sided crack appeared. The first block could be broken in two with little force. In each case the hole had a diameter of 0.5 in. and nearly cylindrical walls over the 3-3/8-in. length. The second block broke into three pieces. Since it appeared that the blocks would not break by themselves because the beam went clean through, a third block was placed under the beam with the 8-in. length in the beam direction. When the 9-kW beam was fired into the block it took 57 sec until the block split into two sections along the full length, although the beam had only penetrated about 4 in. This block is shown in Fig. 11.

An electron beam penetrates into a limestone block deeper than into the other kinds of rocks probably because limestone does not melt but disintegrates chemically into vapors and gases. This is noticeable by an intense blowing action when the electron beam hits the limestone. The vapor makes room for the electron-beam path much quicker than the molten material would do. Hence the actual beam penetration is faster. In passing it may be mentioned here that the electron beam decomposes rock partly because of the heat it produces but also because of the radiation degradation of the molecules bombarded by the electrons. With an electron beam we may generate gases, vapors, perhaps even oxygen and water vapor, by decomposition of rocks. On earth it may not be of great interest, but perhaps someday on the surface of the moon it may be of use.

To complete this report we show in Fig. 12 the photograph of a rock surface, a coarse granite, being bombarded by the electron beam from a greater distance. The beam has spread owing to scattering in the air, but no noticeable loss of total beam power has occurred. Because of the lower power density the surface of the rock only melts; a deep penetration cavity is no longer formed. The formation of the deep cavity is essential for the breakage which we have seen in the other experiments, but underneath the melted surface some superficial cracks were found.

DISCUSSION

Regardless of any considerations concerning the energy efficiency electron-beam rock cutting has certain potential advantages simply from a process point of view. The electron-beam equipment may be designed to be relatively mobile and lightweight. Its interaction with the rock does not produce any mechanical reaction forces, like kickback, on the gun. Therefore, no heavy supports or braces are required to hold the equipment

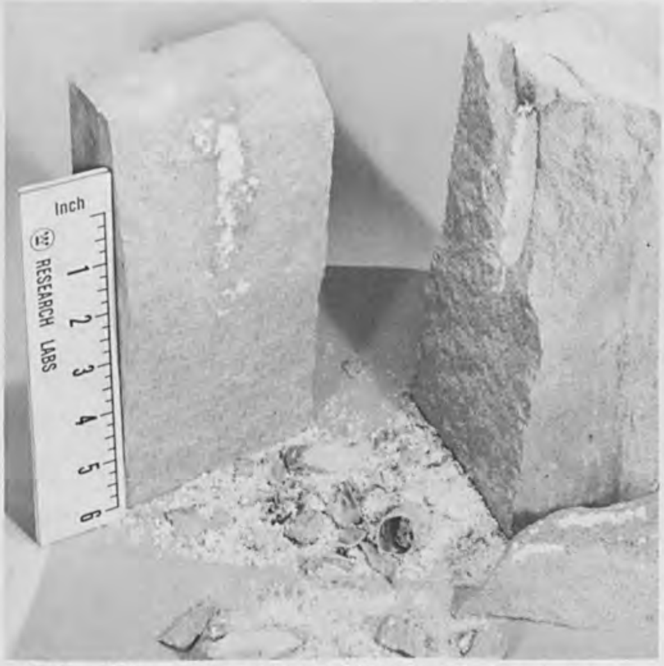

FIG. 11.—Limestone block pierced by a 9-kW electron beam in the direction of the long axis to prevent burning through without breaking; breakage occurred after 57 sec.

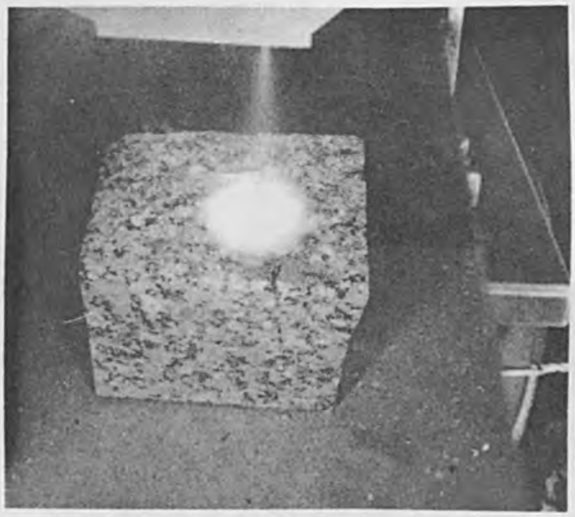

FIG. 12.—Melting of the surface of a granite at 5-in. stand-off distance from the electron gun. No deep cavity is formed anymore and little cracking or spalling occurs.

in place. The process uses electrical energy, which is easily brought in; the conversion of electrical energy into electron-beam energy is very efficient, better than 90%. Although not yet available, a gun could be designed for field use permitting uninterrupted running times into the hundreds of hours. It may seem a small disadvantage that the gun must be maneuvered close to the rock surface, but so must a mechanical cutter. The electron gun produces X rays against which the operator must be shielded. This is no serious problem since a machine of this type has to be operated under remote control in any case. Additional shielding of the operator's booth will require about 1/4 in. of lead.

In addition to these process advantages the above experiments have now shown that the electron-beam piercing method has also an advantage in terms of energy efficiency. For comparison let us discuss some typical figures for rock breakage by other methods.[5] Crushing hard rock (compressive strengths 1000 to 2000 kg/cm^2 with a percussive drill (jack hammer) requires specific energy of 260 J/cm^3. For very hard rock (compressive strengths greater than 2000 kg/cm^2) the specific energy would be 390 J/cm^3. In the same hard rocks a rotary drill of the roller type would require 210 to 840 J/cm^3 and a diamond drill would require 1120 to 4500 J/cm^3. Some specific energy figures for newer experimental drilling techniques are as follows. Pellet drilling of pink quartzite requires 67,000 J/cm^3 input energy. Figures for explosion drilling in limestone and limestone with clay range from 160 J/cm^3 to 685 J/cm^3. Erosion drills using high-pressure water jets have required 11 000 J/cm^3 in sandstone to 56 000 in granite. Ultrasonic drilling in quartz and Jasper requires 19 000 J/cm^3. For flame-jet piercing, which is the only new drilling method that has found widespread applications during the last decades, the specific energy data range from 134 000 J/cm^3 for shale to 3300 J/cm^3 for jasper.

Here the coupling of the energy of the flame jet to the rock determines the limits; it is thought that the jet drilling is only 15 to 50% energy efficient. The energy not going into the rock heats the surrounding gases or is carried away with the combustion products. A variation of this method, the so-called forced flame drill, shows energy efficiencies around 16 000 J/cm^3 in iron quartzite. Limestone cannot be broken or spalled by a flame jet. There are some experiments reported of heating rock by electric currents, either dc or ac or high-frequency current. Conditions must be very favorable to do this effectively. But then very large blocks have been cracked with a specific energy of 10 J/cm^3 for iron quartzite and between 100 and 1000 J/cm^3 for copper ores and granite. Compared with these electric-heating methods the electron-beam method has the great advantage of good coupling of the energy into the rock regardless of the properties (conduction, dielectric constant, etc.) of the rock and may yet attain the same energy efficiency if beams of higher total power are used. Crater formation in rocks by means of an electric arc has also been tried. The surface spalling rates gave specific energy figures between 5000 and 100 000 J/cm^3. Again the energy transfer from the electric arc to the rock poses an insurmountable limit.

Finally it should be mentioned that all of our present data are based on experiments with the relatively small beam power of 9 kW. We can expect the power efficiency of all the processes to increase with an increase in beam power, because the heat losses owing to heat conduction, etc., do not increase proportionally. With an increase in total beam power the cavity drilled in the rock initially will go deeper; this will lead to an increased breakage volume. A further increase in the depth of the cavity can be achieved if the electron beam voltage is increased, even at constant total power. Neither an increase in voltage nor in beam current will pose serious technical problems. Extrapolating to what we may reasonably expect at higher beam powers we may assume with a 24-kW beam a block of 1 ft^3 (28 320 cm^3) can be cracked off a larger block (or broken from a natural rock face with a 1-ft ledge) in 20 sec; then the specific energy figure would amount to 17 J/cm^3. This could more than triple today's excavation rates in hard rock. We believe the electron-beam method and machinery can readily be developed to the point where it can successfully compete with conventional rock drilling methods in many applications.

REFERENCES

1. B. W. Schumacher, "Electron beam cutting of rocks and concrete," in Electron and Ion Beam Science and Technology, Third International Conference, R. A. Bakish, Ed., New York: Electrochemical Society, 1968. (Also Westinghouse Scientific Paper 67-1C2-EWELD-P5, 1 Nov. 1967.)

2. B. W. Schumacher, "Power density limits for the particle penetration laws and the onset of energy phenomena in electron beam targets," ibid. (Also Westinghouse Scientific Paper 67-1C2-EWELD-P1, Aug. 1967.)

3. D. C. Schubert and B. W. Schumacher, "Effect of electron scattering in the metal vapor on the energy dissipation in the cavity present during EB welding," ibid. (Also Westinghouse Scientific Paper 67-1C2-EWELD-P6, December 1967.)

4. P. G. Klemens, "Energy considerations in electron beam welding," ibid. (Also Westinghouse Scientific Paper 67-1C2-EWELD-P4, July 1967.)

5. W. C. Maurer, Novel Drilling Techniques, New York: Pergamon Press, 1968.

PHENOMENA ASSOCIATED WITH ELECTRON-BEAM EVAPORATING

SHELDON S. WHITE

Texas Instruments, Inc., Attleboro, Mass.

During electron-beam (EB) evaporation of copper at high power levels, the slope of the evaporation rate-power curves decrease. Therefore, the percentage of the beam power which is used to evaporate the copper becomes less with increasing power. Measurements and calculations have been made which show that the most likely cause of this phenomenon is the existence of a space charge. This space charge would decrease beam energy and would come from a low-energy source, which is thought to be thermionic emission from the melt.

The power density distribution on the surface of the melt was found to be quite uniform. Therefore, each power level imposed by the beam yields a particular current density and, hence, a specific amount of thermionic emission and specific evaporation rate. By equating thermionic emission with current loss from the filament (less overspray current) divided by emitting area, a surface temperature for the melt may be calculated. This temperature can be used with Langmuir's law to predict evaporation rates which agree with measured rates, thereby proving that Langmuir's law operates for at least single-element EB evaporation. Thermocouple probes into the melt show that a sharp temperature drop exists at the surface of the melt.

INTRODUCTION

The emission characteristics of various vapor sources and film thickness distribution have been analyzed from a theoretical and practical standpoint.[1,2] Vapor emission through apertures and "molecular beaming" when the aperture is in the form of a tube has been the subject of studies by Clausing[3] and Korsunsky and Vekshinsky.[4] Experimental data on profile families for linear and ring sources has been obtained by Bugenis and Preuss[5] using conventional evaporation (non-EB) techniques. Behrndt[6] has strived to obtain uniformly thick deposits using large-area sources and two-source control.

The theory of evaporation of crystals has been treated by Knacke et al.[7] and by Hirth and Pound,[8] following ideas developed by Gibbs,[9] Kessel,[10] Stranski,[11] and Burton et al.[12]

Using the kinetic theory of gases, Langmuir[13] devised the following expression for the equilibrium vapor pressure P_e in free evaporation:

$$P_e = (\dot{m}/\alpha_v)(2\pi RT/M)^{1/2} \tag{1}$$

where $\dot{m}$ = rate of evaporation, g/cm^2-sec
α_v = vaporization coefficient
R = gas constant
T = surface temperature of source
M = molecular weight of vaporizing species

Record of 10th Symposium on Electron, Ion, and Laser Beam Technology (L. Marton, ed.); San Francisco Press, Inc.
Copyright © by The Institute of Electrical and Electronics Engineers, Inc.—Printed in the U.S.A.

The vaporization coefficient is defined here as the ratio of the observed rate of evaporation to the maximum possible rate of vaporization at equilibrium vapor pressure.

The Langmuir equation implies that the rate of vaporization is the equilibrium rate and that no condensation of the evaporant takes place on the sample.

In view of nonequilibrium conditions which are encountered in practice a modification of Langmuir's equation, known as the Hertz-Knudsen equation, is used:

$$J_v = \alpha_v (P_e - P)/(2\pi MkT)^{1/2} \tag{2}$$

where J_v = the net vaporization flux in molecules per unit area per second
P = actual vapor pressure
R = Boltzmann's constant

It has been shown[1,2] that vaporization occurs by a stepwise process that may be summarized as follows:

(1) movement of atoms from a kink position in a monatomic ledge to a position on the ledge;
(2) dissociation of atoms from the ledge to adsorbed positions on the surface;
(3) surface diffusion of the adatoms; and
(4) desorption to the vapor phase.

The final step, desorption, is rate controlling, so that the evaporation rate (and hence α_v) is determined by the adatom concentration, which is fixed by the ledge spacing on the surface.

Small ledge spacings which tend to give $\alpha_v = 1$ as a limit are favored by the presence of surface imperfections, such as dislocations, and by high index surface orientations. Large ledge spacings, which tend to give $\alpha_v = 1/3$ as a limit, can occur only for perfect crystals with low index orientations.

Frank[14] and Cabrera and Vermilyea[15] have considered the influence of adsorbed surface contaminants. They indicated that strongly bound contaminants retard step motion, with the result that α_v is lowered.

In agreement with theory, values of $\alpha_v \approx 1$ have been obtained for the evaporation of metallic polycrystals. Cases where α_v was less than unity are associated with surface contamination owing to poor vacuum or preparation of specimen.

The above literature search turned up very little information on the mechanisms and phenomena associated with evaporation in the electron beam evaporation-condensation process. The main purpose of the research described below was to gain a clearer understanding of the role and importance of some of these mechanisms and phenomena.

EQUIPMENT AND TECHNIQUES

Two different EB evaporating chambers were used in this work. The larger chamber (Fig. 1) consisted of a 5 ft diameter X 6 ft long vacuum chamber, a 20-in. diffusion pump, and a mechanical pump. The pumping time to 5×10^{-5} Torr was 30 min. The chamber had a Temescal gun (Fig. 2)

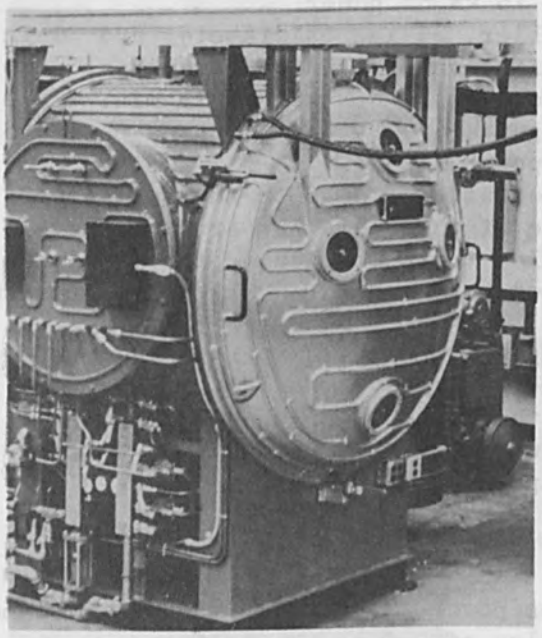

FIG. 1.—Large laboratory EB evaporator.

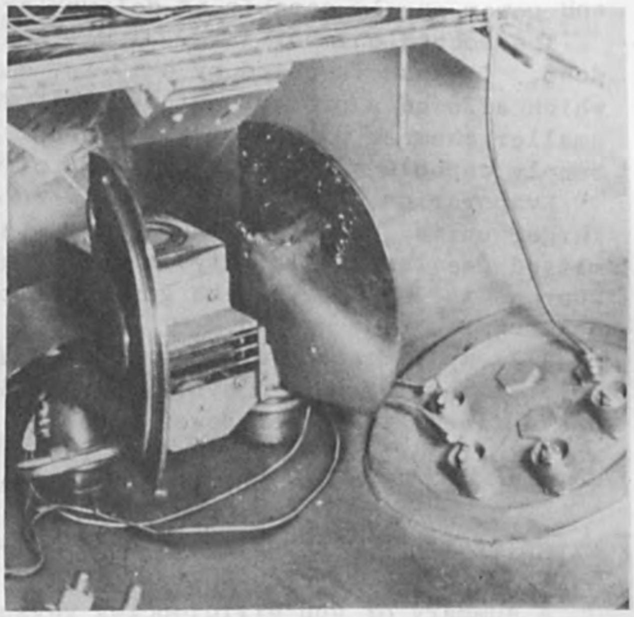

FIG. 2.—EB evaporating gun (75 kW).

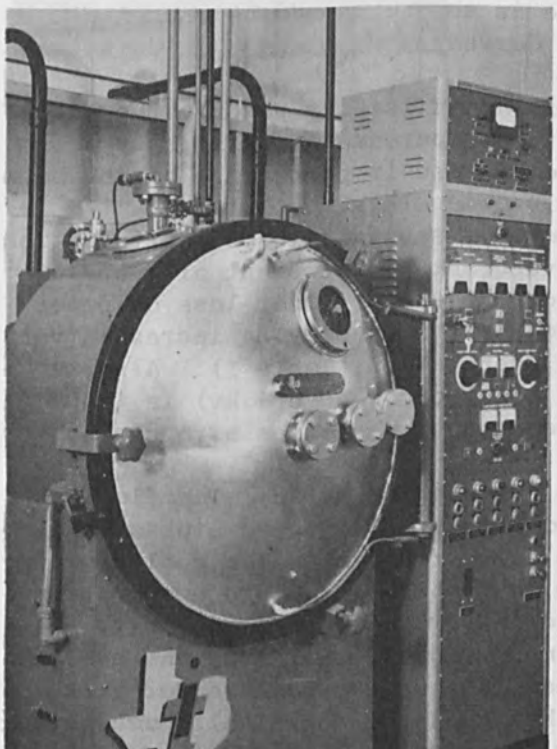

FIG. 3.—Small laboratory EB evaporator.

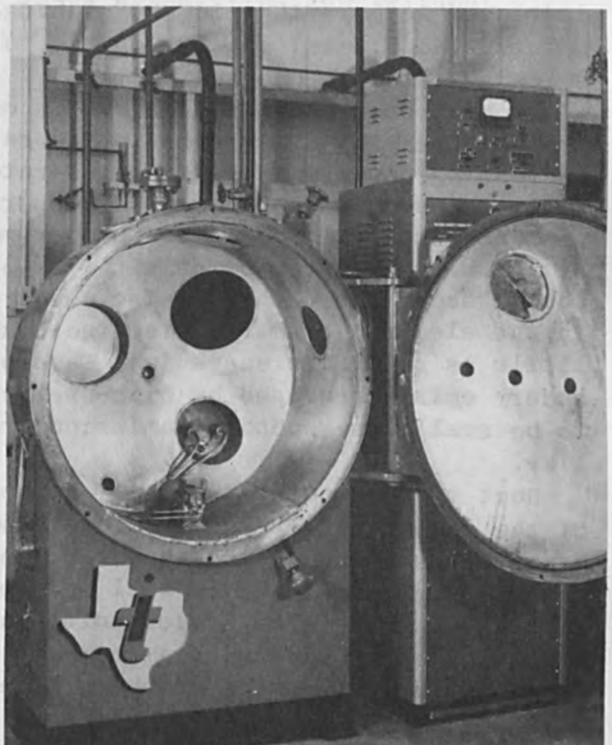

FIG. 4.—EB evaporating gun (10 kW) mounted in the small laboratory EB evaporator.

and power supply capable of delivering 75 kW of power.

The second chamber (Fig. 3) was smaller, 36 in. in diameter and 26 in. deep. It was evacuated by a 10-in. diffusion pump and a mechanical pump, which allowed a pressure of 5 X 10^{-5} Torr to be reached in 18 min. This smaller chamber used another Temescal gun (Figs. 4 and 5) and a power supply capable of delivering 10 kW of power.

Evaporation efficiency curves were obtained from both the smaller and larger units. However, the larger size of the 75-kW gun crucible permitted greater flexibility in positioning thermocouples in the melt, whereas the smaller, 10-kW gun permitted more accurate heat and electrical balances to be measured.

All experimental work was done using OFHC copper, with and without an auxiliary wire feed system for 1/16-in.-diam. wire. Gun efficiency was defined at a given power level as the ratio of actual evaporation rate to theoretical evaporation rate, under the assumption that the entire beam power was converted into evaporation energy.

EXPERIMENTAL PROCEDURE

A summary of gun efficiencies versus power is given in Figs. 6, 7, and 8. For the larger gun, a threshold value of 7.5-10 kW at 10 kv was observed; a corresponding smaller value was required for the smaller gun. This minimum power must be supplied to overcome heat losses to the cooling water in order to melt the charge. The efficiency of operation was increased to more than 50% by a change in the angle of the magnetic poles. The 9.5-in. spacing in Fig. 6 corresponds to magnetic deflection poles parallel to one another.

At high power levels, the slopes of the efficiency-power curves decrease, implying a decrease in the rate of increase of efficiency with increasing power. Therefore, the rate of rise in percentage of the beam which is used to evaporate the copper becomes less.

This result may be due to one or more of several causes: attenuation of the beam by interaction with the evaporant, development of a space charge above the crucible, increased overspray, or other loss of power in the electron beam reaching the crucible. Overspraying increases very little as power increases (see Before Evaporation, Table I). Also, secondary emission caused by high-energy electrons (above 4 kv) is thought to be small, as secondary emission from copper decreases strongly above 1 kv.

Heat measurements were made on the gun cooling water. The flow rate of the cooling water and the inlet and outlet water temperatures were measured as a function of power. The heat transfer to the cooling water can then be calculated as well as the heat which goes into evaporation, into heating the wire feeder unit, and into radiation. Then, with the amount of overspray and beam current measured by insulating the gun and overspray area from the chamber, a heat balance may be made for the crucible. At high power levels, the heat balance works well, accounting for 98 per cent of the imposed power, implying no loss to attenuation of the electron beam or increased overspray (Table II). (It should be noted that the area of overspray can be readily detected by bleeding argon gas into the chamber. The beam path becomes visible as the argon atoms produce a yellow green light when excited by the electrons.)

The effect of pressure was investigated to determine if the electron density could depress evaporation. The pressure due to electron

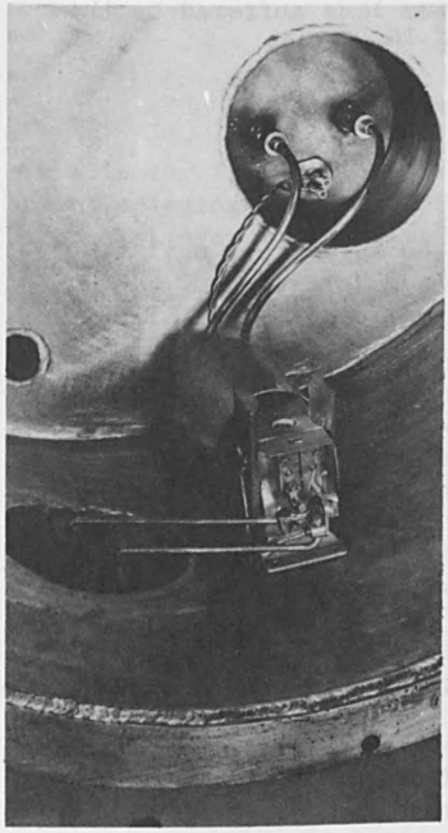

FIG. 5.—EB evaporating gun (10 kW).

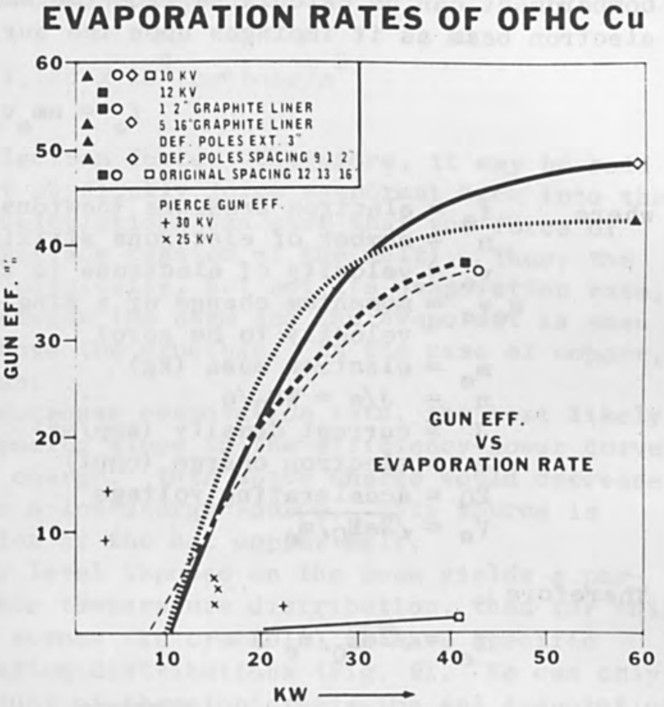

FIG. 6.—Evaporation efficiency curves for the 75-kW evaporating gun (without wire feeding).

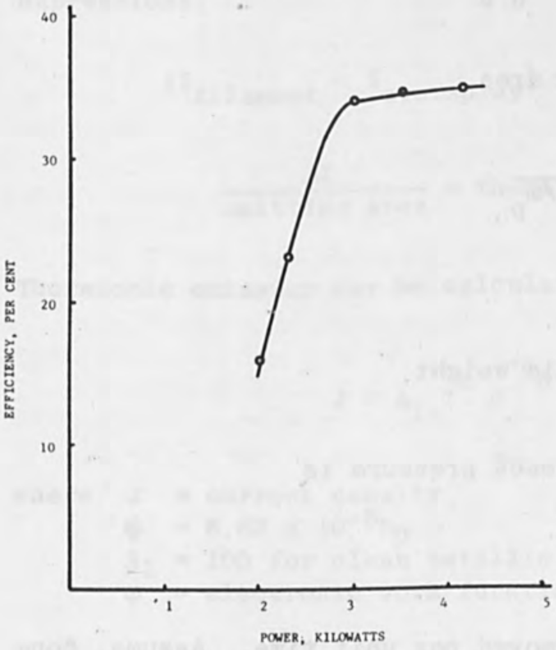

FIG. 7.—Evaporation efficiency curve for the 10-kW evaporating gun (without wire feeding).

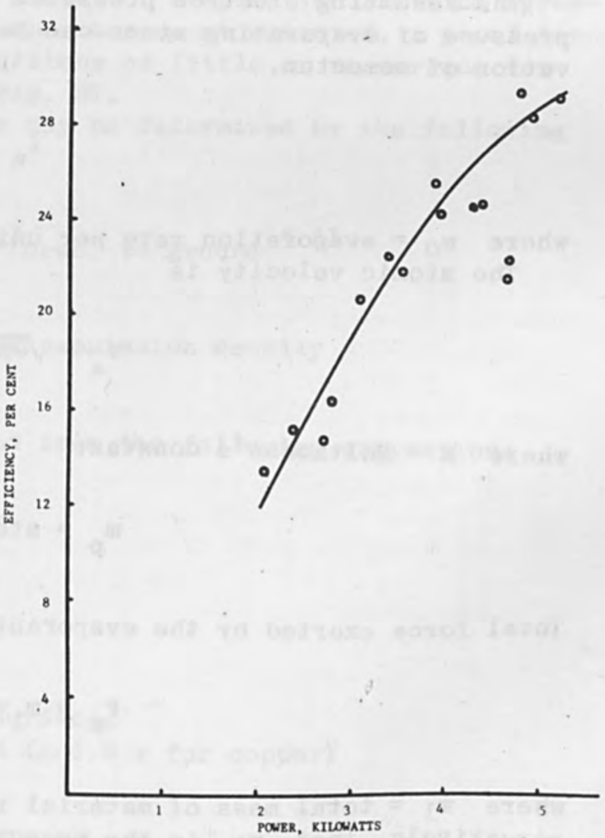

FIG. 8.—Evaporation effiency curve for the 10-kW evaporating gun (with wire feeding).

bombardment can be calculated from the momentum loss suffered by the electron beam as it impinges upon the surface:[16]

$$f_e = nm_e v_e$$

where f_e = electron pressure (newtons/m^2)
n = number of electrons striking the target per unit time
v_e = velocity of electrons is the beam (m/sec)
$m_e v_e$ = momentum change of a single electron (assuming final velocity to be zero)
m_e = electron mass (kg)
n = $J/e = WE_0/e$
J = current density (amp/m^2)
e = electron charge (coul)
E_0 = accelerating voltage
$V_e = \sqrt{2eE_0/m_e}$

Therefore

$$f_e = \sqrt{2eE_0/m_e}\, J$$

$$\text{Force} = f_e x \text{ area} = \pi a^2 f_e = \sqrt{2eE_0/m_e}\, I_0$$

where I_e = total current (amp).

The resulting electron pressures are given in Table III. The back pressure of evaporating atoms can be calculated on the basis of conservation of momentum,

$$f_a = m_0 v_a$$

where m_0 = evaporation rate per unit area.

The atomic velocity is

$$v_a = \sqrt{2KT/m_p}$$

where K = Boltzmann's constant

m_p = atomic weight

Total force exerted by the evaporant back pressure is

$$F_a = m_1 v_a$$

where m_1 = total mass of material removed per unit time. Assume, conservatively, that m_1 is the measured evaporation rate at 10 kv, 20 kW, m_1 = 46.3 g/min, T = 3150°F. Then

$$F_a = 35.60 \text{ newtons}$$

$$f_a = 1.125 \times 10^4 \text{ newtons/m}^2$$

This is far in excess of the electron force. Therefore, it may be said that impinging electrons cannot physically force evaporant back into the crucible (even though similar calculations can show that the force of electrons is greater than the surface tension of the melt). Thus, the melt surface can be suppressed physically, but not its evaporation rate.

Nevertheless, interaction between the beam and the evaporant is seen in the visible light emitted above the crucible. In the case of copper, the color is that of a green gas.

Since beam pressure cannot decrease evaporation rate, the most likely means of accounting for a decreasing slope in the efficiency-power curves is by the existence of a space charge. This space charge would decrease beam energy and would come from a low-energy source. This source is thought to be thermionic emission by the hot copper melt.

If we assume that each power level imposed on the beam yields a particular current density and hence temperature distribution, then for this given temperature distribution across the crucible, we have specific thermionic emission and evaporation distributions (Fig. 9). We can only measure with ease the gross amount of thermionic emission and evaporation taking place over the entire molten area. If we assume that all thermionic emission took place uniformly over the molten surface, we can find an "average" surface temperature by this route. If we use this temperature and Langmuir's law to predict total amount of evaporation and find agreement between this calculated amount and the amount measured, a proof for Langmuir evaporation mode under conditions of little or no surface temperature distribution is obtained (Fig. 9).

The amount of thermionic emission may be determined by the following expressions:

$$(I_{\text{filament}} - I_{\text{overspray}}) - I_{\text{cruc. to ground}} = \Delta I$$

$$\frac{\Delta I}{\text{emitting area}} = \text{thermionic emission density}$$

Thermionic emission may be calculated from the following expression:

$$J = A_1 T^2 e^{-b_0/T}$$

where J = current density
$\varphi = 8.62 \times 10^{-5} b_0$
A_1 = 100 for clean metallic surfaces
φ = electronic work function (≈ 4.0 v for copper)

Therefore

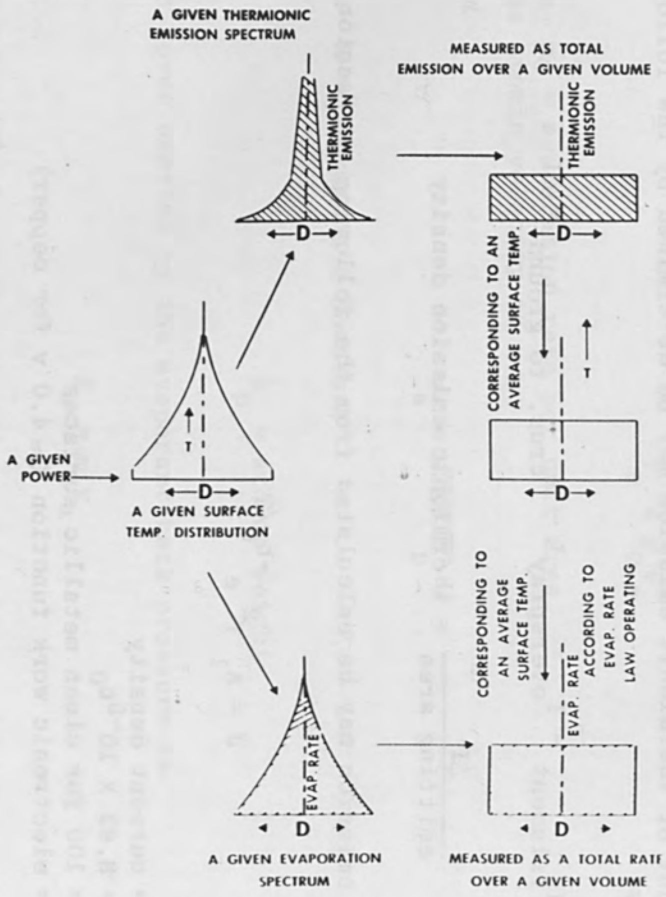
A GIVEN THERMIONIC EMISSION SPECTRUM
THERMIONIC EMISSION
MEASURED AS TOTAL EMISSION OVER A GIVEN VOLUME
THERMIONIC EMISSION
D
A GIVEN POWER
T
D
A GIVEN SURFACE TEMP. DISTRIBUTION
CORRESPONDING TO AN AVERAGE SURFACE TEMP.
T
D
CORRESPONDING TO AN AVERAGE SURFACE TEMP.
EVAP. RATE ACCORDING TO EVAP. RATE LAW OPERATING
EVAP. RATE
D
A GIVEN EVAPORATION SPECTRUM
EVAP. RATE
D
MEASURED AS A TOTAL RATE OVER A GIVEN VOLUME

FIG. 9.—Schematic method of comparing thermionic emission and evaporation rate.

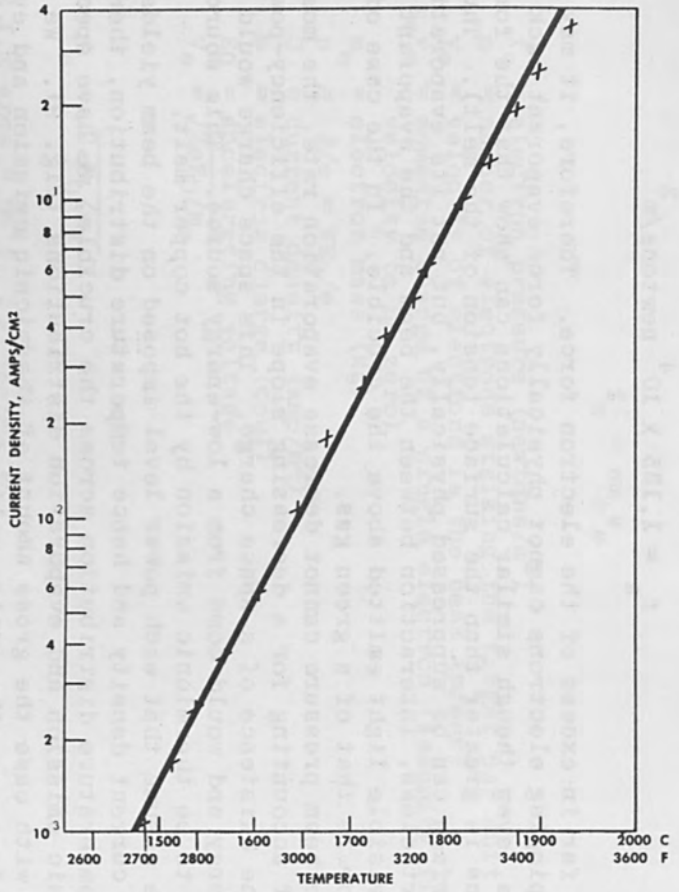

FIG. 10.—Calculated thermionic emission for copper.

$$J = 100\ Te^{-b_0/T}$$

where $b_0 = (4.0/8.62) \times 10^{-5} = 4.64 \times 10^4$

or $J = 100\ T^2e\ -4.64 \times 10^4/T$

From these expressions an average surface temperature may be calculated (Fig. 10), on the assumption that the emitting surface is 6 cm^2 (as estimated by visual observation) in the 10-kW crucible.

The power levels chosen for evaporation rate-thermionic emission interdependence on temperature are shown as circles in Fig. 11 on the evaporation rate vs power curve obtained with the 10-kV gun. Table IV shows the agreement between the evaporation rate calculated from the resultant thermionic emission temperature and measured evaporation. The agreement is well within the 10-percent error of the meters or the visual estimation of emitting surface area.

All of the electrons are stopped within 0.001 in. from the surface of the molten pool. Hence it may be expected that the surface temperature of the metal is superheated. By insertion of shielded W-26% Re thermocouples from the bottom of the 75-kW gun crucible and adjustment of the wire feeding rate so that the protection tube tip was barely washed by the evaporating surface, the experimental temperature shown in Fig. 12 was determined as a function of temperature. The calculated surface temperature (using the Langmuir expression) for the large gun system is shown on the same plot, indicating that a temperature drop of approximately 200°F exists in the surface of the melt.

CONCLUSIONS

In conclusion, the following points may be made:

(1) Changes in evaporation efficiency with increasing power are observed during electron beam evaporation.

(2) The physical pressure of electrons colliding with evaporant does not account for the decrease in slope of the evaporation efficiency-power curves at high power.

(3) Thermionic emission from the melt seems to account for the observed evaporation efficiency.

(4) A proof is offered for Langmuir type of evaporation from the melt.

(5) The surface temperature of the melt is as much as 200°F higher than the bulk temperature of the melt.

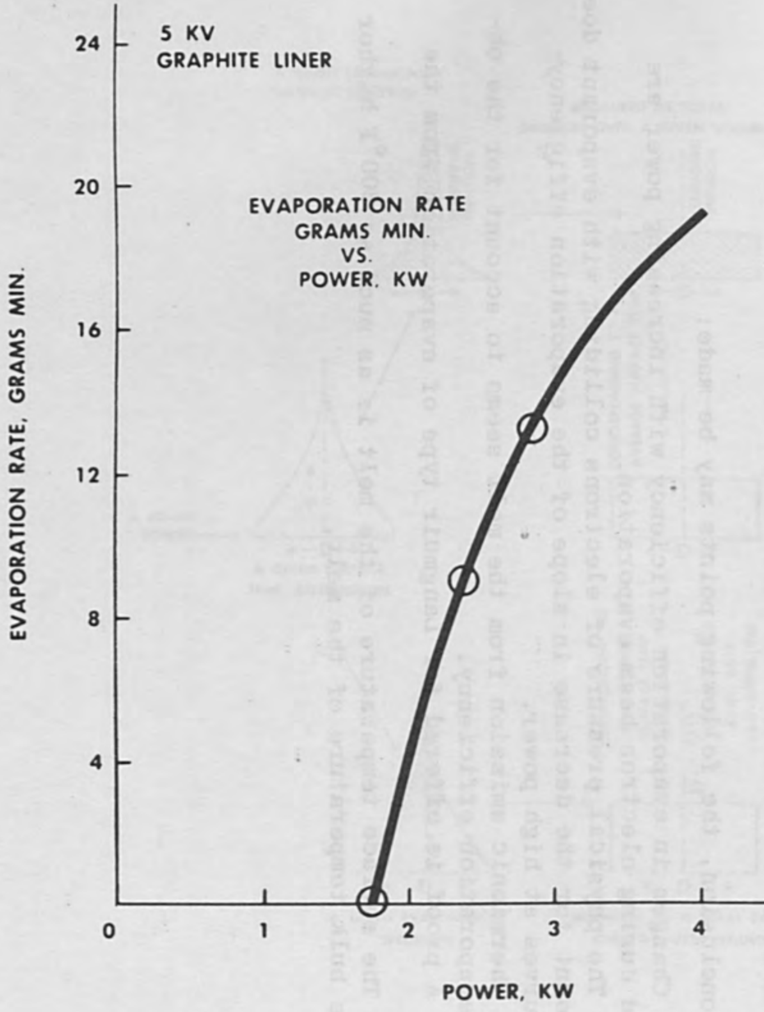

FIG. 11.—Evaporation-rate curve for the 10-kW evaporating gun.

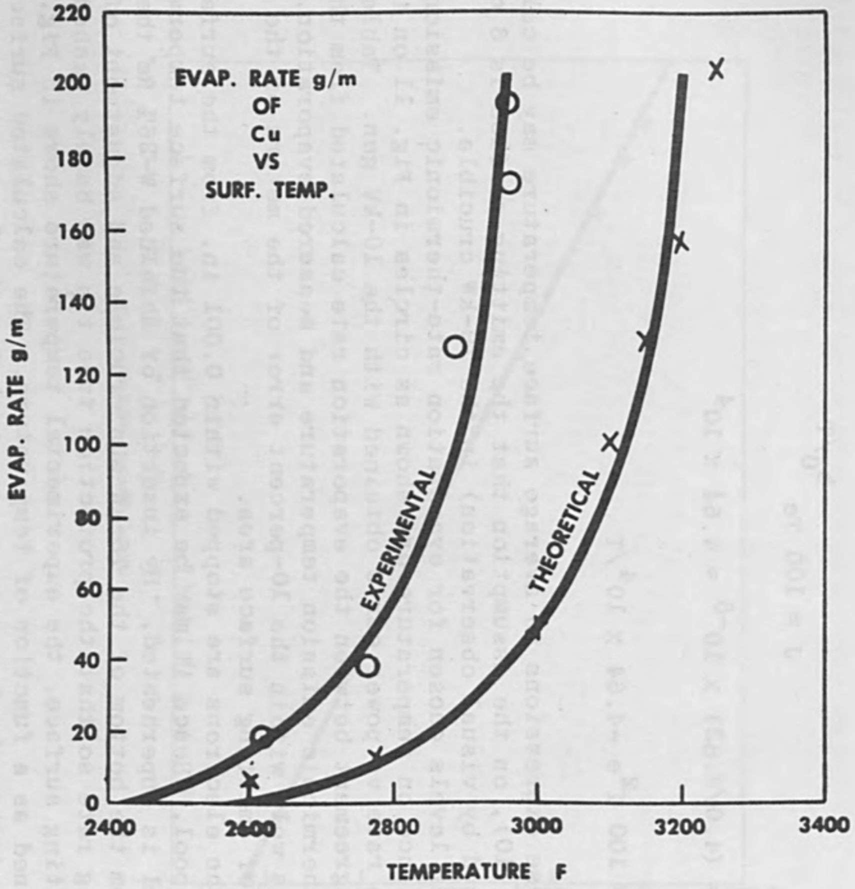

FIG. 12.—Comparison of measured and theoretical surface temperatures.

TABLE I.—Experimental results: Current distribution in EB evaporation.

Voltage (kv)	Before Evaporation			During Evaporation		
	Current on fil.	Current to ground	Current to Overspray	Current on fil.	Current to ground	Current to Overspray
5	0.21	0.18	0.02			
6	0.19	0.17	0.02			
7	0.11	0.10	0.01			
8	0.08	0.07	0.01			
5	0.32	0.30	0.02	0.34	0.30	0.04
6	0.28	0.25	0.04	0.28	0.25	0.03
7	0.24	0.20	0.03	0.24	0.20	0.04
8	0.20	0.18	0.03	0.22	0.18	0.04
5	0.44	0.42		0.48	0.32	0.05
6				0.43	0.27	0.05
7				0.40	0.26	0.05
5				0.57	0.33	0.08
6	0.56	0.52	0.03	0.54	0.33	0.10
7	0.52	0.46	0.04	0.49	0.34	0.09

TABLE II.—Summary of heat-balance calculations. (Heat values have been converted to kilowatts to permit comparison with emitted filament power.)

Power Losses, KW

Run	To cooling water	Heat Cu feed wire	Evap Cu	Overspray	Total loss	Emit.fil power	$\frac{\text{Loss}}{\text{Emit}}$ X100
1	0.56	--	--	0.1	0.66	0.90	73
2	0.60	--	--	0.1	0.70	0.95	74
3	0.94	0.11	0.53	0.15	1.73	2.58	65
4	1.42	0.20	0.98	0.15	2.75	3.42	80
5	2.84	0.24	1.14	0.20	4.42	4.50	98

TABLE III.—Electron pressures.

kW	E_0 (volt)	I_0 (amp)	F_e (newton)	F_e (newton/m^2)
10	10 000	1	106×10^{-3}	0.199
20	10 000	2	212×10^{-3}	0.399
40	10 000	4	425×10^{-3}	0.799
10	12 000	0.834	91×10^{-3}	0.170
20	12 000	1.668	182×10^{-3}	0.340
40	12 000	3.336	364×10^{-3}	0.680

TABLE IV.—Comparison of measured and Langmuir predicted evaporation rates from calculated average temperature given by thermionic emission and open pool of one-half crucible, or 6.0 cm^2 emitting area.

Volt	Amp	kW	I through crucible	Calc'd T°F from th.em.	Measured evap.rate (g/min)	Langmuir pred. based on cal'd T
5000	0.34	1.70	0	0	0	0
5000	0.48	2.40	0.11	3070	8.60	8.28
5000	0.57	2.85	0.16	3120	12.90	11.42

REFERENCES

1. L. Holland and W. Steckelmacker, Vacuum 2: 346, 1952.

2. L. Holland, Vacuum Deposition of Thin Films, New York: John Wiley and Sons, 1960; chap. 5.

3. P. Clausing, Z. Phys. 66: 471, 1930.

4. M. Korsunsky and S. Vekshinsky, J. Phys. Acad. Sci. USSR 9: 399, 1945.

5. C. Bugenis and L. E. Preuss, Trans. Amer. Vac. Soc.: 344, 1963.

6. K. H. Behrndt, ibid., p. 242.

7. O. Knacke, I. N. Stranski, and G. Wolff, Z. Elektrochem. 56: 476, 1952; Z. Phys. Chem. 198: 157, 1951.

8. T. P. Hirth and G. M. Pound, J. Phys. Chemistry 64: 619, 1960.

9. J. W. Gibbs, Collected Works, New Haven, Conn.: Yale University Press, 1948; vol. 1.

10. W. Kossel, Nach. Ges. Wiss. Göttingen 2: 135, 1927.

11. I. N. Stranski, Z. Phys. Chem. 136: 259, 1928; 11: 94, 1931.

12. W. K. Burton, N. Cabrera, and F. C. Frank, Phil. Trans. Roy. Soc. (London) 243(A): 299, 1950.

13. I. Langmuir, Physik Z. 14: 1273, 1913.

14. F. C. Frank, Growth and Perfection of Crystals, New York: John Wiley and Sons, 1958; p. 411.

15. N. Cabrera and D. A. Vermilyea, J. Phys. Chem. 64: 393, 1960.

16. O. C. Wells, A note on the physical principles underlying the cavity in electron beam welding, Proc. Fourth Symposium on Electron Beam Technology (R. Bakish, Ed.), 1962; p. 105.

ENERGY BROADENING IN ACCELERATED ELECTRON BEAMS BY COULOMB INTERACTION

BODO ZIMMERMANN

Fried. Krupp GmbH Zentralinstitut für Forschung und Entwicklung,
Essen, Germany

The velocity distribution of thermionically emitted electrons depends on temperature and quality of the emission surface. However, all experiments that measure the distribution existing immediately at the emission surface have this in common, that the energy spread ΔE_c of the distribution is about equal to Boltzmann constant k times cathode temperature T, that is, at $T = 2300^\circ K$,

$$\Delta E_c \approx kT \approx 0.2 \text{ eV} \tag{1}$$

In the experiment sketched in Fig. 1, much greater energy widths have been measured at high current densities.[1] Between cathode K and anode A an electric field accelerates the emitted electrons, which then drift up to the electrode A_1 in a field-free space before being decelerated to the cathode potential of K_1. The energy spread $\Delta E'$ at K_1 exceeds the energy spread ΔE_c at the cathode. For an acceleration potential of $\langle E \rangle \approx 1$ keV and a current density of $j \approx 5$ A/cm^2, $\Delta E' \approx 2.5$ eV. Calculations have shown that the energy broadening in such electron beams can be quantitatively explained by the Coulomb interaction between the electrons.[2] This was first proposed by Ulmer.[3] In this paper we give an outline of the theory and calculations and discuss the results. Let us first restrict ourselves to the beam configuration shown in Fig.1 and assume that the electrons are moving in a fictitious, ideally reflecting tube, so that the current density remains constant along the beam. This could be approximately realized by a magnetic field.

In order to describe the process of energy broadening, we introduce two magnitudes, the local energy width ΔE and the local internal energy u. Consider a volume element in the beam. The longitudinal momentum components p (these are the momentum components parallel to the beam axis) of the electrons within the volume and the associated energies $E = p^2/2m$ fluctuate about a mean value. We define

$$(\Delta E)^2 = \langle (E - \langle E \rangle)^2 \rangle \tag{2}$$

$$(\Delta p)^2 = \langle (p - \langle p \rangle)^2 \rangle \tag{3}$$

ΔE is a quantitative measure of the energy spread. The last equation yields

$$u = (\Delta p)^2/2m = \langle (p - \langle p \rangle)^2 \rangle / 2m \tag{4}$$

Record of 10th Symposium on Electron, Ion, and Laser Beam Technology (L. Marton, ed.); San Francisco Press, Inc.

Copyright © by The Institute of Electrical and Electronics Engineers, Inc.—Printed in the U.S.A.

for the internal energy per electron, where ΔE and u are connected by a simple but crucial relation:

$$(\Delta E)^2 \approx 4\langle E\rangle u \tag{5}$$

We can see this easily, if we restrict ourselves to two electrons only. Energy and momentum difference are then related by

$$\Delta E = \langle p\rangle \Delta p/m \tag{6}$$

Squaring of (6) yields (5). It has important consequences, which can also easily be derived from the example of two electrons.

If one accelerates two electrons in an electrostatic field, each electron gains the same energy, that is, ΔE remains constant. But the momentum spread diminishes from Δp to $\widetilde{\Delta p}$, in consequence of the quadratic relation between energy and momentum, as shown in Fig. 2. Because the internal energy of the two-electron system is proportional to the square of the momentum difference, it also diminishes. The same conclusion can be drawn from (5): since ΔE remains constant during acceleration, the internal energy u decreases with increasing mean energy $\langle E\rangle$. This means that in an electron beam with energy broadening there occurs an increase of the longitudinal internal energy. But (5) shows that even a small increase of u causes a considerable increase of ΔE.

From (5),

$$d(\Delta E) = 2\,\frac{\langle E\rangle}{\Delta E}\cdot du \gg du \tag{7}$$

for constant $\langle E\rangle$ (in our example $du \approx 5$ meV).

This energy du is delivered--as calculations[2] have shown--by the thermal energy contained in the transverse momentum components of the electrons. The transverse internal energy, which we have not considered until now, is not affected by acceleration and is thus considerably greater after acceleration than the longitudinal internal energy. The exponential function describing the now beginning relaxation process can be replaced for short times t by its linear approximation. Thus we have for the internal energy in the moving system

$$u \approx u_0 + u_\infty \cdot t/\tau \tag{8}$$

[$u_\infty = u(t = \infty) = kT/3$]. This approximation is sufficient to describe all hitherto existing experiments. Now we calculate the relaxation time τ. The energy transfer from the transverse into the longitudinal degree of freedom occurs by encounters between individual electrons. Let us designate the momentum transferred to an electron during the i-th

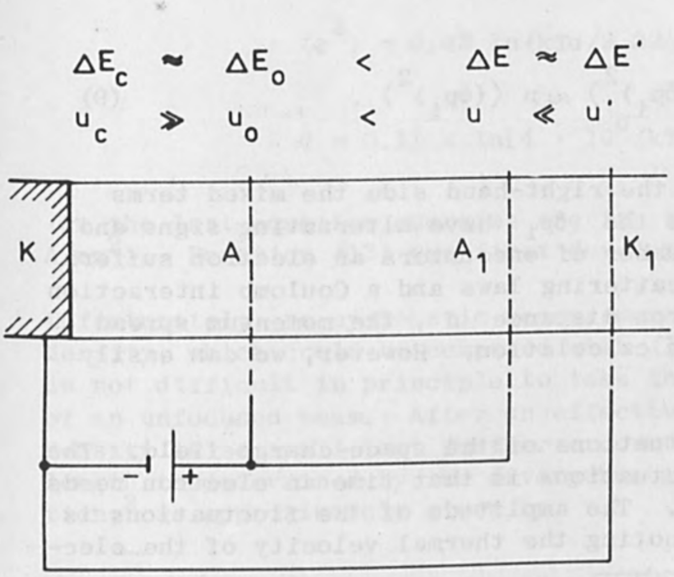
$\Delta E_c \approx \Delta E_o < \Delta E \approx \Delta E'$
$u_c \gg u_o < u \ll u'$
K
A
A_1
K_1
−
+

FIG. 1

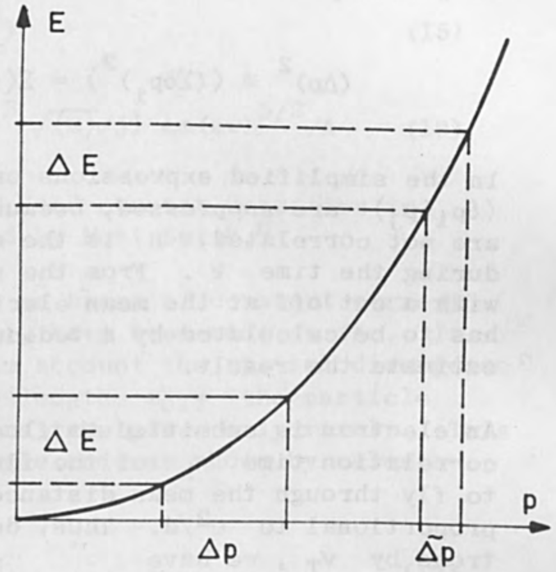

FIG. 2

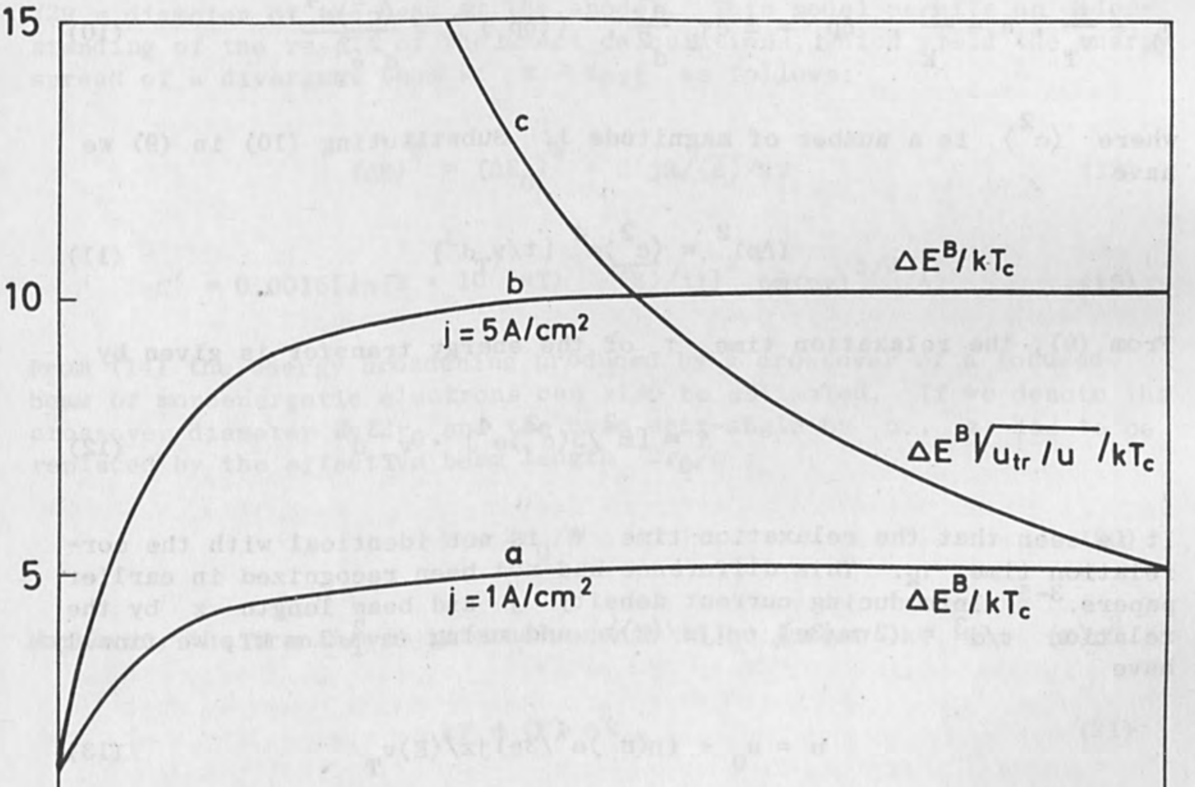

FIG. 3

encounter as δp_i . Then the momentum spread after several encounters is given by

$$(\Delta p)^2 \equiv \langle (\Sigma \delta p_i)^2 \rangle = \Sigma \langle (\delta p_i)^2 \rangle \approx n \ \langle (\delta p_i)^2 \rangle \ . \tag{9}$$

In the simplified expressions on the right-hand side the mixed terms $\langle \delta p_i \delta p_j \rangle$ are suppressed, because the δp_i have alternating signs and are not correlated; n is the number of encounters an electron suffers during the time t . From the scattering laws and a Coulomb interaction with a cut off at the mean electron distance d , the momentum spread has to be calculated by a tedious calculation. However, we can easily estimate the result.

An electron is submitted to fluctuations of the space-charge field. The correlation time τ_k of the fluctuations is that time an electron needs to fly through the mean distance. The amplitude of the fluctuations is proportional to e^2/d. Thus, denoting the thermal velocity of the electrons by v_T , we have

$$\tau_k = \frac{d}{v_T} \ , \ n = \frac{t}{\tau_k} \ , \quad \delta p_i = \pm \, c \tau_k \frac{e^2}{d^2} \ , \quad \langle (\delta p_i)^2 \rangle = \frac{\langle c^2 \rangle e^4}{d^2 v_T^2} \tag{10}$$

where $\langle c^2 \rangle$ is a number of magnitude 1. Substituting (10) in (9) we have

$$(\Delta p)^2 = \langle c^2 \rangle e^4 \ [t/v_T d^3] \tag{11}$$

From (8), the relaxation time τ of the energy transfer is given by

$$\tau = [m^2/3\langle c^2 \rangle e^4] \cdot v_T^3 d^3 \tag{12}$$

It is seen that the relaxation time τ is not identical with the correlation time τ_k. This difference had not been recognized in earlier papers.[3-5] Introducing current density j and beam length z by the relation $t/d^3 = (2\pi m/3e) \cdot (jz/\langle E \rangle)$ and using $mv_T^2/2 = kT$, we finally have

$$u = u_0 + (\pi \langle c^2 \rangle e^4/3e) jz/\langle E \rangle v_T \tag{13}$$

$$(\Delta E)^2 = (\Delta E_0)^2 + Cjz(kT)^{-1/2} \tag{14}$$

where $C = 4\langle c^2 \rangle \sqrt{m/18e^2}$. Exact calculations[2] have shown that $\langle c^2 \rangle$ is not a constant but a function depending to a small extent on the beam parameters:

$$\langle c^2 \rangle = 0.42 \ln(kTd/2.22e^2) \tag{15}$$

$$C = 0.11 \cdot \ln[4 \cdot 10^6 (kT)^3 \sqrt{\langle E \rangle}/j] \text{ cm(ev)}^{5/2}/A \tag{16}$$

(In the last equation energies are in eV and current densities in A/cm^2). Equation (13) was first developed by Mott-Smith.[6]

Unfortunately, no systematic measurements on beams of constant current density, which could be compared with (14), have been made so far. It is not difficult in principle to take into account the spatial divergence of an unfocused beam. After an effective length z_{eff} the particle density is so small that further encounters take place only rarely. This length is determined by the divergence angle and, as shown by calculation,[2] is approximately given by

$$z_{eff} = 0.132\, R\sqrt{\langle E \rangle/kT} \tag{17}$$

(2R = diameter of the beam at the anode). This model permits an understanding of the result of the exact calculations, which yield the energy spread of a divergent beam at $z > z_{eff}$ as follows:

$$(\Delta E)^2 = (\Delta E_0)^2 + C' jR\sqrt{\langle E \rangle/kT} \tag{18}$$

$$C' = 0.0015[\ln(3 \cdot 10^7 (kT)^3 \sqrt{\langle E \rangle}/j)]^2 \text{ cm(ev)}^{5/2}/A \tag{19}$$

From (14) the energy broadening produced by a crossover of a focused beam of monoenergetic electrons can also be estimated. If we denote the crossover diameter by $2r_0$ and the beam semi-angle by α, z has to be replaced by the effective beam length $2r_0/\alpha$:

$$z \rightarrow 2r_0/\alpha \tag{20}$$

Moreover, the transverse internal energy is no longer kT but $\langle E \rangle \alpha^2$:

$$kT \rightarrow \langle E \rangle \alpha^2 \tag{21}$$

Thus the energy broadening caused by a crossover is given by

$$(\Delta E)^2 = (\Delta E_0)^2 + 2\, Cjr_0/\sqrt{\langle E \rangle}\, \alpha^2 \tag{22}$$

This estimate is confirmed by a calculation of Löffler,[7] who obtains C as follows:

$$C_{\text{Löffler}} = (4\pi e^4 \sqrt{m/2}/e)[3.69 + 2\ \ln(8\pi r_0^3\rho) + (1/4)\ln^2(8\pi r_0^3\rho)] \qquad (23)$$

Relativistic beam energies require only a slight modification of (14) in the logarithmic term of C. In (16) $\langle E\rangle$ has to be replaced by

$$\langle E\rangle \rightarrow \langle E\rangle \sqrt{1 + \langle E\rangle/m_0c^2} \qquad (24)$$

where $m_0c^2 = 0.5$ MeV is the rest energy of the electron.

Let us now compare theory with experiment.

Figure 3 shows the dependence of the energy spread of an unfocused beam on the beam length. Only if z is small does the energy spread increase with z . The z independence for the greater beam lengths is experimentally verified.[1] Figure 4 shows the dependence of the energy spread of an unfocused beam on the current density j (at smallest beam diameter). The full lines show the dependence as expected by theory. The points are measured energy spreads. Because C is calculated absolutely we have no free parameter at our disposal. The discrepancy between theory and experiment is probably caused by a dependence of the beam diameter on the current density (induced by the potential of the control grid, which served to vary the beam current).

Figure 5 shows the dependence of the energy spread on the emitter radius. Systematic experiments in this field have not been made up to now. The experiments made to date seem to confirm this dependence.[8]

One remark should be added to the relaxation law (8). In Ref. 3, a linearized relaxation law for ΔE instead of for u was proposed. The more careful analysis has led, however, to (8). It follows from the fact that the broadened velocity distribution is a convolution of the initial distribution and a Boltzmann distribution. From this, the broadened distributions themselves can be calculated.

Figure 6 shows the agreement between the calculated and measured integrated energy distributions. The analytically given distribution makes it now possible to state the relation between the energy widths $\Delta E_{1/2}$ and $\Delta E_{63\%}$ (which are normally taken from the measured distributions) and the energy spread ΔE . The relations are nonlinear and are shown in Fig. 7 for the broadened normal energy distributions (K1/2 and K63%, respectively) and for the broadened total energy distributions (B1/2 and B63%, respectively). Following Ref. 9 we have designated the energy distributions $dn/dE \propto (1/\sqrt{E}) \cdot \exp(-E/kT)$ as (unbroadened) normal energy distribution; and $dn'/dE \propto \sqrt{E} \cdot \exp(-E/kT)$ as total energy distribution, where dn is the number of electrons within the energy interval from E to E + dE .

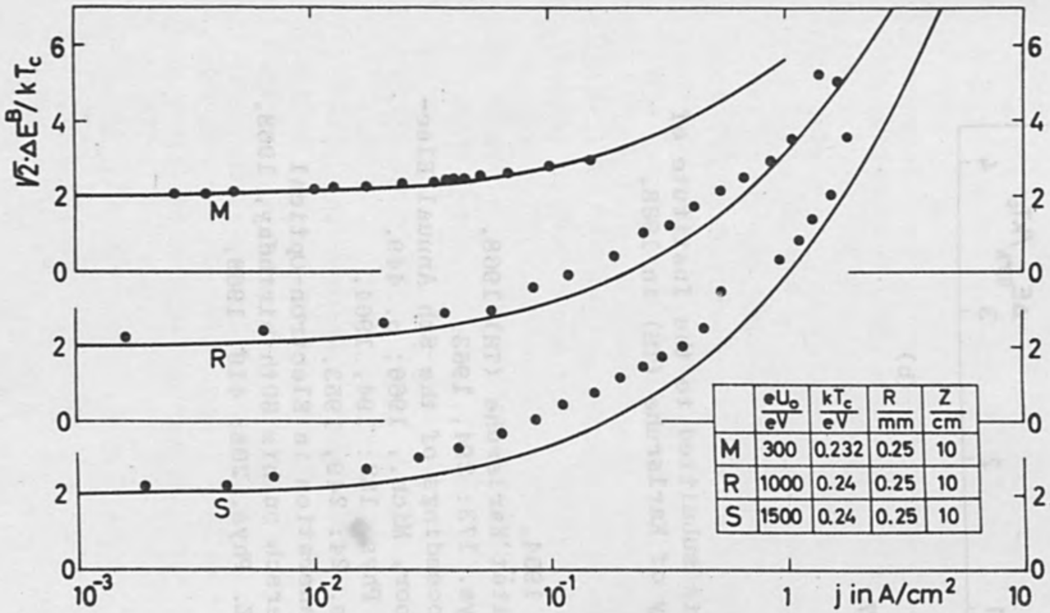

	$\frac{eU_0}{eV}$	$\frac{kT_c}{eV}$	$\frac{R}{mm}$	$\frac{Z}{cm}$
M	300	0.232	0.25	10
R	1000	0.24	0.25	10
S	1500	0.24	0.25	10

FIG. 4

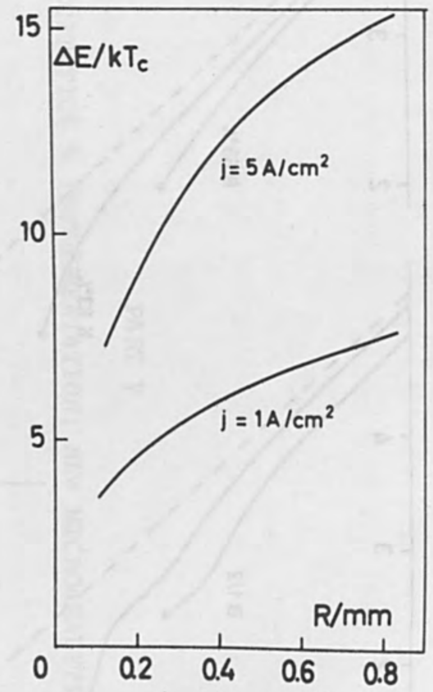

FIG. 5

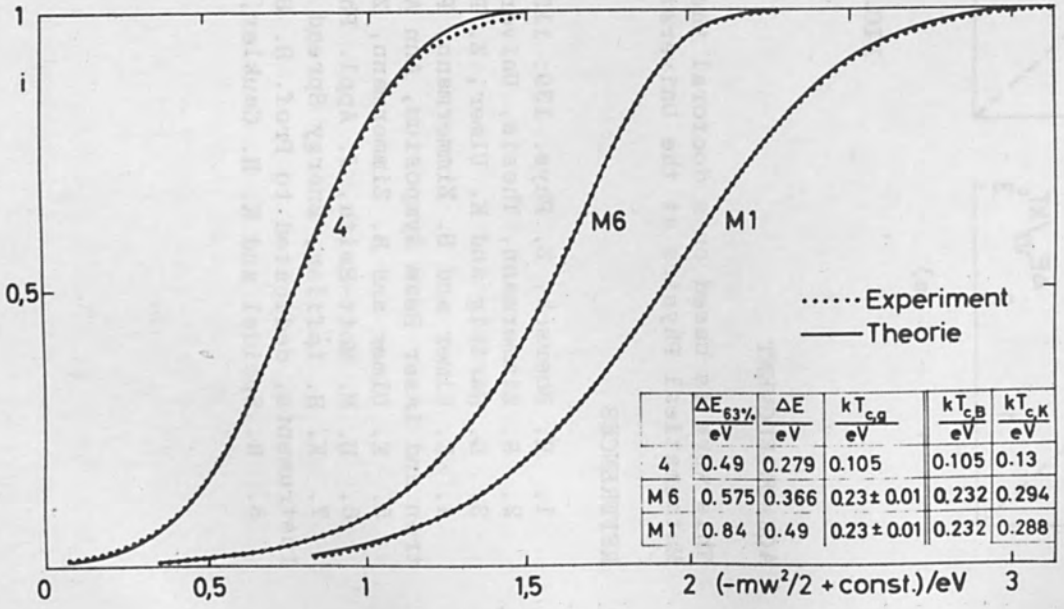

	$\frac{\Delta E_{63\%}}{eV}$	$\frac{\Delta E}{eV}$	$\frac{kT_{c,g}}{eV}$	$\frac{kT_{c,B}}{eV}$	$\frac{kT_{c,K}}{eV}$
4	0.49	0.279	0.105	0.105	0.13
M6	0.575	0.366	0.23 ± 0.01	0.232	0.294
M1	0.84	0.49	0.23 ± 0.01	0.232	0.288

FIG. 6

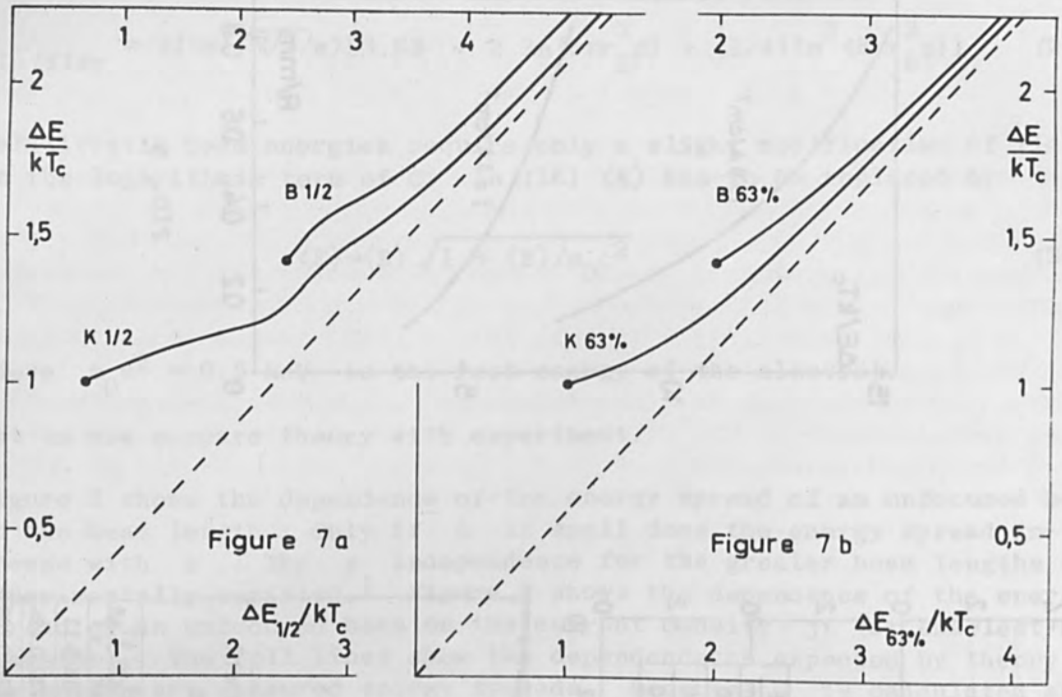

(a) (b)

FIG. 7

ACKNOWLEDGMENT

This work is based on a doctoral thesis submitted to the Institute of Mathematical Physics at the University of Karlsruhe (TH) in 1968.

REFERENCES

1. H. Boersch, Z. Phys. 139: 115, 1954.
2. B. Zimmermann, Thesis, Universität Karlsruhe (TH) 1968.
3. D. Hartwig and K. Ulmer, Z. Phys. 173: 294, 1963.
4. K. Ulmer and B. Zimmermann, Proceedings of the 8th Annual Electron and Laser Beam Symposium, Ann Arbor, Mich., 1966; p. 449.
5. K. Ulmer and B. Zimmermann, Z. Phys. 182: 194, 1964.
6. H. M. Mott-Smith, J. Appl. Phys. 24: 249, 1953.
7. K. H. Löffler, Energy Spread Generation in Electron-Optical Instruments, dedicated to Prof. H. Boersch on his 60th birthday, 1968.
8. R. Speidel and K. H. Gaukler, Z. Phys. 208: 419, 1968.

PART V

LASER EXCITATION & INSTRUMENTATION; NEW MICROANALYTICAL TOOLS

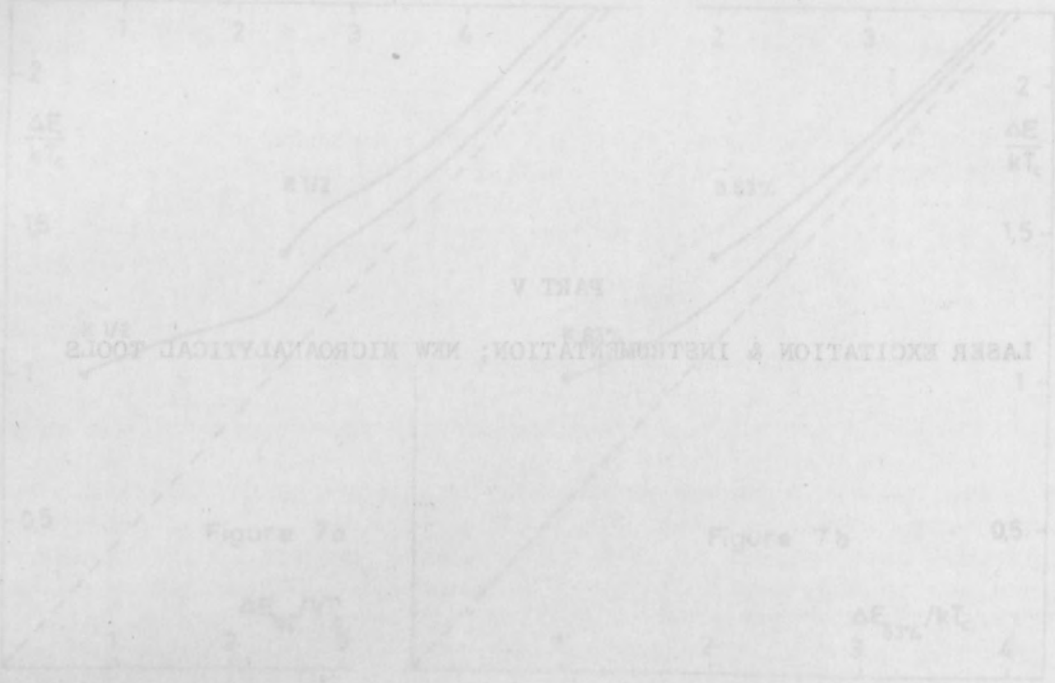

(a) (b)

Fig.

ACKNOWLEDGMENT

This work is based on a doctoral thesis submitted to the Institute of Mathematical Physics at the University of Karlsruhe (TH) in 1968.

REFERENCES

1. H. Boersch, Z. Phys. 139: 115, 1954.
2. B. Zimmermann, Thesis, Universität Karlsruhe (TH) 1968.
3. D. Hartwig and K. Ulmer, Z. Phys. 173: 294, 1963.
4. K. Ulmer and B. Zimmermann, Proceedings of the 6th Annual Electron and Laser Beam Symposium, Ann Arbor, Mich., 1964, p. 449.
5. K. Ulmer and B. Zimmermann, Z. Phys. 182: 194, 1964.
6. D. B. Kott-Smith, J. Appl. Phys. 24 1249, 1953.
7. K. H. Loeffler, Energy Spread Generation in Electron-Optical Instruments, Dedicated to Prof. H. Boersch on his 60th Birthday, 1968.
8. W. Fenstel and K. H. Gaukler, Z. Phys. 208: 419, 1968.

CERAMIC PLASMA CONTAINER FOR ION LASERS

M. NASINI and G. REDAELLI

Technological Research Group, Physics Division, CISE, Milan

R. PRATESI

Istituto di Fisica Superiore dell'Università, Florence

INTRODUCTION

The very high current densities needed for laser action in ionized gases put a severe limitation to the type of materials which can be used for the construction of the plasma containers. Material are needed with high resistance to thermal shocks, discharge erosion, and decomposition. Further, they should present large thermal dissipation and low gas evolution and permeation at the operating temperatures. The lifetime of the laser tube strongly depends on the value of these parameters.

Silica is highly resistant to thermal shocks, but has low thermal conductivity and high gas clean-up rate and suffers decomposition owing to collisions of ionized and neutral (metastable) atoms diffusing away from the discharge. Recently, more or less sophisticated methods of confining the discharge by the use of segmented metal or graphite structures have been used,[1-3] but a gas-replenishing system has been necessary to obtain useful lifetimes. Some ceramic materials satisfy most of the above cited requirements. Beryllia is unique with a high thermal conductivity and good thermal shock resistance. Sealed-off beryllia tubes have been successfully tested for long-life operation without the need of a gas replenishing system,[4,5] Glass-ceramic seal[4] and metal-ceramic seal[5] (moly-manganese) have been employed for medium- and high-power operation, respectively. On the other hand the toxicity of beryllia and the difficulty of finding commercial tubes with high-vacuum tightness properties may limit its utilization.

In this paper we present some preliminary results on a particularly simple method for constructing laser tubes with operation characteristics comparable to those obtained by Conder and Foster.[5] A low-cost, commercially available ceramic material (Sintox) has been employed and the old, quite simple "soldered'seal" technique has been used for the metal-ceramic seal.

CHOICE OF SINTOX

Among commercial ceramics Sintox* presents very good mechanical properties, sufficiently high thermal conductivity (0.054 cal/cm sec °C), extremely low gas permeation and gas evolution (impervious ceramics), and relatively low coefficient of thermal expansion ($6.5\ 10^{-6}/^{\circ}C$) in the temperature range 20-600°C. Moreover its thermal shock resistance is not too small (3.5 cal/sec dm) and it can be safely processed and handled.

---

*Sintox, made by Smith Ltd, England, is the trade name of a ceramic with large content of crystallized alumina embedded in a continuous glassy phase.

Record of 10th Symposium on Electron, Ion, and Laser Beam Technology (L. Marton, ed.); San Francisco Press, Inc.

Copyright © by The Institute of Electrical and Electronics Engineers, Inc.—Printed in the U.S.A.

TECHNIQUES FOR VACUUM JOINT AND DISCHARGE TUBE CONSTRUCTION

Standard technique for glass- or metal-ceramic sealing can be used with Sintox. Glass-ceramic seal and soldered seal techniques have been experimentally tested.

GLASS-CERAMIC SEAL. Discharge tubes (1.2 mm bore, 200 mm long ceramic tube) with glass-Sintox seals have been constructed as reported previously[6] and tested under standard conditions encountered in argon-ion lasers. The upper limit to the current density supported by the discharge tube was determined by the glass-ceramic seal and turned out to be approximately 250 A/cm^2. At higher current densities the ceramic-glass seal was broken. Obviously, if the end bore of the ceramic tube is conically shaped, the current density inside the capillary will be significantly higher than the above value.

SOLDERED SEAL. As is known, ceramic insulators and feedthroughs have been metallized by the thermal reduction of salt solutions of precious metals for many years. The thin, conductive coating thus obtained can then be strengthened by electroplating and soldered connections may be made directly to them. Vacuum-tight joints can be achieved in this manner.[7] This technique was successively overtaken by the well-known moly-manganese process.[8] It is opinion of the authors that with the recently developed materials, soldered seals can with great advantage substitute the moly-manganese technique in the construction of ceramic plasma containers for ion-laser applications. The sealing process is briefly reviewed below.

Both ends of the Sintox tube were externally metallized by thermal reduction of a noble-metal solution to which a small amount of a glass flux powder with the same expansion coefficient of the ceramics has been added. When the mixture is heated, the glaze melts and wets the ceramic. The precious metal then floats to the surface of the glass and forms a continuous and, under particular conditions, very compact layer with excellent adhesion. The bonding strength turns out to be[9,10] higher than 5000 lb/in.^{2} (about one-third that achievable with the moly-manganese process.[11]) The coating is now strengthened by electroplating with copper. Solderability is excellent with soft solders such as lead-tin and gold-tin eutectic alloys (m.p. 185° and 280°C, respectively). Owing to the large differential expansion between the noble-metal coating and the ceramic it is essential to keep the over-all thickness of the coating less than 30 μ (thickness of the copper plating $\sim 10\ \mu$). For the same reason, good metal-ceramic seals can only be attained with sufficiently thin metal parts.

Figure 1 shows a schematic drawing of the soldered ceramic-to-metal seal. Two commercial feedthroughs for high-power vacuum tubes (FIVRE - 3F 25 TA) have been used to connect the Sintox tube to the glass bulbs supporting the electrodes. The OFHC copper pin was drilled and shaped as shown in Fig. 1 to fulfill the requirement cited above and directly soldered to the Sintox tube.

Figure 2 shows the complete discharge tube. An improved version of the LaB_6 cathode[12] has been used (emitting surface 5 cm^2, working temperature 1500°C). A glass jacket placed coaxially to the discharge tube insures good cooling of the graded seals, soldered seals, and ceramic tube with a flow of recirculated de-ionized water. The tube was finally

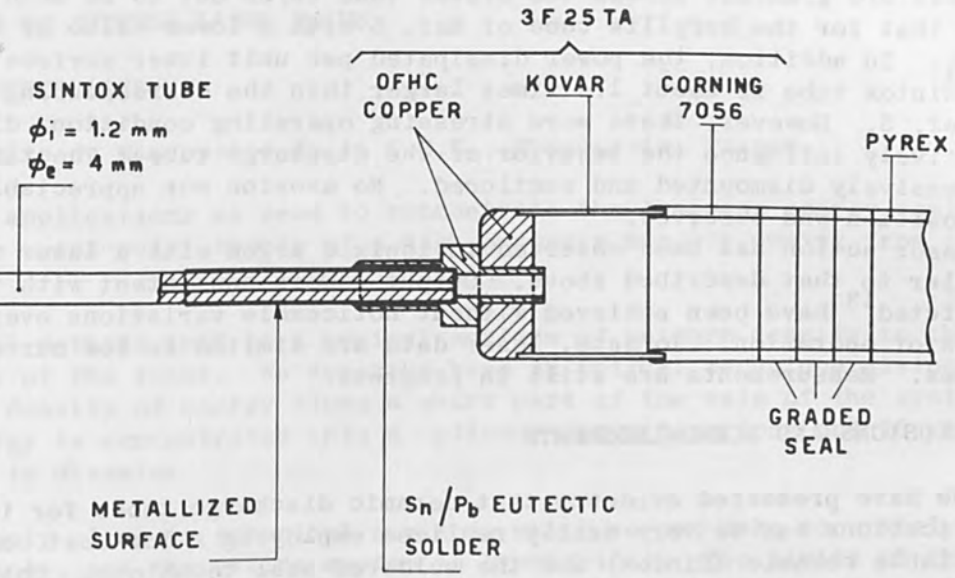
3F25TA
SINTOX TUBE
$\phi_i = 1.2$ mm
$\phi_e = 4$ mm
OFHC COPPER
KOVAR
CORNING 7056
PYREX
GRADED SEAL
METALLIZED SURFACE
Sn/Pb EUTECTIC SOLDER

FIG. 1.—Schematic drawing of soldered metal-Sintox seal.

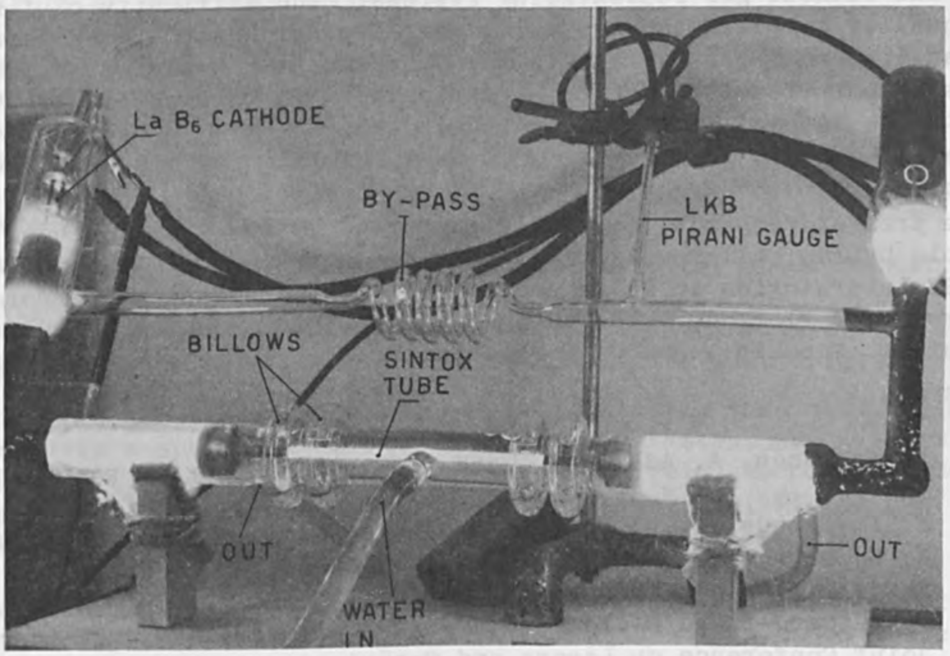
La B6 CATHODE
BY-PASS
LKB PIRANI GAUGE
BILLOWS
SINTOX TUBE
OUT
WATER IN
OUT

FIG. 2.—Discharge tube. The discharge produces a red fluorescence in the Sintox capillary, which appears bright.

evacuated and backed out at 150°C for several hours. After several discharges in pure argon the tube was filled with Ar at about 0.8 Torr and sealed off.

PERFORMANCE OF SINTOX DISCHARGE TUBE

The discharge tube has been tested for gas clean-up, mechanical and thermal resistance, discharge erosion, and decomposition. The discharge current was increased stepwise to 7.2 A (about 637 A/cm^2). No gas clean-up was observed after 100 hours, when the test was terminated. At 7.2 A, 108 W/cm was dissipated in the capillary; assuming $R_2/R_1 = 3.3$

(R_2 denoting the outer radius and R_1 the inner radius) the calculated temperature gradient across the Sintox tube turns out to be much larger than that for the beryllia tube of Ref. 5 with a lower value of the ratio R_2/R_1. In addition, the power dissipated per unit inner surface area of the Sintox tube is about 1.4 times larger than the corresponding value of Ref. 5. However, these more stressing operating conditions did not negatively influence the behavior of the discharge tube. The tube was successively dismounted and sectioned. No erosion nor appreciable decomposition was observed.

Laser action has been observed in ionized argon with a laser tube similar to that described above. Output powers consistent with those predicted[13] have been achieved without noticeable variations over many hours of operation. To date, laser data are limited to low current densities. Measurements are still in progress.

CONCLUSIONS AND ACKNOWLEDGMENTS

We have presented evidence that ceramic discharge tubes for ion laser applications can be very easily realized employing a low-cost commercially available ceramic (Sintox) and the soldered-seal technique. This ceramic can be substituted for beryllia for sealed-off ion lasers with long lifetimes and without gas-replenishing systems. The difficulty of finding high-quality beryllia tubes and the ever-present hazard in processing and handling them can be in this way overcome; the superior characteristics of beryllia seem not to be determinant in this application in the power range reached with ion lasers to date.

The authors are greatly indebted to A. Capelli for his skill in glass blowing.

The present research, partially supported by the CNR, has been made possible by the collaboration between the Technological Research Group of CISE Laboratories in Milan and the Istituto di Fisica Superiore, University of Florence. The authors are greatly indebted to Profs. F. T. Arecchi, U. Facchini, and G. Toraldo di Francia for their interest.

REFERENCES

1. R. Paananen, A. Adams jr., and D. T. Wilson, NEREM Record 7: 238, 1964.
2. E. F. Labuda, E. J. Gordon, and R. C. Miller, JQE 1: 273, 1966.
3. K. G. Hernqvist and J. R. Fendley, JQE 3: 66, 1967.
4. Spectra Physics A^+ laser, Model 141.
5. P. C. Conder and H. Foster, A sealed-off beryllia tube argon ion laser, Joint Conference on Lasers and Optoelectronics, Southampton, England 25-28 March 1969.
6. M. Nasini, R. Pratesi, and G. Redaelli, Research on ceramic discharge tubes for gas lasers: I, Microwave Center Report CM-R79-8.7, October 1967.
7. W. H. Kohl, Handbook of Materials and Techniques for Vacuum Devices, New York: Reinhold Publishing Corp., 1967; p. 455.
8. Ibid., p. 446.
9. A. Sedanka, Bull. Am. Ceram. Soc. 38: 139, 1959.
10. S. J. Stein, Electronic Components Conference, Washington, D. C., 1968.
11. F. Rosebury, Handbook of Electron Tube and Vacuum Technique, Boston: Addison and Wesley Co., 1965; p. 73.
12. M. Nasini and G. Redaelli, Improvements in LaB_6 cathodes with high current density for ion lasers (in preparation).
13. R. Paananen, IEEE Spectrum 3(No. 6): June 1966; p. 88.

FOCUSING OF INTENSE LASER BEAMS

R. H. ROCHEROLLES

Laboratoire de Marcoussis de la C.G.E., Marcoussis, France

In many applications we need to concentrate the luminous energy coming from the quasi-point source of a high-pressure arc, or coming from a laser.

Classical methods lead to a conical surface of uniform density in the vicinity of the focus. We describe here an optical technique giving a uniform density of energy along a short part of the axis of the system; the energy is concentrated into a cylinder about 1 mm long and 10 wavelengths in diameter.

We use only plane or spherical surfaces which we can make accurately and cheaply, and the entire system is symmetrical. The limits of the concentration zone are obtained by diaphragms, and we use the geometrical aberrations of spherical surfaces.

It is well known that the field distribution for a fundamental mode of a spherical Fabry-Perot cavity is gaussian.[1] Consider the mirrors limiting the optical cavity. C_1 and C_2 are their centers of curvature, S_1 and S_2 are their apex on the axis (Fig. 1). The circles having diameters C_1S_1 and C_2S_2 intersect in two points F and F' which are:

(1) The foci of oblate ellipsoids axisymmetrical about Oz and tangent to the mirrors.
(2) The foci of hyperbolas which are the trajectories of the energy: the light rays are orthogonal to the equiphase surfaces (Fig. 2).

This can be demonstrated (however not perfectly) im the following manner. Starting from a spherical wavefront at the first step, and a gaussian distribution of the intensity of the electric field, we compute the resulting field at any point. With some approximations, Pierce has calculated the equipotential surfaces.[2]

Equiphase surfaces at a point M near the axis are thus well represented by parts of spheres whose radius is equal to the diameter of the circle passing through $FF'M$ (Fig. 3).[3] Confocal mirrors represent a case of degeneracy: in this case F and F' are on the median plane.

We define the divergence of a laser beam as the angle φ of the asymptote of the hyperbola corresponding to the envelope of the beam (Fig. 4). On the line FF', we call w_0 the half-width of the beam at $1/e$ of the maximum intensity of the electric field ($1/e^2$ of maximum power).

The circle of radius w_0 contains 84% of total energy and is the minimum spot size. We have the two relations:

$$\pi w_0^2 = \lambda c \qquad \varphi = w_0/c$$

Record of 10th Symposium on Electron, Ion, and Laser Beam Technology (L. Marton, ed.); San Francisco Press, Inc.
Copyright © by The Institute of Electrical and Electronics Engineers, Inc.—Printed in the U.S.A.

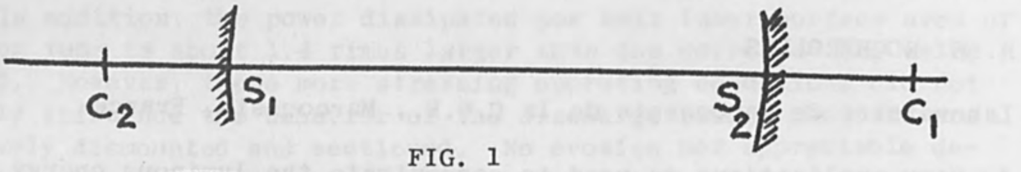

FIG. 1

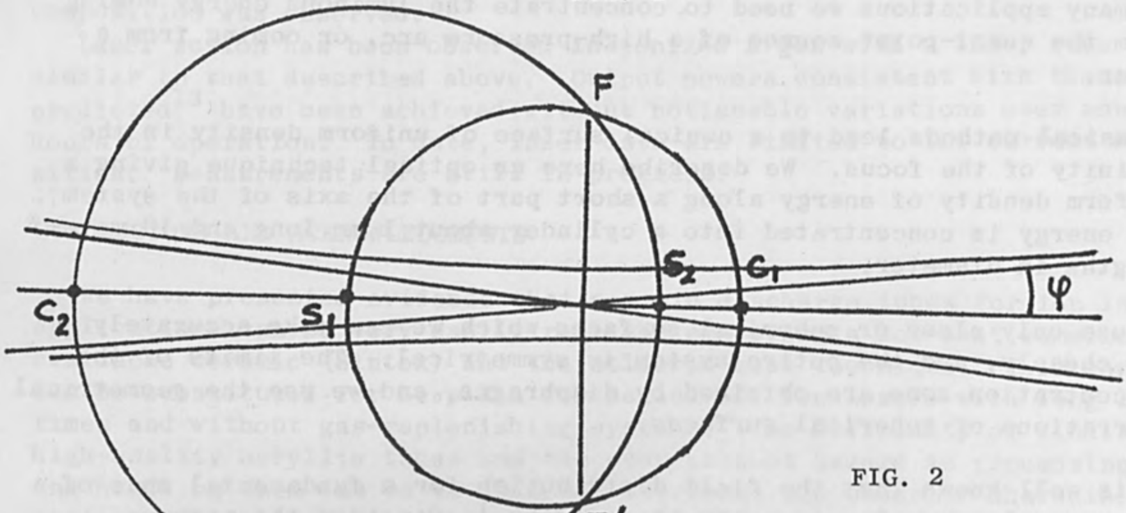
F
C2
S1
S2
C1
φ
F′

FIG. 2

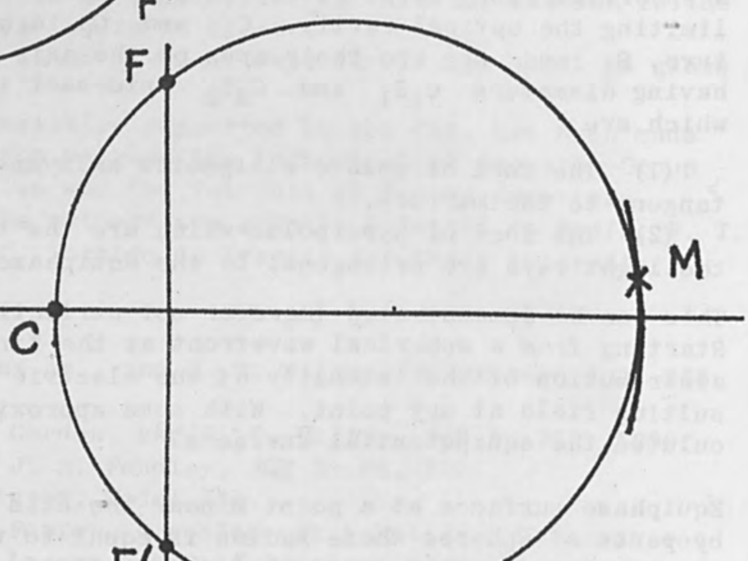

FIG. 3

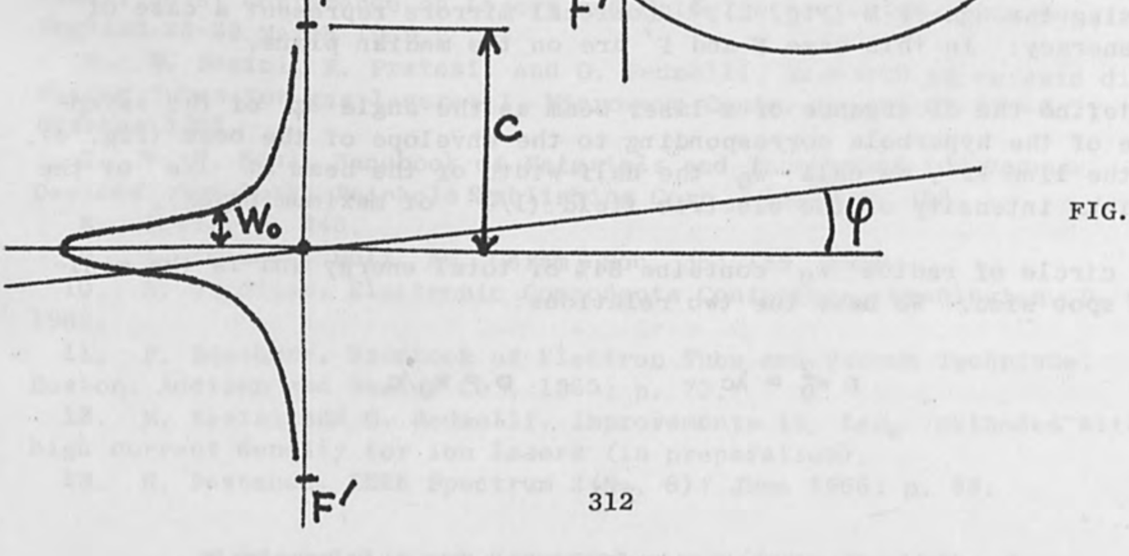

FIG. 4

We see that $w_0\varphi$ is constant $(= \lambda/\pi)$.

Going now to the description of our system, let us begin by examining a classical focusing lens (Fig. 5). In order to have a small focusing region, we employ large objective aperture of the order of F/1 . And working with very high energy lasers, we know that a hole is necessary in the center of the lenses to avoid multiple reflections and damage. In that situation, spherical aberration plays an important role, since paraxial rays have been suppressed and the image is formed with inclined rays. Corrections are important. The best one can do in that way is a cylindrical volume 0.06 mm long and 0.03 mm in diameter, and often worse. Our purpose has been to use directly the geometrical aberrations to concentrate the energy, rejecting the classical image of the source. There is a system in which the axial rays are lost, the Cassegrain telescope (Fig. 7). The central part of the beam is lost:

$$\frac{\varphi}{\Phi} = \frac{f}{F} = \frac{1}{G}$$

We now change the system, making it convergent, reducing the focal length of the main mirror: $F \rightarrow F'$ (Fig. 8). Let us call X the converging distance and N the ratio $N = X/F$. The central part of the beam which is lost is now

$$\frac{\varphi}{\Phi'} = \frac{N}{(N-1)G+1}$$

and the new focal length is

$$F' = \frac{N}{N+1}\,F$$

We compute the aberrations of this system (Fig. 9). In the following example, we take:

$G = 10$
$f = 24$ mm
$F = 240$ mm
$N = 2$
$F' = 160$ mm
$X = 480$ mm

the diameters are

$\varphi = 16$ mm
$\Phi = 160$ mm
$\Phi' = 88$ mm

the fraction of shadow is

$$\frac{\varphi}{\Phi'} = \frac{2}{11}$$

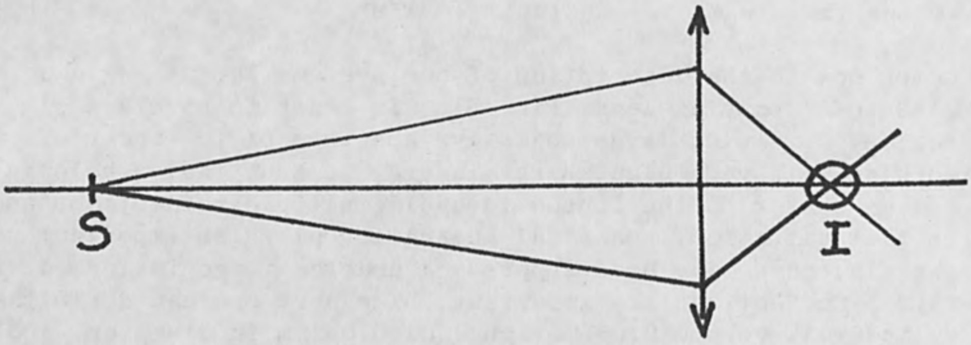

FIG. 5

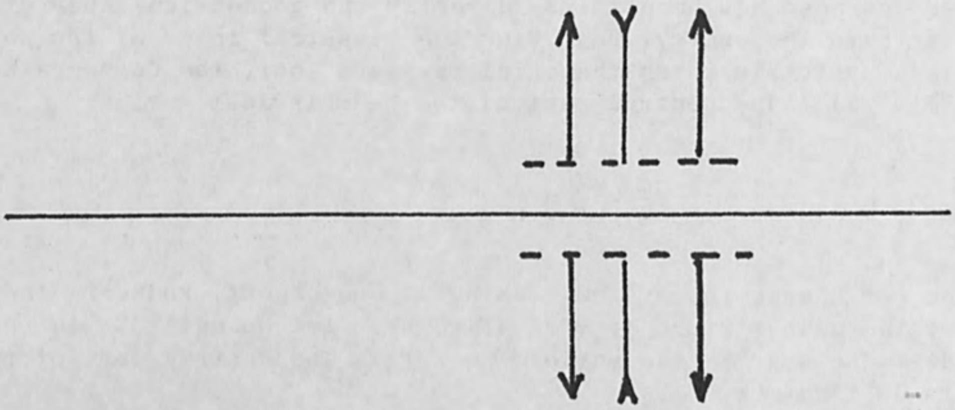

FIG. 6

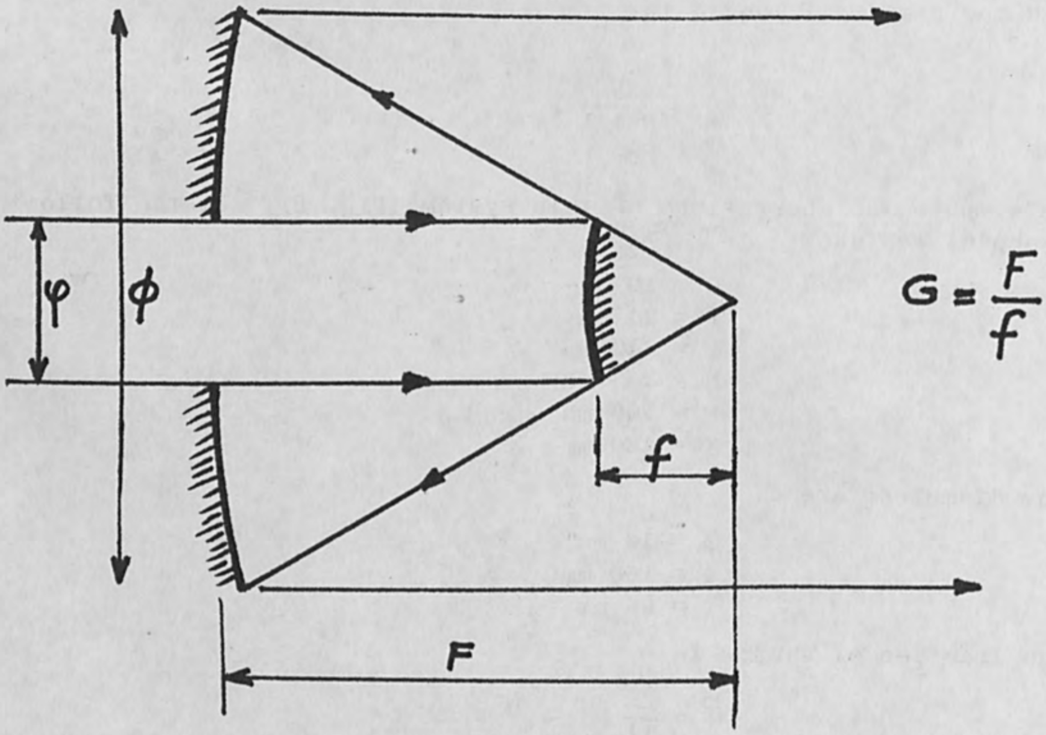

FIG. 7

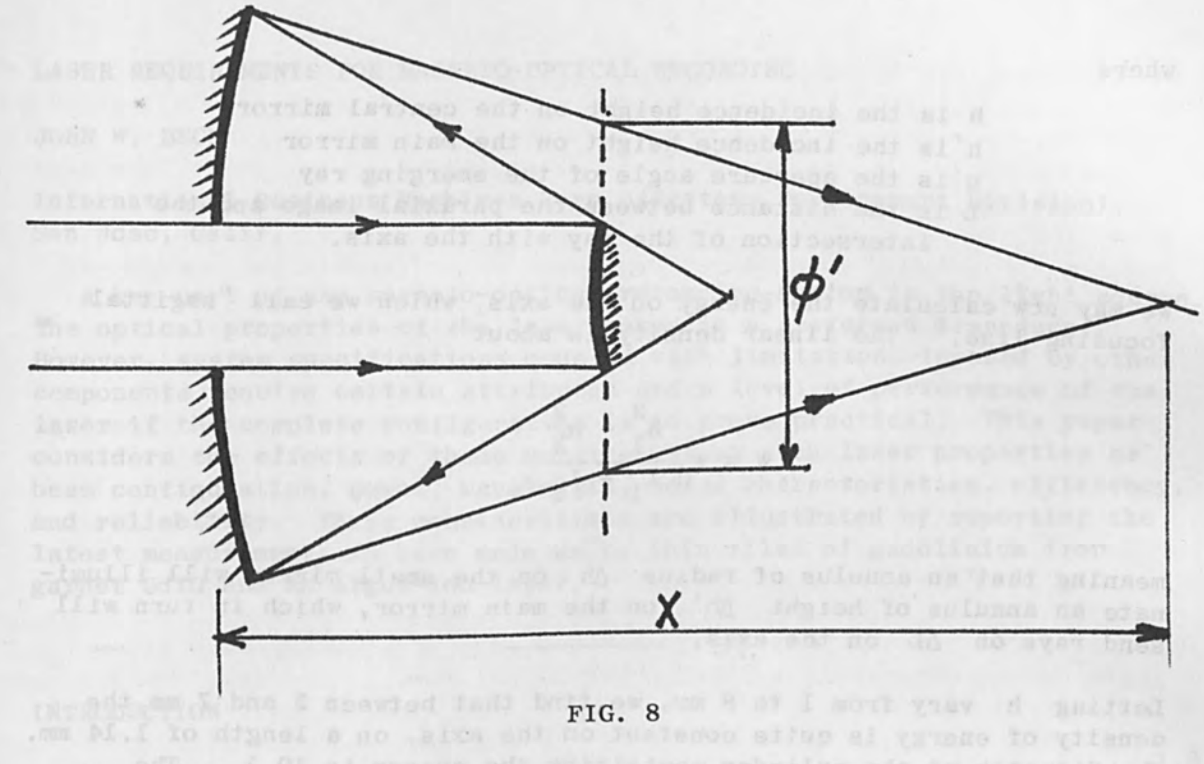

FIG. 8

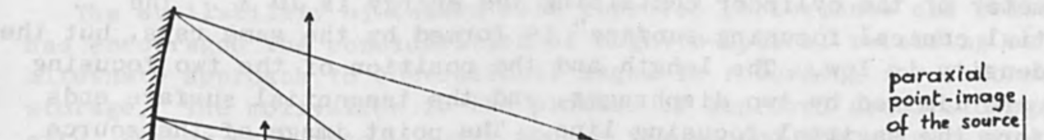
paraxial point-image of the source
u'
h_1
h_2
h'_1
h'_2
L_1
L_2

FIG. 9

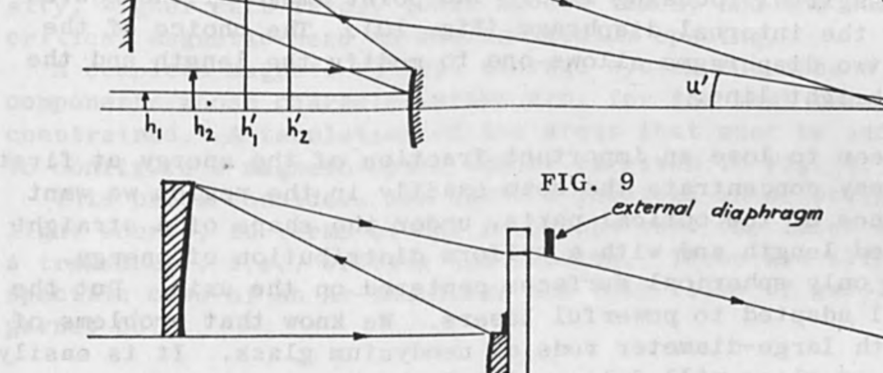
external diaphragm
internal diaphragm

FIG. 10

So we have:

h (mm)	1	2	3	4	5	6	7	8
h' (mm)	10.011	19.994	29.991	39.989	49.972	59.948	69.916	79.862
u'	1° 10'	2° 20'	3° 30'	4° 50'	6°	7° 10'	8° 30'	9° 40'
L μ	52	201	523	891	1414	2040	2799	3430

where

h is the incidence height on the central mirror
h' is the incidence height on the main mirror
u' is the aperture angle of the emerging ray
L is the distance between the paraxial image and the intersection of the ray with the axis.

We may now calculate the energy on the axis, which we call "sagittal focusing line." The linear density is about

$$W = W_0 \frac{h_1^2 - h_2^2}{L_1 - L_2}$$

meaning that an annulus of radius Δh on the small mirror will illuminate an annulus of height $\Delta h'$ on the main mirror, which in turn will send rays on ΔL on the axis.

Letting h vary from 1 to 8 mm, we find that between 3 and 7 mm the density of energy is quite constant on the axis, on a length of 1.14 mm. The diameter of the cylinder containing the energy is 10 λ . The "tangential conical focusing surface" is formed by the same rays, but the energy density is low. The length and the position of the two focusing regions are limited by two diaphragms, and the tangential surface ends 1 mm before the sagittal focusing line. The point image of the source is suppressed by the internal diaphragm (Fig. 10). The choice of the diameter of the two diaphragms allows one to modify the length and the position of the bright line.

This system is seen to lose an important fraction of the energy at first glance. But we may concentrate the beam exactly in the region we want at a great distance of the optical parts, under the shape of a straight element of limited length and with a uniform distribution of energy. For this, we use only spherical surfaces centered on the axis. But the situation is well adapted to powerful lasers. We know that problems of pumping arise with large-diameter rods of neodynium glass. It is easily seen that a tube of glass will deliver its laser energy exactly in the useful region of that aberrant telescope.

BIBLIOGRAPHY

1. G. D. Boyd and J. P. Gordon, BSTJ 40: 489, 1961.
2. J. R. Pierce, Proc. Nat. Acad. Sci. (U.S.) 47: 1808, 1961.
3. P. Laures, "Geometrical approach to Gaussian beam propagation," Applied Optics 6: April 1967.
4. J. P. Gaffard, Internal report, 10 Feb. 1969.

LASER REQUIREMENTS FOR MAGNETO-OPTICAL RECORDING

JOHN W. BECK

International Business Machines Corp. (Systems Development Division),
San Jose, Calif.

A key part of any magneto-optical recording system is the light source. The optical properties of the laser makes it a preferred transducer. However, system specifications coupled with limitations imposed by other components require certain attributes and a level of performance of the laser if the complete configuration is to prove practical. This paper considers the effects of these constraints on such laser properties as beam configuration, power, wavelength, noise characteristics, efficiency, and reliability. These considerations are illustrated by reporting the latest measurements we have made using thin films of gadolinium iron garnet GdIG and an argon-ion laser.

INTRODUCTION

The availability of lasers with improved performance and reliability[1,2] has encouraged the consideration of magneto-optical recording as an alternate approach to conventional magnetic recording for information storage. The motivation is the promise of improved areal storage density, higher data rates, lower access times, and the elimination of critical magnetic-head to storage-medium spacing.

A complete magneto-optical storage system requires a combination of components whose characteristics are, for the most part, interdependently constrained. A tabulation of the areas that must be addressed in order to configure a magneto-optic memory is given in Fig. 1.

This paper considers the factors involved in selecting a suitable light source, in terms of the functions that the laser must perform as a transducer, i.e., writing and reading. These are illustrated for the specific case of an Ar-ion laser and thin films of gadolinium iron garnet GdIG.

THERMOMAGNETIC WRITING

Each method used to write magneto-optically, i.e., Curie point,[3] thermostrictive,[4] temperature-sensitive coercive force,[5] and compensation point,[6] relies on the combination of a nonlocalized magnetic field and the temperature rise caused by a focused beam to switch the direction of magnetization of a small film area. The write energy needed to raise the temperature ΔT of a unit area of a film is given by $C_v t \Delta T$, where C_v is the specific heat and t is the film thickness. The energy absorbed in a unit time is given by $I_0(1 - \epsilon^{-\alpha t})$, where I_0 is the nonreflected incident beam intensity and α is the absorption coefficient of the material. The required write energy per unit area approaches the limit $C_v \Delta T/\alpha$ as αt approaches zero, indicating the desirability of high values of α. The absorption coefficient of magneto-optical materials is wavelength dependent,[7-9] but for some materials the match to suitable laser lines is not optimum. For GdIG[9]

Record of 10th Symposium on Electron, Ion, and Laser Beam Technology (L. Marton, ed.); San Francisco Press, Inc.

Copyright © by The Institute of Electrical and Electronics Engineers, Inc.—Printed in the U.S.A.

at a wavelength λ of 4880 Å, a strong line of the Ar-ion laser, $\alpha = 10^4$/cm. At 4416 Å, a strong line of the He-Cd laser,[10] $\alpha = 3 \times 10^4$/cm.

The distribution of energy in the beam is an important factor in the writing process. To obtain the smallest recorded spots, it follows that the laser beam divergence and diameter should be as small as possible. Since the diffraction-limited spot size will be proportional to wavelength and since electro-optical materials used for deflectors and modulators have optical phase retardations inversely proportional to wavelength,[11] it is usually preferable to work with shorter wavelength lines if not constrained by other material or systems considerations. To obtain the minimum spot size on the storage material, it is also preferable to employ the TEM_{00} transverse mode of gas lasers.[12] To a good approximation the focused spot of such a laser beam is Gaussian if spherical aberration and aperturing effects are minimized.[13]

On very thin films and for a laser beam exposure time much shorter than the thermal diffusion time, the temperature profile on the film matches the intensity distribution of the beam. In addition, the temperature profile of the spot appears to "collapse"; the heat dissipates primarily into the supporting substrate. For a given magnetic bias field, all thermomagnetic writing techniques have a threshold temperature above which the material switches. It can be shown[15] that the ratio of beam energy over the threshold value gives a switched spot size which can be expressed as $x_0 = [\ell n(mn)/2]^{1/2}$, where x_0 is normalized to the $1/\varepsilon^2$ beam radius. The symbol mn is proportional to the ratio of beam energy to threshold energy. Figure 2 is a plot of this expression which shows that operation well above threshold avoids spot size versus beam power sensitivity effects.

Furthermore, operation in excess of threshold tends to reduce defocusing effects, because the increase in beam width caused by defocusing is offset by the decrease of beam intensity per unit area. The plots of Fig. 3 give a simplified picture of this effect. For an optical system with a numerical aperture of 0.1, the change in spot size resulting from a lens to material distance change of 100 μm would be one part in two.

We have written dynamically[9] on 1-μm films of GdIG at $\lambda = 4880$ Å with energies of approximately 1.25 nJ/μm^2. Inasmuch as this figure includes the losses due to scanning and finite beam switching times, as described elsewhere,[16] and represents an absorption of 50% of incident energy and a temperature rise above ambient of 80°C at beam center, it compares well with a previously estimated value[17] of 0.8 nJ/μm^2. Measured values for a 1-μm-thick film normalized to 0.23 nJ/μm^2 are shown plotted in Fig. 2. To obtain high data rates, it is important to minimize the required writing energy. The energy of 1.25 nJ/μm^2 corresponds to a beam-power requirement of 20 mW/MHz for a 5-μm diameter spot.

MAGNETO-OPTICAL READING

For materials such as thin stressed films of GdIG, where the magnetization is perpendicular to the film plane, two magneto-optical effects can be used to sense the state of magnetization: (1) the Faraday effect and (2) circular dichroism. As plots[9] of these effects indicate, both are strongly wavelength dependent. Of available lasers the Ar-ion laser is reasonably useful for the Faraday effect with GdIG. The He-Cd line at 4416 Å is a good match to the circular dichroism spectrum of GdIG.

The minimum power level for reading is determined by signal-to-noise

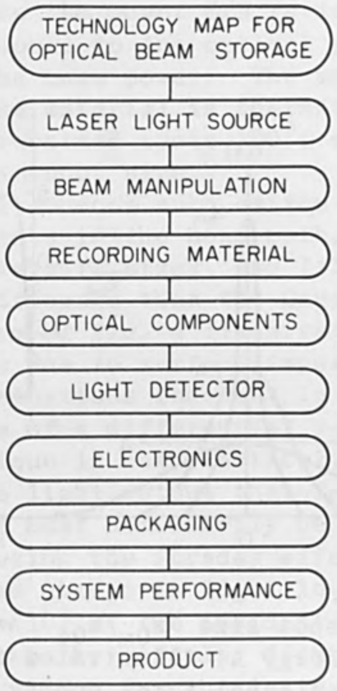
TECHNOLOGY MAP FOR OPTICAL BEAM STORAGE
LASER LIGHT SOURCE
BEAM MANIPULATION
RECORDING MATERIAL
OPTICAL COMPONENTS
LIGHT DETECTOR
ELECTRONICS
PACKAGING
SYSTEM PERFORMANCE
PRODUCT

FIG. 1.—Magneto-optical check list.

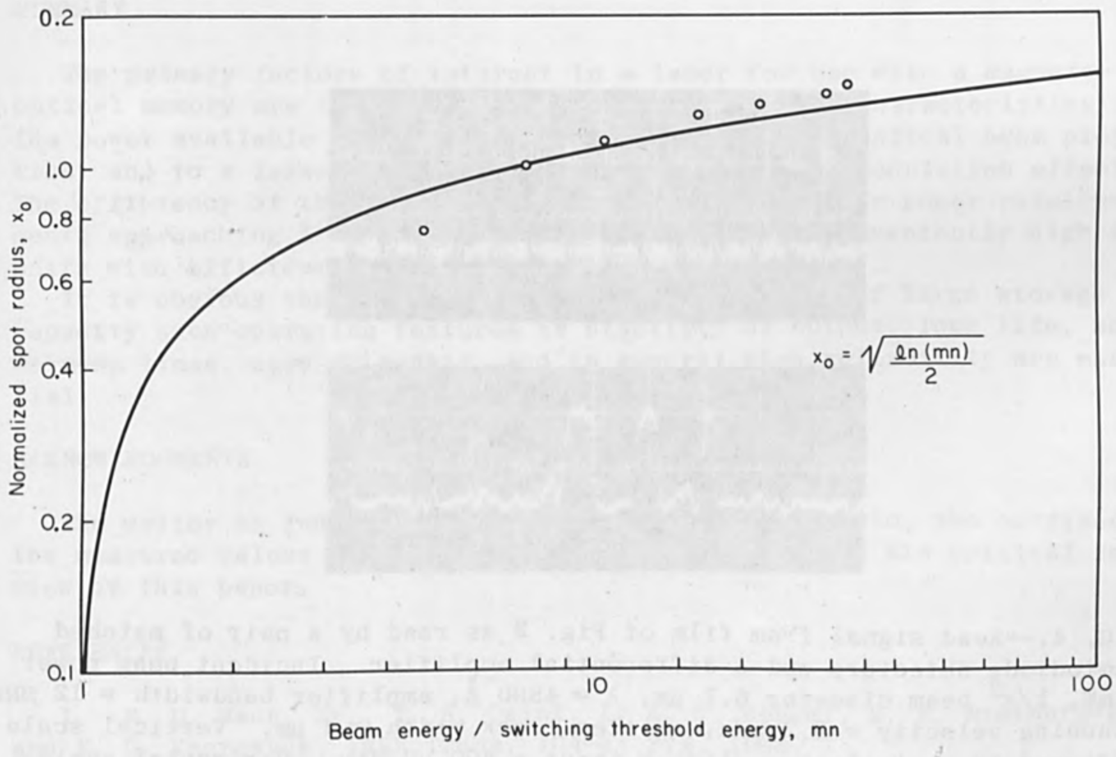

FIG. 2.—Plot of x_0 versus mn for expression $x_0 = \sqrt{[\ell n(mn)]/2}$, where x_0 is equal to the written spot radius normalized to the $1/\epsilon^2$ beam radius. Points represent values measured on 1-μm thick GdIG film crystallized epitaxially on (111)-oriented yttrium aluminum garnet (YAG) substrate. Film temperature 26°C above its compensation temperature of -1°C; magnetic field bias 150 Oe; $1/\epsilon^2$ beam diameter 4.75 μm; threshold writing energy 0.23 nJ/μm^2.

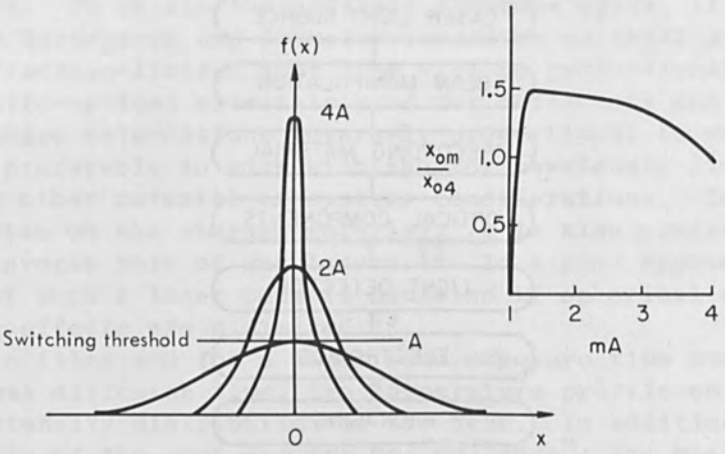

FIG. 3.—Plot of relative spot size x_{0m}/x_{04} as a function of beam energy/threshold writing energy A, illustrated for the case of three normal distribution plots of equal total energy. The case for the multiplier m = 4 corresponds to the best focused spot.

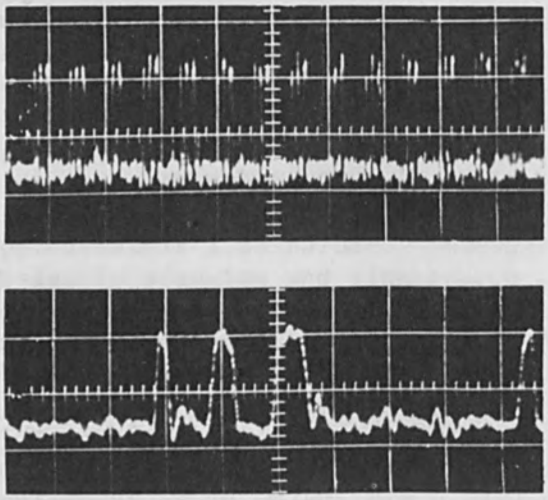

FIG. 4.—Read signal from film of Fig. 2 as read by a pair of matched photodiode detectors and a differential amplifier. Incident beam power 8 mW, $1/\epsilon^2$ beam diameter 6.1 μm, λ = 4880 Å, amplifier bandwidth = 12 MHz, scanning velocity = 8.2 m/s, written track width ≃ 4 μm. Vertical scale referred to equivalent amplifier input = 400 μV/div. Horizontal scale: upper trace = 50 μs/div, lower trace = 5 μs/div.

S/N considerations. Since the power S/N ratio[18] for photodetection and amplification is proportional to the optical power, the S/N ratio can be improved by increasing the beam power. The upper limit to such a procedure is reached when the material is thermally demagnetized. With GdIG samples, we have heated reversed spots 100°C above the compensation temperature with no change in spot size.[9]

Noise terms from other sources such as the laser, unavoidable relative motion of optical components in the beam path, scratches, material inclusions, irregular crystallite sizes, and film magnetic dispersion generally have more significance than the Gaussian noise terms.[19] For example, the read waveform of Fig. 4 illustrates the case where the predominant noise term is due to surface imperfections in the film. The noise contributed by fluctuations inherent in the output of a gas laser[20] can be reduced by the use of a differential reading technique.[21,22] However, when this technique is not practical, the allowable noise percentage modulation of the light output that falls in the passband of the read amplification system must necessarily be small. For single-ended readout near extinction using the Faraday effect with 1-μm-thick films of GdIG at $\lambda = 4880$ Å, the change in light level, i.e., the effective signal, is only 1 part in 10^4 of the incident transmitted light.[9] For 1-μm-thick GdIG films using the circular dichroism effect at $\lambda = 4416$ Å, the signal is 4 parts per 100. For the latter case, the modulation effects would still have to be well under 1 part per 100.

SUMMARY

The primary factors of interest in a laser for use with a magneto-optical memory are the wavelength (to match the film characteristics), the power available (large for high data rates), the optical beam properties, and to a lesser degree the (lack of) intensity-modulation effects. The efficiency of the laser is of consequence since for power requirements approaching 1 W, the primary power becomes inconveniently high for units with efficiencies below about 1/2%.

It is obvious that for a successful configuration of large storage capacity such operating features as stability of output, long life, short warm-up times, ease of repair, and in general high reliability are essential.

ACKNOWLEDGMENTS

The writer is indebted to D. G. Murphy and R. T. Muto, who obtained the measured values of Fig. 2, and R. E. MacDonald for his critical review of this paper.

REFERENCES

1. R. D. Haun, Jr., T. A. Osial, L. A. C. Weaver, K. B. Steinbruegge, and E. G. Vaerewyck, IEEE Trans. IGA-4: 379, 1968.

2. F. P. Gagliano, R. M. Lumley, and L. S. Watkins, Proc. IEEE 57: 114, 1969.

3. L. Mayer, J. Appl. Phys. 29: 1003, 1958.

4. H. J. Kump and P. T. Chang, IBM J. Research Develop. 10: 255, 1966.

5. D. Treves, I. W. Wolf, and N. Ballard, J. Appl. Phys. 40: 976, 1969.

6. J. T. Chang, J. F. Dillon jr., and U. F. Gianola, J. Appl. Phys. 36: 1110, 1965.
7. D. Chen, J. F. Ready, and E. Bernal G., J. Appl. Phys. 39: 3916, 1968.
8. K. Y. Ahn and J. C. Suits, IEEE Trans. MAG-3: 453, 1967.
9. R. E. MacDonald and J. W. Beck, J. Appl. Phys. 40: 1429, 1969.
10. W. T. Silvest, Appl. Phys. Letters 13: 169, 1968.
11. I. P. Kaminow and E. H. Turner, Proc. IEEE 54: 1374, 1966.
12. R. J. Freiberg and A. S. Holsted, Laser Focus 4 (No. 3): 21, 1968.
13. D. J. Innes and A. L. Bloom, Spectra-Physics Laser Tech. Bull. No. 5, Spectra-Physics, Inc., Mountain View, Calif., 1966.
14. N. Goldberg, IEEE Trans. MAG-3: 605, 1967.
15. J. W. Beck, Proc. IEEE 57: 1223, 1969.
16. R. L. Aagard, D. Chen, R. W. Honebrink, G. N. Otto, and F. M. Schmit, IEEE Trans. MAG-4: 416, 1968.
17. C. D. Mee and G. J. Fan, IEEE Trans. MAG-3: 72, 1967.
18. L. K. Anderson and B. J. McMurtry, Proc. IEEE 54: 1335, 1966. Also Appl. Optics 5: 1573, 1966.
19. J. W. Beck, "Noise considerations of optical beam reading," to be published.
20. A. L. Bloom, Proc. IEEE 54: 1262, 1966.
21. J. Miyata and T. Lentz, "MAGOP: A new approach to high density digital magnetic recording," 1962 Large Capacity Memories Conf. Rept.; pp. 117-134.
22. D. Treves, J. Appl. Phys. 38: 1192, 1967.

OBSERVATION OF ELECTRON DIFFRACTION PATTERN ON NONLUMINESCENT TARGET CAUSED BY LASER INTERACTION*

HELMUT SCHWARZ and HEINRICH HORA+

Rensselaer Polytechnic Institute (Hartford Graduate Center),
East Windsor Hill, Conn.

INTRODUCTION

Electron transmission diffraction patterns of thin monocrystal films of SiO_2 and Al_2O_3 were made visible on a nonluminescent screen.[1] The films were optically transparent. An argon-ion laser of 10 W intersected the electron beam of 50 keV energy and a few microamperes of current within the crystal film. The light beam was parallel, 10 to 100 μm wide within the intersection region; it was polarized so that its electric field vector was perpendicular to the thin film and parallel to the electron beam.

A satisfactory explanation for this "modulation of the electron wave" cannot yet be offered. Two theories are briefly outlined:

One theory, based on quantum mechanics, is that the electrons after leaving the laser beam remain in the quantum oscillation state they picked up within the intersection region and then somehow transfer their oscillation state by collective effects due to bremsstrahl processes within the target material, and finally the target material emits light of the frequency corresponding to the electron oscillation state.

A second theory[2] is more classical: the electrons acquire in the ac field of the optical frequency an ac acceleration superimposed on the dc acceleration voltage of 50 kV, since the electrical vector of the light is parallel to the electron beam.

Unfortunately not enough experimental data are available as yet to test the theories proposed.

However, we shall only elaborate somewhat on the first theory, since the second one would require higher fields and a wider interaction region to guarantee enough voltage modulation of the electron acceleration voltage.

EXPERIMENTAL SET-UP

The thin films of SiO_2 and Al_2O_3 of approximately 1000 Å thickness were epitaxially vacuum-deposited. After floating them off their substrate and supporting them with special grids cooled with liquid nitrogen, we observed transmission electron diffraction patterns on a fluorescent screen of zinc sulfide at a distance of 25 cm from the films. For this purpose, usual electron optics were applied to obtain an electron beam of 50 keV energy and a beam current of the order of 1 μA in a spot of a few microns diameter. The electron beam was directed through such an area of the thin film where the diffraction pattern on the screen

---

* Sponsored in part by a "Research Support Award" of the Connecticut Research Commission.

+ Also with Institut für Plasmaphysik, Max Planck Gesellschaft, Garching, Germany.

Record of 10th Symposium on Electron, Ion, and Laser Beam Technology (L. Marton, ed.); San Francisco Press, Inc.

Copyright © by The Institute of Electrical and Electronics Engineers, Inc.—Printed in the U.S.A.

indicated that the beam passed through a monocrystal structure (see upper part of Fig. 1).

The film supporting grid was constructed in such a way that two opposite edges were not obstructed by the grid wires, so that a laser beam could pass through the film lengthwise and perpendicular to the electron beam.

DIFFRACTION PATTERN AS LIGHT ON NONLUMINESCENT TARGET

After the fluorescent screen is replaced by a smooth flat sheet of polycrystalline alumina, the diffraction pattern produced by the electrons obviously becomes invisible. But if a parallel light beam of 10 to 100 μm from an argon ion laser (λ = 4880 Å) of 10 W output is directed symmetrically (Fig. 2) lengthwise through the solid optically transparent film and perpendicular to the electron beam with the electric field vector of the light polarized parallel to the electron beam, the diffraction pattern becomes visible again on the nonluminescent target with the same spot positions as on the fluorescent screen. But this time the spots emit light of the same wavelength as the blue argon laser. However, no wavelength measurements were performed to prove whether this statement is correct; but visual observation made the light appear of the same frequency. The lower part of Fig. 1 shows the diffraction pattern emitted as blue light from the nonluminescent alumina target, whereas the upper part represents the usual picture from a fluorescent zinc sulfide screen. The lower part of Fig. 1 was, of course, not directly photographed by placing a sensitive film at the target, but rather a mirror with a hole for the passage of the electron beam was placed at 45° between target and thin film, so that a picture could be taken from the side through a glass window of the vacuum system.

EXPERIMENTAL PROOF THAT ELECTRONS TRANSFER LIGHT TO NONLUMINESCENT TARGET

The experiment shows that the electrons remain in the state of oscillation of light frequency ω picked up from the photon-electron interaction within the crystal. That the light spots on the nonluminescent alumina target are really due to the arriving electrons is demonstrated by the ability of a magnet of about 300 gauss to displace the spots or even make them disappear. Care was, of course, taken that the photon-electron interaction region was well shielded against this magnet.

TENTATIVE WAVE-MECHANICAL THEORY

WAVE EQUATION AND SOLUTION OF MODULATED ELECTRON. Free electrons are very often describable by classical models even when the limits of quantum theory (Heisenberg's Uncertainty principle) are far exceeded. In particular, the oscillation of a free electron in an electromagnetic wave field does fulfill a classical description which is usually used without restrictions, for example in plasma physics. The experiments reported in this paper show that a free electron passing through a light wave may possess under quantum conditions a state of internal oscillation which cannot be described point-mechanically. Point-mechanically one would expect that the electron would remain in such a state of oscillation only as long as it stays within the light beam and would then move unperturbed in a straight path in some direction determined by the

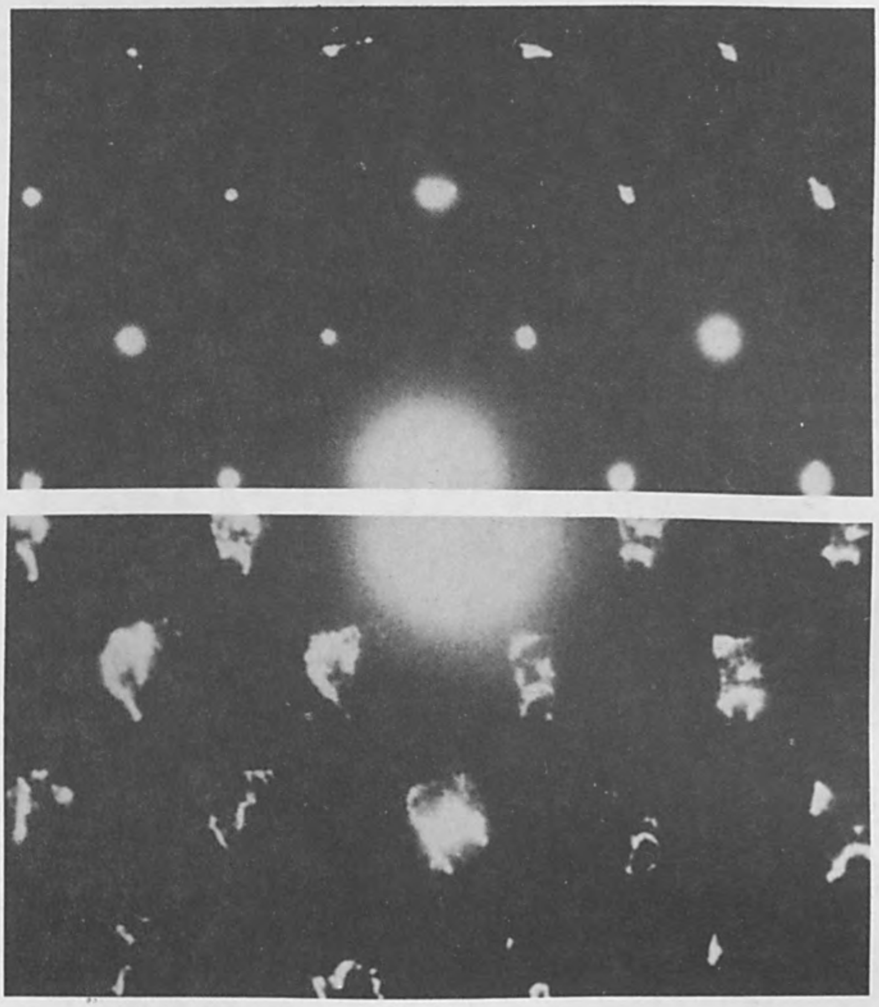

FIG. 1.—Diffraction pattern of 50-keV electrons crossing a 1300-Å-thick SiO_2 crystal. Top: luminescent screen; bottom: nonluminescent alumina when an argon laser beam passes the crystal perpendicularly to the electron beam.

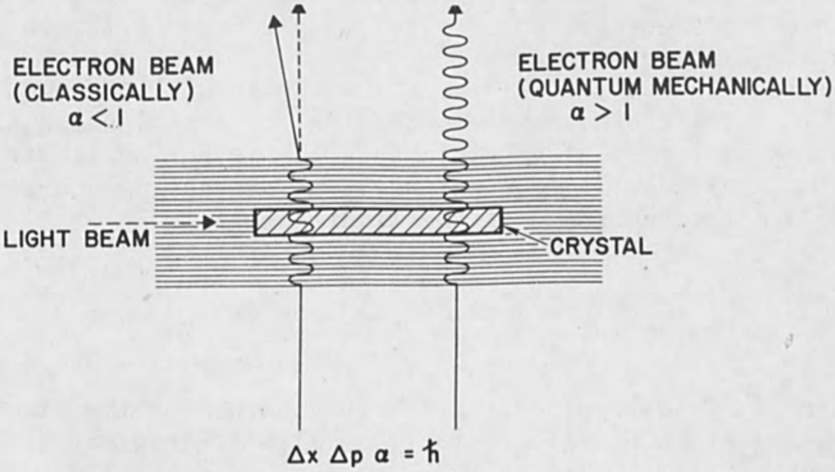
ELECTRON BEAM
(CLASSICALLY)
$\alpha < 1$
ELECTRON BEAM
(QUANTUM MECHANICALLY)
$\alpha > 1$
LIGHT BEAM
CRYSTAL
$\Delta x \, \Delta p \, \alpha = \hbar$

FIG. 2.—Interaction of a light wave beam penetrating along a sheet of SiO_2 and crossed by an electron beam in a classical ($\alpha > 1$) way; α is defined by Eq. (2).

phase and momentum vector at the point of exit (see left side of Fig. 2).

In an electromagnetic wave of maximum electric field strength E_0 and frequency ω, a point-mechanical description of acceleration $\ddot{x}$, velocity $\dot{x}$, and elongation x of an electron from a center at time t is given by

$$\dot{x} = -\frac{e}{m}\,\frac{E_0}{\omega}\cos\omega t\ ;\ x = -\frac{e}{m}\,\frac{E_0}{\omega^2}\sin\omega t \qquad (1)$$

where e is the charge and m is the mass of the electron. This classical description should not hold if $\Delta x = |x_{max}| = (e/m)E_0/\omega^2$ and $\Delta p = |m\dot{x}_{max}| = eE_0/\omega$ lead to $\Delta x\,\Delta p < \hbar$. One can introduce a parameter α into the Heisenberg relation as follows:

$$\Delta x\ \Delta p\ \alpha = \hbar \qquad (2)$$

where α then serves as a criterion as to whether a classical description $(\alpha < 1)$ or a wave-mechanical model $(\alpha > 1)$ should be applied. Using (1) and (2), we find:

$$\alpha = 3.72 \times 10^{-31}\ \omega^3/E_0^2 \qquad (3)$$

For a classical description $(\alpha < 1)$, E_0 must be larger than 1.46×10^8 V/cm for the frequency ω of the blue argon laser line. However, the classical description is also applicable for results observed at much lower field strength as it is well known from the plasma physical description of the inverse bremsstrahlung, from the observation of Thomson scattering in plasmas,[3] from propagation of waves,[4] etc. One consequence of a classical description is that the electron is driven by the electromagnetic field only as long as the field is acting. If an electron beam (Fig. 2) crosses a light beam, the electron oscillates inside the beam and gets a final velocity which generally leads to a change of its original direction; however, no oscillation can occur after the electron beam leaves the light beam.

Our experimental data yield for α a value much larger than 1 $(\alpha \simeq 4 \times 10^6)$. Therefore, a wave-mechanical treatment seems in order. The description of the electron state by a wave function starts from the Hamiltonian H_{int} of the electron and uses an interaction operator[5] simplified to only one frequency ω of the light:

$$H_{int} = q^* q 2\omega^2 \beta = \epsilon_L \cos^2\omega t \qquad (4)$$

where the factor β determines the energy absorbed by the electron, and ϵ_L is the interaction energy of electrons with light given by:

$$\varepsilon_L = n\hbar\, \omega_p^2/(\omega|\tilde{n}|) \tag{5}$$

Use was also made of the known interaction of light with a plasma[6] by introducing the plasma frequency ω_p and the complex refractive index $\tilde{n}$ as it is also analogously[7] applicable for 50-keV electrons in solids. An approximate solution of the wave equation for the electrons as given by

$$\left(-\frac{\hbar^2}{2m}\nabla^2 + \varepsilon_L \cos^2 \omega t\right)\Psi = i\hbar\frac{\partial\Psi}{\partial t} \tag{6}$$

is then

$$\Psi = A \exp\left\{\frac{i}{\hbar}\left[\vec{r}\cdot\vec{p} - (\varepsilon_e + \frac{1}{2}\varepsilon_L)t - \frac{\varepsilon_L}{4\omega}\sin^2 \omega t\right]\right\} \tag{7}$$

showing a modulation of the electron wave at the frequency of the light.

The wave function (7) indicates with its factor

$$\left(\exp\ -\frac{i}{\hbar}\ \frac{\varepsilon_L}{4\omega}\ \sin 2\omega t\right)$$

a phase factor which is also modulated; but for interaction durations $t > (2\omega)^{-1}$ this can be neglected, which is the case in our experiments. Though ε_L is smaller than ε_0 by many orders of magnitude, the bremsstrahlung process of the electrons in the alumina somehow reproduces the light frequency.

DAMPING TIME OF OSCILLATION STATE. The following simple calculation shows that the damping of the oscillations picked up by the electrons is sufficiently slow, so that the state of oscillation of the electrons at the frequency of light is still of high enough energy to cause an emission of radiation at the target. The intensity of dipole radiation of the electron after leaving the light beam is $S = e^4E_0^2/(3c^3m^2)$. The time t^* until the oscillation energy $\varepsilon_0 = e^2E_0^2/(m\omega^2)$ of the electron drops down to 1/e is

$$t^* = \varepsilon_0/S = 3\,c^3 m/(e\omega)^2 \tag{8}$$

We get for the argon laser radiation $t^* = 2.14 \times 10^{-8}$ sec. The time of flight for the electrons to travel the 25 cm from the material sheet to the nonluminescent alumina target is 1.9×10^{-9} sec, which is an order of magnitude shorter than t^* .

ESTIMATE OF INTENSITY OF LIGHT RADIATION CARRIED BY THE ELECTRONS

The oscillation picked up by the electrons acquires approximately the same frequency ω due to collective effects[7] in the sheet, similar to the Thomson scattering in a plasma.[3] The number of photons transported by the electrons can be calculated from (5), taking into account that a few microamperes of electron current constitute a number of electrons large enough to account for the visibility of the spots on the nonluminescent screen. The observed light intensity from the alumina is in rough agreement.

We should like to point out that the theory outlined here has not been confirmed experimentally in all aspects, but that the effect has consistently been observed. More experimental data are needed in order to verify and refine the theory. Different materials should be used and the geometrical and electrical data must be varied.

Preliminary experiments have shown already that slowing down the electrons and increasing correspondingly their number resulted in a substantial decrease of light intensity on the alumina target, whereas the light from the fluorescent screen did not show much decrease in over-all intensity.

It should be mentioned that in the theory of the diffraction of an electron beam by a standing light wave (the Kapitza-Dirac effect[9]), a point-mechanical approach was sufficient to describe the stimulated Thomson scattering. A detailed interpretation of the measurements[10,11] was discussed, taking into account the quantum-mechanical properties of the electrons.[11]

REFERENCES

1. H. Schwarz, Bull. Am. Phys. Soc. 13: 897, 1968.

2. Suggested by W. C. Wang and D. B. Scarl of Polytechnic Institute of Brooklyn, New York, after a colloquium of one of the authors (H. Schwarz) at the Polytechnic Institute of Brooklyn, 9 January, 1969.

3. E. Fünfer, B. Kronast, and H. J. Kunze, Phys. Letters 5: 125, 1963.

4. L. Brillouin, Wave Propagation and Group Velocity, New York: Academic Press, 1960.

5. W. Heitler, The Quantum Theory of Radiation, Oxford University Press, 1966.

6. H. Hora, Phys. Fluids 12: 182, 1969.

7. D. Pines and D. Bohm, Phys. Rev. 85: 338, 1952.

8. H. Hora, Optik 17: 409, 1960.

9. P. L. Kapitza and P. A. M. Dirac, Proc. Cambridge Phil. Soc. 29: 297, 1933.

10. H. Schwarz, H. A. Tourtellotte, and W. W. Gaertner, Phys. Letters 19: 202, 1965; IEEE J. of Quantum Electronics QE-2: 297, 1966.

11. H. Schwarz, Z. Physik 204: 276, 1967.

FEEDBACK CONTROL OF HIGH INTENSITY TRIODE GUNS

Ernö Fóti

Central Research Institute for Physics, Hungarian Academy of Sciences, Budapest

Triode guns are generally used for low-power purposes, though their optical properties allow them to be applied advantageously even in electron beam (EB) machines of medium power, e.g., in EB welding machines of 3-5 kW power like those developed in our laboratories for the instruments industry,[1] where these guns have an extra advantage: good controllability. To make proper use of this advantage of triode guns needs a thorough study of their feedback control properties and behavior as outlined below.

DEFINING CONTROL CRITERIA

An accuracy criterion involving not only process variables but also material properties of the part to be welded is best defined by starting from the heating effect of the beam scanning on the surface of a semi-infinite solid at a constant velocity v along the x axis (Fig. 1). Supposing that the impact surface of the beam constitutes a heat source made up of point sources of strength

$$q = U_a j(r) r \, dr \, d\theta$$

having a gaussian distribution on account of the presumed gaussian distribution of current density

$$j(r) = j_{max} \exp[-(r/r_n)^2]$$

and from the well-known relation

$$T = e^{-v/2\alpha} \varphi(\xi, y, z)$$

which is a solution of the differential equation describing conduction of heat in the quasi-stationary state,[2] where in this case

$$\varphi(\xi, I, z) = \frac{q}{2\lambda R} \exp[-(v/2\alpha)(\xi + R)]$$

the temperature generated by a point source in point P at a distance R from the center of the spot is found by the function

$$\delta T = \frac{U_a j(r) \, dr \, d\theta}{2\pi\lambda u} \exp[-(v/2\alpha)(\xi + R)]$$

Record of 10th Symposium on Electron, Ion, and Laser Beam Technology (L. Marton, ed.); San Francisco Press, Inc.

Copyright © by The Institute of Electrical and Electronics Engineers, Inc.—Printed in the U.S.A.

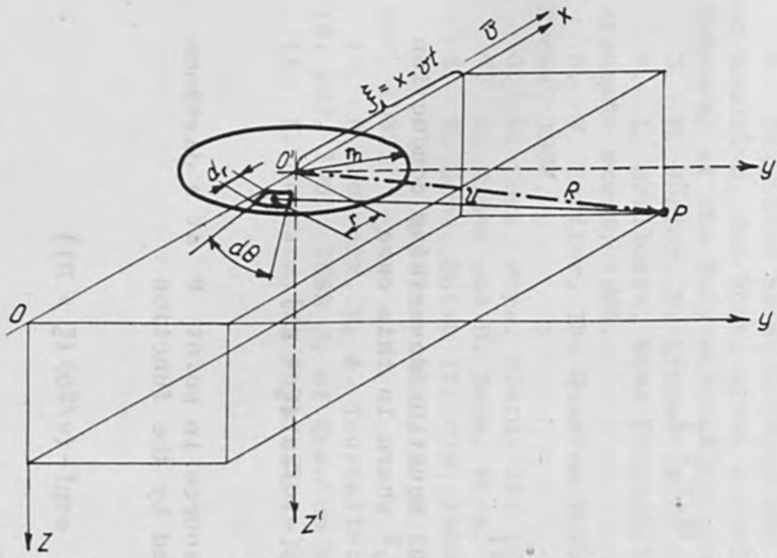
x
$\vec{v}$
$\xi = x - vt$
O'
m
d_r
R
u
P
y'
$d\theta$
r
O
y
Z'
Z

FIG. 1.—Explanation of symbols used in computing control criteria.

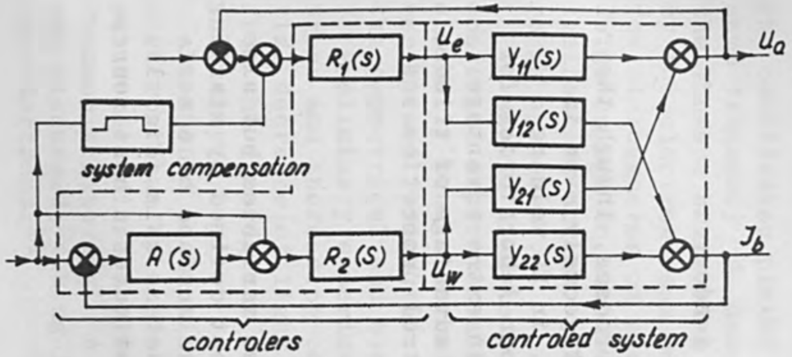
system compensation
$R_1(S)$
U_e
$Y_{11}(S)$
$Y_{12}(S)$
$Y_{21}(S)$
$Y_{22}(S)$
U_a
$A(S)$
$R_2(S)$
U_W
J_b
controlers
controled system

FIG. 2.—Model of the triode-gun control system.

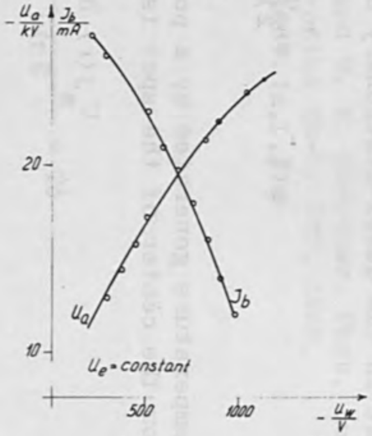

FIG. 3.—Typical static characteristics of a controlled system with magnetic amplifiers.

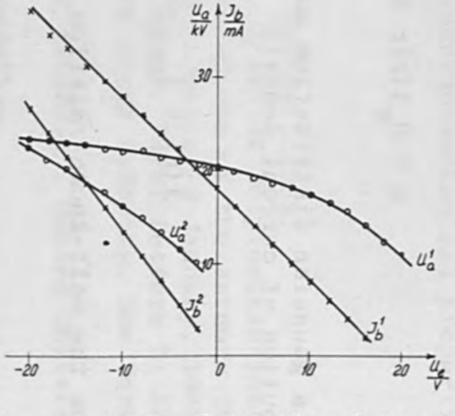

FIG. 4.—Typical static characteristics of a controlled system with magnetic amplifiers (superscript 1) and thyristor power controllers (2).

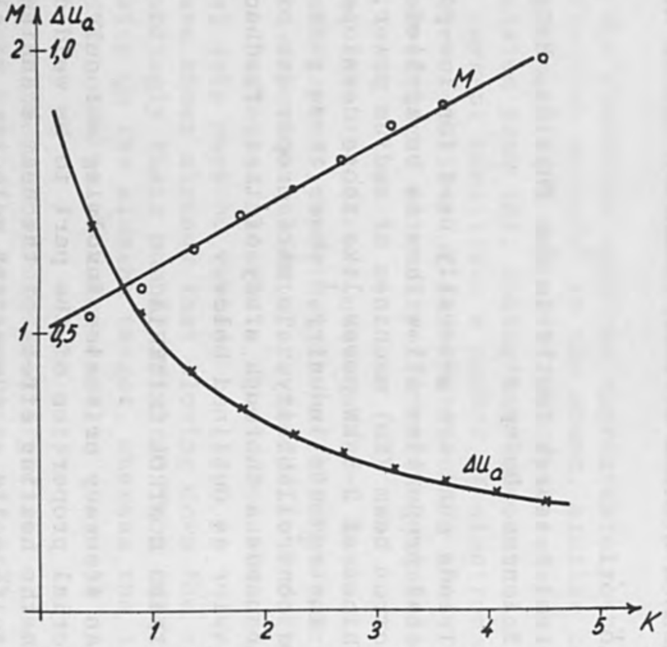

FIG. 5.—Relative steady-state error ΔU_a and overshot of U_a as a function of loop gain when R_1 is purely proportional.

where U_a is acceleration voltage, λ the thermal conductivity and α the thermal diffusivity of the material. Integrating over $0 \leq r \leq r_n$ and $0 \leq \theta \leq 2\pi$, the temperature at point P

$$T = c \, \frac{U_a \cdot I_b}{R} \, e^{-(v/2\alpha)R}$$

provided that $r_n \ll R$, i.e., $R \approx u$ for all point sources and $\xi' = 0$, that is the point P is in the y', z' plane of the coordinate system moving with the beam.

Any small change of the process variables U_a, I_b, and v cause a large change of temperature

$$\Delta T = \frac{\partial T}{\partial U_a} \Delta U_a + \frac{\partial T}{\partial I_b} \Delta I_b + \frac{\partial T}{\partial v} \Delta v$$

Computing the partial derivatives and introducing constants which express relative changes of the respective variables, we obtain

$$k_T = k_{U_a} + k_{I_b} + \frac{vR}{2\alpha} k_v$$

in the pessimistic case.

Since we are now interested in the control of the gun only (that is why we have excluded r_n from our computation) and the term expressing the effect of velocity changes is small (generally of the order of 10^{-3}), the accuracy criterion may be defined by the requirement that the sum of the relative changes of I_b and U_a, or for large signals the relative change of beam power P, must not be greater than the relative change of temperature allowed at a reasonable distance from the weld seam.

As to the dynamic properties we might require that transient overshots do not exceed the steady-state accuracy limit.

MODEL OF THE CONTROLLED SYSTEM

When I_b and U_a are the controlled variables or we take beam power as indirectly controlled variable, the controlled system should contain the high-voltage rectifier, the power amplifier on the primary side of the rectifier (which might be magnetic amplifiers, thyristor power controllers, or any other suitable power elements), and the electron gun. Then the manipulated variables are the input of the primary power element U_e (which is generally a voltage) and the Wehnelt voltage U_W.

In operating an EB machine with a triode gun, usually the acceleration voltage is constantly switched on and the beam current (frequently pulsed) is generated by a signal that controls U_W, so that this part of the system must be of a follower type and the whole system may be represented by the block diagram shown in Fig. 2 (a two-variable canonical representation).

The static characteristics describing the dependence of the controlled variables on each of the manipulated variables while the other is constant are almost linear or can be piecewise linearized as shown by the typical characteristics given in Figs. 3 and 4.

A series of measurements carried out on several machines prove that the dynamic properties of the controlled system are rather uniform. The transfer functions were determined from measured time responses. Y_{11} and Y_{12} might be regarded as critically damped second-order lag (at any rate that should be the aim of proper high-voltage power-supply design) and the transfer functions Y_{21} and Y_{22} in turn best approach first-order lags. The time constants in these functions are generally found to coincide within 10-15 per cent so for a general investigation all time constants of the controlled system may be taken as equal, T_s, and its dynamic properties may be described therefore by the transfer matrix

$$\overline{\overline{y}} = \begin{vmatrix} -\dfrac{A_{s11}}{(1 + sT_s)^2} & -\dfrac{A_{s12}}{(1 + sT_s)^2} \\ \\ -\dfrac{A_{s21}}{1 + sT_s} & \dfrac{A_{s22}}{1 + sT_s} \end{vmatrix} .$$

CHOICE OF CONTROLLERS

The R_1 controller cannot be a simple proportional controller because it would always give either a greater steady-state error or a greater transient overshoot than the permissible static accuracy (about 3 per cent as seen from Fig. 5) gotten from analog-computer simulation. Since an integrating (lag) compensation results in a slower operation and the high-voltage loop is the slower of the two control circuits, R_1 must be a PID/proportional-integrating-differentiating = lag-lead) controller with the transfer function

$$R_1(s) = A_{R1}\left(1 + \frac{1}{sT_{i1}} + \frac{sT_D}{1 + sT_1}\right)$$

The beam-current control loop is much faster and R_2 therefore may be a proportional integrating (lag) controller, its transfer function being

$$R_2(s) = A_{R2}\left(1 + \frac{1}{sT_{i2}}\right)$$

whereas A has the character of an amplifier, that is

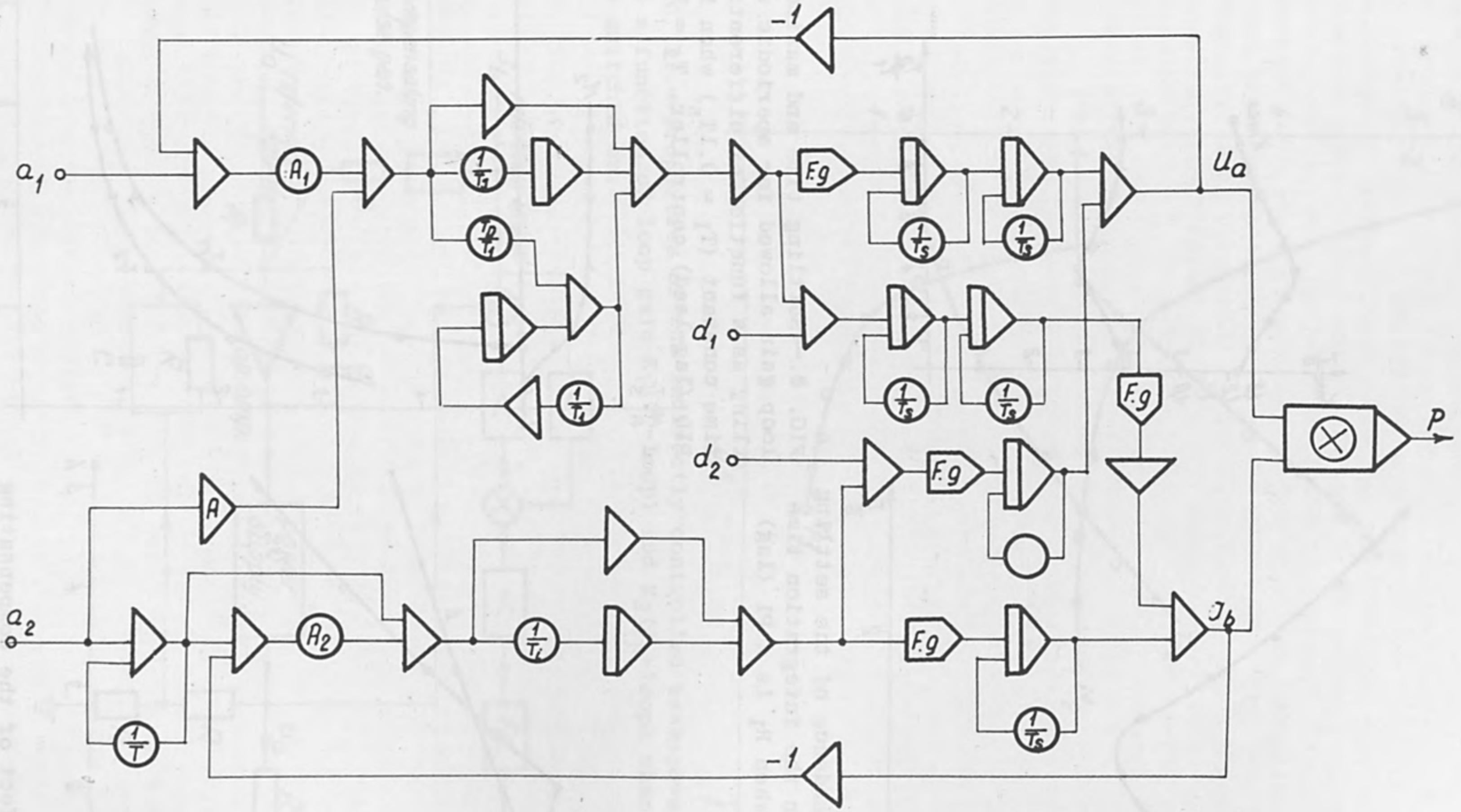
-1
a1
A1
$\frac{1}{T_1}$
$\frac{T_2}{T_1}$
$\frac{1}{T_4}$
F.g
$\frac{1}{T_s}$
Ua
d1
d2
P
A
a2
$\frac{1}{T}$
A2
$\frac{1}{T_i}$
Jb
-1

FIG. 6.—Analog computer program of the model shown in Fig. 2.

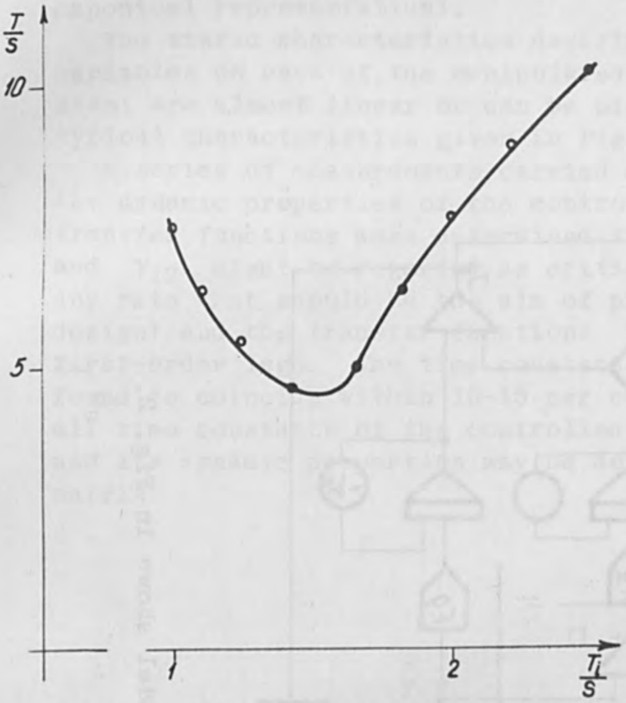

FIG. 7.—Dependence of the settling time of U_a on the integration time constant T_i when R_1 is a PI (lag) controller.

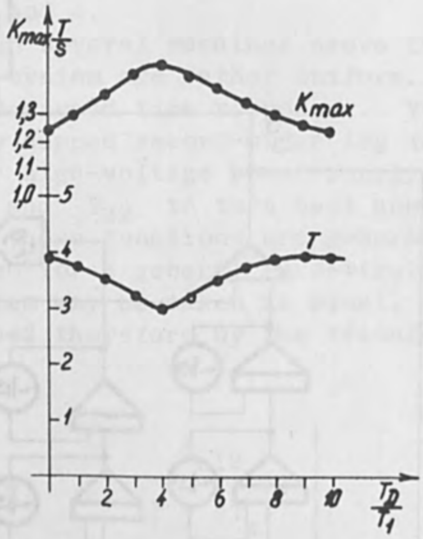

FIG. 8.—Settling time and maximum loop gain allowed for aperiodic settling as a function of differentiating time constant ($T_1 = 0.1T_s$) when R_1 is a PID (lag-lead) controller, $T_i = 1.5T_s$.

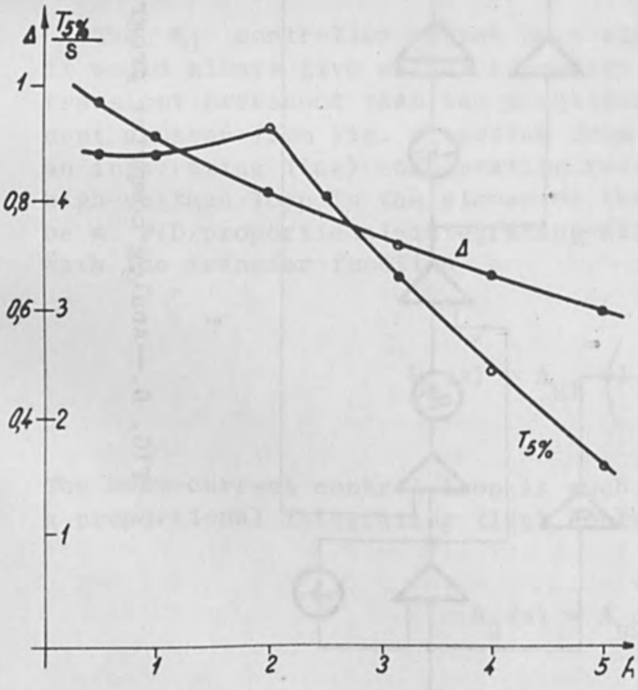

FIG. 9.—Effect of the compensating amplifier A (Fig. 6.) as a function of its gain.

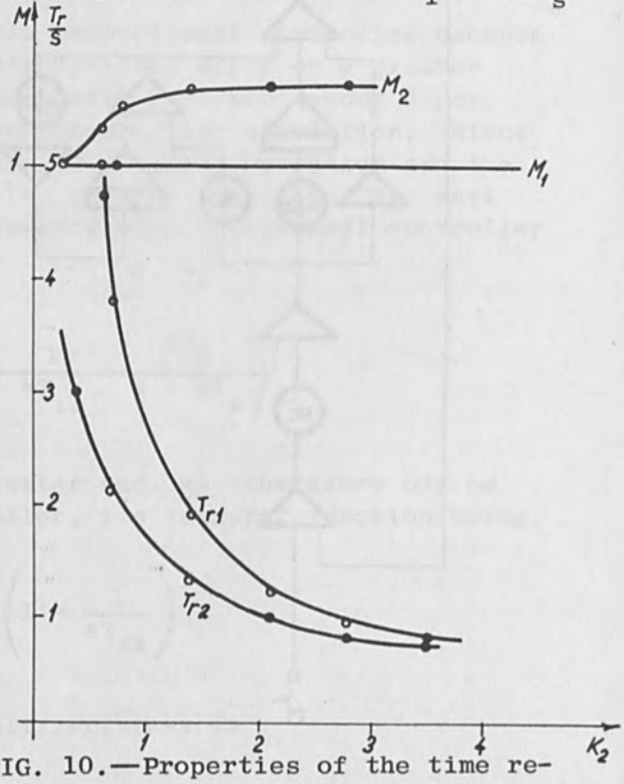

FIG. 10.—Properties of the time response of I_b to a_2 when the loop stands along (subscript 1) and is interconnected with the U_a control-loop (2).

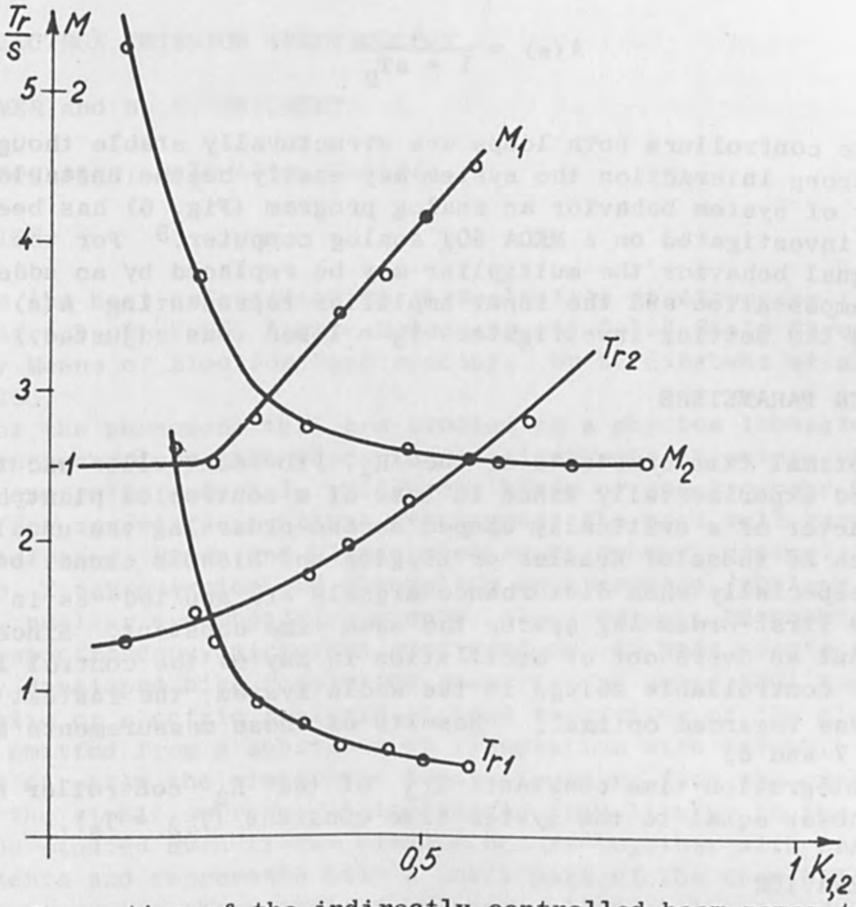

FIG. 11.—Properties of the indirectly controlled beam-power time response as a function of loop gain K_1 (U_a-loop) and K_2 (I_b-loop) when beam current is switched on.

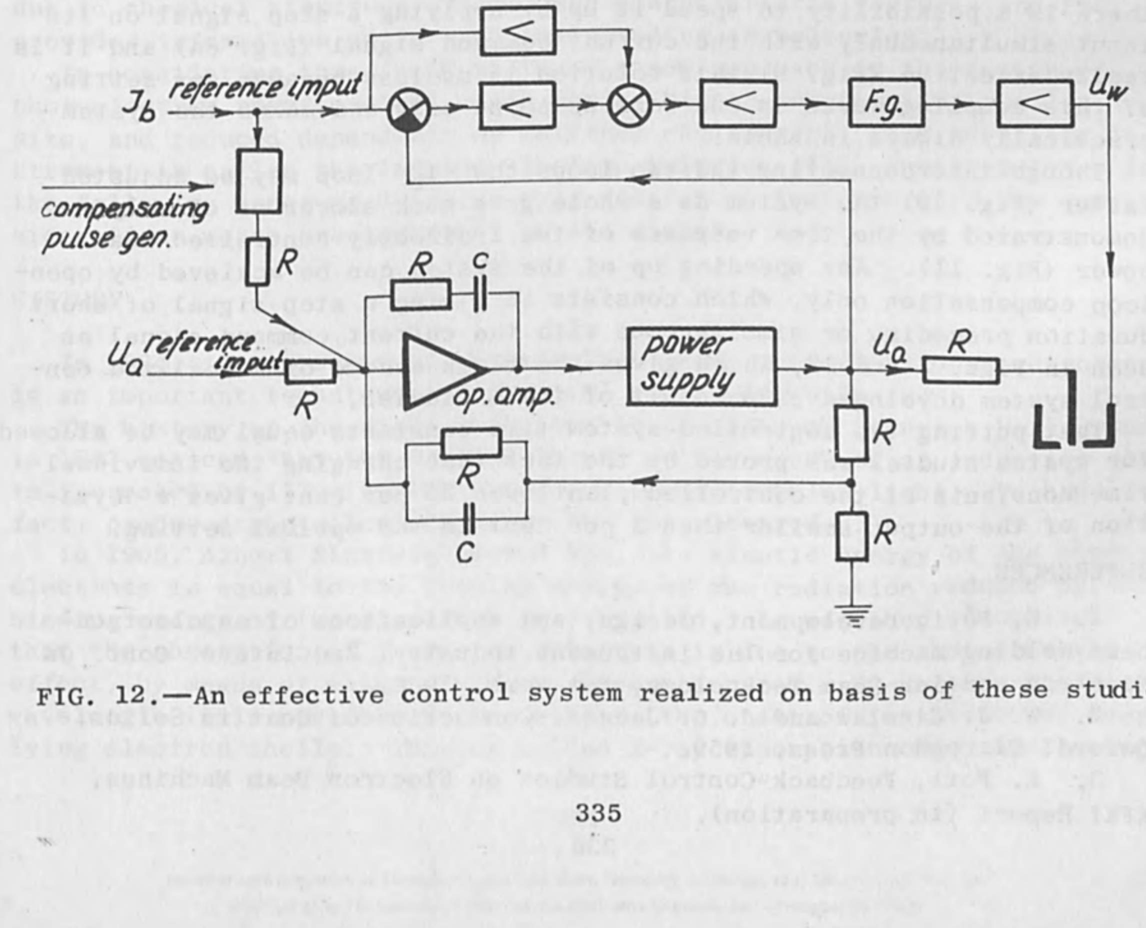

J_b
reference impput
<
<
<
F.g.
<
U_w
compensating
pulse gen.
R
R
C
U_a reference impput
R
op.amp.
power supply
U_a
R
R
R
C
R
R

FIG. 12.—An effective control system realized on basis of these studies.

$$A(s) = \frac{A}{1 + sT_2}$$

With these controllers both loops are structurally stable though because of the strong interaction the system may easily become unstable. For the study of system behavior an analog program (Fig. 6) has been developed and investigated on a MEDA 80T analog computer.[3] For the study of small-signal behavior the multiplier may be replaced by an adder and system compensation and the input amplifier representing A(s) left out. (In the setting investigated $T_s = 1$ sec was adjusted.)

CONTROLLER PARAMETERS

The optimal time constants of the R_1, PID controller had to be determined experimentally since in case of a controlled plant having the character of a critically damped second-order lag the usual tuning rules such as those of Kessler or Ziegler and Nichols cannot be directly applied especially when disturbance signals are applied--as in this case--through a first-order lag having the same time constant. Since try runs showed that an overshoot or oscillation in any of the control loops results in barely controllable swings in the whole system, the fastest aperiodic setting was regarded optimal. Results of these measurements are given in Figs. 7 and 8.

The integration time constant T_{i2} of the R_2 controller may be simply chosen equal to the system time constant ($T_{i2} = T_s$).

SYSTEM BEHAVIOR

As seen from Fig. 8 the high-voltage control loop is rather slow and settling time is 3-4 times as great as the system time constant. Though there is a possibility to speed it up by applying a step signal on its input simultaneously with the current command signal (Fig. 6a) and it is really effective (Fig. 9) this solution is useless because any setting of this coupling works in one working point only and makes the system practically always instable.

Though interconnecting the two loops the I_b loop may be adjusted faster (Fig. 10) the system as a whole gets much slower as clearly demonstrated by the time response of the indirectly controlled beam power (Fig. 11). Any speeding up of the system can be achieved by open-loop compensation only, which consists in giving a step signal of short duration preceding or simultaneous with the current command signal as seen in Figs. 2 and 12, which gives the block scheme of a realized control system developed as a result of these studies.

That putting the controlled system time constants equal may be allowed for system studies was proved by the fact that changing the individual time constants of the controlled plant over 25 per cent gives a deviation of the output smaller than 1 per cent in the optimal setting.

REFERENCES

1. E. Fóti, Development, design, and applications of an electron-beam welding machine for the instrument industry, 2nd Intern. Conf. on Electron and Ion Beam Technology, New York, 1966.

2. W. J. Carslaw and J. C. Jaeger, Conduction of Heat in Solids, Oxford: Clarendon Press, 1959.

3. E. Fóti, Feedback Control Studies on Electron Beam Machines, KFKI Report (in preparation).

INDUCED ELECTRON EMISSION SPECTROSCOPY

J. C. HELMER and N. H. WEICHERT

Varian Associates, Palo Alto, Calif.

INTRODUCTION

Perhaps the best orientation to photoelectron spectroscopy is the first paragraph of "ESCA, Atomic Molecular and Solid State Structure Studied by Means of Electron Spectroscopy," by K. Siegbahn et al., Uppsala, 1967:

"Most of the phenomena that are studied in a physics laboratory and utilized in technology take place in the electronic structure of atoms, molecules and solid material. Different kinds of spectroscopy have been developed for investigating these structures; the most well known being optical, infrared, Raman and ultraviolet spectroscopy, optical rotational dispersion, X-ray emission and absorption spectroscopy, nuclear magnetic resonance, nuclear quadrupole resonance, electron spin resonance, Mössbauer spectroscopy, microwave spectroscopy and mass spectroscopy. A recently developed high resolution spectroscopy named ESCA is based on a magnetic or electric analysis at high resolution of the electrons which are emitted from a substance on irradiation with X-rays. ESCA reproduces directly the electronic level structure from the innermost shells to the atomic surface. All elements from lithium to the heaviest ones can be studied even if the element occurs together with several other elements and represents only a small part of the chemical compound. This spectroscopy is characterized by sharp electron lines and by a high sensitivity. The precision has been brought to the limit set by the inherent widths of the atomic levels themselves. Shifts of inner levels due to chemical structure effects are characteristic features and ESCA provides information on the chemical bonding in molecules."

In considering this field we found a new approach to the design of photoelectron spectrometers which yields higher sensitivity, smaller size, and reduced dependence on external environment. The resulting instrument is called the Induced Electron Emission (IEE) Spectrometer. In the following paper we describe this instrument together with the considerations which are important to its design.

HISTORY

In 1964, it was shown at Uppsala that X-ray photoelectron spectroscopy is an important technique for chemical structure analysis.

The history of the field goes back to the time of Heinrich Hertz, who in 1887 noticed that the maximum length of the spark of an induction coil is increased by illuminating the gap with ultraviolet light. He had, in fact, produced photoelectrons from the gap electrodes.

In 1905, Albert Einstein showed that the kinetic energy of the photoelectrons is equal to the quantum energy of the radiation reduced by the binding energy of the electrons in the solid. It was then recognized that the absorption of X rays in materials is due to the photoelectric effect, by means of which the atoms become ionized. By varying the X-ray wavelength it is possible to investigate the onset of ionization of deep-lying electron shells. This is called X-ray absorption-edge spectroscopy.

Record of 10th Symposium on Electron, Ion, and Laser Beam Technology (L. Marton, ed.); San Francisco Press, Inc.

Copyright © by The Institute of Electrical and Electronics Engineers, Inc.—Printed in the U.S.A.

In 1920, J. Bergengren discovered that the positions of X-ray absorption-edges depend slightly on the types of bonding or valence states of the atoms of the material. This effect was subsequently explained by L. Pauling in 1929 as being due to the charges appearing on atoms from ionic bonding. For example, in the salt NaCl the sodium atom has a positive charge, whereas the chlorine atom has a negative charge. These charges produce electric fields which modify the binding energies of the electrons.

It is clear that one can look either at the absorption of X rays in the direction of the X-ray beam, or at photoelectrons ejected at right angles to the X-ray beam. In the early days, however, electron spectroscopy was not capable of the same resolution as X-ray spectroscopy. In recent years, the group at Uppsala has developed an electron spectrometer whose resolution equals or exceeds that obtained in X-ray spectroscopy, and this development has given rise to the work of which we now speak. In fact, the analysis of photoelectron energies now enables us to measure the binding energies of electrons with a precision that is much higher than could ever have been achieved by the X-ray method. Fantastic resolution has been obtained by D. W. Turner in England, using an ultraviolet light source, in measuring the binding energies of molecular orbital electrons in gas phase molecules by means of photoelectron spectroscopy. In some sense, we are now in communion with Heinrich Hertz.

IEE SPECTROMETER

Being electrostatic, the IEE Spectrometer is shielded by a double layer of mu-metal so that it is not sensitive to the common laboratory environment. The shield is about 1 ft in diameter and 4 ft high. The IEE Spectrometer is operated by, and the data processed by a 620/i Computer. The data and control system is shown in Fig. 1. The analyzer is derived from the rotational-spherical condenser of Purcell. This figure of rotation provides a very large solid angle of acceptance.

Figure 2 shows a schematic of the analyzer itself. Other features which give rise to improved operation are:

(1) The employment of electron retardation between the sample and the spectrometer.

(2) The use of annular slits giving rise to a high source area.

(3) The employment of focus electrodes to adjust the optical axis of the system.

(4) The employment of a filter in front of the electron multiplier of the system.

(5) The ability to vary the analyzer line width electronically from 1.0 to 0.2 eV by changing the energy at which the electrons are analyzed. Normally the energy of analysis is held fixed while the spectrum is swept by applying a voltage to the sample.

The sample is inserted through a vacuum lock and its temperature may be varied by hot or cold gas flowing in the interior of the sample holder. Most commonly, the sample is a solid thin film or a powder. A cylindrical surface is especially convenient for mounting films and powders. However, flat samples can be used as well. Very often the compound of interest is powdered and brushed on the surface of cellophane tape wrapped around the sample holder with the sticky side outwards.

The sample sits in a chamber with thin aluminum walls. Soft X rays from an aluminum X-ray tube pass through the walls and irradiate the

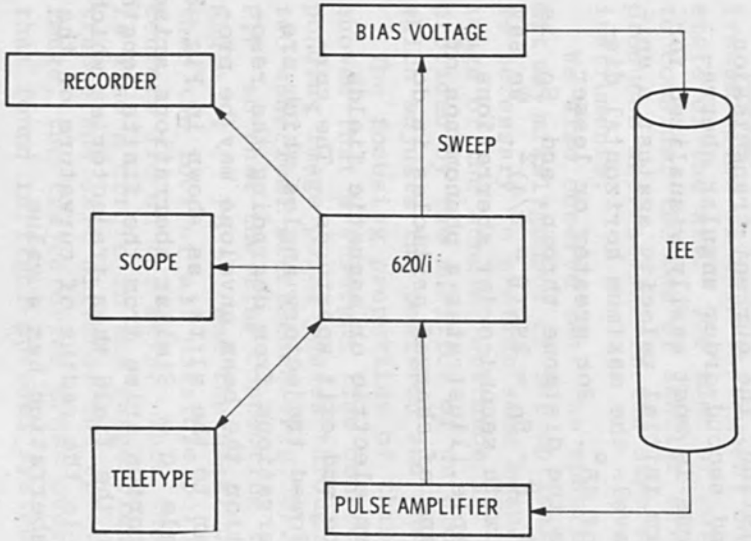
RECORDER
BIAS VOLTAGE
SWEEP
SCOPE
620/i
IEE
TELETYPE
PULSE AMPLIFIER

FIG. 1.—Data and control system.

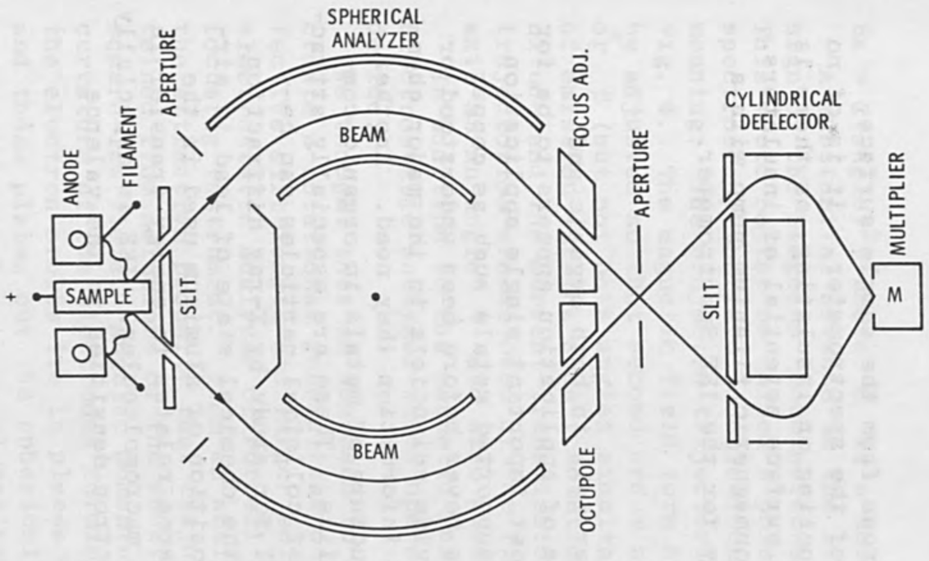
SPHERICAL ANALYZER
APERTURE
FILAMENT
ANODE
SAMPLE
+
SLIT
BEAM
BEAM
FOCUS ADJ.
OCTUPOLE
APERTURE
CYLINDRICAL DEFLECTOR
SLIT
MULTIPLIER
M

FIG. 2.—Analyzer schematic.

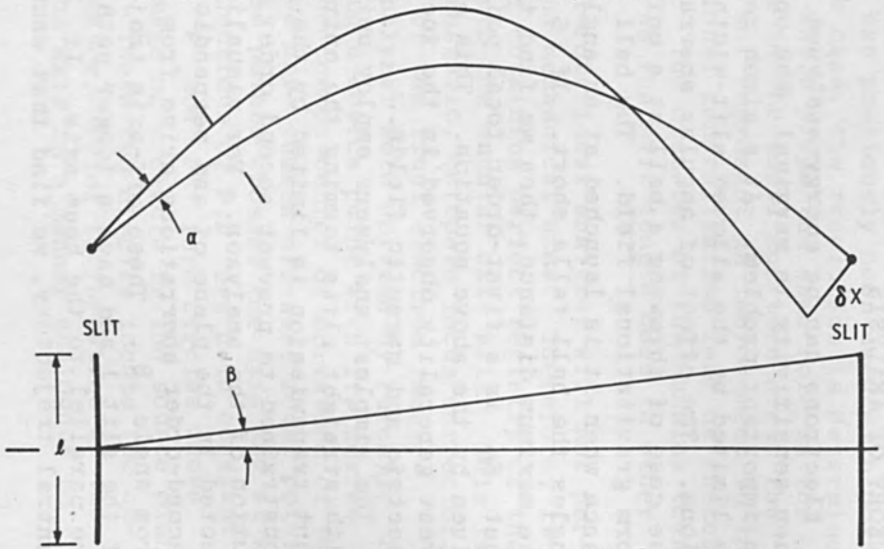
α
SLIT
δx
SLIT
ℓ
β

FIG. 3.—Aberration angles for simple analyzer.

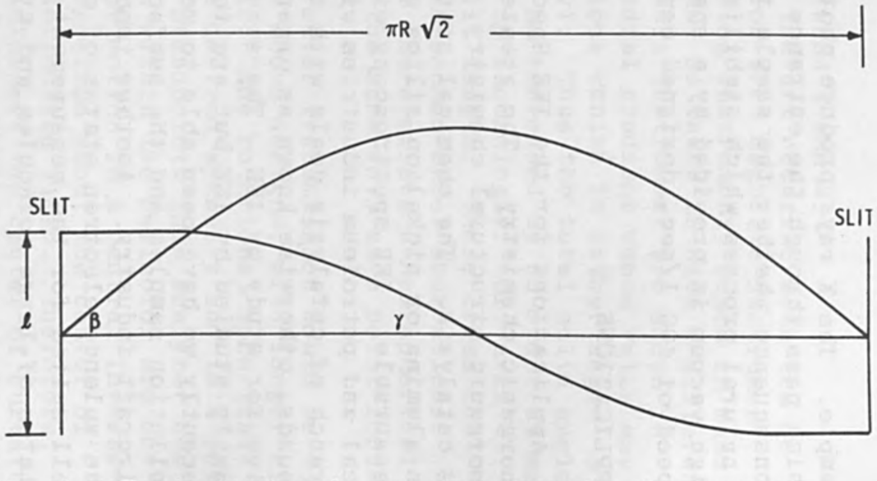
πR √2
SLIT
SLIT
ℓ
β
γ

FIG. 4.—Trajectories in a point-focusing instrument.

sample. The X rays produce photoelectrons from the sample surface, which pass through the entrance slits of the spectrometer. It is of no consequence whether the sample is conducting or insulating, as there is a natural process which stabilizes the surface potential of insulators. High vacuum is provided by a special nonmagnetic titanium pump with a speed of 400 l/sec, designed especially for the IEE Spectrometer.

APPLICATIONS

Applications for the IEE Spectrometer fall in both organic and inorganic chemistry. The greatest area of application appears to be for inorganic structural chemistry. The most important single application is catalysis. The chemical states of supported metals such as copper on alumina or nickel on silica gel have never before been understood or measurable. IEE spectroscopy will provide scientists in the major chemical and petroleum industries with the information they need. Another branch of catalysis deals with the structure of metals in organic compounds, otherwise known as organometallics. These are especially attractive for study by IEE. The structure of colloidal particles can be easily studied by IEE but are too small for study by X-ray diffraction. Recently we have been able to measure the chemical state of lead in air-pollution samples and the surface composition of aluminum used in the aircraft industry. Another important area relates to energy transfer in the valence electron states of organic macromolecules. IEE is especially well suited for the measurement of electron densities in the valence states of large molecules and crystals.

THEORY OF ANALYSIS

Electrons can be energy-analyzed in electric and magnetic fields. When sensitivity is marginal, the optimum design of the analyzer becomes an important problem. At a given resolution, the current transmission is limited by the allowed slit-width and second-order angular aberrations. The effect of angular aberrations is most easily visualized for the case of throwing a ball at a uniform initial velocity against a uniform gravitational field. The ball travels the maximum horizontal distance when it is launched at an angle of 45°. For greater or lesser angles the ball falls short. If S is the distance thrown, and S_0 is the maximum distance, then we find that $S - S_0 = 2S_0(\theta - \pi/4)^2$. We say that S_0 is a first-order focal point with second-order aberrations given by the above equation. This example illustrates a phenomenon of great generality observed in the focusing of charged particles in dc electric and magnetic fields.

The simplest analyzers employ uniform electric or magnetic fields with straight slits forming the entrance and exit apertures. The current transmission is limited by the allowed trajectory angles which are constrained to prevent second order aberrations from degrading the resolution of the analyzer. For visualization the beam envelope may be projected in the plane of and perpendicular to the slits, as shown in Fig. 3. Second-order aberrations arise from angle α. Similar aberrations arise from angle β. These off-axis trajectories arise from the finite length of the slit l and have a longer path in the field than trajectories which are parallel to the beam axis. If R is the radius of curvature of the central trajectory, we find that each aberration has a value

$\delta x = C(\text{angle})^2$, where C is a number between 1 and 2.

A substantial advance in the state of the art occurred with the design of the Siegbahn "double-focusing" iron-free magnetic instrument. This would better be called a point-focusing instrument, since in mass spectroscopy the term "double-focusing" may be taken to have a different meaning. The projected trajectories of this instrument are shown in Fig. 4. The magnetic field form has a radial gradient whose value may be adjusted so that second-order aberrations vanish in either angle α or β (but not both angles simultaneously). Thus the total solid angle of emission (at the same resolution) may be increased by an order of magnitude and the current transmission goes up accordingly. Off-axis trajectories are allowed by the finite slit length. These cross the axis at an angle γ and also give rise to second-order aberrations.

In addition to the magnetic instrument there exists a hemispherical electrostatic analyzer which operates in the same way, as a point-focusing device.

We thought that an approach to even greater transmission would be to create a rotational generalization of the above designs, with longer effective slit length and larger solid angle. The rotational-spherical electrostatic analyzer of Purcell has the desired symmetry and is a point focusing instrument. From an analytical standpoint, this analyzer has the attractive property that trajectories within the deflector are obtained from solutions of the equations for motion in a central inverse-square-law field. Angular momentum is preserved about the center of curvature of the electrodes forming the deflecting field. Therefore, the electron orbits lie in planes which intersect the center of curvature, and these planes cut the spherical electrodes in great circle paths.

The spherical-rotational analyzer has previously been used with point sources and point detectors. In this case, the resolution is determined by the size of the entrance aperture which plays the same role as the slit *width* in other analyzers. Owing to the small aperture area, the transmission of this instrument does not represent an improvement in the state of the art. The idea of rotational generalization lead us instead to consider the use of annular slits. The diameter of the annulus then produces aberrations in the same way as the slit *length* does in other instruments.

We also observe that the spherical-rotational analyzer will not permit any misalignment of the optical and mechanical axes. Therefore, it is necessary to provide some means of obtaining perfect registry of the image of the annular entrance slit onto the annular exit slit. This is provided by the addition of an electrostatic, octupole focus corrector, which adjusts the position and shape of the final electron image.

The focusing properties of this analyzer were derived by Purcell. He showed that a straight line connecting a source point with its corresponding image point passes through the common center of curvature of the two spherical electrodes (Fig. 5). We have chosen off-axis focal points P, P' so that the line connecting these points crosses the axis and at an angle Φ. If Φ and the axial projections of P, P' are held constant then the loci of all possible points P and P' form circles whose centers lie on the axis. Thus the image of a circle in the source plane is also a circle in the image plane. These two circles locate the entrance and exit slits of the spectrometer. Prior to formation of the image, the trajectories cross over the axis in a manner analogous to that found in light-optical systems.

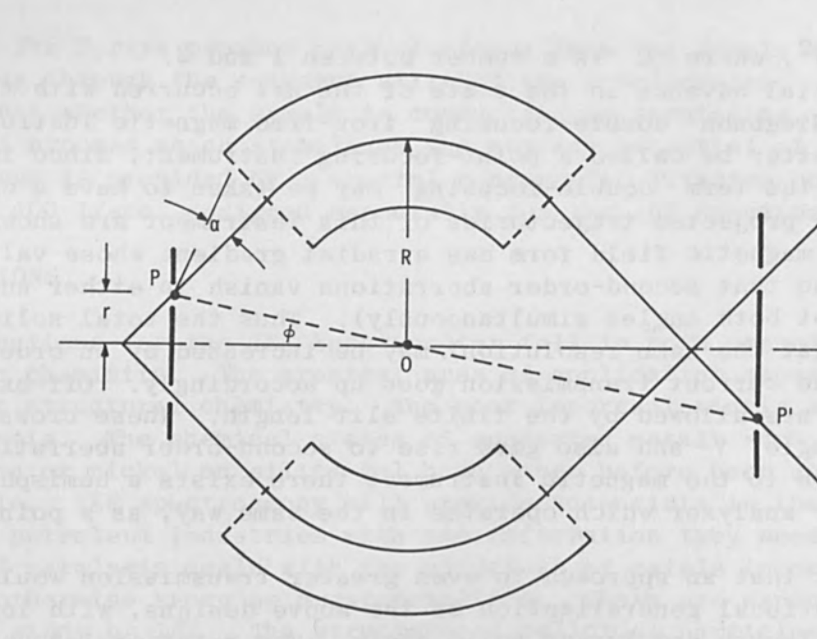

FIG. 5.—Focal-point construction with annular slits.

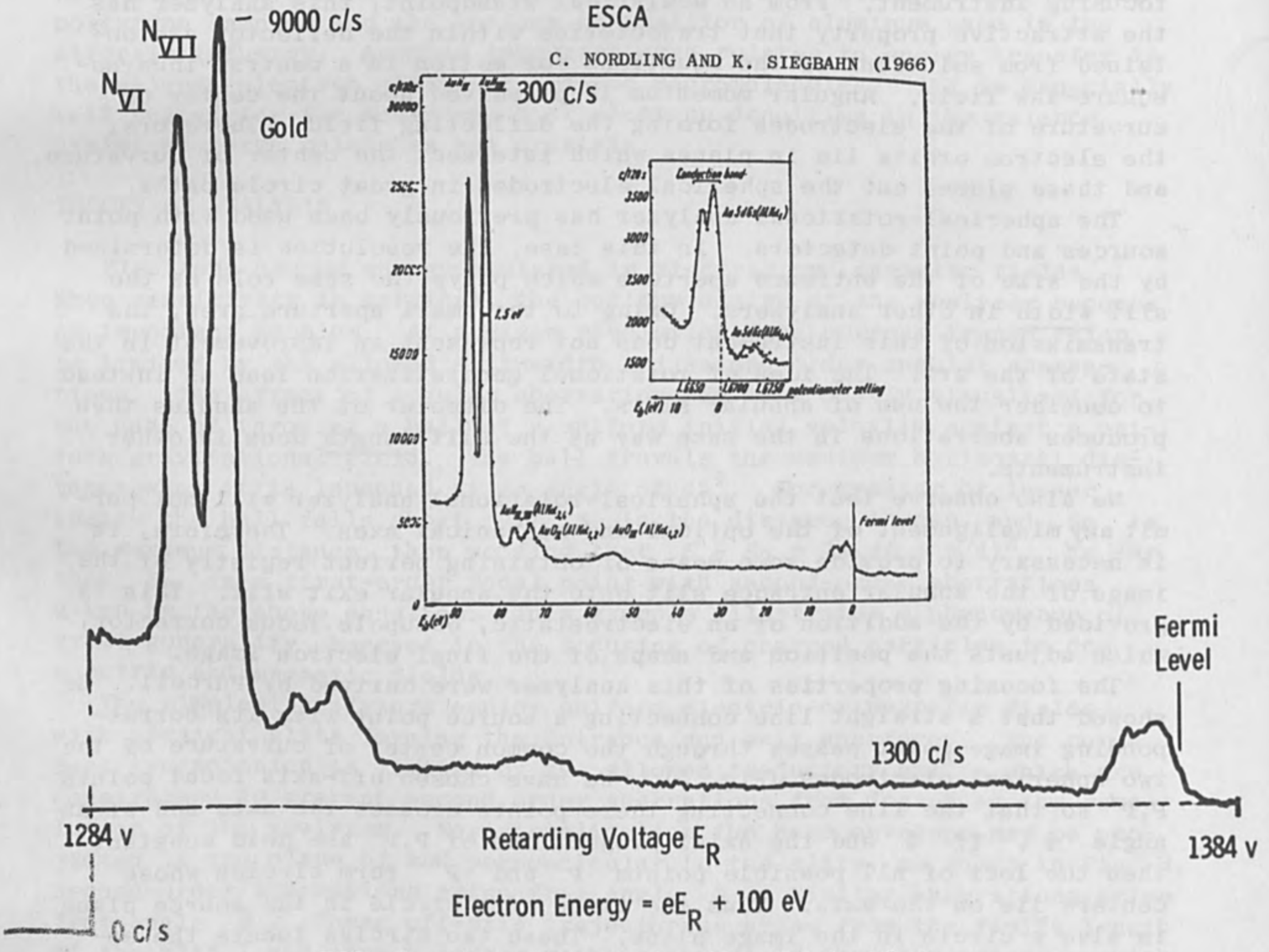

FIG. 6.—Spectrum of the 4f gold doublet.

Our configuration is shown in Fig. 2. Electrons from an annular filament strike the anode of an annular X-ray tube, creating aluminum Kα fluorescence X radiation at a photon energy of 1486 eV. The X rays irradiate a cylindrical sample surface, ejecting photoelectrons in all directions. A fraction of them pass through the annular entrance slit into the region of the spherical analyzer. The electron image of the entrance slit is focused onto an annular exit slit, after which the electron cone is brought to focus on the aperture of an electron multiplier.

Typically, a positive voltage is applied to the sample so that the initial photoelectrons are retarded to 100 eV upon passing through the slit. The geometry of the retarding region does not appear to be critical as long as one insures that all electrons entering the analyzer originate from a strongly irradiated portion of the sample surface. Then the beam intensity will be governed by the brightness conservation law. The spectrum is swept by sweeping the voltage applied to the sample. This has the advantage that the analyzer voltages remain fixed and the line-width contribution of the analyzer remains constant throughout the spectrum. Also, one can reduce the analyzer line width contribution by reducing the energy at which the electrons are analyzed. Nominally, we analyze electrons at an energy of 100 eV. With a spectrometer designed for 1-percent resolution we get a spectrometer contribution of 1 eV, full width, half height. Under these conditions we obtain the spectrum shown in Fig. 6 of the 4f gold doublet. Including the energy width of the aluminum Kα radiation of about 0.9 eV, we obtain a spectrum line width of 2 eV full width, half height, as would be expected. With a power input of 400 W to the X-ray tube, we get an electron counting rate of 9000 counts per second at the peak of the spectrum. This, we observe, is about ten times higher than is normally reported in the ESCA literature, for the same resolution, from instruments of three times larger radius. In addition, we have observed in general that the peak-to-background ratio is comparable to that obtained on other instruments and this is primarily a sample characteristic. Background is produced by bremsstrahlung and by high-energy electrons scattered to lower energies prior to escape from the sample surface. Complete details on the performance of this spectrometer will be published elsewhere.

As an example of work done with the IEE Spectrometer we show in Fig. 7 the carbon spectra from three polyester plastic films, two of which were surface treated with silicon compounds to reduce their permeability, and one of which was untreated. The untreated film exhibits two carbon peaks, the smaller of which represents the CO bonds, as opposed to the CH bonds. In one case, our results suggest that silicon treatment replaces CO bonds by SiO bonds, and an oxidized silicon peak appears (Fig. 8) with a chemical shift of 3 eV corresponding to the chemical formula SiO_2 . In the other case, an intermediate oxidation state of carbon appears on the surface.

It is with pleasure that we acknowledge the continued support and encouragement of Dr. W. A. Anderson and many other members of Varian Corp.

REFERENCES

1. K. Siegbahn, Alpha, Beta and Gamma Spectroscopy, North Holland, 1966; vol. 1, ch. 3, ESCA, Stockholm: Almquist & Wiksells AB, 1967.
2. E. M. Purcell, Phys. Rev. 54: 818, 1938.
3. J. C. Helmer and N. H. Weichert, Appl. Phys. Lett. 13: 266, 1968.

4. H. Hafner, J. A. Simpson, and C. E. Kuyatt, Rev. Sci. Instr. 39: 33, 1968.

5. J. Kessler and N. Weichert, Nucl. Inst. & Meth. 35: 161, 1965.

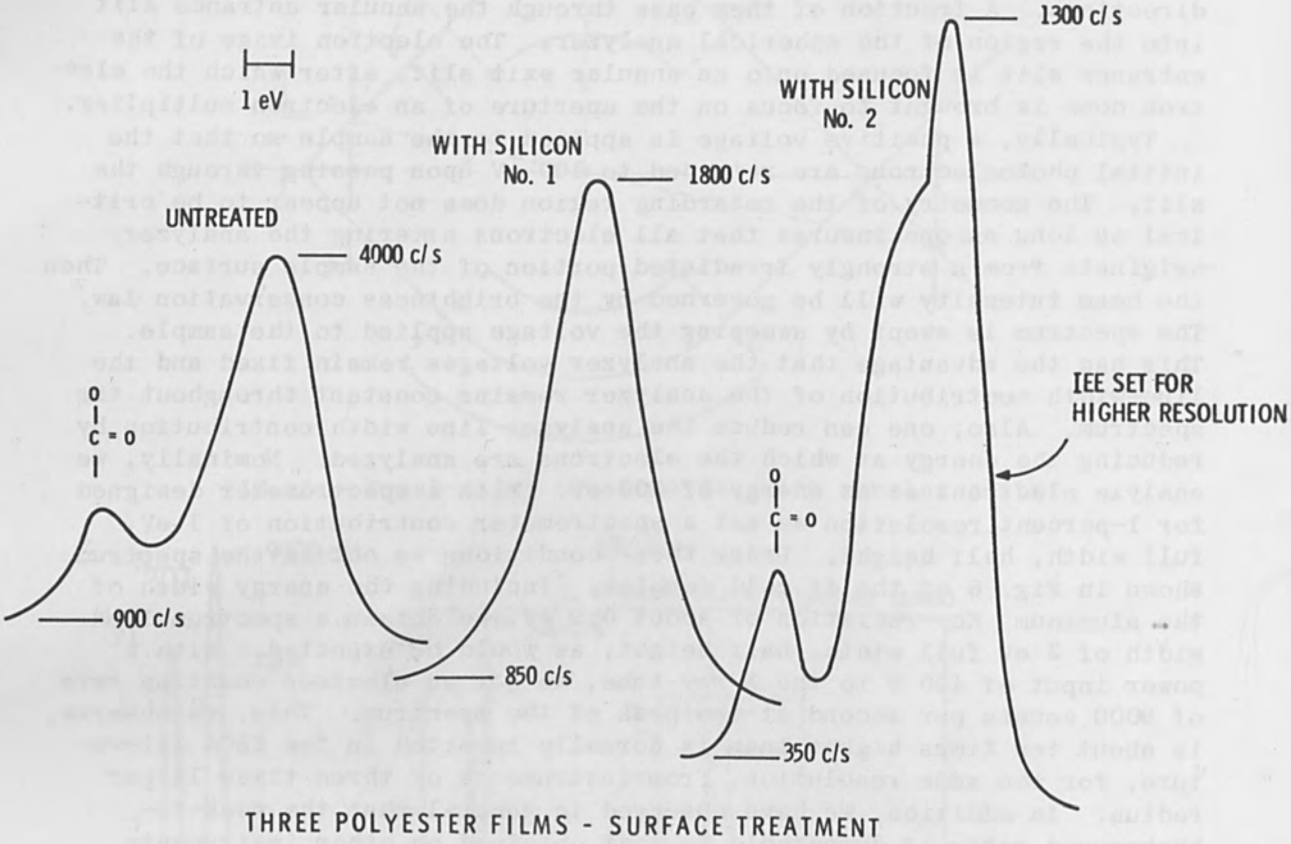

FIG. 7.—Carbon spectra from plastic films.

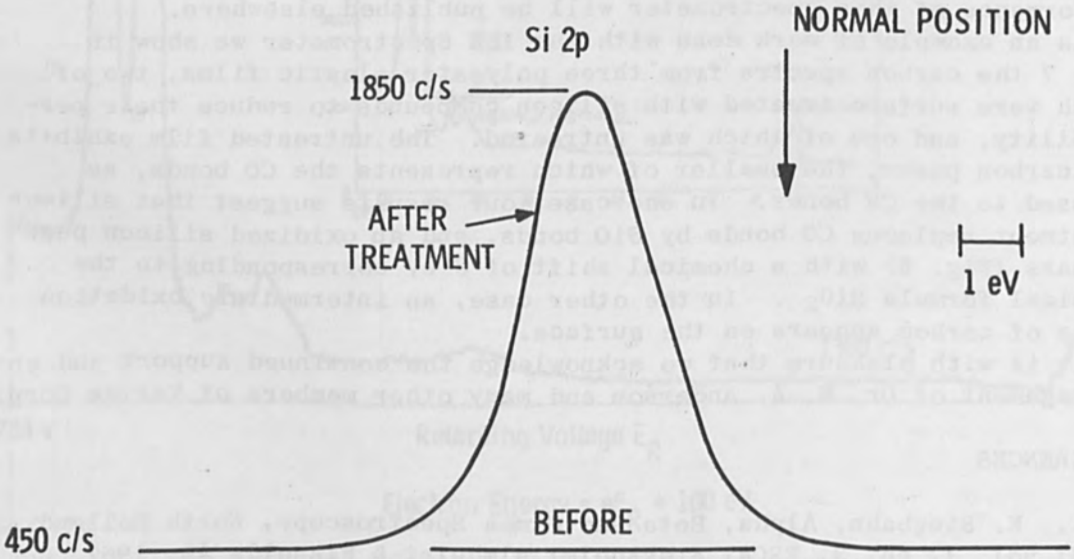

FIG. 8.—Silicon spectrum from treated plastic.

ELECTRON IMPACT SPECTROSCOPY

J. AROL SIMPSON

National Bureau of Standards, Washington, D. C.

Recent developments in electron spectrometer design have made the application of inelastic electron scattering measurements to gas analysis competitive with other techniques. The energy distribution of electrons of an initially monoenergetic electron beam after an encounter with a gas target (the loss spectrum) contains the optical absorption spectrum of the gas. The absorption data extend from the extreme vacuum ultraviolet into the visible with an energy resolution comparable to a 1/2-meter optical grating spectrometer. Its response is linear with concentration over a very wide range and contains between 10^3 and 10^4 resolution widths. This spectrum, by revealing the valence energy states of the gas, is the most intrinsic possible "fingerprint" of the atom or molecule. An instrument has been built to explore the potentialities of this method. The instrument is described and its performance as a trace analyzer for air pollution studies discussed.

INTRODUCTION

One of the ambitions of analysis is to distinguish between various atoms and molecules by virtue of differences in some physical property. The more fundamental or intrinsic this property the more unambiguous the identification. For example, despite the extreme usefulness of the various forms of chromatography, the differential solubility or adsorbability on which they depend is a secondary property which may be shared by any number of otherwise unrelated species. On the other hand, the property of mass, which is used in mass spectrometry, is much more fundamental but is limited by the fact that masses differ by almost exact integers and hence even the mass of such simple species as N_2 and CO differ by only some parts in ten thousand. Optical spectrometry uses the most fundamental of all atomic properties, the number and spacing of the energy levels of the atom or molecule. This spectral fingerprint is unique, since it arises from the same physical property (the outer electron configuration of the species) as do all other chemical and physical properties.

For atomic species emission spectrometry is an extremely powerful analytical tool. Unfortunately, the conditions necessary to excite an emission spectrum are severe enough so that many molecules are disrupted or only weakly excited.

However, the same information is obtainable from absorption spectrometry since for every emission feature arising from a transition from the ground state there is at the same wavelength an absorption feature. The problem which interferes with the full exploitation of this fact is that to measure the absorption spectra one must have light of appropriate wavelength to absorb. Unfortunately, the first few energy levels in simple atoms or molecules lie in the ultraviolet, where the smooth continuum desired is not easily generated. This difficulty has been circumvented to some extent by the development of infrared spectrometry, where

Record of 10th Symposium on Electron, Ion, and Laser Beam Technology (L. Marton, ed.); San Francisco Press, Inc.
Copyright © by The Institute of Electrical and Electronics Engineers, Inc.—Printed in the U.S.A.

blackbody thermal sources are available. The penalty paid here is that no longer can one measure the fundamental atomic levels but rather the vibrational-rotational levels of the molecular ground state. These frequencies are characteristic of particular chemical bonds, C-H, C=0, etc., and are very nearly the same for any molecule containing such a bond. Hence at usual resolutions the "fingerprint" is not so distinctive and interference is a serious problem.

For quantitative work all absorption techniques suffer from the fact that absorption obeys Beer's law, i.e., is exponentially dependent on absorbent concentration, only if the width of the absorbing state is larger than the instrumental bandwidth.[1] For absorbing states much narrower than the instrumental bandwidth, oscillator strength determinations have been reported which are orders of magnitude too small.[2] Furthermore, the amount of light absorbed by a contaminant at low concentration is lost in the noise level of the light source.

Electron impact spectroscopy (EIS) is a method of obtaining optical absorption data which avoids the difficulties of source availability, of narrow lines, and of source noise.

THEORY

Electron impact spectrometry is based on the physical fact that if an atom or molecule is bombarded by an electron whose energy is greater than the energy gap between the ground state and the first excited state of the target, an energy transfer may occur, in which case the target is left in an excited state and the incident electron is deviated from its course and suffers an energy loss precisely equal to the gap between the ground state and the final excited state. If the electron energy is above the ionization potential of the atom and the experiment is repeated a sufficient number of times, the initial monoenergetic beam of electrons is transformed into a loss spectrum with a discrete energy loss in the beam corresponding to every possible energy state in the atom. This fact has been long known[3] and interesting work in the far UV was done by Whiddington and Priestly[4] more than 30 years ago. Figure 1 shows such a spectrum taken on a modern instrument for the very simple helium atom. It is to be noted that unlike photon absorption this process is essentially nonresonant. Any state whose energy is below that of the incident energy can be excited; hence there is no need for a continuum of electron energies. Moreover the apparent line width of a very narrow line becomes the line width of the incident electron beam and the difficulty of relative intensity determinations of narrow lines is eliminated.

It has been shown that if the energy of the electron is high enough (about 20 times ionization energy is sufficient in practice) and if only those electrons that have been deflected through a very small angle (in practice[5] less than 1°) are used then the intensity of the loss peak for a given state is directly related to the optical absorption of that state.[6]

The use of electron spectrometry languished for a long time for lack of sufficient resolution in electron monochromators and analyzers. With the recent interest in oscillator strengths in the far UV and with renewed interest in electron scattering, the technique has recently been taken up by ourselves[7] and others[8] and a resolution of a few millivolts at usable intensities has been obtained.[9] Figure 2 shows the currently available resolution as a function of wavelength as compared to an

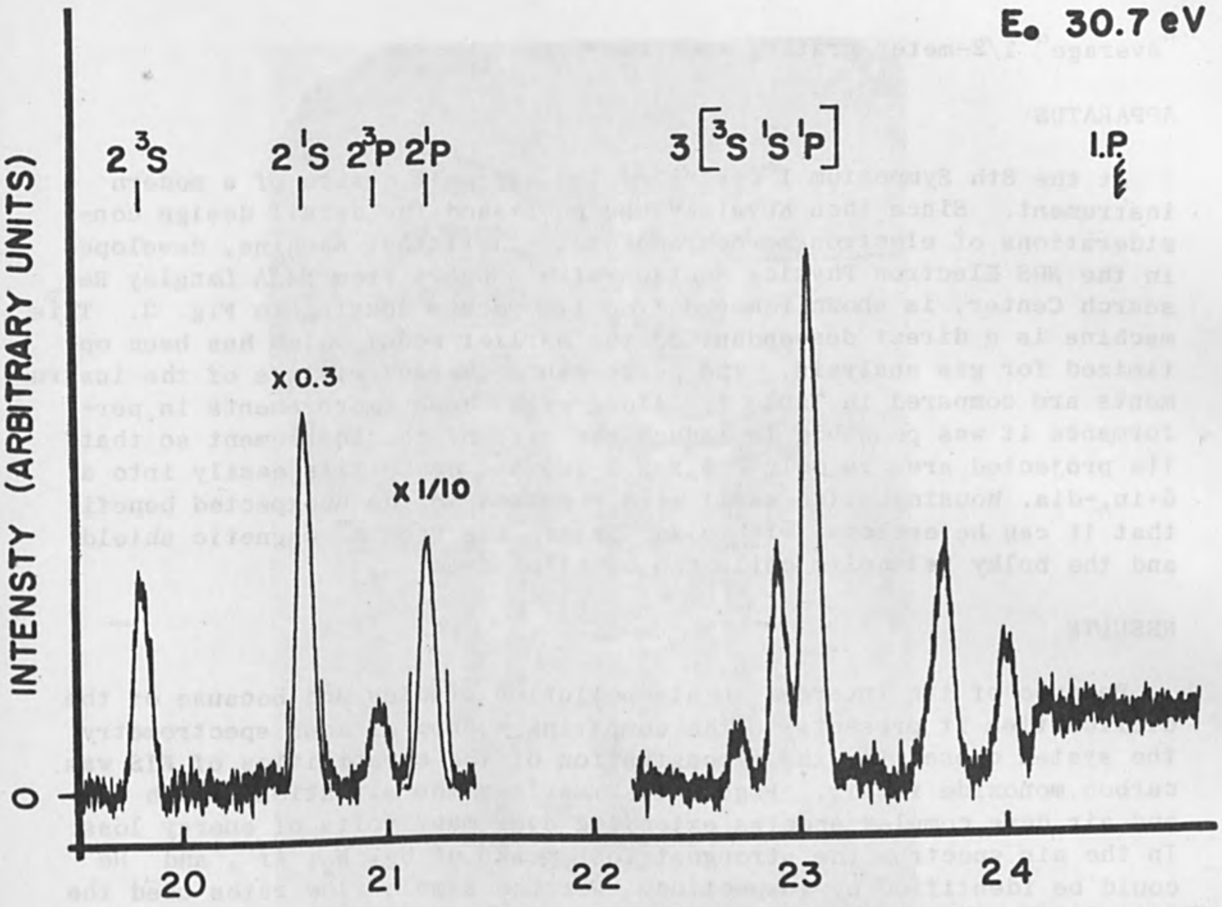

FIG. 1.—Electron impact spectrum of helium. Note that under these impact conditions both allowed and optically forbidden transitions are excited.

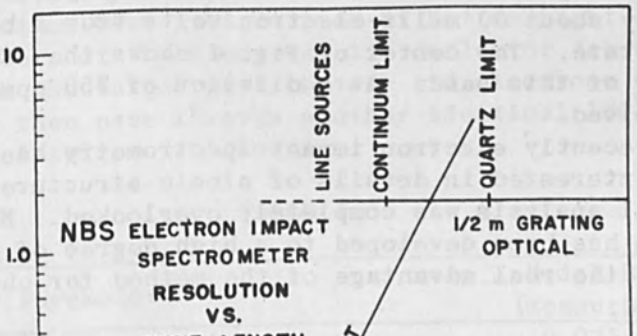

FIG. 2.—Equivalent wavelength resolution of an electron impact spectrometer as a function of wavelength. For comparison the wavelength resolution of an "average" 0.5-m grating optical monochromator is shown.

"average" 1/2-meter grating spectrometer.

APPARATUS

At the 8th Symposium I described the over-all design of a modern instrument. Since then Kuyatt[10] has published the detail design considerations of electron monochromators. The latest machine, developed in the NBS Electron Physics Section with support from NASA Langley Research Center, is shown removed from its vacuum housing in Fig. 3. This machine is a direct descendant of the earlier model which has been optimized for gas analysis. The performance characteristics of the instruments are compared in Table I. Along with these improvements in performance it was possible to reduce the size of the instrument so that its projected area is only 2.5 X 5.5 in. and hence fits easily into a 6-in.-dia. housing. The small size resulted in the unexpected benefit that it can be enclosed within an "inside the vacuum" magnetic shield and the bulky Helmholtz coils can be eliminated.

RESULTS

Because of its interest in air-pollution studies and because of the difficulties it presents to the competing method of mass spectrometry the system chosen for the demonstration of the capabilities of EIS was carbon monoxide in air. Figure 4 summarizes the situation. Both CO and air have complex spectra extending over many volts of energy loss. In the air spectrum the strongest loss peaks of O_2, N_2, Ar , and He could be identified by inspection. For the sample flow rates used the two noble gases are detectable in amounts of about 0.2 nanograms and 0.2 picograms, respectively. In the region just above 11 eV, CO has two peaks, corresponding to the $C^1\Sigma^+$ and $E^1\Sigma^+$ absorptions. These peaks are separated by about 60 milli-electron volts from a broad band believed to be an O_2 state. The center of Fig. 4 shows the CO peak appearing on the shoulder of this band. At a dilution of 250 ppm the CO peak is still well resolved.

Until very recently electron impact spectrometry has been the province of physicists interested in details of atomic structure and its application to chemical analysis was completely overlooked. Nonetheless the instrumentation has been developed to a high degree of performance and reliability and the real advantage of the method for chemical analysis can be exploited.

DISCUSSION

Electron impact spectrometry is best compared with mass spectrometry, which uses instrumentation of comparable complexity and of superficial resemblance, and to absorption spectrometry, which depends on the same atomic or molecular properties.

Compared to mass spectrometry EIS has the following advantages.

(1) Each species has a complex EIS spectrum of many lines or bands which extend over several hundred or thousand data points. These complex spectra are to be compared to the single mass peak of an ion species or the dozen or so peaks of a fragmented complex ion in mass spectrometry. The additional data points obtained with EIS greatly reduce the problems

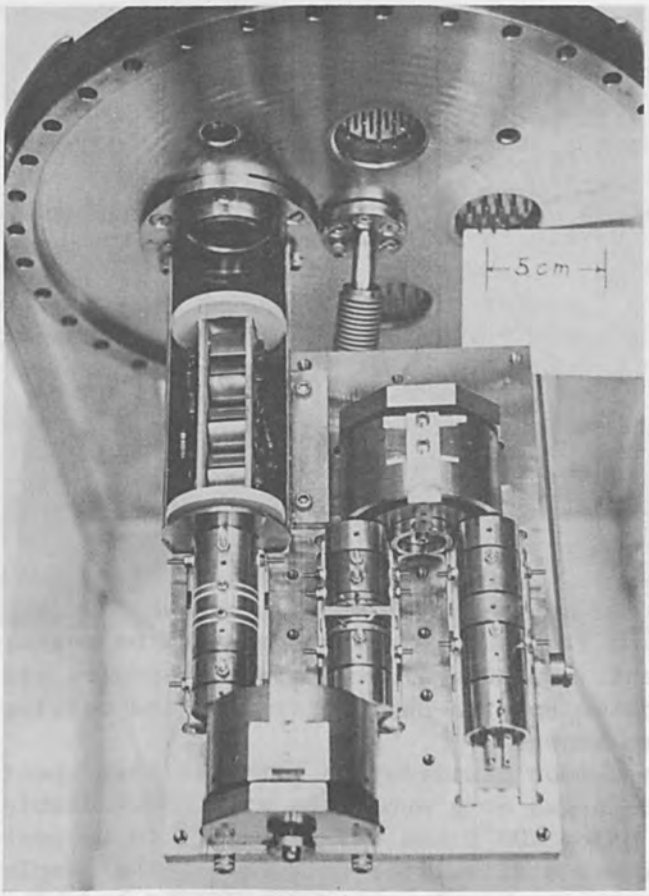

FIG. 3.—The electron impact spectrometer shown outside its evacuated housing. The electron beam is initiated at bottom right and traverses through the 180° turn of the electrostatic deflector (above). The beam then collides with the target gas (center) and electrons scattered in the forward direction then pass through another identical 180° deflector (bottom) to the multiplier (top left).

TABLE I

Parameter	Model B (measured)	Model AN (predicted)
Resolution ΔE (ev)	0.075	0.023
Scattering energy E_0 (eV)	400	50
Scattering chamber current I_0 (A)	$\sim 10^{-7}$	$\sim 10^{-8}$
Relative Born cross section at E_0	1	3.7
Percent Born cross section accepted	12	30
Response at equal path length $\times$(times) density	0.12	1.1
Path length $\times$(times) density (1% of optimum)	10	100
Detector limit (S/N = 1, integration time = 1 sec) (A)	10^{-15}	10^{-18}
Relative sensitivity	1	9200

*Note that increased resolution of Model AN is responsible for decreased scattering chamber current. Some of this loss in sensitivity will be reclaimed in increased peak height for states whose natural width is less than the resolution.

of interference that arise in mixtures, since all data points may be compared with standard spectra.

(2) Mass spectra analysis depends on both the parent species and its ion being at least metastable or identifiable by means of its fragmentation pattern. EIS depends only on the parent being stable, and no reconstruction from fragments is necessary. Also, in the case of fragile species, the fact that the hot filament present in both methods is physically well separated from the sample gas eliminates problems of thermal dissociation.

(3) The physical size of the EIS apparatus does not increase in proportion to the molecular weight of the sample. The apparatus is electrostatic and all dc powered, it is essentially lighter in weight than a magnetic mass spectrometer, and the electrical circuity is simpler than that of rf-type mass spectrometers.

One apparent disadvantage of EIS is that a priori the spectrum of a substance is not known, whereas its atomic mass is; hence standard spectra of all species of interest must be developed. In the case of complex molecules, which usually fragment in a mass spectrometer, this disadvantage is more apparent than real since the fragmentation pattern is also unknown and fragmentation patterns must be measured for all species of interest. Because electron impact spectra are simply related to optical absorption spectra one can draw on the catalog of these spectra where they are known.

EIS shares the common disadvantage with the mass spectrometer that the sample must be a gas or a substance with a detectable vapor pressure at a temperature below 400°C and stable enough to be passed through a tube. The well known difficulties of reducing the sample pressure to 1 torr or below without changing its composition by selective absorption on the inlet walls or by mass separation during flow must also be contended with in quantitative work.

Compared to optical absorption spectroscopy, EIS has the following advantages.

(1) The equivalent wavelength range of EIS is very much larger than any optical instrument of comparable size; it can extend from the visible to the soft X-ray region in a single scan. Since the scan is achieved by electrical means there is no fundamental limit to scan speed and time-resolved analysis is limited only by the speed of response of the detector. Most identification work will be done at energy losses corresponding to the UV region beyond the quartz limit. This is the region where the transitions from the first few excited states to the ground state lie. These "resonance lines" are the strongest lines in any spectrum and the easiest to recognize.

(2) For quantitative work the response of EIS as a function of concentration is easier to interpret than that of optical absorption. In the latter technique the response to a narrow line is linear at extremely low pressures, becomes exponential at slightly higher pressures, and then goes over to approximately a square-root dependence on pressure. The transition regions depend on the natural line width relative to instrument resolution and hence occur at different partial pressures for each constituent. For narrow lines, measurement of the relative intensity relations in a single substance can be an extremely difficult experimental problem.

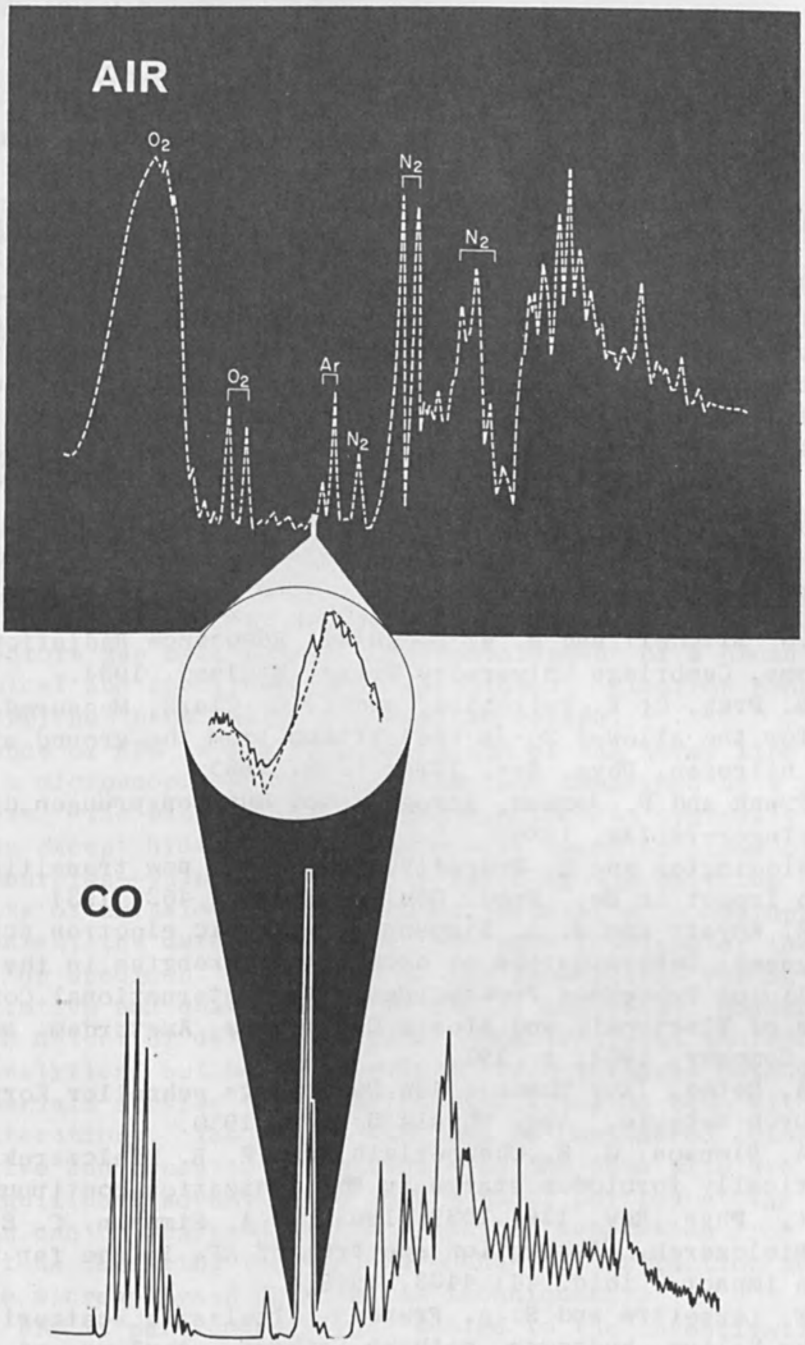

FIG. 4.—A three-part graph demonstrates the sensitivity of the electron-impact spectrometer to carbon monoxide. The upper portion (white dashed curve) provides the full spectrum of breathing air including all of the air's most prominent constituents--oxygen (O_2), nitrogen (N_2), and argon (Ar). The lower graph shows the full carbon monoxide spectrum with the main peak shadowed. The central graph (within the circle) shows an expansion of the spectrum of air as given by the electron impact spectrometer for two conditions: (1) with no carbon monoxide present (dashed curve), and (2) with 250 parts per million of carbon monoxide present (solid curve). Note that in the solid curve there is a definite peak at the same location as the main peak of CO.

In EIS the response R is given by

$$R = ke^{-\sigma_\tau p_\tau} p_s \sigma_s$$

where k is an instrumental constant, the subscript τ refers to total scattering cross section and pressure, and the subscript s refers to the individual species. Hence as long as the species of interest is a minor constituent the response is linear with partial pressure and is independent of natural line width. If one wishes to analyze for major constituents the pressure can be lowered to minimize the effect of the exponential absorption term. Moreover, the fact that the EIS response is a signal on a zero background, instead of a decrease in a large background, is favorable with respect to signal to noise and places less stringent requirements on system stability.

REFERENCES

1. A.C.G. Mitchell and M. W. Zemansky, Resonance Radiation and Excited Atoms, Cambridge University Press, England, 1934.

2. A. B. Prag, C. E. Fairchild, and K. C. Clark, Measured oscillator strengths for the allowed 2p-3s transitions from the ground state of oxygen and nitrogen, Phys. Rev. 137A: 1358, 1965.

3. J. Frank and P. Jordan, Anregung von Quantensprüngen durch Stösse, Berlin: Springer-Verlag, 1926.

4. R. Widdington and H. Priestly, "Note on a new transition produced by electron impact in He," Proc. Roy. Soc. A145: 462, 1934.

5. C. E. Kuyatt and J. A. Simpson, "Inelastic electron scattering from rare gases: Determination of oscillator strengths in the continuum," Atomic Collision Processes Proceedings, IIId International Conference on the Physics of Electronic and Atomic Collisions, Amsterdam: North-Holland Publishing Company, 1964; p. 191.

6. H. A. Bethe, "Zur Theorie des Durchgangs schneller Korpuskularstrahlen durch Materie," Ann. Physik 5: 325, 1930.

7. J. A. Simpson, G. E. Chamberlain, and S. R. Mielczarek, "Excitation of optically forbidden states in the ionization continuum by electron impact," Phys. Rev. 139: 1039, 1965; J. A. Simpson, C. E. Kuyatt, and S. R. Mielczarek, "Absorption spectrum of SF_6 in the far ultraviolet by electron impact," ibid. 44: 4403, 1966.

8. E. N. Lassettre and S. A. Francis, "Inelastic scattering of 390-V electrons by helium, hydrogen, methane, ethane, ethylene and water," J. Chem. Phys. 40: 1208, 1964; J. Geiger and M. Topschowsky, "Übergangwahrscheinlichkeiten im Elektronen- und Schwingungsspektrum des Wasserstoffmoleküls," Z. Naturforsch. 21A: 626, 1966.

9. J. A. Simpson, "High resolution, low energy electron spectrometer," Rev. Sci. Instr. 35: 1698, 1964.

10. C. E. Kuyatt and J. A. Simpson, "Electron monochromator design," Rev. Sci. Instr. 38: 103, 1967.

ELECTRON AND ION MICROPROBE ANALYSIS

KURT F. J. HEINRICH

National Bureau of Standards, Washington, D. C.

This review covers the principles and development of electron probe microanalysis, with particular emphasis on recent developments. The double function of the instrument as a spectrograph and as a microscope is considered. The salient characteristics of the ion beam microprobe are also indicated.

INTRODUCTION

The demand for characterization of increasingly complex and sophisticated materials used in science and technology has prompted an untiring search for new analytical tools. The rapid progress in electronics, nucleonics, electron optics, and in the construction of particle and photon detectors has made possible the development of a broad range of physicochemical and spectroscopical techniques. Electron probe microanalysis (EPM) has been one of the most successful.[1]

The essence of EPM is the interpretation of the X-ray line spectrum emitted by a microscopic volume of a specimen bombarded by a focused electron beam. The excited mass of the specimen is typically 10^{-11} g. All elements except hydrogen and helium emit bands or lines of wavelengths--or photon energies--which are characteristic of the emitting element. The intensity of emission of these lines permits, with appropriate correction procedures, the determination of the mass fraction of the respective element in the specimen. We have thus the foundations for an almost complete qualitative and quantitative elemental analysis. However, it is difficult to detect or determine trace concentrations; therefore, EPM is a microanalytical but not typically a trace-analysis method.

Most materials survive the impact of the electron beam without observable alterations. The method can thus be considered essentially nondestructive and repeated measurements at the same site are possible. The most significant advantage is that a small portion at the surface of the specimen can be analyzed without physical separation from the surroundings, thus obviating the tedious mechanical extraction methods that must precede microanalysis by chemical techniques.

Although EPM is particularly well suited to the investigation of alloys, it can be applied to a very wide range of solid materials including minerals, ceramics and semiconductors, atmospheric dust, and biological specimens. Consequently, the technique has been applied in many areas of science and technology. It will, for example, play a prominent role in the characterization of lunar specimens.

Since the electrons penetrating the specimen act to charge it negatively, the specimen must conduct electricity. Nonconductors must be covered with a thin conductive film (carbon or metal) to prevent charging of the specimen. Such coatings also avoid excessive local heating of the specimen under electron bombardment. The specimen must withstand the vacuum necessary for the formation of the electron beam and for the transmission of soft X rays. Organic materials must thus be dehydrated; this

Record of 10th Symposium on Electron, Ion, and Laser Beam Technology (L. Marton, ed.); San Francisco Press, Inc.

Copyright © by The Institute of Electrical and Electronics Engineers, Inc.—Printed in the U.S.A.

unfortunately precludes the analysis of most biological tissue in vivo.

The positions and shapes of X-ray emission bands in the soft X-ray region suffer slight changes as a function of the chemical state of the emitting element. It is possible to observe such changes in the electron probe microanalyzer and thus to draw conclusions as to the chemical state of such elements in the specimen.[2] This interesting technique is being investigated at present in several laboratories.

The scanning electron microscope antedates the electron probe microanalyzer by more than a decade. In the former instrument, beam currents as low as 10^{-11}-10^{-12} A produce useful images, and beams diameters of the order of a few angstroms can be used. Hence the scanning electron microscope approaches the transmission electron microscope in resolution but has a much greater depth of focus.

Cosslett and Duncumb have shown that the technique of the scanning electron microscope can be incorporated in the electron probe microanalyzer.[3] The scanning electron probe[4] can produce images of the specimen surface using either electron signals (backscattered electrons, secondary electrons, or target current), or X-ray signals (Fig. 1). Hence, both the topography (Fig. 2) and the distribution of elements on the specimen surface can be observed and photographically documented.

The resulting interaction of microscopy and spectrography has been extraordinarily useful in the inspection and characterization of the many types of specimens. Besides, it has stimulated the investigation of phenomena other than X-ray emission, which are useful in analysis, such as cathodoluminescence in the visible and infrared range,[5] the emission of backscattered electrons, and the liberation of gases under the impact of the electron beam.[6] One may thus define EPM as the observation and interpretation of all phenomena caused by the interaction of the electron beam with the specimen, which contribute to the better knowledge of the specimen.

PRESENT STATE OF QUANTITATIVE ELECTRON PROBE MICROANALYSIS

The foundation of the theory of quantitative EPM was laid by R. Castaing, the inventor of the electron probe microanalyzer.[7] He proposed to compare the X-ray intensities emitted by the specimen with those obtained from standards of simple and well-known composition (typically, pure elements). The theory of the corrective calculations has been greatly advanced through the efforts of many investigators[1] and with the aid of increasingly available computers. At present, the errors in the determination of the composition of alloys are usually of the order of 2 percent (mass-fraction) or less.[8] Some difficulties persist with specimens which contain elements differing considerably in atomic number, and particularly in the determination of elements of atomic number below 12.

The analysis of geological materials is usually performed by comparison of the specimen with minerals of similar and well-known composition. Efforts are currently under way to study the analysis of such specimens in a more systematic way, so that the number of needed standards can be reduced. The situation is least satisfactory for biological specimens. The difficulties of preparing the complex biological tissues for analysis, of minimizing their destruction by the electron beam, and of obtaining adequate standards are considerable and progress is slow.[9]

The preparation of well-characterized and microscopically homogeneous

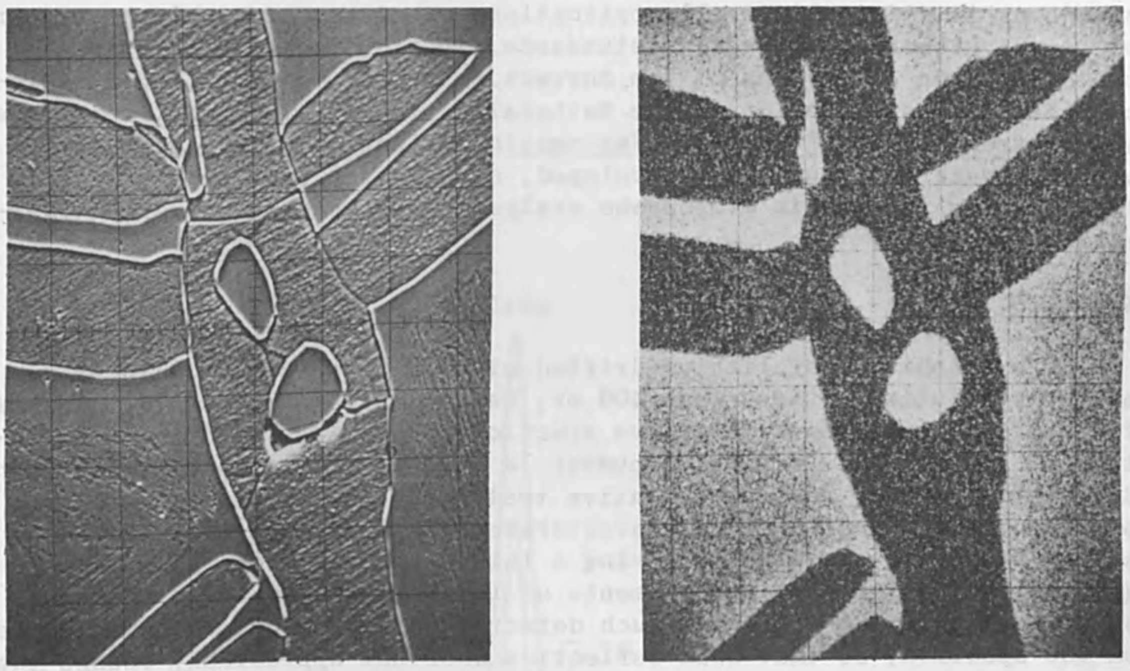

FIG. 1.—Area scans of section of ferrous meteorite: left, scanning electron micrograph obtained from target current, showing topographic features; right, Ni K alpha X-ray scan, showing the distribution of nickel in the light areas. (Scale: 20 µm per large division.)

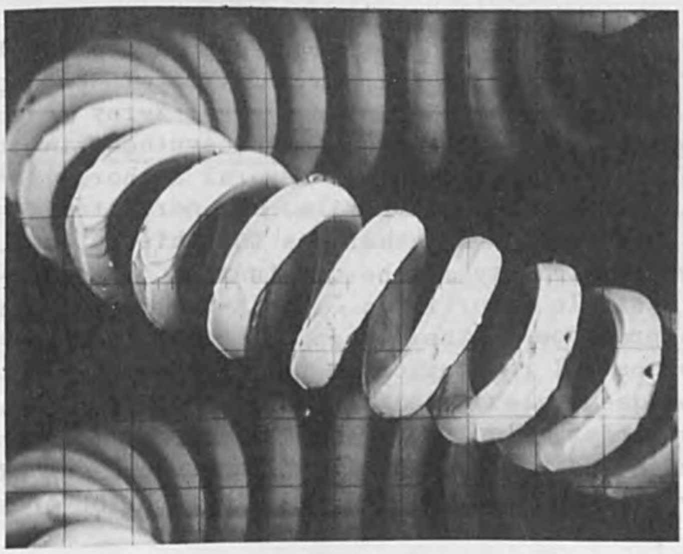

FIG. 2.—Scanning electron micrograph of tungsten filament after recrystallization (from used light bulb). This image, obtained in conventional electron probe microanalyzer, shows capabilities of this instrument as microscope. Note in particular depth of focus. (Scale: 20 µm per large division.)

standards is difficult in all applications of microprobe analysis. Even when pure elements are used as standards, multielement standards are needed for the evaluation of the correction procedures. At the Spectrochemical Analysis Section of the National Bureau of Standards, techniques and instrumentation for the semiautomatic evaluation of homogeneity of standard materials have been developed, and several standards specially designed for the use in microprobe analysis have been prepared and characterized.[10]

NEW DETECTORS

The availability of lithium-drifted silicon detectors,[11] with an energy resolution of less than 400 eV, has prompted a reinvestigation of the application of nondiffractive spectrometry to EPM. The rapid detection of all elements of atomic number 12 or larger is possible with such detectors. Such a rapid qualitative test is of great value when many points of a specimen must be characterized (Fig. 3). Combination with a flow-proportional detector having a thin window extends the rapid qualitative analysis to the elements of lower atomic numbers. Another advantage is in the fact that such detectors do not focus on a small area on the specimen, so that beam deflection does not appreciably change the signal strength. The high efficiency of the silicon detector permits its application in scanning electron microscopes, where the typical beam currents are too low for the use of spectrometers provided with diffracting crystals. Consequently, one may expect in the near future a greater interaction between scanning electron microscopy and EPM.

USE OF COLOR PHOTOGRAPHY IN SCANNING ELECTRON PROBE MICROANALYSIS

The success of scanning electron microscopy cannot fail to increase the interest of the analyst in the capabilities of the electron probe as a microscope. For instance, combining several X-ray images by means of color photography is a very useful means of synthesizing the available information and has been advocated by several authors.[12-14] The availability of rapid-development color films has permitted the design of simple, rapid, and economical techniques for this purpose.[15] A particularly attractive possibility is the combination of target-current and X-ray scans in a single color image. The X-ray scanning image, although specific to the presence of the element emitting the corresponding X-ray line, lacks the spatial resolution of the electron image, since X rays are emitted from deeper levels below the specimen surface than the backscattered and secondary electrons. By superposing in a photocopy process the electron image and up to three X-ray images, we can efficiently combine the topographic information and the distribution of several elements present in the specimen.

QUANTITATIVE PHASE ANALYSIS

Quantitative phase analysis (stereometry) has been performed in the past on the basis of photographic images. The specificity of the electron probe X-ray signals offers an excellent means for the application of this technique as demonstrated by Dörfler, who has extensively described the theory and developed the necessary instrumentation.[16] In Dörfler's technique, compositional differences are used to characterize

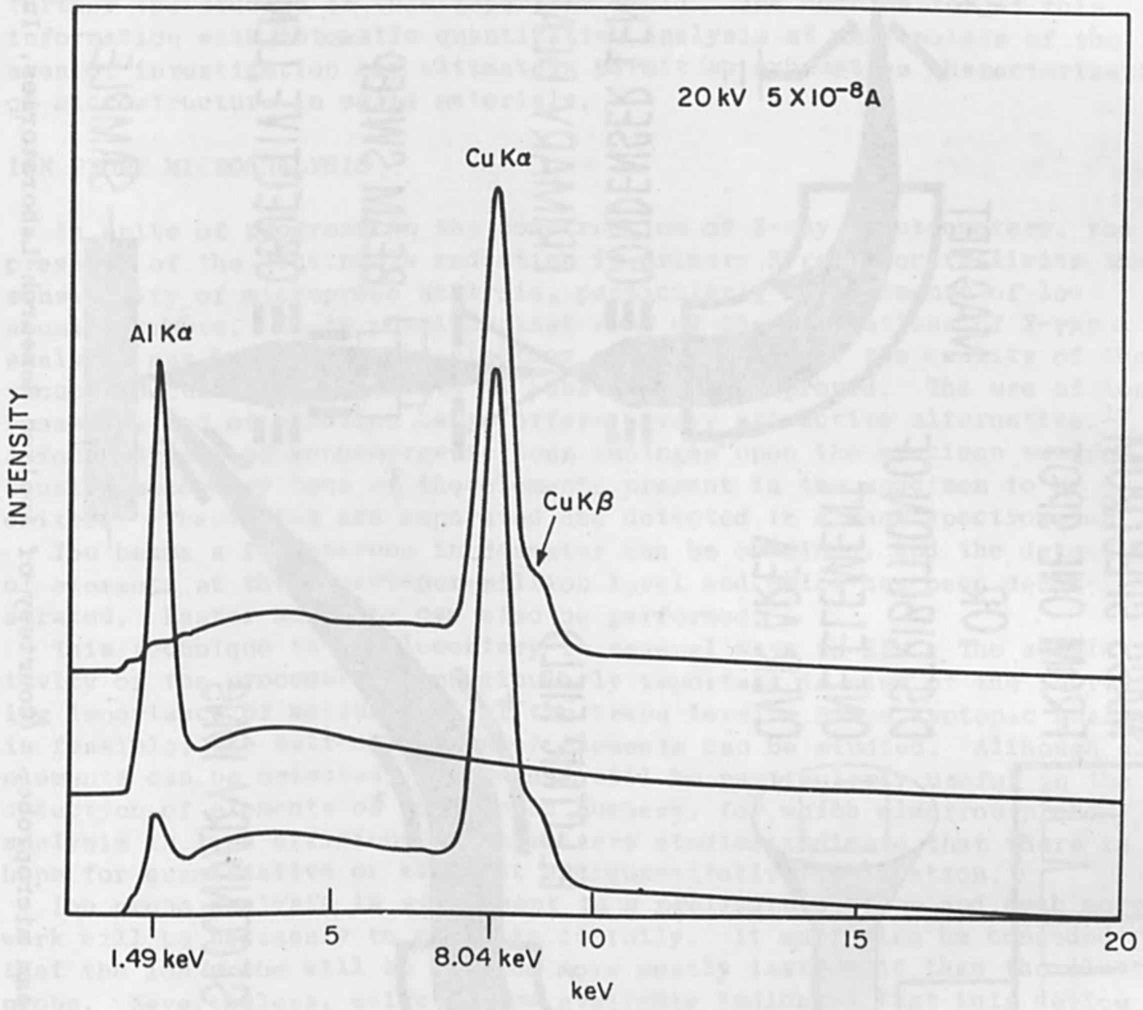

FIG. 3.—Energy spectra of the X radiation emitted from copper, aluminum, and a copper-aluminum alloy, obtained with the use of a lithium-drifted silicon detector. Resolution of this detector was 500 eV at half peak-height. Currently available detectors have a resolution of 250-300 eV.

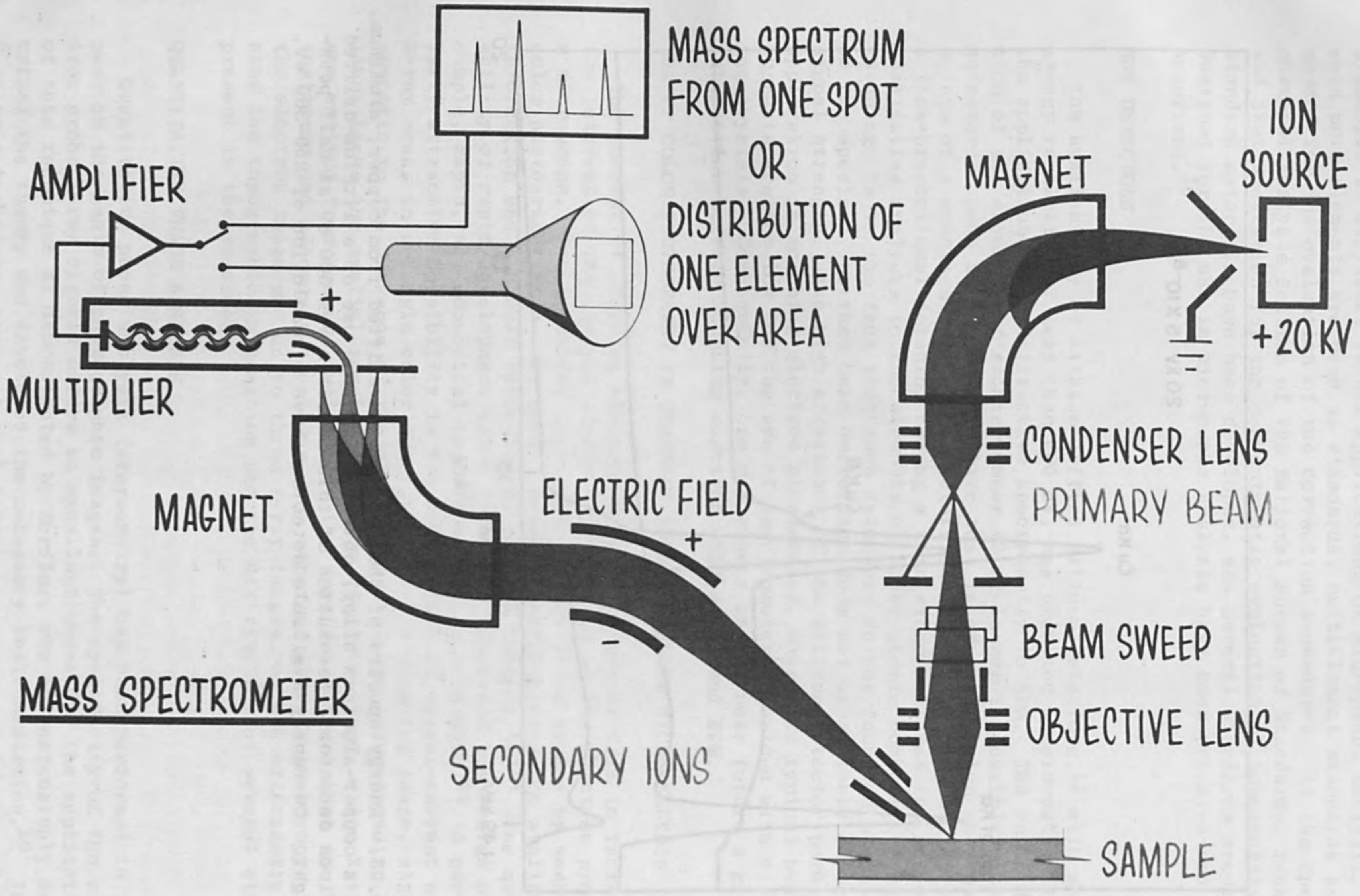
MASS SPECTRUM
FROM ONE SPOT
OR
DISTRIBUTION OF
ONE ELEMENT
OVER AREA
AMPLIFIER
MULTIPLIER
+
−
MAGNET
MASS SPECTROMETER
ELECTRIC FIELD
+
−
SECONDARY IONS
MAGNET
ION
SOURCE
+20 KV
−
CONDENSER LENS
PRIMARY BEAM
BEAM SWEEP
OBJECTIVE LENS
SAMPLE

FIG. 4.—Schematics of an ion beam microprobe. (Courtesy of Applied Research Laboratories, Inc.)

the phases of a multiphase specimen in order to determine the volume fractions, as well as mean diameters of grains, contiguity relations, and other topological characteristics. The development of rapid detectors and the possibility of extensive machine computation will greatly further the studies in this important field. The combination of this information with automatic quantitative analysis at many points of the area of investigation may ultimately permit an exhaustive characterization of microstructure in solid materials.

ION PROBE MICROANALYSIS

In spite of progress in the construction of X-ray spectrometers, the presence of the continuous radiation in primary X-ray spectra limits the sensitivity of microprobe analysis, particularly for elements of low atomic numbers. It is possible that some of the limitations of X-ray analysis may be overcome by electron spectrography if the quality of the vacuum in current instruments is substantially improved. The use of ion beams instead of electron beams offers a very attractive alternative.[17] A focused beam of monoenergetic ions impinges upon the specimen surface, causing secondary ions of the elements present in the specimen to be emitted. These ions are separated and detected in a mass spectrometer.

Ion beams a few microns in diameter can be obtained, and the detection of elements at the 1 part-per-million level and below has been demonstrated. Raster scanning can also be performed.

This technique is complementary in several ways to EPM. The sensitivity of the procedure is particularly important in view of the increasing importance of measurement at the trace level. Since isotopic analysis is feasible, the self-diffusion of elements can be studied. Although all elements can be detected, the method will be particularly useful in the detection of elements of low atomic numbers, for which electron probe analysis is less efficient. Preliminary studies indicate that there is hope for quantitative or at least semiquantitative application.

Ion probe analysis is at present in a preliminary stage and much more work will be necessary to evaluate it fully. It must also be conceded that the ion probe will be an even more costly instrument than the electron probe. Nevertheless, evidence now available indicates that this device will be of great value in microanalysis. In view of the gratifying results obtained with electron-beam instruments, it can be expected that further significant progress in the application of particulate beams to microanalysis will be achieved in the near future.

REFERENCES

1. K.F.J. Heinrich, ed., Quantitative Electron Probe Microanalysis, NBS Special Publication 298, Oct. 1968.

2. J. E. Holliday, Change in shape of the K emission spectra of the light elements with chemical combination, T. D. McKinley, K.F.J. Heinrich, and D. B. Wittry, eds., The Electron Microprobe, New York: John Wiley & Sons, 1966; p. 3.

3. V. E. Cosslett and P. Duncumb, Nature 177: 1172, 1956.

4. K.F.J. Heinrich, Scanning Electron Probe Micro Analysis, NBS Technical Note 278, Feb. 1967.

5. D. F. Kyser and D. B. Wittry, Cathodoluminescence in Gallium Arsenide, The Electron Microprobe (cf. Ref. 2); p. 691.

6. J. Zähringer, Earth and Planetary Science Letters 1: 20, 1966.
7. R. Castaing, Thesis, University of Paris, 1951.
8. K.F.J. Heinrich, Advances in X-Ray Analysis 11: 40, 1968.
9. T. Hall, Some Aspects of the Microprobe Analysis of Biological Specimens, NBS Special Publication 298, Oct. 1968; p. 269
10. NBS Standard Reference Materials 480, 481, and 482.
11. R. Fitzgerald, K. Keil, and K.F.J. Heinrich, Science 159: 528, 1968.
12. P. Duncumb and V. E. Cosslett, in V. E. Cosslett, A. Engstrom, and H. H. Pattee, jr., eds., X-Ray Microscopy and Microradiography, New York: Academic Press, 1957; p. 374.
13. R. Theisen, Mem. Scient. Rev. Métallurgie 60: 189, 1963.
14. K.F.J. Heinrich, Advances in X-Ray Analysis, 7: 382, 1964.
15. H. Yakowitz and K.F.J. Heinrich, J. Res. NBS 73A: 113, 1969.
16. G. Dörfler, Quantitative Evaluation Methods for Alloy Microstructures by Microprobe Analysis, NBS Special Publication 298, Oct. 1968; p. 269.
17. M. F. Hasler and C. A. Andersen, "Analytical methods suitable for the ion microprobe mass analyzer," Proc. 5th Intern. Congress on X-Ray Optics and Microanalysis, Tübingen, 1968 (in press).

PART VI

ELECTRON MICROSCOPES; ELECTRON OPTICS; ELECTRON SCATTERING

6. J. Zähringer, Earth and Planetary Science Letters 1: 20, 1966.
7. R. Castaing, Thesis, University of Paris, 1951.
8. K.F.J. Heinrich, Advances in X-Ray Analysis 11: 40, 1968.
9. T. Hall, Some Aspects of the Microprobe Analysis of Biological Specimens, NBS Special Publication 298, Oct. 1968; p. 269.
10. NBS Standard Reference Materials 480, 481, and 482.
11. R. Fitzgerald, K. Keil, and K.F.J. Heinrich, Science 159: 528, 1968.
12. P. Duncumb and V. E. Cosslett, in V. E. Cosslett, A. Engstrom, and H. H. Pattee, jr., eds., X-Ray Microscopy and Microradiography, New York: Academic Press, 1957; p. 374.
13. R. Theisen, Mem. Scient. Rev. Metallurgie 60: 189, 1963.
14. K.F.J. Heinrich, Advances in X-Ray Analysis, 7: 382, 1964.
15. H. Yakowitz and K.F.J. Heinrich, J. Res. NBS 73A: 113, 1969.
16. G. Dörfler, Quantitative Evaluation Methods for Alloy Microstructures by Microprobe Analysis, NBS Special Publication 298, Oct. 1968; p. 269.
17. M. P. Hasler and C. A. Andersen, "Analytical methods suitable for the ion microprobe mass analyzer," Proc. 5th Intern. Congress on X-Ray Optics and Microanalysis, Tübingen, 1969 (in press).

FURTHER DEVELOPMENTS IN STROBOSCOPIC SCANNING ELECTRON MICROSCOPY

G. S. PLOWS and W. C. NIXON

Engineering Department, Cambridge University, England

The stroboscopic scanning electron microscope, and its use in the observation of high-frequency (7-MHz) microcircuit voltages, were both presented at the Boston Conference on Electron Beam Technology (May 1968), and were fully described in the J. Sci. Instr. (Journal of Physics E), June 1968, Series 2, Vol. 1, pp. 595-600. The instrument can be used to study time-periodic surface voltages on large and complex microcircuits in operation, over a very wide range of frequencies, either by imaging the spatial distribution of surface voltages at a given phase or by displaying the time-dependent voltage waveform at a selected surface point. Among other circuits studied, one is a monolithic integrated-circuit 24-bit dynamic-shift register which uses MOS transistors as active devices. The 100-kHz interleaved clock pulse trains were imaged simultaneously with the input pulse, supplied at 1/24 of the clock rate (about 4 kHz). Successive micrographs showed the input pulse at all stages of its progress through the register. The time-dependent voltage waveforms on selected electrodes of the shift register have been displayed on the screen of the stroboscopic scanning electron microscope.

IMPROVED CONTRAST IN SCANNING ELECTRON MICROSCOPY

J. R. BANBURY and W. C. NIXON

Engineering Department, Cambridge University, England

For conventional scanning microscopy, the secondary-electron detector is placed close to the specimen, which inclined at an angle to the beam, in order to collect as much as possible of the available signal. Contrast arises mainly from point-to-point changes in the secondary-emission coefficient of the specimen, and modifications of this contrast are limited to electronic expansion or contraction within the video amplifier before application of the signal to the display cathode-ray tube.

Little attention has been paid previously to the possibility of increasing the available contrast at the specimen surface. A new detector design has been produced in which the highly efficient scintillator-photomultiplier combination is retained but new electrodes are added to control the electron trajectories between the specimen and the collector. In this way the variable component of the collected signal can be increased and greater information is obtained about the surface under examination.

By altering bias voltages on the electrodes several modes of operation are available, giving enhanced surface detail, sensitivity to magnetic and electric field components parallel and perpendicular to the specimen surface, and voltage contrast. To a considerable extent these effects may be separately observed and the sensitivity can be varied electrically from outside the vacuum chamber.

The system is being developed to optimize the facilities provided by this form of detector, where the improvement in contrast is particularly marked for flat specimens normal to the electron beam and there is no foreshortening of the image.

TRANSMISSION SCANNING ELECTRON MICROSCOPE USING FIELD EMITTERS AND LIQUID HELIUM

DANIEL WEINER

Berkeley, Calif.

A transmission scanning electron microscope has been built which features a field emitting electron source and a cryogenically maintained vacuum. Total field emission currents of about 10^{-5} to 10^{-6} A and focused spot currents of about 10^{-10} to 10^{-11} A have been used in practice. They are stable enough for practical microscope pictures and were achieved with no special care in selection of construction or sample materials. A resolution of several thousand Ångstroms at 5 kV is demonstrated. Methods of improving this to about 20 Å at 10 kV with our single electrostatic demagnifying lens are discussed.

I. INTRODUCTION

The great potential advantages of scanning in transmission electron microscopy have long been recognized.[1] Here the possible resolution is at least as good as in ordinary electron microscopy and one can obtain much more information about the sample being examined.[2] For example we may, in principle, measure the differential elastic and inelastic scattering cross section at each resolved area. This brings the possibility of atomic structure analysis of biological materials much closer.

The use of field emitters[3] as an electron source in such a system has many advantages. Their very great electron brightness allows us to scan our samples in reasonably short times. Their small source size requires less demagnification and hence simpler electron optics.

The main disadvantage of field emitters is the very good vacuum (10^{-9} Torr) needed for useful emitter lifetime in practical systems. This places considerable restrictions on construction materials, sample materials, and cleanliness. By cooling the microscope to cryogenic temperatures, we may get sufficient vacuum[4] without these restrictions. Vacuums of under 10^{-13} Torr have been reported[5] in cryogenic field-emission microscopes. Also cooling may allow use of superconducting lenses,[6] magnetic lens coils, and magnetic shields and provides automatically the best sample environment for ultrahigh resolution.

In this paper we report encouraging preliminary results in such a cryogenic microscope.

II. DESCRIPTION OF THE MICROSCOPE

A schematic of the microscope is shown in Fig. 1. Here electrons from a field emitter (a) of 310 oriented tungsten wire pass through a 1/32-in.-diameter beam-defining aperture (b) in a molybdenum disk that covers one end of the brass cylindrical anode (c). The anode is insulated from ground by glass and mylar spacers so that the total field emission current can be monitored.

The electron beam then passes through an electrostatic deflector formed by four quadrants of a cylinder (d) to a molybdenum disk with an

Record of 10th Symposium on Electron, Ion, and Laser Beam Technology (L. Marton, ed.); San Francisco Press, Inc.

Copyright © by The Institute of Electrical and Electronics Engineers, Inc.—Printed in the U.S.A.

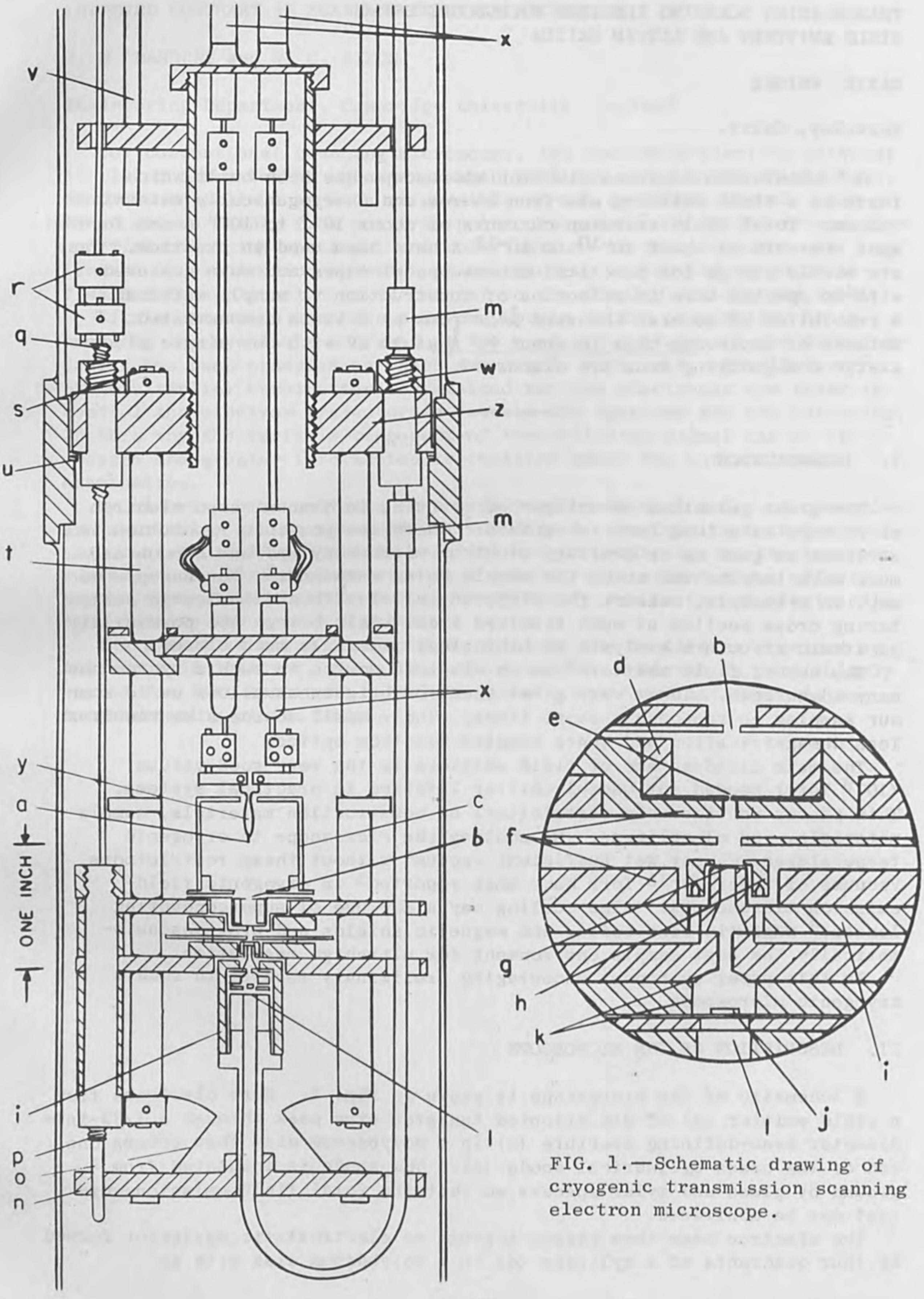
x
v
r
q
m
w
s
z
u
m
t
d
b
x
e
y
a
c
b
f
ONE INCH
g
h
k
i
i
l
j
l
p
o
n

FIG. 1.—Schematic drawing of cryogenic transmission scanning electron microscope.

approximately 0.0015-in. aperture (e). The fraction of the beam transmitted through the aperture is focused by an electrostatic Einzel lens (f) of about 1 mm focal length onto a standard electron microscope sample grid (g).

The sample is held by a cap (h) so that the cap and grid are insulated from the detector support (i). Thus the current through the 0.0015-in. aperture may be monitored.

Electrons that are transmitted through the sample strike a phosphor-coated disk (j). Light thus produced is reflected from polished aluminum surfaces (k) through a quartz light pipe (l). Light loss at necessary breaks in the light pipe is minimized by polishing their ends and connecting them with polished aluminum sleeves (m). The light is detected outside the vacuum by an RCA 931A photomultiplier, powered by a battery pack and connected to the quartz light pipe by a short fiber-optic light pipe.

The sample support is itself supported by a disk (n) held in place by leaf springs (o) and can be moved by turning a differential screw (p). The slot in the differential screw is turned via a fin (not shown) connected by a tube to a graphite lubricated copper screw (q) which is turned from above by a sliding coupling (r). This scheme allows for thermal contraction and decouples the sample somewhat from vibration.

The microscope is held together by four aluminum rods (s) in copper sleeves (t). They may be tightened by vertical set screws between runs. The materials were chosen to tighten the system on cooling. The microscope is pressed against a rim (u) in a copper ring via four steel tubes (v) which also serve as conduits for low-voltage electrical leads. These tubes are connected (via leaf springs) to an O-ring-sealed disk above that holds electrical and mechanical vacuum feedthroughs. The entire microscope assembly may thus be easily removed from the vacuum can from above for modification.

Mechanical, optical, and low-voltage electrical connections are made through 12 symmetrically placed, easily removable copper plugs (w), two of which are shown in the figure. They are sealed sufficiently by vacuum grease. They provide great flexibility.

Standard 10-kV ceramic hermetic seals (x) are used for high-voltage feedthroughs. One pair supports the split disk assembly that holds the 0.0055-in. tungsten field emitter support hairpin (y). The emitter is cleaned in the standard way by passing current through the hairpin. Another high-voltage feedthrough, not shown, replaces one of the copper plugs. It is used to excite the Einzel-lens center electrode and allows biasing it by a few per cent for a fine focusing adjustment.

For clarity many clips, springs, and electrical leads are not shown. Among the mechanical linkages not shown are two that adjust the field-emitter position via eccentric cams. Another is used to rotate the entire anode assembly so that the four deflector quadrants may be used as a stigmator.

Also, the many nonmagnetic stainless-steel Allen set screws are not shown. Of these, three of special interest are in the disk that holds the tubes (v). They press against the 1-in.-diameter copper tube via short pins so that the copper disk (z) connected to the tube may move slightly to seat correctly.

In the vacuum can region above the figure, the tubes (v) pass through two 2.75-in.-diameter, 8 in. apart, rings that prevent the tubes from buckling. Also in this region, the high-voltage lead tubes are split and pass through sleeves so as to allow for thermal contraction.

III. CRYOGENICS

In principle, the ultrahigh vacuum is maintained in the following way. An initial low vacuum (10^{-5} Torr) is obtained throughout the vacuum can with a Vacsorb and an 8 l/sec Vacion pump. The region of the can below the rim (v) is connected to the region above through twelve 1/64-in.-diameter holes in a 1/16 × 1/16 × 2-7/8-in.-diameter greased brass ring. This ring rests between the rim (u) and the copper microscope support disk (z). When liquid helium outside the can reaches the level of the rim, it cools the ring and disk by conduction to 4.2°K. Thus any air in the can below adheres to the walls and any from the relatively poor vacuum above is trapped before it gets through the small holes in the rim[5] or between screw threads in the plugs (w).

In practice, the effective thermal conductivity of the grease (which is used for thermal contact at flat interfaces throughout the microscope) is much poorer than one would expect. Thus the copper disk does not cool easily. For example, it requires about 10 hr to precool the disk with liquid nitrogen to near 77°K as monitored by a temperature sensing resistor imbedded in one of the copper plugs (n).

This procedure requires the following changes. About 1 Torr of air is left in the vacuum can during precooling. This change reduces the precooling time to about 2 hr. Also the liquid-helium level is kept more than 6 in. above the rim so that air is trapped on the can walls above before it reaches the holes in the ring or spaces between threads of the copper plugs. With lower levels of helium, field emitter stability is noticeably affected.

The helium level is monitored by sensing of the resistance change in a current-carrying resistor as it passes through the liquid surface. Use of the pressure in the ion pump as a guide to the correct helium level (10^{-7} to 10^{-8} Torr with a high helium level, 10^{-5} to 10^{-6} Torr with a low level) proved unreliable and caused several field emitter failures early in the work.

IV. STABILITY

The electrical stability of the total field emission current is shown in Fig. 2. In Fig. 2(a), the field emitter voltage of 4900 V is turned off for about 10 sec in the middle of the trace, during which time the current drops from about 1.9 μA to zero. Over many hours about 2 μA of current can be maintained with slow drifts (of ±10 per cent) as long as the helium level is maintained.

In Fig. 2(b), the effect of higher currents on stability is shown. For the central 25 sec of the trace, the voltage is 5900 V and the current is 16 μA (the voltage is 0 and 5000 V in the other plateau regions). This decrease in stability is attributed to heating of the molybdenum disk (b) and its mylar insulators. Earlier experiments using a much thicker metal anode and glass insulators gave about 100 μA of stable current.

The electrical stability of the current in the focused spot is shown in Fig. 3. Throughout the voltage was about 5 kV, the total current was about 2 μA, and the current in the spot was about 10^{-11} A. Figure 3(a) indicates that low-frequency (< 1 sec^{-1}) noise is comparable to that of the total field-emission current. High-frequency noise is shown in Figs. 3(b) and 3(c) where the RC time constants are 0.04 and 4 msec,

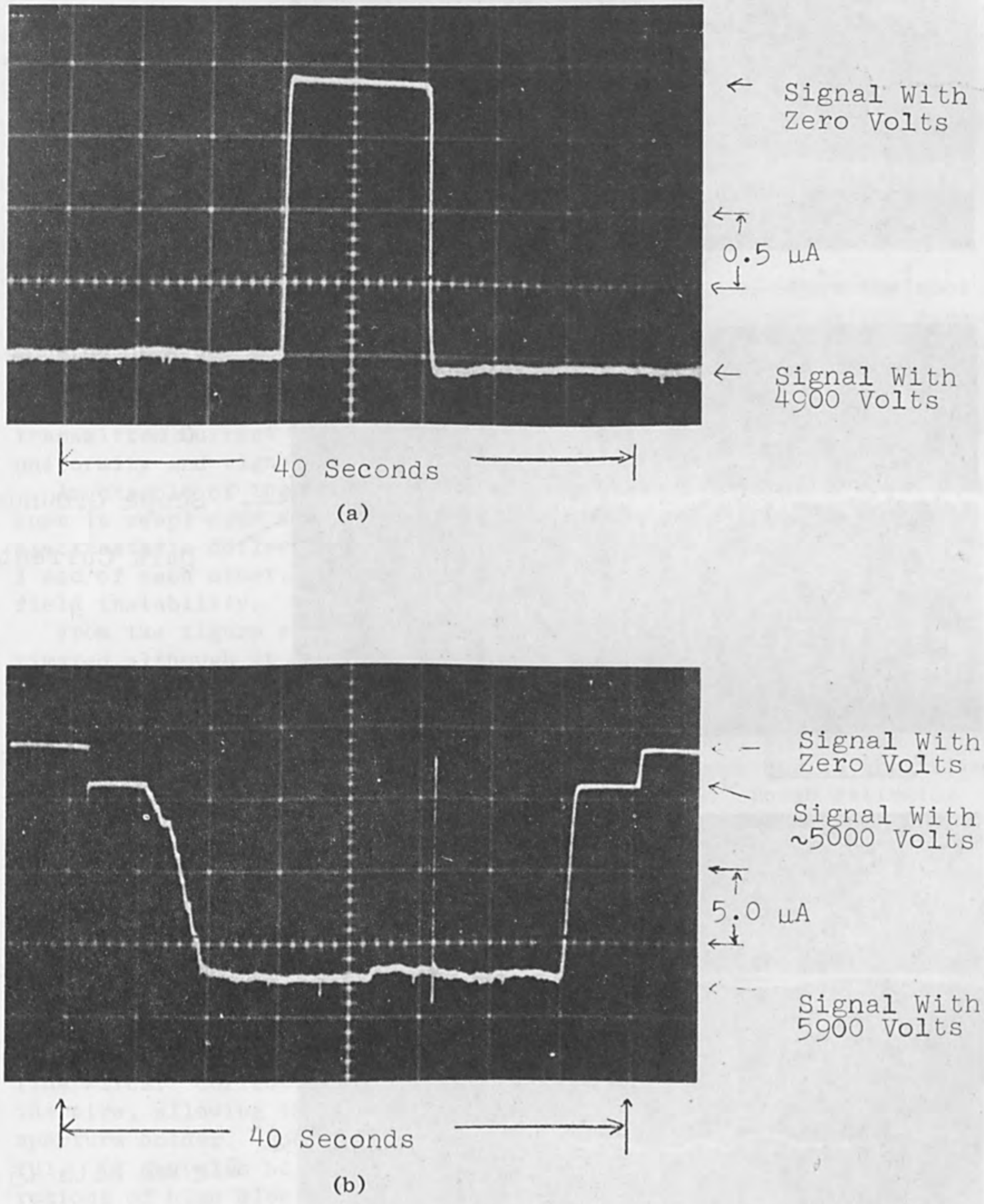

FIG. 2.—Oscillographs showing electrical stability of total field emission current for (a) 1.9 µA and (b) 16 µA.

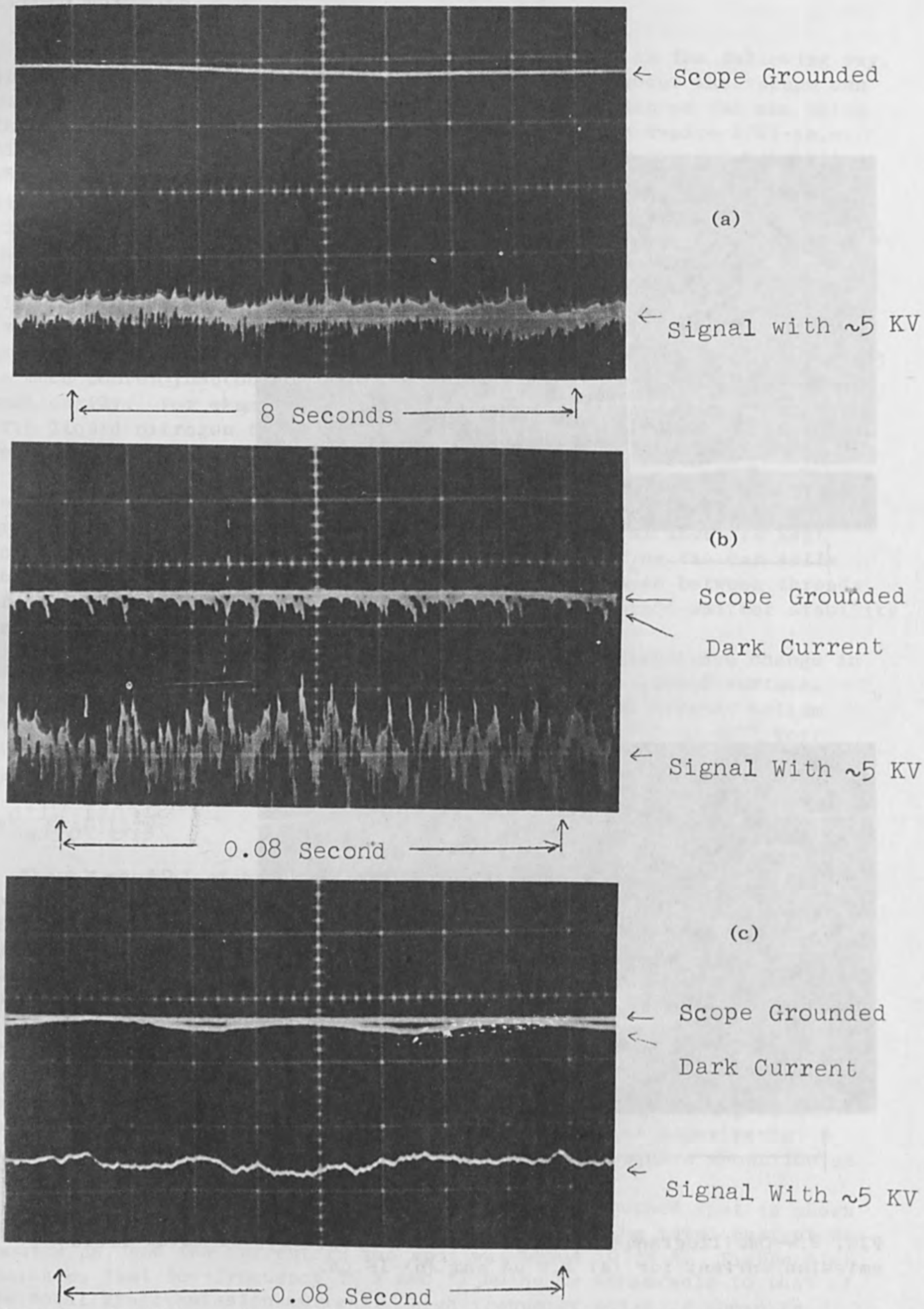

FIG. 3.—Oscillographs showing electrical stability of current in focused spot (a) over 50 sec with an RC time constant t ≈ 0.04 ms, (b) over 0.05 sec with t ≈ 0.04 ms, and (c) over 0.05 sec with t ≈ 4 ms. Photomultiplier dark current is also shown in (b) and (c).

respectively. The dark-current noise is also shown. From these and the known photomultiplier sensitivity we can infer that (1) the short-term instability is dominated by photomultiplier shot noise and (2) the light to the photomultiplier is less than 1 per cent of that expected, probably owing to poor phosphor material.

Our stability is certainly sufficient for resolution measurements in process of improving the microscope. The above indicates that it should be sufficient for actual scanning-microscope pictures, especially when our phosphor is improved. This stability is achieved with no care in cleaning and material selection. For example brass, soft solder, mylar, epoxy, and formvar-coated wire are used in the high-vacuum region. This fact illustrates a great advantage of the cryogenic field emission microscope.

V. RESOLUTION

An example of microscope action is shown in Fig. 4. Here the spot is swept roughly perpendicular to the bars of a 1500-mesh silver screen mounted on a 200-mesh electron microscope sample grid by an external magnetic field. Throughout it was found that the best focus occurred at considerable (more than 0.001-in.) deflections. Nonuniformity of transmitted current peaks is attributed to the effects of phosphor nonuniformity and vignetting by the 1/32-in. aperture.

An example of the resolution obtained is shown in Fig. 5. Here the spot is swept over the edge of a silver screen wire by the internal electrostatic deflectors. Two 1/10-sec. sweeps are made manually within 1 sec of each other. The dual trace is probably due to magnetic biasing field instability. The voltage for both Figs. 4 and 5 was 5 kV.

From the figure a resolution of a few thousand Ångstroms can be estimated although it seems better than that at the left of the figure. For our configuration, we expect 100-Å resolution at 10 kV, dominated by spherical aberration. The difference is probably due to off-axis aberrations (e.g., coma) caused by aperture misalignment, and perhaps to other electron optical asymmetries. It does not seem due to aberrations caused by the lens action of the 1/32-in. aperture. Rough estimates show that for our configuration, the much stronger objective lens always dominates the chromatic and spherical aberration of the system. Thus specially shaped apertures of the type devised by Butler[3] are not needed.

VI. FUTURE WORK

The previously described work suggests many improvements. To attain 100-Å resolution the 0.0015-in. aperture must be better aligned, which might be done by nudging it slightly with leaf springs held taut with fine wires. Current pulses through the wire momentarily heat and expand the wire, allowing the spring momentarily to push against a clip held aperture holder. Room-temperature tests of this technique were successful. It may also be necessary to improve cylindrical symmetry in all regions of high electric field.

The optimum theoretical resolution of our microscope is about 20 Å at 10 kV. This takes into account spherical and chromatic aberration, diffraction, and electron-source size. It will require a 0.7-mil-diameter aperture. This will reduce the current at the focus. To compensate we must improve the phosphor and/or make better thermal contact between the

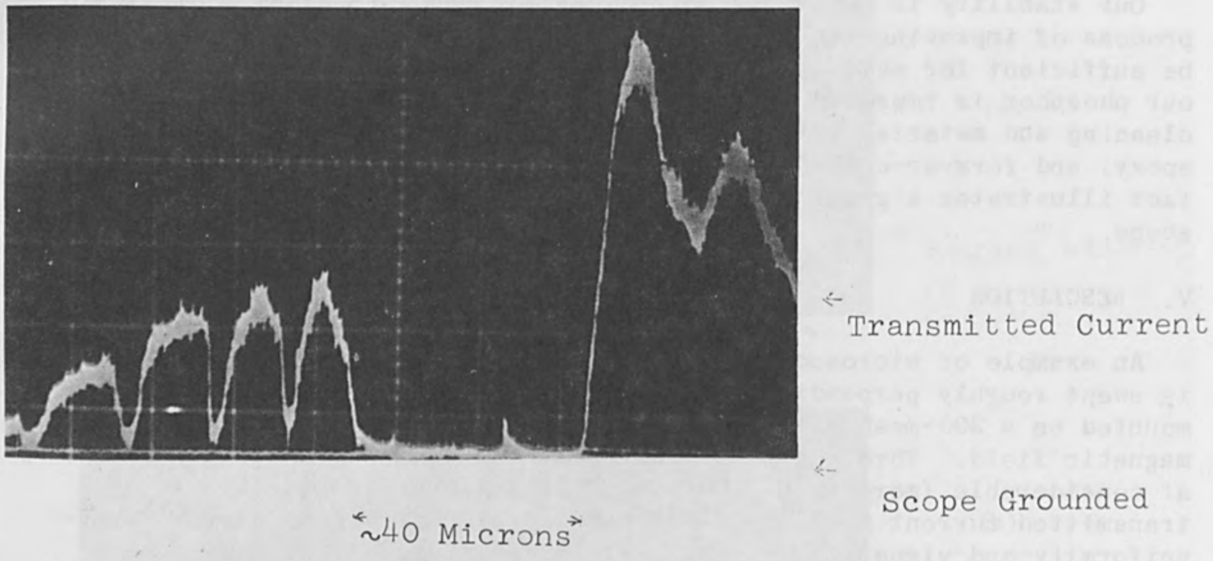

FIG. 4.—Transmitted electron current as focused spot is swept over 1500-mesh silver screen (mounted on 200-mesh microscope sample grid) by magnetic field.

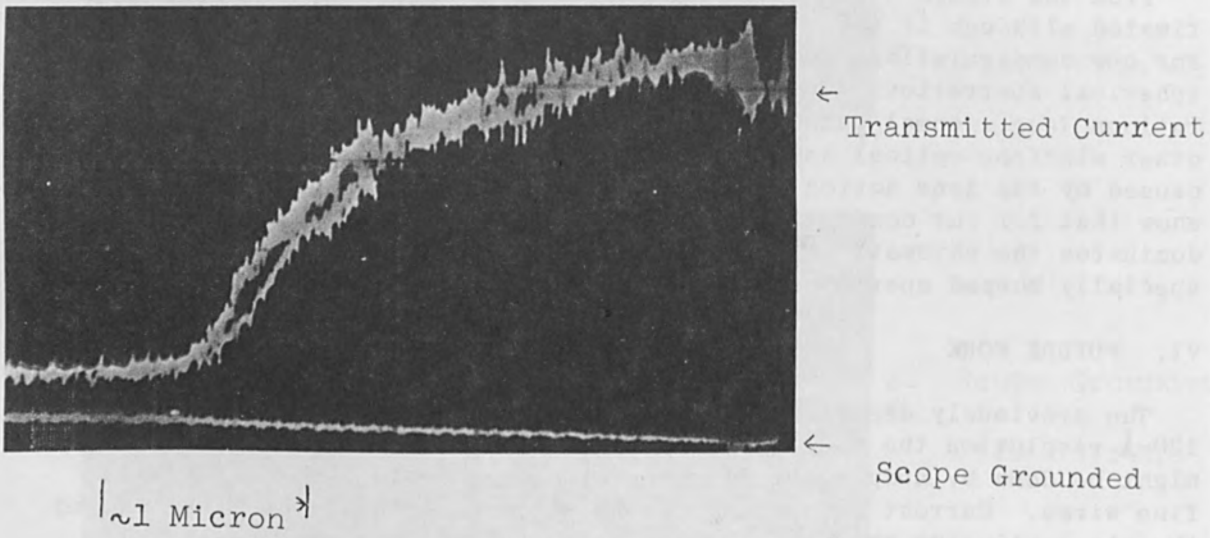

FIG. 5.—Transmitted electron current as focused spot is swept over edge of single silver screen wire.

anode and the helium bath so that the field emitter current may be safely increased. For the latter we may make use of an indium-soldered single-crystal quartz wafer. It serves as a thermal short and an electrical insulator.

To improve the resolution to 10 Å at 10 kV, a miniature magnetic lens excited by Alnico cylinders may be used. Such a lens failed to show a focus earlier in the work, probably owing to a large background of secondary electrons from the long narrow bore of the lens. (Here a Faraday cup detector was used.) Thus special apertures may be needed. Also such a lens considerably restricts the sample holder and detector configuration.

Mechanical vibration[7] may be a problem at higher resolution owing to the relatively thin support and low demagnification of the field-emitter electron source. At present the microscope cart is mounted on four aircraft tire inner tubes as a precaution. A further precaution would be to mount our field emitter on the end of a cylindrical cylinder, tapered on the end instead of on a thin hairpin. This configuration is also less astigmatic and easier to assemble. Several experiments of this type were performed with a 1/16-in.-diameter by 3/4-in.-long cylinder.

Of course a new way must be used to heat the emitter. The most successful way that was tried was to charge two 250-pf capacitors to the voltage needed for 0.1 μA and place them in series with the emitter and a variable resistor. The large current pulse from this voltage doubling would heat the emitter tip[8] enough to clean it when the resistance was lowered to the correct value. In practice the correct resistance value was difficult to find and the emitter tip would often be deformed so that the emitter current would no longer be peaked in the forward direction.

A great convenience would be to substitute screw (or solder) connections for grease to increase thermal conductivity. This method should reduce precooling time and liquid helium consumption (at present about 20 l per 3-hr run). It should also significantly reduce run preparation time. It now requires about 1 day to change the field emitter and sample, clean and grease the microscope, tighten set screws and align the field emitter (via a laser).

Ultimately higher voltages may be used for higher resolution. Also a compact energy analyzer of the counterfield type[9] could be incorporated to measure electron energy losses. However, calculations show that even at 10-Å resolution, single heavy atoms attached to DNA on a 100-Å thick carbon substrate may be detected by measuring small and large angle scattering.

VII. CONCLUSION

The microscope described above is relatively inexpensive and easy to modify. Although marginally useful now, it has a large potential and many simple improvements suggest themselves. Perhaps most important, it may motivate cryogenic scientists to enter the scanning electron microscope field as Crewe's microscope has motivated high-energy scientists.

ACKNOWLEDGMENTS

We wish to thank J. McGee and H. Hodges for expert technical assistance. Also we wish to thank the National Institutes of Health for

support in the design stages of the instrument.

REFERENCES

1. J. Hillier, Encyclopaedia Britanica, vol. 8, p. 335, 1951.
2. A. V. Crewe, Science 154: 729, 1966.
3. A. V. Crewe, D. N. Eggenberger, J. Wall, and L. M. Welter, Rev. Sci. Instr. 39: 576, 1968.
4. R. Gomer, J. Chem. Phys. 20: 1772, 1952.
5. W. R. Savage and F. J. Low, Rev. Sci. Instr. 35: 848, 1964.
6. H. Fernandez Moran, Proc. National Academy of Sciences 53: 445, 1965.
7. A. N. Broers, 26th Annual Meeting, Electron Microscopy Society of America (New Orleans), p. 294 (Sept. 1968).
8. W. P. Dyke, J. K. Trolan, E. E. Martin, and J. P. Barbour, Phys. Rev. 91: 1054, 1953.
9. H. Heil, Bull. Am. Phys. Soc. 7: 488, 1962.

ION THINNING OF ELECTRON MICROSCOPE SPECIMENS

N. J. TIGHE and B. J. HOCKEY

National Bureau of Standards (Inorganic Materials Division,
Institute for Materials Research), Washington, D. C.

INTRODUCTION

The present paper concerns the application of argon ion bombardment to the preparation of ceramic specimens for study by transmission electron microscopy. Ionic thinning was first used for preparing metal specimens for electron microscopy.[1] However, work done by Castaing and Jouffrey[2] showed that most metals suffered severe radiation damage which changed the initial substructure of the samples. Castaing performed thinning experiments on gold foils in the electron microscope and showed the development of dislocation loops at low temperatures and argon-filled bubbles when the specimens were thinned at temperatures over 200°C. The radiation damage, in addition to slow rates of materials removal, discouraged extensive use of ionic thinning for metals which could be thinned readily by electro-chemical methods. Most ceramics are insulators and are chemically inert; thus chemical and electrochemical thinning methods can be used only with great difficulty for single crystals and are not useful for polycrystalline bodies. Ionic thinning has become a useful technique for preparing electron-microscope specimens from ceramic materials because (1) the times necessary for thinning a sample are comparable to those needed for some chemical methods, (2) the radiation damage from argon ions is less severe in ceramics than in metals, and (3) the existing dislocation substructures in a sample are not changed by the thinning method. In this laboratory, a number of ceramic materials have been studied including alumina, magnesia, silica, and zirconia in both single and polycrystalline forms.[3]

Initial work was done with polycrystalline Al_2O_3 because results could be compared with the electron microscopic results of Barber and Tighe on chemically thinned single crystal Al_2O_3 (corundum).[5] Observations on neutron-irradiated corundum showed that point-defect clusters did not interact with grown-in dislocations but that annealing at temperatures in excess of 1000°C caused interaction with increasing temperature, dislocation loops formed, and some precipitation on grown-in dislocations occurred.[5c]

BOMBARDMENT APPARATUS

The ionic bombardment apparatus was that by Paulus and Reverchon.[6] Figure 1 is a schematic of the bombardment chamber showing the positions of the ion guns A, specimen holder B, motor for specimen rotation C, viewing telescope D, and sensor for the ion beam current E. The vacuum system has a diffusion pump with a capacity of 350 l/sec which maintains a pressure of 10^{-3} Torr during operation. The specimen holder consists of two stainless-steel or aluminum plates 3 cm in diameter held together by screws. The details of the ion gun are shown in Fig. 2, where the anode A, cathode B, insulator tubes C, and gas inlet D are marked. The anode-cathode separation is adjustable and for operation at 6 kV is set at 0.8 mm. Teflon insulating tubes are used instead of the original

Record of 10th Symposium on Electron, Ion, and Laser Beam Technology (L. Marton, ed.); San Francisco Press, Inc.
Copyright © by The Institute of Electrical and Electronics Engineers, Inc.—Printed in the U.S.A.

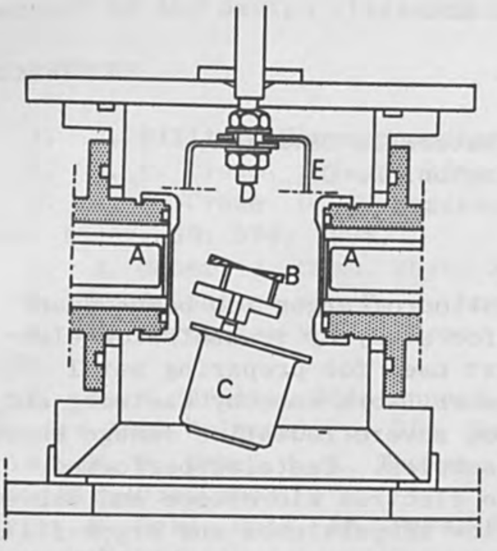

FIG. 1.—Bombardment chamber showing ion guns A, specimen holder B, motor C for specimen rotation.

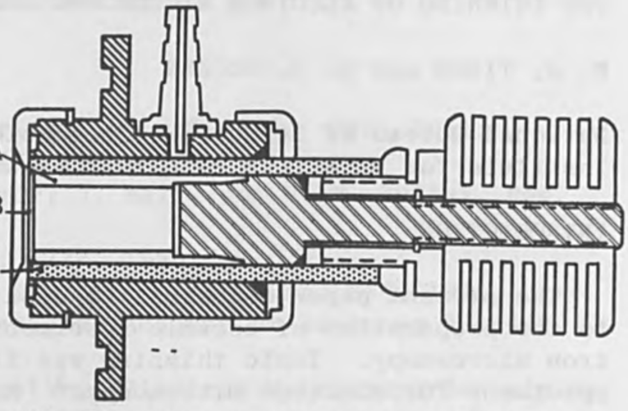

FIG. 2.—Ion gun showing anode A, cathode plate B, insulating tube C, and outer case for attachment to bombardment chamber.

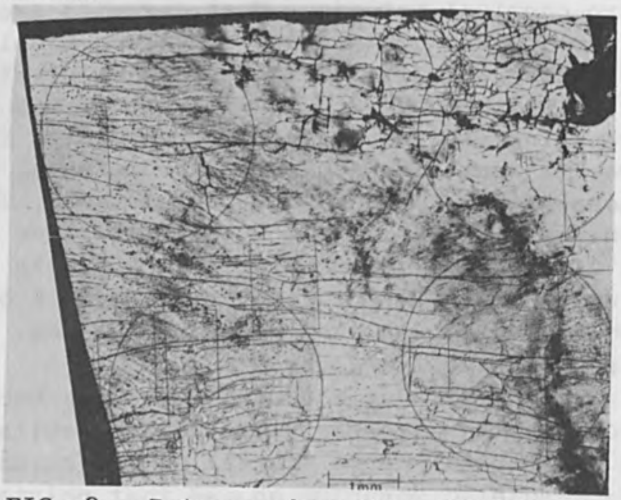

FIG. 3.—Petrographic thin section of Brazil quartz deformed under confining pressure.

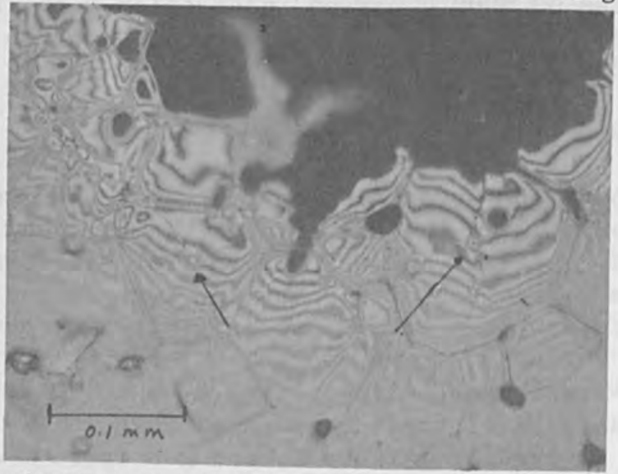

FIG. 4.—Optical micrograph of thin area in polycrystalline alumina specimen; hardness indents are arrowed and fringes are optical interference fringes for green light.

glass tubes but because they expand during operation, the outer brass holder is grooved to allow even gas flow. Both guns are operated from the same power supply and the beam current is varied by adjusting the gas flow.

Prior to ion thinning, disks 3 mm in diameter are cut from mechanically polished sections. The disk thickness is limited only by the fragility of a sample and the depth of polishing damage and typically is 40 to 60 μm. Samples which were particularly fragile or fragmented because of internal strain and fracture resulting from deformation could be prepared by cementing a supporting ring to the thin section or to the disk specimen. It was possible to make four specimens from the quartz sample shown in Fig. 3 by this technique. These supporting rings also are useful for samples which are less than 3 mm in diameter.

Most of the materials were thinned using an operating voltage of 4 to 6 kV and a beam current of 100 A/cm^2 in each gun. Some typical thinning rates are as follows: Al_2O_3, Fe_2O_3, ZrO_2 1 μm/h; SiO_2, Cu_2O, 4 μm/h; MgO, 0.5 μm/h for both single and polycrystalline samples. Progress of thinning was monitored by removing the specimens and measuring the thickness with the fine focus of an optical microscope and during the final stages, by observing the optical interference fringes. The thinning process can be controlled so that special features of interest are in the thin areas. Figure 4 shows a polycrystalline Al_2O_3 sample which was indented and then thinned from one side. Final thinning was carried out carefully so that several hardness indents were in the electron transparent areas. Specimens can be rethinned after observing them in the electron microscope.

SURFACE CONDITION

A surface texture resulted from ionic thinning and can be detected in some of the micrographs included in this paper. Surface attack in the form of pits and sometimes hillocks occurred on one or both surfaces of some single crystal specimens. These features could not be associated uniquely with either dislocations or impurity precipitates and therefore were similar to the randomly occurring features which form on surfaces during thermal etching rather than to dislocation etch pits resulting from chemical etching. Surface texture results from non rotation of the sample, shadowing by particles of dirt or the edges of the specimen holder, and contamination build-up in ion guns and in the chamber.

EXAMPLES OF ION THINNED SPECIMENS

Satisfactory electron-microscope specimens have been prepared from many ceramic materials regardless of composition, porosity, and total strain resulting from deformation. Grain boundaries and pores were not etched preferentially and sufficient thin area--of a few thousand angstroms thickness--was present to obtain information on the microstructure. A few examples are given below.

Figure 5 shows a region in the quartz sample of Fig. 3. The area shows the high dislocation density expected from the deformation, pores, and a fault. Analysis of the deformation substructure is complicated by rapid damage caused by the electron beam during observation. The sequence in Fig. 6 shows the progress of the damage. Small damage centers form and become amorphous and the region under observation becomes

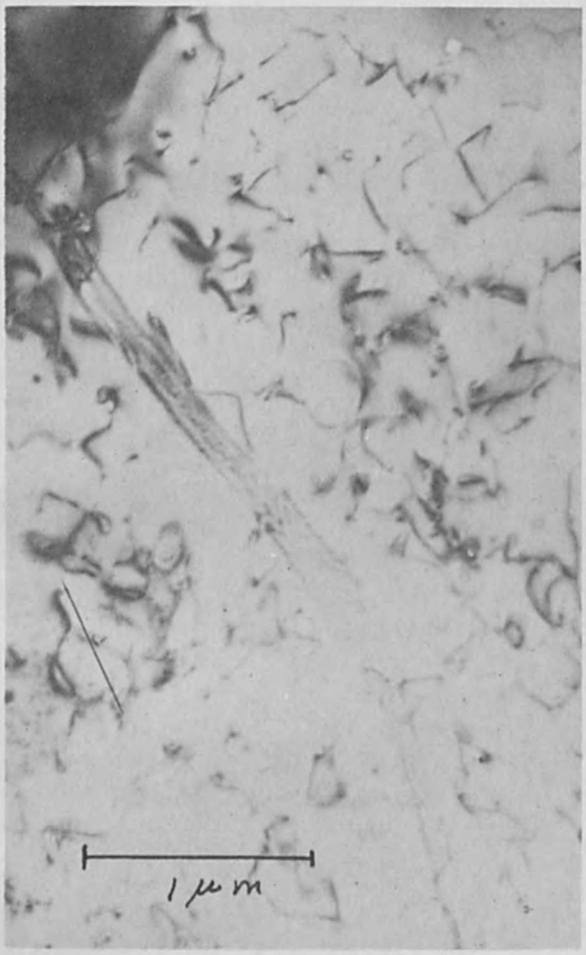

FIG. 5.—Dislocation arrangements in quartz specimen of Fig. 3.

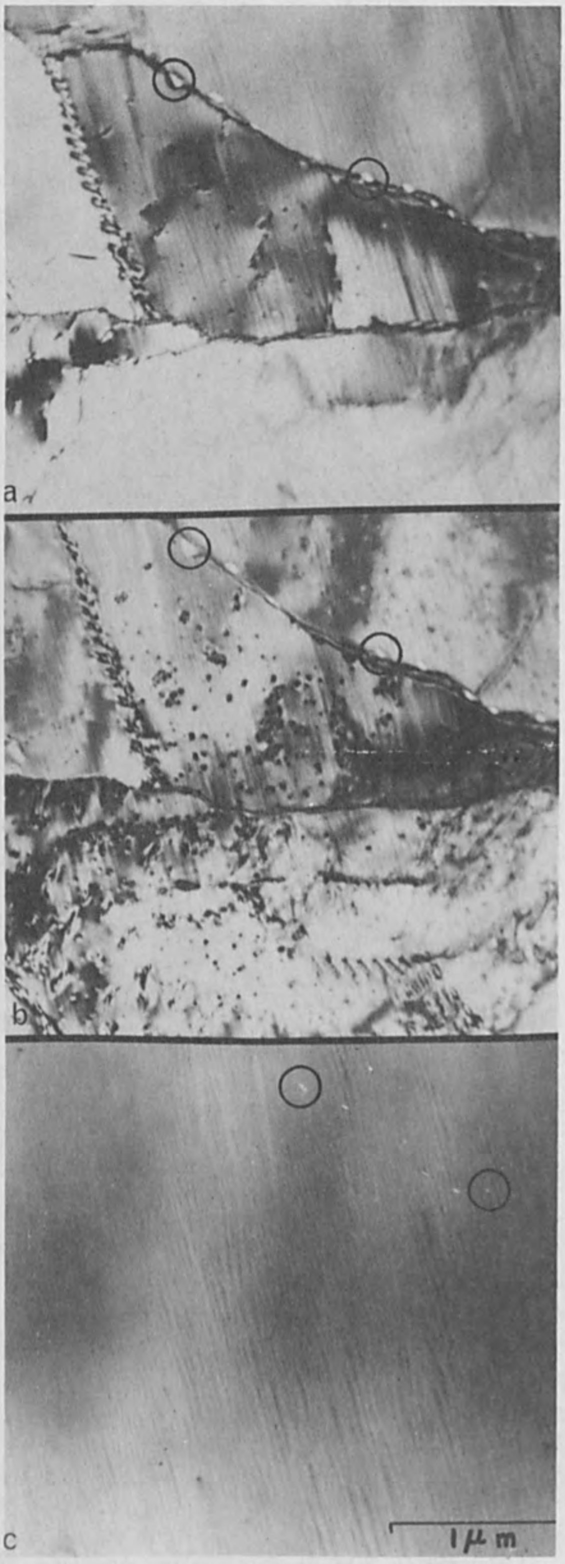

FIG. 6.—Area in Orcopia quartzite showing progress of vitrification induced by electron beam during observation: (a) less than 1/2 min, (b) after 2 min, (c) after about 12 min.

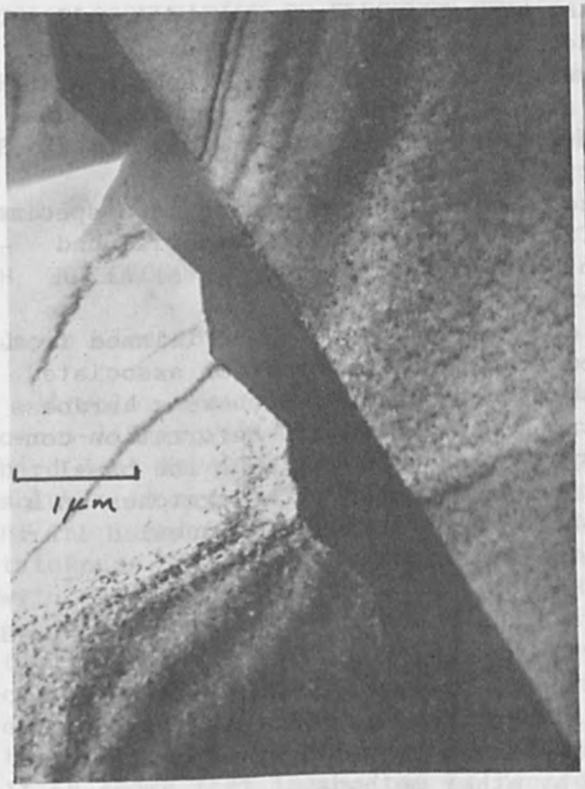

FIG. 7.—Grains in hot-pressed Al_2O_3 sample.

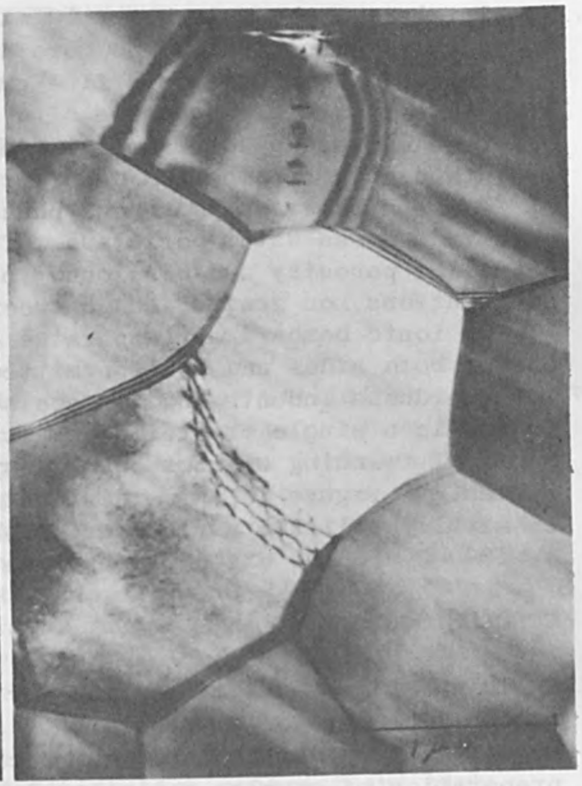

FIG. 8.—Amorphous phase A between MgO grains in periclase refractory brick.

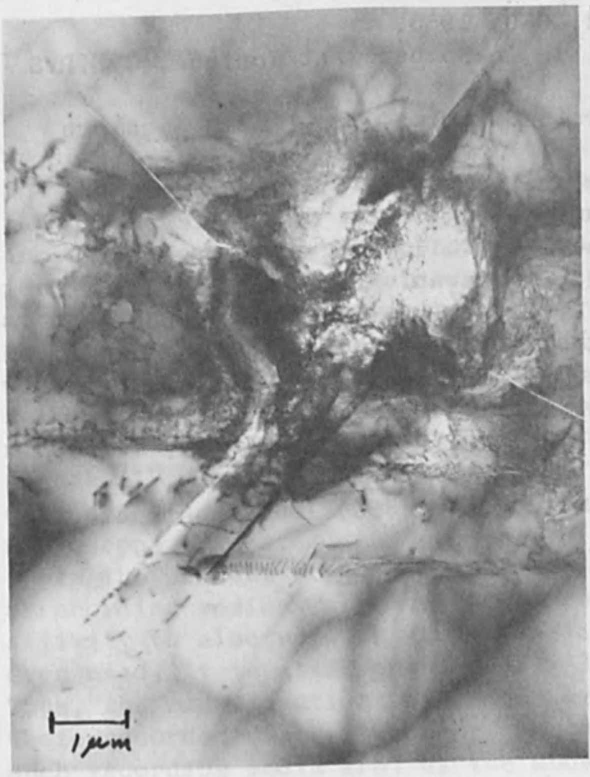

FIG. 9.—Hardness indent in rhombohedral plane of corundum specimen.

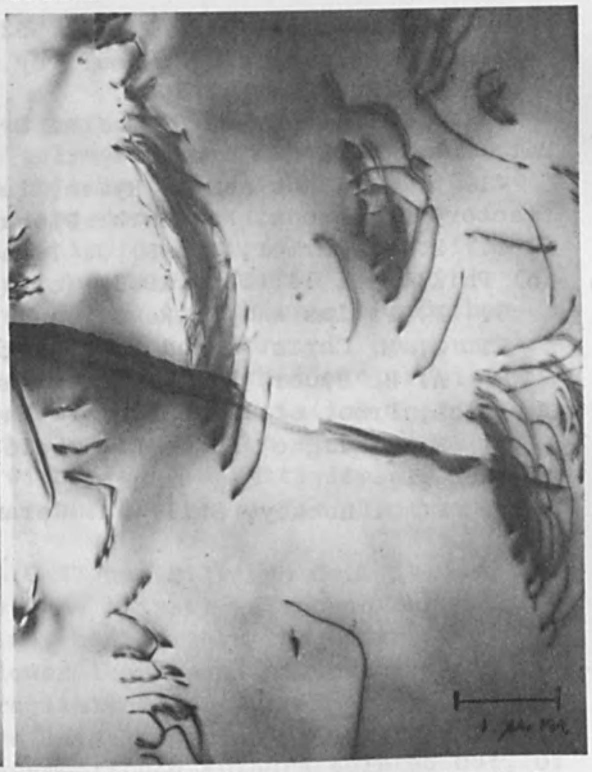

FIG. 10.—Dislocations associated with surface scratches on an alumina (Al_2O_3 + $\frac{1}{4}$% MgO) specimen.

completely amorphous in about 10 min. Vitrification occurred in all of the quartz rocks studied and more details are presented separately.[7]

Figure 7 is an area in a fine-grained hot-pressed Al_2O_3 sample. The area shows the microstructure of a sample deformed 3% by bending. The electron microscopy done on this material provided direct evidence for grain boundary sliding and deformation twinning.[8]

Figure 8 shows an amorphous phase between two MgO grains in a specimen made from a sea-water periclase refractory brick. This material had about 19% porosity and was found to contain second-phase material on dislocations, on grains, and between grains.[9]

The ionic bombardment apparatus allowed specimens to be thinned from one or both sides and thus permitted studies of deformation associated with hardness indents and surface scratches. Figure 9 shows a hardness indent in a single crystal Al_2O_3 (sapphire) specimen. Deformation consists of twinning on rhombohedral systems and some slip on the basal system.[10] Figure 10 shows dislocations associated with scratches on a chemically polished surface of sapphire. The sample was annealed 1 hr at 1000°C and the dislocations have moved slightly.

CONCLUSIONS

Thinning of ceramic material for study by ionic bombardment can be accomplished by ionic bombardment. The process is slow and introduces some radiation damage into the specimens; however, the process permits preparation of samples not possible by other methods.

REFERENCES

1. R. Castaing, Rev. Metall. 52: 669, 1955.
2. R. Castaing and B. Jouffrey, in Le Bombardment Ionique, C.N.R.S. No. 113, 62-69, Paris, 1966.
3. N. J. Tighe, in Ultrafine Grain Ceramics, Proc. 15th Sagamore Mat. Conf. 1968 (in press).
4. N. J. Tighe and A. Hyman, in Anisotropy in Single-Crystal Refractory Compounds, New York: Plenum Press, 1968.
5. D. J. Barber, and N. J. Tighe, (a) Phil. Mag. 11: 495, 1965; (b) Phil. Mag. 14: 531, 1966; (c) J. Am. Ceram. Soc. 51: 611, 1968.
6. M. Paulus and F. Reverchon, J. Phys. Rad. 22: 103A, 1961.
7. J. M. Christie and N. J. Tighe, to be published.
8. A. H. Heuer, R. M. Cannon, and N. J. Tighe, in Ultrafine Grain Ceramics, Proc. of 15th Sagamore Mat. Conf. 1968 (in press).
9. N. J. Tighe and J. R. Kreglo jr., Bull. Am. Ceram. Soc. (in press).
10. B. J. Hockey, Bull. Am. Ceram. Soc. 48: 393, 1969 (abstract).

COLOR OBSERVATION OF ELECTRON MICROSCOPE IMAGES

K. KANAYA, H. KAWAKATSU, and N. ATODA

Electrotechnical Laboratory, Tokyo, Japan

and

H. YOTSUMOTO and A. ONO

Japan Electron Optics Laboratory Co., Tokyo, Japan

A color observation of electron microscope images utilizing the cross-linking phenomenon of a silicone resin is reported. When bombarded by an electron beam, the silicone becomes cross linked and insoluble in organic solvents. An image recorded as thickness variation of the insoluble layer presents interference color corresponding to the thickness. The measured cross-linking characteristics of the silicone with thickness of about 1 μm for 50-keV electrons are found to be in good agreement with a theoretical formula assuming that molecules initially present follow a Poisson distribution. On the basis of the colorimetric theory, optical characteristics governing the appearance of the recorded image are calculated. As a preliminary attempt, electron microscope images of magnification of several thousand are recorded. It is shown that images can be recorded with high contrast and high resolution by the recording method.

I. INTRODUCTION

It is well known that long-chain organic molecules, when bombarded by an electron or an ion beam, become polymerized or cross linked and that these materials are no longer soluble in organic solvents. Since the thickness of the insoluble layer corresponds to the intensity of the incident beam, this phenomenon is available for recording of electron or ion images. Recording methods of this type were reported by many authors[1-5] who used contamination layer formed by electron or ion bombardment. For more sensitive recording media, some organic compounds were investigated.[6] Recently, it has been reported that photoresist such as KPR (Eastman Kodak Co.) may be of great value in fabricating of microelectronic circuits combined with electron or ion exposure techniques.[7-9] In this field, materials with higher sensitivity are required and are also to be utilized as recording media for electron or ion microscope images.

In the present work, Silicone SH 410 (Toray Silicone Co.) is used as a recording medium for electron microscope images. Although the sensitivity to electrons is about ten times higher than the other materials ever used, it is still considerably lower than usual silver halide plates. Thus, the magnifications of images are limited to several thousand. These recorded images, however, can be largely optically enlarged, since such recording media are, as the above-mentioned authors pointed out, of high resolution. This recording method may offer a useful tool of quantitative analysis of electron microscope images, since current intensity

Record of 10th Symposium on Electron, Ion, and Laser Beam Technology (L. Marton, ed.); San Francisco Press, Inc.
Copyright © by The Institute of Electrical and Electronics Engineers, Inc.—Printed in the U.S.A.

transferred from a specimen is uniquely represented by the cross-linked thickness, i.e., the interference color.

II. CROSS-LINKING CHARACTERISTICS

The structure of the recording plate is shown in Fig. 1. On the clean surface of the glass plate, Al is evaporated several hundred angstroms in thickness. The organic substance is coated by use of a spinning table. The organic solution of Silicone SH 410 is applied to the Al-coated glass plate while stationary, after which the plate is spun at about 3000 rpm for 1 min. The thickness and the uniformity of the silicone layer depend on the concentration of the organic solution and the spinning speed. The plate coated with the organic substance is inserted into the normal position of photographic plates of an electron microscope and exposed to an electron image. For developing, the exposed plate is rinsed in trichloro-ethylene and then the cross-linked layer with thickness corresponding to the intensity of the incident remains on the base plate. After that, Al is evaporated on the surface. The thickness of the upper and the lower Al layer determines transmission coefficients of interfaces of the organic layer and is controlled so that brightness and purity of interference color of the transmitted light may be suitable for observation, i.e., about 300 Å in thickness.

Silicone SH 410 is a silicone polymer consisting of dimethylpolysiloxan with vinyl radicals, which is not photosensitive. When bombarded by electrons, double bonds of vinyl radicals change into free radicals and cross linking occurs. The experiments show that the thickness of the insoluble layer of the silicone t (Å) depends on the initial thickness of the organic film t_0 (Å) as well as the amount of exposure. The normalized value t/t_0, however, is a function of exposure charge density q (coul/cm^2) only, which is shown in Fig. 2, where measured values of t/t_0 of four samples different in the initial thickness almost coincide with each other within the experimental errors. Therefore, the relationships between t and q can be represented by

$$t = t_0 \cdot f(q) \tag{1}$$

where $f(q)$ is independent of t_0. From (1), "contrast" is

$$dt/dq = t_0 \cdot df(q)/dq \tag{2}$$

Accordingly, the contrast increases proportionally to the initial thickness t_0. Practically observed contrast, however, is also governed by the optical characteristics of the recording plate, which is theoretically calculated in the next chapter.

As is shown in Fig. 2, when the exposure charge density is less than about 5×10^{-8} coul/cm^2, any cross-linked layer does not remain after developing. Therefore, the recording plate is uniformly exposed more than 5×10^{-8} coul/cm^2, previously to being exposed to a magnified image (for convenience, which is called "pre-exposure"). If the pre-exposure is performed, the average exposure charge density required for recording an image can be reduced, that is, the sensitivity apparently

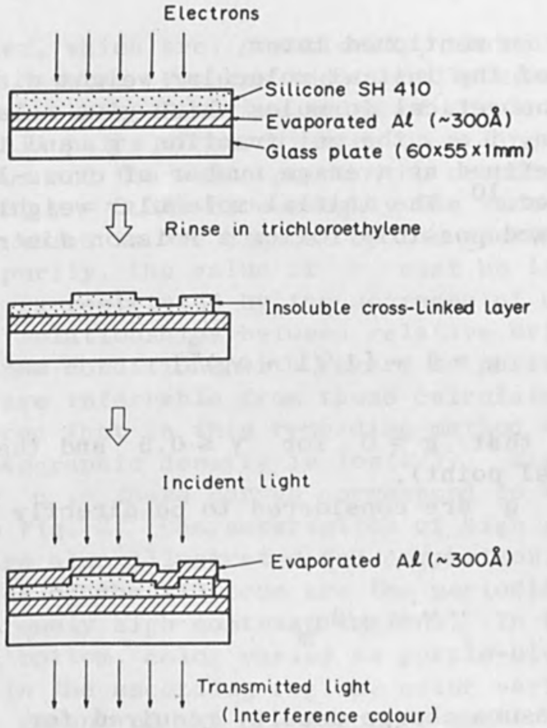
Electrons
Silicone SH 410
Evaporated Aℓ (~300Å)
Glass plate (60x55x1mm)
Rinse in trichloroethylene
Insoluble cross-linked layer
Incident light
Evaporated Aℓ (~300Å)
Transmitted light
(Interference colour)

FIG. 1.—Structure of color recording plate.

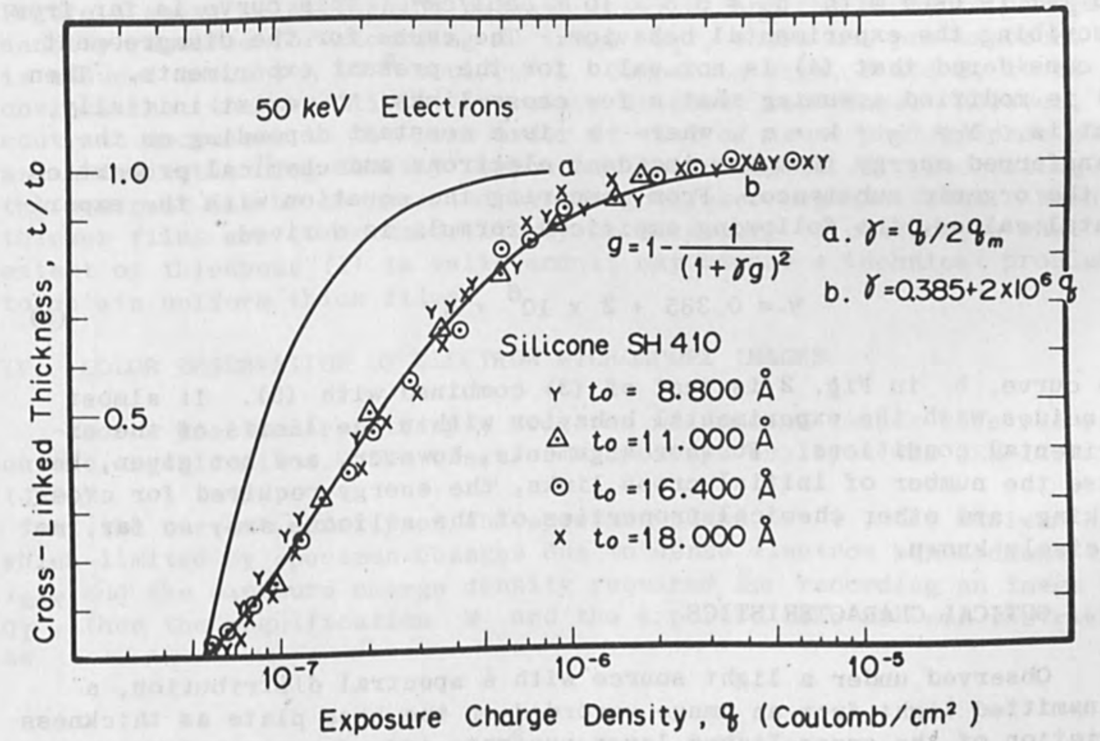

FIG. 2.—Cross-linking characteristics of silicone SH 410 for 50-keV electron.

increases, which will be mentioned later.

For several types of the initial molecular weight distribution of polymer substances, theoretical formulas which give relationships between the insoluble fraction, i.e., the gel fraction g and the cross-linking index γ, which is defined as average number of cross-links per molecule, have been derived.[10] The initial molecular weight distribution of the silicone employed possibly follow a Poisson distribution. For the case,

$$g = 1 - [1/(1 + \gamma g)^2] \qquad (3)$$

From (3), it is shown that $g = 0$ for $\gamma \leq 0.5$ and that gel formation starts at $\gamma = 0.5$ (gel point).

Generally, γ and q are considered to be directly proportional to each other.[6] Then

$$\gamma = q/2q_m \qquad (4)$$

where q_m is the exposure charge density required for γ to reach the gel point. The curve a in Fig. 3 is that of (3) where the gel fraction g is taken to be equivalent to the normalized thickness t/t_0 and (4) is used with $q_m = 5.5 \times 10^{-8}$ coul/cm^2. This curve is far from describing the experimental behavior. The cause for the disagreement is considered that (4) is not valid for the present experiments. Then (4) is modified assuming that a few cross-links γ_0 exist initially, that is, $\gamma = \gamma_0 + k \cdot q$, where k is a constant depending on the transferred energy from the incident electrons and chemical properties of the organic substance. From comparing the equation with the experimental values, the following empirical formula is derived,

$$\gamma = 0.385 + 2 \times 10^6 \cdot q \qquad (5)$$

The curve b in Fig. 2 is that of (3) combined with (5). It almost coincides with the experimental behavior within the limits of the experimental conditions. Further arguments, however, are not given, because the number of initial cross links, the energy required for cross linking, and other chemical properties of the silicone are, so far, not precisely known.

III. OPTICAL CHARACTERISTICS

Observed under a light source with a spectral distribution, a transmitted light from an image recorded on the base plate as thickness variation of the cross-linked layer presents interference color corresponding to the thickness. In order to perform quantitative as well as qualitative analysis of observed images, we must know the interference color and brightness as a function of thickness. For a simplified model, chromaticity coordinates were calculated on the basis of the colorimetric theory.[11] Figure 3 shows calculated color locus for $r^2 = 0.7$ where r is the amplitude reflection coefficients of the interfaces of the interference layer, which are, practically, controlled by the thickness of evaporated Al layers. Figures additionally remarked to the locus are values of nt (n is the refractive index of the interference layer) in terms of mμ. All pairs of coordinates on a line between a point on the spectrum locus and the white point (the coordinates of the light source: $x = 0.33$, $y = 0.33$) have roughly the same hue but differ in purity of color, which is the highest on the spectrum locus. In order to realize high purity, the value of r must be large. The large value of r, however, is restricted by the decrease of brightness. Figure 4 shows calculated relationships between relative brightness Y and thickness nt. Optimum conditions with regard to purity and brightness of observed images are inferrable from these calculated results.

It is considered that in this recording method what is equivalent to the ordinary photographic density is $\log(1/Y)$. Figure 5 shows $\log(1/Y)$ as a function of q. These curves correspond to the curve for $t_0 = 11\,000$ Å in Fig. 2. Characteristics of high resolution plates of Kodac and Fuji are also illustrated for comparison. Distinctive features of characteristics of the silicone are the periodical behavior and the existence of extremely high contrast regions. In the descending region from a peak to a bottom, color varies as purple-blue-green-yellow. On the other hand, in the ascending region, color varies as yellow-orange-red-purple. The amount of the pre-exposure mentioned in Sec. II has to be more precisely chosen from the view point of which region to be utilized. The pre-exposure apparently increases the sensitivity. Figure 6 shows relationships between $\log(1/Y)$ and the exposure charge density required for recording an image q_I, where the pre-exposure q_P is assumed to be 8×10^{-8} coul/cm^2. Comparing Figs. 6 and 5, it is obvious that the sensitivity increases by about ten times. However, the contrast decreases to the same order of that of usual photographic plates and undesirable "fog density" appears. According to (2), decreasing of the contrast can be compensated by using thicker organic films. When thicker films are to be used, it may be necessary to confirm to what extent of thickness (1) is valid and it may become a technical problem to obtain uniform thick films.

IV. COLOR OBSERVATION OF ELECTRON MICROSCOPE IMAGES

For a preliminary attempt, electron microscope images were recorded on the organic films. The electron microscope employed was JEM-120 (JEOL).

If the current density on the specimen plane is i, the maximum of which limited by specimen changes due to dense electron bombardment is i_{max} and the exposure charge density required for recording an image is q_I, then the magnification M and the exposure time T are restricted as

$$q_I = i \cdot T/M^2 \leq i_{max} \cdot T/M^2 \tag{6}$$

Further, the allowable displacement of an image due to the drift, D, also contributes to the restriction to the magnitude of M and T:

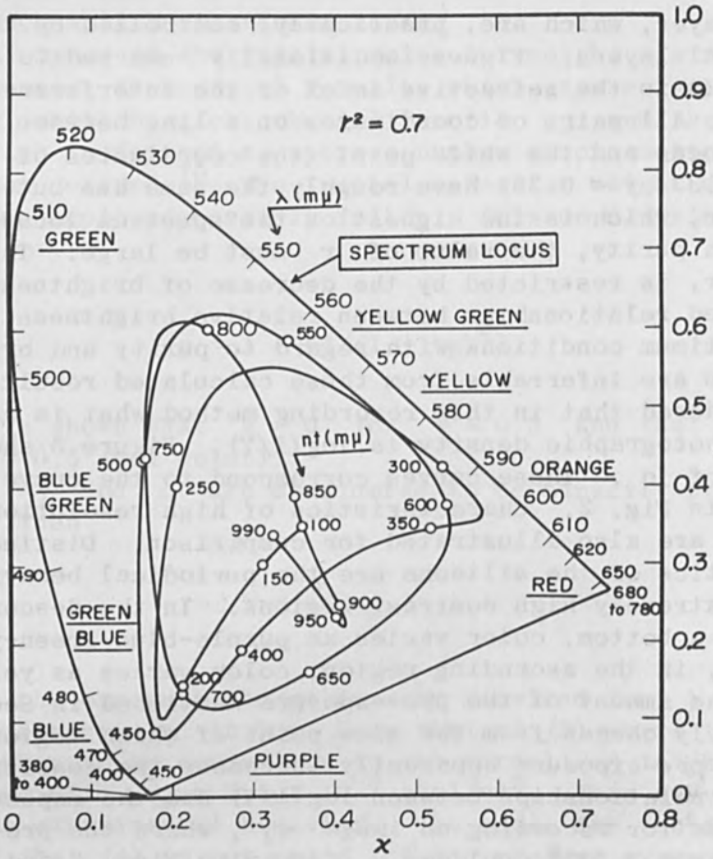

FIG. 3.—Locus of the interference color on the chromaticity diagram.

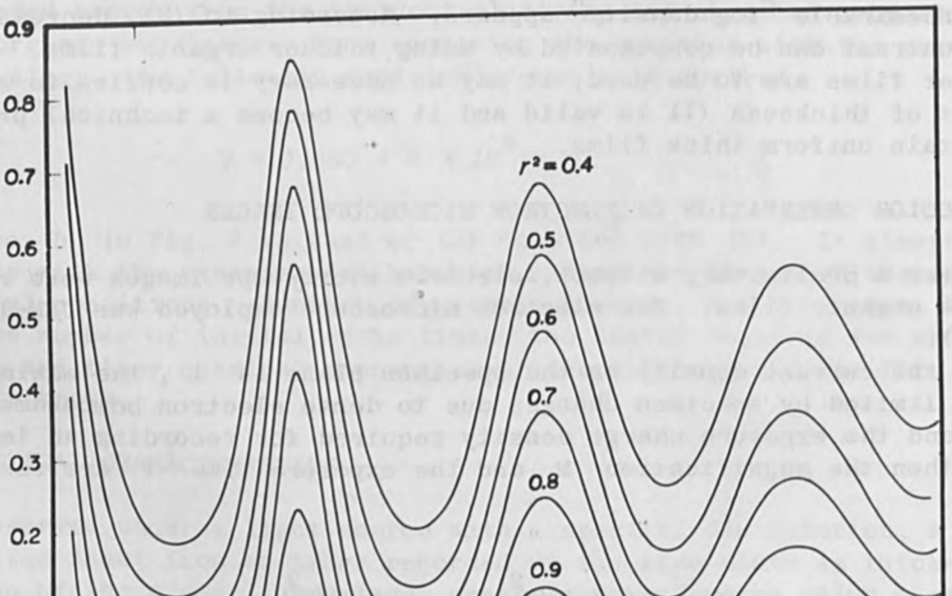

FIG. 4.—Brightness variation with thickness of interference layer.

$$D \geq M \cdot T \cdot d \qquad (7)$$

where d is the drift rate of the specimen. As an example, if $i_{max} = 10^{-1}$ A/cm^2, $d = 1$ Å/sec, $D = 1$ μm, and $q_I = 2 \times 10^{-8}$ coul/cm^2, then (6) and (7) give $MT \leq 10^4$ and $T/M^2 \geq 2 \times 10^{-7}$. Consequently, the magnification is limited to smaller than about X4000 and the exposure

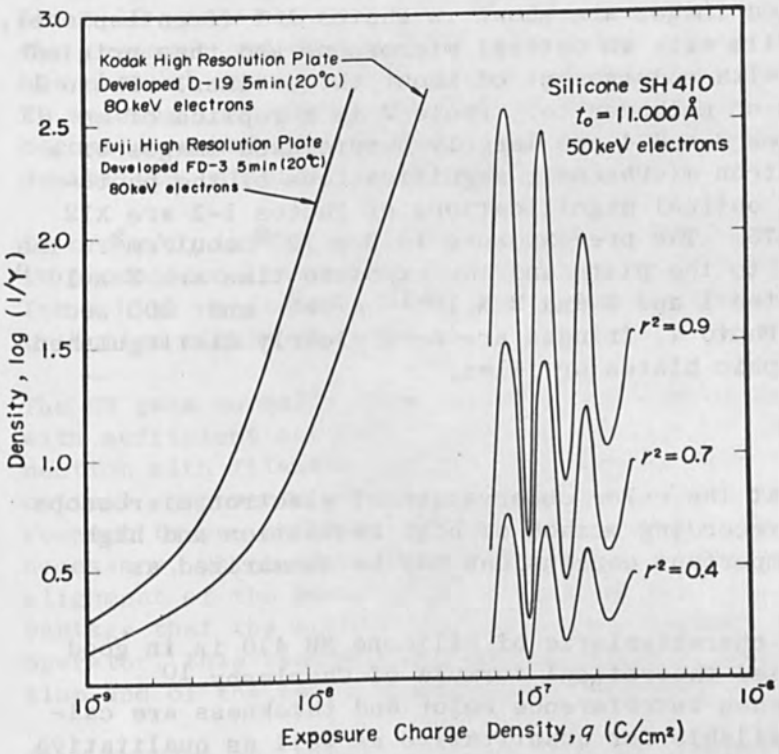

FIG. 5.—Characteristic curves of color recording plate and usual photographic plates.

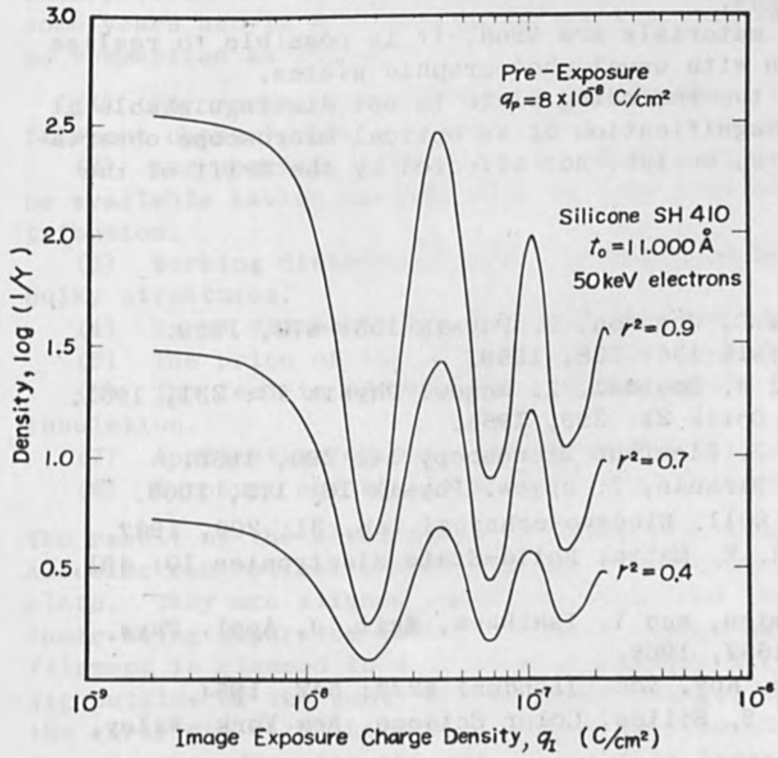

FIG. 6.—Characteristics of the color recording plate when the pre-exposure is 8×10^{-8} coul/cm^2.

time is several seconds. In the experiments, the exposure time was 10-20 sec when the magnification was several thousand. Accordingly, the displacement of images due to the drift might be larger than the value adopted above. Therefore, the resolution of the recording plate is chiefly affected by the drift, whereas the graininess of the recording plate is practically not distinguished at least up to X100 in the magnification of an optical microscope observation.

Photographs of recorded images are shown in Photos 1-4 (frontispiece), taken on a usual color film with an optical microscope and then printed on color printing paper with enlargement of about three times. Photo 1 is interference contours of molybdenite. Photo 2 is a replica of an etched Al crystal. Photos 3 and 4 are largely overfocused images of a plastic micromesh. Electron microscopic magnifications of the photographs are all X1500 and optical magnifications of Photos 1-3 are X12 and that of Photo 4 is X75. The pre-exposure is 9×10^{-8} coul/cm^2. The current density incident to the plate and the exposure time are 2×10^{-9} A/cm^2 and 20 sec for Photos 1 and 2 and 2×10^{-10} A/cm^2 and 200 sec for Photos 3 and 4. In Photo 4, fringes are more clearly distinguished than with usual photographic plates or films.

V. CONCLUDING REMARKS

It has been shown that the color observation of electron microscope images is a very useful recording method of high resolution and high contrast. Some of the important conclusions may be summarized as follows.

1. The cross-linking characteristic of Silicone SH 410 is in good agreement with the modified theoretical formula of Charlesby.[10]
2. Relationships between interference color and thickness are calculated, which may be available for quantitative as well as qualitative analysis of recorded images.
3. If more sensitive materials are used, it is possible to realize much higher contrast than with usual photographic plates.
4. The graininess of the recording plate is not distinguishable at least up to X100 in the magnification of an optical microscope observation and the resolution is, so far, not affected by the drift of the image.

REFERENCES

1. G. Möllenstedt and C. Jönsson, Z. Physik 155: 472, 1959.
2. R. Speidel, Z. Physik 154: 238, 1959.
3. G. Möllenstedt and R. Speidel, Z. angew. Physik 13: 231, 1961.
4. K. Kanaya et al., Optik 21: 399, 1964.
5. S. Matsui et al., J. Electron Microscopy 14: 290, 1965.
6. H. Hamisch and L. Binkele, Z. angew. Physik 16: 145, 1963.
7. K. Kanaya et al., Bull. Electrotechnical Lab. 31: 206, 1967.
8. M. W. Larkin and R. K. Matta, Solid-State Electronics 10: 491, 1967.
9. K. Kanaya, K. Shimizu, and Y. Ishikawa, Brit. J. Appl. Phys. (J. Phys. D, ser. 2) 1: 1657, 1968.
10. A. Charlesby, Proc. Roy. Soc. (London) A222: 542, 1954.
11. G. Wyszecki and W. S. Stiles, Color Science, New York: Wiley, 1967.

A NEW TYPE OF ELECTRON GUN

K. H. STEIGERWALD, W. E. MEYER, and W. SCHEFFELS

Steigerwald Strahltechnik, Munich

About 10 years ago, most of the electron beam (EB) machines were used for research and development work only. Since that time the picture has changed considerably. Great efforts have been made to introduce EB welding into production. From that time on, the EB gun designer has become more and more engaged with such questions as reliability, reproducibility, stability, and running costs.

In order to insure reproducible results many applications of EB welding in production lines with a higher degree of automation ask especially for a high constancy of the spot position and of the power density distribution within the spot.

The EB guns normally used so far often cannot meet these requirements with sufficient accuracy. During the life of the filament and in connection with filament change the geometric position of the electron optical components (filament, bias cup, anode, lens) may change with respect to one another. Therefore, a readjustment of the beam becomes necessary, which, for practical reasons, is normally restricted to an alignment of the beam to the center of the lens. Apart from the disadvantage that the accuracy of this step depends on the quality of the operator, this readjustment cannot inhibit variations of the spot position and of the power density distribution.

This problem and others arising from EB production applications resulted some years ago in a target specification, the main points of which may be summarized as follows:

(1) For normal application no readjustment of the beam (even after filament change) should be necessary.
(2) For special, high precision application a fine adjustment should be available having no influence on spot position and power density distribution.
(3) Working distances up to 2 m should be available for welding of bulky structures.
(4) Rapid filament change should be possible.
(5) The price of the filament should be reduced considerably.
(6) The feed-in of the high voltage should be possible without oil insulation.
(7) Application of soft vacuum within the chamber should be possible.
(8) A robust and simple construction is necessary.

The result of the development is shown in a simplified drawing (Fig. 1). All electron-optical components are fixed close to a central mounting plate. They are aligned during assembly and there is no necessity of their being separated when a filament change has to be made. The ribbon filament is clamped to a filament cartridge with close tolerances in a jig outside of the gun. For filament change, the top seal is opened, the cartridge with the used filament is removed by a special tool, a second cartridge with the new filament is inserted into a fixed position

Record of 10th Symposium on Electron, Ion, and Laser Beam Technology (L. Marton, ed.); San Francisco Press, Inc.

Copyright © by The Institute of Electrical and Electronics Engineers, Inc.—Printed in the U.S.A.

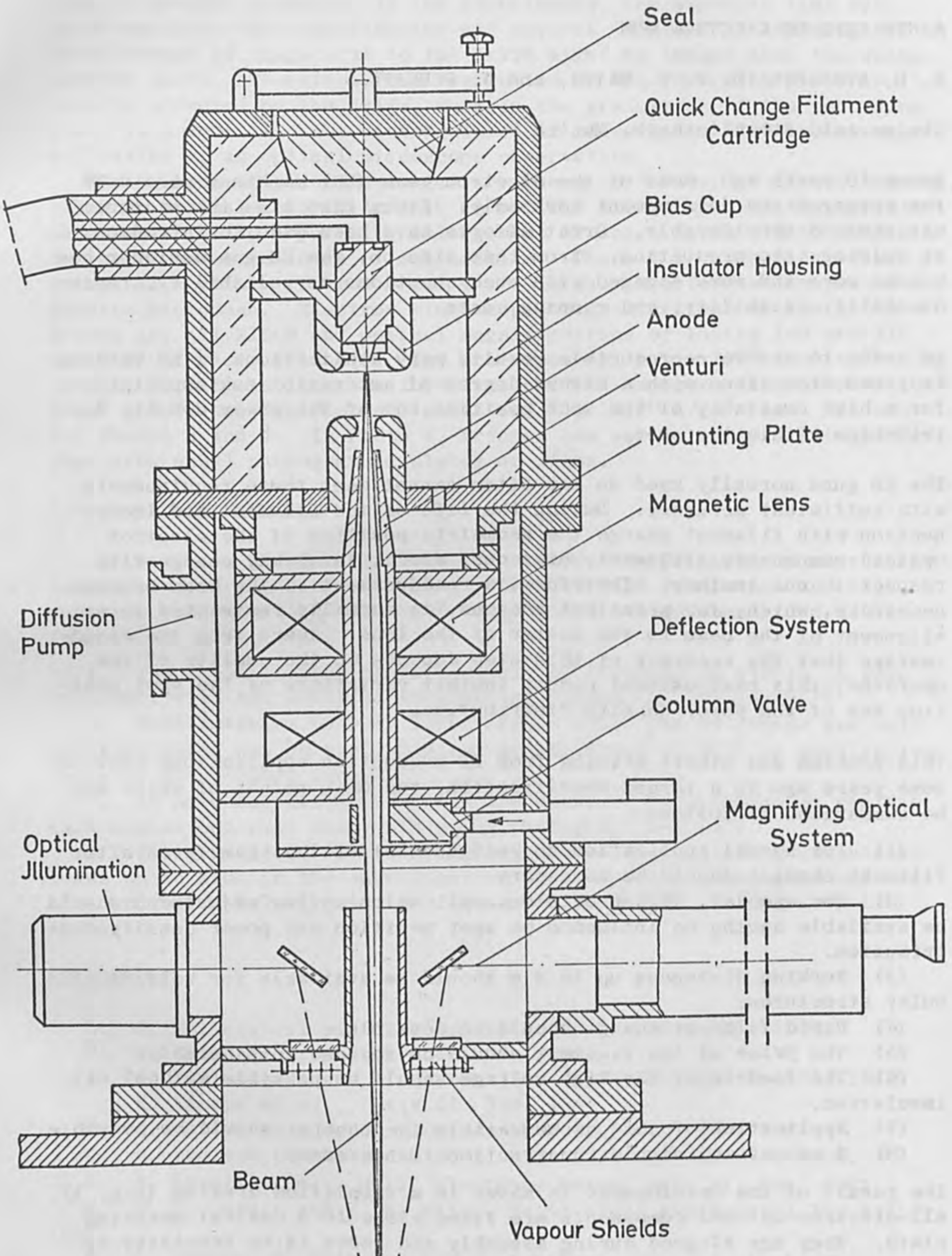
Seal
Quick Change Filament Cartridge
Bias Cup
Insulator Housing
Anode
Venturi
Mounting Plate
Magnetic Lens
Diffusion Pump
Deflection System
Column Valve
Magnifying Optical System
Optical Jllumination
Beam
Vapour Shields
Workpiece

FIG. 1.—Schematic drawing of new EB gun.

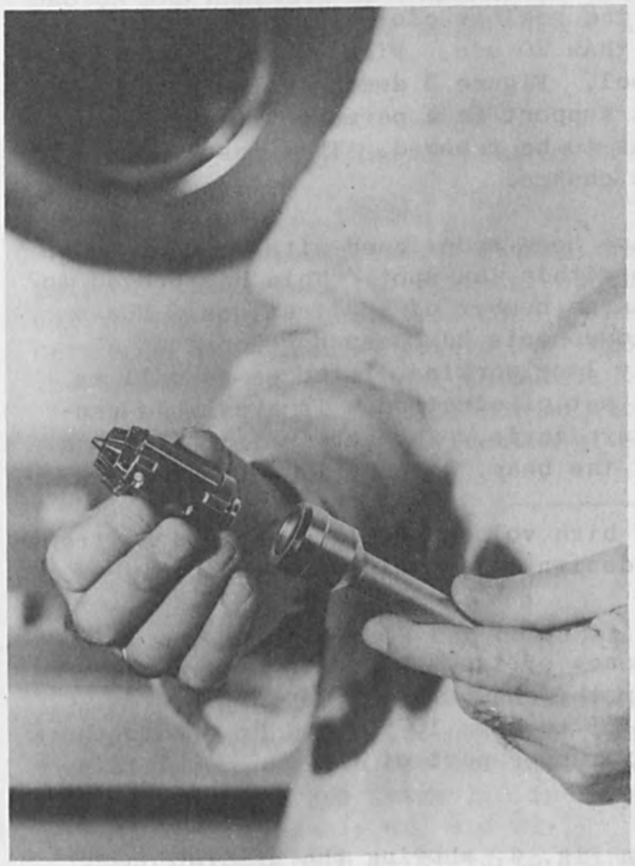

FIG. 2.—Filament cartridge with special tool.

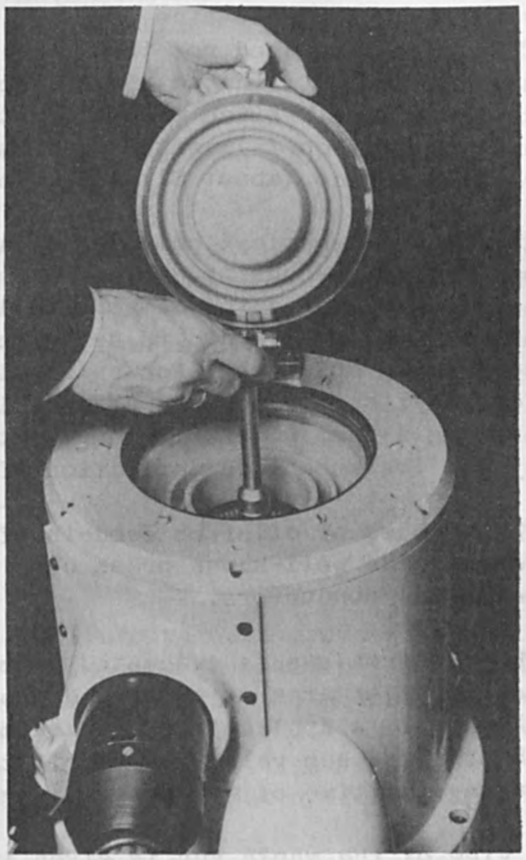

FIG. 3.—Filament change.

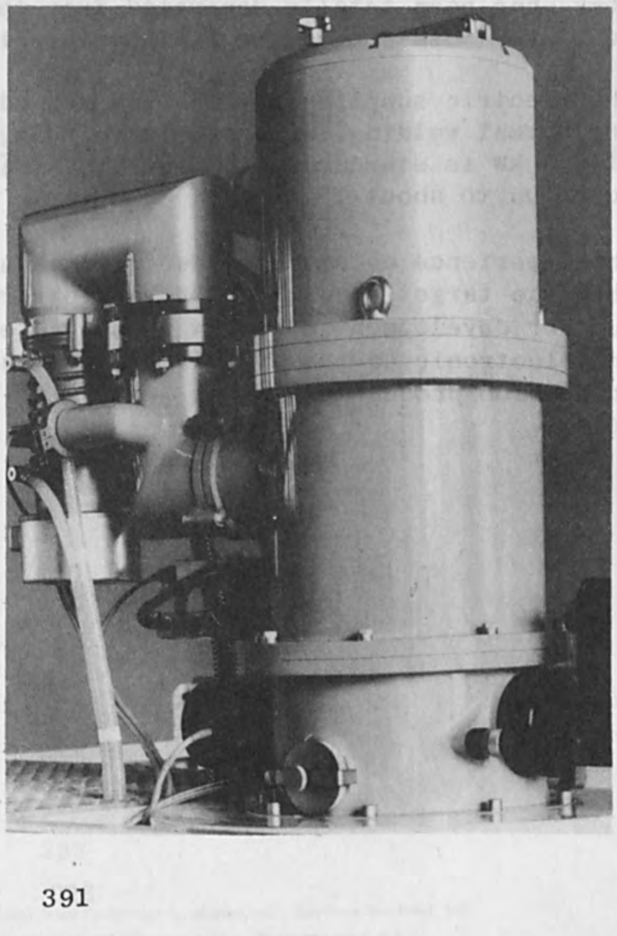

FIG. 4.—View of the new electron beam gun.

with respect to the bias cup, and the seal is closed for evacuation. This procedure need not take more than 20 sec. Figure 2 shows the filament cartridge with the special tool. Figure 3 demonstrates the cartridge change. Since the filament support is a permanent usable part, only the ribbon filament itself has to be renewed. This results in a very low price (about $1) for each change.

All electron-optical components have been redesigned with respect to an optimal power-density distribution within the spot. This has proved to be a most important factor for a large number of applications. For normal welding a standard set of components has been developed as a compromise solution. For extremely long working distances as well as for small spot diameters a special set of electrodes is available generating a beam with a larger aperture angle. The gun is fitted with a system for ac and dc deflection of the beam.

The problem of oil-free feed-in of high voltage could be solved by transferring the well-known press cone design to a cable with three high-potential conductors.

The electron gun is evacuated by means of its own pump system. The acceleration area is separated from the chamber by a Venturi system, which allows application of vacuum up to some 10^{-2} mm of Hg within the chamber. A gun valve closes off the upper part of the gun completely during the time of workpiece change.

A view of the whole gun is given in Fig. 4, showing the simple construction. The optical viewing system, still valuable for some type of work, has been totally separated from the electron optical part of the gun. For mass-production applications it may simply be omitted.

The electric supplies for the gun depend on the type of application. For normal welding, a high-voltage unit of 150 kV with a maximum power of 7.5 kW is standard. The gun itself is capable for application of power up to about 15 kW.

The experience obtained so far with this new type of gun have shown that the target specification has been reached in all important points. Further development must now concentrate on various types of electric and electronic equipment suitable for tape- or computer-controlled production processes.

DESIGN AND ANALYSIS OF SYMMETRICAL AND ASYMMETRICAL ELECTROSTATIC IMMERSION LENSES USING A DIGITAL COMPUTER

A. B. EL-KAREH

Syracuse University (Department of Electrical Engineering),
Syracuse, N. Y.

An analytical expression giving the potential distribution along the axis of symmetrical two-cylinder electrostatic immersion lenses is derived as has already been done by Bertram. The result is used to determine the cardinal points and important aberration coefficients of the lenses using a digital computer.

A similar analysis is performed with asymmetrical electrostatic immersion lenses using a derivation given by Lebedev et al.

I. INTRODUCTION

Electrostatic lenses can be classified into various groups one of which is the immersion lens. Figure 1 shows some examples of immersion lenses. Their common characteristic is the fact that the potentials in the object and image space are constant and unequal. Their name derives from their analogy to the oil-immersion objectives of light optics in which the object and image lie in media of constant but different indices of refraction, namely oil and air.

Some authors have referred to cathode lenses as immersion lenses since the object is here immersed in the lens. This is a misnomer.

It is well known that the paraxial ray equation can be reduced using the substitution $R = r\emptyset^{1/4}$ first suggested by Picht, and becomes

$$\frac{d^2R}{dz^2} = -\frac{3}{16}\left(\frac{\emptyset'}{\emptyset}\right)^2 R \tag{1}$$

Here the primes represent derivatives with respect to z.

For a weak lens, the focal length is given by

$$\frac{1}{f_o} = \frac{3}{16}\left(\frac{\emptyset_i}{\emptyset_o}\right)^{1/4}\int_{z_o}^{z_i}\left[\frac{\emptyset'(z)}{\emptyset(z)}\right]^2 dz \tag{2}$$

and

$$\frac{1}{f_i} = \frac{3}{16}\left(\frac{\emptyset_o}{\emptyset_i}\right)^{1/4}\int_{z_o}^{z_i}\left[\frac{\emptyset'(z)}{\emptyset(z)}\right]^2 dz \tag{3}$$

Record of 10th Symposium on Electron, Ion, and Laser Beam Technology (L. Marton, ed.); San Francisco Press, Inc.

Copyright © by The Institute of Electrical and Electronics Engineers, Inc.—Printed in the U.S.A.

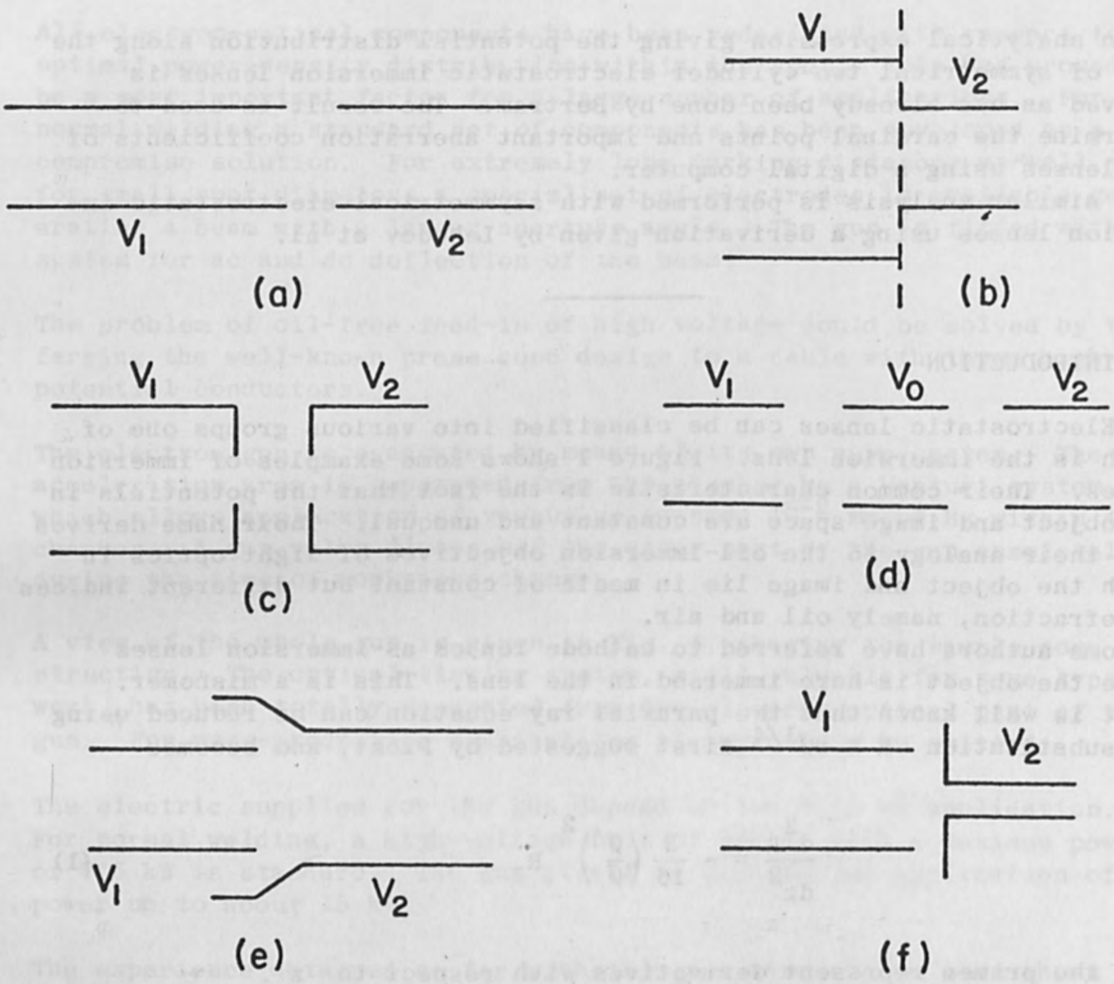
V1
V2
V1
V2
(a)
(b)
V1
V2
V1
V0
V2
(c)
(d)
V1
V2
V1
V2
(e)
(f)

FIG. 1.—Various types of electrostatic immersion lenses.

Record of 10th Symposium on Electron, Ion, and Laser Beam Technology (L. Marton, ed.), San Francisco Press, Inc.

Copyright © by The Institute of Electrical and Electronics Engineers, Inc.—Printed in the U.S.A.

The subscripts o and i refer to object and image side, respectively. As in light optics, we have

$$\left(\frac{\phi_o}{\phi_i}\right)^{1/2} = \frac{f_o}{f_i} \tag{4}$$

When the lens is strong, by which we mean that the height of the ray changes inside the lens, the above relations for focal lengths are no longer valid. The determination of the cardinal points is then made by computing the actual path of the ray through the lens. In any case, the potential distribution along the axis and its derivatives must be determined before the analysis of the lens can be made.

II. AXIAL POTENTIAL DISTRIBUTION OF THE SYMMETRICAL LENS

The potential distribution along the axis of two equidiameter cylinders separated by a distance S was first calculated by Bertram.[1] We shall quickly review the derivation here for the sake of clarity.

It is well known that

$$\phi(r,z) = \frac{1}{2\pi}\int_{-\infty}^{+\infty} a_k J_0(jkr)e^{jkz}\,dk \tag{5}$$

(in which J_0 is the normal Bessel function of the first kind of zero order) is a solution of Laplace's equation

$$\nabla^2\phi = 0 \tag{6}$$

If we consider two cylinders of potentials V_1 and V_2 separated by a distance S and of radius unity and assume that the potential in the gap varies linearly at $r = 1$, we finally obtain

$$\phi(0,z) = \frac{V_1 + V_2}{2} + \left(\frac{V_2 - V_1}{\omega S}\right) \log_e \frac{\cosh \omega z}{\cosh \omega(z - s)} \tag{7}$$

where $\omega = 1.32$. For very small separation, we let $S \to 0$ and obtain

$$\phi(0,z) = \frac{V_1 + V_2}{2} + \left(\frac{V_2 - V_1}{2}\right) \tanh \omega z \tag{8}$$

The value of ω was determined by equating the derivatives with respect to z at $r = 0$ and $z = 0$ of (8) and

$$\phi(0,z) = \frac{V_1 + V_2}{2} + \frac{V_2 - V_1}{\pi} \int_0^{\infty} \frac{\sin kz}{k} \frac{1}{J_0(jkR)} dk \tag{9}$$

which was obtained following the analysis of Bertram. Since $\phi(z)$ and its first and second derivatives are to be used in the analysis of a series of lenses, it was important to determine the accuracy of the simplifications introduced by (7) and (8). Tables I-III represent a computer comparison between the actual numerical integration and the relation given by (8). It can be seen that the error is very small at practically all the points. Where the errors become exceedingly large, at large distances from the lens, the field is very weak and therefore plays an insignificant role in the determination of the course of the trajectory.

Equations (7) and (8) were also checked with values obtained using the relaxation technique and the accuracy was remarkable even for values of $S = 2R$.

III. METHOD OF ANALYSIS OF THE SYMMETRICAL LENS

One way of analysis which looks very attractive because of its simplicity is the method of sectionizing the lens. For a given voltage distribution of the lens system, the parameter $[\phi'(z)/\phi(z)]^2$ is plotted as a function of z. First the center of gravity G on the z axis is determined by finding a line perpendicular to the axis which divides the area under the curve into two equal parts. Next, G_1 and G_2 are obtained as points on the z axis through which lines perpendicular to the axis divide each half area of the curve into two equal areas. Instead of one lens, we place two lenses, one at G_1 and one at G_2, each having reduced focal length given by

$$\left(\frac{1}{F_1}\right)_{\text{at } G_1} = \frac{3}{16} \int_{z_o}^{G} \left[\frac{\phi'(z)}{\phi(z)}\right]^2 dz \tag{10}$$

and

$$\left(\frac{1}{F_2}\right)_{\text{at } G_2} = \frac{3}{16} \int_{G}^{z_i} \left[\frac{\phi'(z)}{\phi(z)}\right]^2 dz \tag{11}$$

Since the areas are equal, $F_1 = F_2 = F$. We can now obtain the corrected reduced focal length F_c

$$\frac{1}{F_c} = \frac{1}{F}\left(1 - \frac{d}{4F}\right) \tag{12}$$

TABLE I.—Potential Ø(z).

Z	Eq. (9)	Eq. (8)	Difference Column 2 - Column 3	Per cent error
0.2	0.406502	0.405318	0.001184	0.291262
0.4	0.759237	0.760033	-0.000795	-0.104767
0.6	1.03068	1.03601	-0.005325	-0.516636
0.8	1.22227	1.23171	-0.009442	-0.772492
1.0	1.35011	1.36154	-0.011437	-0.847114
1.2	1.43253	1.44392	-0.011392	-0.795221
1.4	1.4847	1.49471	-0.010004	-0.673827
1.6	1.51738	1.52547	-0.008089	-0.533102
1.8	1.53769	1.54391	-0.006216	-0.404232
2.0	1.55031	1.55488	-0.004572	-0.294919
2.2	1.55814	1.56139	-0.003256	-0.208963
2.4	1.56295	1.56524	-0.002291	-0.146593
2.6	1.56595	1.56752	-0.001572	-0.100371
2.8	1.56781	1.56887	-0.001055	-0.067276
3.0	1.56894	1.56966	-0.000719	-0.045811

TABLE II.—First derivative Ø′(z).

Z	First Derivative Eq. (9)	First Derivative Eq. (8)	Difference Column 2-Column 3	Per cent Error
0	2.08326	2.07345	0.009808	0.470801
0.2	1.93454	1.9354	-0.000855	-0.044207
0.4	1.56953	1.58803	-0.018503	-1.17890
0.6	1.14775	1.17151	-0.023762	-2.07026
0.8	0.782622	0.798575	-0.015953	-2.03835
1.0	0.511255	0.515637	-0.004382	-0.857171
1.2	0.32582	0.32144	0.0043796	1.34418
1.4	0.204783	0.196022	0.008762	4.27861
1.6	0.127728	0.117942	0.009786	7.66161
1.8	0.079345	0.070391	0.008953	11.284
2.0	0.049174	0.041809	0.007365	14.978
2.2	0.030444	0.024761	0.005683	18.6664
2.4	0.018832	0.014640	0.004192	22.2607
2.6	0.011648	0.008647	0.000300	25.7678
2.8	0.007200	0.005104	0.002096	29.115
3.0	0.004453	0.0030118	0.0014415	32.3695

TABLE III.—Second derivative Ø″(z).

Z	Second Derivative Eq. (9)	Second Derivative Eq. (8)	Difference Column 2-Column3	Per cent Error
0	0	0	0	0
0.2	-1.41007	-1.3184	-0.091661	6.50
0.4	-2.09473	-2.02849	-0.066238	3.16
0.6	-2.02696	-2.03982	-0.012861	-0.63
0.8	-1.5968	-1.65313	0.056328	-3.53
1.0	-1.12603	-1.17994	0.053907	-4.79
1.2	-0.747482	-0.780054	0.032572	-4.36
1.4	-0.480192	-0.492427	0.012235	-2.55
1.6	-0.30304	-0.302382	-0.000658	0.22
1.8	-0.189425	-0.182651	-0.006773	3.58
2.0	-0.117803	-0.109256	-0.008547	7.26
2.2	-0.073050	-0.064977	-0.008072	11.05
2.4	-0.045247	-0.038512	-0.006735	14.89
2.6	-0.027983	-0.022780	-0.005203	18.59
2.8	-0.017323	-0.013458	-0.003865	22.31
3.0	-0.010694	-0.000795	-0.0027484	25.70

where d is the distance between G_1 and G_2 . It is therefore not necessary to determine the location of G .

This method is not very accurate. For example, for a lens of ratio $V_2/V_1 = 10$, it was found that

$$\frac{1}{F} = \frac{3}{16} \int_{z_o}^{z_i} \left(\frac{\phi'}{\phi}\right)^2 dz = \frac{3}{16} \cdot 2.14967$$

or

$$\frac{1}{f} = \left(\frac{1}{10}\right)^{1/4} \frac{3}{16} \cdot 2.14967 = 0.2265$$

or

$$f = 4.42$$

This is the result obtained using the thin-lens formula. The exact value obtained by numerical integration is f = 4.95 . There is, therefore, an appreciable error. Actually this was to be expected because with $V_2/V_1 = 10$ the lens is strong.

The lens is then sectionized and following are the relevant values:

Half area = 2.14967/2 = 1.07483
Position of 1/4 point at z = -0.74505
Position at 3/4 point at z = -0.12715
Distance d between the two points = 0.61790

Corrected focal length

$$\frac{1}{F_c} = \frac{1}{F}\left(1 - \frac{d}{4F}\right) = 0.378$$

and

$$f = \frac{10^{1/4}}{0.378} = 4.7$$

The error is still about 5%. Similar errors were obtained for other values of V_2/V_1 . It is obvious, therefore, that this method is not suitable for the analysis of this type of lens if a sufficient accuracy is required.

Another method was also investigated. It was thoroughly explained by Goddard.[2] We shall review very briefly the analysis presented in his paper. For further details readers are referred to his paper or to a forthcoming book.[3]

By defining

$$\sigma = \frac{\phi_i}{\phi_o}$$

and using the expression for the focal length as given by (2) or (3), we finally obtain

$$f_i = \frac{2.020\sigma^{1/4}}{\left(\frac{\sigma + 1}{\sigma - 1}\right) \log \sigma - 2} \tag{13}$$

This formula is dependable for weak lenses, i.e., for small values of σ. The values of σ can be as high as 4 before serious errors develop. For stronger lenses we use the method of successive approximation. By defining

$$J = \int_{z_o}^{z_i} \left[\frac{\phi'(z)}{\phi(z)}\right]^2 \int_{z_o}^{z} \int_{z_o}^{z_2} \left[\frac{\phi'(z_1)}{\phi(z_1)}\right]^2 dz_1 dz_2 dz \tag{14}$$

and after some lengthy derivations, we finally obtain

$$\frac{1}{f_i} = \sigma^{-1/4} (A - B) \tag{15}$$

where

$$A = \frac{3\omega}{8} \left(\frac{1}{x} \log \sigma - 2\right) \tag{16}$$

and

$$B = \left(\frac{3}{16}\right)^2 J = \left(\frac{3}{16}\right)^2 \frac{\omega}{x} \{4x - 2[(1 + \log(1 - x^2)] \log \sigma$$

$$+ \frac{1}{x}(1 - x^2) \ (\log \sigma)^2 + 2x^2 \beta\} \tag{17}$$

Here $\omega = 1.32$ as before, $x = (\sigma - 1)/(\sigma + 1)$, and β is defined by

$$\beta = \int_{-1}^{+1} \frac{1 - \xi^2}{(1 + x\xi)^2} \log\ (1 + x\ \xi) \log \frac{1 + \xi}{1 - \xi}\, d\xi \tag{18}$$

where $\xi = \tanh \omega z$.

It can readily be seen that A in (15) represents the thin-lens formula given by (13) and B is the second term of the infinite series of the successive approximation; B is appreciably smaller than A . Thus, even by limiting ourselves to up to the second term of the series the results are still accurate.

When an attempt is made to determine the other cardinal points of a lens with separation S , the analysis becomes very complicated. We have thus decided to analyze the lens using a digital computer. The paraxial ray equation (1) was solved numerically using the following formula, which was found to be very accurate and convenient in this case:

$$R_{n+1} = R_n - R_{n-4} - R_{n-5} + \frac{h^2}{48} (67R''_n - 8R''_{n-1} + 122R''_{n-2} - 8R''_{n+2} + 67R''_{n=4}) \tag{19}$$

Here h is the increment. The analysis was started from a point sufficiently outside the field to ascertain that the derivatives along the z axis are zero. The numerical analysis was then performed step by step until a point was reached after passing through the lens where the field is negligible.

In all cases, we started parallel to the axis at a normalized height of 1 . The slope of the trajectory was determined outside the lens and the values of the focal length, midfocal length, and position of the principal plane were all determined.

Using this method a series of lenses was analyzed with spacing $S = 0$ to 2 in steps of 0.1. The voltage ratio was taken from 1.5 to 50 in steps of 0.5. To the best of our knowledge, these are the most complete sets of results available in the literature. Table IV shows a comparison between the results obtained numerically and those obtained analytically. Table V gives a sample of the results for $S = 0.2$.

IV. METHOD OF ANALYSIS OF THE ASYMMETRICAL LENS

In the case in which two coaxial cylinders of unequal diameters are placed end to end, the determination of the axial potential distribution and its derivatives is very complex. An analytical solution was obtained by Lebedev et al.[4] A cylinder of radius b is assumed to be of infinite length and is maintained at zero potential. A coaxial cylinder of radius a and of semi-infinite extent with a thin wall (actually negligible in our case) is at potential V. Although this is not an exact model of the asymmetrical lens, the potential distribution along the axis and its derivatives are practically the same in both cases. The potential along the axis is given by

$$\frac{u}{V} = 1 - \sum_{m=1}^{\infty} \frac{\exp[-(\gamma_m z/a)] J_0(\gamma_m r/a)}{\gamma_m J_1(\gamma_m) K + \left(\frac{j \ \gamma_m}{a}\right)} \tag{20}$$

TABLE IV

V_2/V_1	A	B	f_i Eq.(13)	f_i Eq.(15)	f_i Numerical Analysis
1.5	0.013510	0.000043	81.92	82.18	82.18
2	0.039276	0.000372	30.28	30.57	30.57
2.5	0.068233	0.001133	18.43	18.74	18.74
3	0.097508	0.002334	13.50	13.83	13.83
3.5	0.126059	0.003931	10.85	11.20	11.20
4	0.153507	0.005871	9.21	9.58	9.57
4.5	0.179739	0.008103	8.10	8.49	8.48
5	0.204759	0.010583	7.30	7.70	7.69
5.5	0.228617	0.013272	6.70	7.11	7.10
6	0.251384	0.016139	6.23	6.65	6.64
6.5	0.273135	0.019157	5.85	6.29	6.28
7	0.293944	0.022302	5.53	5.99	5.98
7.5	0.313881	0.025557	5.27	5.74	5.73
8	0.333012	0.028904	5.05	5.53	5.52
8.5	0.351395	0.032331	4.86	5.35	5.33
9	0.369085	0.035825	4.69	5.20	5.18
9.5	0.386130	0.039376	4.55	5.06	5.04
10	0.402575	0.042977	4.42	4.95	4.92
10.5	0.418461	0.046619	4.30	4.84	4.82
11	0.433823	0.050296	4.20	4.75	4.72
11.5	0.448696	0.054002	4.10	4.67	4.64
12	0.463108	0.057733	4.02	4.59	4.56
12.5	0.477089	0.061484	3.94	4.52	4.50
13	0.490663	0.065251	3.87	4.46	4.43
13.5	0.503853	0.069031	3.80	4.41	4.38
14	0.516681	0.072821	3.74	4.36	4.32
14.5	0.529166	0.076619	3.69	4.31	4.28
15	0.541326	0.080422	3.64	4.27	4.23
15.5	0.553178	0.084228	3.59	4.23	4.19
16	0.564737	0.088036	3.54	4.20	4.16
16.5	0.576018	0.091843	3.50	4.16	4.12
17	0.587033	0.095649	3.46	4.13	4.09
17.5	0.597796	0.099452	3.42	4.10	4.06
18	0.608317	0.103251	3.39	4.08	4.03
18.5	0.618608	0.107044	3.35	4.05	4.01
19	0.628678	0.110832	3.32	4.03	3.98
19.5	0.638538	0.114613	3.29	4.01	3.96
20	0.648194	0.118386	3.26	3.99	3.94

All values normalized to cylinder R.

FIG. 5.—Cardinal points of two equidiameter cylinders separated by a distance s = 0.2; f is focal length, z_m is midfocal length, z_p is distance from principal plane to center of lens. (All values normalized to cylinder radius R.)

V_2/V_1	f_i	z_{m_i}	z_{p_i}	f_o	z_{m_o}	z_{p_o}
1.5	82.56	74.62	-7.94	-67.41	-74.78	-7.37
2	30.71	25.79	-4.92	-21.71	-26.05	-4.34
2.5	18.82	14.89	-3.94	-11.90	-15.24	-3.33
3	13.89	10.43	-3.45	- 8.02	-10.85	-2.83
3.5	11.25	8.07	-3.18	- 6.01	- 8.55	-2.54
4	9.62	6.62	-3.00	- 4.81	- 7.15	-2.34
4.5	8.52	5.64	-2.87	- 4.01	- 6.22	-2.20
5	7.73	4.94	-2.79	- 3.46	- 5.55	-2.10
5.5	7.13	4.41	-2.72	- 3.04	- 5.06	-2.02
6	6.67	3.99	-2.68	- 2.72	- 4.68	-1.95
6.5	6.30	3.66	-2.64	- 2.47	- 4.37	-1.90
7	6.00	3.38	-2.61	- 2.27	- 4.13	-1.86
7.5	5.75	3.15	-2.59	- 2.10	- 3.92	-1.82
8	5.54	2.96	-2.58	- 1.96	- 3.75	-1.79
8.5	5.36	2.79	-2.57	- 1.84	- 3.60	-1.77
9	5.20	2.64	-2.56	- 1.73	- 3.48	-1.74
9.5	5.06	2.51	-2.55	- 1.64	- 3.37	-1.73
10	4.94	2.39	-2.55	- 1.56	- 3.27	-1.71
10.5	4.84	2.29	-2.55	- 1.49	- 3.19	-1.69
11	4.74	2.19	-2.55	- 1.43	- 3.11	-1.68
11.5	4.66	2.11	-2.55	- 1.37	- 3.04	-1.67
12	4.58	2.03	-2.55	- 1.32	- 2.98	-1.66
12.5	4.51	1.96	-2.55	- 1.28	- 2.92	-1.65
13	4.45	1.89	-2.56	- 1.23	- 2.87	-1.64
13.5	4.39	1.83	-2.56	- 1.20	- 2.82	-1.63
14	4.34	1.77	-2.57	- 1.16	- 2.78	-1.62
14.5	4.29	1.72	-2.57	- 1.13	- 2.74	-1.61
15	4.25	1.67	-2.58	- 1.10	- 2.70	-1.61
15.5	4.21	1.63	-2.58	- 1.07	- 2.67	-1.60
16	4.17	1.58	-2.59	- 1.04	- 2.64	-1.60
16.5	4.14	1.54	-2.60	- 1.02	- 2.61	-1.59
17	4.10	1.50	-2.60	- 1.00	- 2.58	-1.59
17.5	4.07	1.47	-2.61	- .97	- 2.56	-1.58
18	4.05	1.43	-2.62	- .95	- 2.53	-1.58
18.5	4.02	1.40	-2.62	- .93	- 2.51	-1.58
19	4.00	1.37	-2.63	- .92	- 2.49	-1.57
19.5	3.97	1.34	-2.64	- .90	- 2.47	-1.57
20	3.95	1.31	-2.64	- .88	- 2.45	-1.57
20.00	3.95	1.31	-2.64	-0.88	-2.45	-1.57
20.50	3.93	1.28	-2.65	-0.87	-2.43	-1.56
21.00	3.91	1.25	-2.66	-0.85	-2.41	-1.56
21.50	3.90	1.23	-2.67	-0.84	-2.40	-1.56
22.00	.88	1.20	-2.68	-0.83	-2.38	-1.56
22.50	3.86	1.18	-2.68	-0.81	-2.37	-1.55
23.00	3.85	1.16	-2.69	-0.80	-2.35	-1.55
23.50	3.84	1.14	-2.70	-0.79	-2.34	-1.55
24.00	3.82	1.12	-2.71	-0.78	-2.33	-1.55
24.50	3.81	1.10	-2.72	-0.77	-2.32	-1.55
25.00	3.80	1.08	-2.72	-0.76	-2.30	-1.54
25.50	3.79	1.06	-2.73	-0.75	-2.29	-1.54
26.00	3.78	1.04	2.74	-0.74	-2.28	-1.54
26.50	3.77	1.02	-2.75	-0.73	-2.27	-1.54
27.00	3.76	1.01	-2.75	-0.72	-2.26	-1.54
27.50	3.75	0.99	-2.76	-0.72	-2.25	-1.54
28.00	3.74	0.97	-2.77	-0.71	-2.24	-1.54
28.50	3.74	0.96	-2.78	-0.70	-2.24	-1.54
29.00	3.73	0.94	-2.79	-0.69	-2.23	-1.53
29.50	3.72	0.93	-2.79	-0.69	-2.22	-1.53
30.00	3.72	0.91	-2.80	-0.68	-2.21	-1.53
30.50	3.71	0.90	-2.81	-0.67	-2.20	-1.53
31.00	3.70	0.89	-2.82	-0.67	-2.20	-1.53
31.50	3.70	0.87	-2.83	- .66	-2.19	-1.53
32.00	3.69	0.86	-2.83	-0.65	-2.18	-1.53
32.50	3.69	0.85	-2.84	-0.65	-2.18	-1.53
33.00	3.69	0.84	-2.85	-0.64	-2.17	-1.53
33.50	3.68	0.82	-2.86	-0.64	-2.16	-1.53
34.00	3.68	0.81	-2.87	-0.63	-2.16	-1.53
34.50	3.67	0.80	-2.87	-0.63	-2.15	-1.53
35.00	3.67	0.79	-2.88	-0.62	-2.15	-1.53
35.50	3.67	0.78	-2.89	-0.62	-2.14	-1.52
36.00	3.66	0.77	-2.90	-0.61	-2.13	-1.52
36.50	3.66	0.76	-2.90	-0.61	-2.13	-1.52
37.00	3.66	0.75	-2.91	-0.60	-2.12	-1.52
37.50	3.66	0.74	-2.92	-0.60	-2.12	-1.52
38.00	3.65	0.73	-2.93	-0.59	-2.11	-1.52
38.50	3.65	0.72	-2.93	-0.59	-2.11	-1.52
39.00	3.65	0.71	-2.94	-0.58	-2.11	-1.52
39.50	3.65	0.70	-2.95	-0.58	-2.10	-1.52
40.00	3.65	0.69	-2.96	-0.58	-2.10	-1.52
40.50	3.65	0.68	-2.96	-0.57	-2.09	-1.52
41.00	3.64	0.67	-2.97	-0.57	-2.09	-1.52
41.50	3.64	0.66	-2.98	-0.57	-2.08	-1.52
42.00	3.64	0.66	-2.99	-0.56	-2.08	-1.52
42.50	3.64	0.65	-2.99	-0.56	-2.08	-1.52
43.00	3.64	0.64	-3.00	-0.56	-2.07	-1.52
43.50	3.64	0.63	-3.01	-0.55	-2.07	-1.52
44.00	3.64	0.62	-3.02	-0.55	-2.07	-1.52
44.50	3.64	0.62	-3.02	-0.55	-2.06	-1.52
45.00	3.64	0.61	-3.03	-0.54	-2.06	-1.52
45.50	3.64	0.60	-3.04	-0.54	-2.06	-1.52
46.00	3.64	0.59	-3.04	-0.54	-2.05	-1.52
46.50	3.64	0.59	-3.05	-0.53	-2.05	-1.52
47.00	3.64	0.58	-3.06	-0.53	-2.05	-1.52
47.50	3.64	0.57	-3.07	-0.53	-2.04	-1.52
48.00	3.64	0.56	-3.07	-0.53	-2.04	-1.52
48.50	3.64	0.56	-3.08	-0.52	-2.04	-1.52
49.00	3.64	0.55	-3.09	-0.52	-2.04	-1.52
49.50	3.64	0.54	-3.09	-0.52	-2.03	-1.52
50.00	3.64	0.54	-3.10	-0.51	-2.03	-1.52

in the region $0 \leq r \leq a$ and $z > 0$ and

$$\frac{u}{V} = \frac{1}{\ell n \frac{b}{a}} \sum_{m=1}^{\infty} \frac{K_+\left(\frac{j\gamma_m}{b}\right) e^{\frac{\gamma_m z}{b}}}{\gamma_m^2 J_1^2(\gamma_m)} J_0\left(\frac{\gamma_m a}{b}\right) J_0\left(\frac{\gamma_m r}{b}\right) \qquad (21)$$

in the region $0 \leq r \leq a$ and $z < 0$.

In the above two equations, γ_m are the roots of

$$J_0(\gamma) = 0 \qquad (22)$$

where $J_0(\gamma)$ is the Bessel function of the first kind, order zero, and $J_1(\gamma)$ is of order 1, and

$$K_+\left(\frac{j\gamma_m}{a}\right) = f\left(\frac{b-a}{a}\gamma_m\right) \quad K_+\left(\frac{j\gamma_m}{b}\right) = f\left(\frac{b-a}{b}\gamma_m\right) \qquad (23)$$

The $f(y)$ functions are real functions defined by

$$f(y) = \frac{\left(P\,\frac{by}{b-a}\right) e^{-y/[\pi(c/(b-a) + \pi S)]}}{P\left(\frac{ay}{b-a}\right) Q(y)} \qquad (24)$$

where

$$c = (b-a)\,\ell n\,(b-a) + a\,\ell n\,a - b\,\ell n\,b \qquad (25)$$

and the functions $P(\alpha)$, S, and $Q(\alpha)$ are defined by

$$P(\alpha) = \prod_{n=1}^{\infty} \left(1 + \frac{\alpha}{\gamma_n}\right) e^{-\alpha/\gamma_n}, \quad Q(\alpha) = \prod_{n=1}^{\infty} \left(1 + \frac{\alpha}{\delta_n}\right) e^{-\alpha/\delta_n}$$

and

$$S = \sum_{n=1}^{\infty} \left(\frac{1}{\delta_n} - \frac{1}{\gamma_n}\right) \qquad (26)$$

In the above relations, δ_n are the roots of the cross product

$$J_0\left(\frac{a\delta}{b - a}\right) Y_0\left(\frac{b\delta}{b - a}\right) - J_0\left(\frac{b\delta}{b - a}\right) Y_0\left(\frac{a\delta}{b - a}\right) = 0 \qquad (27)$$

where Y_0 is Bessel's function of the second kind. The series for $P(\alpha)$, $Q(\alpha)$, and S were found not to converge very rapidly. We have instead chosen the following series:

$$\ell n\ P(\alpha) = \ell n\ \frac{\Gamma(3/4)}{\Gamma\left(\frac{3}{4} + \frac{\alpha}{\pi}\right)} - \frac{\alpha}{\pi}\left(\gamma - \frac{\pi}{2} + 3\ \ell n\ 2\right) + \sum_{n=1}^{\infty} \ell n\left(1 + \frac{\alpha}{\gamma_n}\right) - \frac{\alpha}{\gamma_n} - \ell n\left(1 + \frac{\alpha}{\gamma'_n}\right) \qquad (28)$$

$$\ell n\ Q(x) = -\frac{\gamma\alpha}{\pi} - \ell n\ \Gamma\left(1 + \frac{x}{\pi}\right) + \sum_{n=1}^{\infty}\left[\ell n\left(1 + \frac{\alpha}{\delta_n}\right) - \frac{\alpha}{\delta_n} - \mathrm{ln}\left(1 + \frac{\alpha}{n\pi}\right) + \frac{\alpha}{n\pi}\right] \qquad (29)$$

$$S = \frac{1}{2} - \frac{3}{\pi}\ \ell n 2 + \sum_{n=1}^{\infty}\left(\frac{1}{\delta_n} - \frac{1}{n\pi} - \frac{1}{\gamma_n} + \frac{1}{\gamma'_n}\right) \qquad (30)$$

In the above three series we define $\gamma = 0.5772\ldots$, which is Euler's constant, and $\gamma' = n\pi - \pi/4$.

With the above relations, a digital computer program was written to determine the axial voltage distribution and its derivatives. The cardinal points were obtained using exactly the same procedures outlined earlier. Table VI gives an example of the results obtained.

The coefficient of spherical aberration C_s using Scherzer's formula was also computed for each lens. Table VII shows an example of the results for the experimental lens. I is the value of the integral in Scherzer's formula. The spacing is 0.2 in units of R .

V. RESULTS

From the detailed results obtained in both the symmetrical and asymmetrical cases, the following conclusions were drawn.

(a) The focal length in the direction of increasing potential is always greater than the focal length in the direction of decreasing potential.

(b) The focal length of the symmetrical two tube lens with spacing s increases, i.e., the lens gets weaker as the axial spacing of the cylinders increases. The change is small for small spacings but increases as the spacing is increased. At high voltage ratios, the effect

TABLE VI.—Cardinal points of asymmetrical two-cylinder lens of radii a and b and potentials V_2 and V_1, respectively, for b/a = 2.

V_2/V_1	f_i	z_{m_i}	z_{p_i}	f_o	z_{m_o}	z_{p_o}
1.5	118.92	106.93	-11.99	-97.11	-107.99	-10.88
2	45.41	37.58	-7.83	-32.12	-38.8	-6.67
2.5	28.33	21.86	-6.48	-17.93	-23.2	-5.27
3	21.2	15.38	-5.82	-12.25	-16.82	-4.57
3.5	17.37	11.92	-5.45	-9.29	-13.44	-4.15
4	15	9.78	-5.22	-7.51	-11.39	-3.88
4.5	13.4	8.34	-5.06	-6.32	-10.01	-3.69
5	12.25	7.3	-4.96	-5.48	-9.03	-3.54
5.5	11.39	6.51	-4.88	-4.86	-8.29	-3.43
6	10.72	5.89	-4.83	-4.38	-7.73	-3.34
6.5	10.19	5.39	-4.8	-4	-7.27	-3.27
7	9.75	4.98	-4.77	-3.69	-6.9	-3.22
7.5	9.39	4.63	-4.76	-3.43	-6.6	-3.17
8	9.09	4.34	-4.75	-3.22	-6.34	-3.13
8.5	8.83	4.08	-4.74	-3.03	-6.12	-3.09
9	8.6	3.86	-4.75	-2.87	-5.93	-3.06
9.5	8.41	3.66	-4.75	-2.73	-5.77	-3.03
10	8.24	3.48	-4.76	-2.61	-5.62	-3.01
10.5	8.09	3.33	-4.76	-2.5	-5.49	-2.99
11	7.96	3.18	-4.77	-2.4	-5.38	-2.97
11.5	7.84	3.05	-4.79	-2.32	-5.27	-2.96
12	7.73	2.93	-4.8	-2.24	-5.18	-2.94
12.5	7.64	2.82	-4.81	-2.16	-5.1	-2.93
13	7.55	2.72	-4.83	-2.1	-5.02	-2.92
13.5	7.47	2.63	-4.84	-2.04	-4.95	-2.91
14	7.4	2.54	-4.86	-1.98	-4.88	-2.9
14.5	7.34	2.46	-4.88	-1.93	-4.82	-2.89
15	7.28	2.39	-4.89	-1.88	-4.77	-2.88
15.5	7.23	2.32	-4.91	-1.84	-4.72	-2.88
16	7.18	2.25	-4.93	-1.8	-4.67	-2.87
16.5	7.13	2.19	-4.94	-1.76	-4.62	-2.87
17	7.09	2.13	-4.96	-1.72	-4.58	-2.86
17.5	7.05	2.07	-4.98	-1.69	-4.54	-2.86
18	7.01	2.02	-5	-1.66	-4.51	-2.85
18.5	6.98	1.96	-5.02	-1.63	-4.47	-2.85
19	6.95	1.92	-5.03	-1.6	-4.44	-2.84
19.5	6.92	1.87	-5.05	-1.57	-4.41	-2.84
20	6.9	1.83	-5.07	-1.55	-4.38	-2.84
20.5	6.87	1.78	-5.09	-1.52	-4.35	-2.83
21	6.85	1.74	-5.11	-1.5	-4.33	-2.83
21.5	6.83	1.7	-5.13	-1.48	-4.3	-2.83
22	6.81	1.67	-5.14	-1.46	-4.28	-2.83
22.5	6.79	1.63	-5.16	-1.44	-4.26	-2.82
23	6.78	1.6	-5.18	-1.42	-4.24	-2.82
23.5	6.76	1.56	-5.2	-1.4	-4.22	-2.82
24	6.75	1.53	-5.22	-1.38	-4.2	-2.82
24.5	6.73	1.5	-5.23	-1.36	-4.18	-2.82
25	6.72	1.47	-5.25	-1.35	-4.16	-2.81
25.5	6.71	1.44	-5.27	-1.33	-4.14	-2.81
26	6.7	1.41	-5.29	-1.32	-4.13	-2.81
26.5	6.69	1.39	-5.3	-1.3	-4.11	-2.81
27	6.68	1.36	-5.32	-1.29	-4.1	-2.81
27.5	6.67	1.33	-5.34	-1.28	-4.08	-2.81
28	6.67	1.31	-5.36	-1.26	-4.07	-2.81
28.5	6.66	1.29	-5.37	-1.25	-4.06	-2.81
29	6.65	1.26	-5.39	-1.24	-4.04	-2.81
29.5	6.65	1.24	-5.41	-1.23	-4.03	-2.8
30	6.64	1.22	-5.42	-1.22	-4.02	-2.8
30.5	6.64	1.2	-5.44	-1.2	-4.01	-2.8
31	6.63	1.18	-5.46	-1.19	-4	-2.8
31.5	6.63	1.16	-5.47	-1.18	-3.99	-2.8
32	6.63	1.14	-5.49	-1.17	-3.98	-2.8
32.5	6.62	1.12	-5.51	-1.16	-3.97	-2.8
33	6.62	1.1	-5.52	-1.16	-3.96	-2.8
33.5	6.62	1.08	-5.54	-1.15	-3.95	-2.8
34	6.62	1.06	-5.56	-1.14	-3.94	-2.8
34.5	6.61	1.04	-5.57	-1.13	-3.93	-2.8
35	6.61	1.03	-5.59	-1.12	-3.92	-2.8
35.5	6.61	1.01	-5.6	-1.11	-3.91	-2.8
36	6.61	0.99	-5.62	-1.11	-3.9	-2.8
36.5	6.61	0.98	-5.63	-1.1	-3.9	-2.8
37	6.61	0.96	-5.65	-1.09	-3.89	-2.8
37.5	6.61	0.95	-5.67	-1.08	-3.88	-2.8
38	6.61	0.93	-5.68	-1.08	-3.87	-2.8
38.5	6.61	0.92	-5.7	-1.07	-3.87	-2.8
39	6.61	0.9	-5.71	-1.06	-3.86	-2.8
39.5	6.61	0.89	-5.73	-1.06	-3.85	-2.8
40	6.62	0.87	-5.74	-1.05	-3.85	-2.8
40.5	6.62	0.86	-5.76	-1.04	-3.84	-2.8
41	6.62	0.85	-5.77	-1.04	-3.84	-2.8
41.5	6.62	0.83	-5.79	-1.03	-3.83	-2.8
42	6.62	0.82	-5.8	-1.02	-3.82	-2.8
42.5	6.62	0.81	-5.82	-1.02	-3.82	-2.8
43	6.63	0.8	-5.83	-1.01	-3.81	-2.8
43.5	6.63	0.78	-5.85	-1.01	-3.81	-2.8
44	6.63	0.77	-5.86	-1	-3.8	-2.8
44.5	6.63	0.76	-5.87	-1	-3.8	-2.8
45	6.64	0.75	-5.89	-0.99	-3.79	-2.8
45.5	6.64	0.74	-5.9	-0.99	-3.79	-2.8
46	6.64	0.72	-5.92	-0.98	-3.78	-2.8
46.5	6.65	0.71	-5.93	-0.98	-3.78	-2.8
47	6.65	0.7	-5.95	-0.97	-3.77	-2.8
47.5	6.65	0.69	-5.96	-0.97	-3.77	-2.8
48	6.65	0.68	-5.97	-0.96	-3.76	-2.8
48.5	6.66	0.67	-5.99	-0.96	-3.76	-2.8
49	6.66	0.66	-6	-0.95	-3.76	-2.8
49.5	6.67	0.65	-6.01	-0.95	-3.75	-2.8
50	6.67	0.64	-6.03	-0.95	-3.75	-2.8

TABLE VII.—Coefficient of spherical aberration of two-cylinder equidiameter electrostatic lens of spacing s = 0.2 in units of R.

V_2/V_1	I	C_1/M	C_{so}/R	C_{so}/f_o
1.50	3377912.31	0.70	211119.52	3153.39
2.00	135338.79	0.83	8458.67	390.43
2.50	25590.48	0.95	1599.40	134.51
3.00	8769.40	1.07	548.09	68.42
3.50	4081.56	1.18	255.10	42.47
4.00	2280.69	1.28	142.54	29.66
4.50	1436.25	1.39	89.77	22.37
5.00	983.14	1.49	61.45	17.79
5.50	715.21	1.59	44.70	14.70
6.00	544.82	1.69	34.05	12.51
6.50	430.18	1.78	26.89	10.88
7.00	349.49	1.87	21.84	9.63
7.50	290.58	1.96	18.16	8.65
8.00	246.28	2.05	15.39	7.86
8.50	212.08	2.14	13.26	7.22
9.00	185.11	2.22	11.57	6.68
9.50	163.45	2.31	10.22	6.22
10.00	145.78	2.39	9.11	5.83
10.50	131.14	2.46	8.20	5.49
11.00	118.88	2.54	7.43	5.20
11.50	108.49	2.62	6.78	4.94
12.00	99.59	2.69	6.22	4.71
12.50	91.92	2.76	5.74	4.50
13.00	85.24	2.83	5.33	4.32
13.50	79.38	2.90	4.96	4.15
14.00	74.22	2.97	4.64	4.00
14.50	69.63	3.04	4.35	3.86
15.00	65.54	3.10	4.10	3.73
15.50	61.88	3.17	3.87	3.62
16.00	58.57	3.23	3.66	3.51
16.50	55.58	3.29	3.47	3.41
17.00	52.87	3.35	3.30	3.32
17.50	50.39	3.41	3.14	3.23
18.00	48.13	3.47	3.01	3.15
18.50	46.05	3.52	2.88	3.08
19.00	44.13	3.58	2.76	3.01
19.50	42.37	3.63	2.65	2.94

V_2/V_1	Integral	C_1/M	C_{so}/R	C_{so}/f_o
20.00	40.75	3.69	2.55	2.88
20.50	39.23	3.76	2.45	2.82
21.00	37.82	3.79	2.36	2.77
21.50	36.50	3.84	2.28	2.71
22.00	35.27	3.89	2.20	2.66
22.50	34.12	3.94	2.13	2.62
23.00	33.04	3.99	2.06	2.57
23.50	32.03	4.04	2.00	2.53
24.00	31.07	4.08	1.94	2.49
24.50	30.17	4.13	1.89	2.45
25.00	29.32	4.17	1.83	2.41
25.50	28.52	4.22	1.78	2.38
26.00	27.76	4.26	1.74	2.34
26.50	27.04	4.30	1.69	2.31
27.00	26.36	4.34	1.65	2.28
27.50	25.71	4.39	1.61	2.25
28.00	25.09	4.43	1.57	2.22
28.50	24.50	4.47	1.53	2.19
29.00	23.94	4.50	1.50	2.16
29.50	23.40	4.54	1.46	2.13
30.00	22.89	4.58	1.43	2.11
30.50	22.40	4.62	1.40	2.08
31.00	21.94	4.65	1.37	2.06
31.50	21.49	4.69	1.34	2.04
32.00	21.06	4.72	1.32	2.02
32.50	20.65	4.76	1.29	1.99
33.00	20.25	4.79	1.27	1.97
33.50	19.87	4.83	1.24	1.95
34.00	19.50	4.86	1.22	1.93
34.50	19.15	4.89	1.20	1.91
35.00	18.81	4.92	1.18	1.90
35.50	18.48	4.95	1.16	1.88
36.00	18.17	4.99	1.14	1.86
36.50	17.86	5.02	1.12	1.84
37.00	17.57	5.05	1.10	1.83
37.50	17.29	5.08	1.08	1.81
38.00	17.01	5.10	1.06	1.79
38.50	16.75	5.13	1.05	1.78
39.00	16.49	5.16	1.03	1.76
39.50	16.24	5.19	1.02	1.75
40.00	16.00	5.22	1.00	1.73
40.50	15.77	5.24	0.99	1.72
41.00	15.54	5.27	0.97	1.71
41.50	15.33	5.30	0.96	1.69
42.00	15.11	5.32	0.94	1.68
42.50	14.91	5.35	0.93	1.67
43.00	14.71	5.37	0.92	1.66
43.50	14.51	5.40	0.91	1.64
44.00	14.32	5.42	0.90	1.63
44.50	14.14	5.44	0.88	1.62
45.00	13.96	5.47	0.87	1.61
45.50	13.78	5.49	0.86	1.60
46.00	13.61	5.51	0.85	1.59
46.50	13.45	5.54	0.84	1.58
47.00	13.29	5.56	0.83	1.57
47.50	13.13	5.58	0.82	1.55
48.00	12.98	5.60	0.81	1.54
48.50	12.83	5.62	0.80	1.53
49.00	12.69	5.64	0.79	1.53
49.50	12.54	5.66	0.78	1.52
50.00	12.41	5.68	0.78	1.51

is quite small.

(c) The position of the principal planes does not change much with voltage ratio except at very low values.

(d) As the spacing s is increased, a slight movement of the principal planes towards the low voltage cylinder occurs. At high voltage ratios, this effect is negligible.

(e) The lens thickness defined by the separation of the principal planes increases monotonically with voltage ratio.

(f) The focal length increases monotonically with the diameter ratio in an asymmetrical two-cylinder lens. The rate of increase of f decreases as the diameter ratio increases.

(g) The spherical aberration decreases monotonically as the voltage ratio increases.

VI. CONCLUSION

All the results and conclusions agree reasonably well with those already published by previous authors. We have reason to believe that our method of analysis is more accurate and convenient. The entire data obtained are to be published elsewhere and represent, in our opinion, the most complete analysis of the electrostatic immersion lens available in the literature.

REFERENCES

1. S. Bertram, J. Appl. Phys. 13: 496-502, 1942, and Proc. IRE 28: 418-420, 1940.
2. L. S. Goddard, Proc. Phys. Soc. 56: 372, 1944.
3. A. B. El-Kareh, Fundamentals of Electron Optics, in preparation.
4. N. N. Lebedev and I. P. Skalskaya, Zh. Tekhnicheskoi Fiziki 30: 472, 1960.

COMPUTER ANALYSIS OF SYMMETRICAL MAGNETIC LENSES WITH UNSATURATED POLE PIECES

A. B. EL-KAREH and H. G. PARKS*

Syracuse University (Department of Electrical Engineering),
Syracuse, N. Y.

A computer method of analysis for symmetrical magnetic lenses is presented. An analytical expression for the axial magnetic field is derived from a boundary-value solution of the magnetic scalar potential of the lens. Important field, paraxial, and aberration properties of a series of magnetic lenses are calculated with the help of a digital computer.

I. INTRODUCTION

Numerous methods of analyzing magnetic lenses have been described in the literature. Glaser[1] started with a bell-shaped curve given by

$$B(z) = \frac{B_0}{\left[1 + \left(\frac{z}{a}\right)^2\right]^{\mu}} \qquad (1)$$

Here B_0 is the maximum value of the field and a and μ are constants related to the half-amplitude width $2d$, as shown in Fig. 1, by the equation

$$d = a\sqrt{2^{1/\mu} - 1} \qquad (2)$$

Glaser found that for $\mu = 1$, he was able to analyze the lens completely. Unfortunately the field distribution obtained with $\mu = 1$ does not accurately represent the fields found in real lenses. The field decreases much more slowly with increaseing z than the fields in real lenses. The results are given in terms of the parameter

$$k^2 = \frac{e}{8mV_r}(B_0 a)^2 \qquad (3)$$

where e and m are the charge and mass of the electron, respectively, and V_r is the accelerating potential corrected for relativity by

$$V_r = V(1 + 0.978 \times 10^{-6} V) \qquad (4)$$

---

* Now at Xerox Corporation, Rochester, New York.

Record of 10th Symposium on Electron, Ion, and Laser Beam Technology (L. Marton, ed.); San Francisco Press, Inc.

Copyright © by The Institute of Electrical and Electronics Engineers, Inc.—Printed in the U.S.A.

The Glaser field distribution leads to some serious errors in lens analysis. For example, Glaser finds that if C_s, the coefficient of spherical aberration, is plotted as a function of k^2, the curve passes through a minimum. In real lenses C_s decreases monotonically with k^2. The Glaser field distribution is most accurate for lenses with saturated polepieces. However, even in that case it does not truly represent the broadening of the field distribution owing to saturation found in real lenses.

Owing to the inaccuracies of the field model when $\mu = 1$, the results of Glaser's analysis are now primarily used for qualitative rather than quantitative lens analysis, i.e., as a learning model. It should be noted, however, that at the time of its development, which was over 25 years ago, the model was a major breakthrough in the understanding of magnetic lenses and it found wide application in the analysis and design of lenses.

Ramberg[2] published data for a magnetic lens with axial field distribution given by

$$B(z) = B_0 \operatorname{sech}^2\left(2.630 \frac{z}{D}\right) \tag{5}$$

where B_0 is the maximum amplitude of the axial field and D is the bore of the lens. This field distribution was obtained by considering the polepieces of the lens to be magnetic scalar equipotentials and allowing the ratio of gap width to bore diameter, S/D, to become very small. The preceding paper on electrostatic lenses describes a similar case in detail where the case of two equidiameter cylinders of potentials V_1 and V_2 with negligible separation is analyzed. Calculations for the magnetic system would be essentially the same based on the magnetic scalar potential.

Using this field distribution and numerical techniques, Ramberg was able to obtain solutions for the paraxial-ray equation and the aberration coefficients as a function of lens strength. Along with this lens, three types of electrostatic lenses were also considered and the important optical properties of each lens system versus lens strength were presented in graphical form. From this study, Ramberg was then able to conclude that magnetic lenses are superior to electrostatic lenses of comparable dimensions in terms of spherical and chromatic aberrations for the types of lenses used as microscope objectives.

The majority of magnetic lenses found in practice have ratios of gap width to bore diameter in the range of 0.2 to 2.0. The field distribution used by Ramberg, constrained by small values of S/D, is in general too limited for the analysis and design of magnetic lenses. It does, however, present a limiting case with which other methods of lens analysis can be compared.

Van Ments and Le Poole[3] used a combination of experimental and analytical techniques to investigate the optical properties of magnetic lenses. Their method of field measurement was based on the force exerted on a current carrying conductor placed in a magnetic field. They defined a parameter

$$K = \frac{(NI)^2}{V_r} \tag{6}$$

where NI is the number of ampere turns. This is related to the dimensionless parameter k^2 by

$$K = \emptyset k^2$$

$\emptyset$ was found to be constant for a given ratio of gap width to bore diameter, S/D, provided saturation of the lens polepieces was avoided. Van Ments and Le Poole presented optical properties of a series of lenses ($0.2 \le S/D \le 2.2$) using the above-mentioned procedure.

Liebmann and Grad[4] published results for the optical properties of a series ($S/D = 0.2, 0.6, 1.0, 2.0$) of magnetic lenses. The polepieces of the lenses considered were assumed to be scalar magnetic equipotentials and were modeled on a resistance-network analog of ten mesh units per lens radius. The mesh potentials were then recorded to five decimal places and after correction for local errors, the relative accuracy was 2 parts in 10 000. The relative field intensity $H(z)/H(0)$ was obtained by taking first and third differences of the axial potentials. Relative values for the first and second derivatives of the field were obtained in a similar manner from differences of $H(z)/H(0)$ and $H'(z)/H(0)$, respectively.

The optical properties of the lenses were obtained by numerical ray tracing and were presented in graphical form as a function of the parameter

$$k^2 = \frac{e}{8mV_r} (B_0 R)^2 \tag{7}$$

where R is the radius of the bore. This value of k^2 differs from that defined by Glaser, since here R and not a is used. This form is more suitable because the radius is a more easily obtainable parameter than the field halfwidth. A relationship between V_r, NI, and k^2 was defined:

$$\beta = k^2 \frac{V_r}{(NI)^2} \tag{8}$$

β is constant for any given value of S/D.

The above-mentioned work was based on the measurement of the axial magnetic field either experimentally or with the help of a resistor board. This involves a considerable amount of labor for each value of S/D. In addition important errors occur whenever the first or second derivative is calculated. In what follows we shall develop an analytical expression for the axial magnetic field with the help of which the complete optical data will be obtained. This analytical approach was first developed by Lenz.[5]

II. AXIAL MAGNETIC POTENTIAL OF A SYMMETRICAL LENS

Laplace's equation of a rotationally symmetrical lens can be conveniently written in cylindrical coordinates as

$$\nabla^2 \Psi = \frac{1}{r}\frac{\partial}{\partial r}\left(r \frac{\partial \Psi}{\partial r}\right) + \frac{\partial^2 \Psi}{\partial z^2} = 0 \tag{9}$$

where Ψ is the magnetic scalar potential. A general solution of the equation based on the Fourier integral[6] is

$$\Psi(r,z) = \int_{-\infty}^{+\infty} f(\alpha) e^{j\alpha z} I_0(\alpha r)\, d\alpha \tag{10}$$

where $I_0(\alpha r)$ is the modified Bessel function of first kind, order zero, and is defined by the series

$$I_0(\alpha r) = \sum_{k=0}^{\infty} \frac{1}{(k!)^2}\left(\frac{\alpha r}{2}\right)^{2k} \tag{11}$$

In order to solve our problem we need to determine the function $f(\alpha)$ in (10). We do this by using the boundary conditions. Along the bore radius R, (10) becomes

$$\Psi(R,z) = \int_{-\infty}^{+\infty} f(\alpha) e^{j\alpha z} I_0(\alpha R)\, d\alpha \tag{12}$$

which is obviously a function of z only. We note the similarity of (12) with the Fourier inversion integral

$$g(z) = \frac{1}{2\pi}\int_{-\infty}^{+\infty} G(\alpha) e^{j\alpha z} d\alpha \tag{13}$$

which is used to recover $g(z)$ from its Fourier transform $G(\alpha)$. We thus have

$$f(\alpha) = \frac{G(\alpha)}{2\pi I_0(\alpha R)} \tag{14}$$

Therefore, the function $f(\alpha)$ is defined in terms of the Fourier integral of the potential variation along the bore radius of the lens.

The lens excitation NI is assumed to be low enough so that saturation is avoided.

At points far from the bore, the field is parallel to the z axis and

$$H = NI/S \tag{15}$$

In this region the potential varies linearly across the gap with a slope given by (15). Along the bore radius fringe fields exist which cause a curvature in the field lines and the potential distribution. However, as with the case of electrostatic lenses, we can assume a linear variation along the gap without any significant error. We therefore assume the following conditions:

$$\Psi(R,z) = g(z) = \begin{cases} \dfrac{-NI}{2} & z \le -S/2 \\ \dfrac{NI}{S}\, z & |z| < S/2 \\ \dfrac{NI}{2} & z \ge S/2 \end{cases} \tag{16}$$

where g(z) appears as the inclined step as shown in Fig. (1).

Now that the potential along the bore radius has been specified, $f(\alpha)$ can be determined and the solution for $\Psi_{(r,z)}$ completed. From (14) we see that this involves evaluating the Fourier integral $G(\alpha)$ given by the equation

$$G(\alpha) = \int_{-\infty}^{+\infty} g(z) e^{-j\alpha z} dz \tag{17}$$

for the function $g(z)$ given by (16). The function $g(z)$ does not satisfy the classical conditions for existence of the Fourier transform pair defined by (17) and (13), namely the condition of absolute integrability

$$\int_{-\infty}^{+\infty} |g(z)|\, dz < \infty \tag{18}$$

is violated by $g(z)$. However, due to the frequent occurrence of functions such as $g(z)$ in physical problems, techniques have been developed that extend the Fourier theory to encompass them.[7] Here we will follow the limit method presented by Bracewell.[8] First we modify $g(z)$ slightly by letting

$$g_1(z) = e^{-\tau|z|} g(z) \tag{19}$$

where τ is a small positive constant. Equation (19) satisfies the conditions of existence for the Fourier integral and we can, therefore, write

$$G_1(\alpha) = \int_{-\infty}^{+\infty} g_1(z) e^{-j\alpha z} dz \tag{20}$$

We then define a Fourier transform for $G(\alpha)$ which exists in the limit as

$$G(\alpha) = \lim_{\tau \to 0} G_1(\alpha) \tag{21}$$

In view of (16) and (19), (20) becomes

$$G_1(\alpha) = \int_{-\infty}^{-S/2} - \frac{NI}{2} e^{-j\alpha z - \tau|z|} dz + \int_{-S/2}^{+S/2} \frac{NI}{S} z e^{-j\alpha z - \tau|z|} dz + \int_{+S/2}^{\infty} \frac{NI}{2} e^{-j\alpha z - \tau|z|} dz \tag{22}$$

For the magnitude of z we can write

$$|z| = \begin{cases} -z & z \le 0 \\ z & z \ge 0 \end{cases} \tag{23}$$

and substituting this in the preceding equation for $G_1(\alpha)$ we obtain

$$G_1(\alpha) = NI \left\{ - \frac{1}{2} \int_{-\infty}^{-S/2} e^{(\tau - j\alpha) z} dz + \frac{1}{S} \int_{-S/2}^{0} z e^{(\tau - j\alpha) z} dz + \frac{1}{S} \int_{0}^{S/2} z e^{-(\tau + j\alpha) z} dz \right.$$
$$\left. + \frac{1}{2} \int_{S/2}^{\infty} e^{-(\tau + j\alpha) z} dz \right\} \tag{24}$$

If we define

$$a = \tau + j\alpha$$
$$b = \tau - j\alpha \tag{25}$$

(24) becomes upon substitution of (25)

$$G_1(\alpha) = NI\left\{-\frac{1}{2}\int_{-\infty}^{-S/2} e^{bz}dz + \frac{1}{S}\int_{-S/2}^{0} ze^{bz}dz + \frac{1}{S}\int_{0}^{S/2} ze^{-az}dz + \frac{1}{2}\int_{S/2}^{\infty} e^{-az}dz\right\} \tag{26}$$

Taking the limit as τ approaches zero gives

$$G(\alpha) = \lim_{\tau\to 0} G_1(\alpha) = \frac{NI}{2}\,\frac{e^{-j\alpha S/2} + e^{j\alpha S/2}}{j\alpha} + \frac{NI}{S}\left\{\frac{e^{j\alpha S/2}}{(-j\alpha)^2}\left[-(j\alpha S/2) + 1\right] - \frac{e^{-j\alpha S/2}}{(j\alpha)^2}\left[(j\alpha S/2) + 1\right] + \frac{1}{(j\alpha)^2} - \frac{1}{(j\alpha)^2}\right\} \tag{27}$$

which after some simplification gives

$$G(\alpha) = \frac{2NI}{jS\alpha^2}\sin\left(\frac{S\alpha}{2}\right) \tag{28}$$

or

$$f(\alpha) = \frac{NI}{jS\alpha^2}\sin\left(\frac{S\alpha}{2}\right)\cdot\frac{1}{\pi I_0(\alpha R)} \tag{29}$$

Substituting (29) into (10) we obtain

$$\Psi(r,z) = \frac{NI}{\pi S}\int_{-\infty}^{+\infty}\frac{\sin\left(\frac{S\alpha}{2}\right)}{j\alpha^2}\,e^{j\alpha z}\,\frac{I_0(\alpha r)}{I_0(\alpha R)}\,d\alpha \tag{30}$$

This integral can be simplified further by writing

$$\Psi(r,z) = \frac{NI}{\pi S}\left[\int_{-\infty}^{0}\frac{\sin(S\alpha/2)}{j\alpha^2}\,e^{j\alpha z}\,\frac{I_0(\alpha r)}{I_0(\alpha R)}\,d\alpha + \int_{0}^{\infty}\frac{\sin(S\alpha/2)}{j\alpha^2}\,e^{j\alpha z}\,\frac{I_0(\alpha r)}{I_0(\alpha R)}\,d\alpha\right] \tag{31}$$

which after some simplification gives

$$\Psi(r,z) = \frac{NI}{\pi}\int_0^\infty \frac{\sin(S\alpha/2)}{S\alpha/2}\,\frac{\sin(\alpha z)}{\alpha}\,\frac{I_0(\alpha r)}{I_0(\alpha R)}\,d\alpha \tag{32}$$

Equation (32) is the final solution for the scalar magnetic potential of the symmetrical magnetic lens as calculated from the approximate boundary conditions for unsaturated polepieces. For the analysis of magnetic lenses we are interested in the magnitudes of the axial magnetic induction and its derivatives.

The magnetic-field intensity is obtained from the gradient of the scalar potential. Thus, for the axial magnetic induction $B(z)$ we have

$$B(z) = -\mu_0 \left.\frac{\partial\Psi}{\partial z}(r,z)\right|_{z=0} = -\mu_0\,\frac{d\Psi}{dz}(0,z) \tag{33}$$

where $\Psi_{(0,z)}$ is the axial scalar potential variation. We obtain $\Psi_{(0,z)}$ from (32) by letting $r = 0$. Since $I_0(0) = 1$,

$$\Psi_{(0,z)} = \frac{NI}{\pi}\int_0^\infty \frac{\sin(S\alpha/2)}{S\alpha/2}\,\frac{\sin(\alpha z)}{\alpha}\,\frac{1}{I_0(\alpha R)}\,d\alpha \tag{34}$$

Before taking the derivative of (34), we change the variable of integration so that the dependence of the potential and fields on the lens dimensions will be more obvious by defining $t = \alpha R$, and therefore

$$\alpha = t/R$$
$$dt = R\,d\alpha \tag{35}$$

and since $D = 2R$ we obtain

$$\Psi_{(0,z)} = \frac{NI}{\pi}\int_0^\infty \frac{\sin(St/D)\,\sin(2tz/D)}{\frac{S}{D}\,t^2 I_0(t)}\,dt \tag{36}$$

Therefore

$$B(z) = 2\mu_0\,\frac{NI}{\pi S}\int_0^\infty \frac{\sin(St/D)\,\cos(2tz/D)}{t I_0(t)}\,dt \tag{37}$$

for the axial magnetic induction. This equation was first obtained by

Lenz.[5] Similarly we obtain the derivatives of the axial induction as

$$B'(z) = \frac{dB(z)}{dz} = -4\,\frac{\mu_0 NI}{\pi SD}\int_0^{\infty}\frac{\sin(St/D)\ \sin(2tz/D)}{I_0(t)}\,dt \qquad (38)$$

and

$$B''(z) = \frac{d^2B(z)}{dz^2} = -8\,\frac{\mu_0 NI}{\pi SD^2}\int_0^{\infty}\frac{t\ \sin(St/D)\ \cos(2tz/D)}{I_0(t)} \qquad (39)$$

III. NUMERICAL ANALYSIS TECHNIQUES USED IN THE PROGRAM

A program was written in Fortran IV for the analysis of symmetrical magnetic lenses using the field distribution derived above. It is convenient to express the field distribution, and the z,r coordinates in relative units rather than MKS units. The lens bore radius R and the maximum axial field B(0) are used as units of measure. By defining

$$k^2 = \frac{e}{8mV_r}\,B^2(0)\ R^2 \qquad (40)$$

the coefficient of spherical aberration C_s can be written in terms of Scherzer's coefficient C_1

$$\frac{C_s}{R} = \frac{k^2}{2}\int_{-\infty}^{\bar{z}_0}\left[3k^2\bar{B}^4 + (\bar{B}')^2 - \bar{B}^2\left(\frac{\bar{r}'_\alpha}{\bar{r}_\alpha}\right)^2\right]\bar{r}_\alpha^4\,d\bar{z} \qquad (41)$$

and the Glaser definition of C_s is given by

$$\frac{C_s}{R} = \frac{k^2}{12}\int_{-\infty}^{\bar{z}_0}[16k^2\bar{B}^4 + 5(\bar{B}')^2 - \bar{B}\bar{B}'']\bar{r}_\alpha^4\,d\bar{z} \qquad (42)$$

Here $\bar{z} = z/R$, $\bar{B} = B(z)/B(0)$, and the primes represent derivatives with respect to $\bar{z}$. The chromatic aberration coefficient C_c is given by

$$\frac{C_c}{R} = \int_{-\infty}^{z_0}(\bar{r}'_\alpha)^2\,d\bar{z} \qquad (43)$$

The terms of $\bar{z}$ the axial field distribution and its derivatives are expressed as

$$B_{(\bar{z})} = \frac{2\mu_0 NI}{\pi S} \int_0^\infty \frac{\sin(St/D)\ \cos(t\bar{z})}{tI_0(t)}\,dt \tag{44}$$

$$B'_{(\bar{z})} = \frac{-2\mu_0 NI}{\pi S} \int_0^\infty \frac{\sin(St/D)\ \sin(t\bar{z})}{I_0(t)}\,dt \tag{45}$$

and

$$B''_{(\bar{z})} = \frac{-2\mu_0 NI}{\pi S} \int_0^\infty \frac{t\ \sin(St/D)\ \cos(t\bar{z})}{I_0(t)}\,dt \tag{46}$$

At $\bar{z} = 0$ the field is given by

$$B_{(0)} = \frac{2\mu_0 NI}{\pi S} \int_0^\infty \frac{\sin(St/D)}{tI_0(t)}\,dt \tag{47}$$

Another field quantity of interest is the ratio of the maximum axial field $B(0)$ to the field in the polepiece gap, B_p . Since

$$B_p = \mu_0 \frac{NI}{S} \tag{48}$$

we obtain

$$\frac{B_{(0)}}{B_p} = \frac{2}{\pi} \int_0^\infty \frac{\sin(St/D)}{tI_0(t)}\,dt \tag{49}$$

The lens analysis program uses two specific methods of numerical integration. All definite integrals are solved by a modified form of Simpson's rule.[9] The solution of the differential equation is obtained by the Runge Kutta technique.

The value of $\bar{r}$ and $\bar{r}'$ are determined for the interval $|\bar{z}| \le 6.0$ with an increment of $\Delta z = 0.01$. This large interval was needed in order to guarantee that the starting and end points of $\bar{z}$ lie in a field free region for the range of values of S/D which were studied.

As the ray proceeds through the lens we keep track of the value of $\bar{r}$ so that the first axial crossing of the trajectory can be obtained. These values are used to determine the objective optical properties. Since we are only evaluating values of $\bar{r}$ at discrete increments, we note that the ray could cross the axis at one of these points; however, it will more than likely fall within the increment where $\bar{r}$ is not defined by the analysis. We therefore provide for these conditions in the program. If the ray crosses at a point where $\bar{r}$ is evaluated, we set the value of $\bar{z}$ at this point equal to the normalized midfocal length. However, if the ray crosses at an intermediate point, we save the values $\bar{r}$, $\bar{r}'$, and $\bar{z}$ at the increment points immediately to the left and right of where the ray crossed. We then interpolate these values to define the objective properties. If the lens is weak (i.e., k^2 small), the trajectory does not cross the axis within the lens field. In this case the objective properties are set equal to the projective properties which are evaluated from straight-line projections based on the coordinates of the trajectory in the field free region after leaving the lens.

IV. RESULTS OF THE PROGRAM

With the program the most complete set of results on the symmetrical magnetic lens available in the literature were obtained for the range of S/D from 0.01 to 2. It should be borne in mind that for $S/D > 2$, the field model which was derived earlier in this paper is no longer accurate. However, as was stated before, the most widely used values of S/D lie well within that range.

As the ratio of gap width to bore diameter, S/D, increases, the axial field distribution broadens and flattens out near the center of the gap. This is shown in Fig. 2 which, owing to the symmetry of the field, is plotted for positive values of $\bar{z}$ only. We note that for the extreme case $S/D = 2.0$, after which the field model loses its validity, the normalized field has fallen to a value of 0.07 at $\bar{z} = 3.0$. In view of this result and the nature of the field distribution, we see the justification in assuming that the region $|\bar{z}| \geq 6.0$, is field free in the lens analysis program.

The field half value width in relative units, a/R, is plotted versus S/D in Fig. 3. From the figure we see that a/R asymptotically approaches S/D as S/D becomes large. Some values of a/R for some of the lenses analyzed are given in Table I. From these values a correlation can be formed between Glaser's value of k^2, and the Liebmann value of k^2 used in the lens analysis program. The two values of k^2 are related by

$$k^2\big|_{\text{Glaser}} = \left(\frac{a}{R}\right)^2 k^2\big|_{\text{Liebmann}} \qquad (50)$$

Similarly the optical properties determined from the lens analysis program, which are normalized with respect to R, can be normalized with respect to a by dividing them by the value of a/R, if it is so desired.

The ratio of the maximum axial field to the field in the gap at the polepieces versus S/D is given in Fig. 4. With these values one can

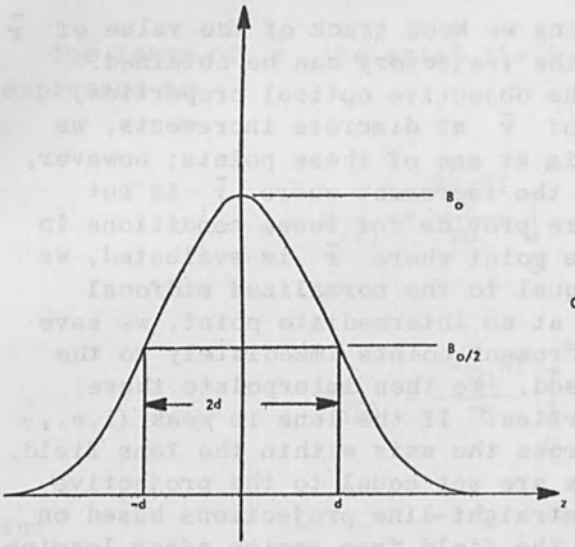

FIG. 1.—Glaser bell-shaped field.

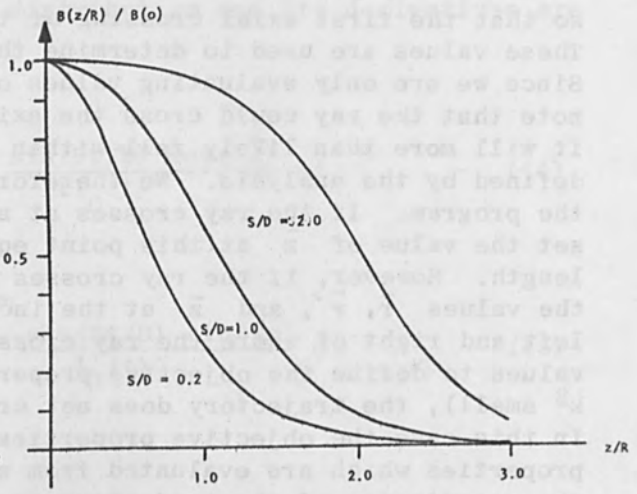

FIG. 2.—Normalized axial fields.

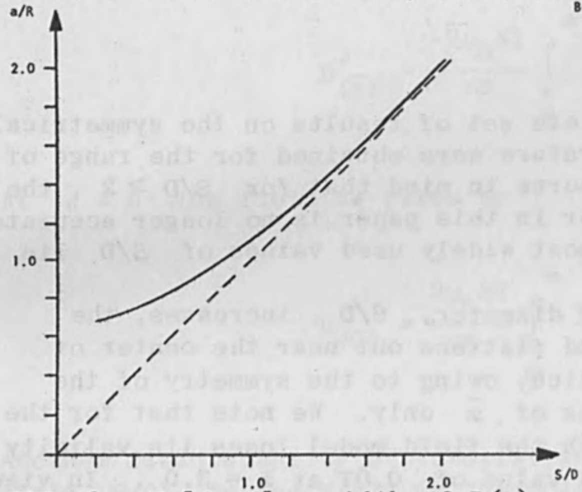

FIG. 3.—Half-value width of B(z)

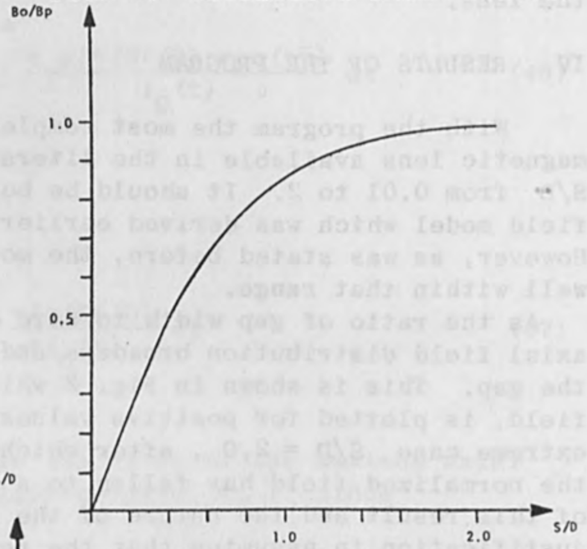

FIG. 4.—$B_{(0)}/B_p$ as function of S/D.

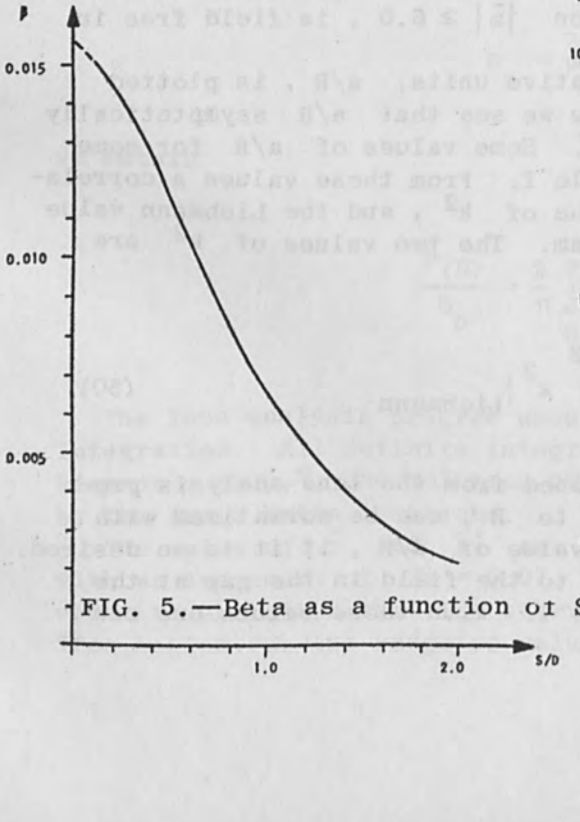

FIG. 5.—Beta as a function of S/D.

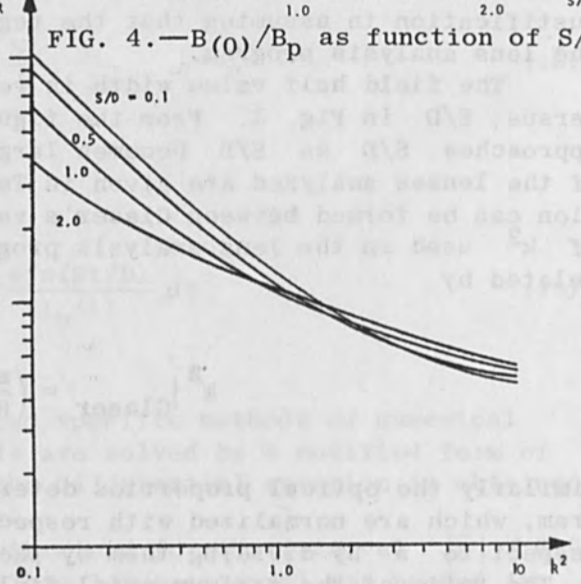

FIG. 6.—Objective focal length as function of lens excitation.

TABLE I

S/D	$B_{(0)}/B_p$	a/R	$\beta \times 10^2$
0.1	0.132	0.667	1.51
0.2	0.259	0.674	1.45
0.3	0.377	0.699	1.37
0.4	0.483	0.733	1.27
0.5	0.577	0.776	1.15
0.6	0.656	0.828	1.04
0.7	0.723	0.886	0.93
0.8	0.778	0.952	0.82
0.9	0.823	1.023	0.73
1.0	0.860	1.099	0.64
1.1	0.889	1.179	0.57
1.2	0.912	1.263	0.50
1.3	0.931	1.350	0.45
1.4	0.945	1.440	0.40
1.5	0.957	1.532	0.35
1.6	0.966	1.625	0.32
1.7	0.973	1.720	0.29
1.8	0.979	1.816	0.26
1.9	0.983	1.912	0.23
2.0	0.987	2.010	0.21

relate a given value of $B_{(0)}$ to the lens excitation NI or vice versa. A more important parameter that can be obtained from these values is β which relates the dimensionless excitation parameter k^2 to the actual electrical parameters NI and V_r of the lens. The relationship between β and k^2 is

$$k^2 = \beta \frac{(NI)^2}{V_r} \qquad (51)$$

We have

$$k^2 = \frac{e}{8mV_r} (B_{(0)} R)^2 \left(\frac{B_p}{B_p}\right)^2 = \frac{e}{8mV_r} \left(\frac{B_{(0)}}{B_p}\right)^2 B_p^2 R^2$$

which becomes

$$k^2 = \frac{e\mu_0^2}{32m} \left(\frac{B_{(0)}}{B_p}\right)^2 \left(\frac{D}{S}\right)^2 \frac{(NI)^2}{V_r} \qquad (52)$$

and β is given by

$$\beta = \frac{e\mu_0^2}{32m}\left(\frac{B_{(0)}}{B_p}\right)^2 \left(\frac{D}{S}\right)^2 = 0.0087\left(\frac{B_{(0)}}{B_p}\right)^2 \left(\frac{D}{S}\right)^2 \qquad (53)$$

Figure 5 shows β versus S/D . Some values for both β and $B_{(0)}/B_p$ are given in Table II for some of the lenses analyzed.

The objective optical properties f_o/R and z_o/R are plotted for the lenses S/D = 0.1, 0:5, 1.0, and 2.0 as a function of k^2 in Figs. 6 and 7. At small values of k^2 the focal length, Fig. 6, is larger for the smaller values of S/D . As k^2 increases f_o/R decreases monotonically. The focal lengths for lenses with smaller values of S/D , however, decrease more rapidly than the lenses with larger values of S/D. This results in a crossover of the focal lengths in the region $0.8 \leq k^2 \leq 3.3$ for the range of lenses considered. The focal lengths then emerge from this crossover region being larger for the larger values of S/D. After the crossover, the focal lengths become more nearly equal as k^2 increases, and continue to decrease at a decreasing rate. This trend is indicated in Fig. 6. The focal lengths at $k^2 = 100$ are 0.36, 0.37, 0.38 and 0.38 for S/D equal to 0.1, 0.5, 1.0, and 2.0, respectively. The midfocal lengths, z_o/R , versus k^2 are given in Fig. 7. Again we see a monotonic decrease as k^2 increases with z_o/R being smaller for larger values of S/D . The midfocal lengths, unlike f_o/R , remain separated as k^2 increases becoming negative in the range $0.8 \leq k^2 \leq 8.0$. This separation is still evident at extremely high values of k^2 . For example, at $k^2 = 100$, z_o/R is -0.65, -0.79, -1.14, and -2.08 for S/D = 0.1, 0.5, 1.0, and 2.0, respectively.

The objective optical properties just discussed are of particular interest when the image or object is immersed in the lens field, e.g., the electron microscope objective lens. In some applications, e.g., the projective lens of the electron microscope and the lens of a magnetically focused CRT, the projective optical properties are of interest. The projective focal lengths are of an oscillatory nature as k^2 increases. This is a result of the multiple crossings of the optical axis by the beam for strong lenses. For practical purposes, only beams that cross the axis once are of interest. In this region the projective focal lengths initially decrease reaching a minimum value and then increase again as k^2 increases. This is shown in Fig. 8 for the series of lenses S/D = 0.1, 0.5, 1.0, and 2.0. As for f_o/R we see that the projective focal length at small k^2 is largest for small values of S/D . In fact, for small values of k^2 , f_o/R and f_p/R are equal. For the range of lenses considered, f_o/R and f_p/R are always equal for $k^2 \leq 0.1$ (i.e., for $S/D \leq 2.0$). This correspondence increases with k^2 for smaller values of S/D up to approximately $k^2 = 1.0$ for S/D = 0.1. The minimum value of f_p is of particular interest since it represents the minimum value of focal length obtainable when the lens is used as a projective lens. Furthermore, operation of the lens at or near this point makes f_p invariant with reasonable fluctuations in k^2 due to the broad shallow nature of the minimums. For the range of lenses considered, the minima fall in the approximate range $0.35 \leq k^2 \leq 3.0$. After the minimum, further increase in k^2 results in a rapid increase of f_p which asymptotically goes to infinity. This corresponds to the value of k^2 when the beam leaves the lens field parallel to the optical axis. The projective midfocal lengths, z_p/R , as a function of k^2 are

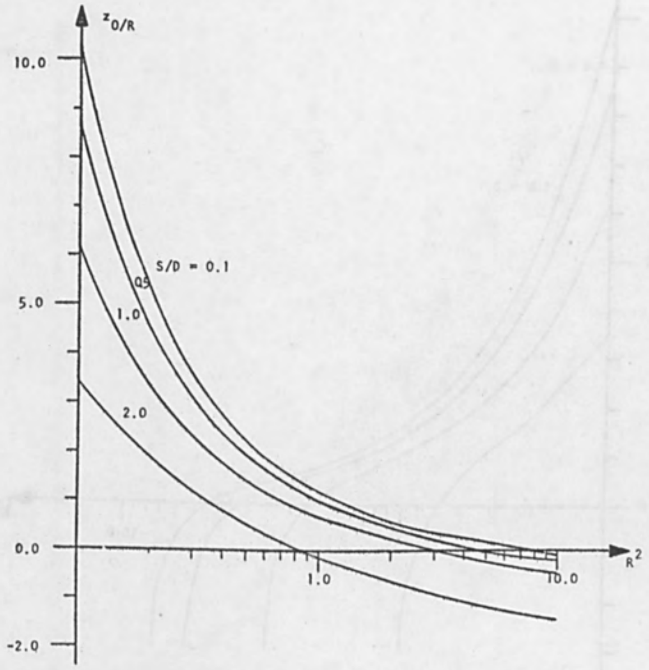

FIG. 7.—Objective midfocal length as function of lens excitation.

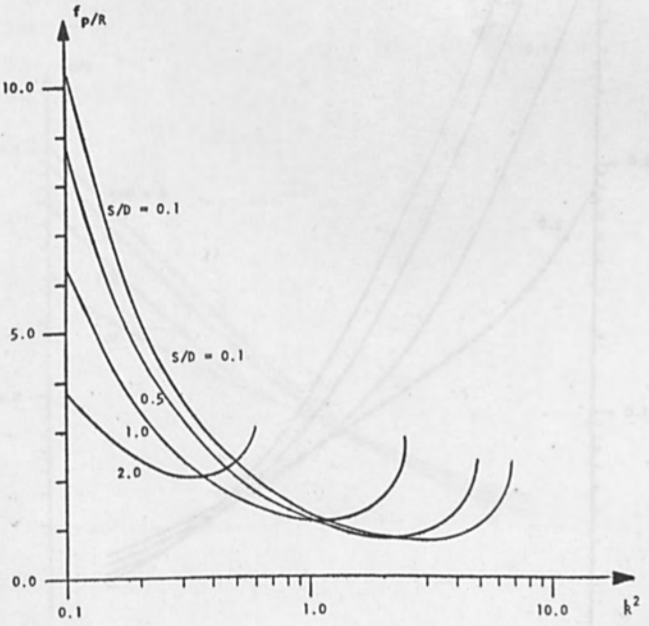

FIG. 8.—Projective focal length as function of lens excitation.

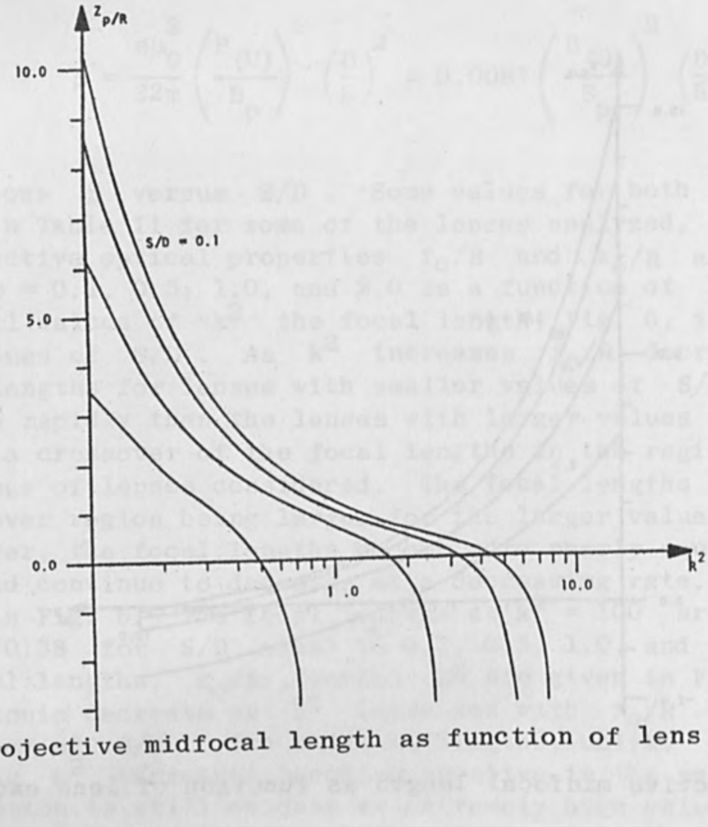

FIG. 9.—Projective midfocal length as function of lens excitation.

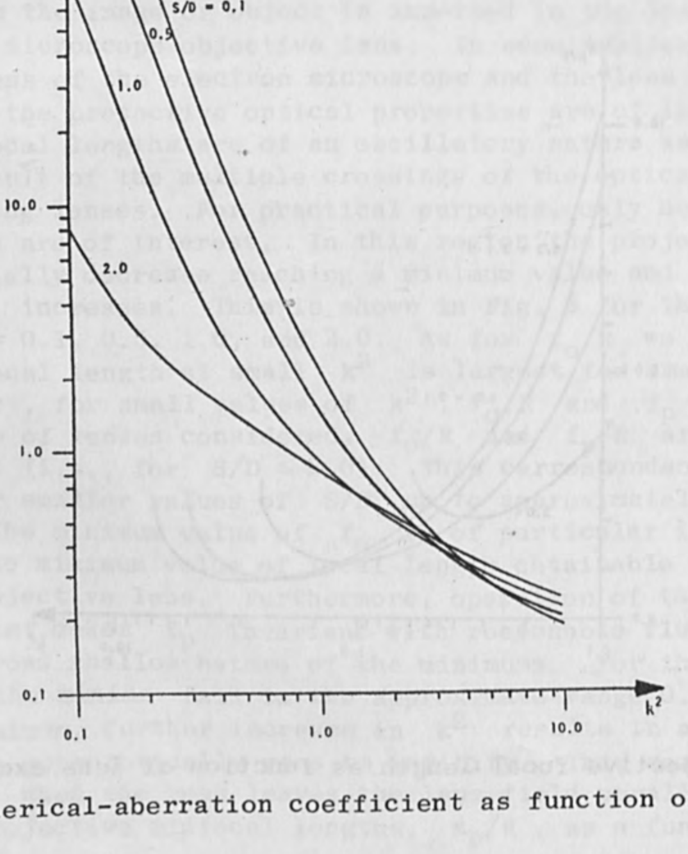

FIG. 10.—Spherical-aberration coefficient as function of lens excitation.

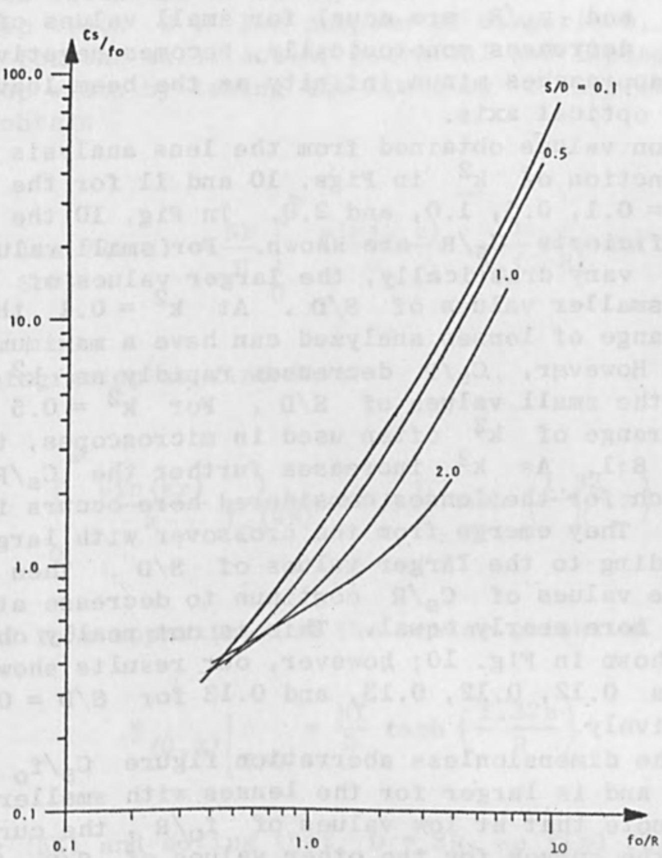

FIG. 11.—Dimensionless aberration constant as function of objective focal length.

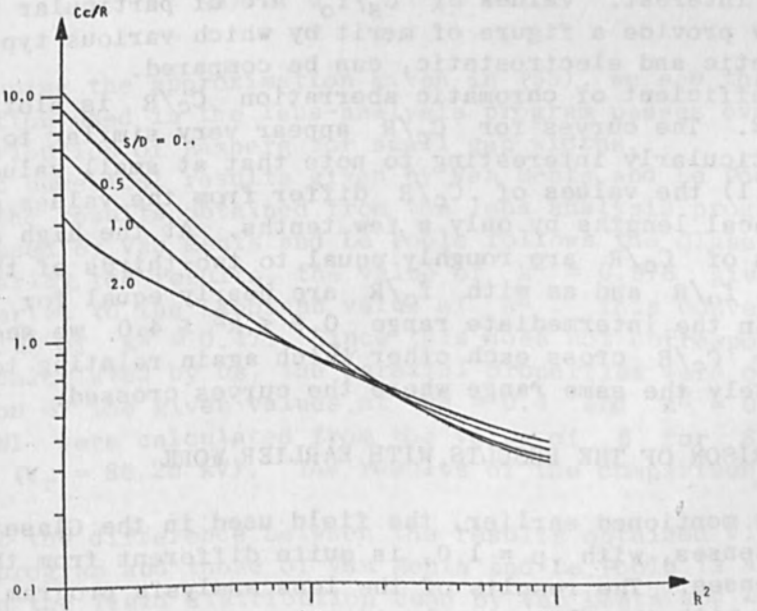

FIG. 12.—Chromatic-aberration coefficient as function of lens excitation.

given in Fig. 9. Just like their corresponding focal lengths, the values of z_p/R and z_o/R are equal for small values of k^2. As k^2 increases, z_p/R decreases monotonically, becomes negative, and then asymptotically approaches minus infinity as the beam leaves the lens parallel to the optical axis.

The aberration values obtained from the lens analysis program are plotted as a function of k^2 in Figs. 10 and 11 for the represented values of $S/D = 0.1$, 0.5, 1.0, and 2.0. In Fig. 10 the spherical aberration coefficients C_s/R are shown. For small values of k^2 the values of C_s/R vary drastically, the larger values of C_sR corresponding to the smaller values of S/D. At $k^2 = 0.1$ the ratio for C_s/R for the range of lenses analyzed can have a maximum value of the order of 80:1. However, C_s/R decreases rapidly as k^2 increases, especially for the small values of S/D. For $k^2 = 0.5$, which approaches the range of k^2 often used in microscopes, this ratio is of the order of 8:1. As k^2 increases further the C_s/R curves cross each other, which for the lenses considered here occurs in the interval $1.4 < k^2 < 5.5$. They emerge from the crossover with larger values of C_s/R corresponding to the larger values of S/D. Then as k^2 continues to increase, the values of C_s/R continue to decrease at a decreasing rate and become more nearly equal. This is not really obvious for the range of k^2 shown in Fig. 10; however, our results show that C_s/R at $k^2 = 100$ is 0.12, 0.12, 0.13, and 0.13 for $S/D = 0.1$, 0.5, 1.0, and 2.0, respectively.

In Fig. 11 the dimensionless aberration figure C_s/f_o increases as f_o/R increases and is larger for the lenses with smaller values of S/D. We also note that at low values of f_o/R, the curve for $S/D = 2.0$ crosses the curves for the other values of S/D. The shape of the curves for $S/D = 0.1$, 0.5, and 1.0 indicate a general crossover of the curves in the neighborhood of $f_o/R = 0.2$. Focal lengths this small correspond to values of $k^2 > 100$ and are, therefore, not of much practical interest. Values of C_s/f_o are of particular interest because they provide a figure of merit by which various types of lenses, both magnetic and electrostatic, can be compared.

The coefficient of chromatic aberration C_c/R is plotted versus k^2 in Fig. 12. The curves for C_c/R appear very similar to those of f_o/R. It is particularly interesting to note that at small values of k^2 (around 0.1) the values of C_c/R differ from the values of their corresponding focal lengths by only a few tenths. At the high end of k^2, the values of C_c/R are roughly equal to two-thirds of the corresponding values of f_o/R and as with f_o/R are nearly equal for the various lenses. In the intermediate range $0.9 \leq k^2 \leq 4.0$ we see that the curves for C_c/R cross each other which again relating to f_o/R is approximately the same range where the curves crossed.

V. COMPARISON OF THE RESULTS WITH EARLIER WORK

As was mentioned earlier, the field used in the Glaser analysis of magnetic lenses, with $\mu = 1.0$, is quite different from the fields found in real lenses. The results of the lens analysis program are thus not comparable with the Glaser analysis.

The field distribution used in the lens-analysis program was derived from the scalar magnetic potential with the assumption that the polepieces of the lens were equipotentials. The field distribution used by Ramberg was also based on equipotential polepieces with the additional constraint of negligible gap width S. For purpose of comparison, then, we return to the equation for the axial scalar potential and impose the constraint of negligible gap width by taking the limit as S approaches zero. Doing this, we obtain

$$\lim_{S\to 0} \Psi(0,z) = \frac{NI}{\pi}\int_0^\infty \frac{\sin(\alpha z)}{\alpha}\,\frac{1}{I_0(\alpha R)}\,d\alpha \qquad (54)$$

By numerical integration we find that

$$\int_0^\infty \frac{\sin(kz)}{k}\,\frac{1}{I_0(kR)}\,dk \approx \frac{\pi}{2}\tanh\left(\frac{1.32}{R}z\right) \qquad (55)$$

Thus, in view of this approximation the scalar potential becomes

$$\Psi(0,z)\Big|_{S\to 0} = \frac{NI}{2}\tanh\left(\frac{1.32z}{R}\right) \qquad (56)$$

Differentiating (56) and noting that D = 2R, we find the axial magnetic induction to be

$$B_{(z)} = B_0\,\mathrm{sech}^2\left(\frac{2.64z}{D}\right) \qquad (57)$$

Therefore, by using the approximation given in (55), we see that the field distribution used in the lens-analysis program passes over into the field distribution of Ramberg for small gap widths.

The specific numerical results given by Van Ments and Le Poole were compared with the results obtained from the lens analysis program. The value of k^2 used by Van Ments and Le Poole follows the Glaser definition. In comparing the results, the value of $k^2 = 0.976$ given by them was first converted to the Liebmann value of k^2. This conversion resulted in a value of $k^2 = 0.47$. Since this does not correspond to a value of k^2 calculated by us, the paraxial properties were obtained by interpolation of the given values at $k^2 = 0.4$ and $k^2 = 0.5$. The ampere turns NI were calculated from the value of β for $S/D = 1.4$ and $V = 80$ kV ($V_r = 86.26$ kV). The results of the comparison are shown in Table II.

We note that the difference between the results obtained with the lens analysis program and those of Van Ments and Le Poole is always less than 5%. Since the field distribution used by Van Ments and Le Poole was obtained experimentally from real lenses we consider the close agreement of the two methods a justification for use of the field equation derived earlier in this paper.

TABLE II.—Comparison of Van Ments and Le Poole's results with the lens-analysis program.

	f_0	z_0	P_0	NI
Van Ments and Le Poole	8.2 mm	6.0 mm	-2.2 mm	3200 At
Lens analysis program	7.9 mm	5.8 mm	-2.1 mm	3199 At
% Difference	3.6	3.33	4.5	0.03

Given: S/D = 1.4, S = 14 mm, D = 10 mm, V = 80 kV, $k^2 = 0.976$

The results given by Liebmann and Grad were compared with results obtained from the lens analysis program. For these cases the values of k^2 corresponding to the different S/D values (0.2, 0.6, 1.0, and 2.0) were computed using the value of β obtained by our program and the values of NI and V_r given by Liebmann and Grad. The comparison is shown in Table III.

From the table we see that for the magnitudes of the fields, the paraxial properties, and the chromatic aberration, the correlation between the methods is very good. The percent error in these quantities ranges from 0% to 5%. For most of these cases, however, it is less than 3%. The percentage error for the spherical aberration coefficient is extremely high. For the four lenses the minimum error is 4.25% for S/D = 1.0 and the maximum error is 30.3% for S/D = 2.0. In view of these large errors the lens analysis program was changed so that the spherical aberration coefficient was calculated using Glaser's definition. The same results were obtained in both cases, with agreement up to the fifth decimal place. The method of calculating C_s/R used by Liebmann and Grad requires evaluation of the first and second derivatives of $\bar{B}$. These derivatives were obtained by successive differencing of the initial potentials read from the resistance-network analog. In our case, the derivatives are obtained from equations, and the field equation provides excellent correlation with the different methods for parameters other than C_s/R . We conclude, therefore, that the values of C_s/R obtained from our analysis are more accurate.

In their paper Liebmann and Grad also presented a table of values of ampere turns NI necessary to obtain a given focal length f_0/R at a fixed anode voltage, $V_r = 6.7 \times 10^4$ V. These values of NI were also calculated from results obtained with the lens analysis program. The results obtained by Liebmann and Grad and those obtained from the lens analysis program are compared in Table IV.

Again we see the results are in excellent agreement for the two methods. For the case $f_0/R = 10.0$ and S/D = 2.0, the percent error is 19.2%. Otherwise, it is always less than 6%. k^2 for this value of f_0/R is found by interpolation over a large range of f_0/R and is, therefore, the probable source of error.

TABLE III.—Comparison of Liebmann and Grad's results with the lens-analysis program.

Source	S/D	0.2	0.6	1.0	2.0
Liebmann & Grad	k^2	1.44	0.94	0.56	0.19
Lens-analysis program		1.36	0.97	0.60	0.20
% Difference		2.68	3.10	7.15	5.3
Liebmann & Grad	H_0 (gauss)	10 500	8450	6500	3800
Lens-analysis program		10 162	8589	6750	3876
% Difference		3.21	1.65	3.85	2.00
Liebmann & Grad	f_0/R	1.00	1.20	1.50	2.40
Lens-analysis program		1.02	1.18	1.45	2.37
% Difference		2.00	1.67	3.33	1.25
Liebmann & Grad	z_0/R	0.84	1.00	1.20	1.85
Lens-analysis program		0.88	1.00	1.21	1.88
% Difference		4.8	0.0	0.84	1.62
Liebmann & Grad	C_s/R	1.05	1.25	1.65	3.8
Lens-analysis program		1.17	1.31	1.58	2.85
% Difference		11.4	4.80	4.25	30.3
Liebmann & Grad	C_c/R	0.81	0.96	1.2	1.9
Lens-analysis program		0.82	0.94	1.14	1.85
% Difference		1.22	2.09	5.0	2.64

TABLE IV.—Comparison of Liebmann and Grad's values with the lens-analysis program.

	f_0/R	S/D = 0.2	S/D = 0.6	S/D = 1.0	S/D = 2.0
Liebmann & Grad	10.0	670	720	810	1000
Lens-analysis program		644	707	846	1192
% Error		3.87	1.80	4.44	19.20
Liebmann & Grad	5.0	960	1060	1170	1500
Lens-analysis program		983	1082	1227	1586
% Error		2.39	2.07	4.87	5.73
Liebmann & Grad	2.0	1600	1800	2000	3000
Lens-analysis program		1622	1757	1996	2986
% Error		1.37	2.39	0.20	0.46
Liebmann & Grad	1.0	2500	2850	3700	6700
Lens-analysis program		2575	2930	3513	6640
% Error		3.00	2.80	5.75	0.89

REFERENCES

1. W. Glaser, Z. Physik 117: 285, 1941.
2. E. G. Ramberg, J. Appl. Phys. 13: 582, 1942.
3. M. Van Ments and J. B. Le Poole, Appl. Sci. Res. 1B: 3, 1947.
4. G. Liebmann and E. M. Grad, Proc. Phys. Soc. B64: 956, 1951.
5. F. Lenz, Z. f. angew. Phys. 2: 448, 1950.
6. A. B. El-Kareh, Fundamentals of Electron Optics, in preparation.
7. A. Papoulis, The Fourier Integral and Its Applications, New York, McGraw-Hill, 1962.
8. R. M. Bracewell, The Fourier Transform and Its Applications, New York: McGraw-Hill, 1965.
9. D. D. McCracken, Fortran with Engineering Applications, New York: John Wiley and Sons, 1969.

PARAXIAL ELECTRON TRAJECTORIES WITH SPACE CHARGE

J. H. McWHIRTER

Westinghouse Research Laboratories, Pittsburgh, Pa.

Gans's approximation is a method for computing electron trajectories near an axis of radial symmetry when the angle between the trajectory and the axis is small. The effect of the electron-beam space charge on the field and thus on the trajectory is neglected. This paper describes an extension to include the effect of the space charge. Several simplifying assumptions are made which permit a simple expression for the electron-beam charge density. The effect of this space charge on the electron trajectory can then be included. The results of calculations which have been made appear to be reasonable.

A calculation of the space-charge-limited current is also obtained as a byproduct.

BACKGROUND

Gans's approximation[1,2] is useful as a means of calculating electron trajectories where the electron path is close to an axis of radial symmetry, the angle between the path and the axis is small, and space charge effects are negligible. The method requires that the axial field be approximated by a series of straight line segments. The off-axis field is approximated by the initial terms of a series solution to Laplace's equation.

APPROACH[3]

The approach which has been taken here is similar to Gans's method. The difference is that a series solution in the radial distance r is obtained for Poisson's equation rather than Laplace's equation. The potential is an even function of r . We neglect the terms including the fourth and higher powers of r , leaving only a term which does not change with r and a term varying with the square of r . The coefficients of this series vary with axial position and are functions of the axial potentials and the charge densities along an axis.

The solution to this problem by any method encounters difficulty in the calculation of space charge. Initially, the electrons come from the cathode in densities which are functions of position, with various initial energies, and at various angles. Each electron affects the field and the position of each electron is in turn influenced by the field. This difficult problem is simplified by means of the following assumptions:

(1) The axial charge density is calculated as if the entire current is uniformly distributed within the beam radius.

(2) The beam radius is defined to be the radial displacement of an electron which leaves the outer edge of the cathode with zero initial velocity.

A mathematical approximation is made which is equivalent to the assumption that the charge is concentrated or "bunched" at discrete planes along the axis.

AN EXAMPLE

The beam profiles have been determined for the electron beam gun configuration in Fig. 1 with several currents.[4] The procedure used was as follows:

(1) The entire field was found by means of numerical field plotting techniques without including the effects of space charge.
(2) The charge density was found by relating the electron velocities to the axial potentials (Eq. 3). The beam diameter was assumed to be equal to the cathode diameter. Since beam diameters are later determined, calculated beam diameters could have been used in an iterative manner. This is an unnecessary refinement since the effect of the charge on the axial potentials is secondary and is more a function of total charge per unit axial distance than it is of charge density.
(3) The entire field is found including the effect of the estimated space charge.
(4) Steps 2 and 3 are repeated until the axial potentials have converged. An over-relaxation factor of 1.5 was applied to the axial potentials in this iterative process and this seemed to hasten convergence. As is shown it is not important for the axial potentials to be precisely consistent with the space charge.

In order to calculate the charge densities, the following formulas are utilized:

$$v = 5.93 \times 10^5 \, \phi^{1/2} \qquad \text{m/sec} \qquad (1)$$

$$\rho = \frac{I}{\pi R^2 v} \qquad \text{coul/m}^3 \qquad (2)$$

where

v is the electron velocity (m/sec)
ϕ is the axial potential with respect to the cathode (V)
ρ is the charge density (coul/m^3)
I is the current (A)
R is the beam radius (m)

If we change to a length unit to inches and combine 1 and 2 we have

$$\rho/\varepsilon_0 = 6.06 \times 10^4 \, \frac{I}{\phi^{1/2} R^2} \qquad \text{V/in.}^2 \qquad (3)$$

RESULTS OF CALCULATIONS

The beam profiles for the gun configuration in Fig. 1 have been calculated for several values of cathode current. The results are shown in Fig. 2, all calculated on the basis of a mesh interval of 0.030 in. which

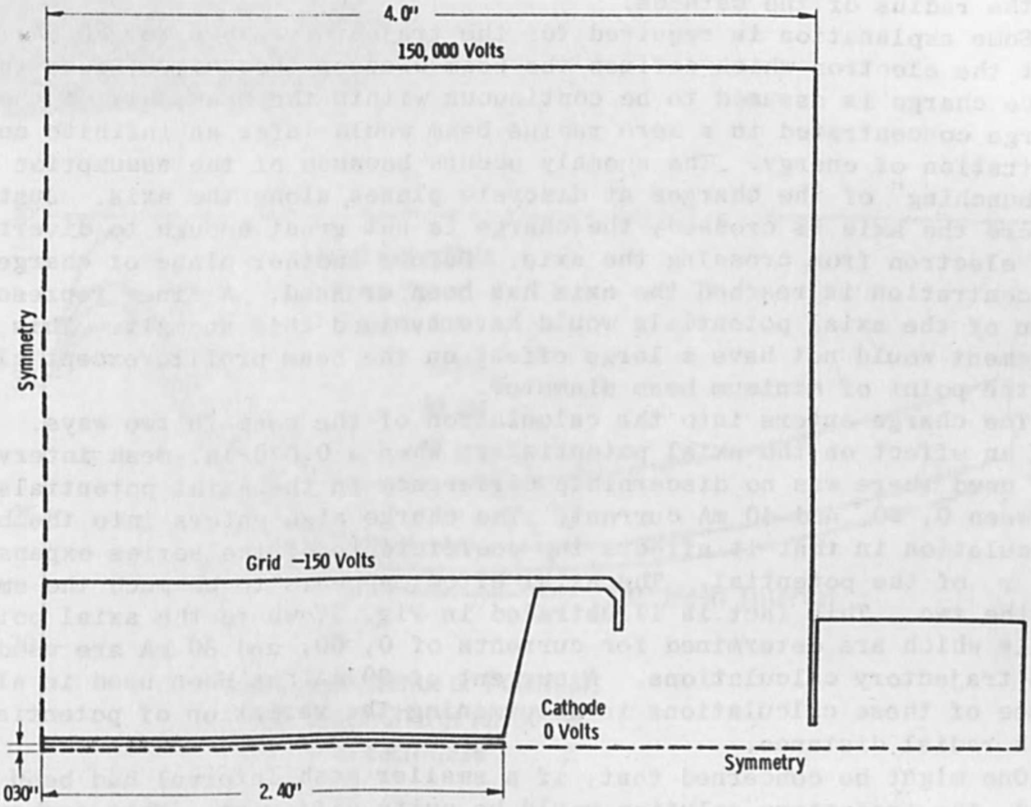
4.0"
150,000 Volts
Symmetry
Grid −150 Volts
Cathode
0 Volts
Symmetry
.030"
2.40"

FIG. 1.—Gun configuration with 30-mil mesh interval.

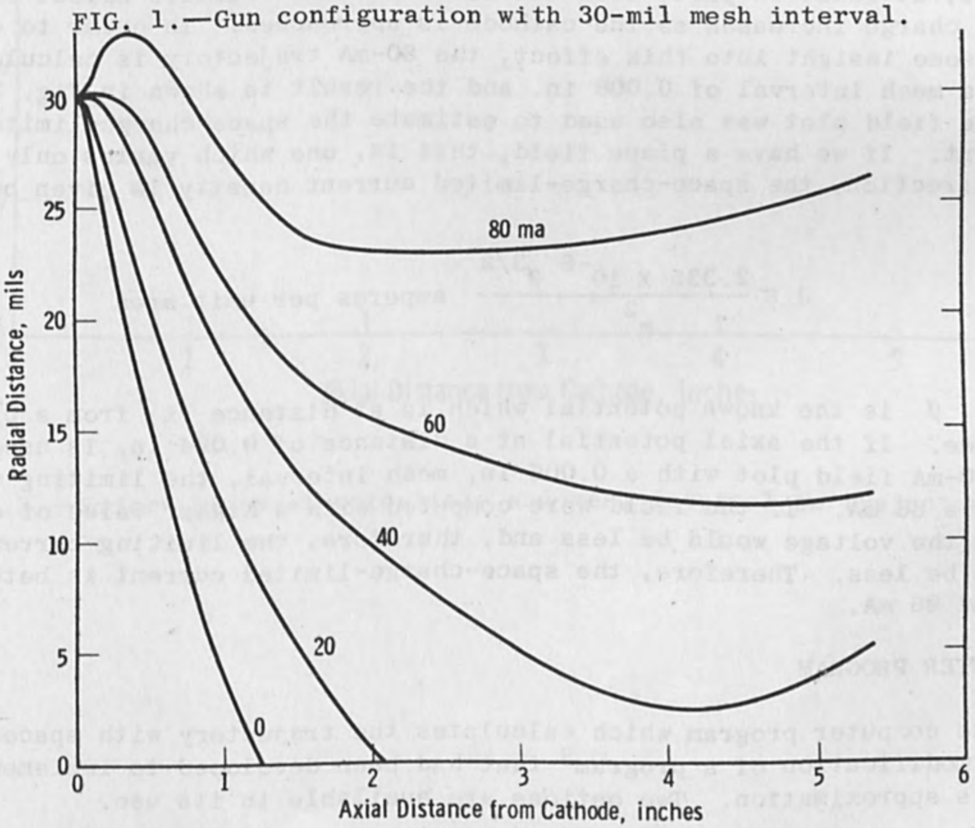

FIG. 2.—Beam radii at various cathode currents.

is the radius of the cathode.

Some explanation is required for the trajectory shown for 20 mA, in that the electron which defines the beam crosses the axis. Since the space charge is assumed to be continuous within the beam, all of the charge concentrated in a zero radius beam would infer an infinite concentration of energy. The anomaly occurs because of the assumption of a "bunching" of the charges at discrete planes along the axis. Just before the axis is crossed, the charge is not great enough to divert the electron from crossing the axis. Before another plane of charge concentration is reached the axis has been crossed. A finer representation of the axial potentials would have avoided this anomaly. This refinement would not have a large effect on the beam profile except close to the point of minimum beam diameter.

The charge enters into the calculation of the beam in two ways. It has an effect on the axial potentials. When a 0.030-in. mesh interval was used there was no discernible difference in the axial potentials between 0, 20, and 40 mA current. The charge also enters into the beam calculation in that it affects the coefficients of the series expansion in r of the potential. The axial effect appears to be much the smaller of the two. This fact is illustrated in Fig. 3, where the axial potentials which are determined for currents of 0, 60, and 80 mA are used in the trajectory calculations. A current of 80 mA has been used in all three of these calculations in determining the variation of potential with radial distance.

One might be concerned that, if a smaller mesh interval had been used, the trajectory solution would be quite different. This concern arises, at least in part, from the fact that the relative effect of the space charge increases as the cathode is approached. In order to establish some insight into this effect, the 80-mA trajectory is calculated with a mesh interval of 0.006 in. and the result is shown in Fig. 3.

The field plot was also used to estimate the space-charge-limited current. If we have a plane field, that is, one which varies only in one direction, the space-charge-limited current density is given by[1]

$$J = \frac{2.335 \times 10^{-6} \phi^{3/2}}{z^2} \text{ amperes per unit area}$$

where ϕ is the known potential which is at distance z from a plane cathode. If the axial potential at a distance of 0.024 in. is used from the 80-mA field plot with a 0.006-in. mesh interval, the limiting current is 86 mA. If the field were computed with a higher value of current, the voltage would be less and, therefore, the limiting current would be less. Therefore, the space-charge-limited current is between 80 and 86 mA.

COMPUTER PROGRAM

The computer program which calculates the trajectory with space charge is a modification of a program[3] that had been developed to implement Gans's approximation. Two options are available in its use.

(a) The trajectory of an electron, whose path determines the outer boundary of the beam, is calculated. In the computations which have been

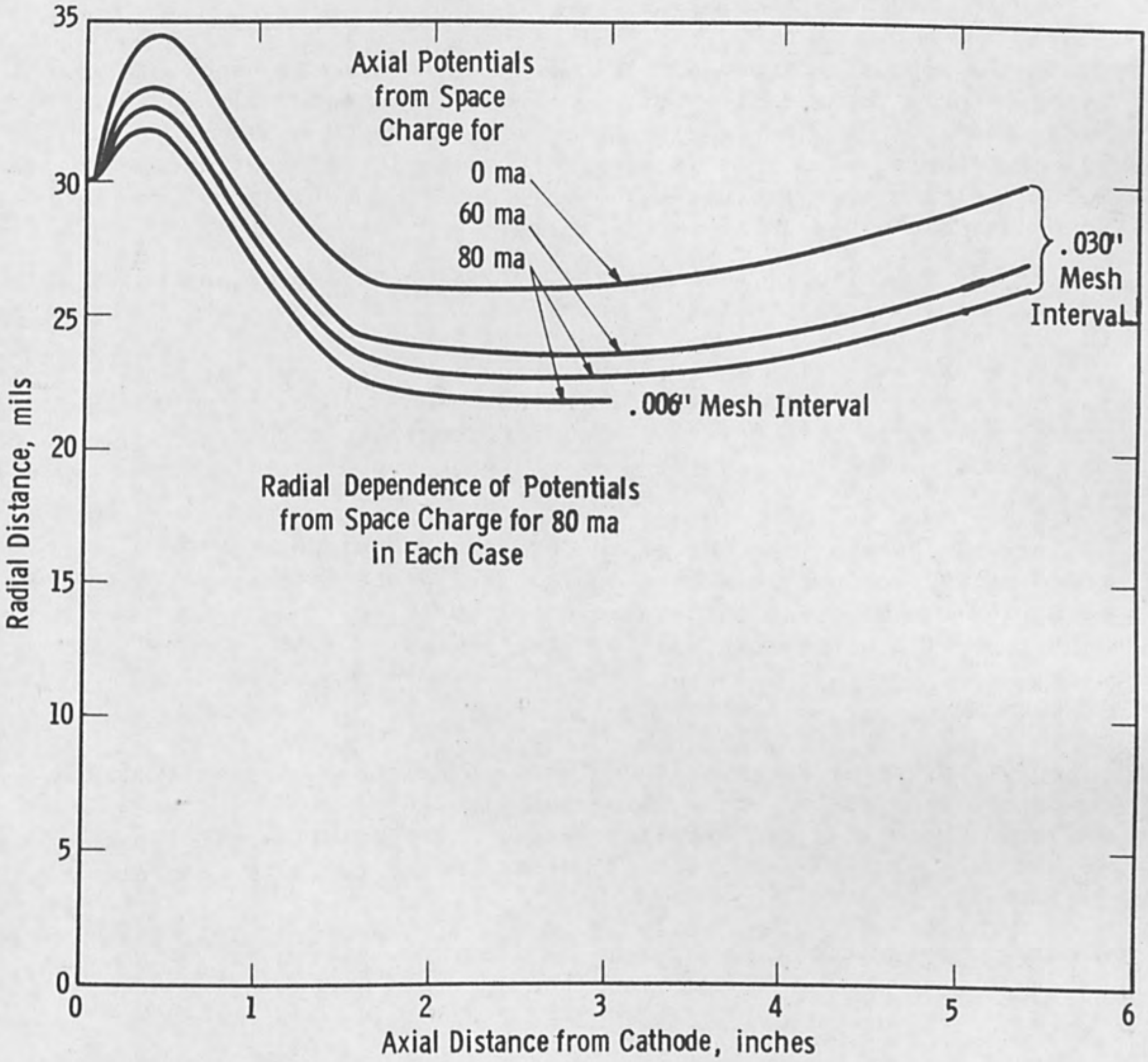

FIG. 3.—Effect of axial potentials and mesh interval on trajectories.

made, this has always been an electron which starts from the outer edge of the cathode with zero initial velocity.

(b) If the beam radius has already been determined, the values of the radii can be part of the input data and the trajectory of an electron with any other initial condition may be determined.

POTENTIAL FUTURE DEVELOPMENT

Gans's approximation was originally intended to be used as a manual calculation. The modification for space charge was designed to be a minor change in an existing computer program which could be easily and quickly incorporated. It is therefore quite likely that the method is not the ultimate in its use of mathematics or computational techniques. Some possible lines of improvement are:

(1) The use of more terms in the series expansion of the potential.

(2) A more elegant solution which does not require the "bunching" of the space charge.

(3) A variable step size in the trajectory tracing which will permit the specification of more detail in the potentials where it is needed.

(4) Automatic interpolation of the potentials so that a smaller step can be used where the direction is changing rapidly without the necessity of specifying the data for each step.

It would be a simple matter to develop an analogous program which would solve problems in an x-y coordinate system with symmetry in the z direction, the electron path being confined to small values of y. The equations will be somewhat different.

REFERENCES

1. K. R. Spangenberg, Vacuum Tubes, New York: McGraw Hill, 1948.

2. R. Gans, Zeit. Techn. Phys. 18: 41, 1937.

3. J. H. McWhirter, Paraxial Electron Trajectories with Space Charge, Scientific Paper 69-162-EWELD-P1, Westinghouse Research Laboratories, Pittsburgh, Pa.

4. J. Lempert, J. F. Lowry, F. D. Seaman, and C. S. Williams, Proc. 7th Annual Electron and Laser Beam Symposium, March 31-April 2, 1965; p. 393.

HIGH-SPEED HIGH-RESOLUTION DEFLECTION SYSTEM

R. F. WOLTER

International Business Machines Corp. (Systems Development Division), San Jose, Calif.

A magnetic deflection system has been developed for use in a high-resolution electron-beam-on-film recorder. Performance of the system has been tested under various operating conditions, and experimental results have been compared with predictions of third-order deflection-aberration theory. Ultimate resolution of 60 000 spot diameters per line (measured at the 1/e points of a Gaussian current distribution) is limited only by energy-spread induced chromatic aberration.

INTRODUCTION

A demand for high-resolution video-on-film recording[1] initiated the development of an electron-gun assembly for a compact electron-beam recorder (Fig. 1). The deflection system presented in this paper is part of the recorder and was designed to meet the resolution specification of 11 000 spot diameters over an 11.4-cm (4.5-in.) line-scan format at a sweep frequency of 8.3 kHz, a beam current of 1.6×10^{-6} A, an accelerating voltage of 15 kV, and a working distance of 12.7 cm (5.0 in.). Contract requirements necessitated the development of a new deflection system since our experience with previously built electron-optical systems has shown that commercially available deflection yokes presently do not have or cannot guarantee the required high-resolution performance.

DEFLECTION YOKE

The deflection yoke shown in Fig. 2 consists of a ferrite core furnished with an approximated sinusoidal current distribution for x and y deflection to generate a homogeneous field for all deflection directions.[2] The number of windings and the yoke configuration have been optimized to achieve a high resonant frequency and therefore a high deflection linearity at fast sweep rates while maintaining a reasonable deflection sensitivity. Fifteen pairs of windings have been used for each deflection direction, and the yoke has an outside diameter $2R_2 = 6.2$ cm, an inside diameter $2R_1 = 3.2$ cm, and a length $L = 3.8$ cm.

Deflection sensitivity can be approximated by

$$\frac{\sin \beta}{IN} = \mu_0 \sqrt{\frac{e}{2mU}}\, \frac{L}{2R_1}\, k$$

where

β = deflection angle
I = deflection current
N = number of pairs of windings per deflection direction

Record of 10th Symposium on Electron, Ion, and Laser Beam Technology (L. Marton, ed.); San Francisco Press, Inc.
Copyright © by The Institute of Electrical and Electronics Engineers, Inc.—Printed in the U.S.A.

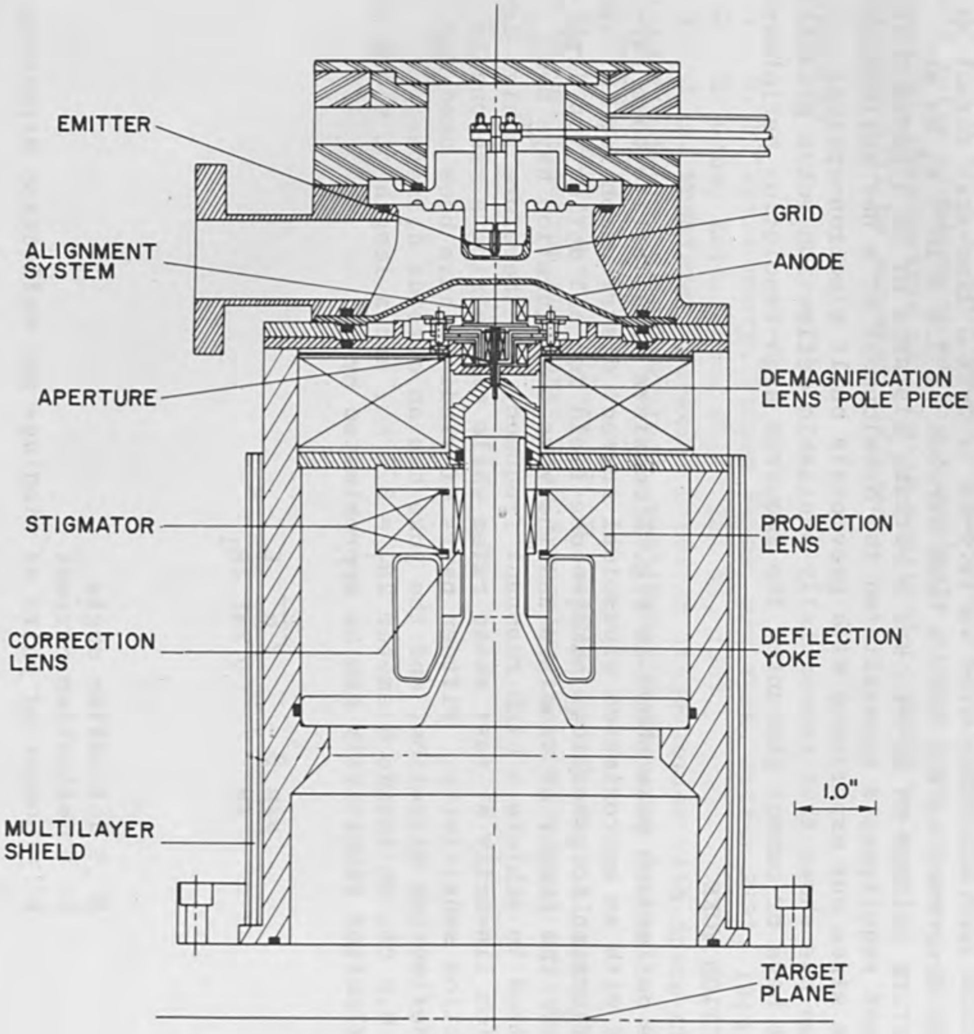
EMITTER
GRID
ALIGNMENT SYSTEM
ANODE
APERTURE
DEMAGNIFICATION LENS POLE PIECE
STIGMATOR
PROJECTION LENS
CORRECTION LENS
DEFLECTION YOKE
1.0"
MULTILAYER SHIELD
TARGET PLANE

FIG. 1.—Electron-gun assembly.

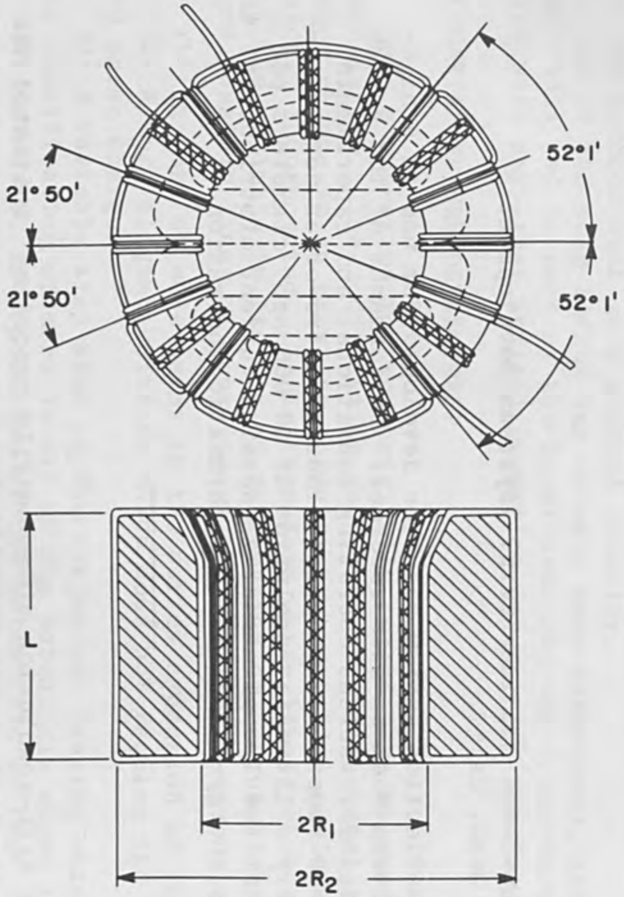
21° 50'
21° 50'
52° 1'
52° 1'
L
2R1
2R2

FIG. 2.—Deflection-yoke current distribution.

μ_0 = induction constant
e = electron charge
m = mass of electron
U = accelerating voltage

The numerical constant k is a function of core material and geometry, where $1 \le k \le 2$.

Measurements have shown the deflection sensitivity to be 4.2°/A at an accelerating voltage of 10kV, and the yoke resonant frequency to be 6.1 MHz.

For calculating deflection aberrations, the on-axis deflection field has been approximated by the on-axis field of a cylinder with radius R_1 and length L , which has sinusoidal current distribution and a center field H_0 :

$$H(0,0,z) = H_0 \left[\frac{z}{\sqrt{z^2 + R_1^2}} \quad \frac{z - L}{\sqrt{(z-L)^2 + R_1^2}} \right]$$

DEFLECTION ABERRATION

The theoretical performance of the deflection yoke has been calculated according to the third-order deflection-aberration theory of Glaser.[3] If we assume space charge and relativistic effects to be negligible, a deflection field symmetrical against the plane of deflection, small deflection angles (i.e., $\sin \beta \simeq \beta$), and aperture angles α small compared to $\beta (\alpha < \beta)$, the main resolution-limiting deflection aberrations are caused by image curvature and astigmatism. In a first approximation, the spot diameter of the deflected beam is a linear function of the aperture angle and proportional to the square of the deflection angle.

Deflection aberrations measured at various working distances, aperture angles (beam semiangles at the target), and deflection angles are shown in Figs. 3 and 4. The spot diameter is defined at the 1/e points of a Gaussian current distribution. Figure 3 demonstrates the linear relationship between the aberration diameter and the aperture angle for three different deflection angles. Operating parameters include the following: working distance = 15 cm, accelerating voltage - 10 kV, and beam current = 0.7×10^{-9} A . The measured spot size as a function of the deflection angle is shown in Fig. 4 for working distances of 16.8 and 10.5 cm, and aperture angles of 0.9×10^{-3} and 1.28×10^{-3} rad, respectively.

A numerical comparison between experimental and theoretical data is given in Fig. 5. The upper solid curve represents the uncorrected spot diameter according to the theory and the small circles on the dotted line are experimental results. The operating parameters are as follows: aperture angle = 10^{-3} rad, accelerating voltage = 10 kV, working distance = 5.9 in., and beam current = 0.7×10^{-9} A .

The resolution expressed in terms of numbers of largest spots per line is about 1000.

CORRECTION ELEMENTS

To improve performance, correction elements have been added to the yoke

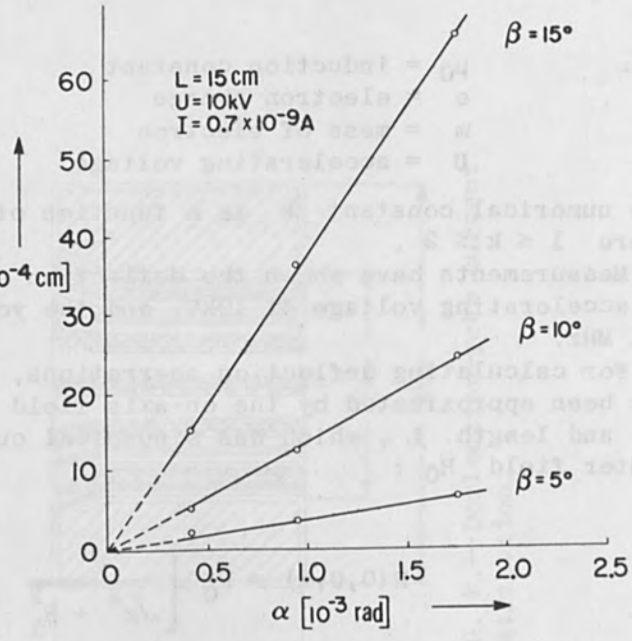

FIG. 3.—Deflection aberration as function of beam semiangle.

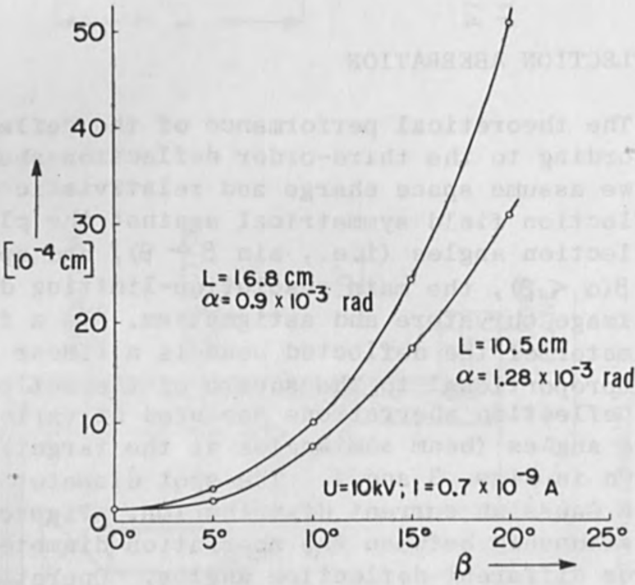

FIG. 4.—Deflection aberration as function of deflection angle.

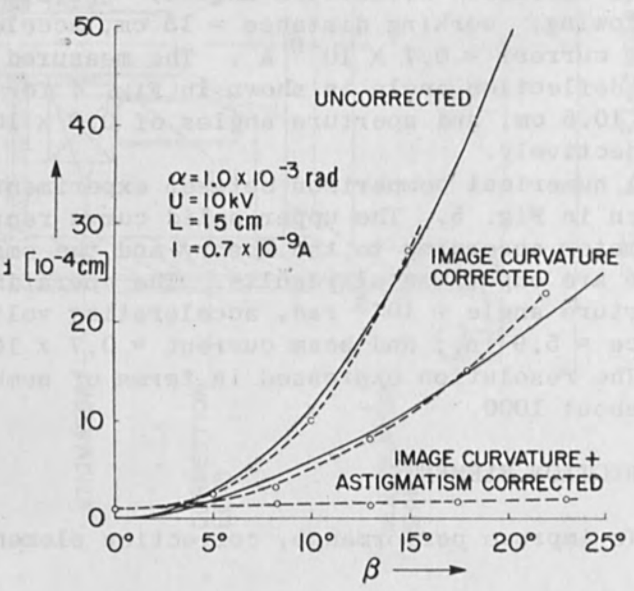

FIG. 5.—Deflection aberration as function of deflection angle (theory and experiment).

as shown in Fig. 6. Incorporated into a projection lens, which is not part of the deflection system, is a dynamic lens for correcting image curvature and a 4-pole stigmator for correcting astigmatism. Furthermore, a 6-pole isoplanator[4] is positioned at the beginning of the deflection yoke, which could be used for correcting any three-fold aberrations.

Theoretical and experimental results for the corrected spot diameter are shown in Fig. 5 as a function of the deflection angle. Correction of image curvature yields an astigmatic spot, whose diameter in deflection direction is shown by the middle solid line. Experimental results are again indicated by small circles on the dotted line.

Correction of image curvature and astigmatism should result in a spot size mainly determined by the spot-focusing system and deflection coma. The system used for the experiments was a modified electron gun from the IBM Photo Digital System,[5] which is designed for a spot diameter of 1×10^{-4} cm. The theoretical deflection coma at the above stated operating conditions is well below 0.5×10^{-4} cm and, therefore, does not show up in Fig. 5. The measured spot size, however, increased by more than 1×10^{-4} cm, indicating that a further aberration must be present. Correction of image curvature and astigmatism increased the resolution of the deflection system under the above-mentioned operating conditions by a factor of about 50.

ENERGY SPREAD

The unanticipated increase in spot size for the image curvature and astigmatism-corrected system indicated that chromatic aberrations could be present. Chromatic deflection aberrations could be caused by the cathode temperature-dependent normal energy spread or by the energy spread owing to interaction of beam electrons.[6,7] Since this energy

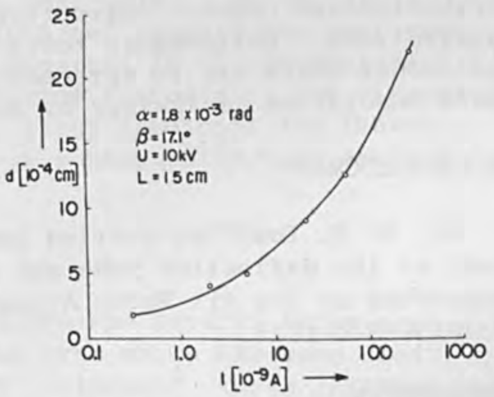

FIG. 7.—Deflection aberration as function of beam current (effect of energy spread).

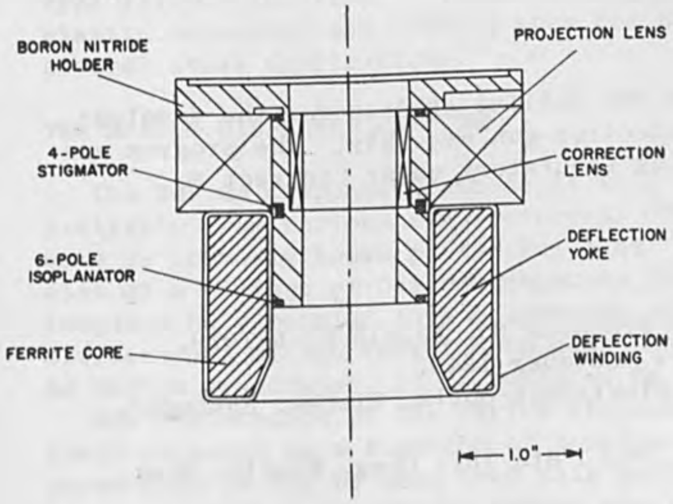

FIG. 6.—Magnetic deflection system with correction elements.

spread is a function of the beam current density, the minimum spot diameter in the deflection direction has been investigated as a function of beam current. The beam current at the target has been increased over three orders of magnitude by modulation of the emission current of the triode-type electron source by means of grid voltage variation while all other operating parameters were kept constant. The diameter of the undeflected spot has been measured to be less than 3×10^{-4} cm for all beam currents. Figure 7 indicates that, with increasing beam current, a growing spot has been observed, a result which qualitatively agrees with the energy-spread theory.

RESOLUTION LIMITATIONS

The resolution of this astigmatism and image-curvature-corrected deflection system is therefore limited under the above-mentioned operating conditions by energy-spread-induced chromatic aberration. Deflection aberrations could be corrected in agreement with the theoretical predictions of third-order aberration theory. Coma aberrations have not been detected in the present system and, therefore, correction of three-fold aberrations by means of the 6-pole isoplanator could not be demonstrated.

Ultimate resolution, measured at a beam current of 0.3×10^{-9} A and a working distance of 5.0 in., was a 1.8×10^{-6}-m spot up to a deflection angle of 0.4366 rad. This resolution is equivalent to a resolution of 60 000 spot diameters per line.

CONCLUSION

A magnetic deflection system has been developed for a high-resolution video-on-film recorder for airborne applications. The system incorporates a ferrite-cored magnetic deflection yoke with a sinusoidal current distribution and dynamic correction elements for third-order deflection aberrations. Performance tests resulted in deflection aberrations measurements which are in agreement with theoretical prediction. The ultimate resolution is limited by energy-spread induced chromatic aberration.

ACKNOWLEDGMENT

Dr. K. H. Loeffler carried out the initial studies for the development of the deflection yoke and electron gun assembly. The program was supported by the Air Force Avionics Laboratory under Contract No. F33615-68-C-1045.

REFERENCES

1. Request for U.S. Air Force Proposal No. F33615-67-R-1979.
2. K. Schlesinger, Electronics, October 1949.
3. W. Glaser, Grundlagen der Elektronen-Optik, Vienna: Springer, 1952.
4. W. D. Riecke and E. Ruska, Proc. 6th Int. Cong. Electr. Micr. 1966.
5. K. H. Loeffler, Proc. 6th Int. Cong. Electr. Micr., 1966.
6. H. Boersch, Z. Phys. 139: 115, 1954.
7. K. H. Loeffler, Z. angew. Phys., June 1969.

LONG-LIFE, HIGH-BRIGHTNESS SOURCES FOR DEMOUNTABLE GUNS

W. C. HUGHES

General Electric Co., Schenectady, N. Y.

INTRODUCTION

In recent years there has been considerable activity in the development of electron beam (EB) devices for industrial application. Included have been electron guns for data recording; joining and machining; and microcircuit inspection, diagnostics, and fabrication. These are, for the most part, demountable systems; that is, the gun is let down to air periodically to insert or remove the target or workpiece.

Demountable guns have always been viewed as a special class by those working in electron optics, because the low vacuum quality found in these systems requires special precautions, often influencing the optical design. Elements which intercept the beam, such as apertures or meshes, are usually avoided, for example, because it is difficult to keep these parts from accumulating an insulating layer. The electron source also requires special attention. Most low-temperature electron emitters, which would be favored in sealed-tube applications, do not perform satisfactorily under poor vacuum conditions. Demountable guns have, therefore, commonly made use of the tungsten hairpin cathode.

The tungsten hairpin has served honorably but there has long been a desire on the part of the designer and user for sources which would last longer, be less fragile, and require less mechanical adjustment. The optics designer would also like to be able to use higher cathode loadings. At loadings above 3 A/cm^2 the life of a 0.005-in.-diameter tungsten hairpin is less than 10 hr even in a good vacuum environment.[1]

In the past 5 years, there has been considerable activity and progress toward sources which display all of these desirable characteristics. Practical emission systems in the 3- to 10-A/cm^2 range using lanthanum hexaboride and thorium carbide have been reported in the literature.[2,3] In this paper a series of sources using barium cathodes of the dispenser type will be described. These units were first developed for thermoplastic recording and reading guns but have subsequently been applied in several other applications.

THE BARIUM DISPENSER CATHODE

The barium dispenser cathode is well known and several types are available from various manufacturers. The type which has been used here is commonly known as the Phillips "B" cathode.[4] These cathodes consist of a mixture of barium compounds dispersed throughout a porous tungsten body mounted in a molybdenum shell. In operation, barium diffuses out of the tungsten to coat the active surface of the cathode. As barium evaporates, it is replaced by the diffusion process.

The performance of the barium dispenser cathode, in terms of zero field emission as a function of temperature, is shown in Fig. 1. From these data it can be seen that this emitter operates at a much lower temperature than any of the others mentioned. There is a direct performance advantage to lower operating temperatures in that higher brightness can be realized for a given loading and the thermal energy spread in the beam is reduced. Furthermore, the operating temperature is low enough to allow the convenience of indirect heating and conventional mounting of the cathode in a ceramic insulator. The "B" cathode can be accurately machined to almost any desired shape. The shape of the emitting surface is retained throughout cathode life. Techniques are also available to reduce emission from undesirable locations. Good configuration control near the cathode is, therefore, possible. This is an important factor for the sources to be described.

These advantages make the barium dispenser cathode attractive but, although they are mechanically rugged, they are not noted for being tolerant of poor vacuum conditions and cannot be used successfully in the average demountable gun. They can be used very successfully in these applications, however, if the vacuum is improved in the area of the cathode itself.

VACUUM SYSTEM

It has been found that the divergent requirements of a poor vacuum at one end of the electron gun and a very good vacuum at the other can be met in a practical manner if the gun is separated into two parts. We have then (Fig. 2) a "lens chamber" and a "source chamber" with a restricted passage for the beam between them.

For many guns the electron optics can be arranged such that this "restriction" is an aperture, 1-2 mils in diameter, located near the source. A 2-mil aperture in a thin plate has a conductance of about 1×10^{-4} ℓ/sec.[5] Considering only this leakage and assuming a lens chamber pressure of 2×10^{-5} torr, a pumping speed of 0.2 ℓ/sec maintains the cathode chamber at 1×10^{-8} torr. Because the pressures involved are low enough for molecular flow conditions to prevail, elaborate gas seals are not required between the two chambers. Metal-to-metal contact between parts constitutes sufficiently leak-tight construction.

The source housing design presently being used is shown in Fig. 3. It has been constructed as a separate unit so as to be easily replaceable at the end of cathode life and so that it can be conveniently cleaned and baked during assembly and activation. A 1-ℓ/sec ion appendage pump is used to maintain vacuum in the unit during operation and storage. Pump life appears to be several years of continuous operation under these conditions. A single layer of magnetic shielding around the magnet is sufficient to reduce the field to less than earth's field at the cathode.

To allow the lens chamber to be let down to atmospheric pressure an elastomer valve is incorporated into the source housing. This valve, shown in Fig. 4, is a simple lever arrangement actuated by rotary motion through a metal bellows seal. If required, the valve can be arranged to spring close in the event of high pressure in the lens chamber. The source can be stored for long periods (years) with this valve closed and the ion pump operating or if dead storage is required a leak-tight crushed copper seal can be made over the mounting flange.

SOURCE OPTICS

In many demountable gun applications the maximum source brightness is required but sensitive control grid operation is not. In these cases, a narrow-angle Pierce optical design[6] is attractive because performance

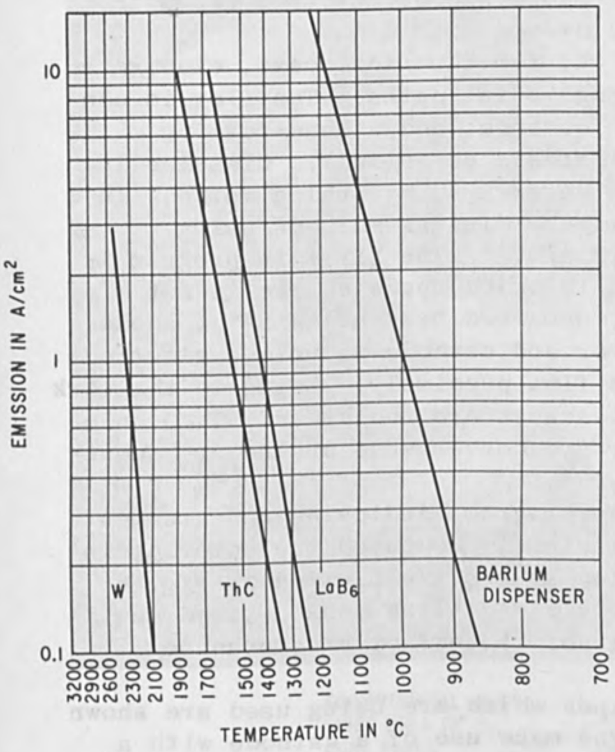

FIG. 1.—Performance of various cathodes.

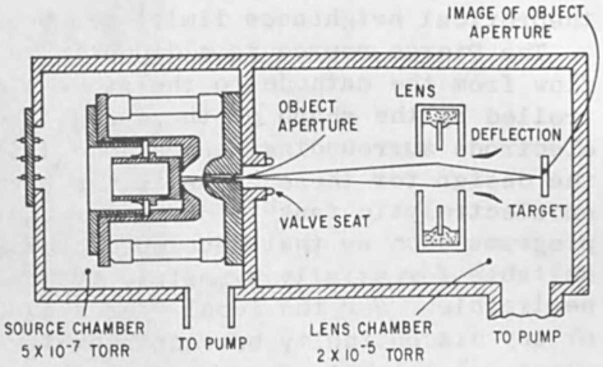
IMAGE OF OBJECT APERTURE
OBJECT APERTURE
LENS
DEFLECTION
TARGET
VALVE SEAT
SOURCE CHAMBER
5 X 10⁻⁷ TORR
TO PUMP
LENS CHAMBER
2 X 10⁻⁵ TORR
TO PUMP

FIG. 2.—Isolation and pumping of cathode chamber.

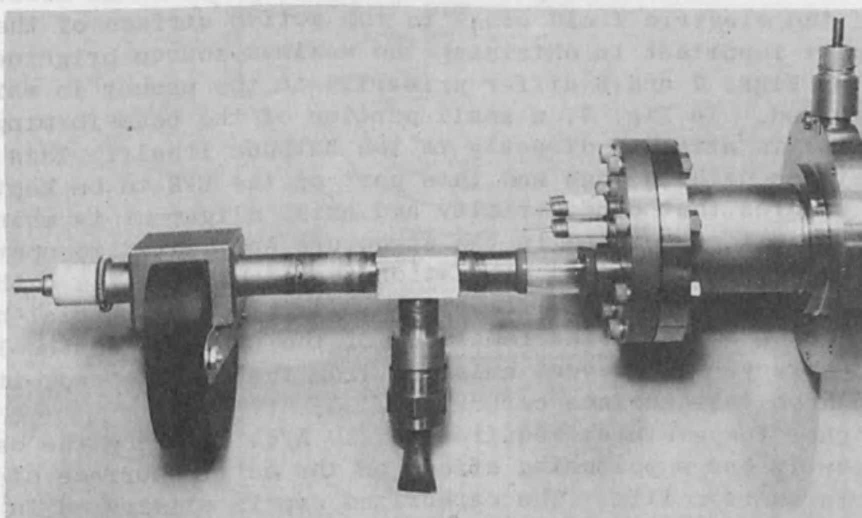

FIG. 3.—Source housing, valve and pump.

can be very accurately predicted and a close approach to the Langmuir theoretical brightness limit[7] can be achieved.

The Pierce source is a diode in which, for the ideal case, electrons flow from the cathode to the anode along radial paths. The flow is controlled by the shape of the anode, the cathode, and a beam-forming electrode surrounding the cathode (at cathode potential). Classically, the design for these elements has been determined by analog methods in an electrolytic tank[8,9] or more recently by digital methods using programs such as that developed by Kirstein.[10] The Kirstein program is suitable for axially symmetric systems in which space charge is not negligible. For the ideal Pierce gun, unmarred by a hole in the anode or any discontinuity between beam former and cathode, a unique electrode shape exists that produces the desired flow precisely. Owing to the work of Radley,[11] these theoretically exact shapes are now known. The equipotential surfaces given by Radley for two convergence angles are shown in Fig. 5.

Digital analysis, using the Kirstein program, indicates an agreement between the program and Radley's conclusions. Computed trajectories in a configuration approximating the Radley shapes are plotted in Fig. 6. The rays are seen to travel along nearly radial lines, as desired, until they deviate near the anode as a result of the effect of the anode aperture.

Examples of practical electrode shapes which are being used are shown in Figs. 7 and 8. Both of these designs make use of a cathode with a 10-mil diameter emitting area. For the applications in which these sources have been used, smaller cathodes would have been acceptable. However, it has not been found practical to go much below 10 mils. The character of the electric field close to the active surface of the cathode is most important in obtaining the maximum source brightness.[12] The designs of Figs. 7 and 8 differ primarily in the manner in which this field is obtained. In Fig. 7, a small portion of the beam-forming electrode (BFE) is attached directly to the cathode itself. This allows the space between cathode edge and this part of the BFE to be kept to a minimum and assures that concentricity and axial alignment is maintained after the cathode is assembled in the structure and heated to operating temperature. Digital computer calculations have shown that a cathode cap only a few mils thick is sufficient to determine the initial beam direction and convergence. The remainder of the BFE need not be located with great accuracy. To prevent emission from the cathode cap, it is necessary to have this surface carburized.[4]

At the higher temperatures required for 10 A/cm^2 loading the carburization apparently has a poisoning effect on the active surface of cathode and results in shorter life. The carburized cap is eliminated in the design shown in Fig. 8. This arrangement produces longer life at 10 A/cm^2 but at the price of some sacrifice in brightness. The design also allows grid control of the beam current as illustrated in Fig. 9. For this particular source the maximum output occurred at about -15 V. Ideally, maximum output would occur at 0 V. At -100 V, the current was reduced to about 3% of its maximum value. The mechanical construction for a typical source is shown in Fig. 10.

PERFORMANCE

From the viewpoint of cathode performance, in the environment provided

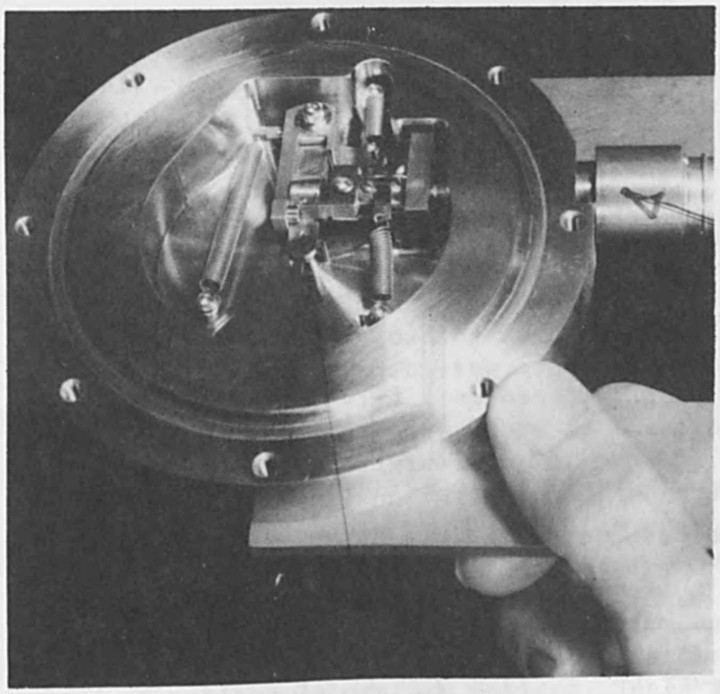

FIG. 4.—Cathode chamber valve.

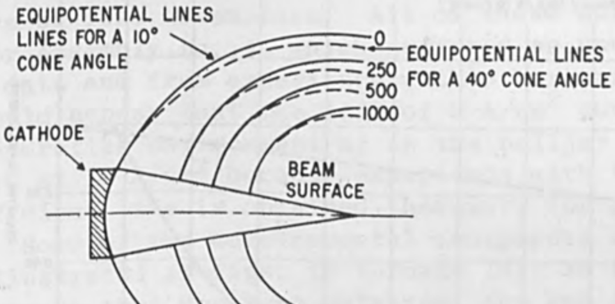
EQUIPOTENTIAL LINES
LINES FOR A 10° CONE ANGLE
0
250
500
1000
EQUIPOTENTIAL LINES FOR A 40° CONE ANGLE
CATHODE
BEAM SURFACE

FIG. 5.—Equipotentials for Radley configuration.

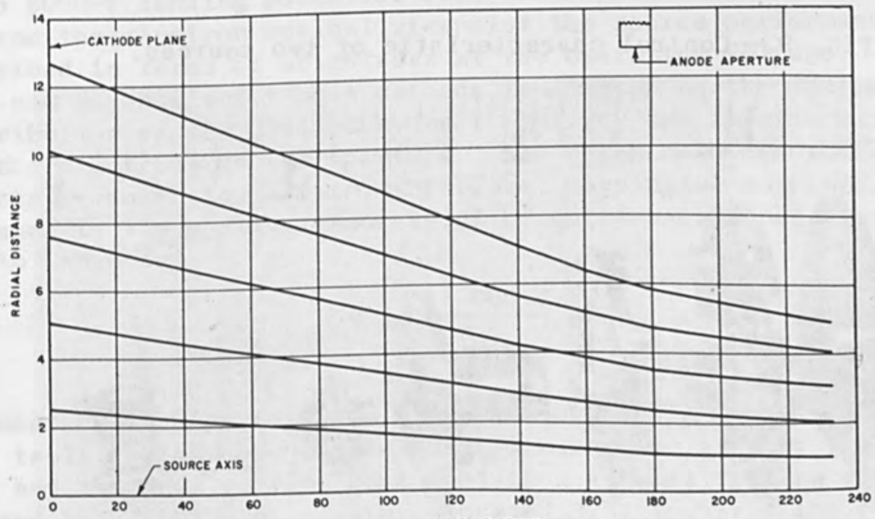

FIG. 6.—Computed electron trajectories for Radley electrode shapes.

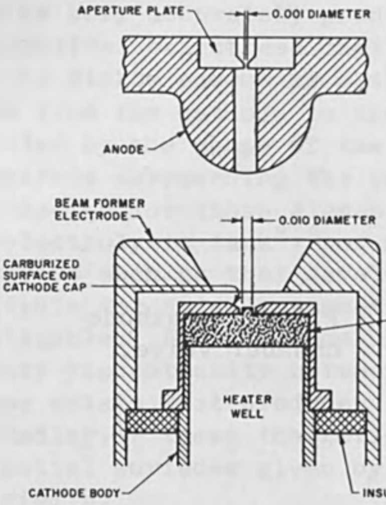
APERTURE PLATE
0.001 DIAMETER
ANODE
BEAM FORMER ELECTRODE
0.010 DIAMETER
CARBURIZED SURFACE ON CATHODE CAP
BARIUM DISPENSER INSERT
HEATER WELL
CATHODE BODY
INSULATOR

FIG. 7.—Source using capped cathode.

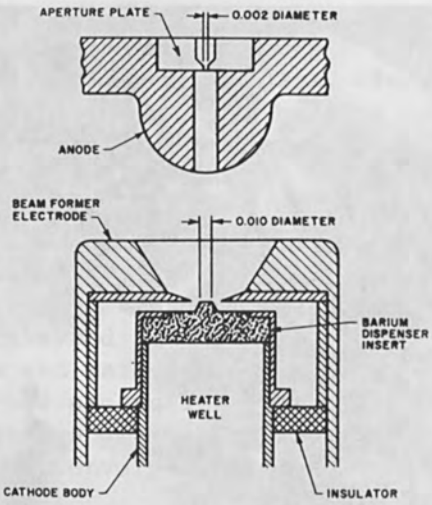
APERTURE PLATE
0.002 DIAMETER
ANODE
BEAM FORMER ELECTRODE
0.010 DIAMETER
BARIUM DISPENSER INSERT
HEATER WELL
CATHODE BODY
INSULATOR

FIG. 8.—Source with isolated beam former.

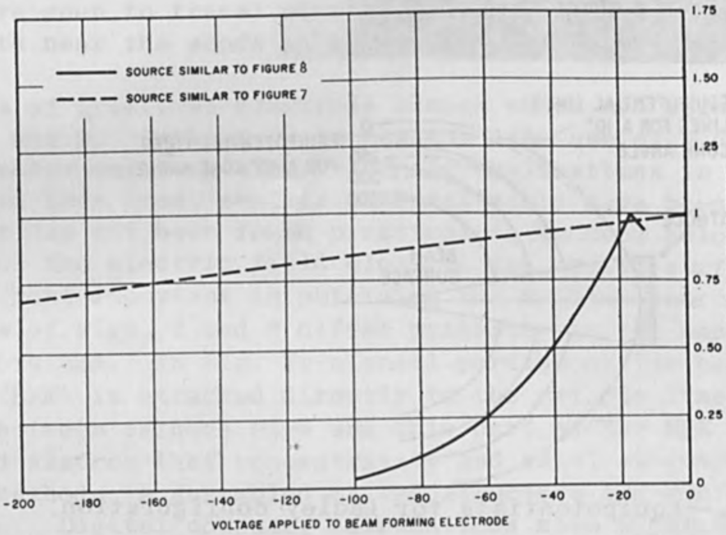

FIG. 9.—Control characteristic of two sources.

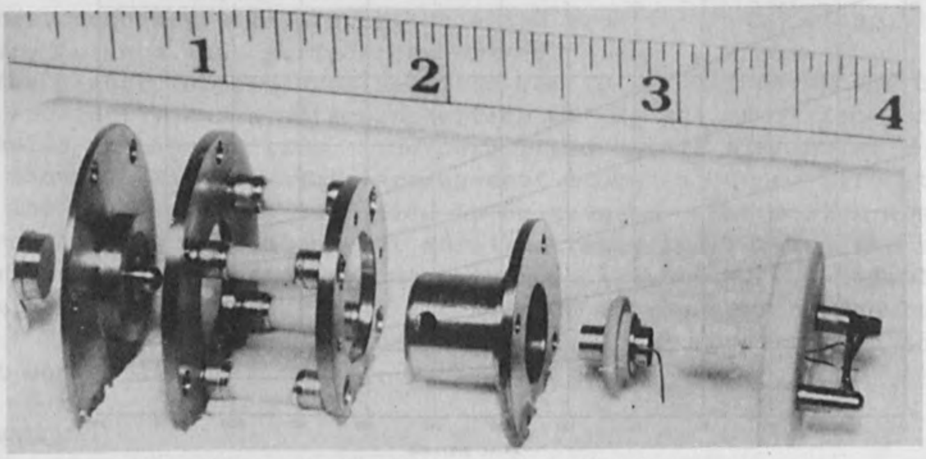

FIG. 10.—Construction of typical source.

by the vacuum techniques described above, the most important parameters are cathode loading and life. Life is always difficult to specify accurately, especially for a developmental device where the design is continually changing and few samples are tested, but the testing which has been done provides at least a rough estimate. The data come from sources which have been run to failure under simulated conditions and from sources which have been used in actual equipments.

Tests of the first type have been made in ion-pumped belljars at pressures of 5×10^{-7} torr and below. Under these conditions it appears that several thousand hours can be obtained at 3 A/cm^2 and about 1000 hr at 10 A/cm^2. Cathode loading figures used in this report are the total cathode current divided by the area of the cathode tip. The beam current gradually decreases with time as shown in a typical performance curve (Fig. 11). The life stated above is the time at which the beam current falls to 70% of its original value.

Tests under actual operating conditions are more meaningful than a simulated test can ever be, but the unique history of each device makes it difficult to generalize about life. Some cathodes, for example, have been used on several machines over a period of years. One such device, assembled and activated almost four years ago, is still operating at near its original performance. To illustrate the life that has been experienced in various laboratory devices, Table I has been prepared showing the performance of five assemblies. All of these units are still operating except for Assembly No. 4, which suffered an unusual heater failure.

From these data and from experience with other units not included in Table I, it would appear that the life of 3-A/cm^2 guns is of the same order in the operating environment as in the belljar tests. Results are less conclusive at 10 A/cm^2 because experience with these units is more limited. Sufficient life is obtained, however, for practical use in many applications. Some of the developmental equipments which are using these sources are illustrated in Figs. 12 through 14. To illustrate the overall gun performance that has been obtained, the gun in Fig. 12 produces a 4-μ-diameter spot with a beam current of 1 μA at a 1000-V landing potential from a 3-A/cm^2 source. The thermoplastic recorder gun (Fig. 14) produces a spot approaching 5 μ in diameter with a beam current of 20 μA at an 8000-V landing potential from a 10-A/cm^2 source.

From the electron optical viewpoint the source performance is best described in terms of brightness at the operating voltage. The brightness that can be obtained from a cathode is limited by the thermal velocity distribution of the electrons, space charge, and imperfections in focusing the electrons on the aperture. For these cathodes thermal velocity effects predominate. It is, therefore, meaningful to compare their performance to the maximum theoretical brightness in A/cm^2/steradian according to Langmuir[7]

$$(B_T)_{max} = j_0 \frac{11\,600\ V}{\pi T} \qquad (1)$$

A summary of the performance of three sources is given in Table II. For this table, brightness was calculated using the area of the object aperture and the beam current contained in a 1.9-milliradian solid angle as defined by a 0.013-in. aperture located 3.37 in. from the object aperture. For the best gun the brightness obtained is about 70% of the value given by (1).

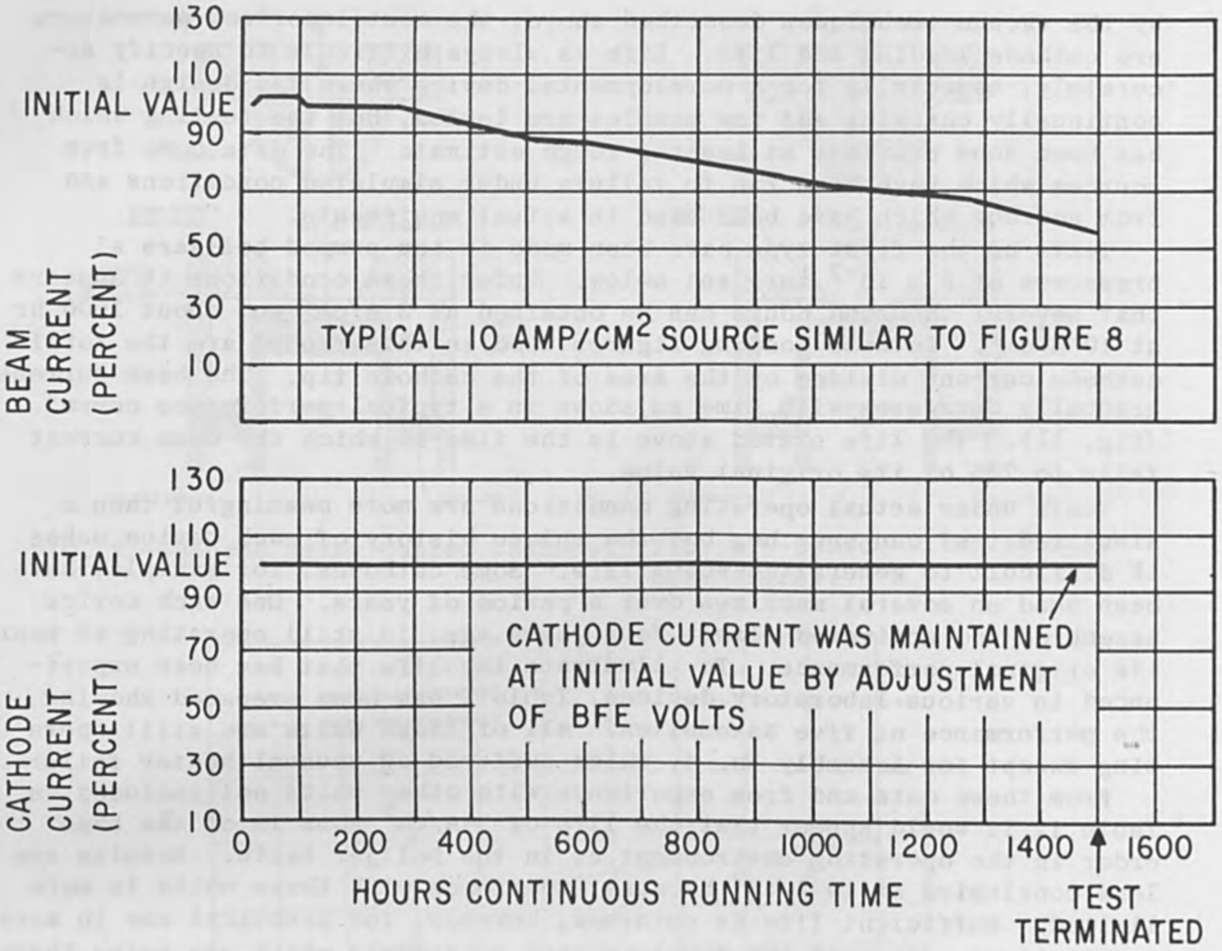

FIG. 11.—Temporal performance of a 10-A/cm^2 source.

TABLE I.—Lifetimes of various sources.

NOMINAL CATHODE LOADING (Amps/cm^2)	APPLICATION	TOTAL TIME SINCE ACTIVATION (Months)	HOURS OF USE	REMARKS
3	THERMOPLASTIC RECORDER & OTHERS	44	280	STILL OPERATING
3	THERMOPLASTIC RECORDER	21	480	STILL OPERATING
3	FLY'S EYE LENS TEST DEVICE	22	4900	STILL OPERATING
10	THERMOPLASTIC RECORDER	21	70	HEATER OPENED
3	FLY'S EYE LENS DEVICE	7	780	STILL OPERATING

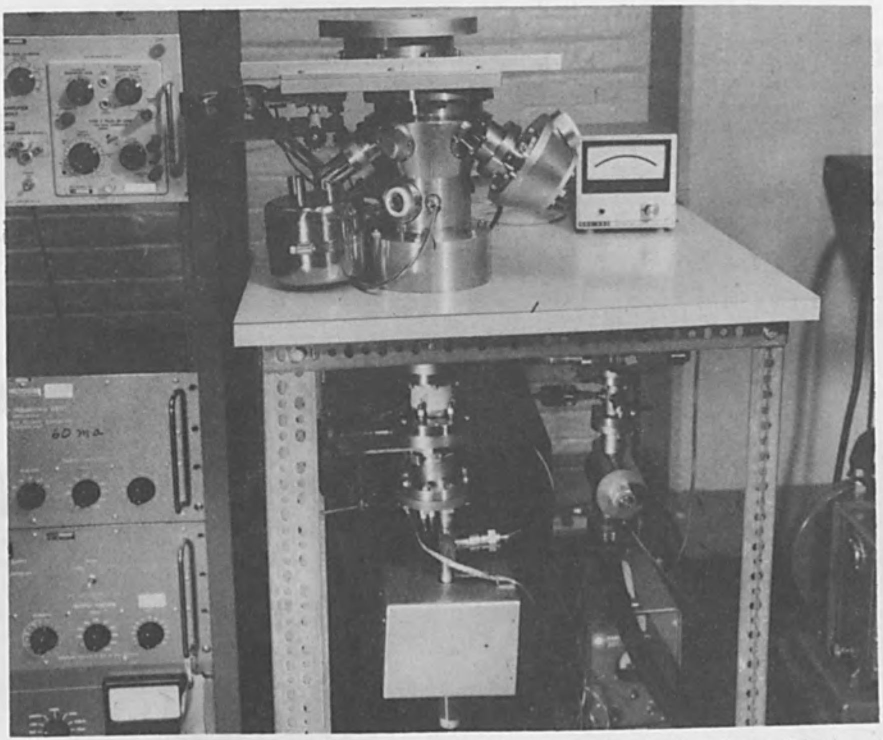

FIG. 12.—Device for testing integrated circuits.

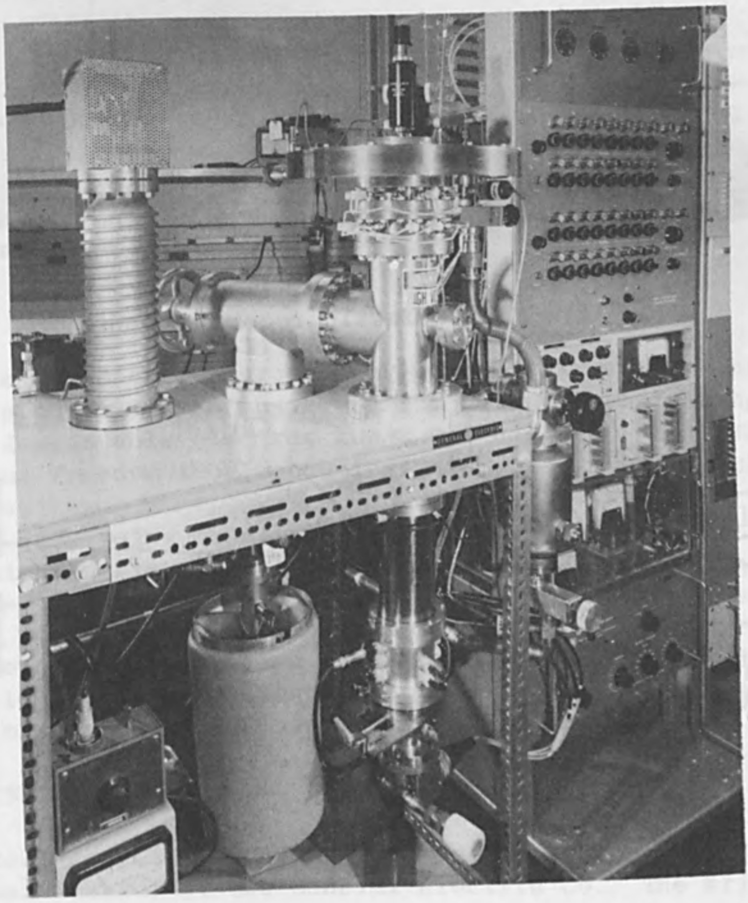

FIG. 13.—Fly's eye lens device.

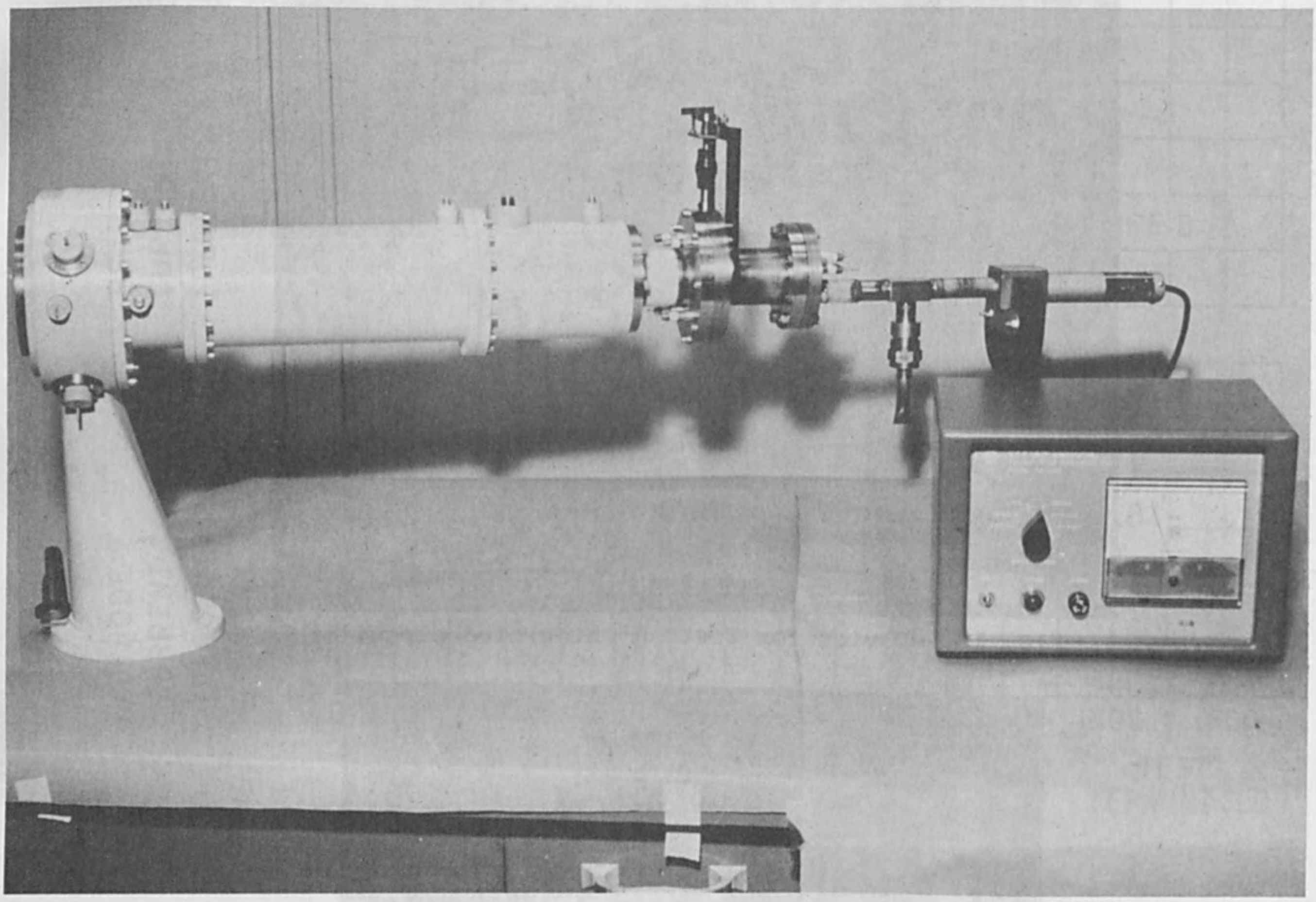

FIG. 14.—Thermoplastic recording gun.

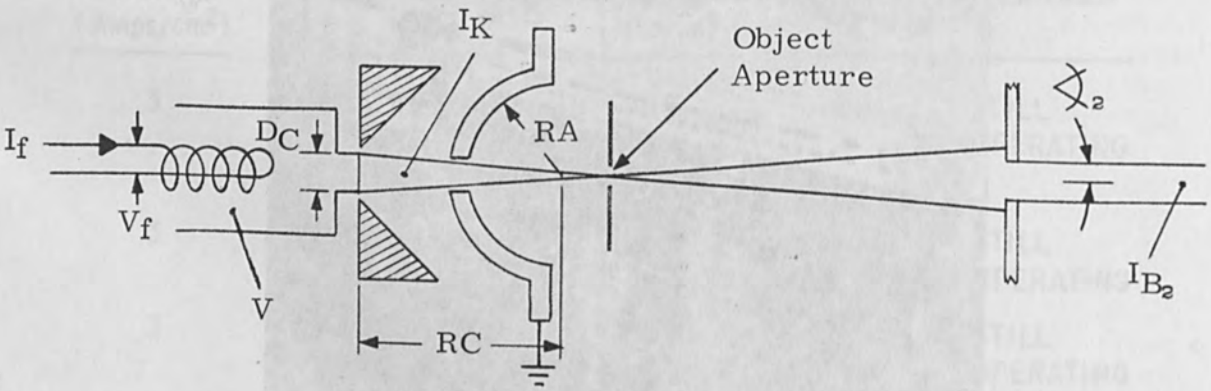
I_K
Object Aperture
I_f
D_C
RA
α_2
V_f
V
RC
I_{B_2}

TABLE II.—Performance of various sources.

Current and voltage		$3\ A/cm^2$, 6 kV	$10\ A/cm^2$, 6 kV	$10\ A/cm^2$, 8 kV
Configuration	Figure	4	6	6
	RC/RA	2.22	2.17	2.36
Heater	V_f	10.2	9.2	10.5
	I_f	0.87	0.93	1.0
Cathode	Temperature (°K)	1433	1468	1468
	I_k (mA)	1.9	6	6
	V (kV)	-6	-6	-8
	A/cm^2	3.75	11.85	11.85
Aperture output	Beam current (μA)	1.2	23	20
	Radian	1.35×10^{-3}	1.9×10^{-3}	1.39×10^{-3}
Brightness (A/cm^2 - steradian)	Actual	4.14×10^4	10×10^4	16.2×10^4
	Theoretical	5.78×10^4	17.8×10^4	23.8×10^4
	Actual/Theoretical	0.72	0.56	0.68

ASSEMBLY AND ACTIVATION

During assembly the sources are treated very much as if they were going into a sealed tube. The parts are cleaned with solvents and demineralized water and given a vacuum bake. They are then assembled and the source housing is sealed, evacuated, and baked while pumping with an external ion pump. The ion appendage pump is started and the copper tube for the external pump is pinched off. The cathode is activated on the schedule recommended by the manufacturer using only the appendage pump to maintain the vacuum.

CONCLUSIONS

Experience with these sources over the past five years has demonstrated the practicality of using barium cathodes at loadings up to $10\ A/cm^2$ in demountable electron guns. It has been shown that long life, stability, and freedom from mechanical adjustment can be achieved in these applications.

While the life being experienced at the present time is much higher than is obtainable with tungsten cathodes, it is shorter than has been demonstrated for barium dispensers in diode tests under ideal conditions. This finding would indicate that there is a possibility for life improvement. Barium cathodes are also known to be capable of loadings much higher than $10\ A/cm^2$, suggesting that improvements in the direction of higher loadings may also be possible.

ACKNOWLEDGMENTS

The sources described in this report were developed at the Research and Development Center of the General Electric Co. The writer is especially indebted to J. E. Wolfe for much of the early work on source

design, H. L. Lester for advice and encouragement throughout the program, D. C. Peroutky for the mechanical design of the sources, and J. F. Bedard for most of the source assembly and test.

REFERENCES

1. R. N. Bloomer, "The lives of electron microscope filaments," Brit. J. Appl. Phys. 8: 83-85, 1957.
2. H. H. Glascock jr., J. Appl. Phys. 37: 4995, 1966.
3. A. N. Broers, J. Sci. Instr. 2: 273, 1969.
4. Roberto Levi, "Improved impregnated cathode," J. Appl. Phys. 26: 639, 1955.
5. M. Pirani and J. Yarwood, Principles of Vacuum Engineering, New York: Reinhold Publishing Corp., 1961.
6. J. R. Pierce, Theory and Design of Electron Beams, New York: D. Van Nostrand, 1954.
7. D. B. Langmuir,"Theoretical limitations of cathode ray tubes," Proc. IRE 25: #8, 977, August 1937.
8. K. R. Spangenberg, Vacuum Tubes, New York: McGraw Hill, 1948.
9. R. Helm, K. R. Spangenberg, and L. M. Field, "Cathode-design procedure for electron beam tubes," Elec. Communication 24: No. 1, 1947.
10. P. T. Kirstein and J. S. Hornsby, "A Fortran program for the numerical analysis of curvilinear electrode systems with an emitting surface," CERN Report 63-6, Accelerator Research Division, 25 April 1963.
11. D. E. Radley, "Electrodes for convergent pierce-type electron guns," J. Electronics and Control 15: 469-477, 1964.
12. R. J. Lomax, "The effect of the inclination of the focusing electrodes on electron beam formation," ibid. 6: No. 1, 1959.

POINT-CATHODE ELECTRON GUN ANALYSIS

H. YAMAZAKI and T. E. EVERHART

University of California, Berkeley

SUMMARY

Recently, a specific model of a point-cathode electron gun was analyzed to determine the source size, position, magnification, and electron-optical brightness.[1] In this model, both the grid voltage and the anode voltage of a three-electrode gun affected the electric field at the cathode tip, which is an important parameter of electron emission in both field-emission and Schottky-emission guns. In field-emission guns in particular, it is desirable to operate so that only one applied voltage determines the electron emission, to insure current stability. This voltage is applied to the electrode closest to the cathode, or first anode; the second anode is placed at the desired beam voltage. This system has been used by Crewe et al.,[2] and experimental points were presented for a given electrode configuration. Since that electrode configuration closely approximates the so-called hyperbolic electrodes[3] which were assumed in the previous model, a modified analysis based on hyperbolic fields suggested itself to us. This modified model is relatively straightforward, and produces theoretical curves in excellent agreement with the experimental points of Crewe et al.[2]

The three-electrode guns used previously for field emission require a fixed voltage for the desired electron emission; if a given total accelerating voltage or beam voltage is desired, all electrode voltages are fixed. Under these circumstances, the only way the source position can be adjusted up and down the gun axis is by mechanically moving the tip. If a four-electrode gun is used, it should be possible to adjust the axial position of the apparent source by varying the potential on the fourth electrode. The first-order analysis of this case has been carried out for a variety of electrode shapes, and this conclusion has been verified. However, no experimental confirmation of the predicted performance of a four-electrode electron gun has been obtained yet.

We gratefully acknowledge helpful discussions with R. Speidel and J. C. Wiesner. One of us (H. Y.) was supported in part by the National Institutes of Health.

REFERENCES

1. T. E. Everhart, "Simplified analysis of point-cathode electron sources," J. Appl. Phys. 38: 4944-4957, 1967.

2. A. V. Crewe, D. N. Eggenberger, J. Wall, and L. M. Welter, "Electron gun using a field-emission source," Rev. Sci. Instr. 39: 576-583, 1968.

3. K. Schlesinger, "Focus-reflex modulation of electron guns," IRE Trans. ED-8: 224-230, 1961.

Record of 10th Symposium on Electron, Ion, and Laser Beam Technology (L. Marton, ed.); San Francisco Press, Inc.

Copyright © by The Institute of Electrical and Electronics Engineers, Inc.—Printed in the U.S.A.

DIRECT MEASUREMENT OF ELECTRON ENERGY LOSS IN SOLIDS

P. H. HOFF and T. E. EVERHART

University of California, Berkeley

A knowledge of the distribution of energy loss vs penetration depth for kilovolt electrons is of great importance in the scanning electron microscopy of semiconductors. For the mode of operation where the video signal is derived from the electron-beam-induced current, it is necessary to know the density and location of beam-created electron-hole pairs in order to reach a quantitative understanding of the beam-induced effects in the semiconductor and to relate these to the video signal.

If the assumption is made that the generation at every point is directly proportional to the local energy dissipation at that point, the problem of finding the generation function becomes one of finding dE/dx vs x. In particular, an analytical expression would be especially desirable from the standpoint of mathematical manipulations. Expressions for dE/dx vs x have been proposed by Everhart et al.,[1] by Kyser and Wittry,[2] and by Klein.[3] The expression of Everhart et al. was a cubic polynomial fit to the experimental data of Grün.[4] Kyser and Wittry used a Gaussian approximation, and Klein used a function which was basically a product of linear and exponential terms. The latter two functions each contain one or more undetermined parameters. In addition, both are symmetrical about some value of penetration depth. The experimental data of Grün, however, indicate some asymmetry about its peak point.

Grün measured the ionization of gas by an electron beam, but it is not obvious a priori that his measurements are applicable to the solid targets which are of interest to us. On the other hand, Schumacher and Mitra[5] used Grün's data by introducing a linear scaling factor for the density of the solid target to gage thin metal films and obtained good agreement. Furthermore, Grün's curve of dE/dx vs x is in good qualitative agreement with published experimental and theoretical results for solid targets of atomic number $Z < 30$.

One of the most attractive features of the Grün curve of dE/dx vs x is that it is the basis of a definition of electron range which is highly consistent over the range of voltage from 5 to 54 kV. Figure 1 shows the basis on which the Grün range is defined. Figure 2 shows a log-log plot of the Grün range vs the primary beam energy. The small point scatter is evident. An experimental determination of dE/dx for solid targets seemed in order. In particular, it was desired to see whether postulating the range-energy relationship of Grün led to an energy loss vs depth function quantitatively similar to his result for gases.

In the experiment, metal-oxide-semiconductor sandwiches were fabricated and subsequently bombarded while a bias was applied between the metal and the semiconductor. The electron beam creates carriers in the normally insulating oxide. After a transient current associated with the accumulation of a hole space charge very near the oxide-cathode interface, a steady state current associated with electron drift through the oxide is

Record of 10th Symposium on Electron, Ion, and Laser Beam Technology (L. Marton, ed.); San Francisco Press, Inc.

Copyright © by The Institute of Electrical and Electronics Engineers, Inc.—Printed in the U.S.A.

observed.[6] The magnitude of this electron current is taken to be directly proportional to the amount of power dissipated in the oxide, i.e., to the integral of the dE/dx between the values of x corresponding to the oxide boundaries.[7] Grün found that if the ordinate of a plot of dE/dx is normalized to the primary beam energy, and the abscissa is normalized to the Grün range as defined in Fig. 1, the resulting plot is essentially the same for all beam energies in the range he investigated. It is this universal curve that we attempted to find by experiment. Changing the beam voltage thus has the effect of imposing different parts of the energy-loss curve upon the oxide region, as illustrated in Fig. 3. By experimental measurements of beam power and induced current for beam voltages between 6 and 20 kV, and by introducing the appropriate normalization for both axes for each point, data are obtained which by a method of selfconsistent calculations can be used to construct a curve of the residual energy function, E vs x. Such a curve is shown in Fig. 4.

It should be pointed out that Grün's normalization convention is

$$\int_{-\infty}^{\infty} \frac{d(E/E_0)}{dx}\, dx = 1 \tag{1}$$

The electron beam enters the gas space at $x = 0$. Thus Grün's normalization includes backscattering. Using the fact that for a given target, the backscattered energy for kilovolt electrons is essentially independent of primary beam energy,[8,9] the normalization condition may be expressed by the following equation, where f is that fraction of the primary beam energy which is actually dissipated in the target.

$$\int_{0}^{\infty} \frac{d(E/fE_0)}{dx}\, dx = 1 \tag{2}$$

Since Grün's gas space backscattered only about 2% of the primary beam energy, only slight renormalization of his ordinate is necessary to allow a comparison with our experimental results.

Once the data for a curve of E vs x have been obtained, a seventh-order polynomial is fitted to it by a least-squares computer program as shown in Fig. 4. The polynomial expression is differentiated to give dE/dx. The resulting curve is shown in Fig. 5 along with other published results. The curve of Bishop[10] is based on a Monte-Carlo calculation for 29-kV electrons on copper. Cosslett and Thomas[11] combined experimental measurements of backscatter from copper for 20-kV electrons with a theoretical expression relating backscatter and dE/dx. Agreement of our data with those of both Grün and Bishop is within experimental error.

Although more extensive measurements yet to be performed will undoubtedly improve the accuracy, we have found that the following expression

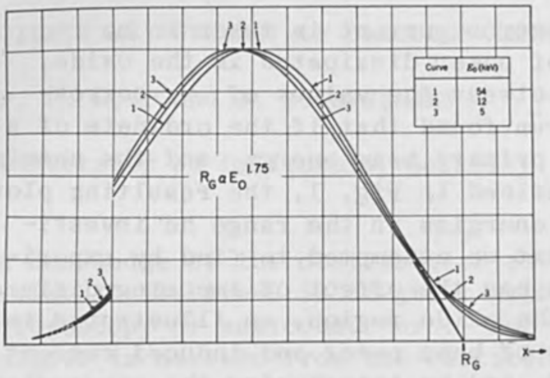

FIG. 1.—Grün's "universal curve" of dE/dx, which defines R_G, the Grün range.

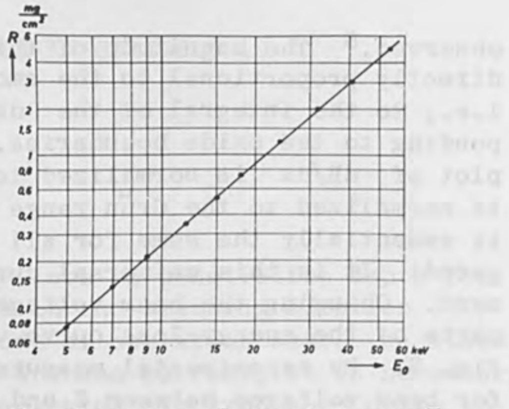

FIG. 2.—Log-log plot of R_G vs E_0, showing excellent fit between Grün's data and the slope of 1.75.

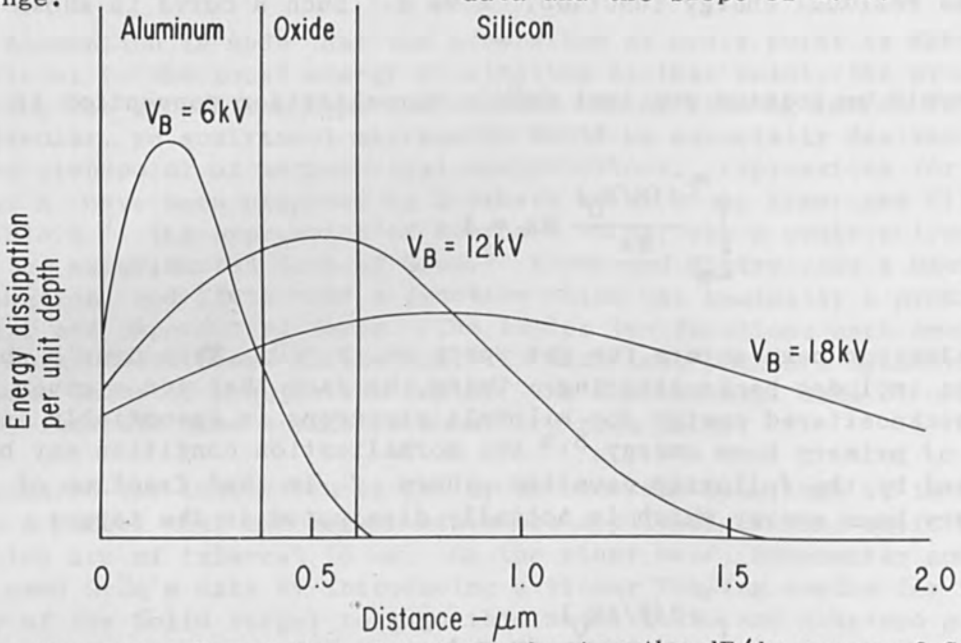

FIG. 3.—The three-layer MOS structure showing the dE/dx curve of Grün imposed on the structure for three different values of beam voltage. In each case the area under the curve in the oxide is proportional to energy dissipated in the oxide at that beam voltage. (After MacDonald and Everhart.[6])

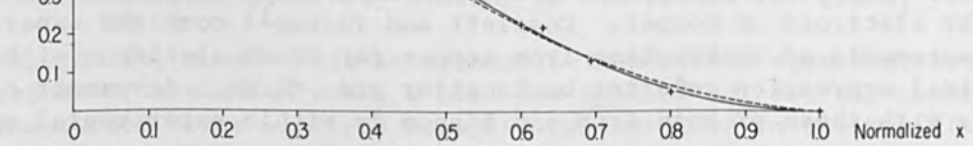

FIG. 4.—Residual beam energy vs penetration into target. Crosses are experimental points. The dashed line is a least-squares fit to those points. The solid line is the integral of the cubic polynomial fit to Grün's dE/dx curve as given by Everhart et al.[1]

represents experimental results quite well.

$$\lambda(y)\ \frac{d(E/fE_0)}{dy} = 0.76 + 5.44y - 11.64y^2 + 5.64y^3\ ;\ (0 \le y \le 1)\ ;\ y = x/R_G \tag{3}$$

The disadvantage of simple power-series representation is that a small change in the curve being represented often results in a substantial change in each of the coefficients. This problem may be minimized by expressing the curve in orthogonal polynomials. Then if small changes are made in the curve, the coefficients of the lower-order polynomials are essentially unchanged, and the perturbation of the curve is evidenced in the coefficients of the higher-order terms. Orthogonal expansion not only has this stabilizing effect on the coefficients, but it also insures that if the expression is truncated at any given order term, the best possible approximation to the function for that order expansion results.

On the interval $0 \le y \le 1$ orthogonal polynomials with unity weight are the shifted Legendre polynomials. In terms of these functions, the normalized energy loss function becomes

$$\lambda(y) = 1.00P_0(2y - 1) - 0.57P_1(2y - 1) - 0.53P_2(2y - 1) + 0.28P_3(2y - 1) \tag{4}$$

This may be compared to the cubic approximation to Grün's curve as published by Everhart et al. (renormalized as described to exclude backscatter)

$$\lambda(y) = 1.00P_0(2y - 1) - 0.49P_1(2y - 1) - 0.59P_2(2y - 1) + 0.18P_3(2y-1) \tag{5}$$

The form of the argument of the Legendre polynomials is due to the fact that the region of orthogonality for these functions is from -1 to 1. Hence the $P_n(y)$ are not orthogonal on the interval $0 \le y \le 1$ and an expansion in terms of them would not have the desirable characteristics that motivated the expansion originally.

In summary, an experimental method has been developed for measuring the rate of energy loss in solid targets. The results obtained from so doing are in good agreement with those of Grün for gases, provided that appropriate scaling factors are introduced for density, and provided that the 1.75 power range-energy relationship of Grün is postulated.

The authors acknowledge with gratitude partial financial support by the Joint Services Electronics Program at the University of California in Berkeley. Thanks are also due to Mrs. D. McDaniel for assistance in device fabrication and to Mr. N. Susta for the line drawings.

REFERENCES

1. T. E. Everhart, A. J. Gonzales, P. H. Hoff, N. C. MacDonald, Proc. Intl. Congress for Electron Microscopy, Tokyo: Maruzen Co., 1966; pp. 201-202.
2. P. F. Kyser and D. B. Wittry, Proc. IEEE 55: 733, 1967.
3. C. Klein, Raytheon Technical Memorandum T-786, 6 May 1968.
4. A. E. Grün, Z. Naturforschung 12A: 89-95, 1957.
5. B. W. Schumacher and S. S. Mitra, Electronics Reliability and Microminiaturization 1: 321-331, 1962.
6. N. C. MacDonald and T. E. Everhart, J. Appl. Phys. 39: 2433-2447, 1968.
7. P. H. Hoff and T. E. Everhart, to be published. The question of what factors determine the induced current through the oxide is a key one. Available evidence will be presented and discussed in a forthcoming paper.
8. E. J. Sternglass, Phys. Rev. 95: 345-358, 1954.
9. K. A. Wright and J. G. Trump, J. Appl. Phys. 33: 687-690, 1962.
10. H. E. Bishop, Proc. Phys. Soc. 85: 855-866, 1965.
11. V. E. Cosslett and R. N. Thomas, Brit. J. Appl. Phys. 16: 779, 1965.

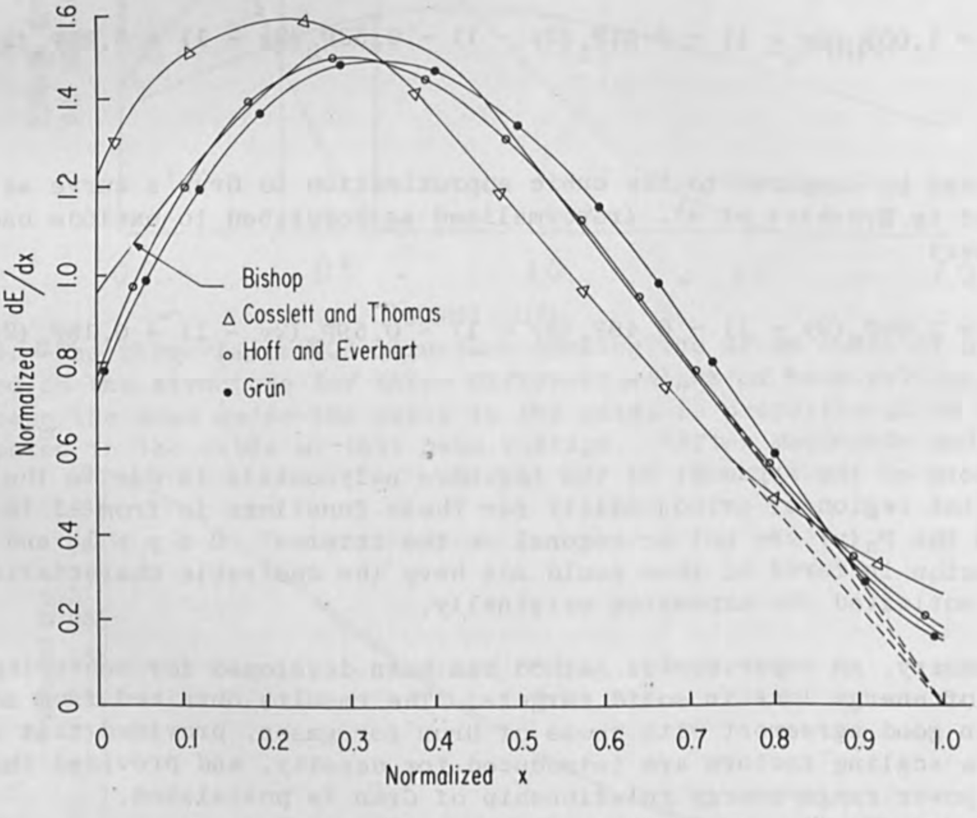

FIG. 5.—Curves of dE/dx vs x according to Grün, Bishop, Cosslett and Thomas, and the present work. Details on each of the curves are given in the text. All have been normalized to the Grün range and unity area.

COMPUTATION OF SMALL-ANGLE SCATTERING AND ITS IMPORTANCE FOR ELECTRON BEAM WELDING

D. C. SCHUBERT

Westinghouse Research Laboratories, Pittsburgh, Pa.

Calculated current density distributions of electrons scattered by gas atoms from a high-voltage beam of infinitesimal cross section are reported. Uniform gas density along the entire electron path is assumed. Calculations were carried out on the B-5500 digital computer, using the Born approximation and X-ray form factors found in the literature. Results are presented in form suitable for scaling in pressure and beam length. The difference of present configuration from that of scattering from a point source causes a striking difference in current density distributions at small radius from the corresponding point source distributions.

I. INTRODUCTION

Small-angle scattering of electrons by gas atoms tends to degrade the power density for atmospheric and semivacuum electron beam (EB) welders. The electron beam, carrying several kilowatts of power, is generated in a region maintained at a vacuum of about 10^{-4} Torr, but the objects to be welded are at a much higher pressure, and to get there the beam passes through narrow apertures in one or more barriers which are the walls of differentially pumped vacuum chambers. Electrons are scattered out of the main beam while traversing these intermediate-pressure chambers, as well as in the high-pressure region between the last aperture and the workpiece. The scattered electrons reduce the power density of the main beam, they carry power to positions where it is no longer desirable to melt the target (producing "nail head" welds), and sometimes they may damage the apertures. A less than optimum power density distribution in the beam may, of course, have many other reasons. To distinguish between these other effects and the unavoidable effect of electron scattering we should know its contribution to the current-density distribution in any selected plane in the welding machine. This paper presents scatter distribution curves derived from scatter theory in order to permit an independent assessment of the significance of electron scattering in welding.

II. DEFINITION OF TERMS

The situation which we want to consider is illustrated in Fig. 1. An electron beam of current I_0 is passing through a gas of density ρ and pressure P, over a certain path of length L which is defined by two planes, one located at $Z = 0$, the second located at $Z = L$. The scatter current distribution in the plane $Z = L$ is calculated. As a first approximation we assume the beam to be of infinitesimal width and coincident with the axis Z. Since we have a line-beam of finite length L, the scatter current is composed of electrons coming from every location along the beam path, but the analytical equations for scattering are

Record of 10th Symposium on Electron, Ion, and Laser Beam Technology (L. Marton, ed.); San Francisco Press, Inc.

Copyright © by The Institute of Electrical and Electronics Engineers, Inc.—Printed in the U.S.A.

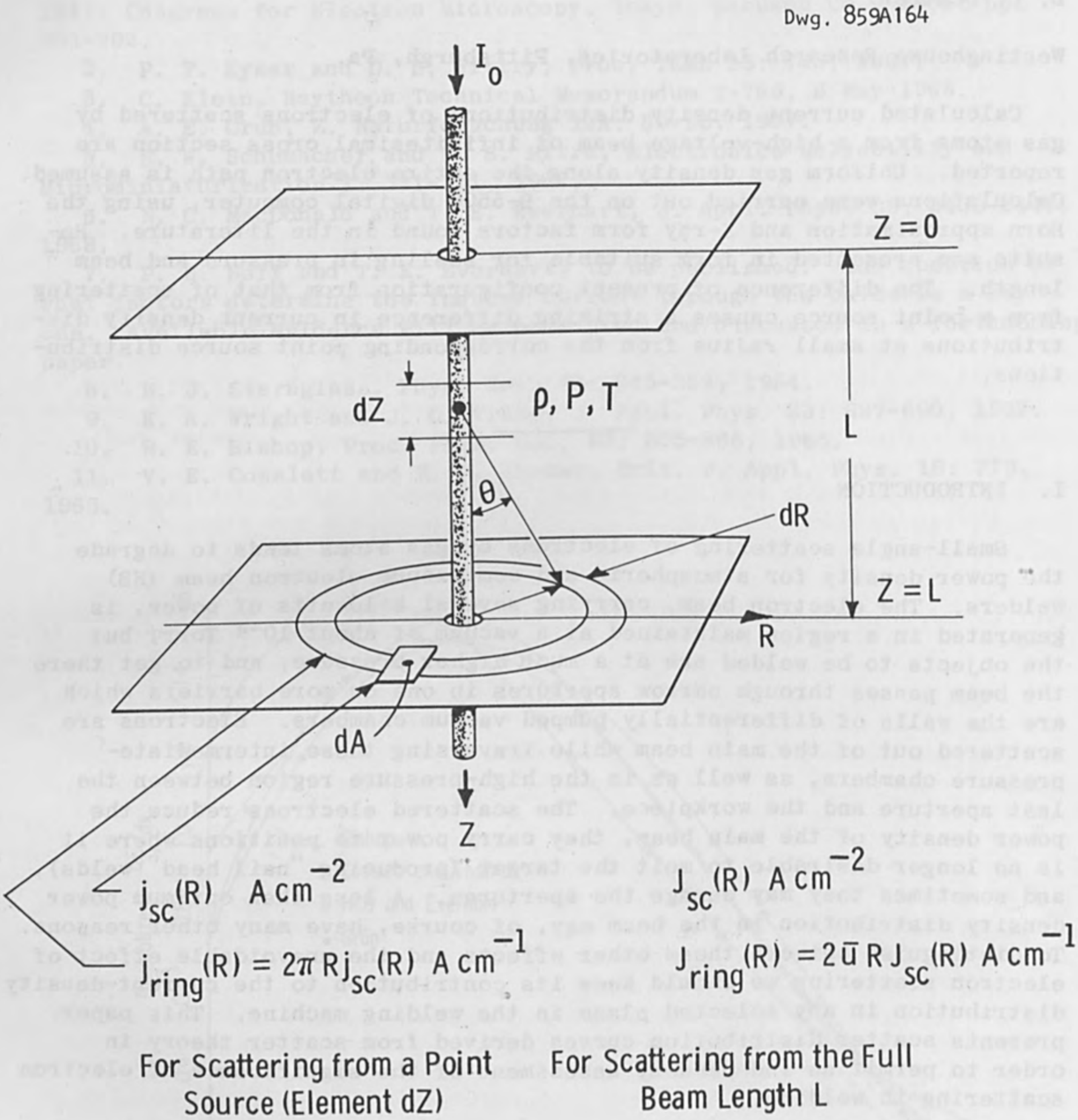
Dwg. 859A164
I_o
Z = 0
ρ, P, T
dZ
L
θ
dR
Z = L
R
dA
Z
j_sc (R) A cm^-2
J_sc (R) A cm^-2
j_ring (R) = 2π R j_sc (R) A cm^-1
J_ring (R) = 2π R J_sc (R) A cm^-1
For Scattering from a Point Source (Element dZ)
For Scattering from the Full Beam Length L

FIG. 1.—Scattering configuration and scattering nomenclature.

conventionally given for scattering from a point source through a certain scattering angle θ .

In order to get the scatter current from the full length of the beam we have first to calculate the contribution to the scatter current density from any one beam element of length dZ at position Z . To distinguish clearly between the two types of scatter current, the one coming from the line element dZ and the one coming from the full length of the beam, we have used lower-case letters for the point-scatter intensity and capital letters for the scatter intensity from the full length of the beam, as shown in Fig. 1 where $j_{sc}(R)$ and $J_{sc}(R)$ represent the local current density dI/dA from a beam element of dZ and from the entire beam, respectively. Here dI is the current, which could be found experimentally from electrons scattered onto the element dA .

Since our problem exhibits cylindrical symmetry it is convenient to define another quantity, namely the current per centimeter width scattered into the ring area of radius R and width dR . This quantity is called $j_{ring}(R)$, or $J_{ring}(R)$ respectively. There is a simple geometric relationship between j_{sc} and j_{ring} , as indicated in Fig. 1.

Assuming for the moment that the scatter current density J_{sc} has been calculated, as well as $J_{ring}(R)$, we see immediately some other geometrical relationships. Integrating over the current density $J_{ring}(R)$ between R_1 and R_2 will give us the scatter current falling into the area between R_1 and R_2 . This current value can also be obtained if a table is produced for the scatter current falling outside a given radius R_1 , R_2 , etc., and the relevant values are subtracted from one another. For large values of R this leads to a subtraction of two relatively small numbers, giving us a higher numerical accuracy than that obtainable if we would subtract the two figures for the large scatter currents which fall inside the radii R_1 , R_2 , etc. For this reason we have computed the values

$$I_{sc}(R_1) = \int_{R_1}^{\infty} J_{ring}(R)\,dR \tag{1}$$

$I_{sc}(R_1)$ represents scatter current which falls outside a certain radius R_1 . This may be the current intercepted, for instance, by an aperture of diameter $D = 2R_1$. This is also identical with the current loss of the main beam as long as the pressure is low and the majority of the electrons are only scattered once. The scattering into angles larger than 90° is also neglected.

At higher pressures, with $R_1 \ll L$, $I_{sc}(R_1)$ may be interpreted as I_0 times the number of scatter events per incoming electron in which the effective displacement

$$D_{eff} = (L-Z)\tan\theta \tag{2}$$

is greater than R_1 . In this sense we can accept values of I_{sc} greater than I_0 . Taking into consideration the independence of successive random random scattering events we can show that if we assign to each scattered electron an R value equal to the largest value of D_{eff} in its individual scatter history, we thus define a current distribution $I_{thru}(R_1)$ which may be easily calculated; this is the current that would pass through an aperture of radius R_1 with R assigned as indicated above. This is certainly a better approximation to the multiply scattered current that would pass through the aperture than $I_0 - I_{sc}(R_1)$. The probability of each beam electron being assigned in the above manner to the circle of radius R and width dR may be shown to be

$$\frac{dI_{thru}}{I_0} = \frac{I_{thru}\, dI_{sc}(R)}{I_0^2} \tag{3}$$

Integrating this and setting $I_{thru}(R=\infty) = I_0$, we obtain

$$I_{thru}(R) = I_0 e^{-I_{sc}(R)/I_0} \tag{4}$$

The current which is lost from the beam through multiple scattering in this approximation is then

$$I_{loss}(R) = I_0(1 - e^{-I_{sc}(R)/I_0}) \tag{5}$$

Although this derivation of I_{loss} is not strictly accurate it gives reasonable indication of the current loss in the transition region from single scattering to multiscattering. On the other hand I_{thru} is a reasonable number for the current retained in a welding beam focus of radius R (e.g., identical to the width of a finite beam).

A systematic extension of the calculations to the case of finite diameter primary beams will be presented at a later time.

Having in the above paragraphs defined some of the geometric relationships, let us now consider how J_{sc} can be calculated from j_{sc}, which is first calculated from scattering cross section data.

III. SCATTERING EQUATIONS AND CROSS SECTIONS

Since the beam voltage in which we are most interested, namely 150 kV, is in the range at which the Born approximation works well, and extensive Born data can be found in the literature, we made this the basis of our small angle scattering calculations. In nonrelativistic form, the elastic and inelastic cross sections are given (in cm^2/atom) as:

$$\sigma_{\omega,el} = F^2(X) = \frac{4}{a^2q^4}[Z - f(\eta)]^2 \qquad \sigma_{\omega,in} = \frac{4}{a^2q^4}S(\eta) \qquad (6)\ (7)$$

where $X = [\sin(\theta/2)]/\lambda$, $\lambda = h/p$ = wave length of electron, h = Planck's constant, $q = 2\pi\Delta p/h$, Δp = magnitude of momentum change to the electron as a result of the collision, $\eta = qa$, $a = h^2/4\pi^2e^2m_0$ is the Bohr radius for hydrogen, e = electronic charge, m_0 = rest mass of the electron, and Z = atomic number of scattering atoms; F is called the Born wave amplitude and is listed[1] as a function of X; cgs units are used for all quantities.

To use (6) and (7), one must determine θ and q for each tabular value of X or η , and then use the equation to calculate σ_ω . It is well known that

$$\Delta p = 2\, mv_1 \sin\,(\theta/2) \tag{8}$$

in the case of elastic scattering and

$$\Delta p = m\sqrt{v_1^2 + v_2^2 - 2v_1v_2\cos\theta} \tag{9}$$

for inelastic scattering where v_1 and v_2 are the electron velocities before and after the collision; f is called form factor in X-ray diffraction, and the function S , introduced by Morse, was calculated and presented in graphs by Lenz.[2] In the case of 150-kV electrons, the tables and graphs take us to angles of only a few degrees. For larger angles the Rutherford (Coulomb) scattering formula may be used. Since at 150 kV relativistic effects are already appreciable it seemed advisable to include relativistic corrections at both large and small angles. Thus, for large angles we used Mott's formula for Coulomb scattering:[3]

$$\sigma_{\omega,el}(\theta) = \frac{Z^2e^4}{4m^2v^4\sin^4\frac{\theta}{2}}\,(1-\beta^2)\left[1 - \beta^2\sin^2\frac{\theta}{2} + \pi\alpha\beta\,\sin\frac{\theta}{2}\left(1 - \sin\frac{\theta}{2}\right)\right] \tag{10}$$

where $\beta = v/c$, v = electron velocity, c = velocity of light, and $\alpha = Z/137$. It was not obvious in the text whether m was intended to mean the rest mass m_0 or the dynamic mass $m_0/\sqrt{1-\beta^2}$. We found, however, that use of the rest mass m_0 gives consistency with relativistic forms of (6) and (7), which we shall consider next. The second bracketed expression in (10) gives the effect of spin, and differs only negligibly from 1 at small angles, but the remainder of the Rutherford $\sigma_{\omega,el}$ should join smoothly with the relativistic form of (6), namely[1]

$$\sigma_{\omega,el} = \frac{F^2}{1-\beta^2} \tag{11}$$

Likewise in the use of (6) and (7) it was not clear whether X, q, and η should be computed by classical or relativistic methods, although it was noted in the tables[1] for F that the tabulated values of F were to be multiplied by $(1 - \beta^2)^{-1/2}$. We can get internal consistency in (6) if both expressions for $\sigma_{\omega,el}$ are divided by $(1 - \beta^2)$ and the independent variables X and q are either both computed classically or both computed relativistically. Since $f(\eta)$ approaches zero for large η, substitution of $f = 0$ into (6) should give consistency with the Mott equation (10) without the spin term. The unique choice of alternatives which makes such consistency possible was for X and q to be computed relativistically, i.e., using $m = m_0/\sqrt{1-\beta^2}$ and for Mott's m to be simply m_0. Since second forms of (6) and (7) are often written together as a single expression for total cross section,[2] it seemed reasonable to apply the same relativistic treatment to (7) as to (6). Finally, to avoid an artificial break in our curves when we passed from the Born formula to the Mott formula, we decided to include the spin term in the Born formulae. In the equation for inelastic scattering (7) S approaches Z as η becomes large. Hence it seemed reasonable to extend equation (7) to large angles with Z replacing S, or equivalently to apply equation (10) to large angle inelastic scattering with Z^2 replaced by Z.

In summary then, the formulae which we used for computation were:

Small angle elastic:

$$\sigma_{\omega,el}(\theta) = F^2(X)G(\beta,\theta); \left[x = \sin\frac{\theta}{2}\Big/\lambda \ ; \quad \lambda = \frac{h}{p} = \frac{h\sqrt{1-\beta^2}}{m_0 v}\right] \qquad (12a)$$

Small angle inelastic:

$$G_{\omega,in} = \frac{4a^2}{\eta^4} S(\eta)G(\beta,\theta) \qquad (12b)$$

Large angle elastic:

$$\sigma_{\omega,el}(\theta) = \frac{Z^2 e^4}{4m_0^2 v^4 \sin^4\frac{\theta}{2}} G(\beta,\theta) \qquad (12c)$$

Large angle inelastic:

$$\sigma_{\omega,in}(\theta) = \frac{Z e^4}{4m_0^2 v^4 \sin^4\frac{\theta}{2}} G(\beta,\theta) \qquad (12d)$$

where

$$G(\beta,\theta) = (1 - \beta^2)\left[1 - \beta^2\sin^2\frac{\theta}{2} + \pi\alpha\beta\sin\frac{\theta}{2}\left(1 - \sin\frac{\theta}{2}\right)\right] \qquad (12e)$$

In relating v and β^2 to the beam voltage V, we define a relativistic potential

$$\varphi^* = \frac{V}{510\ 976} \qquad (13a)$$

which is related to β by the equation

$$(\varphi^* + 1)^2 = \frac{1}{1-\beta^2} \qquad (13b)$$

from which

$$\beta^2 = \frac{2\varphi^* + \varphi^{*2}}{(1+\varphi^*)^2} \qquad (13c)$$

$$v = \frac{c\sqrt{2\varphi^* + \varphi^{*2}}}{1+\varphi^*} \qquad (13d)$$

In the case of inelastic scattering equation (13d) is used to calculate velocities v_1 and v_2 separately using the volt energy after collision $V_2 = V_1 - V_{loss}$. The typical loss voltage was taken as half of the ionization potential of the scattering atom. In the region of very low η values, $S(\eta)$ varies as the square of η and only the fact that the condition $V_2 < V_1$ leads to a nonzero value for η at $\theta = 0$ in (12b), prevents $\sigma_{\omega,in}(\theta)$ from becoming infinite. This means that the peak value of $\sigma_{\omega,in}(\theta)$ is determined entirely by the assumed value of V_{loss}. Further consequences of this almost singular behavior of $\sigma_{\omega,in}(\theta)$ will be discussed with the results of the computations.

COMPUTATION OF SCATTER CURRENT DENSITIES

The above equations give us the scatter cross section in cm^2/steradian-atom. This result must be related to our scatter current densities defined in the previous chapter. The current which is due to that scatter probability can be expressed as

$$j_\omega(\theta) = I_0 \sigma_\omega(\theta) N\, dZ \qquad (14)$$

where N is the number of atoms/cm^3 and dZ is the length of the beam element. The relationship between j_ω and j_{sc} depends upon the geometric orientation of the surface element dA with respect to the point of scatter; in our simple case of Fig. 1 the relationship becomes

$$j_{sc} = j_\omega d\omega/dA \qquad (15)$$

with

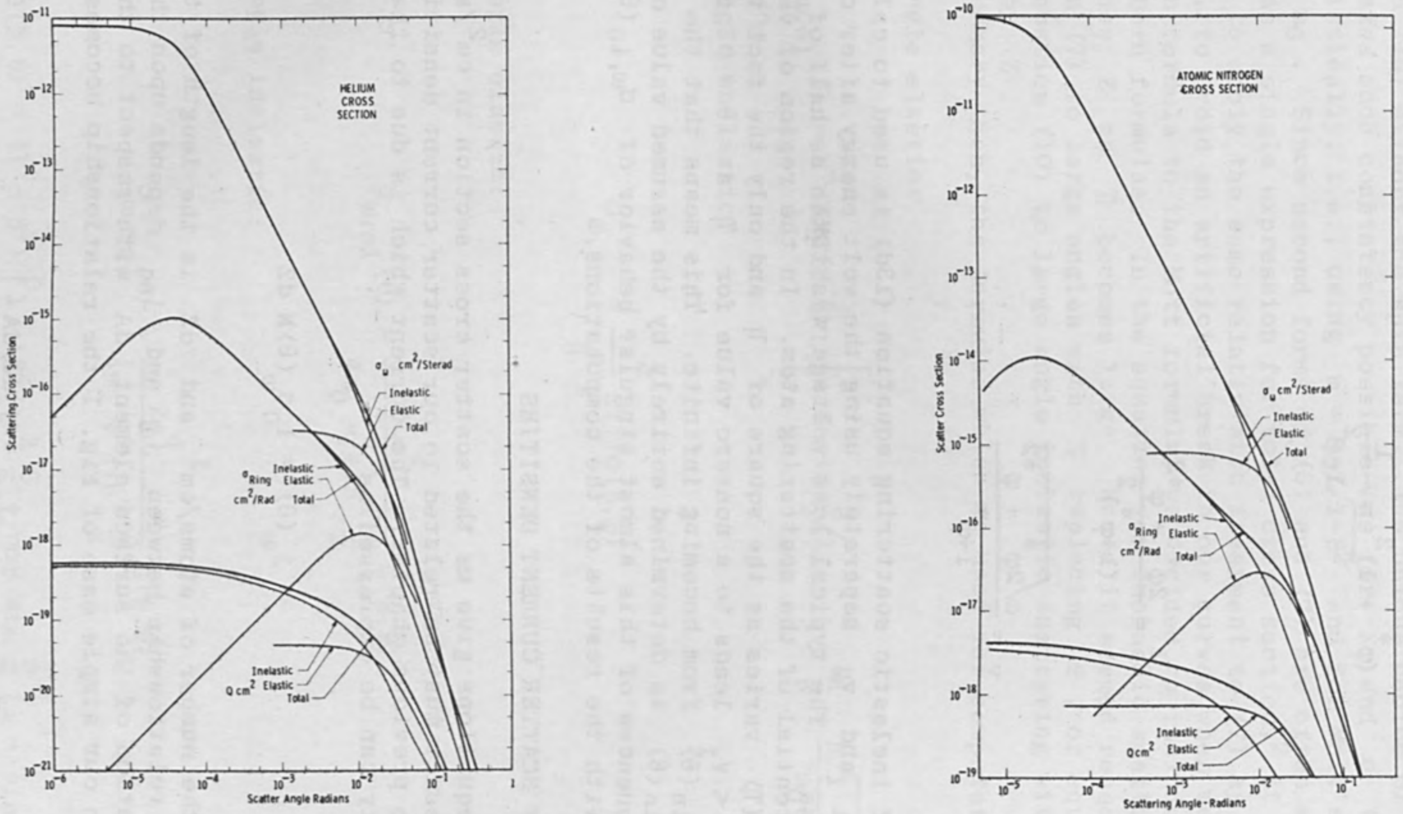

(a) (b)

FIG. 2.—Calculated scattering cross sections for (a) helium, (b) nitrogen.

$$d_{\omega} = \frac{\cos\theta}{R^2 + (L - Z)^2}\, dA \tag{16}$$

From this one can derive the following:

$$j_{sc}(R) = \frac{I_0 N \sin^2\theta}{R^2} \cos\theta\, \sigma_{\omega}(\theta)\, dZ \tag{17}$$

$$j_{ring}(R) = \frac{I_0 2\pi \sin^2\theta}{R} \cos\theta\, \sigma_{\omega}(\theta) N dZ \tag{18}$$

where $j_{sc}(R)$ is related to $j_{ring}(R)$ as shown in Fig. 1.

For small angles this simplifies to

$$j_{ring}(R) = I_0 2\pi \sin\theta\, \sigma_{\omega}(\theta) \frac{N}{(L - Z)}\, dZ \tag{19}$$

$$= I_0\, \sigma_{ring}(\theta) \frac{N}{(L - Z)}\, dZ \tag{20}$$

The term $2\pi \sin\theta\, \sigma_{\omega}(\theta)$ in (19) can be considered another cross section which we have designated $\sigma_{ring}(\theta)$. It represents the probability for scattering into a cone mantle region with half angle θ and width $d\theta$. This is of some importance because σ_{ring} behaves differently at small angles from σ_{ω}. While σ_{ω} becomes constant for $\theta \to 0$, $\sigma_{ring} \to 0$ for $\theta \to 0$. As a consequence the scatter cross section σ_{ring}, if plotted over θ, starts at 0 and shows a peak at some small but finite angle θ.

Numerical values for $\sigma_{\omega}(\theta)$ and $\sigma_{ring}(\theta)$ have been computed using the input data from Refs. 1 and 2. Details of the computation, programmed on a B-5500 digital computer, will not be discussed here.

As an additional quantity Fig. 2 shows the so-called partial cross section Q which is defined as follows:

$$Q = \int_{\theta_1}^{\pi} \sigma_{ring}(\theta)\, d\theta \tag{21}$$

This quantity represents cross section for the scattering of an electron beyond a given angle θ_1. For $\theta_1 = 0$ we get

$$Q_0 = \int_{0}^{\pi} \sigma_{ring}\, d\theta \tag{21a}$$

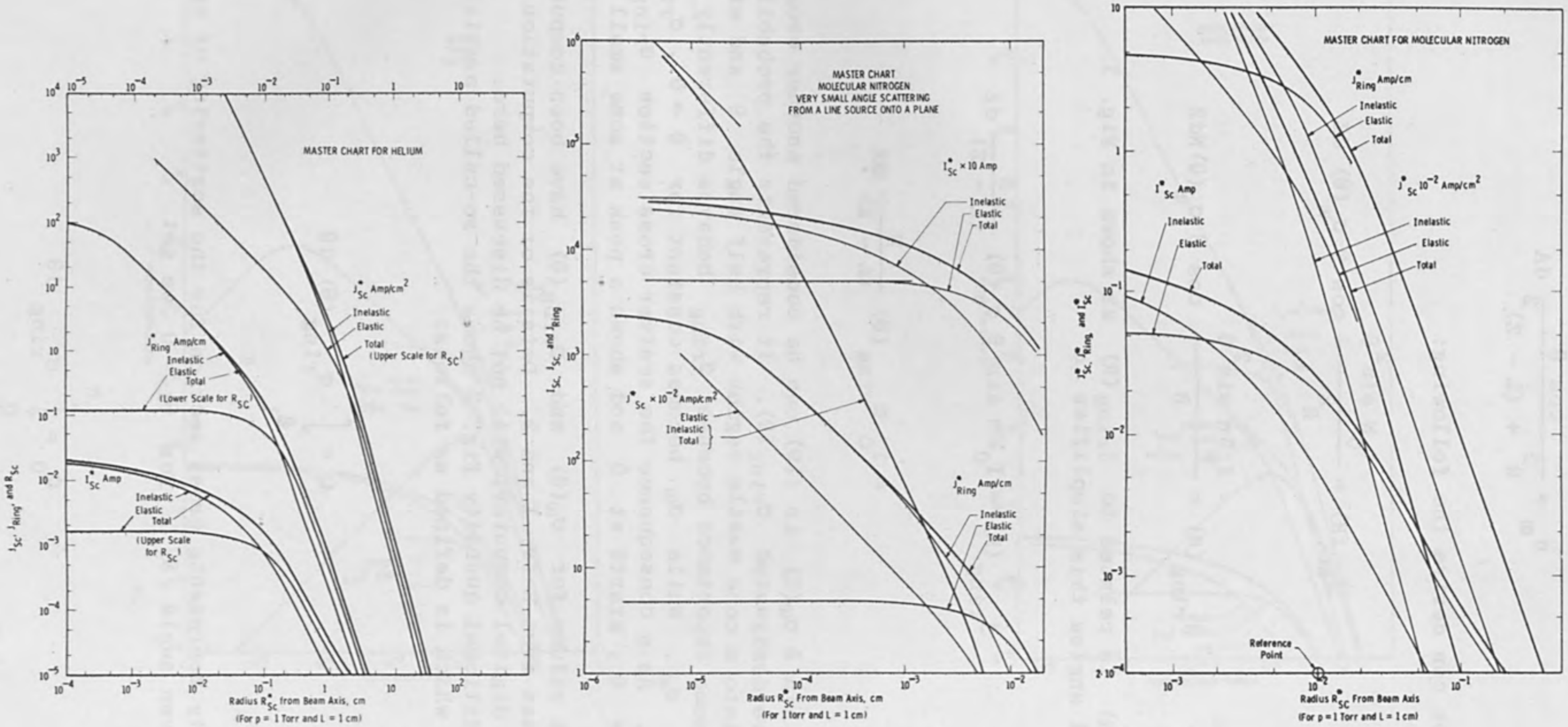

(a) (b) (c)

FIG. 3.—Master charts for scatter current and current density distributions for (a) helium, (b) nitrogen, (c) nitrogen at extremely small radius.

which is called the total scattering cross section. The above value of $j_{sc}(R)$ is not yet the quantity which we need for our later computations; we have to integrate (17) over dZ. This can best be done by substituting $Z = L - R \cot \theta$ and integrating over θ. Then we obtain

$$J_{sc}(R) = \frac{N}{R} I_0 \int_{\mathrm{arc\,cot}(L/R)}^{\pi/2} \sigma_\omega(\theta) \cos \theta \, d\theta \qquad (22)$$

Combining this result with the definition of $J_{ring}(R)$ gives us also

$$J_{ring}(R) = 2\pi I_0 N \int_{\mathrm{arc\,cot}(L/R)}^{\pi/2} \sigma_\omega(\theta) \cos \theta \, d\theta \qquad (23)$$

The above equations give us the scatter current density from a line source as a function of radius R in the lower plane at which the line source ends. After these quantities are known, it is a simple matter to calculate, for instance, $I_{sc}(R)$ according to (1) by integrating over dR.

The results of these computations for helium and for nitrogen as the scatter medium are presented in the forms of graphs in Fig. 3. The properties of these charts and the quantities represented therein are discussed in the next section.

CHARTS FOR SCATTERING FROM A LINE SOURCE

The graphs in Fig. 3 are drawn for the particular conditions $P = 1$ Torr, $L = 1$ cm, and $T = 0°$C, and all quantities are marked with an asterisk. These charts are called master charts because they may be readily converted into graphs corresponding to any desired values of P, L, and T; we see from (23) that $J_{ring}(R)$ depends upon R and L in the combination of the ratio L/R only, and not on either of them separately. Apart from this ratio J_{ring} is proportional to initial beam current I_0 and density ρ. On the other hand, J_{sc} in (22) depends not only on L/R but also on $1/R = 1/(L \tan \theta)$; and the integration of (1) for $I_{sc}(R)$ uses the term $dR = L \sec^2 \theta \, d\theta$. The above two expressions contain functions of the ratio L/R and coefficient terms $1/L$ and L, respectively. We therefore must multiply J^*_{sc} by $1/L$ to arrive at J_{sc} and multiply I^*_{sc} by L to obtain I_{sc}. Considering the gas laws we arrive at the following conversion formulas which permit us to go from the data on the master graph to any other values of I_0, L, and ρ, P, or T which we may want to use:

$$J_{sc}(R) = \frac{P I_0}{L\left(1 + \frac{T}{273}\right)} \, , \, J^*_{sc}(R) \qquad (24a)$$

a finite value as arc cot L/R approaches zero, whereas $1/R^*$ remains as a coefficient. Following these facts, we should expect the shapes of $J^*_{ring}(R^*)$ and $I^*_{sc}(R^*)$ essentially to match $\sigma_{ring}(\theta)$ and $Q(\theta)$ in the small angle Rutherford scattering region and to have larger slope in the range $R^* < 0.01$. These characteristics are confirmed in the curves.

A set of curves, converted from the nitrogen master chart (as previously explained) to actual conditions as found in a semivacuum welder is given in Fig. 4. From the chart we see that for scattering to a radius of 1 mm, $I_{sc}(R) = 30$ mA and $J_{sc}(R) = 0.25$ A/cm^2. This indicates that somewhat more than 30% of a 2-mm-diameter beam would be scattered outside the main beam cross section. Without scattering the current density would have been 32 A/cm^2 but at a distance of 1 mm from the boundary of the original cross section, current density has fallen to the neighborhood of 0.25 A/cm^2. Clearly this is too low to melt metal and current scattered this far must be considered as effectively lost.

Another way to look at beam degradation due to scattering is to look at I_{thru}, i.e., the fraction of current retained in the beam, passing through an aperture of $D = 2R$. From the graph of Fig. 6(b), (24), and (4) we have calculated Table I. Distances L have been chosen to resemble work spacings typical for nonvacuum welding.

TABLE I

Gas	L	Fraction of beam current I_0 passing through aperture of diameter $D = 2R$ (Pressure P = 760 Torr)		
	(cm)	D = 0.1 cm	D = 0.2 cm	D = 0.5 cm
He	0.3	0.997	0.9986	0.9992
	0.6	0.984	0.994	0.9977
	1.2	0.862	0.969	0.9907
N_2	0.3	0.944	0.974	0.986
	0.6	0.675	0.886	0.958

We see with a beam path of 1.2 cm in helium 97% of the beam remains in a 0.2-cm spot (e.g., giving a 0.2-cm-wide weld at 1/2 in. working distance). In nitrogen, even at 0.6-cm distance only 89% of the beam is retained in the same spot.

REFERENCES

1. International Tables for X-Ray Crystallography, 3: 201-226. Birmingham, England: Kynoch Press, 1962.

2. H. Wyrwich and F. Lenz, "Berechnung der differentiellen Wirkungsquerschnitte für die Streuung mittelschneller Elektronen an Atomen aus Hartree-Funktionen," Zeit. für Naturforsch. 13a: 515-523, 1958.

3. N. F. Mott and H. S. W. Massey, The Theory of Atomic Collisions, Oxford: Clarendon Press, 1965; 3rd ed., p. 235.

ANGULAR DISTRIBUTION OF BACKSCATTERED ELECTRONS

D. M. HART

International Business Machines Corp. (Systems Development
Division), San Jose, California

The angular distribution of backscattered electrons has been determined from targets of different atomic number at various angles of the primary beam. The two targets chosen were materials with vastly different atomic numbers, i.e., aluminum and tantalum. This was done to determine experimentally the effect of the atomic number Z and the angle of incidence φ on the backscatter fraction η.

Polar diagrams, representing the angular distribution of the backscattered electrons, show that η is considerably greater for the high-Z material Ta than for the low-Z material, Al. Also, the dependence of the backscatter fraction η on the angle of incidence φ is apparent, particularly for large angles of incidence.

It appears that for large angles of incidence the backscatter for aluminum is greater than tantalum. This is probably due to the fewer orbital electrons in the low Z material, i.e., less stopping power, and ease of escape from the shallow penetration depths as a result of the large incident angle.

INTRODUCTION

Electron beam readout of information recorded in the form of variations in surface topography requires an understanding in the distribution of the backscattered electrons relative to angle of incidence of the impinging electron beam. This information allows optimization of detector positioning relative to the slope of the recorded information.

The angular distribution, as well as the energy distribution of the backscattered electrons, depends on the interaction of the incident electrons with the target nuclei and electrons. Owing to the difference in masses, the principal effect of the target nuclei is to change the direction of the incident electron, whereas the principal effect of the target electrons is to decrease the velocity of it. Experimentally, then, it has been shown[2,3] that as the atomic number of the target increases, there is a greater influence on the incoming electron, in that the direction of an incident electron may be changed several times through successive nuclear scatterings.

The following experimental work shows the influence of the atomic number of the target, the angle of incidence of the primary beam, and the energy of the primary beam on the backscattered electrons.

EXPERIMENTAL WORK

The prime purpose of this work was to determine the angular distribution of backscattered electrons from targets of different atomic number at various incident angles of the primary beam. For our experiments a rotatable Faraday cage was selected as the electron collector, and a rotatable target was used for providing changes in the angle of incidence.

The directional distribution of greatest interest was in a plane perpendicular to the rotational axis of the target. We expected that the greatest change in the number of backscattered electrons would occur in this plane as a function of a change in the angle of incidence φ. Here, then, was where the Faraday cage collector was rotated.

The collector was rectangular in cross section with sufficient area to collect a useful quantity of electrons. The quantity of electrons collected as a function of angle of incidence are those electrons that are backscattered within the solid pyramidal angle. Figure 1 shows the collection concept.

Electron current measured at the collector is not meaningful in terms of high-energy backscatter from the target unless some measure is taken to minimize the effects of backscatter and low-energy secondary electron emission from the collector. Since the backscatter fraction η is a direct function of atomic number,[3] the collector must be constructed of material having a low atomic number. When high-energy backscatter electron distribution is required, it is important to eliminate the collection of true secondary electrons that emanate from the target and from surfaces within the recording chamber. The secondary electrons that emanate from the chamber surface are eliminated by the configuration of the Faraday cage collector. The true secondaries (that is, those electrons that emanate from the target with energies less than 50 eV) are eliminated by applying a retarding field at the entrance to the collector.

To determine the backscatter distribution as a function of the angle of incidence, the target could be set at any angular position from 0° to 90° relative to the beam. Care was taken in the fabrication of the target holder to insure that the axis of rotation of the target was on the surface of the target. This prevents the electron beam from moving across the target surface, and prevents any change in position of the backscatter source relative to the collector.

EXPERIMENTAL APPARATUS

The primary beam of electrons is produced by a conventional demountable electron optical system using a triode gun with a tungsten hairpin filament. The beam is first bent off axis to prevent possible contamination of the target by tungsten evaporation, and then repositioned on the electron optical axis by a magnetic turning field.

A single magnetic lens, located approximately three times its focal length from the first crossover at the gun, is used to focus the beam to a spot size of approximately 0.5 mm on the target. Accelerating potentials of 10 and 20 kV were used to determine experimentally the dependence of η on the initial kinetic energy. The beam is positioned on the target by applying a balanced voltage to a set of electrostatic deflection plates located just below the magnetic lens. The focal length of the final lens is sufficiently long to prevent any interaction between the magnetic and electrostatic fields with the backscattered electrons that emanate from the target.

Figure 2 shows the electron collection chamber. It consists of a 6-in.-diameter copper cylinder with a demountable endplate. The endplate supports the entire target and collector assembly for ease of sample handling. Distribution of the backscattered electrons is measured in terms of electron current and angle of collection in the plane perpendicular to the axis of rotation. The collection angle is measured by using an

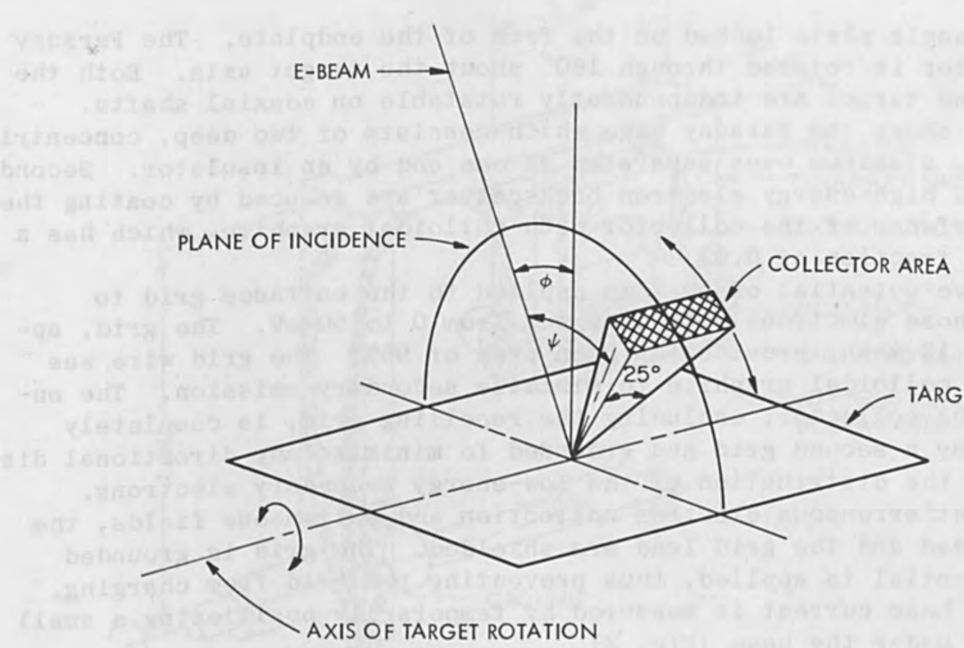
E-BEAM
PLANE OF INCIDENCE
φ
ψ
COLLECTOR AREA
25°
TARGET
AXIS OF TARGET ROTATION

FIG. 1.—Collection concept.

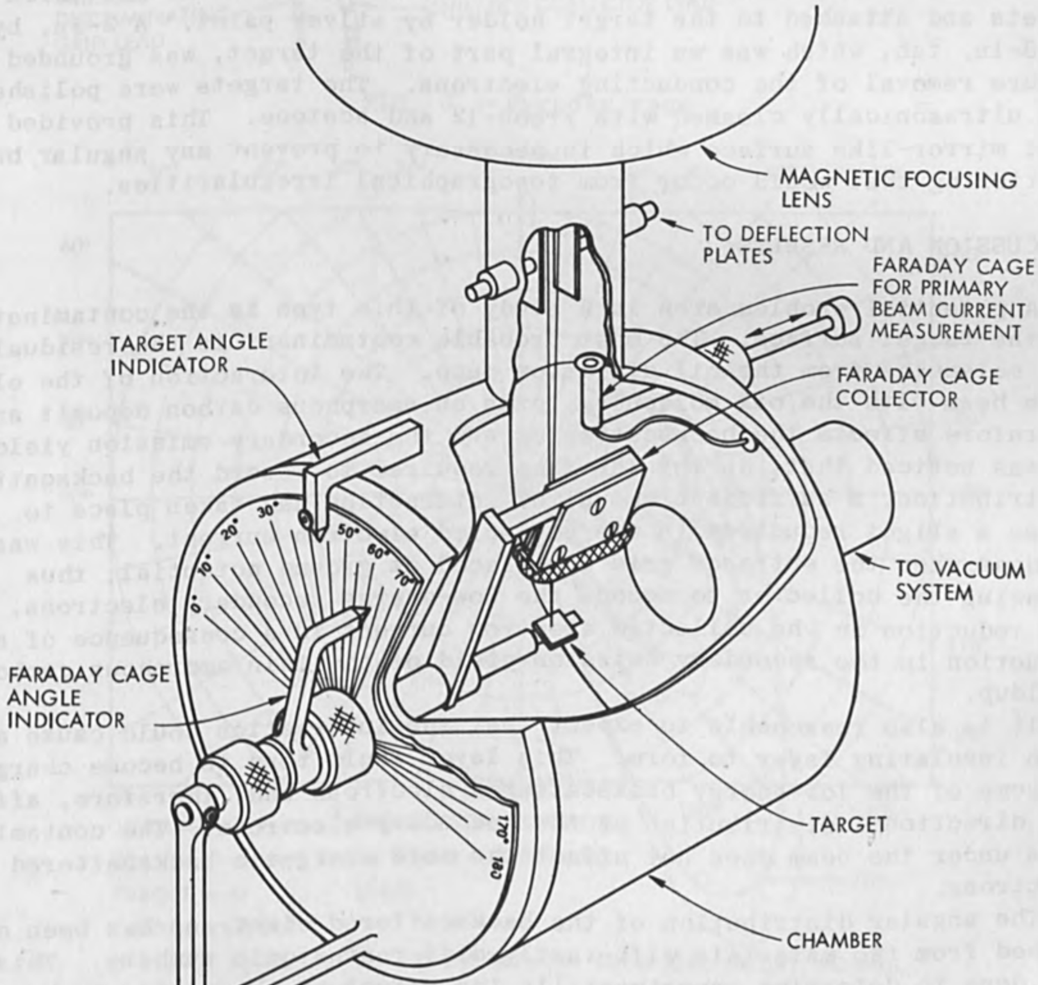
MAGNETIC FOCUSING LENS
TO DEFLECTION PLATES
FARADAY CAGE FOR PRIMARY BEAM CURRENT MEASUREMENT
TARGET ANGLE INDICATOR
FARADAY CAGE COLLECTOR
TO VACUUM SYSTEM
FARADAY CAGE ANGLE INDICATOR
TARGET
CHAMBER
0
10
20
30
50
60
70
180

FIG. 2.—Experimental electron-collector chamber.

adjustable angle plate locked on the face of the endplate. The Faraday cage collector is rotated through 180° about the target axis. Both the collector and target are independently rotatable on coaxial shafts.

Figure 3 shows the Faraday cage which consists of two deep, concentric, rectangular, aluminum cups separated at one end by an insulator. Secondary emission and high-energy electron backscatter are reduced by coating the interior surfaces of the collector with colloidal graphite, which has a backscatter fraction of 0.07.

A negative potential of 50 V is applied to the entrance grid to eliminate those electrons with energies from 0 to 50 eV. The grid, approximately 12 mesh, provides an open area of 95%. The grid wire was coated with colloidal graphite to minimize secondary emission. The entrance to the collector, including the repelling grid, is completely surrounded by a second grid and grounded to minimize any directional disturbance in the distribution of the low-energy secondary electrons.

To prevent erroneous electron collection and extraneous fields, the collector lead and the grid lead are shielded. The grid is grounded when no potential is applied, thus preventing the grid from charging. The primary beam current is measured by temporarily positioning a small Faraday cup under the beam (Fig. 2).

The metal targets were cut into 1/4-in. squares from 10-mil-thick sheets and attached to the target holder by silver paint. A 2-in. by 1/16-in. tab, which was an integral part of the target, was grounded to insure removal of the conducting electrons. The targets were polished and ultrasonically cleaned with Freon-12 and acetone. This provided a flat mirror-like surface which is necessary to prevent any angular backscattering that would occur from topographical irregularities.

DISCUSSION AND RESULTS

A potential problem area in a study of this type is the contamination of the target surface. The most probable contaminant is the residual oil molecules from the oil diffusion pump. The interaction of the electron beam with the oil molecules forms an amorphous carbon deposit and therefore affects the backscattering and the secondary emission yield. It was noticed that, during the time required to record the backscatter distribution, a sufficient amount of interaction had taken place to cause a slight reduction in the collected electron current. This was evident when the entrance grid was placed at ground potential, thus allowing the collector to accept the low-energy secondary electrons. The reduction in the collected electron current is a consequence of a reduction in the secondary emission yield of the thin amorphous carbon buildup.

It is also reasonable to expect that the interaction could cause a thin insulating layer to form. This layer would tend to become charged by some of the low-energy backscattered electrons and, therefore, affect the directional distribution of the secondary electrons. The contaminated area under the beam does not affect the more energetic backscattered electrons.

The angular distribution of the backscattered electrons has been obtained from two materials with vastly different atomic numbers. This was done to determine experimentally the effect of the atomic number Z and the angle of incidence φ on the backscatter fraction η.

Figures 4 through 7 are polar diagrams representing the angular

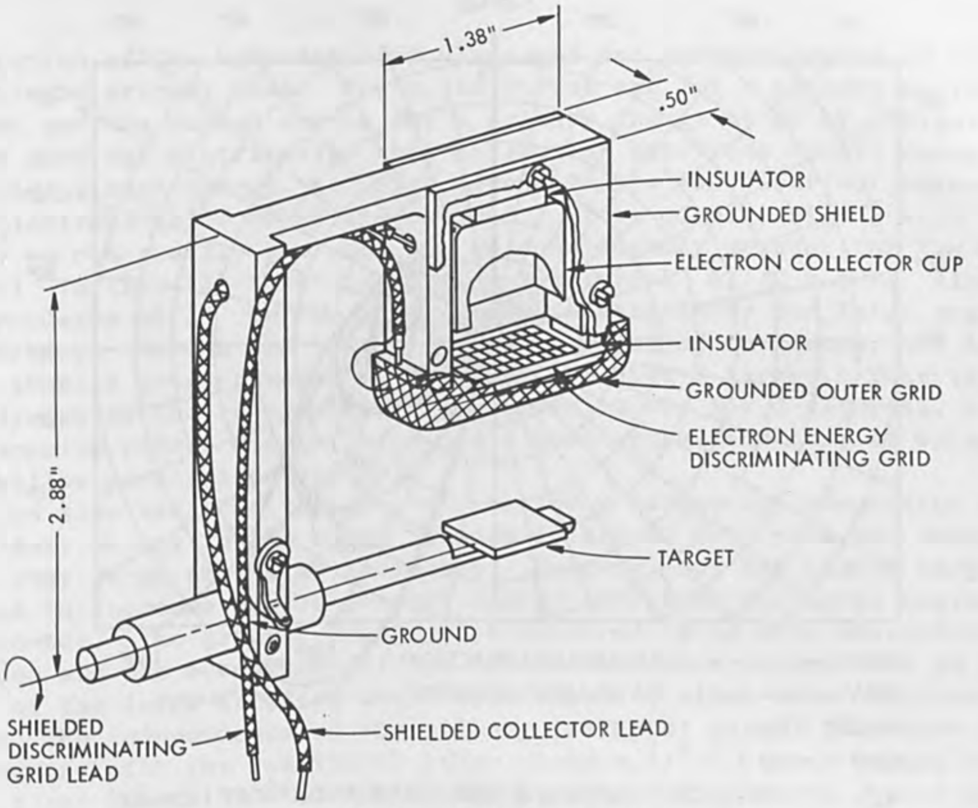
1.38"
.50"
INSULATOR
GROUNDED SHIELD
ELECTRON COLLECTOR CUP
INSULATOR
GROUNDED OUTER GRID
ELECTRON ENERGY DISCRIMINATING GRID
2.88"
TARGET
GROUND
SHIELDED DISCRIMINATING GRID LEAD
SHIELDED COLLECTOR LEAD

FIG. 3.—Faraday cage.

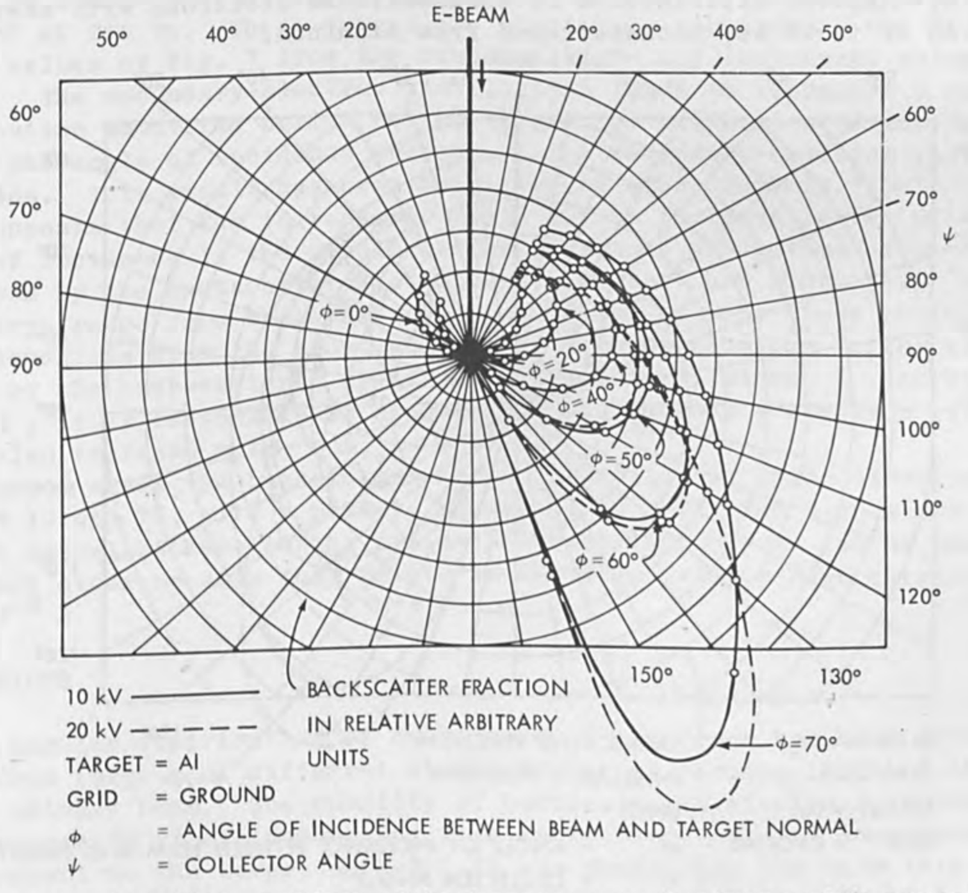

FIG. 4.—Angular distribution of backscattered electrons with energies from 0-20 keV backscattered from aluminum.

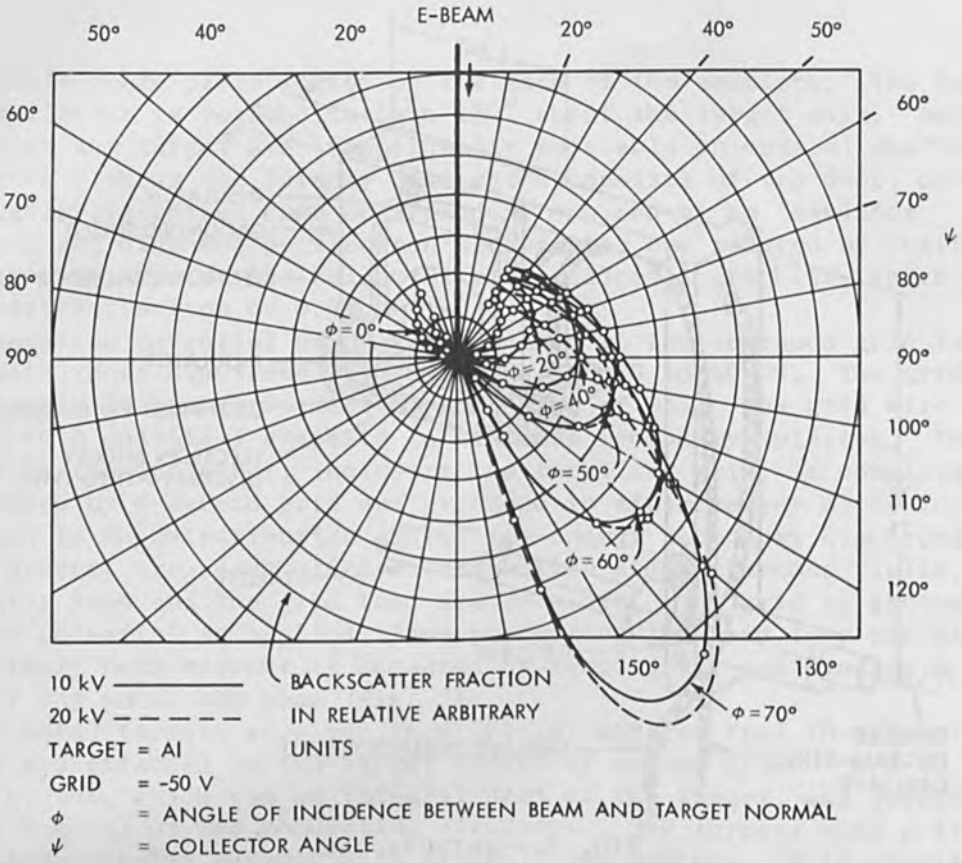

FIG. 5.—Angular distribution of backscattered electrons with energies from 50 eV to 20 keV backscattered from aluminum.

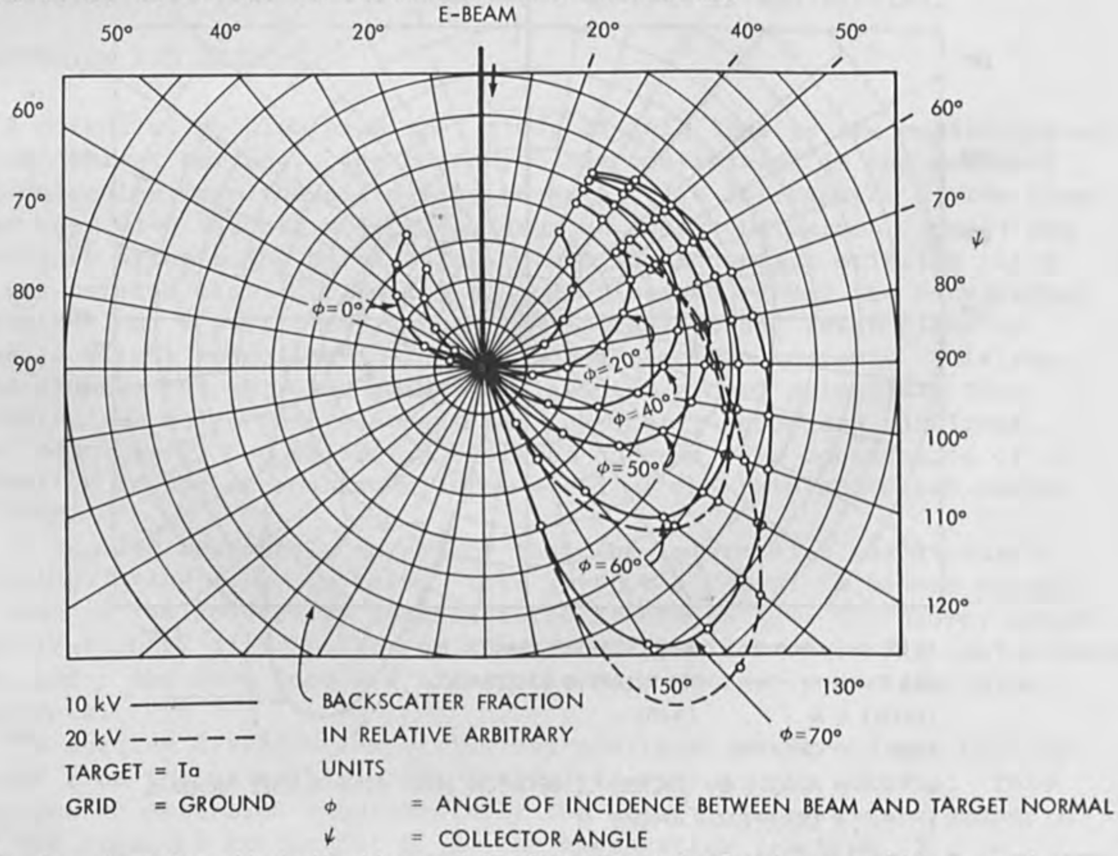

FIG. 6.—Angular distribution of backscattered electrons with energies from 0 to 20 keV backscattered from tantalum.

distribution of the backscattered electrons for various angles of incidence of the primary beam. The solid curves are for a primary energy of 10 kV and the dashed curves for a primary energy of 20 kV. Figures 4 and 6 show the distribution when collecting electrons of all energies up to the primary energy, and Figs. 5 and 7 show the distribution when those electrons below 50 eV are omitted. If we compare Fig. 5 with Fig. 7, we can readily see that η is considerably greater for the high-Z material Ta (Z = 73) than for the low-Z material Al (Z = 13). Also, the dependence of η on φ is apparent, particularly for large angles of incidence. We can see that, for large angles of incidence, the low-Z target shows a greater value of η than the high-Z target. This is probably due to the fewer orbital electrons in the low Z material, i.e., less stopping power, single large angle scattering, and ease of escape from shallow penetration depths.

We can also see that the η for the low Z target is independent of the primary energy in the range between 10 and 20 keV, with the exception of the very large angles of incidence. However, for the high-Z target, η tends to increase as the primary energy increases for large angles of incidence. The greater penetration depth of these more energetic electrons and the occurrence of the interaction near the surface as a result of the large incident angle would tend to allow more electrons to escape. The independence of the primary energy at normal incidence is in agreement with the results of other workers.[1,2,3] Lower values shown in the first 30° to 120° of the 20-keV primary-energy curve appear to be a reduction in the contribution of the low-energy electrons.

Figure 8 shows the distribution of the low-energy secondary electrons below 50 eV for Ta. These curves are plotted by subtracting the high-energy values of Fig. 7 from the combined high- and low-energy values of Fig. 6. The secondary-electron distribution tends to represent a cosine distribution about the normal to the target for all angles of incidence. But as the angle of incidence increases, the secondary-emission yield increases. This result has been confirmed by other workers.[4,5]

It appears that the increase in yield for an increase in the primary angle of incidence is the result of the increased production of secondary electrons by the backscattered electrons. Kanter[6] has shown that "for the energy range from a few keV to several tens of keV, close to 40% of all secondaries from the front surface of a thick aluminum target was formed by the backscattered electrons." Therefore, since η increases with φ, it is reasonable to expect that the secondary electron yield would also increase with φ.

Figure 9 shows the backscattering as a function of angle of incidence for Z = 13 and 73, with a primary energy of 10 keV. The values for η are not actual backscattering ratios; however, the curves can be compared with each other because they relate to the same primary beam current of 47×10^{-9} A.

CONCLUSIONS

The angular distribution of backscattered electrons has been determined from targets of different atomic number at various incident angles of the primary beam. The quantity of backscattered electrons increase with increasing atomic number and with increasing angle of incidence with respect to the target normal. It was found that for very large angles (i.e., 70°) the quantity of backscattered electrons from Al

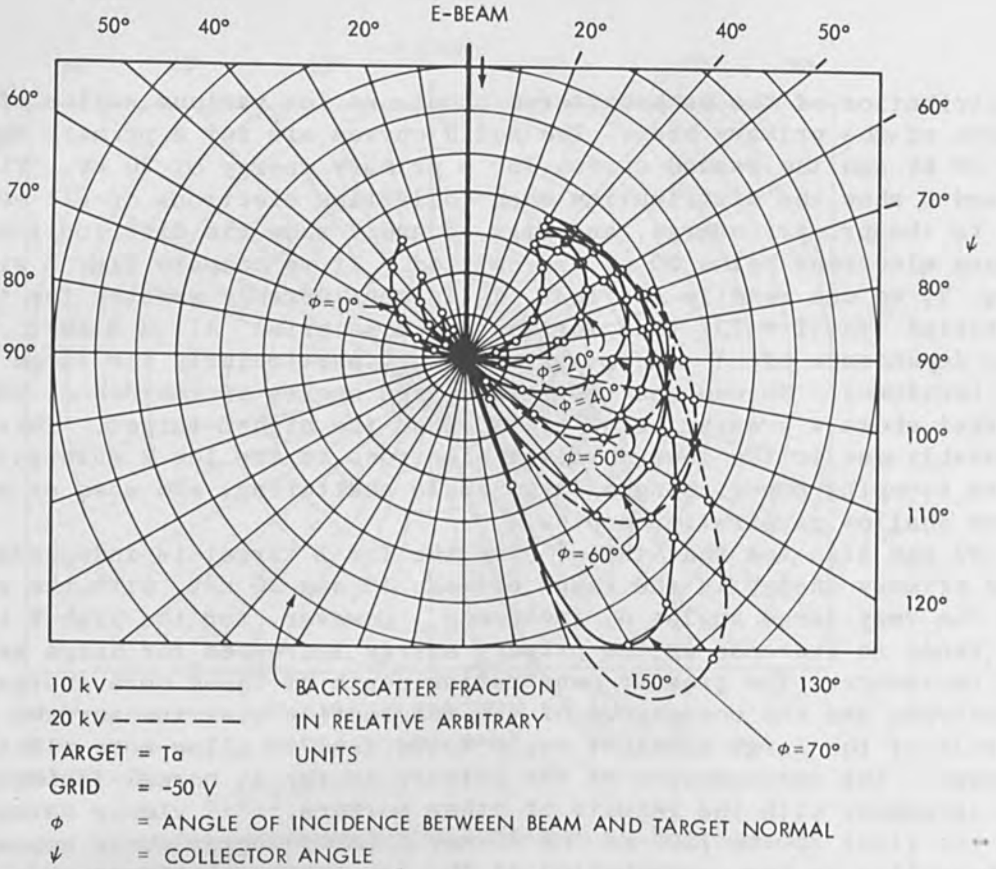

FIG. 7.—Angular distribution of backscattered electrons with energies from 50 eV to 20 keV backscattered from tantalum.

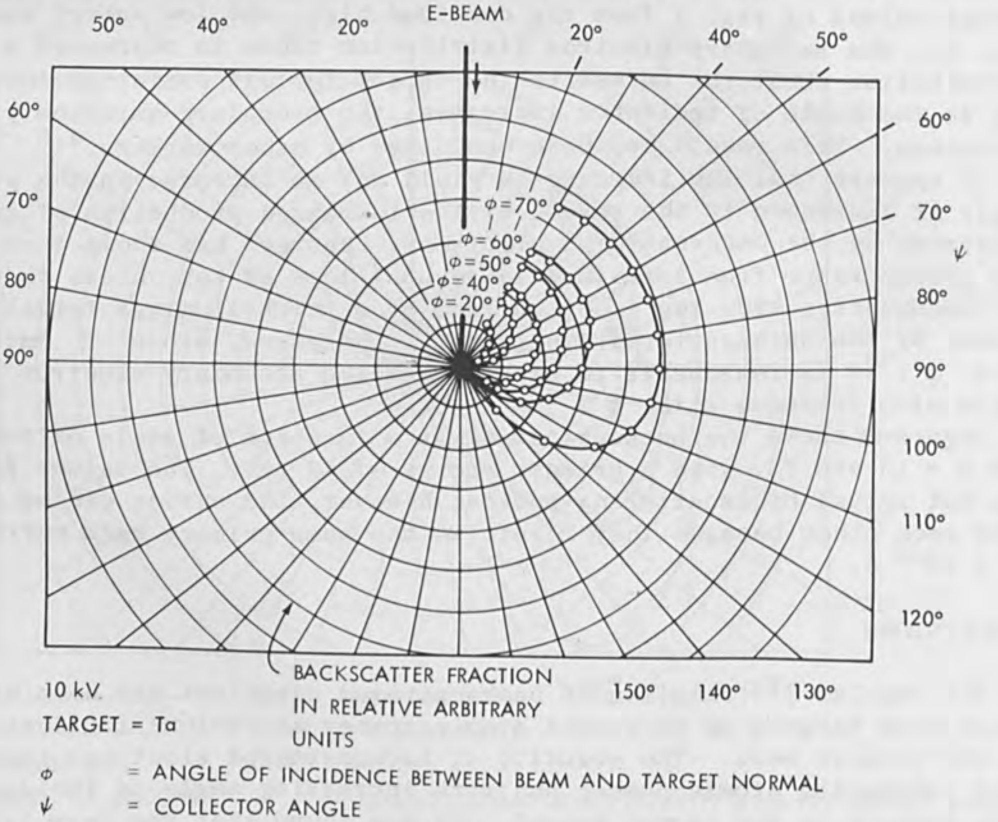

FIG. 8.—Angular distribution of backscattered electrons with energies below 50 eV backscattered from tantalum.

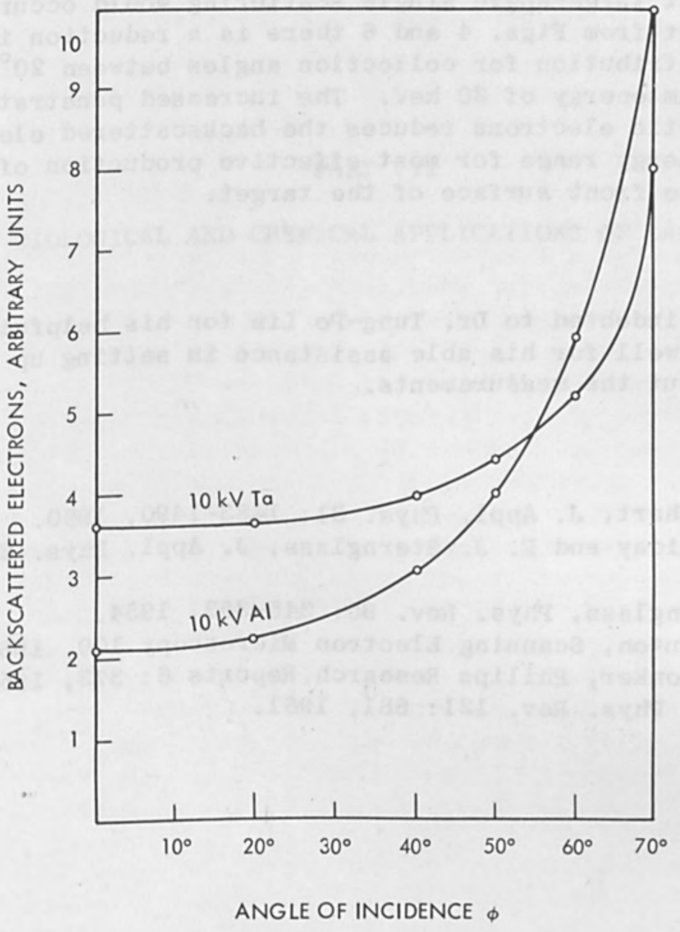

FIG. 9.—Backscattered electrons as a function of angle of incidence for Z = 13 and Z = 73, with a primary energy of 10 keV.

exceeded that of tantalum by approximately 20% (Fig. 9). It appears that this may be due to the decreased stopping power of aluminum and the ease of escape of the electrons from the shallow penetration depth. That is, if D is the penetration depth and φ is the angle of incidence between the beam and target normal, then the distance of escape is D cos φ. Also, there is less chance for multiple scattering and, therefore, it is more probable that large-angle single scattering would occur.

It appears that from Figs. 4 and 6 there is a reduction in the secondary electron contribution for collection angles between 20° and 120° for a primary beam energy of 20 keV. The increased penetration depth of these more energetic electrons reduces the backscattered electrons which would be in an energy range for most effective production of secondary electrons from the front surface of the target.

ACKNOWLEDGMENTS

The author is indebted to Dr. Tung-Po Lin for his helpful discussions and to D. C. Caldwell for his able assistance in setting up the apparatus and in carrying out the measurements.

REFERENCES

1. T. E. Everhart, J. Appl. Phys. 31: 1483-1490, 1960.
2. J. E. Holliday and E. J. Sternglass, J. Appl. Phys. 28: 1189-1193, 1957.
3. E. J. Sternglass, Phys. Rev. 95: 345-353, 1954.
4. P. R. Thornton, Scanning Electron Microscopy 100, 1968.
5. J. L. H. Jonker, Philips Research Reports 6: 372, 1951.
6. H. Kanter, Phys. Rev. 121: 681, 1961.

PART VII

BIOLOGICAL AND CHEMICAL APPLICATIONS OF LASERS

BIOLOGICAL RESEARCH WITH LASERS (Invited Paper)

Charles Süsskind

University of California, Berkeley

The course that biomedical applications of the laser have followed since its invention is so reminiscent of earlier instances of what we should today call bioengineering that it is tempting to seek a characteristic pattern. One need not think farther back than uhf and microwaves to see the sequence: invention, realization that biological interactions are possible, various medical applications (diagnostic, clinical, therapeutical), appreciation of hazards, protective legislation, and study and elucidation of the basic mechanism of interaction. The same pattern may be discerned in other instances, for example X rays and indeed the development of all electrophysiology. The several stages are not always of equal length and often overlap and interact. In the case of microwaves, for example, recent legislation[1] has given a new impetus to the study of basic questions in the U.S.; and lasers are following a similar, though considerably foreshortened, path.

Because of the manifold possibilities offered by a device capable of delivering a highly concentrated and easily controlled dose of thermal energy to tissue--in some cases, deep-seated tissue--it is not surprising that extensive use was made of laser rays before the mechanism by which they interact with biological materials was properly understood. The spectacular successes of laser techniques in ophthalmic surgery were reported in 1967 at the 9th Symposium in Berkeley, the Record of which devoted an entire section to the biological effects of lasers and also contained reports from most of the groups carrying on basic research in the field in America; e.g., on the mechanism of damage from thermochemical changes, on apparently frequency-specific photochemical effects, and on the increase of absorption at specific wavelengths by vital staining.[2] Other photochemical effects that have been studied include rapid absorption changes in photosynthetic organisms under pulsed laser radiation[3] and the susceptibility of various organisms to photosensitization by laser light.[4] From the program of the 1969 Gordon Conferences it is evident that this work is being vigorously carried forward, mainly by the same groups.[5]

The engineer who approaches this particular field hoping to contribute his mite to the advancement of biological knowledge by technological means should be forewarned that he is laboring in a fairly sophisticated vineyard. Even if the principal effect of laser light on tissue should prove to be thermal, it remains to show by what means energy is transferred and propagated, what role is played by vaporization and by acoustical effects, and whether photosynthesis is affected by the physical peculiarities of laser light--all questions requiring extensive familiarity with highly advanced branches of science.

A pilot experiment made in connection with the last question may serve to illustrate what pitfalls await the unwary. The comparison of the efficiency of coherent and incoherent radiation in producing photosynthesis was a virgin field--or almost so: one other preliminary report came to our attention after our measurements were completed.[6] (As in our tests, coherent radiation was reported to be more efficient at the same light intensity.) Moreover, it was tempting to think of interactions

Record of 10th Symposium on Electron, Ion, and Laser Beam Technology (L. Marton, ed.); San Francisco Press, Inc.

Copyright © by The Institute of Electrical and Electronics Engineers, Inc.—Printed in the U.S.A.

between visible light and cellular organisms in terms of electromagnetic resonances, in the manner of microwaves and artificial dielectrics.[7]

The details of our experiments have been reported elsewhere.[8] Briefly, seaweed was irradiated alternately with an He-Ne cw laser at 6328 Å and with filtered light (at almost the same frequency) from a tungsten lamp; the amounts of oxygen evolved in the two cases were compared after compensation for meters, filters, and the action spectrum of the sample over a 1000-Å range straddling the center frequency. The results of the first test showed that 2.75 times more oxygen was evolved by coherent light than by incoherent light. But a second test, made several months later at 10 times the power level and with somewhat different filters, gave a ratio of 32. That was certainly unexpected, if only from the viewpoint of the quantum efficiencies implied by a 32-fold enhancement.

What could be the possible explanation of these large and widely ranging ratios (2.75 to 32)? The other research team[6] had also obtained better efficiencies with lasers than with ordinary light but the ratios ranged only from 1.2 to 2.0--depending on whether the ambient temperature was 25 or 30°C. Here was one possible explanation: we had not monitored the temperature. Other questions presently suggested themselves. The incoherent light had not been polarized: would that produce differences resulting from the structure of the chloroplasts? Did variations in the relative absorbance by the sample chlorophyll over the filter passband account for the ratios differing from unity? Did the coherent light so alter the absorption spectrum as to produce appreciable bleaching around the operating frequency--i.e., "burn a hole" in the spectrum? Did the action of the oxygen electrode depend on light intensity? Did the optical inhomogeneities characteristic of the interaction of laser light with biological samples cause "hot spots" that produced greater local response at the level of individual chloroplasts?[9] (Such hot spots might be eliminated by the use of a diffusing plate that would nevertheless preserve coherence;[10] and conversely, there are methods for processing laser light by which its coherence may be lessened to any desired degree.)

It is thus evident that the question, Does coherent light produce a photosynthetic effect different from that produced by incoherent light? cannot be answered by a quick and simple experiment. Even if all the uncertainties enumerated above are resolved by a greatly elaborated experiment, one would still like to be able to vary the most obvious parameter, frequency, once laser technology is equal to that desideratum. Other elaborations will doubtless arise from further experimentation. The scientific and technological "pay-off" resulting from a thorough understanding of the mechanism of interaction would be high--not only for medicine, but possibly also for agriculture, water pollution, and other applied fields. But it is manifest that he who expects to base such understanding on a crucial experiment involving only one or two parameters, as is often successfully done in the physical sciences, is not likely to be rewarded by useful results.

ACKNOWLEDGMENT

The experimental work reported was carried out with the support of Joint Services Electronics Program under grant AF-AFOSR 139-67 at the Electronics Laboratory of the University of California in Berkeley; a first report appeared in an internal memorandum, Memo ERL-M233, in December 1967.

REFERENCES

1. Public Law 90-602, 18 October 1968.

2. R.F.W. Pease, ed., Record of the IEEE 9th Annual Symposium on Electron, Ion, and Laser Beam Technology, San Francisco: San Francisco Press, 1967. (See esp. articles by C. Hu et al., pp. 371-378; D. E. Rounds et al., pp. 363-370; and R. Storb et al., pp. 391-395.

3. W. W. Hildreth et al., Plant Physiol. 41: 983-991, 1966; Biochem. et Biophys. Acta 153: 197-202, 1968.

4. J. D. Macmillan et al., Photochem. and Photobiol. 5: 555-565 and 567-577, 1966.

5. Science 163: 1085, 1969.

6. E. P. Karlander and R. W. Kraus, Biochem. and Biophys. Acta 153: 312-314, 1968.

7. See, for instance, C. Süsskind, J. Brit. IRE 12: 49-62, 1952.

8. C. Süsskind and I. Garro, Non-Ionizing Radiation 1: 45-46, 1969.

9. D. E. Rounds, Pasadena, Calif., private communication.

10. L. D. Siebert, Proc. IEEE 56: 1242-1243, 1968.

Q-SWITCHED NEODYMIUM LASER EFFECTS ON TISSUE

G. C. RIGGLE

Biomedical Engineering and Instrumentation Branch, DRS

and

R. C. HOYE, J. FARMER*, and A. S. KETCHAM

National Cancer Institute
National Institutes of Health, Bethesda, Md.

INTRODUCTION

Previous reported work indicates that laser radiation can destroy normal and tumor tissue.[1-4] With both the ruby (693.4-nm) and neodymium (1060-nm) wavelengths used in the conventional mode (pulse length of 1 to 3 msec), the mechanism of tissue destruction is caused primarily by thermal energy transfer. Detailed studies of the histology of the high-energy neodymium laser tissue interaction identified a nonuniformity in the pattern of tissue treated by this form of energy. A zone of tissue surrounding the epicenter of the impact site contained cells (normal and tumor) which morphologically and functionally were not completely destroyed.[5]

Reports[6,7] of high-power ruby laser radiation indicated the biological effects in tissue were similar, whether treatment was administered using high energy with low power or high power with low energy.

This study was designed to investigate the effect of high-power neodymium laser radiation on normal and tumor tissue.

MATERIALS AND METHODS

THE LASER. Both the high-energy and the high-power systems used in our studies were developed by the Eastman Kodak Co. (Fig. 1). The high-power module consists of an oscillator-amplifier combination, with Q switching in the oscillator produced by a rotating mirror driven by a 400-Hz motor. Oscillator output ranges from 50 to 75 MW (4 joules) and the amplifier up to 400 MW in a single 40-ns pulse. The amplifier rod output end is Brewster angle-shaped, resulting in an elliptically shaped output beam.

A Fresnel plate was used to divert 8 per cent of the exit energy into a TRG energy monitor. Nitrogen gas purged the reflective chambers and cooled the rods and flash lamps. Output power levels were controlled by time-spacing successive laser discharges.

Studies were made with unfocused and partially focused beams. At 350 MW unfocused, the average power density was 140 MW/cm^2 (5.0 J). Partially focused beams were developed by placing the target surface 120 mm from a 170-mm focal length plano-convex lens. Power density at this surface averaged 450 MW/cm^2 (17.0 J). All energies were delivered in a single spike potential.

---

*Now at Department of Surgery, Duke University, Durham, N. C.

Record of 10th Symposium on Electron, Ion, and Laser Beam Technology (L. Marton, ed.); San Francisco Press, Inc.
Copyright © by The Institute of Electrical and Electronics Engineers, Inc.—Printed in the U.S.A.

NORMAL TISSUE. In the treatment of normal tissue, the intact abdominal skin areas of 3-month-old New Zealand white rabbits were irradiated. The animal was anesthetized and the hair over the anterior abdominal wall shaved. The skin surface was positioned at right angles to the beam of incident laser light. Following treatment of the skin in various areas, the abdominal cavity was opened through a midline incision and intra-abdominal organs inspected for evidence of damage. The suspensory ligaments of the liver were then incised and the anterior surface of this organ positioned at right angles to the beam of incident laser light. Areas of the liver exposed to laser treatment were identified with diagrams and photographs so that at the time of sectioning, 6 days to 10 weeks later, these areas could be adequately evaluated. Following treatment, the abdominal cavity was closed and the animal allowed to recover.

To evaluate the transmission of laser light through the organ being treated, 2 X 2-cm segments of exposed film or pieces of black cardboard were placed either in a subcutaneous pocket under the skin or under the segment of liver being treated. At selected time intervals after irradiation (6 days to 10 weeks), individual animals were killed. Areas of the treated tumor were sectioned and stained with hematoxylin and eosin for later examination under light microscopy.

TUMOR TISSUE. The heavily pigmented mouse tumor, S-91 melanoma in CDF_1 mice, was used. In experiments with high-energy neodymium laser, this tumor-host system was, of the six systems studied, the most sensitive to laser radiation. Freshly excised tumor tissue was mixed with saline in a ratio of 1:10, and 0.01 cc of this suspension (approximately 300 000 viable cells) was injected beneath the skin on the dorsal flank of the mouse. At the time of laser treatment the mouse was anesthetized and the skin (previously shaved) overlying the tumor on the muscles of the dorsal flank was either opened or left intact. The tumor was positioned so that its anterior surface was at right angles to the beam of incident laser light. Following treatment, the mice were individually housed and the growth rate of each tumor recorded by measuring its major and minor diameter every two days.

Four experiments were conducted, each of which used 40 mice, bearing tumors that had been simultaneously injected. At the time of laser treatment, the size of the tumors in each of the experiments was: I - 1-2 mm; II - 3-4 mm; III - 4-5 mm; and IV - 5-6 mm.

In each experiment the mice were randomly divided into 4 groups of 10 each and treated as follows:

(1) Skin opened over tumor at time of laser treatment, then closed.
(2) Skin not opened over tumor at time of laser treatment.
(3) Skin opened and closed only; no laser treatment.
(4) Skin not opened; no laser treatment.

In each experiment, as the animals began to die, the entire group was killed and the presence and size of distant metastases noted.

RESULTS

GROSS EFFECTS. Normal Tissue. A beam of incident laser light, unfocused or partially focused, directed on the nonpigmented abdominal

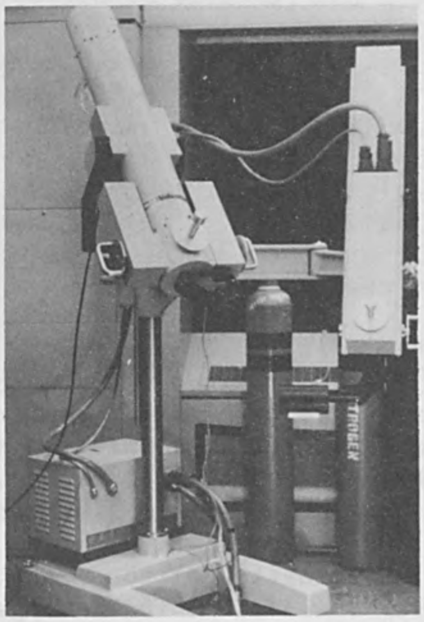

FIG. 1.—Experimental neodymium laser system. High-energy module (1000 J, 2-ms pulse) is mounted on the left arm and the 400-MW, 40-ns high-power unit on the right arm.

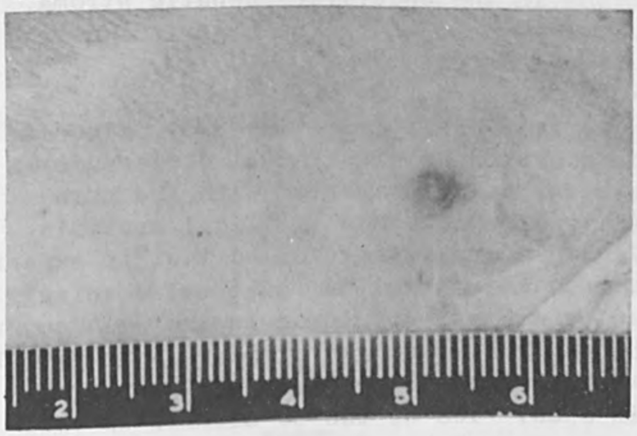

FIG. 2.—Abdominal skin area of rabbit treated with a high-power laser pulse. Beam center was positioned 1.5 mm above the 3-mm scale mark.

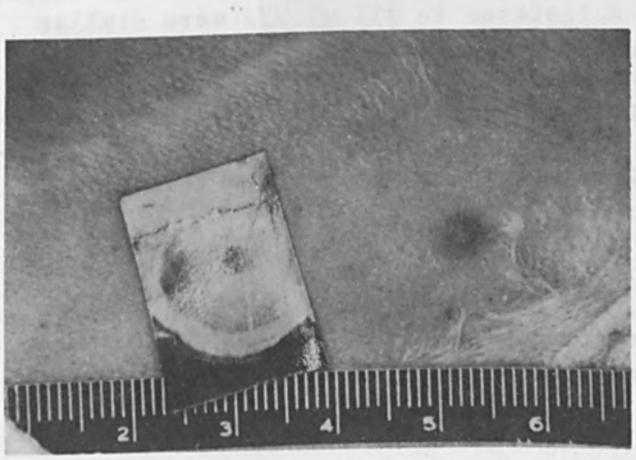

FIG. 3.—Nonabsorption of high-power laser light. Film, placed between the abdominal skin wall and peritoneal sac, is blanched from high-power laser energy transmitted through the wall. Laser beam center was positioned similar to Fig. 2. Film blanching effect is comparable to that produced by direct exposure.

skin of a rabbit, produced no effect (Fig. 2). Previously exposed film, placed under the skin tissue, was blanched from the laser energy transmitted through the skin wall (Fig. 3). Immediately after laser treatment, it was difficult to determine where the laser radiation had been administered. No adverse tissue effects were observed in later examinations.

Unfocused laser energy directed at the surface of rabbit liver was ineffective. With partial focusing, a slight drying and wrinkling of the capsule was apparent. No other effects were noted at the site, either immediately after, or 10 weeks after exposure.

Tumor Tissue. Skin blanching developed on the shaved area of the dorsal flank of mice injected with tumor cell suspensions (Fig. 4). The tumor site was later surgically exposed and examination revealed no tumor tissue disruption. On the exposed S-91 melanoma (Fig. 5), a slight disruption of the tumor substance and a small amount of hemorrhage occurred with both unfocused and partially focused laser light (Fig. 6).

MICROSCOPIC EFFECTS. Examination of the areas of liver treated with high-power neodymium laser revealed minimal changes. No alteration occurred in the architecture of the hepatic cells or change in the staining characteristics of the nucleus or cytoplasm. In the sections of liver treated with partially focused radiation, there was a slight thickening of the capsule without any alteration in the underlying hepatic stroma. A similar alteration in the capsule was noted on the undersurface of the liver when film or cardboard was placed under it.

EFFECT ON TUMOR GROWTH RATE. The growth curves of the S-91 melanoma in the four experiments performed indicated no significant difference in experiments II, III, and IV between the animals treated with the skin either open or intact. These results were combined for final analysis as indicated on Graph B of Fig. 7. This analysis revealed that in experiments II, III, and IV, the growth rate of control and of treated animals was similar. In experiment I, the growth rate of tumor in the high-power neodymium-treated group and in the control group was similar (A in Fig. 7); the only difference represented was a delay in the onset of tumor growth in the group treated with the skin open. Two of the 10 animals in this group had no tumor development.

Autopsy analysis of the presence or absence and location of distant metastases in all groups revealed metastases occurring only in the lungs. The size and number of pulmonary metastases in all groups were similar and no difference was noted between the treated and the control groups.

Exposed film and black cardboard placed beneath tissue and organs being treated were markedly blanched and appeared similar to effects produced with direct exposure. The laser's effect on photographic film suggested that tissue absorbed little energy at the neodymium wavelength.

REFERENCES

1. A. S. Ketcham, R. C. Hoye, and G. C. Riggle, "A surgeon's appraisal of the laser," Surg. Clinics of North America 47: 1249, 1967.

2. G. C. Riggle and R. C. Hoye, "Effects of laser energy on living tissue," IEEE Intl. Conv. Record 15(pt. 9): 94, 1967.

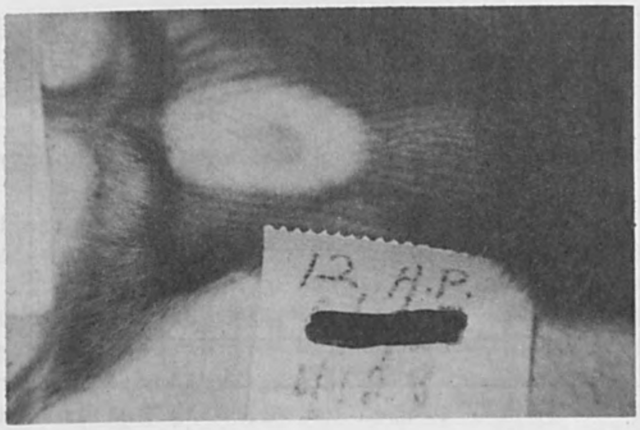

FIG. 4.—Effects of an unfocused pulse on unexposed tumor. An S-91 melanoma implant is outlined in the center of the blanched area. The tumor was later examined after surgical exposure and revealed no tumor disruption.

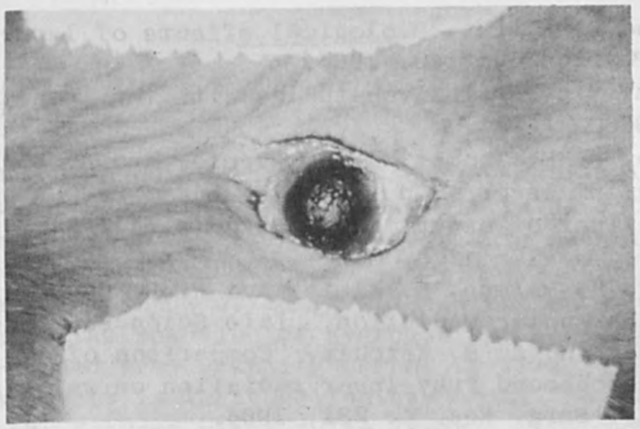

FIG. 5.—Prelaser view of exposed 5-mm tumor. Surgically exposed site with epidermal skin in tension.

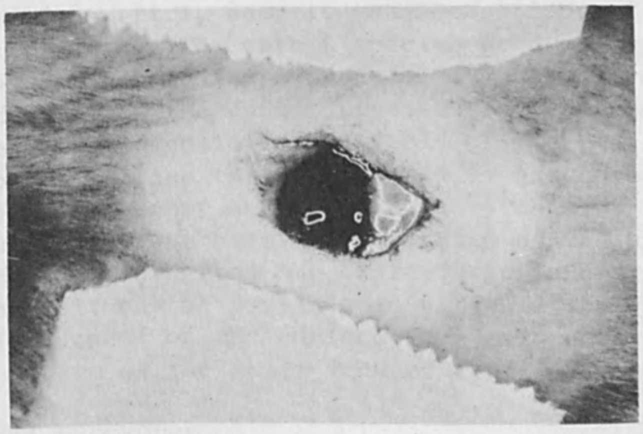

FIG. 6.—Postlaser effect on tumor. Slight hemorrhaging of tumor surface occurred with a minimal disturbance to the tumor mass.

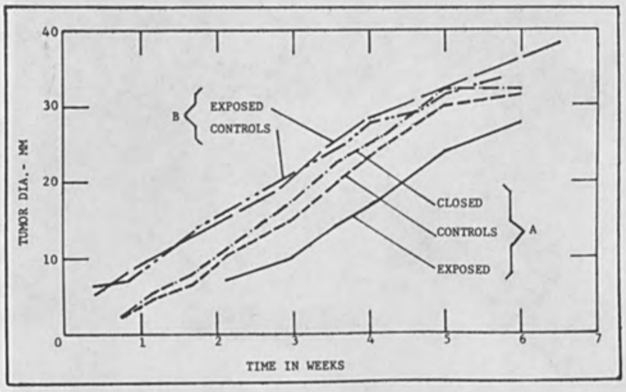

FIG. 7.—Growth rate of tumors exposed to high-power neodymium pulses: (A) record of experiment I (1- to 2-mm tumors); (B) record of experiment IV (5- to 6-mm tumors).

3. S. Fine and E. Klein, "Biological effects of laser radiation," Adv. Biol. Med. Physics 10: 149, 1965.

4. L. Goldman, "Investigative studies with the laser," Southern Med. Jour. 61: 735, 1968.

5. R. C. Hoye, L. B. Thomas, G. C. Riggle, and A. S. Ketcham, "Effects of neodymium laser on normal tissue and Vx2 carcinoma transplanted into the liver of experimental animals," J. Nat. Cancer Inst. 41: 1071, 1968.

6. S. Fine, T. H. Maiman, E. Klein, and R. E. Scott, "Biological effects of high peak power radiation," Life Sciences 3: 209, 1964.

7. J. P. Minton and A. S. Ketcham, "Comparison of the effect of microsecond and nanosecond ruby laser radiation on rat tissues and mouse melanoma," J. Surg. Res. 4: 281, 1964.

LASER-INDUCED CHEMICAL REACTION

SUSUMU NAMBA, PIL HYON KIM, and KO TAKI

Institute of Physical and Chemical Research, Yamato-machi Saitama, Japan

Hydrogen and hydrocarbons (ethylene, methane, ethane, and cyclopropane) reacted with the carbon vapor produced from the carbon target by irradiation of the pulse ruby laser. The main product was acetylene. From the distribution of the reaction products, it is assumed that diatomic carbon contained in the carbon vapor plays a main role in the reaction with hydrogen and hydrocarbons.

By irradiation of the giant pulse laser, the breakdown of hydrocarbons was observed. The main reaction product caused by the breakdown was also acetylene. In the mixture gas of argon at high partial pressure and ethylene or methane, the breakdown of argon gas was observed and the reaction products were obtained. In this case, it may be suggested that the reactions occur by the energy transfer from argon excited by the breakdown to the substrate gas.

1. INTRODUCTION

When the intense laser beam is focused on a suitable target, its surface material is heated and vaporized. It is of interest to study the chemical reaction of an organic or inorganic material with a vapor produced by laser irradiation.

In this paper, two kinds of laser-induced chemical reactions will be described. One is the reaction of hydrogen and hydrocarbons with a carbon vapor produced from graphite carbon by irradiation of the focused ruby laser. The other is the reaction caused by the gas breakdown which is produced by the focused giant pulse laser.

The carbon target was used by the following reason. First, there have been many investigations for the reactions of carbon species which were produced by nuclear recoil reaction,[1] photolysis of carbon suboxide,[2] explosion of silver acetylide,[3] carbon arc,[4] and heating of carbon filament.[5] Therefore, it is easy to make comparison of the laser-induced reaction with the other. The carbon species produced by laser irradiation seems to be similar to those produced by carbon arc or heating of carbon filament, because the carbon species are produced by a thermal process. Second, the composition and yield of the reaction products (low hydrocarbon gases) are easily analyzed by gas chromatography.

Although the carbon vapor has been known to consist of C_1 , C_2 , C_3 .....species by other authors,[5,6] the ratio of the species is different from case to case. From the distribution and the ratio of the reaction products, it may be possible to estimate the ratio of the carbon species which depend on the surface temperature of carbon target and clarify the mechanism of the laser-induced chemical reaction.

II. EXPERIMENTAL PROCEDURE

The target material employed was Shimadzu spectroscopic electrode graphite preheated under vacuum. The ruby laser used was the normal

Record of 10th Symposium on Electron, Ion, and Laser Beam Technology (L. Marton, ed.); San Francisco Press, Inc.

Copyright © by The Institute of Electrical and Electronics Engineers, Inc.—Printed in the U.S.A.

laser whose output energy and pulse duration were 3 joules and 0.5 ms, and the giant pulse laser whose output power and pulse width were 30 MW and 20 ns, respectively.

The laser beam was focused by a lens of 30 mm focal length on the carbon target in a 7-cm^3 Pyrex cell filled with hydrogen or vapor of hydrocarbon, as shown in Fig. 1. After irradiation of 10-20 pulses, the reaction products were analyzed by gas chromatography using a silicagel column. Figure 2 shows an example of recorder trace in an analysis of reaction products formed from hydrogen and carbon vapor. The quantitative analysis was made by using inner standards. The yield of C_3 and C_4 compounds were determined by means of the analyses of propane (C_3H_8) and butane (C_4H_{10}) produced by the catalytic reduction of all products.

Spectroscopic analysis of the carbon vapor was also performed by a grating spectroscope.

III. RESULT AND DISCUSSION

A. REACTION WITH CARBON VAPOR PRODUCED BY NORMAL LASER.[7] The products in the reaction with hydrogen are listed in Table I. The main product is acetylene (C_2H_2) and carbon vapor produced almost reacts with hydrogen. The trace of methane, C_3, and C_4 compounds are detected, but ethylene (C_2H_4) is not detected. As far as the main product is concerned, the result is similar to that in the reaction of a graphite filament with hydrogen at about 3200°K. In our experiment, the temperature at the surface of carbon target irradiated by normal laser was estimated at 3000-4000°K.[8]

TABLE I.—Yield of products in the reaction with hydrogen (normal laser irradiation).

Products	Yield ($\times 10^{-6}$ moles)
Methane	0.3-0.4
Acetylene	15.0-20.0
Ethylene	0
C_3-compounds	0.1
C_4-compounds	1.0
C_3/C_4	0.1

Hydrogen: 700 Torr.
Carbon consumed: $3.0 - 4.0 \times 10^{-5}$ moles.
Laser: 10 pulses.

In the reaction of hydrogen with the carbon atom produced by recoil reaction, CH, CH_2, and CH_3 radicals are produced and undergo further reaction to produce acetylene, ethylene, and others. But ethylene was not detected in our case. Since it was suggested that addition of methyne (CH)[9] to an ethylene molecule gives pentene-1 (C_5H_{10}), the carbon target was irradiated in the mixture of hydrogen and ethylene (8:1). But pentene-1 was not detected. From above results, acetylene precursor might be mainly C_2 in our case. Though methane may be the reaction

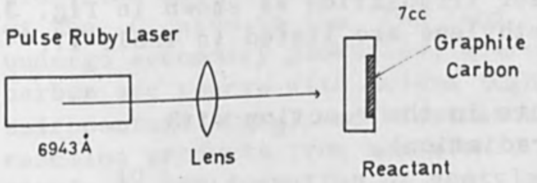
Pulse Ruby Laser
6943 Å
Lens
7cc
Graphite
Carbon
Reactant

FIG. 1.—Experimental block diagram.

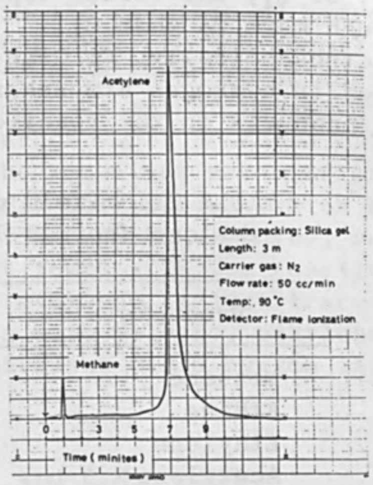

FIG. 2.—Recorder trace in analysis of reaction products formed from hydrogen and carbon vapor.

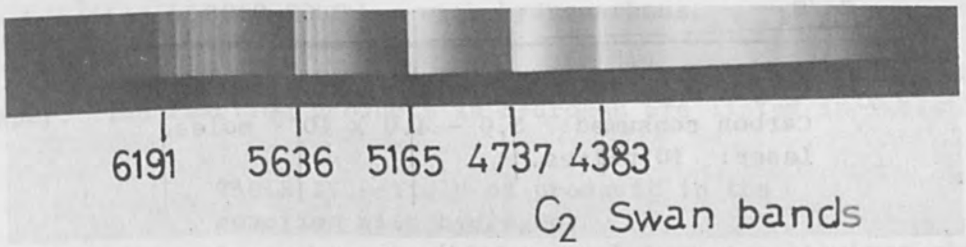
6191
5636
5165
4737
4383
C2 Swan bands

FIG. 3.—Emission spectrum of carbon vapor in hydrogen atmosphere.

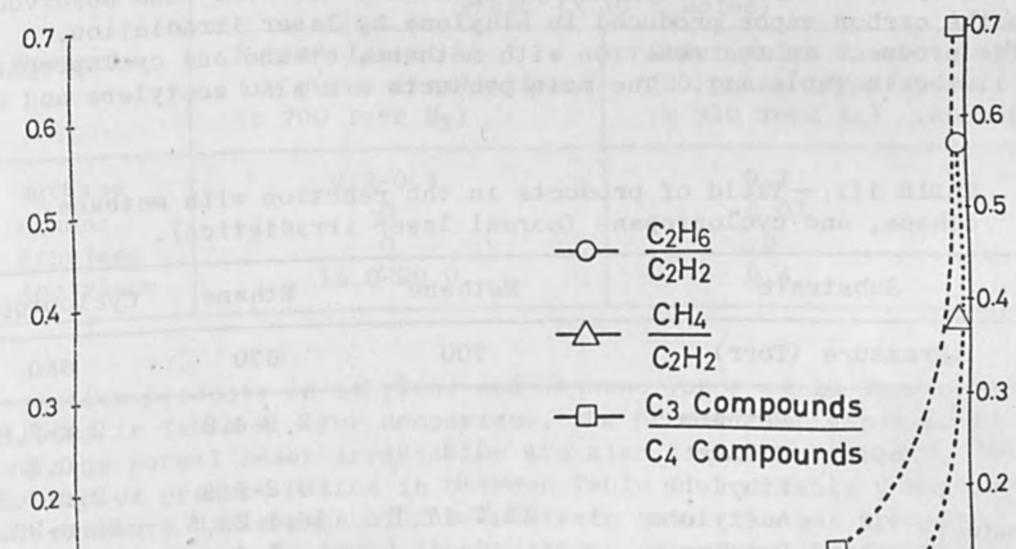

FIG. 4.—Relation between product ratios and ethylene mol fraction in the mixture of ethylene and argon.

product of C_1, the carbon vapor produced by laser irradiation will contain much more C_2 than C_1.

Spectroscopically, C_2 Swan bands were observed from the carbon vapor produced in hydrogen atmosphere by laser irradiation as shown in Fig. 3.

The products in the reaction with ethylene are listed in Table II.

TABLE II.—Yield of products in the reaction with ethylene (normal laser irradiation).

Products	Yield ($\times 10^{-6}$ moles)
Methane	0.15-0.22
Ethane	0.06-0.08
Ethylene	-
Acetylene	24.0-26.0
Vinylacetylene	0.5
Diacetylene	3.5-4.0
C_3-compounds	0.12-0.15
C_4-compounds	4.0-4.5
C_3/C_4	0.03-0.05

Ethylene: 700 Torr.
Carbon consumed: 3.0 - 4.0 $\times 10^{-5}$ moles.
Laser: 10 pulses.

The main products are acetylene and C_4 compounds such as diacetylene and vinylacetylene. Spectroscopically, C_2 Swan bands were also observed from the carbon vapor produced in ethylene by laser irradiation.

The products in the reaction with methane, ethane and cyclopropane are listed in Table III. The main products are also acetylene and C_4 compounds.

TABLE III.—Yield of products in the reaction with methane, ethane, and cyclopropane (normal laser irradiation).

Substrate		Methane	Ethane	Cyclopropane
Pressure (Torr)		700	670	680
Products ($\times 10^{-6}$ moles)	Methane	-	2.9-4.2	2.6-2.8
	Ethane	1.1	-	0.1
	Ethylene	0	4.2-6.6	2.0-2.3
	Acetylene	12.7-17.1	16.1-23.5	22.6-23.2
	Propane	-	1.4	-
	Propylene	0.31-0.41	-	14.5-16.6
	C_3-compounds	0.5-0.7	1.4-2.7	-
	C_4-compounds	1.8-3.9	3.6-4.0	8.8-10.0
	C_3/C_4	0.1-0.4	0.4-0.7	-

Carbon consumed: 3.0 - 4.0 $\times 10^{-5}$ moles.
Laser: 10 pulses.

The reaction products and ratio of products are different from those in the recoil reaction of hydrocarbons or in the reaction of hydrocarbons with carbon vapor produced by the carbon arc. In the recoil reaction, the most common primary processes have been shown to be addition of the C atom to the C-H and C=C bonds; the resulting adducts undergo secondary processes; whereas the carbon vapor produced by the carbon arc reacts with butens (C_4H_8) and the resulting products are spiropentane (C_5H_8) and bisethanoallen (C_7H_8) derivatives, which are reaction products from monoatomic and triatomic carbon species, respectively,[10] but formation of acetylene is not found. In the reaction with methane, the main product is acetylene but ethylene is just trace as listed in Table III. If carbon atom reacts with methane, ethylene and acetylene are to be produced almost in equivalent yield by the insertion mechanism:[11]

$$C + CH_4 \rightarrow (CH_3 - \overset{\cdot}{\underset{\cdot}{C}} - H) \rightarrow C_2H_2 \text{ and } C_2H_4$$

In our case, from the fact that the product distribution consists of C_2 and C_4 compounds, it seems likely that the reaction may occur in the combination of C_2 species with hydrocarbons.

B. REACTION INDUCED BY GIANT PULSE LASER.[12] (1) Reaction with Carbon Vapor. The reaction products in hydrogen are listed in Table IV.

TABLE IV.—Yield of products in the reaction with hydrogen.

Products	Yield ($\times 10^{-6}$ moles)	
	Normal laser (10 pulse irradiation in 700 Torr H_2)	Giant pulse laser (20 pulse irradiation in 720 Torr H_2)
Methane	0.3-0.4	0.1
Ethane	0	0.01
Ethylene	0	0
Acetylene	15.0-20.0	0.4

The reaction products in ethylene and methane vapor at 10 Torr pressure are listed in Table V. For comparison, the products obtained at 10 Torr pressure by normal laser irradiation are also listed in Table V. The difference of product ratios in between Table II and Table V may be due to the pressure difference of the substrate gas. The gas pressure (10 Torr) was chosen to avoid the breakdown caused by the focused giant pulse laser. At higher pressure (more than 100 Torr) the breakdown was observed as mentioned later.

Although the ratios of methane and ethane to acetylene are higher than in the case of the normal laser, the main products are C2 compounds. It seems that the carbon species produced by the giant pulse laser is different from that produced by the normal laser, and the fraction of

TABLE V.—Yield of products in the reaction with ethylene and methane vapor at 10 Torr pressure.

Substrates	Products	Yield (X 10^{-6} moles)	
		Normal laser (10 pulse irradiation)	Giant pulse laser (12 pulse irradiation)
Ethylene	Methane	0.007	0.014
	Ethane	trace	0.009
	Acetylene	1.6	0.47
	C_3-compounds	trace	0.018
	C_4-compounds	0.48	0.19
Methane	Ethane	0.022	0.084
	Acetylene	1.52	0.32
	C_3-compounds	0.02	0.024
	C_4-compounds	0.5	0.19

monoatomic carbon (C_1) increases. The result may be due to the difference of the surface temperature of the carbon target. The estimated temperature[13] in the giant pulse laser is much higher than in normal laser.

(2) Reaction Caused by Breakdown. The breakdown[14] of gas by the focused giant pulse laser is well known. The yields of products in the breakdown of various substrates at 720 Torr pressure are listed in Table VI. In this case, the carbon target was not used. The main product is also acetylene, and spectroscopically C_2 Swan bands were observed as observed by Adelman[15] in the breakdown of organic vapors. At high pressure of the substrate (for example at 720 Torr), the reaction products and their ratios in the reaction with the carbon target

TABLE VI.—Product yields in the breakdown of various substrates at 720 Torr pressure.

	Yield (X 10^{-6} moles) in 10 pulse irradiation			
Substrates Products	Methane	Ethane	Ethylene	Cyclopropane
Methane		0.5-0.7	0.05-0.08	0.4-0.5
Ethane	0.1-0.2		0.2-0.3	0.02
Ethylene	0	0.3-0.5		0
Acetylene	0.5-0.7	1.1-1.4	1.7-2.7	0.8-1.2
C_3-compounds	0.1	0.3	0.03	
C_4-compounds	0.1	0.2	0.4-0.5	0
Propane				0.1
Propylene				1.5-2.0

were almost the same as that in the breakdown without the carbon target. When the laser beam was focused on the carbon target, the breakdown of gases was also observed in the focal region. These facts suggest that the products are formed mainly by the reaction of substrate with C_2 produced in the breakdown, even if the carbon target is used.

The breakdown was not observed at 10 Torr in ethylene or methane, because it is hard to produce a breakdown at the lower pressure. But in the mixture of 10 Torr ethylene and 750 Torr argon, the breakdown was observed, and argon lines were detected spectroscopically. The product ratios of C_3 compounds to C_4 compounds and CH_4/C_2H_2, C_2H_6/C_2H_2 are plotted as a function of the partial pressure of ethylene in the mixture as shown in Fig. 4. The interaction of argon (I.P. = 15.7 eV) with ethylene (I.P. = 10.5 eV) is not found until at the pressure of 100 Torr ethylene and 660 Torr argon (ethylene mol fraction is 0.15) because the ratios of CH_4/C_2H_2 and C_2H_6/C_2H_2 are constant. The drastic change of the ratios in the mixture of 10 Torr ethylene and 750 Torr argon (mol fraction is 0.013) may show some interaction of ethylene with argon. It may be considered to be the energy transfer from argon to ethylene. In the case of the γ-radiolysis of 10^{19} eV dose at room temperature in the mixture of 10 Torr ethylene and 750 Torr argon, the product ratios are different from that in laser irradiation, as shown in Table VII. For reference, Lampe's result[16] is also listed. This difference might be considered to depend on the excited energy state of ethylene.

TABLE VII.—Relative yield in the γ-radiolysis and in the laser irradiation in the mixture of ethylene and argon.

	Relative G value in γ-radiolysis			Relative yield in laser irradiation
Ethylene mol fraction in Ar	1.0*	0.7*	0.013	0.013
Products				
Methane			0.13	0.38
Ethane	0.26	0.18	0.16	0.57
Acetylene	1.00	1.00	1.00	1.00
n-butane	0.33	0.26	0.18	0.35
C_3-compounds			0.17	0.27

* From Ref. (16).

The methane and argon system also showed an almost similar result to the ethylene and argon system, and the condensable product was only ethane at the pressure of 10 Torr methane and 750 Torr argon. In the presence of nitric oxide (4 Torr) as radical scavenger, the breakdown of the mixture of methane (12 Torr) and argon (744 Torr) did not give ethane. This suggests that the reaction involves the following free radical processes:

$$Ar^* + CH_4 \rightarrow CH_4^* \rightarrow \cdot CH_3 + H$$

$$2 \cdot CH_3 \rightarrow C_2H_6$$

The fact may be the evidence for the energy transfer from argon to methane. In the radiolysis of methane[17] and methane-argon mixture,[18] the main products are hydrogen and ethane, but acetylene is not formed. The result is similar to that in laser induced reaction.

From the above results, it may be concluded that the focused giant pulse laser also produces mainly diatomic carbon (C_2) in the breakdown of organic vapors and C_2 is considered to play the dominant role in the reaction.

REFERENCES

1. M. Marshall, G. MacKay and R. Wolfgang, J. Am. Chem. Soc. 86: 4741, 1964; H. J. Ache and A. P. Wolf, ibid. 88: 888, 1966.
2. K. D. Bayes, ibid. 84: 4077, 1962.
3. K. Taki, to be published in Bull. Chem. Soc. Japan.
4. P. S. Skell and R. R. Engel, J. Am. Chem. Soc. 88: 4883, 1966.
5. J. T. Clarke and B. R. Fox, J. Chem. Phys. 46: 827, 1967.
6. H. A. Chupka and M. G. Inghram, J. Phys. Chem. 59: 100, 1955; J. Drowart, R. P. Burns, G. DeMaria, and M. G. Inghram, J. Chem. Phys. 31: 1131, 1959; J. Berkowitz and W. A. Chupka, ibid. 40: 2735, 1964; J. E. Mentall and R. W. Nicholls, ibid. 46: 2881, 1967.
7. K. Taki, P. H. Kim, and S. Namba, Bull. Chem. Soc. Japan 42: 823, 1969.
8. S. Namba, P. H. Kim, S. Nakayama, and I. Ida, Japan. J. Appl. Phys. 4: 153, 1965.
9. J. Nicholas, G. MacKay, and R. Wolfgang, J. Am. Chem. Soc. 88: 1065, 1966.
10. P. S. Skell, L. D. Wescott, jr., J. P. Golstein, and R. R. Engel, ibid. 85: 1023, 1963.
11. C. MacKay and R. Wolfgang, ibid. 83: 2399, 1961; G. Stöcklin and A. P. Wolf, ibid. 85: 229, 1963.
12. K. Taki, P. H. Kim, and S. Namba: to be published in Bull. Chem. Soc. Japan.
13. S. Namba, P. H. Kim and A. Mitsuyama, J. Appl. Phys. 37: 3330, 1966; S. Namba, P. H. Kim, T. Itoh, T. Arai, and H. Schwarz, Record 9th IEEE Symposium on Electron, Ion, and Laser Beam Technology, Berkeley, May 1967, p. 86.
14. R. G. Meyer and A. F. Haught, Phys. Rev. Letters 11: 401, 1963; R. W. Minck, J. Appl. Phys. 35: 252, 1964.
15. A. H. Adelman, J. Chem. Phys. 45: 3152, 1966.
16. F. W. Lampe, Rad. Research 10: 691, 1959.
17. F. W. Lampe, J. Phys. Chem. 79: 1055, 1957; K. Yang and D. J. Manno, ibid. 63: 752, 1959.
18. G. G. Meisels, W. H. Hamill, and R. R. Williams jr., J. Am. Chem. Soc. 61: 1456, 1957.

LASER DETECTION OF VISIBLE AIR POLLUTION

J. J. WILHELMI* and A. P. SZEWS

Marquette University College of Engineering, Milwaukee, Wis.

There are many facets to the problem of air pollution. This paper considers only one aspect of the air pollution problem--the detection and measurement of visible air pollution such as smoke, dust, and other particulate wastes emitted by a chimney.

When asked the question about what life would be like in our country 50 years from now, the Director of the Institute for Atmospheric Research (and men from similar institutions) declared that many of our major urban areas will be uninhabitable in less than 50 years because of air pollution.[1]

Laws will be enacted to limit air pollution, but these laws cannot come into being if there is no accurate way to measure air pollution.

The purpose of this paper is to show that:

(a) the present method for measuring visible air pollution is archaic and inconsistent;
(b) uniform standards of pollution measurement based on the old method can be utilized;
(c) constant monitoring of emission is possible; and
(d) monitoring of emission can result in lower plant operating costs.

There is only one statutory standard for the measurement of visible emission--the Ringlemann smoke chart. One type of Ringlemann smoke chart is shown in Fig. 1. This is a reproduction of the Ringlemann type smoke chart used by the Milwaukee County Air pollution Control Agency. The chart contains five shaded areas which are grids obscuring 20, 40, 60, 80, and 100 per cent of the white card.

To determine the Ringlemann number, the shaded areas on the white card are compared with the smoke at the chimney top against a sky background (as seen through the hole in the center of the card). Ringlemann 2, the permitted maximum emission shade in Milwaukee County (and many other communities), is a shade that obscures 40% of the white card. Since the ratio of the brightness of the sky compared to a white card can vary from 5:1 to 0.6:1 in normal weather conditions,[2] the same smoke appears to compare with different Ringlemann numbers under different conditions.

The Ringlemann method for measuring visible air pollution, in its present form, leaves much room for improvement. Feasibility studies done at Marquette University indicate that a laser can be used to detect and measure visible air pollution with significant advantages over the present method.

To conduct these studies, a 4-in. square column was fabricated from clear acrylic plastic. This column was made 4 ft long in order to eliminate

---

*Currently with Collins Radio Company, Newport Beach, Calif.

Record of 10th Symposium on Electron, Ion, and Laser Beam Technology (L. Marton, ed.); San Francisco Press, Inc.

Copyright © by The Institute of Electrical and Electronics Engineers, Inc.—Printed in the U.S.A.

PLIBRICO SMOKE CHART

RINGELMANN TYPE

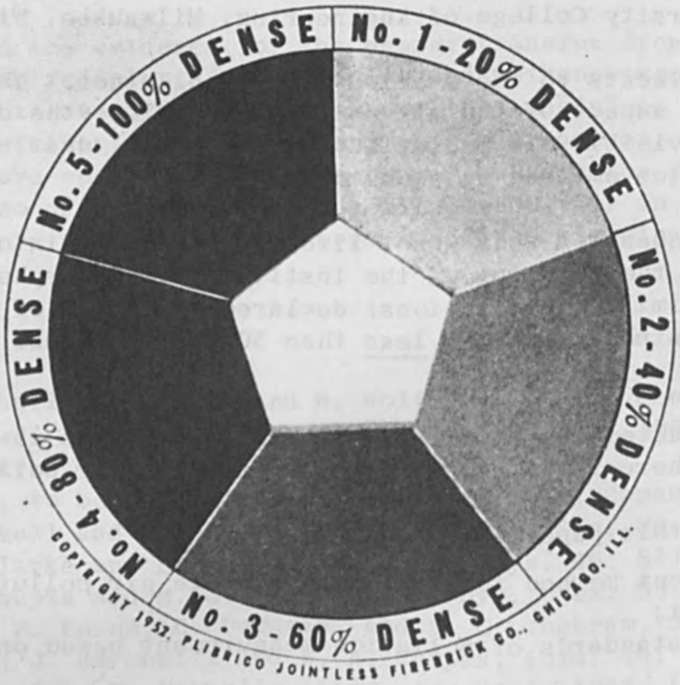
No. 1-20% DENSE
No. 2-40% DENSE
No. 3-60% DENSE
No. 4-80% DENSE
No. 5-100% DENSE
COPYRIGHT 1952, PLIBRICO JOINTLESS FIREBRICK CO., CHICAGO, ILL.

INSTRUCTIONS

This miniature Ringelmann smoke scale will enable the observer to conveniently grade the density of smoke issuing from the stack.

The scale should be held at arm's length at which distance the dots in the scale will blend into uniform shades.

Then compare the smoke (as seen through the hole) with the chart, determining the shade in the chart most nearly corresponding to the shade or density of the smoke. Experienced observers often record in half chart numbers. By recording the changes in smoke density, the average "percentage of smoke density" for any period of time can be determined.

Observer's line of observation should be at right angles to the direction of smoke travel.

Observer should not be less than 100 ft. nor more than 1/4 mile from the stack.

Observer should avoid looking towards bright sunlight. The background immediately beyond the top of the stack should be free of buildings or other dark objects.

Copr. 1946, Plibrico Jointless Firebrick Co.

FIG. 1

any turbulence at the inlet and outlet from affecting the smooth flow of smoke at the point of measurement. An exhaust fan was mounted at the top of the column and a chamber for commercial smoke bombs was provided at the bottom. An 80-mW H-N gas laser (provided through a National Science Foundation grant) and an optical power meter tuned to the laser frequency of 6328 Å were placed on opposite sides of the column at the half way point. The recorder output of the power meter was connected to an oscilloscope. This oscilloscope was equipped with a camera to record the variations in the transmitted power of the laser during the time smoke was present in the column. The equipment used in this feasibility study is shown in Fig. 2.

A smoke test was made with a 30-sec smoke bomb. The oscillogram in Fig. 3 shows laser power detected versus time. The smoke bomb was lit and placed in the chamber and the door was closed. As the smoke bomb burned, the density of the smoke drawn through the column increased, and the laser power detected by the optical power meter decreased reaching zero power when the density of the smoke in the column was greatest. This is shown in the first trace starting at the upper left in Fig. 3. As the smoke bomb burned out, the density of the smoke in the column decreased and the optical power detected gradually increased. This is shown in the second trace starting at the lower left in Fig. 3. The horizontal time scale in this oscillogram is 5 sec/cm; the vertical scaling is equivalent to 8.3 mW/cm. The first smoke test lasted approximately 90 sec.

Another smoke bomb was ignited and placed in the chamber at the base of the column--only the chamber door was left open. The oscillogram of the laser power detected versus time is shown in Fig. 4. (The short horizontal line at the upper right is the start of the second trace.) Inspection of Fig. 4 indicates that this system is sensitive to rapid changes in the smoke density. These variations in smoke density were caused by air turbulence at the base of the column due to the open chamber door and nonuniform emission of smoke from the smoke bomb. It can also be observed that with the smoke chamber door open and the mixing of smoke and air, even at maximum smoke density in the column, the laser power detected is greater than zero--about 9 to 10 mW. Also, the period of maximum smoke density is shortened because there is no buildup of smoke in the chamber as there was in the first smoke test.

The advantages of a laser measurement and detection system are three:

1. Uniform standards of pollution based on the spirit of the Ringlemann number can be utilized. A chart of Ringlemann numbers and the corresponding percent obscuration for a fixed optical path length is shown in Fig. 5.[3] This chart shows the correlation between Ringlemann numbers and the percent obscuration caused by the smoke emitted from the chimney. This chart is based on the assumption that the average sky brightness is 1.7 times the brightness of a white card.[4] If the measurement is taken across the outlet diameter of a chimney, Ringlemann 1 corresponds to 52% obscuration, Ringlemann 2 to 64%, Ringlemann 3 to 76%, and Ringlemann 4 to 88%.
2. Constant monitoring is possible. A chart recorder can monitor chimney emission around the clock and make a permanent record of emission detected. This can be an asset to the local air pollution control agencies whose detection methods are nonexistent after sundown.

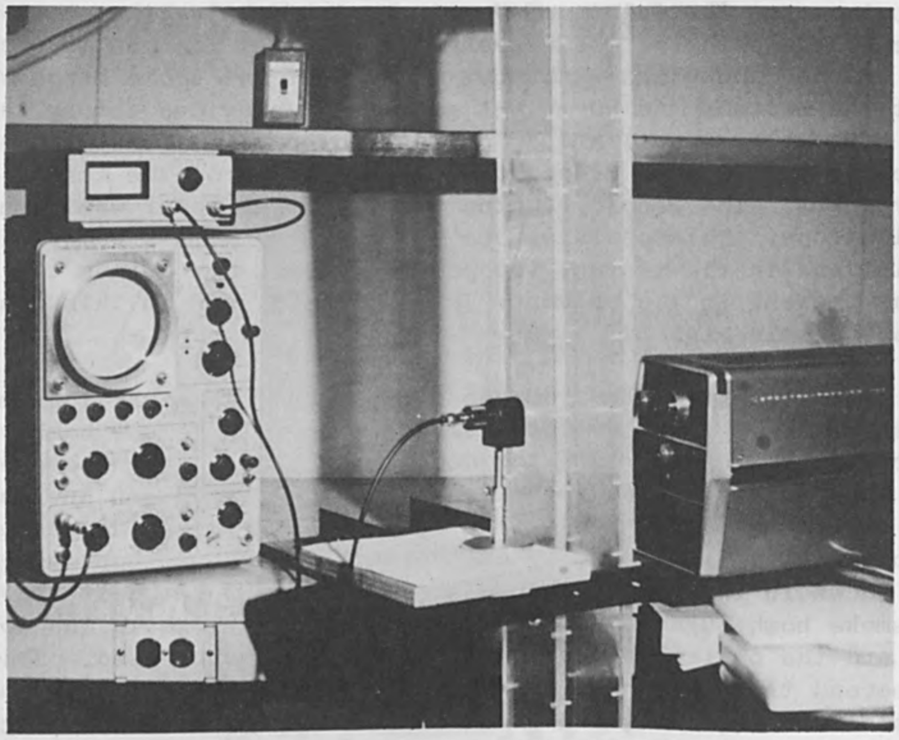

FIG. 2.—The laser, smoke column, optical power detector, and oscilloscope used in this study.

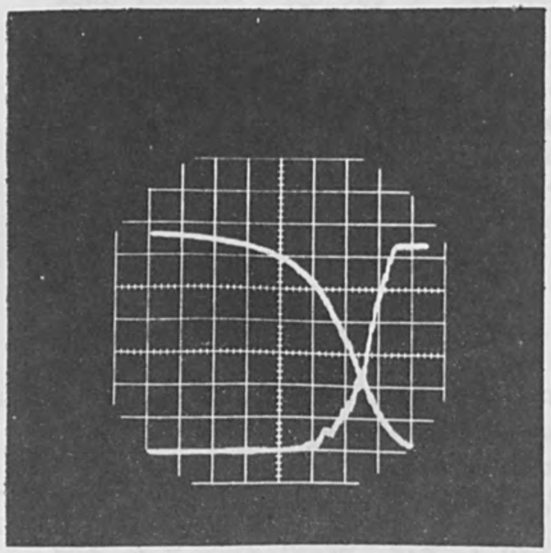

FIG. 3.—Laser power detected vs time (closed chamber).

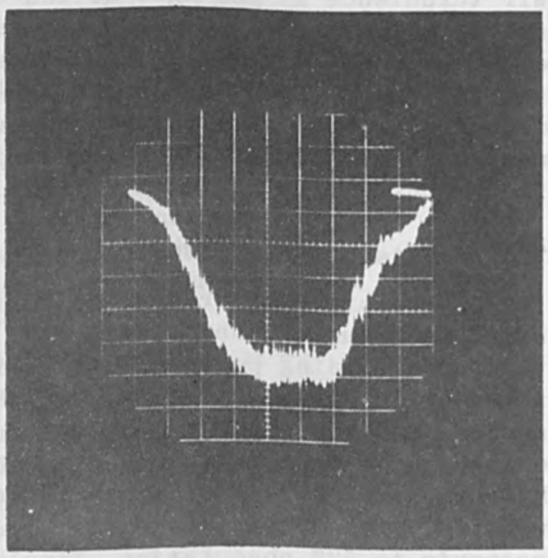

FIG. 4.—Laser power detected vs time (open chamber).

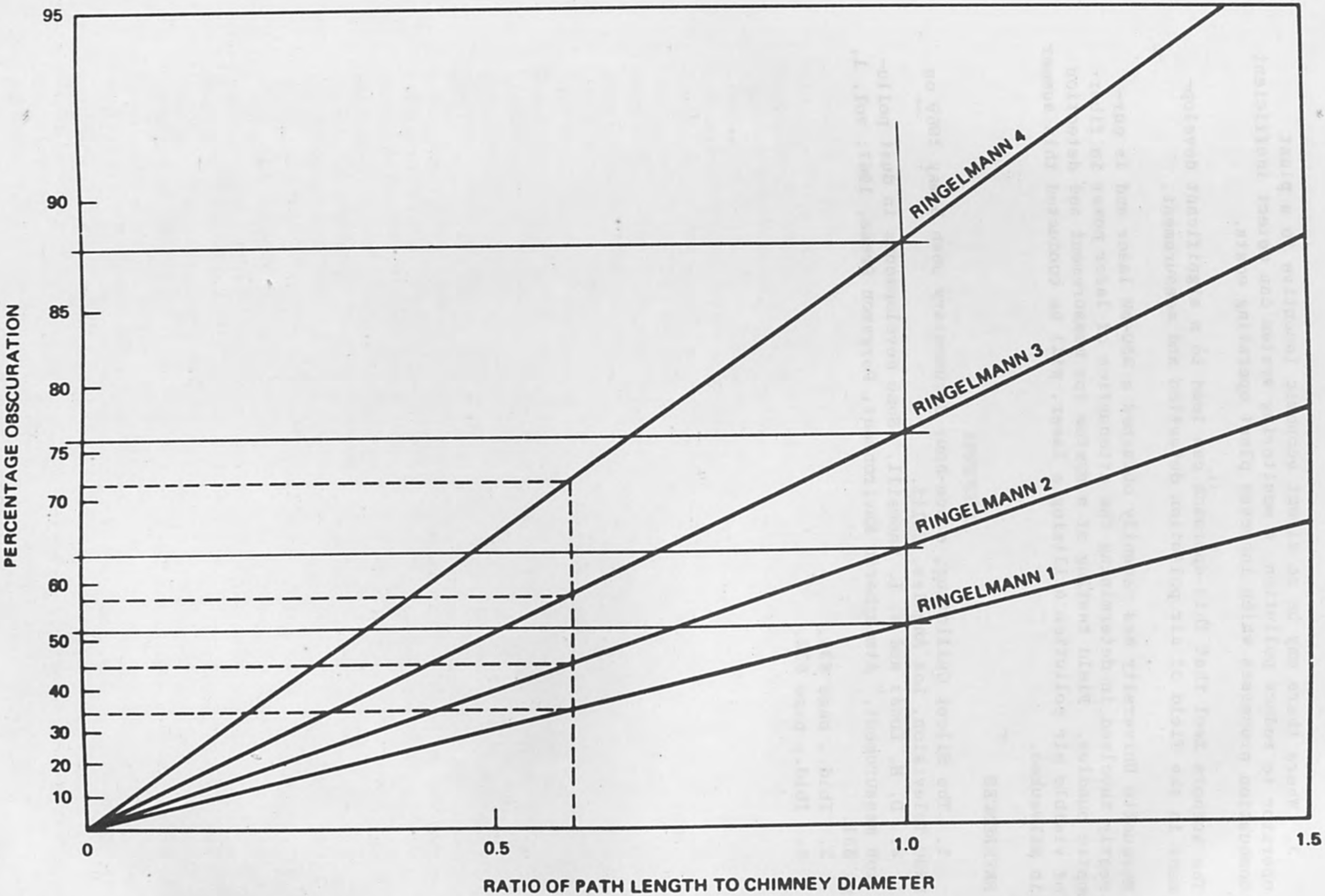

FIG. 5.—Calibration of optical-density measuring instruments in Ringelman numbers for differing optical path lengths.

3. Where there may be no direct economic incentive to a plant operator to reduce pollution, a monitoring system can detect inefficient combustion processes which increase plant operating costs.

The authors feel that this approach can lead to a significant development in the field of air pollution detection and measurement.

Marquette University has recently obtained a 250-mW laser and is currently involved in determining the attenuation of laser power in fiber optic bundles. Field testing of a system for measurement and detection of visible air pollution utilizing a laser, will be conducted this summer in Milwaukee.

REFERENCES

1. The Silent Guillotine, a one-hour documentary seen 8 May 1969 on KNBC Television, Los Angeles, Calif.
2. D. H. Lucas and W. L. Snowsill, "Some developments in dust pollution measurement," Atmospheric Environment, Pergamon Press, 1967; vol. 1, p. 631.
3. Ibid., page 633.
4. Ibid., page 632.

APPENDIX

3. Where there may be no direct economic incentive to a plant operator to reduce pollution, a monitoring system can detect inefficient combustion processes which increase plant operating costs.

The authors feel that this approach can lead to a significant development in the field of air pollution detection and measurement.

Marquette University has recently obtained a 220-mW laser and is currently involved in determining the attenuation of laser power in fiber optic bundles. Field testing of a system for measurement and detection of visible air pollution utilizing a laser, will be conducted this summer in Milwaukee.

REFERENCES

1. The Silent Guillotine, a one-hour documentary seen 8 May 1969 on KNBC Television, Los Angeles, Calif.
2. D. H. Lucas and W. L. Snowsill, "Some developments in dust pollution measurement," Atmospheric Environment, Pergamon Press, 1967; vol. 1, p. 631.
3. Ibid., page 633.
4. Ibid., page 634.

BIBLIOGRAPHY ON THE SCANNING ELECTRON MICROSCOPE

Oliver C. Wells

IBM Watson Research Center, Yorktown Heights, N.Y. 10598.

ABSTRACT: Approximately 450 literature references to the scanning electron microscope are cited in this bibliography. Instrumental aspects and applications are both covered. Applications include both biological and non-biological work. References are indexed by subject matter. Co-authors are cross-indexed.

INTRODUCTION AND ACKNOWLEDGMENTS

This bibliography contains references of interest to users of the scanning electron microscope (SEM). Theory, applications and instrumental aspects are covered. High brightness electron guns and non-thermal irradiation effects in silicon dioxide have been selectively included. X-ray analysis and thermal effects were excluded. Conference Proceedings were listed in full up to 1967; and selectively thereafter. Citations are listed alphabetically by the lead author, and conference proceedings are listed by the editor. References having more than 4 authors are listed as Author, Coauthor, Coauthor and xx others (year). Numbers in square brackets [xx] refer to the position of the reference in the main list.

Biological and non-biological references are included in the same reference list. This was done to avoid subdividing the work of authors who have published in both fields. Biological citations are indicated by the letter B beside the reference. These are catalogued in the subject index under "Biological, (subdivision)".

An earlier version of this bibliography was published as pp. 412-438 in Pease [318]. It was assembled with the help of authors who sent reprints of their work; and I shall be very grateful for new information to be included in later versions. If readers send reprints then it would help greatly if they could also suggest the correct classification for each of them in the subject index; and also prepare microabstracts of the type that are included after some references in this list. Microabstracts refer to papers published in conference proceedings that otherwise would not be cited; errors; forward references; special cross-references; and points of special interest. Notification of errors will be greatly appreciated. I am grateful to G.R. Booker, A.N. Broers, Miss E.E. Brown, Miss I. Corvin, T.E. Everhart, T.L. Hayes, J. Heslop-Harrison, O. Johari, D. Kynaston, I. Minkoff, C. Munakata, W.C. Nixon, R.F.W. Pease, G. Pfefferkorn, P. Pinard, A. Rezanovich, F. Rossi, P.A. Sandberg, R.F.M. Thornley, P.R. Thornton and several others, all of whom either supplied references or sent reprints of their work.

These pages were processed using the TEXT360 text-handling system. The input file for TEXT360 was prepared by a bibliographic program which inserted new references at the correct alphabetic point in the existing list, renumbered the updated list, cross-referenced the coauthors and updated the reference numbers in the subject index. The final pages were photocomposed by Alphanumeric Inc. from a modified TEXT360 print tape. I am grateful for advice from colleagues at IBM concerning these programs.

LIST OF CONFERENCES

A list of conferences by location and year is given below following the list of sponsoring organizations:

A Alloyd Electronics Corp.
B All-Union Conferences on Electron Microscopy (USSR).
C British Paper and Board Makers' Association.

Record of 10th Symposium on Electron, Ion, and Laser Beam Technology (L. Marton, ed.); San Francisco Press, Inc.

Copyright © by The Institute of Electrical and Electronics Engineers, Inc.—Printed in the U.S.A.

D Electrochemical Society.
E Electron Microscope Society of America.
F Engis Equipment Co.
G German Society for Electron Microscopy.
H IIT Research Institute.
I International Association of Research Institutes for the Graphic Arts Industry.
J International Federation of Electron Microscope Societies (International Conferences).
K International Federation of Electron Microscope Societies (Regional Conferences).
L Institute of Electrical and Electronics Engineers.
M Institute of Physics.
N Institution of Electrical Engineers.
O The Physical Society of Japan.
P RCA Laboratories.
Q University of Denver.

1956 M Leeds: Challice [78].
1956 K Stockholm: Sjostrand [366].
1957 et seq., Q Denver: Mueller [273].
1958 J Berlin: Bargmann [18].
1960 K Delft: Houwink [205].
1961 A Boston: Bakish [13].
1961 C Oxford: Bolam [33].
1962 J Philadelphia: Breese [58].
1964 K Prague: Titlebach [418].
1964 P Princeton: Kurshan [231].
1964 D Toronto: Bakish [14].
1964 D Washington: McKinley [262].
1965 C Cambridge: Bolam [34].
1965 I Finland: is cited in Lyne [245].
1966 J Kyoto (electron microscope): Uyeda [421].
1966 O Kyoto (semiconductors): no editor; see Wittry [448].
1966 N London: no editor; see Chang [80].
1966 Michigan: Haddad [166].
1967 E Chicago: Arceneaux [6].
1967 B Novosibirsk: see Spivak [380].
1968 L Berkeley: Pease [318].
1968 D Boston: Bakish [15].
1968 et seq., H Chicago: Johari [210].
1968 et seq., F Chicago: (available from Engis Equipment Co).
1968 G Munster: will be published in BEDO (Beitrage zur elektronenmikroskopischen Direktabbildung von Oberflachen).
1968 E New Orleans: Arceneaux [7].
1968 K Rome: Bocciarelli [32].
1969 L Karlsruhe: will be published in BEDO.
1969 L Washington: Marton [253].

INDEX OF REFERENCES BY SUBJECT

Airplane Accident:
  Clancey [89].

Barium Titanate:
  Robinson [343].

Bibliographies:
  Corvin [96],
  Heinrich [179].

Biological:
- survey:
  - Fromme [146],
  - Hayes [175].
- see Fossils, Papermaking.

Biological, specimen preparation:
- bacteria:
  - Boyde [51].
- critical point drying:
  - Horridge [204].
- examine while frozen:
  - Thornley [406].
- freeze drying:
  - Blumcke [30],
  - Boyde [53],
  - Small [367],
  - Thornley [406],
  - Washburn [430].
- freeze etching:
  - Peveling [320].
- graded solvents:
  - Barber [17],
  - Blumcke [30],
  - Jaques [209].
- hard biological tissues:
  - Green [154].
- ion etching:
  - (blood cells) Lewis [243],
  - (dental) Boyde [40],
  - (dental) Stewart [383].
- replicas:
  - Chapman [84].
- sectioning:
  - McDonald [258].
- see Specimen Preparation (non-biological).

Biological, human:
- blood cells:
  - Clarke [90, 91],
  - Hayes [171],
  - Lewis [243],
  - Salsbury [346-348].

- bone:
  - Boyde [55],
  - Chatterji [87],
  - Hobdell [194].
- chromosomes:
  - Christenhusz [88],
  - Neurath [287],
  - Pawlowitzki [309].
- dental:
  - Boyde [40-56],
  - Fromme [145],
  - Hoffman [195, 196],
  - Lester [239-241],
  - Poole [329, 330],
  - Stewart [383],
  - (following laser irradiation) Vahl [422, 423].
  - see Dental Fillings.
- kidney:
  - Morgenroth [271].
- lung:
  - Jaques [209].
- ocular:
  - (trabecular meshwork) Spencer [375].
- soft tissues (various):
  - (sectioned) McDonald [258].
- synovial membranes:
  - Fujita [147].

Biological, mammals:
- cilia:
  - (rabbit) Barber [17].
- lymph-node cells:
  - (rat) Clarke [92].
- mitochondria:
  - (rat) Kurahasi [230].
- ocular:
  - (rabbit cornea) Blumcke [30].
- scar tissue:
  - (rat) Forrester [144].
- villi:
  - (rat) Thornley [406].

Biological, insects:
- Bernhard [29],
- Hinton [191-193],
- Oatley [299],
- Smith, K.C.A., [369],
- Smith, D.S., [368],
- Sokoloff [374],
- (insect, alive) Pease [317],
- (insect, alive) Hayes [172].

Biological, microorganisms and fungus:
- Bartlett [19],
- (dental bacteria) Boyde [51],
- (algae) Dwornik [126],
- Gray [153],
- (effect of antibiotics) Greenwood [160],
- Jones [212].

Biological, other animal:
- (chick embryo fibroblasts) Boyde [54],
- (echinoderm calcite) Curry [108],
- (ammanoids) Erben [128],
- (nematode cuticle) Green [154],
- (xylariaceae) Greenhalgh [159],
- (fossil) Gross [161],
- (onychiurus) Hale [167],
- (organelles) Heslop-Harrison [183],
- (gecko foot) Hiller [190],
- (rotifer jaw) Koehler [225],
- (house cricket eggshell) McFarlane [260],
- (mollusc teeth) Runham [345],
- (meal worm grub) Smith [369],
- (amoeba) Smith [369],
- (shore crab) Thornton [410],
- (mollusc shell) Wise [443].

Biological, Foraminifera:
- Be [23],
- Honjo [199, 201],
- Jannin [208],
- Malapris [252].

Biological, pollen:
- Bourreil [37],
- Burrichter [72],
- (fossil pollen) Drew [124],
- Echlin [127],
- Heslop-Harrison [180-184],
- Reyre [337], [338],
- Thornhill [404].

Biological, other plants:
- chromosomes:
  - Guervin [163].
- leaves:
  - (spinach leaf) Pease [316].
- lichen:
  - Peveling [320],
  - Reznik [339].
- wax cover:
  - Amelunxen [5].
- wood:
  - Resch [334].
  - see Papermaking.

Cadmium Sulphide:
  Flogel [140].

Cathodes:
  dispenser:
    Ahmed [1, 2],
    Beck [24].
  field emission:
    (sealed-off SEM) Zworykin [451],
    (demountable) Crewe [99, 100, 102, 103].
  lanthanum hexaboride pointed rod:
    Broers [62, 63].
  oxide cathodes:
    te Gude [395].
  tungsten hairpin:
    (brightness) Wittry [444],
    (thermal etching) Thornley [405],
    (single crystal on point) Grote [162].

Cement Fractures:
  Chatterji [85, 86],
  Tooper [419].

Ceramics:
  by low voltage method:
    Thornley [407].
  see Glass Ceramics.

Composite Materials:
  Fairing [138],
  Majumdar [251],
  (in dental fillings) Riedel [341].

Coates Patterns:
  effect first recognised:
    Coates [93].
  theory:
    Booker [35],
    Schulson [352, 353],
    Shaw [358],
    Van Essen [425].
  applied:
    Coates [94],
    Holt [198].
  see Crystal Orientation Contrast.

Cold Stage:
  joule cooling unit:
    Wayte [431].
  by evaporating water in vacuum:
    Cross [105].

Corrosion:
  Castle [76],
  Pfefferkorn [324],
  Ugiansky [420].

Crystal Orientation Contrast:
  in polycrystalline nickel:
    Knoll [220].
  reversed with small specimen tilt (acknowledged to Christenhusz):
    Pfefferkorn [324].
  see Coates Patterns.

Crystals:
  graphite crystals:
    Minkoff [266-268].
  quartz crystals:
    Dwornik [126].
  tungsten crystal:
    Grote [162].
  crystals decomposing by heat:
    Bowden [38],
    McAuslan [256],
    Oatley [299],
    Smith [370, 373].
  twin structures:
    Schwuttke [355].
  see Coates Patterns; Ice; Phosphors; Semiconductors.

Dental Fillings:
  Riedel [341, 342].

Dielectric Films:
  examined by induced signal method:
    Green [157].
  see Irradiation Effects; Integrated Circuits; Iron Oxide; Low Voltage Method.

Disc Recording:
  Woodward [450].

Dislocations: see Gallium Arsenide (by luminescent method); Image, luminescent; Image, induced signal; Semiconductors.

Display, methods of:
  cathode ray tube:
    Knoll [220],
    Heinrich [177].
  storage tube:
    Brookshier [66].
  deflection modulated:
    Chang [83],
    Everhart [137],
    Wittry [449].
  see Image Processing; Instrument Design.

Dust Particles:
  Pfefferkorn [323].

Electron Beam Fabrication (involving principles of SEM):
  formation of structure:
    Broers [59-61],
    Chang [81],
    Larkin [238],
    Matta [255],
    O'Keeffe [304],
    Pease [314].
  registration:
    Wells [436, 438].

Electron collector:
  secondary electron:
    (scintillator/light-pipe) Everhart [132],
    (channel multiplier) Hughes [207],
    (pair of collectors) Kimoto [214],
    (back through lens) Tamura [392],
    (back through lens) Zworykin [451].
  secondary electron energy analyser:
    Wells [439].
  transmitted electron energy analyser:
    Crewe [100].
  variable impact energy:
    Paden [306, 307].
  see Image.

Electron Gun: see Cathodes.

Electroplating:
  metal on metal:
    Richards [340].
  metal on plastic:
    Heymann [185].

Energy Analyser: see Electron Collector; Image.

Explosion Fragments:
    Clancey [89].

Fabrics and Fibres:
    Bobkowicz [31],
    Challice [78],
    Culpin [107],
    Reumuth [335],
    Sikorski [365],
    Smith [369],
    Thompson [402].

Fibres: see Fabrics; Papermaking.

Field Emission: see Cathodes.

Fossils:
    Bens [25],
    Dwornik [126],
    Hay [170],
    Honjo [200],
    Kimoto [216],
    Sandberg [349].
  see Biological, pollen; Biological, other animal; Geological.

Fractures:
  in iron oxide:
    Howes [206].
  see Composite Materials; Metallurgical.

Friction and Wear:
  in metal:
    Bowden [39].
  see Disk Recording.

Gallium Arsenide:
  by secondary electron method:
    Drummond [125],
    Northrop [295],
    Shaw [359],
    Thornton [409, 410].
  by luminescent method:
    Casey [74, 75],
    Kyser [235],
    Holt [197],
    Shaw [361, 362],
    Wittry [445-448].
  Gunn effect:
    Robinson [344].

Gallium phosphide:
    Alfrey [3],
    Everhart [131],
    Sulway [389].

Geological:
  calcite-clay mixtures:
    Noel [294].
  chalk:
    Hancock [168].
  feldspars:
    Nissen [291].
  lithographic calcite:
    Laffitte [236].
  minerals by luminescent method:
    Long [244].
  quartz crystals:
    Dwornik [126].
  sand:
    Cailleux [73].
  sedimentary rocks:
    Leuteritz [242],
    Noel [294].
  see Fossils.

Germanium:
  etched surface:
    Allen [4].
  p-n junctions in:
    Everhart [129, 130],
    Oatley [296],
    Wells [435, 437].
  irradiation of:
    Ovsyuk [305].

Glass:
    Korda [229].

Glass Ceramics:
    Majumdar [250].

Gravure Cells:
    Goode [151, 152].

Gunn Effect: see Gallium Arsenide.

Gypsum Plaster:
    Majumdar [251].

Hot Stage:
    Knoll [224],
    McAuslan [256],
    Smith [370].

Ice:
  evaporating in SEM:
    Cross [105, 106].
  examined by replicas:
    Odencrantz [302, 303].

Image, backscattered electron:
  theory:
    McMullan [263-265],
    Vercensini [429].
  to analyse materials:
    Heinrich [178],
    Shirai [363].
  compared with secondary electron image:
    Everhart [129, 130],
    Kimoto [215].
  escape area measured:
    Pease [311].
  see Coates Patterns.

Image, Deflection-Modulated: see Display.

Image, induced signal:
  in semiconductors:
    Everhart [133, 134],
    Higuchi [186, 188],
    Lander [237],
    Munakata [274-285],
    Thornton [411, 415],
    Wells [436, 438].
  transverse induced signal:
    Munakata [274-285],
  transverse induced signal image:
    Matare [254],
    McAvoy [257].
  in dielectric films:
    Green [157].
  see Integrated Circuits.

Image, luminescent:
  method first demonstrated (acknowledged to McMullan):
    Smith [369].
  monochromatic:
    Williams [442].
  see Geology; Phosphor Crystals; Semiconductors.

Image, secondary electron:
  to examine surface topography:
    Knoll [220, 221],
    Zworykin [451],
    Smith [370-371],
    Everhart [129, 130],
    see Surfaces.
  to reveal mechanical strain:
    Davoine [116].
  contrast formation:
    Everhart [129, 130],
    Spivak [378, 379],
    Wells [439].
  see Coates Patterns; Crystal Orientation Contrast; Magnetic contrast; Voltage Contrast.

Image, transmitted electron:
  with energy analyser:
    Crewe [99, 100].
  without energy analyser:
    von Ardenne [8, 9],
    McMullan [263],
    Smith [369].
  water vapor cell:
    Smith [370],
    Thornley [405].

Image Contrasts: see Coates Patterns; Crystal Orientation Contrast; Image; Magnetic Contrast; Stroboscopic Method; Voltage Contrast.

Image Processing:
  multiple exposure to obtain difference:
    Everhart [129].
  differentiate to enhance contrasts:
    (semiconductor induced signal image)
      Lander [237],
    (Coates Patterns) Shaw [358].

Image Resolution: see Resolution.

Instrument Design:
  method proposed:
    Stintzing [386],
    Knoll [220].
  made from glass:
    Knoll [220],
    Theile [398],
    te Gude [396].
  metal, oil pumped:
    von Ardenne [8, 9],
    Zworykin [451],
    McMullan [265],
    Bernard [26],
    Smith [370-372],
    Kimura [219],
    Stewart [384].
  ultra-high vacuum:
    Crewe [99, 100, 103],
    Haas [164, 165].
  quadrupole lenses:
    Crewe [101].
  combined with x-ray microanalyser:
    Cosslett [97, 98],
    Kushnir [232-234].
  first commercial model:
    Stewart [384].
  Faraday cage:
    Hill [189].
  see Cathodes; Cold Stage; Display; Electron Collector; Hot Stage; Image; Resolution; Specimen Stub; Vidicon-Type Electron Optics.

Insulators: see Dielectric Films; Low Voltage Method.

Integrated Circuits:
    Everhart [133-135],
    Kimura [218],
    Mackintosh [249],
    Sulway [390],
    te Gude [397],
    Thornhill [403],
    Thornton [414].
  see Low Voltage Method; Semiconductors.

Ion Etching:
  non-biological:
    Broers [59-61],
    Pease [312],
    Stewart [382].
  see Biological, specimen preparation.

Iron Oxide:
  layers:
    Castle [76, 77],
    Howes [206],
    Knoll [223],
    Pease [312].
  particles:
    Themelis [399-401].
  see Corrosion.

Irradiation Effects (non-thermal):
  in germanium:
    Ovsyuk [305].
  in silicon dioxide:
    Green [156],
    MacDonald [248],
    Nealey [286],
    O'Keeffe [304],
    Speth [376],
    Szedon [391],
    Thornton [414],
    Varker [426],
    Wells [440].

Lithographic Calcite:
    Laffitte [236].

Low Voltage Method:
  to examine insulators:
    Thornley [405-407].
  to reduce electron penetration:
    Bernard [28],
    Davoine [117].
  to measure work functions:
    Haas [164, 165].
  to examine dielectric films:
    Da Silva [113],
    Harris [169].
  to examine integrated circuits:
    Bauer [21, 22].

Magnetic Contrast:
  in normal SEM image:
    Banbury [16],
    Dorsey [123],
    Joy [213],
    Vertsner [427].
  by SEM shadow method:
    Thornley [408].

Metallurgical:
  diffusion couple:
    Shirai [364].
  metal fractures:
    McGrath [261],
    Morris [272],

- Tipper [417].
- eutectic alloys:
  - Day [120, 121].
- by luminescent method:
  - Heinrich [177].
- survey:
  - Johari [211],
  - Predel [331].
- see Corrosion; Electroplating; Image; Surfaces; Whiskers.

Microdeformation: see Surfaces.

Microfossils: see Fossils.

Mode (conductive, emissive, luminescent): see Image.

Nylon Spinneret:
- Wells [433].

Orientation-Dependent Patterns: see Coates Patterns.

Paint Films:
- Brooks [65],
- Pfefferkorn [322].

Papermaking:
- initial evaluation:
  - Atack [10].
- wood fracture, chipping and pulping:
  - Atack [11],
  - Buchanan [67],
  - Debaise [122],
  - Forgacs [141, 143],
  - Green [158],
  - Horn [203],
  - Koran [226, 227],
  - Smith [371],
  - Teder [393, 394].
- paper:
  - Baker [12],
  - Buchanan [68-71],
  - Forgacs [142],
  - (printability) Lyne [245],
  - Pye [333],
  - Sennett [356],
  - Sepall [357],
  - Smith [371],
  - Washburn [430].

Particles: see Dust; Explosion Fragments; Iron Oxide; Biological, pollen.

Phosphor Crystals:
- by secondary electron method:
  - Pinard [326].
- by luminescent method:
  - Bernard [27],
  - Williams [441],
  - Davey [114],
  - Davoine [117-119],
  - Korda [228],
  - Pinard [325],
  - Shaw [360, 361],
  - Smith [369].

Pollen: see Biological, pollen.

Replicas: see Specimen Preparation; Biological, specimen preparation.

Resolution:
- best resolution for a time:
  - Knoll [220],
  - von Ardenne [8, 9],
  - Zworykin [451],
  - McMullan [265],
  - Smith [370-372],
  - Pease [310, 313],
  - (in transmission) Crewe [103],
  - (in reflection) Broers [64].
- resolution calculated:
  - Brachet [57],
  - Zworykin [451, 452],
  - Smith [373],
  - Everhart [129],
  - Pease [313].

Retarding Field Method: see Electron Collector; Vidicon-Type Electron Optics.

Semiconductors:
- survey:
  - Thornton [416].
- breakdown of junctions:
  - Davies [115],
  - Gaylord [150],
  - Neve [288-290],
  - Sulway [387].
- action of light on P-N junctions:
  - Vertsner [428].
- crystal defects in:
  - Czaja [109-112],
  - Lander [237],
  - Thornton [410],
  - Wittry [445-448].
- depletion layers:
  - MacDonald [246],
  - Everhart [136].
- diffusions:
  - MacDonald [247].
- inversion layers:
  - Green [155],

Higuchi [187],
Lander [237],
Sulway [388].
time-varying effects:
Northrop [295],
Saparin [351],
see Stroboscopic Methods.
beam-induced potentials:
Chang [82],
Wells [439].
see Irradiation Effects; Gallium Arsenide; Gallium Phosphide; Germanium; Image, induced signal; Integrated Circuits; Zinc Selenide.

Shadow Method: see Magnetic Contrast.

Silicon Dioxide: see Irradiation Effects.

Specimen Preparation:
test specimens:
Schur [354].
metallizing:
Boult [36],
Smith [369].
replicas:
(ice crystals) Odencrantz [303].
wood fibres:
Washburn [430].
see Biological, specimen preparation.

Stereomicrographs: theory of:
Kimoto [217],
Wells [434].

Specimen Stub:
Sandberg [350].

Stroboscopic Method:
Plows [327, 328],
Robinson [344].

Surfaces:
chemically etched:
(aluminum) Everhart [130],
(germanium) Allen [4],
(very deeply) Day [120, 121].
etched plastic:
Heymann [185].
electron beam machined:
Chang [79, 80].
laser irradiated:
Baston [20].
spark machined:
Cole [95].
thermally etched:
Thornley [405].
deformed in the microscope:
Gane [148],
Smith [370].
barium titanate:
Robinson [343].
see Composite Materials; Fractures; Ion Etching.

Survey Papers (most recent):
Kimoto [217],
Mackintosh [249],
Minkoff [269],
Mollenstedt [270],
Nixon [292, 293],
Oatley [297-300],
Pease [319],
Pfefferkorn [321],
Pruden [332],
Reumuth [336].

Textiles: see Fabrics.

Vidicon-Type Electron Optics in SEM:
Bauer [21, 22],
Flemming [139],
Haas [164, 165],
Harris [169].

Voltage Contrast:
surrounding a charged particle:
Knoll [222].
at a p-n junction:
Oatley [296],
Everhart [130],
Thornton [413].
high field:
Drummond [125],
Spivak [377, 379].
see Electron Collector; Semiconductors.

Water Vapor, specimens examined in:
Smith [370],
Thornley [405].

Wear: see Disc Recording; Friction.

Whisker Growth:
Morris [272],
Pease [312, 315],
Gardner [149],
Thornton [412].

Zinc Selenide:
Williams [441].

Zinc Sulphide:
Shaw [360].
see Phosphor Crystals.

LIST OF REFERENCES

** **Ackerman, M.**, see Sokoloff [374].

[1] **Ahmed, H.**, (1962). "Studies on high current density thermionic cathodes," Ph.D. Diss., Cambridge Univ.

[2] ---- and Beck, A.H.W., (1963). "Thermionic emission from dispenser cathodes," J. Appl. Phys., vol. 34, pp. 997-998.

** ---- see Beck [24].

[3] **Alfrey, G.F.**, and Wiggins, C.S., (1960). "Electroluminescence at grain boundaries in gallium phosphide," pp. 747-750 in Solid State Phys. in Electronics and Telecommunications (Proc. Int. Conf. held in Brussels 1958), M. Desirant and J.L. Michiels, Eds., Academic Press, N.Y.

[4] **Allen, J.W.**, and Smith, K.C.A., (1956). "Electron microscopy of etched germanium surfaces," J. Electronics, vol. 1, pp. 439-443 and 2 plates.

** **Alvarado, J.**, see Spencer [375].

** **Amand, P.St.**, see Odencrantz [303].

B [5] **Amelunxen, F.**, Morgenroth, K., and Picksak, T., (1967). "Investigations on the epidermis with the Stereoscan electron microscope" (in German), Z. Pflanzenphysiologie, vol. 57, pp. 79-95.

** ---- see Burrichter [72].

** **Amer, N.M.**, see Pease [317].

** **Ampola, M.G.**, see Neurath [287].

[6] **Arceneaux, C.J.**, (Ed.) (1967). Proc. 25th. Annual Meeting Electron Microscopy Society of America, Chicago, Aug./Sept. 1967, Claitors Publishing Division, Louisiana.

[7] ---- (Ed.) (1968). Proc. 26th. Annual Meeting Electron Microscopy Society of America, New Orleans, Sept. 1968, (same publisher).

[8] **Ardenne, M. von**, (1938a). "The scanning electron microscope. Practical construction" (in German), Z. Techn. Physik, vol. 19, pp. 407-416.

[9] ---- (1938b). "The scanning electron microscope. Theoretical fundamentals" (in German), Z. Physic, vol. 109, pp. 553-572.

[10] **Atack, D.**, and Smith, K.C.A., (1956). "The scanning electron microscope - A new tool in fibre technology," Pulp Paper Mag. Canada, vol. 57, pp. 245-251; convention issue.

[11] ----, May, W.D., Morris, E.L., and Sproule, R.N., (1961). "The energy of tensile and cleavage fracture of black spruce," Tappi, vol. 44, pp. 555-567.

** ---- see Forgacs [142].

** **Backmann, R.**, see Morgenroth [271].

[12] **Baker, D.L.**, and Sepall, O., (1965). "A new dimension in papermaking - carboxyethylation," Pulp Paper Mag. Canada (Technical Section), vol. 66, pp. T449-T455. (Has 4 SEM images.)

[13] **Bakish, R.A.**, (Ed.) (1961). Proc. Third Symposium on Electron Beam Technology, Alloyd Electronics Corp., Boston.

[14] ---- (Ed.) (1965). First Int. Conf. Electron and Ion Beam Science and Technology, Toronto, May 1964. John Wiley and Sons, New York, 1965.

[15] ---- (Ed.) (1968). Electron and Ion Beam Science and Technology. Third Int. Conf. (Boston, May 1968. Electrochem. Soc.)

[16] **Banbury, J.R.**, and Nixon, W.C., (1967). "The direct observation of domain structure and magnetic fields in the scanning electron microscope," J. Sci. Inst., vol. 44, pp. 889-892. (See Joy and Jakubovics, 1968.)

B [17] **Barber, V.C.**, and Boyde, A., (1968). "Scanning electron microscopic studies of cilia," Z. fur Zellforschung, vol. 84, pp. 269-284.

** ---- see Boyde [53].

[18] **Bargmann, W.**, Mollenstedt, G., Niehrs, H., and 3 others (Ed.) (1960). Proc. Fourth Int. Conf. on Electron Microscopy, Berlin, Sept. 1958. Springer Verlag, Berlin, 1960.

B [19] **Bartlett, G.A.**, (1967). "Scanning electron microscope: potentials in the morphology of microörganisms," Science, vol. 158, pp. 1318-1319, front cover and index page.

[20] **Baston, T.J.**, and Bowden, F.P., (1968). "Localized damage of metal crystals by laser irradiation," Nature (London), vol. 218, pp. 150-152.

[21] **Bauer, K.**, (1966). "New electron-optical technique for imaging surfaces and indentifying areas" (in German), Z. fur angew.

Physik, vol. 20, pp. 294-301. (Vidicon-type electron optics.)

[22] ---- and Bloss, W., (1967). "Scanning technique with slow electrons for investigation of integrated circuits," Electronics Letters, vol. 3, pp. 475-477. (Vidicon-type electron optics.)

[23] **Be, A.W.H.**, (1968). "Shell porosity of recent planktonic Foraminifera as a climatic index," Science, vol. 161, pp. 881-884 and front cover for Aug. 30 issue.

[24] **Beck, A.H.W.**, and Ahmed, H., (1963). "The activation process in dispenser cathodes," J. Electronics and Control, vol. 14, pp. 623-627.

** ---- see Ahmed [2].

B [25] **Bens, E.M.**, and Drew, C.M., (1967). "Diatomaceous earth: scanning electron microscope of 'Chromosorb P'," Nature (London), vol. 216, pp. 1046-1048.

** **Berggren, W.A.**, see Honjo [199].

[26] **Bernard, R.**, and Davoine, F., (1957). "The scanning electron microscope" (in French), Ann. de L'Univ. de Lyon, Third Series, Sciences, Section B, vol. 10, pp. 78-86 and 4 plates.

[27] ----, Davoine, F., and Pinard, P., (1959). "Extension of the technique of scanning electron microscopy to the observation of fluorescent substances" (in French), C.R. Acad. Sci., vol. 248, pp. 2564-2566.

[28] ---- and Davoine, F., (1960). "Scanning electron microscopy" (in French), pp. 273-276 in Bargmann et al (1960). (Describes low-voltage SEM.)

** ---- see Davoine [117].

B [29] **Bernhard, C.G.**, (1967). "Structural and functional adaptation in a visual system," Endeavour, vol. 26, pp. 79-84 in May issue. (Has SEM images of insect eyes.)

** **Bikov, M.V.**, see Spivak [379].

** **Blaschke, R.**, see Heymann [185], Hiller [190], Morgenroth [271], Nissen [291], Pawlowitzki [309], Pfefferkorn [321, 322, 323], Predel [331] and Resch [334].

** **Bloss, W.**, see Bauer [22].

B [30] **Blumcke, S.**, and Morgenroth, K., (1967). "The stereo ultrastructure of the external and internal surface of the cornea," J. Ultrastructure and Res., vol. 18, pp. 502-518.

[31] **Bobkowicz, A.J.**, (1963). "The effects of turbulence on the flow characteristics of model fibre suspensions," Ph.D. Diss., McGill Univ. (Contains SEM images of damaged fibres.)

[32] **Bocciarelli, D.S.**, (1968). "Electron Microscopy 1968," Pre-Cong. Abs. of papers presented at the Fourth European Regional Conf. held in Rome, Sept. 1-7, 1968. Tipografia Poliglotta Vaticana. Vol. 1, Non-Biology; Vol. 2, Biology.

[33] **Bolam, F.**, (Ed.) (1962). "The Formation and Structure of Paper," Trans. Oxford Symp., Sept. 1961, Technical Section of British Paper and Board Makers Association, London, E.C.4, England.

[34] ---- (Ed.) (1966). "Consolidation of the paper web," Trans. of the Symposium held at Cambridge, Sept. 1966, Technical Section of British Paper and Board Makers Association, London, E.C.4, England.

[35] **Booker, G.R.**, Shaw, A.M.B., Whelan, M.J., and Hirsh, P.B., (1967). "Some comments on the interpretation of the 'Kikuchi-like reflection patterns' observed by scanning electron microscopy," Phil. Mag., vol. 16, pp. 1185-1191. (See Coates, 1967.)

** ---- see Shaw [358].

[36] **Boult, E.H.**, and Brabazon, E.J., (1968). "A rotating device for use in metallizing non-conducting scanning electron microscope specimens," J. Sci. Inst. (J. Phys. E), Series 2 vol. 1, pp. 565-566.

B [37] **Bourreil, P.**, and Reyre, Y., (1968). "Preliminary study of pollen grains of the graminaceous Aristides in the scanning electron microscope" (in French), C.R. Acad. Sci. Paris, vol. 267 D, pp. 398-401 and 2 plates.

[38] **Bowden, F.P.**, and McAuslan, J.H.L., (1956). "Slow decomposition of explosive crystals," Nature (London), vol. 178, pp. 408-410.

[39] ---- and Childs, T.H.C., (1968). "Friction and deformation of metals at extremely low temperatures," Nature (London), vol. 219, pp. 1333-1335.

** ---- see Baston [20] and Gane [148].

B [40] **Boyde, A.**, and Stewart, A.D.G., (1962a). "A study of the etching of dental tissues with argon ion beams," J. Ultrastructure Res., vol. 7, pp. 159-172.

B [41] ---- and Stewart, A.D.G., (1962b). "Investigation of the erosion of tooth sections with an argon ion beam," Paper QQ-9 (2 pages) in Breese (1962).

B [42] ---- and Stewart, A.D.G., (1963). "Scanning electron microscopy of the surface of developing mammalian dental enamel," Nature (London), vol. 198, pp. 1102-1103.

B [43] ----, Switsur, V.R., and Stewart, A.D.G., (1963). "An assessment of two new physical methods applied to the study of dental tissues," pp. 185-193 in Proc. 9th. ORCA Cong. (Permagon Press.) (European Organization for Caries Research.)

B [44] ---- and Quilliam, T.A., (1966). "The scanning electron microscope," Medical and Biological Illustration, vol. 16, pp. 116-117. (Shows SEM images of developing African elephant molar tooth enamel.)

B [45] ---- (1967a). "Direct visualisation of the site of development of enamel prism sheaths," Naturwissenschaften, vol. 54, pp. 252-253.

B [46] ---- (1967b). "The development of enamel structure," Proc. Roy. Soc. Medicine, vol. 60, pp. 923-928.

B [47] ---- and Lester, K.S., (1967a). "The structure and development of marsupial enamel tubules," Z. Zellforsch., vol. 82, pp. 558-576.

B [48] ---- and Lester, K.S., (1967b). "Electron microscopy of resorbing surfaces of dental hard tissues," Z. Zellforsch., vol. 83, pp. 538-548.

B [49] ---- and Lester, K.S., (1967c). "An electron microscope study of fractured dentinal surfaces," Calc. Tiss. Res., vol. 1, pp. 122-136.

B [50] ---- and Jones, S.J., (1968). "Scanning electron microscopy of cementum and Sharpey fibre bone," Z. Zellforsch., vol. 92, pp. 536-548.

B [51] ---- and Lester, K.S., (1968). "A method of preparing bacterial plaque lining carious cavities for examination by scanning electron microscopy," Archs. Oral Biol., vol. 13, pp. 1413-1419 and 2 plates.

B [52] ---- (1969). "Correlation of ameloblasts with enamel prism pattern: use of scanning electron microscope to make surface area measurements," Z. Zellforsch., vol. 93, pp. 583-593.

B [53] ---- and Barber, V.C., (1969). "Freeze-drying methods for the scanning electron microscopical study of the protozoon Spirostomum ambiguum and the statocyst of the cephalopod mollusc Loligo vulgaris," J. Cell Sci., vol. 4, pp. 223-239.

B [54] ----, Grainger, F., and James, D.W., (1969). "Scanning electron microscopic observations of chick embryo fibroblasts in vitro, with particular reference to the movement of cells under others," Z. Zellforsch., vol. 94, pp. 46-55.

B [55] ---- and Hobdell, M.H., (1969). "Scanning electron microscopy of lamellar bone," Z. Zellforsch., vol. 93, pp. 213-231.

B [56] ---- and Reith, E.J., (1969). "The pattern of mineralization of rat molar dentine," Z. Zellforsch., vol. 94, pp. 479-486.

** ---- see Barber [17], Hobdell [194], Lester [239, 240, 241] and Stewart [383].

** **Brabazon, E.J.**, see Boult [36].

[57] **Brachet, C.**, (1946). "Note on the resolution of the scanning electron microscope" (in French), Bull. L'Assoc. Tech. Mar. et Aero., No. 45, pp. 369-378.

** **Bradford, A.**, see Thornton [412].

** **Brandis, E.K.**, see Schwuttke [355].

[58] **Breese, S.S.**, (Ed.) (1962). Proc. Fifth Int. Cong. for Electron Microscopy, Philadelphia. Aug./Sept. 1962. Academic Press, New York, 1962.

** **Bremer, C.G.**, see Wells [439].

[59] **Broers, A.N.**, (1965a). "Selective ion beam etching in the scanning electron microscope," Ph.D. Diss., Cambridge Univ.

[60] ---- (1965b). "Micromachining by sputtering through a mask of contamination laid down by an electron beam," pp. 191-204 in Bakish (1965).

[61] ---- (1965c). "Combined electron and ion beam processes for microelectronics," Microelectronics and Reliability, vol. 4, pp. 103-104 and 1 plate.

[62] ---- (1967). "Electron gun using long-life lanthanum hexaboride cathode," J. Appl. Phys., vol. 38, pp. 1991, 1992 and 3040. (See

also pp. 1-6 in Pease 1967a; but main reference follows.)

[63] ---- (1969a). "Some experimental and estimated characteristics of the lanthanum hexaboride rod cathode electron gun," J. Sci. Inst. (J. Phys. E), Series 2, vol. 2, pp. 273-276.

[64] ---- (1969b). "A new high resolution reflection scanning electron microscope," Rev. Sci. Inst., Aug. 1969 issue. (30 AU probe diameter; 50 AU point to point separation.)

** ---- see Pease [312].

[65] **Brooks, L.E.**, Sennett, P., and Morris, H.H., (1967). "Scanning electron micrographs of pigmented paint films," J. Paint Technology, vol. 39, pp. 472-483.

[66] **Brookshier, W.K.**, and Gilroy, J., (1965). "Display system for use with a scanning electron energy analyzing microscope," IEEE Trans. on Nuclear Science, vol. NS-12, pp. 104-110.

[67] **Buchanan, J.G.**, and Smith, K.C.A., (1960). "Preliminary studies of damage in papermaking wood chips using the scanning electron microscope," pp. 547-550 in Houwink and Spit (1960).

[68] ---- and Lindsay, R.A., (1962). "A note on structure of paper as revealed by the scanning electron microscope," pp. 101-117 in Bolam (1962).

[69] ---- and Washburn, O.V., (1962a). "Some experimental observations with a bearing on the paper 'A new theory of the shrinkage, structure and properties of paper'," pp. 422-425 in Bolam (1962).

[70] ---- and Washburn, O.V., (1962b). "The surface and tensile fractures of chemical fibre handsheets as observed with the scanning electron microscope," Pulp Paper Mag. Canada (Technical Section), vol. 63, pp. T485-T493.

[71] ---- and Washburn, O.V., (1964). "The surface and tensile fractures of groundwood handsheets as observed with the scanning electron microscope," Pulp Paper Mag. Canada (Technical Section), vol. 65, pp. T52-T60.

** ---- see McGrath [261], Pye [333] and Washburn [430].

** **Buchner, Th.**, see Christenhusz [88].

** **Buck, T.M.**, see Lander [237].

** **Buckley, T.**, see Sikorski [365].

** **Bucklow, I.A.**, see Cole [95].

B [72] **Burrichter, E.**, Amelunxen, F., Vahl, J., and Giele, T., (1968). "Investigation of pollen and spores with the scanning electron microscope" (in German), Z. Pflanzenphysiologie, vol. 59, pp. 226-237.

** **Cahn, R.W.**, see Gardner [149].

[73] **Cailleux, A.**, and Schneider, H., (1968). "Erosion of sand studied by scanning electron microscopy" (in French), Science Progres - La Nature (Paris), no. 3395 pp. 92-94.

** **Camp, A.S.**, see Hayes [172, 173] and Pease [317].

** **Cartz, L.**, see Thornley [407] and Tooper [419].

[74] **Casey, H.C.**, (1967). "Investigation of inhomogeneities in GaAs by electron beam excitation," J. Electrochem. Soc., vol. 114, pp. 153-158.

[75] ---- and Kaiser, R.H., (1967). "Analysis of n-type GaAs with electron beam excited radiative recombination," J. Electrochem. Soc., vol. 114, pp. 149-153.

[76] **Castle, J.E.**, and Masterton, H.G., (1966a). "The role of diffusion in the oxidation of mild steel in high temperature aqueous solutions," Corrosion Science, vol. 6, pp. 93-104.

[77] ---- and Masterton, H.G., (1966b). "Applications of the scanning electron microscope to oxide surfaces," Anti-Corrosion Methods and Materials, vol. 1, pp. 6-11.

[78] **Challice, C.E.**, and Sikorski, J., (Ed.) (1957). "Summarised proceedings of a conference on the electron microscopy of fibres - Leeds, January 1956," Brit. J. Appl. Phys., vol. 8, pp. 1-26. (Has SEM image of wool fibre surface.)

[79] **Chang, T.H.P.**, and Nixon, W.C., (1966a). "Scanning electron microscopy and electron beam effects on silicon surfaces," pp. 193-194 in Uyeda (1966).

[80] ---- and Nixon, W.C., (1966b). "Electron beam machining of silicon observed with the scanning electron microscope," Paper 23 (3 pages) in Proc. Joint IERE-IEE Conf. on Applications of Thin Films in Electronic Engineering, London 1966. (IERE Conf. Proc. no. 7.)

[81] ---- and Nixon, W.C., (1967a). "Electron beam formation of 800 AU wide aluminium lines," J. Sci. Inst., vol. 44, pp. 231-234.

[82] ---- and Nixon, W.C., (1967b). "Electron beam induced potential contrast on unbiased planar transistors," Solid-State Electronics, vol. 10, pp. 701-704 and 2 plates.

[83] ---- and Nixon, W.C., (1968). "Scan-modulation display in scanning electron microscopy," J. Royal Microscopical Soc., vol. 88, pt. 2, pp. 143-149.

B [84] **Chapman, B.**, (1967). "Polystyrene replicas for scanning reflexion electron microscopy," Nature (London), vol. 216, pp. 1347-1348.

** **Chase, B.D.**, see Holt [197].

[85] **Chatterji, S.**, and Jeffery, J.W., (1966). "Three-dimensional arrangement of hydration products in set cement paste," Nature (London), vol. 209, pp. 1233-1234. (Shows SEM images of fractured cement surfaces.)

[86] ---- and Jeffery, J.W., (1967). "Strength development in calcarious cements," Nature (London), vol. 214, pp. 559-561.

B [87] ---- and Jeffery, J.W., (1968). "Changes in structure of human bone with age," Nature (London), vol. 219, pp. 482-484.

** ---- see Majumdar [250].

** **Chentsov, Yu.V.**, see Vertsner [427, 428].

** **Childs, T.H.C.**, see Bowden [39].

B [88] **Christenhusz, R.**, Buchner, Th., and Pfeiffer, R.A., (1967). "Visualization of human somatic chromosomes by scanning electron microscopy," Nature (London), vol. 216, pp. 379-380.

** ---- see Pawlowitzki [309].

[89] **Clancey, V.J.**, (1968). "Comet G-ARCO: solving the riddle," New Scientist, vol. 39, pp. 533, 534, 536 and 537. (SEM examined explosion fragments.)

B [90] **Clarke, J.A.**, and Salsbury, A.J., (1967). "Surface ultramicroscopy of human blood cells," Nature (London), vol. 215, pp. 402-404.

B [91] ----, Salsbury, A.J., and Rowland, G.F., (1968). "The scanning electron microscope: II," Science J., vol. 4, pp. 54-61 in August issue.

B [92] ----, Salsbury, A.J., and Willoughby, D.A., (1968). "The effects of various antisera on the surfaces of sensitised rat lymph-node cells," J. Pathology and Bacteriology, vol. 96, pp. 235-238.

** ---- see Salsbury [346, 347, 348].

** **Coalson, J.**, see Jaques [209].

[93] **Coates, D.G.**, (1967). "Kikuchi-like reflection patterns observed in the scanning electron microscope," Phil. Mag., vol. 16, pp. 1179-1184. (See Booker et al, 1967.)

[94] ---- (1968). "Improvements in the orientation effect observed by scanning electron microscopy," Physica Status Solidi, vol. 27, pp. K11-K13 and 1 plate.

** ---- see Shaw [358].

[95] **Cole, M.**, Bucklow, I.A., and Grigson, C.W.B., (1961). "Technique for the rapid, accurate and strain-free machining of metallic single crystals," Brit. J. Appl. Phys., vol. 12, pp. 296-297.

** **Coq, C. Le**, see Guervin [163].

[96] **Corvin, I.**, (1968). "Bibliography on the scanning electron microscope and some related subjects," pp. 157-185 in Johari (1968a).

[97] **Cosslett, V.E.**, and Duncumb, P., (1957). "A scanning microscope with either electron or x-ray recording," pp. 12-14 in Sjostrand and Rhodin (1957).

[98] ---- (1967). "Scanning microscopy with electrons and x-rays," J. Electron Microscopy (Japan), vol. 16, pp. 51-64.

** **Coutts, M.D.**, see Woodward [450].

[99] **Crewe, A.V.**, (1963). "A new kind of scanning microscope," J. de Microscopie (Paris), vol. 2, pp. 369-371.

[100] ---- (1966). "Scanning electron microscopes: is high resolution possible?" Science, vol. 154, pp. 729-738. (Shows SEM images of thin films obtained by collecting electrons with specified energy loss.)

[101] ----, Eggenberger, D.N., and Welter, L.M., (1967). "Experiments with quadrupole lenses in a scanning electron microscope," J. Appl. Phys., vol. 38, pp. 4257-4266.

[102] ----, Eggenberger, D.N., Wall, J., and Welter, L.M., (1968). "Electron gun using a field emission source," Rev. Sci. Ins., vol. 39, pp. 576-583.

[103] ----, Wall, J., and Welter, L.M., (1968). "High resolution scanning transmission electron microscope," J. Appl. Phys, vol. 39, pp. 5861-5868.

[104] ----, Isaacson, M., and Johnson, D., (1969). "A simple scanning electron microscope," Rev. Sci. Inst., vol. 40, pp. 241-246.

[105] **Cross, J.D.**, and Cross, P.M., (1968). "Scanning electron microscopy of materials containing water without a refrigeration stage," J. Sci. Inst. (J. Phys. E), Series 2, vol. 1, pp. 1123-1124.

[106] ---- (1969). "Scanning electron microscopy of evaporating ice," Science, vol. 164, pp. 174-175.

** **Cross, P.M.**, see Cross [105].

[107] **Culpin, M.J.**, and Dunderdale, K.F., (1965). "Studies of fibre surfaces in a scanning electron microscope," pp. 421-422 in Titlebach (1965).

** ---- see Thornton [409].

B [108] **Currey, J.D.**, and Nichols, D., (1967). "Absence of organic phase in echinoderm calcite," Nature (London), vol. 214, pp. 81-83.

[109] **Czaja, W.**, and Wheatley, G.H., (1964). "Simultaneous observation of diffusion-induced dislocation slip patterns in silicon with electron beam scanning and optical means," J. Appl. Phys., vol. 35, pp. 2782-2783.

[110] ---- and Patel, J.R., (1965). "Observations of individual dislocations and oxygen precipitates in silicon with a scanning electron beam method," J. Appl. Phys., vol. 36, pp. 1476-1482.

[111] ---- (1966a). "Detection of partial dislocations in silicon with the scanning electron beam technique," J. Appl. Phys., vol. 37, pp. 918-919.

[112] ---- (1966b). "Response of Si and GaP p-n junctions to a 5- to 40-keV electron beam," J. Appl. Phys., vol. 37, pp. 4236-4248.

** **Dagg, D.I.**, see Tipper [417].

[113] **Da Silva, E.M.**, and White, P., (1961). "A method for detecting imperfections in thin insulating films," pp. 830-835 in 1961 Trans. of the Eighth National Vacuum Symp. (American Vacuum Society) combined with Second Int. Cong. on Vacuum Science Pergamon Press, New York, N.Y.

[114] **Davey, J.P.**, (1965). "Electron microprobe scanning system for the study of cathodoluminescence," Ph.D. Diss., Cambridge Univ.

[115] **Davies, I.G.**, Hughes, K.A., Sulway, D.V., and Thornton, P.R., (1966). "The direct observation of electrical leakage paths due to crystal defects by use of the scanning electron microscope," Solid-State Electronics, vol. 9, pp. 275-279.

** ---- see Sulway [387] and Thornton [416].

[116] **Davoine, F.**, (1957). "Secondary electron emission of metals under mechanical strain" (in French), Ph.D. Diss., L'Univ. de Lyon.

[117] ----, Bernard, R., and Pinard, P., (1960). "Fluorescence of alkali halides observed with a scanning electron microscope, (in French), pp. 165-168 in Houwink and Spit (1960).

[118] ----, Pinard, P., and Martineau, M., (1960). "Observation of cadmium sulfide bombarded with electrons of 5 kev energy" (in French), J. Phys. Rad., vol. 21, pp. 121-124.

[119] ---- and Pinard, P., (1965). "Study of cathodoluminescence by scanning electron microscopy" (in French), pp. 113-114 in Titlebach (1965).

** ---- see Bernard [26, 27, 28].

[120] **Day, M.G.**, and Hellawell, A., (1967). "The structure of modified aluminum-silicon eutectic alloy," J. Institute Metals, vol. 95, p. 377.

[121] ---- and Hellawell, A., (1968). "The microstructure and crystallography of aluminum-silicon eutectic alloys," Proc. Roy. Soc. A., vol. 305, pp. 473-491 and plates 5-12.

[122] **Debaise, G.R.**, Porter, A.W., and Pentoney, R.E., (1966). "Morphology and mechanics of wood fracture," Materials Research and Standards, vol. 6, pp. 493-499.

** **Der-Shvarts, G.V.**, see Kushnir [233].

** **Dickinson, H.G.**, see Heslop-Harrison [184].

[123] **Dorsey, J.R.**, (1966). "Scanning electron probe measurement of magnetic fields," abstract no. 10, First National Conf. on Electron Probe Microanalysis, available from L. Marton, Ed., College Park, Maryland.

B [124] **Drew, C.M.**, and Tschudy, B.D., (1968). "Aquilapollenites: fossil pollen as seen under the scanning electron microscope," Geol. Soc. America Bull., vol. 79, pp. 1829-1932 and 2 plates.

** ---- see Bens [25] and Hoffman [195, 196].

** **Drexel, J.**, see Sennett [356].

[125] **Drummond, I.W.**, and Thornton, P.R., (1965). "Studies of electrical high-field regions in high resistivity GaAs with the scanning electron microscope," pp. 287-288 in Titlebach (1965).

** ---- see Thornton [409].

** **Duncumb, P.**, see Cosslett [97].

** **Dunderdale, K.F.**, see Culpin [107].

[126] **Dwornik, E.J.**, (1965). "Use of the scanning electron microscope in geologic studies," U.S. Geol. Survey Prof. Paper 550-D pp. D209-D213.

B [127] **Echlin, P.**, (1968). "Pollen," Scientific American, vol. 218, pp. 4, 80-90, 146 and front cover in April issue.

** **Eggenberger, D.N.**, see Crewe [101, 102].

B [128] **Erben, H.K.**, Flajs, G., and Siehl, A., (1968). "Ammonoids: early ontogeny of ultamicroscopical shell structure," Nature (London), vol. 219, pp. 396-398.

** **Evans, W.A.**, see Sulway [388].

[129] **Everhart, T.E.**, (1958). "Contrast formation in the scanning electron microscope," Ph.D. Diss., Cambridge Univ. (Available in part as ERL-M161 from Electronics Research Laboratory, College of Engineering, Univ. of Calif., Berkeley, Calif. 94720.)

[130] ----, Wells, O.C., and Oatley, C.W., (1959). "Factors affecting contrast and resolution in the scanning electron microscope," J. Electronics and Control, vol. 7, pp. 97-111.

[131] ----, Smith, K.C.A., Wells, O.C., and Oatley, C.W., (1960). "Recent developments in scanning electron microscopy," pp. 269-273 in Bargmann et al (1960).

[132] ---- and Thornley, R.F.M., (1960). "Wide-band detector for micro-microampere low-energy electron currents," J. Sci. Inst., vol. 37, pp. 246-248.

[133] ----, Wells, O.C., and Matta, R.K., (1963). "Evaluation of passivated integrated circuits using the scanning electron microscope," Extended abstracts (Electrochem. Soc.), Electronics Division, vol. 12, no. 2, pp. 2-4. (New York Meeting, Oct. 1963.)

[134] ----, Wells, O.C., and Matta, R.K., (1964a). "Evaluation of passivated integrated circuits using the scanning electron microscope," J. Electrochem. Soc., vol. 111, pp. 929-936.

[135] ----, Wells, O.C., and Matta, R.K., (1964b). "A novel method of semiconductor device measurements," Proc. IEEE, vol. 52, pp. 1642-1647.

[136] ---- (1966a). "Certain semiconductor applications of the scanning electron microscope," pp. 665-676 in McKinley et al (1966).

[137] ---- (1966b). "Deflection-modulation CRT display," Proc. IEEE, vol. 54, pp. 1480-1482.

** ---- see MacDonald [246, 247, 248], Oatley [296] and Wells [436, 438].

[138] **Fairing, J.D.**, (1967). "Examination of fracture surfaces by scanning electron microscopy," J. Composite Materials, vol. 1, pp. 208-210.

** **Fang, F.F.**, see Speth [376].

** **Fetisov, D.V.**, see Kushnir [232, 233, 234].

** **Finnegan, W.G.**, see Odencrantz [303].

** **Flajs, G.**, see Erben [128].

[139] **Flemming, J.P.**, (1968). "A low energy scanned electron beam potential probe," J. Sci. Inst. (J. Phys. E), Series 2, vol. 1, pp. 1179-1182. (Vidicon-type electron optics.)

[140] **Flogel, P.**, Nebauer, E., and 3 others (1968). "Electron microprobe and scanning electron microscope investigations on plate-shaped CdS single crystals," Physica Status Solidi, vol. 29, pp. K89-K90 and 1 plate.

[141] **Forgacs, O.L.**, (1961). "Structural weaknesses in softwood pulp tracheids," Tappi, vol. 44, pp. 112-119.

[142] ---- and Atack, D., (1962). "Distribution of chemical woodpulp and groundwood through the thickness of newsprint," pp. 721-747 in Bolam (1962).

[143] ---- (1963). "The characterization of mechanical pulps," Pulp Paper Mag. Canada (Technical Section), pp. T89-T118; Convention issue.

B [144] **Forrester, J.C.**, Hunt, T.K., Hayes, T.L., and Pease, R.F.W., (1969). "Scanning electron microscopy of healing wounds," Nature (London), vol. 221, pp. 373-374.

B [145] **Fromme, H.G.**, Riedel, H., and Vahl, J., (1967). "Investigations of the inner structure of dental enamel and dentine with the scanning electron microscope" (in Germane, Deutsche Zahnarztliche Z., vol. 22, pp. 395-400.

B [146] ---- (1968). "Forms of biological material in the scanning electron microscope" (in German), Natur und Museum, vol. 98, pp. 482-490.

B [147] **Fujita, T.**, Inoue, H., and Kodama, T., (1968). "Scanning electron microscopy of the normal and rheumatoid synovial membranes," Archivum Histologicum Japonicum, vol. 29, pp. 511-522.

** ---- see Kurahasi [230].

[148] **Gane, N.**, and Bowden, F.P., (1968). "Microdeformation of solids," J. Appl. Phys., vol. 39, pp. 1432-1435.

[149] **Gardner, Mrs. G.A.**, and Cahn, R.W., (1966). "The use of a scanning electron microscope to examine whisker growth on an iron-aluminium alloy," J. Materials Science, vol. 1, pp. 211-212.

** **Gauvin, W.H.**, see Themelis [400, 401].

** **Gavrilovic, J.**, see Holt [198].

[150] **Gaylord, J.W.**, (1966). "Microplasma observations in silicon junctions using a scanning electron beam," J. Electrochem. Soc., vol. 113, pp. 753-754.

** **Gibbs, D.F.**, see Hinton [193].

** **Giele, T.**, see Burrichter [72].

** **Gilroy, J.**, see Brookshier [66].

[151] **Goode, F.N.**, (1966a). "New views of gravure cells," Gravure Mag., vol. 12, pp. 26-29 in issue for October.

[152] ---- (1966b). "Pictures of gravure cells by the Stereoscan method," Print in Britain, vol. 14, pp. 34-36.

** **Grainger, F.**, see Boyde [54].

B [153] **Gray, T.R.G.**, (1967). "Stereoscan electron microscopy of soil microorganisms," Science, vol. 155, pp. 1668-1670.

B [154] **Green, C.D.**, (1967). "Preparation of nematodes for examination under the stereoscan electron microscope," Nematologica (Leiden), vol. 13, pp. 279-282 and 2 plates.

[155] **Green, D.**, and Nathanson, H.C., (1965). "Observation of inversion layers under insulated-gate electrodes using a scanning electron microscope," Proc. IEEE vol. 53, pp. 183-184.

[156] ----, Sandor, J.E., O'Keeffe, T.W., and Matta, R.K., (1965). "Reversible changes in transistor characteristics caused by scanning electron microscope examination," Appl. Phys. Letters, vol. 6, pp. 3-4.

[157] ---- (1966). "A method of examination of semiconductor oxides with a scanning electron microscope," pp. 375-384 in Haddad (1966).

** ---- see Matta [255] and McAvoy [257].

[158] **Green, H.V.**, (1962). "Compression-caused transverse discontinuities in tracheids," Pulp Paper Mag. Canada, (Technical Section), vol. 63, pp. T155-T168.

B [159] **Greenhalgh, G.N.**, (1967). "A note on the conidial scar in the Xylarioceae," The New Phytologist, vol. 66, pp. 65-66 and 2 plates.

B [160] **Greenwood, F.**, and O'Grady, F., (1969). "Antibiotic-induced surface changes in microorganisms demonstrated by scanning electron microscopy," Science, vol. 163, pp. 1076-1077.

** **Grigson, C.W.B.**, see Cole [95].

B [161] **Gross, W.**, Vahl, J., and Ziegler, W., (1968). "Investigations of sieve plates of Dartmuthia (Osteostraci) with the scanning electron microscope" (in German), Palaont.

Z., vol. 42, pp. 73-82 and plates 8-10.

[162] **Grote, K.H. von,** (1967). "Growth of tungsten single-crystals at wire tips" (in German), Naturwissenschaften, vol. 21, pp. 558-559.

B [163] **Guervin, C.,** and Coq, C. Le, (1968). "Use of the scanning electron microscope in caryology" (in French), C.R. Acad. Sci. Paris, vol. 266 D, pp. 1239-1241 and 1 plate.

[164] **Haas, G.A.,** and Thomas, R.E., (1963). "Investigation of the patch effect in uranium carbide," J. Appl. Phys., vol. 34, pp. 3457-3465. (These workers used a scanning electron beam of very low energy in ultra-high vacuum.)

[165] ---- and Thomas, R.E., (1966). "Electron beam scanning technique for measuring surface work function variations," Surface Science (Holland), vol. 4, pp. 64-88. (See comment above.)

** **Hachenberg, O.,** see Knoll [224].

[166] **Haddad, G.I.,** (Ed.) (1966). Proc. Eighth Annual Electron and Laser Beam Symp., Univ. of Michigan, April 1966.

** **Hagon, P.J.,** see Nealey [286].

** **Hahne, D.,** see Riedel [342].

B [167] **Hale, W.G.,** and Smith, A.L., (1966). "Scanning electron microscope studies of cuticular structures in the genus Onychiurus (Collembola)," Rev. Ecol. Biol. Sol (Paris), vol. 3 pp. 343-354.

B [168] **Hancock, J.M.,** and Kennedy, W.J., (1967). "Photographs of hard and soft chalks taken with a scanning electron microscope," Proc. Geol. Soc. London, no. 1643 (Dec.), pp. 249-252 and 4 plates.

** **Handy, R.M.,** see O'Keeffe [304].

[169] **Harris, F.H.,** (1964). "Low velocity electron probe investigation of thin dielectric films," pp. 227-232 in Proc. National Electronics Conf., Chicago.

** **Hashimoto, H.,** see Kimoto [214, 215].

B [170] **Hay, W.W.,** and Sandberg, P.A., (1967). "The scanning electron microscope, a major breakthrough for micropaleontology," Micropaleontology, vol. 13, pp. 407-418.

** ---- see Sandberg [349] and Wise [443].

B [171] **Hayes, T.L.,** Pease, R.F.W., and McDonald, L.W., (1966). "Applications of the scanning electron microscope to biologic investigations," Laboratory Investigation, vol. 15, pp. 1320-1326.

B [172] ----, Pease, R.F.W., and Camp, A.S., (1967). "Stereoscopic scanning electron microscopy of living Tribolium confusum," J. Insect Physiol., vol. 13, pp. 1143-1145 and 2 plates.

B [173] ----, Pease, R.F.W., McDonald, L.W., and Camp, A.S., (1967). "A device for multidimensional electron microscopy," Clin. Res., vol. 15, p. 116.

B [174] ---- and McDonald, L.W., (1968). "Three-dimensional analysis of human blood and marrow using the scanning electron microscope," Clin. Res., vol. 16, p. 121.

B [175] ---- and Pease, R.F.W., (1968). "The scanning electron microscope: principles and applications in biology and medicine," pp. 85-137 in Advances in Biological and Medical Phys., vol. 12, J.H. Lawrence and J.W. Gofman, Ed., Academic Press, N.Y.

B [176] ---- and Pease, R.F.W., (1969). "The scanning electron microscope: a nonfocused, multi-informational image," in the monograph, "Data extraction and processing of optical images in the medical and biological sciences," W.E. Tolles, Ed., The New York Academy of Sciences, Annals, vol. 157, pp. 497-509.

** ---- see Forrester [144], Koehler [225], McDonald [258, 259], Pease [316, 317], Sokoloff [374] and Spencer [375].

[177] **Heinrich, K.F.J.,** (1962). "Oscilloscope readout of electron microprobe data," pp. 291-300 in Mueller and Fay (1962).

[178] ---- (1963). "Interrelationships of sample composition, backscatter coefficient, and target current measurement," pp. 325-339 in Mueller, Mallett and Fay (1963).

[179] ---- (1966). "Bibliography on electron probe microanalysis and related subjects," pp. 979-1030 in McKinley et al (1966).

** ---- see McKinley [262].

** **Hellawell, A.,** see Day [120, 121].

** **Hendy, J.C.,** see Richards [340].

B [180] **Heslop-Harrison, J.,** (1968a). "Wall development in the microspore tetrad of Lilium longiflorum," Canadian J. Botany, vol. 46, pp. 1185-1192. (Deals with the exine, tracing early morphogenesis.)

B [181] ---- (1968b). "Pollen wall development," Science, vol. 161, pp. 230-237, index page and front cover for July 19 issue. (General review of work on pollen grain wall.)

B [182] ---- (1968c). "Tapetal synthesis of pollen coat substances in Lilium longiflorum," New Phytologist, vol. 67, pp. 779-786. (Includes one SEM image of the pollen wall.)

B [183] ---- (1968d). "The emergence of pattern in the cell walls of higher plants," pp. 118-150 in "The Emergence of Order in Developing Systems," 1968 Symp. Soc. Dev. Biology, M. Locke (Ed.), Developmental Biology, Supplement 2, Academic Press, N.Y. (Shows endothecial thickenings of spore walls.)

B [184] ---- and Dickinson, H.G., (1968). "Time relationships of the sporopollenin synthesis associated with tapetum and microspores in Lilium," Planta, vol. 84, pp. 199-214. (Has 2 SEM images of spores and tapetum.)

[185] **Heymann, K.,** Riedel, W., Blaschke, R., and Pfefferkorn, G., (1968). "Scanning electron microscopy of etched plastics and metals electroplated onto plastics" (in German), Kunststoffe, vol. 58, pp. 309-312.

[186] **Higuchi, H.,** Tauchi, S., and Kimura, H., (1964). "Amplification of bombarding electron beam current in transistors," Extended abstracts (Electrochem. Soc.), Electronics Division, vol. 13, No. 1, pp. 140-141 (Toronto Meeting, May 1964).

[187] ---- and Maki, M., (1965). "Observations of channels of MOS field-effect transistors using the scanning electron microscope," Japan. J. Appl. Phys., vol. 4, pp. 1021-1022.

[188] ---- and Tamura, H., (1965). "Measurement of the lifetime of minority carriers in semiconductors with a scanning electron microscope," Japan. J. Appl. Phys. vol. 4, pp. 316-317.

** ---- see Kimura [218, 219].

[189] **Hill, B.H.,** (1968). "Simple device for measuring beam current in a scanning electron microscope," Rev. Sci. Inst., vol. 39, p. 1369.

B [190] **Hiller, U.,** and Blaschke, R., (1967). "Examination of the gecko foot" (in German), Naturwissenschaften, vol. 54, pp. 344-345.

** **Hillier, J.,** see Zworykin [451].

B [191] **Hinton, H.E.,** (1966a). "Plastron respiration in marine insects," Nature (Lond.), vol. 209, pp. 220-221.

B [192] ---- (1966b). "The spiracular gill of the fly, Antocha bifida, as seen with the scanning electron microscope," Proc. R. Ent. Soc. London (A), vol 41, pp. 107-115 and 1 plate.

B [193] ---- and Gibbs, D.F., (1969). "Diffraction gratings in Phalacrid beetles," Nature (London), vol. 221, pp. 953-954.

** **Hirsh, P.B.,** see Booker [35].

B [194] **Hobdell, M.H.,** and Boyde, A., (1969). "Microradiography and scanning electron microscopy of bone sections," Z. Zellforsch., vol. 94, pp. 487-494.

** ---- see Boyde [55].

B [195] **Hoffman, S.,** McEwan, W.S., and Drew, C.M., (1968). "Scanning electron microscopy of dental enamel," J. Dental Res., vol. 47, p. 842.

B [196] ----, McEwan, W.S., and Drew, C.M., (1969). "Scanning electron microscopy studies of dental enamel," J. Dental Res., Apr-May issue.

** **Hohling, H.J.,** see Vahl [424].

[197] **Holt, D.B.,** and Chase, B.D., (1968). "Scanning electron beam excited charge collection micrography of GaAs lasers," J. Materials Science, vol. 3, pp. 178-182.

[198] ----, Gavrilovic, J., and Jones, M.P., (1968). "Scanning electron beam anomalous transmission patterns," J. Materials Science, vol. 3, pp. 553-558.

B [199] **Honjo, S.,** and Berggren, W.A., (1967). "Scanning electron microscope studies of planktonic Foraminifera," Micropaleontology, vol. 13, pp. 393-406 and 4 plates.

B [200] ----, Minoura, N., and Okada, H., (1967). "Study of nannofossils by the scanning electron microscope," J. Fac. Science Hokkaido Univ., Series IV, Geol. and Mineralogy, vol. 13, pp. 427-431 and plates 51 and 52.

B [201] ---- and Okada, H., (1968). "Scanning electron microscopy of planktonic Foraminifera: a preparation technique," J. Fac. Science Hokkaido Univ., Series IV, Geol. and Mineralogy, vol. 14, pp. 71-76 and plates 17-19.

** ---- see Kimoto [216].

[202] **Hopf, D.**, (1941). "Image formation of conducting surface layers in the scanning electron microscope" (in German), Ph.D. Diss., Technische Hochschule Berlin.

[203] **Horn, R.A.**, and Simmonds, F.A., (1968). "Microscopical and other fibre characteristics of high-yield sodium bisulfite pulps from balsam fir," Tappi, vol. 51, pp. 67A-73A.

B [204] **Horridge, G.A.**, and Tamm, S.L., (1969). "Critical point drying for scanning electron microscopic study of ciliary motion," Science, vol. 163, pp. 817-818.

[205] **Houwink, A.L.**, and Spit, B.J., (Ed.) (1961). Proc. European Regional Conf. on Electron Microscopy, Delft, Aug. 1960. De Nederlandse Vereniging Voor Electronenmicroscopie, Delft, 1961.

[206] **Howes, V.R.**, (1967). "Observations of a metal-oxide interface," Nature (London) vol. 216, pp. 362. (Shows cross-section of a fractured oxide film.)

[207] **Hughes, K.A.**, Sulway, D.V., Wayte, R.C., and Thornton, P.R., (1967). "Application of secondary electron channel multipliers to scanning electron microscopy," J. Appl. Phys., vol. 38, pp. 4922-4923.

** ---- see Davies [115], Neve [288, 289], Shaw [359], Sulway [387, 388] and Thornton [411, 414].

** **Humiston, L.E.**, see Odencrantz [302].

** **Humpage, J.**, see Richards [340].

** **Hunt, T.K.**, see Forrester [144].

** **Hutchinson, J.D.**, see Thornley [408].

** **Ichinokawa, T.**, see Shirai [363, 364].

** **Ing, D.W.**, see McAvoy [257].

** **Inoue, H.**, see Fujita [147].

** **Isaacson, M.**, see Crewe [104].

** **Ivanov, R.D.**, see Spivak [378].

** **Jakubovics, J.P.**, see Joy [213].

** **James, D.W.F.**, see Thornton [412].

** **James, D.W.**, see Boyde [54].

B [208] **Jannin, F.**, (1968). "On the topology and size of pores in some Nodosariidae in Albian strata from the Prefecture Aube" (in French), C.R. Acad. Sci. Paris, vol. 266 D, pp. 321-324 and 2 plates.

** ---- see Malapris [252].

B [209] **Jaques, W.E.**, Coalson, J., and Zervins, A., (1965). "Application of the scanning electron microscope to human tissues - A preliminary survey," Exp. and Molecular Pathology, vol. 4, pp. 576-580.

** **Jeffery, J.W.**, see Chatterji [85, 86, 87] and Majumdar [250].

[210] **Johari, O.**, (Ed.) (1968a). "The scanning electron microscope - the instrument and its applications," Proc. Seminar held at IIT Reseach Institute, Chicago, April 30-May 1.

[211] ---- (1968b). "Comparison of transmission electron microscopy and scanning electron microscopy of fracture surfaces," J. Metals, vol. 20, pp. 26-32 in June issue.

** **Johnson, D.**, see Crewe [104].

** **Johnson, N.W.**, see Poole [330].

B [212] **Jones, D.**, (1967). "Examination of mycological specimens in the scanning electron microscope," Trans. Br. Mycol. Soc., vol. 50, pp. 690-691 and 1 plate.

** **Jones, M.P.**, see Holt [198].

** **Jones, S.J.**, see Boyde [50].

[213] **Joy, D.C.**, and Jakubovics, J.P., (1968). "Direct observation of magnetic domains by scanning electron microscopy," Phil. Mag., vol. 17, pp. 61-69. (See Banbury and Nixon, 1967.)

** **Juleff, E.M.**, see Varker [426].

** **Kaiser, R.H.**, see Casey [75].

** **Kennedy, W.J.**, see Hancock [168].

[214] **Kimoto, S.**, and Hashimoto, H., (1966). "Stereoscopic observation in scanning microscopy using multiple detectors," pp. 480-489 in McKinley et al (1966).

[215] ----, Hashimoto, H., and Sato, M., (1966). "On a scanning electron microscope," pp. 197-198 in Uyeda (1966). (Compares backscattered image and secondary electron image from same area.)

B [216] ---- and Honjo, S., (1968). "Scanning electron microscope as a tool in geology and biology," J. Fac. Science Hokkaido Univ., Series IV, Geol. and Mineralogy, vol. 14, pp. 57-69 and plates 11-16.

[217] ---- and Russ, J.C., (1969). "The characteristics and applications of the scanning electron microscope," American Scientist, vol. 57, pp. 112-133.

[218] **Kimura, H.,** Higuchi, H., Maki, M., and Tamura, H., (1966). "Observation of semiconductor elements using scanning electron microscope," J. Electron Microscopy (Japan), vol. 15, pp. 21-25.

[219] ----, Higuchi, H., Tamura, H., and Maki, M., (1966). "New scanning electron microscope and its applications," pp. 195-196 in Uyeda (1966).

** ---- see Higuchi [186] and Tamura [392].

[220] **Knoll, M.,** (1935). "Static potential and secondary emission of bodies under electron irradiation" (in German), Z. Techn. Phys., vol. 11, pp. 467-475.

[221] ---- and Theile, R., (1939). "Scanning electron microscope for determining the topography of surfaces and thin layers" (in German), Z. Phys., vol. 113, pp. 260-280.

[222] ---- (1941a). "Deflecting action of a charged particle in the electric field of a secondary emitting cathode" (in German), Naturwissenschaften, vol. 29, pp. 335-336.

[223] ---- (1941b). "Demonstration of the existence of oxidised layers on iron with the scanning electron microscope" (in German), Phys. Z., vol. 42, pp. 120-122 and one plate.

[224] ----, Hachenberg, O., and Randmer, J., (1944). "On the mechanism for secondary electron emission from inside ionic crystals" (in German), Z. Physik, vol. 122, pp. 137-162.

** **Kodama, T.,** see Fujita [147].

B [225] **Koehler, J.K.,** and Hayes, T.L.; (1969). "The rotifer jaw: a scanning transmission electron microscope study," J. Ultrastructure Res., in press.

** **Komolova, L.F.,** see Spivak [380].

[226] **Koran, Z.,** (1967). "Electron microscopy of radial tracheid surfaces of black spruce separated by tensile failure at various temperatures," Tappi, vol.50, pp. 60-67.

[227] ---- (1968). "Electron microscopy of tangential tracheid surfaces of black spruce produced by tensile failure at various temperatures," Svensk Papperstidning, in press.

[228] **Korda, E.J.,** Pruden, L.H., and Williams, J.P., (1967). "Scanning electron microscopy of a P-16 phosphor - cathodoluminescent and secondary electron emission modes," Appl. Phys. Letters, vol. 10, pp. 205-206.

[229] ----, Pruden, L.H., and Williams, J.P., (1969). "Three-dimensional and stereo observations in glass and ceramic systems," J. Amer. Ceramic Soc., vol. 52, pp. 46-51.

** ---- see Pruden [332].

** **Kruger, J.,** see Ugiansky [420].

** **Krygin, V.M.,** see Vertsner [428].

B [230] **Kurahasi, K.,** Tokunaga, J., Fujita, T., and Miyahara, M., (1969). "Scanning electron microscopy of isolated mitochondria I," Archivum Histologicum Japonicum, vol. 30, pp. 217-232.

[231] **Kurshan, J.,** (Ed.) (1964). Proc. Symp. on Analytical Characterization of Materals (available from RCA Laboratories, Princeton, New Jersey). (See also pp. 24-30 in Physics Today, issue for July 1964.)

[232] **Kushnir, Yu.M.,** Fetisov, D.V., Raspletin, K.K., and 4 others (1961). "Scanning electron microscope and x-ray microanalyzer," Bull. Acad. Sci. USSR Physical Series (USA), vol. 25, pp. 709-714, 1962. Translated from Izv. Akad. Nauk SSSR Ser. Fiz., vol. 25, pp. 695-700; (1961).

[233] ----, Fetisov, D.V., Der-Shvarts, G.V., and 9 others (1963). "Scanning electron microscope-x-ray microanalyser with magnetic electron optics," Bull. Acad. Sci. USSR Physical Series (USA), vol. 27, pp. 1146-1151. Translated from Izv. Acad. Nauk SSSR Ser. Fiz., vol. 27, pp. 1166-1172.

[234] ----, Fetisov, D.V., Raspletin, K.K., and 5 others (1963). "Improvement of a scanning microscope and local x-ray microanalyser and some applications of the instrument," Bull. Acad. Sci. USSR Physical Series (USA), vol. 27, pp. 421-425. Translated from Izv. Acad. Nauk SSSR Ser. Fiz., vol. 27, pp. 415-419.

** **Kyaw, H.,** see Sulway [389] and Thornton [414].

[235] **Kyser, D.F.,** and Wittry, D.B., (1966). "Cathodoluminescence in gallium arsenide," pp. 691-714 in McKinley et al (1966).

** ---- see Wittry [445, 446, 448].

** **Laakso, C.W.,** see Matare [254] and Nealey [286].

[236] **Laffitte, R.,** and Noel, D., (1967). "On the formation of lithographic calcites" (in French), C.R. Acad. Sci. Paris, vol. 264 D, pp. 1379-1382 and 2 plates.

[237] **Lander, J.J.**, Schreiber, H., Buck, T.M., and Mathews, J.R., (1963). "Microscopy of internal crystal imperfections in silicon p-n junction diodes by use of electron beams," Appl. Phys. Letters, vol. 3, pp. 206-207.

[238] **Larkin, M.W.**, and Matta, R.K., (1967). "The electron beam fabrication of small geometry transistors," Solid-State Electronics, vol. 10, pp. 491-496 and 4 plates.

** ---- see Matta [255].

** **Lenz, F.**, see Mollenstedt [270].

B [239] **Lester, K.S.**, and Boyde, A., (1967). "Electron microscopy of predentinal surfaces," Calc. Tiss. Res., vol. 1, pp. 44-54.

B [240] ---- and Boyde, A., (1968a). "The question of von Korff fibres in mammalian dentine," Calc. Tiss. Res., vol. 1, pp. 273-287.

B [241] ---- and Boyde, A., (1968b). "Some preliminary observations on caries ('remineralization') crystals in enamel and dentine by surface electron microscopy," Virchows Arch. Abt. A Path. Anat., vol. 344, pp. 196-212.

** ---- see Boyde [47, 48, 49, 51].

[242] **Leuteritz, K.**, Pietzner, H., and Vahl, J., (1969). "Investigation of cosmic dust in sedimentary rocks" (in German), Fortschr. Geol. Rheinld. u. Westf., vol. 17, pp. 1-8, 10 plates and 9 caption pages.

** **Levin, E.R.**, see Woodward [450].

** **Lewis, C.**, see Thornton [412].

B [243] **Lewis, S.M.**, Osborn, J.S., and Stuart, P.R., (1968). "Demonstration of an internal structure within the red blood cell by ion etching and scanning electron microscopy," Nature (London), vol. 220, pp. 614-616.

** **Lindsay, R.A.**, see Buchanan [68].

** **Lomunov, R.I.**, see Vertsner [427].

[244] **Long, J.V.P.**, (1962). "Recent advances in electron-probe analysis," pp. 276-290 in Mueller and Fay (1962).

[245] **Lyne, L.M.**, (1967). "The application of the scanning electron microscope to the study of printability," pp. 295-313 in "Paper in the printing process," Proc. Eighth Int. Conf. of Printing Research Institutes, Aulanko, Finland, 1965. W.H. Banks, Ed. Pergamon Press, N.Y.

[246] **MacDonald, N.C.**, and Everhart, T.E., (1965). "Direct measurement of the depletion layer width variation vs applied bias for a p-n junction," Appl. Phys. Letters, vol. 7, pp. 267-269.

[247] ---- and Everhart, T.E., (1967). "Scanning electron microscope investigation of planar diffused p-n junction profiles near the edge of a diffusion mask," J. Appl. Phys., vol 38, pp. 3685-3692.

[248] ---- and Everhart, T.E., (1968). "Selective electron-beam irradiation of metal-oxide-semiconductor structures," J. Appl. Phys., vol. 39, pp. 2433-2447.

** ---- see Robinson [344].

[249] **Mackintosh, I.M.**, (1965). "Applications of the scanning electron microscope to solid-state devices," Proc. IEEE, vol. 53, pp. 370-377.

** ---- see Thornhill [403].

[250] **Majumdar, A.J.**, Nurse, R.W., Chatterji, S., and Jeffery, J.W., (1966). "Three-dimensional view of phase separation in glass ceramics," Nature (London), vol. 211, pp. 622-624.

[251] ----, Ryder, J.F., and Rayment, D.L., (1968). "Fracture studies in glass-reinforced gypsum plaster using the scanning electron microscope," J. Materials Science, vol. 3, pp. 561-563 and front cover.

** **Maki, M.**, see Higuchi [187] and Kimura [218, 219].

B [252] **Malapris, M.**, and Jannin, F., (1967). "Use of scanning electron microscope for study of Foraminifera" (in French), C.R. Acad. Sci. Paris, vol. 264 D, pp. 247-249 and 1 plate.

** **Marszalek, D.S.**, see Small [367].

** **Martineau, M.**, see Davoine [118].

[253] **Marton, L.**, (Ed.) (1969). Record IEEE 10th. Ann. Symp. on Electron, Ion, and Laser Beam Technology held at Gaithersburg, Md., May, 1969. (San Francisco Press; see Pease 1967a.)

** **Mason, S.G.**, see Sepall [357].

** **Massarani, B.**, see Spivak [379].

** **Masterton, H.G.**, see Castle [76, 77].

[254] **Matare, H.F.**, and Laakso, C.W., (1968). "Scanning electron beam display of dislocation space charge," Appl. Phys. Letters, vol. 13, pp. 216-218. (Obtained image using transverse photovoltage effect.)

** **Mathews, J.R.**, see Lander [237].

[255] **Matta, R.K.**, Green, D., and Larkin, M.W., (1965). "The use of the scanning electron microscope in the fabrication of an integrated circuit," Extended abstracts (Electrochem. Soc.), Electrothermics and Metallurgy Division, vol. 3, no. 1, pp. 32-33. (San Francisco Meeting, May 1965.)

** ---- see Everhart [133, 134, 135], Green [156], Larkin [238], Thornhill [404] and Wells [436, 438].

** **Matteudi, G.**, see Pinard [326].

** **May, W.D.**, see Atack [11].

[256] **McAuslan, J.H.L.**, and Smith, K.C.A., (1957). "The direct observation in the scanning microscope of chemical reactions," pp. 343-345 in Sjostrand and Rhodin (1957).

** ---- see Bowden [38].

[257] **McAvoy, B.R.**, Green, D., Ing, D.W., and Ure, R.W., (1969). "Study of inhomogeneities in GaAs using a scanning electron microscope," Appl. Phys. Letters, vol. 14, pp. 16-18.

B [258] **McDonald, L.W.**, Pease, R.F.W., and Hayes, T.L., (1967). "Scanning electron microscopy of sectioned tissue," Laboratory Investigation, vol. 16, pp. 532-538.

B [259] ---- and Hayes, T.L., (1969). "Correlation of scanning electron microscope and light microscope images of individual cells in human blood clots," Experimental and Molecular Pathology, in press.

** ---- see Hayes [171, 173, 174].

** **McEwan, W.S.**, see Hoffman [195, 196] and Odencrantz [303].

B [260] **McFarlane, J.E.**, (1965). "The surface structures of various layers of the house cricket eggshell as seen in the scanning electron microscope," Canadian J. Zool., vol. 43, pp. 911-913.

[261] **McGrath, J.T.**, Buchanan, J.G., and Thurston, R.C.A., (1962). "A study of fatigue and impact fractures with the scanning electron microscope," J. Inst. Metals (England) vol. 91, Pt 1, pp. 34-39.

[262] **McKinley, T.D.**, Heinrich, K.F.J., and Wittry, D.B., (Eds.) (1966). The Electron Microprobe, Proc. Symp. held in Washington, D.C., Oct. 1964. John Wiley and Sons, New York, 1966.

[263] **McMullan, D.**, (1952). "Investigations relating to the design of electron microscopes," Ph.D. Diss., Cambridge Univ.

[264] ---- (1953a). "The scanning electron microscope and the electron-optical examination of surfaces," Electronic Engineering (England), vol. 25, pp. 46-50.

[265] ---- (1953b). "An improved scanning electron microscope for opaque specimens," Proc. IEE (England), vol. 100, Pt II, pp. 245-259.

[266] **Minkoff, I.**, (1966a). "Observations of spherulitic graphite growth with the scanning electron microscope," Acta Metallurgica, vol. 14, pp. 551-552.

[267] ---- (1966b). "Hole formation in crystal growth by surface adsorbtion of an impurity," Phil. Mag., vol. 12, pp. 1083-1086.

[268] ---- and Nixon, W.C., (1966). "Scanning electron microscopy of graphite growth in iron and nickel alloys," J. Appl. Phys., vol. 37, pp. 4848-4855.

[269] ---- (1967). "Applications of the scanning electron microscope in materials science," J. Materials Science, vol. 2, pp. 388-394.

** **Minoura, N.**, see Honjo [200].

** **Miyahara, M.**, see Kurahasi [230].

[270] **Mollenstedt, G.**, and Lenz, F., (1963). "Electron emission microscopy," pp. 251-329 in Advances in Electronics and Electron Physics, L. Marton and C. Marton, Ed., Academic Press, N. Y.

** ---- see Bargmann [18].

B [271] **Morgenroth, K.**, Backmann, R., and Blaschke, R., (1968). "On the forms of deposits of calcium oxalate in the human kidney in oxalosis" (in German), Beitr. Path. Anat., vol. 136, pp. 454-463.

** ---- see Amelunxen [5] and Blumcke [30].

** **Morris, E.L.**, see Atack [11].

** **Morris, H.H.**, see Brooks [65] and Sennett [356].

[272] **Morris, W.G.**, (1965). "Scanning electron microscopy of the surface structure of iron whiskers;" Ph.D. Diss., MIT.

** **Morton, G.A.**, see Zworykin [452].

** **Moss, J.S.**, see Sikorski [365].

[273] **Mueller, W.M.**, or Mueller et al, beginning (1957). Advances in X-Ray Analysis, Proc. Sixth et seq. Annual Conferences on

Application of X-Ray Analysis, Univ. of Denver. Plenum Press, New York, N.Y.

[274] **Munakata, C.**, (1965). "Measurement of the homogeneity of a semiconductor with an electron beam," Japan. J. Appl. Phys., vol. 4, p. 815.

[275] ---- (1966a). "Detection of resistivity striations in a Ge crystal with an electron beam," Japan. J. Appl. Phys., vol. 5, p. 336.

[276] ---- (1966b). "On the voltage induced by an electron beam in a bulk semiconductor crystal," Japan. J. Appl. Phys., vol. 5, pp. 756-763.

[277] ---- (1966c). "Applications of the barrier electron voltaic effect," pp. 357-374 in Haddad (1966).

[278] ---- (1966d). "Measurement of minority carrier lifetime with a non-ohmic contact and an electron beam," Microelectronics and Reliability, vol. 5, pp. 267-270 and 2 plates.

[279] ---- and Todokoro, H., (1966). "A method of measuring lifetime for minority carriers induced by an electron beam in germanium," Japan. J. Appl. Phys., vol. 5, p. 249.

[280] ---- (1967a). "Detection of resistivity variation in a semiconductor pellet with an electron beam," Microelectronics and Reliability, vol. 6, pp. 27-33 and 2 plates.

[281] ---- (1967b). "An electron beam method of measuring diffusion voltage in semiconductors," Japan. J. Appl. Phys., vol. 6, p. 274.

[282] ---- (1967c). "Measurement of potential distribution in a semiconductor crystal with an electron beam," Japan. J. Appl. Phys., vol. 6, pp. 548-549.

[283] ---- (1967d). "An electron beam method of measuring resistivity distribution in semiconductors," Japan. J. Appl. Phys., vol. 6, pp. 963-971.

[284] ---- (1968a). "An application of beta conductivity to measurement of resistivity distribution," J. Sci. Inst. (J. Phys. E), Series 2, vol. 1, pp. 639-642.

[285] ---- (1968b). "Voltage signal due to electron-beam-induced conductivity in semiconductors," Japan. J. Appl. Phys., vol. 7, pp. 1051-1055. (See pp. 580-585 in Bakish, 1968.)

** **Nathanson, H.C.**, see Green [155].

[286] **Nealey, C.C.**, Laakso, C.W., and Hagon, P.J., (1966). "Planar silicon device analyses with the electron microprobe microanalyser," pp. 748-783 in McKinley et al (1966). (Has data on irradiated planar silicon transistors.)

** **Nebauer, E.**, see Flogel [140].

B [287] **Neurath, P.W.**, Ampola, M.G., and Vetter, H.G., (1967). "Scanning electron microscopy of chromosomes," The Lancet, vol. 2 for 1967, pp. 1366-1367.

[288] **Neve, N.F.B.**, Hughes, K.A., and Thornton, P.R., (1966). "Scanning electron microscope as a means of studying microplasmas at high resolution," J. Appl. Phys., vol. 37, pp. 1704-1709.

[289] ----, Sulway, D.V., Hughes, K.A., and Thornton, P.R., (1966). "The scanning electron microscope as a means of investigating second breakdown and similar phenomena," IEEE Trans. on Electron Devices, vol. ED-13, pp. 639-642.

[290] ---- and Thornton, P.R., (1966). "Electrical effects of crystal imperfections studied by scanning electron microscopy," Solid-State Electronics, vol. 9, pp. 900-901 and 2 plates.

** ---- see Shaw [359] and Thornton [413].

** **Newman, P.H.**, see Sikorski [365].

** **Nichols, D.**, see Currey [108].

** **Niehrs, H.**, see Bargmann [18].

[291] **Nissen, H.U.**, and Blaschke, R., (1968). "The fracture surfaces of feldspars in scanning and transmission electron micrographs," Photographische Korrespondenz, vol. 104, pp. 105-107.

[292] **Nixon, W.C.**, (1964). "Scanning electron microscopy," J. Royal Microscopical Soc., vol. 83, pts. 1 and 2, pp. 213-216. Reprinted in Microelectronics and Reliability, vol. 4, pp. 55-57; 1965.

[293] ---- (1969). "Scanning electron microscopy," Contemporary Physics, vol. 10, pp. 71-96.

** ---- see Banbury [16], Chang [79, 80, 81, 82, 83], Minkoff [268], Oatley [298], Paden [307], Pease [313, 314] and Plows [328].

[294] **Noel, D.**, (1968). "Nature and origin of the alternating strata of calcite-clay mixtures and calcites in upper Barremian near Angles (Vocontien hollow, Prefecture Basses-Alpes)" (in French), C.R. Acad. Sci. Paris, vol. 266 D, pp. 1223-1225 and 2 plates.

** ---- see Laffitte [236].

[295] **Northrop, D.C.,** Thornton, P.R., and Trezise, K.W., (1964). "Electrical transients in high resistivity gallium arsenide," Solid-State Electronics vol. 7, pp. 17-30.

** **Nurse, R.W.,** see Majumdar [250].

[296] **Oatley, C.W.,** and Everhart, T.E., (1957). "The examination of p-n junctions with the scanning electron microscope," J. Electronics, vol. 2, pp. 568-570 and 1 plate.

[297] ---- (1958). "The scanning electron microscope," New Scientist (England), pp. 153-155 in issue for 12 June.

[298] ----, Nixon, W.C., and Pease, R.F.W., (1965). "Scanning electron microscopy," pp. 181-247 in Advances in Electronics and Electron Physics, vol. 21, L. Marton, Ed., Academic Press, New York, N.Y.

B [299] ---- (1966a). "The scanning electron microscope," Spectrum (Central Office of Information, London), March 1966, pp. 6-8.

[300] ---- (1966b). "New electron-probe instruments," Electronics and Power, vol. 12, pp. 282-285.

[301] ---- (1966c). "The scanning electron microscope," Science Progress (Oxford), vol. 54, pp. 483-495.

** ---- see Everhart [130, 131] and Smith [369].

[302] **Odencrantz, F.K.,** and Humiston, L.E., (1968). "Replicator for ice crystals," Rev. Sci. Inst., vol. 39, pp. 1870-1872.

[303] ----, McEwan, W.S., Amand, P.St., and Finnegan, W.G., (1968). "Mechanism for multiplication of atmospheric ice crystals: apparent charge distribution on laboratory crystals," Science, vol. 160, pp. 1345-1346 and front cover.

** **O'Grady, F.,** see Greenwood [160].

** **Okada, H.,** see Honjo [200, 201].

[304] **O'Keeffe, T.W.,** and Handy, R.M., (1967). "Fabrication of planar silicon transistors without photoresist," Solid-State Electronics, vol. 11, pp. 261-266 and 2 plates. (Describes enhanced etch-rate effect.)

** ---- see Green [156].

** **Onoguchi, A.** see Shirai [363, 364].

** **Osborn, J.S.,** see Lewis [243].

[305] **Ovsyuk, V.N.,** and Smirnov, L.S., (1965). "Effect of electron bombardment on the surface states of germanium," Soviet Physics - Solid State (USA), vol. 6, pp. 2413-2418. Translated from Fiz. Tver. Tela, vol. 6, pp. 3031-3037.

[306] **Paden, R.S.,** (1968). "Scanning and transmission electron microscopy with energy analysis and variable impact energy," Ph.D. Diss., Cambridge Univ.

[307] ---- and Nixon, W.C., (1968). "Retarding field scanning electron microscopy," J. Sci. Inst. (J. Phys. E), Series 2, vol. 1, pp. 1073-1080.

[308] **Paris, J-P.,** (1965). "Time-dependent changes in the properties of semiconducting and ionic crystals under bombardment with medium-energy electrons" (in French), Ph.D. Diss., Lyon Univ.

** ---- see Pinard [326].

** **Patel, J.R.,** see Czaja [110].

** **Pavlyuchenko, O.P.,** see Spivak [378].

B [309] **Pawlowitzki, I.H.,** Blaschke, R., and Christenhusz, R., (1968). "Representation of chromosomes in the scanning electron microscope after contact with enzymes" (in German), Naturwissenschaften, vol. 55, pp. 63-64.

[310] **Pease, R.F.W.,** (1963). "High resolution scanning electron microscopy," Ph.D. Diss., Cambridge Univ.

[311] ---- (1965). "The determination of the area of emission of reflected electrons in a scanning electron microscope," J. Sci. Inst., vol. 42, pp. 158-159.

[312] ----, Broers, A.N., and Ploc, R.A., (1965). "Scanning electron microscopy of the growth and subsequent sectioning by sputtering of iron oxide films," pp. 389-390 in Titlebach (1965).

[313] ---- and Nixon, W.C., (1965a). "High resolution scanning electron microscopy," J. Sci. Inst., vol. 42, pp. 31-35.

[314] ---- and Nixon, W.C., (1965b). "Microformation of filaments," pp. 220-230 in Bakish (1965).

[315] ---- and Ploc, R.A., (1965). "Scanning electron microscopy as applied to the oxidation of iron," Trans. Met. Soc. AIME, vol. 233, pp. 1949-1954.

B [316] ---- and Hayes, T.L., (1966). "Scanning electron microscopy of biological material," Nature (London), vol. 210, p. 1049. (Observes selectively absorbed cathodoluminescent dyes by the luminescent method.)

B [317] ----, Hayes, T.L., Camp, A.S., and Amer, N.M., (1966). "Electron microscopy of living insects," Science, vol. 154, pp. 1185-1186.

[318] ---- (Ed.) (1967a). Record IEEE 9th. Ann. Symp. on Electron, Ion and Laser Beam Technology, Berkeley, 9-11 May 1967 (San Francisco Press, 255 12th. St., San Francisco, Calif.).

[319] ---- (1967b). "The scanning electron microscope," IEEE Spectrum, vol. 4, pp. 96-102 in issue for October.

** ---- see Forrester [144], Hayes [171, 172, 173, 175, 176], McDonald [258], Oatley [298] and Sokoloff [374].

** **Pentoney, R.E.,** see Debaise [122].

** **Pereverzev, N.A.,** see Spivak [377].

B [320] **Peveling, E.,** and Vahl, J., (1968). "Possibilities of freeze etching for scanning electron microscopy" (in German), Z. Wissenschaftliche Mikroskopie und Mikroskopische Technik, vol. 69, pp. 11-17.

** ---- see Reznik [339].

[321] **Pfefferkorn, G.,** and Blaschke, R., (1967). "Scanning electron microscope for surface investigations" (in German), Umschau in Wiss. und Technik, vol. 18, pp. 584-590.

[322] ---- and Blaschke, R., (1968a). "New possibilities of surface investigation in paint research with electron microscopic scanning" (in German), Fette Seiffen Anstrichmittel, vol. 70, pp. 413-417.

[323] ---- and Blaschke, R., (1968b). "Scanning electron microscopy of dust particle surfaces" (in German), Staub Reinhaltung der Luft, vol. 28, pp. 440-444.

[324] ---- and Schur, K., (1968). "Examination of corroded metal surfaces" (in German), Werkstoffe und Korrosion, vol. 19, pp. 855-862.

** ---- see Heymann [185], Predel [331] and Vahl [422, 424].

** **Pfeiffer, R.A.,** see Christenhusz [88].

** **Picksak, T.,** see Amelunxen [5].

** **Pietzner, H.,** see Leuteritz [242].

[325] **Pinard, P.,** (1964). "Study of cathodoluminescence using the scanning electron microscope" (in French), Ph.D. Diss., L'Univ. de Lyon.

[326] ----, Paris, J-P., and Matteudi, G., (1964). "Secondary electron emission from cadmium sulfide" (in French), C.R. Acad. Sci. Paris, vol. 259, pp. 2187-2189.

** ---- see Bernard [27] and Davoine [117, 118, 119].

** **Ploc, R.A.,** see Pease [312, 315].

[327] **Plows, G.S.,** (1968). "Stroboscopic scanning electron microscopy," Ph.D. Diss., Cambridge Univ.

[328] ---- and Nixon, W.C., (1968). "Stroboscopic scanning electron microscopy," J. Sci. Inst. (J. Phys. E), Series 2, vol. 1, pp. 595-560.

B [329] **Poole, D.F.G.,** (1966). "The use of the microscope in dental research," British Dental J., vol. 121, pp. 71-79.

B [330] ---- and Johnson, N.W., (1967). "The effects of different demineralizing agents on human enamel surfaces studied by scanning electron microscopy," Archs. Oral Biol. (G.B.), vol. 12, pp. 1621-1634 and 4 plates.

** **Porter, A.W.,** see Debaise [122].

[331] **Predel, B.,** Pfefferkorn, G., and Blaschke, R., (1967). "Use of the scanning electron microscope in metals research," Praktische Metallographie (Stuttgart), vol. 4, pp. 559-573.

[332] **Pruden, L.H.,** Korda, E.J., and Williams, J.P., (1967). "Characterisation of surface topography with the scanning electron microscope," Amer. Cer. Soc. Bull., vol. 46, pp. 750-755.

** ---- see Korda [228, 229].

[333] **Pye, I.T.,** Washburn, O.V., and Buchanan, J.G., (1966). "Structural changes in paper on pressing and drying," pp. 353-367 in Bolam (1966).

** **Quilliam, T.A.,** see Boyde [44].

** **Ramberg, E.G.,** see Zworykin [452].

** **Randmer, J.,** see Knoll [224].

** **Raspletin, K.K.,** see Kushnir [232, 234].

** **Rayment, D.L.,** see Majumdar [251].

** **Reimer, L.,** see Schur [354].

** **Reith, E.J.,** see Boyde [56].

B [334] **Resch, A.,** and Blaschke, R., (1968). "Application of the Stereoscan electron microscope in wood anatomy" (in German), Planta (Berlin), vol. 78, pp. 85-88.

[335] **Reumuth, H.,** (1967a). "A new electron microscope Stereoscan 1966 and its first results from textiles" (in German), Z. fur die gesamte Textilindustrie, vol. 69, pp. 227-236.

[336] ---- (1967b). "Comparison of capabilities and principles between light microscopy, transmission microscopy and the new scanning electron microscope Stereoscan 1966" (in German), Melliand Textilberichte, vol. 5, pp. 489-501.

B [337] **Reyre, Y.**, (1968a). "Additional information on the structure and shape of prepollens in genera Classopollis (Pflug) Pocock and Jansonius. Applications in paleobotany and stratigraphy" (in French), C.R. Acad. Sci. Paris, vol. 266 D, pp. 1233-1235 and 2 plates.

B [338] ---- (1968b). "Value in taxonomy of the topography of pollens of Gymnosperms and Chlamydosperms" (in French), C.R. Acad. Sci. Paris, vol. 267 D, pp. 160-162 and 1 plate.

** ---- see Bourreil [37].

B [339] **Reznik, H.**, Peveling, E., and Vahl, J., (1968). "Different forms of holdfast-organs in some lichens. Studies with the Stereoscan scanning electron microscope and the transmission microscope" (in German), Planta (Berlin), vol. 78, pp. 287-292.

** **Rhodin, J.**, see Sjostrand [366].

[340] **Richards, H.D.**, Humpage, J., and Hendy, J.C., (1968). "Topography control of plated wire memory elements," IEEE Trans. on Magnetics, vol. MAG-4, pp. 351-355.

B [341] **Riedel, H.**, and Vahl, J., (1967). "Experimental investigation of tooth filling materials" (in German), Deutsche Zahnarztliche Z., vol. 22, pp. 476-486.

B [342] ----, Vahl, J., and Hahne, D., (1968). "Investigation of topography of 3M Addent 35 with the scanning electron microscope" (in German), Deutsche Zahnarztliche Z., vol. 23, pp. 199-204. (Continues above reference.)

** ---- see Fromme [145].

** **Riedel, W.**, see Heymann [185].

[343] **Robinson, G.Y.**, and White, R.M., (1967). "Scanning electron microscopy of ferroelectric domains in barium titanate," Appl. Phys. Letters, vol. 10, pp. 320-323 and vol. 11, p. 141.

[344] ----, White, R.M., and MacDonald, N.C., (1968). "Probing of Gunn effect domains with a scanning electron microscope," Appl. Phys. Letters, vol. 13, pp. 407-408.

** **Rowland, G.F.**, see Clarke [91].

B [345] **Runham, N.W.**, and Thornton, P.R., (1967). "Mechanical wear of the gastropod radula: a scanning electron microscope study," J. Zool., Lond., vol. 153, pp. 445-452.

** **Russ, J.C.**, see Kimoto [217].

** **Ryder, J.F.**, see Majumdar [251].

B [346] **Salsbury, A.J.**, and Clarke, J.A., (1967). "New method for detecting changes in the surface appearance of human red blood cells," J. Clinical Pathólogy, vol. 20, pp. 603-610.

B [347] ---- and Clarke, J.A., (1968). "The surface appearance of blood cells," Triangle, The Sandoz J. of Medical Science, vol. 8, pp. 260-266.

B [348] ----, Clarke, J.A., and Shand, W.S., (1968). "Red cell surface changes in cold agglutination," Clin. and Exp. Immunology, vol. 3, pp. 313-322.

** ---- see Clarke [90, 91, 92].

B [349] **Sandberg, P.A.**, and Hay, W.W., (1967). "Study of microfossils by means of the scanning electron microscope," J. Paleontology, vol. 41, pp. 999-1001 and 2 plates.

[350] ---- (1968). "A new specimen stub for stereophotography with the scanning electron microscope," Micropaleontology, vol. 14, pp. 489-498.

** ---- see Hay [170].

** **Sandor, J.E.**, see Green [156] and Szedon [391].

[351] **Saparin, G.V.**, Spivak, G.V., and Stepanov, S.S., (1966). "Observation of the p-n junction at small constant and alternating bias with the scanning electron microscope," pp. 609-610 in Uyeda (1966).

** ---- see Spivak [377, 379, 380].

** **Sato, M.**, see Kimoto [215].

** **Schneider, H.**, see Cailleux [73].

** **Schreiber, H.**, see Lander [237].

[352] **Schulson, E.M.**, (1969). "Some considerations of selected-area channelling in the scanning electron microscope," J. Sci. Inst. (J. Phys. E), Series 2, vol. 2, pp. 361-364.

[353] ---- and Van Essen, C.G., (1969). "Optimum conditions for generating channelling patterns in the scanning electron microscope," J. Sci. Inst. (J. Phys. E), Series 2, vol. 2, pp. 247-251.

** ---- see Van Essen [425].

** **Schulte, C.**, see Schur [354].

[354] **Schur, K.**, Schulte, C., and Reimer, L., (1967). "Resolution and contrast of steps in the surface by imaging with the scanning electron microscope" (in German), Z. fur angew. Physik, vol. 23, pp. 405-412.

** ---- see Pfefferkorn [324].

[355] **Schwuttke, G.H.**, and Brandis, E.K., (1968). "Scanning electron microscopy of twin structures in silicon web dendrite crystals," J. Electrochem. Soc., Solid State Science, vol. 115, pp. 669-671.

** **Sedov, N.N.**, see Spivak [378, 380].

[356] **Sennett, P.**, Drexel, J., and Morris, H.H., (1967). "Effect of pigment particle shape on the surface profile of light weight coated sheets," Tappi, vol. 50, pp. 560-571.

** ---- see Brooks [65].

[357] **Sepall, O.**, and Mason, S.G., (1961). "Influence of surface roughness upon the measurement of tritium radioactivity in paper and other sheets," Tappi, vol. 44, pp. 899-905. (Has 4 SEM images.)

** ---- see Baker [12].

** **Shand, W.S.**, see Salsbury [348].

[358] **Shaw, A.M.B.**, Booker, G.R., and Coates, D.G., (1969). "Further comments on the origin of orientation-dependent patterns obtained in the scanning electron microscope," J. Sci. Inst. (J. Phys. E), Series 2, vol. 243-246.

** ---- see Booker [35].

[359] **Shaw, D.A.**, Hughes, K.A., Neve, N.F.B., and 3 others (1966). "Crystal mosaic structures and the lasing properties of GaAs laser diodes,", Solid-State Electronics, vol. 9, pp. 664-665 and 2 plates.

[360] ----, Wayte, R.C., and Thornton, P.R., (1966). "Scanning electron microscopy observations of ZnS phosphor grains at high resolution," Appl. Phys. Letters, vol. 8, pp. 289-291.

[361] ----, Sulway, D.V., Wayte, R.C., and Thornton, P.R., (1967). "Simultaneous observation of surface detail and cathodoluminescence in the scanning electron microscope," J. Appl. Phys., vol. 38, pp. 887-888.

[362] ---- and Thornton, P.R., (1968). "Cathodoluminescent studies of laser quality GaAs," J. Materials Science, vol. 3, pp. 507-518.

** ---- see Thornton [416].

[363] **Shirai, S.**, Onoguchi, A., and Ichinokawa, T., (1966). "Atomic number analysis by specimen current in scanning electron microscope," pp. 199-200 in Uyeda (1966).

[364] ----, Onoguchi, A., and Ichinokawa, T., (1967). "Absorbed specimen current anomaly of Cu-Zn diffusion couple in electron scanning microscope," Japan. J. Appl. Phys., vol. 6, pp. 277-278.

** **Siehl, A.**, see Erben [128].

[365] **Sikorski, J.**, Moss, J.S., Newman, P.H., and Buckley, T., (1968). "A new preparation technique for examination of polymers in the scanning electron microscope," J. Sci. Inst. (J. Phys. E), Series 2, vol. 1, pp. 29-31.

** ---- see Challice [78].

** **Simmonds, F.A.**, see Horn [203].

[366] **Sjostrand, F.S.**, and Rhodin, J., (Ed.) (1957). Electron Microscopy. Proc. Stockholm Conf. Sept. 1956. Almquist and Wiksells, Uppsala; Academic Press, N.Y., 1957.

** **Skolnick, L.P.**, see Ugiansky [420].

B [367] **Small, E.B.**, and Marszalek, D.S., (1969). "Scanning electron microscopy of fixed, frozen, and dried protozoa," Science, vol. 163, pp. 1064-1065, index page and front cover.

** **Smirnov, L.S.**, see Ovsyuk [305].

** **Smith, A.L.**, see Hale [167].

B [368] **Smith, D.S.**, (1968). "Insect cells: their structure and function," Oliver and Boyd, Edinburgh.

[369] **Smith, K.C.A.**, and Oatley, C.W., (1955). "The scanning electron microscope and its fields of application," Brit. J. of Appl. Phys., vol. 6, pp. 391-399.

[370] ---- (1956). "The scanning electron microscope and its fields of application," Ph.D. Diss., Cambridge Univ.

[371] ---- (1959). "Scanning electron microscopy in pulp and paper research," Pulp and Paper Mag. Canada (Technical Section), vol. 60, pp. T366-T371.

[372] ---- (1960). "A versatile scanning electron microscope," pp. 177-180 in Houwink and Spit (1960).

[373] ---- (1961). "Scanning," pp. 241-251 in "Encyclopedia of Microscopy," G.L. Clark, Ed., Reinhold Publishing Corp., New York, N.Y.

** ---- see Allen [4], Atack [10], Buchanan [67], Everhart [131] and McAuslan [256].

** **Snelling, M.A.**, see Stewart [384].

** **Snyder, R.L.**, see Zworykin [451].

B [374] **Sokoloff, A.**, Hayes, T.L., Pease, R.F.W., and Ackerman, M., (1967). "Tribolium castaneum: morphology of 'Aureate' revealed by the scanning electron microscope," Science, vol. 157, pp. 443-445

B [375] **Spencer, W.H.**, Alvarado, J., and Hayes, T.L., (1968). "Scanning electron microscopy of human ocular tissues: Trabecular meshwork," Investigative Ophthalmology, vol. 7, pp. 651-662.

[376] **Speth, A.J.**, and Fang, F.F., (1965). "Effects of low-energy electron irradiation on Si-insulated gate FET's," Appl. Phys. Letters, vol. 7, pp. 145-146.

** **Spit, B.J.**, see Houwink [205].

[377] **Spivak, G.V.**, Saparin, G.V., and Pereverzev, N.A., (1962). "Potential distribution in a p-n junction as observed by electron-optical scanning," Bull. Acad. Sci. SSSR Physical Series (USA), vol. 26, pp. 1362-1365. Translated from Izv. Akad. Nauk SSSR Ser. Fiz., vol. 26, pp. 1339-1342.

[378] ----, Ivanov, R.D., Pavlyuchenko, O.P., and Sedov, N.N., (1963). "Mechanism of contrast formation in mirror, emission and scanning electron-optical systems," Bull. Acad. Sci. USSR Phys. Ser. (USA), vol. 27, pp. 1120-1127. Translated from Izv. Akad. Nauk SSSR Ser. Fiz., vol. 27, pp. 1139-1146.

[379] ----, Saparin, G.V., Massarani, B., and Bikov, M.V., (1965). "Contrast of images of a p-n junction in the scanning electron microscope" (in German), pp. 285-286 in Titlebach (1965).

[380] ----, Saparin, G.V., Sedov, N.N., and Komolova, L.F., (1967). "Theory of contrast formation at a p-n junction" (in Russian), Izv. Acad. Nauk SSSR Ser. Fiz., vol. 32, pp. 1124-1129.

** ---- see Saparin [351].

[381] **Spreadbury, P.J.**, (1958). "Investigations relating to the design of a simple scanning electron microscope," Ph.D. Diss., Cambridge Univ.

** **Sproule, R.N.**, see Atack [11].

** **Stepanov, S.S.**, see Saparin [351].

[382] **Stewart, A.D.G.**, (1962). "Investigation of the topography of ion bombarded surfaces with a scanning electron microscope," pp. D12-D13 in Breese (1962).

B [383] ---- and Boyde, A., (1962). "Ion etching of dental tissues in a scanning electron microscope," Nature (London), vol. 196, pp. 81-82.

[384] ---- and Snelling, M.A., (1965). "A new scanning electron microscope," pp. 55-56 in Titlebach (1965).

[385] ---- and Thompson, M.W., (1969). "Microtopography of surfaces eroded by ion-bombardment," J. Materials Science, vol. 4, pp. 56-60.

** ---- see Boyde [40, 41, 42, 43].

** **Stiefel, S.W.**, see Ugiansky [420].

[386] **Stintzing, H.**, (1929). German Patent No. 485,155. "Method and device for automatically assessing, measuring and counting particles of any type, shape and size," Date of application - 13 May 1927. Granted Oct. 1929.

** **Stuart, P.R.**, see Lewis [243].

[387] **Sulway, D.V.**, Davies, I.G., Hughes, K.A., and 2 others (1966). "Localized breakdown in Ge mesa diodes due to inclusions," Microelectronics and Reliability, vol. 5, pp. 323-327 and 3 plates.

[388] ----, Hughes, K.A., Evans, W.A., and Thornton, P.R., (1966). "Direct observation of MOS transistor channel pinch-off by scanning electron microscopy," Appl. Phys. Letters, vol. 8, pp. 296-298.

[389] ----, Kyaw, H., and Thornton, P.R., (1967). "Some factors affecting the yield of GaP crystal lamps," Solid-State Electronics, vol. 10, pp. 545-553 and 4 plates.

[390] ----, Thornton, P.R., and Turner, M.J., (1968). "Direct observation of electrical faults in planar transistors made in epitaxially grown silicon," Solid-State Electronics, vol. 11, pp. 567-568 and 1 plate.

** ---- see Davies [115], Hughes [207], Neve [289], Shaw [361] and Thornton [411, 413].

** **Switsur, V.R.**, see Boyde [43].

[391] **Szedon, J.R.,** and Sandor, J.E., (1965). "The effect of low-energy electron irradiation of metal-oxide-semiconductor structures," Appl. Phys. Letters, vol. 6, pp. 181-182.

** **Tamm, S.L.,** see Horridge [204].

[392] **Tamura, H.,** and Kimura, H., (1968). "New method of detecting secondary electrons on scanning electron microscope," J. Electron Microscopy (Japan), vol. 17, pp. 106-111.

** ---- see Higuchi [188] and Kimura [218, 219].

** **Tauchi, S.,** see Higuchi [186].

[393] **Teder, A.,** (1964a). "The properties of spruce pulps as related to paper structures observed with the scanning electron microscope," Svensk Papperstidn, vol. 67, pp. 670-685.

[394] ---- (1964b). "The effect of drying, heat treatment and beating on the papermaking properties of birch pulps," Svensk Papperstidn, vol. 67, pp. 911-923.

[395] **Te Gude, H.,** (1940). "Investigation of barium paste cathodes with the scanning electron microscope" (in German), Ph.D. Diss., Technische Hochschule Berlin.

[396] ---- (1945). "The scanning electron electron microscope - an imaging method using secondary electrons" (in German), Funk und Ton, vol. 7, pp. 373-383.

[397] ---- (1965). "Automatic inspection and fabrication of integrated circuits with the scanning electron microscope" (in German), Internationale Elektronische Rundschau, vol. 19, pp. 479-482, 567 and 570.

[398] **Theile, R.,** (1938). "Resistance-sensitive scanning electron tubes" (in German), Die Telefunken Rohre, number 13, pp. 90-126 in the August issue.

** ---- see Knoll [221].

[399] **Themelis, N.J.,** (1961). "Studies in the reduction of iron oxides in particulate systems," Ph.D. Diss., McGill Univ. (Contains SEM images of iron oxide particles.)

[400] ---- and Gauvin, W.H., (1962). "Reduction of iron oxide in gas-conveyed systems," A.I.Ch.E. J., vol. 8, pp. 437-444.

[401] ---- and Gauvin, W.H., (1963). "A generalized rate equation for the reduction of iron oxides," Trans. Met. Soc. of AIME, vol. 227, pp. 290-300. (Figures 4 through 7 show SEM images of iron oxide particles.)

** **Thomas, R.E.,** see Haas [164, 165].

[402] **Thompson, A.B.,** (1967). "A third generation of synthetic fibre materials," The Advancement of Science (G.B.), vol. 24, pp. 150-161.

** **Thompson, M.W.,** see Stewart [385].

[403] **Thornhill, J.W.,** and Mackintosh, I.M., (1965). "Application of the scanning electron microscope to semiconductor device structures," Microelectronics and Reliability, vol. 4, pp. 97-100.

B [404] ----, Matta, R.K., and Wood, W.H., (1965). "Examining three-dimensional microstructures with the scanning electron microscope," Grana Palynologica (Almquist and Wiksells), vol. 6, pp. 3-6 and 2 plates. (Contains SEM images of pollen grains.)

[405] **Thornley, R.F.M.,** (1960a). "New applications of the scanning electron microscope," Ph.D. Diss., Cambridge Univ.

[406] ---- (1960b). "Recent developments in scanning electron microscopy," pp. 173-176 in Houwink and Spit (1960).

[407] ---- and Cartz, L., (1962). "Direct examination of ceramic surfaces with the scanning electron microscope," J. Amer. Ceramic Soc., vol. 45, pp. 425-428.

[408] ---- and Hutchinson, J.D., (1968). "Magnetic field measurements in the scanning electron microscope," Appl. Phys. Letters, vol. 13, pp. 249-250 (Describes a new version of the shadow method.)

** ---- see Everhart [132].

[409] **Thornton, P.R.,** Culpin, M.J., and Drummond, I.W., (1963). "Direct observation of the high-field regions in GaAs," Solid-State Electronics, vol. 6, pp. 532-533 and 2 plates.

[410] ---- (1965). "The scanning electron microscope," Science J. (London), pp. 66-71 in the Nov. issue.

[411] ----, Hughes, K.A., Sulway, D.V., and Wayte, R.C., (1966). "Quantitative measurements by scanning electron microscopy - 1, the use of conductivity maps," Microelectronics and Reliability, vol. 5, pp. 291-298 and 2 plates.

[412] ----, James, D.W.F., Lewis, C., and Bradford, A., (1966). "Silicon whisker growth by the vapor-liquid-solid process," Phil. Mag., vol. 14, pp. 165-177.

[413] ----, Neve, N.F.B., and Sulway, D.V., (1966). "Quantitative measurements by scanning electron microscopy - 2, the use of emissive micrographs," Microelectronics and Reliability, vol. 5, pp. 299-303 and 3 plates.

[414] ----, Hughes, K.A., Kyaw, H., and 2 others (1967). "Failure analysis of microcircuitry by scanning electron microscopy," Microelectronics and Reliability, vol. 6, pp. 9-16 and 4 plates.

[415] ---- (1968). Scanning Electron Microscopy - Applications to Materials and Device Science, Chapman and Hall, London.

[416] ----, Davies, I.G., Shaw, D.A., and 2 others (1969). "Device failure analysis by scanning electron microscopy," Microelectronics and Reliability, vol. 8, pp. 33-53 and 3 plates.

** ---- see Davies [115], Drummond [125], Hughes [207], Neve [288, 289, 290], Northrop [295], Runham [345], Shaw [360, 361, 362], Sulway [388, 389, 390] and Wayte [431].

** **Thurston, R.C.A.**, see McGrath [261].

[417] **Tipper, C.F.**, Dagg, D.I., and Wells, O.C., (1959). "Surface fracture markings on alpha iron crystals," J. Iron and Steel Institute, vol. 193, pp. 133-141.

[418] **Titlebach, M.**, (Ed.) (1965). Electron Microscopy. Proc. Third European Regional Conf. Prague, Sept. 1964. Pub. House of Czechoslovak Academy of Sciences, Prague.

** **Todokoro, H.**, see Munakata [279].

** **Tokunaga, J.**, see Kurahasi [230].

[419] **Tooper, B.**, and Cartz, L., (1966). "Structure and formation of magnesium oxychloride sorel cements," Nature (Lond.), vol. 211, pp. 64-66.

** **Trezise, K.W.**, see Northrop [295].

** **Tschudy, B.D.**, see Drew [124].

** **Turner, M.J.**, see Sulway [390].

[420] **Ugiansky, G.M.**, Skolnick, L.P., Kruger, J., and Stiefel, S.W., (1968). "Rate-controlled step in stress corrosion cracking," Nature (London), vol. 218, pp. 1156-1157.

** **Ure, R.W.**, see McAvoy [257].

[421] **Uyeda, R.**, (Ed.) (1966). "Electron Microscopy 1966," Sixth Int. Cong. Electron Microscopy, Kyoto, Aug./Sept. 1966. Vol. 1, Non-Biology; Vol. 2, Biology. Maruzen Co.. Tokyo, 1966.

B [422] **Vahl, J.**, and Pfefferkorn, G., (1967). "Scanning electron microscopical investigations of changes in enamel and dentine following laser irradiation" (in German), Deutsche Zahnarztliche Z., vil. 22, pp. 386-394.

B [423] ---- (1968). "Electron microscopical and x-ray crystallographic investigations of teeth exposed to laser rays," Caries Res., vol. 2, pp. 10-18.

B [424] ----, Pfefferkorn, G., and Hohling, H.J., (1968). "Submicroscopic investigations of human saliva stones" (in German), Deutsche Zahnarztliche Z., vol. 23, pp. 39-44.

** ---- see Burrichter [72], Fromme [145], Gross [161], Leuteritz [242], Peveling [320], Reznik [339] and Riedel [341, 342].

** **VanCouvering, A.**, see Wittry [449].

[425] **Van Essen, C.G.**, and Schulson, E.M., (1969). "Selected area channeling patterns in the scanning electron microscope," J. Materials Science, in press.

** ---- see Schulson [353].

[426] **Varker, C.J.**, and Juleff, E.M., (1967) "Electron beam recording in SiO_2 with direct read-out using the electron beam induced current at a p-n junction," Proc. IEEE, vol. 55, pp. 728-729.

[427] **Vertsner, V.N.**, Lomunov, R.I., and Chentsov, Yu.V., (1966). "Utilization of slow electrons in a scanning electron microscope," Bull. Acad. Sci. USSR Phys. Ser. (USA), vol. 30, pp. 806-808. Translated from Izv. Akad. Nauk SSSR Ser. Fiz., vol. 30, pp. 778-780. (Shows magnetized areas on recording tape.)

[428] ----, Chentsov, Yu.V., and Krygin, V.M., (1967). "Scanning electron microscope observation of the action of light on the potential distribution in a p-n junction," Soviet Physics - Solid State (USA), vol. 9, pp. 391-393. Translated from Fiz. Tver. Tela, vol. 9, pp. 512-515.

** **Vetter, H.G.**, see Neurath [287].

[429] **Vincensini, P.-D.**, (1969). "Formation of backscattered electron images in the scanning electron microscope" (in French), J. de Microscopie (Paris), vol. 8, pp. 1-20.

** **Wall, J.**, see Crewe [102, 103].

[430] **Washburn, O.V.**, and Buchanan, J.G., (1964). "Changes in web structure on pressing and drying," Pulp Paper Mag. Canada. (Technical Section), vol. 65, pp. T400-T408.

** ---- see Buchanan [69, 70, 71] and Pye [333].

[431] **Wayte, R.C.**, and Thornton, P.R., (1967). "A specimen cooling stage for the scanning electron microscope," J. Sci. Inst., vol. 44, pp. 806-808. (Joule expansion unit.)

** ---- see Hughes [207], Shaw [360, 361] and Thornton [411].

[432] **Wells, O.C.**, (1957). "The construction of a scanning electron microscope and its application to the study of fibres," Ph.D. Diss., Cambridge Univ.

[433] ---- (1959). "Examination of nylon spinneret holes by scanning electron microscopy," J. Electronics and Control, vol. 7, pp. 373-376.

[434] ---- (1960). "Correction of errors in electron stereomicroscopy," Brit. J. Appl. Phys., vol. 11, pp. 199-201. (Refers to case when the lines of sight are separated by a large angle.)

[435] ---- (1962). "Electron beams in microelectronics," pp. 354-381 in Introduction to Electron Beam Technology, R. Bakish, Ed., J. Wiley and Sons, New York, N.Y. (Earlier version was pp. 291-321 in Bakish 1961.)

[436] ----, Everhart, T.E., and Matta, R.K., (1963). "Automatic positioning of device electrodes using the scanning electron microscope," Extended abstracts (Electrochem. Soc.), Electronics Division, vol. 12, no. 2, pp. 5-10. (New York Meeting, Oct. 1963.)

[437] ---- (1964). "Scanning electron microscope," pp. 32-34 in Kurshan (1964).

[438] ----, Everhart, T.E., and Matta, R.K., (1965). "Automatic positioning of device electrodes using the scanning electron microscope," IEEE Trans. on Electron Devices, vol. ED-12, pp. 556-563.

[439] ---- and Bremer, C.G., (1968). "Voltage measurement in the scanning electron microscope," J. Sci. Inst. (J. Phys. E), Series 2, vol. 1, pp. 902-906. (Included cylindrical mirror electrostatic energy analyser between specimen and secondary electron detector.)

[440] ---- (1969). "An irradiation effect in thermally grown SiO_2," Appl. Phys. Letters, vol. 14, pp. 5-6.

** ---- see Everhart [130, 131, 133, 134, 135] and Tipper [417].

** **Welter, L.M.**, see Crewe [101, 102, 103].

** **Wheatley, G.H.**, see Czaja [109].

** **Whelan, M.J.**, see Booker [35].

** **White, P.**, see Da Silva [113].

** **White, R.M.**, see Robinson [343, 344].

** **Wiggins, C.S.**, see Alfrey [3].

** **Williams, J.P.**, see Korda [228, 229] and Pruden [332].

[441] **Williams, P.M.**, and Yoffe, A.D., (1968). "Scanning electron microscope studies of cathodoluminescence in ZnSe single crystals," Phil. Mag., vol. 18, pp. 555-560.

[442] ---- and Yoffe, A.D., (1969). "Monochromatic cathodoluminescence image in the scanning electron microscope," Nature (London), vol. 221, pp. 952-953.

** **Willoughby, D.A.**, see Clarke [92].

B [443] **Wise, S.W.**, and Hay, W.W., (1968). "Scanning electron microscopy of molluscan shell structures," (in two parts), Trans. Amer. Microscopical Soc., vol. 87, pp. 411-430.

[444] **Wittry, D.B.**, (1957). "Two improvements in electron sources for electron probes," Rev. Sci. Inst., vol. 28, p. 58.

[445] ---- and Kyser, D.F., (1964). "Use of electron probes in the study of recombination radiation," J. Appl. Phys., vol. 35, pp. 2439-2442.

[446] ---- and Kyser, D.F., (1965). "Cathodoluminescence at p-n junctions in GaAs," J. Appl. Phys., vol. 36, pp. 1387-1389.

[447] ---- (1966). "Cathodoluminescence and impurity variations in Te-doped GaAs," Appl. Phys. Letters, vol. 8, pp. 142-144.

[448] ---- and Kyser, D.F., (1966). "Surface recombination velocities and diffusion lengths in GaAs," pp. 312-316 in Proc. Int. Conf. on the Physics of Semiconductors, Kyoto, 1966. Published in J. Physical Society Japan, vol. 21, Supplement, 1966.

[449] ---- and VanCouvering, A., (1967). "Stereoscopic display system for electron microprobe instruments," J. Sci. Inst., vol. 44, pp. 294-295.

** ---- see Kyser [235] and McKinley [262]

** **Wood, W.H.**, see Thornhill [404].

[450] **Woodward, J.G.**, Coutts, M.D., and Levin, E.R., (1968). "The scanning electron microscope. A new tool in disc-recording research," J. Audio Eng. Soc., vol. 16, pp. 258-265. (See also Stereo Review, October 1968.)

** **Yoffe, A.D.**, see Williams [441, 442].

** **Zervins, A.**, see Jaques [209].

** **Ziegler, W.**, see Gross [161].

[451] **Zworykin, V.K.**, Hillier, J., and Snyder, R.L., (1942). "A scanning electron microscope," ASTM Bull., no. 117, pp. 15-23.

[452] ----, Morton, G.A., Ramberg, E.G., and 2 others (1945). "Electron optics and the electron microscope," John Wiley and Sons, New York, N.Y.

** Wood, W.H., see Thornhill [604]

[450] Woodward, L.G., Curtis, M.D., and Levin, E.R., (1963). "The scanning electron microscope. A new tool in disc-recording research," J. Audio Eng. Soc. vol. 16, pp. 258-265. (See also Sonic Review, October 1968.)

** Yoffe, A.D., see Williams [441], 442]

** Zervins, A., see Jaques [209]

** Ziegler, N., see Gross [161]

[451] Zworykin, V.K., Hillier, J., and Snyder, R.L., (1942). "A scanning electron microscope," ASTM Bull., no. 117, pp. 15-23.

[452] —, Morton, G.A., Ramberg, E.G., and 2 others (1945). "Electron optics and the electron microscope," John Wiley and Sons, New York, N.Y.

AUTHOR INDEX

AUTHOR PAGE

Ando, S. 249
Andrews, M. L. 117
Angelo, R. W. 259
Aoki, M. 249
Aritome, H. 197
Asmus, J. F. 241
Atoda, N. 381

Baker, F. S. 241
Bakish, R. 3
Banbury, J. R. 364
Barber, R. B. 225
Barnard, G. M. 247
Bauer, S. J. 164
Beck, J. W. 317
Boncoeur, M. 15, 43
Brewster, J. L. 209
Broers, A. N. 107

Chang, T. H. P. 97
Chernow, F. 189
Chun, M. K. 231
Clark, J. J. 117
College, R. R. 51
Condon, J. J. 131
Cosslett, V. E. 165

El-Kareh, A. B. 393,407
Everhart, T. E. 453,454

Farmer, J. 487
Flinchbaugh, D. E. 247
Fóti, E. 329

Graybill, S. E. 155

Hammer, D. A. 117
Hart, D. M. 473
Hatzakis, M. 107
Heinrich, K. F. J. 353
Helmer, J. C. 337
Hockey, B. J. 375
Hoff, P. H. 454
Hora, H. 323
Hoye, R. C. 487
Hughes, W. C. 441

Ikeda, T. 183
Iwai, S. 203

AUTHOR PAGE

Kanaya, K. 381
Kasprzak, L. A. 217
Kawakatsu, H. 381
Ketcham, A. S. 487
Kikuchi, M. 249
Kim, P. H. 493
König, D. 87

Linke, S. 117
Linn, D. L. 225

Marton, L. iii
Masuda, K. 197
Matting, A. 61
Meyer, W. E. 87,389
Minkowitz, S. 248

McNeill, W. H. 155
McWhirter, J. H. 429

Namba, S. 197,203,493
Nasini, M. 307
Nixon, W. C. 363,364

Okada, K. 249
Ono, A. 381

Parks, H. G. 407
Plows, G. S. 363
Pratesi, R. 307
Privoznik, L. J. 77

Raheja, R. K. 71
Rapin, M. 43
Redaelli, G. 307
Riggle, G. C. 487
Rocherolles, R. H. 311

Sato, K. 249
Scheffels, W. 389
Schubert, D. C. 459
Schumacher, B. W. 29,271
Schwarz, H. 323
Seaman, F. D. 29
Sepold, G. 61
Simpson, J. A. 345
Smith, T. C. 177
Spence, P. 143
Spitz, H. Y. 233

AUTHOR INDEX (Cont'd)

AUTHOR PAGE

Steigerwald, K. H. 87,389
Stewart, A. D. G. 97
Sugano, T. 249
Süsskind, C. 484
Szews, A. P. 501

Taki, K. 493
Taylor, C. R. 271
Tencza, A. D. 259
Tighe, N. J. 375
Tokuyama, T. 183
Trivelpiece, A. W. 163
Tsuchimoto, T. 183

Uglum, J. R. 155
Ury, M. 117

Wåhlin, L. 189
Weichert, N. H. 337
Weiner, D. 365
Wells, O. C. 509
White, S. S. 285
Wilhelmi, J. J. 501
Wolter, R. F. 435

Yamazaki, H. 453
Yonas, G. 143
Yotsumoto, H. 381

Zimmerman, B. 297